PSI-1283/
TR-1745

TOXIC SUBSTANCES FROM COAL COMBUSTION – A COMPREHENSIVE ASSESSMENT

Final Report

Dr. C.L. Senior
Physical Sciences Inc.
20 New England Business Center
Andover, MA 01810-1077

Prof. F. Huggins, Prof. G.P. Huffman, Dr. N. Shah, and Dr. N. Yap
University of Kentucky
Lexington, KY 40506-0059

Prof. J.O.L. Wendt and Mr. W. Seames
University of Arizona
Tucson, AZ 85721

Dr. M.R. Ames
Massachusetts Institute of Technology
Cambridge, MA 02139

Prof. A.F. Sarofim, Ms. S. Swenson, and Prof. J.S. Lighty
University of Utah
Salt Lake City, UT 84112

Dr. A. Kolker, Dr. R. Finkelman, Dr. C.A. Palmer, and Mr. S.J. Mroczkowski
U.S. Geological Survey
Reston, VA 20192

Prof. J.J. Helble, Mr. R. Mamani-Paco, and Mr. R. Sterling
University of Connecticut
Storrs, CT 06269

Mr. G. Dunham and Mr. S. Miller
University of North Dakota
Energy & Environmental Research Center
Grand Forks, ND 58202

DOE Contract No. DE-AC22-95PC95101
U.S. DEPARTMENT OF ENERGY
Federal Energy Technology Center
P.O. Box 10940
Pittsburgh, PA 15236

July 2001

TABLE OF CONTENTS

Section Page

ABSTRACT xxxix

1. EXECUTIVE SUMMARY 1-1

1.1 Coal Properties 1-3
1.2 Combustion Zone Behavior 1-4
1.3 Post-Combustion Behavior of Semi-Volatile Metals 1-5
1.4 Post-Combustion Behavior of Mercury 1-7
1.5 Field Data Evaluation 1-9
1.6 Model Development 1-11

2. INTRODUCTION AND PROGRAM OVERVIEW 2-1

2.1 Introduction 2-3
2.2 Program Overview 2-8

3. RESULTS AND DISCUSSION 3-1

3.1 Coal Characterization (UK, USGS, MIT) 3-3
3.1.1 Coal Composition 3-3
3.1.2 Coal Mineralogy 3-8
3.1.3 Trace Element Content of Coals by Selective Leaching and Microprobe Analyses 3-17
3.1.4 Element Speciation by XAFS Spectroscopy 3-51
3.1.5 Characterization High Arsenic Coals from U.S.G.S 3-63
3.1.6 Summary and Recommendations 3-66

3.2 Combustion Zone Transformations (UU, MIT) 3-67
3.2.1 Single Particle Combustion Studies 3-67
3.2.2 Chlorine Studies 3-84
3.2.3 Summary 3-86

3.3 Post-Combustion Transformations of Semi-Volatile Elements (UA,UK,UC) 3-87
3.3.1 Background and Motivation 3-87
3.3.2 Bench-scale Investigations of Arsenic Behavior Post-Combustion 3-117
3.3.3 Large Scale Integrated Combustion Studies 3-146
3.3.4 Summary and Recommendations 3-338

3.4 Post-Combustion Transformations of Mercury (EERC, UK, UC) 3-341
3.4.1 Background and Motivation 3-341
3.4.2 Kinetic Modeling of Gaseous Mercury Oxidation 3-354
3.4.3 Bench-scale Investigations of Gaseous Mercury Oxidation 3-366

TABLE OF CONTENTS (Continued)

Section — Page

3.4.4 Mercury-Ash Interactions in Fixed Bed Tests 3-398
3.4.5 Trace Metal Speciation on Solid Samples 3-450
3.4.6 Summary and Recommendations 3-480

3.5 Field Data (PSI, UC) 3-483
3.5.1 Semi-volatile Trace Metals 3-483
3.5.2 Mercury Field Data 3-502

3.6 Model Development (PSI, UU, UC) 3-512
3.6.1 Overview 3-512
3.6.2 Coal Mineralogy 3-512
3.6.3 Modeling Vaporization from Single Particles 3-522

4. SUMMARY 4-1

4.1 Coal Properties 4-3
4.2 Combustion Zone Behavior 4-4
4.3 Post-Combustion Behavior of Semi-Volatile Metals 4-5
4.4 Post-Combustion Behavior of Mercury 4-7
4.5 Field Data Evaluation 4-9
4.6 Model Development 4-11

5. REFERENCES 5-1

APPENDIX A: Phase II Coal Results A-1

APPENDIX B: Composition and Analyses of Phase I Coals B-1

APPENDIX C: Comparison of Whole Coal Elemental Compositions for Original and Blind Replicate Analyses C-1

APPENDIX D: CCSEM Mineral Compositions of Phase II Coals D-1

APPENDIX E: Trace Metal Content of Mineral Grains by Electron Microprobe Analysis E-1

APPENDIX F: USGS Leaching Results F-1

APPENDIX G: Trace Metal Content of Mineral Grains by SHRIMP-RG Analysis G-1

TABLE OF CONTENTS (Continued)

Section		Page
APPENDIX H:	Trace Metal Content of Mineral Grains by Laser Ablation Mass Spectrometry	H-1
APPENDIX I:	Procedures For Large Scale Combustion Experiments	I-1
APPENDIX J:	Quality Assurance And Control For Large Scale Combustion Studies	J-1
APPENDIX K:	Experimental and Sampling Conditions for Large Scale Combustion Studies	K-1
APPENDIX L:	Measurements of Gaseous Mercury Oxidation in Bench-scale Reactor	L-1
APPENDIX M.	Correlations Between Calculated Mercury Removal and Speciation with ICR Data	M-1
APPENDIX N.	Distribution of Elements in Mineral Categories Bases for Major Coal Types	N-1
APPENDIX O.	Mineral Size Distributions for U.S. Coals Based on Rank.	O-1

LIST OF FIGURES

Figure No.		Page
2-1.	Inorganic compounds in coal.	3-5
2-2.	Classification of trace elements by behavior during combustion	3-6
2-3.	Possible transformation pathways of inorganic elements during pulverized coal combustion	3-7
2-4.	Phase II program organization.	3-9
3-1.	Distribution of Fe/S ratio in mineral particles with more than 80% of emitted X-rays from Fe and S for the Ohio coal measured using a ultrathin window X-ray detector	3-10
3-2.	(Na+K+Ca)-Al-Si ternary diagrams demonstrating the difference in aluminosilicate mineralogy among the three project coals	3-12
3-3.	Mössbauer spectra of the three project coals.	3-14
3-4.	Mössbauer spectra of top and bottom layers of Illinois #6 coal	3-16
3-5.	Selective leaching results for Fe, Cu, As, and Se	3-23
3-6.	Selective leaching results for Rare Earth Elements (REE) showing chondrite-normalized pattern for whole coals and rank dependence of HCl fraction	3-40
3-7.	Results of coal oxidation experiments showing constant percent Fe leached by HCl despite heating and wet-dry cycling.	3-41
3-8.	Selective leaching data for Hg	3-42
3-9.	Summary of electron microprobe data for pyrite in Phase II samples.	3-43
3-10.	Electron microprobe aluminum map showing distribution of clay minerals used to locate targets for SHRIMP-RG analysis of illite/smectite, and reflected light image of the same area showing distribution of illite/smectite and SHRIMP-RG analysis points	3-45
3-11.	SHRIMP-RG results for illite/smectite.	3-46
3-12.	SHRIMP-RG results for pyrite in Phase II samples and Phase I Illinois #6 and Pittsburgh samples	3-49

LIST OF FIGURES (Continued)

Figure No. Page

3-13. Laser ablation ICP-MS results for pyrite in Phase II Ohio 5/6/7 sample and Phase I Illinois #6 and Pittsburgh samples. 3-50

3-14. Arsenic XANES spectra of the North Dakota lignite and of the same sampling of the Ohio coal taken at three different times. 3-52

3-15. Unnormalized and normalized arsenic XANES spectra for the Ohio coal residues after different stages of the USGS leaching protocol. 3-53

3-16. Unnormalized and normalized arsenic XANES spectra for North Dakota Lignite residues after different stages of the USGS leaching protocol. 3-54

3-17. Correlation between the XAFS step-height and the concentration of arsenic in the leached residues. 3-54

3-18. Cr XANES spectra of physically-separated fractions of the Ohio bituminous coal. 3-57

3-19. Cr XANES spectra of leached fractions of the Ohio bituminous coal residues after different stages of the USGS leaching protocol. 3-57

3-20. Cr XANES spectra of leached fractions of the North Dakota lignite residues after different stages of the USGS leaching protocol. 3-59

3-21. Unnormalized XANES spectra of Zn in leached residues of Ohio #5 coal, and normalized XANES spectra of the same fractions. 3-60

3-22. XANES spectra of zinc standards. 3-61

3-23. Zn difference XANES spectrum obtained by subtracting the Zn XANES spectrum of the HCl-leached residue from that of the amm. acetate-leached residue. 3-61

3-24. Se XANES spectra of the Ohio raw coal, the Ohio tailings fraction, and the North Dakota lignite. 3-62

3-25. As XANES spectra for USGS high arsenic coals. 3-63

3-26. As XAFS/RSFs spectra for USGS high arsenic coals 3-64

3-27. LSQ-fitted As XANES spectra for two USGS high arsenic coals 3-65

3-28. Schematic of the drop tube furnace. 3-67

LIST OF FIGURES (Continued)

Figure No. Page

3-29. Photograph of the drop tube furnace. 3-68

3-30. Mass distribution of ash from different combustion gas compositions. 3-72

3-31. The ash has a definite bimodal distribution 3-73

3-32. Appearance of submicron ash from the Ohio coal: the chemistry of the submicron ash has high variabilityunder pyrolyzing conditions, at 100% oxygen, and at 50% oxygen in carbon dioxide. 3-73

3-33. Effect of oxygen concentration on amount of various elements in the submicron ash..... 3-78

3-34. Fraction of selected elements in submicron ash as a function of O_2 concentration for La and Au, Cr and Co, Hg, and Sm, Br, Cl, Sm, Au, Sb, La. 3-79

3-35. Fraction of selected major elements in submicron ash as a functionof oxygen concentration for combustion in N_2 and CO_2..... 3-80

3-36. Fraction of Mn, Cr, and Zn in submicron ash as a function of oxygen concentration for combustion of Ohio coal in O_2/N_2 and O_2/CO_2..... 3-81

3-37. Fraction of Cs, Mn, Cl, Br, Cr, Mo in submicron ash as a function of oxygen concentration for combustion of ND lignite in O_2/N_2 and O_2/CO_2..... 3-82

3-38. Fraction of selected elements in submicron ash as a function of oxygen concentration for combustion of Wyodak coal in O_2/N_2 and O_2/CO_2..... 3-83

3-39. Mercury from the Ohio coal shows a decrease in capture on submicron particles with carbon dioxide 3-84

3-40. Simulated temperature-dependent equilibrium profiles of arsenic during combustion of the six study coals under baseline conditions..... 3-97

3-41. Simulated temperature-dependent equilibrium profiles of arsenic omitting AsO as a valid product..... 3-101

3-42. Simulated temperature-dependent equilibrium profiles of selenium during combustion of the six study coals under baseline conditions..... 3-105

3-43. Simulated temperature-dependent equilibrium profiles of antimony during combustion of the six study coals under baseline conditions..... 3-110

LIST OF FIGURES (Continued)

Figure No. Page

3-44. Simulated temperature-dependent equilibrium profiles of antimony when SbO is omitted as a valid combustion product. 3-113

3-45. Schematic diagram of reactor assembly. 3-118

3-46. Cahn micro balance calibration check results for known sample weights. 3-119

3-47. Reactor temperature control test. 3-120

3-48. Equilibrium data generated by FACT for nitrogen-arsenic trioxide system 3-121

3-49. A comparison of calculated and measured vaporization for the nitrogen–arsenic trioxide system 3-121

3-50. Results of preliminary calcium silicate experiments arsenic trioxide concentration of 13 ppm. 3-124

3-51. Results of varying arsenic trioxide concentrations with calcium silicate. 3-124

3-52. Results of the duplicate experiments with calcium oxide as the reacting solid at 26 ppm. 3-125

3-53. A comparison of calcium oxide and calcium silicate results at 26 ppm arsenic trioxide vapor. 3-125

3-54. Results from duplicate experiments for calcium oxide with arsenic trioxide concentration of 13 ppm. 3-126

3-55. Effectiveness factor plots for nth order kinetics for spherical solids, and first-order reaction on different solid geometries. 3-128

3-56. Results from triplicate experiments for calcium oxide with arsenic oxide equal to 26 ppm. 3-130

3-57. Results from triplicate experiments for dicalcium silicate at 26 ppm As_2O_3 vapor. 3-131

3-58. Results of triplicate experiments for calcium mono-silicate with 26 ppm As_2O_3 vapor 3-131

3-59. Results of triplicate experiments for calcium oxide at 13 ppm As_2O_3 vapor. 3-132

3-60. Results of triplicate experiments for dicalcium oxide at 13 ppm As_2O_3 vapor 3-132

LIST OF FIGURES (Continued)

Figure No. Page

3-61. Results from triplicate experiments for calcium oxide with 26 ppm arsenic oxide in air. 3-134

3-62. Results from triplicate experiments for di-calcium silicate at 26 ppm As_2O_3 vapor in air 3-135

3-63. Results of triplicate experiments for calcium mono-silicate with 26 ppm As_2O_3 vapor in air 3-135

3-64. XRD pattern of product formed from reacting dicalcium silicate 26 ppm As_2O_3 vapor 3-138

3-65. XRD pattern of product formed from reacting mono-calcium silicate 26 ppm As_2O_3 vapor. 3-138

3-66. XRD pattern of product formed from reacting calcium silicate 26 ppm As_2O_3 vapor 3-139

3-67. XRD pictograph of product formed from reacting mono-calcium silicate with 26 ppm As_2O_3 vapor. 3-139

3-68. XRD pictograph of product formed from reacting di-calcium silicate with 26 ppm As_2O_3 vapor. 3-140

3-69. XRD pictograph of product formed from reacting calcium oxide with 26 ppm As_2O_3 vapor. 3-140

3-70. XRD pictograph of product formed from reacting calcium oxide with 26 ppm As_2O_3 vapor. 3-141

3-71 XRD pictograph of calcium arsenate reference material 3-141

3-72. Arsenic concentration distribution as a function of equal magnitude of surface reaction rate and condensation. 3-145

3-73. Arsenic distribution for various surface reaction rate. 3-145

3-74. Overall schematic of University of Arizona combustion system. 3-147

3-75. Schematic of compressed air supply system. 3-149

3-76. Furnace refractory and upper zircar section. 3-152

LIST OF FIGURES (Continued)

Figure No.		Page
3-77.	Simple schematic of furnace outlet line piping.	3-155
3-78.	Simplified drawing of total fly ash sample collector.	3-157
3-79.	Simplified schematic of particle sampling system.	3-159
3-80.	Simplified schematic of the Berner low pressure impactor.	3-160
3-81.	Typical temperature profile of the Pittsburgh seam coal under baseline screening experimental conditions.	3-173
3-82.	Total ash particle size distributions for the Pittsburgh seam coal sampled at three locations.	3-174
3-83.	Major element differential distributions for the Pittsburgh seam coal sampled at three locations	3-175
3-84.	Trace element differential distributions for the Pittsburgh seam coal sampled at three locations	3-175
3-85.	Typical temperature profile of the Illinois #6 coal under baseline screening experimental conditions.	3-182
3-86.	Total ash particle size distributions for the Illinois #6 coal sampled at three locations	3-183
3-87.	Major element differential distributions for the Illinois #6 coal sampled at three locations	3-183
3-88.	Trace element differential distributions for the Illinois #6 coal sampled at three locations	3-184
3-89.	Typical temperature profile of the Kentucky coal under baseline screening experimental conditions.	3-189
3-90.	Total ash particle size distributions for the Kentucky coal sampled at three locations.	3-190
3-91.	Major element differential distributions for the Kentucky coal sampled at three locations	3-190

LIST OF FIGURES (Continued)

Figure No. Page

3-92. Trace element differential distributions for the Kentucky coal sampled at three locations 3-191

3-93. Typical temperature profile of the Ohio coal under baseline screening experimental conditions. 3-197

3-94. Total ash particle size distributions for the Ohio coal sampled at three locations 3-198

3-95. Major element differential distributions for the Ohio coal sampled at two locations 3-198

3-96. Trace element differential distributions for the Ohio coal sampled at three locations 3-199

3-97. Typical temperature profile of the Wyodak coal under baseline screening experimental conditions. 3-205

3-98. Total ash particle size distributions for the Wyodak coal sampled at three locations 3-206

3-99. Major element differential distributions for the Wyodak coal sampled at three locations 3-206

3-100. Trace element differential distributions for the Wyodak coal sampled at three locations 3-207

3-101. Typical temperature profile of the North Dakota coal under baseline screening experimental conditions. 3-213

3-102. Total ash particle size distributions for the North Dakota coal sampled at three locations 3-213

3-103. Major element differential distributions for the North Dakota coal sampled at three locations 3-214

3-104. Trace element differential distributions for the North Dakota lignite sampled at three locations 3-215

3-105. Differential distributions for Wyodak doping experiments: oxygen enrichment without doping 3-219

LIST OF FIGURES (Continued)

Figure No. Page

3-106. Differential distributions for Wyodak doping experiments: arsenic doping with no oxygen enrichment 3-220

3-107. Differential distributions for Wyodak doping experiments: arsenic doping with oxygen enrichment 3-220

3-108. Differential distributions for Wyodak doping experiments: selenium doping with no oxygen enrichment 3-221

3-109. Differential distributions for Wyodak doping experiments: selenium doping with oxygen enrichment 3-221

3-110. Differential distributions for Wyodak doping experiments: antimony doping with no oxygen enrichment 3-222

3-111. Differential distributions for Wyodak doping experiments: antimony doping with oxygen enrichment 3-222

3-112. Differential distributions for Wyodak doping experiments: iron doping with no oxygen enrichment 3-223

3-113. Differential distributions for Wyodak doping experiments: iron doping with oxygen enrichment 3-224

3-114. Differential distributions for Ohio special experiments: CO_2 addition with no calcium addition. 3-226

3-115. Differential distributions for Ohio special experiments: calcium addition with no CO_2 addition 3-227

3-116. Differential distributions for Ohio special experiments: calcium addition with CO_2 addition 3-228

3-117. Differential distributions for Kentucky SO_2 addition experiments 3-230

3-118. Differential distributions for Pittsburgh calcium addition experiments 3-231

3-119. Differential distributions for Pittsburgh iron doping experiments 3-232

3-120. The effect of combustion temperature on the volatility of calcium, iron, and aluminum during the combustion of Wyodak coal 3-237

LIST OF FIGURES (Continued)

Figure No. Page

3-121. Particle size dependence of selenium in supermicron fly ash particles 3-242

3-122. Particle size dependence of selenium in submicron fly ash particles for all six study coals sampled at Port 14. 3-243

3-123. Differential mass distributions of selenium, calcium, iron, and total ash for the six study coals sampled at Port 14..... 3-245

3-124. Cross correlation of Pittsburgh selenium to calcium and iron at baseline screening experimental conditions sampled at Port 14 for the supermicron region..... 3-246

3-125. Cross correlation of Pittsburgh selenium to calcium and iron differential distribution curves at baseline screening experimental conditions sampled at Port 14 for the supermicron region 3-247

3-126. Comparison of selenium differential distributions when adjusting the selenium-to-calcium ratio at constant maximum combustion temperature in the Wyodak coal 3-250

3-127. Comparison of selenium differential distributions when adjusting the selenium-to-calcium ratio of the Wyodak coal with combustion near the Ohio maximum combustion temperature. 3-251

3-128. Comparison of selenium differential distributions when adjusting the selenium-to-calcium ratio of the Ohio with combustion at the Ohio maximum combustion temperature..... 3-252

3-129. Comparison of selenium differential distributions when adjusting the selenium-to-calcium ratio of the Ohio with combustion at the Wyodak maximum combustion temperature..... 3-253

3-130. Particle size dependence of selenium in supermicron fly ash particles for all six study coals sampled at Port 4. 3-258

3-131. Particle size dependence of selenium in submicron fly ash particles for all six study coals sampled at Port 4. 3-259

3-132 Differential mass distributions of selenium, calcium, iron, and total ash for the six study coals sampled at Port 4. 3-260

3-133. Summary of selenium partitioning mechanisms. 3-262

LIST OF FIGURES (Continued)

Figure No. Page

3-134. Particle size dependence of arsenic in supermicron fly ash particles for all six study coals sampled at Port 14. 3-268

3-135. Particle size dependence of arsenic in submicron fly ash particles for all six study coals sampled at Port 14. 3-269

3-136. Differential mass distributions of arsenic, calcium, iron, and total ash for the six study coals sampled at Port 14. 3-270

3-137. Comparison of arsenic differential distributions when adjusting the arsenic-to-calcium ratio at constant maximum combustion temperature in the Wyodak coal. 3-274

3-138. Comparison of arsenic differential distributions when adjusting the arsenic -to-calcium ratio of the Wyodak coal with combustion near the Ohio maximum combustion temperature. 3-274

3-139. Comparison of arsenic differential distributions when adjusting the arsenic -to-calcium ratio of the Wyodak coal to the Ohio and Kentucky distributions with combustion near the Ohio maximum combustion temperature. 3-275

3-140. Comparison of arsenic differential distributions when adjusting the arsenic-to-calcium ratio of the Ohio with combustion at the Ohio maximum combustion temperature. 3-276

3-141. Comparison of arsenic differential distributions when adjusting the arsenic-to-calcium ratio of the Ohio with combustion at the Wyodak maximum combustion temperature. 3-276

3-142. Particle size dependence of arsenic in supermicron fly ash particles for all six study coals sampled at Port 4. 3-282

3-143. Particle size dependence of arsenic in submicron fly ash particles for all six study coals sampled at Port 4. 3-283

3-144. Differential mass distributions of arsenic, calcium, iron, and total ash for the six study coals sampled at Port 4. 3-284

3-145. Summary of arsenic partitioning mechanisms. 3-286

3-146. Particle size dependence of antimony in supermicron fly ash particles for all six study coals sampled at Port 14. 3-293

LIST OF FIGURES (Continued)

Figure No. Page

3-147. Particle size dependence of antimony in submicron fly ash particles for all six study coals sampled at Port 14. 3-293

3-148. Differential mass distributions of antimony, calcium, iron, aluminum, and total ash for the six study coals sampled at Port 14. 3-295

3-149. Comparison of antimony differential distributions when adjusting the antimony-to-calcium ratio at constant maximum combustion temperature in the Wyodak coal. 3-299

3-150. Comparison of antimony differential distributions when adjusting the antimony-to-calcium ratio of the Wyodak coal with combustion near the Ohio maximum combustion temperature. 3-299

3-151. Comparison of antimony differential distributions when adjusting the antimony-to-calcium ratio of the Ohio with combustion at the Ohio maximum combustion temperature. 3-300

3-152. Comparison of antimony differential distributions of the Ohio coal at two different combustion temperatures 3-301

3-153. Comparison of antimony differential distributions when adjusting the antimony-to-calcium ratio of the Ohio coal with combustion at the Wyodak maximum combustion temperature. 3-301

3-154. Particle size dependence of antimony in supermicron fly ash particles for all six study coals sampled at Port 4. 3-305

3-155. Particle size dependence of antimony in submicron fly ash particles for all six study coals sampled at Port 4. 3-306

3-156. Differential mass distributions of antimony, calcium, iron, aluminum, and total ash for the six study coals sampled at Port 4 3-307

3-157. Summary of antimony partitioning mechanisms. 3-309

3-158. Particle size dependence of cobalt in supermicron fly ash particles for all six study coals sampled at Port 14. 3-314

3-159. Particle size dependence of cobalt in submicron fly ash particles for all six study coals sampled at Port 14. 3-315

LIST OF FIGURES (Continued)

Figure No. Page

3-160. Differential mass distributions of cobalt, calcium, iron, aluminum, and total ash for the Pittsburgh, Kentucky, and Wyodak coals sampled at Port 14. 3-316

3-161. Differential mass distributions of cobalt, aluminum, iron, and calcium for the Pittsburgh baseline, Ca-doped, and Fe-doped experiments supermicron region sampled at Port 14. 3-318

3-162. Differential mass distributions of cobalt, aluminum, iron, and calcium for the Kentucky baseline and SO_2-doped experiments supermicron region sampled at Port 14. 3-319

3-163. Differential mass fraction distributions of cobalt for the Wyodak coal at two combustion temperatures sampled at Port 14. 3-320

3-164. Particle size dependence of cobalt in supermicron fly ash particles for all six study coals sampled at Port 4. 3-323

3-165. Particle size dependence of cobalt in submicron fly ash particles for all six study coals sampled at Port 4. 3-323

3-166. Differential mass distributions of cobalt, iron, and aluminum, for the Pittsburgh, Kentucky, and Wyodak coals sampled at Port 4. 3-324

3-167. Particle size dependence of cesium in supermicron fly ash particles for five coals sampled at Port 14. 3-331

3-168. Particle size dependence of thorium in supermicron fly ash particles for five coals sampled at Port 14. 3-332

3-169. Particle size dependence of cerium in supermicron fly ash particles for five coals sampled at Port 14. 3-333

3-170. Particle size dependence of cesium in submicron fly ash particles for five coals sampled at Port 14. 3-333

3-171. Particle size dependence of thorium in submicron fly ash particles for five coals sampled at Port 14. 3-334

3-172. Particle size dependence of cerium in submicron fly ash particles for five coals sampled at Port 14. 3-334

LIST OF FIGURES (Continued)

Figure No. Page

3-173. Cross correlation of cesium to aluminum, iron, and calcium in supermicron-sized impactor stages for Wyodak and North Dakota fly ash sampled at Port 14. 3-335

3-174. Vapor pressure - temperature data for Hg and $HgCl_2$ 3-344

3-175. Rate constant of HgCl + Cl reaction as a function of temperature from 273 to 973 K. 3-356

3-176. Hg conversion as a function of HCl concentration at 773 K using global kinetics. 3-357

3-177. Hg conversion as a function of HCl concentration at 973 K using global kinetics. 3-357

3-178. Hg conversion as a function of Cl_2 concentration at 773 K using global kinetics. 3-358

3-179. Hg conversion as function of Cl_2 concentration at 973 K using global kinetics..... 3-358

3-180. Hg conversion for two different cooling rates using global kinetics. 3-359

3-181. Fraction of elemental mercury converted for two different cooling rates using elementary reaction mechanism. 3-360

3-182. Hg conversion as a function of Cl atom concentration at 773 K and 1 second residence time using elementary reaction mechanism. 3-360

3-183. High temperature mercury oxidation at 200 K/s. 3-362

3-184. High temperature mercury oxidation at 500 K/s. 3-362

3-185. Calculated boiler temperature profile used in kinetic calculations. 3-364

3-186. Calculated cooling rates for boiler temperature profile. 3-364

3-187. Conversion of Hg to $HgCl_2$ using boiler temperature profiles for calculations begun at 1370 K. 3-365

3-188. Conversion of Hg to $HgCl_2$ using boiler temperature profiles for calculations begun at 970 K. 3-365

3-189. Experimental system for mercury oxidation experiments..... 3-367

3-190. Mercury generation system 3-367

LIST OF FIGURES (Continued)

Figure No. Page

3-191. Permeation rate as a function of bath temperature (°C). 3-368

3-192. Temperature profile in quartz tube reactor. 3-370

3-193. Temperature profile with varying heating tape settings 3-371

3-194. Temperature sampling points through quartz tube reactor. 3-372

3-195. Temperature as a function of distance 3-372

3-196. Gas velocity as a function of distance. 3-372

3-197. Ontario Hydro sampling train. 3-374

3-198. Comparison of HCl oxidation results with literature reported data. 3-383

3-199. Fraction of elemental mercury as a function of initial chlorine concentration. 3-386

3-200. Results of oxidation experiments in the presence of Cl_2 3-391

3-201. SEM micrograph of alumina powder used as fly ash surrogate. 3-395

3-202. Number size distribution of alumina particles taken from SEM micrographs. 3-395

3-203. Mercury conversion in the absence and presence of alumina particles. 3-396

3-204 Schematic of the EERC bench-scale system 3-399

3-205. Plot of outlet mercury concentration as a function of time, from one run with three different mercury CEMs 3-401

3-206. Outlet mercury concentration from three repeat runs of the same test conditions 3-401

3-207. SEM photograph of Ohio ash sample (590 times magnification). 3-406

3-208. SEM photograph of Ohio ash sample (4,890 times magnification). 3-407

3-209. SEM photograph of Ohio ash sample (7,230 times magnification). 3-407

3-210. SEM photograph of Ohio ash sample (28,600 times magnification). 3-408

3-211. SEM photograph of North Dakota lignite ash sample (343 times magnification). 3-409

LIST OF FIGURES (Continued)

Figure No. Page

3-212. SEM photograph of North Dakota lignite ash sample (1,070 times magnification). ... 3-409

3-213. SEM photograph of North Dakota lignite ash sample (4,370 times magnification). ... 3-410

3-214. SEM photograph of North Dakota lignite ash sample (17,500 times magnification). ... 3-410

3-215. SEM photograph of North Dakota lignite ash sample (4,370 times magnification). ... 3-411

3-216. SEM photograph of North Dakota lignite ash sample (7,160 times magnification). ... 3-411

3-217. SEM photograph of Wyodak ash sample (378 times magnification). ... 3-412

3-218. SEM photograph of Wyodak ash sample (3,020 times magnification). ... 3-413

3-219. SEM photograph of Wyodak ash sample (6,290 times magnification). ... 3-413

3-220. SEM photograph of Wyodak ash sample (1,440 times magnification). ... 3-414

3-221. SEM photograph of Wyodak ash sample (11,400 times magnification). ... 3-414

3-222. SEM photograph of Wyodak ash sample (14,800 times magnification). ... 3-415

3-223. SEM photograph of Wyodak ash sample (24,900 times magnification). ... 3-415

3-224. Mössbauer spectra of Comanche fly-ash and Blacksville Hopper ash. ... 3-418

3-225. Sulfur XANES of first set of samples from EERC. ... 3-419

3-226. Sulfer XANES of second set of samples from EERC. ... 3-420

3-227. Examples of LSQ fitted sulfur XANES spectra for EERC ash samples ... 3-423

3-228. Outlet mercury concentration as a function of time for Ohio blend ash at 250 and 350°F. ... 3-427

3-229. Outlet mercury concentration as a function of time for Wyodak ash at 250 and 350° F. ... 3-427

LIST OF FIGURES (Continued)

Figure No. Page

3-230. Outlet mercury concentration as a function of time for the North Dakota lignite ash at 250 and 350° F and the Coal Creek ash at 350°F. 3-428

3-231. Outlet mercury concentration as a function of time for the Ohio blend fly ash, ashed at 400 and 750°C and evaluated at 300°F, and the results from the baseline tests at 250 and 350°F. 3-430

3-232. Outlet mercury concentration as a function of time for the Wyodak samples ashed at 400 and 750°C and evaluated at 350°F, and the results from the baseline tests at 250 and 350°F. 3-430

3-233. Outlet mercury concentration as a function of time for the Blacksville ash at 250 and 350°F. 3-431

3-234. Outlet mercury concentration as a function of time for the Valmy ash at 250 and 350°C. 3-432

3-235. Outlet mercury concentration as a function of time for the Valmont ash at 250 and 350°F. 3-432

3-236. Outlet mercury concentration as a function of time for the Comanche ash at 250 and 350°F. 3-433

3-237. Outlet mercury concentration as a function of time for the AA ash at 250 and 350°F. 3-434

3-238. Outlet mercury concentration as a function of time for the DA ash at 250 and 350°F. 3-434

3-239. Outlet mercury concentration as a function of time for the GA and DMA ashes at 250°F. 3-435

3-240. Outlet mercury concentration as a function of time for the MA ash at 250 and 350°F with 75 ppm HCl and with 50 ppm HCl at 250°F. 3-435

3-241. Outlet mercury concentration as a function of time for the Dale Station ash at 250°F. 3-436

3-242. Outlet mercury concentration as a function of time for the Dale Station ash at 250°F with 150 mg ash. 3-437

LIST OF FIGURES (Continued)

Figure No. Page

3-243. Outlet mercury concentration as a function of time for the Black Thunder ash at 250 and 350°F. 3-438

3-244. Outlet mercury concentration as a function of time for the Cordero Rojo ash at 250 and 350°F. 3-438

3-245. Outlet mercury concentration as a function of time for the Absaloka ash at 250 and 350°F. 3-439

3-246. Percent oxidation of elemental mercury as a function of ash LOI. 3-440

3-247. Percent oxidation of elemental mercury as a function of ash surface area. 3-440

3-248. Percentage of elemental mercury capture at 100% breakthrough as a function of ash LOI. 3-441

3-249. Percentage of elemental mercury capture at 100% breakthrough as a function of ash surface area. 3-441

3-250. Outlet mercury concentration as a function of time for the Ohio blend fly ash, ashed at 400 and 750°C and evaluated at 300°F, and the results from the baseline tests at 250 and 350°F with $HgCl_2$ injection. 3-444

3-251. Outlet mercury concentration as a function of time for the Wyodak fly ash, ashed at 400 and 750°C and evaluated at 300°F, and the results from the baseline tests at 250 and 350°F with $HgCl_2$ injection. 3-444

3-252. Outlet mercury concentration as a function of time for the Blacksville fly ash, ashed at 400 and 750°C and evaluated at 300°F, and the results from the baseline tests at 250 and 350°F with $HgCl_2$ injection. 3-445

3-253. Outlet mercury concentration as a function of time for the Valmy fly ash, ashed at 400 and 750°C and evaluated at 300°F, and the results from the baseline tests at 250 and 350°F with $HgCl_2$ injection. 3-445

3-254. Outlet mercury concentration as a function of time for the AA, DA, and GA fly ashes at 350°F with $HgCl_2$ injection. 3-446

3-255. Outlet mercury concentration as a function of time for the DMA fly ash at 250 and 350°F with $HgCl_2$ injection. 3-447

LIST OF FIGURES (Continued)

Figure No. Page

3-256. Outlet mercury concentration as a function of time for the MA fly ash at 250 and 350°F with $HgCl_2$ injection. 3-447

3-257. Outlet mercury concentration as a function of time for the Black Thunder and Cordero Rojo ashes at 350°F with $HgCl_2$ injection. 3-448

3-258. Outlet mercury concentration as a function of time for theAbsaloka fly ash at 250 and 350°F with $HgCl_2$ injection. 3-448

3-259. Percentage of $HgCl_2$ capture at 100% breakthrough as a function of ash LOI. 3-449

3-260. Percentage of $HgCl_2$ capture at 100% breakthrough as a function of ash surface area. 3-449

3-261. XANES and EXAFS/RSFs of arsenic compounds produced in bench-scale study designed to determine arsenic speciation during pulverized coal combustion 3-450

3-262. XANES of arsenic and chromium on a filter used to collect fly-ash and particulate matter from the UA combustion unit. 3-451

3-263. XANES spectra of chromium in three fly-ash samples from EERC. 3-452

3-264. Definition of the IPD parameter from Hg XANES spectrum of a carbon-based sorbent 3-456

3-265. Diagram showing the relationship of the IPD parameter to different possible mercury sorption species represented by different ligand types. 3-457

3-266. Simulated mercury XANES spectra for mixtures of elemental mercury and mercuric chloride based on weighted additions of the experimental spectra for the two end-members. 3-459

3-267. Comparison of the relationship between the HR and IPD XANES parameters calculated for simulated spectra of mixtures of elemental mercury and mercuric sulfide or mercuric chloride and experimental determinations for mercury in various sorbent materials. 3-459

3-268. Hg XANES spectra of high mercury sorbent samples prepared at UA. 3-461

3-269. Hg XANES spectra of low mercury sorbent samples prepared at UA. 3-461

3-270. Hg EXAFS/RSFs for high mercury sorbents prepared at UA. 3-462

LIST OF FIGURES (Continued)

Figure No. Page

3-271. Hg RSFs for low mercury sorbents prepared at UA. 3-463

3-272. Hg XANES spectra of very low mercury sorbent samples prepared at PSI. 3-463

3-273. Hg XANES spectra of three lignite-activated carbons (LAC) from UNDEERC and the Cherokee fly-ash sample from ADA Technologies. 3-464

3-274. Chlorine XANES spectra of three lignite-activated carbons (LAC) from UNDEERC. 3-466

3-275. Sulfur XANES spectra of three lignite-activated carbons (LAC) from UNDEERC and the Cherokee fly-ash from ADA Technologies. 3-466

3-276. Correlation between carbon content and mercury content for fractions of ADA baghouse-hopper fly-ash separated by triboelectrostatic separation, and partitioning of mercury among different fractions separated from the Cherokee fly-ash by a laboratory-scale triboelectrostatic method. 3-468

3-277. Mercury XANES spectra (left) and first-derivative spectra (right) of fractions of Cherokee fly-ash separated in a laboratory-scale triboelectrostatic separation technique 3-469

3-278. Hg XANES and first derivative spectra for sorbent samples from Drs. Ghorishi and Gullett (US EPA) 3-471

3-279. Plot of IPD values for different carbon-based sorbents and two lime-based sorbents for comparable experiments. 3-472

3-280. Hg XANES spectra of activated carbon felt samples obtained from Dr. Brian Gullett, US EPA and co-workers. 3-473

3-281. Mercury XANES and first derivative spectra of pre-treated carbon felts exposed to a mercury-laden flue gas 3-474

3-282. Sulfur XANES spectra of ACN and BPL carbon felt materials 3-475

3-283. Histogram of IPD values for mercury sorption experiments on various sorbent materials in four investigations conducted at UA, at PSI and at Illinois State Geological Survey and Radian (ISGS) 3-476

3-284. Plot of RSF peak positions against IPD values for mercury compounds and for various sorbents. 3-478

LIST OF FIGURES (Continued)

Figure No. Page

3-285. Fly ash particle size distributions obtained from field measurements and used to assign baseline size distribution at ESP inlet 3-491

3-286. Particle penetration through cold-side electrostatic precipitators as a function of particle size 3-492

3-287. Arsenic emissions data obtained from field measurements as a function of C*PM/fa as per Eq. (3-46) 3-495

3-288. Arsenic emissions data obtained from field measurements as a function of C*PM/fa, plotted according to Eq. (3-47) 3-496

3-289. Comparison of field measurements of chromium emissions with empirical model derived from database fit and partitioning / penetration model described by Eqs. (3-48) through (3-51) 3-496

3-290. Chromium emissions data obtained from field measurements as a function of C*PM/fa as per Eq. (3-46) 3-497

3-291. Comparison of field measurements of arsenic emissions with empirical model derived from database fit,and partitioning/penetration model described by Eqs. (3-48) through (3-51). 3-498

3-292. Comparison of field measurements of arsenic emissions from 12 Canadian boilers with empirical model derived from database fit, using U.S. database, and partitioning/penetration model described by Eqs. (3-48) through (3-51) 3-500

3-293. Comparison of field measurements of selenium emissions with empirical model derived from database fit and partitioning/penetration model described by Eqs. (3-48) through (3-51) 3-501

3-294. Observed speciation of mercury in the stacks of coal-fired power plants (as percent elemental mercury) as a function of coal chlorine content. 3-507

3-295. Speciation of mercury (in terms of gaseous elemental) at the inlet to air pollution control devices as a function of coal chlorine content 3-508

3-296. Speciation of mercury (in terms of gaseous elemental) at the inlet to air pollution control devices as a function of device temperature 3-508

LIST OF FIGURES (Continued)

Figure No. Page

3-297. Particulate mercury (as fraction of particulate and oxidized mercury) at the inlet to the particulate control device for cold-side devices. 3-509

3-298. Flow chart for engineering model for ash formation. 3-513

3-299. Fraction of calcium in the minerals as a function of CaO content of ash for Powder River Sub-bituminous coals. 3-518

3-300. Fraction of magnesium in the minerals as a function of MgO content of ash for Powder River Sub-bituminous coals. 3-518

3-301. Distribution of silicon among the mineral categories for sub-bituminous coals..... 3-519

3-302. Distribution of silicon among the mineral categories for different coal types, based on average values in a given coal type. 3-520

3-303. Distribution of kaolinite minerals by diameter of mineral grains for Appalachian bituminous coals and subbituminous coals. 3-521

3-304. Elkhorn-Hazard: Mineral composition as a function of coal particle size, predicted by ToPEM. 3-523

3-305. Illinois 6: Mineral composition as a function of coal particle size, predicted by ToPEM. 3-523

3-306. Pittsburgh: Mineral composition as a function of coal particle size, predicted by ToPEM 3-524

3-307. Wyodak: Mineral composition as a function of coal particle size, predicted by ToPEM. 3-524

3-308. Elkhorn-Hazard: Bulk ash composition predicted by ToPEM and estimated from CCSEM data. 3-525

3-309. Illinois 6: Bulk ash composition predicted by ToPEM and estimated from CCSEM data..... 3-525

3-310. Pittsburgh: Bulk ash composition predicted by ToPEM and estimated from CCSEM data..... 3-525

LIST OF FIGURES (Continued)

Figure No. Page

3-311. Wyodak: Bulk ash composition predicted by ToPEM and estimated from CCSEM data. 3-526

3-312. Cumulative mass distribution of coal particles as a function of coal particle size. 3-526

3-313. Mineral content that corresponds to various sizes of coal particles, as predicted by ToPEM for the four coals. 3-526

3-314. Cumulative distribution of mineral mass in the various sizes of coal particles. 3-527

3-315. Partial pressure of vaporized metals calculated for 20-3% O_2 (0-14% bulk CO_2) at 1750 K gas temperature. 3-536

3-316. Ash vaporization for 20%, 14% and 3% bulk O_2 (0%, 3% and 14% CO_2). 3-536

3-317. Sodium vaporization for 20%, 14% and 3% bulk O_2 (0%, 3% and 14% CO_2). 3-537

3-318. Iron vaporization for 20%, 14% and 3% bulk O_2 (0%, 3% and 14% CO_2). 3-537

3-319. Elkhorn-Hazard: Submicron ash composition predicted from bulk ash for 20%, 14% and 3% bulk O_2 (0%, 3% and 14% CO_2). 3-537

3-320. Illinois 6: Submicron ash composition predicted from bulk ash for 20%, 14% and 3% bulk O_2 (0%, 3% and 14% CO_2). 3-538

3-321. Pittsburgh: Submicron ash composition predicted from bulk ash for 20%, 14% and 3% bulk O_2 (0%, 3% and 14% CO_2). 3-538

3-322. Wyodak: Submicron ash composition predicted from bulk ash for 20%, 9.5% and 3% bulk O_2 (0%, 3% and 14% CO_2). 3-538

3-323. Fraction of Al that vaporizes at 14% O_2 using equilibrium Eq. (8), and using equilibrium Eq. (5) 3-539

3-324. Fraction of Fe that vaporizes at 14% O_2 using equilibrium Eq. (9) and using equilibrium Eq. (3) 3-539

3-325. Elkhorn-Hazard: Submicron ash composition predicted for 20% O_2 predicted by ToPEM for different sizes of coal particles. 3-540

LIST OF FIGURES (Continued)

Figure No. Page

3-326. Illinois 6: Submicron ash composition predicted for 20% O_2 predicted by ToPEM for different sizes of coal particles. 3-540

3-327. Pittsburgh: Submicron ash composition predicted for 20% O_2 predicted by ToPEM for different sizes of coal particles. 3-540

3-328. Wyodak: Submicron ash composition predicted for 20% O_2 predicted by ToPEM for different sizes of coal particles. 3-541

3-329. Ash vaporization for 20% bulk O_2 from ToPEM and from the bulk ash model. 3-542

3-330. Sodium vaporization for 20% bulk O_2 from ToPEM and from the bulk ash model. ... 3-542

3-331. Iron vaporization for 20% bulk O_2 from ToPEM and from the bulk ash model. 3-542

LIST OF TABLES

Table No.		Page
2-1	Task Breakdown	3-9
3-1.	Coal Properties Phase II Program Coals (As-received basis)	3-4
3-2.	Coal Ash Composition (wt%, sulfur-free basis)	3-4
3-3.	Forms of Sulfur in Phase II Coals (wt%, as-received basis)	3-5
3-4.	Coal Particle Size Distribution for Phase II Coals (in wt%)	3-5
3-5.	Trace Element Concentrations in Phase II Coals by Neutron Activation Analysis (as received basis)	3-6
3-6.	Elemental Concentrations for Phase II Whole Coals	3-7
3-7.	Semi-Quantitative Mineralogy by X-Ray Diffraction	3-8
3-8.	Mineralogy of PSI Phase II Coals Determined by SEM.	3-9
3-9.	Size Distribution of Major Minerals in Wyodak Coal	3-11
3-10.	Size Distribution of Major Minerals in North Dakota Lignite	3-11
3-11.	Size Distribution of Major Minerals In Ohio Coal	3-11
3-12.	Mössbauer Results for Phase II Project Coals	3-14
3-13.	Mössbauer Data for Top and Bottom Layers of Coal Samples from UU	3-15
3-14.	Representative Electron Microprobe Analyses for Pyrite in Phase II Coals	3-44
3-15.	Representative Electron Microprobe Analyses for Illite/Smectite in Phase II Coals	3-44
3-16.	As XANES Results of Least-Squares Fitting - Project Coals	3-52
3-17.	As Contents of Residues (by INAA) Remaining After Leaching Experiments	3-53
3-18.	Estimates of Arsenic Forms Remaining After Each Leaching Step in the Ohio Coal	3-55
3-19.	Relative Step-Heights and Concentrations for Chromium in Leached Coal Residues	3-58

LIST OF TABLES (Continued)

Table No.		Page
3-20.	Relative Step-Heights and Concentrations for Zinc in Leached Coal Residues	3-60
3-21.	Results of Mössbauer and As XANES Spectral Fitting on USGS High-As Coals	3-64
3-22.	Combustion Gas Compositions for Drop Tube Experiments	3-69
3-23.	Cascade Impactor Cutoff Diameters	3-69
3-24.	Coefficients for the Rate Constant Approximations as Determined from Data on Temperature Increases in the Furnace	3-71
3-25.	Fraction of Each Element Recovered in the Submicron Ash for the Ohio Coal	3-75
3-26.	The Fraction of Each Element Collected in the Submicron Ash of ND Lignite	3-76
3-27.	The Fraction of Each Element Collected on the Final Filter for Wyodak	3-77
3-28.	Composition of Synthetic Flue Gas (concentrations in ppm) Used in Experiments to Test Interference with Methods for Measurement of Chlorine Speciation	3-85
3-29.	Sources of Thermodynamic Data	3-95
3-30.	Thermodynamic Equilibrium Simulations Performed to Evaluate the Chemistry of Arsenic, Selenium, and Antimony during Pulverized Coal Combustion	3-96
3-31.	Possible Arsenic Products from Thermodynamic Simulation	3-104
3-32.	Possible Selenium Products from Thermodynamic Simulation	3-108
3-33.	Possible Antimony Products from Thermodynamic Simulation	3-116
3-34.	Molar Rates of Arsenic Deposition for Calcium Oxide Experiment	3-129
3-35.	Results of Kinetic Rate Calculations	3-129
3-36.	Molar Rates of Arsenic Oxide Reaction for Reactants at 26 ppm Vapor Concentration	3-133
3-37.	Molar Rates of Arsenic Oxide Reaction for Reactants at 13 ppm Vapor Concentration	3-133
3-38.	Results of Kinetic Rate Calculations at 26 ppm	3-133

LIST OF TABLES (Continued)

Table No.		Page
3-39.	Results of Kinetic Rate Calculations at 13 ppm	3-133
3-40.	Molar Rates of Arsenic Oxide Reaction for Reactants at 26 ppm Arsenic Oxide Vapor Concentration	3-136
3-41.	Results of Kinetic Rate Calculations at 26 ppm	3-136
3-42.	Comparison of Experimental and Analytical Arsenic Absorbed	3-136
3-43.	Flue Gas Residence Times at Particle Sampling Locations	3-169
3-44.	Proximate/Ultimate Analysis of the Pittsburgh Seam Coal	3-170
3-45.	Pittsburgh Seam Coal	3-171
3-46.	Pittsburgh Seam Coal Ash Elemental Composition	3-171
3-47.	Enrichment Factors for Key Elements in Pittsburgh Seam Fly Ash Sampled at Port 4b	3-176
3-48.	Enrichment Factors for Key Elements in Pittsburgh Seam Fly Ash Sampled at Port 12	3-176
3-49.	The Solubility of Key Pittsburgh Seam Fly Ash Elements in EPA TCLP Leaching Solutions Sampled at Port 4b and Port 12	3-177
3-50.	Proximate/Ultimate Analysis of the Illinois #6 Coal	3-178
3-51.	Illinois #6 Coal Ash Characterization	3-179
3-52.	Illinois #6 Coal Ash Elemental Composition	3-179
3-53.	Enrichment Factors for Key Elements in Illinois #6 Fly Ash Sampled at Port 4b	3-184
3-54.	Enrichment Factors for Key Elements in Illinois #6 Fly Ash Sampled at Port 12	3-185
3-55.	Proximate/Ultimate Analysis of the Kentucky Coal	3-185
3-56.	Kentucky Coal Ash Characterization	3-186
3-57.	Kentucky Coal Ash Elemental Composition	3-186

LIST OF TABLES (Continued)

Table No.		Page
3-58.	Enrichment Factors for Key Elements in Kentucky Fly Ash Sampled at Port 4	3-191
3-59.	Enrichment Factors for Key Elements in Kentucky Fly Ash Sampled at Port 14	3-192
3-60.	The Solubility of Key Kentucky Fly Ash Elements in EPA TCLP Leaching Solutions Sampled at Port 4 and Port 14	3-192
3-61.	Proximate/Ultimate Analysis of the Ohio Coal	3-193
3-62.	Ohio Coal Ash Characterization	3-193
3-63.	Ohio Coal Ash Elemental Composition	3-194
3-64.	Enrichment Factors for Key Elements in Ohio Fly Ash Sampled at Port 4	3-199
3-65.	Enrichment Factors for Key Elements in Ohio Fly Ash Sampled at Port 14	3-200
3-66.	The Solubility of Key Ohio Fly Ash Elements in EPA TCLP Leaching Solutions Sampled at Port 4 and Port 14	3-200
3-67.	Proximate/Ultimate Analysis of the Wyodak Coal	3-201
3-68.	Wyodak Coal Ash Characterization	3-201
3-69.	Wyodak Coal Ash Elemental Composition	3-202
3-70.	Enrichment Factors for Key Elements in Wyodak Fly Ash Sampled at Port 4	3-207
3-71.	Enrichment Factors for Key Elements in Wyodak Fly ash Sampled at Port 14	3-207
3-72.	The Solubility of Key Wyodak Fly Ash Elements in EPA TCLP Leaching Solutions Sampled at Port 4 and Port 14	3-208
3-73.	Proximate/Ultimate Analysis of the North Dakota Lignite	3-209
3-74.	North Dakota Lignite Ash Characterization	3-209
3-75.	North Dakota Lignite Ash Elemental Composition	3-210
3-76.	Enrichment Factors for Key Elements in North Dakota Fly Ash Sampled at Port 4	3-215

LIST OF TABLES (Continued)

Table No.		Page
3-77.	Enrichment Factors for Key Elements in North Dakota Fly Ash Sampled at Port 14	3-216
3-78.	The Solubility of Key North Dakota Fly Ash Elements in EPA TCLP Leaching Solutions Sampled at Port 4 and Port 14	3-216
3-79.	Forms of Occurrence of Selenium in the Six Study Coals	3-238
3-80.	Mass Fraction of Selenium in Vapor, Submicron, and Supermicron Regimes at Three Combustor Sample Locations	3-239
3-81.	Selenium Enrichment* Factors for Submicron-Sized Fly Ash Samples	3-240
3-82.	Correlation Coefficients for Selenium vs. Calcium and Iron in Fly Ash Particles from the Six Study Coals Sampled at Port 14	3-248
3-83.	Selenium Partitioning Mechanism Hypotheses and Validation Test Matrix	3-249
3-84.	Comparison of Selenium Mass Concentration Values	3-254
3-85.	A Comparison of Absolute Selenium Concentration Values from Pittsburgh Seam Coal Cation Doping Experiments	3-254
3-86.	Summary of Selenium Solubility in Fly Ash from Baseline Screening Experiments	3-256
3-87.	Environmental Impact of Selenium in Fly Ash Particles	3-257
3-88.	Correlation Coefficients for Selenium Versus Calcium and Iron in Fly Ash Particles from the Six Study Coals Sampled at Port 4	3-261
3-89.	Primary Partitioning Mechanisms for Selenium during the Combustion of the Six Study Coals	3-263
3-90.	Forms of Occurrence of Arsenic in the Six Study Coals	3-265
3-91.	Mass Fraction of Arsenic in Vapor, Submicron, And Supermicron Regimes at Three Combustor Sample Locations	3-266
3-92.	Arsenic Enrichment Factors1 for Submicron-Sized Fly Ash Samples	3-267

LIST OF TABLES (Continued)

Table No. Page

3-93. Correlation Coefficients for Arsenic vs. Calcium and Iron in Fly Ash Particles from the Six Study Coals Sampled at Port 14 3-271

3-94. Arsenic Partitioning Mechanism Hypotheses and Validation Test Matrix 3-273

3-95. Comparison of Arsenic Mass Concentration Values 3-277

3-96. Comparison of Arsenic Mass Concentration Values 3-278

3-97. A Comparison of Absolute Arsenic Concentration Values 3-278

3-98. Summary of Arsenic Solubility in Fly Ash 3-279

3-99. Correlation Coefficients for Arsenic Versus Calcium and Iron 3-285

3-100. Primary Partitioning Mechanisms for Arsenic during the Combustion of the Six Study Coals 3-287

3-101. Forms of Occurrence of Antimony in the Six Study Coals 3-288

3-102. Mass Fraction of Antimony in Vapor, Submicron, and Supermicron Regimes at Three Combustor Sample Locations 3-289

3-103. Antimony Enrichment Factors for Submicron-Sized Fly Ash Samples 3-291

3-104. Correlation Coefficients for Antimony versus Calcium, Iron, and Aluminum 3-296

3-105. Antimony Partitioning Mechanism Hypotheses and Validation Test Matrix 3-298

3-106. Comparison of Antimony Mass Concentration Values 3-302

3-107. Comparison of Absolute Antimony Concentration Values 3-303

3-108. Summary Of Antimony Solubility in Program 3-303

3-109. Correlation Coefficients for Antimony vs. Calcium, Iron, and Aluminum 3-308

3-110. Primary Partitioning Mechanisms for Antimony during the Combustion of the Six Study Coals 3-310

3-111. Cobalt Enrichment Factors for Submicron-Sized Fly Ash Samples 3-312

LIST OF TABLES (Continued)

Table No. Page

3-112. Mass Fraction of Cobalt in Vapor, Submicron, and Supermicron Regimes at Three Combustor Sample Locations 3-313

3-113. Correlation Coefficients for Cobalt Versus Calcium, Iron, and Aluminum in Fly Ash Particles from the Pittsburgh, Kentucky, and Wyodak Study Coals Sampled at Port 14 3-317

3-114. Summary of Cobalt Solubility in Fly Ash from Baseline Screening Experiments 3-321

3-115. Correlation Coefficients for Cobalt Versus Calcium, Iron, and Aluminum in Fly Ash Particles from the Pittsburgh, Kentucky, and Wyodak Study Coals Sampled at Port 4 3-325

3-116. Primary Partitioning Mechanisms for Cobalt During the Combustion of the Six Study Coals 3-326

3-117. Cesium, Thorium, and Cerium Enrichment Factors for Submicron-Sized Fly Ash Samples 3-327

3-118. Mass Fraction of Cesium, Thorium, and Cerium in Vapor, Submicron, and Supermicron Regimes at Two Combustor Sample Locations 3-330

3-119. Primary Partitioning Mechanisms for Cesium, Thorium, and Cerium During the Combustion of Five Coals 3-337

3-120. Mercury Emission Inventory for U.S. Sources, kg/yr 3-341

3-121. Speciated Mercury Emission Inventory for U.S. Sources, kg/yr 3-342

3-122. Physical/Chemical Properties of Mercury and Some of Its Compounds 3-343

3-123. Characteristics of Experiments Conducted Under Isothermal Conditions 3-346

3-124. Characteristics of Experiments Conducted with a Temperature Gradient 3-347

3-125. Niksa et al. Rate Constants for Hg Oxidation 3-353

3-126. Initial Conditions for Global and Elementary Kinetics 3-359

3- 127. Initial Conditions and Temperatures for Mercury Kinetic Calculations 3-361

3-128. Time-Temperature History of Effluent Gas 3-363

LIST OF TABLES (Continued)

Table No. Page

3-129. Mercury Concentrations for Different Constant Heating Bath Temperatures 3-369

3-130. Radiation Corrected Temperatures at Outlet of Mixing Chamber 3-369

3-131. Volumetric Flow Rates and Velocities at Different Distances from the Center of the Mixing Chamber (31slpm) 3-373

3-132. Residence Times and Cooling Rates at Different Sampling Points 3-373

3-133. Trace Mercury Speciation Measurement Methods 3-373

3-134. Carbon Adsorption Experimental Results 3-388

3-135. Combined Carbon Adsorption-Ontario Hydro Experimental Runs 3-389

3-136. Physical Conditions at Different Quartz Tube Reactor Sampling Ports 3-393

3-137. Flue Gas Mixture for Bench-Scale Tests 3-400

3-138. Results of Ash Analysis 3-402

3-139. Characteristics of Eastern Bituminous Coal Ash Samples 3-404

3-140. Surface Area and LOI of Ash Samples for Morphological Analysis 3-405

3-141. Mössbauer Data for First Set of EERC Fly-Ash Samples 3-417

3-142. Mössbauer Data for the Second Set of Samples from EERC 3-421

3-143. Results of Least-Squares Fitting S XANES Spectra – EERC Ash Samples 3-422

3-144. Results from Tests with Hg0 Injection 3-424

3-145. Mössbauer Data 3-429

3-146. Results from Tests with $HgCl_2$ Injection 3-443

3-147. Estimates of Cr(VI) Contents of EERC Ash Samples 3-453

3-148. Hg XAFS Systematics for Mercury Compounds 3-457

LIST OF TABLES (Continued)

Table No. Page

3-149. Experimental Results for Coal-Based Chars After Exposure to Hg-Laden Flue Gas in UA Combustion Unit 3-462

3-150. Experimental Results for Zeolite and Activated Carbon Sorbents 3-464

3-151. Mercury XAFS Systematics for EERC LAC Sorbent Samples 3-465

3-152. Hg, S and Cl Step-Height Data for EERC LAC Sorbent Samples 3-465

3-153. Mercury XAFS Parametric Data for the Hg-Enriched ADA Cherokee Ash 3-467

3-154. Data for Triboelectrostatic separation on ADA Cherokee Fly-Ash Sample 3-467

3-155. Hg XAFS Systematics of Various Sorbents from Ghorishi and Gullett (EPA) 3-472

3-156. Hg XAFS Systematics of Carbon “Felt” Sorbents from Gullett (EPA) 3-474

3-157. Trace Metal Enrichment in Submicron Fly Ash Particulate 3-484

3-158. Trace Element Capture Efficiencies: Field Data Facilities Utilizing ESP Alone for Particulate Control 3-486

3-159. Emissions Factors for Selected Trace Metals Emitted by Utility Pulverized Coal Combustion (lb/1012 Btu) Median (Range) 3-487

3-160. Average Capture Efficiency for Selected Trace Metals 3-487

3-161. Partitioning Functions used in Development of Emissions Model 3-493

3-162. Fraction of Trace Element Associated with Submicron Ash 3-499

3-163. Summary of APCD and Coal Type Information for ICR Data Sets 3-504

3-164. Average Values of Inlet Mercury Speciation and Removal of Gaseous Mercury Species for Combinations of Coal and APCD 3-505

3-165. Correlations Between Mercury Removal and Chlorine Content: Fractional Removal and Coefficient of Regressions (RSQ) 3-510

LIST OF TABLES (Continued)

Table No. Page

3-166. Average Error of Prediction for ICR Values Versus Calculated Values, Where Calculated Values Were Derived from Correlations from Species-Based Model and Correlations Based on Total Removal or Stack Speciation with Chlorine Content 3-511

3-167. Common Minerals Occurring in US Coals 3-514

3-168. Properties of Coals in Mineralogy Database 3-517

3-169. Average Atomic Ratios in Selected Minerals from CCSEM Analysis 3-520

3-170. Amount of Excluded Mineral Particles as Calculated by ToPEM 3-522

3-171. Bulk Composition of Gas Phase after Volatile Combustion 3-533

3-172. Bulk Composition of Gas Phase after Overall Combustion 3-533

3-173. Equilibrium Equations and Constants for Vaporization of Metals 3-534

3-174. Calculated Partial Pressure of Metals under Various Assumptions 3-536

ABSTRACT

The Clean Air Act Amendments of 1990 identify a number of hazardous air pollutants (HAPs) as candidates for regulation. Should regulations be imposed on HAP emissions from coal-fired power plants, a sound understanding of the fundamental principles controlling the formation and partitioning of toxic species during coal combustion will be needed. With support from the National Energy Technology Laboratory (NETL), the Electric Power Research Institute, and VTT (Finland), Physical Sciences Inc. (PSI) has teamed with researchers from USGS, MIT, the University of Arizona (UA), the University of Kentucky (UK), the University of Connecticut (UC), the University of Utah (UU) and the University of North Dakota Energy and Environmental Research Center (EERC) to develop a broadly applicable emissions model useful to regulators and utility planners. The new Toxics Partitioning Engineering Model (ToPEM) will be applicable to *all* combustion conditions including new fuels and coal blends, low-NO_x combustion systems, and new power generation plants. Development of ToPEM will be based on PSI's existing Engineering Model for Ash Formation (EMAF).

The work discussed in this report covers the Phase II program. Five coals were studied (three in Phase I and two new ones in Phase II). In this work UK has used XAFS and Mössbauer spectroscopies to characterize elements in project coals. For coals, the principal use was to supply direct information about certain hazardous and other key elements (iron) to complement the more complete indirect investigation of elemental modes of occurrence being carried out by colleagues at USGS. Iterative selective leaching using ammonium acetate, HCl, HF, and HNO_3, used in conjunction with mineral identification/quantification, and microanalysis of individual mineral grains, has allowed USGS to delineate modes of occurrence for 44 elements. The Phase II coals show rank-dependent systematic differences in trace-element modes of occurrence. The work at UU focused on the behavior of trace metals in the combustion zone by studying vaporization from single coal particles. The coals were burned at 1700 K under a series of fuel-rich and oxygen-rich conditions. The data collected in this study will be applied to a model that accounts for the full equilibrium between carbon monoxide and carbon dioxide. The model also considers many other reactions taking place in the combustion zone, and involves the diffusion of gases into the particle and combustion products away from the particle. A comprehensive study has been conducted at UA to investigate the post-combustion partitioning of trace elements during large-scale combustion of pulverized coal combustion. For many coals, there are three distinct particle regions developed by three separate mechanisms: 1) a submicron fume, 2) a micron-sized fragmentation region, and 3) a bulk (>3 μm) fly ash region. The controlling partitioning mechanisms for trace elements may be different in each of the three particle regions. A substantial majority of semi-volatile trace elements (e.g., As, Se, Sb, Cd, Zn, Pb) volatilize during combustion. The most common partitioning mechanism for semi-volatile elements is reaction with active fly ash surface sites. Experiments conducted under this program at UC focused on measuring mercury oxidation under cooling rates representative of the convective section of a coal-fired boiler to determine the extent of homogeneous mercury oxidation under these conditions. In fixed bed studies at EERC, five different test series were planned to evaluate the effects of temperature, mercury concentration, mercury species, stoichiometric ratio of combustion air, and ash source. Ash samples generated at UA and collected from full-scale power plants were evaluated. Extensive work was carried out at UK during this program to

develop new methods for identification of mercury species in fly ash and sorbents. We demonstrated the usefulness of XAFS spectroscopy for the speciation of mercury captured on low-temperature sorbents from combustion flue gases and developed XAFS parameters for such analyses. We demonstrated that all mercury sorption processes appeared to involve chemisorption rather than physisorption. This work aimed to develop a model that predicts the vaporization of metals during coal combustion and to incorporate this model into the existing Engineering Model for Ash Formation (EMAF). The model is based on theoretical analysis for metal vaporization, experimental data and data correlations. The existing program, EMAF, was substantially modified to accommodate the vaporization sub-model.

SECTION 1

EXECUTIVE SUMMARY

1. EXECUTIVE SUMMARY

1.1 Coal Properties

The coals in Phase II were chosen in an attempt to (1) represent a broad range of elemental forms of occurrence and (2) represent the major coal ranks and commercial coal seams used for pulverized coal power generation in the U.S.

A bituminous coal from Ohio coal was selected for study. The particular coal sample was a blend of three seams: Ohio 5, Ohio 6, and Ohio 7. The second coal in Phase II was a lignite from North Dakota (Hagel Bed). This coal is burned at a mine-mouth utility power plant in North Dakota. While lignites are not major steam producing coals throughout the United States, they are important regionally. The mineralogy of lignites from this seam is different from other coals. This coal is also burned at a full scale power plant which will be sampled for trace element emissions in another DOE-sponsored program. The third coal was from the Wyodak seam. This is a sub-bituminous coal from the Powder River Basin and is an important steam coal.

In this work the University of Kentucky (UK) has used XAFS and Mössbauer spectroscopies to characterize elements in project coals. For coals, the principal use was to supply direct information about certain hazardous and other key elements (iron) to complement the more complete indirect investigation of elemental modes of occurrence being carried out by colleagues at USGS.

- For comparing speciation information, XAFS experiments should be conducted directly on the residues from the leaching experiments. Using the identical fractions enables the assumptions in the leaching protocol to be tested and provides cleaner fractions for the XAFS investigation.

- Arsenic principally exists in association with pyrite in U.S. bituminous coals and as As^{3+}-O species in lower rank coals. Both forms are easily oxidized to arsenate forms.

- Chromium was found largely in organic association in both bituminous and lower-rank coals. Cr associated with clays (illite) was relatively minor in all three coals.

- Iron was found to be present predominantly as pyrite in all three coals; minor Fe^{2+}/clay and/or siderite were also present, more so in the lower-iron, lower-rank coals. Jarosite was a common oxidation product of pyrite.

- Zinc was not present as zinc sulfide (sphalerite), except possibly in minor amount in the bituminous coal. The major zinc forms in all three coals remain to be identified.

- Selenium is largely associated with pyrite in the bituminous coal; its contents in the lower rank coals were too low to obtain useful information.

Iterative selective leaching using ammonium acetate, HCl, HF, and HNO_3, used in conjunction with mineral identification/quantification, and microanalysis of individual mineral grains, has allowed USGS to delineate modes of occurrence for 44 elements in the Ohio 5/6/7, Wyodak, and North Dakota Program coals. These results provide basic information on the distribution of elements in these coals, information needed for characterization and combustion model development.

The Phase II coals show rank-dependent systematic differences in trace-element modes of occurrence. For example, the Ohio 5/6/7 sample shows a greater proportion of chalcophile elements residing in pyrite, compared to the two lower rank coals. These associations are quantified by selective leaching results for each element, and supporting data where obtainable. Microanalysis shows that each of the Phase II coals have pyrite containing isolated domains enriched in one or more potentially harmful elements. Pyrite in the Ohio 5/6/7 coal has the most arsenic-rich micro-domains (approaching 2.0 wt. %), but these show no appreciable enrichment in associated chalcophile elements. Grain-scale concentrations of other chalcophile elements (e.g., Cd, Se) may be higher in pyrite in the two lower rank coals, but pyrite is less abundant in these coals than the Ohio 5/6/7 sample. The association of mercury and pyrite was confirmed using laser ablation ICP-MS, for the Ohio 5/6/7 sample, and for the Illinois #6 and Pittsburgh coals studied in Phase I. Chromium and other transition metals in illite/smectite were determined using the SHRIMP-RG ion microprobe, providing concentrations of silicate-hosted metals, at levels below those that can be quantified with the electron microprobe.

1.2 Combustion Zone Behavior

The work at the University of Utah (UU) focused on the behavior of trace metals in the combustion zone by studying vaporization from single coal particles. The coals were burned at 1700 K under a series of fuel-rich and oxygen-rich conditions. The combustion atmosphere varied from 0 to 100% oxygen with the balance being either nitrogen or carbon dioxide. The nitrogen provided an inert environment for the reaction. Carbon dioxide was used to investigate the governing reaction for metal reduction. Carbon dioxide was expected to keep the metals in their less volatile oxidized state, and also to affect the particle temperature. The impact of the carbon dioxide is particularly important since early interpretations of the vaporization data did not properly account for the gas composition in the pores.

After combustion, the particles were rapidly cooled by addition of nitrogen gas through a water-cooled probe. An Andersen Mark II cascade impactor, located directly below the furnace collected and sized the particles. A side stream of the final exhaust was pulled through a small activated carbon plug to absorb any gas phase mercury and complete the mass balance. After collection, selected impactor stages, representing the residual and submicron ash, and the carbon plug were analyzed using instrumental neutron activated analysis (INAA).

During pyrolysis, the volatile organics are removed, and the remaining char is often assumed to include all of the mineral components of coal. Surprisingly, a number of elements showed enrichment in the submicron ash under pyrolyzing conditions. It appears likely that, with the exception of mercury, these elements were associated with volatile compounds.

Mercury is not associated with organics, but is more likely enriched because of the ability of carbon to absorb mercury.

As the oxygen concentration was increased, there was an enrichment of several elements in the submicron ash. Several significant minor elements were also reduced in the submicron ash by using a carbon dioxide rich atmosphere. These data support the hypothesis that the carbon dioxide controls vaporization rates for metal species according to the governing reaction. The carbon lowers the reaction constant, however the affect cannot simply be explained with empirical models because of the intricacies of the carbon dioxide reactions.

The data collected in this study will be applied to a model that accounts for the full equilibrium between carbon monoxide and carbon dioxide. The model also considers many other reactions taking place in the combustion zone, and involves the diffusion of gases into the particle and combustion products away from the particle.

UU also investigated chlorine speciation in the flue gas because one possible means of reducing emissions of mercury is to reduce elemental mercury by reacting it with a radical chloride ion. It has been suggested that sulfur dioxide would interfere with the speciation, so this was first tested that theory with a synthetic flue gas.

1.3 Post-Combustion Behavior of Semi-Volatile Metals

A comprehensive study has been conducted at UA to investigate the post-combustion partitioning of trace elements during large-scale combustion of pulverized coal combustion. For many coals, there are three distinct particle regions developed by three separate mechanisms: 1) a submicron fume, 2) a micron-sized fragmentation region, and 3) a bulk (>3 μm) fly ash region. The controlling partitioning mechanisms for trace elements may be different in each of the three particle regions. A substantial majority of semi-volatile trace elements (e.g., As, Se, Sb, Cd, Zn, Pb) will volatilize during combustion. The most common partitioning mechanism for semi-volatile elements is reaction with active fly ash surface sites. Only the least volatile of these elements (e.g., cobalt) are expected to undergo significant vapor-to-solid phase partitioning by homogeneous nucleation. The presence of this mechanism is coal-specific.

The submicron and fragmentation particle regions typically contain more active fly ash surface sites than the bulk fly ash region. The maximum combustion temperature affects the availability of active calcium and iron surface sites on submicron particles. Therefore, for most coals/combustion conditions, increasing the combustion temperature will decrease the vapor-phase emission of those trace elements that form oxy-anions during volatilization. The maximum combustion temperature does not affect the availability of active aluminum surface sites on submicron particles. Therefore, the recovery of volatilized trace elements that partition by reaction with active anion surface sites may be unaffected by combustion temperature.

Although not predicted by thermodynamic simulation, many volatilized trace elements appear to form oxy-anions during combustion. Volatilized transition metals (e.g., cobalt) may form simple oxides, oxy-anions, or a combination of both during combustion.

Sulfur will inhibit the reaction of most volatilized trace element oxy-anions with iron surface sites. The effect of sulfur on calcium reactivity appears to be less than the effect on iron reactivity. Sulfur content does not appear to affect the reactivity of aluminum surface sites. Therefore, coal sulfur content is an important parameter affecting the partitioning of many trace elements (e.g., selenium, arsenic) but not others (e.g., antimony, cesium). For coals with moderate (> 1 wt% as SO_2) to high sulfur contents (e.g., Pittsburgh, Illinois), volatilized trace elements that form oxy-anions will partition by reaction with active calcium surface sites if sufficient sites are available. For coals with low (<1 wt% as SO_2) sulfur contents (e.g., Kentucky, Wyodak, and North Dakota), volatilized trace elements that form oxy-anions will partition by reaction with active iron and/or calcium surface sites (depending on the reactivity of the individual trace element with iron versus calcium and the ratio of available iron to calcium surface sites). Volatilized trace elements that form oxy-anions will not partition by reaction for coals having a moderate to high sulfur content and low calcium content (e.g., Ohio) because there are insufficient active cation surface sites available for reaction.

Unreacted trace elements present on fly ash surfaces are usually very soluble in slightly acidic and acidic aqueous environments. The solubility of reacted trace elements present on fly ash surfaces is reaction product-dependent. Differences in partitioning mechanisms has a greater effect on trace element solubility from fly ash than which particle region the trace element resides in. Useful information can be obtained from leaching size-segregated fly ash samples collected on greased impactor membranes.

The following, element-specific conclusions can be derived from this work:

1. The volatilized form of antimony can have a substantial impact on the vapor phase emission. Almost all antimony present as antimony chloride is expected to leave in the flue gas and the remainder will partition as unreacted antimony to fly ash surfaces.

2. Volatilized selenium is more reactive with iron surface sites than with calcium surface sites. Therefore, coal sulfur content has a substantial impact on selenium partitioning.

3. Volatilized selenium is more reactive with both iron and calcium surface sites than arsenic or antimony.

4. Volatilized arsenic and antimony have similar reactivities with iron or calcium surface sites.

5. Volatilized selenium, arsenic, and antimony appear to form oxy-anions. These oxy-anions will react with active surface sites if available. Contrary to thermodynamic simulation predictions, formation of Al-As, Al-Se, or Al-Sb complexes were not observed under any of the conditions studied.

6. The forms of occurrence of selenium on fly ash surfaces can be distinguished by the solubility properties of the most likely forms of occurrence in slightly acidic and acidic aqueous leachates.

7. The forms of occurrence of arsenic on fly ash surfaces cannot be distinguished by the solubility properties of the most likely forms of occurrence in slightly acidic and acidic aqueous leachates.

8. All of the dominant forms of occurrence of antimony and cobalt on fly ash surfaces evaluated during this study were very soluble in slightly acidic and acidic aqueous leachates.

1.4 Post-Combustion Behavior of Mercury

Combustion processes remain the major source of mercury emissions to the atmosphere. Electric utility boilers are the largest emitting single source category in this inventory, accounting for one-third of the anthropogenic emissions to the air in the U.S. Anthropogenic mercury emissions from human activity take three forms: gaseous elemental mercury, gaseous divalent mercury, and particulate mercury. Mercury circulates in the environment in different chemical forms and different physical states. Inorganic forms exist in three oxidation states: elemental, monovalent, or divalent. Mercury in the atmosphere can return to the surface of the earth by either dry or wet deposition. In the case of gaseous divalent mercury, it can be subject to rapid wet or dry deposition. Divalent mercury is soluble in water and it can also adhere to particles in the air. It has a residence time of several days to a week. Mercury in its elemental state can be expected to disperse on a regional and global scale. The oxidation rate of Hg^0 to Hg^{+2} is on the order of a year, indicative of long atmospheric residence times.

The form of mercury emitted from point sources is a critical variable in modeling the patterns and amount of mercury deposited from the atmosphere. During combustion, mercury escapes from the burning fuel as an elemental vapor, which may persist in elemental form or may be oxidized to the +2 (mercuric) state. The three most likely gas phase mercury compounds in combustion systems - Hg, HgO, and $HgCl_2$ - are all volatile at stack and air pollution control device temperatures. At furnace exit temperatures, all of the mercury is expected to remain as the thermodynamically favored elemental form in the gas. As the gas cools after combustion, oxidation reactions can occur, significantly reducing the concentration of elemental mercury by the time the post-combustion gases reach the stack. Measurements of the concentration of mercury species taken in the stacks of pilot and full scale coal combustion systems show more than half of the vapor phase mercury as the oxidized form that is likely to be $HgCl_2$. The range of observed values is broad.

Many laboratory studies in the literature have suggested that the presence of chlorine species (HCl and Cl_2), temperature and cooling rates were the most important factors affecting mercury oxidation. Molecular chlorine readily reacted with mercury. In the presence of a cooling rate (i.e., non-isothermal conditions), kinetic limitations were evident, according to several of the studies. Further, surface reactions may contribute, although high conversion by homogeneous pathways is reported under certain conditions.

Experiments conducted under this program at the University of Connecticut (UC) therefore focused on measuring mercury oxidation under cooling rates representative of the convective section of a coal-fired boiler to determine the extent of homogeneous mercury oxidation under these conditions.

Although the oxidation of elemental mercury in the convective pass is assumed to proceed primarily via gas-phase reaction, experimental evidence suggests that some fly ash can catalyze oxidation of elemental mercury. Iron oxide has been shown to promote this oxidation. Other constituents in the fly ash (carbon, calcium compounds) may also contribute. The presence of acid gases (HCl, SO_2, NO, NO_2) in the flue gas has also been shown to cause oxidation in the presence of fly ash. Thus, the coal composition (in terms of chlorine content and ash composition), the operation of the combustion system (in terms of unburned carbon in the ash), and temperature and residence time in the particulate control device will all affect mercury speciation in the gas and the amount of mercury adsorbed on the particulate matter.

Experiments conducted at the Energy & Environmental Research Center (EERC) at the University of North Dakota measured oxidation of elemental mercury and adsorption of elemental and mercuric chloride on ash samples. The ash samples were in a heated fixed bed reactor.

Gaseous Mercury Oxidation

Kinetic modeling of reactions of mercury with chlorine species under different cooling rate conditions established the importance of cooling rates as one of the main factors determining the degree of mercury oxidation in post-coal combustion. Kinetic calculations showed that the chemistry involving Cl atom reactions with mercury is fast. Therefore the presence of high concentrations of Cl atoms causes rapid mercury oxidation to occur, and the degree to which Cl_2 and HCl generate Cl atoms is important.

The results of mercury oxidation experiments under different chlorine concentrations showed that, relative to what has been reported in the literature, much higher chlorine concentrations are needed to obtain higher mercury oxidation. At typical HCl concentrations (100 ppmv) no reaction is observed with mercury. We demonstrated that total mercury oxidation can be achieved at cooling rates of 400 K/s by increasing the amount of chlorine up to 500 ppmv.

Mercury-Ash Interactions

In the original scope of work, five different test series were planned to evaluate the effects of temperature, mercury concentration, mercury species, stoichiometric ratio of combustion air, and ash source. Tests were run at temperatures of 250 and 350°F. With the tests with elemental mercury injection, there was no clear temperature effect. Oxidation of the elemental mercury either increased or decreased or was not affected by increasing temperature. With elemental mercury capture, there appeared to be a slight effect, but this can be attributed to physisorption of the elemental mercury on the ash samples. With the $HgCl_2$ injection tests, capture efficiency increased with decreasing temperature. Again, this can be attributed to physisorption on the ash surface. The objective was to identify a temperature to optimize

interactions between the mercury in the simulated flue gas and the ash samples. Based on the results, there was no need to find an "optimum" temperature for either the elemental or $HgCl_2$ tests. The temperatures used were adequate for observation of effects. Tests were planned to find optimum mercury concentrations, but again the baseline concentrations were adequate. The main body of the testing performed was to identify reactive ash samples and determine the effects of ash properties on capture, oxidation of elemental mercury, and reduction of oxidized mercury. As a result, 17 different ash samples were evaluated with elemental mercury or $HgCl_2$ injection. The results from these tests and analysis of the ash samples indicate there is a slight correlation between LOI and oxidation of elemental mercury across the fixed bed of ash. This effect was more evident with the bituminous and subbituminous ashes. There was also a general trend of increasing oxidation with increasing surface area. These trends most likely represent increasing active sites on the carbon that is in the ash. There was no correlation between temperature and the amount of oxidation of elemental mercury. There was also no correlation between LOI, surface area, and capture of elemental mercury. Also, no conclusions could be made about the effect of ash type on oxidation or capture of elemental mercury. Results from tests where ash samples were ashed at 400 and 750°C to remove carbon and evaluated in the fixed bed showed this process rendered active ashes inert. The baseline Wyodak ash which showed capacity for capture and oxidation of elemental mercury showed no reactivity even after the low-temperature ashing at 400°C. This was observed with all the ash samples that were ashed. The loss of active sights when the carbon was ashed is most likely responsible for the change in reactivity and not a change in the inorganic matter in the ash.

Results from the tests with $HgCl_2$ in the simulated flue gas indicate there is increased capture of $HgCl_2$ at lower temperatures. However, this is most likely due to physisorption and not an ash surface effect. As expected, the ash samples did not reduce $HgCl_2$ across the fixed bed.

Extensive work was carried out at UK during this program to develop new methods for identification of mercury species in fly ash and sorbents. We demonstrated the usefulness of XAFS spectroscopy for the speciation of mercury captured on low-temperature sorbents from combustion flue gases and developed XAFS parameters for such analyses. We demonstrated that all mercury sorption processes appeared to involve chemisorption rather than physisorption. Chloride, sulfide, iodide and oxygen anions were all shown to be effective for capturing mercury. The mechanism of capture reflects the gas-phase composition in terms of the speciation of mercury and of acid-gas components.

1.5 Field Data Evaluation

Semi-Volatile Trace Metals

Based on a review of field data, a model for the emission of trace elements from electric utility coal-fired power plants has been developed. The model partitions trace elements among fly ash particles as a function of ash particle size, and incorporates size-dependent particulate penetration through electrostatic precipitators to obtain emissions estimates. Comparison with recent field measurements and a database-derived model demonstrated that improved agreement could be obtained for relatively volatile elements such as arsenic and selenium. In contrast,

agreement for chromium was comparable to that obtained with the database-derived model, and was attributed to the relatively low volatility of this element. A review of the literature in this area suggests that this conclusion may be restricted to facilities combusting bituminous coals, as facilities firing sub-bituminous coals generally produced greater fractions of chromium in the submicron ash particulate. The partitioning model might thus be a more appropriate mechanism for predicting chromium emissions for such facilities.

Although the fraction of an element in the submicron size range was treated as an adjustable parameter in this study, the values obtained for each of these elements were consistent with partitioning data reported in both field and laboratory studies. It is therefore concluded that for volatile elements such as arsenic and selenium, a model based upon partitioning and overall ESP capture efficiency offers the most accurate predictions of trace element emissions, even for facilities contained within the PISCES database. Recommended values for arsenic are 14% in the submicron range, and for selenium, 20% vapor and 30% in the submicron fly ash size range. Further improvement in emissions prediction could be achieved by measuring the size-dependent particulate penetration though an ESP at an individual facility, but given the general absence of such data, the results presented herein suggest that an average value coupled to an overall particulate collection efficiency can provide improved predictions of trace element emissions. It is anticipated that first principles prediction of elemental partitioning, when coupled to the model presented herein, will provide the most accurate model of trace element emissions for all coals over a broad range of combustion conditions.

Mercury

Data from the EPA Information Collection Request (ICR) may be used to increase our knowledge of the effect of coal type, combustion system, and air pollution control devices on mercury speciation and emissions. These data must be evaluated carefully, however, if they are to be useful. In many cases, critical information may be missing or measurements in error. Several sources of inaccuracy in the predictions were identified, specifically,

- Lack of ash composition data which could be used to improve the prediction of the adsorption of mercury on fly ash the oxidation of mercury in particulate control devices;
- Uncertainty in the measurement of coal chlorine, a key parameter for mercury oxidation in flue gas;
- Over-reporting of oxidized mercury by the Ontario Hydro method when applied to flue gas containing high ash loadings;
- Poor mercury mass balance closure.

Air Pollution Control Devices (APCDs) have not previously been tuned to maximize mercury capture; such a strategy may be considered in the future, if mercury regulations are imposed. Most APCDs have been associated with reductions in mercury emissions, although the speciation of mercury is very important in determining the magnitude of reduction. However, a considerable increase in our understanding of the behavior of mercury in APCDs will be required

even to get consistent mercury reductions without having an impact on removal efficiency of particulate, SO_2 or NO_x. With these caveats in mind, wet FGD's, dry scrubbers, and fabric filters can all remove a significant amount (circa 50%) of the gaseous mercury in the flue gas under certain conditions. Fabric filters showed an average of 40 to 85% decrease in elemental mercury and a 25% decrease in oxidized mercury. The large decrease in elemental mercury suggests that some of the elemental mercury is being oxidized across the bag filter. SDAs produce decreases in oxidized mercury (50 to 60%) and elemental mercury (20 to 30%). ESPs and HESPs have a smaller effect on gaseous mercury. For bituminous coals, ESPs and HESPs appear to decrease elemental mercury (perhaps via oxidation). For low rank coals, precipitators have a smaller effect on gaseous mercury; ICR data do indicate a number of cases in which gaseous mercury (elemental or oxidized) increases across the precipitator, particularly for low rank coals.

1.6 Model Development

This work aimed to develop a model that predicts the vaporization of metals during coal combustion and to incorporate this model into the existing Engineering Model for Ash Formation (EMAF). The model is based on theoretical analysis for metal vaporization, experimental data and data correlations. The existing program, EMAF, was substantially modified to accommodate the vaporization sub-model.

The new Toxics Partitioning Engineering Model (ToPEM) was used to model the combustion and ash vaporization of coals used in Phase I. In certain coals, vaporization from excluded minerals and the smallest coal particles has a significant impact on the composition of the vaporized material. The vaporization equations were revised, so the effect of metal concentration in the coal is accounted for more accurately. The effects of the bulk CO_2 and char temperature were examined in detail. The calculated values for metal vaporization were compared with measured values from four different coals obtained in Phase I. The best agreement between the amount of vaporization and the composition of the submicron ash was obtained by assuming that the coal particles burn in 20% oxygen.

SECTION 2

INTRODUCTION AND PROGRAM OVERVIEW

2. INTRODUCTION AND PROGRAM OVERVIEW

2.1 Introduction

Before electric utilities can plan or implement emissions minimization strategies for hazardous pollutants, they must have an accurate and site-specific means of predicting emissions in all effluent streams for the broad range of fuels and operating conditions commonly utilized. Development of a broadly applicable emissions model useful to utility planners first requires a sound understanding of the fundamental principles controlling the formation and partitioning of toxic species during coal combustion. Physical Sciences Inc. (PSI) and its team members will achieve this objective through the development of an "Engineering Model" that accurately predicts the formation and partitioning of toxic species as a result of coal combustion. The "Toxics Partitioning Engineering Model" (ToPEM) will be applicable to all conditions including new fuels or blends, low-NO_x combustion systems, and new power systems being advanced by DOE in the Combustion 2000 program.

Based on a goal of developing and delivering this ToPEM model, a 5-year research program was proposed. This program is divided into a 2-year Phase I program and a 3-year Phase II program. The objective of the ongoing Phase II program is to develop an experimental and conceptual framework for the behavior of selected trace elements (arsenic, selenium, chromium, and mercury) in combustion systems and incorporate these concepts into a new engineering model. This Phase II objective will be achieved by a team of researchers from USGS, the Massachusetts Institute of Technology (MIT), the University of Arizona (UA), the University of Kentucky (UK), the University of Connecticut (UC), the University of Utah (UU), the University of North Dakota Energy & Environmental Research Center (EERC) and PSI. Model development and commercialization will be carried out by PSI.

The ultimate goal of this DOE, Federal Energy Technology Center-sponsored project was to develop a broadly applicable trace metal emissions model for coal-fired electric utility boilers.

In order to reach this goal, the program must:

1) Identify forms of occurrence of trace metals in coal feedstocks,
2) Define solid-phase to vapor-phase transformations in the flame zone,
3) Define vapor-phase to solid-phase transformations after the material leaves the flame zone, and
4) Determine the forms of occurrence of trace elements in the gaseous and solid material leaving the combustor and its impact on the environment.

This report documents work associated with the third and fourth of these areas. Defining vapor-phase to solid-phase transformations after the material leaves the flame zone has been studied in detail while a more limited effort has been made towards determining the forms of occurrence of trace elements in the gaseous and solid material leaving the combustor and its impact on the environment.

One of the unique aspects of this research is the use of experimental facilities that allow trace element partitioning to be studied under practical coal combustion conditions. Where practical means that the experimental conditions simulate the particle concentrations, residence times, and temperature profiles of commercial scale combustors.

2.1.1 The Combustion of Pulverized Coal

Coal is one of the primary fossil fuels used to generate energy. Unfortunately, it is also one of the most complex. Coal is a heterogeneous mixture of organic and inorganic compounds. The composition varies from coal seam to coal seam and in fact, the exact composition varies within the coal seam both horizontally and vertically [1-4]. To reduce the rate of build-up of deposits in boilers and to increase the efficiency of char oxidation [5], coal is typically pulverized into a fine powder prior to combustion.

One of the main focus areas in coal research is mitigating the impact of coal combustion upon the environment. This research is primarily divided into two general areas: combustion of organic compounds – that is, mitigation of soot – and mitigation of the inorganic compounds that are sent through the burner with the coal.

The types of plants that made up the original sediment layers and the age of the coal primarily determines the organic content. One of the main ways of categorizing (ranking) coals is by the "coalification" or structure of the organic portion of the coal. The primary categories for coals [5] are:

1. Anthracites,
2. Carbonaceous coals,
3. Bituminous coals,
4. Sub-bituminous coals, and
5. Lignites.

Anthracites have the highest carbon content (93-95 wt% total carbon) and lowest hydrogen content (2.5 wt%). Thus, the carbon molecules are closer to the elemental carbon state than the lower rank coals. By contrast, lignites are often still very plant-like in nature and have complicated carbon molecular structures. The carbon and hydrogen contents of lignites are typically 59 to 75 wt% and 4.5 to 5.5 wt%, respectively [5]. Bituminous and sub-bituminous coals are commonly utilized in the U.S. pulverized coal combustion. These coals have total carbon contents of 80 to 91 wt% and 75 to 80 wt%, respectively. This research utilized four bituminous coals, one sub-bituminous coal, and one lignite.

Inorganic compounds get into coal in a number of ways as illustrated in Figure 2-1. Much of the inorganic material was included in the original sediment layers which formed the organic structure of the coal. This material is usually organically bound in the final coal product. Larger chunks of inorganic material in the original sediment layers may not be incorporated into the organic structure but end up as an inclusion – that is, the structure forms around it. Other inorganic material entered the sediment layer after it was decomposed. This material tends to be located between coal particles and is known as excluded minerals. Other inorganic material is mixed into the coal during geological events after the coal seam has formed and during mining operations. These also constitute excluded minerals [5].

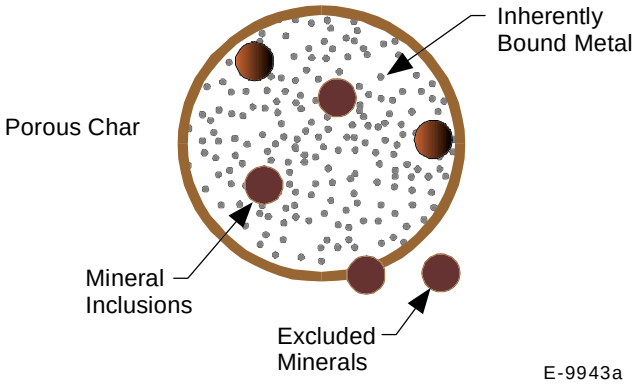

Figure 2-1. Inorganic compounds in coal.

2.1.2 The Environmental Impact of Trace Elements from Pulverized Coal Combustion

An important issue facing the coal-fired electric utility industry is the environmental impact resulting from the release of semi-volatile trace metals contained in the coal feed-stock [6]. Before electric utilities can plan or implement emissions minimization strategies for hazardous trace elements, they must have an accurate means of predicting the emissions in all effluent streams for the broad range of fuels and operating conditions commonly utilized [7].

General Concepts

Every coal contains at least some small quantity of every element that naturally occurs in the earth's crust. Because the chemical composition of these elements is complex and difficult to define, coal research typically classifies these chemical compounds by the element of interest. Thus, we refer in this work to arsenic, selenium, etc.

Trace metals that enter the combustor with coal are of environmental concern [6, 8-16] when they leave the combustion system in one of the following three forms:

1. As vapor emitted in the flue gas,
2. Included in submicron particles, or
3. Included in the larger, supermicron particles that make up the fly and bottom ash.

Figure 2-2 shows some of the more important trace elements classified based on their behavior after pulverized coal combustion in commercial applications. The low volatile species in Group 3 are usually incorporated in large, inorganic solid structures that are collected as bottom and fly ash. These typically are not believed to be of significant environmental concern. Group 2 elements, often termed "semi-volatile trace elements", may undergo vaporization in the flame but are not typically emitted in appreciable quantities as flue gas since they tend to return to the solid phase in the boiler. Notable exceptions are Se and Sb in most coals and As and Cd in some coals. Group 2 elements are commonly found in high concentrations in submicron particles. Group 3 elements are highly volatile and a significant fraction of these elements will leave with the flue gas. How these elements partition during combustion depends upon:

1. The form of occurrence in the coal,
2. The volatility of the trace element, and
3. The vapor-to-solid phase transformation mechanisms available to the metal in the combustor.

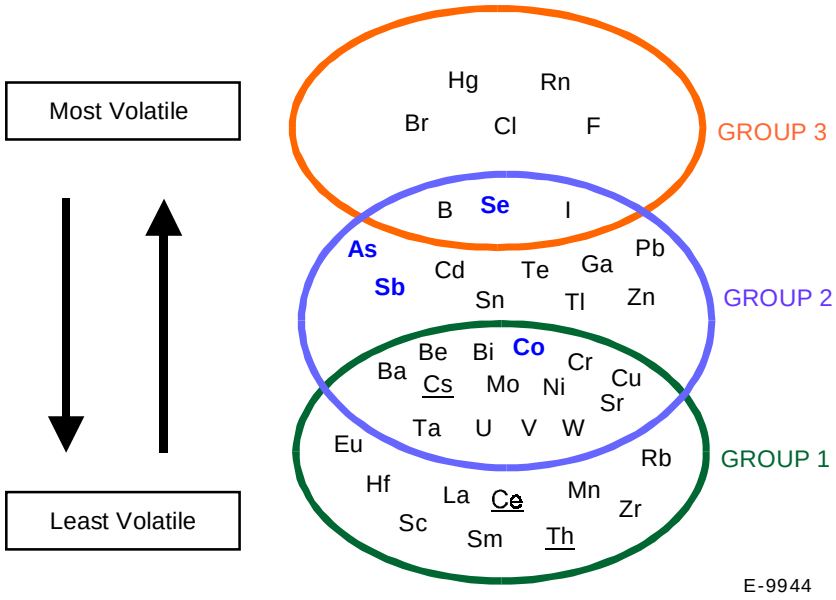

Figure 2-2. Classification of trace elements by behavior during combustion (developed from data given in Meij [17].

Figure 2-3 illustrates the current understanding of the possible transformation pathways of the coal feedstock's inorganic elements in a commercial combustor. Inorganic elements can be present in included or excluded mineral fractions or may be bound in the organic matrix of the coal particles fed to the combustor [6, 18]. As the carbon chains break apart and oxidize, the inorganics are exposed to the high temperature environment of the char particle. Much of the material in the larger inorganic fractions never vaporizes, but moves through the combustor (subject to softening, melting, and coalescence) to form the bulk of the bottom and fly ash [10, 19]. However, some of the material in the larger inorganic fractions plus material in small inorganic fractions does vaporize during combustion. In general, the less volatile the element, the sooner it is expected to partition back to the solid phase.

The major refractory elements (iron, silica, aluminum, and calcium) are believed to vaporize as suboxides formed by reduction with carbon monoxide (CO) in the immediate vicinity of the burning char particle [15, 20, 21]. As the molecules diffuse out of the reducing atmosphere of the char, they are oxidized. These oxides are not very volatile and will nucleate while still in the flame zone to form a submicron fume [20, 22-27]. The submicron fume is typically only 1 to 7% of the total fly ash mass but has a very high particle number density [27, 28].

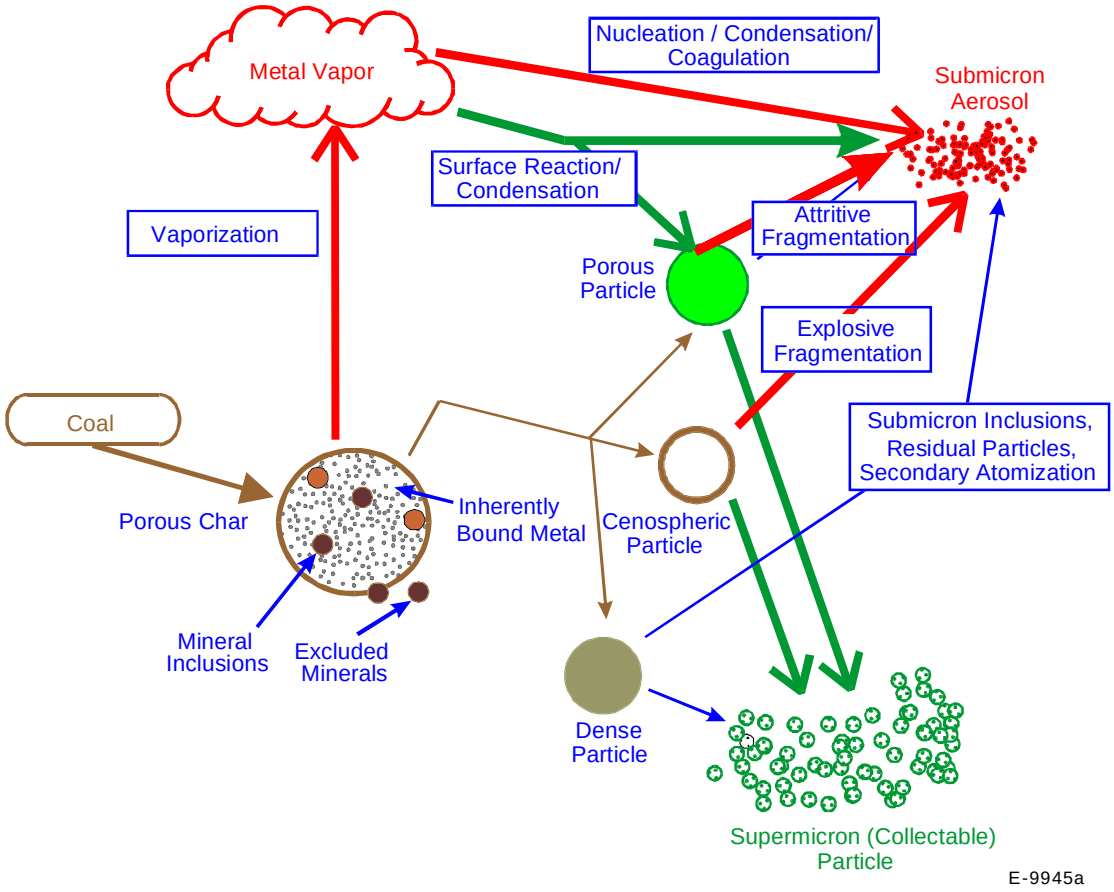

Figure 2-3. Possible transformation pathways of inorganic elements during pulverized coal combustion.

The fractionation of larger particles to submicron-sized particles also contributes to the submicron fume [26, 27, 29]. The contribution from fractionation is highly coal dependent.

The volatility of trace elements in the coal is highly dependent on the forms of occurrence. Bool and Helble [29] determined that elements associated with the coal organic matrix and those associated with reactive mineral pyrite were highly volatile while those associated with silicate or oxide minerals were relatively non-volatile.

Due to the low concentration of trace elements compared to the major species in the coal, there is a very high probability that a volatilized trace element molecule will contact submicron or supermicron particles prior to reaching the supersaturation conditions required for nucleation. Therefore, most of the volatilized trace element molecules are expected to heterogeneously partition onto the surfaces of both submicron and supermicron particles [30] prior to the exit of the combustion system.

Submicron particles formed by nucleation of major elements have a high number density [28]. The combination of small size and high number density leads to a very high surface area density (surface area/unit mass). Thus, there will be an enrichment (i.e., higher

concentration) of volatilized trace elements onto submicron particles compared to the bulk fly ash [24, 31].

While supermicron particles have a lower specific surface area than submicron particles, the total surface area available on supermicron particles exceeds the total available on submicron particles. As a result, the supermicron particle region will contain a higher mass fraction of the total trace elements available than the submicron particles.

Impacts from Submicron Particle Emissions

Trace elements contained in submicron particles are of concern because the collection efficiency of electrostatic precipitators and filter bag control equipment is lower for submicron particles than for supermicron particles [10, 32, 33].

It has also been shown that the residence time of submicron particles in an atmospheric aerosol is an order of magnitude longer than for supermicron particles. Esmen and Corn [34] estimated the mean residence time of submicron particles to be 100 to 1000 hours while the mean residence time of supermicron particles is 10 to 100 hours. Thus, greater emission of submicron particles from commercial coal combustion sources may represent a greater risk of trace element inhalation into human and animal respiratory systems. Once present in the lungs, submicron particles have been shown to defeat the human respiratory filtration system and tend to become lodged in the lungs [24, 33, 35, 36].

The lower removal efficiency in flue gas particle collection equipment may also increase the deposition of submicron particles in the downwind environment and subsequent migration into the water table [36, 37].

Impacts from Bulk Fly Ash Disposal and Utilization

For supermicron particles, often known as bulk fly ash, an important concern is the forms of occurrence of trace elements on or within the particle matrix and the consequences of these forms of occurrence for leachability of potentially toxic trace elements during fly ash disposal or reutilization [37-41]. Vaporized trace elements that redeposit onto the surface of supermicron particles are more likely to leach into moisture sources that non-volatilized trace elements bound within particle fragments. The chemical form of the trace element on the particle surface can substantially affect the solubility of that trace element in aqueous environments.

2.2 Program Overview

Our general approach to the development of the ToPEM model is to break the process for toxic formation into sub-processes, each of which will be addressed by team members who are experts in the area. Ultimately, this will result in new sub-models which will be added to the existing Engineering Model for Ash Formation (EMAF) to create ToPEM. Table 2-1 describes the work breakdown structure for the Phase II program. Figure 2-4 illustrates the relationship between the elements of the Phase I work breakdown structure and the sub-processes. Each of the areas identified in the figure will be addressed in the Phase II program as described below.

Table 2-1. Task Breakdown

Technical Task	Team Member
Program management	PSI
Coal acquisition, characterization	PSI
Coal, ash trace element characterization	PSI
Coal characterization -- forms of occurrence	UK, USGS
Coal, ash trace element characterization and mercury capture and analysis	MIT
Mechanistic study: dilute bench scale combustion tests plus equilibrium, kinetic modeling	UU
Large scale tests at 100,000 Btu/h facility	UA
Mechanistic study of kinetic rates for gas-phase reactions	UC
Mercury-fly ash interactions at bench scale	EERC
Speciation of Hg (and other elements) on ash and sorbents	UK
Fundamental Engineering Model development	PSI
Inorganic emissions: literature survey and model validation	UC

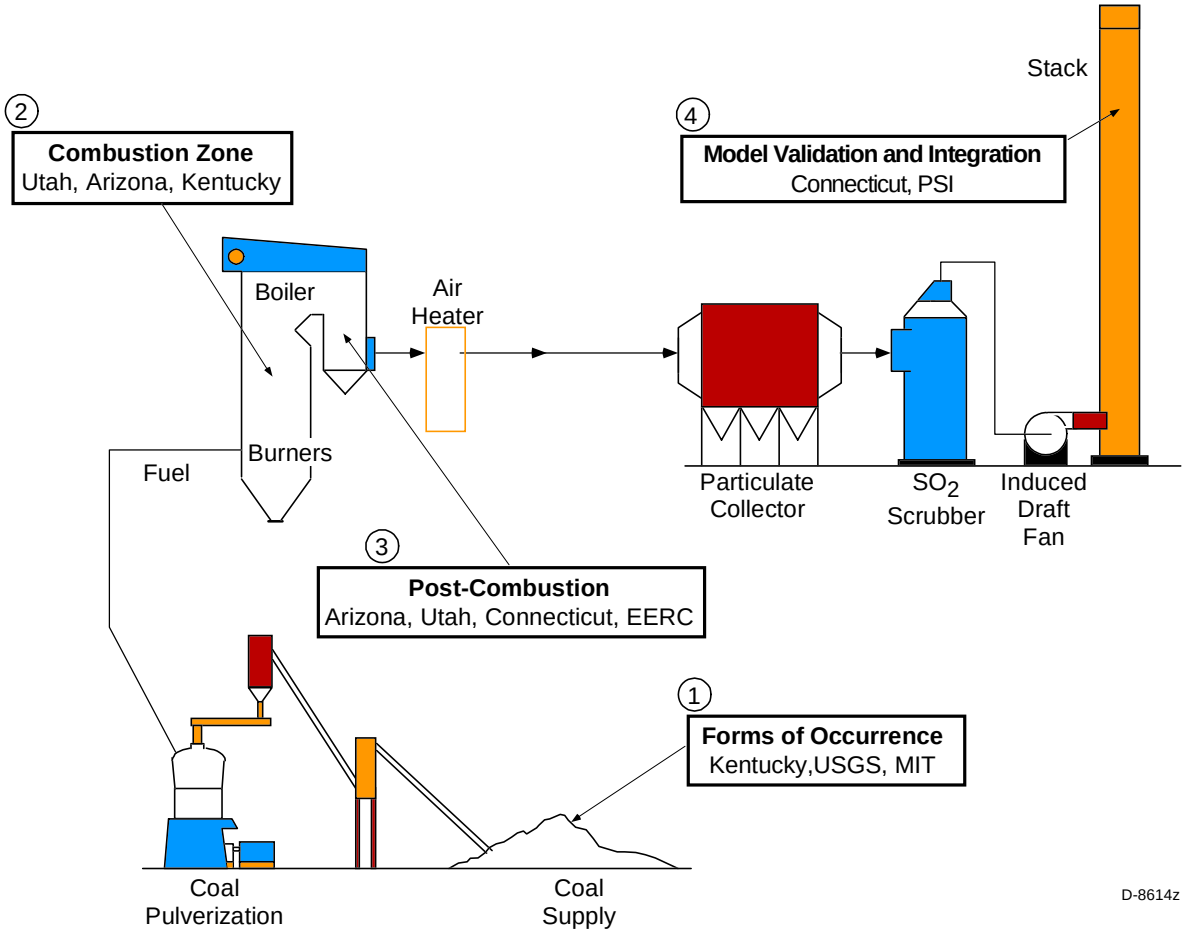

Figure 2-4. Phase II program organization.

Forms of Occurrence of Trace Elements in Coal

One of the most important questions to be answered in the program as a whole is whether the form of a particular element in the coal affects its form of emission at the end of the process. The answer to this question will determine the shape of the sub-models that must be developed in this program. Thus, a detailed understanding of the forms of individual trace elements in coal provides a foundation for much of the rest of the program. Key issues that will be addressed in Phase II are the specific mineral associations of individual elements and the relationship between trace metal form and "standard" coal analyses.

Because of the importance of elemental form (e.g., sulfate versus silicate mineral) on partitioning, it is critical that coals representing a broad range of elemental forms be examined in this program. In Task 2 we will select and acquire a total of three coals for study in this program. The coals chosen will represent a broad range of elemental forms of occurrence taken from the major coal ranks and commercial coal seams used for pulverized coal power generation in the U.S. Once selected, fresh coal samples will be acquired and distributed to team members. These samples will be subjected to ultimate, proximate, and ASTM ash analysis. Coal samples will be analyzed for trace element concentrations by Neutron Activation Analysis (NAA) at the MIT Nuclear Reactor Laboratory (Task 5.2).

Advanced analytical techniques such as Mössbauer spectroscopy and Computer-Controlled Scanning Electron Microscopy (CCSEM) will be used by UK (Task 3) to determine the major mineral species present in the program coals and the combustion generated ash. Whole coal samples and density segregated coal samples will be studied. This analysis will provide important insight on the minerals present in the coal, how they interact during the combustion process, and how this interaction may affect the partitioning of toxic elements.

Another important issue is the form-of-occurrence of the trace elements in the coal. In this task the mode of occurrence of As, Cr, and Se will be determined by combining XAFS and the Mössbauer/CCSEM derived data discussed above. Hg will also be evaluated where possible.

Other less critical trace elements (Mn, Ni, Zn, Pb, U, etc.) may also be evaluated, especially if their abundance is unusually high in any of the program coals. In addition, the form-of-occurrence of Cl and S in coals and chars will be investigated.

As a complement to the XAFS analysis mentioned above, a unique protocol developed by USGS will be used in Task 4 to analyze selected raw coal, and size and density segregated coal, samples for trace element forms of occurrence. This protocol combines low temperature (< 200EC) ashing, chemical analysis, x-ray diffraction, coal segregation via flotation, ammonium acetate and selected acid leaching, electron microbeam measurements, and low and moderate temperature heating tests to determine the forms of elements in coal. Because of the unique combination of existing testing and analytical facilities available at USGS, the work will be conducted at USGS laboratories.

Combustion Zone Transformations

The effect of coal type and combustion conditions on the emission of the toxic trace elements will be investigated using the UU laminar-flow drop tube reactor (Task 5.1). The fundamental mechanisms of toxic species formation and partitioning will be determined from careful examination of the ash formed under a variety of combustion conditions. Measurements will be made of the partitioning of the trace elements in the three coals as a function of temperature and equivalence ratio. These measurements will provide the baseline data on the fraction vaporized. Individual size-segregated ash samples (collected with a cascade impactor) will then be analyzed by NAA for total composition and other analyses as needed, for example, Auger and STEM for surface composition, TEM and SEM for particle morphology, and possibly water washing and/or chemical leaching to determine the solubility of selected trace elements in the ash samples. Samples will also be submitted to UK for chemical species analysis by XAFS and other techniques.

Post-Combustion Transformations

The goal of this task is an increased understanding of the transformations of selected metals as the flue gases cool following the high temperature combustion zone. Bench scale experimentation will be carried out by several organizations as well as large scale combustion measurements. Advanced analytical methods will be used extensively to understand speciation of trace elements in the post-combustion flue gas.

At UC (Task 10) experiments will focus on determination of trace vapor-ash particle reactions rates in post-combustion gases, including

- Identification of the rate controlling phenomena in the oxidation of arsenic under combustion conditions
- Relative rates of gas-phase reaction of elemental mercury with HCl and Cl_2 under combustion conditions
- Measurement of rates of heterogeneous conversion of HCl to Cl_2 in the presence of coal combustion products such as iron oxide, iron sulfate, and fly ash samples.

Interactions of mercury with ash and ash components at lower temperatures will be the focus of the effort at EERC in Task 11. A bench-scale sorbent evaluation system will be used to increase our understanding of the interactions between gas-phase mercury and coal ash. Experiments will explore the effects of temperature and the interactions between elemental mercury or mercuric chloride and fly ash samples generated under oxidizing conditions, the effect of mercury concentration on the interactions between elemental mercury and fly ash, and the effect of coal combustion conditions on the ash and ultimately on the interaction between mercury and ash.

On a larger scale in Task 6, UA will determine how both coal composition, detailed mineralogy and combustion conditions (including low NO_x conditions) govern the fate of toxic metals under practical time/temperature, self sustained, yet still aerodynamically well defined, pulverized coal combustion conditions. Program coals will be burned in the UA self-sustained

combustor under premixed conditions. The baseline tests will employ the naturally occurring temperature profile for each coal at a stoichiometric ratio of 1.2. Samples will be withdrawn at several ports, representing a range of temperatures and residence times. Complete impactor samples will be collected and analyzed for each toxic metal (11 as listed in the CAAA plus U and Th) plus major elements. This will yield the particle size segregated toxic metal composition, which can be compared to data obtained from other tasks of this program. These data will then be examined to determine particle size dependence in order to infer possible mechanisms governing the fate of each metal.

Model Validation

UC will conduct a more in-depth review of the relevant field data on inorganic emissions (Task 9.2). In Phase II we will emphasize use of the field data to validate the models we will develop. The Phase II effort focuses on data from the following sources:

- EPRI PISCES
- DOE Program
- VTT (Finland)
- KEMA (Netherlands).

Important issues to be addressed when reviewing these data include mass balance closure, methods of analysis and sample collection, effect of APCD, effect of bulk coal ash chemistry, particle size distribution, and speciation of Hg.

Model Development

In Task 9.1, data obtained from subcontractor and PSI tasks will be combined to create a comprehensive model of the transformations of important inorganic species during combustion. This model, denoted the ToPEM, will be based on an existing model (the PSI Engineering Model for Ash Formation which predicts ash particle size and composition distributions – EMAF). Because the development of this model is strongly dependent on the mechanistic, equilibrium, and kinetic information being developed under the experimental tasks, ToPEM will incorporate information on the mechanisms controlling species behavior, equilibrium modeling where appropriate and kinetic modeling to mimic kinetic constraints on species behavior. During the later stages of the Phase II work, sufficient detailed information will be available to support specific modifications to EMAF in order to describe the combustion transformations of important inorganic trace elements. Based on the experimental studies, equilibrium modeling, and kinetic modeling, it will be clear which modifications are required. Once complete, the model will be validated using a combination of laboratory and field data. As part of the validation effort, coal and size fractionated ash samples collected from operating utility boilers will be provided by Dr. Esko Kauppinen of VTT, Finland. Once validated, the ToPEM will be used to simulate the behavior of these and other coals under utility boiler conditions. The results from these simulations will then be compared to field data from PISCES obtained through EPRI participation in this program, DOE field sampling campaigns, and other relevant data in the literature. This validation procedure will ensure that the model developed as the result of the proposed research efforts accurately predicts the behavior of toxic metals species from a wide range of coals during the combustion process in any combustion system.

SECTION 3

RESULTS AND DISCUSSION

3. RESULTS AND DISCUSISON

3.1 Coal Characterization (UK, USGS, MIT)

3.1.1 Coal Composition

One of the primary goals of this program is to determine the mechanisms that govern the partitioning of trace elements into forms that may be emitted from commercial power plants, with the ultimate goal of developing a model framework to predict potential emissions. For this reason it is extremely important that the coals (and the experimental conditions) used in this program be directly applicable to commercial systems. By studying coals that are either currently in widespread use, for which a great deal of operational information exists, or are potentially attractive as 'compliance coals', we can facilitate the use of the information obtained in this program in the full scale systems.

Another important criterion for coal selection is the mode-of-occurrence of the trace elements in the coals. As one of the technical objectives of the program is to explore the link between the mode-of-occurrence of a given element in coal and its partitioning into potentially emitted phases (i.e., submicron fume or vapor), it is important to pick coals that should have a wide range of modes of occurrence for selected elements. As this information is not always readily apparent, at least two coals were selected based on either knowledge gained in previous programs at PSI or knowledge of the general trends of trace elements with other coal parameters, such as ash content and sulfur content. In addition, in order to facilitate XAFS analysis of the coals, efforts were taken to maximize the arsenic concentrations in the coal, while still only utilizing those coals that are suitable for use in commercial power plants.

The coals in Phase II were chosen in an attempt to (1) represent a broad range of elemental forms of occurrence and (2) represent the major coal ranks and commercial coal seams used for pulverized coal power generation in the U.S. A bituminous coal from Ohio coal was selected for study. The particular coal sample was a blend of three seams: Ohio 5, Ohio 6, and Ohio 7. This blend was made for testing at McDermott Technologies Clean Environment Development Facility (CEDF). The CEDF test program, also sponsored by DOE, is intended to study mercury emissions from coal-fired combustion systems and the interactions of mercury and air pollution control devices such as scrubbers. A similar coal, a blend of Ohio 5 and 6 seams, is burned at a full scale power plant which is currently being sampled for trace element emissions in another DOE-sponsored program.

The second coal in Phase II is a lignite from North Dakota (Hagel Bed). This coal is burned at a mine-mouth utility power plant in North Dakota. While lignites are not major steam producing coals throughout the United States, they are important regionally. The mineralogy of lignites from this seam is different from other coals. A pulverized sample was obtained from EERC. This coal is also burned at a full scale power plant which will be sampled for trace element emissions in another DOE-sponsored program.

The third coal is from the Wyodak seam. This is a sub-bituminous coal from the Powder River Basin and is an important steam coal. The Phase I Wyodak sample was obtained through ABB. Since there was not enough of the Phase I material left for Phase II, a fresh sample was

procured from a power plant which burns this coal. Both Phase I and Phase II samples came from the same mine, although the samples were mined approximately 2 years apart. Approximately 1.5 tons of coal were shipped from the power plant to EERC. The coal was pulverized this quarter and shipped to UA.

Upon receipt of the three Phase II coals, geochemical splits of each coal were prepared and sent to Geochemical Testing, Inc., of Somerset, PA for coal analyses not available at the USGS. These tests include proximate analysis, ultimate analysis, heating value, forms of sulfur, free swelling index, and ash fusion temperature. Complete coal testing results are included in Appendix A. These results are reported on an as-received basis, on a dry basis, and on a dry ash-free basis.

Tables 3-1 through 3-3 summarize the coal composition analyses. The coal particle size distribution is shown in Table 3-4. The Ohio coal has a moderate sulfur content (2.62 wt%, as received) which is intermediate between the Phase I Illinois and Pittsburgh coals. (For reference, analyses for the Phase I coals are given in Appendix B.) The ash is lower in iron than the Illinois and Pittsburgh coals. The North Dakota lignite has a substantial amount of water as well as a moderately high (~10%) ash content.

Table 3-1. Coal Properties Phase II Program Coals (As-received basis)

	Wyodak	**Ohio 5,6,7**	**ND Lignite**
Proximate, wt%			
Moisture	25.81	2.33	35.88
Volatile matter	34.85	39.19	28.15
Fixed carbon	33.31	48.78	26.59
Ash	6.03	9.70	9.38
Heating Value, Btu/lb	8,869	12,865	6,392
Ultimate, wt%			
Hydrogen	6.51	5.07	6.59
Carbon	51.19	71.07	38.57
Nitrogen	0.72	1.37	0.42
Sulfur	0.32	2.62	0.63
Chlorine	0.0026	0.0974	0.0036
Oxygen	35.23	10.17	44.41
Ash	6.03	9.7	9.38

Table 3-2. Coal Ash Composition (wt%, sulfur-free basis)

	Wyodak	**Ohio 5,6,7**	**ND Lignite**
SiO_2	43.28	38.09	22.00
Al_2O_3	17.17	39.41	20.38
Fe_2O_3	6.32	13.03	11.75
TiO_2	1.38	2.04	0.50
P_2O_5	1.78	0.51	0.13
CaO	22.74	2.24	30.25
MgO	4.03	1.02	8.00
Na_2O	1.67	0.92	5.12
K_2O	0.45	2.55	1.38
BaO	0.68	0.20	0.50
SrO	0.49		

Table 3-3. Forms of Sulfur in Phase II Coals (wt%, as-received basis)

	Wyodak	Ohio 5, 6, 7	ND Lignite
Sulfate	0.01	0.02	0.09
Pyritic	0.04	1.39	0.18
Organic	0.27	1.21	0.36

Table 3-4. Coal Particle Size Distribution for Phase II Coals (in wt%)

Size Range, microns	Wyodak	Ohio 5, 6 & 7	North Dakota Lignite
2.2-2.6	1.7	0.6	0.3
2.6-3.0	1.7	0.8	1.0
3.0-3.4	1.8	1.2	1.2
3.4-4.0	1.6	1.4	1.3
4.0-4.6	1.9	1.1	0.9
4.6-5.3	2.7	1.1	0.9
5.3-6.2	3.7	1.2	1.5
6.2-7.2	4.4	1.8	2.2
7.2-8.3	4.4	3.1	2.9
8.3-9.6	3.9	3.3	3.4
9.6-11	3.6	2.5	3.1
11-13	4.1	2.2	2.9
13-15	4.9	3.2	3.1
15-17	5.5	5.0	4.6
17-20	5.7	6.4	6.9
20-23	5.3	6.6	7.7
23-27	3.9	4.7	5.7
27-37	3.0	4.0	4.6
31-36	3.1	5.2	5.6
36-42	3.7	6.9	7.2
42-49	4.3	7.8	7.8
49-57	5.0	7.9	7.4
57-66	5.5	7.1	6.3
66-76	5.4	6.1	5.0
76-88	4.7	4.7	3.7
88-102	3.3	3.1	2.3
102-118	1.3	1.1	0.8

Total sulfur contents range from 0.32 wt·% (as-received) in the Wyodak to 2.62 wt·% in the Ohio sample, about half of the total sulfur is pyritic and half is organic. In the North Dakota sample (total sulfur 0.62 wt·%), the organic sulfur content is 0.36 wt·%, and the pyritic sulfur fraction is exactly half that of the organic sulfur. The remainder of the sulfur in the North Dakota sample (0.09%) is present as sulfate, consistent with the presence of barite in this sample. In the Wyodak sample, the majority of the sulfur is organic.

The lignite has more sulfur than the Wyodak coal and about 1/3rd of the sulfur is pyritic, indicating that this coal will have a significant amount of pyrite. This can also be seen from the ash analysis since the ash has a moderate amount of iron oxide. The ash is also high in calcium, magnesium, and sodium. These are probably organically associated to some degree. The

Wyodak sample contained more moisture, as received, than the Phase I sample. The ash contains somewhat less calcium than the Phase I sample.

The chlorine contents of the Wyodak coal and the North Dakota lignite are low, 26 ppmw and 36 ppmw, respectively. The Ohio bituminous coal, on the other hand, has a chlorine content of 974 ppmw which is in the range of values for U.S. bituminous coals.

Table 3-5 presents the elemental composition of the raw coal samples as measured by neutron activation analysis (NAA) at MIT.

Table 3-5. Trace Element Concentrations in Phase II Coals by Neutron Activation Analysis (as received basis)

Element (μg/g)	**Wyodak**	**+/-**	**Ohio 5, 6, 7**	**+/-**	**ND Lignite**	**+/-**
Al	5400	400	11100	390	5400	400
Ti	530	160	670	190	330	120
Fe	2300	170	15100	650	5300	350
Ca	**7900**	**680**	**1400**	**220**	**13000**	**540**
Mg	1700	540	760	450	3100	950
Na	660	60	350	43	2400	180
K	2300	1800	2500	780	<3200	
Cl	62	26	880	120	170	55
Sc	1.40	0.09	3.90	0.25	1.20	0.09
V	14.0	1.8	23.0	2.5	11.0	1.5
Cr	7.3	0.6	19.0	1.7	8.5	1.1
Mn	8.2	0.4	19.0	0.7	44.0	1.6
Co	5.1	0.4	5.8	0.5	6.4	0.6
Zn	52	13	39	9	57	14
Ga	9.7	5.2	11.0	5.4	17.0	
As	1.4	0.2	19.0	1.9	8.1	0.8
Se	1.08	0.75	1.40	0.77	1.50	1.40
Br	1.2	0.3	23.0	6.2	1.9	0.5
Rb	20.0		21.0	8.6	32.0	7.8
Sr	100	37	100	38	120	50
Mo	1.5	0.4	7.6	1.8	0.7	0.3
Cd	0.24	0.20	0.40	0.30	0.21	0.20
In	0.07	0.04	0.06	0.07	0.12	0.12
Sb	0.40	0.03	2.30	0.18	0.91	0.08
Cs	2.50	0.50	0.63	0.30	0.50	0.36
Ba	380	53	102	43	420	75
La	4.00	0.25	9.40	0.60	3.10	0.33
Ce	7.4	0.5	14.0	0.8	4.3	0.6
Nd	2.6	0.6	11.0	2.1	1.8	0.6
Sm	0.60	0.05	2.00	0.17	0.50	0.04
Eu	0.25	0.08	0.38	0.15	0.27	0.08
Yb	0.30	0.06	1.10	0.20	0.40	0.10
Lu	0.04	0.01	0.22	0.05	0.04	0.01
Au (ng/g)	5.0	2.7	3.0	2.0	1.7	0.9
Hg	0.13	0.01	0.15	0.01	0.13	0.01
Th	1.30	0.10	2.70	0.26	1.20	0.14
U	0.70	0.05			0.80	0.06

Additionally, splits of the three Phase II coals were also sent to USGS Energy Program Laboratories in Denver for bulk elemental analysis using methods described in a previous section. These results are shown in Table 3-6. These results are used as the elemental totals that selective leaching fractions are compared to. A series of blind replicate analyses of the three program coals is given in Appendix C.

Table 3-6. Elemental Concentrations for Phase II Whole Coals
(Values are in ppm on a dry basis)

Element	Ohio	Wyodak	ND	Element	Ohio	Wyodak	ND
Li	11	3.7	5.1	**Te**	<0.2	<0.2	<0.3
Be	2.6	0.3	0.8	**Cs**	0.75	0.136	0.58
B	86	42	130	**Ba**	66	450	590
Na	280	860	3800	**La**	9.82	5.60	4.96
Mg	340	1900	4000	**Ce**	18.4	9.3	7.8
Al	9100	7400	9000	**Sm**	2.17	0.96	0.75
Si	19000	13000	25000	**Eu**	0.427	0.193	0.149
P	270	570	170	**Tb**	0.319	0.11	0.111
K	1600	190	1700	**Yb**	0.98	0.42	0.49
Ca	1100	11000	15000	**Lu**	0.137	0.049	0.070
Sc	3.8	1.9	1.9	**Hf**	0.61	0.59	0.61
Ti	580	670	410	**Ta**	0.20	0.159	0.137
V	25	18	15	**W**	1.1	0.48	2.99
Cr	15.3	7.9	11.5	**Au**	<1.0	<0.9	<1.5
Mn	20	8.2	59	**Hg**	0.18	0.13	0.08
Fe	14700	3030	7870	**Tl**	1.3	<0.2	<0.3
Co	4.91	5.66	9.1	**Pb**	9.1	1.9	1.5
Ni	18	4.8	4.3	**Bi**	<0.2	<0.2	<0.3
Cu	9.6	14	5.5	**Th**	2.14	1.85	1.67
Zn	21	8.2	12	**U**	1.25	0.73	1.12
Ga	6.0	2.5	2.3				
Ge	9.8	0.37	1.3				
As	17.8	1.74	10				
Se	1.78	1.31	0.97				
Br	18.7	1.1	2.58				
Rb	11.3	2.1	7.2				
Sr	100	260	420				
Y	9.7	3.5	4.8				
Zr	14	18	26				
Nb	3.0	2.8	3.1				
Mo	4.9	1.1	2.3				
Ag	<0.2	<0.2	<0.3				
Cd	0.1	0.1	<0.1				
Sn	1.0	<0.9	<1.5				
Sb	1.94	0.23	0.70				

The Wyodak coal is generally similar to the Phase I sample in terms of trace element concentrations. Zn and Co are noted to be higher than in the Phase I sample. The new coals (Ohio 5,6,7 and North Dakota lignite) show similar trace element concentrations to the previously studied coals with a few exceptions. Both coals have higher arsenic levels than any others studied in the program. The Ohio coal has the highest arsenic concentration, 19 ppmw. All three Phase I coals show mercury concentrations of about 0.13 ppmw.

3.1.2 Coal Mineralogy

Semi-quantitative determination of sample mineralogy by X-ray diffraction (XRD) of low-temperature ash (LTA) has been completed by USGS and is summarized in Table 3-7. Values listed as trace (tr) range from <1 to 3%; values ≤ 5% are considered trace constituents by this method. Samples with an asterisk were treated with ammonium acetate prior to ashing. Bassanite ($CaSO_4 * ½ H_2O$) is probably an artifact of the ashing process, formed by combination of organic Ca and S, but may also form by dehydration of gypsum. Other possible trace constituents that could not be resolved with certainty are listed below. Phases are listed in boldface where they also have been found in preliminary SEM (Table 3-8). For the North Dakota sample, these are chlorite, apatite, rutile, and anatase (not distinguishable from rutile in SEM). For the Wyodak sample, these are siderite, apatite, and rutile. For the Ohio sample, these are calcite, siderite, chlorite, hematite, apatite, rutile, and barite.

Mineralogy of the three phase II coals determined by SEM/EDX is summarized in Table 3-8. The Ohio 5/6/7 coal contains all of the five most common major phases: quartz, illitic clay, kaolinitic clay, pyrite and calcite. The illite grains in this sample are large (some larger than 50 μm) and well formed, appropriate for further studies using electron microprobe and SHRIMP-RG ion microprobe. The North Dakota and Wyodak samples appear to lack calcite. From the XRD results, it is likely that kaolinite is present in the North Dakota sample. SEM and XRD also show that proportions of illite and kaolinite are very different in the three coals. The Ohio 5/6/7 and North Dakota samples have sub-equal amounts of these clay minerals, whereas kaolinite is by far the dominant clay mineral the Wyodak sample. Pyrite was observed in three coals, and is most abundant in the Ohio 5/6/7 sample (Tables 3-7 and 3-8).

The minor or trace phases found, and their compositions are shown in the lower part of Table 3-8. Each of the three samples contains a TiO_2 phase (probably rutile), monazite (REE phosphate) and sphalerite (ZnS). Barite ($BaSO_4$) and an iron-oxide or hydroxide phase are common in both the North Dakota and Wyodak samples. An interesting suite of accessory silicates is present in the North Dakota sample, including epidote, chlorite, and probable, alkali-feldspar. The presence of these phases suggests a detrital metamorphic contribution to the coal basin.

Table 3-7. Semi-Quantitative Mineralogy by X-Ray Diffraction
(whole ash basis)

Sample	QTZ	FLD	SID	ILL	KOL	PY	BAS	SPL	MAR	HEM
North Dakota	38	tr	tr	12	16	tr	28			tr
North Dakota*	47	tr	tr	12	12	tr	20	tr		tr
Wyodak	26				46		28	tr		
Wyodak*	30				46	tr	23			
Ohio	19	tr		21	43	12	tr	tr	Tr	

where QTZ = quartz; FLD = feldspar; SID = siderite; ILL = illite; KOL = kaolinite; CHL = chlorite; PY = pyrite; BAS = bassanite; SPL = sphalerite; MAR = marcasite; and HEM = hematite

Table 3-8. Mineralogy of PSI Phase II Coals Determined by SEM.
Mineral Phases Observed in SEM are Indicated by an X.

		Ohio	North Dakota	Wyodak
Major Phases				
Quartz		X	X	X
Illite		X	X	X
Kaolinite		X	X	X
Pyrite		X	X	X
Calcite		X		
Minor or Trace Phases				
Epidote	*Fe-Mg-Ca-Al silicate*		X	
Chlorite	*Fe-Mg-Al silicate*		X	
Alkali-feldspar	*K-Al-silicate*		X	
Zircon	$ZrSiO_4$		X	X
Barite	$BaSO_4$		X	X
FeO(OH) phase		X	X	X
TiO_2 phase		X	X	X
Apatite	*Ca-phosphate*	X	X	
Crandellite	*Ca-Al phosphate*			X
Goyazite	*Sr-Al-REE phosphate*		X	
Monazite	*REE phosphate*	X	X	X
Sphalerite	ZnS	X	X	X
Chalcopyrite	$CuFeS_2$			X

3.1.2.1 CCSEM Investigation of Coal Mineralogies

In addition to the spectroscopic work reported in the main body of the Annual Report, UK also performed computer-controlled scanning electron microscopy (CCSEM) analyses of the discrete mineral matter in the three project coals. These results are described herein

The coal minerals analysis (CMA) was performed as described previously [7], but on a new SEM with an ultrathin window detector. This change in detector window thickness necessitated some minor changes in the mineral sorting routine, as the coal minerals analysis scheme was originally designed for a significantly thicker X-ray detector window. The significant variation in X-ray energy of the characteristic K_α emission lines of the elements between Na and Fe results in increasing absorption by the detector window with decreasing energy of the X-rays from Fe to Na. Hence, the significant reduction in window thickness of the new CCSEM detector relative to the original has the effect of preferentially enhancing the X-ray intensities of lower Z elements. Since the classification scheme is based on ratios of the emitted X-rays by different elements, the further apart are two elements in the periodic table, the more the ratio is affected by the difference in window thickness to the point where the classification scheme gives erroneous results.

Using our previous scheme based on a thick window detector, the current particle-by-particle data sets did not yield sensible results for iron sulfates and sulfides because of the difference in absorption of the X-rays of S and Fe by the thin window detector. The binary distribution of Fe/S ratio for all particles in which the X-ray intensity ratio, $(I_{Fe} + I_s)/\Sigma I_i$,

exceeded 0.8 occurred at about 0.76 for the Ohio coal (Figure 3-1). However, as can also be seen from Figure 3-1, the Fe/S distribution is quite sharp and clearly represents a single major Fe-S mineral in the coal. From the Mössbauer data for the Ohio coal (Table 3-9), it is apparent that this distribution can only arise from pyrite as it is the only major Fe,S-bearing mineral in the coal. Hence, a correction factor was calculated from these data to bring the maximum in the Fe/S ratio in line with the value of 0.66 established for this ratio in the thick window detector SEM. Once this change was made, the CMA was re-run and the weight percentage of "Pyrite" increased from 5 wt% to 40 wt%, while the "Misc Sulf" category shrank from 27 wt% to 2 wt%. In addition, a few particles were re-classified as "Ferrous Sulfate", where none had been seen previously in the uncorrected version. Again, this is consistent with the Mössbauer data, which indicates the minor presence of szomolnokite, a ferrous sulfate. Pyrite contents in the other two coals, were also significantly enhanced by the application of the new correction factors.

Data for the discrete mineral species in the three coals are summarized in Tables 3-9 through 3-11. Detailed composition information is given in Appendix D. Each of the three coals is quite distinctive in its discrete mineral composition. The Ohio coal contains illite as the most common clay, whereas the Wyodak coal contains kaolinite as the predominant clay and the North Dakota lignite has appreciable montmorillonite in it. The latter mineral is indicative of a high content of sodium in this coal. The amounts of pyrite are also quite different among the three coals. Figure 3-2 shows the ternary plots for the aluminosilicate minerals in the three coals. The Wyodak coal also contains a significant amount (~10 wt%) of a Ca-Al-P mineral, tentatively identified as crandallite ($CaAl_3(PO_4)_2(OH)_5.H_2O$) or deltaite ($Ca(Al_2,Ca)(PO_4)_2(OH)_4.H_2O$).

Mössbauer Analysis of Coal Samples. ^{57}Fe Mössbauer spectroscopy was performed on all three project coals and on the physically separated fractions of the Ohio coal in order to characterize the forms of iron present in the coals and to estimate the weight percentage of sulfur contained in the coals as pyritic sulfur, using the method described elsewhere [42, 43]. The spectra of the

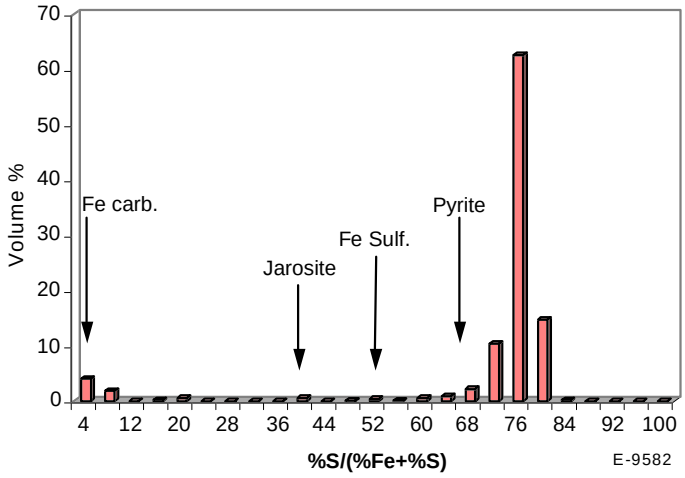

Figure 3-1. Distribution of Fe/S ratio in mineral particles with more than 80% of emitted X-rays from Fe and S for the Ohio coal measured using a ultrathin window X-ray detector. Note the displacement of the distribution peak from the anticipated position for pyrite determined by a thick window detector.

Table 3-9. Size Distribution of Major Minerals in Wyodak Coal

Mineral Species	Wt. %	20 µm	2.5 µm	0.3 µm
		200 µm	20 µm	2.5 µm
Quartz	37.9	23	56	21
Kaolinite	20.1	7	52	41
Misc. Silicates	15.1	20	36	44
Misc. Phosphate	8.6	7	46	47
Misc. Mixed	7.4	5	42	53
Minor Minerals	11.0	14	35	51
Grand Totals	**100**	**16**	**48**	**36**

Table 3-10. Size Distribution of Major Minerals in North Dakota Lignite

Mineral Species	Wt. %	20 µm	2.5 µm	0.3 µm
		200 µm	20 µm	2.5 µm
Quartz	24.4	31	46	24
Illite	12.6	13	59	28
Montmorillonite	5.8	20	40	40
Misc. Silicates	21.9	18	45	37
Pyrite	9.6	22	71	7
Gypsum	5.1	13	75	12
Misc. Sulf.	5.9	17	54	28
Misc. Mixed	7.9	21	35	44
Minor Minerals	6.8	20	44	36
Grand Totals	**100**	**21**	**50**	**29**

Table 3-11. Size Distribution Of Major Minerals In Ohio Coal

Mineral Species	Wt. %	20 µm	2.5 µm	0.3 µm
		200 µm	20 µm	2.5 µm
Quartz	10.4	12	62	27
Kaolinite	8.4	10	40	50
Illite	16	14	57	29
Misc. Silicates	16.5	14	56	31
Pyrite	39.3	53	39	8
Minor Minerals	9.3	40	36	25
Grand Totals	**100**	**31**	**47**	**22**

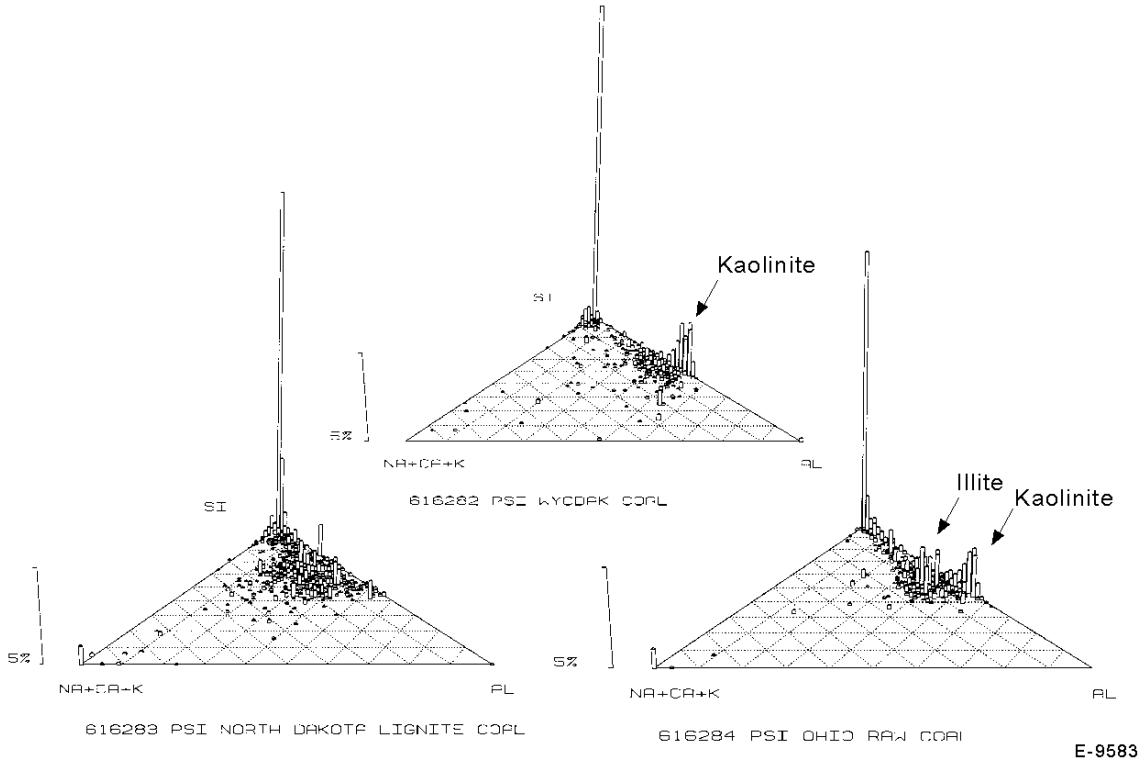

Figure 3-2. (Na+K+Ca)-Al-Si ternary diagrams demonstrating the difference in aluminosilicate mineralogy among the three project coals.

three coals are shown in Figure 3-3 and the results of the computerized analyses are summarized in Table 3-12. The dominant iron-bearing phase in all three coal samples is pyrite, but the two lower sulfur, low-rank coals also contain appreciable iron as clays, sulfates, or carbonates. Pyritic sulfur contents, calculated as described elsewhere [42, 43], are also listed in Table 3-12. These data are used in conjunction with the CCSEM data obtained on the project coals to provide detailed mineralogical descriptions of the coals, as well as for understanding aspects of the occurrence of pyrite-associated trace elements.

It can be seen from the Table 3-12 that the Ohio coal has almost all of its iron present as iron in pyrite or its oxidation products (jarosite and szomolnokite), which are relatively minor. The two lower-rank coals have significantly more of their iron in other primary forms (clay or siderite), but also contain significantly higher fractions of their iron as jarosite, $(Na,K)Fe_3(SO_4)_2(OH)_6$, than the Ohio coal. The presence of jarosite and szomolnokite in the coals themselves is important because it indicates that the pyrite in all three coals has started to oxidize as a consequence of pulverization and exposure of the coal to air. As will be discussed below, this has an important and pronounced effect on the speciation of arsenic.

Mössbauer Analysis of Stored Coal Samples. It was postulated by Dr. Sarofim and co-workers (UU) that storage of coal samples in jars for long periods of time might lead to (a) a segregation of pyrite to the bottom of the jar due to its high specific gravity; and (b) a gradation of coal oxidation between the coal at the top of the jar and the coal at the bottom of the jar. Both of these effects

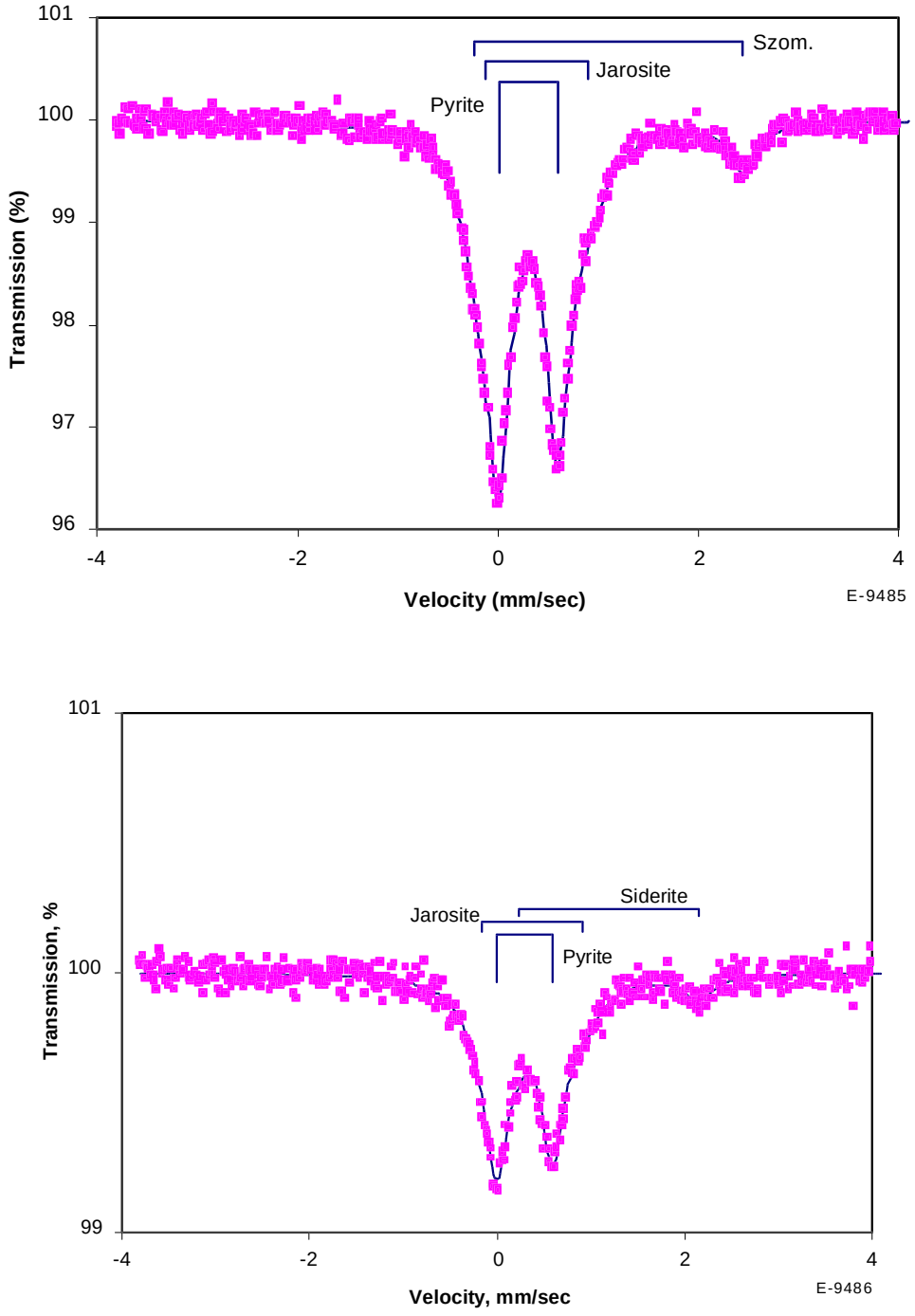

Figure 3-3. Mössbauer spectra of the three project coals.

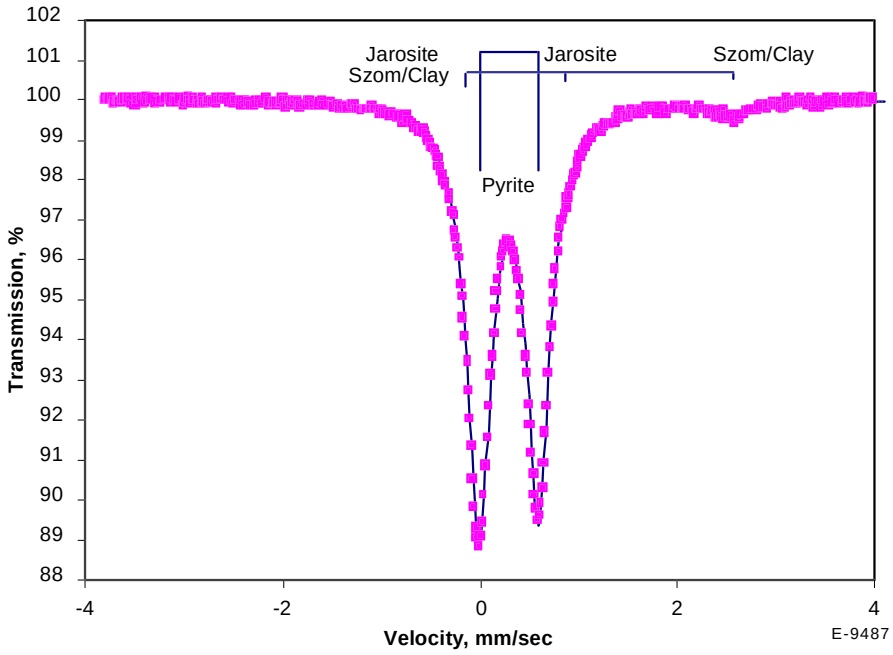

Figure 3-3. (Continued) Mössbauer spectra of the three project coals.

Table 3-12. Mössbauer Results for Phase II Project Coals

Coal Sample	Iron-Bearing Mineral	I.S., Q.S.* mm/sec	% Fe	Pyritic Sulfur wt % of coal
North Dakota lignite	Pyrite	0.30, 0.60	68	0.23
	Jarosite	0.39, 1.03	20	
	Clay	1.10, 2.69	12	
Wyodak	Pyrite	0.30, 0.59	67	0.05
	Jarosite	0.38, 1.08	22	
	Siderite	1.19,1.92	11	
Ohio, raw	Pyrite	0.29, 0.60	88	1.14
	Jarosite	0.36, 1.00	6	
	Clay/Szom.	1.21, 2.70	6	
Ohio, tailings	Pyrite	0.29, 0.60	90	8.8
	Jarosite	0.37, 1.03	6	
	Clay	1.16, 2.64	4	
Ohio, concentrate	Pyrite	0.29, 0.60	91	0.99
	Jarosite	0.36, 1.01	5	
	Clay/Szom	1.20, 2.68	4	
Ohio, HYM fraction	Pyrite	0.29, 0.60	>98	21.4
	Clay/Szom	--- , ---	<2	

*I.S. and Q.S. are the isomer shift and quadrupole splittings, respectively [43, 44].

might contribute to a significant difference in the combustion behavior of the coal from the top and bottom of the jar. To test this hypothesis, various coals that had been stored in jars for long periods of time were divided into top and bottom fractions and subjected to iron Mössbauer spectroscopy. The results for the different fractions are summarized in Table 3-13 and representative spectra are shown in Figure 3-4.

For all samples except the Wyodak samples, the differences between the Mössbauer spectra of the top and bottom layers were not significant in either pyrite content (wt% pyritic sulfur in Table 3-13) or in oxidation, as measured by the ratio of sulfate Fe to pyritic iron. For the Wyodak samples, some significant differences were noted in the ratio of the pyrite:sulfate minerals that may indicate more pronounced oxidation of the top layer.

Table 3-13. Mössbauer Data for Top and Bottom Layers of Coal Samples from UU

Sample ID	Phase	I.S. mm/sec	Q.S. mm/sec	Wdth mm/sec	%Fe	%Pyr S
10. Wyodak Bottom Layer	Pyrite	0.31	0.63	0.4	75	0.035
	Jarosite	0.36	1.27	0.4	25	
9. Wyodak Top Layer	Pyrite/Marcasite	0.32	0.56	0.37	48	0.05
	Jarosite	0.37	1.17	0.37	43	
	Siderite?	1.23	1.86	0.37	9	
8. Pittsburgh Bottom Layer	Pyrite	0.3	0.61	0.28	85	0.75
0.4511 g	Szomolnokite	1.24	2.74	0.27	15	
7. Pittsburgh Top Layer	Pyrite	0.3	0.64	0.29	85	0.69
0.4463 g	Szomolnokite	1.24	2.74	0.3	15	
6. ND Lignite Bottom Layer	Pyrite	0.31	0.61	0.34	66	0.27
0.615 g	Jarosite	0.37	1.13	0.49	22	
5. ND Lignite Top Layer	Pyrite	0.3	0.63	0.38	71	0.23
0.6038 g	Jarosite	0.37	1.23	0.41	16	
	Fe2+/Clay	1.08	2.64	0.42	13	
4. Illinois #6 Bottom Layer	Pyrite	0.29	0.58	0.27	78.5	1.07
0.4566 g	Jarosite	0.31	1.16	0.32	3.5	
	Szomolnokite	1.24	2.7	0.24	18	
3. Illinois #6 Top Layer	Pyrite	0.3	0.61	0.29	79.5	1.15
0.4579 g	Jarosite	0.36	1.19	0.29	1.0	
	Szomolnokite	1.24	2.74	0.29	19.5	
2. Elkhorn Bottom Layer	Pyrite	0.3	0.58	0.33	55	0.15
0.4463 g	Jarosite	0.33	1.14	0.31	12	
	Fe2+/Clay	1.13	2.52	0.46	33	
1. Elkhorn, Top Layer	Pyrite	0.32	0.61	0.36	59	0.17
0.4782 g	Jarosite	0.34	1.25	0.23	8	
	Fe2+/Clay	1.13	2.56	0.45	33	

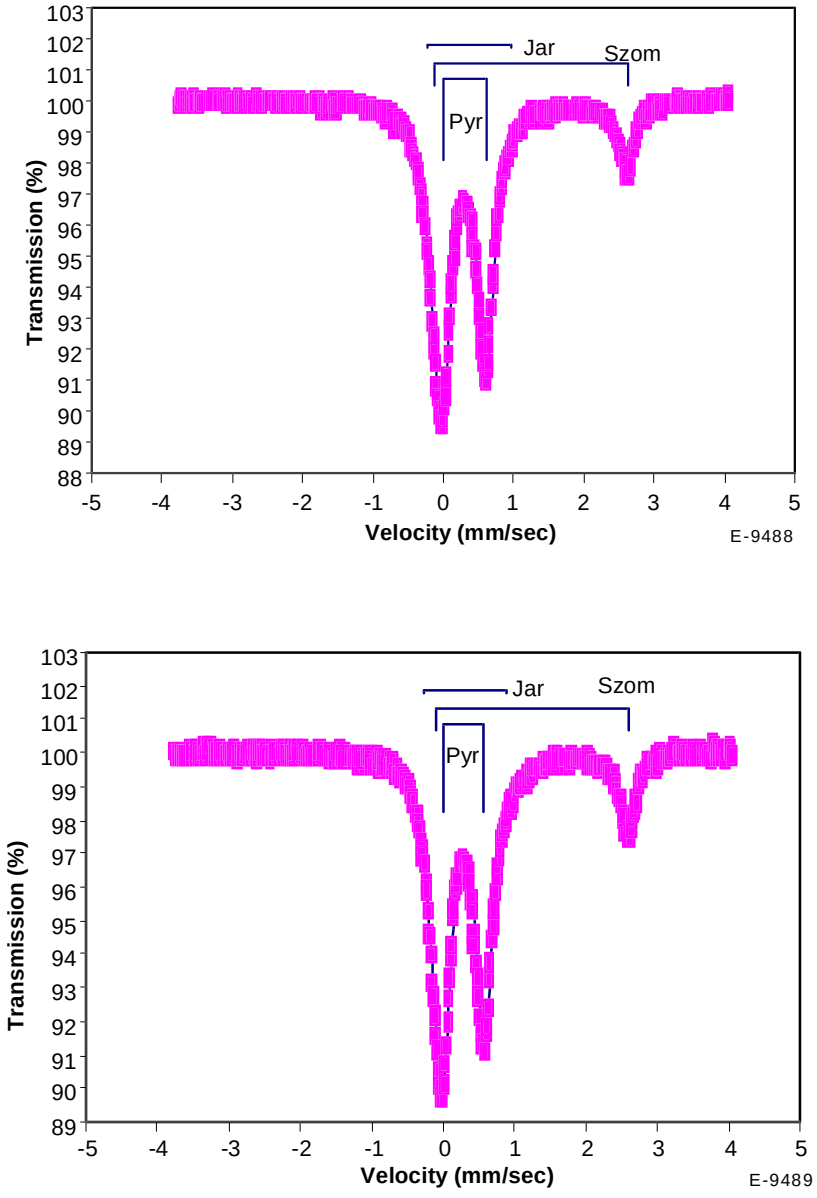

Figure 3-4. Mössbauer spectra of top and bottom layers of Illinois #6 coal.

Comparison of the data in Table 3-12 with those in Table 3-13 allows us to assess the change in oxidation state of the iron with time, since the data in Table 3-12 were collected about 2 years prior to the data summarized in Table 3-13. Unfortunately, the Ohio coal was not included in the suite of coals analyzed at the later date. The data for the North Dakota lignite obtained in 2000 showed little difference from that obtained in 1998, indicating that the pyrite in this coal does not oxidize at a significant rate. However, the lignite does appear to show some significant changes, particularly the top layer fraction from the storage jar, which contains almost half of the iron in the form of jarosite 2 years later.

3.1.3 Trace Element Content of Coals by Selective Leaching and Microprobe Analyses

3.1.3.1 New Approaches In Phase II

The USGS approach to the Phase II investigation is similar to that used in Phase I, with some fundamental additions. In Phase II, leaching data were obtained for 6 elements: Fe, As, Se, Cr, Ni, and Hg, in the three Phase I coals. In the Phase II investigation, leaching data have been obtained for more than 40 elements in three additional coals. A new method for Hg analysis, using a direct mercury analyzer (DMA) procedure has been developed as part of this study. Leaching results are presented in similar detail to those reported in Phase I for only six elements. Pyrite digestion problems encountered in the HNO_3 step of the leaching procedure in Phase I and early in Phase II, have been corrected by adopting a new procedure for this stage of the process. Microanalysis of Phase II coals by electron microprobe was conducted using a similar approach to the Phase I work, but in Phase II, these analyses were followed by trace-element microanalysis with the USGS SHRIMP-RG ion microprobe at Stanford University, and the USGS laser ablation ICP-MS system in Denver. The ion probe analyses confirm the residence of transition metals and other elements of interest in illite/smectite, an important clay mineral in the three Phase II coals. This mode of occurrence is indicated by HF-soluble leaching fractions, and by Phase I and II electron microprobe analyses, indicating that elements such as Cr are present in illite at levels that approach the detection limit of this method. Detailed electron microprobe studies of sulfides in the three Phase II coals was followed by semi-quantitative SHRIMP-RG ion microprobe work and reconnaissance laser ablation ICP-MS analysis. The laser ablation ICP-MS provides quantitative results for a range of chalcophile elements, including Hg, the first direct determinations we have made for mercury in organic or inorganic constituents of coal.

3.1.3.2 Methods

The USGS procedure is intended to determine quantitatively or semi-quantitatively the mode of occurrence of trace elements in coal. This is accomplished by an iterative selective leaching protocol, used in combination with a range of complementary techniques. In the leaching protocol, the amount of each element removed by four different reagents is compared to the concentration of that element in the whole coal to obtain the fraction of an element residing in a given coal component. The sequence of leaching steps, and the intended results, are as follows: 1) exchangeable cations, and a fraction of the carbonate-hosted cations are removed by ammonium acetate; 2) cations primarily associated with carbonates and monosulfides such as galena, sphalerite and chalcopyrite are removed by hydrochloric acid; 3) silicate-associated cations are removed by hydrofluoric acid; and 4) elements associated with di-sulfides (pyrite and marcasite) are removed by nitric acid. Elements not leached by any of the four reagents may be present in the organic portions of the coal, or in insoluble phases such as zircon or titanium dioxides. Additionally, where mineral grains are completely encased by the organic matrix, these “shielded” grains may not be completely digested. As an internal check, leaching results are obtained for both the solid residues (by INAA) and leachates (by ICP-MS and ICP-AES). Element-specific methods are used for selenium (hydride generation) and mercury (see section on mercury). Quantitative results are obtained by interpreting the leaching data together with the results obtained by complementary techniques such as electron microprobe analysis. The microprobe is especially useful for pyrite grains, as many of the elements of interest are present

at concentration levels above the detection limit of about 100 ppm. Other essential components of the USGS procedure include semi-quantitative determination of mineralogy by X-ray diffraction (XRD) analysis of low temperature ash (LTA), and confirmation of mineralogy for operator-selected grains using a scanning electron microscope (SEM) equipped with an energy-dispersive X-ray analyser (EDX). The USGS approach complements results obtained by X-ray absorption fine structure (XAFS) by our colleagues at UK (as discussed in Section 3.1.4). The USGS technique also provides data for elements such as Se and Hg, whose concentrations are commonly too low to obtain XAFS spectra, and for elements with atomic numbers beyond the routine XAFS atomic number range of about 20 to 42 (Ca to Mo). For elements that are common to the two approaches, such as As and Cr, comparison of results obtained by the USGS and by XAFS provides an important confirmation of our results.

Low Temperature Ash/X-Ray Diffraction

To prepare mineral concentrates for X-ray diffraction analysis (XRD), coal samples are subjected to a low temperature (< 200°C) ashing procedure (LTA) in which the bulk of the organic matter is slowly consumed in an oxygen plasma, without altering the mineralogy by phase transformations that generally occur at higher temperatures. The low rank of the North Dakota sample required slight modifications to the standard leaching procedure. Lignites tend to have a high concentration of cations associated with carboxyl groups. These cations neutralize the oxygen plasma during ashing, thus significantly reducing the rate at which ashing occurs. An additional problem with lignites is that the fixation of sulfur as sulfate is much higher than in bituminous coals. As the ashing progresses, this fixed sulfate coats the remaining particles, shielding the surfaces from the oxygen plasma and further hampering the ashing process. Increased formation of sulfates also may obscure the X-ray diffractogram making it difficult to interpret. To prevent these complications, prior to the ashing procedure, the North Dakota sample was treated with an ammonium acetate leach to remove the carboxyl bound cations, and prevent fixation of the organic sulfur as sulfate.

To obtain semi-quantitative information on the minerals present in the coals, samples of LTA were pressed into pellets and analyzed using an automated X-ray diffractometer. Diffraction of Cu Kα X-rays was measured over the interval from 4^{o} to 60^{o} 2θ. Counts were collected at 0.5 seconds per step. The data were processed using a computer program for semi-quantitative mineral analysis by X-ray diffraction [45]. The XRD results were used in conjunction with SEM and electron microprobe data.

Bulk Analysis and Leaching Procedure

Bulk coal analyses utilize a combination of techniques that have been optimized by the USGS for multi-element analysis of coal [46]. In this procedure, ground coal is ashed at 525°C, and analyzed by ICP-AES and ICP-MS. Acid digestions are used for analysis of Li, Be, Na, Sc, V, Cr, Mn, Co, Ni, Cu, Zn, Sr, Y, and Th, by ICP-AES, and for analysis of Ga, Ge, As, Rb, Nb, Mo, Ag, Cd, Sn, Sb, Te, Cs, Au, Tl, Pb, Bi, and U, by ICP-MS. Sinter digestions are used for analysis of B, Mg, Al, Si, K, Ca, Ti, Fe, Zr, and Ba, by ICP-AES, and for analysis of Hf, Ta, and W, by ICP-MS. Element-specific methods on whole ground coal are used for Se (hydride generation) Cl (ion selective electrode) and Hg (see section on mercury).

The sequential selective leaching procedure used in this study is similar to that described by [47], which was modified from that of [48]. Quadruplicate 5 g samples were sequentially leached with 35 ml each of 1N ammonium acetate (CH_3COONH_4), 3N hydrochloric acid (HCl), concentrated hydrofluoric acid (HF; 48%), and 2N (1:7) nitric acid (HNO_3). CH_3COONH_4 removes elements bonded onto exchangeable sites, water-soluble compounds, and some carbonates. HCl dissolves carbonates, iron oxides, monosulfides and certain chelated organic compounds. HF solublizes silicates, and nitric acid dissolves disulfides, especially pyrite. For the first three leaching stages (CH_3COONH_4, HCl, and HF) each sample was shaken in conical bottom 50 ml polypropylene tubes, for 18 hours on a Burrell[1] wrist-action shaker. Formation of gas during some leaching steps requires that each tube be enclosed in double polyethylene bags, closed with plastic coated wire straps. The bags allow gas to escape, but prevent the release of liquid. The HNO_3 digestion was carried out in an Erlenmeyer flask, similar to the method for the determination of pyritic sulfur [49]. This "flask method" is more effective at dissolving pyrite than digestion in tubes, because the partially de-mineralized coal from the first three leaching steps has very low density, forming a protective layer of sediment that covers pyrite concentrated at the bottom of the conical tubes.

Approximately 0.5 g of residual solid was removed for instrumental neutron activation analysis (INAA) and cold vapor atomic absorption analysis (CVAA) for mercury, following at each stage of the leaching procedure. Leachate solutions were analyzed by ICP-AES and ICP-MS. Chemical data for the leachates and the solid residues were processed to derive the mean percentages of each element leached by each of the four solvents. The analytical errors were estimated to be ±2 to ±25% for these data, but errors are generally within ±5%, absolute.

Elements not leached by any of the four reagents may be present in the organic portions of the coal, or in insoluble phases such as zircon or titanium dioxides. Additionally, where mineral grains are completely encased by the organic matrix, these "shielded" grains may not be completely digested. As an internal check, leaching results are obtained for both the solid residues (by INAA, or Hg-specific method) and leachates (by ICP-MS and ICP-AES).

At each step of the leaching process, the samples are leached in duplicate. Early on in Phase II a problem with the normality of the HNO_3 used in that step of the leaching process necessitated re-leaching of the North Dakota and Ohio samples (in duplicate). Later, adoption of the flask method for the HNO_3 step of the procedure necessitated a second round of re-leaching for each of the samples. Results for the first three steps of the procedure (ammonium acetate, HCl, HF) were not affected by these modifications. As a result, leaching results given in this report are based on three duplicate leachings (six samples total) for the North Dakota and Ohio samples, and two duplicate leachings (four samples total) for the Wyodak sample, with the exception of the HNO_3 step. Results for the HNO_3 step are based on the final duplicate leaching, using the flask method (two samples for each coal).

---

[1]Use of trade names and trademarks in this publication is for descriptive purposes only and does not constitute endorsement by the U. S. Geological Survey.

Electron Microprobe and SEM

Electron microprobe analysis and scanning microscopy were conducted on pellets prepared from powdered coal. The pellet formation procedure follows ASTM D2797-85 [50] technique for anthracite and bituminous coal, as modified by Pontolillo and Stanton [51]. In this procedure, approximately 7 to 8 g of crushed sample is impregnated under pressure with Armstrong C4 epoxy. The resultant mold is cured overnight at 60 °C. The pellet is ground and polished using ASTM D2797-85 procedure [50] as modified by Pontolillo and Stanton [51]. The epoxy-coal pellet is first ground until flat and smooth, with a 15-μm diamond platen and then using 600-grit SiC paper. Rough polishing is done with 1-μm alumina and final polishing is completed with 0.06-μm-colloidal silica. Ultrasonic cleaning after each step insures a final product free of extraneous abrasive material.

A JEOL-840 scanning electron microscope (SEM) equipped with a Princeton Gamma-Tech. energy-dispersive X-ray analytical system (EDX) and/or an ETEC Autoscan SEM with a Kevex EDX, was used for SEM examination of the coals. Mineral identifications are based on morphology, and major-element composition of grains. Both secondary electron imaging (SEI) and backscattered electron imaging (BSE) modes were used in coal sample characterization. The BSE mode is especially sensitive to variation in mean atomic number and is useful for showing within-grain compositional variation. By optimizing the BSE image, the presence of trace phases containing elements with high-atomic number can be revealed. Samples were scanned initially to obtain an overall view of the phases present. This was followed by a series of overlapping traverses in which the relative abundance of the phases was assessed. This approach allows the operator to select phases for analysis by EDX and interpret textural relations. EDX analysis provides information on elements having concentrations at roughly the tenth-of-percent level or greater. Typical operating conditions for SEM analysis are: accelerating potential of 10 to 30 kV, magnifications of ~50->10,000 times and working distances ranging from 15 to 20 mm (ETEC Autoscan) and 25 or 39 mm (JEOL-840). SEI and BSE images were used as a guide to locate phases of interest for electron microprobe analysis.

A fully-automated, five spectrometer microprobe instrument (JEOL JXA 8900R Superprobe) was used to quantitatively determine element concentrations in pyrite, illite, and carbonates, by the wavelength-dispersive technique. In our microprobe analysis of pyrite the following elements were measured: Fe, S, As, Ni, Cu, Zn, Se, and Co. Natural and synthetic standards were used. A beam current of 3.0×10^{-8} amps and a voltage of 20 KeV were used in the analysis of sulfides. For quantitative analysis, the probe beam diameter was fully focused, giving an actual working diameter of about 3 μm. The minimum detection limit for microprobe analysis of pyrite was about 100 ppm for each of the trace elements analyzed, using peak counting times of 60 seconds and 30-second upper and lower backgrounds. For Co, the detection limit is limited to about 500 ppm (0.05 wt%) due to an interference with Fe giving a constant background in pyrite of 400 to 500 ppm. Co results shown in Appendix E are background corrected. Analysis counting statistics have a large uncertainty as the detection limit is approached.

SHRIMP-RG Ion Microprobe

Analyses of transition metals and other elements in illite/smectite in the Phase II coals were obtained using the Stanford-USGS SHRIMP-RG ion microprobe at Stanford University. A procedure was developed for analyzing illites using the O_2^- duoplasmatron ion source. Calibration was achieved using aluminosilicate standard glasses that included National Institute of Standards and Technology (NIST) SRM 610 and 612, and USGS standards GSE and GSD, synthetic standards prepared for the USGS by Corning Glass Works, Inc., and glass prepared from powdered USGS rock standard BHVO-1.

Concentrations were obtained by determining the counts/ppm for standards and calculating the concentrations of unknowns by comparing their raw counts to the standard data for glasses whose composition approximates that of the illites. Analysis points were initially subjected to a 1 to 3 min burn-in to stabilize the response. The burn-in was followed by a "short" analysis, consisting of four, seven, or eight elements, to confirm the identity of the grains selected and minimize the contribution of overlapping grains. This was followed by a "long" analysis in which the initial group of elements was repeated together with about ten additional elements or masses. In the August 1999 runs, the short analyses were followed directly by "long" analyses in which the initial seven elements (Mg, Al, Ca, Si, ^{52}Cr, K, and Fe) were re-determined and combined with analyses of Sc, Ti, V, ^{53}Cr, Mn, Co, Ni, Cu, Zn, Rb, and Sr. The same procedure was used to measure these elements in reference standards. A similar procedure was followed in February 2000, except that all the short runs were conducted successively, followed by a series of long runs for only the most promising grains. This modification minimized magnet instability caused by changes to its within-run scan range.

SHRIMP-RG data were also obtained for pyrite in the three Phase II coals and for the Illinois #6 and Pittsburgh samples from Phase I of the program. Minor or trace elements determined include Ti, Cr, Mn, Co, Ni, Cu, Zn, As, Se, Cd, Sb, and Pb, using the oxygen duoplasmatron source. Because suitable standards, offering a close matrix match to the pyrite unknowns, were not available, quantitative results were not obtained. However, the results show relative differences among the samples, when the response for trace elements is plotted as ratios versus ^{32}S or ^{57}Fe, whose content in pyrite is assumed to be uniform. Because the ionization efficiency differs for each element, and relative sensitivity factors (a measure of ionization efficiency) for pyrite are not well known, the ratios determined cannot be used to compute concentrations using Fe or S as an internal standard.

Laser Ablation ICP-MS

Reconnaissance laser ablation ICP-MS data were obtained for pyrite in the Ohio 5/6/7 coal, and for the Illinois #6 and Pittsburgh samples from Phase I. The system used is located in USGS labs at the Denver Federal Center, and consists of a pulsed Nd(YAG) laser coupled to a dedicated ICP-MS. In order to obtain results for Hg at the 0.5 ppm level, instrument conditions included a 50 μm spot, and a laser pulse rate of 20 Hz at 75% energy. These conditions give an excavation rate of about 3 μm/sec. NIST SRM 2710 was used for analysis of Hg, and USGS standard GSE was used for other elements determined, including Cr, Mn, Co, Ni, Cu, Zn, As, Se, Mo, Cd, Sb, Tl, and Pb. Fe was used as an internal standard, and its concentration was fixed at the Fe content of stoichiometric pyrite. Ablated material is introduced into the ICP-MS analyzer

as an argon plasma, therefore, matrix match between standards and unknowns is not critical. Laser ablation ICP-MS data were not obtained for pyrite in the Wyodak and North Dakota samples, because these do not contain pyrite grains large enough to analyze with the 50 μm spot.

3.1.3.3 Leaching Studies

Leaching studies of the three Phase II coals provide semi-quantitative information on the modes of occurrence of trace elements in coal. Leaching results were obtained for 44 elements, ranging from Li to U, in each of the Phase II coals. Our Phase II leaching results show excellent recoveries, totaling 100% or less in all cases. Recoveries less than 100% are acceptable because the procedure does not digest organic portions of the coal, which may be host to a significant fraction of metallic elements, especially in the two low rank coals.

Leaching results are reported in Table F-1 (Appendix F), with the results expressed as a percentage fraction of a given element removed in each stage of the leaching procedure. This compilation is based on weighted averages of replicate analyses of leachate solutions and solid residues. Results are discussed below by coal, and by element, listed in order of atomic number. Leaching data are also shown in Figure 3-5 containing stacked-bar plots for each of the elements. For illustrative purposes, in the first portion of Figure 3-5, elements are grouped by affinities (e.g., chalcophile, lithophile, exchangeable, etc.). Leaching results in the remainder of Figure 3-5 are shown in order of atomic number. Finally, in Table F-2 (Appendix F), we have interpreted the elemental proportions residing in various constituents of the three Phase II coals, based on integrating the results of leaching studies, other results in this study, and our experience with other samples.

Element Associations

The leaching procedure gives a semi-quantitative accounting of the distribution of elements among dominant element modes of occurrence in coal. These include silicates (leached by HF), carbonates (leached by HCl and ammonium acetate), monsulfides (leached by HCl), di-sulfides (leached by HNO_3), loosely bound ions (leached by ammonium acetate), and element-organic complexes (not removed by any solvent). Additionally, information on elements hosted by minor or trace phases, such as phosphates, sulfates, and oxides, can be obtained with knowledge of the leaching behavior of these phases.

Examination of the leaching data is facilitated by using a few definitions: ***Dominant*** element associations are indicated where the amount of an element leached by a given solvent exceeds that of any other solvent, and that of the unleached fraction, and is ≥ 35%. ***Significant*** element associations are indicated for any leached fraction ≥ 25%. Where no leached fraction exceeds the unleached fraction, and the unleached fraction is >50%, that element is said to be ***organic dominant***. ***Subsidiary*** associations are cases where the fraction of an element leached is ≥ 10%. ***Mixed*** associations refer to cases where there are multiple subsidiary associations. ***Bimodal*** associations are cases where the element occurs almost entirely in two forms whose proportion is subequal. These definitions are intended to help us provide consistent descriptions of the results, and do not replace the quantitative or semi-quantitative determinations.

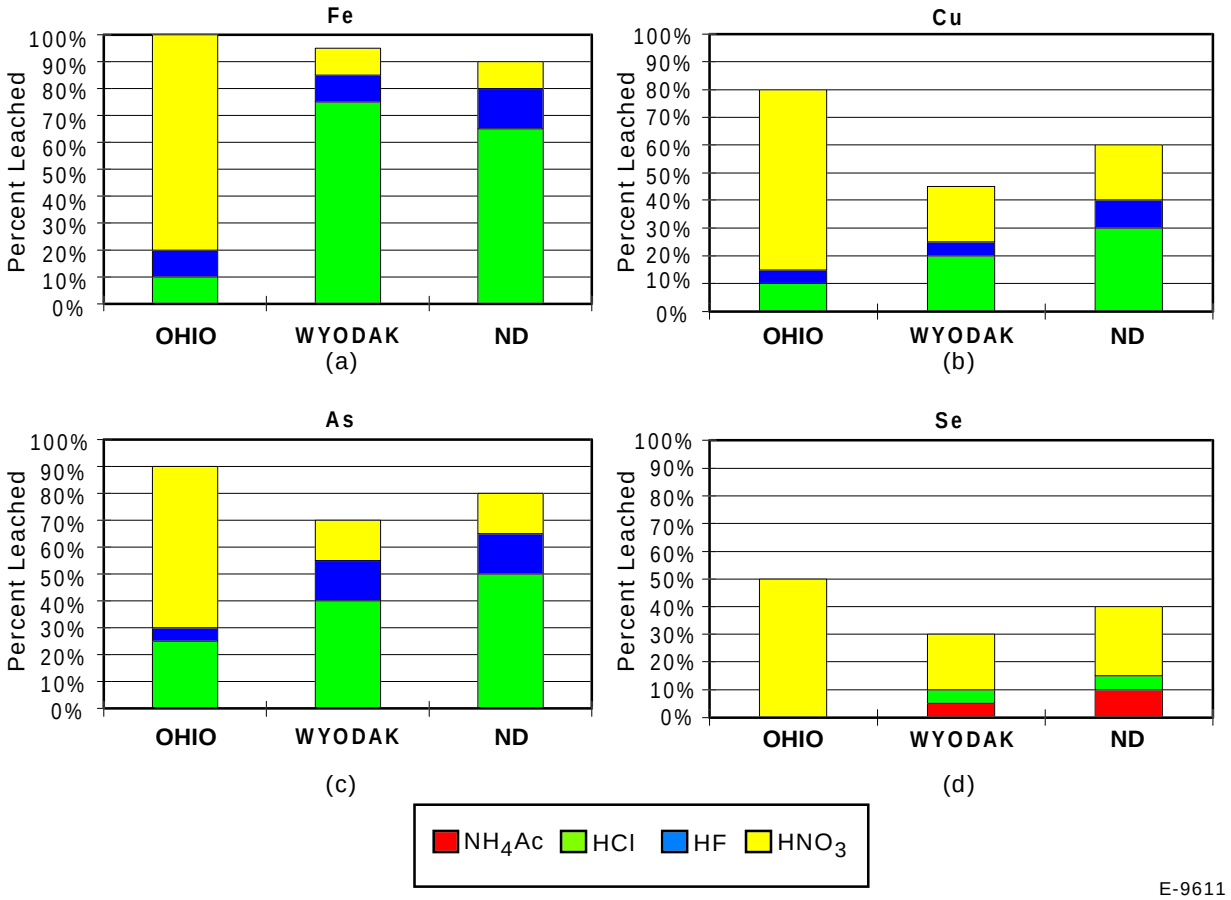

Figure 3-5. Leaching results. (a)-(d) Selective leaching results for Fe, Cu, As, and Se, showing a chalcophile association (primarily in Ohio 56/7).

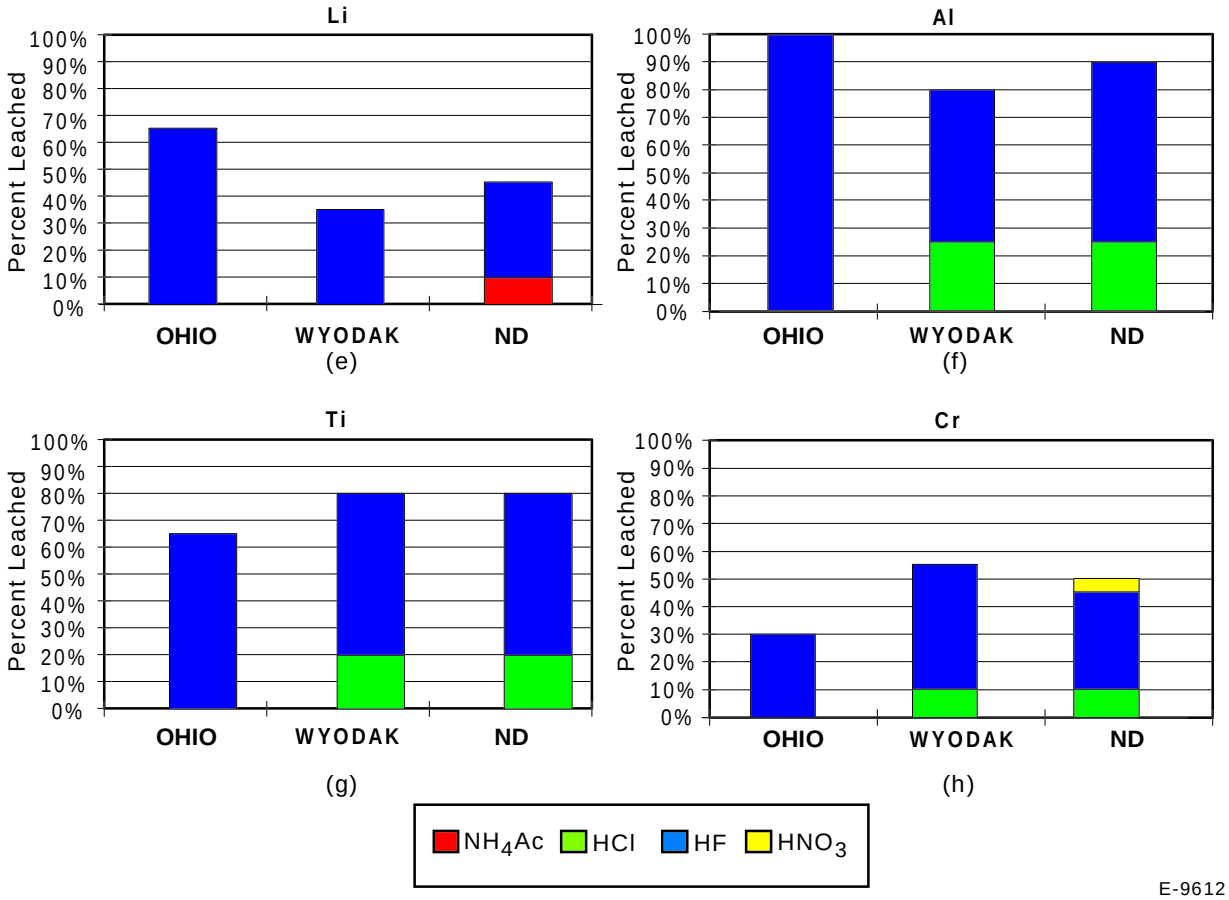

Figure 3-5. Leaching results (continued). (e)-(h) Leaching data for elements Li, Al, Ti, Cr, showing lithophile association.

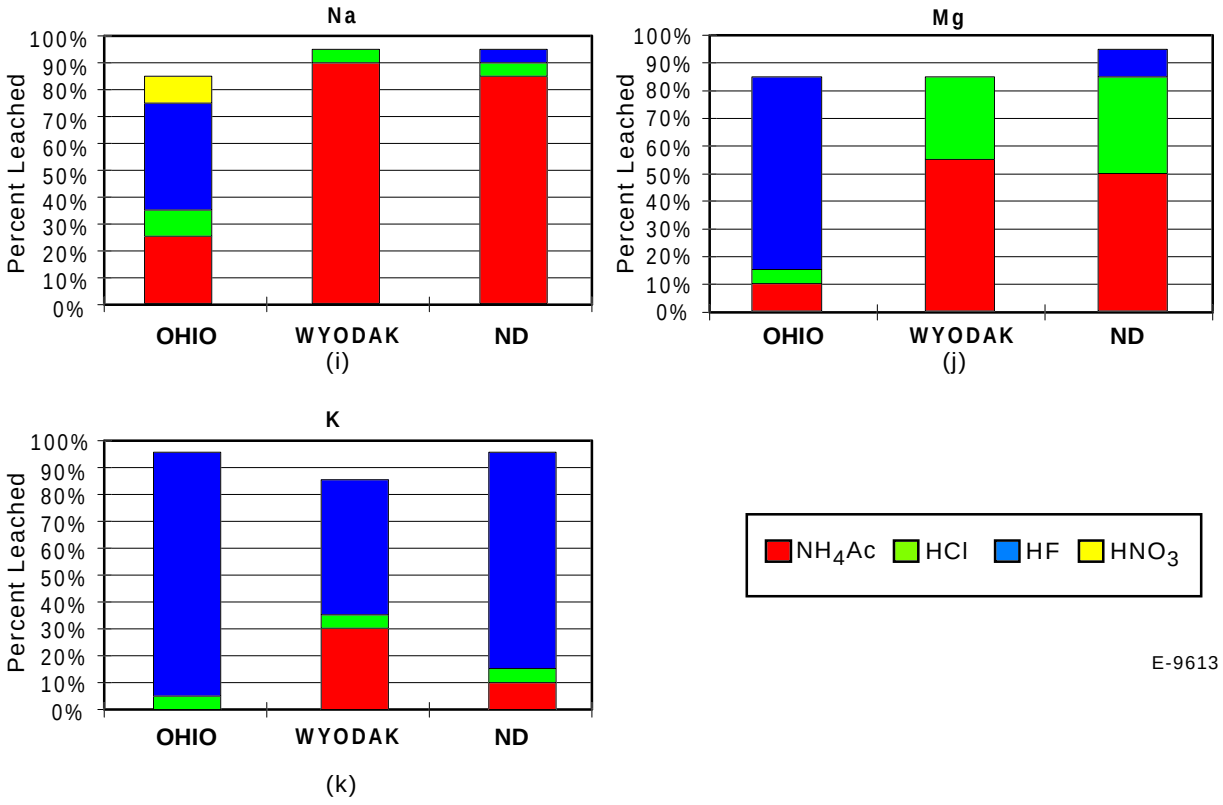

Figure 3-5. Leaching results (continued). (i)-(k) Selective leaching results for elements Na, Mg, K, showing exchangeable component.

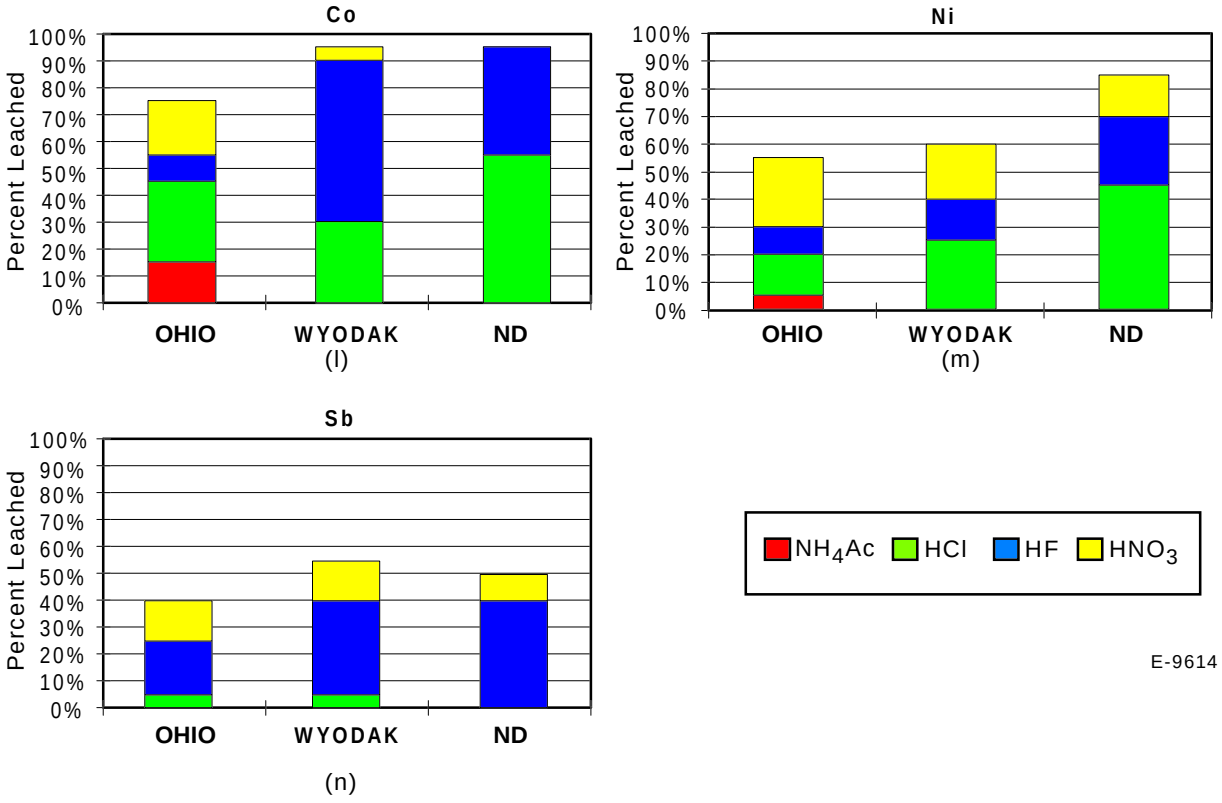

Figure 3-5. Leaching results (continued). (l)-(n) Selective leaching results for elements Co, Ni, and Sb, showing a mixed association.

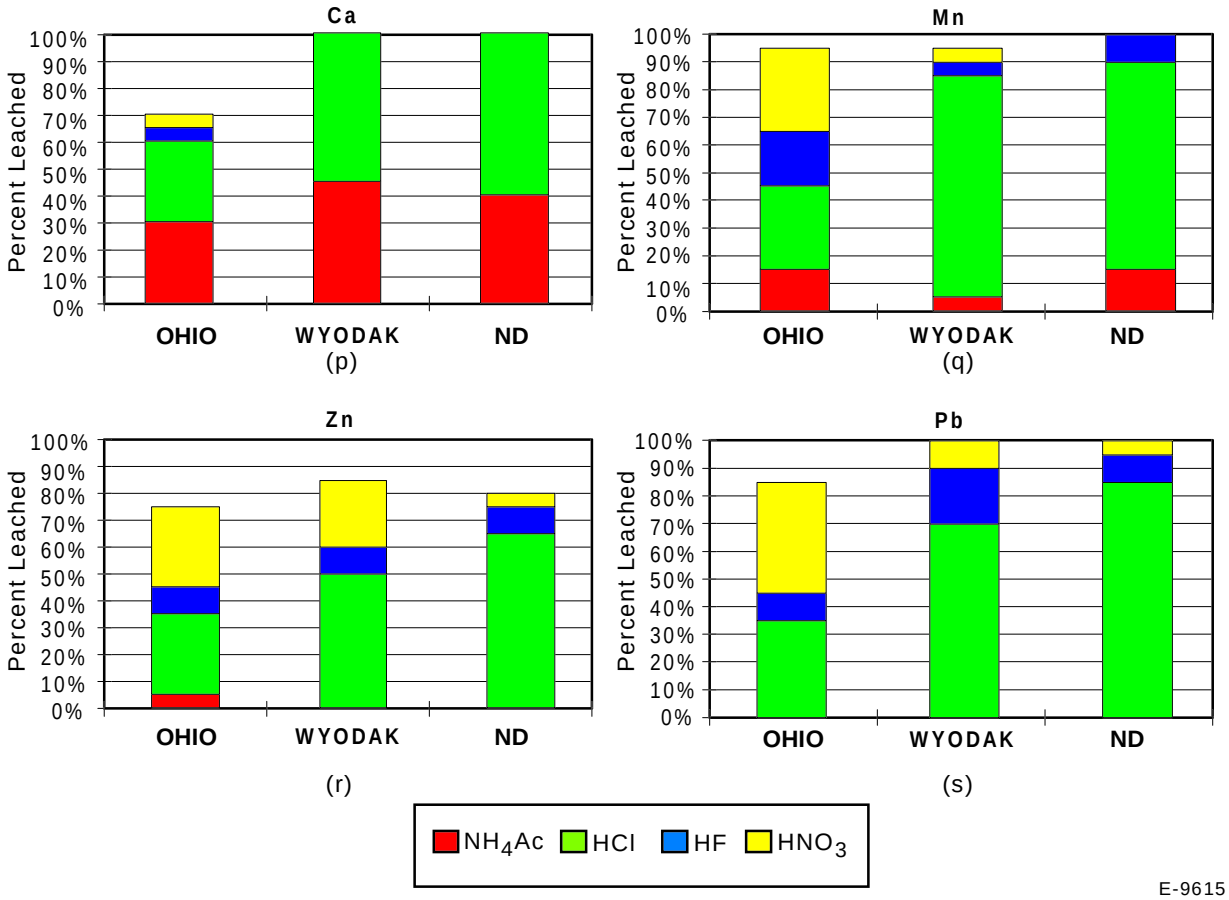

Figure 3-5. Leaching results (continued). (p)-(s) Selective leaching results for selected elements showing a carbonate (Ca, Mn) or monosulfide (Zn, Pb) association.

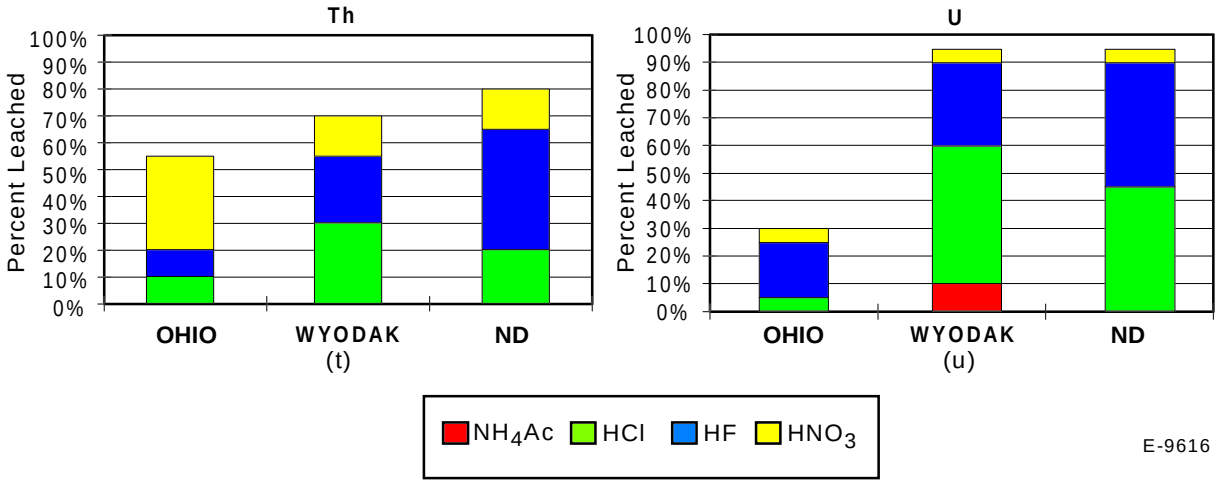

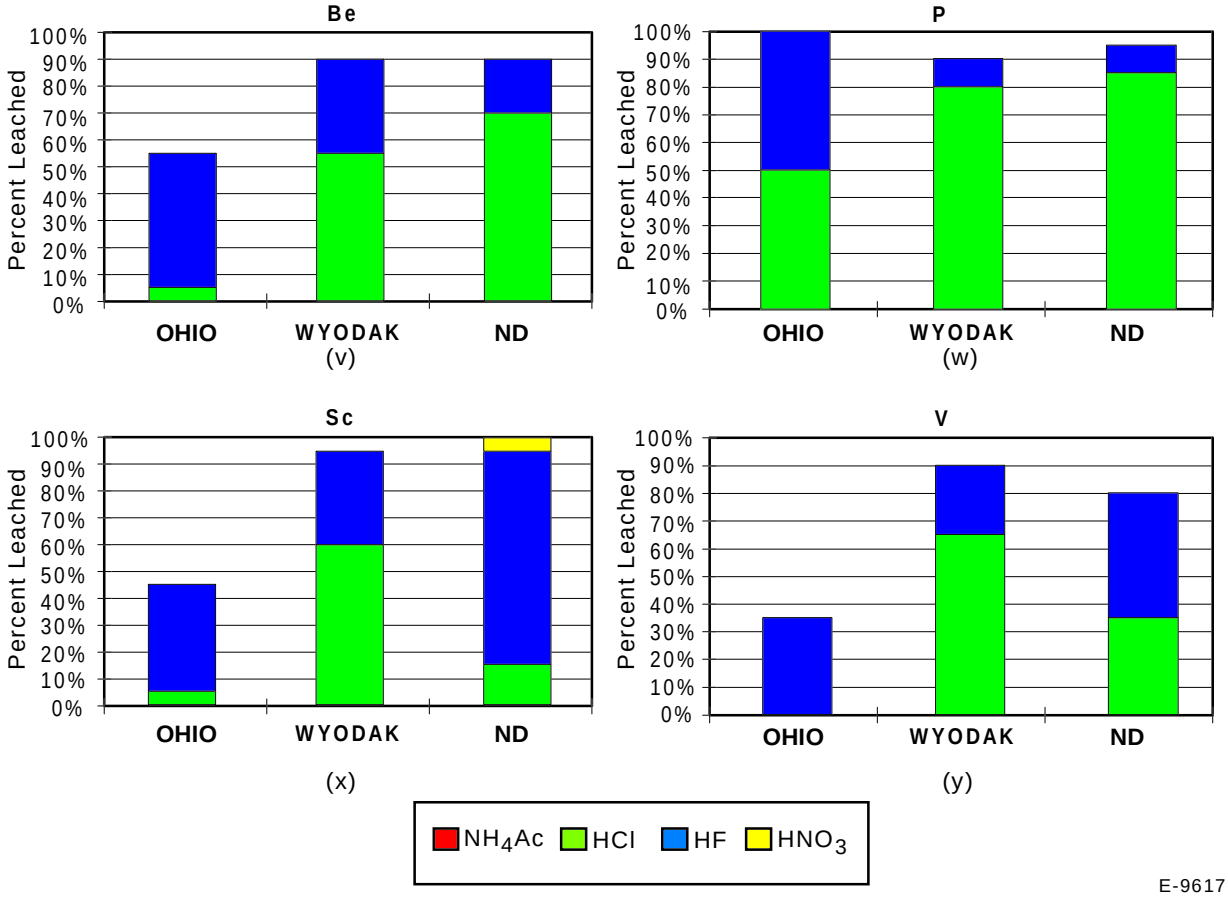

Figure 3-5. Leaching results (continued). (t)-(u) Selective leaching results for radionuclides Th and U. (v)-(y) Selective leaching results for elements Be, P, Sc, V, not shown in Figure 3-5a through 3-5u (by atomic number).

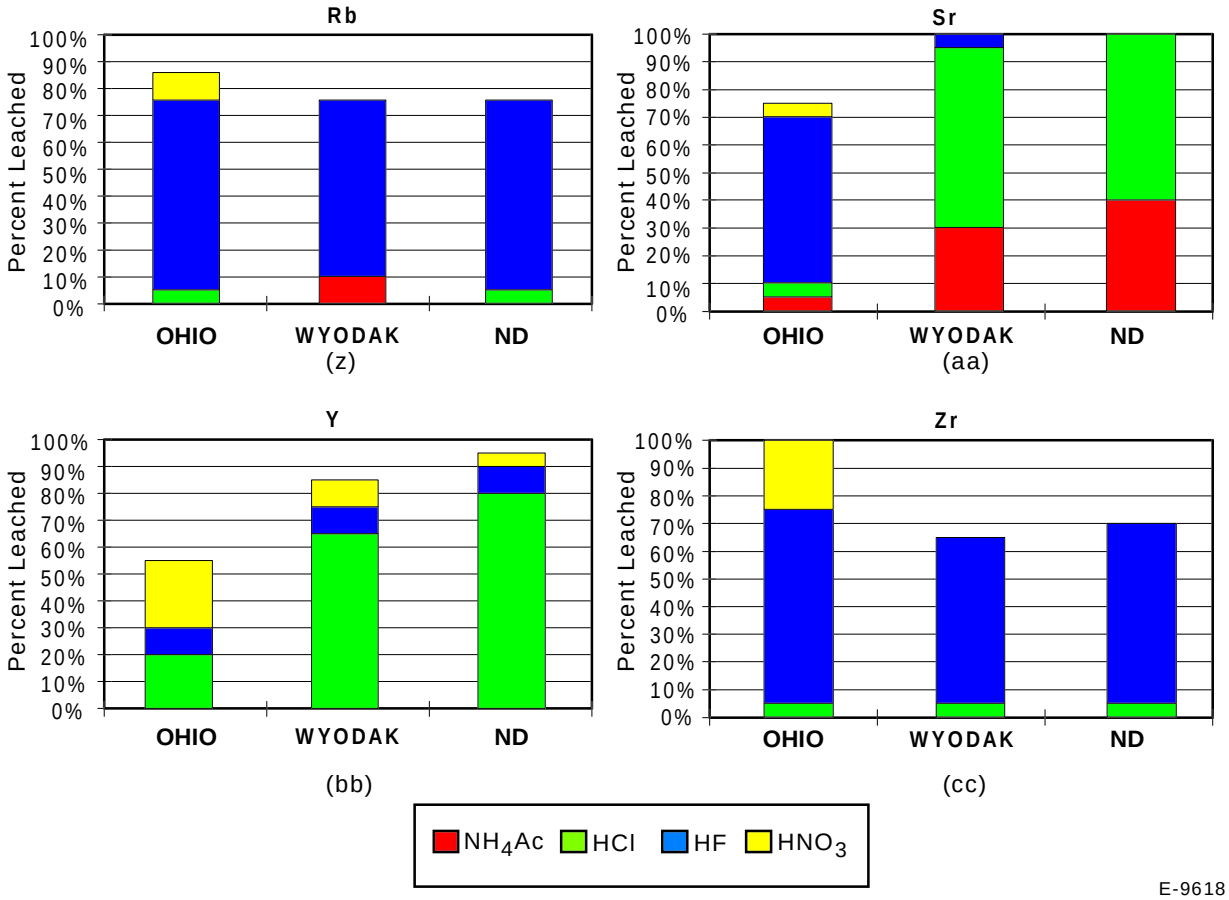

Figure 3-5. Leaching results (continued). (z)-(cc) Selective leaching results for Rb, Sr, Y, Zr.

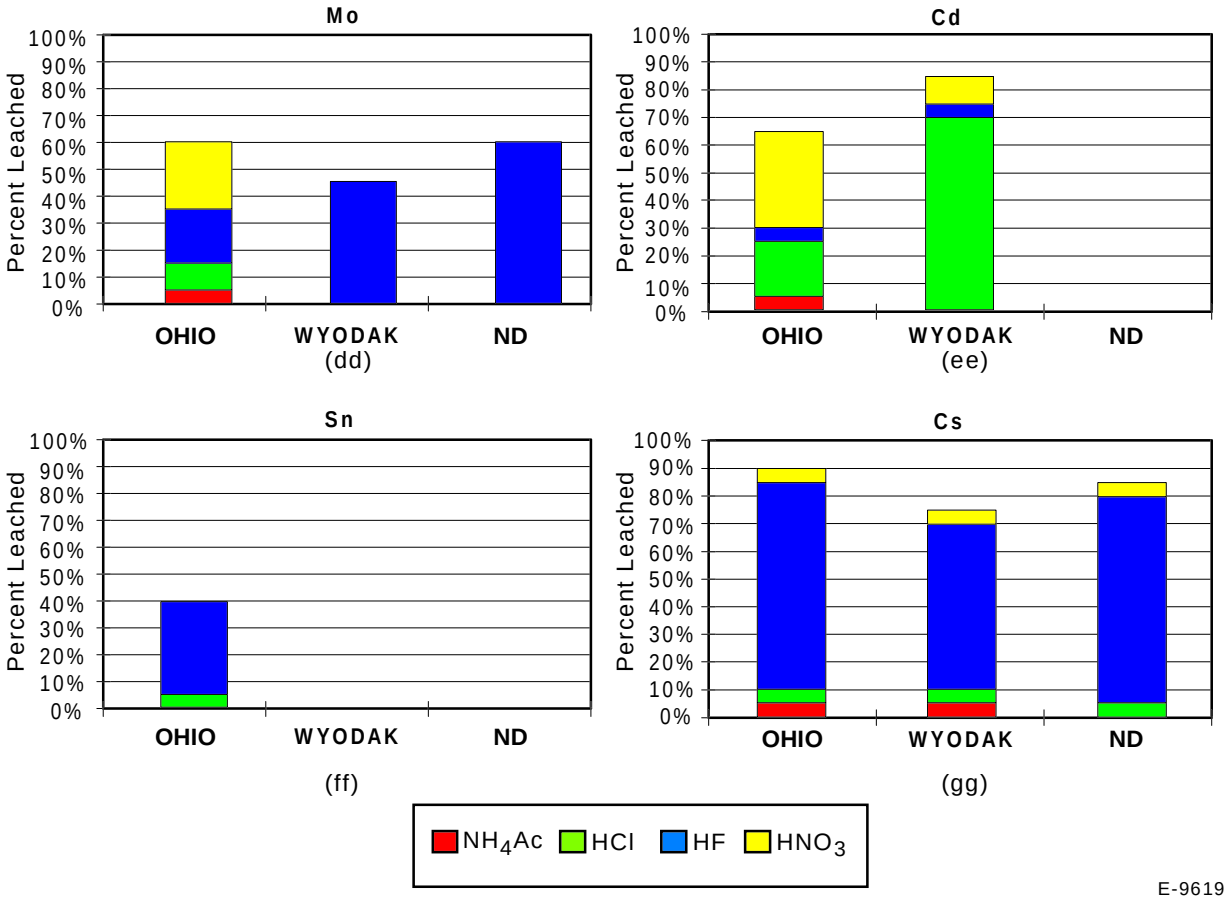

Figure 3-5. Leaching results (continued). (dd)-(gg) Selective leaching results for Mo, Cd, Sn, Cs.

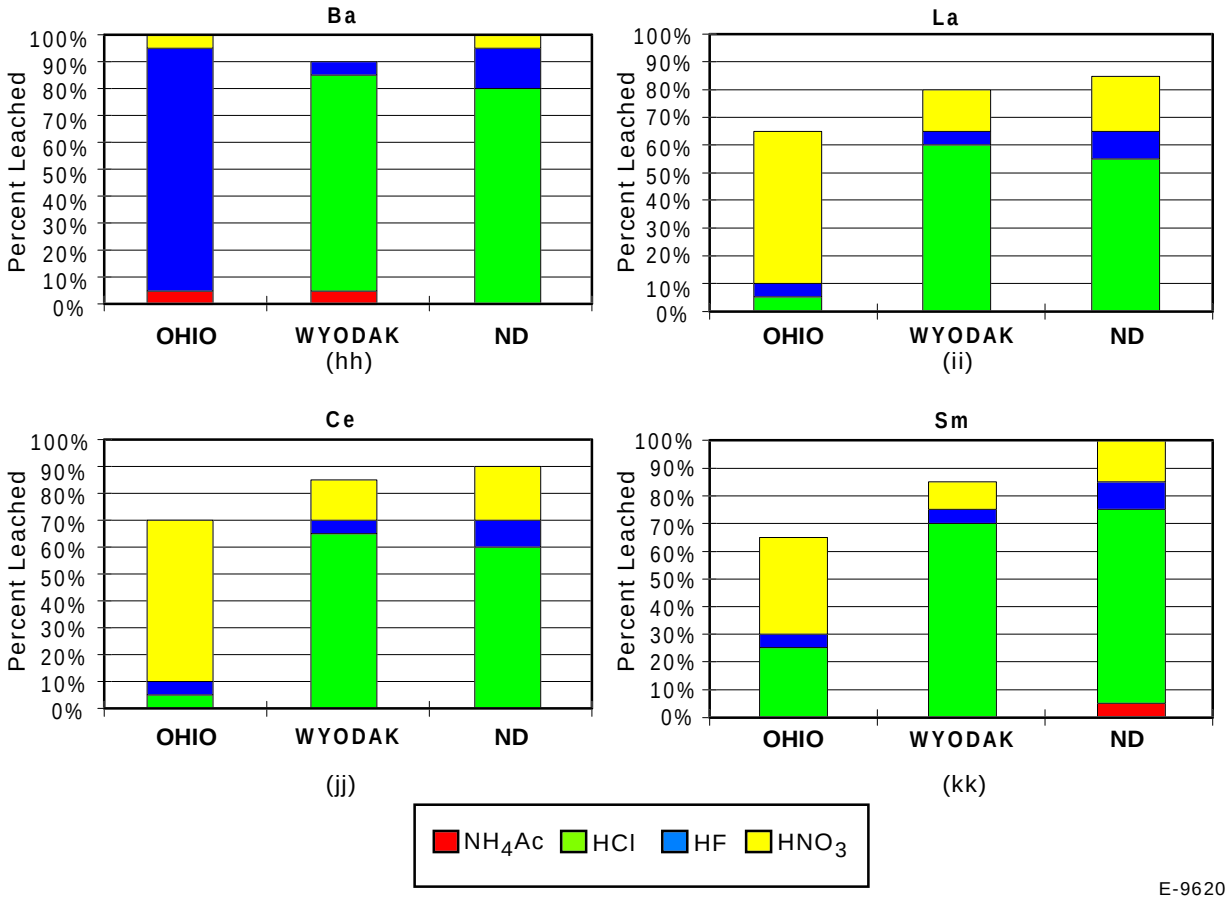

Figure 3-5. Leaching results (continued). (hh)-(kk) Selective leaching results for Ba, La, Ce, Sm.

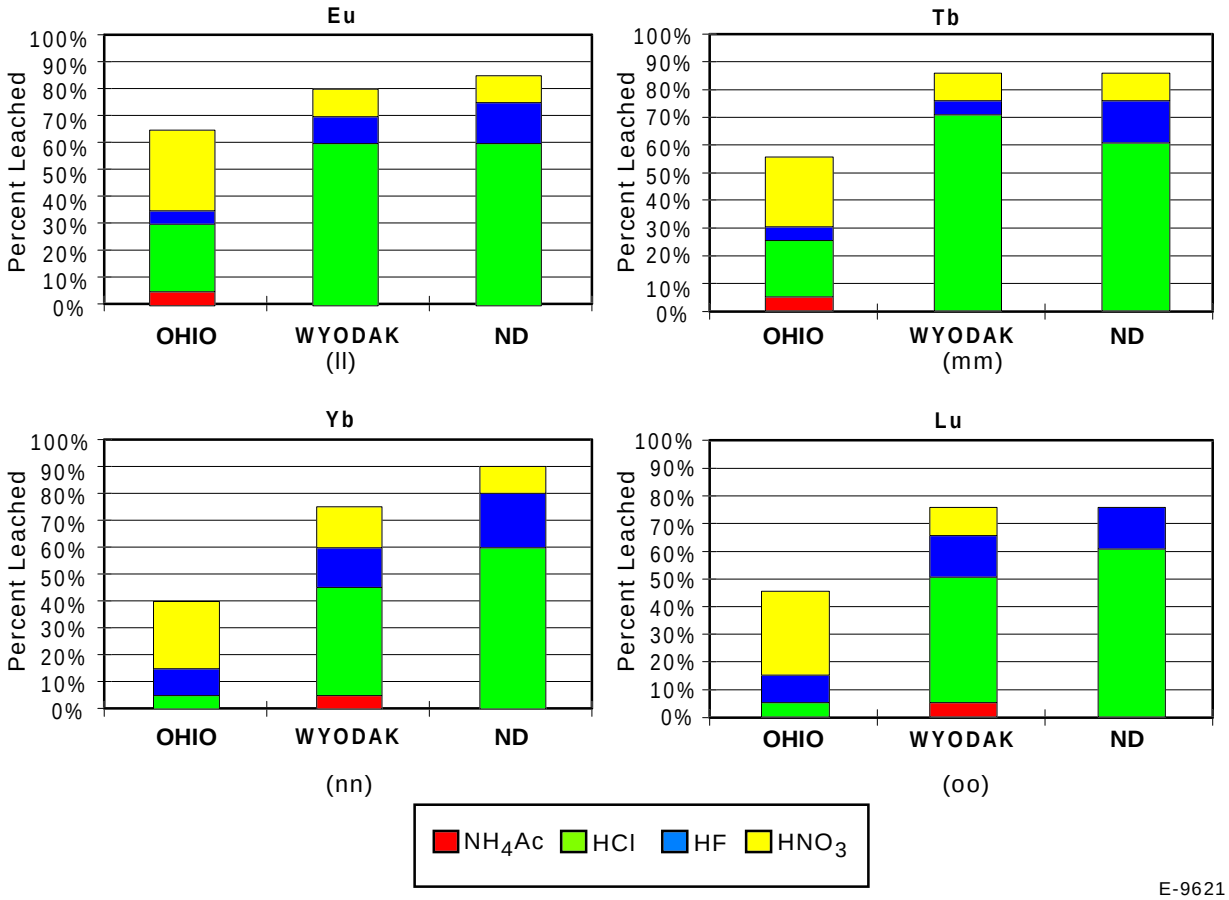

Figure 3-5. Leaching results (continued). (ll)-(oo) Selective leaching results for Eu, Tb, Yb, Lu.

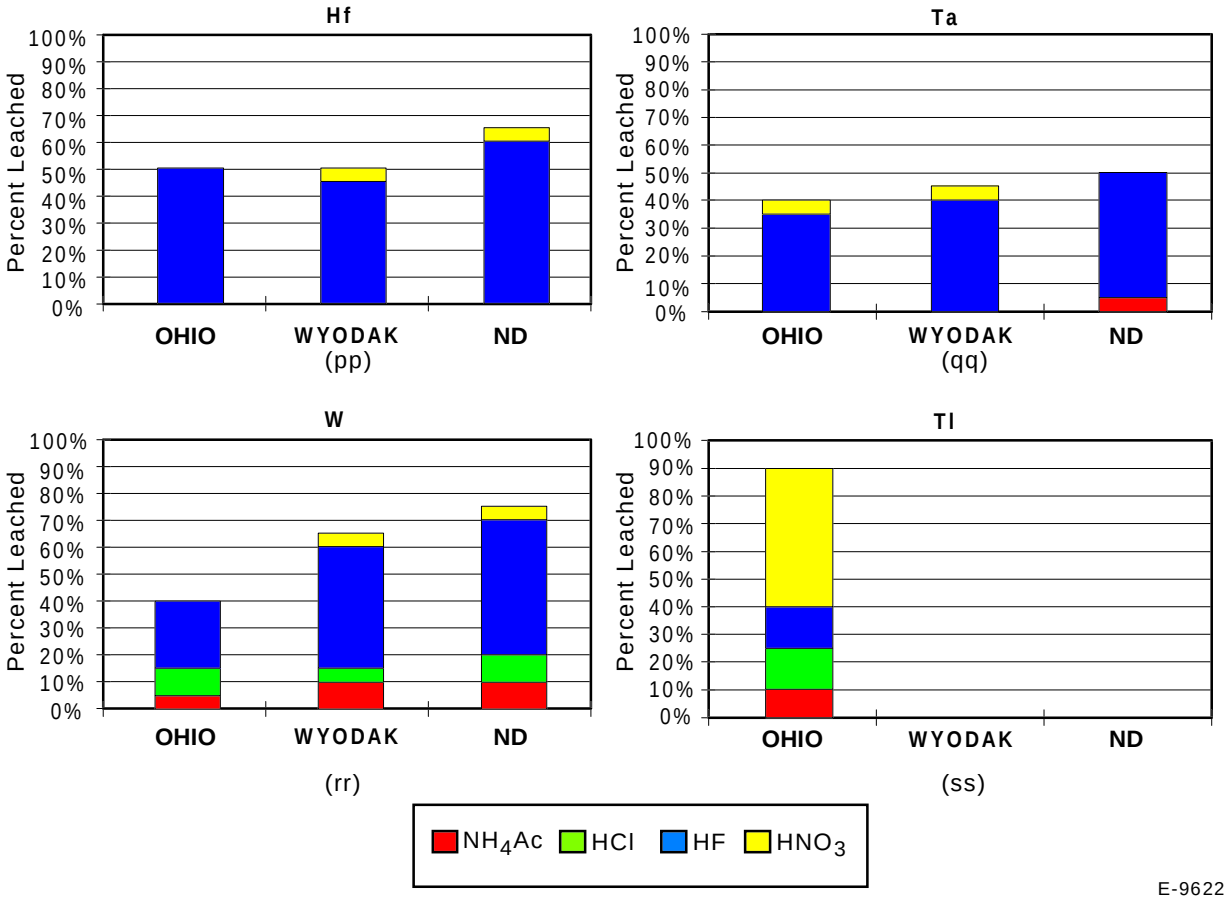

Figure 3-5. Leaching results (continued). (pp)-(ss) Selective leaching results for Hf, Ta, W, Tl.

Ohio 5/6/7: For the Ohio 5/6/7 coal, a dominant silicate association is indicated for Li, Be, Na, Mg, Al, K, Ti, Rb, Sr, Zr, Cs, and Ba. Significant silicate associations in Ohio 5/6/7 are indicated for Sc, V, Cr, Sn, Ta, and W. Many elements partition into clay minerals such as kaolinite and/or illite-smectite, as confirmed by microanalysis. Non-clay silicate-hosted elements include a dominant fraction of Zr and a significant fraction of U, both of which are present in zircon. A dominant sulfide association is indicated for Fe, Cu, As, Tl, and Pb. Each of these trace elements has been found in pyrite, although Cu more commonly occurs as chalcopyrite ($CuFeS_2$). Several elements that generally do not occur in pyrite (REE, Th) were also found to be HNO_3 leachable, possibly due to silicate-encapsulated phosphates. Significant sulfide associations were found for Mn, Ni, Zn, Se, Mo, and Cd. Bimodal element associations are indicated for Se (sulfide/organic) and Hf (silicate/organic). Se is known to occur in pyrite, whereas Hf can substitute for Zr in zircon. Mn, Co, Ni, Zn, Mo, and Cd show mixed associations in the Ohio 5/6/7 sample, and Sc, V, Cr, Sn, Sb, Yb, Lu, Ta, W, and U are organic dominant.

Wyodak: For the Wyodak coal, a dominant silicate association is indicated for Al, K, Ti, Co, Rb, Zr, and Cs, and W. Significant silicate associations are indicated for Li, Be, Sc, V, Cr, Mo, Sb, Hf, Ta, Th, and U. There are no dominant sulfide (pyrite) element associations in the Wyodak coal, consistent with its low (0.05 wt. %) pyritic sulfur content. Zn is the only element that shows a significant (25%) pyrite association. Many elements are dominantly HCl-leachable in the Wyodak sample, including Be, P, Ca, Sc, V, Mn, Fe, Zn, As, Sr, Y, Cd, Ba, REE, Pb, and U. No one phase is responsible for this behavior. Elements such as Mg, Ca, Mn, Fe, and Sr are present in carbonate minerals that undergo some dissolution in ammonium acetate, and more complete digestion in HCl. For example, Sr is 30% ammonium acetate leachable and 65% HCl leachable. Other HCl-dominant elements such as Zn and Pb, occur in HCl-soluble monsulfides such as sphalerite (ZnS) and galena (PbS). Cadmium (70% HCl leachable) is known to substitute in the sphalerite structure. Significant HCl leachable fractions found for elements such as Co (30%) and Ni (25%), which do not occur in common monosulfides, probably reflect limited substitution of these elements in carbonates. Overall, Ni shows a mixed association, as does Th. The dominant (50%) fraction of HCl-leachable As found for the Wyodak coal is likely an arsenate phase, as shown by XAFS study of our Phase II leached residues (see section on XAFS). Organic dominant elements in the Wyodak sample include Li, Cu, Se, Mo, and Ta.

North Dakota: Dominant silicate associations in the North Dakota sample include Al, K, Sc, Ti, V, Rb, Zr, Mo, Cs, Hf, W, and Th. Significant silicate associations are Cr, Co, Ni, Sb, Ta, and U. Uranium shows a bimodal silicate/HCl-leachable distribution. There are no dominant sulfide (pyrite) element associations in the North Dakota sample. Only Se shows a significant (25%) sulfide association. As in the Wyodak sample, the North Dakota sample contains many HCl-leachable element forms. Dominant HCl-leachable elements include Be, P, Ca, Mn, Fe, Co, Ni, Zn, As, Sr, Y, Ba, REE, and Pb. Significant HCl-leachable fractions include Mg, Al, V, Cu, and U. The behavior of Li and Se is organic dominant.

Leaching Results by Element

Lithium: Lithium has a dominant (65%) silicate association in the Ohio 5/6/7 coal and significant (35% each) fractions in the Wyodak and North Dakota samples, which both show organic dominant (65%W, 55%ND) forms of Li (Figure 3-5e).

Beryllium: Beryllium has a dominant (50%) silicate association in the Ohio 5/6/7 coal. The Wyodak and North Dakota samples show dominant HCl-leachable forms (55%W, 70%ND) and subsidiary (35%W, 20%ND) silicate associations (Figure 3-5v).

Sodium: Sodium has a dominant (40%) silicate association and a subsidiary exchangeable association (25%) in the Ohio 5/6/7 sample. In the two lower rank coals, Na has a dominant exchangeable association (90% in W, 85% in ND; Figure 3-5i).

Magnesium: Magesium has a dominant (70%) silicate association in the Ohio 5/67/7 coal. In the Wyodak and North Dakota samples, Mg is dominantly exchangeable (55% in W, 50% in ND), and has a subsidiary HCl-leachable form (30% in W, 35% in ND; Figure 3-5j).

Aluminum: Aluminum has a dominant (100%) silicate association in the Ohio 5/67/7 coal. In the Wyodak and North Dakota samples, Al has a dominant silicate association (55% in W, 65% in ND), and a subsidiary (25% in W and ND) HCl-leachable association (Figure 3-5f).

Phosphorus: In the Ohio 5/6/7 sample, P has a bimodal HF-leachable (50%) and HCl-leachable (50%) association. The HCl-leachable form probably represents phosphate minerals such as apatite ($Ca_5(PO_4)_3(OH,F,Cl)$), whereas the HF-leachable form may be explained by phosphate minerals encased in silicates, rather than the presence of P in solid solution in silicates. In the two lower rank coals, P shows a dominant HCl-leachable form (80% in W, 85% in ND), indicating a phosphate association (Figure 3-5w).

Potassium: Potassium has a dominant (90%) silicate association in the Ohio 5/6/7/ blend. In the Wyodak and North Dakota samples, K has a dominant (50% in W, 80% in ND) silicate association, and a subsidiary (30% in W, 10% in NA) exchangeable fraction (Figure 3-5k).

Calcium: In each of the Phase II coals, Ca has a dominant carbonate and/or exchangeable association. This is expressed for the Ohio 5/6/7 by a mixed ammonium acetate (30%), HCl (30%) and unleached (30%) association. For the two lower rank coals Ca occurs as bimodal association of ammonium acetate leachable (45% in W, 40% in ND) and HCl-leachable Ca (55% in W, 60% in ND; Figure 3-5p).

Scandium: The Ohio 5/6/7 coals shows a significant (40%) silicate association for Sc, which is organic-dominant (55% unleached) in this sample. The Wyodak sample shows a dominant (60%) HCl-leachable form of Sc and a subsidiary (35%) silicate association. The North Dakota sample has a dominant (80%) silicate association, and a subsidiary (15%) HCl-leachable fraction (Figure 3-5x).

Titanium: Titanium shows a dominant silicate association in each of the samples (65% in O, 60% in W and ND). Some of the HF-leachable Ti may be due to inclusions of titanium dioxide in silicates. SEM of leached residues shows that TiO_2 minerals are not completely digested by the leaching procedure. Each of the two lower rank coals show subsidiary (20%) HCl-leachable Ti forms (Figure 3-5g).

Vanadium: The Ohio 5/6/7 coal shows a significant (35%) silicate association for V, which is organic-dominant (65% unleached) in this sample. The Wyodak sample shows a dominant (65%) HCl-leachable form and a subsidiary (25%) silicate-hosted form. The North Dakota sample contains V dominantly as silicates (45%), but with a subsidiary (35%) HCl-hosted form (Figure 3-5y).

Chromium: The Ohio 5/6/7 coal shows a significant (30%) silicate association for Cr, which is organic-dominant (70% unleached) in this sample. The Wyodak sample shows a bimodal distribution of silicate (45%) and organic (45% unleached) forms, as well as a subsidiary HCl-leachable (10%) form. The North Dakota sample has a significant (35%) silicate form of Cr, a subsidiary (10%) HCl-leachable form, and is organic dominant (50% unleached; Figure 3-5h).

Manganese: Manganese has a mixed association (15-30% for each solvent) in the Ohio 5/6/7 sample. The significant fraction of Mn in pyrite in this sample (20%) may reflect the fact that the Mn content of this sample is low (20 ppm), less than half the average for U.S. coals (43 ppm). In the two lower rank coals, Mn is dominantly carbonate-hosted, with HCl-leachable fractions of 80% (W) and 75% (ND; Figure 3-5q).

Iron: Iron shows a dominant (80%) sulfide (pyrite) association in the Ohio 5/6/7 sample, and subsidiary (10% each) HCl-leachable and HF-leachable forms, probably Fe in carbonates and in illite/smectite. In the two low rank coals, a dominant (75% in W, 65% in ND) HCl-leachable form of iron is present, probably carbonate. Each of the two low rank coals show subsidiary (10% in W, 15% in ND) HF-leachable forms, probably illite/smectite, and subsidiary (10% in each) HNO_3-leachable Fe, representing pyrite-hosted Fe. Pyritic sulfur contents of the three coals (1.42 wt. % in O, 0.05 wt. % in W, 0.28 wt. %) broadly reflect the differences in pyrite-associated Fe indicated by the leaching data (Figure 3-5a).

Cobalt: Cobalt shows a mixed association in the Ohio 5/6/7 sample, with the fraction leached by each of the four solvents, and the unleached fraction, all exceeding 10%. The HCl fraction (30%) and the HNO_3 fraction (20%) are the two most abundant leached fractions in the Ohio 5/6/7 sample. These data indicate that carbonate, silicate (illite), organic, and pyritic forms of Co are present. The two lower rank coals each show roughly bimodal distributions of HCl-leachable (30% in W, 55% in ND) and HF-leachable (60% in W, 40% in ND) Co (Figure 3-5l).

Nickel: Nickel shows a mixed association in each of the three coals. Only the North Dakota sample shows a dominant leached fraction (45%), an HCl-leachable form. Significant Ni (25%) is leached by HF in the Wyodak sample. A significant pyrite association is indicated by

HNO_3-leachable Ni (25%) in the Ohio 5/6/7 sample, as confirmed by microanalysis (Figure 3-5m).

Copper: In the Ohio 5/6/7 sample, Cu is dominantly (65%) leached by HNO_3, with subsidiary (10%) HCl-leachable Cu, and a 20% unleached fraction. These results indicate a dominant pyrite association and a subsidiary chalcopyrite and organic associations. The Wyodak sample, Cu is organic dominant (55% unleached). Both lower rank coals have equal or subequal fractions (20% in W, 30% in ND) of HCl-leachable Cu (chalcopyrite) and HNO_3-leachable (20% in W, 20% in ND) Cu in pyrite (Figure 3-5b).

Zinc: In the Ohio 5/6/7 coal, Zn shows a mixed association in which there are significant (30% each) HCl- and HNO_3-leachable fractions, corresponding to sphalerite and pyrite associations, and a subsidiary (25%) organic association. In the two lower rank coals Zn is dominantly in sphalerite (50% in W, 65% in ND), with subsidiary silicate (10%), pyrite (25%), and organic (15%) associations in the Wyodak sample, and subsidiary silicate (10%) and organic (20%) associations in the North Dakota sample (Figure 3-5r).

Arsenic: The distribution of As in the three coals is similar to that for Fe. In the Ohio 5/6/7 sample, As is dominantly (60%) in pyrite, with a subsidiary (25%) HCl-leachable form, probably arsenate. In the two lower rank coals, the arsenate(?) form is dominant (40% in W, 50% in ND), with subsidiary organic (30% in W, 20% in ND) and pyrite-hosted (15% in each) As. The two lower rank coals also show subsidiary (15% in each) HF-leachable As. XAFS study of leached residues (below) shows that HF removes arsenate not removed by HCl, rather than As that is structurally bound in silicates. However, some of this arsenic may be interstitial to finely disseminated clays and released by their digestion in HF (Figure 3-5c).

Selenium: Selenium shows a bimodal pyritic (50%) and organic (50%) association in the Ohio 5/6/7 coal. In the two lower rank coals, Se in organic-dominant (70% in W, 60% in ND) with a subsidiary (20%) pyrite association in the Wyodak sample, and a significant (25%) pyrite association in the North Dakota sample (Figure 3-5d).

Rubidium: Rubidium is dominantly (65 to 70%) hosted by silicates in each of the three Phase II coal samples (Figure 3-5z).

Strontium: Strontium is dominantly (60%) silicate-hosted in the Ohio 5/6/7 sample. In the two lower rank coals, Sr is dominantly carbonate-hosted. The sum of ammonium-acetate and HCl-leachable fractions in these samples is 95% (W) to 100% (ND). The ammonium-acetate leachable fraction ranges from 30% (W) to 40% (ND), permitting a subsidiary portion of exchangeable Sr (Figure 3-5aa).

Yttrium: In the Ohio 5/6/7 sample, Y follows a mixed distribution, with a significant (25%) fraction leached by HNO_3. In the two lower-rank coals, HCl-leachable forms are dominant (65% in W, 80% in ND), probably phosphates such as apatite, the crandallite group $(Ca,Ba,Sr)Al_3(PO_4)_2(OH)_{5*}H_2O$, or xenotime ($YPO_4$; Figure 3-5bb).

Zirconium: Zirconium is dominantly (60 to 70%) hosted by silicates (zircon) in each of the three Phase II coal samples (Figure 3-5cc).

Molybdenum: Molybdenum shows a mixed association in the Ohio 5/6/7 sample, with significant (25%) sulfide-hosted Mo. The Wyodak sample is organic dominant (55%) with a significant (45%) HF-leachable component, probably in clays. The North Dakota sample shows a dominant HF-leachable component (60%) with a significant (40%) organic component (Figure 3-5dd).

Cadmium: In the Ohio 5/6/7 coal sample, Cd has 3 major forms, including pyrite (35%), organic (35%), and a subsidiary (20%) HCl-leachable form, likely representing Cd in sphalerite. In the Wyodak sample, the HCl-leachable form is dominant. Cd leaching data were not determined for the North Dakota sample, as its whole coal Cd concentration is below the detection limit (<0.1 ppm; Figure 3-5ee).

Tin: For the Ohio 5/6/7 coal, Sn is organic dominant (60% unleached), and there is a significant (35%) silicate association. Sn leaching data were not determined for the Wyodak and North Dakota samples, as their whole coal Sn concentrations are each below the detection limit (Figure 3-5ff).

Antimony: Antimony is organic dominant (60% unleached) in the Ohio 5/6/7 coal, with subsidiary HF- (20%) and HNO_3-leachable (15%) forms. The Wyodak sample shows a mixed association with significant (35%) silicate-hosted Sb. The North Dakota sample has a bimodal silicate (40%) and organic (50%) Sb, with a subsidiary (10%) sulfide-hosted form (Figure 3-5n).

Cesium: Cesium shows a dominant (75% in O, 60% in W, 75% in ND)) silicate association in each of the three Phase II coals. The data indicate a subsidiary (10% in O, 25% in W, 15% in ND) organic Cs fraction in each sample (Figure 3-5gg).

Barium: Leaching results for the Ohio 5/6/7 sample shows a dominant (90%) silicate association. In the two lower rank coals, Ba has a dominant (80% in each) HCl-leachable association, probably Ba in barite ($BaSO_4$; Figure 3-5hh).

Light REE (La, Ce): In the Ohio 5/6/7 sample, La and Ce are dominantly leached by HNO_3 (55% La, 60% Ce). In the Wyodak sample, these elements are dominantly leached by HCl (60% La, 65% Ce). La and Ce in the North Dakota sample are also dominantly leached by HCl (55% La, 60% Ce; Figure 3-5ii-jj).

Middle REE (Sm, Eu, Tb): Middle REE show a mixed association in the Ohio 5/6/7 sample, whereas an HCl-leachable form is dominant in the two lower rank coals (60 to 70% for each element in each coal; Figure 3-5kk-mm).

Heavy REE (Yb, Lu): In the Ohio sample, the heavy REE are organic dominant (55% unleached Lu, 60% unleached Yb), with significant (25 to 30%) HNO_3-leachable fractions, and a subsidiary (10%) HF-leachable fraction. The Wyodak sample has a dominant (40 to 45%) HCl-leachable

fraction, and a significant organic component (25% for each). The North Dakota sample shows a dominant HCl-leachable form for Yb and Lu (60% each; Figure 3-5nn-oo).

Hafnium: Hafnium shows a similar bimodal silicate(50 to 45%)/organic (50% in each) association for the Ohio and Wyodak samples. In the North Dakota sample, the silicate form of Hf is dominant (60%), with a significant (35%) organic Hf component (Figure 3-5pp).

Tantalum: The occurrence of Ta is similar for each of the three Phase II coals. In each coal, Ta is organic dominant (50 to 60%), with a significant (35 to 45%) silicate fraction (Figure 3-5qq).

Tungsten: In the Ohio 5/6/7 sample, W is organic dominant (60%), with a significant silicate fraction (25%), and a subsidiary (10%) HCl-leachable fraction. In the two lower rank coals, the silicate fraction of W is dominant (45% in W, 50% in ND), with a significant (35% in W, 25% in ND) organic fraction (Figure 3-5rr).

Thallium: A pyrite association is dominant (50%) for Tl in the Ohio sample, with subsidiary (10 to 15%) amounts of Tl leached by each of the other solvents. Tl leaching results were not determined for the two lower rank coals because the whole-coal Tl values of these samples are below the detection limit.

Lead: Lead shows a mixed distribution for the Ohio sample, in which the main modes of occurrence are as HNO_3 leachable Pb (40%, in pyrite), and as HCl-leachable Pb (35%, likely as galena). HCl-leachable Pb is the dominant Pb form in the two lower rank coals (70% in W, 85% in ND; Figure 3-5ss).

Thorium: Thorium shows a mixed association in each of the three Phase II coals. The Ohio sample has a significant HNO_3-leachable (35%), and unleached (45%) fractions. The Wyodak coal has significant HCl-and HF-leachable Th fractions. In the North Dakota sample, the silicate Th fraction is dominant (45%; Figure 3-5t).

Uranium: Uranium shows a strongly organic dominant mode (70%) in the Ohio sample, with a subsidiary (20%) silicate fraction. The Wyodak sample shows a dominant HCl-leachable U mode, with a significant (30%) silicate fraction, and a subsidiary (10%) exchangeable form. The North Dakota sample has a bimodal HCl (45%) and silicate (45%) distribution of U forms (Figure 3-5u).

Systematic Differences by Rank

Systematic differences in trace element modes of occurrence among the three Phase II coals are attributable to the difference in their rank. For example, in bituminous coals such as the Ohio 5/6/7, it is common for chalcophile elements (As, Cu, Se, Hg, etc.) to occur primarily in pyrite, whereas in low rank coals, the fractions of these elements in organic or HCl-soluble forms generally exceed those in pyrite (e.g., As, Figure 3-5c). A number of other elements (Co, Ni, Mn, Mo) showing some pyrite association in bituminous coals have little or no pyrite association in low rank coals. Low rank coals also show markedly different modes of occurrence for Sr, Ba,

and REE than bituminous coals. The association of Sr with carbonates and Ba with barite decreases with rank, except in coals containing these minerals in cleat-fillings or other late diagenetic forms. REE data for the three Phase II coals, and other coal samples we have analyzed, shows that the proportion of HCl-soluble REE, probably as REE phosphates, is far greater in low rank coals (Figure 3-6).

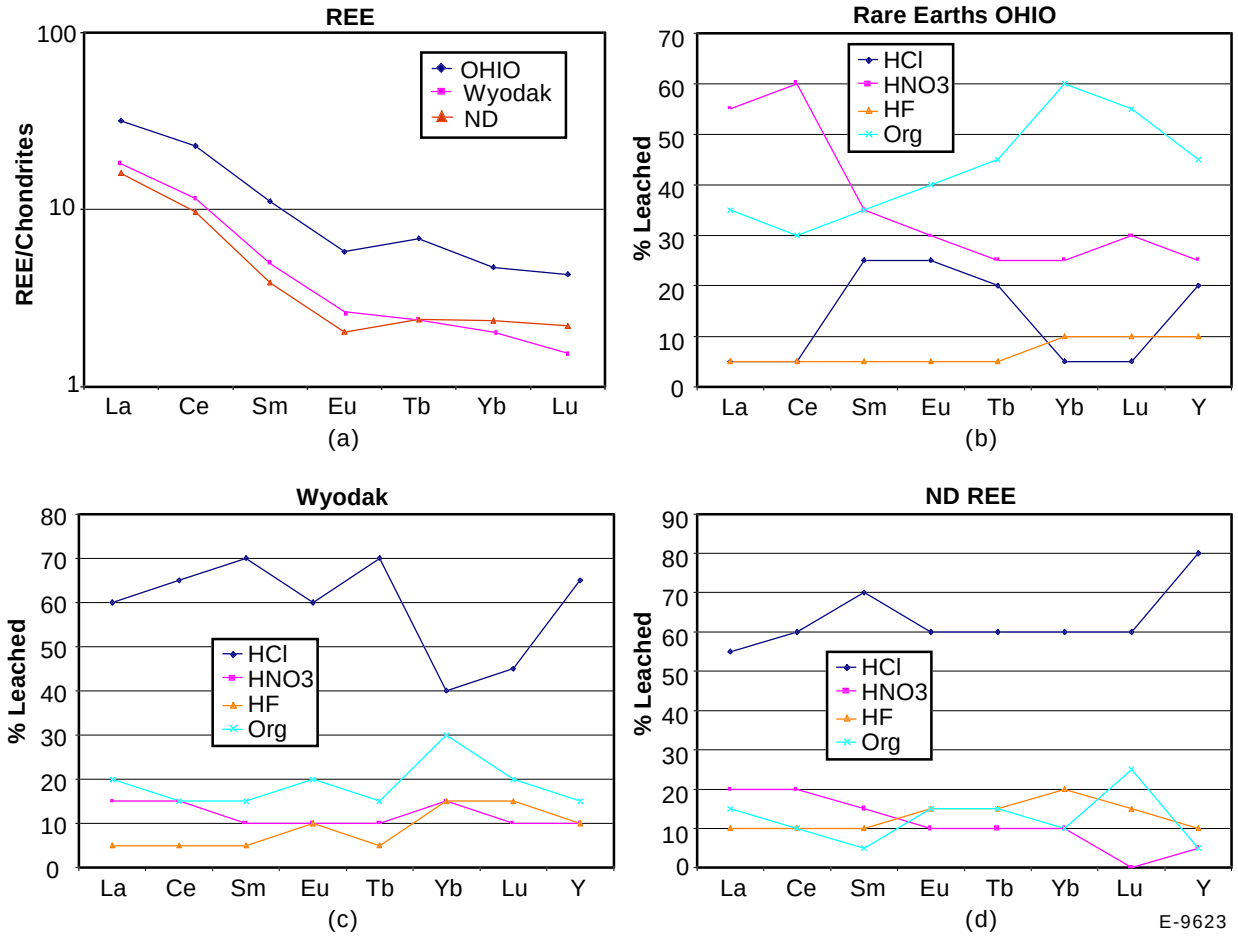

Figure 3-6. Selective leaching results for Rare Earth Elements (REE) showing chondrite-normalized pattern for whole coals (a) and rank dependence of HCl fraction (blue curve in (b)-(d)). REE fraction leached by HCl is greatest in Wyodak and North Dakota Samples ((c)-(d)).

Comparison with XAFS

To help integrate the leaching and XAFS portions of this project, XAFS splits were taken from each of the leaching steps conducted. Arsenic XAFS spectra were obtained by Frank Huggins for leached residues of the Ohio and North Dakota samples. These results (discussed more fully in Section 3.1.4) show that HCl removes arsenate, HF has little effect on As, and that HNO_3 removes pyritic arsenic (results for Ohio 5/6/7 only). The XAFS results show that a small

amount of residual arsenic remains after leaching. Arsenate forms extracted by HCl and ammonium acetate are believed to be oxidation products from the other major arsenic forms, resulting from exposure of the powdered coal samples to air. These results are consistent with Phase I XAFS results for bituminous coals [52], showing that significant fractions of arsenate can result from in-situ oxidation.

3.1.3.4 Coal Oxidation Experiments

A series of leaching experiments was devised to test the possibility that the leaching process itself results in pyrite oxidation in-situ. In these experiments, baseline HCl leaching experiments for the Wyodak and North Dakota samples were repeated after heating the coal to 75°C in air, or wet-dry cycling of the coal while heating at the same temperature (75°C). The results, expressed as percent iron leached by HCl, are within analytical uncertainty for all determinations, indicating the neither heating or wetting and drying, both of which take place during the leaching procedure, has a measurable effect on the fraction of Fe leached by HCl (Figure 3-7). This fraction should increase if pyrite is being oxidized by the leaching procedure.

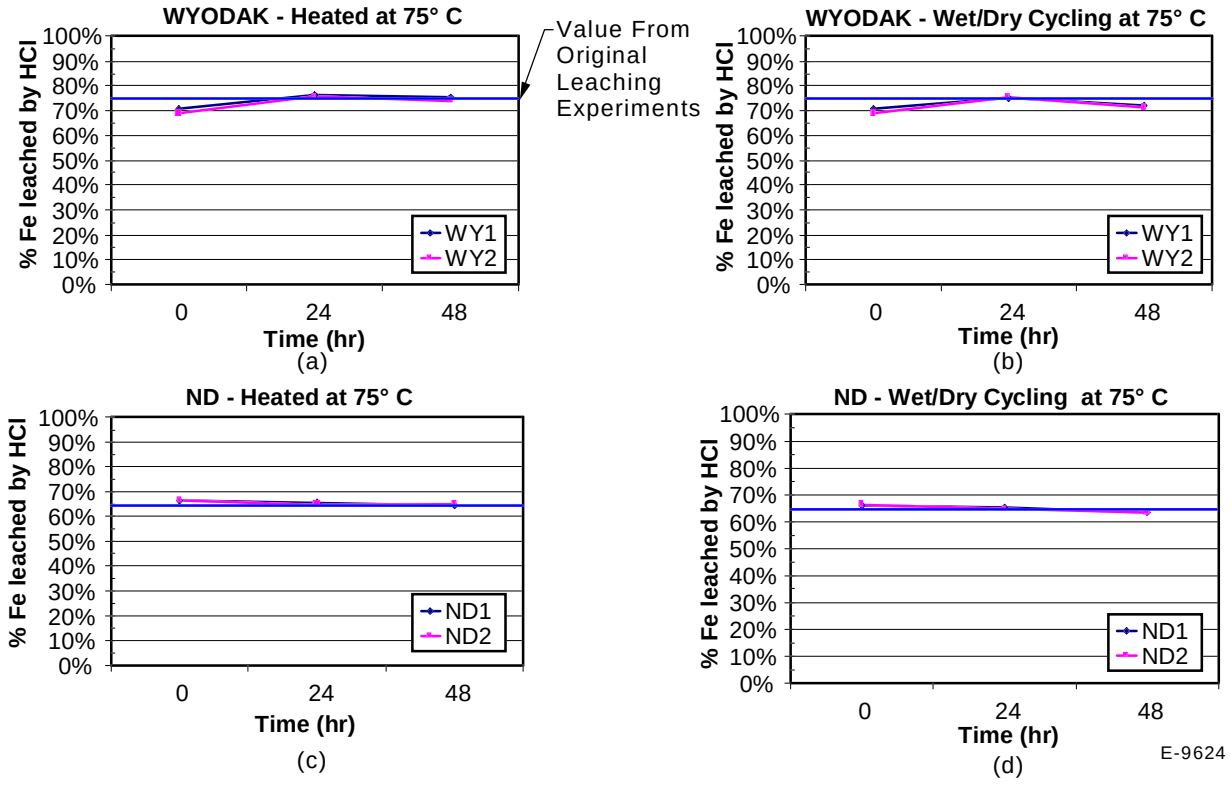

Figure 3-7. Results of coal oxidation experiments showing constant percent Fe leached by HCl despite heating and wet-dry cycling.

3.1.3.5 Mercury Analysis

A direct mercury analyzer (DMA) was delivered to our Denver laboratories in March 2000. Compared to the cold-vapor atomic absorption (CVAA) method used in Phase I, this method offers better detection limits for small solid samples having low Hg concentrations, such as our leached residues. CVAA remains a reliable method for samples having Hg concentrations >100 ppb. DMA method development revealed problems with Hg carry-over from sample to sample, and a problem with the automatic sample introduction device that necessitated return of the instrument to the manufacturer. Changes in the gas mixture supplied to the instrument eliminated the carry-over problem. Periodic sample introduction problems persist, even after repair of the instrument by the factory, nonetheless, the instrument is providing acceptable analyses on a one-at-a-time basis. Hg analysis of leaching solid residues by direct mercury analyzer (DMA) was finally completed during the reporting period. The DMA method offer the advantages of lower detection limits, and the capability of determining small sample sizes, compared to the cold-vapor atomic absorption (CVAA) method used in Phase I, and for Phase II whole coals.

Mercury leaching results for the three phase two coals, using DMA data for the leaching splits, are shown in Figure 3-8. The results indicate a pyrite association for Hg in each of the coals, a finding confirmed for the Ohio 5/6/7 sample by direct analysis of individual pyrite grains, using laser-ablation inductively-coupled-plasma mass spectrometry (ICP-MS; see below). Surprisingly, pyrite is the dominant mercury form even in the two low rank coals. For other chalcophile elements (e.g. As, Cu, Se), the low rank coals show a much less pronounced pyrite association than the Ohio 5/6/7 sample, in which the proportion of pyrite is much greater.

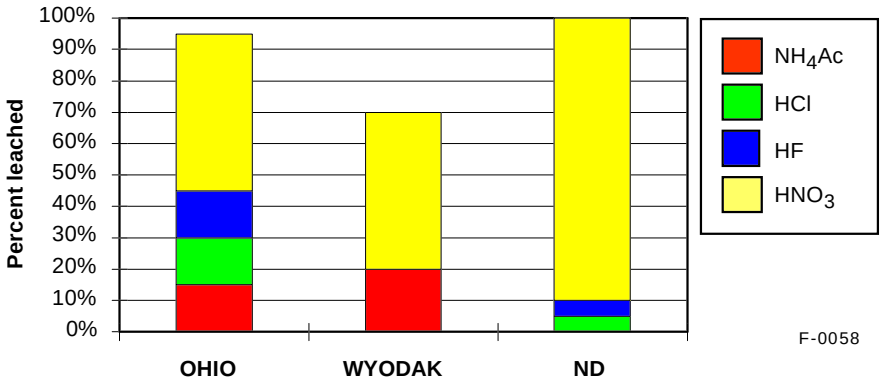

Figure 3-8. Selective leaching data for Hg. For the Ohio and Wyodak samples, percent mercury leached is relative to amount in bulk coals (180 ppb, 130 ppb, respectively) determined by coal-vapor atomic absorption (CVAA). For North Dakota sample, bulk Hg by CVAA is below 100 ppb, and DMA is considered more reliable. For North Dakota, leaching residue after ammonium acetate was used as whole coal value, and no ammonium acetate leached split is reported.

3.1.3.6 Electron Microprobe

Microprobe studies concentrated on pyrite, illite-smectite, and carbonates present in the Phase II coals. Complete analytical results are given in Appendix E. Results for pyrite are plotted in Figure 3-9, and representative analyses are shown in Table 3-14. In the Ohio 5/6/7 coal, with the exception of 1 pyrite grain, whose arsenic content ranges for 0.02 to 1.79%, arsenic contents of pyrites determined are all below 0.4 wt % and there is no correlation between arsenic content and concentrations of other chalcophile elements (Figure 3-9a-d). In the Wyodak coal, arsenic in pyrite ranges from negligible to about 0.5 wt %, with some correlation between contents of As and other chalcophile elements, especially Se (Figure 3-9d). Arsenic in North Dakota pyrite is generally below 0.40 wt % with the exception of 1 subhedral grain whose arsenic content ranges from 0.18 to 0.84 wt % (Figure 3-9). This grain is also enriched in Se (0.02 to 0.07 wt %) and Ni (0.00 to 0.12 wt %; Figure 3-9).

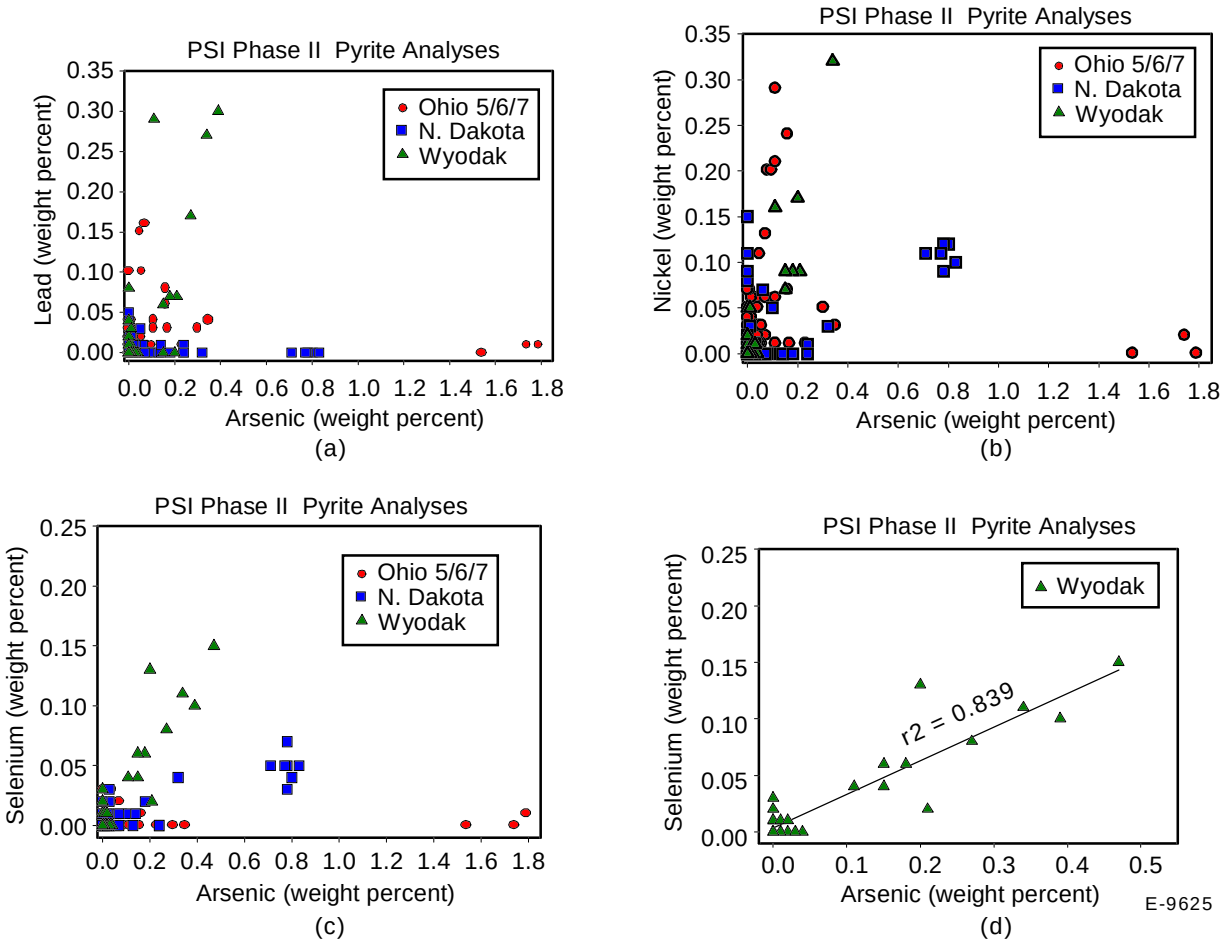

Figure 3-9. Summary of electron microprobe data for pyrite in Phase II samples.

Table 3-14. Representative Electron Microprobe Analyses for Pyrite in Phase II Coals

	1	2	3	4	5	6	7	8	9
S	53.07	53.22	53.19	53.07	53.35	52.78	51.97	52.90	54.23
Fe	47.36	46.48	46.94	45.63	47.06	47.43	46.10	47.43	44.61
Co*	0.00	0.00	0.03	0.01	0.00	0.01	0.01	0.01	0.11
Ni	0.00	0.06	0.02	0.29	0.01	0.00	0.10	0.00	0.49
Cu	0.00	0.02	0.00	0.15	0.02	0.03	0.03	0.00	0.01
Zn	0.00	0.00	0.00	0.00	0.00	0.02	0.00	0.00	0.01
As	0.00	0.11	1.74	0.11	0.00	0.02	0.83	0.01	0.27
Se	0.01	0.00	0.00	0.00	0.00	0.01	0.05	0.00	0.08
Cd	0.02	0.01	0.01	0.02	0.00	0.00	0.00	0.04	0.01
Pb	0.02	0.00	0.01	0.00	0.00	0.00	0.00	0.01	0.17
Total	100.48	99.90	101.94	99.28	100.44	100.30	99.09	100.40	99.99

1-5 Ohio 5/6/7; 6-7 North Dakota; 8-9 Wyodak.
*Results for Co are background-subtracted and analyses are re-calculated to original totals.

Microprobe data for illite/smectite show considerable major element variability in the contents of K, Mg, Fe, and to a lesser degree, Al, and Si. This is due to fine-scale intergrowth of clay minerals, overlap with adjacent grains, and differing degrees of substitution of these elements in the illite structure (Table 3-15; Appendix E). In most grains, SiO_2 in illite/smectite averages about 50 wt % and Al_2O_3 averages about 30 wt % (Table 3-15). Prior electron microprobe elemental mapping (Figure 3-10) and the presence of Fe, Mg, and K, were used to identify illite/smectite grains during SHRIMP-RG analyses (see below). Compared to the Ohio 5/6/7 sample, the North Dakota illites have slightly lower Al_2O_3 contents, and the Wyodak sample has a greater fraction of kaolinite. Unlike the illite/smectite, kaolinite shows little or no solid solution, and is essentially stoichiometric $Al_4Si_4O_{10}(OH)_8$, giving an Al_2O_3 content of about 40 wt % and an SiO_2 content of about 50 wt % (Table 3-15). The clay mineral analyses do not sum to 100% because of structural water and/or hydroxyls, that are not determined.

Table 3-15. Representative Electron Microprobe Analyses for Illite/Smectite in Phase II Coals

	1	2	3	4*	5	6	7	8	9
SiO_2	49.15	50.44	50.19	49.61	49.42	51.89	50.30	46.99	48.20
TiO_2	0.35	0.04	0.24	0.00	0.02	0.24	0.70	0.44	0.09
Al_2O_3	29.69	31.83	34.39	41.67	31.62	29.67	29.69	35.13	36.45
Cr_2O_3	0.03	0.01	0.01	0.00	0.01	0.02	0.01	0.00	0.00
MgO	2.60	1.38	1.29	0.02	2.13	1.74	2.30	0.40	0.87
CaO	0.02	0.07	0.12	0.02	0.13	0.32	0.08	0.11	0.08
MnO	0.01	0.01	0.00	0.00	0.00	0.01	0.01	0.03	0.00
FeO	4.67	2.32	1.71	0.13	2.85	4.26	4.57	0.72	2.20
Na_2O	0.11	0.08	0.17	0.00	0.14	0.10	0.10	0.89	0.06
K_2O	8.20	1.73	4.75	0.00	6.53	4.96	6.30	7.45	3.75
Total	94.83	87.91	92.86	91.45	92.85	93.21	94.06	92.16	91.70

1-4 Ohio 5/6/7; 5-7 North Dakota; 8-9 Wyodak.
*Analysis 4 is kaolinite.

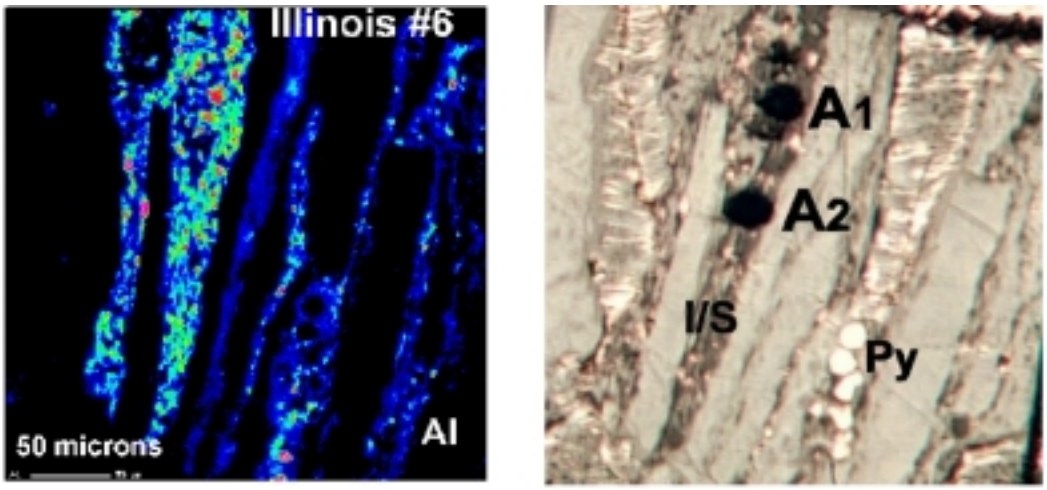

Figure 3-10. (a) Electron microprobe aluminum map showing distribution of clay minerals used to locate targets for SHRIMP-RG analysis of illite/smectite. (b) Reflected-light image of the same area showing distribution of illite/smectite and SHRIMP-RG analysis points. Example is Phase I Illinois #6 sample.

Electron microprobe data were also obtained for calcite in the Ohio 5/6/7 coal. The following elements were determined (as oxides)- Mn, Mg, Pb, Ca, Sr, Ba, and Zn. The results confirm that Mg, Fe, Sr, and Mn are commonly present at trace to minor element levels in calcite, and measurable concentrations of Ba, Pb, and Zn were found in a few cases. Results for calcite in the Phase II Ohio 5/6/7 sample are given in Appendix E.

3.1.3.7 SHRIMP-RG Ion Microprobe

Concentrations of trace metals in illite/smectite in the three Phase II coals were obtained by determining the counts/ppm for standard glasses whose composition approximates that of the illites, and calculating the concentrations of unknowns by comparing their raw counts to the standard data. Calibration results were obtained using SRM 610, GSE, and BHVO-1 standards. Comparison of results using different standards for the same Ohio 5/6/7 illite/smectite, is given in Table G-1 (Appendix G). For most elements, the GSE standard gives the lowest concentrations, and these can be considered minima. GSE is the only standard determined in both illite/smectite SHRIMP-RG runs, providing a uniform basis for comparing data. Table G-2 (Appendix G) shows the reproducibility of counts/concentration for the GSE standard in four runs over a 2-day period in February 2000. Total deviation ranges from 5.8 to 12.5%, except for Rb (20.9%) and Sr (17.9%). In each of the two illite/smectite SHRIMP-RG sessions, results were obtained for Mg, Al, Ca, Si, Sc, Ti, V, Cr, Mn, Co, Ni, Rb, and Sr. Four additional elements, K, Fe, Cu, and Zn, were determined in the second session.

SHRIMP-RG results for Mg, V, Cr, Mn, and Ni, are shown in Figure 3-11. Contents of transition metals are correlated with Mg content, a proxy for the illite (ferromagnesian) component in clays that show both solid solution to smectite and fine-scale intergrowth with other clay minerals, such as kaolinite. Contents of V and Cr show similar ranges in the illite/smectites, and appear to be correlated (Figure 3-11e). Quantifying the concentration of

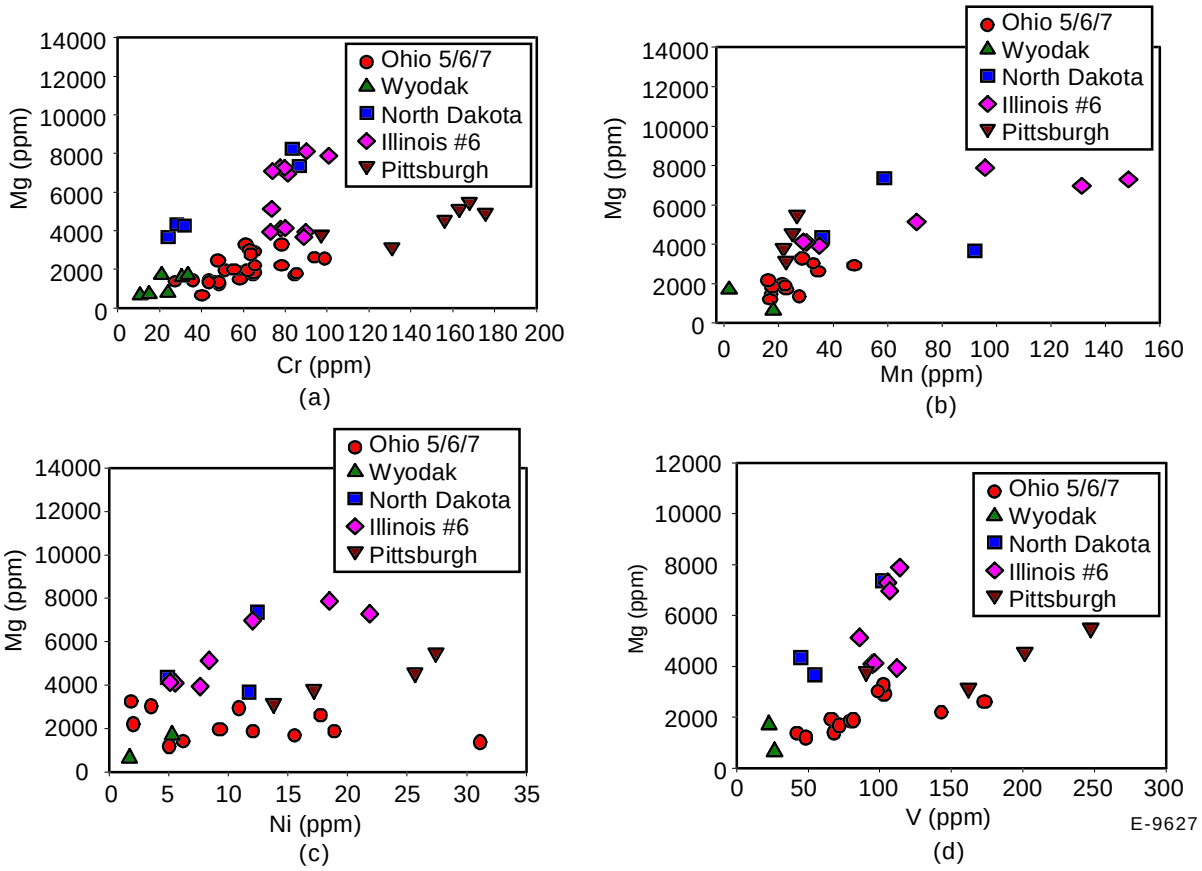

Figure 3-11. SHRIMP-RG results for illite/smectite. (a)-(d) SHRIMP-RG results for illite/smectite in Phase II samples and Phase I Illinois #6 and Pittsburgh samples.

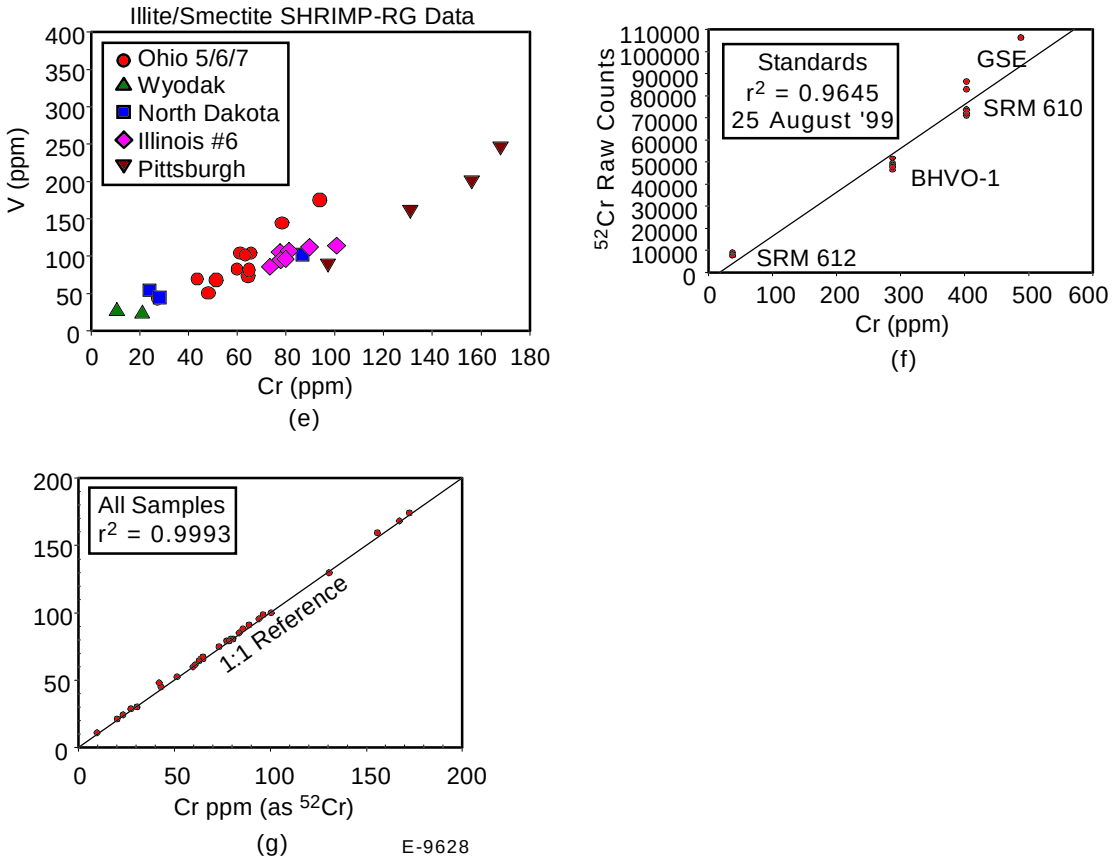

Figure 3-11. SHRIMP-RG results for illite/smectite (continued). (e)-(g) Additional SHRIMP-RG results for illite/smectite.

Cr was the highest priority of the study, and therefore, Cr was determined twice, as ^{52}Cr and as ^{53}Cr. Using this approach, the natural ratio of $^{53}Cr/^{52}Cr$ (0.1134) was easily reproduced to three decimal places. Concentrations obtained using the two chromium isotopes were generally within 1% (absolute), for calibrations obtained using the same standard (Figure 3-11g).

The capabilities of the SHRIMP-RG instrument for investigating Hg in sulfides, and arsenic on the surfaces of ash particles, were also investigated. In the Spring of 2000, laboratory staff brought online a new, more energetic duoplasmatron ion source, producing a Cs primary beam, that we considered necessary to ionize elements such as arsenic and mercury, not readily ionized by the oxygen primary beam used to analyze illite/smectite. Test results on HgS, using the Cs beam, showed insufficient Hg ionization. This was also found to be the case for Hg ionization tests on HgS using the O_2^- source. Test determinations of As in flyash, using the oxygen primary beam, show sufficient mass resolution to determine ^{75}As, but the Cs source, which will be available again periodically, is needed to obtain higher count rates.

In January 2001, SHRIMP-RG ion probe data were obtained for pyrite in the three Phase II coals and for the Illinois #6 and Pittsburgh samples from Phase I of the program. Minor or trace elements determined include Ti, Cr, Mn, Co, Ni, Cu, Zn, As, Se, Cd, Sb, and Pb, using the oxygen duoplasmatron source. Because suitable standards, offering a close matrix match to the pyrite unknowns, were not available, quantitative results were not obtained. However, the results show relative differences among the samples, when the response for trace elements is plotted as ratios vs. ^{32}S or ^{57}Fe, whose content in pyrite is assumed to be uniform. Because the ionization efficiency differs for each element, and relative sensitivity factors (a measure of ionization efficiency) for pyrite are not well known, the ratios determined cannot be used to compute concentrations using Fe or S as an internal standard.

Results were obtained for Cd whose contents are mostly below the electron microprobe detection limit, and Sb, not determined by microprobe. Results for Cd, Se, and possibly other elements, show enrichment in pyrite present in the two low rank coals (North Dakota and Wyodak) relative to pyrite in the Ohio 5/6/7 sample, and two other bituminous coals from Phase I (Figure 3-12). Note that count rates for Cd, Sb, and As are all similar, even though arsenic in pyrite is generally more abundant than the other two elements. This suggests that relative sensitivity factors (RSF's) for these elements in pyrite are like those in silicate matrices, in which RSF's for Cd and Sb are similar, and the RSF for As is lower [54].

Laser Ablation ICP-MS

Reconnaissance laser ablation ICP-MS data were obtained for pyrite in the Ohio 5/6/7 coal, and for the Illinois #6 and Pittsburgh samples from Phase I. The system used is located in USGS labs at the Denver Federal Center, and consists of a pulsed Nd(YAG) laser coupled to a dedicated ICP-MS. In order to obtain results for Hg at the 0.5 ppm level, instrument conditions included a 50 μm spot, and a laser pulse rate of 20 Hz at 75% energy. These conditions give an excavation rate of about 3 μm/sec NIST SRM 2710 was used for analysis of Hg, and USGS standard GSE was used for other elements determined, including Cr, Mn, Co, Ni, Cu, Zn, As, Se,

Mo, Cd, Sb, Tl, and Pb. Fe was used as an internal standard, and its concentration was fixed at the Fe content of stoichiometric pyrite. Ablated material is introduced into the ICP-MS analyzer as an argon plasma, therefore, matrix match between standards and unknowns is not critical. Laser ablation ICP-MS data were not obtained for pyrite in the Wyodak and North Dakota samples, because these do not contain pyrite grains large enough to analyze with the 50 μm spot.

Results of the reconnaissance laser ablation ICP-MS analysis of pyrite in the Ohio 5/6/7 sample are given in Table H-1 (Appendix H). As in the SHRIMP-RG determination of Cr in illite, Hg was determined using two isotopes, ^{200}Hg (23.1% of Hg) and ^{202}Hg (29.9% of Hg). Each isotope provided acceptable results; there is a slight bias towards higher contents using the more abundant isotope (Figure 3-13a). The data show the most mercury-rich pyrites are also enriched in other metals (Figure 3-13b-c).

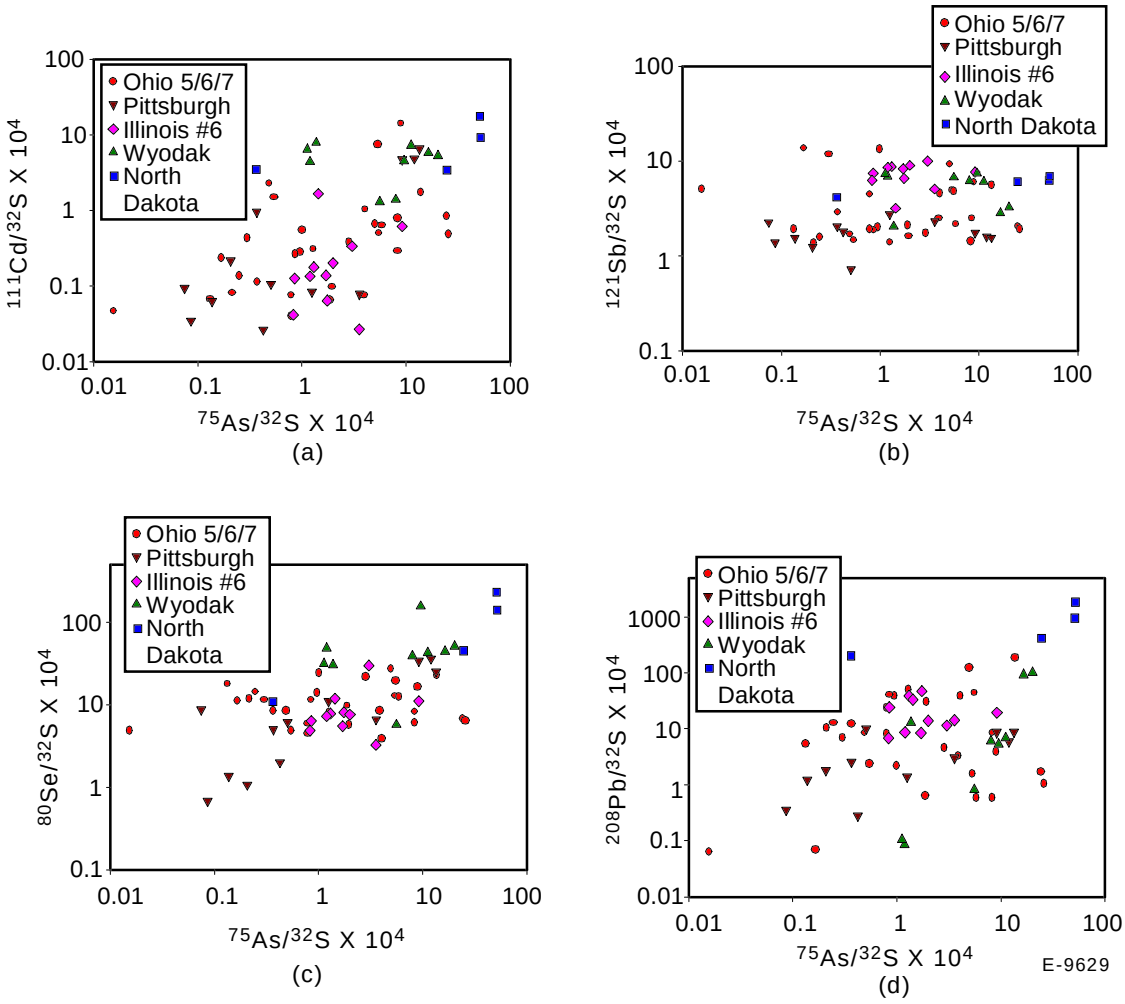

Figure 3-12. SHRIMP-RG results for pyrite in Phase II samples and Phase I Illinois #6 and Pittsburgh samples.

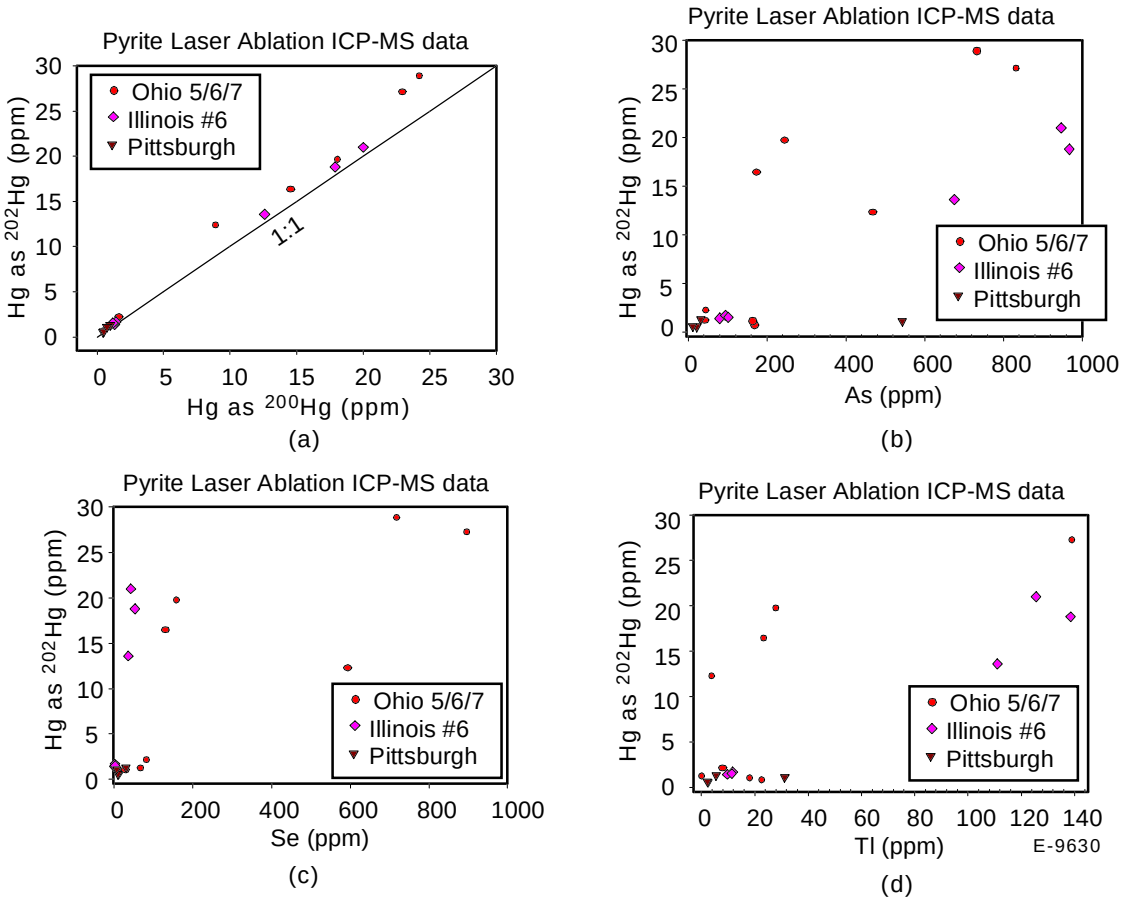

Figure 3-13. Laser ablation ICP-MS results for pyrite in Phase II Ohio 5/6/7 sample and Phase I Illinois #6 and Pittsburgh samples.

3.1.3.8 Phase I Follow-up Studies

As new techniques were applied to the three Phase II samples, these techniques were used to obtain additional results for samples studied in Phase I of the program. This includes selective leaching of the Phase I Elkhorn/Hazard coal using the flask method and electron microprobe analysis of calcite in the Phase I Pittsburgh and Illinois #6 coals. The Pittsburgh and Illinois #6 samples were also used to analyze illite/smectite and pyrite by SHRIMP-RG and pyrite by laser ablation ICP-MS. Leaching results for the Phase I Elkhorn/Hazard sample, and electron microprobe results for calcite in Phase I coals have been presented in previous interim reports. New results for Phase I coals by SHRIMP-RG and laser ablation ICP-MS are included here.

3.1.4 Element Speciation by XAFS Spectroscopy

For the direct elucidation of elemental occurrences in coal, we have demonstrated, in Phase I of the study [7] as well as in other studies [54], the value of performing XAFS spectroscopy not just on the coal itself, but also on various fractions prepared from the coal. Such fractions can be prepared either by float-sink in high specific-gravity liquids (e.g., perchloroethylene and bromoform) or by separation according to surficial properties (e.g., Denver cell, froth flotation) or by combination of both methods. It was felt that such separations would need to be performed for the three new project coals and were generously carried out for us by Dr. B.K. Parekh, Associate Director of the U.K. Center for Applied Energy Research (CAER), and his staff. However, only the Ohio coal was effectively separated by such methods. Fractions from such separations were then subjected to both XAFS spectroscopy and Mössbauer spectroscopy. The information obtained was used to complement the more general, but indirect speciation methods based on a leaching behavior protocol carried out by U.S. Geological Survey personnel.

In due course, however, it was felt that the *best* approach to take would be to carry out such spectroscopic characterization on the *chemical* fractions generated in the leaching protocol itself, as this would enable a better comparison between the indirect leaching protocol and the direct XAFS spectroscopic method to be made. XAFS results from both suites of fractions prepared from the project coals are reported herein.

Arsenic. The arsenic XANES spectra of two of the project coals (Ohio bituminous and North Dakota lignite) are shown in Figure 3-14. The arsenic content of the Wyodak coal is only about 1/10 of that in the other two coals. The spectrum of the Ohio raw bituminous coal was recorded at three different times: at both SSRL (05/1998) and NSLS (07/1998), about 2 months apart, and finally again at SSRL (03/2001), after almost 3 years. As can be seen the quality of the data at SSRL is somewhat better, but the difference is not that marked. The As XAFS spectra of the fractions were also obtained at NSLS in July 1998, except for the HYM fraction that was measured in February 1999. As with the investigation of As in Phase I bituminous coals, both As/pyrite and arsenate forms are readily apparent in the spectra of the Ohio bituminous coal and fractions. Using the procedure previously described [55], quantitative estimates of the major As forms in these coals have been made and are summarized in Table 3-16. The difference in relative peak heights between the spectra of the raw Ohio coal taken 2 months apart indicates on-going oxidation of arsenical pyrite to arsenate. However, although a significant initial change was observed during the first 2 months, only a further similar-sized change was noted for the interval of almost 3 years, between 07/1998 and 03/2001. The arsenic in the North Dakota lignite was significantly more oxidized than that in the Ohio bituminous coal and could only be satisfactorily fit with an As^{3+}-O component, which might actually be a primary component [56].

In October 1999, for each project coal, we received a complete suite of the residues after each step of the USGS leaching protocol for trace-element speciation [52] from our colleagues at the USGS. Arsenic XAFS data were then obtained for most of these coal samples during an XAFS session at beam-line X-18B at the National Synchrotron Light Source, Brookhaven National Laboratory, during the period October 28-31, 1999. By means of using a combination

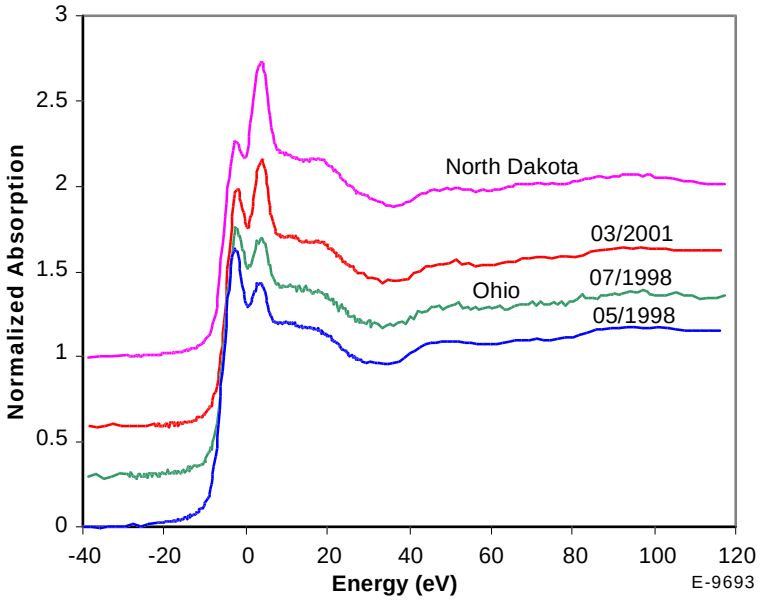

Figure 3-14. Arsenic XANES spectra of the North Dakota lignite and of the same sampling of the Ohio coal taken at three different times.

Table 3-16. As XANES Results of Least-Squares Fitting - Project Coals

Coal Sample (mo/yr)	As/Pyrite	As^{3+}-O	As/Arsenate	ΔP*, eV
Ohio Raw (05/98)	87		13	6.5
Ohio Raw (07/98)	84		16	6.3
Ohio, Concentrate (07/98)	80		20	6.1
Ohio, Tailings (07/98)	86		14	6.6
Ohio, HYM (02/99)	>90		<10	--
Ohio Raw (03/01)	80		20	6.1
ND Lignite (07/98)	28	18	54	6.4

*ΔP is the difference in eV between the positions of the two peaks.

of Soller slits, a 6μ Ge filter, maximum operating voltage (2.8 GeV) for the synchrotron, and multiple scanning, some surprisingly good quality results were obtained for the arsenic in the Ohio and North Dakota sample suites. Even some of the Wyodak samples, with less than 1 ppm As, provided spectra that could be used to estimate the oxidation state of arsenic. The arsenic contents of the residue fractions, determined by instrumental neutron activation analysis (INAA) after each extraction, are summarized in Table 3-17. A more detailed account of the work summarized here has been given elsewhere [57].

Table 3-17. As Contents of Residues (by INAA) Remaining After Leaching Experiments

	Ohio Bituminous As in ppm	Wyodak Subbit. As in ppm	N. D. Lignite As in ppm
After amm. acet. leach	19.1	1.7	11.0
After HCl leach	15.1	1.0	5.2
After HF leach	15.2	0.7	3.6
After HNO_3 leach	0.9	0.4	1.6

Arsenic XAFS spectra were collected from the various fractions using as many as ten scans for each sample. The spectra are shown in Figures 3-15a and 3-15b for the Ohio bituminous coal and in Figures 3-16a and 3-16b for the North Dakota lignite. Figures 3-15a and 3-16a show the unnormalized spectra, whereas Figures 3-15b and 3-16b show the same spectra normalized to the edge step and hence, these latter groupings of spectra have the effect of concentration removed from them. By comparison of the spectra for the physically-separated fractions obtained earlier (Figure 3-14), it is clear that the North Dakota lignite is significantly more oxidized in the chemically-separated fractions provided by USGS personnel. There is now no indication of any arsenic associated with pyrite.

The analytical data in Table 3-17 can be correlated with the step-height determined from XAFS spectra, which is also an approximate measure of the arsenic concentration. This correlation is shown in Figure 3-17. The correlations between the analytical data and the XAFS edge-step heights for the two coals show a reasonable approximation to a linear relationship. For the Ohio bituminous coal, the correlation coefficient (r^2) exceeds 98%, whereas it is about 90% for the North Dakota lignite. This result indicates that both analyses are consistent with each other.

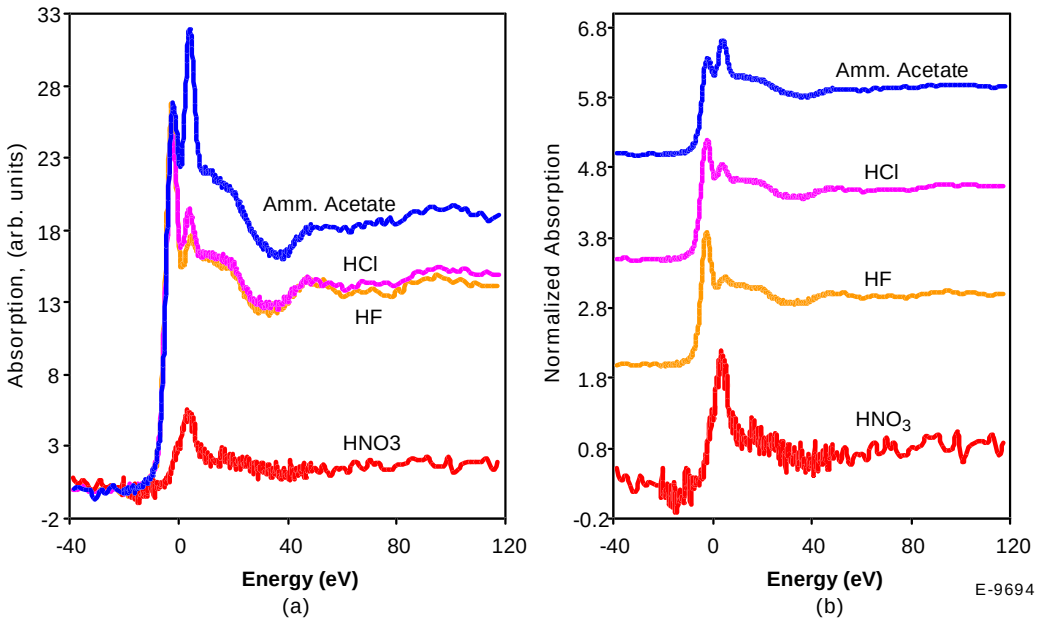

Figure 3-15. Unnormalized (a) and normalized (b) arsenic XANES spectra for the Ohio coal residues after different stages of the USGS leaching protocol.

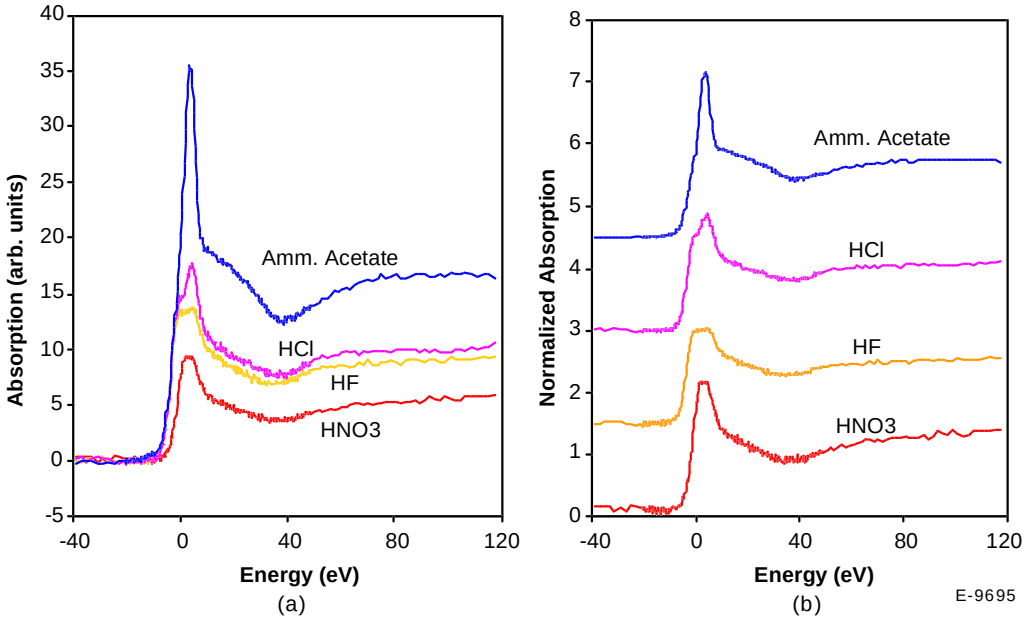

Figure 3-16. Unnormalized (a) and normalized (b) arsenic XANES spectra for North Dakota Lignite residues after different stages of the USGS leaching protocol.

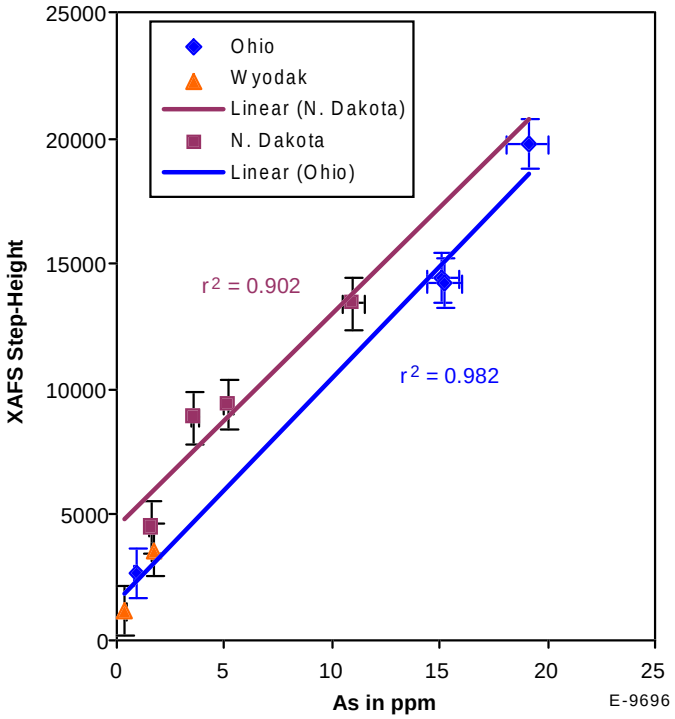

Figure 3-17. Correlation between the XAFS step-height and the concentration of arsenic in the leached residues.

The As XANES data for the leached residues clearly show, by the reduction in intensity of the major peak at about 4.0 eV in Figures 3-15 and 3-16, that the HCl treatment removes principally, if not exclusively, arsenate from both the Ohio and North Dakota coals. This observation confirms more definitively the similar conclusion made in Phase I of this study [7, 52] based on a less direct comparison of leaching data and arsenic XAFS data for various coals. The data show also that the HF treatment has little effect, except for removing some very minor amounts of arsenate remaining after the HCl treatment. For the Ohio coal, as indicated by the reduction in intensity of the peak at about –2.3 eV, the HNO_3 treatment removes all of the pyritic arsenic. However, no such phase is present in the North Dakota lignite. Rather for this coal, the HNO_3 treatment appears to be removing an As^{3+} phase, as the peak that is removed is close to 0 eV. For both coals, there is a small residue of arsenic that remains after all the leachings. It is not arsenical pyrite or As^{3+}, but rather more like an arsenate phase.

The calibrated least-squares fitting model, developed previously [55], was used to quantify the arsenic speciation in the Ohio bituminous coal samples. For this coal, it was decided to fit only the two major arsenic forms present: arsenical pyrite and arsenate. The arsenic speciation results for the Ohio bituminous coal obtained using this procedure are summarized in Table 3-18. The least-squares fitting model has not yet been modified for application to the low-rank coals and their different arsenic species.

Table 3-18. Estimates of Arsenic Forms Remaining After Each Leaching Step in the Ohio Coal

Leachant	% As as As/pyrite	% As as Arsenate	ppm As as As/pyrite	ppm As as Arsenate
Amm. acetate 19.1 ppm As remains	75	25	14.3	4.8
HCl 15.1 ppm As remains	93	7	14.0	1.1
HF 15.2 ppm As remains	>95	<5	>14.4	<0.8
HNO_3 0.9 ppm As remains	<10	>90	<0.1	>0.8

Based on the least-squares fitting analysis, the concentration of arsenic as As/pyrite after the first three leaching steps is approximately the same, 14 ± 1 ppm. This indicates that none of the three reagents, ammonium acetate, HCl, or HF removes significant arsenic as As/pyrite. As has been postulated previously [55], the presence of arsenic in pyrite appears to make pyrite more reactive to oxidation. However, for this particular coal, it does not appear that any arsenic associated with pyrite is leached prior to the HNO_3 treatment. The HF leach appears to remove only the minor arsenate remaining after the HCl leach. The HNO_3 leach removes all of the arsenic as arsenical pyrite and appears to leave a small residue of arsenate on the carbonaceous materials. It should be noted that the arsenate in the HNO_3 residue is higher than that remaining after the HF leach, suggesting that it has been formed during the nitric acid leach.

It would appear that the use of arsenic XAFS spectroscopy to examine arsenic in leached residues of coals from a sequential leaching protocol for elemental speciation in coals has provided an unparalleled insight into the leaching characteristics of arsenic from coal and enables a rather complete assessment of the assumptions behind using sequential leaching for arsenic speciation to be made. XAFS spectroscopy shows clearly that the major fraction of arsenic leached from both coals by HCl is arsenate and that HNO_3 removes much of the remaining arsenic in both coals. Leaching with HF has little effect on the arsenic content of both coals examined and appears restricted to removing any arsenate species that remains after the HCl leach. Such an observation suggests that there is no arsenic associated with silicates in these coals, even though minor fractions of arsenic are removed by HF leaching. The arsenic associated with pyrite in the bituminous coal is removed effectively by nitric acid, but a quite different form is removed from the lignite by nitric acid. The XAFS data suggest that this arsenic phase may be an As^{3+} species, but it remains yet to be positively identified. Finally, a small fraction of the arsenic (5-15%) remains in the coal after the final nitric acid leach. It is suspected that this may be an organoarsenate formed by a side reaction between the arsenic leached from the coal and new oxygen functionality on the coal introduced by oxidative reaction of the coal macerals with nitric acid.

Chromium. Significant XAFS investigation of chromium in the three project coals was attempted with only limited success for the Ohio coal. The two lower-rank coals generally exhibited rather poor quality spectra, most likely because they contain greater quantities of calcium, which can contribute significantly to the background noise at the chromium K-edge. As for arsenic, both physically separated fractions and the USGS leached residues were examined for chromium in the Ohio and North Dakota coals. Only the raw coal was examined for the Wyodak coal, which had the lowest Cr content of the three coals.

Chromium XANES of the physically separated fractions of the Ohio coal are shown in Figure 3-18. The two major peaks in the Cr XANES spectra are quite well resolved, although the prominence and asymmetry of the two peaks become more pronounced in the sequence: organic (float) fraction < raw coal < tailings (sink) fraction. As also shown in Figure 3-18, the derivative of the chromium XANES spectrum of the tailings fraction is of reasonably good quality and exhibits the characteristic three-peaked pattern similar to that observed for chromium in the layer silicates, illite and muscovite [58, 59]. This is a clear indication that the chromium in the tailings fraction is mostly associated with the clay mineral illite. The characteristic spectral features of Cr/illite are less obvious in the raw coal and organic fraction, indicating that at least one other major chromium form is present in the coal, presumably the CrOOH phase postulated to exist in organic association [58-60].

The Cr XANES data for the leached samples of the Ohio bituminous coal are shown in Figure 3-19. These data appear to show significant differences when compared with the data obtained for the samples of the Ohio bituminous coal prepared by float/sink techniques (Figure 3-18). However, the spectra of the ammonium acetate and HCl leached coals are similar to those obtained from the raw and organic fractions. The biggest change comes after the HF leach, when the second peak degrades to a broad shoulder, and the spectra at this and the subsequent nitric-acid leach stage are dissimilar to any of those observed for the physically-separated fractions. The explanation for this is readily apparent. The HF leach removes the

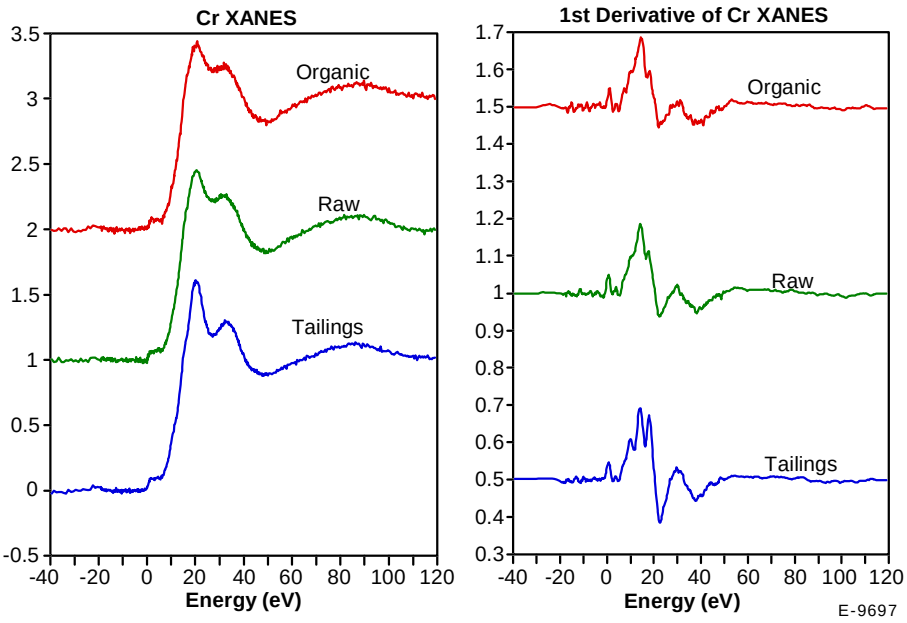

Figure 3-18. Cr XANES spectra of physically-separated fractions of the Ohio bituminous coal.

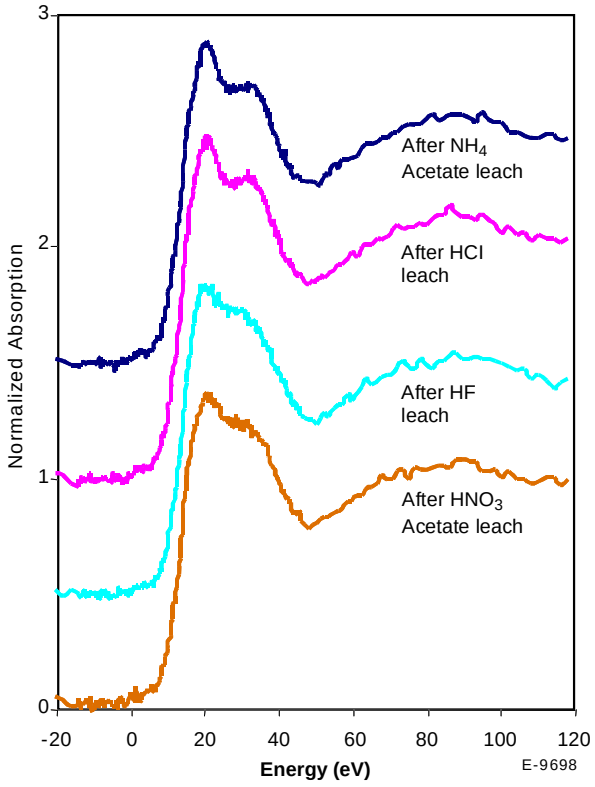

Figure 3-19. Cr XANES spectra of leached fractions of the Ohio bituminous coal residues after different stages of the USGS leaching protocol.

aluminosilicate fraction, i.e., the Cr/illite that is abundant in the tailings fraction, leaving only organically-associated chromium. The spectrum that is observed after the HF leach more closely resembles that of poorly crystallized CrOOH, which is thought to constitute much of the chromium in organic association in U.S. bituminous coals, than does the spectrum of the organic fraction in the physically separated suite of samples.

These spectra appear to be compatible with previous investigations [42, 59] of Cr in bituminous coals, in which chromium is believed to occur in two principal forms: as Cr in the clay mineral illite (Cr/illite) and as a predominantly organically-associated phase, thought to be a poorly crystalline chromium oxyhydroxide (CrOOH). The major distinguishing feature of these two occurrences of chromium is the prominence of the shoulder peak in their XANES spectra at about 30 eV. On examining the spectra shown in Figures 3-18 and 3-19, the spectra with the least prominent shoulder peaks are the HNO_3- and HF-leached coal samples, whereas the most prominent shoulder peak occurs in the spectrum of the float/sink tailings fraction. These spectra represent the two extremes and must come closest to the spectra of CrOOH and Cr/illite, respectively. All other Cr XANES spectra shown in Figures 3-18 and 3-19 (viz., the amm. acetate and HCl-leached coals, the raw coal and the organic float/sink fraction) can be simulated from weighted additions of these two extreme spectra.

Data for the Cr contents and step-heights of the leached samples are summarized in Table 3-19. From the significant but relatively small changes in step-height and in Cr content between the HCl- and HF-leached samples, it is estimated that only about 15 to 25% of the Cr in the Ohio coal can be Cr/illite. The other leaching solutions have little or no effect on Cr in the Ohio coal. The chromium XAFS spectral data (Figure 3-20) and step-height data (Table 3-19) for the North Dakota lignite appear somewhat similar to those for the Ohio bituminous coal. However, the overall absorption background for the lignite was higher than that for the bituminous coal due presumably to the abundance of Ca in the sample, which gave rise to a significantly poorer signal/noise ratio and a less certain interpretation. Again, the largest change is seen for the HF leach stage indicating that a minor fraction (25 to 50%) of the Cr exists as Cr associated with clays, while the major fraction is relatively unaffected by any of the leaching solutions, although the nitric acid leach may be somewhat effective in removing some Cr.

Table 3-19. Relative Step-Heights and Concentrations for Chromium in Leached Coal Residues

	Ohio Bituminous Coal		**N. Dakota Lignite**	
Sample	**Step-hgt**	**Cr in ppm**	**Step-hgt**	**Cr in ppm**
After amm. acetate leach	0.22	15	0.18	11
After HCl leach	0.23	15	0.18	12
After HF leach	0.19	11	0.14	5
After HNO_3 leach	0.20	9	0.10	4

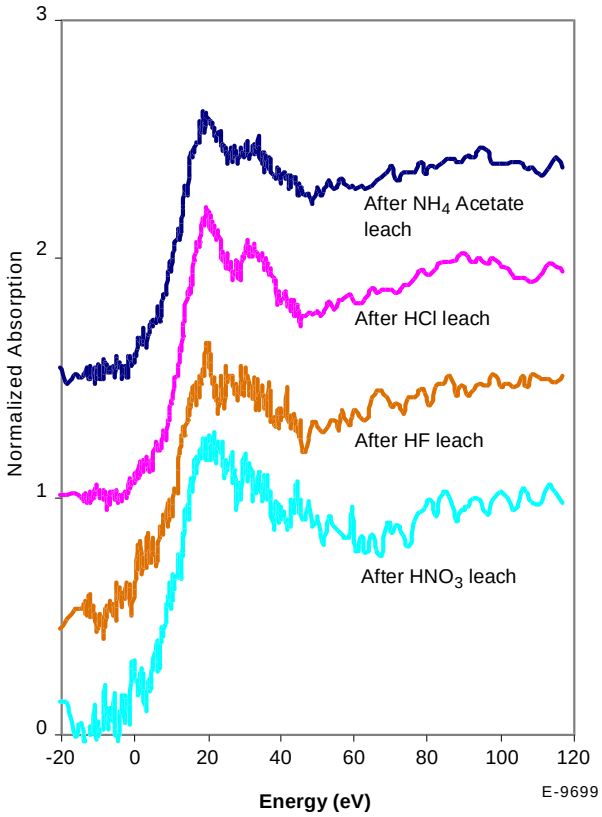

Figure 3-20. Cr XANES spectra of leached fractions of the North Dakota lignite residues after different stages of the USGS leaching protocol.

The chromium XANES of the Wyodak coal was rather noisy; but it appeared to be mostly organically-bound Cr as there was little or no evidence for Cr/illite in the spectrum derivative.

Zinc. XAFS data for zinc were obtained on the USGS leached residues from the Ohio and North Dakota project coals; zinc XANES spectra are shown for the Ohio residues after various stages of the leaching procedure in Figure 3-21. The HCl leaching is effective in removing a significant fraction of the zinc from the Ohio coal, which, according to the leaching scheme protocol, should be considered to be sphalerite, ZnS. As shown in Table 3-20, the step-height drops by about 50% between the ammonium acetate leach and the HCl leach. The shape of the zinc XANES spectrum also changes significantly between the ammonium acetate and HCl leached residue stages (Figure 3-21). Whereas the spectrum of the ammonium acetate leach residue has a flattened appearance, the spectrum after the HCl leach has a much more pronounced main peak. A suite of XANES spectra for various zinc compounds is shown in Figure 3-22. None of the spectra of the standards is close to any of the spectra shown in Figure 3-21. For certain, sphalerite is not a significant component of any of the fractions, although it is conceivable that a small fraction (<20% of the Zn) might be present in the amm. acetate leached sample. However, attempts to subtract the spectrum of the HCl-leached residue from that of the amm. acetate leached residue did not result in a spectrum that resembled that of ZnS (Figure 3-23).

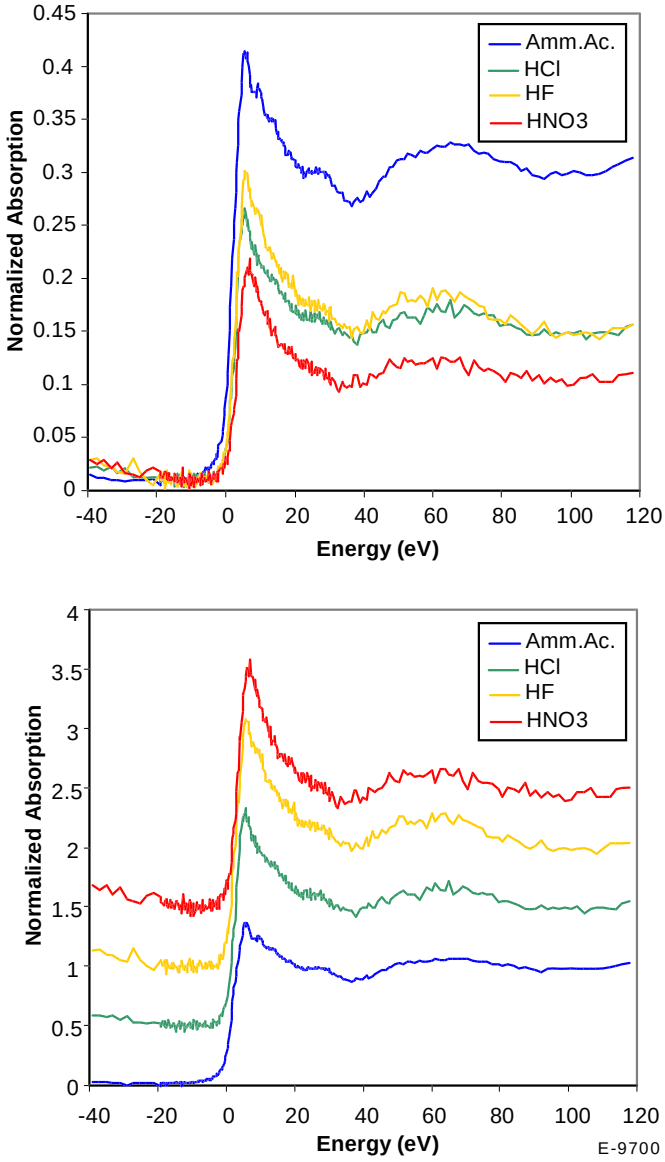

Figure 3-21. Top: unnormalized XANES spectra of Zn in leached residues of Ohio #5 coal; bottom: normalized XANES spectra of the same fractions.

Table 3-20. Relative Step-Heights and Concentrations for Zinc in Leached Coal Residues

Sample	Ohio Bituminous Coal		N. Dakota Lignite	
	Step-hgt	Zn in ppm	Step-hgt	Zn in ppm
After amm. acetate leach	0.31	24	0.16	12
After HCl leach	0.15	18	0.08	<6
After HF leach	0.14	10	0.11	<2
After HNO_3 leach	0.10	4	<0.05	<2

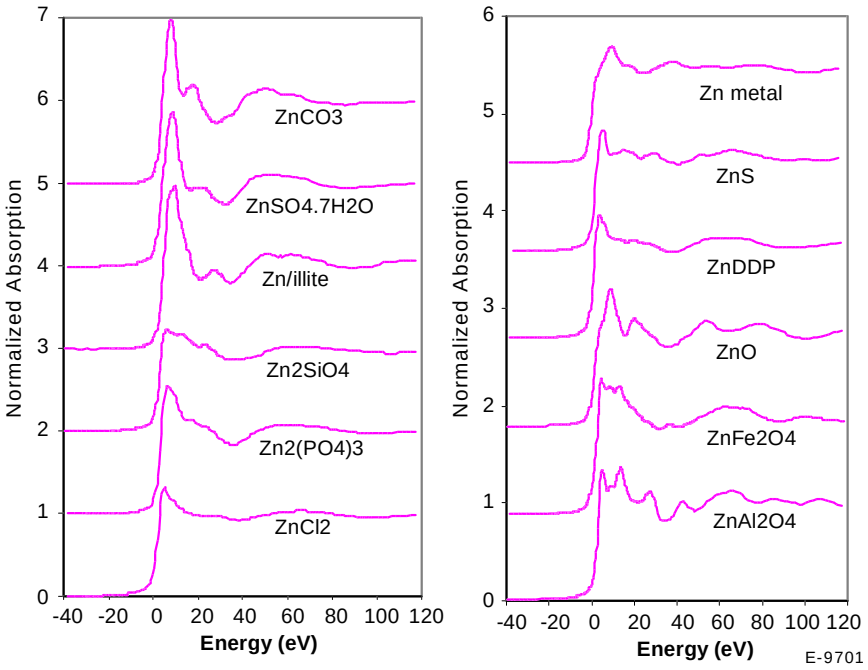

Figure 3-22. XANES spectra of zinc standards.

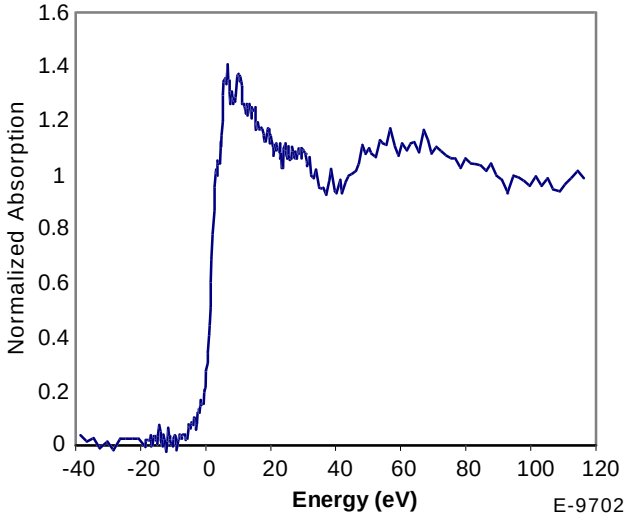

Figure 3-23. Zn difference XANES spectrum obtained by subtracting the Zn XANES spectrum of the HCl-leached residue from that of the amm. acetate-leached residue.

Zinc XAFS data for the leached fractions of the North Dakota lignite were also obtained. However, the spectra were poorer in quality that those obtained for the Ohio coal. But again, although a large change was seen at the HCl-leach stage (Table 3-20), the spectra did not identify zinc sulfide as the zinc constituent leached from the lignite residues at that stage.

Selenium. Some spectra of selenium in project coals were obtained at NSLS in July 1998, but the quality of the data reflects the low selenium contents of the coals: 2.1 ppm for the Ohio coal, 0.8 ppm for the North Dakota lignite and 1.2 ppm for the Wyodak subbituminous coal. The collected data are shown in Figure 3-24. Despite the relatively poor quality of the data, the Se XANES spectra for the Ohio coal and fraction do appear to indicate a significant Se/pyrite association as the spectra are similar to data obtained previously with coals of higher Se content [58]. This observation is consistent with the leaching results obtained for Se, which shows that almost all of the Se is removed from the Ohio coal only during the final HNO_3 leaching stage when pyrite is expected to be leached from the coal.

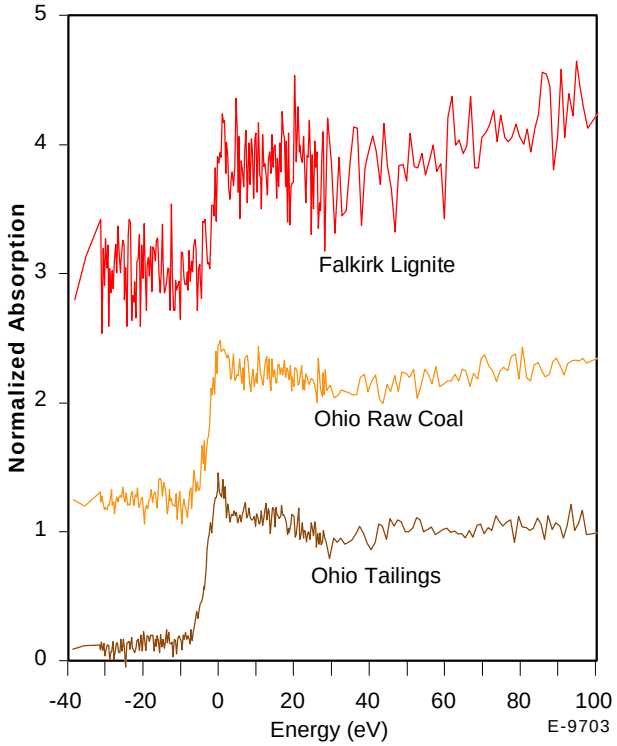

Figure 3-24. Se XANES spectra of the Ohio raw coal, the Ohio tailings fraction, and the North Dakota lignite.

3.1.5 Characterization High Arsenic Coals from USGS

Five high arsenic coals received from H. E. Belkin, USGS were investigated by both arsenic XAFS and iron Mössbauer spectroscopies in order to get a better understanding of the nature of oxidized arsenic in coals, which is so prevalent in virtually all coals as a result of the facile oxidation of reduced arsenic forms, especially arsenical pyrite. As is normally done, the arsenic XAFS spectra of the five high-As coals were divided into separate XANES and EXAFS regions for analysis. The resulting arsenic XANES spectra are shown in Figure 3-25. It is clear by visual inspection that these spectra, with a main peak and an obvious shoulder, indicate the presence of at least two different arsenic forms in each sample, with the possible exception of sample JL-As6-97A. The spectrum of this last sample indicates only the presence of significant arsenate (AsO_4^{3-}), based on the peak position of the main peak. The radial structure functions (RSFs) derived from analysis of the EXAFS regions are shown in Figure 3-26. Only a relatively poor quality RSF was obtained from sample JL-As1-97A, owing to the poor signal/noise ratio in the EXAFS region. The RSFs shown in Figure 3-26, especially the top four, are similar; all show one major peak at about 1.25 Å that, as previous work [7, 52, 60] has documented, clearly corresponds to the As-O distance in the AsO_4^{3-} anion unit. However, the spectra are slightly different in that the RSF peak at 1.25 Å is more intense for the JL-As6-97A sample and less intense for the JL-As1-97A sample than for the other samples and may therefore indicate a somewhat higher and lower relative fractions of arsenic as arsenate, respectively, in these samples. In addition, the top four RSF spectra indicate a small but significant peak at around 2.7 Å (denoted by the dashed line in Figure 3-15(b). This peak may indicate the presence of a small fraction of arsenic as As_2O_3, since this oxide has a significant peak at about 2.8 Å (its main peak at about 1.35 Å can not be seen as it is hidden by the much larger arsenate peak at about 1.25 Å).

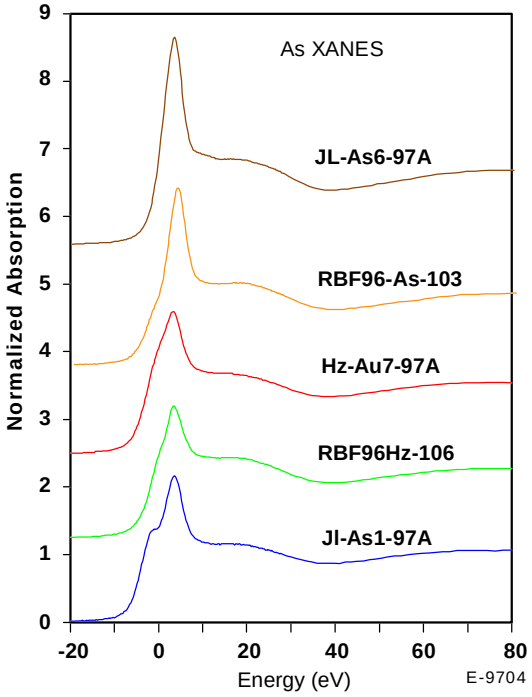

Figure 3-25. As XANES spectra for USGS high arsenic coals.

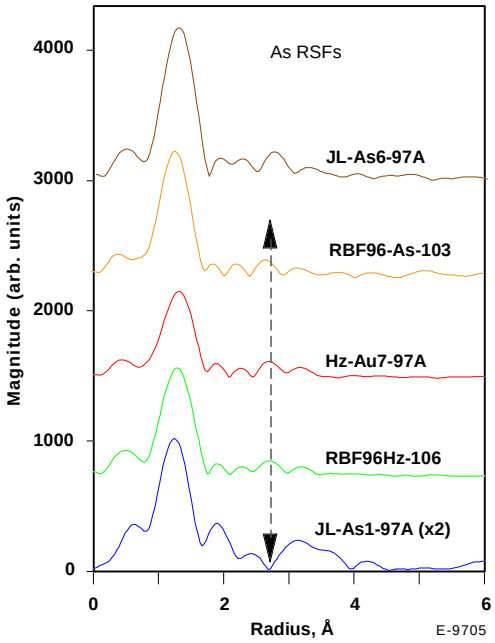

Figure 3-26. As XAFS/RSFs spectra for USGS high arsenic coals.

Only one of the RSF spectra (for sample JL-As1-97A) showed any evidence for a peak at about 1.9 - 2.0 Å that could be attributed to arsenical pyrite. As a result, the mixture of different forms in sample JL-As1-97A (see discussion below and data in Table 3-21) may also have been a contributing factor as to why a relatively poor RSF was obtained with this particular sample.

Table 21. Results of Mössbauer and As XANES Spectral Fitting on USGS High-As Coals

Coal Sample	Mössbauer, % Fe			XANES, % As			
	Pyr	Jar	Other	As/Pyr	As/Sulf.	As/Oxide	Arsenate
JL-As1-97A	82	11	7**	40	14		46
RBF96-Hz-106	91	9			7	24	69
Hz-Au7-97A	64	29	7**		18	25	57
JL-As6-97A	<5	<10	>90*			12	88
RBF96-As-103	60	40		22		11	67

*superparamagnetic FeOOH; ** unknown

The individual arsenic XANES spectra have been subjected to least-squares fitting in order to identify and quantify the different forms of arsenic in the samples. Initially, two-peak fits were tried; but there was no consistency in the location of the peak at lower energy, although the prominent arsenate peak was fitted precisely each time. It was clear that the behavior is more complicated than that indicated by just two peaks, in agreement with inferences from earlier work [54]. We next tried a constrained three-peak fit: one peak for the arsenate absorption peak at 3 to 4 eV; and then two peaks for two absorptions among the following three different types of arsenic forms: a peak at about -2.3 eV for arsenical pyrite; a peak at -1.5 eV for arsenic sulfide forms (AsS, As_2S_3) and a peak at 0.0 eV for As^{3+} oxide forms (e.g., As_2O_3) (see Ref. 59 for data on arsenic standard compounds). Fits were tried with all four peaks; but typically one of the peaks would tend to zero height and would then be dropped from the analysis so that the final fit consisted of three peaks, in which the two peaks at lowest energy were constrained to occur at a certain peak positions.

Such fitting was reasonably robust and two examples are given in Figure 3-27. The results of such fitting are summarized in Table 3-21.

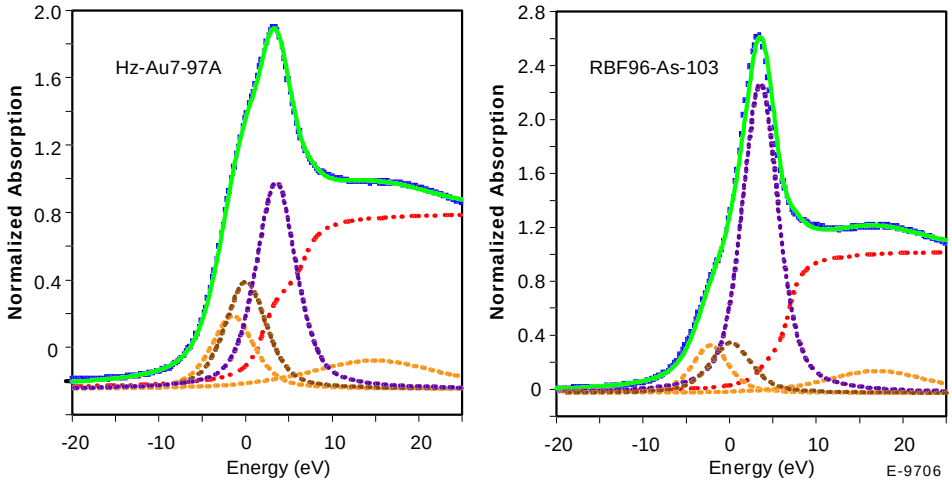

Figure 3-27. LSQ-fitted As XANES spectra for two USGS high arsenic coals. The three peaks correspond to As-S species (Hz-Au7-97A) or As/Pyrite (RBF-As-103) at lowest energy and, in both coals, to As(III)-O and As(V)-O at higher energy. The very broad peak at highest energy is a fitting artifact.

Also summarized in Table 3-21 are the results of the ^{57}Fe Mössbauer analysis for the five samples. Examples of the fitted spectra were shown in Subsection 3.1.2 (e.g., Figure 3-4). Except for sample JL-As6-97A, the Mössbauer spectra of all samples were dominated by iron as pyrite, ranging from 60 to 91% of the iron. The sulfate phase, jarosite, is next most common iron-bearing form, ranging from 9 to 40% of the iron. Sample JL-As6-97A exhibits a quite different Mössbauer spectrum to those of the other four samples. No pyrite or jarosite could be identified in this sample and it appears that all of the iron is present as paramagnetic or superparamagnetic goethite (α-FeOOH).

It is clear that there are some significant differences between the iron Mössbauer and arsenic XAFS data for these samples. Only for the most oxidized sample (JL-As6-97A), for which both techniques indicate that the iron and arsenic in this sample are almost completely oxidized, is there any apparent agreement between the two methods. For the other four samples, the arsenic XANES results always indicate much less arsenic as arsenical pyrite and much more arsenic in oxidized forms than the corresponding Mössbauer data for iron as pyrite and iron in oxidized forms. Of course, there is no reason to expect a 1:1 correlation between these two. In fact, for most of these coals it is likely that the much if not all of the arsenic was introduced into the coal by a completely different mechanism than one which incorporates the arsenic in pyrite. In at least two cases (RBF96-Hz-106 and Hz-Au7-97A), there is no evidence for any arsenical pyrite in the sample, although substantial amounts of iron as pyrite are present in the coal. The presence of significant [As^{3+}-O], which has been noted in the fitted XANES spectra of some of the samples, may correspond also with the observation of a small peak near 2.7 Å in the RSF (indicated by the arrow in Figure 3-26). It is tempting to attribute this RSF peak to the presence of a small fraction of As_2O_3, as this arsenic oxide has a very prominent peak at about this position in its RSF [60]. Evidence for the presence of an intermediate [As-S] phase is restricted to the XANES fitting.

3.1.6 Summary and Recommendations

In this work UK has used XAFS and Mössbauer spectroscopies to characterize elements in project coals. For coals, the principal use was to supply direct information about certain hazardous and other key elements (iron) to complement the more complete indirect investigation of elemental modes of occurrence being carried out by colleagues at USGS.

Coal:

- For comparing speciation information, XAFS experiments should be conducted directly on the residues from the leaching experiments. Using the identical fractions enables the assumptions in the leaching protocol to be tested and provides cleaner fractions for the XAFS investigation.
- Arsenic principally exists in association with pyrite in U.S. bituminous coals and as As^{3+}-O species in lower rank coals. Both forms are easily oxidized to arsenate forms.
- Chromium was found largely in organic association in both bituminous and lower-rank coals. Cr associated with clays (illite) was relatively minor in all three coals.
- Iron was found to be present predominantly as pyrite in all three coals; minor Fe^{2+}/clay and/or siderite were also present, more so in the lower-iron, lower-rank coals. Jarosite was a common oxidation product of pyrite.
- Zinc was not present as zinc sulfide (sphalerite), except possibly in minor amount in the bituminous coal. The major zinc forms in all three coals remain to be identified.
- Selenium is largely associated with pyrite in the bituminous coal; its contents in the lower rank coals were too low to obtain useful information.

Iterative selective leaching using ammonium acetate, HCl, HF, and HNO_3, used in conjunction with mineral identification/quantification, and microanalysis of individual mineral grains, has allowed USGS to delineate modes of occurrence for 44 elements in the Ohio 5/6/7, Wyodak, and North Dakota Program coals. These results provide basic information on the distribution of elements in these coals, information needed for characterization and combustion model development. The Phase II coals show rank-dependent systematic differences in trace-element modes of occurrence. For example, the Ohio 5/6/7 sample shows a greater proportion of chalcophile elements residing in pyrite, compared to the two lower rank coals. These associations are quantified by selective leaching results for each element, and supporting data where obtainable. Microanalysis shows that each of the Phase II coals have pyrite containing isolated domains enriched in one or more potentially harmful elements. Pyrite in the Ohio 5/6/7 coal has the most arsenic-rich micro-domains (approaching 2.0 wt %), but these show no appreciable enrichment in associated chalcophile elements. Grain-scale concentrations of other chalcophile elements (e.g., Cd, Se) may be higher in pyrite in the two lower rank coals, but pyrite is less abundant in these coals than the Ohio 5/6/7 sample. The association of mercury and pyrite was confirmed using laser ablation ICP-MS, for the Ohio 5/6/7 sample, and for the Illinois #6 and Pittsburgh coals studied in Phase I. Chromium and other transition metals in illite/smectite were determined using the SHRIMP-RG ion microprobe, providing concentrations of silicate-hosted metals, at levels below those that can be quantified with the electron microprobe.

3.2 Combustion Zone Transformations (UU, MIT)

3.2.1 Single Particle Combustion Studies

3.2.1.1 Reaction Zone Experiments in the Drop Tube Furnace

Coal combustion products may have several fates. They may fragment and drop to the bottom as super micron residual ash, become vaporized and recondense as submicron particles, or they may escape as vapor in the outgoing flue gas. This study focused on the behavior of trace metals in the combustion system. We have worked to determine which fate trace metal species predominately take. The experiments were conducted in the MIT laminar entrained flow reactor that is now at UU (Figures 3-28 and 3-29). All combustion products were pulled through the cascade impactor for size segregation, and the gases were then filtered through activated carbon to absorb any remaining metals. These samples were sent to MIT for instrumental neutron activated analysis.

All experiments were conducted in an Astro Industrial Model 1000-3560 drop tube furnace. The furnace is optimized for single particle, non-sustained combustion at temperatures up to 1750 K. It is electrically heated by a graphite heating element, which is separated from the combustion zone with an alumina silicate muffle tube. Combustion gases pass through a honeycomb flow straightener at the furnace entrance to ensure laminar flow. Because combustion is diffusion limited, the local atmosphere of the burning particle may be much different from that of the bulk gas. Oxygen is quickly depleted near the particle, resulting in locally reducing conditions. Coal particles enter the furnace by gas entrainment through a syringe feeding system.

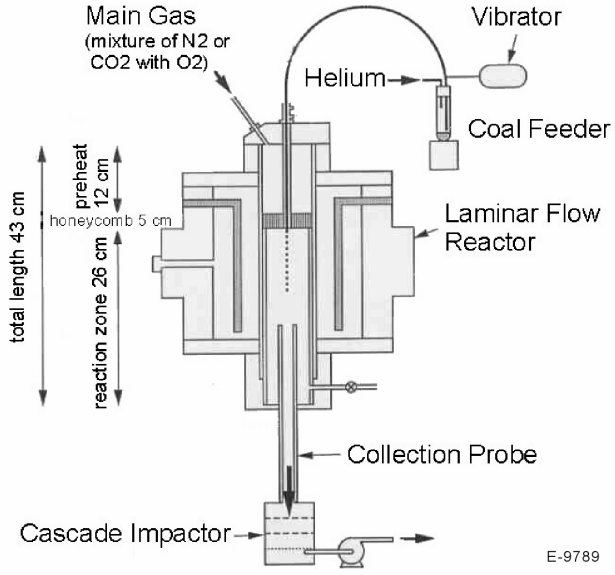

Figure 3-28. Schematic of the drop tube furnace.

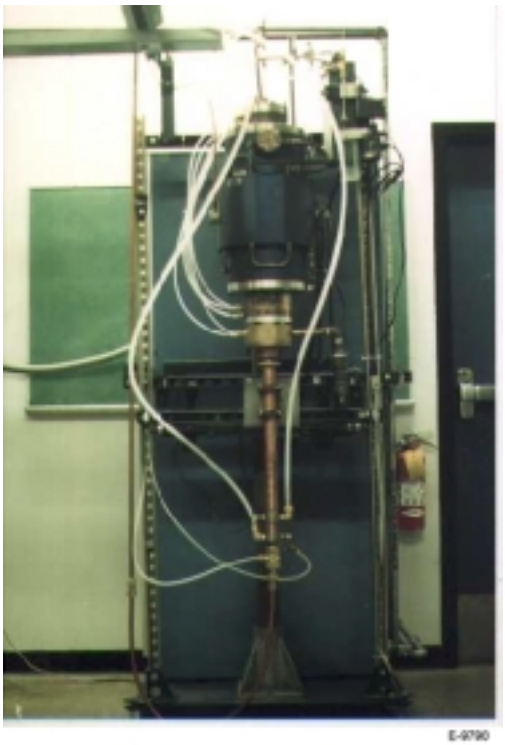

Figure 3-29. Photograph of the drop tube furnace.

Before combustion, the coals were sized according to ASTM sieving methods. Sizing was necessary because residual ash from ultra-fine particles would have been collected in the submicron range along with particles formed through condensation. Very large particles can clog the feeding system. To limit these problems, the size range of 53-74 microns was chosen. As moisture can also cause clogging in the feeding system, the coals were dried according to ASTM methods.

The coals were burned at 1700 K under a series of fuel rich and oxygen rich conditions (Table 3-22). The coal was entrained in helium to increase diffusion of the main gas, which entered adjacent to the coal, and was fed at a rate of approximately 0.02 grams of coal per minute in 5 ml per minute of helium. Below the honeycomb flow straightener, the particles contacted the main gas, which flowed at 6 liters per minute. The combustion atmosphere varied from 0 to 100% oxygen with the balance being either nitrogen or carbon dioxide. The nitrogen provided an inert environment for the reaction. Carbon dioxide was used to investigate the governing reaction:

$$MO(s) + CO(g) = CO_2(g) + M(g) \qquad (3\text{-}1)$$

where M represents a metal species. Carbon dioxide was expected to drive the reverse reaction, thus keeping metals in their less volatile oxidized state, and also to affect the particle temperature. The impact of the carbon dioxide is particularly important since early interpretations of the vaporization data did not properly account for the gas composition in the pores [61, 62]. This has been pointed out by Haynes [63] who has developed a model to account for surface and gas phase reactions on the carbon monoxide-carbon dioxide ratio.

Table 3-22. Combustion Gas Compositions for Drop Tube Experiments

Oxygen	Nitrogen	Carbon Dioxide
0%	100%	0%
20%	80%	0%
50%	50%	0%
100%	0%	0%
20%	0%	80%
50%	0%	50%

The vertical alignment of the furnace ensured that all combustion products were available for analysis with no loss in the reactor. Before beginning any experiments, the furnace alignment was checked at room temperature. Coal was entrained with all gases entering, and 99% of coal fed was collected below the furnace.

After combustion, the particles were rapidly cooled to between 120 and 140°C by addition of 21 liters per minute of nitrogen gas through a water-cooled probe. An Andersen Mark II cascade impactor, located directly below the furnace collected and sized the particles (Table 3-23). Material can be lost in the impactor due to particle bouncing and re-entrainment to lower stages. To minimize these losses, all stages of the impactor were lined with Durapore Millipore filters coated with Apiezon H grease, except the final filter, which was ungreased. This grease was chosen because it is low in metal contaminates. For application, the grease was diluted with toluene and a thin film was applied with an airbrush. The filters were then dried overnight at 120°C and the mass was recorded.

Table 3-23. Cascade Impactor Cutoff Diameters

Stage	Size Range (microns)
Pre-Separator	> 10.0
0	9.0 - 10.0
1	5.8 - 9.0
2	4.7 - 5.8
3	3.3 - 4.7
4	2.1 - 3.3
5	1.1 - 2.1
6	0.7 - 1.1
7	0.4 - 0.7
Final Filter	< 0.4

A side stream of the final exhaust was pulled through a small activated carbon plug to absorb any gas phase mercury and complete the mass balance. After collection, selected impactor stages, representing the residual and submicron ash, and the carbon plug were analyzed using instrumental neutron activated analysis (INAA). This is a nondestructive method, which measures the concentration of most elements larger than sodium.

The length of sampling time of each experiment was from 10 to 45 min, depending on the combustion atmosphere. The sampling time was selected to allow maximum particle collection without overloading the cascade impactor. After collection, all of the stages were weighed. The weights were used to determine the mass balance of the system and identify the separation between the residual and submicron ash.

The time of experiments was from 10 to 45 min depending on the burning conditions. The time length was selected to allow maximum particle collection without overloading the cascade impactor. After collection, the stages were all weighed. Weights were used to determine mass balance of the system and to find the breaking point between the residual and submicron ash.

The reaction rate constant k was approximated as a linear function of temperature, where

$$\frac{\partial x_i}{\partial t} = -k \cdot x \tag{3-2}$$

and

$$k = C_1 \cdot \frac{1}{T} + C_2 \tag{3-3}$$

Coefficients 1 and 2 are presented in Table 3-24.

The initial analysis showed a pronounced bimodal size distribution (Figure 3-30) between residual and fume ash, with the exception of 100% oxygen. At 100% nitrogen, all residual ash was collected above stage 0, indicating that the residual ash was greater than 9 microns (aerodynamic diameter). At 20% and 50% oxygen, the residual ash distribution was broader, with a substantial ash amount of residual ash to stage 4, or greater than 2.1 microns aerodynamic diameter, for Wyodak and ND Lignite. At 100% oxygen, there was no clear distinction between residual and submicron ash. The ash collected on the final filter represented particles smaller than 0.4 microns aerodynamic diameter. This material was considered to be the fume.

Table 3-24. Coefficients for the Rate Constant Approximations as Determined from Data on Temperature Increases in the Furnace

ND Lignite			Ohio (5/6/7)			Wyodak		
Element	**C_1**	**C_2**	**Element**	**C_1**	**C_2**	**Element**	**C_1**	**C_2**
Mg	3809.6	-0.2973	Mg	4638.6	-1.7648	Mg	2847.2	0.4442
Al	1956.5	1.4325	Va	753.12	0.2865	Va	-535.26	0.7282
Ti			Al	7412.3	-2.8201	Al	236.24	1.9545
Va	2474.7	-0.3029	Na	1565.4	-0.0528	Na	-3068.5	1.719
Na	1697.4	0.197	Ti	4430.1	-1.6855	Ti	-5063.9	3.2131
Mn	5017.9	-0.9501	Mn	2995.2	-0.3522	Mn	3794.8	-0.2394
Sr	-5491.6	3.5535	Sr	3764.2	-1.0087	Sr	-3988.3	2.1553
Ba	-8626.5	5.4575	Ca	3400.2	-0.1273	Ca	-1948.5	1.9281
Cl	2996.5	-2.1587	Ba	-939.67	1.023	Ba	-3483.1	2.6421
Ca	2417.7	0.9832	Sc	3245.5	0.0287	Sc	-5619.4	3.9223
Sc	-6954	3.9532	Cl	4835.2	-2.1046	Cl	-5254.4	3.171
Cr	1980.7	0.6149	Sr	1320	0.3582	Cr	846.55	0.5238
Fe	-6589.8	4.1463	Fe	4199.9	-0.6638	Fe	3485.9	0.2648
Br	-2537.2	1.971	Br	6170.2	-1.5142	Br	-5616.8	3.7527
Co	-7061.2	4.4208	Co	2223.4	0.1042	Co	2283.4	0.2352
La	3528.1	-0.4437	La	4893	-0.5862	La	1473.5	1.5002
As	1198.3	0.8031	As	-32.488	0.7341	As	2227.7	-0.299
Ce	-5321.8	3.0253	Ce	1505.3	-0.0355	Ce	2240.3	0.181
Nd			Nd	5546	-2.11	Nd	-7696.6	4.4424
Mo	-5936.1	3.7609	Mo	3890.1	-0.7157	Mo	2322.5	0.6601
Sm	1812.4	1.0966	Sm	4047.3	-0.2578	Sm	2254.7	1.0125
Sb	-3595.4	2.7408	Sb	471.22	0.526	Sb	649.76	-0.857
Zn	1496.7	1.0831	Zn	1834.3	0.2263	Zn	640.76	0.6
Cs	-5872.1	3.6316	Cs	7298.2	-1.991	Cs	-6324.2	3.3689
Hg	6652.4	-1.9411	Hg			Hg	-2429	1.525
Au	-6209	4.0805	Au	-2930.5	1.8069	Au	6640	-0.958

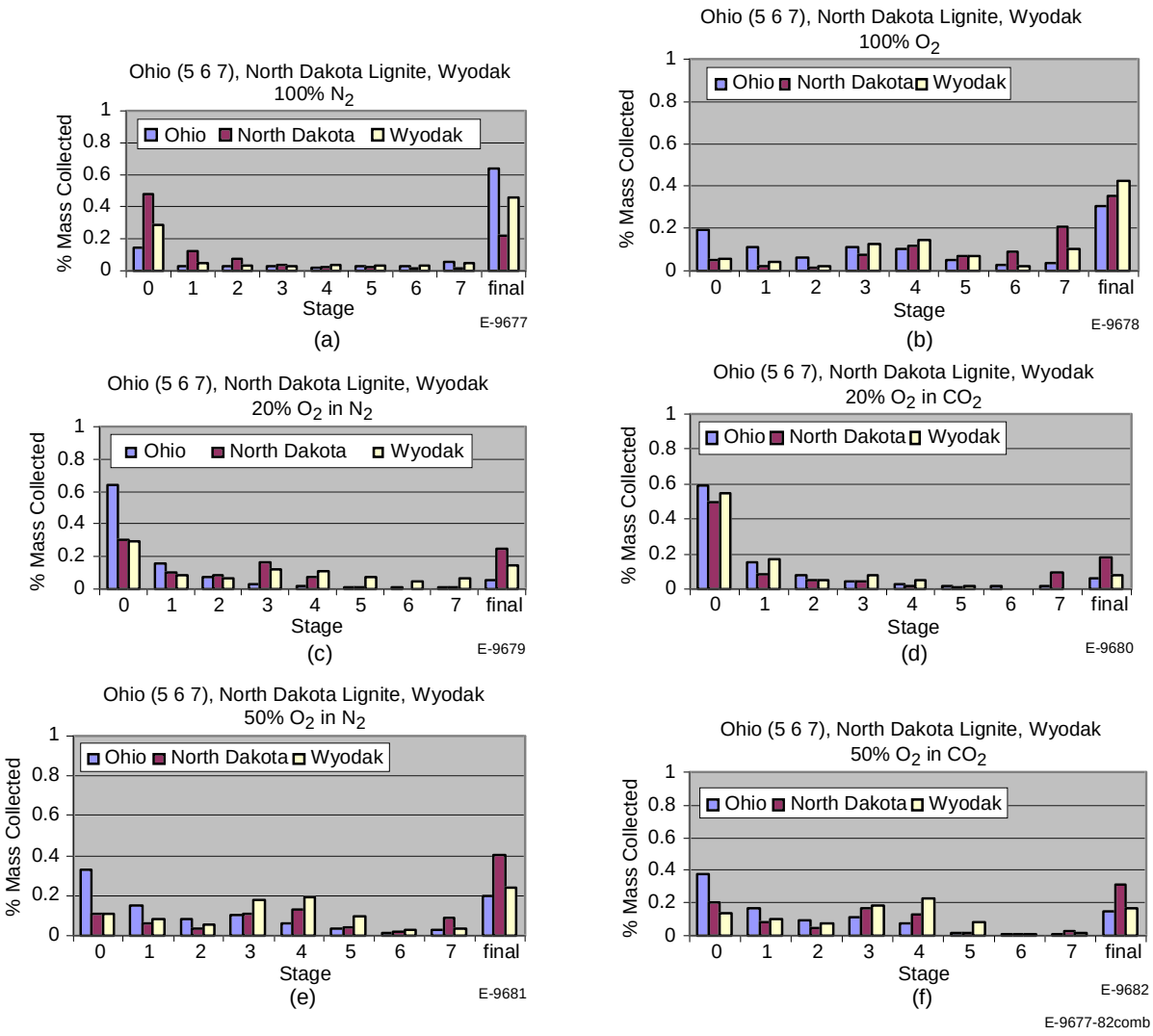

Figure 3-30. Mass distribution of ash from different combustion gas compositions: (a) 100% N_2, (b) 100% O_2, (c) 20% O_2 in N_2, (d) 20% O_2 in CO_2, (e) 50% O_2 in N_2, (f) 50% O_2 in CO_2.

Scanning electron microscopy of the Ohio coal ash shows cenosphere formation and swelling of the residual ash (Figure 3-31a). Agglomerations of submicron particles are shown in Figure 3-31b.

The color of the super micron ash ranged from black to powdery white depending on the extent of the combustion. The submicron ash showed a greater variation in color (Figure 3-32). The effects of the combustion condition on vaporization were seen. Ash collected from pyrolyzing conditions had a greenish color, probably due to reduced chromium content. At 20% oxygen, the ash was a dark gray, and at 100% oxygen, the oxidizing atmosphere was manifest as reddish ash.

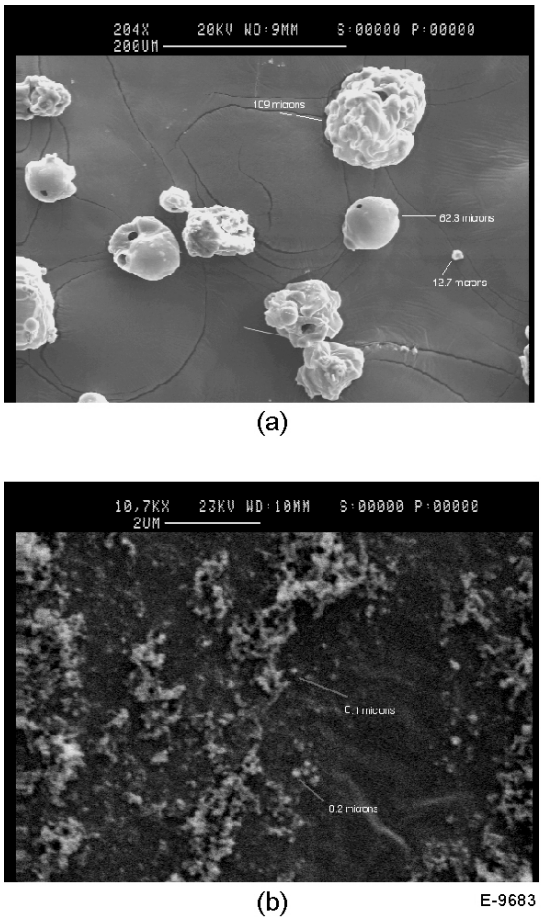

Figure 3-31. The ash has a definite bimodal distribution. Large particles are captured on the first stages of the cascade impactor and measure >10 microns (a). The sub-micron particles are captured on the final filter (b). These particles measuring 0.1 and 0.2 microns appear to be conglomerations of even smaller particles.

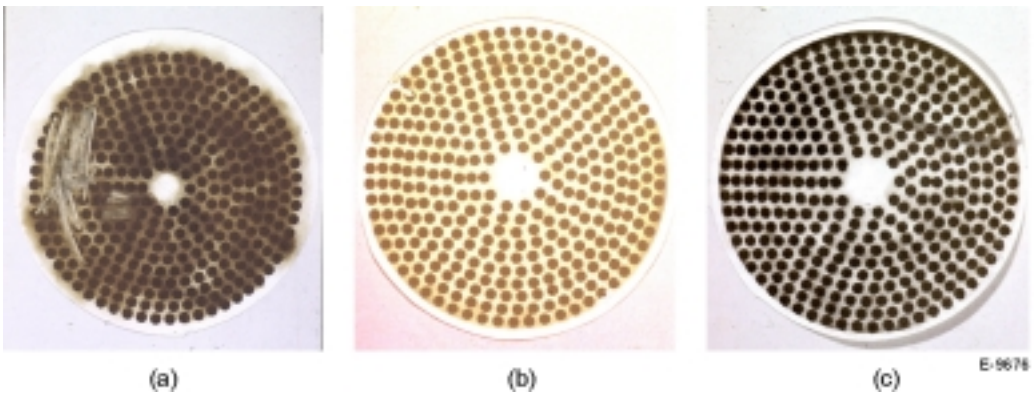

Figure 3-32. Appearance of submicron ash from the Ohio coal: the chemistry of the submicron ash has high variability, which can be seen here (a) under pyrolyzing conditions, (b) at 100% oxygen, and (c) at 50% oxygen in carbon dioxide.

For the Ohio coal, the residual ash was collected primarily on stage 0 of the impactor and all submicron ash was collected on the final filter. With North Dakota Lignite, the residual ash was collected on stages 0-3. Both stages 0 and 3 were analyzed with INAA along with the final filter, which had collected the bulk of the submicron ash. The ash from the Wyodak coal had a similar collection pattern and again stages 0, 3, and the final filter were analyzed. At 100% oxygen, all stages were analyzed for all coals.

Information on 32 elements with atomic weights greater than 20 amu was obtained through INAA. All information is given as the fraction of an element in the raw coal collected in the ash. For the Ohio coal, Table 3-25 contains information on the fraction of each element in the raw coal that was collected on the final filter. The same information for ND Lignite is in Table 3-26 and for Wyodak is in Table 3-27.

As the oxygen concentration was increased, there was an enrichment of several elements in the submicron ash (Figure 3-33). For the Ohio coal, these elements were magnesium, potassium, chromium, manganese, iron, cobalt, arsenic, molybdenum. antimony, and lanthanum. For ND Lignite, the elements were aluminum, barium, vanadium, manganese, chromium, iron, cobalt, and arsenic. For the Wyodak coal, increased oxygen affected the vaporization of aluminum, vanadium, calcium, arsenic, lanthanum, samarium, thorium, and uranium. This is expected because temperature rises as oxygen concentration is increased. Sodium was the only major element that was not enriched as temperature increased. This is because sodium is soluble in silicate glass and, thus, it is retained with silicon in the supermicron ash.

During pyrolysis, the volatile organics are removed, and the remaining char is often assumed to include all of the mineral components of coal. Surprisingly, a number of elements showed enrichment in the submicron ash under pyrolyzing conditions. This phenomena has been previously seen with titanium, which is associated with the organic volatiles [64]. For the Ohio coal, the elements chromium, cobalt, mercury, lanthanum, and gold showed an increased fraction in the submicron ash under pyrolyzing conditions (Figure 3-34a). The ND Lignite showed enrichment of chlorine, gold, manganese, lanthanum, bromine, antimony, and samarium (Figure 3-34b). It appears likely that, with the exception of mercury, these elements were associated with volatile compounds. Mercury is not associated with organics, but is more likely enriched because of the ability of carbon to absorb mercury. The mercury was probably absorbed by the high carbon content of submicron particles formed under pyrolyzing conditions.

The fraction of the major elements collected in the submicron ash was decreased in the presence of carbon dioxide. Iron and magnesium were reduced for the Ohio coal (Figures 3-35a and 35b), sodium was reduced in the ND Lignite (Figure 3-35c), and with the Wyodak coal, iron, magnesium, aluminum, and sodium were all reduced (Figure 3-35d-g).

Table 3-25. Fraction of Each Element Recovered in the Submicron Ash for the Ohio Coal. ND Indicates that a Concentration Was Not Detected Through INAA.

	100% N_2	20% O_2 w/ N_2	50% O_2 w/ N_2	100% O_2	20% O_2 w/ CO_2	50% O_2 w/ CO_2
Mg	0.0087	0.0145	0.0496	0.1258	0.0074	0.0379
Al	0.0080	0.0087	0.0072	0.01290	0.0018	0.0498
Ti	ND	ND	0.0451	0.1408	ND	0.0266
V	ND	0.0947	0.4137	0.4801	0.0559	0.7043
Na	1.1073	0.5759	0.2789	0.2936	0.2486	0.3713
Mn	0.0120	0.0412	0.1427	0.2004	0.0199	0.0677
Sr	ND	ND	ND	0.0706	ND	ND
Ba	ND	0.0212	0.0132	0.3711	ND	ND
Cl	1.2560	0.3288	0.0963	0.1094	0.1277	0.1995
K	ND	0.0317	0.0993	0.1521	0.0373	0.0744
Ca	0.1549	ND	0.0320	0.0999	ND	ND
Sc	ND	0.0022	0.0181	0.0855	0.0008	0.0123
Cr	0.2223	0.138072	0.2748	0.2878	0.0540	0.2459
Fe	0.0030	0.0066	0.0575	0.1011	0.0034	0.0534
Co	0.0676	0.0575	0.1773	0.2271	0.0423	0.2019
Se	ND	ND	ND	ND	ND	0.0170
As	0.1880	0.2772	0.3205	0.4214	0.2277	0.4141
Br	0.2469	ND	0.0199	0.0036	0.0325	0.0142
La	0.0023	0.0023	0.0058	0.0216	0.0011	0.0052
Ce	0.0117	ND	0.0352	0.1924	0.0038	0.0271
Nd	ND	ND	0.0006	0.0712	ND	0.0047
Eu	ND	ND	ND	0.2342	ND	ND
Sm	0.0030	0.0031	0.0162	0.0482	0.0025	0.0130
Lu	ND	ND	ND	0.0077	ND	ND
Th	ND	ND	0.0048	0.0539	ND	0.0173
U	ND	ND	ND	ND	ND	ND
Zn	0.1502	0.3457	0.2397	0.2043	0.1655	0.2396
Mo	0.0090	0.0356	0.0436	0.0951	0.0142	0.0632
Cd	ND	ND	ND	ND	ND	ND
Sb	0.0584	0.2627	0.3139	0.3765	0.2684	0.2210
Cs	ND	ND	ND	0.0022	ND	ND
Hg	0.6249	0.2787	0.1252	ND	0.0996	0.0004
Au	0.0005	0.0003	0.0001	ND	ND	0.7849

Table 3-26. The Fraction of Each Element Collected in the Submicron Ash of ND Lignite.
NA Indicates Not Available Because of Too Few Data Points.
ND Is Not Detected Through INAA.

	100% N_2	20% O_2 w/ N_2	50% O_2 w/ N_2	100% O_2	20% O_2 w/ CO_2	50% O_2 w/ CO_2
Mg	0.0155	0.0404	0.1834	0.1258	NA	NA
Al	0.0003	0.0012	0.0062	0.0129	ND	ND
Ti	NA	NA	NA	0.1408	NA	NA
V	0.0341	0.0428	0.1578	0.4801	NA	ND
Na	0.1181	0.2404	0.2196	0.2935	0.2367	0.1960
Mn	0.0070	0.1047	0.1902	0.2004	0.0152	0.1889
Sr	NA	0.0484	0.1810	0.0706	NA	0.1325
Ba	ND	0.0084	0.0330	0.3711	ND	0.0175
Cl	1	0.8969	0.6705	0.1094	0.7758	0.6156
K	NA	NA	NA	0.1521	NA	NA
Ca	0.0032	0.0002	0.0547	0.0999	0.0011	0.0267
Sc	NA	NA	0.0332	0.0853	0.0010	0.0085
Cr	0.0286	0.0458	0.1075	0.2878	0.0452	0.0829
Fe	NA	0.0678	0.1000	0.1011	0.0024	0.1342
Co	ND	0.0634	0.0760	0.2271	0.0073	0.0910
Se	ND	0.0378	0.0152	ND	0.1066	0.0357
As	0.0598	0.1075	0.1121	0.4214	0.1311	0.1122
Br	0.4149	0.2186	0.2264	0.0036	0.2053	0.0293
La	0.0064	NA	0.0406	0.0216	0.0009	0.0079
Ce	NA	NA	0.1038	0.1924	NA	0.0608
Nd	ND	ND	ND	0.0712	ND	ND
Eu	NA	NA	NA	0.234	NA	NA
Sm	0.0096	0.0019	0.0620	0.0482	0.0006	0.0082
Lu	NA	NA	0.0927	0.0077	0.0556	0.0637
Th	NA	NA	0.0556	0.0539	NA	NA
U	0.0324	ND	0.7297	NA	0.0105	0.0436
Zn	0.0101	0.0436	0.0329	0.2043	0.0595	0.0419
Mo	NA	0.0776	0.1386	0.0951	0.0715	0.1233
Cd	NA	NA	NA	NA	NA	NA
Sb	0.3566	0.1578	0.1052	0.3765	0.1368	0.1214
Cs	NA	0.1647	0.1243	0.0022	0.0825	0.0997
Hg	0.0330	0.0066	ND	ND	ND	ND
Au	0.4229	0.1730	0.0297	0.2862	ND	0.0127

Table 3-27. The Fraction of Each Element Collected on the Final Filter for Wyodak. ND is not detected through INAA.

	100% N_2	20% O_2 w/ N_2	50% O_2 w/ N_2	100% O_2	20% O_2 w/ CO_2	50% O_2 w/ CO_2
Mg	0.0056	0.0571	0.8072	0.2362	0.0135	0.3348
Al	0.0005	0.0041	0.0148	0.0746	0.0030	0.0079
Ti	ND	ND	ND	0.1362	ND	ND
V	0.0234	0.1232	0.2812	0.5595	0.1106	0.1845
Na	0.4182	0.3914	0.4658	0.3875	0.3529	0.3826
Mn	0.0071	0.2501	0.5626	0.3224	0.0420	0.3866
Sr	ND	ND	0.1931	0.3594	ND	0.1022
Ba	ND	0.0444	0.2499	0.2059	0.0103	0.1255
Cl	11.4921	4.7827	3.1113	3.7028	5.4415	4.3447
K	ND	ND	ND	ND	ND	ND
Ca	0.0051	0.0108	0.1650	0.7904	0.0059	0.0632
Sc	ND	0.5488	0.0452	0.1616	0.0038	0.0171
Cr	0.1139	0.2685	0.3219	0.2979	0.0527	0.1769
Fe	ND	0.1806	0.6292	0.4535	0.0384	0.4456
Co	ND	0.1494	0.3599	0.2247	0.0443	0.2309
Se	ND	ND	ND	ND	ND	ND
As	0.3135	0.2809	0.5633	0.5752	0.2070	0.2547
Br	0.7579	0.2762	0.1720	0.5070	0.1140	0.1528
La	0.0048	0.0055	0.0320	0.1087	0.0040	0.0115
Ce	ND	ND	0.1778	0.2798	0.0792	0.0408
Nd	ND	ND	ND	0.0675	1.3553	ND
Eu	ND	ND	0.1001	0.1542	ND	ND
Sm	0.0042	0.0084	0.0687	0.2808	0.0076	0.0242
Lu	ND	ND	0.0415	0.1737	ND	ND
Th	ND	0.0250	0.0943	0.1941	ND	ND
U	ND	0.1259	0.6521	0.6875	0.1554	0.2972
Zn	0.1603	0.1203	0.0756	0.0590	0.0630	0.0893
Mo	ND	0.1420	0.2159	0.1804	0.0810	0.1058
Cd	ND	4.5049	ND	ND	ND	ND
Sb	0.4594	0.1857	0.3190	0.2656	0.1521	0.2431
Cs	ND	ND	ND	ND	ND	ND
Hg	0.1428	ND	ND	0.3495	ND	ND
Au	ND	0.0944	0.0157	0.0836	ND	ND

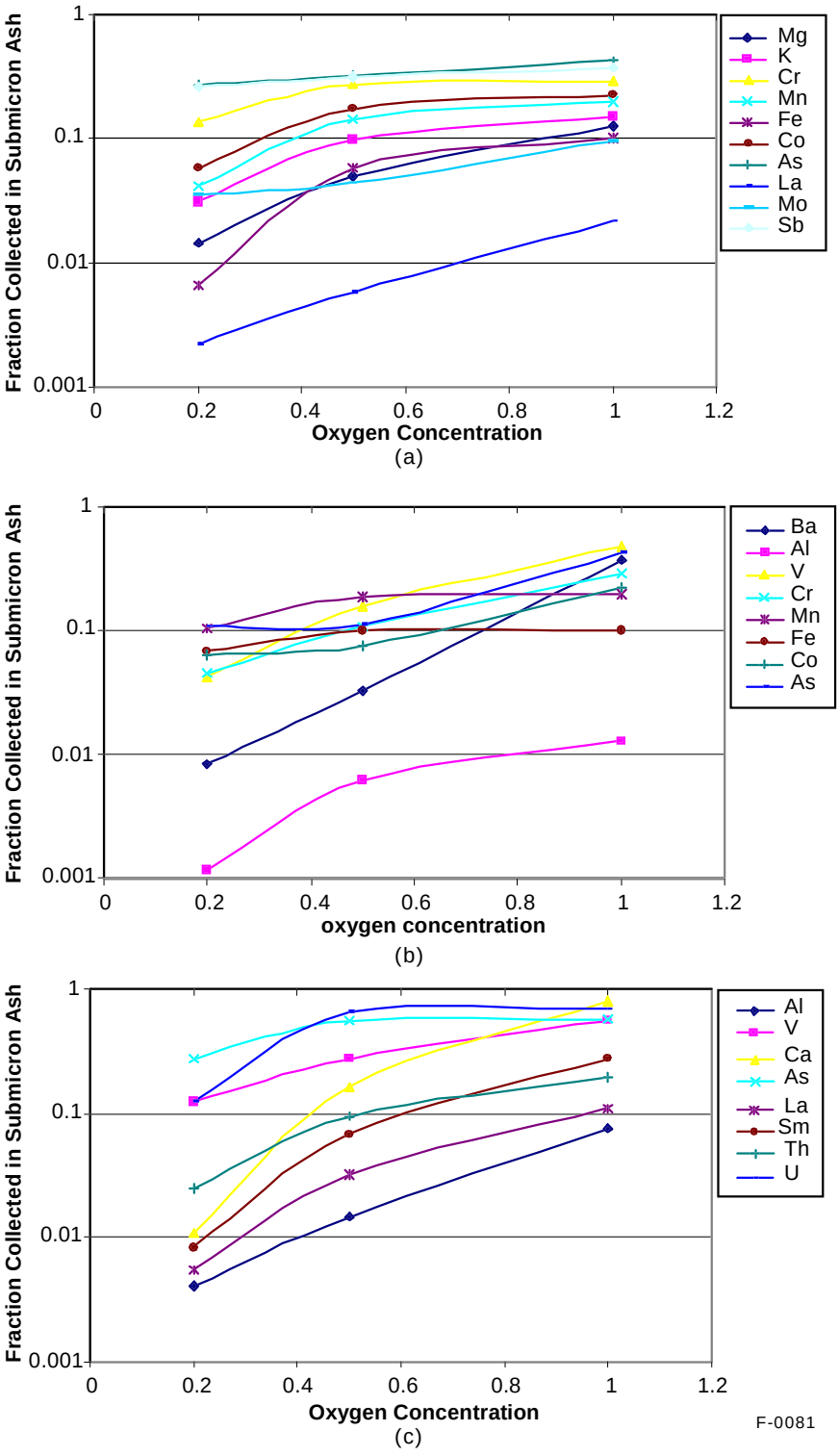

Figure 3-33. Effect of oxygen concentration on amount of various elements in the submicron ash (for combustion in O_2-N_2 mixtures); (a) Ohio, (b) North Dakota Lignite, (c) Wyodak.

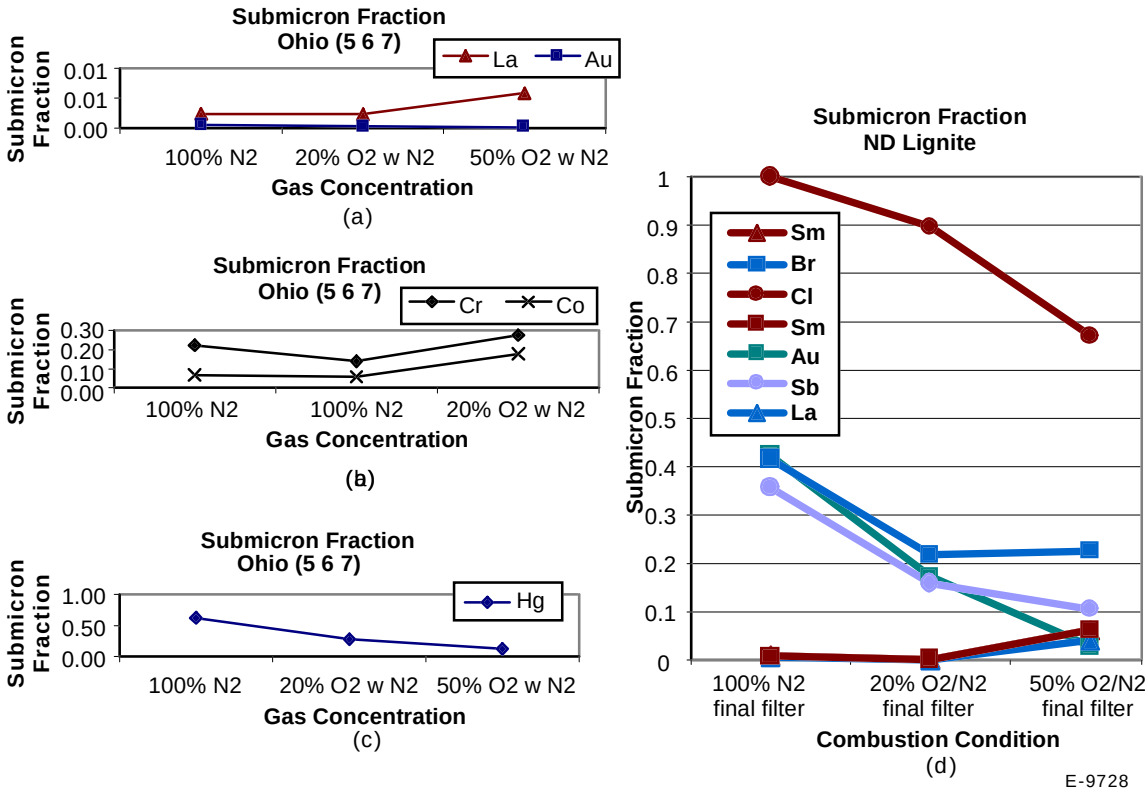

Figure 3-34. Fraction of selected elements in submicron ash as a function of O_2 concentration (O_2/N_2 mixtures) for (a) La and Au, (b) Cr and Co, (c) Hg, and (d) Sm, Br, Cl, Sm, Au, Sb, La.

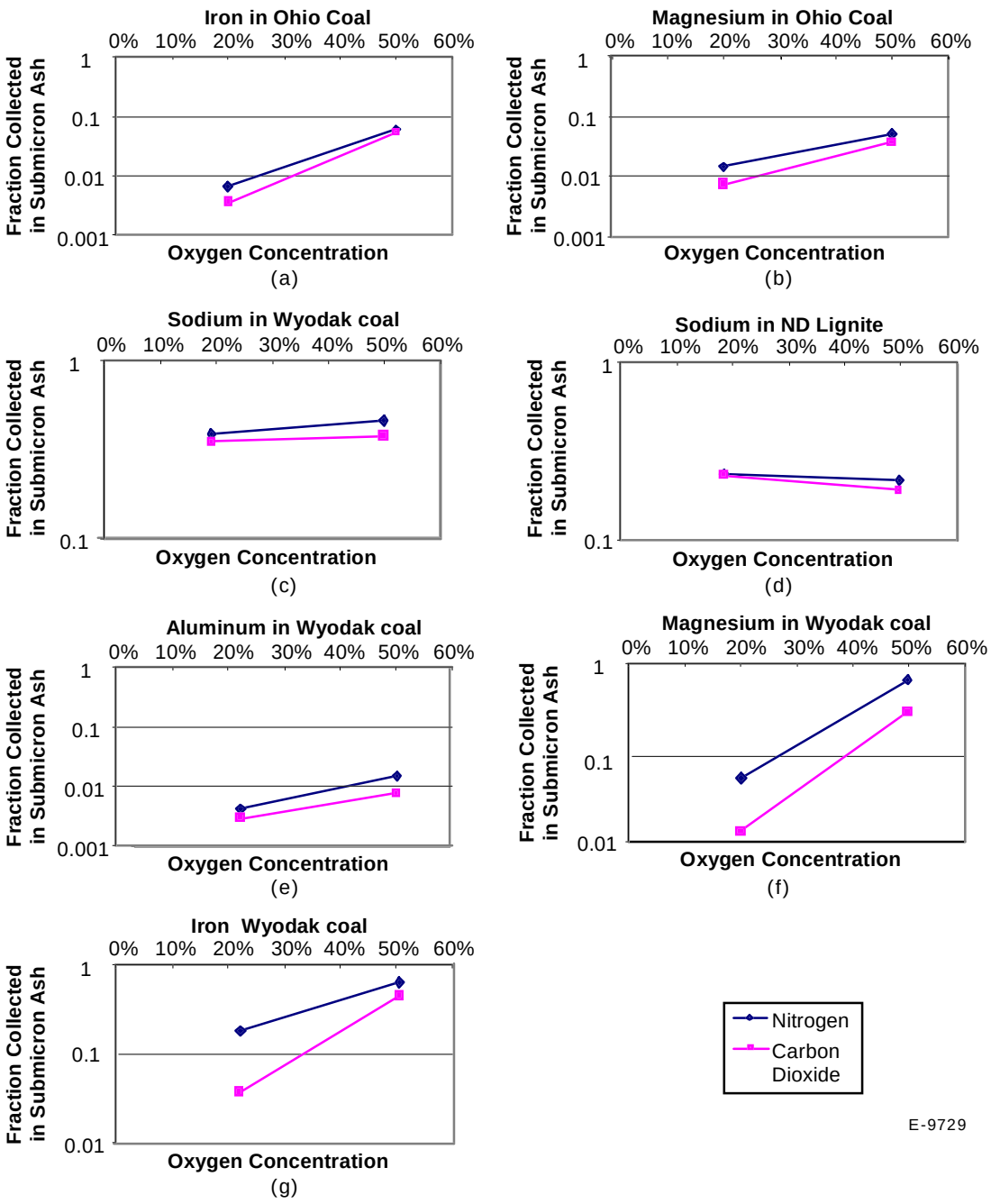

Figure 3-35. Fraction of selected major elements in submicron ash as a functionof oxygen concentration for combustion in N_2 and CO_2.

Several significant minor elements were also reduced in the submicron ash by using a carbon dioxide-rich atmosphere. These include manganese, chromium, and zinc for the Ohio coal (Figure 3-36). From the ND Lignite, cesium, manganese, chlorine, bromine, chromium, and molybdenum were reduced (Figure 3-37). The Wyodak coal showed reduction of many of these along with some other interesting elements including arsenic, zinc, antimony, and barium (Figure 3-38).

Mercury levels in the submicron ash showed the same pattern with the Ohio coal (Figure 3-39), however the carbon dioxide effect on mercury can be explained by the role of soot in the ash. At lower oxygen concentrations, the carbon content of the ash is increased. Because of its reactivity with carbon, the vapor phase mercury is collected with the submicron ash.

These data support the hypothesis that the carbon dioxide controls vaporization rates for metal species according to the governing reaction. The carbon dioxide lowers the reaction constant. However, the affect cannot simply be explained with empirical models because of the intricacies of the carbon dioxide reactions. Past research has assumed that during combustion in an oxygen/nitrogen atmosphere, all the vapor phase carbon was present as carbon monoxide. At moderate temperatures, that was a reasonable assumption. However, at high temperatures, the CO/CO_2 ratio decreases as some solid carbon converts to carbon dioxide at the particle surface. In the pores, the CO/CO_2 has a different equilibrium from the reaction:

$$CO + 1/2\ O_2 = CO_2\ . \qquad (3\text{-}4)$$

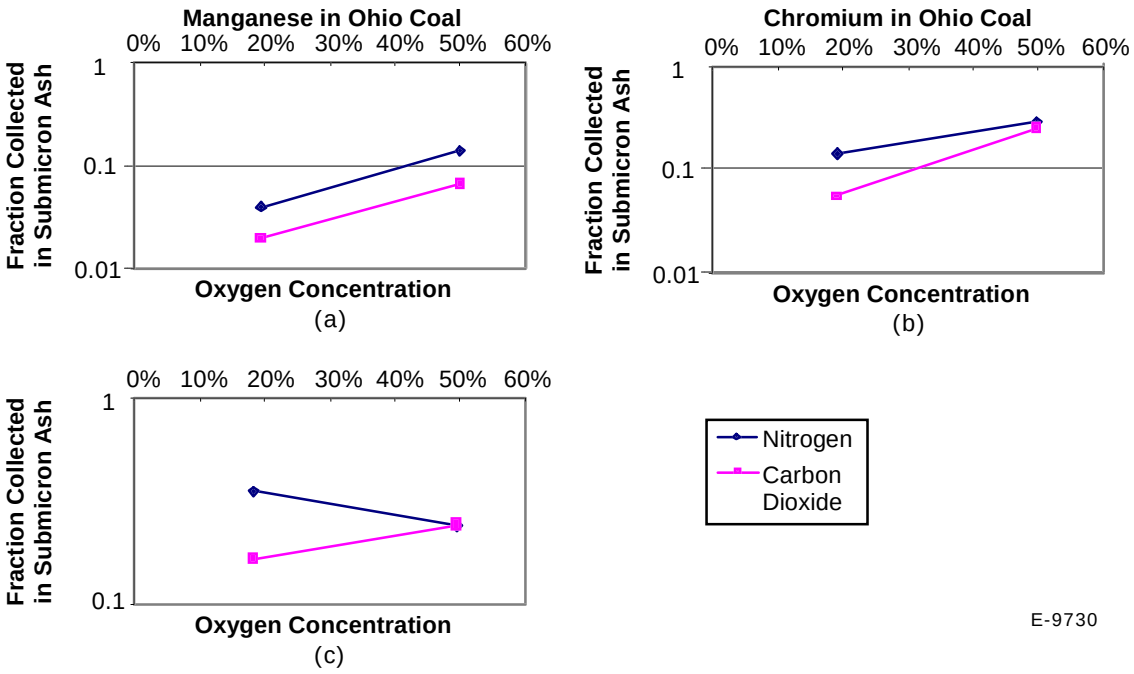

Figure 3-36. Fraction of Mn, Cr, and Zn (a-c) in submicron ash as a function of oxygen concentration for combustion of Ohio coal in O_2/N_2 and O_2/CO_2.

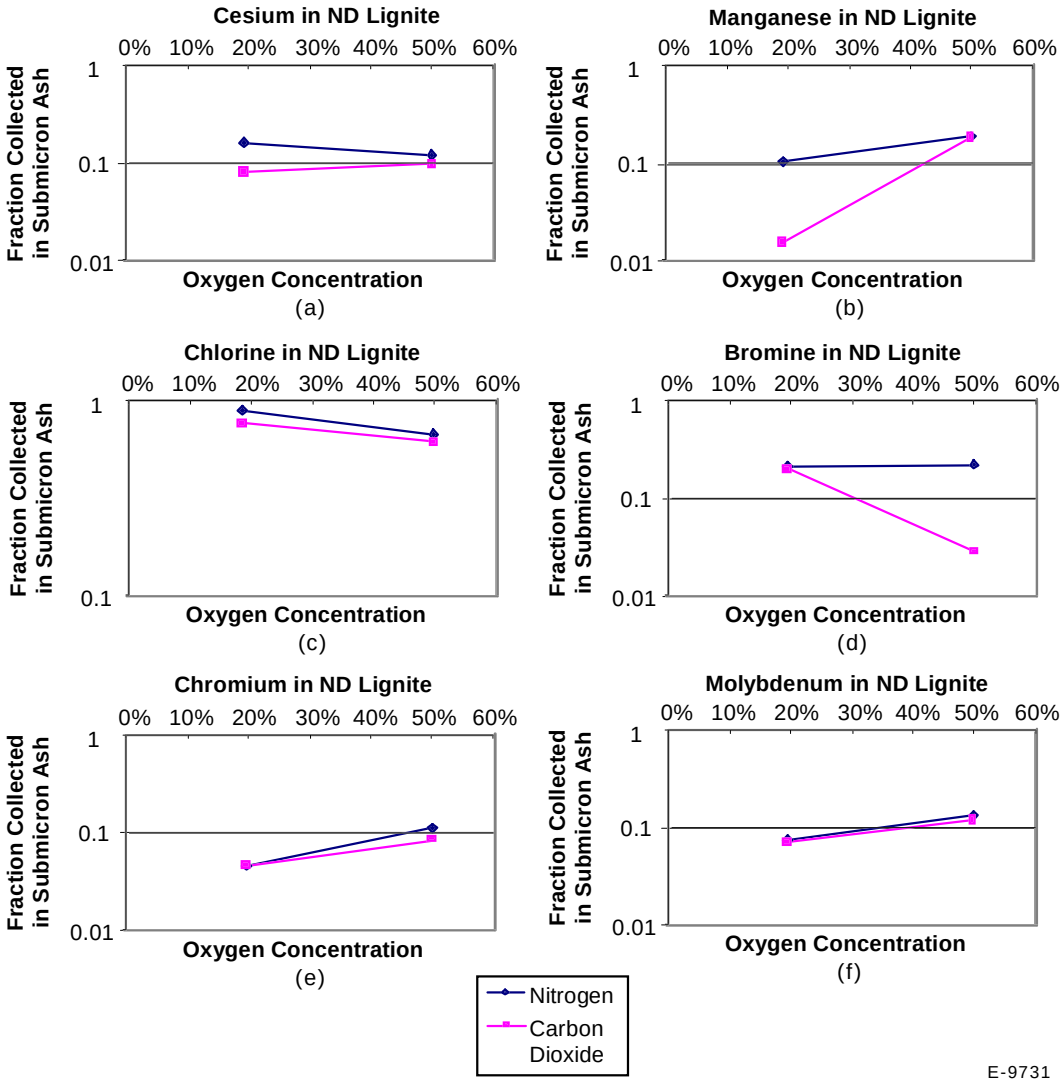

Figure 3-37. Fraction of Cs, Mn, Cl, Br, Cr, Mo in submicron ash as a function of oxygen concentration for combustion of ND lignite in O_2/N_2 and O_2/CO_2.

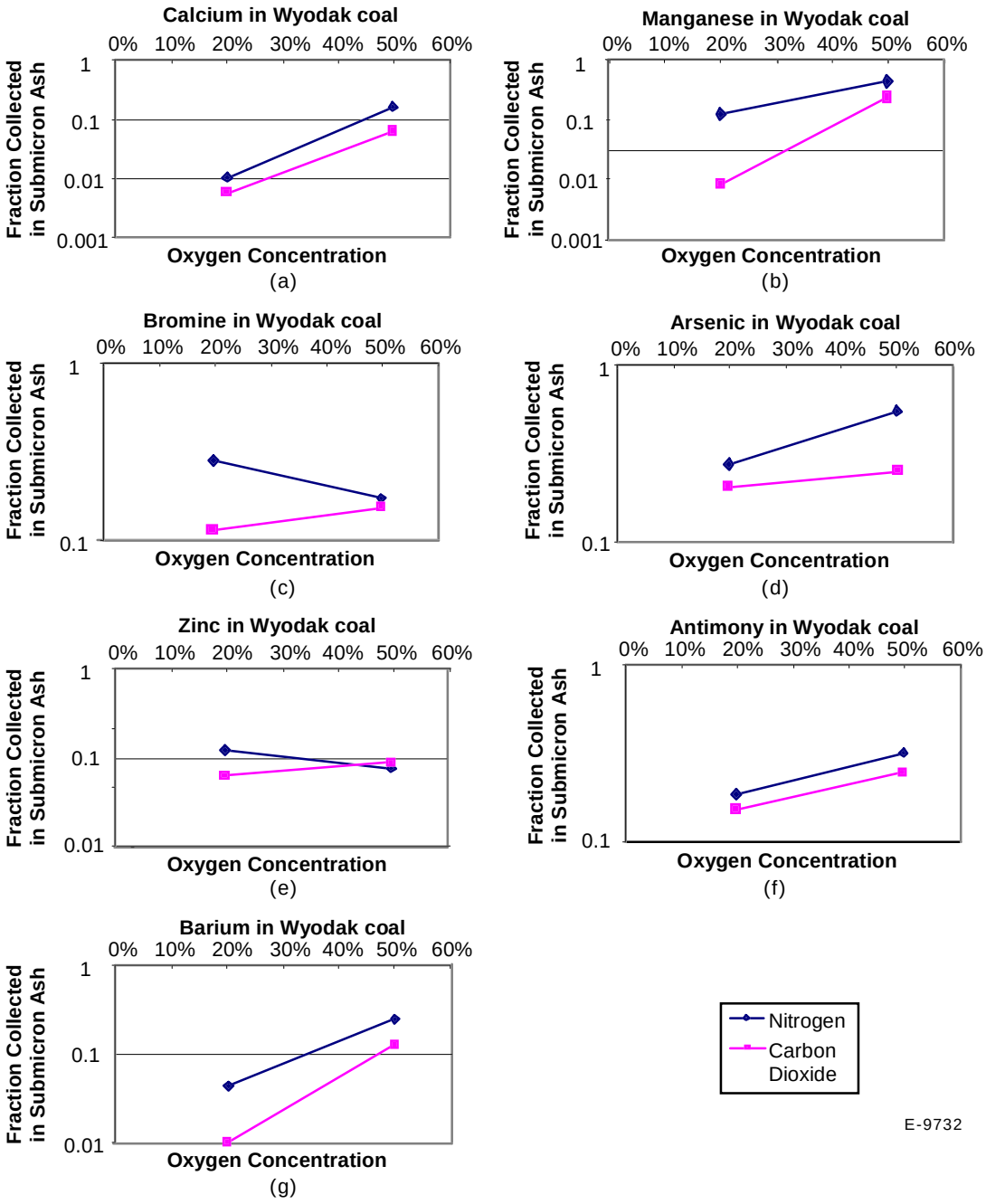

Figure 3-38. Fraction of selected elements in submicron ash as a function of oxygen concentration for combustion of Wyodak coal in O_2/N_2 and O_2/CO_2.

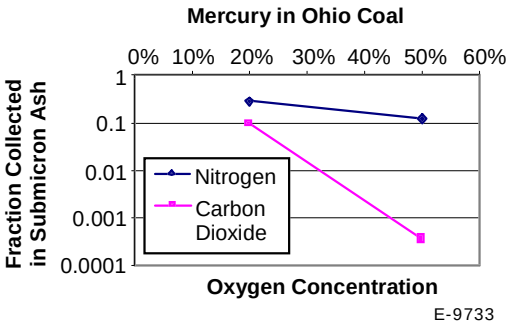

Figure 3-39. Mercury from the Ohio coal shows a decrease in capture on submicron particles with carbon dioxide. This is not due to the governing reactions, but is associated with the soot fraction of the particles, and absorption of mercury on carbon.

The third parameter affecting the CO/CO_2 balance is the boundary condition, which can manually be controlled. This study has investigated the CO/CO_2 ratio in the boundary layer. Burning in an atmosphere of carbon dioxide serves to decrease the CO/CO_2 ratio to levels that can decrease metal vaporization according to Eq. (3-1). While much of this reduction is due to the governing reaction, temperature effects come into play for elements not present as metal oxides.

The previous studies by Quann [62, 66, 66] have attempted to model these effects for a limited number of metals. The usefulness of these studies is limited, however, because of the simplified approach to the equilibrium of gaseous species. Quann's [65] model was based on an assumption that all CO_2 was produced during Eq. (3-1), therefore the partial pressure of CO_2 was equal to the partial pressure of the metal species when burning in an oxygen-nitrogen atmosphere. This assumption has come under scrutiny by Haynes [63], who pointed out the relevance of the other mechanisms for CO_2 formation.

The data collected in this study will eventually be applied to a model similar to one developed by Haynes [63], which accounts for the full equilibrium between carbon monoxide and carbon dioxide. The model also considers many other reactions taking place in the combustion zone, and involves the diffusion of gases into the particle and combustion products away from the particle. From this information, predictions of metal behavior in combustion will be improved.

3.2.1.2 Low Temperature Volatilization

The INAA results for low temperature volatilization experiments were returned to us. They were inconclusive and we will take a closer look to find out what may be causing our sample variation.

3.2.2 Chlorine Studies

One possible means of reducing mercury emissions is to reduce elemental mercury through reactions with free radical chloride in the post combustion zone. The resulting mercury chloride can be easily scrubbed from the exhaust. To determine the extent to which mercury can be removed as a salt, it is important to know the concentration of free chlorine. It is known that

the bulk of the chlorine is released as hydrochloric acid, with just a few percent as Cl_2. The amount of chlorine released as Cl_2 is indicative of the concentration of free radical chlorine at mercury reaction temperatures. In order to measure the HCl/Cl_2 ratio, we attempted to use EPA method 26A. This is a wet sampling technique that uses a series of acidic and basic solutions to collect the chlorine. There is some concern that the presence of SO_2 in flue gas will interfere with the collection through the reaction

$$SO_2 + Cl_2 + 2H_2O = 4H^+ + 2Cl^- + SO_4^{-2} \quad (3\text{-}5)$$

This reaction causes Cl_2 to be retained in the first impingers with the HCl.

The sampling train was set up by connecting a series of four impingers. The first two impingers contained 100 ml of 0.1 N sulfuric acid to capture the hydrochloric acid. Chlorine gas has a low solubility in acid solutions; it was captured in impingers three and four, which contained 100 ml of 0.1 N sodium hydroxide. The impingers were immersed to the fluid level in an ice water bath. The impingers were followed by a tube filled with silica gel desiccant to absorb any water vaporized in the system.

We tested EPA method 26A on a synthetic flue gas with and without SO_2 to evaluate the importance of Eq. (3-5). The concentrations of chlorine, hydrochloric acid, and sulfur dioxide were selected to approximate the concentrations in the flue gas from the Ohio coal (Table 3-28). The tests ran for 30 min each. The contents of each impinger were measured. Then, the impingers were rinsed twice with distilled water, which was added to the impinger solution. Sodium thiosulfate was added to the basic solutions to ensure that all of the chlorine ionized. The concentration of chloride ion was measured with a selective ion probe. Sulfur dioxide was found to interfere with the chlorine speciation, even at low concentrations.

We attempted a second method for chlorine speciation, which used a potassium iodide solution to collect the chlorine gas [67]. This system was set up similar to EPA method 26A, but the collection train was split into two parallel sections. One half contained 0.2 M dibasic potassium phosphate buffered with 0.1 M potassium hydroxide to collect both hydrochloric acid and chlorine gas. The other half contained a solution of 0.1 M potassium iodide buffered with 0.1 M acetic acid and 0.1 M sodium acetate. Chlorine gas reacts with the potassium iodide in this solution, displacing the iodide. The chlorine concentration was determined by measuring the iodine ion concentration. The chlorine concentration in the basic solution was measured directly, and the concentration of HCl in the gas was determined by subtracting the Cl_2 concentration. Selective ion probes were used to measure total chlorine concentration and free iodine, which is equivalent to the chlorine gas. Sulfur dioxide was found to interfere with the chlorine measured by this method, Eq. (3-5) presumably has a faster reaction time than the Cl_2/KI reaction.

Table 3-28. Composition of Synthetic Flue Gas (Concentrations in ppm) Used in Experiments to Test Interference with Methods for Measurement of Chlorine Speciation

Test	Cl_2	HCl	SO_2
1	5	0	0
2	0	65	0
3	5	65	0
4	5	65	100
5	5	65	2000

3.2.3 Summary

The work at UU focused on the behavior of trace metals in the combustion zone by studying vaporization from single coal particles. The coals were burned at 1700 K under a series of fuel rich and oxygen rich conditions. The combustion atmosphere varied from 0 to 100% oxygen with the balance being either nitrogen or carbon dioxide. The nitrogen provided an inert environment for the reaction. Carbon dioxide was used to investigate the governing reaction for metal reduction. Carbon dioxide was expected to keep the metals in their less volatile oxidized state, and also to affect the particle temperature. The impact of the carbon dioxide is particularly important since early interpretations of the vaporization data did not properly account for the gas composition in the pores.

After combustion, the particles were rapidly cooled to between 120 and 140°C by addition of 21 liters per minute of nitrogen gas through a water-cooled probe. An Andersen Mark II cascade impactor, located directly below the furnace collected and sized the particles. A side stream of the final exhaust was pulled through a small activated carbon plug to absorb any gas phase mercury and complete the mass balance. After collection, selected impactor stages, representing the residual and submicron ash, and the carbon plug were analyzed using instrumental neutron activated analysis (INAA).

During pyrolysis, the volatile organics are removed, and the remaining char is often assumed to include all of the mineral components of coal. Surprisingly, a number of elements showed enrichment in the submicron ash under pyrolyzing conditions. It appears likely that, with the exception of mercury, these elements were associated with volatile compounds. Mercury is not associated with organics, but is more likely enriched because of the ability of carbon to absorb mercury.

As the oxygen concentration was increased, there was an enrichment of several elements in the submicron ash. Several significant minor elements were also reduced in the submicron ash by using a carbon dioxide rich atmosphere. These data support the hypothesis that the carbon dioxide controls vaporization rates for metal species according to the governing reaction. The carbon lowers the reaction constant, however the affect cannot simply be explained with empirical models because of the intricacies of the carbon dioxide reactions.

The data collected in this study will be applied to a model that accounts for the full equilibrium between carbon monoxide and carbon dioxide. The model also considers many other reactions taking place in the combustion zone, and involves the diffusion of gases into the particle and combustion products away from the particle.

UU also investigated chlorine speciation in the flue gas because one possible means of reducing emissions of mercury is to reduce elemental mercury by reacting it with a radical chloride ion. It has been suggested that sulfur dioxide would interfere with the speciation, so this was first tested that theory with a synthetic flue gas. Sulfur dioxide was found to interfere with the chlorine speciation. A new system was erected using a potassium iodide solution to collect chlorine gas.

3.3 Post-Combustion Transformations of Semi-Volatile Elements (UA, UK, UC)

3.3.1 Background and Motivation

As discussed in the Phase I final report, certain semi-volatile trace elements are worthy of study because their emission factors from coal-fired power plants are not always predictable from the collection efficiency of the particulate control device. The reason for this is that these elements have substantial vaporization during combustion and the subsequent partitioning between large (easy to collect) and small (harder to collect) ash particles appears to depend on the coal rank (that is, on the composition of the ash).

Arsenic and selenium are the most important semi-volatile elements. We have also looked at antimony, cobalt, and the radionuclides, although not in as much detail. In the first section (3.3.1) we examine the behavior of some of these elements based on available literature and new thermodynamic calculations. At UC, laboratory experiments were performed on the kinetics of arsenic-ash interactions as detailed in Section 3.3.2. At UA, larger, self-sustained combustion experiments were performed with the primary focus on arsenic, selenium, antimony, and cobalt. Cobalt was also studied. It is representative of a large group of the transition metals which constitute the least volatile members of Group 2. Analysis was also performed for three radionuclides – cesium (from volatility group 2, Figure 2-2), thorium (from volatility group 1, Figure 2-2), and cerium (from volatility group 1, Figure 2-2) -- without performing all of the detailed experimental and analytical work carried out for the four elements listed above. Of these three, cerium and thorium are transition metals while cesium is a Group I salt.

Originally cadmium and chromium were also going to be investigated at the UA combustor (Section 3.3.3). Unfortunately, credible experimental results could not be obtained for these elements with the experimental equipment utilized. Cadmium results were invalid because of contamination of the furnace surfaces from other experiments being performed during the same time period using the same equipment. The lag-resistant refractory utilized during the furnace rebuild between Phases I and IIa (see Section 3.3.3 for details) became a source of chromium contamination during subsequent experiments.

3.3.1.1 Behavior of Semi-Volatile Elements

Arsenic

Arsenic is one of the more important of the trace toxic metals related to coal combustion due to its volatility and toxicity. Raask [1] lists the arithmetic mean concentration of arsenic in U.S. coals as 15 ppm but the arsenic concentration in coal can vary substantially between coals and even within a given coal seam [1-4]. Gluskoter et al. [2] reports variations in the arsenic concentration from Illinois basin coals of 1.0 to 120 ppm with an arithmetic mean value of 14 ppm. Arsenic is most commonly associated with pyrite horizons in fractured coal [60, 68, 69]; most likely as sulfides.

Arsenic is a group 15 element located in the 3rd column of the p-block of the periodic table of elements. It is located immediately below phosphorus and immediately above antimony.

For all the elements in this group, the ground state electronic configuration is ns^2np^3 which results in common oxidation states of +3 (III) and +5 (V). Other oxidation states are rarely encountered naturally for arsenic [70]. Arsenic is typically described as a metalloid or semi-metal. In certain environments, arsenic exhibits some of the properties of metals.

Arsenic has a normal melting point of 1090 K [70] and it sublimes at a normal boiling point of 889K. Arsenic trioxide, As_2O_3 or As_4O_6 (often referred to as arsenic (III) oxide) is the most common form of occurrence. Arsenic trioxide belongs to a class of molecules known as oxy-anions. Oxy-anions readily accept additional electrons and can be very reactive with cations. Arsenic trioxide has a sublimation temperature of 466 K and, if present in the coal, is expected to vaporize readily. Arsenic pentoxide (arsenic (V) oxide) is another common oxy-anion form observed in coal fly ash.

Previous work in Phase I of this program on the mode of occurrence of arsenic in coal [56] suggests that arsenic is largely associated with pyrite in bituminous coals. XAFS work has shown that the arsenic in bituminous coals substitutes for sulfur in the pyrite structure. Significant amounts of arsenate (AsO_4^{3-}) are sometimes present due to the oxidation of arsenic-containing pyrite. In subbituminous coals, arsenate has been observed, but arsenic is often not associated with pyrite primarily, but present as As^{3+}, probably ion-exchanged into the organic matrix. This organically associated arsenic oxidizes to arsenate over time.

Depending on the forms of occurrence in the coal and transformation mechanism involved, arsenic-containing compounds may exit the furnace in the vapor, as part of sub-micron size aerosol particles, or as part of larger, supermicron particles. The specific path by which arsenic transforms from the vapor phase to the condensed phase is important in assessing the toxicity of the waste product.

Due to the low concentration of arsenic compared to the major species in the coal, there is a very high probability that a volatilized arsenic molecule will contact submicron or supermicron particles prior to reaching the supersaturation conditions necessary for nucleation. Therefore, a majority of the volatilized arsenic is expected to heterogeneously partition onto the surfaces of both submicron and supermicron particles [30].

Previous research has shown that the collection efficiency in ESP control equipment is significantly lower for submicron particles than for larger particles [10, 31, 32]. Coupled with this, it has been shown that arsenic concentrations are significantly higher in the submicron aerosol fume than in larger particles in the supermicron regime [6, 9-16, 24, 25, 32, 71-73]. Thus, the deposition of submicron particles in the downwind environment may represent a greater risk of arsenic migration into the water table than supermicron particles [36, 37]. However, Swaine [37] monitored the deposition of arsenic at various locations downwind of the Wallerawang power plant in Australia using accumulation in moss. His results indicate arsenic depositions at 1.8 km to be of the same order of magnitude as arsenic deposition from litter decay and the application of fertilizer. At 27.4 km, arsenic depositions were substantially lower, on the order of rock weathering [37].

Selenium

Selenium is also one of the more important of the trace toxic metals due to its volatility and toxicity. Gluskoter et al. [2] reports variations in the selenium concentration from Illinois basin coals of 0.4 to 7.7 ppm with an arithmetic mean value of 2.2 ppm while Raask [1] lists typical coal selenium concentrations as 1-5 ppm. Finkelman [68, 69] reports that for most coals, selenium is associated with organic constituents. However, since selenium can substitute readily for sulfur in many sulfide minerals, it will also be associated with pyrite and other mineral sulfides [68, 69].

Selenium is directly adjacent to arsenic in Group VI of the Periodic Table. It is located immediately below sulfur and above tellurium. Selenium's ground state electronic configuration is $4s^2 4p^4$ which results in common oxidation states of +4 (IV) and +6 (VI). Selenium is typically described as a metalloid or semi-conductor.

Selenium has a normal melting point of 490K and a normal boiling point of 958 K [74]. Selenium dioxide, SeO_2, is the most common oxy-anion formed with SeO_3 (Se_2O_6) another common form of occurrence. Selenium readily substitutes for sulfur and, to a lesser extent, tellurium. As such, selenium reacts with Group 1 and 2 salts such as Na, Mg, and Ca. Selenium oxy-anions readily react with d-block transition metals such as iron.

For many coals, selenium is primarily bound in organic matter of coal. In this form it is expected to volatilize during combustion [48]. To verify this hypothesis, Finkelman et al. [48] performed volatilization experiments on fly ash samples from ten coals at 823 K including three of the coals utilized in the present study (although from different samples).

The Se volatilization rates for the three study coals were:

- Wyodak sub-bituminous = 94%
- Illinois #6 = 98%
- Pittsburgh = 94%.

This conclusion is reinforced by data provided by Eary et al. [75] who report surface enrichment for solid-phase selenium from fly ash particles to be 93% of the total selenium present in the ash. Again indicating a significant Se volatilization percentage during combustion.

Due to the low concentration of selenium compared to the major species in the coal, there is a very high probability that a volatilized selenium molecule will contact submicron or supermicron particles prior to reaching the supersaturation conditions necessary for nucleation. Therefore, a majority of the volatilized selenium is expected to heterogeneously partition onto the surfaces of both submicron and supermicron particles [30]. However since selenium (as SeO_2) is highly volatile at post-combustion temperatures, a significant minority of the selenium will exit the combustor in the vapor phase.

Pupp et al. [76] gives the following equations for the vapor pressure and volatility of SeO_2 as a function of temperature:

$$\text{Vapor Pressure (SeO2):}\ \log(p) = 12.233 - 6045/T \quad (3\text{-}6)$$

$$\text{Volatility (Se):}\ \log(c) = \log(p) + 3.982 - \log(T) \quad (3\text{-}7)$$

where: P = vapor pressure, kPa
T = temperature (K)
c = volatility, g/m^3

Andren et al. [77] report that 32% of the selenium at the Allen Steam Plant leaves in the vapor phase.

Antimony

The behavior of antimony is one of the more interesting of the trace metals encountered during coal combustion. Antimony forms typically have much higher normal boiling points than the comparable forms of arsenic or selenium so less volatilization is expected from comparable forms of occurrence. The partitioning results from many studies [28, 32, 65, 72, 78-81] report the partitioning behavior of antimony as similar (in terms of volatility, submicron particle enrichment, and emission) to arsenic and selenium while in other studies, antimony partitioning is reported to behave similar to less volatile trace elements such as lead and cadmium [17, 29, 30]. These differences are most likely due to differences in the forms of occurrence of antimony in the coal feedstock.

Raask [1] lists the arithmetic mean concentration of antimony in U.S. coals as 1.1 ppm but the antimony concentration in coal can vary substantially between coals and even within a given coal seam [1, 2]. Gluskoter et al. [2] reports variations in the antimony concentration from Illinois basin coals of 0.1 to 8.9 ppm with an arithmetic mean value of 1.3 ppm. Unlike arsenic and selenium, there is relatively little information on the modes of occurrence of antimony in coal. Finkelman [69] suggests that for most coals, antimony is probably present in solid solution in pyrite and as minute accessory sulfides (e.g., stibnite, Sb_2S_3) dispersed throughout the organic matrix. However antimony may also be associated with organic constituents.

Antimony is a group 15 element located in the 3rd column of the p-block of the periodic table of elements. It is located immediately below arsenic and immediately above bismuth. For all the elements in this group, the ground state electronic configuration is ns^2np^3 which results in common oxidation states of +3 (III) and +5 (V). Other oxidation states are rarely encountered naturally for antimony [70]. Antimony is often classified as a metalloid or semi-metal but is also commonly classified as a metal.

Antimony has a normal melting point of 904 K [70] and a normal boiling point of 1908 K. Antimony trioxide, Sb_4O_6 (often referred to as antimony (III) oxide) is a common mineral form of occurrence known as seramontite or valentinite. Antimony trioxide is an

oxy-anion and thus readily accepts additional electrons and can be very reactive with cations. Antimony trioxide has a melting temperature of 928 K and sublimation temperature of 1698 K. At these temperatures, vaporization during coal combustion is expected for most coals. For lower rank coals, the maximum combustion temperature may be lower than the sublimation temperature and volatilization may depend upon the proximity of the antimony to burning char particles (where the local temperature will be substantially higher than the bulk gas temperature). Antimony pentoxide (antimony (V) oxide) has been observed in mixed valent oxides with Sb_4O_6. Sb_2O_5 is not as stable as As_2O_5 [70].

Antimony (III) sulfide (commonly known as stibnite) is one of the most common forms of occurrence in coal. It has a melting temperature of 819 K and is expected to vaporize in the coal combustion process. Similarly, antimony trichloride has a melting point of 347 K and a boiling point of 496 K. It should readily vaporize in the combustor if present in the coal feedstock.

Unlike arsenic, intermetallic p-block – antimony compounds have not been commonly observed. Intermetallic d-block compounds such as $FeSb_2$ and $CrSb_2$ are much more common than their arsenic analogs and may be present in coal or coal fly ash.

Depending on the forms of occurrence in the coal and transformation mechanism involved, antimony-containing compounds may exit the furnace in the vapor, as part of sub-micron size aerosol particles, or as part of larger, supermicron particles. The specific path by which antimony transforms from the vapor phase to the condensed phase is important in assessing the toxicity of the waste product.

Due to the low concentration of antimony compared to the major species in the coal, there is a very high probability that a volatilized antimony molecule will contact submicron or supermicron particles prior to reaching the supersaturation conditions necessary for nucleation. Therefore, a majority of the volatilized antimony is expected to heterogeneously partition onto the surfaces of both submicron and supermicron particles [30].

Previous research has shown that the collection efficiency in ESP control equipment is significantly lower for submicron particles than for larger particles [10, 31, 32]. Coupled with this, it has been shown that for many coals antimony concentrations are significantly higher in the submicron aerosol fume than in larger particles in the supermicron regime [28, 32, 65, 72, 78-81]. Thus, the deposition of submicron particles in the downwind environment may represent a greater risk of antimony migration into the water table than supermicron particles [36, 37].

Cobalt

Cobalt is not typically considered to be of environmental concern to the same extent as arsenic, selenium, or antimony. However, cobalt is on the list of metals regulated under Title III of the Clean Air Amendment Act [6].

Raask [1] lists the arithmetic mean concentration of cobalt in U.S. coals as 7 ppm but the cobalt concentration in coal can vary substantially between coals and even within a given coal

seam [1, 2]. Gluskoter et al. [2] reports variations in the cobalt concentration from Illinois basin coals of 2.0 to 34 ppm with an arithmetic mean value of 7.3 ppm. There is a high degree of uncertainty as to the modes of occurrence of cobalt in coal [6]. Cobalt is most likely associated with sulfide minerals in pyrite fractions. However, some of the cobalt most probably occurs in fine-grained accessory sulfide minerals or in organic association (particularly in lower ranked coals). In tests by Finkelman [68], cobalt was found to not be associated with silicate materials.

Cobalt belongs to the first triad of Group VIII of the periodic table. Like iron, the most common oxidation states are +2 (II) and +3 (III) [82]. It has normal melting and boiling temperatures of 1768 K and 3143 K, respectively. Thus, Co is considerably less volatile than As, Se, or Sb. Co^{2+} oxides fairly easily, having a reduction potential of –0.28 V compared to –0.447 V for Fe^{2+} [83]. The +2 oxidation state is preferred to the +3 oxidation state. The reduction reaction:

$$Co^{3+} + e^{-} \rightarrow CO^{2+} \qquad (3\text{-}8)$$

has a reduction potential of +1.83 V whereas the analogous iron reaction has a reduction potential of +0.771 V. Cobalt oxide, CoO, has a normal melting point of 2068 K. At this temperature, volatilization during coal combustion will depend upon proximity to burning char molecules. Unlike As, Se, and Sb, cobalt has not been observed to form oxy-anions. Cobalt is thus expected to act as a cation in gas-solid reactions with fly ash surface compounds.

Cobalt readily substitutes for iron. CoS is likely one of the most common forms of occurrence in coal. Its melting temperature, 1389 K, is low enough that volatilization during coal combustion is expected. Cobalt (II) chloride ($CoCl_2$) and cobalt (III) chloride ($CoCl_3$) are both stable compounds. Hydrated forms of both chlorides form readily in the presence of water molecules in the solid solution. The melting temperature of $CoCl_2$ is 1322 K [83].

Depending on the forms of occurrence in the coal and transformation mechanism involved, cobalt-containing compounds may exit the furnace in the vapor, as part of sub-micron size aerosol particles, or as part of larger, supermicron particles. Non-volatilized cobalt remaining bound in bulk fly ash particle fragments are not expected to be of great environmental concern. However for volatilized cobalt, the specific path by which vapor phase cobalt transforms to the condensed phase is important in assessing the toxicity of the waste product.

Due to the low concentration of cobalt compared to the major species in the coal, there is a possibility that a volatilized cobalt molecule will contact submicron or supermicron particles prior to reaching the supersaturation conditions necessary for nucleation. However, supersaturation will be reached more rapidly (as the molecule migrates away from the burning carbon particles) for cobalt than for As, Se, or Sb during coal combustion. While most of the volatilized cobalt is expected to heterogeneously partition onto the surfaces of both submicron and supermicron particles [30], a portion may also homogeneously nucleate and form a portion of the submicron fume. It is not currently possible to distinguish between these two partitioning mechanisms in the submicron regime due to the low concentration of cobalt compared to the number density of submicron particles.

Previous research has shown that the collection efficiency in ESP control equipment is significantly lower for submicron particles than for larger particles [10, 31, 32]. Many studies report cobalt concentrations higher in the submicron aerosol fume than in larger particles in the supermicron regime [28, 32, 65]. However, other studies report cobalt concentration depletion in the submicron aerosol fume [72, 78, 79]. Thus the deposition of submicron particles in the downwind environment may represent a greater risk of cobalt migration into the water table than supermicron particles [36, 37]. This risk appears to be related to the specific properties of the coal burned and the combustion system employed.

Swaine [37] monitored the deposition of cobalt at various locations downwind of the Wallerawang power plant in Australia using accumulation in moss. His results indicate cobalt depositions at 1.8 km to be an order of magnitude higher than cobalt deposition from litter decay and the application of fertilizer. At 27.4 km, cobalt depositions were of the same order of magnitude as cobalt deposition from litter decay and the application of fertilizer.

Radionuclides (Cesium, Thorium, and Cerium)

All fossil fuels contain low levels of naturally occurring radioactive substances. The concentrations of the radioactive isotopic forms of radionuclides in U.S. coals have been well-documented [84, 85]. The quantity of radionuclides discharged to the atmosphere depends upon the concentration of the radionuclides in the coal and the partitioning of radionuclides between gaseous, sub-micron particle, and supermicron particle phases in the combustion and post-combustion zones of the combustor [6, 9, 10, 12-16].

Determining the impact of radioactive emissions from coal combustion continues to be an on-going area of study. Changes in the radioactivity of soil and water samples downwind of coal-burning power plants have been documented at a number of different sites over the past 30 years [85-90]. A better understanding of the specific path by which radionuclides transform from the vapor phase to the condensed phase is necessary in order to model and predict radionuclide emissions, the radioactive contribution to the environment from radionuclides, and for assessing the toxicity of the waste product.

The radioactive isotopic forms of radionuclides have been classified by the International Atomic Energy Agency based on their potential impact on human health [91]. Among the radioactive isotopes classified as "high toxicity" are: Th^{232}, Th^{230}, Th^{228}, and Th^{227}. Within the group classified as "medium toxicity" are: Ce^{144}, Cs^{124}, Cs^{137}, Th^{234}, Cs^{135}, Ce^{141}, Cs^{136}, Ce^{143}, Th^{231}, and Cs^{131}. This study does not attempt to identify the fraction of the radionuclides present in fly ash as radioactive isotopes. Rather, we focused on quantifying the size-segregated concentrations of the elements corresponding to the radioactive isotopes, listed above and then investigating possible post-combustion partitioning mechanisms of these elements during coal combustion.

Cesium is located in Group IA of the periodic table; below sodium, potassium, and rubidium. Its normal oxidation state is +1 (I), its melting temperature is 301 K, and its normal boiling point is 942 K [83]. The oxide form, Cs_2O decomposes at a melting temperature of 673 K and thus is expected to volatilize during coal combustion if present. Since cesium will

readily substitute for other group IA and group IIA salts (e.g., Na, K, Mg, Ca), cesium sulfides and sulfates can be expected to be common forms of occurrence in coals. Cs_2S_3 has a boiling point of 1053 K while Cs_2SO_4 has a melting point of 1283 K [83] and thus these forms are expected to volatilize during coal combustion if present. CsCl has a boiling point of 1563 K. This form should volatilize during combustion of bituminous coals but volatilization during combustion of lower rank coals may be dependent on proximity to oxidizing carbon molecules.

Thorium is the second member of the actinide series of the periodic table and has a normal oxidation state is +4 (IV). Its normal melting temperature is 1072 K and its normal boiling point is 3699 K [83]. The oxide form, ThO_2, has a melting temperature of 3573 K and a boiling temperature of 4673 K. Thorite, $ThSiO_4$, and thorianite, ThO_2+UO_2, are the most common natural forms of occurrence [83]. Thorium sulfide, ThS_2 has a melting point of 2198 K while $ThCl_4$ sublimes at 1043 K. Only thorium chloride is expected to vaporize readily at the bulk gas combustion temperature during combustion. For most other forms volatilization during coal combustion will depend on proximity to oxidizing carbon particles.

Cerium is the second member of the lanthanide series of the periodic table and has normal oxidation states of +3 (III) and +4 (IV). The two oxide forms corresponding to the +3 and +4 oxidation states are Ce_2O_3 and CeO_2, respectively. The melting temperature of Ce_2O_3 is 1965 [83]. Ce_2S_3 decomposes at 2373 K while $Ce_2(SO_4)_3$ decomposes at 1193 K. The +4 sulfate form, $Ce(SO_4)_2$ decomposes at a very low temperature (468 K). By contrast, $CeCl_3$ has a melting temperature of 1116 K and a boiling temperature of 2000vK. Only cerium sulfate is expected to vaporize readily at the bulk gas combustion temperature during combustion. For most other forms volatilization during coal combustion will depend on proximity to oxidizing carbon particles.

Of the three radionuclides studied, only cesium has been found in previous work to have higher concentrations in the submicron aerosol fume than in larger particles in the supermicron regime. Cesium is reported to be enriched in submicron particles in the following studies: Kaleta and Tomza [72] (Brown coal); Markowski and Filby [81]; and McElroy et al. [73]. However, no enrichment or depletion of cesium is reported in the following studies: Coles et al. [34]; and Kaleta and Tomza [72] (Hard coal).

No studies were identified where thorium is reported to be enriched in submicron particles. No enrichment or depletion of thorium in submicron particles is reported in the following studies: Block and Dams [79]; Coles et al. [34]; Klein et al. [92]; Quann et al. [62]; Kaleta and Tomza [72]; and Markowski and Filby [81].

No studies were identified where cerium is reported to be enriched in submicron particles. No enrichment or depletion of cerium in submicron particles is reported in the following studies: Coles et al. [34]; Damle et al. [14]; Gladney et al. [93]; Klein et al. [92]; Smith [28]; Kaleta and Tomza [72]; and Markowski and Filby [81].

3.3.1.2 Thermodynamic Equilibrium Modeling of Semi-Volatile Elements

Thermodynamic equilibrium simulation is a useful tool to assist in understanding the chemistry of complex combustion environments. In the present study, equilibrium simulations were executed for three trace elements – arsenic, selenium, and antimony – for the six coals studied under this research program.

Simulations were performed using the NASA CEA equilibrium code [94]. CEA determines the equilibrium environment by minimizing the Gibbs free energy of the reaction environment. Gaseous species are treated as ideal gases and gaseous mixtures are also considered to be ideal. All condensed species are treated as pure. Other commercially available thermodynamic simulation packages include: FACT, MTDATA, MINGTSYS, SOLGASMIX [95], STANJAN [96], and ALEX [97]. The most influential reaction parameters are composition, temperature, and stoichiometry [95]. Similar simulations have been performed by others [6, 29, 96, 97].

Thermodynamic data used in these simulations came from a number of different sources. A list of the references used to compile the thermodynamic data is shown in Table 3-29. A listing of all of the thermodynamic equilibrium simulations performed in this study is given in Table 3-30.

The first set of calculations simulates the combustion conditions in the baseline screening experiments for three key trace elements – arsenic, selenium, and antimony – with no constraints on the compounds available for formation. Actual coal compositions and combustion conditions were utilized in all simulations. Isothermal simulations were performed at intervals of 100 K to generate a series of temperature profiles ranging from well above the maximum combustion temperature (2200 K) to below the furnace outlet temperature (300 K). Each trace element was simulated separately with the major coal components (carbon, hydrogen, oxygen, nitrogen, sulfur, and chlorine) plus the major inorganic ash components (Fe_2O_3, CaO, SiO_2, and Al_2O_3). As described in Section 2, Introduction, the number density of particles present in the flue gas is expected to exceed the number of gas-phase molecules for each trace element. Therefore, the probability for contact of two gas-phase trace element molecules is less than the probability for contact of a gas-phase trace element molecule with a particle.

Table 3-29. Sources of Thermodynamic Data

[98]	Barin, 1995	[110]	Ruzinov and Guljanickij, 1975
[99]	Knacke, et al., 1991	[111]	Karapet, et al. 1970
[100]	Glusko, et al.., 1965	[112]	Karapet and Karapet, 1970
[101]	Glusko, et al., 1968	[113]	Karapet, et al, 1977
[102]	Glusko, et al., 1970	[114]	Karapet, 1978
[103]	Glusko, et al., 1971	[115]	Phillips, et al., 1988
[104]	Glusko, et al., 1972	[116]	Mills, 1974
[105]	Pankratz and King, 1982	[117]	Kubaschewski and Evans, 1951
[106]	Pankratz, 1984a	[118]	Kubaschewski and Catterall, 1956
[107]	Pankratz, 1984b	[119]	Kubaschewski, et al., 1983
[108]	Pankratz, et. al, 1987	[120]	Kubaschewski, et al., 1993
[109]	Pankratz 1995	[121]	Fabricius, et al., 1994

Table 3-30. Thermodynamic Equilibrium Simulations Performed to Evaluate the Chemistry of Arsenic, Selenium, and Antimony during Pulverized Coal Combustion

Run #	Coal	Element Studied	Simulation Conditions
1	Illinois	Arsenic	Unconstrained Baseline Screening Combustion*
2		Arsenic	AsO Omitted as Valid Combustion Product
3		Selenium	Unconstrained Baseline Screening Combustion
4		Antimony	Unconstrained Baseline Screening Combustion
5		Antimony	SbO Omitted as Valid Combustion Product
6	Pittsburgh	Arsenic	Unconstrained Baseline Screening Combustion
7		Arsenic	AsO Omitted as Valid Combustion Product
8		Selenium	Unconstrained Baseline Screening Combustion
9		Antimony	Unconstrained Baseline Screening Combustion
10		Antimony	SbO Omitted as Valid Combustion Product
11	Ohio	Arsenic	Unconstrained Baseline Screening Combustion
12		Arsenic	AsO Omitted as Valid Combustion Product
13		Selenium	Unconstrained Baseline Screening Combustion
14		Antimony	Unconstrained Baseline Screening Combustion
15		Antimony	SbO Omitted as Valid Combustion Product
16	Kentucky	Arsenic	Unconstrained Baseline Screening Combustion
17		Arsenic	AsO Omitted as Valid Combustion Product
18		Selenium	Unconstrained Baseline Screening Combustion
19		Antimony	Unconstrained Baseline Screening Combustion
20		Antimony	SbO Omitted as Valid Combustion Product
21	Wyodak	Arsenic	Unconstrained Baseline Screening Combustion
22		Arsenic	AsO Omitted as Valid Combustion Product
23		Selenium	Unconstrained Baseline Screening Combustion
24		Antimony	Unconstrained Baseline Screening Combustion
25		Antimony	SbO Omitted as Valid Combustion Product
26	North Dakota	Arsenic	Unconstrained Baseline Screening Combustion
27		Arsenic	AsO Omitted as Valid Combustion Product
28		Selenium	Unconstrained Baseline Screening Combustion
29		Antimony	Unconstrained Baseline Screening Combustion
30		Antimony	SbO Omitted as Valid Combustion Product

*Baseline screening combustion conditions are described in Section 3.3.3.

In the second set of simulations, constraints were placed on the formation of simple oxides for arsenic and antimony (e.g., AsO, SbO). Previous research [29, 60] has shown that these trace elements form oxy-anions during combustion (e.g., As_2O_3, Sb_2O_3, SeO_2). Simple oxides were inhibited to more accurately simulate the combustion products expected to be generated during combustion [29].

Simulating Arsenic Partitioning during Coal Combustion

The predicted forms of occurrence of arsenic resulting from the combustion of the six study coals under baseline screening conditions (i.e., 20% excess air) are shown in Figure 3-40. For all six coals, arsenic-sulfur compounds are predicted above 2000 K.

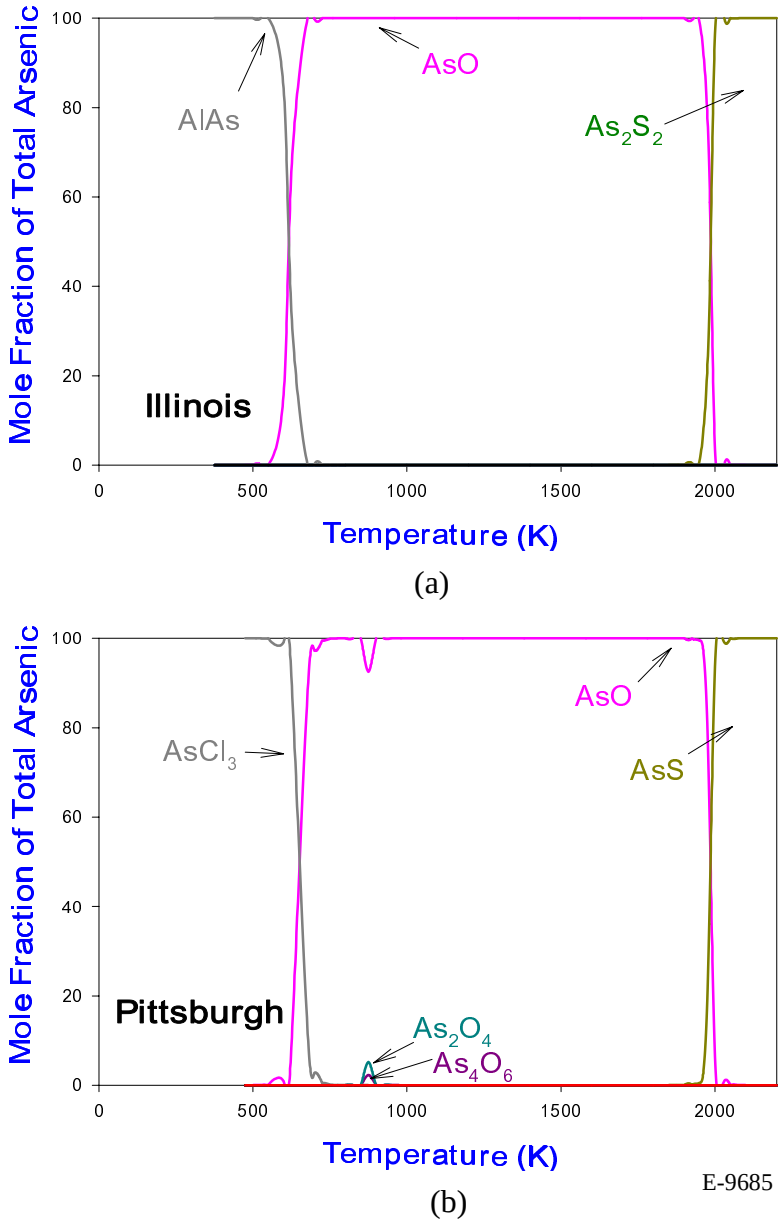

Figure 3-40. Simulated temperature-dependent equilibrium profiles of arsenic during combustion of the six study coals under baseline conditions.

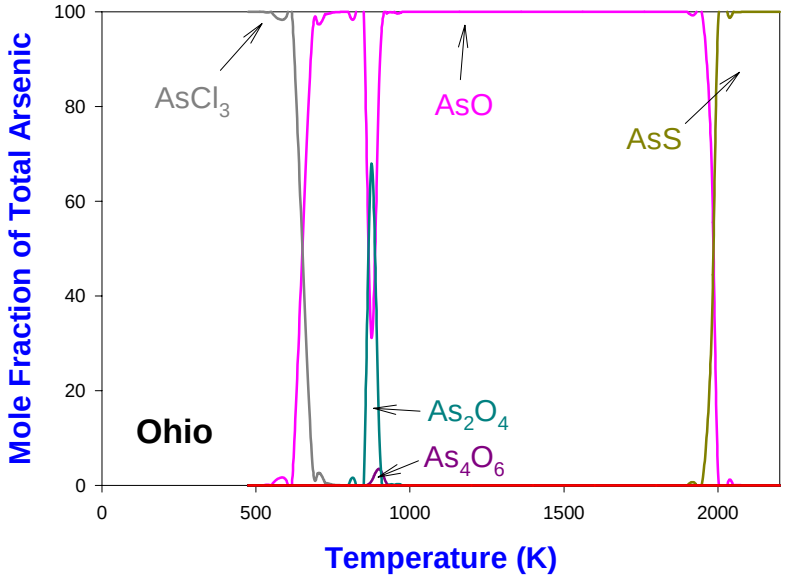

(c)

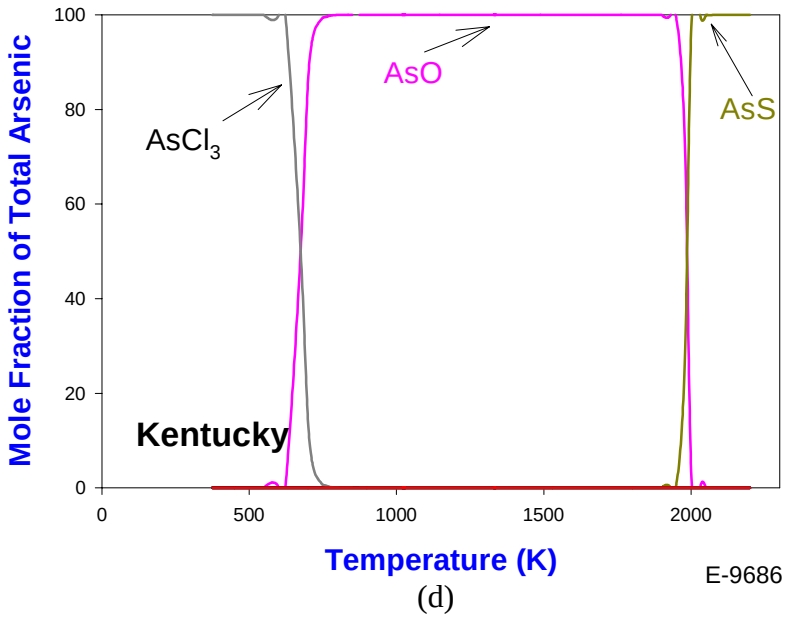

(d)

Figure 3-40. (Continued) Simulated temperature-dependent equilibrium profiles of arsenic during combustion of the six study coals under baseline conditions.

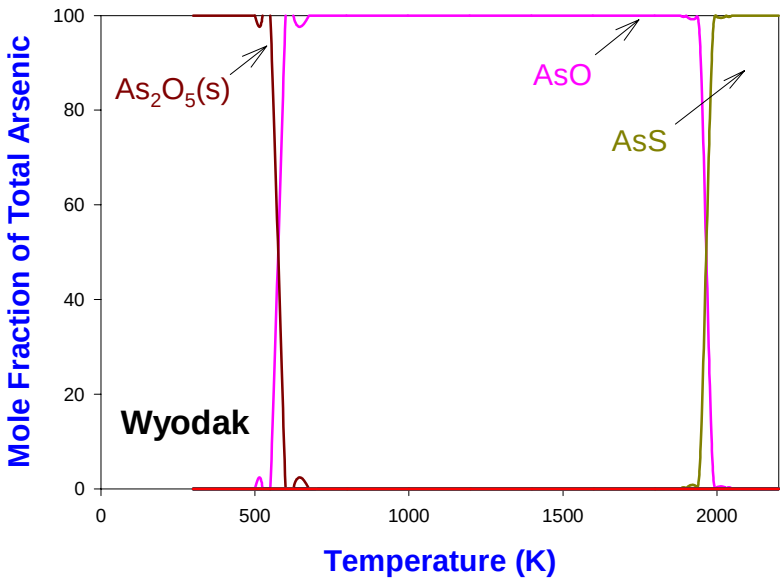

(e)

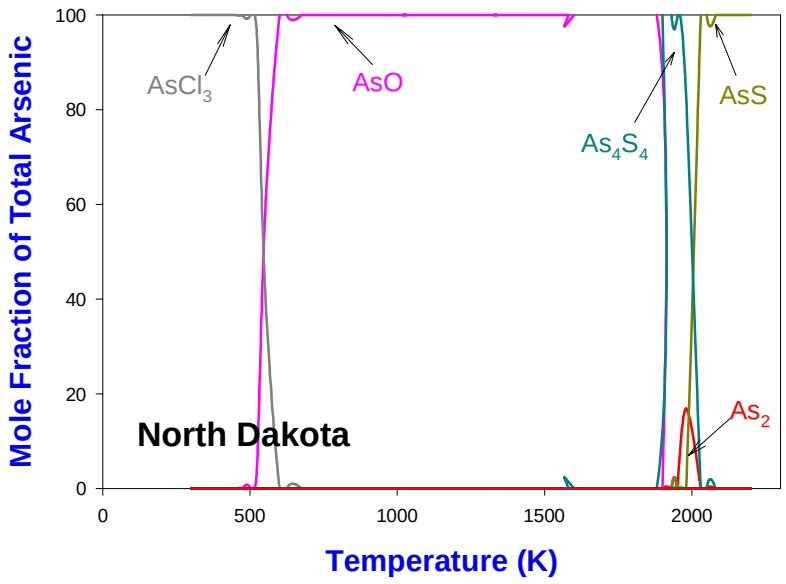

(f)

Figure 3-40. (Continued) Simulated temperature-dependent equilibrium profiles of arsenic during combustion of the six study coals under baseline conditions.

However, AsO is predicted in the region bounding the maximum combustion temperatures (1430 to 1665 K), the Port 4 (Port 4b in Phase I) particle sampling temperatures (1230 to 1520 K), and the Port 14 (Port 12 in Phase I) particle sampling temperatures (840 to 1190 K) for the experiments performed in this research program. A portion of the arsenic is predicted to be present as oxy-anions (As_2O_4, As_4O_6) for the Pittsburgh and Ohio coals. For the Pittsburgh coal less than 10% is predicted to be present in this form. Up to 65% of the Ohio coal arsenic is expected to be present in an oxy-anion form in the narrow temperature range of 850 to 900 K. Arsenic is not predicted in an oxy-anion form for the other four coals.

All of the baghouse inlet port samples were collected below 600 K. AsO is not predicted below 600 K. For the Illinois coal, the predicted form is AlAs(s). The predicted form for the Pittsburgh, Ohio, Kentucky, and North Dakota coals is $AsCl_3(g)$. The formation of $AsCl_3(g)$ at low temperatures is not supported by the experimental partitioning results presented in Section 3.3.3. During Wyodak coal combustion, $As_2O_5(s)$ is predicted.

The simulation results when arsenic oxide (AsO) is omitted as a valid combustion product are shown in Figure 3-41 for all six coals. For all six coals, a mixture of oxy-anions are predicted in the post-combustion zone temperature range. The Illinois results predict the formation of oxy-anions - $As_4O_6(g)$, $As_2O_4(s)$, and $Ca_3(AsO_4)_2(s)$ - plus elemental arsenic in the form of As and As_2. The Pittsburgh results are similar, the oxy-anions $As_4O_6(g)$, $As_2O_4(s)$, and $Ca_3(AsO_4)_2(s)$ are predicted along with As and As_2. In addition, a portion of the arsenic is predicted to form $AsCl_3(g)$.

Although the Ohio coal has a much lower calcium content than the Illinois or Pittsburgh coals, $Ca_3(AsO_4)_2(s)$ is still predicted as one of the oxy-anions forms along with $As_4O_6(g)$ and $As_2O_4(s)$. The elemental forms As and As_2 are also predicted. By contrast, $Ca_3(AsO_4)_2(s)$ is not predicted as one of the oxy-anions formed during the combustion of the Kentucky coal. The Kentucky coal calcium content is similar to the Ohio coal. However, a much higher fraction is predicted in the form $AsCl_3(g)$.

The results for both the Wyodak subbituminous coal and North Dakota lignite are similar to the Illinois coal results.

Below 700 K, $AlAsO_4(s)$ is the predicted form of occurrence for the four bituminous coals (Illinois, Pittsburgh, Ohio, and Kentucky) while $As_2O_5(s)$ is predicted for the two low rank coals (Wyodak and North Dakota).

The constrained simulation results appear to be more reflective of the actual partitioning of arsenic during pulverized coal combustion. Results in subsequent sections will show that vapor-phase arsenic is reactive with cation surface sites available on fly ash particles. This reaction mechanism is more likely with vapor-phase arsenic in an oxy-anion form, such as As_2O_4 rather than a simple oxide form (i.e., AsO). It should be noted that thermodynamic data for Fe-As reaction products were not available for use in these simulations. Therefore, it was not possible to assess whether the formation of Fe-As oxy-anion complexes is thermodynamically favorable. A listing of all possible arsenic products available in the thermodynamic database are shown in Table 3-31.

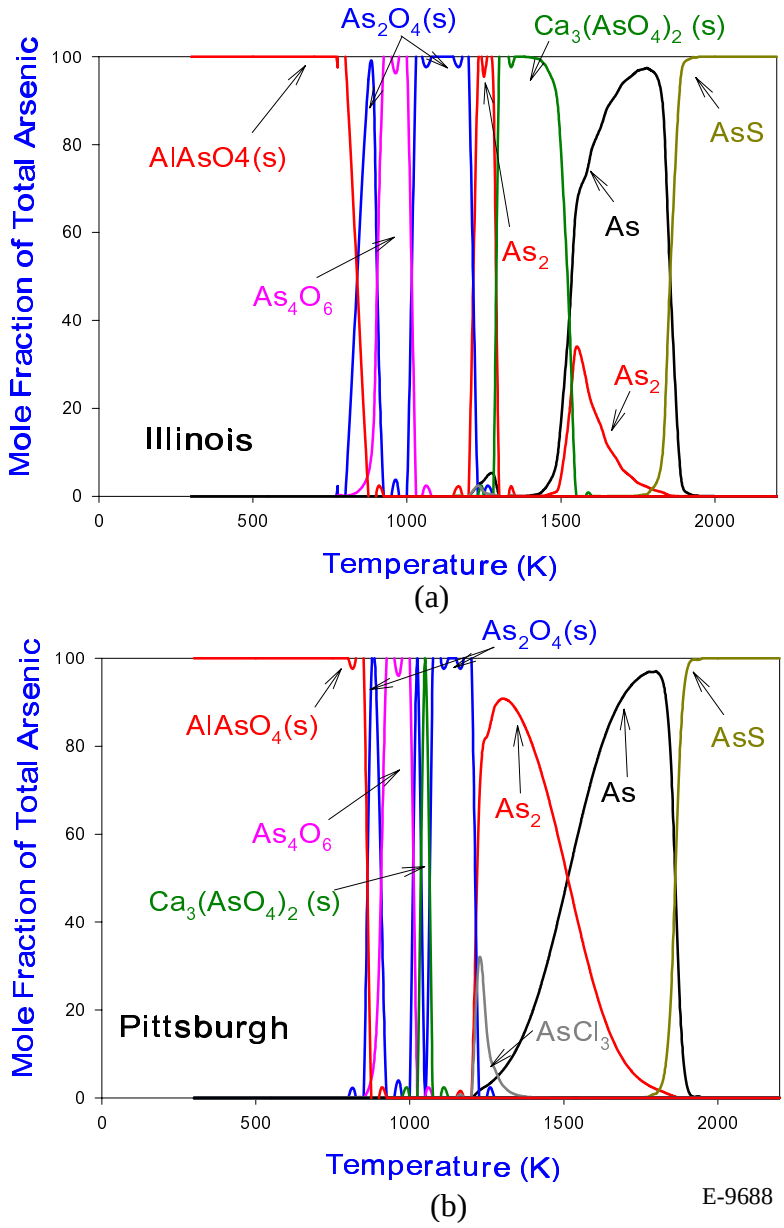

Figure 3-41. Simulated temperature-dependent equilibrium profiles of arsenic omitting AsO as a valid product.

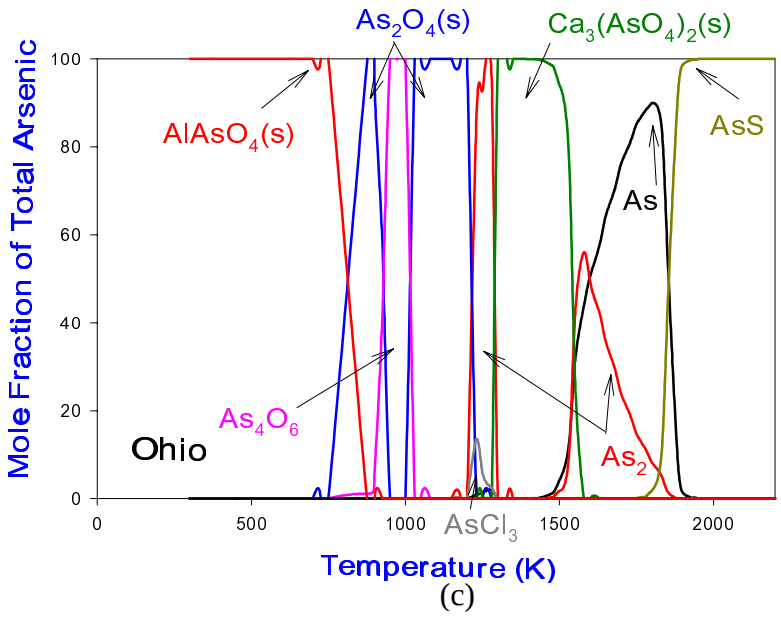

(c)

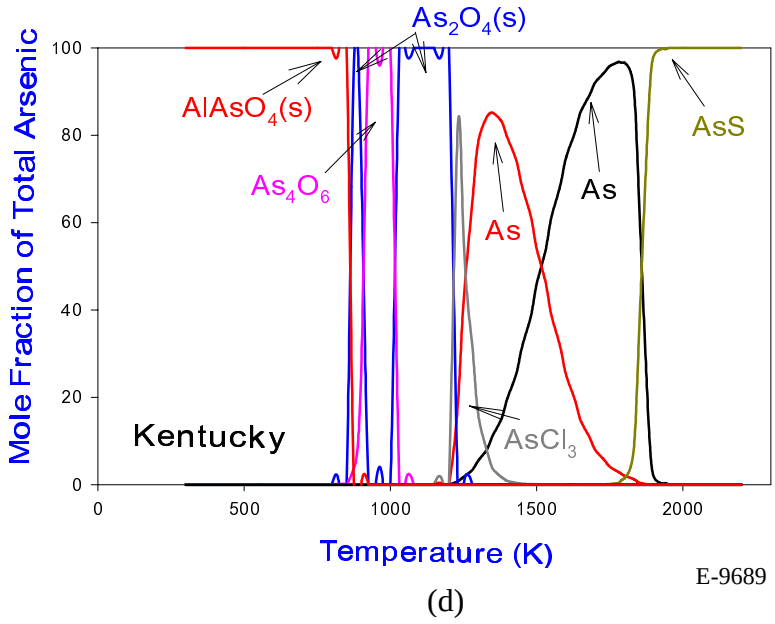

(d)

Figure 3-41. (Continued) Simulated temperature-dependent equilibrium profiles of arsenic omitting AsO as a valid product.

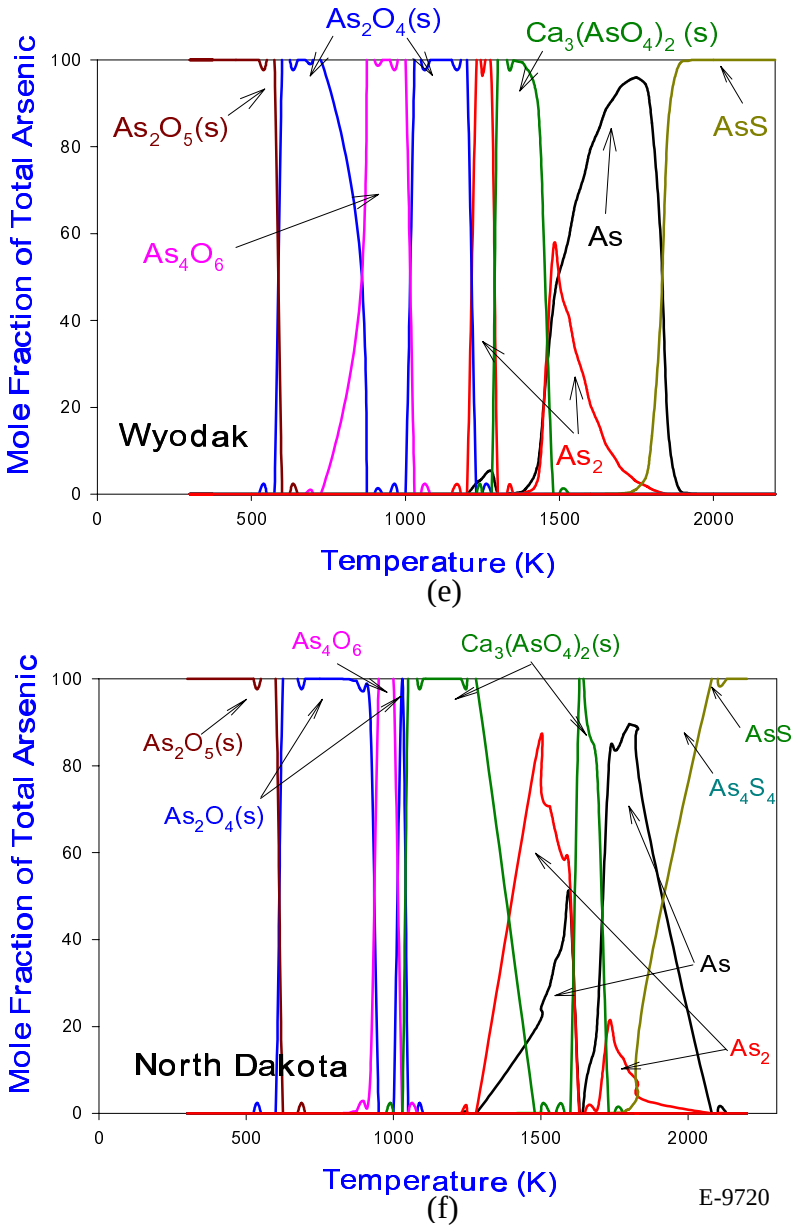

Figure 3-41. (Continued) Simulated temperature-dependent equilibrium profiles of arsenic omitting AsO as a valid product.

Table 3-31. Possible Arsenic Products from Thermodynamic Simulation

Gas Phase	Liquid Phase	Solid Phase
AsI_3	As_4S_4	$Cd_3(AsO_4)_2$
As	As_2O_3	$Be_3(AsO_4)_2$
As_2	As_2S_2	$Ni_{11}As_8$
As_3	As_2S_3	As
As_4	$AsCl_3$	$TlAsO_4$
As4O6	AsI_3	$Sr_3(AsO_4)_2$
$AsBr_3$	AsF_3	$Ni_3(AsO_4)_2$
$AsCl_3$	As_2Te_3	NiAs
AsH_3		Ni_5As_2
AsO		$Cr_3(AsO_4)_2$
AsSe		$CrAsO_4$
AsF_3		$Ca_3(AsO_4)_2$
AsF_5		$Ba_3(AsO_4)_2$
AsTe		As_4S_4
$Hg_3(AsO_4)_2$		As_2O_5
$As(H_3)_3$		As_2S_2
$AsH(H_3)_2$		As_2S_3
$AsH_2(H_3)$		As_2Se_3
As_2S_3		As_4S_4
Na_3As		AsI_3
		AlAs
		$AlAsO_4$
		Ag_3AsO_4
		Cd_3As_2
		As_2Te_3
		$Hg_3(AsO_4)_2$
		MnAs
		$Mn_3(AsO_4)_2$
		$Pb_3(AsO_4)_2$
		$BAsO_4$
		As_2O_4
		Na_3AsO_4
		$3Na_2O*As_2O_5$

Simulating Selenium Partitioning During Coal Combustion

The predicted forms of occurrence of selenium resulting from the combustion of the six study coals under baseline screening conditions (i.e., 20% excess air) are shown in Figure 3-42. The predicted forms of occurrence for all six coals are nearly identical and consists of a mixture of Se, SeO, and SeO_2 above 1600 K. Below 1600 K only SeO_2 is predicted to occur. Solid phase selenium is not predicted for any of the coals studied. These results are not supported by the experimental partitioning data. As shown in Section 3.3.3, the experimental results indicated the reaction of SeO_2 with calcium and iron active cation fly ash surface sites.

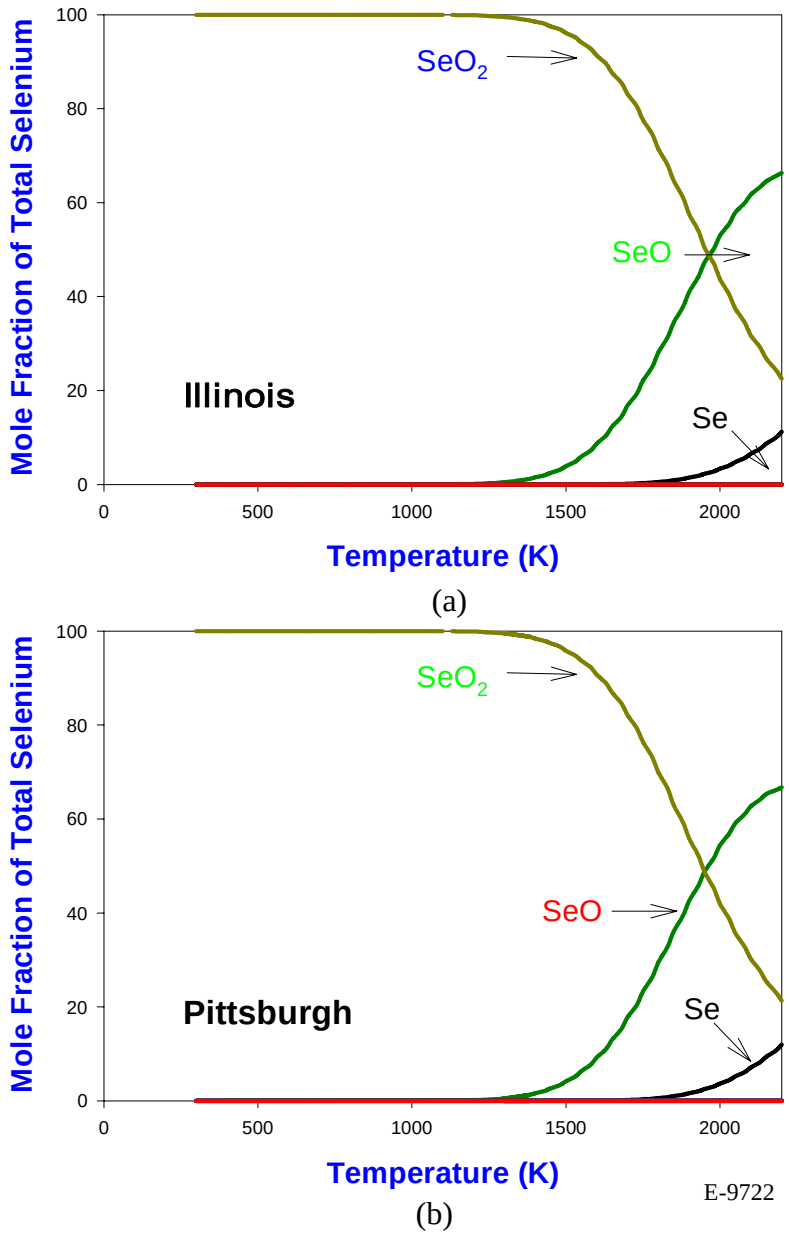

Figure 3-42. Simulated temperature-dependent equilibrium profiles of selenium during combustion of the six study coals under baseline conditions.

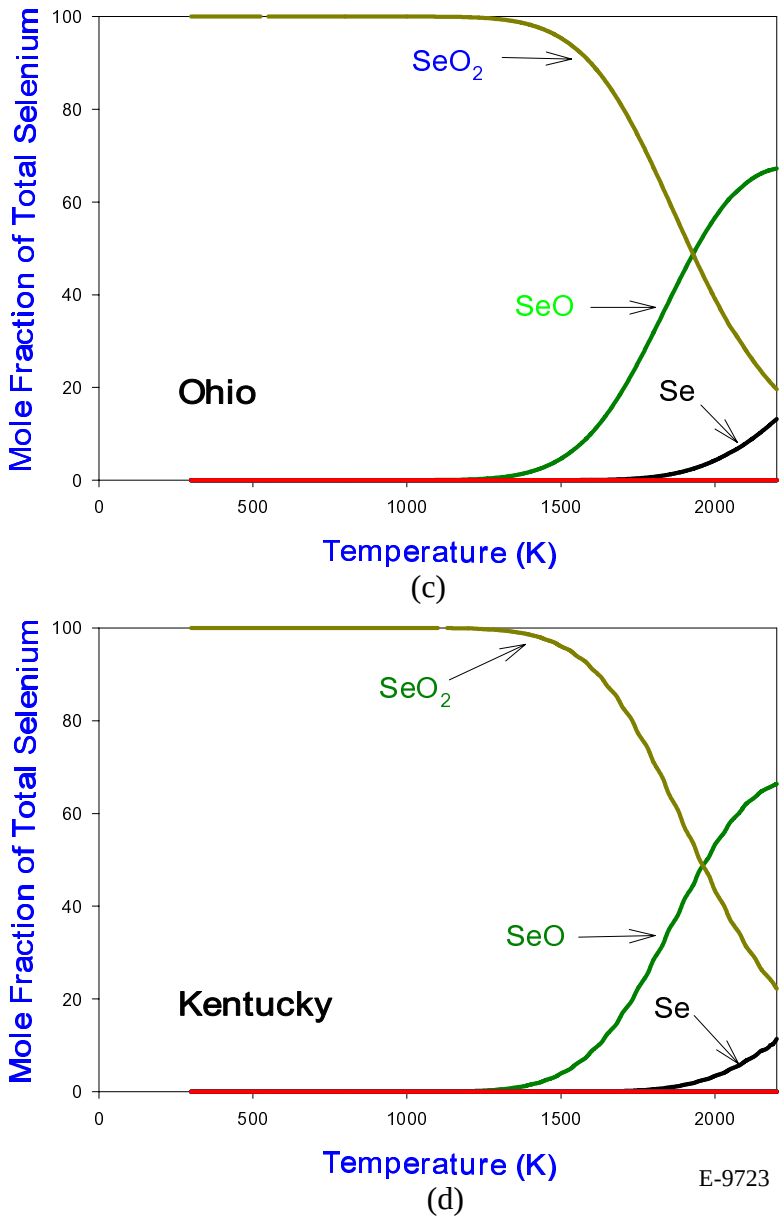

Figure 3-42. (Continued) Simulated temperature-dependent equilibrium profiles of selenium during combustion of the six study coals under baseline conditions.

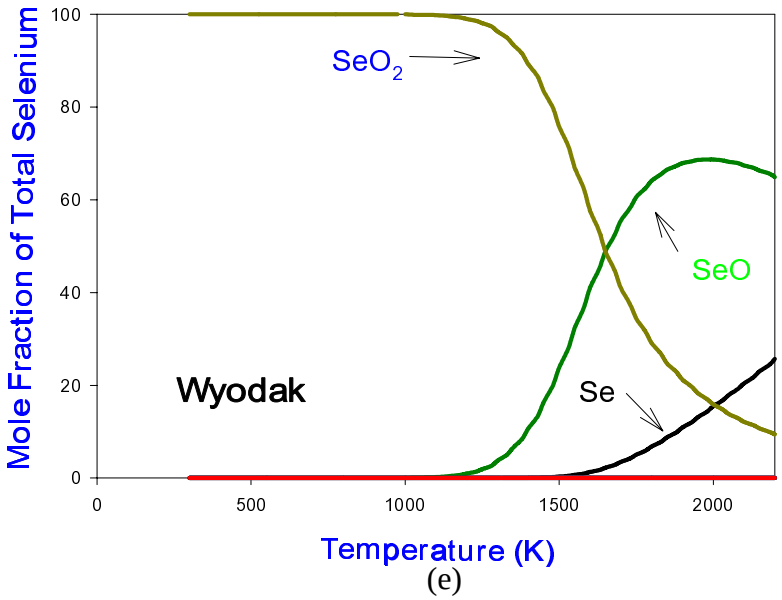

(e)

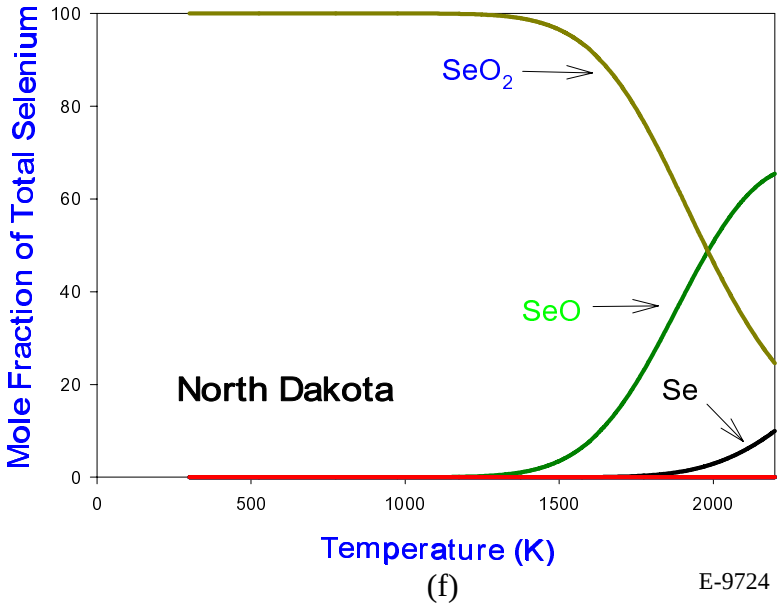

(f)

E-9724

Figure 3-42. (Continued) Simulated temperature-dependent equilibrium profiles of selenium during combustion of the six study coals under baseline conditions.

A listing of all of the possible selenium products available in the simulation database is shown in Table 3-32.

Table 3-32. Possible Selenium Products from Thermodynamic Simulation

Gas Phase	Liquid Phase	Solid Phase
Se	Se_2Cl_2	TlSe, $NiSe_2$
Se_2	TlSe	Tl_2Se, Se
Se_2Cl_2	Se	Se_2Cl_2, $SeCl_4$
Se_3	Sb_2Se_3	Sb_2Se_3, $NiSeO_3$
Se_4	$CdSeO_3$	HgSe, CaSe
Se_5	PbSe	As_2Se_3
Se_{56}	SeO_3	Al_2Se_3
Se_7		Ag_2Se_3
Se_8		$CdSeO_3$
$SeCl_2$		CdSe
SeO		$HgSeO_3$
SeO_2		MnSe
SbSe		PbSe
HgSe		$PbSeO_3$
AsSe		$PbSeO_4$
Al_2Se_2		$CaSeO_4$
PbSe		SeO_3
$SeBr_2$		Se_2O_5
Se_2Br_2		$CaSeO_3*2H_2O$
SeF		$CaSeO_4*2H_2O$
SeF_2		$SiSe_2$
SeF_4		$FeSe_{0.96}$
SeF_5		$FeSe_{0.961}$
SeF_6		FeSe
AlSe		$FeSe_{1.14}$
Al_2Se		$FeSe_{1.143}$
SiSe		$FeSe_{1.333}$
$SiSe_2$		$FeSe_2$
$Fe_2(SeO_3)_3$		MgSe
SSe		$MgSeO_3$
		$MgSeO_4$
		$MgSeO_3*6H_2O$
		Na_2Se
		Na_2Se_2
		Na_2SeO_4

Simulating Antimony Partitioning During Coal Combustion

The predicted forms of occurrence of antimony resulting from the combustion of the six study coals under baseline screening conditions (i.e., 20% excess air) are shown in Figure 3-43. For all six coals, antimony-oxide compounds are predicted to be the dominant form above 2000 K. SbS is also predicted to be present as a minor form of occurrence. AlSb(L) and AlSb(s) are predicted as the major forms of occurrence below 1700 K. SbO is also predicted in this temperature region for the Illinois and North Dakota coals. Unlike the other coals, the North Dakota lignite results predict the formation of vapor phase Sb-Cl compounds below 600 K. This is consistent with experimental results where the majority of the antimony leaves the combustor in the vapor phase for the combustion of North Dakota lignite.

The simulation results when antimony oxide (SbO) is omitted as a valid combustion product are shown in Figure 3-44 for all six coals. For the four bituminous coals and the Wyodak subbituminous coal, AlSb(L) and AlSb(s) are predicted as the major forms of occurrence below 1700 K. SbS and SbCl are also predicted forms of occurrence for the Illinois coal. The North Dakota lignite results predict a mixture of SbS, AlSb(L), and Sb_2O_4 from 600 to1700 K. Below 600 K, $SbCl_3$ and $SbCl_5$ are predicted. It should be noted that only a limited subset of potential Ca-Sb solid-phase products are available in the simulation database. Further, information on Fe-Sb solid-phase products is unavailable.

The formation of AlSb complexes do not appear to be supported by the experimental results presented in Section 3.3.3.

A listing of all of the possible antimony products available in the simulation database is shown in Table 3-33.

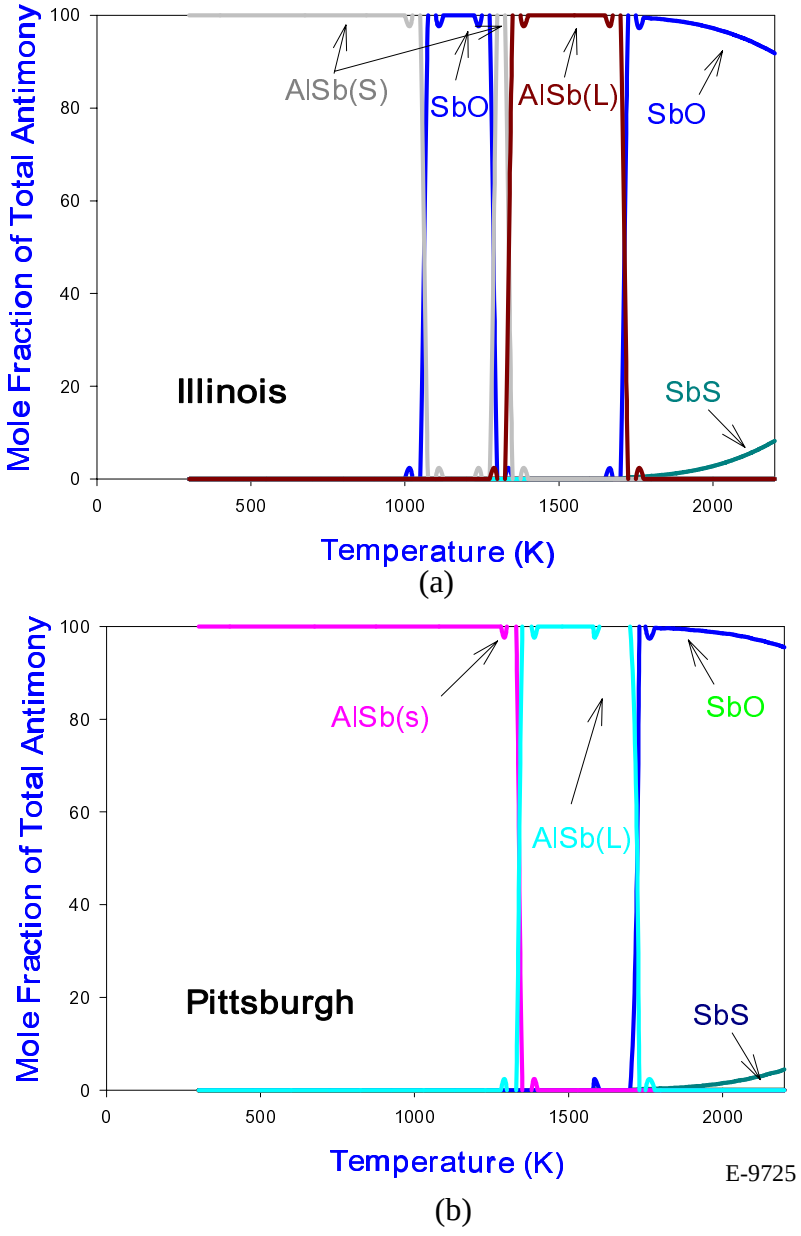

Figure 3-43. Simulated temperature-dependent equilibrium profiles of antimony during combustion of the six study coals under baseline conditions.

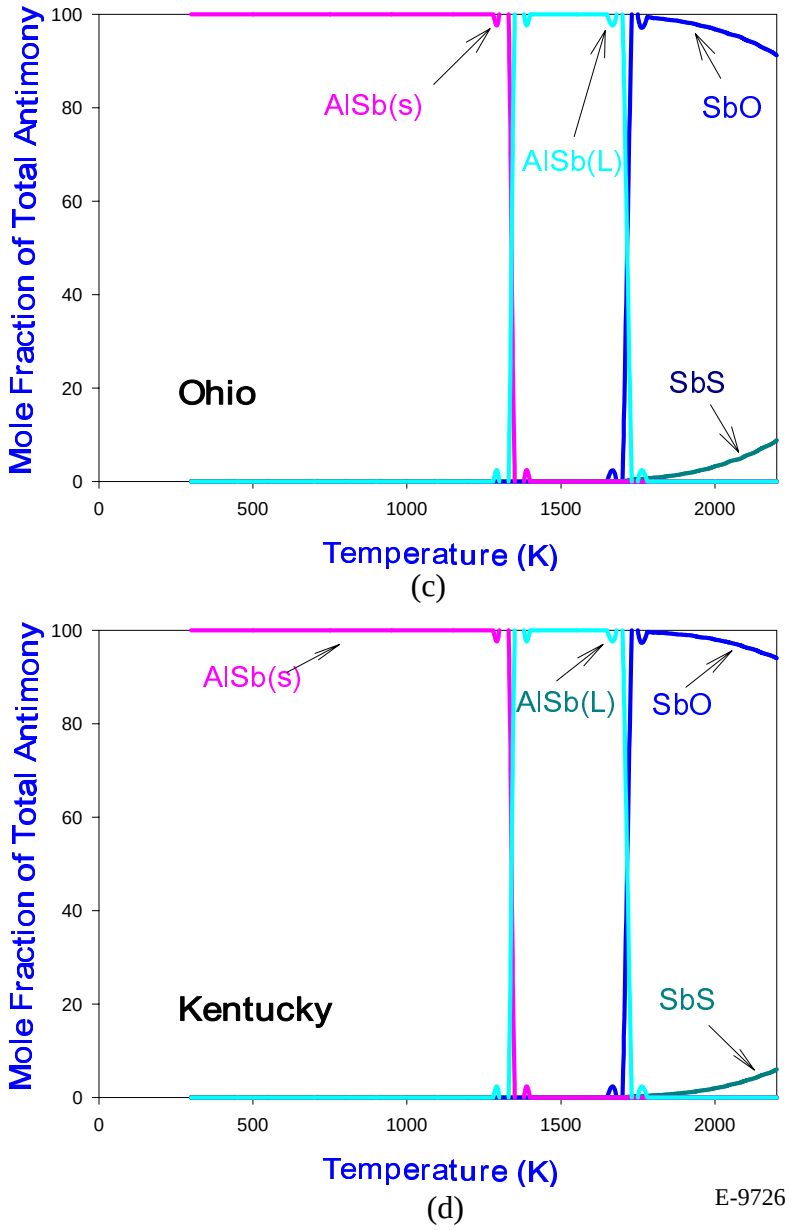

Figure 3-43. (Continued) Simulated temperature-dependent equilibrium profiles of antimony during combustion of the six study coals under baseline conditions.

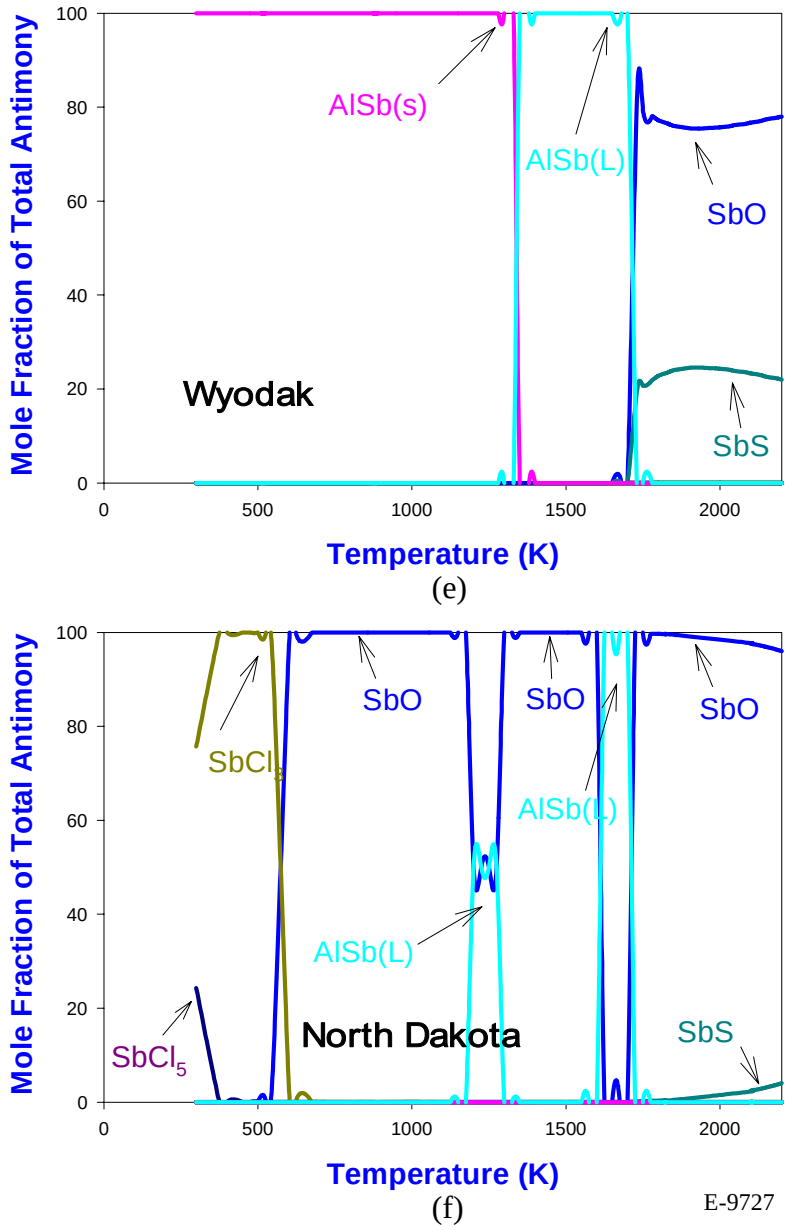

Figure 3-43. (Continued) Simulated temperature-dependent equilibrium profiles of antimony during combustion of the six study coals under baseline conditions.

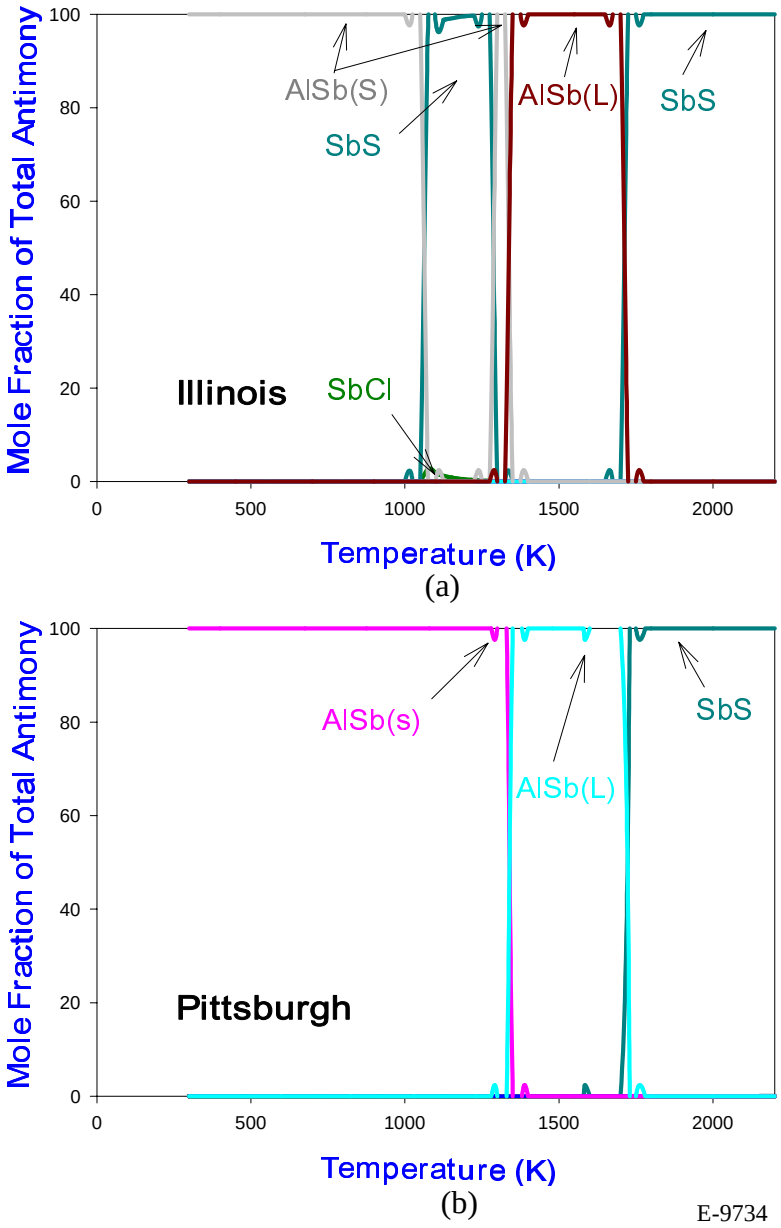

Figure 3-44. Simulated temperature-dependent equilibrium profiles of antimony when SbO is omitted as a valid combustion product.

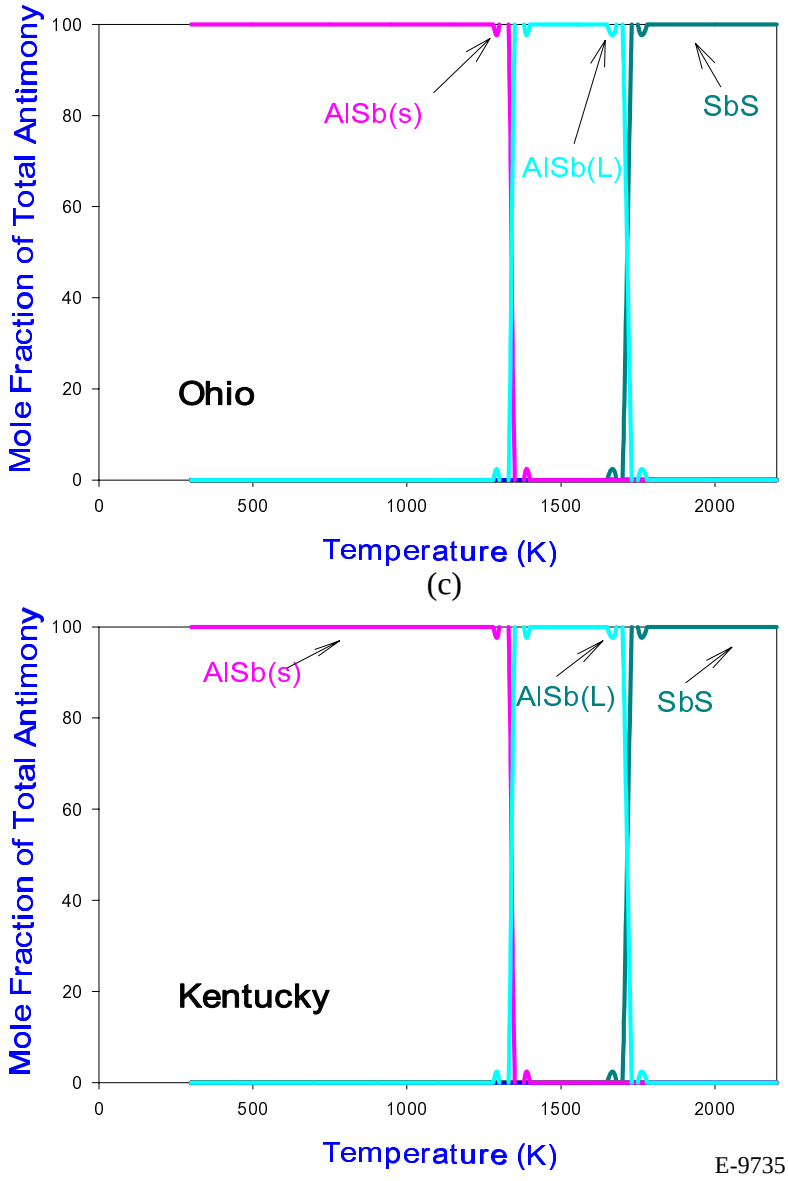

Figure 3-44. (Continued) Simulated temperature-dependent equilibrium profiles of antimony when SbO is omitted as a valid combustion product.

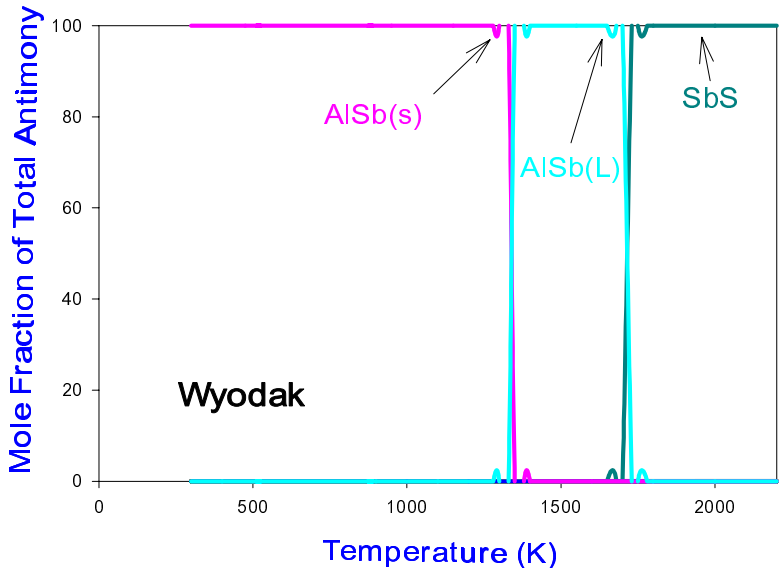

(e)

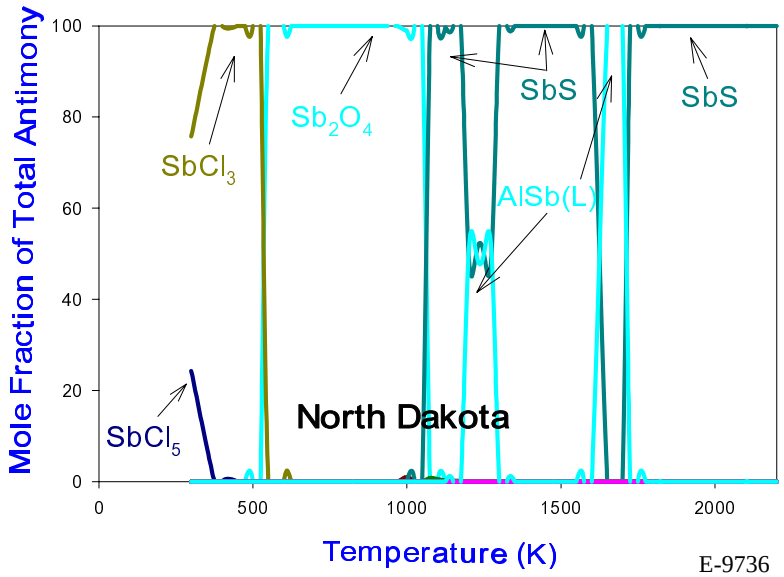

(f)

Figure 3-44. (Continued) Simulated temperature-dependent equilibrium profiles of antimony when SbO is omitted as a valid combustion product.

Table 3-33. Possible Antimony Products from Thermodynamic Simulation

Gas Phase	Liquid Phase	Solid Phase
SbI_3	AlSb	AlSb
Sb	Sb_2O_3	Sb_2O_4
Sb_2	Sb_2S_3	SbOCl
Sb_2S_3	Sb_2Te_3	Sb
Sb_2S_4	Sb	SbI_3
Sb_4O_6	$SbCl_3$	SbZn
Sb_4	Sb_2Se_3	Sb_2O_3
$SbCl_3$	$SbBr_3$	Sb_2O_5
SbH_3	SbF_3	Sb_2S_3
SbO		$Sb_2(SO_4)_3$
SbSe		Sb_2Te_3
SbF_3		Sb_2Se_3
SbF		$SbBr_3$
Sb_3S_2		$SbCl_3$
$SbBr_3$		SbF_3
Sb_4S_3		SbI_3
SbCl		NiSb
$SbCl_5$		Ca_3Sb_2
SbS		CdSb
$(SbS)_2$		MnSb
$(SbS)_3$		Mn_2Sb
$(SbS)_4$		SbO_2
		Mg_3Sb_2

3.3.2 Bench Scale Investigations of Arsenic Behavior Post-Combustion

3.3.2.1 Background

As discussed elsewhere in this report, arsenic in coal occurs in two different forms and these depend upon the rank of the coal. In bituminous coal, arsenic largely occurs in pyrite, where it substitutes for sulfur in the pyrite structure. In low rank coals, arsenic occurs in the form of an oxygenated complex. During combustion, arsenic vaporizes and eventually partitions between the vapor phase and particulate matter. Prior research has shown that it is the interaction of fly ash particles with arsenic vapor that determines the final partitioning of trace metals such as arsenic in these respective phases. As a consequence, several studies have been carried out detailing the interaction of trace metals such as arsenic with a variety of solid sorbents.

For arsenic, Wouterlood and Bowling [122] have shown that activated carbon is an effective sorbent, trapping arsenic oxide vapor at temperatures of 200^{o}C. Hydrated lime was also found to very effective for capturing arsenic oxide. Experiments conducted by Mahuli et al. [123] showed that hydrated lime also captured arsenic oxide by forming an irreversible calcium arsenate product [$Ca_3(AsO_4)_2$] at temperatures of 600 and 1000^{o}C. Subsequent experiments by Jadhav et al. [124] showed that lime effectively captured arsenic oxide vapor over a temperature range of 300 to 1000 ^{o}C. These experiments showed that below 600^{o}C the stable dicalcium orthoarsenate [$Ca_3(AsO_4)_2$] was formed, whereas dicalcium pyroarsenate($Ca_2AS_2O_7$) was the product formed in the range of 700 to 900^{o}C.

During this project experiments were conducted in our lab to ascertain what compounds are formed when and if calcium oxide and calcium silicate present in fly ash react with arsenic. These experiments were not focused on development of sorbents; rather, the objective was to determine the effect of surface reaction with calcium compounds in determining arsenic partitioning under post combustion conditions. These experiments entailed contacting an arsenic solution generated from an organic source (cacodylic acid solution) with particles of several types including silica, dicalcium silicate, calcium doped sol-gel silica and calcium oxide. Subsequent XAFS analyses of these particles showed that the As^{+5} oxidation state was the predominant form of arsenic in all of the solids except silica (discussed in Section 3.4.5), indicating the formation of calcium arsenate.

To model the reaction of arsenic with these calcium particles, the chemical kinetics and in particular the specific reaction rate of *vapor phase* arsenic with these solids must first be determined. In this study the interaction of calcium and calcium silicates with arsenic oxide vapors was therefore investigated over a range temperature(600 to 1000^{o}C). The intrinsic kinetics of these reactions were studied for the same temperature range.

3.3.2.2 Experimental Set-up

The experimental setup for the experiments to be carried out for extracting kinetic rates for arsenic surface reaction with different adsorbents is shown in Figure 3-45. It has four main components: a toxic gas generation section, a reactor assembly, a residual toxic gas scrubber section, and a data acquisition component.

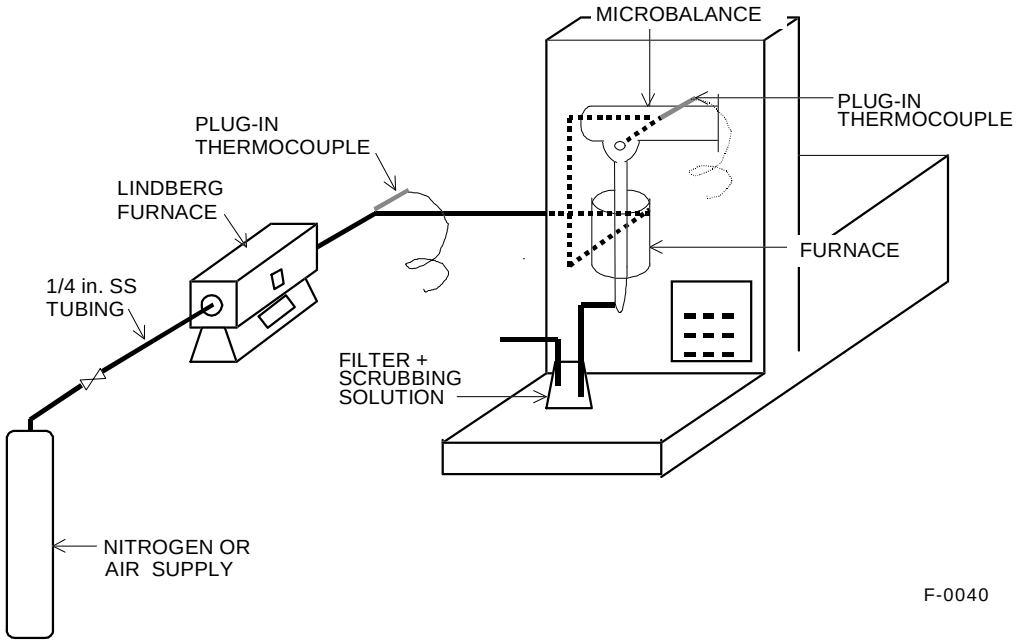

Figure 3-45. Schematic diagram of reactor assembly.

The toxic gas supply assembly consists of 25.4 mm OD quartz tube housed in a Lindberg furnace to which a carrier gas supply was attached. A ceramic boat was used to hold the source of arsenic inside the quartz tubing. Arsenic trioxide was used as the source of arsenic for all experiments. The outlet from the quartz tubing was connected to the reactor assembly by 6.35 mm stainless steel tubing wrapped in heat tapes. Provision was made for in-line vapor temperature monitoring by the insertion of a plug in thermocouple at the exit from the toxic gas assembly and at the entrance to the reactor.

The reactor assembly was made up of a microbalance from which a sample pan suspended using a platinum hang down wire. Sorbent samples were held on the pan enclosed in a quartz tube where the reaction temperature was provided by a Cahn furnace controlled by a microprocessor. A constant reaction temperature was accomplished using a thermocouple inserted in the reaction zone and a feedback control loop.

A 3.13 mm OD Pyrex tube connected the scrubbing assembly to the reactor from which all residual toxic gases were bubbled through a scrubbing solution of HNO_3 in a flask. The resulting scrubbed gas was then vented to the atmosphere through 3.13 mm OD Pyrex tube inside a fume hood.

All the measuring devices were wired to a data acquisition board connected to Desktop computer where software component of data acquisition system was used to monitor real time measurements.

3.3.2.3 Calibration of Microbalance

Prior to the start of these experiments the balance was zeroed and then calibrated to ensure measurement integrity. The calibration exercise involves using a sample of known weight to electronically calibrate the microbalance signal. This is accomplished by placing a 100 mg weight on the sample pan and adjusting the microbalance voltage until the measurement on the computer reads the sample weight. To complete this exercise, several measurements were taken on the microbalance and compared with measurements from an Omega scale. The results are shown in Figure 3-46.

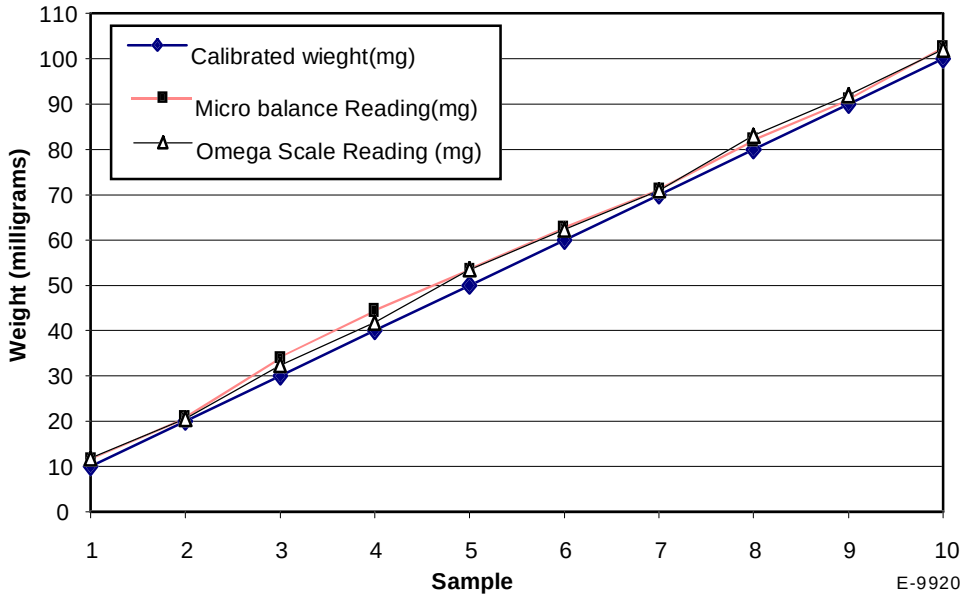

Figure 3-46. Cahn micro balance calibration check results for known sample weights.

3.3.2.4 Cahn Furnace Temperature Control

To establish the capability of the microprocessor a set of temperature control experiments were conducted. This involved tuning the controller by varying the controller gain and reset parameters to reduce lag time and to ensure steady control. A typical result from these exercises is shown in Figure 3-47.

From the above it can be seen that a steady reactor temperature can be achieved with the controls available on the microprocessor.

3.3.2.5 Arsenic Vaporization Data

FACT equilibrium software was used to conduct thermodynamic calculations to determine the temperature - vapor concentration relationship for a vapor stream in contact with the heated arsenic trioxide solid. Inputs for the simulation were:

(a) The equivalent number of moles of nitrogen or oxygen for a fixed flow rate of gas calculated using the ideal gas equation at ambient temperature and the operating gas pressure.

(b) The equivalent number of moles for a fixed mass of solid arsenic trioxide.

Equilibrium simulations were performed for incremental changes in solid arsenic trioxide mass and gas flow rates for a temperature range of 0 to 200°C.

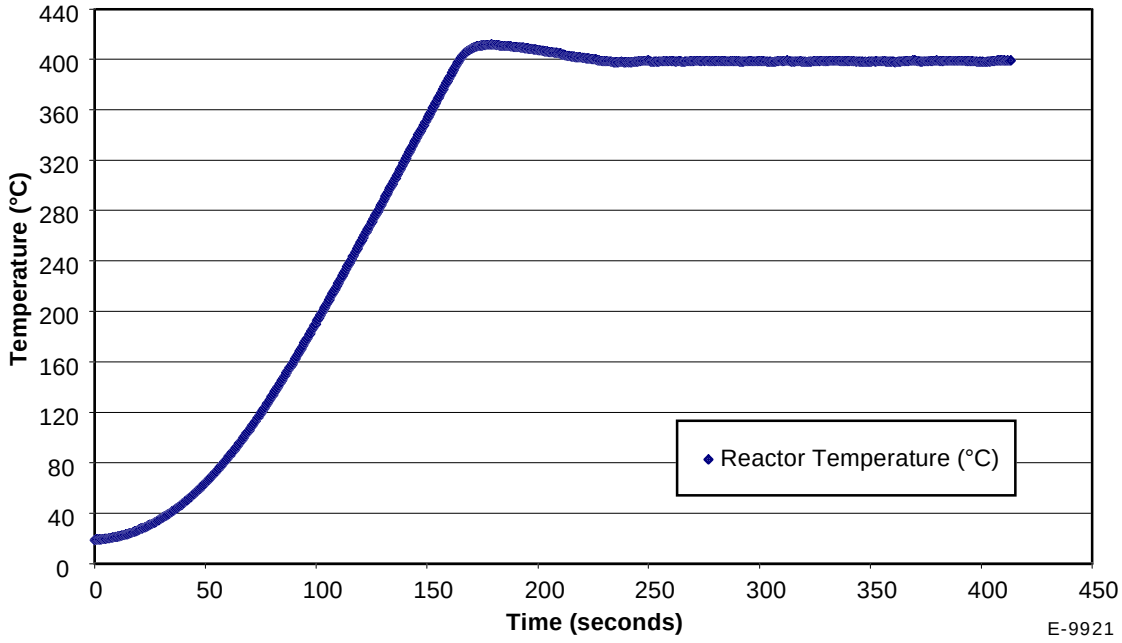

Figure 3-47. Reactor temperature control test.

Because of the capacity limitation of the ceramic boat and decrease in accuracy of the microbalance due to turbulence around the sample pan at high gas flow rates, experiments were generally limited to low (laminar) flow conditions. The input gas flow rate range was therefore in the range of 0.14 to 0.2 slpm and the range mass of solid mass was 0.25 to 1.0 gram. The results for a nitrogen flow rate of 0.16 slpm and a solid mass of 1 gram are shown in Figure 3-48.

To verify these results, a series of vaporization experiments were done using the same gas flow rate but at significantly smaller solid mass because of the sample pan capacity constraint. In these experiments, arsenic trioxide was placed in sample pan suspended in the microbalance and heated to the target temperatures using the Cahn furnace controls. Because of difficulties encountered while trying to control furnace temperature using the PI controls, the programmable control feature of the microprocessor was used to provide a steady vaporization temperature. For each experiment, the weight loss by the sample was recorded for 30 to 60 min. The data were then curve fitted to ascertain the vaporization rate. A comparison of the experimental and simulation results showed good agreement (Figure 3-49).

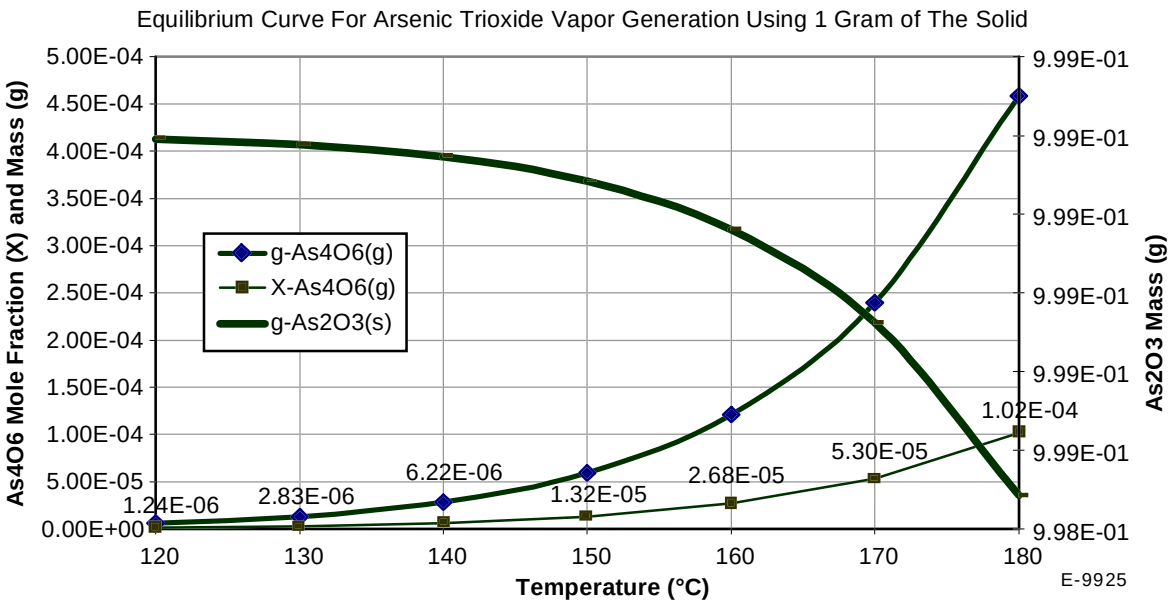

Figure 3-48. Equilibrium data generated by FACT for nitrogen-arsenic trioxide system

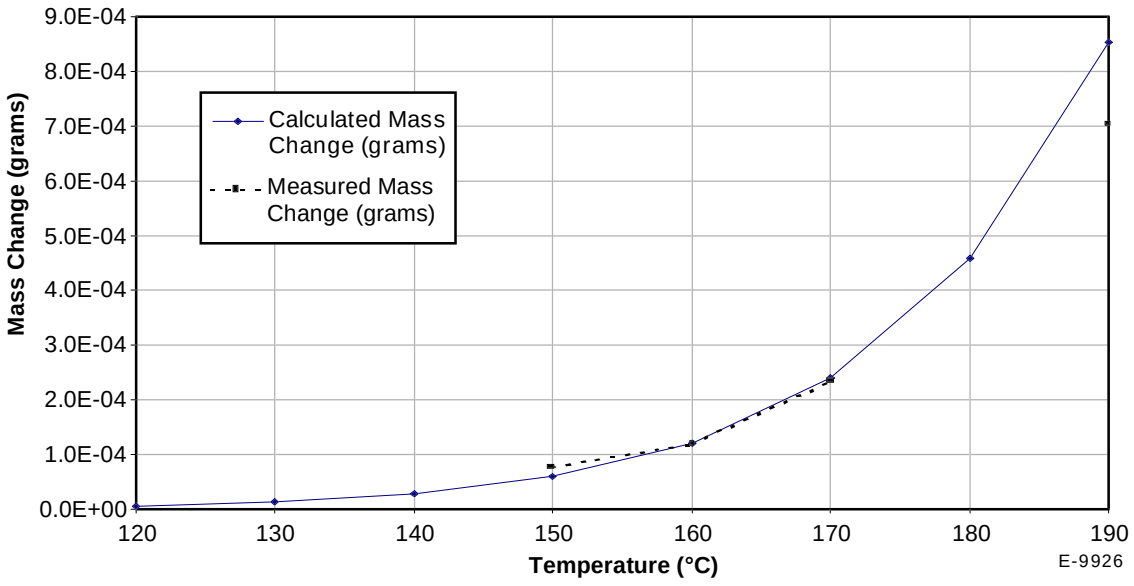

Figure 3-49. A comparison of calculated and measured vaporization for the nitrogen–arsenic trioxide system

3.3.2.6 Arsenic Experiments

Summary of Experimental Procedure

Experiments were conducted using the sequence of actions listed below:

1. Add arsenic source to ceramic boat under a fume hood and insert boat into quartz tube housed by the Lindberg Furnace. Seal both ends of tube.

2. Seal experimental setup and introduce carrier gas to check for leaks. If leaks are present at the joints, replace O-rings.

3. Calibrate the micro-balance using the following procedure:

    a) Place a 100 mg calibrated weight on the sample pan.

    b) Use the two-point calibration option available in the instrunet software to calibrate the mass output range for 0 to 100 mg reading full scale at 100 mg.

    c) Electrically suppress 90 mg and reset the recorder(instrunet) range to read 10 mg.

    d) Adjust the recorder calibration on microbalance until instrunet readout reads full scale.

    e) Electrically suppress 9 mg on the above scale and reset the recorder range to 1 mg.

    f) Adjust the recorder calibration on the balance so the instrunet output reads full scale.

    g) Remove the 100 mg calibrated weight and reset the recorder range to the desired range.

    h) Using calibrated weights of 10, 50 and 100 mg record the microbalance output readings for the respective weight on the sample pan.

4. Mount sample pan with fix masses of sorbent dispersed in 1 to 3 mg of quartz wool on micro- balance and seals all glassware junctions.

5. Using the recorder zero suppression, electrically suppress the sample weight until the output weight signal reads zero.

6. Record this recorder zero suppression reading as the weight of the sample.

7. Open carrier gases supply line to the Lindberg furnace and set flow meter to the target value. Check for leaks.

8. With the system leak free, start heating vapor transfer line with heating tapes.

9. Using data acquisition software monitor inline gas temperature.

10. At an inline gas temperature of 200°C, set Cahn furnace temperature to target value and place controller in AUTO control.

11. At targeted reaction temperature, set Lindberg furnace to target vaporization temperature and start vaporization.

12. Use data logger to record sample mass change and system temperatures for 1 hour.

13. At the end of one hour the reaction temperature is immediately reduced and the reactor is cooled by forced airflow from a fan.

14. The vapor generation reactor is simultaneously shutdown.

Preliminary Experiments

Twelve preliminary experiments were performed using two sorbents. Six experiments were done using calcium oxide as the reacting solid and six were carried out using calcium silicate.

For the calcium silicate experiments, the mass of reacting solid ranged from 15 to 20 mg with the reactor temperatures set to 400 to 1000^{o}C at intervals of 200^{o}C. To examine the temperature dependence of this reaction, four experiments were conducted with arsenic vapor concentrations of 13 ppm. Two experiments were conducted at a reactor temperature of 1000^{o}C with arsenic concentrations of 13 and 26 ppm to determine the effect of arsenic vapor phase concentration on the reaction rate. For experiments conducted at varying temperatures, the results showed an increase in reaction rate for increases in temperature over the range of 400 to 1000^{o}C. This was in agreement with the established trends (Figure 3-50). The results of the two experiments conducted at varying arsenic vapor concentrations clearly showed that increasing the vapor concentration increases the amount reacted (Figure 3-51).

Similarly, calcium oxide experiments were conducted with the mass of reacting solid ranging from 15 to 20 mg. However, the reactor temperatures used were 800 and 1000^{o}C respectively. To examine experimental reproducibility, five experiments were carried out at arsenic vapor concentration of 26 ppm at a reaction temperature of 1000^{o}C. One experiment was carried at a reactor temperature of 800^{o}C with arsenic concentration of 13 ppm.

From the results shown in Figure 3-52, reproducibility was not achieved indicating that the operating conditions were not the same for each run. This problem will be addressed in the next set of experiments.

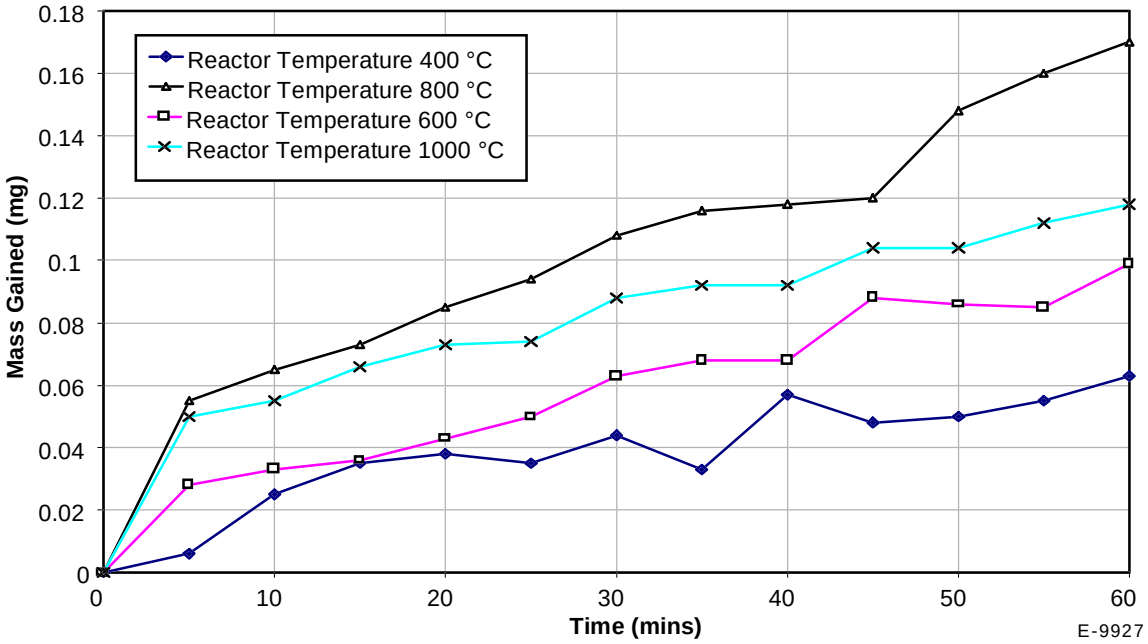

Figure 3-50. Results of preliminary calcium silicate experiments arsenic trioxide concentration of 13 ppm.

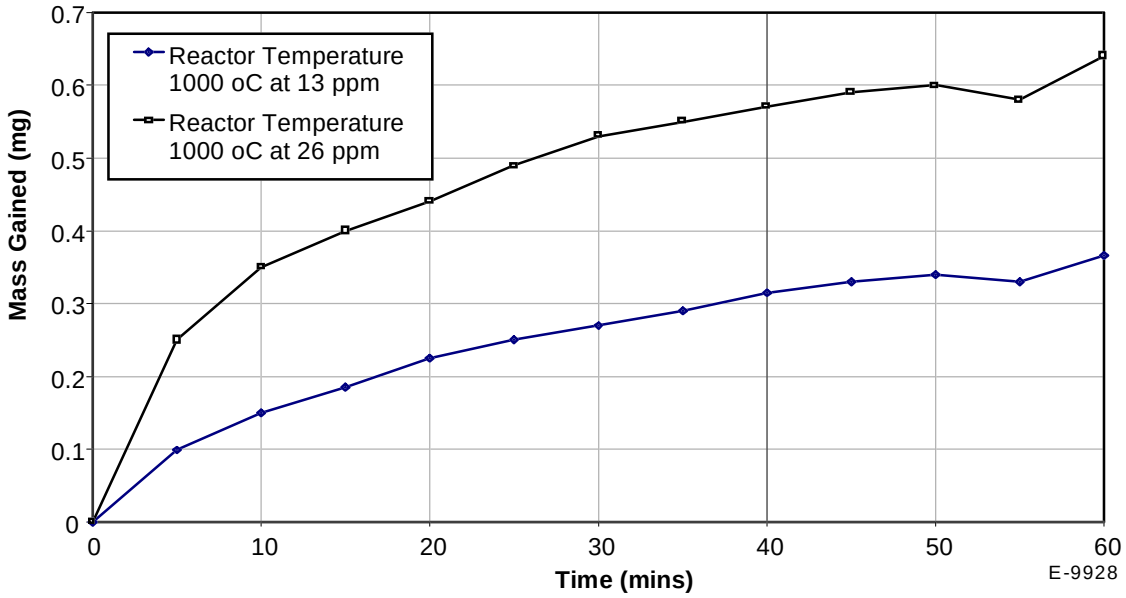

Figure 3-51. Results of varying arsenic trioxide concentrations with calcium silicate.

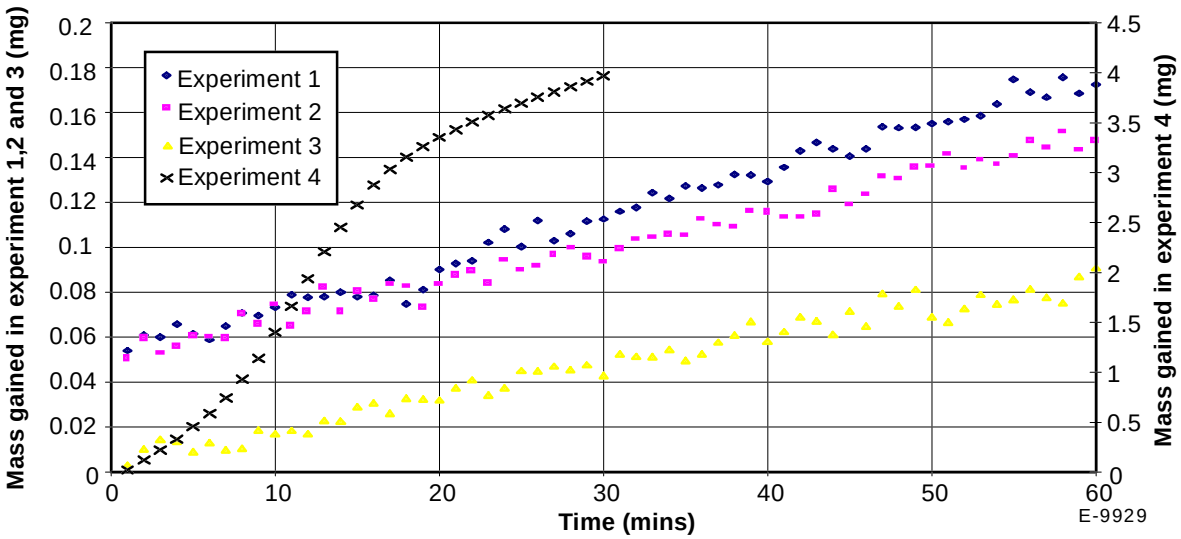

Figure 3-52. Results of the duplicate experiments with calcium oxide as the reacting solid at 26 ppm.

For a preliminary insight into the possible effects of different adsorbents on the reaction rate, the experiments conducted at arsenic vapor concentration of 13 ppm and reactor temperature 1000°C for calcium oxide and calcium silicate were compared. The trends are shown in Figure 3-53. From the data presented it appears that calcium silicate reacts with arsenic vapor at a faster rate. This appearance might be indicative of the availability of calcium within each solid matrix for reaction.

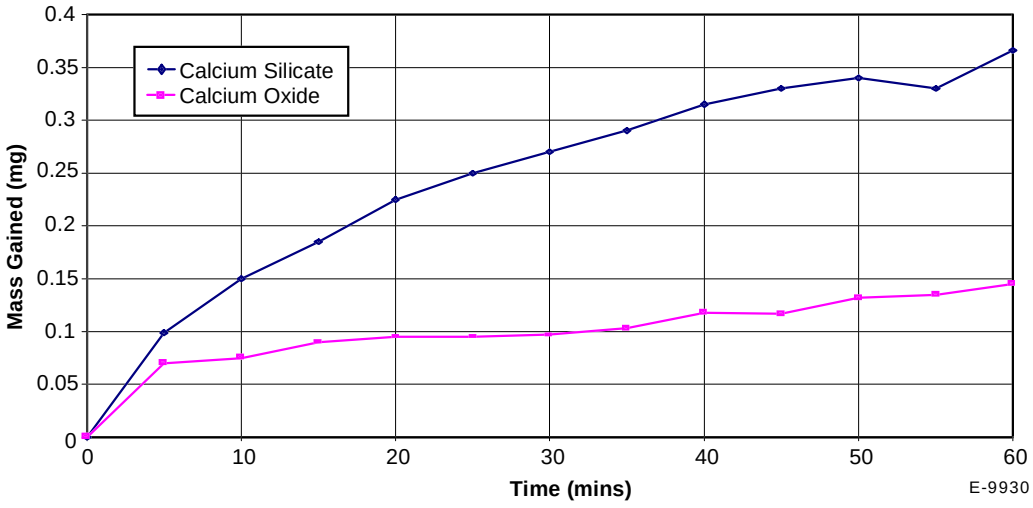

Figure 3-53. A comparison of calcium oxide and calcium silicate results at 26 ppm arsenic trioxide vapor.

Preliminary Kinetic Rate Experiments with Calcium Oxide

Five experiments were conducted in sequence using calcium oxide as the adsorbent with arsenic vapor concentration of 13 ppm and reaction temperature of 600°C for 1 hour. This procedure was repeated at reactor temperatures of 800°C and 1000°C respectively. In the above experiments, all leaks were minimized by constantly inspecting the O-ring joints for deterioration and replacing them where necessary. Arsenic sinks (cold spots) were minimized by wrapping these areas with insulation and heating tapes. Prior to the start of each experiment the microbalance was recalibrated using a two point calibration. This entailed zeroing the balance and calibrating its output for a known weight of 100 mg. As a part of this exercise all other microbalance ranges were also calibrated.

All real time data collected were extracted to a spreadsheet and curve fitted to determine a mass based reaction rate. From the observed trends it was noted the that for the first 10 min of each reaction the mass rates were higher that those for the latter 50 min of reaction time. In all cases the reaction temperature was constant throughout the experiment and the inline gas temperatures were maintained above 200°C.

A summary table and a plot of the final results normalized using the mass reacting absorbent is shown in Figure 3-54.

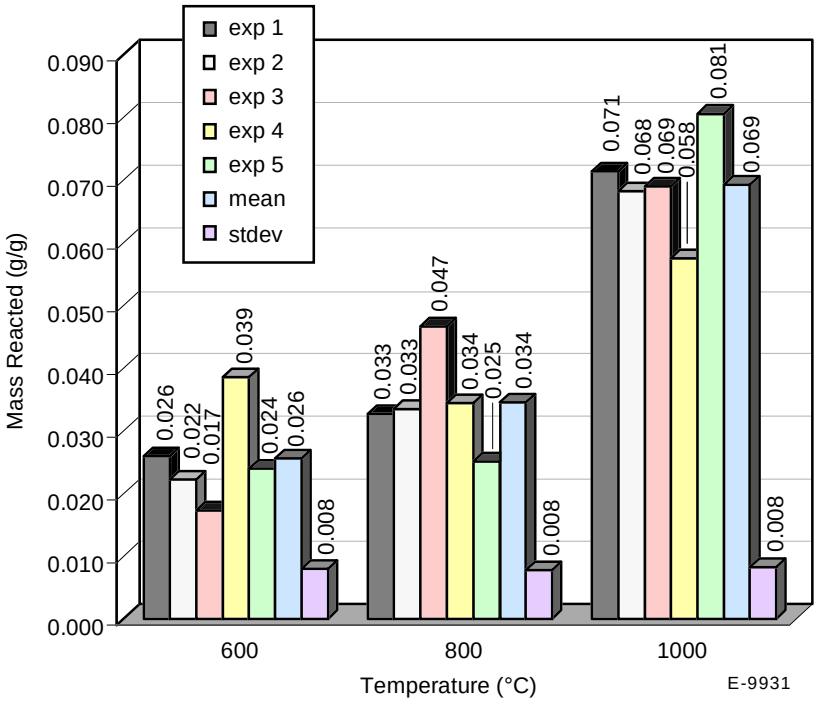

Figure 3-54. Results from duplicate experiments for calcium oxide with arsenic trioxide concentration of 13 ppm.

3.3.2.7 Development of Rate Equation

For any gas-solid reaction the overall rate of reaction per unit surface area is influenced by diffusion, both internal and external, and by surface reaction. Under certain operating conditions, however, the effect of either diffusion or surface reaction can be neglected. The general expression accounting for both effects is as follows:

$$-r_a'' = \frac{\eta * C_a^n * k_1 * k_c * S_o^m}{k_c * S_o^m + \eta * \rho_b * k_1 * S_a^m}$$

where η = internal effectiveness factor
k_1 = specific reaction rate
k_c = mass transfer coefficient
S_o = external surface area
S_a = internal surface area
ρ_b = bulk density of solids
C_a = concentration of gas reactant
n = reaction order
m = surface area order

From prior knowledge, the internal surface area of the commercial calcium oxide is zero because of its non-porous nature. The above equation therefore reduces to:

$$-r_a'' = \eta * k_1 * C_a^n$$

To simplify the above equation further correlations of internal effectiveness factor for the gas-solid reaction were needed. From these relationships, the effectiveness factor is dependent on the Thiele modulus that is a ratio of surface reaction rate to diffusion rate for various solid geometrical shapes.

The Thiele modulus is proportional to internal surface area therefore for solids with negligible internal surface area the thiele modulus is approximately zero. From Figure 3-55, the corresponding effectiveness factor is one for reaction orders and geometry stated. Therefore the rate expression becomes

$$-r_a'' = k_1 * C_a^n$$

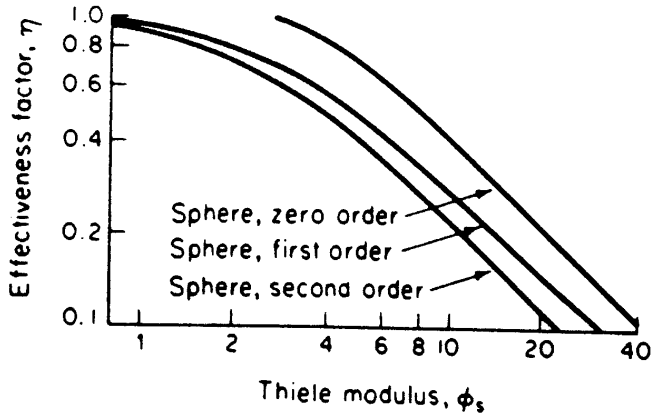

Zero order $\phi_{s0} = R\sqrt{k_0 S_a \rho_p / D_e C_{A0}}$

First order $\phi_{s1} = R\sqrt{k_1 S_a \rho_p / D_e}$

Second order $\phi_{s2} = R\sqrt{k_2 S_a \rho_p C_{A0} / D_e}$

(a)

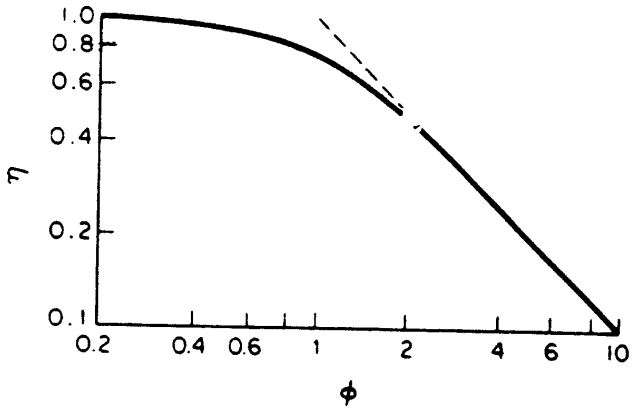

Sphere $\phi = (R/3)\sqrt{k_1 S_a \rho_p / D_e}$

Cylinder $\phi = (R/2)\sqrt{k_1 S_a \rho_p / D_e}$

Slab $\phi = L\sqrt{k_1 S_a \rho_p / D_e}$

(b)

E-9932

Figure 3-55. (a) Effectiveness factor plots for nth order kinetics for spherical solids; (b) First-order reaction on different solid geometries.

3.3.2.8 Discussion on Preliminary Kinetic Rate Result

The standard deviation of +- 0.008 gram per gram of each set of experiments is indicative of similar operating conditions for all sets. In keeping with the established knowledge the normalized mass reacted increased with increases in temperature. To obtain the Arrhenius equation for the Ca-As surface reaction, the result from these experiments and the rate equation below were used to determine activation energy and frequency factor.

$$-r_{As} = k*S_o^m*C_{Aso}^n$$

where $-r_{As}$ = rate of moles of arsenic reacted with calcium oxide (mol/sec)
k = specific surface reaction rate(m/sec)
S_o^m = surface area of calcium oxide (m^2/g)
C_{Aso}^n = initial concentration of arsenic vapor (mol/m^3).

Mahuli et al. [123] showed that both n and m were approximately one. The surface reaction can therefore be assumed to be first order with respect to surface area and initial arsenic concentration. The B.E.T surface area of calcium oxide was measured (nitrogen adsorption, single point analysis) and determined to be 3.86 m^2/g. From the ideal gas equation the initial arsenic concentration was calculated to be 0.00335 g/m^3. From the real time data of mass reacted versus time, the rate of reaction was observed to occur faster in the first 10 min and then slower in the latter 50 min of each experiment as discussed above. Based on these observations, the specific reaction rate was calculated to provide bounds for the expected values. From the curve fitting exercise used for the real time data, the rates of reaction for these two regions at the respective reactor temperatures were obtained and are shown in Table 3-34.

Table 3-34. Molar Rates of Arsenic Deposition for Calcium Oxide Experiment

Reactor Temperature(°C)	Region One (mol/sec)	Region Two (mol/sec)
600	8.08e-10	4.54e-10
800	1.92e-09	7.49e-10
1000	2.37e-09	1.40e-09

Using these data and the rate equation, specific reaction rates were obtained for the Ca-As interaction. To obtain the activation energy, ln(ks) was plotted versus 1/T and the resulting data were curved fit. From the slope and intercept, the frequency factors and activation energies for the two regions were obtained. Table 3-35 shows the results of the above exercise.

Table 3-35. Results of Kinetic Rate Calculations

Parameters	Region One	Region Two
Frequency factor(mol/sec)	9.86e-05	5.256e-05
Activation energy(J/mol)	34126.47	34627.81
R-squared	0.9747	0.9824

Mahuli et al. [123] showed that for the Ca-As interaction at a vapor concentration of 65 ppm, a reactor temperature of 600^{o}C and the same reaction time, the frequency factor was 0.00056 moles per seconds. The activation energy for a comparable temperature range was 43,540 J/mol.

3.3.2.9 Results of Experiments with Calcium Oxide and Calcium Silicates under Inert Conditions

Using the procedure developed from the previous set of experiments, calcium oxide, dicalcium silicate and mono-calcium silicate were all used as sorbents. It must be noted that the ratio of calcium oxide to silica varies for each sorbent. Each set of experiments was performed in triplicate with the absorbent dispersed on 1 to 3 mg of quartz wool.

Summary tables and plots for each set of experiments are shown below in Figures 3-56 to 3-60.

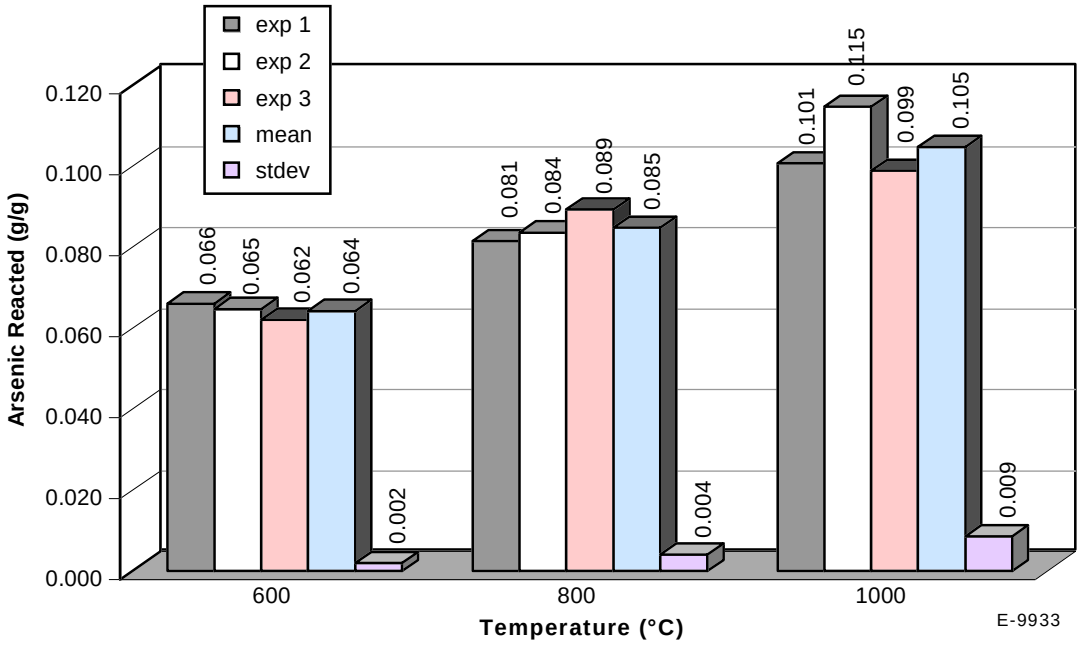

Figure 3-56. Results from triplicate experiments for calcium oxide with arsenic oxide equal to 26 ppm.

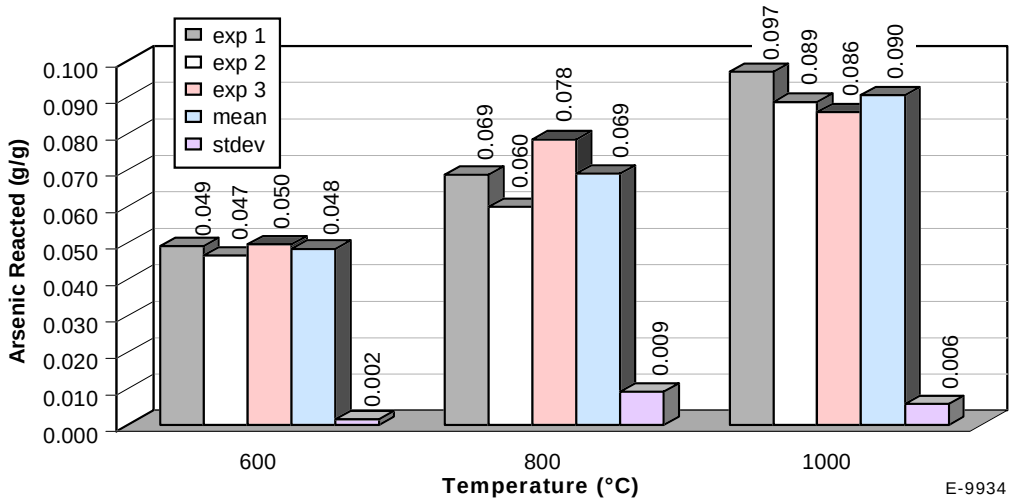

Figure 3-57. Results from triplicate experiments for dicalcium silicate at 26 ppm As_2O_3 vapor.

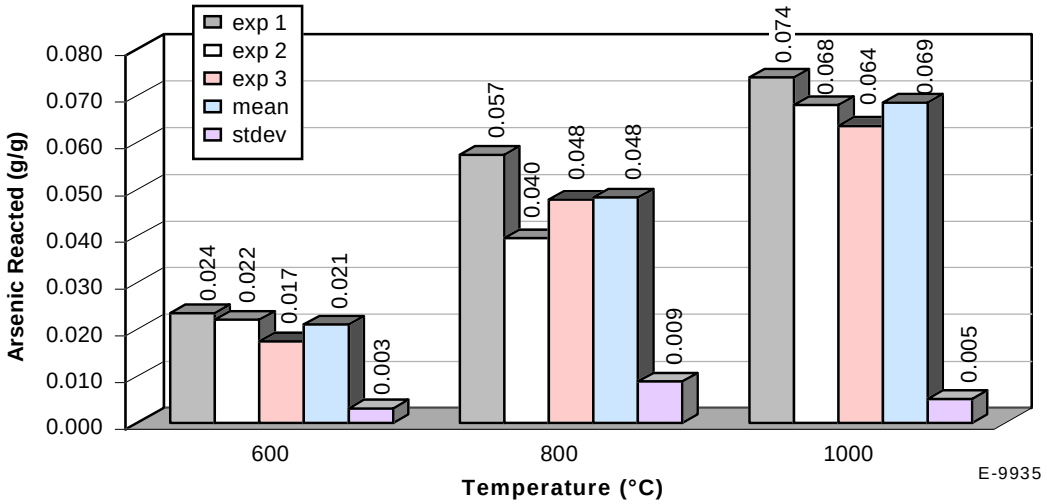

Figure 3-58. Results of triplicate experiments for calcium mono-silicate with 26 ppm As_2O_3 vapor.

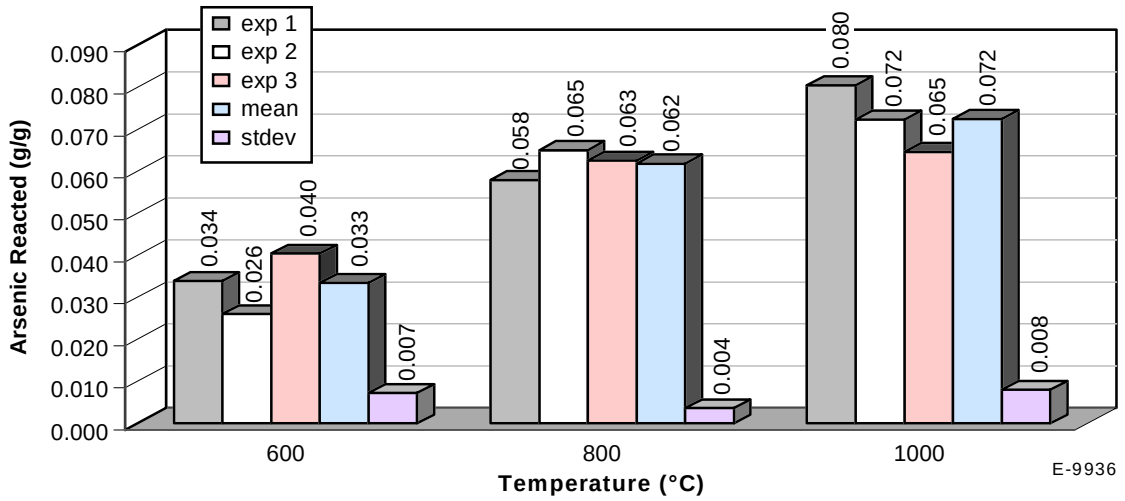

Figure 3-59. Results of triplicate experiments for calcium oxide at 13 ppm As_2O_3 vapor.

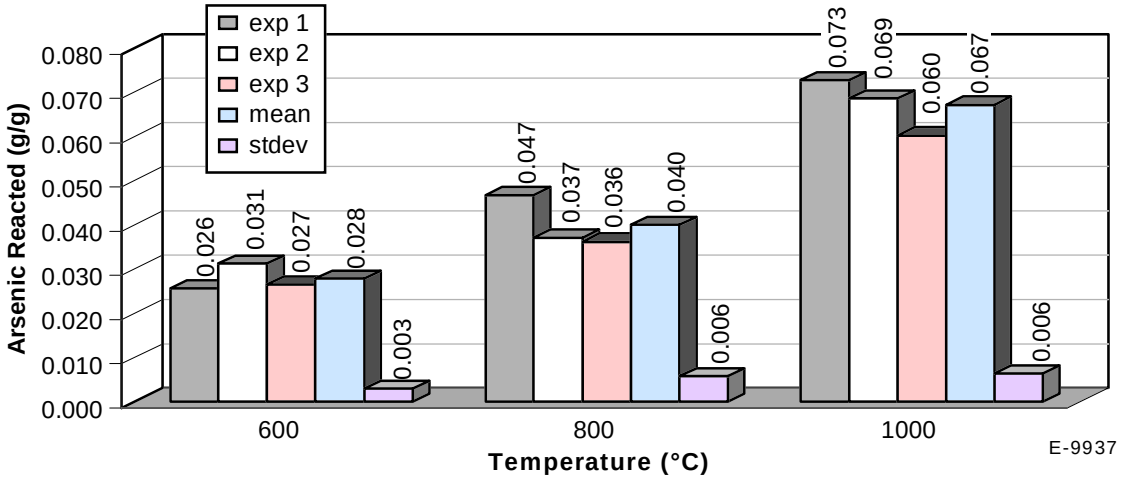

Figure 3-60. Results of triplicate experiments for dicalcium oxide at 13 ppm As_2O_3 vapor.

3.3.2.10 Reaction Rate Determination for Reaction in an Inert Environment

Curve fitting the data from the above experiments gives the rate of reaction for each absorbent at the respective reactor temperatures. Tables 3-36 and 3-37 show the results obtained.

Table 3-36. Molar Rates of Arsenic Oxide Reaction for Reactants at 26 ppm Vapor Concentration

Reactor Temperature (^{o}C)	Calcium Oxide	Dicalcium Silicate	Mono-calcium Silicate
600	1.38e-9	1.00e-9	5.47e-10
800	1.84e-9	1.49e-9	1.28e-09
1000	2.18e-9	1.89e-9	1.58e-09

Table 3-37. Molar Rates of Arsenic Oxide Reaction for Reactants at 13 ppm Vapor Concentration

Reactor Temperature (^{o}C)	Calcium Oxide	Dicalcium Silicate
600	6.47e-10	6.14e-10
800	1.30e-09	8.70e-10
1000	1.62e-09	1.47e-10

Using the above data and the rate equation developed, the specific reaction rates were extracted for the gas-solid reactions involving each ash compound. The activation energy and frequency factors were determined in similar manner as in the preliminary experiments. Tables 3-38 and 3-39 show the results of this exercise.

Table 3-38. Results of Kinetic Rate Calculations at 26 ppm

Absorbent	Frequency Factor (m/s)	Activation Energy (kJ/mol)
Calcium oxide	8.8e-04	19.3
Di-calcium silicate	4.9e-03	23.4
Mono-calcium silicate	1.0e-02	33.8

Table 3-39. Results of Kinetic Rate Calculations at 13 ppm

Absorbent	Frequency Factor (m/s)	Activation Energy (kJ/mol)
Calcium oxide	2.8e-03	26.9
Di-calcium silicate	1.1e-02	28.3

Comparing the specific reaction rate results of experiments done in a nitrogen atmosphere at 13 and 26 ppm for calcium oxide and di-calcium silicate (Tables 3-38 and 3-39) showed variation in the activation energy for the calcium oxide. This can be attributed to the fluctuations in vapor concentration at 13 ppm. From the vaporization curve shown previously (Figure 3-49),

it is clear that a concentration of 13 ppm could not be achieved consistently due to limitation within the experimental set-up. The slight differences in activation energy and pre-exponential factor therefore seem reasonable and do not lead to appreciable differences in the rate constant over the temperature range 600 to 1000°C.

3.3.2.11 Results Of Experiments with Calcium Oxide and Calcium Silicates Under Oxidizing Conditions

Using the procedure developed from the previous set of experiments, calcium oxide, di-calcium silicate and mono-calcium silicate were used as solid reactants in oxygen-containing atmospheres. It must be noted that the ratio of calcium oxide to silica varies for each solid reactant. Each set of experiments was performed in triplicate with the absorbent dispersed on 1 to 3 mg of quartz wool.

Summary tables and plots for each set of experiments are shown below in Figures 3-61 through 3-63.

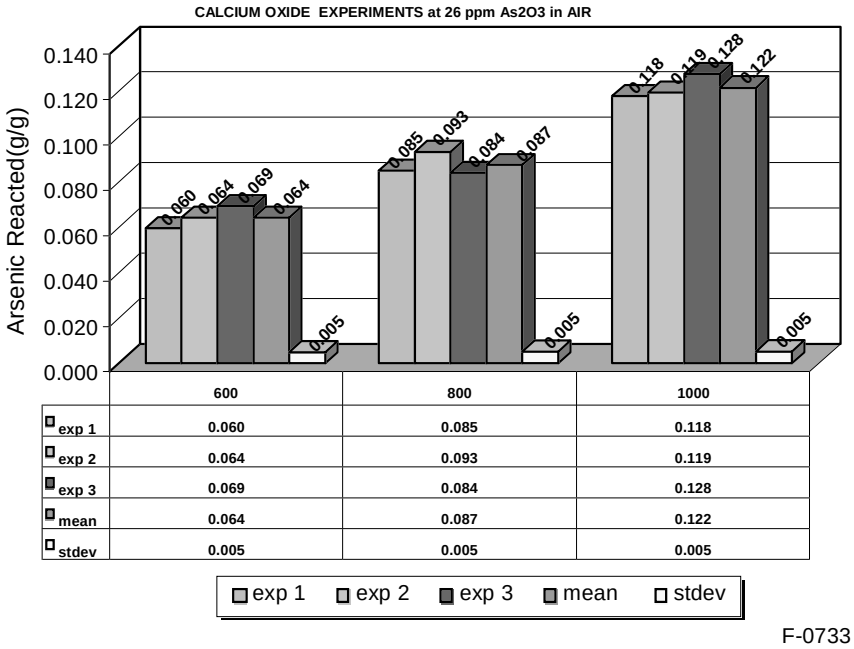

Figure 3-61. Results from triplicate experiments for calcium oxide with 26 ppm arsenic oxide in air.

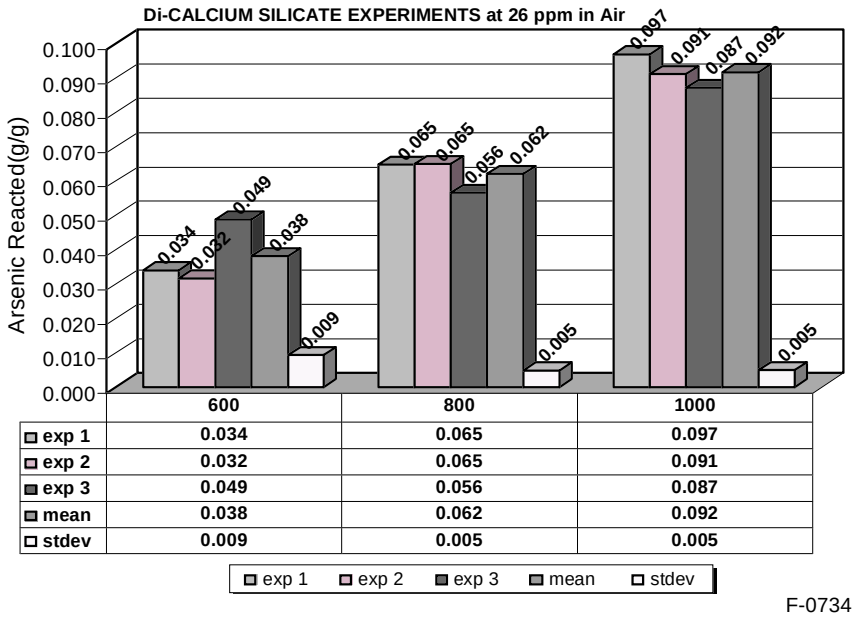

Figure 3-62. Results from triplicate experiments for di-calcium silicate at 26 ppm As_2O_3 vapor in air

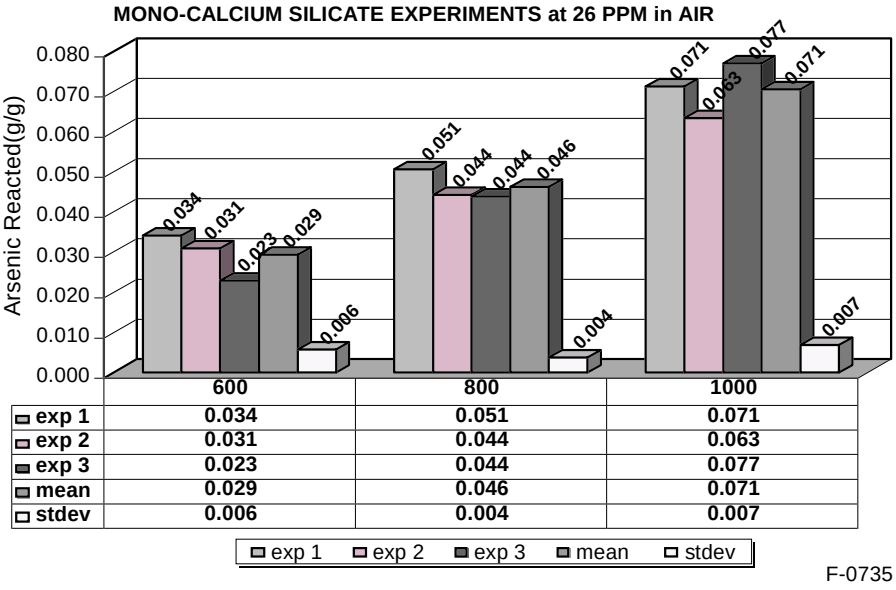

Figure 3-63. Results of triplicate experiments for calcium mono-silicate with 26 ppm As_2O_3 vapor in air

3.3.2.12 Reaction Rate Determination for Reaction in an Oxidizing Environment

Curve fitting the real time data from the above experiments gives the rate of reaction for each reactant at the respective reactor temperatures. Results are shown in Table 3-40. Table 3-41 shows the kinetic parameters associated with these experiments.

Table 3-40. Molar Rates of Arsenic Oxide Reaction for Reactants at 26 ppm Arsenic Oxide Vapor Concentration

Reactor Temperature (^oC)	Calcium Oxide	Di-calcium Silicate	Mono-calcium Silicate
600	1.37e-9	8.05e-10	5.81e-10
800	1.83e-9	1.21e-09	9.76e-10
1000	2.56e-9	1.89e-09	1.49e-09

Table 3-41. Results of Kinetic Rate Calculations at 26 ppm

Absorbent	Frequency Factor (m/s)	Activation Energy (KJ/mol)
Calcium oxide	1.4e-03	22.9
Di-calcium silicate	7.2e-03	28.1
Mono-calcium silicate	5.5e-03	30.0

It must be noted that Jadhav et al. [124] showed that for the Ca-As reaction using calcium oxide as solid reactant, under oxidizing conditions and over a temperature range of 300 to 500^oC the activation energy was 21.3 kJ/mol for a vapor concentration of 14 ppm.

3.3.2.13 Sample Characterization

Sample Arsenic Mass Determination

Quantification of samples was done using ICP-OES (optical emission spectroscopy). technique. Table 3-42 shows a comparison of experimental versus ICP-OES results.

Table 3-42. Comparison of Experimental and Analytical Arsenic Absorbed

SAMPLE	SAMPLE NAME AND TEMPERATURE	SAMPLE LAB CODE	Galbraith Result	Calculated Concentation
1	Calcium Oxide at 600 C 13 ppm	COP13	0.0259	0.0223
2	" " " 800 C "	COP6	0.0282	0.0320
3	" " " 1000 C "	COP8	0.0364	0.0377
4	Calcium Silicate at 600 C 13 ppm	CSP8	0.0125	0.0146
5	" " " 800 C "	CSP10	0.0204	0.0199
6	" " " 1000 C "	CSP11	0.0488	0.0448
7	Calcium Oxide at 600 C 26 ppm	2COP8	0.0505	0.0423
8	" " " 800 C "	2COP5	0.0422	0.0461
9	" " " 1000 C "	2COP2	0.074	0.0749
10	Calcium Silicate at 600 C 26 ppm	2CSP8	0.017	0.0269
11	" " " 800 C "	2CSP6	0.0325	0.0390
12	" " " 1000 C "	2CSP4	0.048	0.0569

3.3.2.14 Conclusions

To determine the accuracy and consistency of our TGA measurements, selected samples were analyzed by ICP-OES. A comparison of the TGA results versus ICP-OES measurements is shown in Table 3-42. Evaluating the results sample-by-sample showed no significant biases at the given temperatures for the solid reactants used. In all cases differences are less than 1% indicating that the TGA experiments were accurate measurements of the rate of gas-solid reaction occurring.

From the results of the kinetic calculations shown in Tables 3-38, 3-39 and 3-41 it can inferred that the ratio of Ca/SiO2 influences the extent of interaction between Ca in the solid matrix and arsenic oxide vapor. The data clearly show that calcium oxide is the most effective solid reactant used while mono-calcium silicate was least effective at 26 ppm arsenic oxide vapor. From the real time data the rate of reaction decreases as the ratio of calcium to silica in the solid reactant decreases.

For each solid reactant the experiment performed in air and nitrogen respectively showed minimal differences in the reactivity on mass of solid reacted basis. From Figures 3-57 and 3-61, respectively, reactions with calcium oxide as the solid reactant showed an average difference of less than a percent with the greatest difference of 1.7% occurring at 1000^{o}C. Therefore, it can be deduce that the oxygen present in the predominantly inert atmosphere is sufficient to facilitate reaction. In addition the specific reaction rates under both experimental conditions showed minimal differences.

Similarly for di-calcium silicate, Figures 3-58 and 3-62 showed that the average difference in the reactivity of the solid reactant in both experimental environment was less than a percent. However the largest deviation of one percent occurred at a reactor temperature of 600^{o}C. A similar analysis of the results shown in Figures 3-59 and 3-63 for mono-calcium silicate indicated that trends are same as aforementioned solid reactants.

Comparing the specific reaction rate results of experiments done in a nitrogen atmosphere at 13 and 26 ppm for calcium oxide and di-calcium silicate (Tables 3-38 and 3-39) showed variation in the activation energy for the calcium oxide. This can be attributed to the fluctuations in vapor concentration at 13 ppm. From the vaporization curve shown previously (Figure 3-49), it is clear that a concentration of 13 ppm could not be achieved consistently due to limitation within the experimental set-up. The slight differences in activation energy and pre-exponential factor therefore seem reasonable and do not lead to appreciable differences in the rate constant over the temperature range 600 to 1000^{o}C.

The results from the XRD analyses of the products formed are shown in Figures 3-64 through 3-70. The XRD pictographs for products formed at reactor temperatures 800^{o}C and 1000^{o}C are consistent with the XRD standard pictograph for the monoclinic crystal structure of calcium arsenate (Figure 3-71). However the products formed at a reactor temperature of 600^{o}C are that of the rhombohedral crystal structure of calcium arsenate.

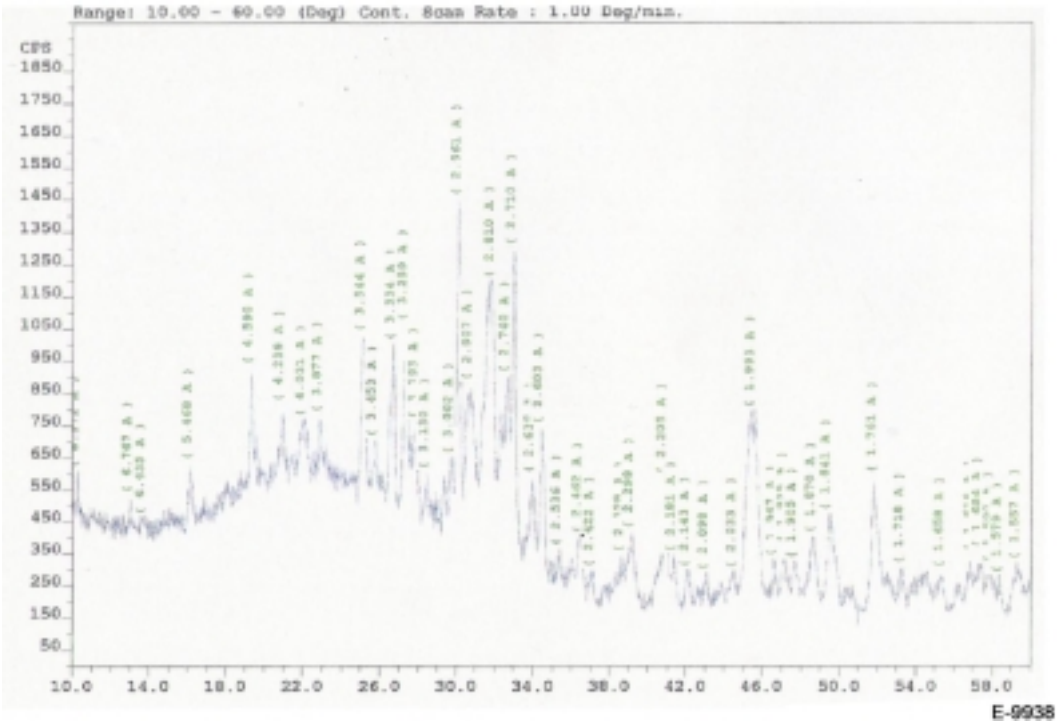

Figure 3-64. XRD pattern of product formed from reacting dicalcium silicate 26 ppm As_2O_3 vapor.

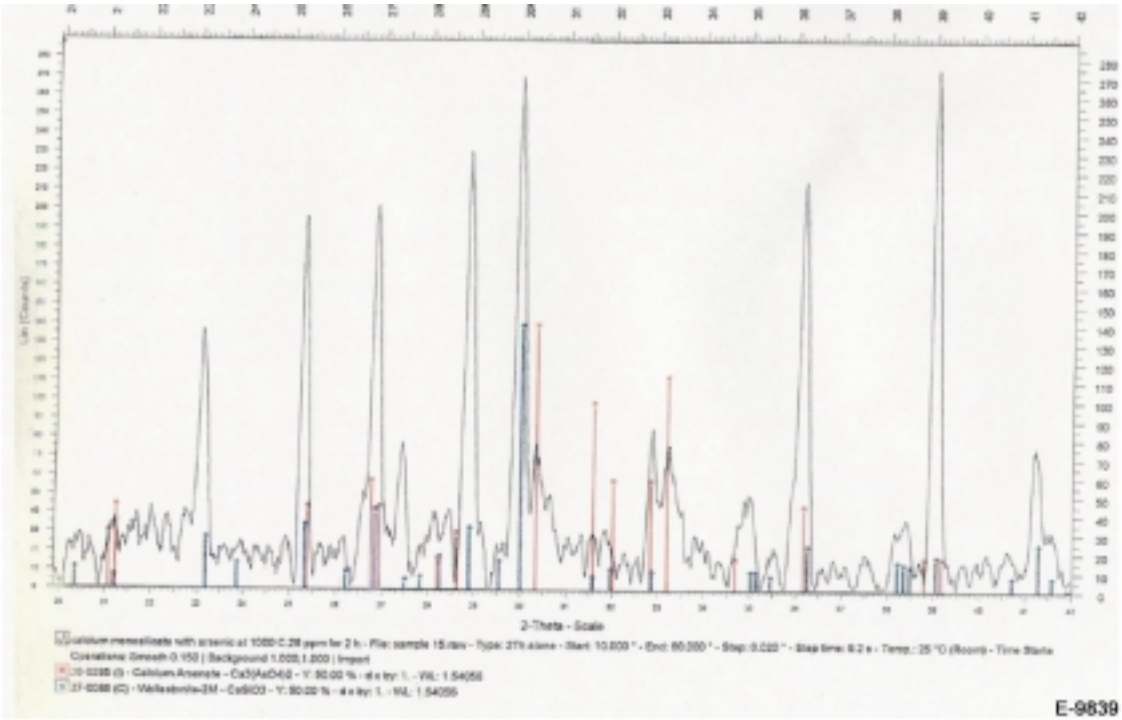

Figure 3-65. XRD pattern of product formed from reacting mono-calcium silicate 26 ppm As_2O_3 vapor.

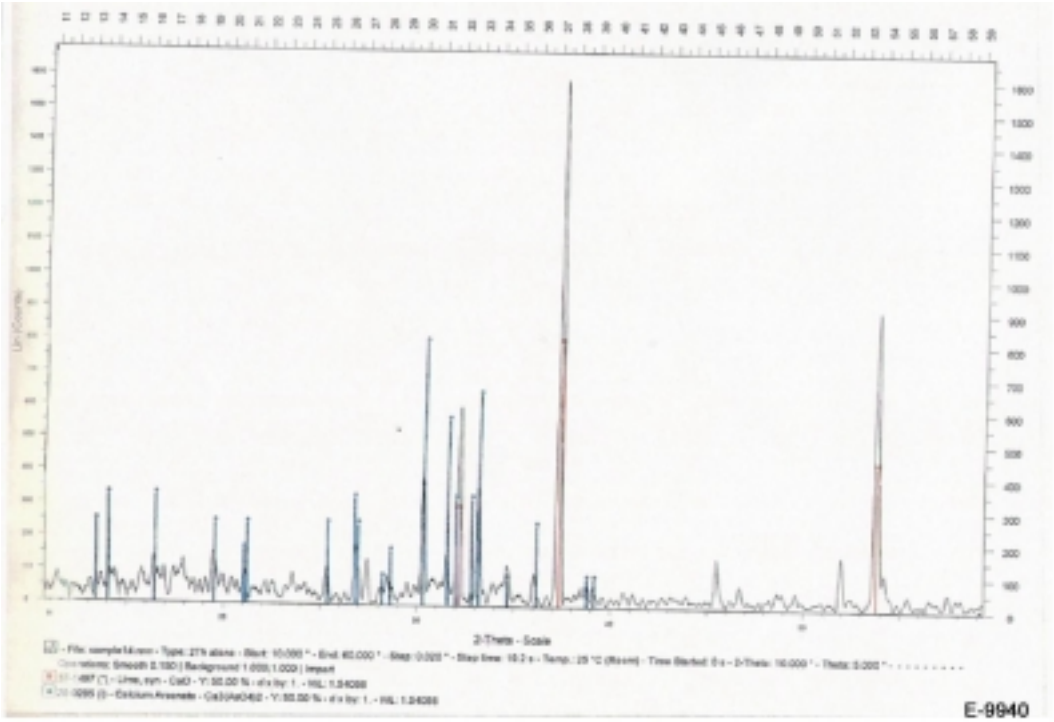

Figure 3-66. XRD pattern of product formed from reacting calcium silicate 26 ppm As_2O_3 vapor.

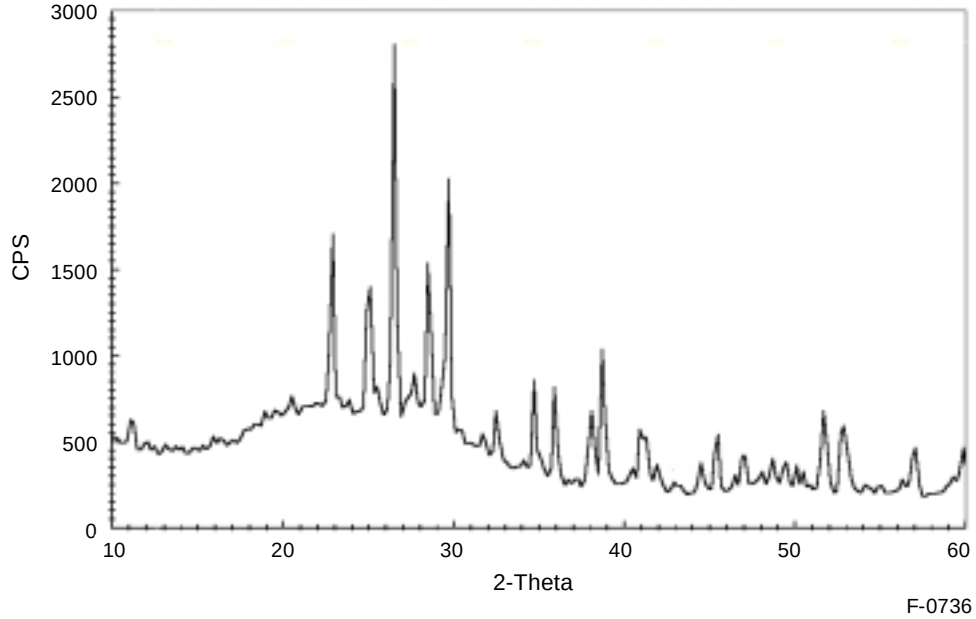

Figure 3-67. XRD pictograph of product formed from reacting mono-calcium silicate with 26 ppm As_2O_3 vapor.

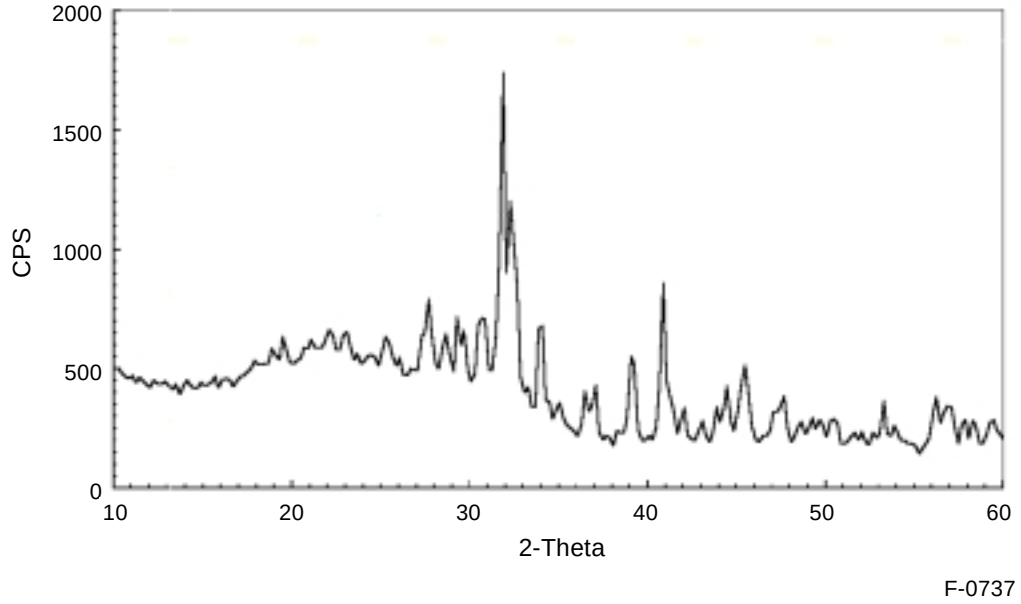

Figure 3-68. XRD pictograph of product formed from reacting di-calcium silicate with 26 ppm As_2O_3 vapor.

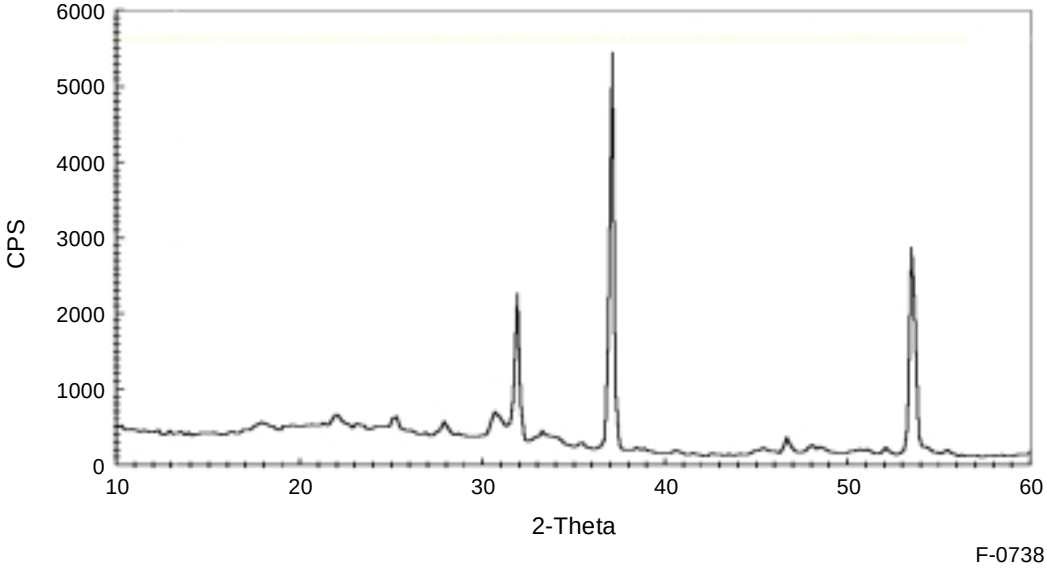

Figure 3-69. XRD pictograph of product formed from reacting calcium oxide with 26 ppm As_2O_3 vapor.

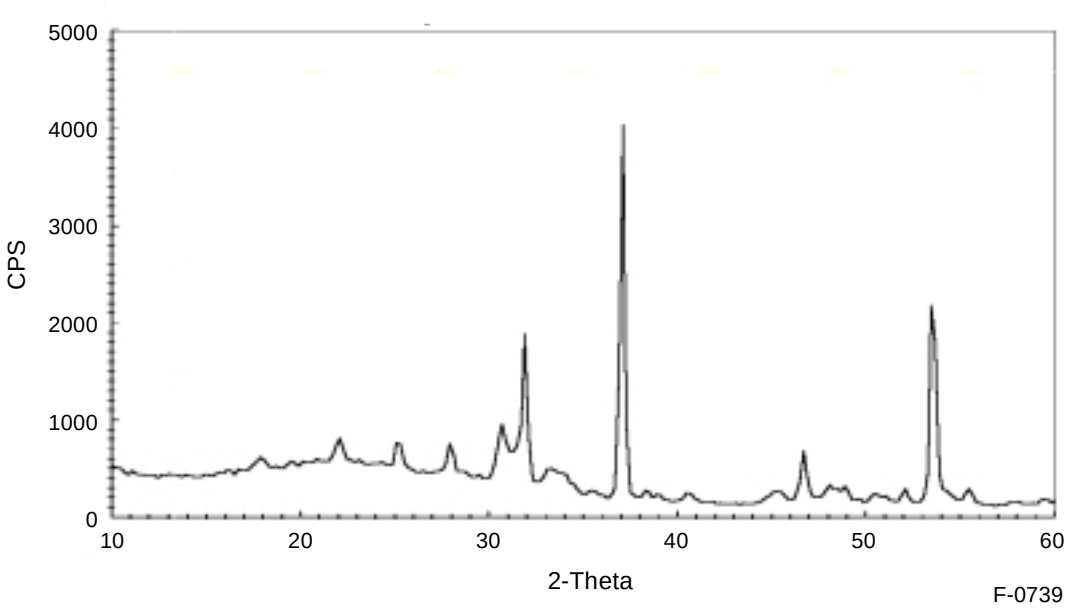

Figure 3-70. XRD pictograph of product formed from reacting calcium oxide with 26 ppm As_2O_3 vapor.

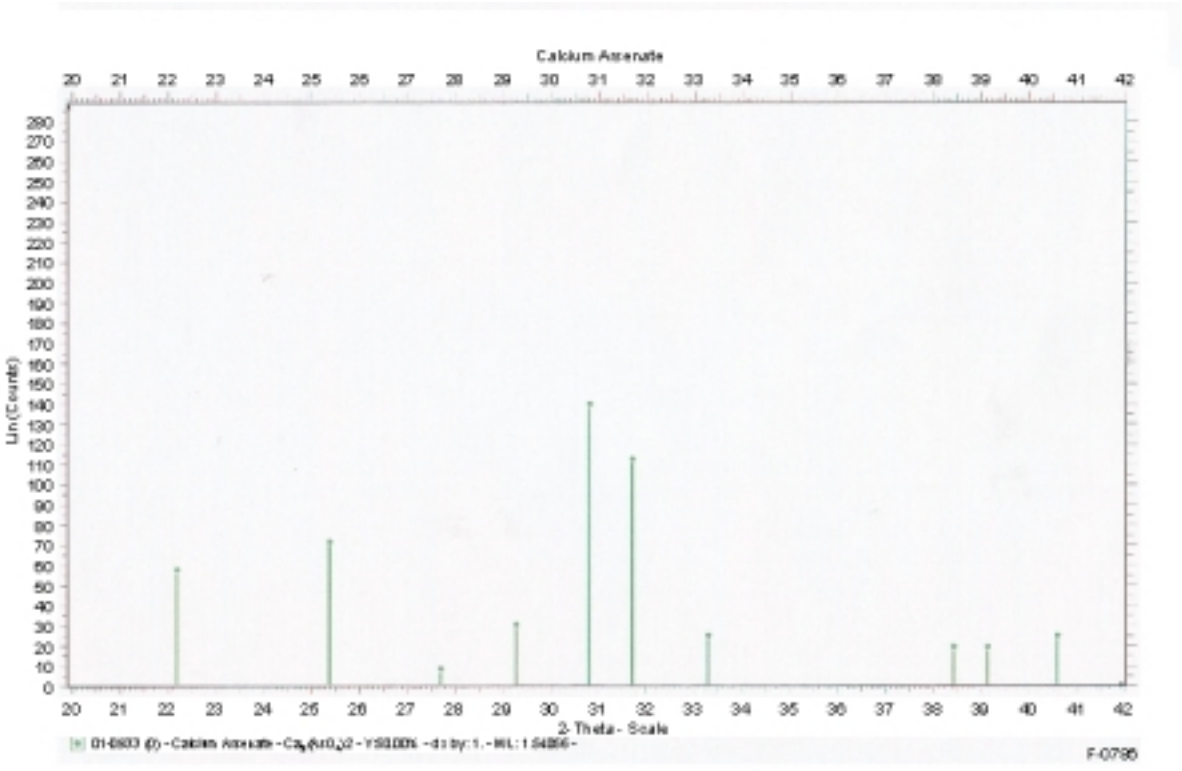

Figure 3-71. XRD pictograph of calcium arsenate reference material.

3.3.2.15 Arsenic Modeling

Introduction

Prior research including that conducted with coal at UA and with synthetic ash particles earlier at UC during this program has indicated that arsenic can interact with calcium containing compounds under post combustion conditions. These interaction produces a compound with a distinct As(V)peaks determined by XAFS spectroscopy at UK and is suggestive of calcium arsenate formation. If the interaction expected occurs via surface reaction and the latter is the dominant enrichment mechanism then arsenic concentrations in the final ash will scale calcium oxide surface concentrations and particle surface area. Because it is difficult to measure accurately the surface concentration of calcium oxide the concentration of arsenic is typically reported as a function of fly ash particle size and the distribution then examined for trends characteristic of surface reaction. If the surface reaction controls the distribution of arsenic in the fly ash particles the arsenic concentration in the ash particles will scale with 1/dp where dp is ash particle diameter assuming spherical particles [125]. If the surface condensation is instead the controlling mechanism then the arsenic concentration will scale with particle diameter as $(1/dp)^n$, where n=1 for the free molecular regime and n=2 for the continuum regime [125, 126].

This limit analysis has proven useful when one mechanism is clearly dominant in determining the partitioning of arsenic and other volatile trace elements contained within coal. For example, data reported in the Quarterly Report #12 suggest that during the combustion of North Dakota lignite coal in the UA facility, Se and Cr concentration scale as $(1/dp)^2$ in the continuum regime, suggesting surface condensation, whereas As concentration scale as (1/dp), suggesting surface reaction. Apart from the Se data, however, there is considerable scatter and the results for the other program coals such as the Ohio blend obtained at the same facility demonstrate no clear trend in concentration as a function of particle size.

When no clear concentration trend is apparent, it may be a result of limited vaporization suggesting that mineral reaction and coalescence processes are dominant. Lack of a clear trend may, however result from competition between surface reaction and condensation even when the majority of a trace metal vaporizes during combustion. To assess this, a dynamic model for condensation and surface reaction was constructed. Mineral reaction was also incorporated by apportioning a portion of the trace metal in the ash particles as function of particle mass and then parametrically examining concentration trends with less than complete metal vaporization. Several different temperature gradients were also considered as these will affect the distribution between condensation and surface reaction. Effort to date have thus focused on examining the effects of parallel and competing mechanism on the concentration of arsenic in the fly ash particles as a function of particles size for conditions of either complete or partial arsenic vaporization.

Model Development

Assuming that the fly ash particle size distribution is fixed and hence condensation does not affect particle size, the arsenic concentration distribution can be determined by incorporating heterogeneous condensation, surface reaction and mineral coalescence (mass apportionment mechanism) as a function of temperature. With known temperature gradient, this also provides concentration as a function of time permitting the assessment of the temporal evolution of the arsenic concentration distribution.

In this model, a particle diameter of 1 μm was set as the boundary between the continuum and free molecular regimes. Note that it is a simple modification to allow this transition point to vary with temperature through the computation of the temperature dependent mean free path. This variation is relative small with Lambda in air varying from approximately 0.6 μm at 2000 K to 0.1 μm at 400 K.

Particle Concentration Equations

For particles in the continuum regime, the concentration distribution can be determined from the flux equations as Described by Neville and Sarofim [126]. Treating the size distribution as discretized and summing over discrete time steps, the concentration in the larger particles is thus given by

$$C(d)=(1-\Theta)*(Co/Ca)* R_{si} + \sum_{0}^{t}\sum_{dp1}^{dp}(W_i/MW_i)*\Theta *Co*(1-f)/\sum\sum F(d,t)n(d) \quad (3\text{-}9)$$

where Θ = fraction of arsenic vaporized during combustion
Co = arsenic concentration in the parent coal
Ca = mass of residual ash per mass of coal
n(d) = number (size) distribution of fly ash particles
f = arsenic concentration(fraction) in the free molecular mode
F(d,t) = flux of arsenic vapor to ash particles
W_i = mass fraction of arsenic on particles I
MW_i = molecular weight of arsenic
t = time
xi = size fraction.

For the free molecular mode the concentration distribution can again be derived from the work of Sarofim and Neville [126], modified to account for the time dependence of the processes as:

$$C(d)= (W_i/MW_i)* \sum_{0}^{t}\sum_{dpo}^{dp1}\Theta *Co*f/ \sum\sum(F(d,t)*n(d)) \quad (3\text{-}10)$$

The determination of the concentration thus requires the establishment of flux equations allowing for both heterogeneous surface condensation and surface reaction as a function of temperature.

Particle Heterogenuous Condensation Flux Equations

The rate of mass transfer to the larger particles was derived from the Fuchs-Sutugen relationship and is given as:

$$F(d,t)=2*\pi*P_i*d*cfs*D_f(P-P_s)/RT \quad (3\text{-}11)$$

where D_f = diffusivity of arsenic in air
P,P_s = vapor pressure of arsenic far from and near the surface of the particles

T = combustion temperature
cfs = Fuchs-Sutugen correction factor.

The diffusivity D_f was estimated from the Chapman Enskog equation for binary diffusion. Mass Transfer to the sub-micron particles was derived from the kinetic theory of gases and is given as:

$$F(d,t)= \psi*\pi*d^2*(P-P_s)/(2\pi MRT)0.5$$

where ψ= the accommodation coefficient.

All the above variables are defined as before.

Particle Surface Reaction Flux Equations

For surface reaction controlled conditions the flux of arsenic vapor to the larger particles(super-micron) is given as

$$F(d,t)= k_r*\pi*d^2*P_s/RT \quad (3\text{-}12)$$

where k_r is the surface reaction rate for the interaction of arsenic vapor with the particles. For this model it is assumed that this rate is determined by the reaction of arsenic oxide vapor with calcium embedded in the particle matrix.

The surface reaction flux for the sub-micron particles is given as

$$F(d,t)= k_{r1}*\pi*d^2*P_s/RT \quad (3\text{-}13)$$

where k_{r1} = $q*D_f/2.6\lambda$
D_f = binary diffusion of the gases
λ = mean free path of the gas
q = the probability of collision of the arsenic vapor with the particle surface.

3.3.2.16 Parametric Modeling Study

For this study data for fly ash particles were obtained from a combustion experiment conducted at UA. A typical combustion temperature profile for a coal fired plant was used to simulate temperature variation with time. Equilibrium calcium suggested that under these conditions arsenic oxides would not be present as condensed phase oxide species at temperatures above 1100 K. For this reason it was assumed that above 1100 K the only method of arsenic enrichment in the particles was through the surface reaction mechanism. At temperatures below 1100 K, however it was assumed that both heterogeneous condensation and surface reaction could occur simultaneously.

To examine the effects of important parameters on the concentration distribution of arsenic, the following case studies were simulated:

Case I: Varying the surface reaction rate on the sub-micron particles using the specific reaction rates for calcium oxide, di-calcium silicate and mono-calcium silicate.

Case II: Allow for 50% reaction by condensation 50% surface reaction in each size bin.

Results

In Figure 3-72 the results demonstrate the predicted effects surface reaction rate and condensation. For the smaller particles there is a d^{-1} concentration dependence. In contrast, the larger particles showed a d^{-2} suggesting heterogeneous condensation dominance. From Figure 3-73 it can be deduced that for the time scale chosen the various reaction used are identical for calcium oxide, di-calcium silicate and mono-calcium silicate.

Figure 3-72. Arsenic concentration distribution as a function of equal magnitude of surface reaction rate and condensation.

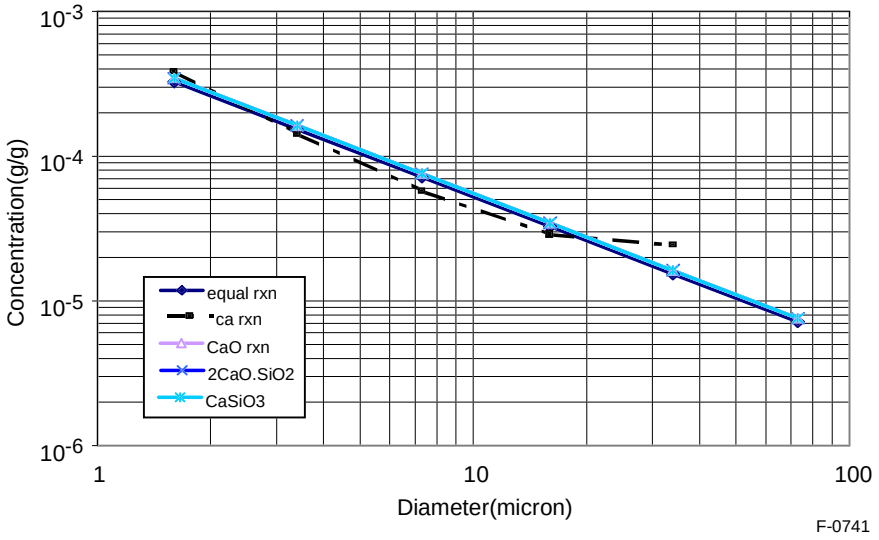

Figure 3-73. Arsenic distribution for various surface reaction rate.

3.3.3 Large Scale Integrated Combustion Studies

Experimental work for this research program was carried out at UA in three phases. The first phase corresponds to Phase I of the DOE contract sponsoring this work and consisted of experiments and subsequent analytical work associated with the baseline screening tests for the Pittsburgh seam coal and the Illinois #6 coal sampled at Ports 4b (combustion zone; initial furnace configuration – see Section 3.3.3.1) and Port 12 (post-combustion zone; initial furnace configuration).

The second phase is a portion of Phase II of the DOE contract, denoted in this work as Phase IIa. This phase consisted of experiments and subsequent analytical work associated with the baseline screening tests for the Ohio 5/6/7 blend, Wyodak PRB subbituminous, North Dakota lignite, and Kentucky Elkhorn/Hazard blend coals sampled at Port 4 (combustion zone; rebuilt furnace configuration – see Section 3.3.3.1), Port 14 (post-combustion zone; rebuilt furnace configuration), and the baghouse inlet port plus baseline screening test for the Pittsburgh seam coal and Illinois #6 coal sampled at the baghouse inlet port. Also included in this phase were the total ash samples collected for use by other members of the DOE contract team.

The third phase, a portion of Phase II of the DOE contract denoted in this work as Phase IIb, consisted of special experiments and analytical work for hypothesis testing.

3.3.3.1 Experimental Equipment and Facilities

This section provides a description of the equipment and facilities utilized during the course of this work. Systems and facilities developed or acquired during the course of this project are described in detail while the description of facilities developed and described by other researchers are summarized.

Many of the experimental systems changed over the course of the 4.5 years required to complete this work. A number of other projects were completed in parallel to this project and most of the work efforts to improve and maintain the combustion equipment were collaborative. While the evolution of equipment and facilities was continuous, there was one major rebuild program associated with the combustion furnace that divided the project from a facilities standpoint into two principle phases. The first phase corresponds to Phase I of the DOE research contract supporting this work. This phase included baseline screening experiments for the Illinois #6 and Pittsburgh seam coals. The second phase corresponds to Phase II scope of work for the DOE contract. This phase included baseline screening experiments for the Ohio, Wyodak, North Dakota, and Kentucky coals (denoted in this work as Phase IIa) and special doping combustion experiments for the Wyodak, Ohio, Kentucky, and Pittsburgh coals (denoted in this work as Phase IIb).

Dimensions given in this section are provided in the units of construction so that future users will have an easier time modifying or repairing the facilities. Metric equivalents (when required) are also provided.

Combustion Facility Overview

A 6 in. (0.152 m) internal diameter by approximately 7 m vertical length downflow combustor was used for all of the combustion experiments performed in this work. A schematic of the combustion system is shown in Figure 3-74. Natural gas was used to heat the furnace above the auto-ignition temperature of coal (typically as close to the steady-state combustion conditions as possible). Coal was premixed with the combustion air and fed to a laminar-flame burner located at the top of the furnace. Combustion gases and solid particles traveled down the furnace following laminar streamlines. An ash trap located at the bottom of the furnace collected fly ash particles whose momentum precluded travel into the horizontal furnace outlet line. The furnace outlet line was used to transport the material from the furnace to a baghouse for removal of the remaining fly ash particulate. The flue gas was then cooled to near atmospheric conditions. Water condensing out of the flue gas was collected in a series of collection pots. Flue gas was educted from the furnace system using a ring compressor and discharged at the roof of the building.

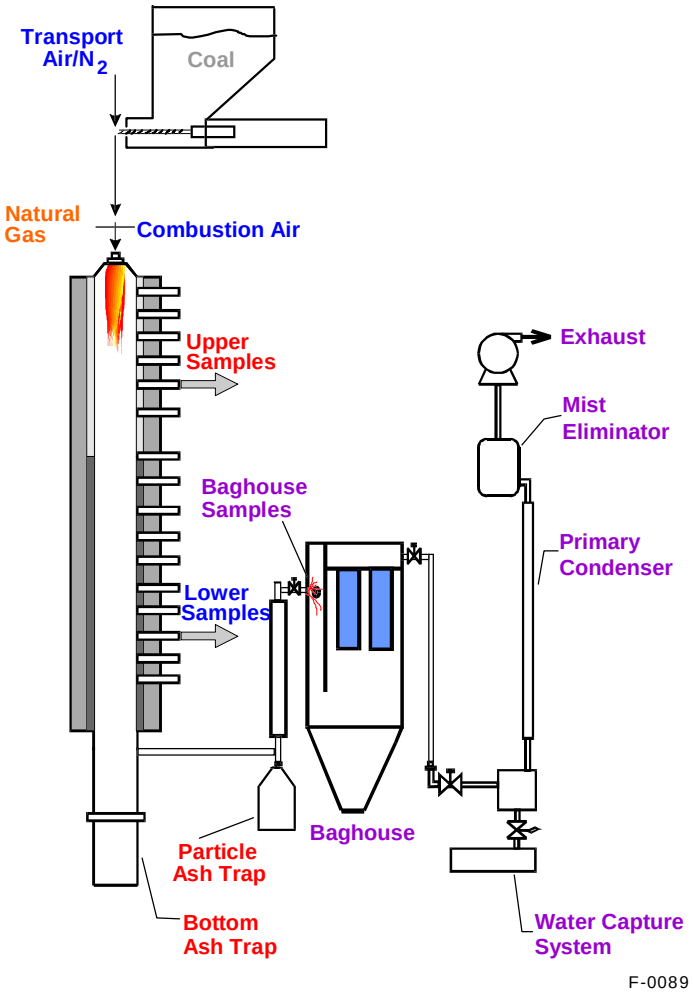

Figure 3-74. Overall schematic of University of Arizona combustion system.

Two inch (0.0508 m) nominal diameter sample ports located approximately every 0.3 m could be used to investigate the conditions within the furnace by a variety of sampling equipment. The temperature within the furnace was primarily monitored using a portable R-type thermocouple. Gas composition was monitored using O_2, CO, CO_2, and NO_x continuous analyzers. Particle composition was investigated using inertial-based size-segregated impactors.

Analysis of particle composition was performed by neutron activation at MIT [7] and in-house by atomic adsorption spectroscopy, atomic emission spectroscopy, and graphite furnace adsorption spectroscopy.

Coal Acquisition and Storage

Six coals were acquired and pulverized for this work under the direction of PSI [7] (see Section 3.1.1) for use by all researchers working under the DOE research contract. All coals were maintained in an oxygen-depleted environment to simulate coal behavior within the coal pile at a major utility and to avoid oxidation of key trace elements during storage.

Phase I coals were shipped in heavy plastic bags purged with argon and stored in barrels. As these barrels were not hermetically sealed, the environment within the barrels was replaced with argon on a periodic basis to avoid oxidation and sealed using a heavy polypropylene material to provide a hermetic seal.

Phase II coals were shipped in heavy plastic bags purged with argon and stored in hermetically sealed barrels. The environment in these barrels was not disturbed until the barrels were opened for use in the laboratory. All opened barrels were purged with argon and sealed using a heavy polypropylene material to provide a hermetic seal.

Air Supply Systems

Compressed air was used for:

1. Primary combustion air
2. Coal transport air
3. UV detector purge
4. Flue gas cooling
5. Coal feeder vibration air
6. Lime transport air
7. Dope system atomization
8. Utility uses.

A simple schematic showing the complete air supply system is shown in Figure 3-75. A detailed description of the air supply system is provided in Appendix I.

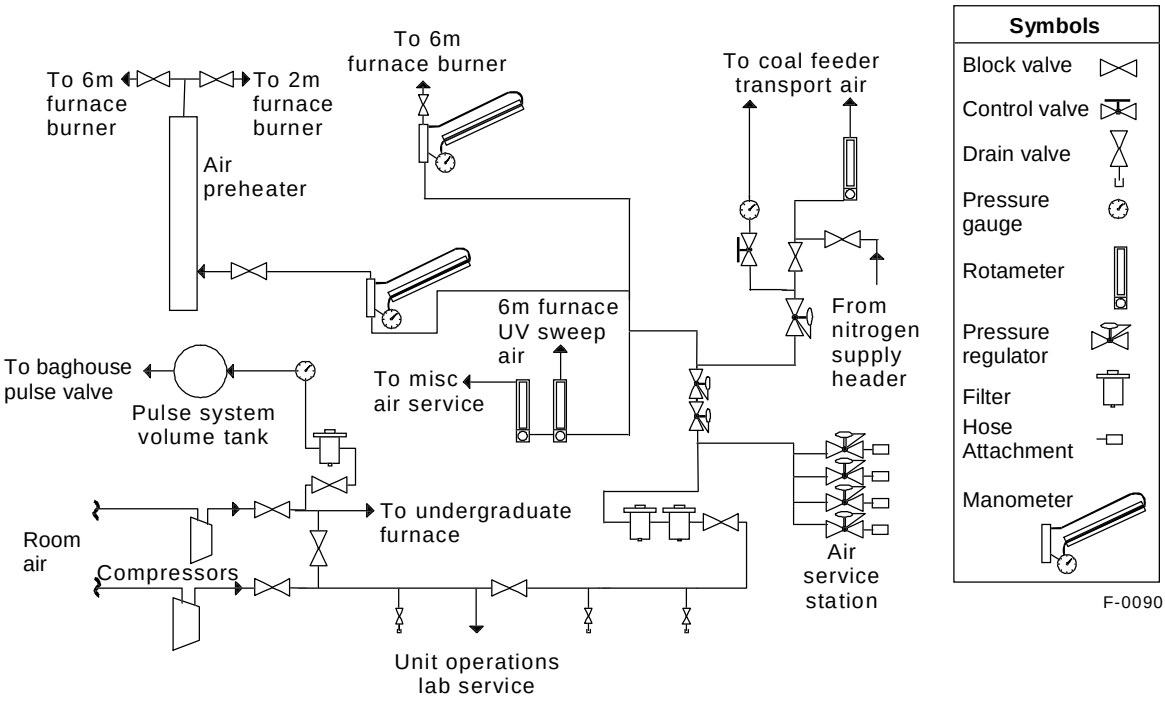

Figure 3-75. Schematic of compressed air supply system.

Coal Feeder Systems

For all experiments an existing Acrison Series 105 single rotating screw type feeder was refurbished and utilized to meter and control the coal feed to the furnace. The screw used was an Acrison auger (Model #1.5x14-7/8 LG 5/8 Hub, SS 105-10-1-2-2). A variable speed motor powers the feeder. Control is accomplished by changing the turning rate of the screw (Acrison Model 050-1 RPM controller). Transport air or nitrogen was used to blow the coal particles off of the screw tip and carry the coal to the burner.

A large coal hopper having a capacity of 1/3 to 1/2 standard barrel (depending on the density of the coal) corresponding to 10-25 run-hours at 2.2 kg/hr was attached to this feeder. Two pneumatic vibrators were used to reducing the tendency of coal particles to stick, bridge or form “worm-holes” (vertical tunnels) in the feed hopper (especially for high moisture coals like the North Dakota lignite). The first vibrator is located on the discharge tee where the coal particles disengage from the screw tip and are combined with the transport air. This vibrator was operated at 30 psig (308 kPa) supply air pressure. The second vibrator was located at the rear of the hopper and operated at 60 psig (515 kPa) supply air pressure. To reduce acoustic emission, outlet air from each vibrator was routed to an empty coal barrel prior to discharge to the environment.

This feeder has one disadvantage. It is not possible to accurately calibrate the coal feed rate due to the configuration of the burner utilized in the experiments. The transport air/coal was inducted into the burner premix section by the combustion air. Attempts to calibrate the feeder

offline resulted in significant under prediction of the coal that would be fed to the furnace for a given screw turning rate. When using this feeder it was necessary to set the air flow rates used in combustion (main air, transport air, UV sweep air, atomizer air) at the theoretical flow rates predicted from combustion calculations and then to set the coal feed rate to match the predicted excess oxygen and CO_2 concentration. This method is accurate as long as there are no leaks in the upper portion of the furnace. Unfortunately this was not the case for many of the experiments performed and the accuracy of the coal feed rate reported in the Results section of this dissertation should be considered approximate.

Combustion Burner

An existing carbon steel laminar-flame burner was utilized for all experimental work. The burner was made of standard schedule 40 carbon steel pipe fittings which allows easy disassembly for maintenance. Air and coal are mixed together in a ½ in. diameter (0.0127 m) side arm of the burner and routed into the body of the burner where the diameter is increased through standard reducer fittings to 2 in. (0.051 m) nominal diameter. Capability exists to add various attachments depending on the experimental requirements. For example, a thermocouple was sometimes added in the inlet air tee to measure the air temperature at the inlet of the burner, an SO_2 supply line was added for the Kentucky doping experiments, a feeder line was added to in-line mix pulverized coal into the coal/air mixture for the Ohio and Pittsburgh calcium doping experiments, and an air blast atomizer was installed through the top of the burner and radiant shield for the Wyodak arsenic, selenium, antimony, and iron doping experiments as well as the Pittsburgh iron doping experiments.

A two-tier water-cooled radiant shield was located near the bottom of the original burner body. This shield insured that coal would not ignite in the burner. The shield was constructed by installing eight brass 1/8 in. (0.00318 m) diameter tubes in each tier. The two tiers were installed perpendicular to each other, creating a grid. Coal and air exited the burner through the opening in the grid. Brass inlet and outlet caissons were used to route water to/from the shield tubes. The tubes were braised to the outlet of the burner body and casinos. Braise connections (for the radiant shield and gas inlet jets) are the weakest point of the burner. RTV high-temperature adhesive was used to seal leaks as they developed in the braising.

Natural gas connections were located just above the radiant shield. One-eighth inch (0.00318 m) diameter brass tubes were mounted at a 15 deg (from vertical) angle to improve the mixing of gas with air at the burner discharge. The jet tubes were sealed to the outlet of the burner body by braising.

An extension was added to the bottom of the burner at the first major rebuild to allow connection to revised furnace mounting bolts. For the Wyodak and Pittsburgh doping tests in Phase IIb, the innermost radiant shield tubes were bent slightly to allow a ¼ in. (0.00635 m) diameter atomizer tube to be inserted through the center of the burner.

A description of the natural gas supply and safety systems plus the radiant shield cooling water supply system can be found in Johnson [127].

Flame Doping System

A system was designed and constructed to allow liquid solutions to be atomized and sprayed into the flame under a swirl flame gas burner. The system allows specified concentrations of metals to be doped into the combustion flame in the furnace. A small laboratory-scale metering pump (Fluid model QV) is used to pump liquid from a reservoir to the inner 1/16 in. (0.0016 m) diameter stainless steel tube of an atomizer. Compressed air, controlled by a rotameter (Matheson Gas Products model FM-1050) is routed to the ¼ in. (0.0064 m) diameter annulus of the stainless steel atomizer. The air picks up the liquid and the mixture is forced through orifices in the atomizer tip, resulting in a fine spray of liquid droplets. When installed in the center of the burner, the atomizer nozzle was located ¼ in. (0.0064 m) below the burner outlet.

Combustion Furnace

The original combustion furnace inherited in 1995 consisted of an upper section of cast thermal-insulating refractory [128] coupled to a lower section made of fibrous alumina (Zircar) cylinders. The entire furnace was insulated using Thermal Ceramics kaowool blanket insulation. Due to the thermal cycling experienced during startup and shutdown of the furnace, the upper section eventually cracked and began leaking. When the leaks became excessive, the first major rebuild in 1997 was effected.

A disadvantage of the original furnace was the inability of the furnace to resist slag and ash buildup on the inner wall of the upper refractory. As a result, coal combustion was limited to between 8 and 12 hours (depending on the coal type) before a slag shelf would develop that covered over ½ the opening of the furnace. This slag shelf was removed by physical impaction using a carbon steel stake mounted on a 2 in. (0.0508 m) diameter carbon steel pipe.

The original furnace utilized mullite ceramic tubes for the UV detection port, pilot port, and all sample ports. These mullite tubes shattered throughout the entire length of the furnace, resulting in significant leakage. Two inch nominal (0.0508 m) brass gate valves were used to isolate the sample ports from the outside environment when not in use. Sample probes were connected to the sample ports using 2 in. nominal (0.0508 m) carbon steel threaded pipe unions.

Below the last sample port, the fibrous alumina section was connected to a 6 in. (0.152 m) diameter schedule 40 stainless steel pipe section. A 1 ½ in. (0.0381 m) stainless steel outlet line was welded perpendicularly in this pipe. A mating flange was installed on the bottom of the section where it connected to the ash trap. The trap was constructed of the same 6 in. (0.152 m) schedule 40 stainless steel pipe (approximately 12 in. [0.305 m] in length) with ¼ in. (0.00636 m) stainless steel plating welded on as the bottom of the trap. A baffle was added upstream of the outlet line to improve ash disengagement from the gas stream leaving the furnace.

The upper section of the furnace was redesigned and rebuilt in the 1997 rebuild. A slag resistant refractory (Thermal Ceramics HPM-95) was utilized for the body of the furnace and an insulating refractory (Thermal Ceramics 2800-LI) for the inlet cap. The refractory rests on

2 x 2 in. (0.0508 x 0.0508 m) alumina beams (Zircar RS-100 coil post). These beams are supported by 2 x 4 in. (0.0508 x 0.1016), ¼ in. (0.006 m) thick stainless steel rectangular channel beams. Photographs of the exterior of the rebuilt furnace refractory section (after curing) are shown in Figure 3-76. A more detailed description can be found in Davis [129].

Figure 3-76. Furnace refractory and upper zircar section.

All ports in the furnace were redesigned. The new ports utilized dense, moldable alumina (Zircar AX moldable) for all of the sample ports, the UV port, and the pilot port. The ports were custom molded on-site. The brass gate valves were replaced with full-ported 2 in. nominal (0.0508 m) diameter brass ball valves to make opening and closing easier.

The upper 6 ft (0.152 m) of the fibrous alumina section was also replaced with nested cylinders of fibrous alumina cylinder sections. The inner cylinders are made of low-silica alumina (Zircar ALC-15) with a 6 in. (0.152 m) inner diameter and 8 in. (0.203 m) outer diameter. The outer cylinders are made of an alumina-silica fibrous mixture (Zircar ASH) with an 8 in. (0.203 m) inner diameter and 10 in. (0.254 m) outer diameter. Refractory and alumina sections were sealed together using moldable alumina (Zircar AX moldable). The top cap was also sealed to the refractory section using moldable alumina. A new stainless steel burner mounting plate was sealed to the top cap using moldable alumina. Due to uneven expansion during heating, stainless steel support bars were added on top of the mounting plate to retain its shape during furnace heat up.

The refractory section was insulated with a 2 in. (0.0508 m) thick layer of Thermal Ceramics Cerachem, a high temperature blanket insulation made of alumina, silica, and zirconia fibers. Around this layer a 4 in. (0.102 m) thick layer of Thermal Ceramics Kaowool blanket

insulation was installed. The alumina section was insulated with a 4 in. (0.102 m) thick layer of Thermal Ceramics Kaowool blanket insulation.

After the rebuild it was possible to burn coal for 40 to 100 hours (depending on coal type) without cleanout of slag/ash buildup. A 6 in. (0.152 m) chimney sweep brush mounted on a ¾ in. (0.0191 m) carbon steel pipe was used to clean the furnace.

Flue Gas Outlet/Treating System

This section describes the equipment used to treat the flue gas that exits the furnace prior to its discharge into the atmosphere.

Furnace Outlet Line and Baghouse

Flue gas from the furnace outlet was routed to a baghouse, where one micron-rated GoreTex filters were used to remove particulate from the gas stream. The original outlet line was 1.5 in. (0.0381 m) schedule 40 stainless steel pipe sloped at around a 5 deg (up from horizontal) angle into the original baghouse. A water-cooled jacket was installed on this line to allow the temperature to be reduced in the flue gas entering the baghouse. The filter material had a maximum temperature rating of 523 K. Even with the cooling jacket, the gas entering the baghouse could exceed this temperature under certain bituminous coal combustion conditions.

An air/water atomized purge system was installed to reduce the flue gas temperature below the filter cartridge maximum temperature rating. An atomizer was installed in the stainless steel section of the furnace (below the last sample port but above the furnace outlet line). The air flow rate was manually controlled using a pressure regulator. The water was manually controlled by a needle valve. Cooling by air purge was used for all bituminous coal experiments conducted with the original baghouse. Although the water atomization system was commissioned and tested in bituminous coal service, in actual practice, water atomization was never required.

The original baghouse was made entirely of stainless steel and the bags were mounted horizontally. A bag pulse system was installed in the back of the baghouse. This pulse system never worked properly and the filter cake was removed by manual shock vibrations induced by impaction of a rubber mallet to the filter mounting plates. After around one year's operation, the sealing system around the rear of the filters failed and erosion opened a gap that allowed particulate to bypass the filters. Due to the design of the baghouse, it was not possible to repair the damage.

A ¾ in. (0.0191 m) stainless steel bypass line was used during furnace warmup or whenever the original baghouse was taken out of service. Due to the small diameter of this bypass line, the pressure drop during bypass operation was excessive. Therefore, a 1.5 in. (0.0381 m) diameter stainless steel bypass line was installed shortly after commissioning.

A new baghouse was commissioned in 1997 to replace the damaged stainless steel baghouse. A simple schematic of this baghouse is shown as part of Figure 3-74. This baghouse

was constructed of carbon steel. The same filter cartridges were utilized but were hung vertically. The new pulse system included a volume tank and quick opening "pop" valves (BHA) to effectively remove the filter cake. The pulse valves were operated by a solenoid-based electrical control system with the capability of manual or automatic (based on time) operation.

Flue gas entered the baghouse horizontally near the top of the unit. A deflector plate was used to route the gas nearer the bottom of the unit to insure a more even distribution of gas through the membranes. The cleaned gas exits horizontally near the top of the unit. A sample port was added to the baghouse perpendicular to the inlet but between the inlet port and the deflector plate. This allowed sampling of the flue gas entering the baghouse; simulating particulate collector inlet conditions in a commercial combustor.

External wall heaters were installed on two sides of the baghouse to reduce condensation during heatup. The original heaters were resistance heating elements mounted in an 18 x 18 in. (0.457 x 0.457 m) polymer square. The polymer failed after around 1 year. Four 7 W Chromalox strip electrical resistance heaters sheaved in carbon steel were then installed to replace the original heaters. An automatic control system was provided with the strip heaters. Control was provided by a Watlow model 935 PID controller operating on the signal from a K-type thermocouple mounted in the center of the baghouse between the bags. An Omega 25A solid state relay was used to energize the heating strips. The baghouse was also insulated with 2 in. (0.0508 m) of Knauff fiberglass insulating panels.

The furnace outlet line was redesigned and modified to match the new baghouse. Standard pipe fittings were used in the redesign to simply maintenance. Existing furnace outlet pipe spools, including the spool with the water cooling jacket were reutilized. These spools were mated to a new carbon steel inlet spool using insulated gasket and bolt inserts to minimize galvanic corrosion. Brass ball valves were used to isolate the baghouse. The presence of a vertical run in the furnace outlet line induced additional particulate to disengage from the gas and collect in the lowest elbow. Therefore, a particle trap was installed below this elbow to collect this material without plugging the furnace outlet line (see Figure 3-74). The trap was made from a 3 x 6 in. (0.0762 x 0.152 m) schedule 40 carbon steel nipple and other carbon steel fittings. A brass gate valve was used for isolation and removal during operation.

The increased volume in the new baghouse provided additional cooling of the flue gas by expansion. This cooling was sufficient to maintain the flue gas temperature below the maximum rated temperature of the filter cartridges without the use of the upstream cooling water jacket or the air/water atomization purge system under all coal combustion conditions experienced.

A 2 in. nominal (0.058 m) schedule 40 carbon steel bypass line was installed for the new baghouse. This bypass line is isolated from the furnace outlet line using a bronze gate valve. The bypass line is routed up the side supports of the furnace and is then connected to the building vent ducting.

A connection constructed of carbon steel pipe fittings was included in the furnace outlet line to allow the flue gas to be routed to temporary devices. This connection was isolated from the furnace outlet line by a 2 in. nominal (0.0508 m) ball valve. This connection was used to collect total ash samples in a single filter bag fly ash collector for use by other researchers on the overall DOE project.

A simple schematic of the furnace outlet line including the bypass line and temporary connection manifold is shown in Figure 3-77.

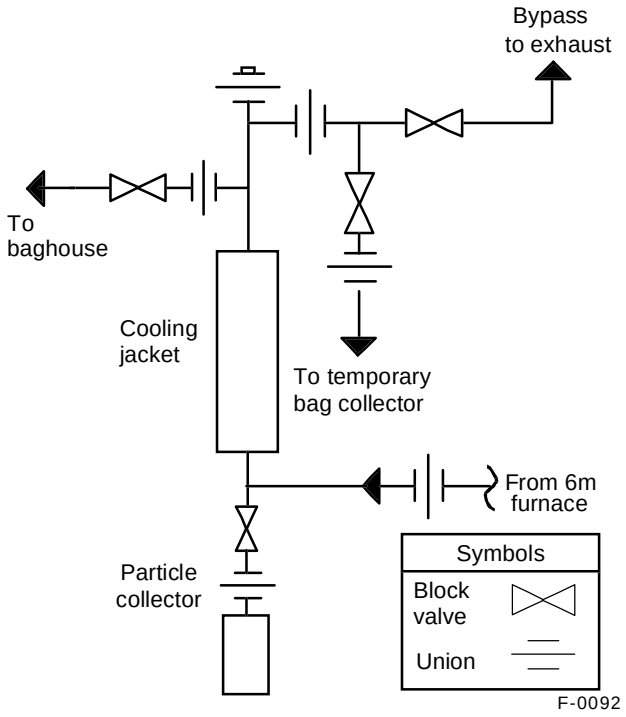

Figure 3-77. Simple schematic of furnace outlet line piping.

Baghouse Outlet Line/Condensing System/Water Collection System

Gas from the baghouse was routed to a vertical 1 ½ in. (0.0381 m) schedule 40 water-jacketed stainless steel pipe. In this piping section, the gas was cooled to near atmospheric conditions. Acidic water condenses out of the gas in this piping section. Much of this water ran down the pipe walls.

A water collection system was used to remove water from the flue gas piping. A simple schematic of the water collection system is shown as part of Figure 3-74. The design was constrained by three limitations:

1) The piping system operated under a vacuum of up to 42 in. of water (78.5 mm Hg; 10.5 kPa),
2) There was limited space available underneath the piping system, and
3) Increases in the pressure drop in the piping system had to be kept to a minimum.

The system installed consisted of two water collection boxes. Baghouse outlet gas was routed into the upper box where the velocity of the gas was reduced by an order of magnitude. This provided cooling and allowed disengagement of any liquid that condensed in the baghouse outlet line or in the upper water box. Baffling in the upper box was used to avoid flue gas channeling and increase gas residence time in the box; increasing liquid disengagement. The outlet of the upper box was immediately below the vertical, water-jacketed pipe. Liquid dropping from the vertical piping section would also be collected in the upper box.

The lower box was connected to the upper box by a 2 in. (0.0508 m) diameter butterfly valve. A butterfly was used because of the space limitations for the collection system. During normal operation, the valve remains open and liquid drains from the upper box into the lower. This box has a capacity of six gallons ($0.0227 m^3$); enough for approximately 48 hours of operation of either gas or coal combustion. To drain the liquid from the lower box, the butterfly valve was closed and the drain valve was opened. Piping from the drain valve routed water to the building sump.

Excessive corrosion was experienced in the water collection system due to the use of the wrong insulating gasket material between the upper box and the stainless steel vertical pipe. Therefore, a new baghouse outlet gas cooling and water collection system was installed in 2000. The new system replaced the vertical water-jacketed cooling system and the two box water collection system. A single pass shell and tube heat exchanger was installed in the baghouse outlet line. Twenty 5/8 in. (0.0159 m) ID x ¾ in. (0.0191 m) OD x 0.91 m long teflon tubes were used in order to handle the maximum temperature (523 K) and acidic condensate (particularly when injecting SO_2 or Cl_2 into the flue gas) that could be expected in the baghouse outlet flue gas. The shell was constructed from 10 in. nominal (0.254 m) diameter PVC pipe and fittings. Tygon tubes with Swaglok fittings were used for the inlet and outlet cooling water connections. Drainage from the tubesheet was accomplished manually by dual ball valves installed in 1 in. (0.0254 m) transparent PVC piping. The wastewater was routed to the building sump. The flue gas leaving the condenser was routed through 1 ½ in. nominal (0.0381 m) PVC piping to the existing knockout pot (see next paragraph below).

The use of a vertical, upflow condenser (the vertical, water-jacketed stainless steel pipe described above) in the original design for flue gas cooling introduced entrainment problems into the system. To alleviate these problems, a 12 in. (0.304 m) diameter x 3 ft (0.914 m) long PVC knockout pot was installed at the outlet of the vertical, water-jacketed stainless steel pipe. This pot was only partially effective in removing liquid drops from the flue gas. Therefore, the pot was replaced by a slightly large pot (4 ft [1.22 m] long) containing a demister pad in 1998. Even with the demister pad, some liquid drops and some fine particulate matter were still present in the flue gas so a polycarbonate filter/coalescer in the outlet line of the knockout pot in 1999 to improve removal of liquid and particulate matter.

Flue Gas Vacuum Compressor

Flue gas from the filter/coalescer was routed through a vacuum ring compressor. The original compressor was a Fuji model 209A-7W centrifugal ring compressor rated at 1/3 hp (249 W) and provided approximately 34 in. H2O (63.5 mm Hg, 8.5 kPa) of vacuum. This compressor was replaced with a larger capacity Fuji model 309A-7W compressor rated at ½ hp (373 W) in 1999. The new compressor provides approximate 45 in. H2O (84.0 mm Hg, 11.2 kPa) of vacuum.

Flue gas from the compressor was routed to the building vent system and discharged to the atmosphere. Blowers on the building vent system provide approximately 6 in. H2O (11.2 mm Hg, 1.5 kPa) additional vacuum for the flue gas system.

Total Ash Collection System

A collection system was designed and constructed to collect all of the ash contained in the flue gas prior to entering the baghouse. Inlet and outlet piping spools of 1 ½ in. (0.0381 m) schedule 40 carbon steel were connected to the temporary connection manifold on the furnace outlet line, to the collector, and the baghouse inlet sample port using threaded unions. A simple schematic of the collector is shown in Figure 3-78. The collector consisted of a bottom box made from carbon sheet steel. The upper section was fitted to the bottom section with gaskets and held in place with latches. A tubesheet was installed near the top of the upper section. A vertical filter bag rated to 523 K and 1-micron filtration size (BHA) was hung on a 27.5 in. (0.699 m) long support cage (BHA Rolled Flange Top/Pan Bottom, 11GA Rigid Cage) and sealed to the tubesheet using RTV adhesive. The inlet nozzle was just below the tubesheet. A baffle directed inlet flue gas downward to reduce channeling in the collector. The outlet nozzle was located just above the tubesheet. The tubesheet was fitted to the upper section with gaskets and held in place by support braces welded to the top cover. Handles were fitted to the tubesheet so that the filter bag could be lifted and manually cleaned without having to dismantle the collector. The top cover was fitted to the upper section with gaskets and held in place by latches.

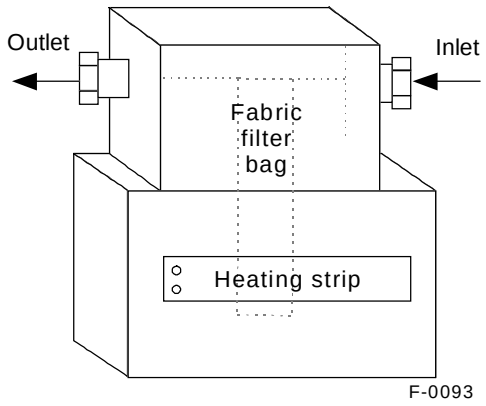

Figure 3-78. Simplified drawing of total fly ash sample collector.

Four 4 W, 7 in. (0.178 m) long carbon steel sheathed electrical heating strips (Chromalox) were attached to the bottom section of the collector. A temperature control system was used to control the heating strips. A Watlow model 935 PID controller operating on an input signal from a "K-type" thermocouple flush mounted to the upper section of the collector was used. An Omega 10A solid state relay supplied the electrical power to the heating strips. The entire control system is portable with plug-in connections from the control panel for the thermocouple signal and electrical power supply. The collector was insulated with 2 in. (0.0508 m) thick Knauff fiberglass insulation.

Process Monitoring Equipment

Temperature Probes

The gas temperature within the furnace was measured at the centerline using a portable bare-wire, ceramic shielded, R-type thermocouple probe connected to a LabTech data acquisition system, DAQ [127]. Each thermocouple lead (Omega Engineering) was threaded into an opening in a ¼ in. (0.0064 m) ceramic sheath (Alfa Aesar) and connected to the DAQ using standard R-type thermocouple connectors and extension wires (Omega, various parts). A cold-junction block thermocouple input board was installed in the DAQ computer to accept this signal.

In Phase I it was discovered that the ¼ in. (0.0064 m) sheath was insufficient to withstand stress from slag impaction and ash buildup. A second ½ in. (0.0127 m) diameter hollow ceramic sheath was added to provide increased strength. At the higher temperature ports, the dual sheath system was still too brittle and weak to withstand slag impaction so moldable alumina (Zircar AX moldable) was added to the outer surface. The moldable is not nearly as brittle as the fired ceramic and thus was able to withstand slag impaction and ash buildup.

Flue Gas Composition Monitoring

A portable water-cooled, stainless steel, gas-sampling probe was used to measure the centerline gas composition profile [127]. Gases were extracted using a vacuum pump through the probe, tygon tubing, and a conditioning system. First the gas entered a carbon steel knockout chamber, constructed of pipe and fittings, to allow any liquid formed in the probe and outlet tubing to drop out of the gas. The gas then was routed through a stainless steel coil mounted inside of a small refrigerator to cool the gas to below atmospheric temperature. Then the gas entered a glass knockout chamber so that liquid formed in the coil could be removed. From the glass knockout chamber the gas passed through a particle filter (Speedaire), then into a PVC surge chamber. From the PVC surge chamber the gas was separated into the individual analyzer manifolds. Each manifold utilized a pressure regulator (Speedaire) and a rotameter (Matheson Gas Products model FM-1050) to control the pressure and flow into the individual analyzers. Excess gas was routed through a bypass line into the building vent system. Backpressure on the inlet system was maintained by a manual needle valve on the bypass line.

The original analyzer system used in Phase I consisted of Beckman CO and CO_2 analyzers (model 864 infrared analyzer), a Beckman O_2 (model 755R paramagnetic) analyzer, and a Thermal Electron NO_x (Chemiluminescent Series 10) analyzer. The obsolete CO and CO_2

analyzers were replaced in 1997 with a combined CO/CO_2 analyzer from California Analytics (NIR model ZRH). The original analyzer enclosure is described by Johnson [127]. The analyzer enclosure was replaced with a standard, double-wide instrument rack in 1997. At this time the DAQ hardware and software (LabTech/LabView) were also upgraded. All analyzers have individual readouts plus connection to the DAQ.

Particulate Sampling System

Particle sampling was carried out using a portable, water-cooled, stainless steel, aspirated isokinetic sampling probe [127]. Samples extracted by the probe from the centerline of the furnace were routed through tygon tubing to a Berner Low Pressure Impactor [130] using a dilution nitrogen gas stream and a vacuum pump. The DAQ was used to control the sampling process. Nitrogen flow rate was controlled using a mass flow controller (Sierra model #810C-DR-13) operating on a signal input from a PID controller block in the DAQ. A high performance vacuum pump (Rietschle with a Baldor 3-phase 3HP [2.24 kW] motor) was used to reduce the pressure at the BLPI outlet to below 8 psia (55.2 kPa). The bottom stage of the BLPI acts as a sonic orifice to control the total flow rate from the sampling probe. A wet test meter (Precision Scientific) was connected to the BLPI outlet so that the actual flow rate through the BLPI could be measured. A simplified schematic of the particle sampling system is shown in Figure 3-79.

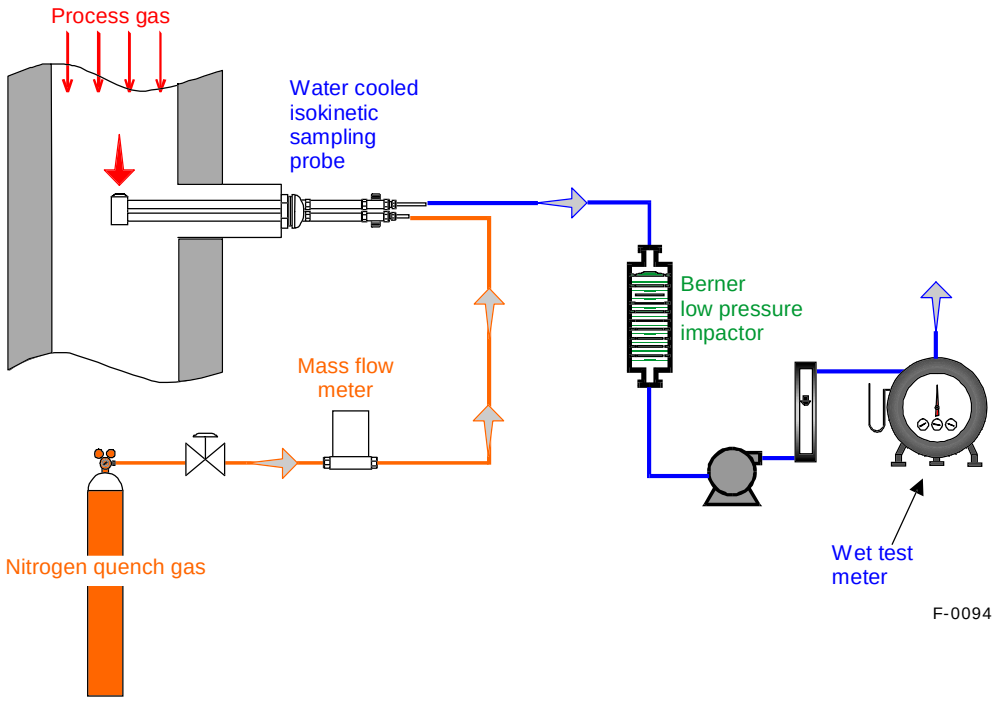

Figure 3-79. Simplified schematic of particle sampling system.

A portion of the outlet gas from the wet test meter was routed to the gas conditioning system. This allowed the NO_x and CO concentrations to be monitored and used to adjust the isokinetic flow rate for particulate sampling of 10 min or longer. Due to the time required to measure the gas composition, the isokinetic flow rate must be determined prior to sampling for sampling times of less than 10 min.

The BLPI utilizes low pressure and high jet velocities to allow size segregation of particles in the submicron range. The BLPI consists of eleven collection plates (stages) designed to collect particles of decreasing size as follows: 15.7, 7.33, 3.77, 1.98, 0.973, 0.535, 0.337, 0.168, 0.0926, 0.0636, and 0.0324 (50% aerodynamic cutoff diameter – in μm). A simplified schematic of the BLPI is shown in Figure 3-80.

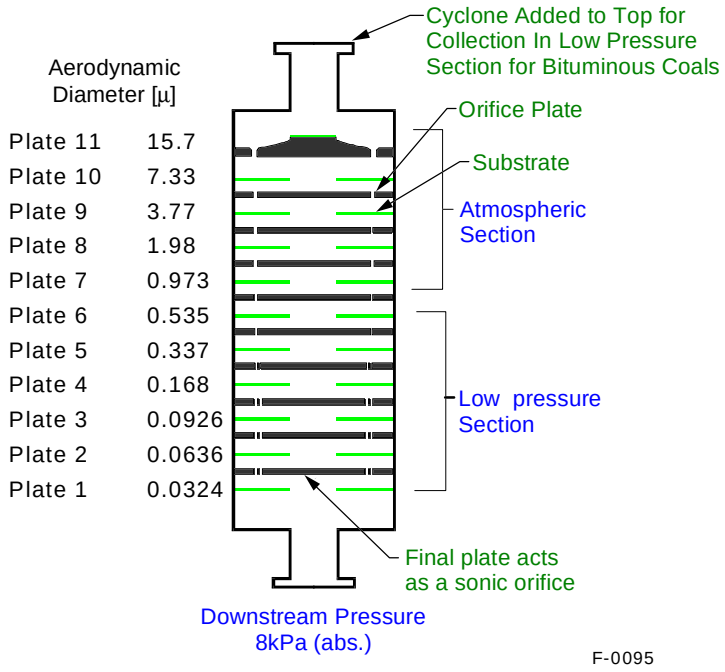

Figure 3-80. Simplified schematic of the Berner low pressure impactor.

Due to the high loading of large, supermicron size particles in bituminous coals, the BLPI must be utilized in two separate configurations in order to obtain a complete particle size distribution. Configuration #1 was used for collection of small particles, those below 0.973 microns. In this configuration a cyclone is used on the inlet of the impactor to collect most of the larger particles (>1 micron). Therefore, no appreciable particle content will appear on the upper stages (7-11). This allows the sampling time to be extended long enough to collect a significantly large sample of small diameter particulate matter (see results section for actual sampling times). Without this cyclone, particles would bounce off the upper stages, severely skewing the data and plugging the jet orifices.

Configuration #2 was used to determine the particle size distribution of large particles. In this configuration the cyclone was removed and particles were collected in the entire impactor but over a shorter sampling period. This configuration yielded measurable quantities of size segregated particulate matter in the upper stages but not in the lower, sub-micron stages.

For the lower rank coals, a complete particle size distribution could be obtained without utilizing the cyclone.

The collection plates were lined with a 0.4 μm thick polycarbonate membrane (Osmonics 2751 "w/1.182 ctr hole") coated with high purity grease (Apiezon L). The grease was dissolved in either high purity toluene (Phases I, IIa, and the Wyodak tests in IIb) or high purity hexane (Ohio tests in IIb). A small atomization-type air sprayer was used to atomize the grease and solvent. An even coating was sprayed on one surface of the membranes. The membranes were allowed to dry under a fume hood for at least 48 hours in enclosed Petrie dishes for Phase I. To improve the stability of the membranes, a vacuum dessicator was utilized in Phase II. Membranes in Petrie dishes were placed in the vacuum dessicator for at least 24 hours prior to use. Blank membranes were weighed just prior to impactor loading (typically in the morning of the same run day – a time gap of between 1-5 hours from weighing and loading) on a micro-balance (Ohaus Analytical Plus) to an accuracy of +/- 25 μg in Phase I, +/- 15 μg in Phase IIa, and +/- 5 μg in Phase IIb. Despite these precautions, negative weights were sometimes realized during testing for some of the smallest diameter impactor stages. Gravimetric error represented a significant source of uncertainty for these experiments. A more complete discussion of the errors associated with gravimetric measurements is given in Appendix J, Quality Control.

When operating in Configuration #1 (with the cyclone), stages 1-6 contained membranes while stages 7-11 were lined with grease-coated aluminum foil or membrane backing paper (dried and weighed as described above). Similarly, when the cyclone was not utilized (Configuration #2), stages 6-11 contained membranes while stages 1-5 were lined with grease-coated aluminum foil. When no cyclone was used, all 11 impactor stages contained membranes.

Analytical Equipment

A subset of the impactor samples collected was selected for elemental analysis. In Phase I, all analytical work was conducted by neutron activation (NAA) at MIT [7]. For Phase II, NAA results were supplemented by in-house analyses. Major elements were analyzed by atomic adsorption spectroscopy (AAS) or atomic emission spectroscopy (AES) using an existing Perkin-Elmer model 2380 atomic adsorption spectrophotometer and hollow cathode lamps from Starna Cells. Trace elements were analyzed by a new graphite furnace atomic spectroscopy (GFAA) with Zeeman background correction using a Perkin-Elmer model 4110 ZL and hollow cathode or electrodeless discharge lamps from Perkin-Elmer. A Neslab model CFT-75 refrigerated recirculator was used as the GFAA instrument cooling unit. Installation required supply of 220V power for the GFAA, 110V power for the chiller, and a dedicated ventilation system.

3.3.3.2 Experiments

Baseline Screening Experiments

Pittsburgh Seam Coal Baseline Screening Tests

UA's pilot-scale downflow laboratory combustion furnace was used to test the partitioning of toxic metals in the Phase I baseline screening experiments for the Pittsburgh seam coal during the time period January 29, 1997 through February 20, 1997. The objectives of these experiments were:

1. To obtain toxic metal partitioning data under test conditions which simulate the time/temperature combustion and post-combustion conditions of commercial scale utility boilers at 20% excess oxygen.

2. To investigate the differences in toxic metal partitioning from samples collected immediately after char burnout compared to samples collected near the furnace exit and to samples collected at the entrance to the baghouse.

A summary of the experiments performed is given in Appendix K, Table K-1. Experimental conditions for the particle sample sets collected are summarized in Table K-2. Ten matched impactor sets were collected during these tests. A matched sample set consists of six membranes from a 1st collection test for particulate on atmospheric stages -- 6-11 -- of the BLPI without the preseparator cyclone attached to the BLPI inlet and six membranes from a 2nd collection test performed immediately before or after the 1st test collecting particulate on the subatmospheric stages -- 1-5 -- of the BLPI with a cyclone.

Additional Pittsburgh seam coal baseline screening experiments were conducted during the time period August 1-3, 1999. The purpose of these experiments was to collect size-segregated particle samples from the baghouse inlet sampling port, which is equivalent to sampling at the particulate collection device in a commercial combustor. In addition, special samples were collected at Ports 4 and 14 to validate the leaching protocol developed as a part of this research project (see below). A summary of the experiments performed is shown in Table K-1. A summary of the experimental conditions for the particle sample sets collected is shown in Table K-2. A total of 18 coal-burning hours and nine impactor sets (one matched set with and without cyclone at Port 4, two matched sets with and without cyclone at Port 14, and three unmatched sets without cyclone at the baghouse inlet port) were collected during these tests. A single collection test, performed without the BLPI inlet cyclone, can be used at the baghouse inlet port due to the removal of a portion of the larger particles in the upstream ash and particle traps.

Illinois #6 Coal Baseline Screening Tests

The downflow laboratory combustion furnace was used to test the partitioning of toxic metals in the Phase I baseline screening experiments for the Illinois #6 coal during the time period February 25, 1997 through March 5, 1997. The objectives of these experiments were the same as those listed above.

A summary of the experiments performed is given in Table K-3. Experimental conditions for the particle sample sets collected are summarized in Table K-4. Thirteen impactor sets (six matched sample sets with and without cyclone plus one additional unmatched set without cyclone) were collected during these tests.

An additional Illinois #6 coal baseline screening experiment was conducted on March 15, 1999. The purpose of this experiment was to collect size-segregated particle samples from the baghouse inlet sampling port. A summary of the experiment performed is included in Table K-3. Experimental conditions for the particle sample sets collected are summarized in

Table K-4. Three unmatched impactor sets from the baghouse inlet sampling port were collected.

Ohio 5/6/7 Blend Coal Baseline Screening Tests

The downflow laboratory combustion furnace was used to test the partitioning of toxic metals in the Phase II baseline experiments for the Ohio 5/6/7 blend coal during the time period November 19, 1998 through December 22, 1998. The objectives of these experiments were the same as listed above except that samples from both the furnace and the baghouse were collected during the same series of experiments. The experiments performed are summarized in Table K-5. Experimental conditions for the particle sample sets collected are summarized in Table K-6.

Table K-6 shows the sampling conditions for the most important sample sets collected during the experiments. Seven matched sets of particulate samples were collected from Port 4 of the furnace, which is located immediately after the end of the combustion zone (around 0.5 residence seconds from the burner). Five matched sets of particulate samples were collected from Port 14, which is located near the bottom of the furnace (around 2.2 residence seconds from the burner) and represents a snapshot of the flue gas in the post-combustion zone. These five samples sets were taken immediately after one of the sample sets from Port 4 so that sample sets from the most similar combustion conditions possible could be selected for analysis.

Four sample sets were taken from the inlet to the baghouse. The baghouse samples are taken after partial segregation of large particles in an ash trap and a small particle trap. Therefore, it was found that a single collection test, performed without the BLPI inlet cyclone, could be used to collect size-segregated samples. This was performed for sample set 16 only.

Wyodak Power River Basin Subbituminous Coal Baseline Screening Tests

The downflow laboratory combustion furnace was used to test the partitioning of toxic metals in the Phase II baseline screening experiments for the Wyodak subbituminous coal during the time period March 15, 1999 through March 29, 1999. The objectives of these experiments were the same as listed above except that samples from both the furnace and the baghouse were collected during the same series of experiments. The experiments performed are summarized in Table K-7.

A total of 12 sets of particulate samples were collected during 6 test runs. All experiments were performed at a coal feed rate of 2.2 kg/hr. Due to the lower energy content of this subbituminous coal compared to the Ohio bituminous coal, combustion gases experienced a longer residence time in the furnace. Experimental conditions for the particle sample sets collected are summarized in Table K-8.

Five sets of particulate samples were collected from Port 4 of the furnace, which is located immediately after the end of the combustion zone (around 1.4 residence seconds from the burner). Four sets of particulate samples were collected from Port 14, which is located near the bottom of the furnace (around 6.6 residence seconds from the burner) and represents a snapshot

of the flue gas in the post-combustion zone. Each of these sample sets was collected immediately after one of the sample sets from Port 4 so that sample sets could be selected for analysis from the most similar combustion conditions possible. Three sample sets were taken from the inlet to the baghouse and represent particulate collection device sampling conditions. The baghouse samples are taken after partial segregation of large particles in an ash trap and a small particle trap. Each of these samples sets were taken immediately after one of the sample sets from Port 14 so that sample sets could be selected for analysis with the most similar combustion conditions possible.

A single collection test, performed without the BLPI inlet cyclone, was used to collect all size-segregated sample sets using the BLPI at all three sampling locations due to a smaller mean particle size for the Wyodak fly ash compared to the mean particle size for the bituminous coals tested under this program.

North Dakota Falkirk Seam Lignite Baseline Screening Tests

The downflow laboratory combustion furnace was used to test the partitioning of toxic metals in the baseline experiments for the Phase II North Dakota lignite. The objectives of these experiments were the same as those listed above except that samples from both the furnace and the baghouse were collected during the same series of experiments.

A total of 15 sets of particulate samples were collected during 6 test runs. All experiments were performed at a coal feed rate of 2.2 kg/hr. Due to the lower energy content of this lignite compared to other Phase I and Phase II coals, combustion gases experienced a longer residence time in the furnace.

Five sets of particulate samples were collected from Port 4 of the furnace, which is located immediately after the end of the combustion zone (around 1.9 residence seconds from the burner). Five sets of particulate samples were collected from Port 14 which is located near the bottom of the furnace (around 9.4 residence seconds from the burner) and represents a snapshot of the flue gas in the post-combustion zone. A pair of sample sets at Port 14 were collected as soon as practical after a pair of the sample sets from Port 4 so that sample sets could be selected for analysis with the most similar combustion conditions possible. Five sample sets were taken from the inlet to the baghouse. The baghouse samples are taken after partial segregation of large particles in an ash trap and a small particle trap.

A single collection test, performed without the BLPI inlet cyclone, was used to collect all size-segregated sample sets at all sampling locations due to a smaller mean particle size for the North Dakota fly ash compared to the mean particle size for the bituminous coals previously tested under this program.. The sample sets and test runs are summarized in Tables K-4 through K-9. Table K-10 shows the sampling conditions for the most important sample sets.

East Kentucky Elkhorn/Hazard Blend Coal Baseline Screening Tests

The downflow laboratory combustion furnace was used to test the partitioning of toxic metals in the baseline experiments for the Phase I Kentucky Elkhorn/Hazard bituminous coal. The objectives of these experiments were the same as those listed above except that samples from both the furnace and the baghouse were collected during the same series of experiments.

A total of 15 sets of particulate samples were collected during 6 test runs. Five matched sets (a matched sample set consists of six membranes from a 1st collection test for particulate on atmospheric stages -- 6-11 -- of the BLPI without the preseparator cyclone attached to the BLPI inlet and six membranes from a 2nd collection test performed immediately before or after the 1st test collecting particulate on the subatmospheric stages -- 1-5 -- of the BLPI with a cyclone) of particulate samples were collected from Port 4 of the furnace, which is located immediately after the end of the combustion zone (around 0.7 residence seconds from the burner). Five matched sets of particulate samples were collected from Port 14 which is located near the bottom of the furnace (around 2.9 residence seconds from the burner) and represents a snapshot of the flue gas in the post-combustion zone. Each of these sample sets was collected as soon as practical after one of the sample sets from Port 4 so that sample sets could be selected for analysis with the most similar combustion conditions possible.

Five sample sets were taken from the inlet to the baghouse. The baghouse samples are taken after partial segregation of large particles in an ash trap and a small particle trap.

The sample sets and test runs are summarized in Tables K-4 through K-11. Table K-12 shows the sampling conditions for the most important sample sets.

Experiments for Hypothesis Testing

Based on the results obtained during the baseline screening experiments, a series of hypotheses were developed concerning how specific trace elements partition in the furnace. The hypotheses are summarized in Section 3.3.3.3. A series of special experiments were designed and conducted to test the validity of these hypotheses.

Wyodak As/Se/Sb Doping Tests

A series of experiments were designed to take advantage of the differences in the trace element-to-calcium ratios of the Wyodak and Ohio coals. In the Wyodak doping tests, solid phase elemental arsenic, selenium, or antimony was dissolved in dilute acid (arsenic and selenium were dissolved in the dissolving acid described in Appendix J diluted as 100 ml of acid in 4 liters with water while antimony was dissolved in dilute nitric acid). The quantity of each element dissolved was calculated to produce an overall trace element-to-calcium ratio in the combustion flame when burning Wyodak coal plus 10 ml/min of doping solution equal to the trace element-to-calcium ratio when burning the Ohio coal.

To investigate the impact of combustion temperature upon trace element partitioning, experiments were conducted at both the natural Wyodak maximum combustion temperature (for

a 20% excess oxygen combustion) and with an elevated maximum combustion temperature. Elevated combustion temperature was achieved by enriching the main combustion air with oxygen while maintaining the overall excess oxygen content of the combustion environment at 20%.

The original intention was to add enough oxygen so that the maximum combustion temperature burning the Wyodak coal would match the natural combustion temperature of the Ohio coal. Unfortunately, limitations were experienced due to flame lift in the furnace. The existing burner had no provision to increase the exit velocity from the burner. As the oxygen content was increased and nitrogen diluent decreased, the exit velocity decreased and the flame became shorter. Eventually the flame began impinging upon the upper plate of the furnace. This plate was not designed to handle the increased temperatures and began to deform.

A compromise solution was found that provided an elevated temperature 50 K below the Ohio combustion temperature (compared to 100 to 150 K under natural combustion conditions) as measured at Port 1 of the furnace.

The sample sets and test runs are summarized in Table K-13. Duplicate complete impactor sample sets were obtained at both Ports 4 and 14 for each experimental condition. Table K-14 shows the sampling conditions for the most important sample sets. Also included is the concentration of trace element in the doping liquid solution for each test.

Ohio Ca Doping Tests

A special set of experiments were designed and implemented using the Ohio 5/6/7 blend coal to complement the results from the Wyodak doping experiments described above. A list of these experiments in provided in Table K-15. In these experiments, pulverized, hydrated lime (Global Stone Tenn Luttrell; see Ref. [129]) was blended into the coal feedstock at the burner inlet to simulate an Ohio coal containing increased calcium in excluded inorganic fractions. The rate of lime added to the coal decreased the arsenic-to-calcium ratio during Ohio coal combustion to match the arsenic-to-calcium ratio of the Wyodak coal. This also resulted in a selenium-to-calcium ratio very close to the selenium-to-calcium ratio of the Wyodak coal.

To investigate the impact of combustion temperature upon trace element partitioning, experiments were conducted at both the natural Ohio maximum combustion temperature (for a 20% excess oxygen combustion) and with a depressed maximum combustion temperature. Depression of the combustion temperature was achieved by diluting the main combustion air with CO_2 while maintaining the excess oxygen content at 20%. The amount of CO_2 added was adjusted until the maximum combustion temperature matched the natural maximum combustion temperature for the Wyodak coal.

To make these tests more efficient, only the supermicron regime was investigated. Therefore, membranes were only collected from impactor stages 6-10 during particle sampling without the inlet preseparator cyclone. Duplicated impactor sets were collected at both Ports 4 and 14 for each set of experimental conditions. The sampling conditions of these sample sets are listed in Table K-16.

Wyodak Fe Doping Tests

Examination of the cation distributions for the Wyodak baseline screening tests (these are provided in Section 3.3.3.4) revealed that the iron and calcium distributions were very similar in shape. As a result, it was not possible to determine whether the oxy-anions (i.e., arsenic, selenium, and antimony) were reacting with one or other of the cations or with both of them.

The Wyodak coal has a low sulfur content and a low trace element-to-calcium ratio. These experiments were designed to determine if the oxy-anions were more partial to calcium or to iron. To accomplish this, solid phase iron nitrate nonohydrate was dissolved in water. The quantity of iron dissolved was calculated to produce an overall selenium-to-iron ratio in the combustion flame when burning Wyodak coal plus 15 ml/min of doping solution equal to the selenium-to-iron ratio when burning the Ohio coal. A summary of the experiments performed is shown in Table K-17.

To make these tests more efficient, only the supermicron regime was investigated. Therefore, membranes were only collected from impactor stages 6-10 during particle sampling without the inlet preseparator cyclone. Duplicated impactor sets were collected at both Ports 4 and 14 for each set of experimental conditions. The sampling conditions for the particulate samples are listed in Table K-18.

Kentucky SO_2 Doping Tests

A series of experiments were designed and implemented using the East Kentucky Elkhorn/Hazard blend coal to investigate the role of fly ash surface cation sulfation in the partitioning of oxy-anion trace elements during combustion of a low sulfur coal having a high trace element-to-calcium ratio. The experiments are summarized in Table K-19.

In these experiments, SO_2 was blended into the main combustion air. The amount of SO_2 added was adjusted so that the sulfur present in the combustion environment when burning the Kentucky coal was equivalent to the sulfur present in the combustion environment (on a molar basis) when burning the Ohio coal.

To make these tests more efficient, only the supermicron regime was investigated. Therefore, membranes were only collected from impactor stages 6-10 during particle sampling without the inlet preseparator cyclone. Duplicated impactor sets were collected at both Ports 4 and 14 for each set of experimental conditions. The sampling conditions for the particulate samples are listed in Table K-20.

Pittsburgh Ca/Fe Doping Tests

Examination of the cation distributions for the Pittsburgh baseline screening tests (these are provided in Section 3.3.3.4), revealed that the iron and calcium distributions were very similar in shape. As a result, it was not possible to determine whether the oxy-anions (i.e., arsenic, selenium, and antimony) were reacting with one or other of the cations or with both of them.

The Pittsburgh coal has a high (relative to other coal in this study) sulfur content and a low trace element-to-calcium ratio. These experiments were designed to determine if the oxy-anions were more partial to calcium or to iron. In the first set of experiments, we blended pulverized, hydrated lime (Global Stone Tenn Luttrell; see Ref. [129]) into the coal feedstock at the burner inlet to simulate a Pittsburgh coal containing increased calcium in excluded inorganic fractions. The rate of lime addition was adjusted to increase the calcium content in the feedstock by 50 mol %. A summary of the experiments is given in Table K-21.

In the second set of experiments, solid phase iron nitrate nonohydrate was dissolved in water. The quantity of iron dissolved was calculated so that the increase in iron content in the combustion flame when burning Pittsburgh coal plus 10 ml/min of doping solution compared to burning natural Pittsburgh coal was equal on a molar basis to the increase in calcium content produced during the first special set of Pittsburgh coal combustion experiments. A summary of the experiments performed is included in Table K-21.

To make these tests more efficient, only the supermicron regime was investigated. Therefore, membranes were only collected from impactor stages 6-10 during particle sampling without the inlet preseparator cyclone. Duplicated impactor sets were collected at both Ports 4 and 14 for each set of experimental conditions. The sampling conditions for the particulate samples are listed in Table K-22.

3.3.3.3 Results

The purpose of this section is to document the results obtained during all of the experimental work associated with this research project. A detailed discussion and analysis of these results is provided in Section 3.3.3.3.

The first section presents the results from baseline screening experiments conducted with six different coals. These results document the size-segregated partitioning of many trace elements as well as provide the basis for an initial evaluation of the mechanisms controlling trace element partitioning.

A series of hypotheses were developed based on the information garnered from the baseline experimental results. The second section below presents the results from a series of special experiments designed to test the validity of these hypotheses. Four of the six study coals were utilized in these experiments.

Baseline Screening Combustion Experiments

A series of experiments were conducted with each of the six program coals to define the fly ash generated during commercially typical combustion conditions. Each coal was burned using air as the oxidizing medium at a coal feed rate of approximately 2.2 kg/hr. The total oxygen in the combustion environment was manipulated so that the flue gas generated during combustion contained oxygen equivalent to 20 mol% of the total oxygen consumed during combustion (i.e., combustion occurred at a stoichiometric ratio of 1.2 mole O_2 to 1 mole Σfuel molecules) as measured at Port 4 (Port 4b in Phase I) of the furnace.

For each coal, the typical temperature profile, the particle size distribution of fly ash at three sampling locations, and size-dependent elemental distributions for many of the major and trace elements in the fly ash at three sampling locations were determined. The three sampling locations were the same for all three coals. Port 4 (Port 4b in Phase I) was used to represent the condition of the fly ash near the end of the combustion zone (where the combustion zone is defined as that point in the furnace where virtually all of the carbon has oxidized). Port 14 (Port 12 in Phase I) was used to represent the condition of fly ash in the post-combustion zone of the furnace (near the furnace exit in a commercial combustor). The baghouse inlet port was used to represent the condition of fly ash at the particle collection device. Samples from this location can be compared to data obtained from other laboratory, pilot scale, and commercial scale combustors. This provides some insight into the relevance of these results to those obtained at other installations. It should be noted that the baghouse inlet port samples were not obtained in the laminar streamlines of the furnace nor was sampling performed isokinetically. These samples are also extracted after partial segregation of particles from the flue gas.

Sampling at constant flue gas residence time in the post-combustion zone was originally considered. For the four bituminous coals, this sampling basis results in the same sampling locations as were actually used. However, the two lower rank coals have substantially lower carbon contents and thus generate a smaller gas volume for the same mass of coal fed to the burner. Unfortunately it was not possible to sample the flue gas during combustion of these coals at the same residence time in the furnace at the 2.2 kg/hr feed rate. Further, the capability was not available to increase the coal feed rate sufficiently to generate enough flue gas volume to replicate the bituminous coal flue gas velocity in the furnace. Therefore the decision was made to sample lower rank coals at the same physical location as the bituminous coals even though the residence times in the furnace were substantially longer. Residence times at the Port 4 (Port 4b in Phase I) and Port 14 (Port 12 in Phase I) sample locations are shown in Table 3-43.

Table 3-43. Flue Gas Residence Times at Particle Sampling Locations

Coal	Port 4 Residence Time (seconds from burner)	Port 14 Residence Time (seconds from burner)
Pittsburgh Seam	0.5[1]	2.2[2]
Illinois #6	0.5[1]	2.2[2]
Kentucky Elkhorn/Hazard	0.7	2.9
Ohio 5/6/7 Blend	0.7	3.2
Wyodak PRB	1.4	6.6
North Dakota Falkirk	1.9	9.4

1. Port 4b for Phase I experiments
2. Port 12 for Phase I experiments

The following subsections document the results on a coal-by-coal basis. As will be shown in Section 3.3.3.4, some of the key parameters affecting the partitioning of trace elements during pulverized coal combustion are:

- The forms of occurrence of trace elements and major inorganic elements (i.e., calcium, iron, and aluminum) in the feed coal
- The maximum combustion temperature (affected primarily by the carbon content and moisture content of the feed coal)
- The ratio of oxy-anion trace elements (volatilized) to surface active cations (i.e., calcium and iron)
- The ratio of cationic trace elements (volatilized) to surface active anions (i.e., aluminum)
- The sulfur content of the feed coal.

Information contained in the experimental results related to each of these areas is highlighted for each coal in the information that follows. A detailed analysis of the results on a trace element-by-trace element basis is provided in Section 3.3.3.4.

Pittsburgh Bituminous Seam Coal

The Pittsburgh seam coal is a bituminous coal. This coal has the highest carbon content of all of the coals tested in this program. The sulfur content is intermediate; lower than the Illinois #6 and Ohio sulfur contents but higher than the Kentucky, Wyodak, and North Dakota sulfur contents. The moisture content is low at 1.4 wt%. The proximate/ultimate analysis of this coal as determined by others [7] is provided in Table 3-44. Characterization of the major ash components (as determined by others) is provided in Table 3-45 [7]. The elemental composition of the Pittsburgh coal ash (as determined by others) is provided in Table 3-46. The silica content is lower than the Illinois #6, Kentucky, and Wyodak coals but higher than the Ohio and North Dakota coals. Aluminum (as Al_2O_3) accounts for almost 23 wt% of the ash. The ratio of Fe_2O_3 to CaO is 4.3 by weight. The arsenic content is higher than most of the coals studied but the selenium content is the lowest. The antimony content is also one of the lowest among the coals studied.

Table 3-44. Proximate/Ultimate Analysis of the Pittsburgh Seam Coal*

Proximate	**wt%**
Fixed Carbon	61.99
Volatile Matter	30.22
Moisture	1.44
Ash	7.01
Heating Value (kJ/kg)	
Ultimate	
Carbon	76.62
Hydrogen	4.80
Nitrogen	1.48
Sulfur	1.64
Oxygen	6.91
Chlorine	0.098
Moisture	1.44
Ash	7.01

* from Ref. [7].

Table 3-45. Pittsburgh Seam Coal
Ash Characterization [1]

Component	wt%
SiO_2	42.92
Al_2O_3	22.87
Fe_2O_3	19.18
TiO_2	1.08
CaO	4.51
MgO	0.97
Na_2O	1.28
K_2O	1.21
SO_3	5.40
P_2O_5	0.57

1. Ref. [7]

Table 3-46. Pittsburgh Seam Coal Ash Elemental Composition

a) Mineralogical Characterization[1]

CCSEM[2] Determinations	wt %
Quartz	11
Kaolinite	9
Illite	13
Montmorillonite	0.5
Misc. Silicates	29
Pyrite	18
Siderite	0.5
Calcite	6
Misc. Carbonates	2
Unclassified	11

1. Ref. [7]
2. CCSEM = computer controlled scanning electron microscopy

b) Trace Element Forms of Occurrence[1]

Element	Form	Wt%
Arsenic	Organic	0
	Mono-sulfides	10
	Silicates	0
	Pyrite/sulfides	80
Selenium	Organic	5
	Mono-sulfides	5
	Silicates	0
	Pyrite/sulfides	90
Antimony	Organic	55
	Mono-sulfides	10
	Silicates	15
	Pyrite/sulfides	20

1. Determine by selective leaching, from Ref. [7]

Table 3-46. (Continued) Pittsburgh Seam Coal Ash Elemental Composition
c) Elemental Analysis

Chemical Composition	By NAA (ppmw)	By ICP-MS (ppmw)	By ICP-AES (ppmw)
Ag	—	0.15	—
As	4.1	4.75	—
Au	9.5×10^{-4}	0.73	—
B	—	—	29.9
Ba	110	—	116.9
Be	—	—	0.6
Bi	—	0.15	—
Br	17	—	—
Cd	0.06	0.06	—
Ce	8.8	—	—
Co	2.5	—	2.4
Cr	13	—	8.8
Cs	0.55	0.59	—
Cu	—	—	5.3
Eu	0.2	—	—
Fe	8220	—	—
Ga	—	3.58	—
Ge	—	3.07	—
Hg	0.11	—	0.09[1]
La	4.5	—	—
Li	—	—	5.4
Lu	0.063	—	—
Md	—	2.08	—
Mn	—	—	13.1
Mo	0.85	—	—
Na	600	—	—
Nb	—	1.46	—
Ni	—	—	6.6
Pb	—	3.14	—
Rb	8	7.15	—
Sb	0.26	0.29	—
Sc	1.8	—	1.9
Se	0.62	—	0.96[2]
Sm	0.78	—	—
Sn	—	0.73	—
Sr	160	—	124.1
Te	—	0.15	—
Th	1.2	—	1.2
Tl	—	0.15	—
U	0.31	0.41	—
V	—	—	11.7
Y	—	—	2.9
Zn	17	—	6.1
Zr	—	—	21.2

1. By Cold Vaporization Method
2. By Hydride Method

Temperature Profile

The temperature profile of the Pittsburgh seam coal, obtained using the Phase I furnace in the 1997 test program, is shown in Figure 3-74. The maximum combustion temperature, interpolated from Figure 3-81 is 1600 K. The temperatures of the Port 4b and Port 12 sampling locations are also shown in Figure 3-81.

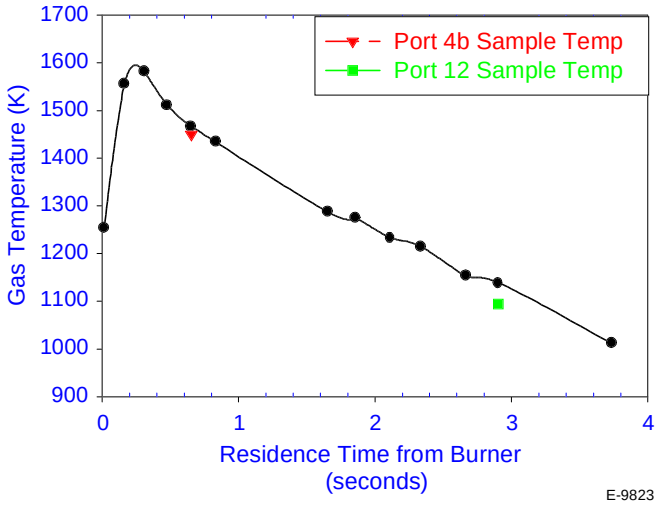

Figure 3-81. Typical temperature profile of the Pittsburgh seam coal under baseline screening experimental conditions.

Size-Segregated Distributions

Size-segregated BLPI samples were used to determine the total ash particle size distribution (PSD) at all three sampling locations. The typical PSD was determined from the average of all sample sets considered to be representative of baseline combustion conditions. Impactor distribution data is commonly displayed in a differential distribution format. For this work, the method documented by Markowski and Ensor [131] was used. In this method the mass concentration of ash collected on a given impactor stage (g/Nm^3) is divided by the difference between the $\log_{10}$ of the particle size of two adjacent impactor stages ($\log_{10}$[microns]).

Differential ash PSDs for the Pittsburgh seam coal at all three sampling locations are shown in Figure 3-82. For this coal, the Port 4b sampling location is 0.5 residence seconds below the burner and the Port 12 sampling location is 2.2 residence seconds below the burner. The distributions shown in Figure 3-82 can be divided into three regions (with indistinct transition regions that vary somewhat depending on the coal and sampling location): material that was present in the furnace in the vapor phase, material associated with submicron particles, and material associated with supermicron particles. For the sampling system employed in this work, Davis et al. [132] have demonstrated that (for flue gases generated by the combustion of gas flames doped with 100 ppmv semi-volatile metals) the smallest particle sizes (below about 0.1 microns) in the profile primarily represent vapor-phase material that nucleates in the sample probe.

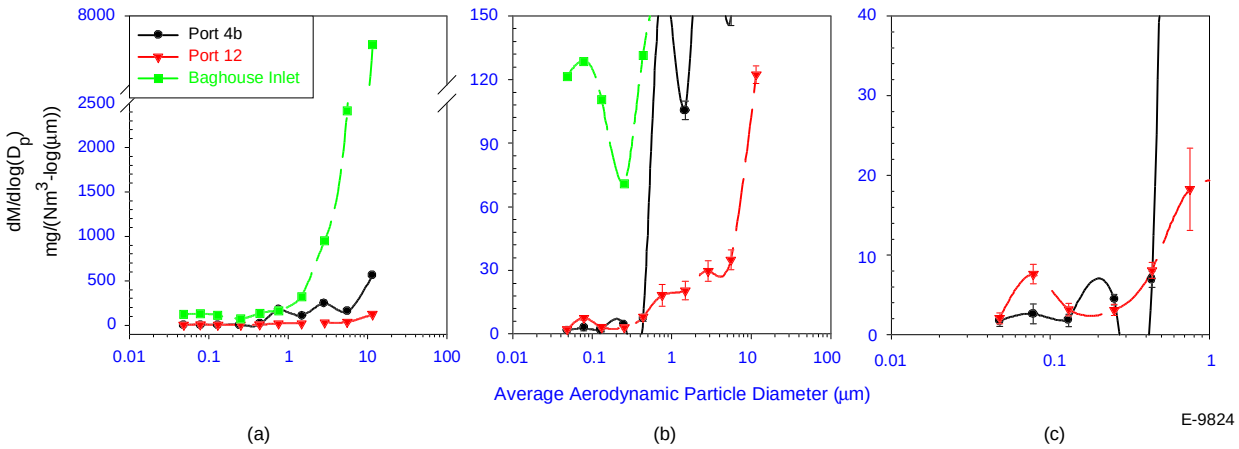

Figure 3-82. Total ash particle size distributions for the Pittsburgh seam coal sampled at three locations: a) total PSD, b) expanded supermicron PSD, c) expanded submicron PSD.

Caution must be taken in interpreting the results from the baghouse inlet port PSD since partial removal of particles in two upstream traps has occurred. These traps are expected to preferentially remove larger particles.

The Port 4b and Port 12 PSDs both show an intermediate maximum in the supermicron region at around 3 µm average aerodynamic particle diameter and an intermediate maximum in the vapor phase region at around 0.08 µm average aerodynamic particle diameter. This intermediate maximum suggests that there are three solid phase modes of occurrence – 1) bulk, supermicron fly ash; 2)micron-sized fragmentation ash; and 3) submicron fume – rather than the two modes described in Section 2.1. This additional mode of occurrence may affect trace element partitioning (see Section 3.3.3.4).

Sample sets that most closely duplicated the typical PSD were selected for elemental analysis. For the samples from Ports 4b and 12, analyses of all species were performed on a single sample set at each location by INAA at MIT. Duplicate sample sets from the baghouse inlet sampling location were analyzed by AAS/AES/GFAA at Arizona. The average of the results from the two in-house sample sets was used to generate typical elemental distributions for the baghouse inlet sampling location.

Differential elemental distributions can also be calculated using the method of Markowski and Ensor [131]. These distributions were generated for calcium, iron, arsenic, selenium, antimony, and cobalt. The major elemental differential distributions at all three sampling locations are shown in Figure 3-83 while the trace elemental differential distributions at all three sampling locations are shown in Figure 3-84. Notice in Figure 3-83 that the distributions of calcium and iron are very similar in shape. There is a distinctive maximum for all elements at around 1 µm average aerodynamic particle diameter at both Port 4b and Port 12 sampling locations related to the micron fragmentation mode.

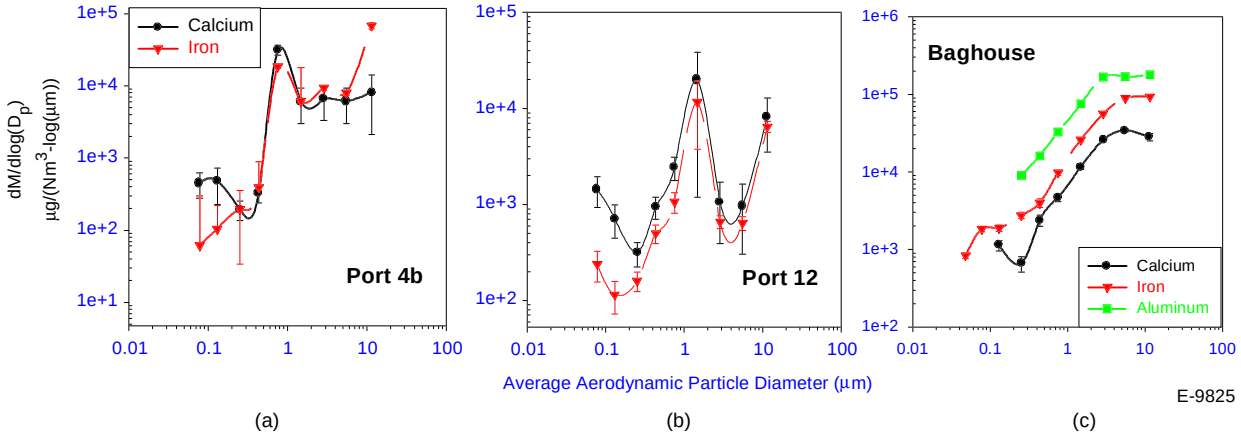

Figure 3-83. Major element differential distributions for the Pittsburgh seam coal sampled at three locations: a) Port 4b - 0.5 residence seconds, b) Port 12 – 2.2 residence seconds, c) baghouse inlet.

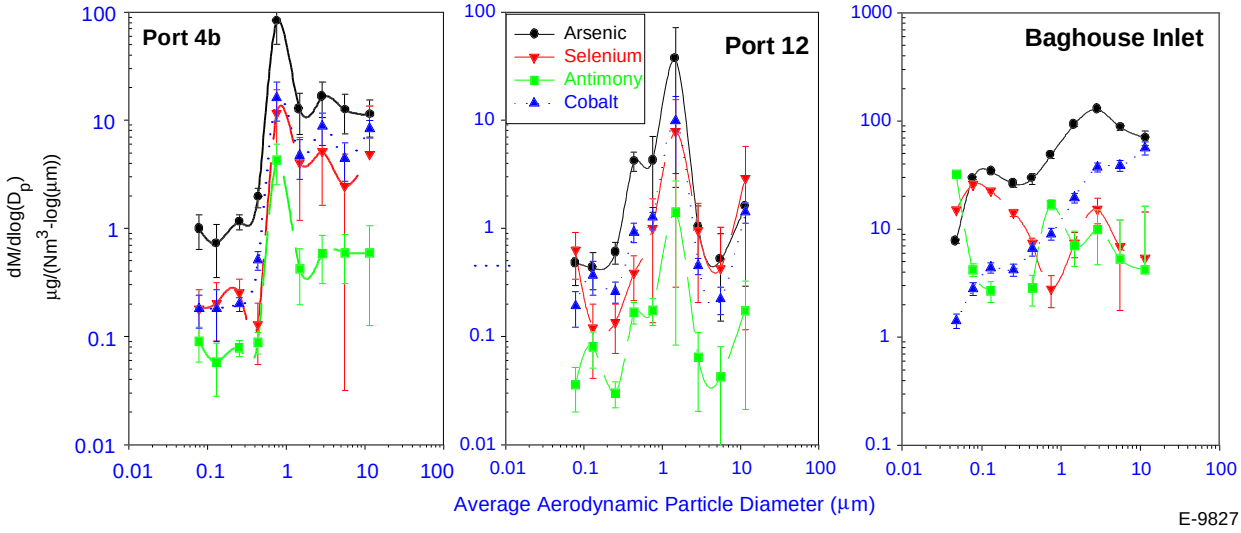

Figure 3-84. Trace element differential distributions for the Pittsburgh seam coal sampled at three locations: a) Port 4b - 0.5 residence seconds, b) Port 12 – 2.2 residence seconds, c) baghouse inlet.

Calculating an enrichment factor can normalize the elemental concentrations on each impactor stage. There are a number of commonly used methods for calculating enrichment factors from impactor distribution data. In this work the method described by Haynes et al. [11] was chosen. This method is based on referencing the elemental mass collected on each individual impactor stage to the mass average concentration of the element for all impactor stages collected. The enrichment factor, $E_{i,x}$ is defined as:

$$E_{i,x} = M_{i,x} / (\Sigma_N M_{i,x} / N) \quad (3\text{-}14)$$

where: $E_{i,x}$ = Enrichment factor of element i on impactor stage x
$M_{i,x}$ = Mass of element i collected on impactor stage x
$\Sigma_N M_{i,x}$ = Sum of mass of element i collected on all impactor stages
N = Number of impactor stages

Port 4b enrichment factors for arsenic, selenium, antimony, and cobalt are shown in Table 3-47 while Port 12 enrichment factors are shown in Table 3-48. It is not possible to calculate meaningful enrichment factors for elements in samples from the baghouse inlet sample port. A significant portion of the supermicron fly ash has settled out of the flue gas prior to this sampling location. Therefore it is not possible to determine the true mass average concentration of any element in the fly ash.

Table 3-47. Enrichment Factors (E_f) for Key Elements in Pittsburgh Seam Fly Ash Sampled at Port 4b

Aerodynamic 50% Particle Cutoff Diameter (microns)

Element	**0.03**	**0.06**	**0.09**	**0.17**	**0.34**	**0.54**	**0.98**	**1.98**	**3.77**	**7.33**	**15.7**
As		4.54	11.14	3.33	5.66	3.58	1.33	1.21	1.13	0.19	0.18
Se		3.43	12.96	3.06	1.56	2.08	1.76	1.57	0.92	0.34	0.45
Sb		4.66	9.98	2.55	2.89	2.07	0.50	0.48	0.60	0.11	0.11
Co		2.38	7.92	1.69	4.23	2.00	1.42	1.84	1.15	0.41	0.93

Table 3-48. Enrichment Factors (E_f) for Key Elements in Pittsburgh Seam Fly Ash Sampled at Port 12

Aerodynamic 50% Particle Cutoff Diameter (microns)

Element	**0.03**	**0.06**	**0.09**	**0.17**	**0.34**	**0.54**	**0.98**	**1.98**	**3.77**	**7.33**	**15.7**
As		0.55	1.19	1.68	4.56	2.03	15.59	0.31	0.13	0.11	0.09
Se		2.27	1.03	1.18	1.31	1.50	10.43	0.89	0.33	0.65	0.99
Sb		0.40	2.14	0.81	1.75	0.81	5.75	0.19	0.10	0.12	0.08
Co		0.57	2.64	1.88	2.59	1.57	10.81	0.35	0.14	0.26	0.69

All four trace elements show enrichment in the submicron particle region compared to the supermicron particles at both the Port 4b and Port 12 sample locations. This implies that the primary mechanism for partitioning to submicron particles is volatilization of the trace element during combustion and redeposition onto fly ash surfaces. This will be discussed in more detail in Section 3.3.3.4.

Trace Element Solubility

One sample set from the Port 4b sampling location and one sample set from the Port 12 sampling location were selected for a solubility study. Impactor stages 3, 4, and 5 (representing the submicron region) and stages 8, 9, and 10 (representing the supermicron region) from each sample set were subjected to the leaching protocol described by Seames [133]. The solubility of arsenic, selenium, antimony, and cobalt in the pH 2.8 EPA Method 1310 solution and the pH 4.9 EPA Method 1310 solution were determined by GFAA analysis at Arizona. Solubility results for all elements in both leaching solutions at both sampling locations are shown in Table 3-49.

Table 3-49. The Solubility of Key Pittsburgh Seam Fly Ash Elements in EPA TCLP Leaching Solutions Sampled at Port 4b and Port 12

Element	Submicron Size % Soluble at pH 4.9	Submicron Size % Soluble at pH 2.9	Supermicron Size % Soluble at pH 4.9	Supermicron Size % Soluble at pH 2.9
Port 4b				
Arsenic	45%	66%	42%	67%
Selenium	42%	67%	50%	65%
Antimony	16%	85%	52%	80%
Cobalt	52%	80%	19%	53%
Port 12				
Arsenic	20%	41%	28%	37%
Selenium	29%	51%	0%	0%
Antimony	12%	87%	9%	86%
Cobalt	25%	45%	9%	24%

Antimony is highly soluble in both leaching fluids. Arsenic, selenium, and cobalt in the Port 4b particles are more soluble than those collected at Port 12. This may indicate a difference in the form of occurrence of the trace elements at different locations in the furnace. For arsenic and antimony there is no clear difference in the solubility in the submicron versus supermicron particles. Selenium and cobalt show more difference between the two size regimes. This difference may also indicate a difference in the partitioning mechanism. A discussion of the possible forms of occurrence related to these solubility values is provided in Section 3.3.3.4.

Illinois #6 Bituminous Coal

The Illinois #6 coal is also a bituminous coal. The proximate/ultimate analysis of this coal is provided in Table 3-50. The carbon content is higher than the Wyodak and North Dakota coals but lower than the other three bituminous coals – Pittsburgh, Kentucky, and Ohio.

Table 3-50. Proximate/Ultimate Analysis of the Illinois #6 Coal[1]

Proximate	wt%
Fixed Carbon	53.16
Volatile Matter	33.27
Moisture	3.31
Ash	10.26
Ultimate	
Carbon	67.70
Hydrogen	4.73
Nitrogen	1.18
Sulfur	3.60
Oxygen	9.50
Chlorine	0.034
Moisture	3.31
Ash	10.26

1. From Ref. [7]

The sulfur content is the highest of all the coals studied. The moisture content is low at 3.3 wt%. This combination of low carbon content and high sulfur content will tend to reduce the availability of action cation sites on fly ash particle surfaces. This may reduce the fraction of trace elements that partition due to a surface reaction mechanism. In the evaluation shown in Section 3.3.3.4 this will be revealed by less definition in the particle size dependence modeling and the trace element to cation correlation analysis compared to the Pittsburgh and Kentucky coals.

Characterization of the major ash components is provided in Table 3-51. The elemental composition of the Illinois #6 coal ash is provided in Table 3-52. The silica content is lower than the Kentucky coal but higher than all of the other coals studied. Aluminum (as Al_2O_3) accounts for 17 wt% of the ash. The ratio of Fe_2O_3 to CaO is 5.0 by weight. The arsenic and selenium content is intermediate than most of the coals studied but the antimony content is one of the lowest among the coals studied.

Temperature Profile

The temperature profile of the Illinois #6 coal, obtained using the Phase I furnace in the 1997 test program, is shown in Figure 3-85. The maximum combustion temperature, interpolated from Figure 3-85, is 1600 K.

Table 3-51. Illinois #6 Coal Ash Characterization[1]

Component	wt%
SiO_2	44.38
Al_2O_3	17.35
Fe_2O_3	19.80
TiO_2	0.91
CaO	4.00
MgO	0.85
Na_2O	0.63
K_2O	1.80
SO_3	4.62
P_2O_5	0.12

1. From Ref. [7]

Table 3-52. Illinois #6 Coal Ash Elemental Composition

a) Mineralogical Characterization[1]

CCSEM[2] Determinations	wt %
Quartz	13
Kaolinite	5
Illite	11
Misc. Silicates	23
Pyrite	30
Misc. Sulf.	2
Siderite	0.5
Calcite	3
Misc. Carbonates	1
Unclassified	12

1. From Ref. 7.
2. CCSEM = computer controlled scanning electron microscopy

Table 3-52. (Continued) Illinois #6 Coal Ash Elemental Composition

b) Trace Element Forms of Occurrence[3]

Element	Form	Wt%
Arsenic	Organic	0
	Mono-sulfides	20
	Silicates	0
	Pyrite/sulfides	60
Selenium	Organic	50
	Mono-sulfides	0
	Silicates	0
	Pyrite/sulfides	50
Antimony	Organic	
	Mono-sulfides	
	Silicates	
	Pyrite/sulfides	

3. Determine by selective leaching, from Ref. 7.

Table 3-52. (Continued) Illinois #6 Coal Ash Elemental Composition

c) Elemental Analysis

Chemical Composition	By NAA (ppmw)	By ICP-MS (ppmw)	By ICP-AES (ppmw)
Ag	—	0.21	—
As	2.7	3.09	—
Au	5.1×10^{-4}	1.03	—
B	—	—	154.5
Ba	52	—	43.3
Be	—	—	1.1
Bi	—	0.21	—
Br	3.7	—	—
Cd	0.15	0.41	—
Ce	9.3	—	—
Co	0.6	—	3.6
Cr	14	—	18.5
Cs	0.99	1.24	—
Cu	—	—	8.2
Eu	0.19	—	—
Fe	13700	—	—
Ga	—	3.81	—
Ge	—	5.36	—
Hg	0.22	—	—
La	4.7	—	—
Li	—	—	7.8
Lu	0.0054	—	—
Md	2.08	—	—
Mn	—	—	37.1
Mo	4.9	—	—
Na	400	—	—
Nb	—	2.06	—
Ni	—	—	12.4
Pb	—	13.39	—
Rb	13	15.45	—
Sb	0.38	0.44	—
Sc	2.2	—	2.7
Se	2.2	—	2.9[4]
Sm	0.9		—
Sn		1.03	—
Sr	nd[5]	—	27.8
Te		0.21	—
Th	0.095	—	1.5
Tl	—	0.67	—
U	nd	1.75	—
V	—	—	25.8
Y	—	—	4.5
Zn	70	—	73.1
Zr	—	—	29.9

4. By Hydride Method
5. nd = below detection limit

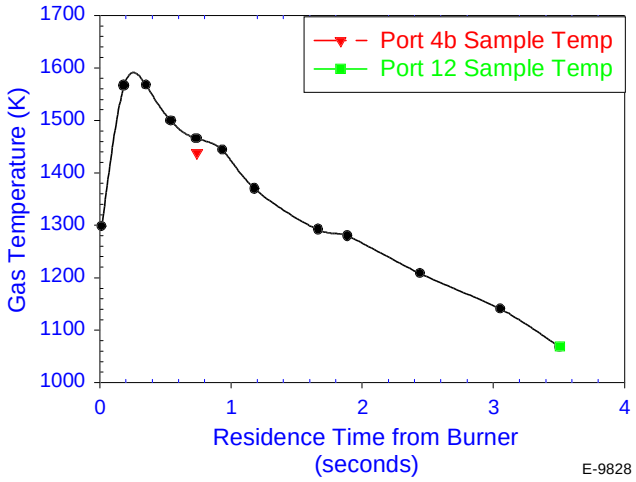

Figure 3-85. Typical temperature profile of the Illinois #6 coal under baseline screening experimental conditions.

Size-Segregated Distributions

Size-segregated BLPI samples were used to determine the total ash PSD at all three sampling locations. The typical PSD was determined from the average of all sample sets considered to be representative of baseline combustion conditions. Differential ash PSDs for the Illinois #6 coal at all three sampling locations are shown in Figure 3-86. For this coal, the Port 4b sampling location is 0.5 residence seconds below the burner and the Port 12 sampling location is 2.2 residence seconds below the burner. Like the Pittsburgh coal, both the Port 4b and Port 12 PSDs show an intermediate maximum in the supermicron region – at 3 μm average aerodynamic particle diameter for Port 4b and approximately 1.5 μm for Port 12 – indicating that a fragmentation particle mode is generated in addition to the submicron fume and bulk supermicron particle fractions.

Sample sets that most closely duplicated the typical PSD were selected for elemental analysis. For the samples from Ports 4b and 12, analyses of all species were performed on a single sample set at each location by INAA at MIT. Duplicate sample sets from the baghouse inlet sampling location were analyzed by AAS/AES/GFAA at Arizona.

Differential elemental distributions were calculated using the method of Markowski and Ensor [131] for calcium, iron, aluminum, arsenic, selenium, antimony, and cobalt. The major elemental differential distributions at all three sampling locations are shown in Figure 3-87 while the trace elemental differential distributions at all three sampling locations are shown in Figure 3-88. The shape of the calcium and iron distributions have more variation between them compared to the Pittsburgh distributions; particularly in the submicron region. The arsenic, selenium, and antimony distributions are similar in shape in the submicron and supermicron regions (variations are more pronounced in the vapor phase region below 1 μm) indicating that the partitioning mechanisms are probably similar. However, the cobalt distribution at Port 12 is distinctly different from the other trace elements suggesting a different mechanism may dominate cobalt partitioning.

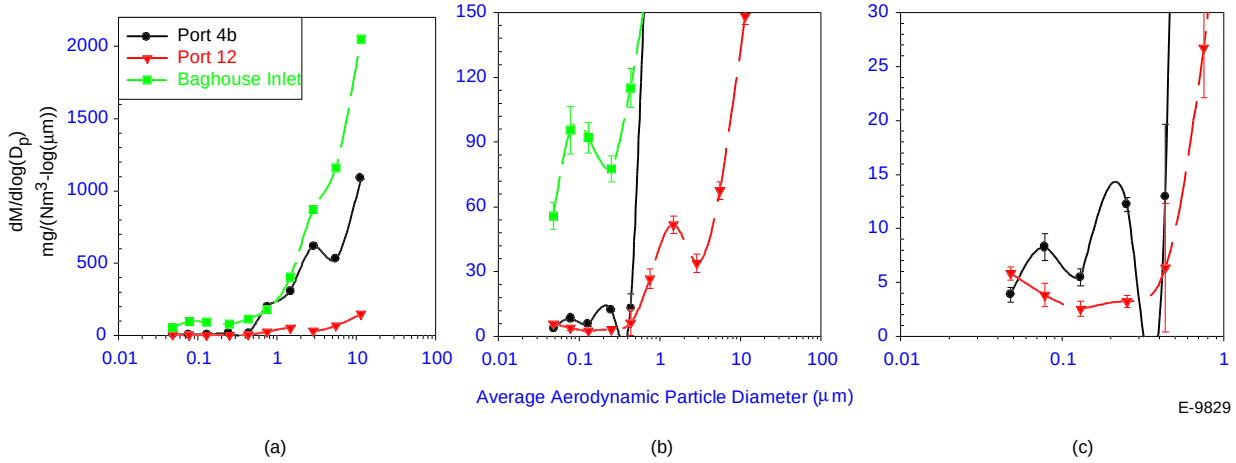

Figure 3-86. Total ash particle size distributions for the Illinois #6 coal sampled at three locations: (a) total PSD, (b) expanded supermicron PSD, (c) expanded submicron PSD.

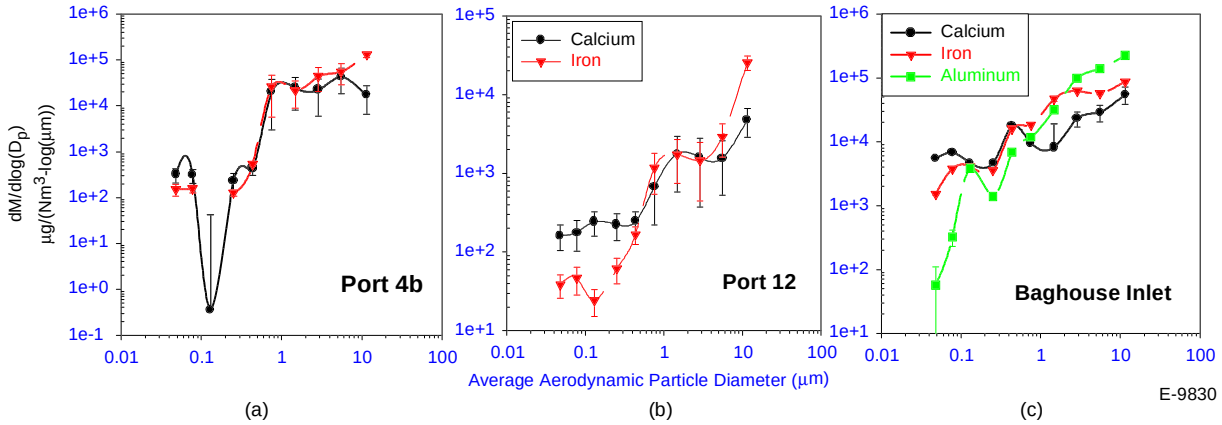

Figure 3-87. Major element differential distributions for the Illinois #6 coal sampled at three locations: (a) port 4b - 0.5 residence seconds, (b) port 12 – 2.2 residence seconds, (c) baghouse inlet.

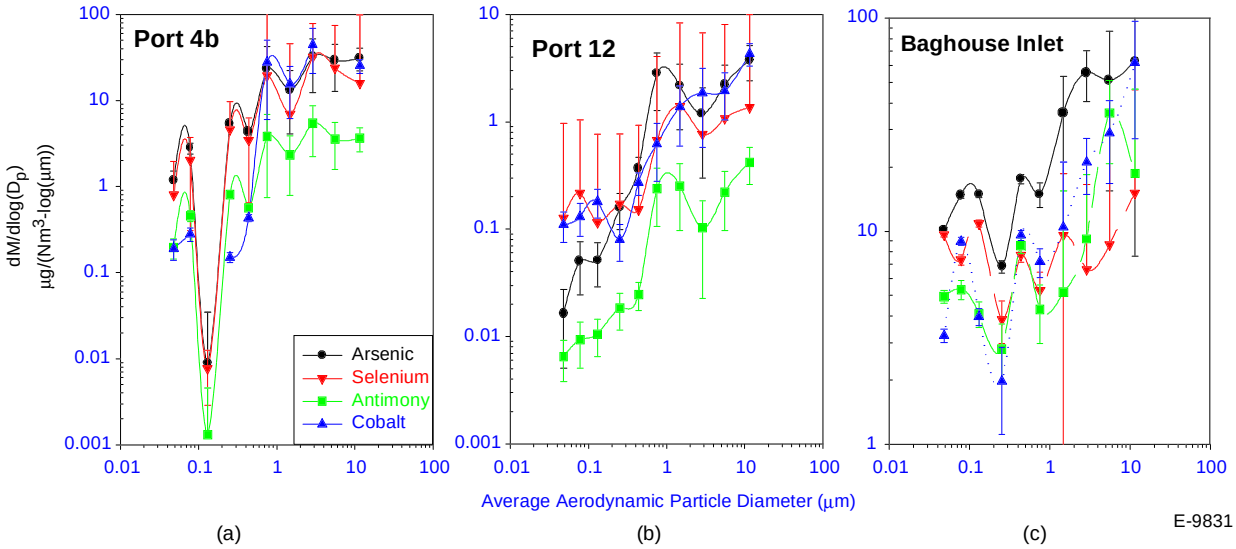

Figure 3-88. Trace element differential distributions for the Illinois #6 coal sampled at three locations: (a) Port 4b - 0.5 residence seconds, (b) Port 12 – 2.2 residence seconds, (c) baghouse inlet.

Calculating an enrichment factor can normalize the elemental concentrations on each impactor stage. Port 4b enrichment factors for arsenic, selenium, antimony, and cobalt are shown in Table 3-53 while Port 12 enrichment factors are shown in Table 3-54. All four trace elements are enriched on the submicron particles from the Port 12 sample location. As, Se, and Sb are enriched on the submicron particles from the Port 4b sample. These results suggest that the primary mechanism for partitioning to submicron particles is volatilization of the trace element during combustion and redeposition onto fly ash surfaces. (This will be discussed in more detail in Section 3.3.3.4.) A likely outlier Co sample at impactor stage 9 precludes determination of meaningful Co enrichment data at Port 4b.

Table 3-53. Enrichment Factors (E_f) for Key Elements in Illinois #6 Fly Ash Sampled at Port 4b

Aerodynamic 50% Particle Cutoff Diameter (microns)

Element	**0.03**	**0.06**	**0.09**	**0.17**	**0.34**	**0.54**	**0.98**	**1.98**	**3.77**	**7.33**	**15.7**
As	48.27	52.76	0.26	68.06	52.18	17.81	6.65	8.14	8.58	4.51	2.79
Se	40.08	47.03	0.27	71.93	51.30	18.27	4.33	10.00	8.69	2.82	1.28
Sb	52.43	57.31	0.25	68.17	44.70	19.34	7.73	9.08	6.99	3.47	1.72
Co	0.41	0.29	0.00	0.10	0.28	1.16	0.42	0.61	626.46	0.20	0.15

Table 3-54. Enrichment Factors (E_f) for Key Elements in Illinois #6 Fly Ash Sampled at Port 12

Aerodynamic 50% Particle Cutoff Diameter (microns)

Element	0.03	0.06	0.09	0.17	0.34	0.54	0.98	1.98	3.77	7.33	15.7
As	0.24	0.56	0.65	3.05	2.61	4.39	1.50	1.41	0.96	0.61	0.25
Se	3.38	4.27	2.59	5.85	1.90	1.87	1.72	1.60	0.83	0.39	0.12
Sb	0.75	0.80	1.02	2.75	1.34	2.89	1.36	0.94	0.74	0.53	0.36
Co	1.99	1.65	2.64	1.92	2.23	1.15	1.15	2.58	1.00	0.83	0.57

Kentucky Elkhorn/Hazard Bituminous Coal Blend

The East Kentucky Elkhorn/Hazard coal is a bituminous coal which has a higher carbon content than all of the other coals tested in this program except for the Pittsburgh seam coal. The sulfur content is the lowest of the bituminous coals studied. The moisture content is low at 2.3 wt%. The combination of high carbon content and low sulfur content is expected to improve the availability of action cation sites compared to other coals being studied in this program. The proximate/ultimate analysis of this coal is provided in Table 3-55.

Table 3-55. Proximate/Ultimate Analysis of the Kentucky Coal[1]

Proximate	wt%
Fixed Carbon	56.46
Volatile Matter	33.80
Moisture	2.33
Ash	7.41
Ultimate	
Carbon	74.87
Hydrogen	4.59
Nitrogen	1.43
Sulfur	0.82
Oxygen	8.38
Chlorine	0.17
Moisture	2.33
Ash	7.41

1. From Ref. 7

Characterization of the major ash components is provided in Table 3-56 and the elemental composition of the ash is provided in Table 3-57. The silica content is the highest of all of the coals studied. Aluminum (as Al_2O_3) accounts for over 34 wt% of the ash. There is substantially less iron and calcium in this coal compared to the Pittsburgh and Illinois #6 coals. The ratio of Fe_2O_3 to CaO is also lower at 2.8 by weight. The arsenic, selenium, and antimony concentrations are higher than most of the coals studied.

Table 3-56. Kentucky Coal Ash Characterization[1]

Component	wt%
SiO_2	55.83
Al_2O_3	34.27
Fe_2O_3	5.18
TiO_2	1.71
CaO	1.84
MgO	0.60
Na_2O	0.32
K_2O	1.53
SO_3	1.45
P_2O_5	0.23

1. From Ref. 7

Table 3-57. Kentucky Coal Ash Elemental Composition

a) Mineralogical Characterization[1]

CCSEM[2] Determinations	wt %
Quartz	12
Kaolinite	26
Illite	15
Misc. Silicates	29
Pyrite	6
Misc. Sulf.	0.5
Siderite	1
Calcite	1
Misc. Carbonates	2
Misc. Phosphates	2
Unclassified	5

1. From Ref. 7
2. CCSEM = computer controlled scanning electron microscopy

Table 3-57. (Continued) Kentucky Coal Ash Elemental Composition

b) Trace Element Forms of Occurrence[3]

Element	Form	Wt%
Arsenic	Organic	0
	Mono-sulfides	30
	Silicates	5
	Pyrite/sulfides	35
Selenium	Organic	65
	Mono-sulfides	15
	Silicates	0
	Pyrite/sulfides	20
Antimony	Organic	70
	Mono-sulfides	5
	Silicates	15
	Pyrite/sulfides	5

3. Determine by selective leaching, from Ref. 7

Table 3-57. (Continued) Kentucky Coal Ash Elemental Composition

c) Elemental Analysis

Chemical Composition	By NAA (ppmw)	By ICP-MS (ppmw)	By ICP-AES (ppmw)
Ag	—	0.16	—
As	4	5.12	—
Au	9.8e-4	0.8	—
B	—	—	14.4
Ba	130	—	112
Be	—	—	3
Bi	—	0.16	—
Br	25	—	—
Cd	0.31	0.06	—
Ce	27	—	—
Co	6.2	—	7
Cr	20	—	14.4
Cs	0.45	0.48	—
Cu	—	—	19.2
Eu	0.37	—	—
Fe	2970	—	—
Ga	—	8	—
Ge	—	3.84	—
Hg	0.13	—	0.05[4]
La	14	—	—
Li	—	—	18.4
Lu	0.24	—	—
Md	—	2.08	--
Mn	—	—	13.6
Mo	4	—	—
Na	340	—	—
Nb	—	3.2	—
Ni	—	—	12
Pb	—	8.8	—
Rb	5.1	6.56	—
Sb	1	1.2	—
Sc	3.9	—	3.8
Se	3.1	—	4.5[5]
Sm	2.5	—	—
Sn	—	0.8	—
Sr	120	—	136
Te	—	0.16	—
Th	4.3	—	3.5
Tl	—	0.32	—
U	1.9	2.16	—
V	—	—	23.2
Y	—	—	12.8
Zn	18	—	6.2
Zr	—	—	56

4. By Cold Vaporization Method
5. By Hydride Method

Temperature Profile

The temperature profile of the Kentucky coal obtained using the Phase II furnace in the 1999 test program is shown in Figure 3-89. The maximum combustion temperature, interpolated from Figure 3-89, is 1665 K.

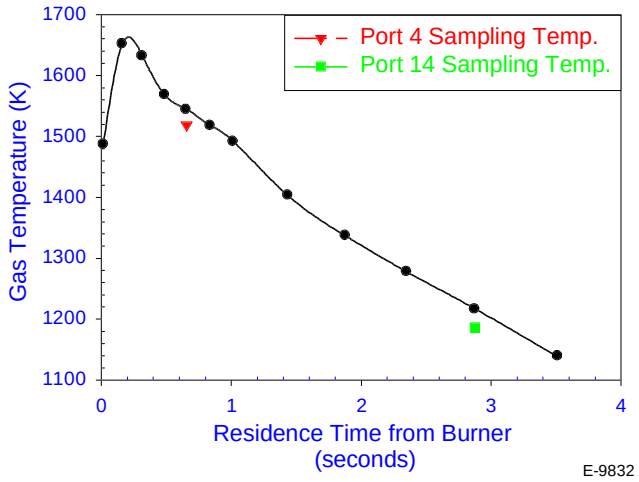

Figure 3-89. Typical temperature profile of the Kentucky coal under baseline screening experimental conditions.

Size-Segregated Distributions

The typical PSD at each sampling location was determined from the average of all size-segregated BLPI sample sets considered to be representative of baseline combustion conditions. Differential ash PSDs for the Kentucky coal at all three sampling locations are shown in Figure 3-90. For this coal, the Port 4 sampling location is 0.7 residence seconds below the burner and the Port 14 sampling location is 2.9 residence seconds below the burner. An intermediate maximum is shown in the supermicron region for the Port 4 sample at around 3 μm but not for the Port 14 sample.

Sample sets that most closely duplicated the typical PSD were selected for elemental analysis. Triplicate sample sets from the Port 4, Port 14, and baghouse inlet sampling locations were analyzed by AAS/AES/GFAA at Arizona.

Differential elemental distributions were calculated using the method of Markowski and Ensor [131] for calcium, iron, aluminum, arsenic, selenium, antimony, and cobalt. The major elemental differential distributions at all three sampling locations are shown in Figure 3-91. while the trace elemental differential distributions at all three sampling locations are shown in Figure 3-92. Calcium, iron, and aluminum distributions shown distinct differences between them. The arsenic and selenium distributions at Ports 4 and 14 are very similar indicating similar partitioning mechanisms. The antimony distributions are more similar to arsenic and selenium than the cobalt distributions.

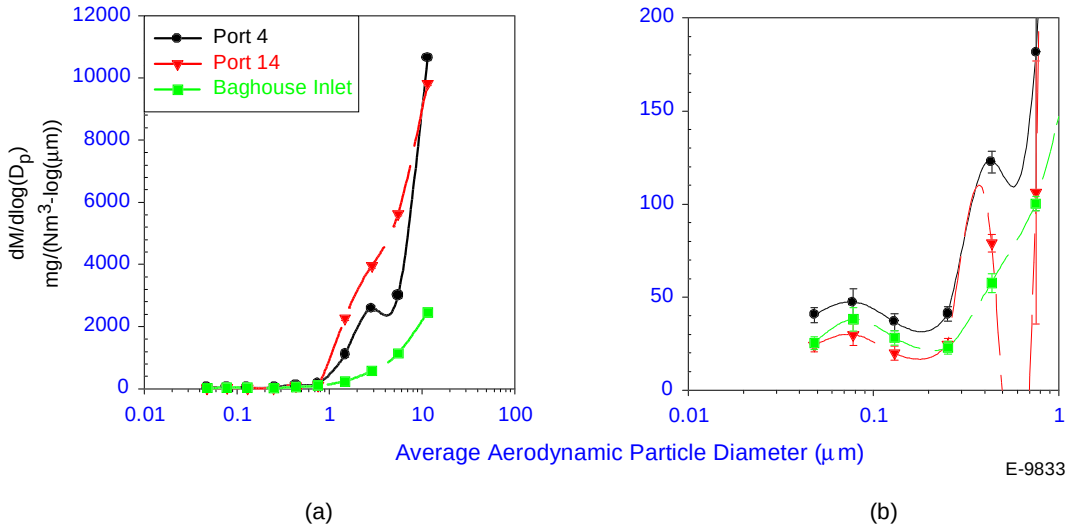

Figure 3-90. Total ash particle size distributions for the Kentucky coal sampled at three locations: (a) total PSD, (b) expanded submicron PSD.

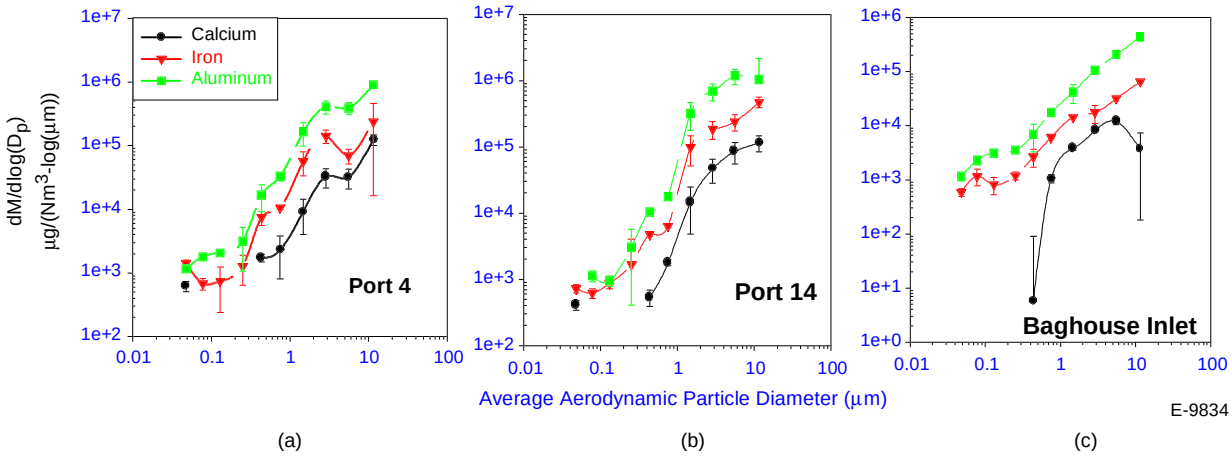

Figure 3-91. Major element differential distributions for the Kentucky coal sampled at three locations: (a) Port 4 - 0.7 residence seconds, (b) Port 14 – 2.9 residence seconds, (c) baghouse inlet.

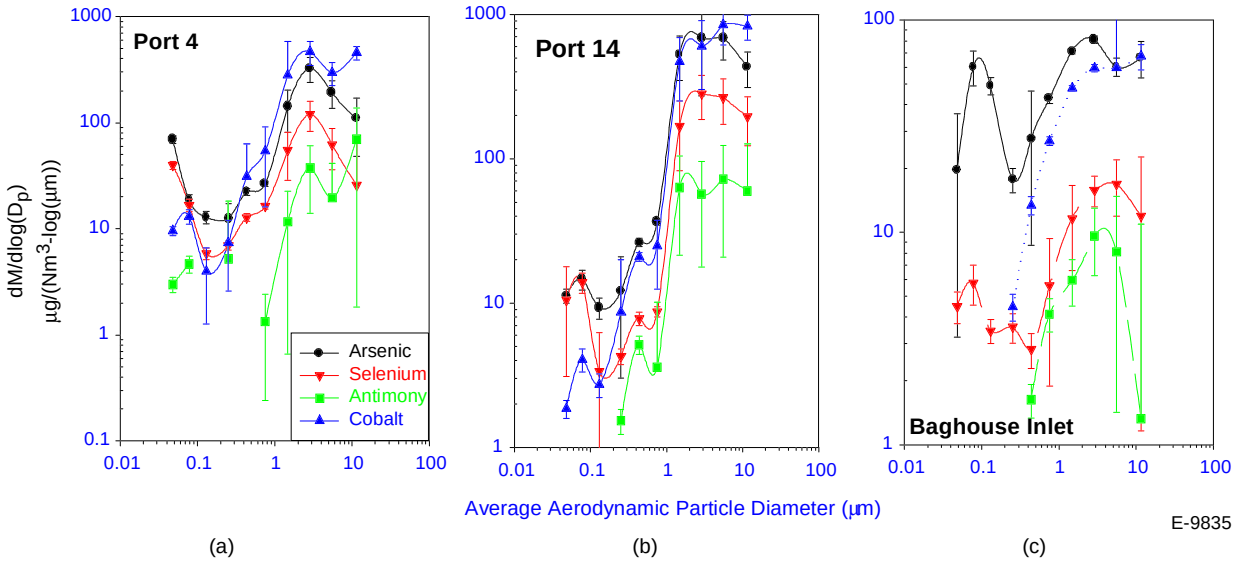

Figure 3-92. Trace element differential distributions for the Kentucky coal sampled at three locations: (a) Port 4 - 0.7 residence seconds, (b) Port 14 – 2.9 residence seconds, (c) baghouse inlet.

Calculating an enrichment factor can normalize the elemental concentrations on each impactor stage. Port 4 enrichment factors for arsenic, selenium, antimony, and cobalt are shown in Table 3-58 while Port 14 enrichment factors are shown in Table 3-59. All four trace elements are enriched in the submicron particles at both Port 4 and 14 sample locations compared to the supermicron particles. This implies that the primary mechanism for partitioning to submicron particles is volatilization of the trace element during combustion and redeposition onto fly ash surfaces.

Trace Element Solubility

Selected impactor stages (3, 4, and 5 representing the submicron region and 8, 9, and 10 representing the supermicron region) were subjected to the leaching protocol described by Seames [133]. The solubility of arsenic, selenium, antimony, and cobalt in the pH 2.8 EPA Method 1310 solution and the pH 4.9 EPA Method 1310 solution were determined by GFAA analysis at Arizona. Solubility results for all elements in both leaching solutions at both sampling locations are shown in Table 3-60.

Table 3-58. Enrichment Factors (E_f) for Key Elements in Kentucky Fly Ash Sampled at Port 4

Aerodynamic 50% Particle Cutoff Diameter (microns)

Element	**0.03**	**0.06**	**0.09**	**0.17**	**0.34**	**0.54**	**0.98**	**1.98**	**3.77**	**7.33**	**15.7**
As	36.34	8.27	7.36	6.36	3.82	3.08	2.73	2.65	1.34	0.22	0.82
Se	55.51	19.84	8.96	9.52	5.88	5.06	2.82	2.62	1.16	0.14	0.64
Sb	8.48	11.31	0.00	14.42	0.00	0.84	1.22	1.65	0.74	0.75	1.54
Co	2.79	3.27	1.27	2.10	2.98	3.50	3.02	2.12	1.17	0.51	0.75

Table 3-59. Enrichment Factors (E_f) for Key Elements in Kentucky Fly Ash Sampled at Port 14

Aerodynamic 50% Particle Cutoff Diameter (microns)

Element	0.03	0.06	0.09	0.17	0.34	0.54	0.98	1.98	3.77	7.33	15.7
As	795.99	4.57	4.79	4.57	4.78	3.25	3.34	2.28	1.69	1.19	0.43
Se	319.97	10.57	11.31	4.12	4.23	2.40	1.99	1.79	1.74	1.14	0.48
Sb	97.09	0.00	0.00	0.00	4.97	5.21	2.71	2.23	1.15	1.03	0.48
Co	983.76	0.61	1.07	1.08	2.77	2.09	1.86	1.64	1.20	1.19	0.66

Table 3-60. The Solubility of Key Kentucky Fly Ash Elements in EPA TCLP Leaching Solutions Sampled at Port 4 And Port 14

Element	Submicron Size % Soluble at pH 4.9	Submicron Size % Soluble at pH 2.9	Supermicron Size % Soluble at pH 4.9	Supermicron Size % Soluble at pH 2.9
Port 4				
Arsenic	16%	57%	18%	60%
Selenium	13%	69%	0%	58%
Antimony	3%	56%	47%	86%
Cobalt	20%	57%	3%	30%
Port 14				
Arsenic	38%	63%	17%	41%
Selenium	0%	43%	0%	55%
Antimony	66%	94%	51%	84%
Cobalt	43%	81%	5%	29%

Antimony is highly soluble from both size regimes at both sample locations. Cobalt in the submicron particles is much more soluble than cobalt in the supermicron particles, which suggests there may be a difference in the form of occurrence between the two regimes. Solubility of arsenic and selenium is similar in submicron versus supermicron particle regimes. There is a slight decrease in As and Se solubility at Port 14 compared to Port 4.

Ohio 5/6/7 Bituminous Coal Blend

The Ohio 5/6/7 blend coal is another bituminous coal. The proximate/ultimate analysis of this coal is provided in Table 3-61. The carbon content is higher than the carbon content of the Illinois #6, Wyodak, and North Dakota coals but lower than the carbon content of the Pittsburgh and Kentucky coals. The sulfur content is high; lower than the Illinois #6 sulfur content but higher than the sulfur content in all of the other study coals. The moisture content is low at 2.3 wt%.

Table 3-61. Proximate/Ultimate Analysis of the Ohio Coal[1]

Proximate	wt%
Fixed Carbon	48.78
Volatile Matter	39.19
Moisture	2.33
Ash	9.70
Heating Value kJ/kg	29,900
Ultimate	
Carbon	71.07
Hydrogen	5.07
Nitrogen	1.37
Sulfur	2.62
Oxygen	10.17
Chlorine	0.0974
Moisture	2.33
Ash	9.70

1. From Ref. 7

Characterization of the major ash components is provided in Table 3-62. The elemental composition of the Ohio coal ash is provided in Table 3-63. The silica content is lower than the Illinois #6, Pittsburgh, Kentucky and Wyodak coals but higher than the North Dakota coal. Aluminum (as Al_2O_3) accounts for over 39 wt% of the ash. The calcium content is low and the ratio of Fe_2O_3 to CaO is 5.8 by weight. The arsenic content is significantly higher than any of the other coals studied. The antimony content is high and the selenium content is intermediate among the coals studied. The combination of high sulfur content and low calcium content will reduce the availability of the active surface sites necessary for surface reaction of As, Se, and Sb.

Table 3-62. Ohio Coal Ash Characterization[1]

Component	wt%[1]
SiO_2	38.09
Al_2O_3	39.41
Fe_2O_3	13.03
TiO_2	2.04
CaO	2.24
MgO	1.02
Na_2O	0.92
K_2O	2.55
BaO	0.20
P_2O_5	0.51

1. Sulfur-free basis

Table 3-63. Ohio Coal Ash Elemental Composition[1]

a) Mineralogical Characterization[1]

XRD[2] Determinations	wt %
Quartz	19
Kaolinite	43
Illite	21
Pyrite	12
Siderite	0.5
Feldspar	tr[4]
Bassanite	tr
Sphalerite	tr
Marcasite	tr

b) Trace Element Forms of Occurrence[3]

Element	Form	Wt%
Arsenic	Organic	0
	Mono-sulfides	30
	Silicates	5
	Pyrite/sulfides	35
Selenium	Organic	40
	Mono-sulfides	5
	Silicates	0
	Pyrite/sulfides	55
Antimony	Organic	
	Mono-sulfides	
	Silicates	
	Pyrite/sulfides	

Table 3-63. (Continued) Ohio Coal Ash Elemental Composition[1]

c) Elemental Analysis

Chemical Composition[5]	MIT/NAA (ppmw)	USGS[6] (ppmw)
Si	nd[7]	14096
Al	11100	6751
Ti	670	430
Fe	15100	10906
Ca	1400	816
Mg	760	252
Na	350	208
K	2500	1187
P	nd	200
Cl	880	nd
Li	nd	8
Be	nd	2.6
B	nd	64
Sc	3.90	2.8
V	23.0	19
Cr	19.0	11.4
Mn	19.0	15
Co	5.8	3.64
Ni	nd	13
Cu	nd	7.1
Zn	39	16
Ga	11.0	4
Ge	nd	7.3
As	19.0	13.2
Se	1.40	1.32
Br	23.0	13.9
Rb	21.0	8.4
Sr	100	74
Y	nd	7.2

Table 3-63. (Continued) Ohio Coal Ash Elemental Composition[1]

c) (Continued) Elemental Analysis

Chemical Composition[5]	MIT/NAA (ppmw)	USGS[6] (ppmw)
Zr	nd	10
Nb	nd	2.2
Mo	7.6	3.6
Ag	nd	<0.2
Cd	0.40	0.1
In	0.06	nd
Sn	nd	1
Sb	2.30	1.44
Te	nd	<0.2
Cs	0.63	0.56
Ba	102	49
La	9.40	7.29
Ce	14.0	13.7
Nd	11.0	nd
Sm	2.00	1.61
Eu	0.38	0.317
Tb	nd	0.237
Yb	1.10	0.73
Lu	0.22	0.102
Hf	nd	0.45
Ta	nd	0.1
W	nd	0.8
Au	3.e-3	<1
Hg	0.15	0.13
Tl	nd	1.0
Pb	nd	6.8
Bi	nd	<0.2
Th	2.70	1.59
U	—	0.93

1. From Section 3.1.1
2. XRD = X-ray Diffraction
3. tr = trace
4. Determine by selective leaching, from Section 3.1.3
5. From Section 3.1.1
6. Optimal results from ICP-MS, ICP-AES, NAA, Hydride (Se), and Cold Vaporization (Hg)
7. nd = not determined by this method

Temperature Profile

The temperature profile of the Ohio coal, obtained using the Phase II furnace in the 1998 test program, is shown in Figure 3-93. The maximum combustion temperature, interpolated from this figure, is 1640 K.

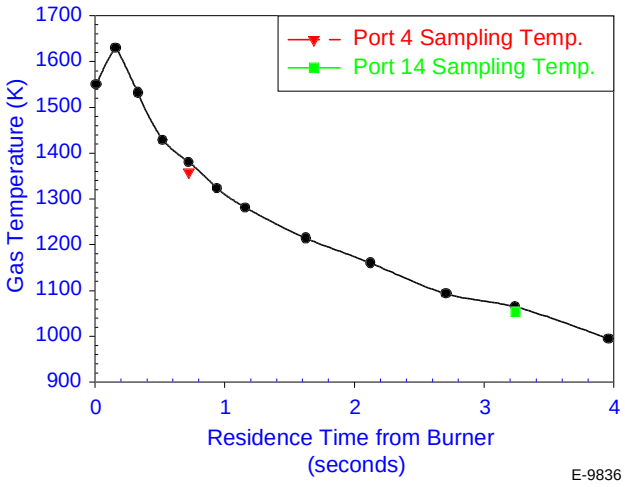

Figure 3-93. Typical temperature profile of the Ohio coal under baseline screening experimental conditions.

Size-Segregated Distributions

A typical PSD was generated at each sampling locations from all size-segregated BLPI samples considered to be representative of baseline combustion conditions. These are shown in Figure 3-94. For this coal, the Port 4 sampling location is 0.7 residence seconds below the burner and the Port 14 sampling location is 3.2 residence seconds below the burner. The Port 14 PSD has an intermediate maxima in the supermicron region at around 2 μm indicating a fragmentation particle region in addition to the bulk supermicron and submicron fume regions.

The sample sets that most closely duplicated the typical PSD were selected for elemental analysis. One sample set each from the Port 4 and Port 14 sampling locations were analyzed by INAA at MIT. Two additional sample sets from the Port 4 and Port 14 sampling locations plus three sample sets from the baghouse inlet sampling location were analyzed by AAS/AES/GFAA at Arizona.

The submicron particles are primarily silica and iron with significant sodium present. There is very little aluminum or calcium present. By contrast, the supermicron particles have a substantial aluminum content in addition to substantial silica and iron content. Calcium content is low and fairly evenly distributed between supermicron and submicron particles.

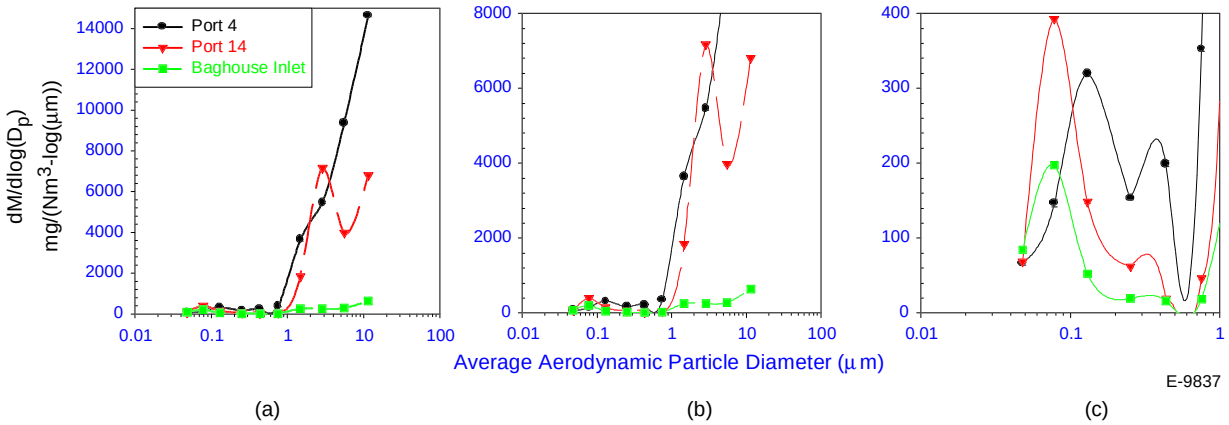

Figure 3-94. Total ash particle size distributions for the Ohio coal sampled at three locations: (a) total PSD, (b) expanded supermicron PSD, (c) expanded submicron PSD.

Differential elemental distributions were calculated using the method of Markowski and Ensor [131] for calcium, iron, aluminum, arsenic, selenium, antimony, and cobalt. The major elemental differential distributions at the Port 4 and Port 14 locations are shown in Figure 3-95 (baghouse major species data are not available) while the trace elemental differential distributions at all three sampling locations are shown in Figure 3-96. The calcium and iron distributions are distinctly different. The aluminum distributions are somewhat similar to the calcium distributions. There is a substantially higher fraction of collected As, Se, and Sb in the vapor phase region than for any other coal studied. This higher vapor-phase fraction for these trace elements indicates that there are not enough active cation surface sites for reaction of As, Se, and Sb with Ca and Fe.

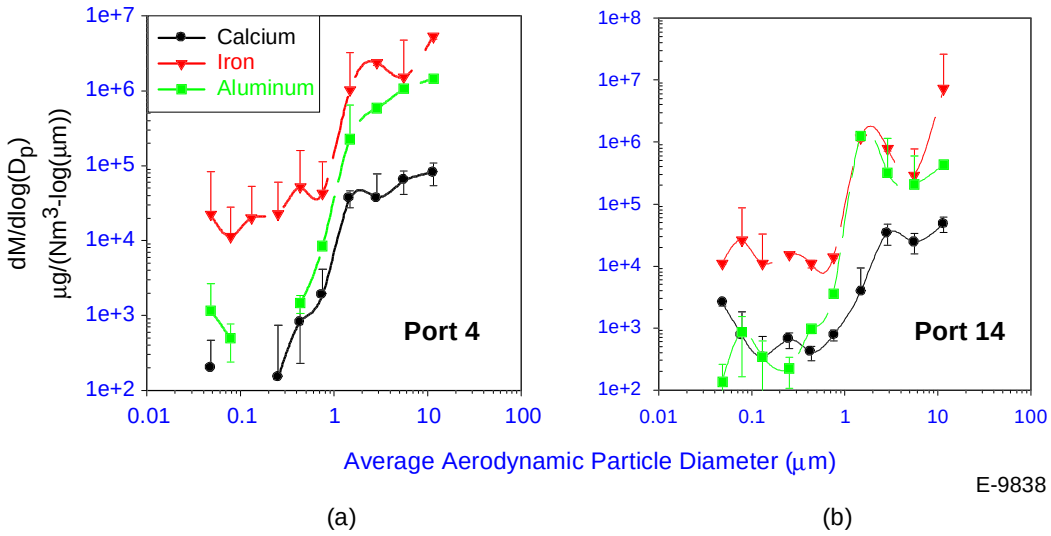

Figure 3-95. Major element differential distributions for the Ohio coal sampled at two locations: (a) Port 4 - 0.7 residence seconds and (b) Port 14 – 3.2 residence seconds.

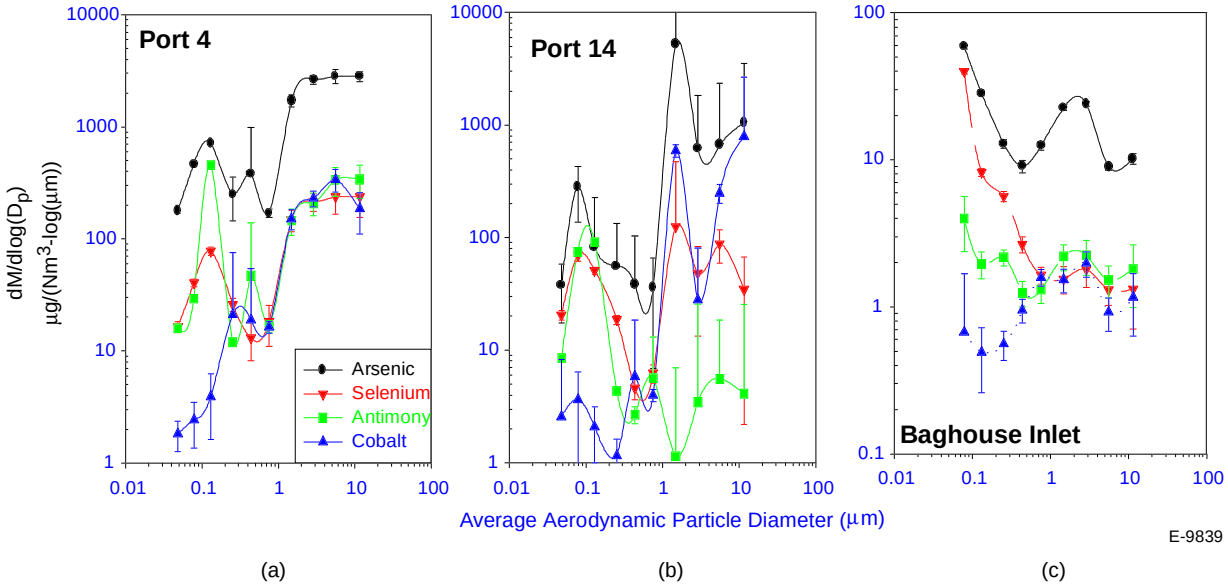

Figure 3-96. Trace element differential distributions for the Ohio coal sampled at three locations: (a) Port 4 - 0.7 residence seconds, (b) Port 14 – 3.2 residence seconds, (c) baghouse inlet.

Calculating an enrichment factor can normalize the elemental concentrations on each impactor stage. Port 4 enrichment factors for arsenic, selenium, antimony, and cobalt are shown in Table 3-64 while Port 14 enrichment factors are shown in Table 3-65. All four trace elements are enriched in the submicron particles in the Port 4 samples compared to the supermicron particles. As and Co are enriched in the submicron particles in the Port 14 samples but antimony is not. The data for selenium at this location is mixed and no trend can be discerned. It should be noted that the selenium concentration in these samples is near the detection limit of the GFAA. These enrichment results are different from those of the other three bituminous coals and suggest that the partitioning mechanisms for trace elements during Ohio coal combustion may be different from the other coals tested. This difference in partitioning mechanism will be examined in detail in Section 3.3.3.4.

Table 3-64. Enrichment Factors (E_f) for Key Elements in Ohio Fly Ash Sampled at Port 4

Aerodynamic 50% Particle Cutoff Diameter (microns)

Element	0.03	0.06	0.09	0.17	0.34	0.54	0.98	1.98	3.77	7.33	15.7
As	8.02	9.50	6.78	4.92	5.78	1.45	1.42	1.45	0.92	0.58	0.86
Se	8.78	9.88	8.71	6.06	2.35	1.86	1.46	1.41	0.91	0.58	0.77
Sb	4.67	3.92	27.92	1.53	4.61	0.92	0.79	0.75	0.71	0.45	2.43
Co	1.03	0.62	0.46	5.19	3.58	1.75	1.57	1.59	1.37	0.48	0.68

Table 3-65. Enrichment Factors (E_f) for Key Elements in Ohio Fly Ash Sampled at Port 14

Aerodynamic 50% Particle Cutoff Diameter (microns)

Element	0.03	0.06	0.09	0.17	0.34	0.54	0.98	1.98	3.77	7.33	15.7
As	1.40	1.84	1.41	2.29	5.02	1.99	7.23	0.22	0.43	0.39	0.98
Se	28.71	17.13	33.09	28.81	22.85	12.98	6.54	0.65	2.13	0.49	0.97
Sb	18.89	28.96	93.38	10.69	20.99	18.54	0.09	0.07	0.21	0.09	0.19
Co	0.47	0.11	0.17	0.23	3.74	1.07	4.00	0.05	0.78	1.44	0.55

Trace Element Solubility

One sample set from the Port 4 sampling location and one sample set from the Port 14 sampling location were selected for leaching. Impactor stages 3, 4, and 5 (representing the submicron region) and stages 8, 9, and 10 (representing the supermicron region) from each sample set were subjected to the leaching protocol described by Seames [133]. The solubility of arsenic, selenium, antimony, and cobalt in the pH 2.8 EPA Method 1310 solution and the pH 4.9 EPA Method 1310 solution were determined by GFAA analysis at Arizona. Solubility results for all elements in both leaching solutions at both sampling locations are shown in Table 3-66.

Table 3-66. The Solubility of Key Ohio Fly Ash Elements in EPA TCLP Leaching Solutions Sampled at Port 4 and Port 14

Element	Submicron Size % Soluble at pH 4.9	Submicron Size % Soluble at pH 2.9	Supermicron Size % Soluble at pH 4.9	Supermicron Size % Soluble at pH 2.9
Port 4				
Arsenic	52%	92%	21%	52%
Selenium	14%	32%	0%	32%
Antimony	36%	74%	49%	61%
Cobalt	95%	100%	0%	69%
Port 14				
Arsenic	39%	64%	49%	84%
Selenium	0%	0%	0%	11%
Antimony	21%	63%	25%	50%
Cobalt	0%	100%	37%	62%

Antimony is less soluble from Ohio fly ash compared to Pittsburgh and Kentucky. By contrast, cobalt and arsenic are more soluble. There are distinct differences in the solubility at Port 4 versus Port 14 for arsenic and selenium.

Wyodak Power River Basin Sub-Bituminous Coal

The Wyodak Power River Basin coal is the only subbituminous coal included in this study. The carbon content is lower than the bituminous coals and higher than the North Dakota lignite. The sulfur content is very low at 0.3 wt % while the moisture content is very high at 25.8 wt %. The proximate/ultimate analysis of this coal is provided in Table 3-67.

Table 3-67. Proximate/Ultimate Analysis of the Wyodak Coal[1]

Proximate	**wt%**
Fixed Carbon	33.31
Volatile Matter	34.85
Moisture	25.81
Ash	6.03
Heating Value, kJ/kg	20,610
Ultimate	
Carbon	51.19
Hydrogen	6.51
Nitrogen	0.72
Sulfur	0.32
Oxygen	35.23
Chlorine	0.0026
Moisture	25.81
Ash	6.03

1. From Ref. 7

Characterization of the major ash components is shown in Table 3-68 and the elemental composition of the Wyodak coal ash is provided in Table 3-69. The silica content is intermediate; lower than the Pittsburgh and Kentucky coals and higher than the Illinois #6, Ohio, and North Dakota coals. Aluminum (as Al_2O_3) accounts for 17 wt% of the ash. The iron content is low and the calcium content is very high. The ratio of Fe_2O_3 to CaO is 0.28 by weight. The arsenic content is lower than most of the coals studied and the selenium content is intermediate. The antimony content is one of the lowest among the coals studied.

Table 3-68. Wyodak Coal Ash Characterization[1]

Component	**wt%[1]**
SiO_2	43.28
Al_2O_3	17.17
Fe_2O_3	6.32
TiO_2	1.38
CaO	22.74
MgO	4.03
Na_2O	1.67
K_2O	0.45
BaO	0.68
P_2O_5	0.49

1. Sulfur-free basis

Table 3-69. Wyodak Coal Ash Elemental Composition[1]

a) Mineralogical Characterization[1]

XRD[2] Determinations	wt %
Quartz	26
Kaolinite	46
Bassanite	28
Pyrite	tr[3]
Sphalerite	tr

1. From Section 3.1.2
2. XRD = X-ray diffraction
3. tr = trace

b) Trace Element Forms of Occurrence[1]

Element	Form	Wt%
Arsenic	Organic	5
	Mono-sulfides	25
	Silicates	15
	Pyrite/sulfides	25
Selenium	Organic	70
	Mono-sulfides	0
	Silicates	0
	Pyrite/sulfides	30
Antimony	Organic	55
	Mono-sulfides	5
	Silicates	40
	Pyrite/sulfides	0

1. Determined by selective leaching, from Ref. 7

Table 3-69. (Continued) Wyodak Coal Ash Elemental Composition[1]

c) Elemental Analysis

Chemical Composition[5]	**MIT/NAA (ppmw)**	**USGS[6] (ppmw)**
Si	nd[7]	9645
Al	5400	5490
Ti	530	430
Fe	2300	2248
Ca	7900	8161
Mg	1700	1410
Na	660	638
K	2300	141
P	nd	423
Cl	62	nd
Li	nd	2.7
Be	nd	0.3
B	nd	31
Sc	1.40	1.4
V	14.0	13
Cr	7.3	5.9
Mn	8.2	6.1
Co	5.1	4.20
Ni	nd	3.6
Cu	nd	10
Zn	52	6.1
Ga	9.7	1.9
Ge	nd	0.27
As	1.4	1.29
Se	1.08	0.97
Br	1.2	0.8
Rb	20.0	1.6
Sr	100	193
Y	nd	2.6

Table 3-69. (Continued) Wyodak Coal Ash Elemental Composition[1]

c) (Continued) Elemental Analysis

Chemical Composition	MIT/NAA (ppmw)	USGS (ppmw)
Zr	nd	13
Nb	nd	2.1
Mo	1.5	0.8
Ag	nd	<0.2
Cd	0.24	0.1
In	0.07	nd
Sn	nd	<0.9
Sb	0.40	0.17
Te	nd	<0.2
Cs	2.50	0.101
Ba	380	334
La	4.00	4.2
Ce	7.4	6.9
Nd	2.6	nd
Sm	0.60	0.71
Eu	0.25	0.143
Tb	nd	0.08
Yb	0.30	0.31
Lu	0.04	0.036
Hf	nd	0.44
Ta	nd	0.118
W	nd	0.36
Au	5.0.e-3	<9e-4
Hg	0.13	0.10
Tl	nd	<0.2
Pb	nd	1.4
Bi	nd	<0.2
Th	1.30	1.37
U	0.70	0.54

1. From Section 3.1.1
2. XRD = X-ray diffraction
3. tr = trace
4. Determine by selective leaching, from Ref. 7
5. From Ref. 7
6. Optimal results from ICP-MS, ICP-AES, NAA, Hydride (Se), and Cold Vaporization (Hg)
7. nd = not determined by this method

Temperature Profile

The temperature profile of the Wyodak coal, obtained using the Phase II furnace in the 1999 test program, is shown in Figure 3-97. The maximum combustion temperature, interpolated from Figure 3-97, is 1480 K. This is 120 to 180 K lower than the bituminous coal combustion temperatures.

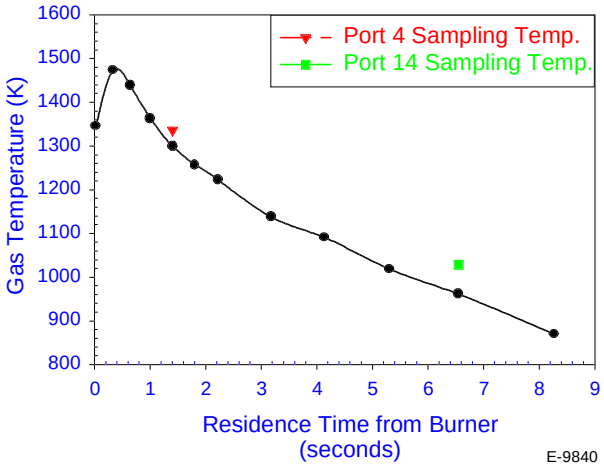

Figure 3-97. Typical temperature profile of the Wyodak coal under baseline screening experimental conditions.

Size-Segregated Distributions

Size-segregated BLPI samples were used to determine the total ash PSD at all three sampling locations. The typical PSD was determined from the average of all sample sets considered to be representative of baseline combustion conditions. Differential ash PSDs for the Wyodak coal at all three sampling locations are shown in Figure 3-98. For this coal, the Port 4 sampling location is 1.4 residence seconds below the burner and the Port 14 sampling location is 6.6 residence seconds below the burner. Both Port 4 and Port 14 PSDs have intermediate maxima in the supermicron region at around 2 μm average aerodynamic particle diameter indicating a fragmentation fly ash mode in addition to the bulk supermicron and submicron fly ash modes.

Sample sets that most closely duplicated the typical PSD were selected for elemental analysis. Selected stages (3, 4, 5, 8, 9, and 10) from one sample set each from the Port 4 and Port 14 sampling locations were analyzed by INAA at MIT. Two additional sample sets from the Port 4 and Port 14 sampling locations plus three sample sets from the baghouse inlet sampling location were analyzed by AAS/AES/GFAA at Arizona.

Submicron particles from the Wyodak fly ash are composed primarily of aluminum, calcium, and iron but contain very little silica. There is significant sodium and magnesium present in the submicron particles. Supermicron particles are composed of silica, aluminum, and calcium. The iron content is fairly evenly distributed between submicron and supermicron particles but the supermicron particles appear to have more calcium than the submicron particles.

Differential elemental distributions were calculated using the method of Markowski and Ensor [131] for calcium, iron, aluminum, arsenic, selenium, antimony, and cobalt. The major elemental differential distributions at all three sampling locations are shown in Figure 3-99 while the trace elemental differential distributions at all three sampling locations are shown in

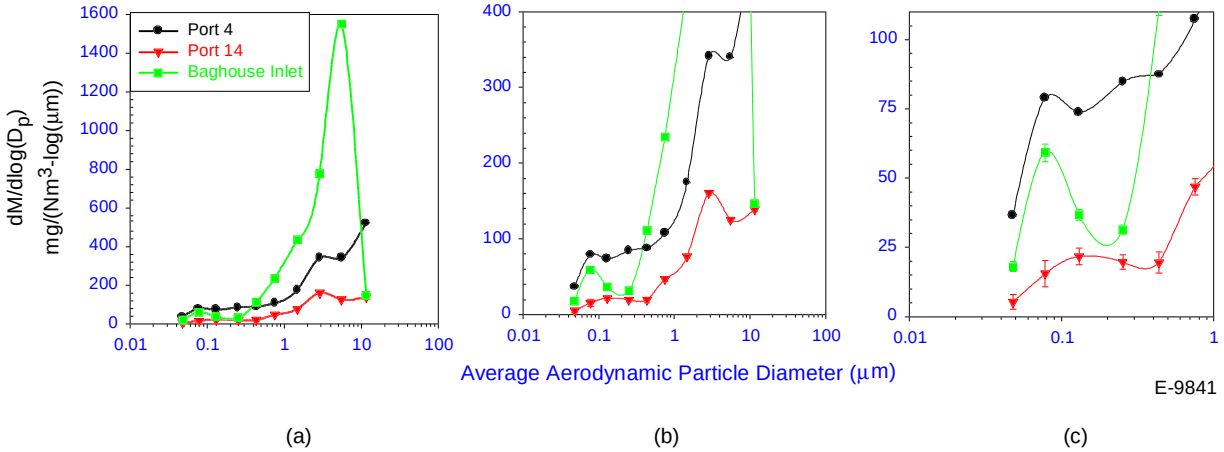

Figure 3-98. Total ash particle size distributions for the Wyodak coal sampled at three locations: (a) total PSD, (b) expanded supermicron PSD, (c) expanded submicron PSD.

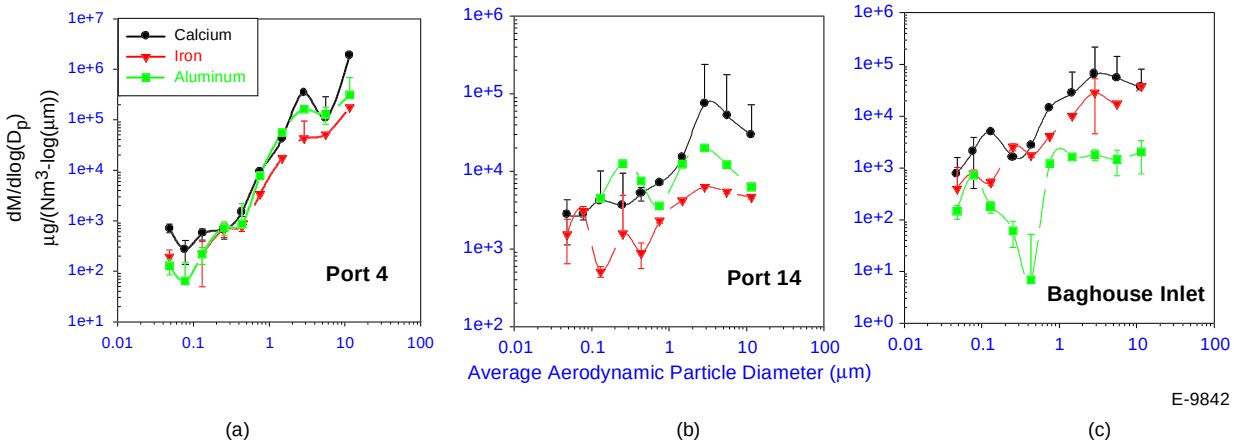

Figure 3-99. Major element differential distributions for the Wyodak coal sampled at three locations: (a) Port 4 –1.6 residence seconds, (b) Port 14 – 6.6 residence seconds, (c) baghouse inlet.

Figure 3-100. Fe, Ca, and Al distributions are very similar in the supermicron region but show differences in the submicron region. As, Se, and Co distributions are fairly similar but the Sb distributions are different in shape.

Calculating an enrichment factor can normalize the elemental concentrations on each impactor stage. Port 4 enrichment factors for arsenic, selenium, antimony, and cobalt are shown in Table 3-70 while Port 14 enrichment factors are shown in Table 3-71. Enrichment of all four trace elements is observed in the submicron sizes for the Port 14 samples while depletion is observed for the Port 4 submicron sizes. These results indicate that trace element volatilization is occurring later during Wyodak combustion than the bituminous coals described above. The timing of trace element partitioning is explored in detail below.

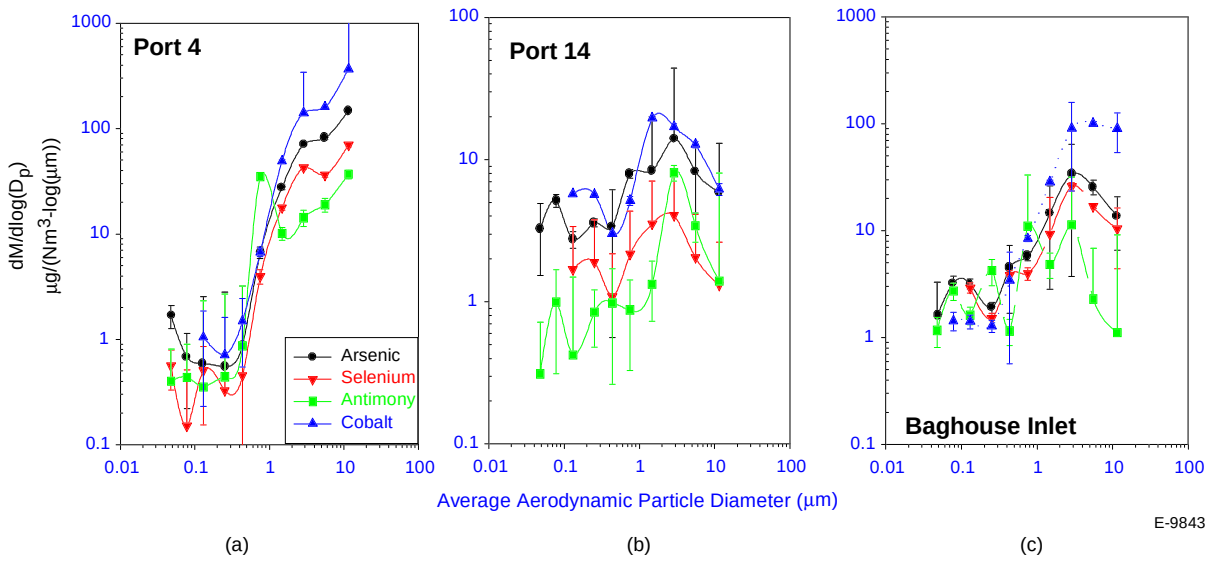

Figure 3-100. Trace element differential distributions for the Wyodak coal sampled at three locations: (a) Port 4 – 1.6 residence seconds, (b) Port 14 – 6.6 residence seconds, (c) baghouse inlet.

Table 3-70. Enrichment Factors (E_f) for Key Elements in Wyodak Fly Ash Sampled at Port 4

Aerodynamic 50% Particle Cutoff Diameter (microns)

Element	0.03	0.06	0.09	0.17	0.34	0.54	0.98	1.98	3.77	7.33	15.7
As	0.23	0.044	0.040	0.033	0.051	0.32	0.81	1.06	1.22	1.45	1.13
Se	0.16	0.020	0.071	0.040	0.054	0.38	1.06	1.31	1.12	1.41	0.64
Sb	0.17	0.084	0.073	0.079	0.15	4.94	0.88	0.63	0.84	1.07	1.27
Co			0.035	0.021	0.04	0.16	0.70	1.02	1.17	1.75	0.44

Table 3-71. Enrichment Factors (E_f) for Key Elements in Wyodak Fly ash Sampled at Port 14

Aerodynamic 50% Particle Cutoff Diameter (microns)

Element	0.03	0.06	0.09	0.17	0.34	0.54	0.98	1.98	3.77	7.33	15.7
As	6.8	3.7	1.4	2.0	1.9	1.9	1.2	0.97	0.73	0.47	0.58
Se			3.1	3.8	2.2	1.8	1.8	1.0	0.65	0.37	
Sb	2.2	2.4	0.71	1.6	1.8	0.68	0.63	1.8	1.0	0.37	0.58
Co			2.3	2.5	1.3	0.94	2.2	0.91	0.87	0.38	0.83

Trace Element Solubility

The leaching protocol described by Seames [133] was to perform a solubility study on selected impactor stages (3, 4, and 5 representing the submicron region and 8, 9, and 10 representing the supermicron region) for one sample set from the Port 4 sampling location and one sample set from the Port 14 sampling location. The solubility of arsenic, selenium, antimony, and cobalt in the pH 2.8 EPA Method 1310 solution and the pH 4.9 EPA Method 1310 solution were determined by GFAA analysis at Arizona. Solubility results for all elements in both leaching solutions at both sampling locations are shown in Table 3-72.

Table 3-72. The Solubility of Key Wyodak Fly Ash Elements in EPA TCLP Leaching Solutions Sampled at Port 4 and Port 14

Element	Submicron Size % Soluble at pH 4.9	Submicron Size % Soluble at pH 2.9	Supermicron Size % Soluble at pH 4.9	Supermicron Size % Soluble at pH 2.9
Port 4				
Arsenic	30%	59%	13%	51%
Selenium	0%	32%	0%	0%
Antimony	2%	15%	29%	91%
Cobalt	0%	0%	16%	63%
Port 14				
Arsenic	33%	49%	18%	42%
Selenium	0%	26%	n/d	n/d
Antimony	50%	100%	91%	100%
Cobalt	45%	65%	60%	76%

Except for the Port 4 submicron sample, antimony is very soluble. Submicron and supermicron regime results are similar for arsenic and selenium. Port 14 samples show a slight decrease in arsenic and selenium solubility compared to Port 4 samples. Cobalt in supermicron particles appears to be more soluble than cobalt in submicron particles.

North Dakota Falkirk Seam Lignite Coal

The North Dakota Falkirk Seam coal is the only lignite included in this study. As a lignite, it has the lowest carbon content of the coals studied. It also has the highest moisture content. The sulfur content is low at 0.63 wt%. The proximate/ultimate analysis of this coal is shown in Table 3-73.

Characterization of the major ash components is given in Table 3-74 and the elemental composition of the North Dakota lignite ash is provided in Table 3-75. The silica content of this ash is the lowest of the coals studied whereas the calcium content is the highest of the coals studied. Aluminum (as A_2O_3) accounts for over 20 wt% of the ash and the iron to calcium ratio is 0.39. The arsenic content is the second highest of the coals studied. Selenium and antimony concentrations are intermediate.

Table 3-73. Proximate/Ultimate Analysis of the North Dakota Lignite[1]

Proximate	**wt%**
Fixed Carbon	26.59
Volatile Matter	28.15
Moisture	35.88
Ash	9.38
Heating Value, kJ/kg	14,850
Ultimate	
Carbon	38.57
Hydrogen	6.59
Nitrogen	0.42
Sulfur	0.63
Oxygen	44.41
Chlorine	0.0036
Moisture	35.88
Ash	9.38

1. From Section 3.1.1

Table 3-74. North Dakota Lignite Ash Characterization[1]

Component	**wt%[1]**
SiO_2	22.00
Al_2O_3	20.38
Fe_2O_3	11.75
TiO_2	0.50
CaO	30.25
MgO	8.00
Na_2O	5.12
K_2O	1.38
BaO	0.50
P_2O_5	--

1. Sulfur-free basis

Table 3-75. North Dakota Lignite Ash Elemental Composition[1]

a) Mineralogical Characterization[1]

XRD[2] Determinations	wt %
Quartz	38
Kaolinite	16
Illite	12
Bassanite	28
Feldspar	tr[3]
Pyrite	tr
Siderite	tr
Sphalerite	tr
Marcasite	tr

1. From Section 3.1.2
2. XRD = X-ray diffraction
3. tr = trace

b) Trace Element Forms of Occurrence[4]

Element	Form	Wt%
Arsenic	Organic	0
	Mono-sulfides	60
	Silicates	10
	Pyrite/sulfides	15
Selenium	Organic	75
	Mono-sulfides	5
	Silicates	0
	Pyrite/sulfides	20
Antimony	Organic	
	Mono-sulfides	
	Silicates	
	Pyrite/sulfides	

4. Determine by selective leaching, from Section 3.1.3

Table 3-75. (Continued) North Dakota Lignite Ash Elemental Composition[1]

c) Elemental Analysis

Chemical Composition[5]	MIT/NAA (ppmw)	USGS[6] (ppmw)
Si	nd[7]	18548
Al	5400	6677
Ti	330	304
Fe	5300	5839
Ca	13000	11129
Mg	3100	2968
Na	2400	2819
K	<3200	1261
P	nd	126
Cl	170	nd
Li	nd	3.8
Be	nd	0.8
B	nd	96
Sc	1.20	1.4
V	11.0	11
Cr	8.5	8.5
Mn	44.0	44
Co	6.4	6.8
Ni	nd	3.2
Cu	nd	4.1
Zn	57	9
Ga	17.0	1.7
Ge	nd	1.0
As	8.1	7.4
Se	1.50	0.72
Br	1.9	1.91
Rb	32.	5.3
Sr	120	312
Y	nd	3.6

5. From Section 3.1.1
6. Optimal results from ICP-MS, ICP-AES, NAA, Hydride (Se), and Cold Vaporization (Hg)
7. nd = not determined by this method

Table 3-75. (Continued) North Dakota Lignite Ash Elemental Composition[1]

c) (Continued) Elemental Analysis

Chemical Composition	MIT/NAA (ppmw)	USGS (ppmw)
Zr	nd	19
Nb	nd	2.3
Mo	0.7	1.7
Ag	nd	<0.3
Cd	0.21	<0.1
In	0.12	nd
Sn	nd	<1.5
Sb	0.91	0.52
Te	nd	<0.3
Cs	0.50	0.43
Ba	420	438
La	3.10	3.68
Ce	4.3	5.8
Nd	1.8	nd
Sm	0.50	0.56
Eu	0.27	0.111
Tb	nd	0.082
Yb	0.40	0.36
Lu	0.04	0.052
Hf	nd	0.45
Ta	nd	0.102
W	nd	2.22
Au	1.7e-3	<1.5e-3
Hg	0.13	0.06
Tl	nd	<0.2
Pb	nd	1.1
Bi	nd	<0.3
Th	1.20	1.24
U	0.80	0.83

Temperature Profile

The temperature profile of the North Dakota lignite, obtained using the Phase II furnace in the 1999 test program, is shown in Figure 3-101. The maximum combustion temperature, interpolated from Figure 3-101, is 1430 K. This is 50 K below the maximum combustion temperature of the Wyodak coal and 180 to 230 K below the bituminous coal combustion temperatures.

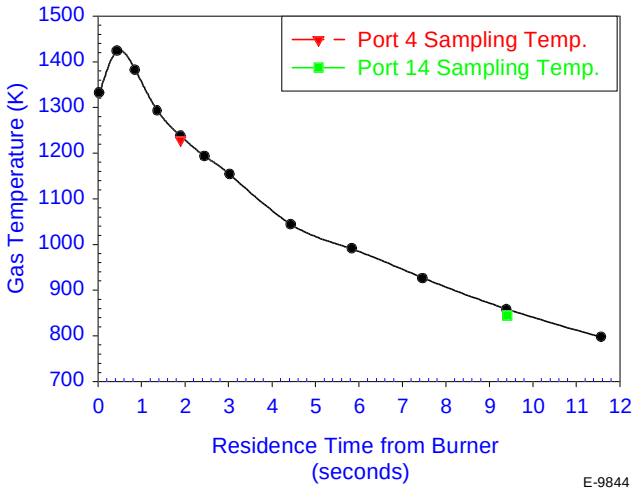

Figure 3-101. Typical temperature profile of the North Dakota coal under baseline screening experimental conditions.

Size-Segregated Distributions

Typical PSDs, determined from the average of all sample sets considered to be representative of baseline combustion conditions, at all three sampling locations, are shown in Figure 3-102. For this coal, the Port 4 sampling location is 1.9 residence seconds below the burner and the Port 14 sampling location is 9.4 residence seconds below the burner. There are no intermediate supermicron region maxima for the Port 4 or Port 14 PSDs.

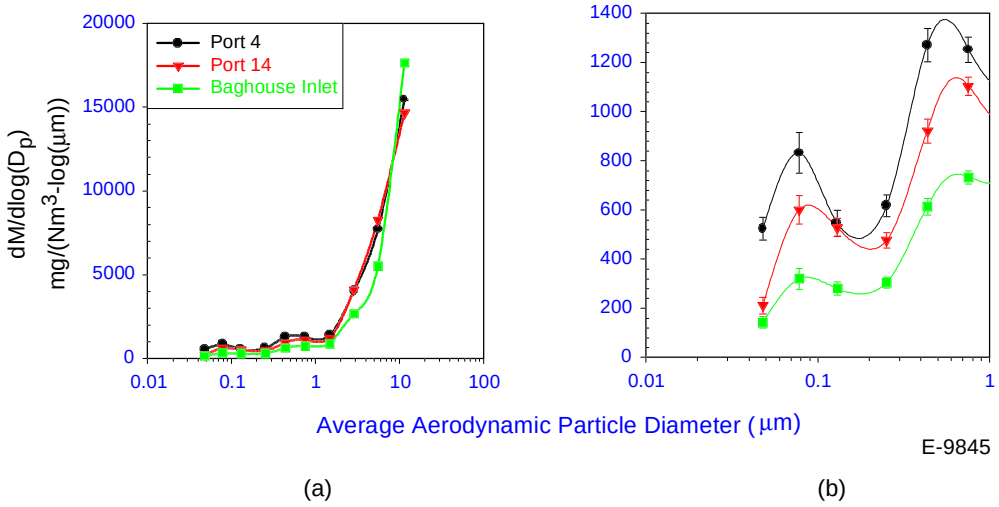

Figure 3-102. Total ash particle size distributions for the North Dakota coal sampled at three locations: (a) total PSD and (b) expanded submicron PSD.

Sample sets that most closely duplicated the typical PSD were selected for elemental analysis. Selected stages (3, 4, 5, 8, 9, and 10) from one sample set each from the Port 4 and Port 14 sampling locations were analyzed by INAA at MIT. Two additional sample sets from the Port 4 and Port 14 sampling locations plus three sample sets from the baghouse inlet sampling location were analyzed by AAS/AES/GFAA at Arizona.

Submicron particles are composed primarily of aluminum, silica, and sodium. The concentrations of iron and calcium are also substantial. All major elements appear to be fairly evenly distributed between submicron and supermicron particles.

Differential elemental distributions were calculated using the method of Markowski and Ensor [131] for calcium, iron, aluminum, arsenic, selenium, antimony, and cobalt. The major elemental differential distributions at all three sampling locations are shown in Figure 3-103 while the trace elemental differential distributions at all three sampling locations are shown in Figure 3-104. The distributions of Ca, Fe, and Al are very similar in the supermicron region but differ significantly in the submicron region. The As and Co distributions are very similar while Sb distributions are distinctly different from any of the other distributions. The presence of substantial vapor-phase antimony is consistent with the results from the thermodynamic equilibrium simulations (see Section 3.3.1). The simulations indicate that $SbCl_3(g)$ is the favored form of Sb for the North Dakota flue gas at post-combustion temperatures.

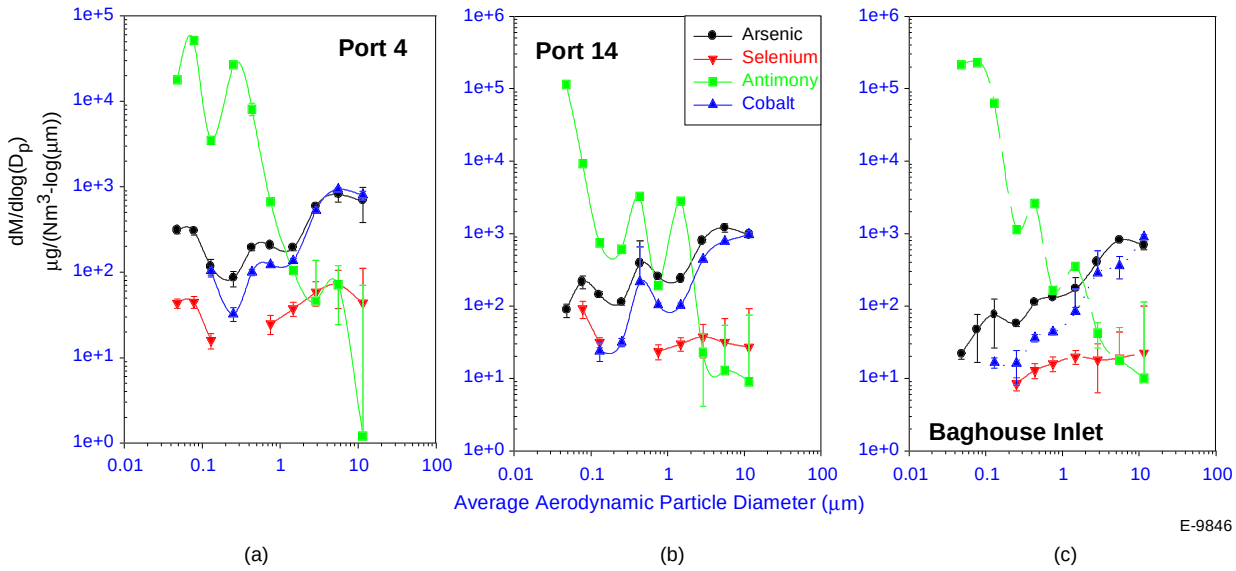

Figure 3-103. Major element differential distributions for the North Dakota coal sampled at three locations: (a) Port 4 –1.9 residence seconds, b) Port 14 – 9.3 residence seconds, (c) baghouse inlet.

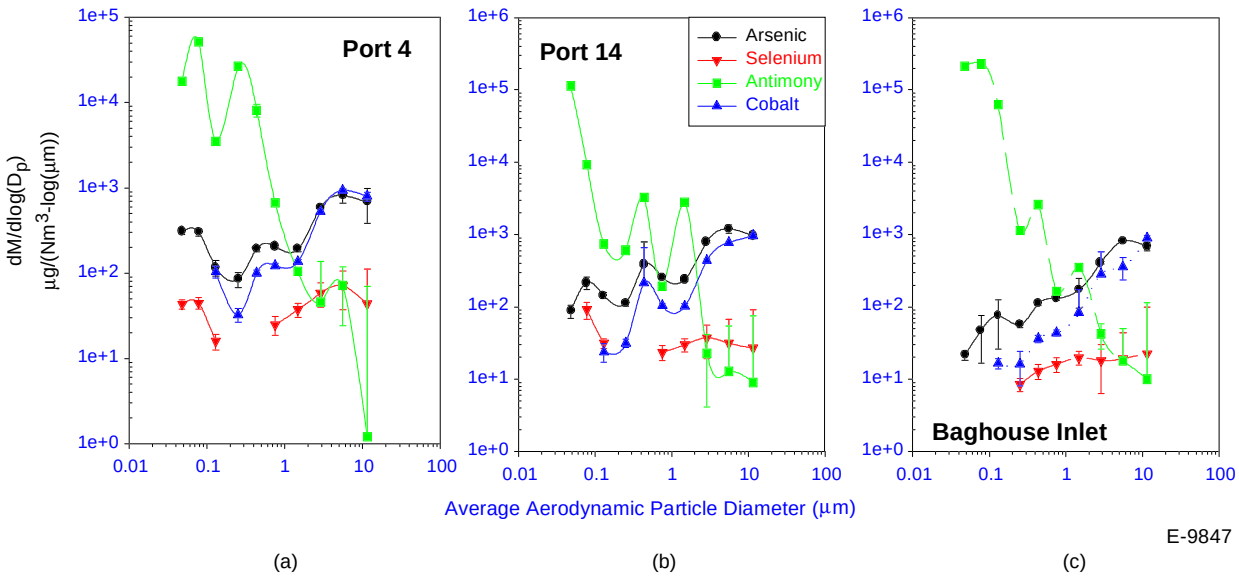

Figure 3-104. Trace element differential distributions for the North Dakota lignite sampled at three locations: (a) Port 4 – 1.9 residence seconds, (b) Port 14 – 9.3 residence seconds, (c) baghouse inlet.

Calculating an enrichment factor can normalize the elemental concentrations on each impactor stage. Port 4 enrichment factors for arsenic, selenium, antimony, and cobalt are shown in Table 3-76 while Port 14 enrichment factors are shown in Table 3-77. Arsenic shows enrichment in submicron particles at both sample locations. Antimony results are too variable to draw conclusions. For many of the submicron stages selenium was below the detection limit of the GFAA. Cobalt results are mixed.

Trace Element Solubility

One sample set from the Port 4 sampling location and one sample set from the Port 14 sampling location were selected for the solubility study. Impactor stages 3, 4, and 5 (representing the submicron region) and stages 8, 9, and 10 (representing the supermicron region) from each sample set were subjected to the leaching protocol described by Seames [133]. The

Table 3-76. Enrichment Factors (E_f) for Key Elements in North Dakota Fly Ash Sampled at Port 4

Aerodynamic 50% Particle Cutoff Diameter (microns)

Element	**0.03**	**0.06**	**0.09**	**0.17**	**0.34**	**0.54**	**0.98**	**1.98**	**3.77**	**7.33**	**15.7**
As	6.1	3.8	2.2	1.4	1.6	1.7	1.5	1.5	1.1	0.46	1.0
Se	9.4	6.1	3.3			2.3	3.2	1.7	1.1	0.32	
Sb	9.9	14	1.6	19	5.2	0.70	0.16	0.18	0.57	0.03	0.50
Co			2.3	0.63	0.95	1.2	1.2	1.6	1.5	0.62	1.5

Table 3-77. Enrichment Factors (E_f) for Key Elements in North Dakota Fly Ash Sampled at Port 14

Aerodynamic 50% Particle Cutoff Diameter (microns)

Element	**0.03**	**0.06**	**0.09**	**0.17**	**0.34**	**0.54**	**0.98**	**1.98**	**3.77**	**7.33**	**15.7**
As	3.3	2.9	2.2	1.9	3.3	1.8	1.6	1.5	1.2	0.52	0.83
Se		24	9.3			3.3	3.9	1.4	0.59	0.29	
Sb	51	3.6	0.65	0.65	0.99	0.35	7.6	0.19	0.22	0.36	1.6
Co			0.56	0.81	2.9	1.2	1.1	1.3	1.2	0.81	1.1

solubility of arsenic, selenium, antimony, and cobalt in the pH 2.8 EPA Method 1310 solution and the pH 4.9 EPA Method 1310 solution were determined by GFAA analysis at Arizona. Solubility results for all elements in both leaching solutions at both sampling locations are shown in Table 3-78.

Table 3-78. The Solubility of Key North Dakota Fly Ash Elements in EPA TCLP Leaching Solutions Sampled at Port 4 And Port 14

Element	**Submicron Size % Soluble at pH 4.9**	**Submicron Size % Soluble at pH 2.9**	**Supermicron Size % Soluble at pH 4.9**	**Supermicron Size % Soluble at pH 2.9**
Port 4				
Arsenic	31%	49%	17%	59%
Selenium	0%	0%	0%	0%
Antimony	68%	72%	8%	59%
Cobalt	44%	83%	35%	56%
Port 14				
Arsenic	47%	71%	10%	61%
Selenium	0%	0%	0%	0%
Antimony	48%	100%	28%	50%
Cobalt	33%	62%	42%	76%

Antimony is very soluble; although solubility for this ash is less than for most of the other coals studied. Selenium was found to be insoluble in all conditions.

Special Condition Combustion Experiments

A series of experiments were performed to investigate hypotheses developed for the partitioning of arsenic, selenium, and antimony during pulverized coal combustion. In these experiments, combustion conditions were maintained at the baseline screening combustion experimental conditions except for the variable(s) of interest. The main parameters manipulated were: trace element concentration (arsenic, selenium, or antimony), major element concentration (sulfur, calcium, or iron), and maximum combustion temperature via oxygen or CO_2 addition (actually, the gas temperature measured at Port 1, the second sample port from the burner, was

controlled since the maximum combustion temperature, per the temperature profiles, is located slightly above this sample port).

This suite of variables was manipulated to investigate the following hypotheses:

1. Arsenic partitioning is controlled by surface reaction with calcium and/or iron active surface sites if a particle size dependence analysis indicates that surface reaction is the dominant mechanism for the heterogeneous partitioning of volatilized arsenic to fly ash surfaces

2. Selenium partitioning is controlled by surface reaction with calcium and/or iron active surface sites if a particle size dependence analysis indicates that surface reaction is the dominant mechanism for the heterogeneous partitioning of volatilized arsenic to fly ash surfaces

3. Antimony partitioning is controlled by surface reaction with calcium and/or iron active surface sites if a particle size dependence analysis indicates that surface reaction is the dominant mechanism for the heterogeneous partitioning of volatilized arsenic to fly ash surfaces

4. Increasing the combustion temperature increases the availability of active cation surface sites and thus increases the recovery of As, Se, and Sb out of the fly ash by surface reaction

5. Increased sulfur inhibits the recovery of As, Se, and Sb by occupying active cation surface sites

6. Sulfur preferentially occupies iron surface sites compared to calcium surface sites.

7. Selenium is more reactive with active iron surface sites than with active calcium surface sites

8. Arsenic and antimony are more reactive with calcium surface sites than with iron surface sites

9. Antimony acts as an oxy-anion and reacts with cation surface sites rather than with anion surface sites (as predicted by equilibrium simulation results)

10. Volatilized cobalt is a simple oxide and reacts with anion surface sites

The results from these experiments are provided below. A detailed analysis of the results and the feasibility of each of these hypotheses are discussed in detail in Section 3.3.3.4.

Wyodak As/Se/Sb/Fe Doping Experiments

A series of special experiments were performed using the Wyodak coal. This coal was selected because:

1) As, Se, and Sb all showed a particle size dependence indicating partitioning was controlled by surface reaction mechanisms,
2) There were apparent correlations between As, Se, and Sb with calcium,
3) Temperature could be manipulated by oxygen enrichment, and
4) Full impactor sets could be collected without utilizing the preseparator inlet cyclone on the BLPI (increasing the reliability of the results).

In these experiments, As, Se, Sb, or Fe were dissolved in solution (dilute acid or water) and injected into the furnace 0.64 cm below the outlet of the burner using an air atomizer system (see Section 3.3.3.1 for a description of the facilities used in these tests). For the trace element doping experiments, the quantity of As, Se, or Sb added to the combustion environment was adjusted so that the As-to-Ca, Se-to-Ca, or Sb-to-Ca ratio matched the corresponding ratio during combustion of the Ohio blend coal. In some of the experiments, oxygen was added to the main combustion air to increase the maximum combustion temperature in the furnace.

Particulate sampling was performed at both Port 4 and Port 14. Duplicate, complete impactor sets were collected at each combustion condition/sampling location combination for the As, Se, and Sb doping experiments (see Appendix K for a list of the experiments performed). For the Fe doping experiments duplicate, partial impactor sets (only the top 5 full size stages -- 6-10) were collected. Submicron particle samples were not collected for the Fe doping experiments. Size-segregated BLPI samples were used to determine the total ash PSD at both sampling locations. The typical PSD was determined from the average of all sample sets considered to be representative of baseline combustion conditions. Differential ash PSDs at both sampling locations are shown as follows:

Figure 3-105: Oxygen enrichment with no doping
Figure 3-106: No oxygen enrichment with arsenic doping
Figure 3-107: Oxygen enrichment with arsenic doping
Figure 3-108: No oxygen enrichment with selenium doping
Figure 3-109: Oxygen enrichment with selenium doping
Figure 3-110: No oxygen enrichment with antimony doping
Figure 3-111: Oxygen enrichment with antimony doping
Figure 3-112: No oxygen enrichment with iron doping
Figure 3-113: Oxygen enrichment with iron doping

Sample sets that most closely duplicated the typical PSD were selected for elemental analysis. One sample set each from the Port 4 and Port 14 sampling locations were analyzed for Ca, Fe, and Al by AAS and for trace elements by GFAA at Arizona.

Differential elemental distributions are shown with the total ash PSDs in Figures 3-105 through 3-113. An assessment of how well these tests support partitioning hypotheses is included in Section 3.3.3.4.

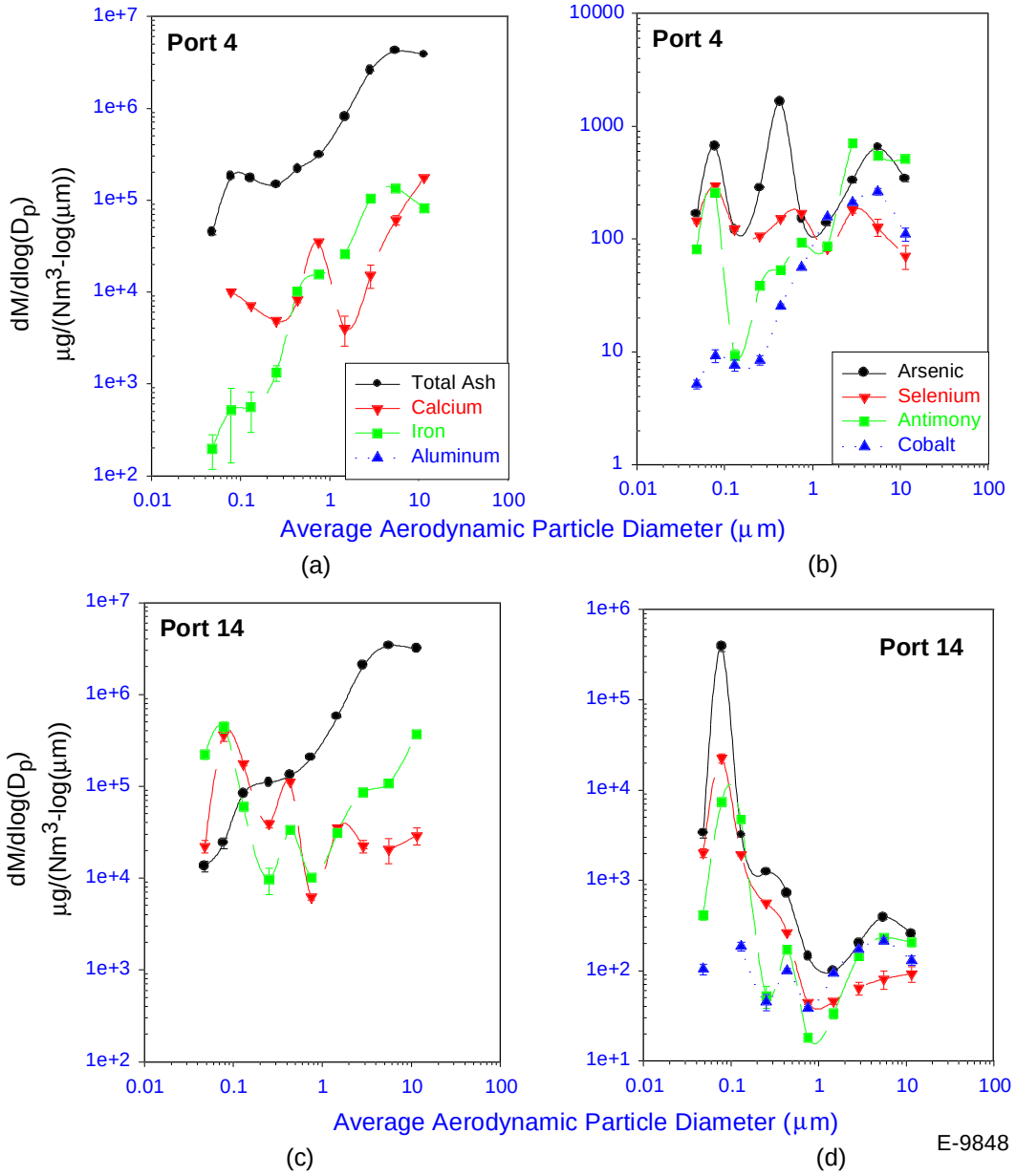

Figure 3-105. Differential distributions for Wyodak doping experiments: oxygen enrichment without doping; (a) total ash and major element PSDs at Port 4 – 1.6 residence seconds, (b) trace element PSDs at Port 4 – 1.6 residence seconds, (c) total ash and major element PSDs at Port 14 – 6.6 residence seconds, and (d) trace element PSDs at Port 14 – 6.6 residence seconds.

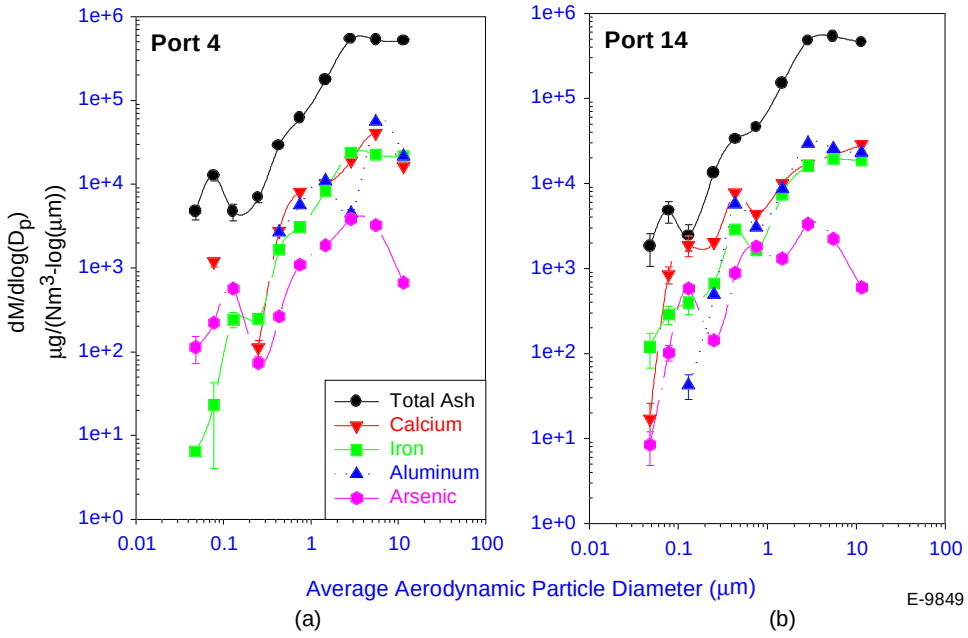

Figure 3-106. Differential distributions for Wyodak doping experiments: arsenic doping with no oxygen enrichment; (a) at Port 4 – 1.6 residence seconds and (b) at Port 14 – 6.6 residence seconds.

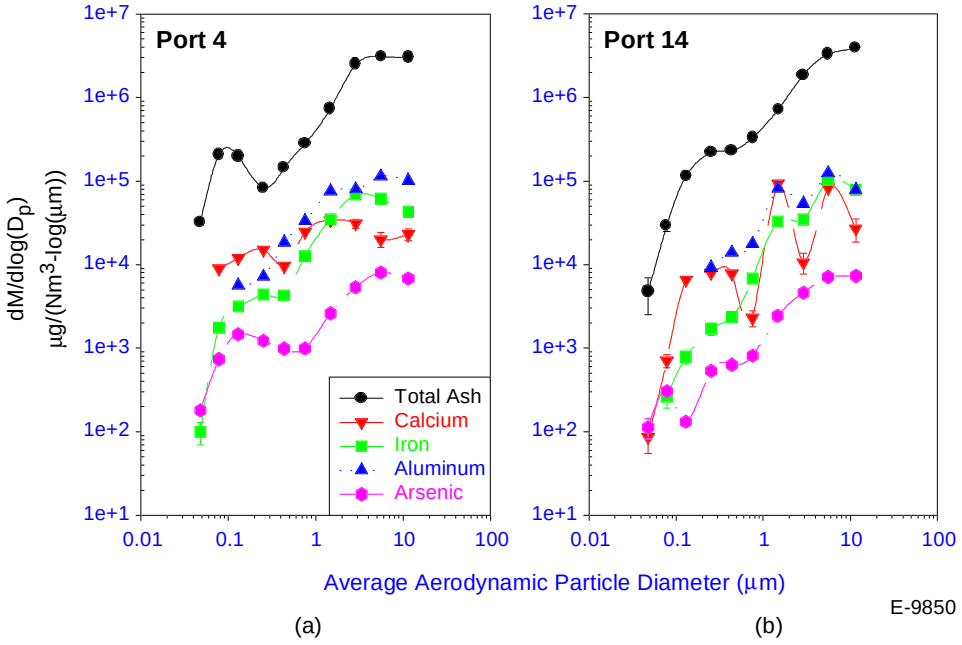

Figure 3-107. Differential distributions for Wyodak doping experiments: arsenic doping with oxygen enrichment; (a) at Port 4 – 1.6 residence seconds and (b) at Port 14 – 6.6 residence seconds.

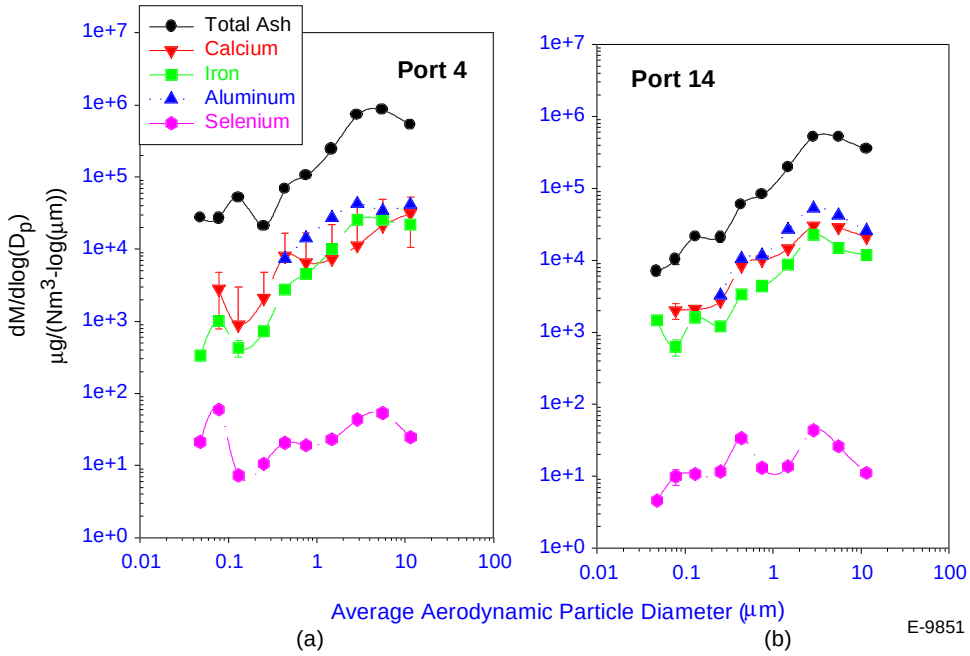

Figure 3-108. Differential distributions for Wyodak doping experiments: selenium doping with no oxygen enrichment; (a) at Port 4 – 1.6 residence seconds and (b) at Port 14 – 6.6 residence seconds.

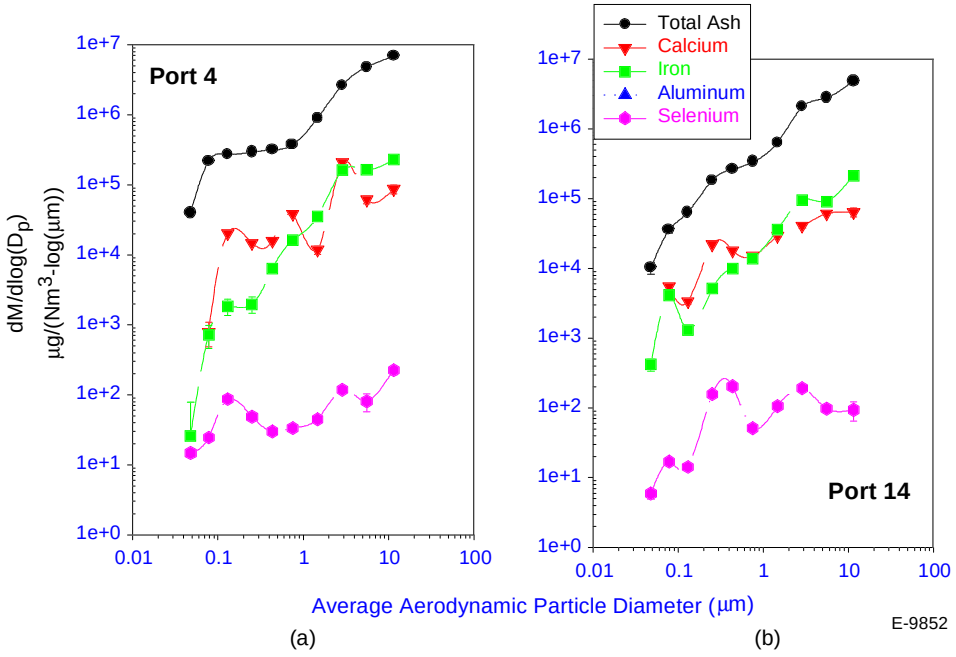

Figure 3-109. Differential distributions for Wyodak doping experiments: selenium doping with oxygen enrichment; (a) at Port 4 – 1.6 residence seconds and (b) at Port 14 – 6.6 residence seconds.

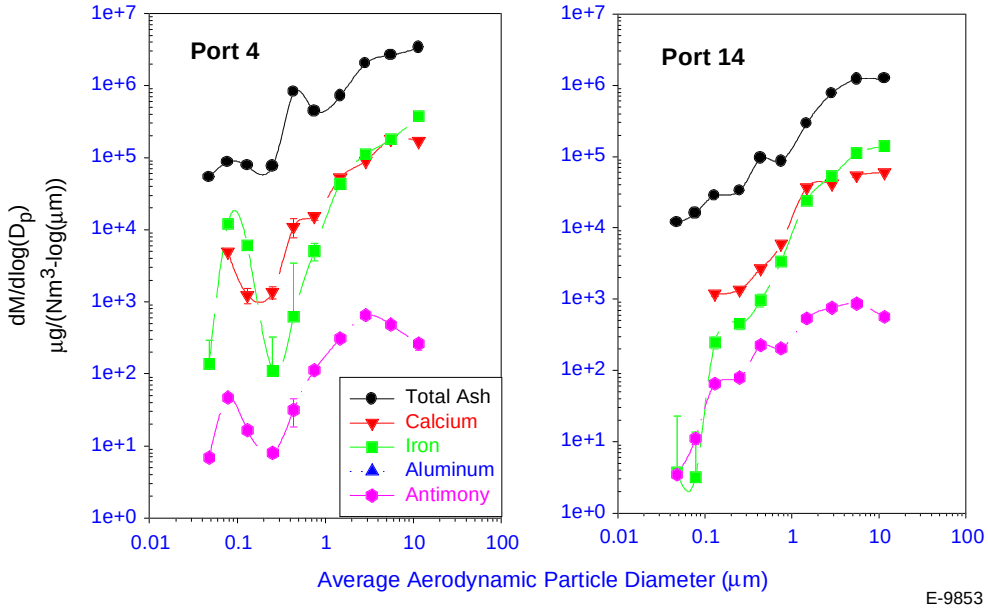

Figure 3-110. Differential distributions for Wyodak doping experiments: antimony doping with no oxygen enrichment; (a) at Port 4 – 1.6 residence seconds and (b) at Port 14 – 6.6 residence seconds.

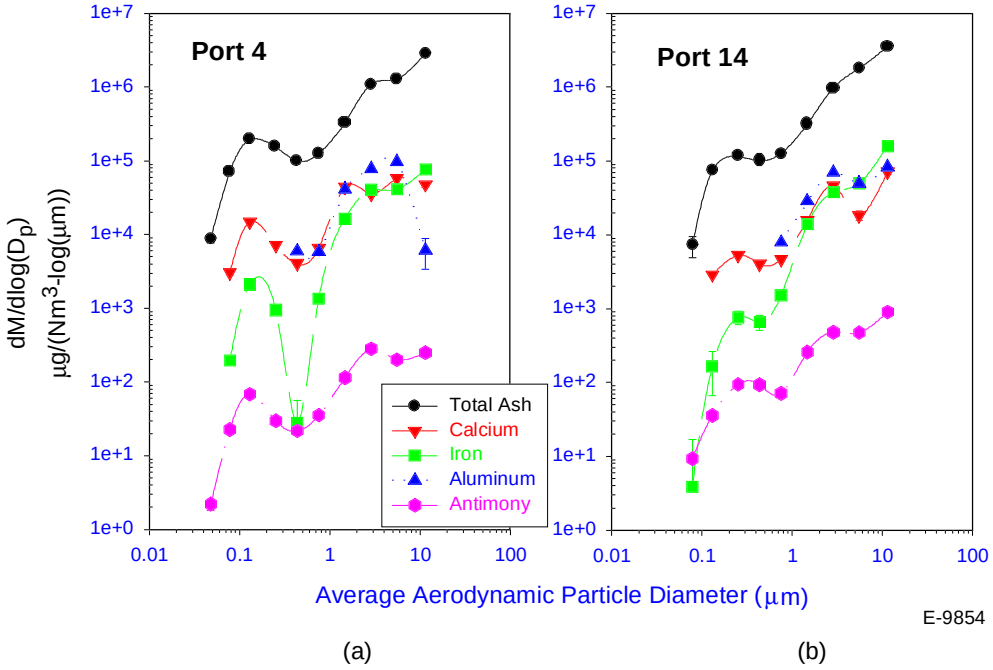

Figure 3-111. Differential distributions for Wyodak doping experiments: antimony doping with oxygen enrichment; (a) at Port 4 – 1.6 residence seconds and (b) at Port 14 – 6.6 residence seconds.

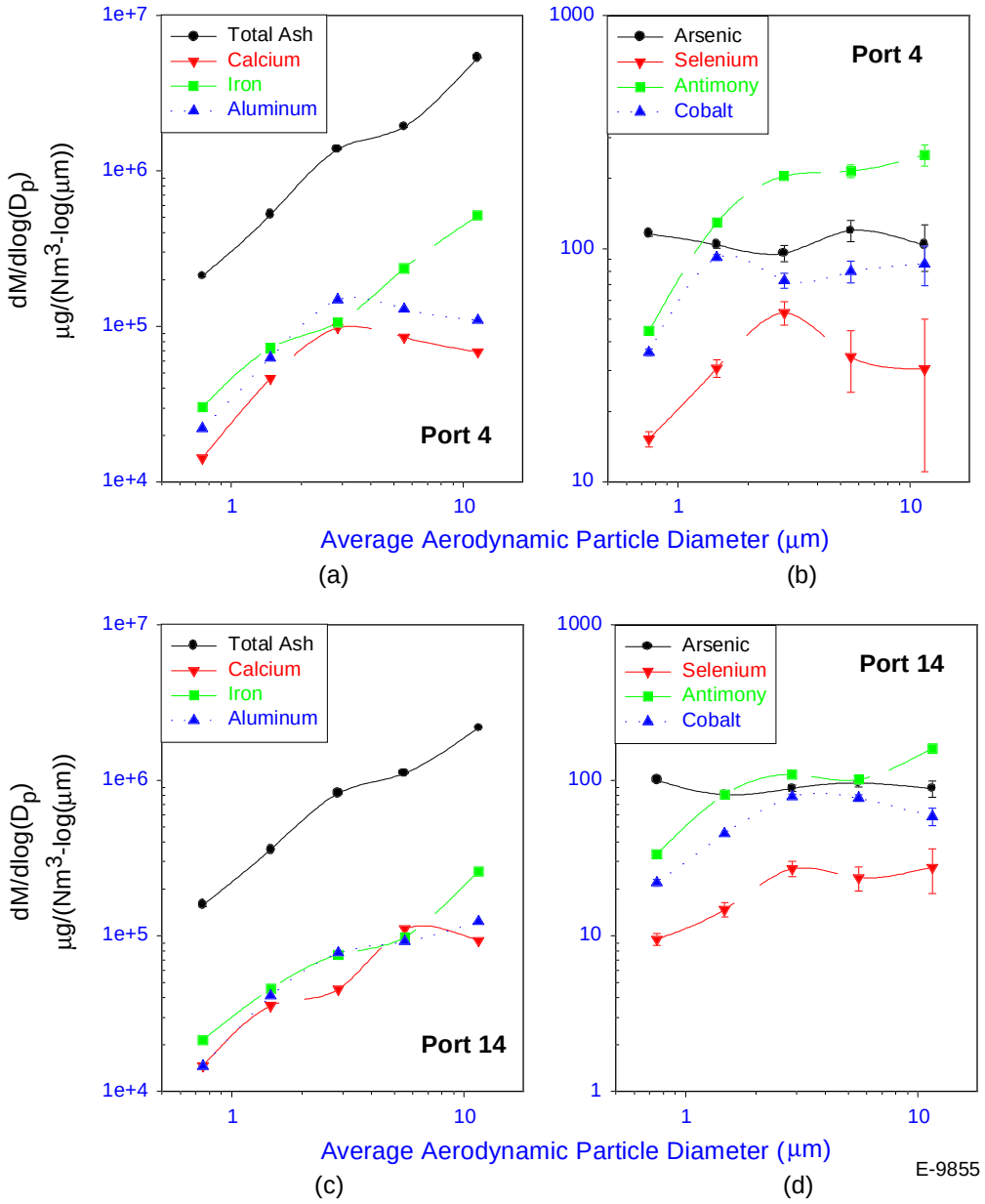

Figure 3-112. Differential distributions for Wyodak doping experiments: iron doping with no oxygen enrichment; (a) total ash and major element PSDs at Port 4 – 1.6 residence seconds, (b) trace element PSDs at Port 4 – 1.6 residence seconds, (c) total ash and major element PSDs at Port 14 – 6.6 residence seconds, and (d) trace element PSDs at Port 14 – 6.6 residence seconds.

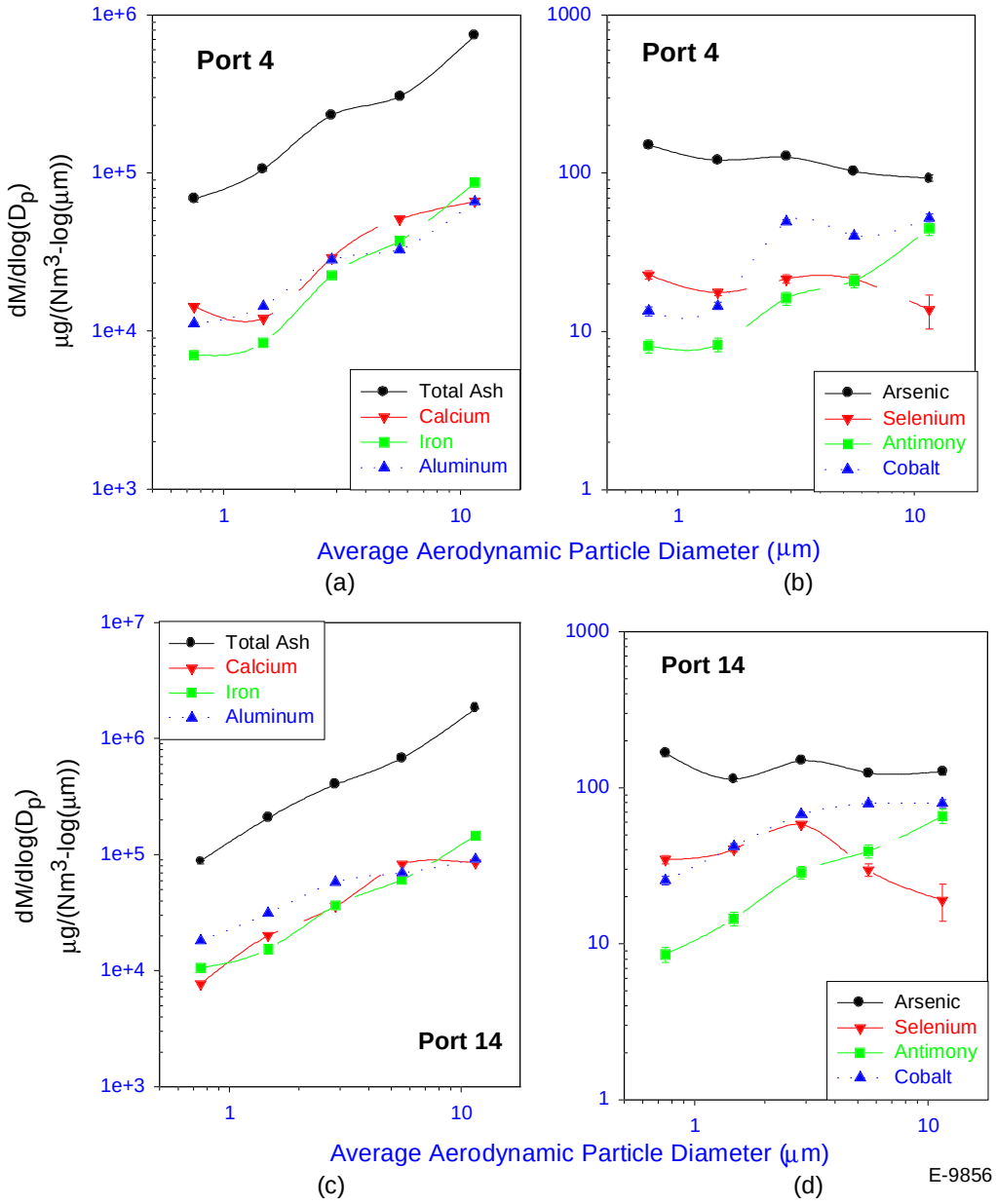

Figure 3-113. Differential distributions for Wyodak doping experiments: iron doping with oxygen enrichment; (a) total ash and major element PSDs at Port 4 – 1.6 residence seconds, (b) trace element PSDs at Port 4 – 1.6 residence seconds, (c) total ash and major element PSDs at Port 14 – 6.6 residence seconds, and (d) trace element PSDs at Port 14 – 6.6 residence seconds.

Ohio Ca Doping Experiments

A series of special experiments were performed using the Ohio coal. The Ohio coal was chosen because no particle size dependence was apparent for As, Se, or Sb. Further, none of the elemental distributions for these trace elements from the baseline combustion experiments correlates to the cation distributions.

In these experiments, calcium in the form of hydrated, pulverized lime was blended into the inlet air/fuel mixture at the top of the burner (see Section 3.3.3.1 for a description of the facilities used in these tests). The amount of calcium added decreased the As-to-Ca ratio to match the As-to-Ca ratio when burning the Wyodak coal. This also decreased the Se-to-Ca ratio to within 10% of the Se-to-Ca ratio of the Wyodak coal. The Sb-to-Ca ratio was within 25% of the Sb-to-Ca ratio of the Wyodak coal. In some of the experiments, carbon dioxide was added to the main combustion air to decrease the maximum combustion temperature in the furnace to match the maximum combustion temperature of the Wyodak coal.

Particulate sampling was performed at both Port 4 and Port 14. Duplicate sets of particle samples were collected on the top five full-size impactor stages (stages 6-10) at each combustion condition/sampling location combination (see Appendix K for a list of the experiments performed). Submicron particle samples were not collected. Size-segregated BLPI samples were used to determine the total ash supermicron PSD at both sampling locations. The typical supermicron PSD was determined from the average of all sample sets considered to be representative of baseline combustion conditions. Differential ash PSDs at both sampling locations are shown as follows:

Figure 3-114: CO_2 addition, no calcium addition
Figure 3-115: No CO_2 addition, Ca addition
Figure 3-116: CO_2 addition, Ca addition.

Sample sets that most closely duplicated the typical PSD were selected for elemental analysis. One sample set each from the Port 4 and Port 14 sampling locations were analyzed for Ca, Fe, and Al by AAS and for As, Se, Sb, and Co by GFAA at Arizona.

Differential elemental distributions are shown with the total ash PSDs in Figures 3-114 through 3-116. A discussion of these results is provided in Section 3.3.3.4.

Kentucky SO_2 Doping Experiments

A series of special experiments were performed using the Kentucky coal. The key parameters in the Kentucky coal are similar to the Ohio coal except for the sulfur content. As, Se, and Sb all show a particle size dependence for the Kentucky coal fly ash samples indicating partitioning controlled by surface reaction.

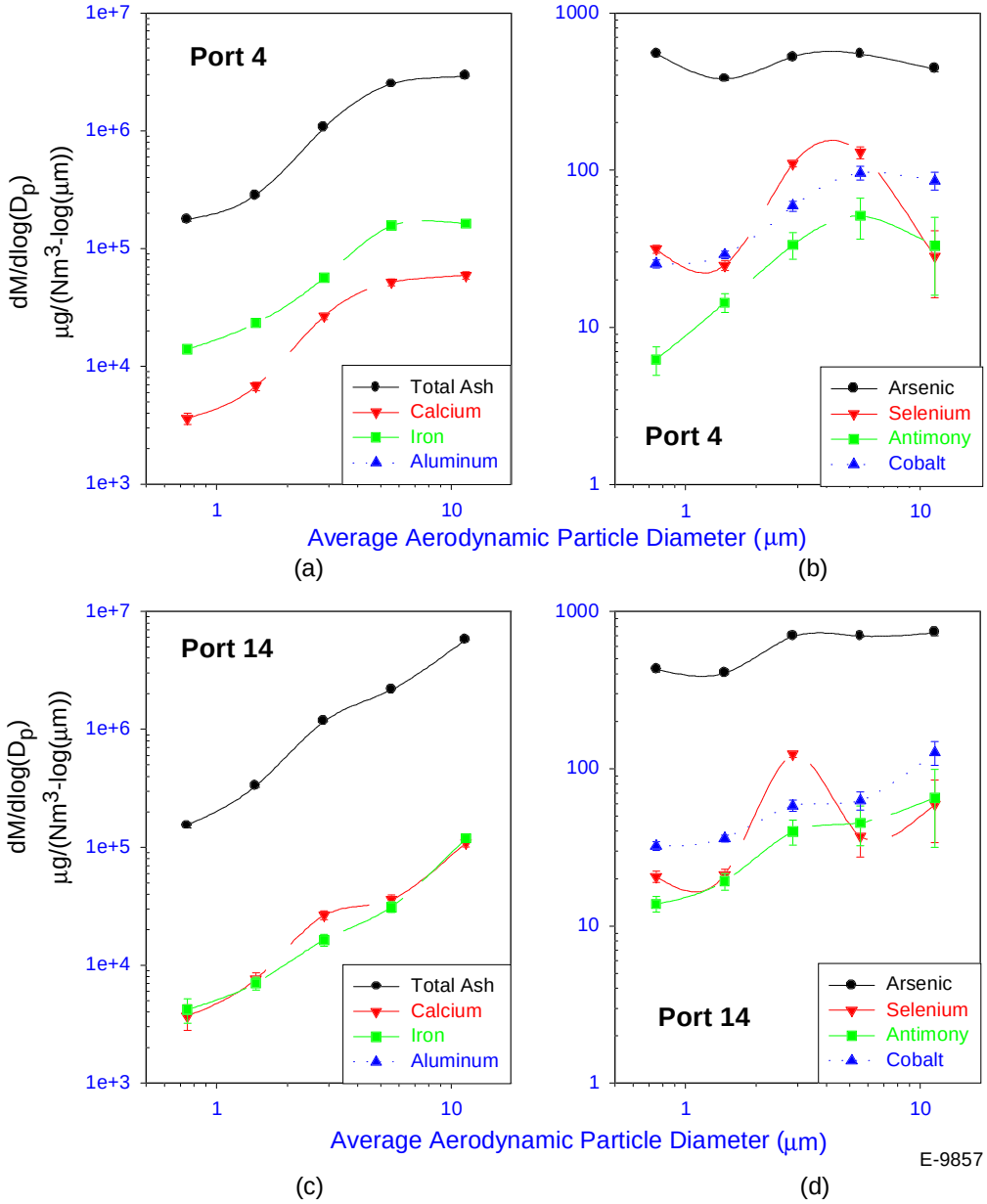

Figure 3-114. Differential distributions for Ohio special experiments: CO_2 addition with no calcium addition; (a) total ash and major element PSDs at Port 4 – 0.7 residence seconds, (b) trace element PSDs at Port 4 – 0.7 residence seconds, (c) total ash and major element PSDs at Port 14 – 3.2 residence seconds, and (d) trace element PSDs at Port 14 – 3.2 residence seconds.

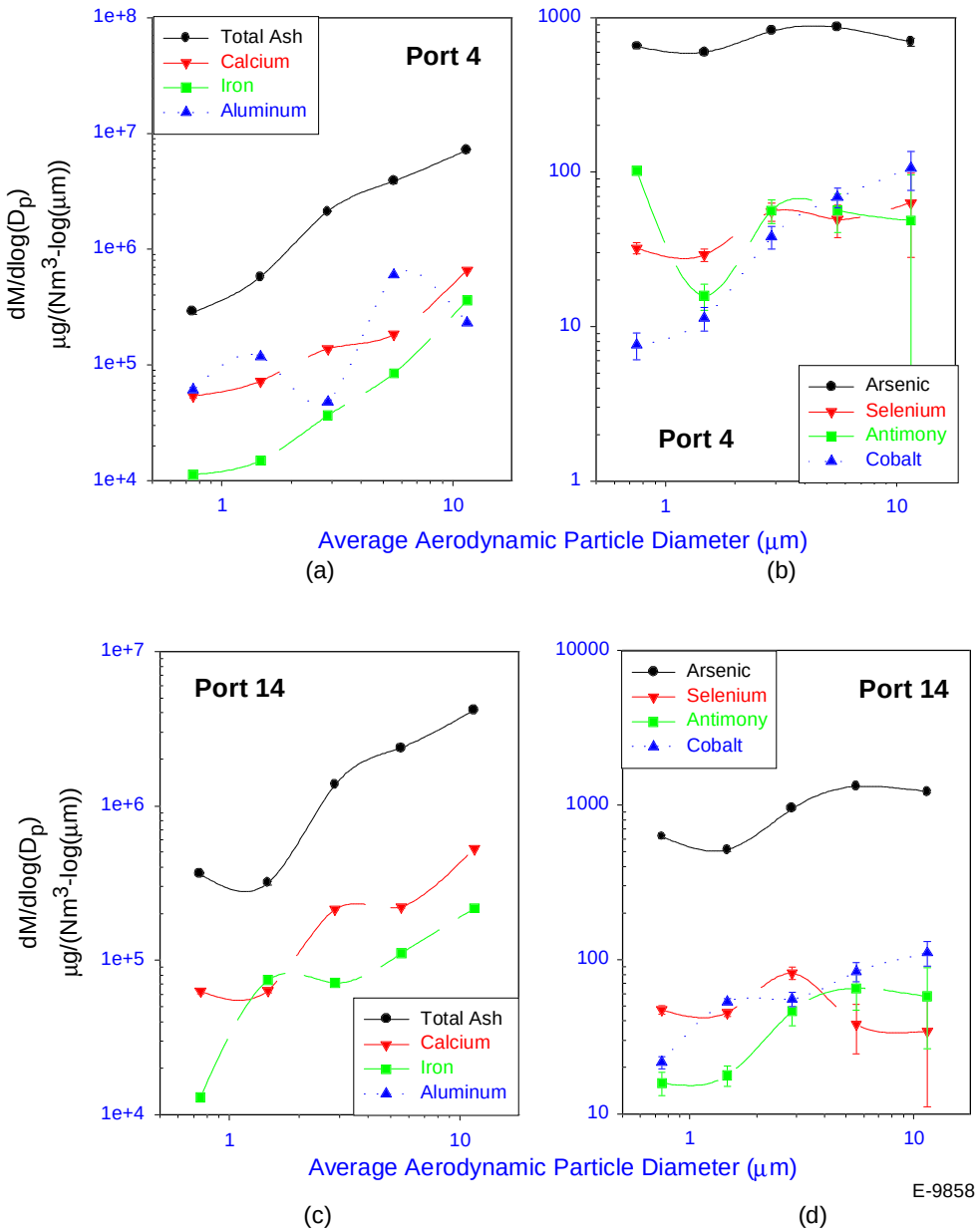

Figure 3-115. Differential distributions for Ohio special experiments: calcium addition with no CO_2 addition; (a) total ash and major element PSDs at Port 4 – 0.7 residence seconds, (b) trace element PSDs at Port 4 – 0.7 residence seconds, (c) total ash and major element PSDs at Port 14 – 3.2 residence seconds, and (d) trace element PSDs at Port 14 – 3.2 residence seconds.

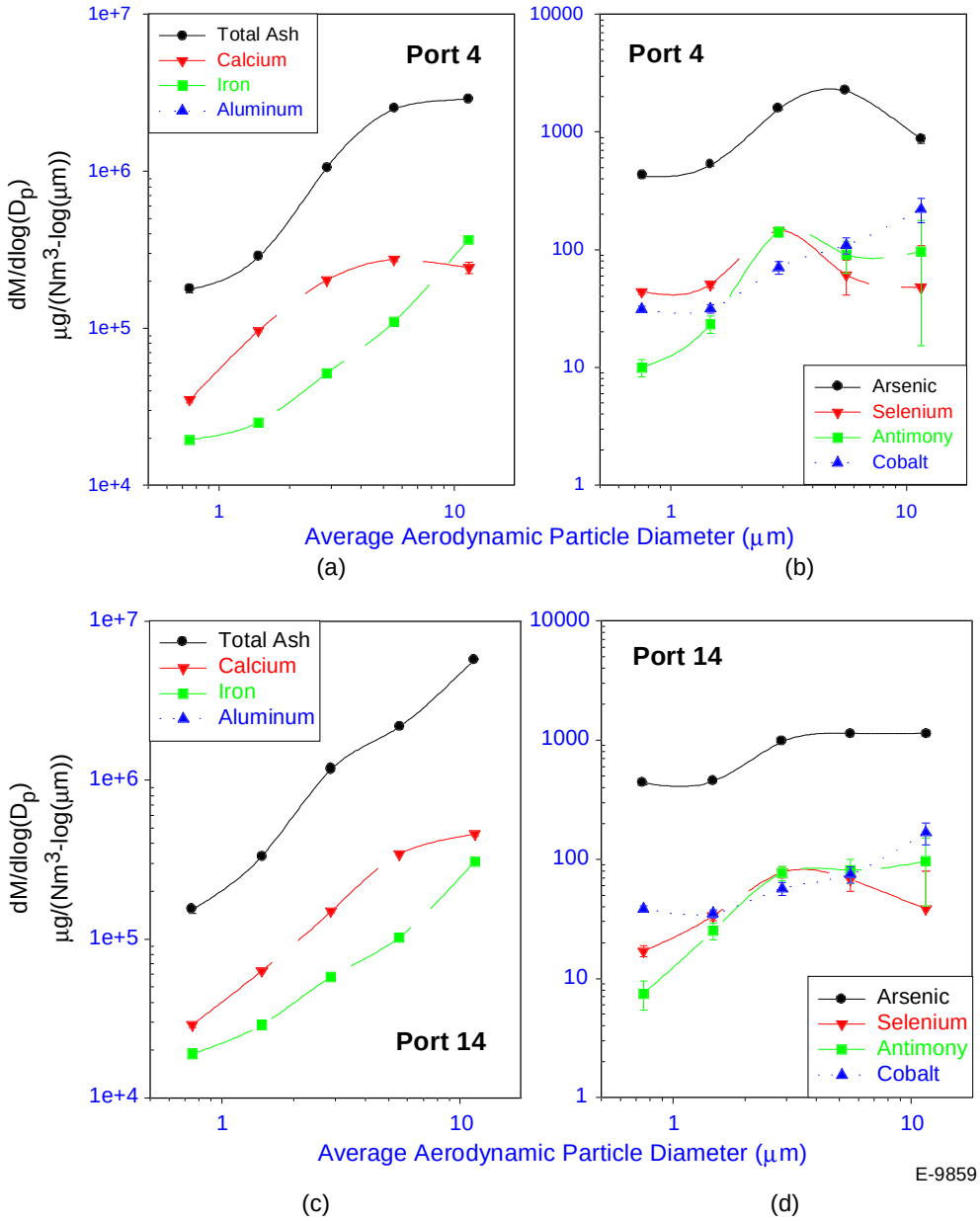

Figure 3-116. Differential distributions for Ohio special experiments: calcium addition with CO_2 addition; (a) total ash and major element PSDs at Port 4 – 0.7 residence seconds, (b) trace element PSDs at Port 4 – 0.7 residence seconds, (c) total ash and major element PSDs at Port 14 – 3.2 residence seconds, and (d) trace element PSDs at Port 14 – 3.2 residence seconds.

In these experiments, sulfur dioxide was blended into the main inlet air (see Section 3.3.3.1 for a description of the facilities used in these tests) to increase the overall sulfur content in the combustion environment. The amount of SO_2 added increased the sulfur content in the combustion environment to match the sulfur content during combustion of the Ohio coal.

Particulate sampling was performed at both Port 4 and Port 14. Duplicate sets of particle samples were collected on the top five full-size impactor stages (stages 6-10) at each combustion condition/sampling location combination (see Appendix K for a list of the experiments performed). Submicron particle samples were not collected. Size-segregated BLPI samples were used to determine the total ash supermicron PSD at both sampling locations. The typical supermicron PSD was determined from the average of all sample sets considered to be representative of baseline combustion conditions. Differential ash PSDs at both sampling locations are shown in Figure 3-117.

Sample sets that most closely duplicated the typical PSD were selected for elemental analysis. One sample set each from the Port 4 and Port 14 sampling locations were analyzed for Ca, Fe, and Al by AAS and for As, Se, Sb, and Co by GFAA at Arizona. Differential elemental distributions are shown with the total ash PSDs in Figure 3-117. An assessment of the results is included in Section 3.3.3.4.

Pittsburgh Ca/Fe Doping Experiments

A series of special experiments were performed using the Pittsburgh coal. In half of these experiments, calcium in the form of hydrated, pulverized lime was blended into the inlet air/fuel mixture at the top of the burner (see Section 3.3.3.1 for a description of the facilities used in these tests). In the other experiments, iron dissolved in water was injected into the furnace just below the burner (see Section 3.3.3.1 for a description of the facilities used in these tests). In the baseline combustion experiments, the elemental distributions of calcium and iron are very similar for the Pittsburgh coal. This set of experiments was designed to determine if As, Se, and Sb are more reactive in the coal combustion/post-combustion partitioning environment with one cation versus the other.

Particulate sampling was performed at both Port 4 and Port 14. Duplicate sets of particle samples were collected on the top five full-size impactor stages (stages 6-10) at each combustion condition/sampling location combination (see Appendix K for a list of the experiments performed). Submicron particle samples were not collected. Size-segregated BLPI samples were used to determine the total ash supermicron PSD at both sampling locations. The typical supermicron PSD was determined from the average of all sample sets considered to be representative of baseline combustion conditions. Differential ash PSDs for the calcium addition experiments at both sampling locations are shown in Figure 3-118. Differential ash PSDs for the iron doping experiments at both sampling locations are shown in Figure 3-119.

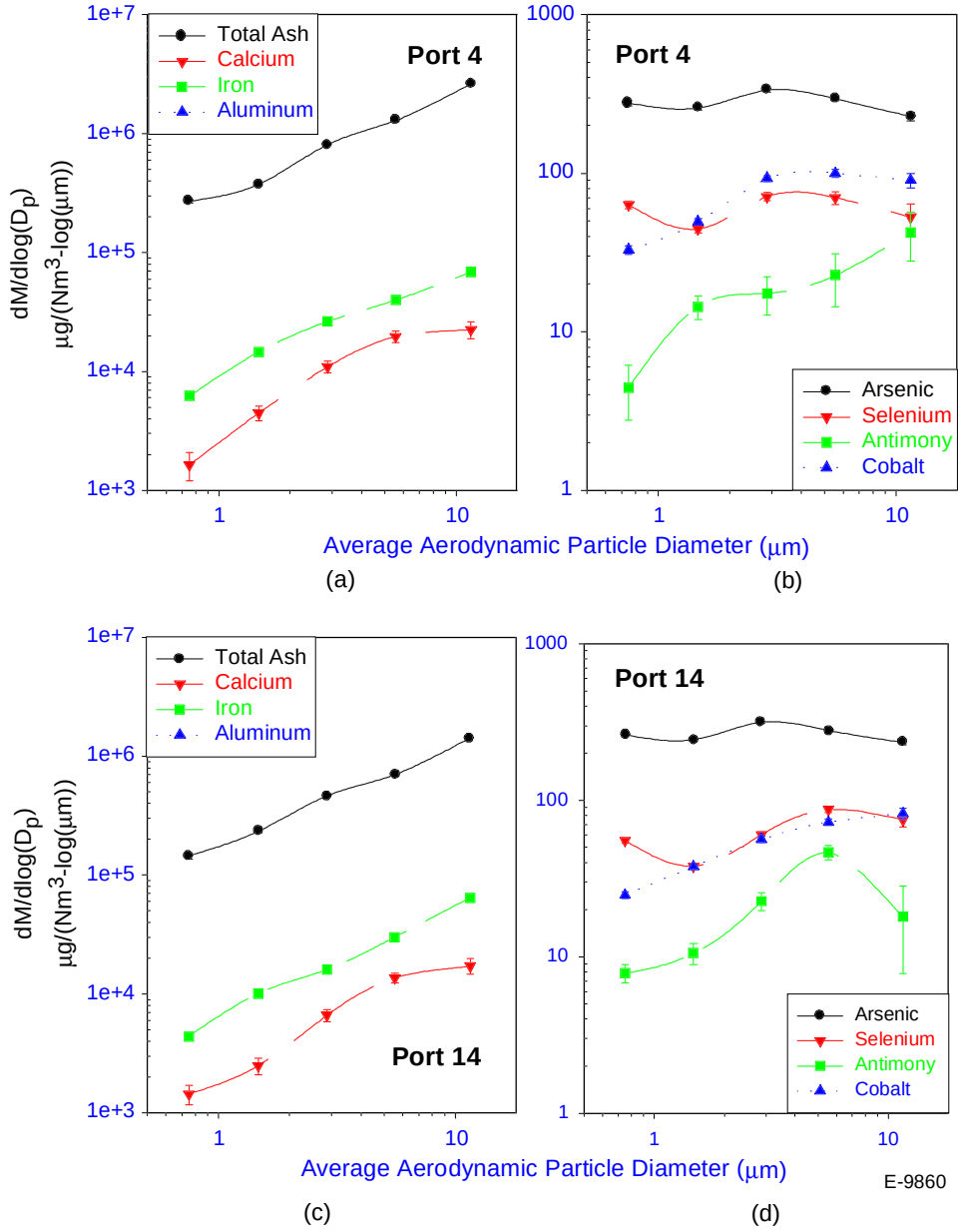

Figure 3-117. Differential distributions for Kentucky SO_2 addition experiments; (a) total ash and major element PSDs at Port 4 – 0.7 residence seconds, (b) trace element PSDs at Port 4 – 0.7 residence seconds, (c) total ash and major element PSDs at Port 14 – 2.9 residence seconds, and (d) trace element PSDs at Port 14 – 2.9 residence seconds.

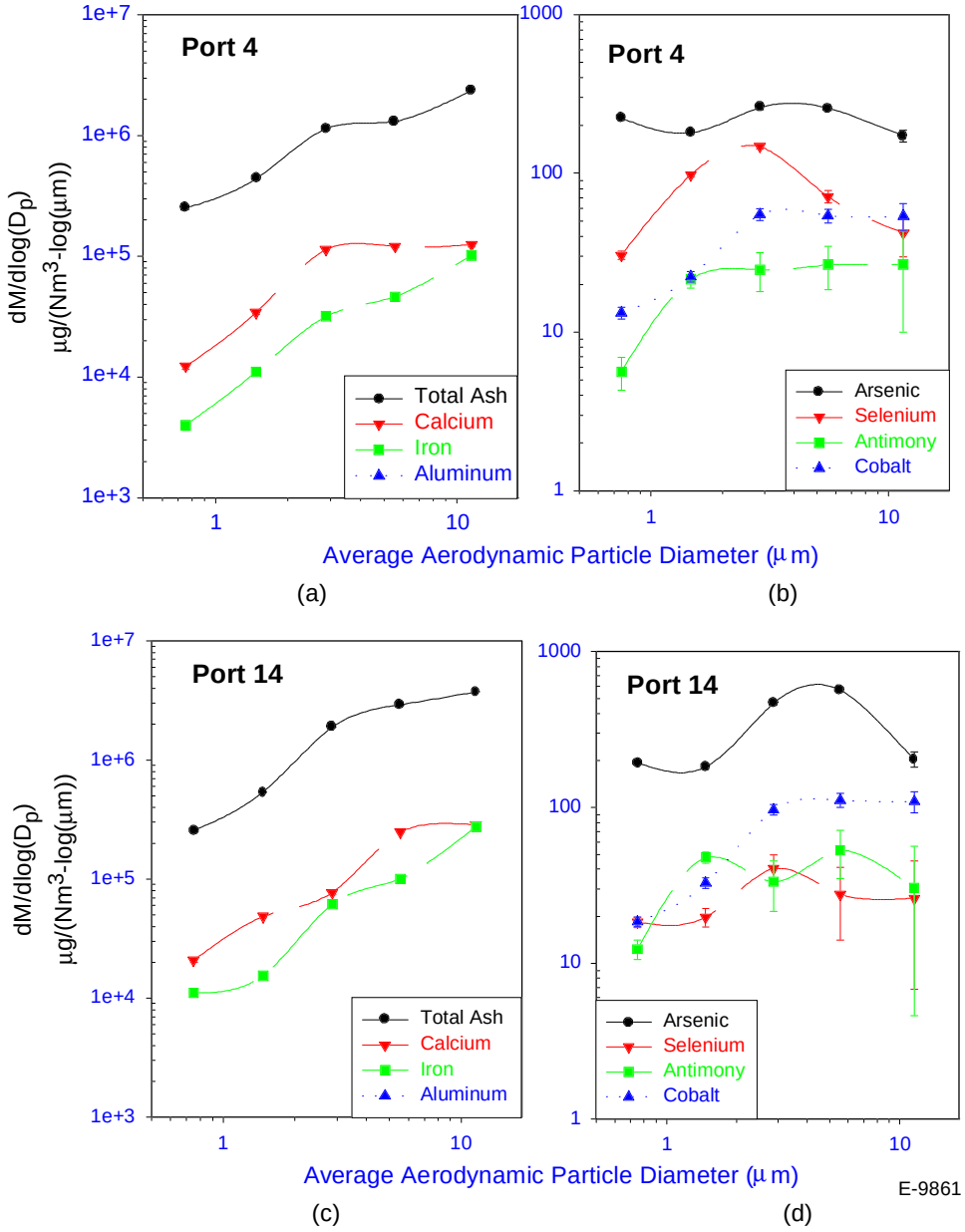

Figure 3-118. Differential distributions for Pittsburgh calcium addition experiments; (a) total ash and major element PSDs at Port 4 – 0.5 residence seconds, (b) trace element PSDs at Port 4 – 0.5 residence seconds, (c) total ash and major element PSDs at Port 14 – 2.2 residence seconds, and (d) trace element PSDs at Port 14 – 2.2 residence seconds.

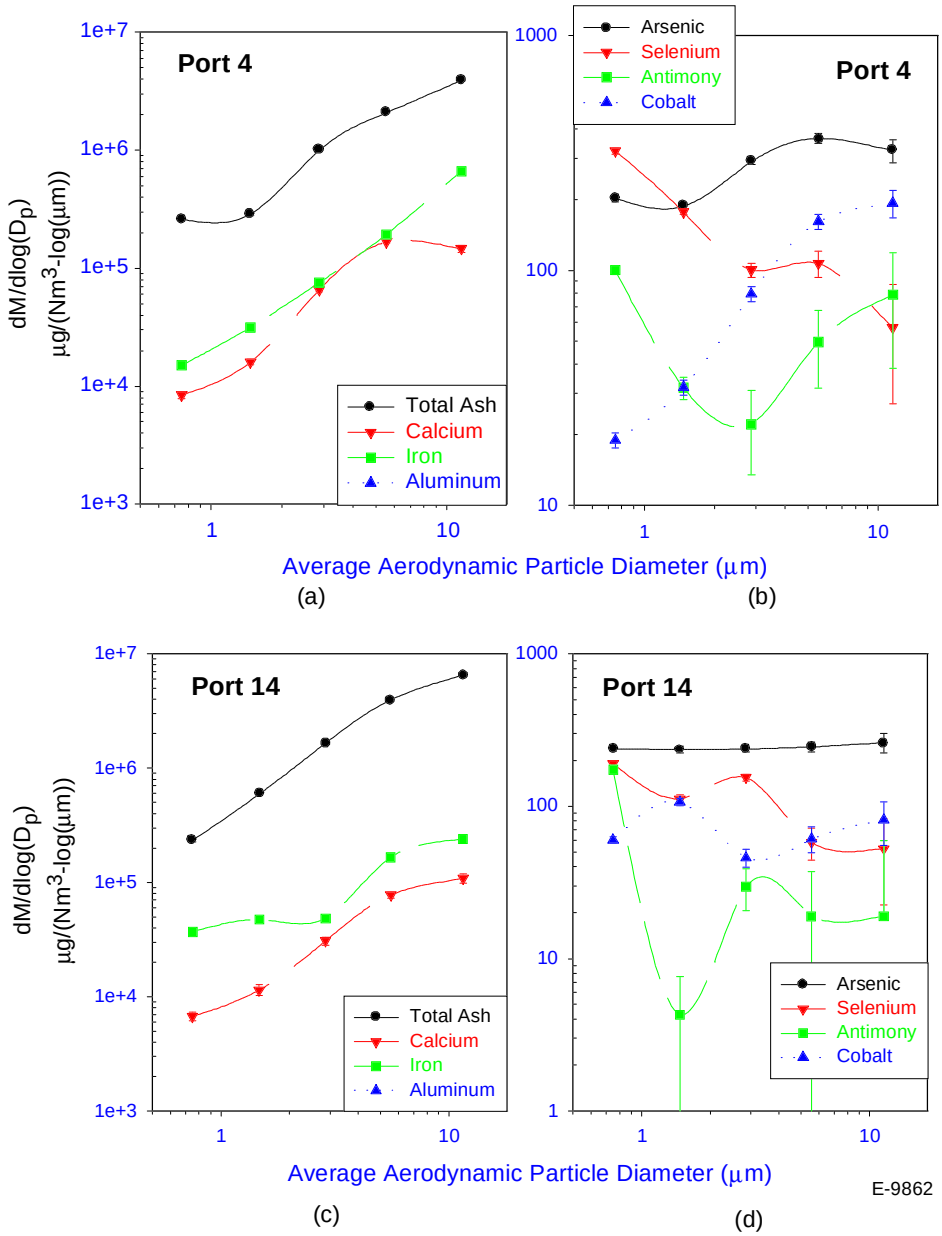

Figure 3-119. Differential distributions for Pittsburgh iron doping experiments; (a) total ash and major element PSDs at Port 4 – 0.5 residence seconds, (b) trace element PSDs at Port 4 – 0.5 residence seconds, (c) total ash and major element PSDs at Port 14 – 2.2 residence seconds, and (d) trace element PSDs at Port 14 – 2.2 residence seconds.

Sample sets that most closely duplicated the typical PSD were selected for elemental analysis. One sample set each from the Port 4 and Port 14 sampling locations were analyzed for Ca, Fe, and Al by AAS and for As, Se, Sb, and Co by GFAA at Arizona. Differential elemental distributions are shown with the total ash PSDs in Figures 3-118 and 3-119.

3.3.3.4 Analysis of Results

This work has focused on defining vapor-phase to solid-phase transformations of trace elements during pulverized coal combustion. The results presented in Section 3.3.3.3 have been evaluated in detail to identify the mechanisms governing the partitioning of semi-volatile trace elements (and to a lesser extent trace elements with lower volatility). How these elements partition during combustion depends upon:

- The form of occurrence of the trace element and potential reactants in the coal,
- The volatility of the trace element and potential reactants during combustion, and
- The vapor-to-solid phase transformation mechanisms available to the metal in the combustor.

A detailed evaluation was performed of the partitioning of selenium, arsenic, antimony, and cobalt. The issues addressed by this evaluation included:

- Assessment of volatility,
- Quantification of vapor-phase emission under the experimental conditions,
- Confirmation of heterogeneous partitioning as the primary mechanism for vapor-to-solid phase transformation,
- Identification of the most likely rate-controlling transport mechanism for vapor-to-solid phase partitioning,
- Identification of the most likely reactants when surface reaction is the rate-controlling transport mechanism,
- Assessment of the environmental impact of trace element leachability from submicron and supermicron fly ash particles, and
- Assessment of the timing of the various partitioning processes.

From this evaluation, hypotheses were developed for the mechanisms and parameters governing the partitioning of the specific trace element examined. These hypotheses are:

- Arsenic, selenium, and antimony partitioning is controlled by surface reaction with calcium and/or iron active surface sites if a particle size dependence analysis indicates that surface reaction is the dominant mechanism for the heterogeneous vapor-to-solid phase partitioning to fly ash surfaces.

- Increasing the combustion temperature increases the availability of active cation surface sites and thus increases the recovery of As, Se, and Sb out of the fly ash by surface reaction.

- Increased sulfur inhibits the recovery of As, Se, and Sb by occupying active cation surface sites.

- Sulfur preferentially occupies iron surface sites compared to calcium surface sites.

- Selenium is more reactive with active iron surface sites than with active calcium surface sites.

- Arsenic and antimony are more reactive with calcium surface sites than with iron surface sites.

- Volatilized cobalt is a simple oxide and reacts with anion surface sites (i.e., aluminum).

In this section, data are provided supporting or refuting the hypotheses proposed.

A less detailed evaluation was performed for the partitioning of three radionuclides – cesium, thorium, and cerium – during pulverized coal combustion. This evaluation provides directional information related to:

- Quantification of vapor-phase emission under the experimental conditions,
- Assessment of the probability of heterogeneous partitioning as the primary mechanism for vapor-to-solid phase transformation,
- Identification of the most likely rate-controlling transport mechanism for vapor-to-solid phase partitioning,
- Assessment of the timing of the various partitioning processes.

Samples were collected and analyzed from two different locations in the experimental furnace. Most of the analysis provided below is based on samples taken at Port 14 and represent typical conditions near the end of a commercial combustor (post-combustion zone conditions). To gain insight into the timing of trace element partitioning, samples were also collected and analyzed from Port 4. This sampling location is located about 0.6 m below the location in the furnace where the maximum combustion temperature occurs. Based on visual observation of the combusting coal particles, the vast majority of carbon burnout has occurred prior to this location during combustion of a bituminous coal. This location has been chosen to represent conditions that approximate the conditions in the commercial combustion just after primary carbon oxidation is completed (combustion zone conditions).

Fly Ash Particle Surface Sites

Due to the low concentration of trace elements compared to the major species in the coal, there is a very high probability that a volatilized trace element molecule will contact submicron or supermicron particles prior to reaching the supersaturation condition necessary to initiate homogeneous nucleation. Therefore, the availability of potential reactants on the surface of submicron and supermicron particles may be significant in the partitioning of the trace element.

Both submicron and supermicron fly ash particles have been shown to be primarily spherical in shape. A scanning electron microscopic (SEM) examination of bulk Wyodak, North Dakota, and Ohio fly ash particles found that the vast majority of inorganic particles are spherical. Mamane et al. [134] observed that over 95% of the particles in both submicron and supermicron regions were spheres having "rather smooth" surfaces for fly collected in-stack at a commercial combustor. Smith [28] and Helble et al. [135] found similar results. In addition, the vast majority of particles (<100 μm diameter) are essentially non-porous in nature [136]. Porous particles are typically hollow cenospheres filled with smaller, essentially non-porous spheres [137]. For most supermicron particles, smaller particles adhere to the particle surface, substantially increasing the surface area and roughness of the particle [136-140].

Fly ash particle surfaces primarily consist of a solid matrix composed of various solid-phase oxidized silica, aluminum, iron, and calcium structures (see results in Section 3.3.3.3). The oxidized forms of silica, iron, and calcium are cationic and the oxidized form of aluminum is anionic. When bound in the inorganic structure of the bulk fly ash particle, these species are believed to have limited reactivity for other elements. However, when these species volatilize and recondense to the solid phase, active surface sites are expected to be present. Active sites are also expected when larger particles fragment into smaller-sized particles.

The major refractory elements (iron, silica, aluminum, and calcium) are believed to vaporize as suboxides formed by reduction with carbon monoxide (CO) in the immediate vicinity of the burning char particle [15, 20, 21]. As the molecules diffuse out of the reducing atmosphere of the char, they are oxidized. These oxides are not very volatile and will nucleate while still in the flame zone to form a submicron fume [20-26].

The oxide forms of silica, aluminum, iron, and calcium have boiling points substantially above the bulk gas temperature in the combustion zone. As a result, volatilization is dependent on the forms of occurrence in the coal and the proximity to burning carbon molecules where the temperature is substantially higher than the bulk gas temperature [15]. The relative volatility of these oxides is: $CaO > Fe_2O_3 > Al_2O_3 > SiO_2$.

If this theory of submicron fume formation (volatilization of refractory elements with subsequent nucleation and coagulation to form submicron particles) is correct, then changing the combustion temperature should change the composition of the submicron particles. A set of special experiments was performed to investigate the effect of combustion temperature on the partitioning (and thus by inference the volatility) of calcium, iron, aluminum, and silicon during coal combustion. In these experiments, the maximum temperature of Wyodak coal combustion was increased 60 K (as measured at Port 1[1]) by adding oxygen to the main combustion air. Evaluation of this hypothesis can be performed using a differential mass fraction distribution analysis.

A comparison of the differential mass fraction distributions for calcium, iron, aluminum and silicon are shown in Figure 3-120. The results show the greatest increase in the mass fraction in the submicron stages of calcium for the 1580 K case compared to the 1520 K case. Iron also shows an increase in the mass fraction in the submicron stages for the 1580K results compared to the 1520 K results but not as significantly as calcium. Increasing the combustion temperature had no appreciable effect on the aluminum or silicon distributions. These results are consistent with the hypothesis stated above. The results shown in Figure 3-120 also helps to evaluate another important parameter during coal combustion – namely carbon burnout. Incomplete carbon burnout can affect the liberation of organically-associated trace elements and the degree of volatilization of major species (and thus the formation of active cation and anion surface sites). One way of minimizing incomplete carbon burnout is to enrich the combustion air with oxygen. If incomplete carbon burnout is significant, there will be an increase in the volatilization (and thus the submicron particle formation) of all major inorganic elements in the results from experiments with O_2-enriched combustion. However, the results in Figure 3-120 indicate that submicron major element enrichment at higher oxygen combustion conditions is selective (i.e., only calcium and iron show increases in the submicron region). Therefore, carbon burnout was not considered to be an important parameter in these experiments.

To further support this conclusion, total bulk ash samples from the Wyodak coals were analyzed for carbon content (by low of ignition analysis) and examined by SEM. The results show that carbon present in the Wyodak fly ash is most likely due to soot formation. Unburned carbon is not expected to be present in significant quantities.

The fractionation of larger particles to submicron-sized particles also contributes to the submicron fume [21, 26-28]. The contribution from fractionation is highly coal dependent. In addition, based on the particle size distributions shown in Section 3.3.3.3, a micron-sized fragmentation-based particle region is formed under baseline combustion conditions for many of the coals studied. The presence of this region affects the shape of the elemental differential distributions of both major and trace element inorganic species. Where possible, the impact of this region on trace element partitioning is addressed in the discussions that follow.

[1] Based on the temperature profile in Figure 3-97, the actual maximum is located slightly above this port.

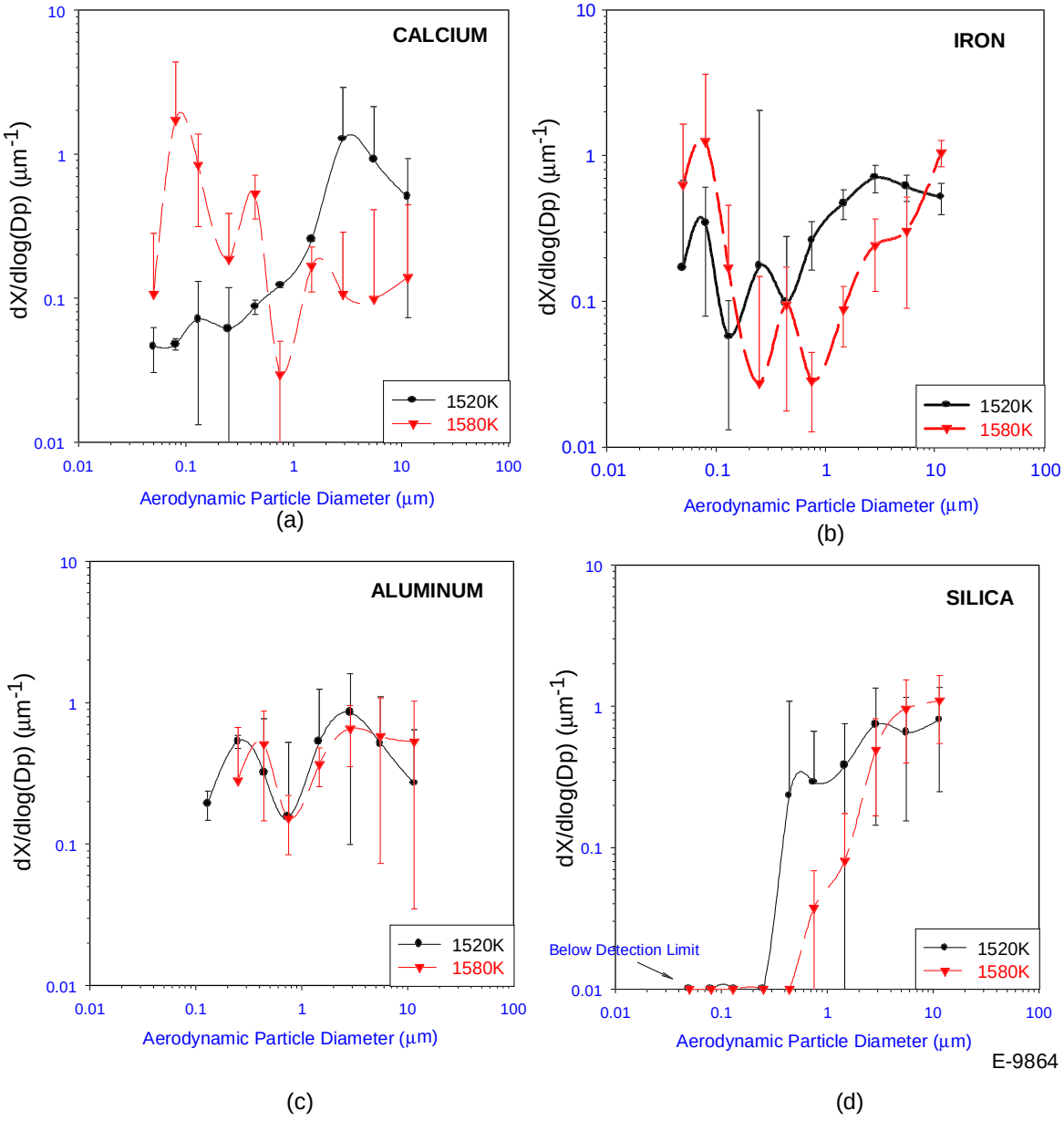

Figure 3-120. The effect of combustion temperature on the volatility of calcium, iron, and aluminum during the combustion of Wyodak coal; (a) calcium, (b) iron, (c) aluminum, and (d) silica

Selenium

Selenium Volatility

Finkleman and coworkers [7, 141, 142] determined the forms of occurrence of selenium for the six coals utilized in this study. The results are summarized in Table 3-79. The majority of the selenium for all six coals was not leachable by any of the solvents. Finkleman et al. [48] has concluded that Se bound in organic matter in a manner similar to sulfur would not be liberated by any of the solvents used. If the Se is primarily bound in organic matter, it is expected to volatilize during combustion [48]. Therefore for all six study coals, most of the selenium in the coal feedstock is expected to volatilize during combustion.

Table 3-79. Forms of Occurrence of Selenium in the Six Study Coals

Coal	Ammonium Acetate Leachable (organic)	HCl Leachable (mono-sulfide)	HF Leachable (silicate)	HNO_3 Leachable (pyrite/sulfide)	Unleached (Organic)
Pittsburgh	0%	5%	0%	90%	5%
Illinois	10%	0%	0%	50%	40%
Kentucky	10%	15%	0%	20%	55%
Ohio	5%	5%	0%	55%	35%
Wyodak	10%	0%	0%	30%	60%
North Dakota	15%	5%	0%	20%	60%

Results from thermodynamic equilibrium simulations predict that SeO_2 (with less than 5% SeO) is the favorable form of occurrence at the combustion temperatures of all six coals studied in this research.

Vapor-to-Particle Surface Selenium Transport Mechanisms

Due to the low concentration of selenium compared to the major species in the coal, there is a very high probability that a volatilized selenium molecule will contact submicron or supermicron particles prior to reaching the supersaturated conditions necessary for nucleation. Therefore, a majority of the volatilized selenium is expected to heterogeneously partition onto the surfaces of both submicron and supermicron particles [30]. However since selenium (as SeO_2) has a high volatility at post-combustion temperatures, a significant minority of the selenium will exit the combustor in the vapor phase. In this study the average mass fraction of selenium still in the vapor phase at the post-combustion zone sampling location (Port 14) for the baseline screening experiments was 13 wt%. However, there was significant variation between coal types (see Table 3-80).

Table 3-80. Mass Fraction of Selenium in Vapor, Submicron, and Supermicron Regimes at Three Combustor Sample Locations

Coal/Location	Average Sampling Temperature (K)	Vapor Regime (Wt%)	Submicron Regime (Wt%)	Supermicron Regime (Wt%)
Pittsburgh				
Port 4	1440	0.9	36	63
Port 14	1140	3.0	8.5	89
Baghouse Inlet	470	6.2	1.5	92
Illinois				
Port 4	1410	1.8	22	76
Port 14	1130	5.5	14	81
Baghouse Inlet	220	29	18	53
Ohio				
Port 4	1330	9.8	4.7	86
Port 14	1040	23	6.0	71
Baghouse Inlet	610	66	20	14
Kentucky				
Port 4	1490	15	8.3	77
Port 14	1150	1.9	1.6	96
Baghouse Inlet	490	14	13	73
Wyodak				
Port 4	1080	0.6	2.2	97
Port 14	760	8.7	27	64
Baghouse Inlet	210	3.5	10.5	86
North Dakota				
Port 4	1250	26	6.9	67
Port 14	870	34	9.2	56
Baghouse Inlet	400	nd[1]	28	72
Average All Coals				
Port 4		8.9	13	78
Port 14		13	11	76
Baghouse Inlet		20	15	65

All samples were below the analytical detection limit

For all of the study coals, most of the selenium partitions back to the solid phase prior to exiting the combustor. For four of the coals – Pittsburgh, Illinois #6, Wyodak, and Kentucky – very little (<9 wt%) of the selenium is still in the vapor phase at Port 14. By contrast, thermodynamic simulation (see Section 3.3.1) predicts vapor-phase SeO_2 as the most favorable form of occurrence for selenium at post-combustion temperatures.

The average mass fraction of selenium still in the vapor phase at the baghouse inlet sampling port for the baseline screening experiments was 20 wt%. It should be noted that a portion of the bulk fly ash particles has been removed from the flue gas prior to this sample. For comparison, Andren et al. [78] report that 32% of the selenium at the Allen Steam Plant leaves in the vapor phase.

Submicron particles formed by the submicron fume formation mechanism above, have a high number density [27]. The combination of small spherical size and high number density leads to a very high surface area density (surface area/unit mass). Thus, there will be an enrichment (i.e., increase in the concentration) of selenium onto submicron particles [24, 30] compared to supermicron particles. Selenium enrichment factors for fly ash particles from the baseline screening experiments sampled at the Port 14 (post-combustion zone) sampling location are given in Table 3-81[2]. All of the submicron fly ash samples taken at the post-combustion zone sampling location (Port 14) show enrichment of selenium (values greater than 1.0). Selenium enrichment on submicron particles has previously been observed by numerous researchers [8, 9, 12, 13, 18, 31, 34, 35, 72, 78, 80, 81, 143, 144].

Table 3-81. Selenium Enrichment* Factors for Submicron-Sized Fly Ash Samples

Coal/Location		Aerodynamic Particle Diameter (μm)			
		0.17	**0.34**	**0.54**	**Average**
Pittsburgh	Port 14	1.2	1.3	1.5	1.3
	Port 4	3.1	1.6	2.1	2.2
	Differential	-1.9	-0.25	-0.57	-0.9
Illinois	Port 14	5.8	1.9	1.9	3.2
	Port 4	2.3	1.6	0.59	1.5
	Differential	3.5	0.25	1.3	1.7
Kentucky	Port 14	4.1	4.2	2.4	3.6
	Port 4	9.5	5.9	5.1	6.8
	Differential	-5.4	-1.6	-2.7	-3.2
Ohio	Port 14	29	23	13	22
	Port 4	6.1	2.4	1.9	3.4
	Differential	23	21	11	18
Wyodak	Port 14	3.8	2.2	1.4	2.5
	Port 4	0.04	0.05	0.38	0.16
	Differential	3.8	2.2	1.4	2.5
North Dakota	Port 14	nd**	nd	3.3	--
	Port 4	nd	nd	2.3	--
	Differential	--	--	1.0	--

* The enrichment factor, $E_{i,x}$ is defined as:

$$E_{i,x} = M_{i,x} / (\Sigma_N M_{i,x} / N)$$

** nd = concentration of element on this impactor stage was below the analytical detection limit

[2] See Eq. (3-14) for the definition of the enrichment factors employed in this work.

While supermicron particles have a lower specific surface area than submicron particles, the total surface area available on supermicron particles exceeds the total available on submicron particles. As a result, the supermicron particle region will contain a higher mass fraction of the total selenium available than the submicron particles. In the current work, the average selenium mass fraction in the supermicron particles was 76 wt% (see Table 3-80 for individual values). These results (selenium concentration enrichment on submicron particles and higher total selenium mass on supermicron particles) are consistent with a partitioning mechanism dominated by the heterogeneous partitioning of selenium to the surfaces of submicron and supermicron particles.

Vapor phase selenium is believed to form an oxy-anion of the form SeO_2 [29, 35, 145, 146], although some researchers believe that gaseous selenium will also be present in the elemental state [77] or as seleneous acid [147]. SeO_2 is also predicted by the thermodynamic simulation results presented in Section 3.3.1. When SeO_2 contacts the particle surface it has the potential to stay with the particle or to bounce off. The oxy-anion is more likely to adhere to the particle when contact is near an active cation surface site (attractive bonding). The probability that SeO_2 will remain on the fly ash surface is primarily due to the number of active cation sites on the particle surface.

SeO_2 will become incorporated into the particle if subsequent reaction between the anion and cation (chemical bonding) occurs. The probability that chemical reaction will occur depends upon the rate at which the anion can migrate across the particle surface to the cation site and the kinetic reaction rate between the anion and cation.

Because of the volatility of selenium, gas-phase concentrations of SeO_2 (up to 250 mg/m^3 at 423 K) are sufficient in many systems to initiate physical condensation prior to the stack. Therefore, condensed SeO_2 may also be present on the particle surfaces for particles collected at low temperatures. Condensation is not expected to be significant for the samples collected at Ports 4 and 14 in the current study due to the relatively high temperatures at the sampling conditions; although the baghouse inlet port samples were collected at a temperature low enough for condensation to occur.

To determine the rate limiting mechanism, a number of researchers have analyzed partitioning behavior from the gas phase to particle surfaces using particle size dependence models based on transport theory [13, 16, 28, 29, 35, 71, 79]. For the supermicron particles, it can be shown that (assuming that the particles are spherical in shape and traveling at the same speed as the surrounding gas) transport of a selenium molecule from the vapor phase to the particle surface controlled by gas film transfer will follow an inverse dependence to the square of the particle diameter ($1/D_p^2$). Similarly, if transport is controlled by exterior surface reaction (assuming the particles are non-porous), the selenium distribution will follow an inverse dependence to the particle diameter ($1/D_p$; [6][3].

[3] For porous particles, a $1/D_p$ dependence may also indicate pore diffusion-controlled reaction.

The particle size dependence of selenium associated with supermicron fly ash particles for the six study coals at the Port 14 sampling location is shown in Figure 3-121. The Illinois, Kentucky, and Wyodak selenium distributions follow a near 1/Dp dependence which indicates that volatile selenium partitions to supermicron particles by a mechanism controlled by exterior surface reaction. The North Dakota selenium distribution follows a near $1/Dp^2$ dependence indicating that gas film transfer controls the transport rate of selenium from the vapor phase to the particle surface. For the Ohio and Pittsburgh coals the results show no particle size dependence in the post-combustion zone.

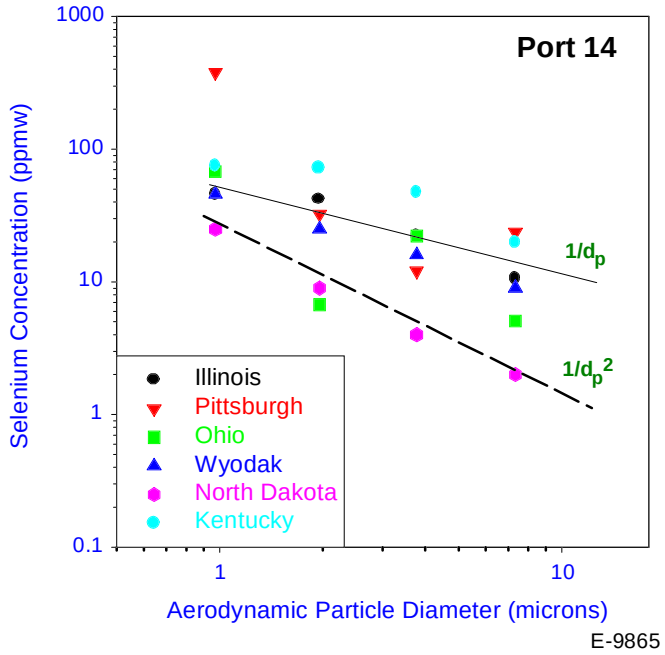

Figure 3-121. Particle size dependence of selenium in supermicron fly ash particles for all six study coals sampled at Port 14.

For comparison, Biermann and Ondov [13] report a $1/D_p^2$ selenium size dependence for fly ash particles sampled at the end of the post-combustion zone; although a $1/D_p$ dependence was found to be equally valid for particles greater than 0.8 μm in diameter.

Submicron particles are typically in the transition size range between particles sizes in which continuum mechanics are valid and smaller size ranges that approach the Knudsen region where the particles are similar in size to the mean free path of molecules in the surrounding gas [13, 148]. Therefore, a particle-size dependence analysis for submicron particles is less useful in determining the rate-limiting mechanism (diffusive, kinetic, etc.).

If free molecular regime transport theory is assumed applicable, a $1/D_p$ dependence for selenium would be evidence for either gas film transfer limited or surface reaction limited transport [6, 29]. The size-segregated concentration of selenium in submicron particles from the current study is shown in Figure 3-122 for the six study coals at the Port 14 sampling location.

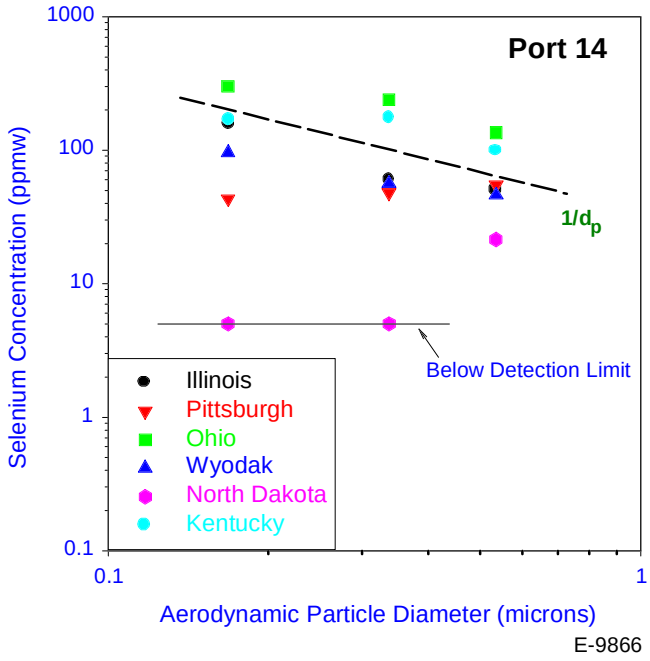

Figure 3-122. Particle size dependence of selenium in submicron fly ash particles for all six study coals sampled at Port 14.

There appears to be a decrease in concentration with particle size for the Illinois, Kentucky, Ohio, and Wyodak coals on the order of a $1/D_p$ dependence. These results imply that a transport process limits the partitioning of selenium to submicron particle surfaces for these coals. No particle size dependence is apparent for the Pittsburgh and North Dakota coals.

In the study by Smith et al. [9] the selenium concentration is independent of particle size in the submicron region. However, Bool and Helble [29] report a $1/D_p^2$ dependence for selenium in experiments with black thunder and washed Pittsburgh coals using a BLPI. However when the data for the supermicron particle sizes is eliminated, this dependence is no longer apparent.

Fly Ash Surface Selenium Reaction Mechanisms

Bool and Helble [29] have proposed a reaction of SeO_2 with iron cations or calcium cations as the most likely partitioning mechanisms, depending upon the coal composition. Work with other oxy-anions (e.g., arsenic) and the success of lime sorbents to remove Se and SO_2 [145, 149] reinforce this hypothesis. Ghosh-Dastidar et al. [150] report substantially higher solid-phase selenium recoveries from Ca-based sorbents acting on artificially generated Se-rich flue gas compared to kaolinite-, alumina-, or silica-based sorbents. Similar results were reported by Gullett and Ragnunathan [149] using sorbents with actual coal combustion. Unfortunately, no iron-based sorbents were utilized in either study.

The potential for Se-Fe or Se-Ca reactions as a dominant partitioning mechanism can be evaluated by comparing the total ash size distribution and the size distributions of iron, calcium, and selenium. The differential mass concentration distributions of selenium, calcium, iron, and the total ash from full impactor sets for all six coals under baseline combustion conditions at the Port 14 sampling location are shown in Figure 3-123.

To examine the results more carefully, the distributions were decomposed into their submicron and supermicron components. Then the correlation between selenium and calcium/iron was analyzed in two ways. First the cross correlation between the absolute concentration values on each relevant impactor stage was evaluated. Figure 3-124 shows an example for the Pittsburgh baseline coal sampled at Port 14. This is an example of a distribution that follows both the calcium and iron distributions more closely than the total ash distribution. However, these distributions are too similar to discern the difference (Pearson's correlation coefficient, R^2, values of 0.67 for Se versus Ca compared to 0.37 for Se versus Fe).

Second, the correlation between the differential distribution curves was evaluated. This involved fitting a curve through the differential data in the region of interest and then plotting data derived from the selenium curve versus data derived from the calcium and iron curves (interpolating between the actual discrete data points on the differential distributions). For the supermicron region, two 2^{nd} order polynomials were fit through the five data points. The polynomial through the data from the smaller diameter impactor stages represents the distribution in the near micron-sized fragmentation region while the data from the larger diameter impactor stages represents the distribution in the larger, bulk fly ash.

For example, two 2^{nd} order polynomials were fit through the five data points in the supermicron region (with the central data point in common between the two curves) for the Pittsburgh supermicron distribution. The combined curve fit is shown in Figure 3-125a. Next, data points were generated from the curves for all three elements (selenium, calcium, and iron, respectively). The overall cross correlation plot between the values generated from each curve was then constructed (Figure 3-125b). Positive correlations were found for both (R^2 values of 0.83 for Se versus Ca and 1.0 for Se versus Fe). However, examination of the Se versus Ca curve in Figure 3-125b suggests that there may be a good correlation for calcium values above 10,000 but not below 10,000. Figure 3-125b can be decomposed into two cross correlation curves for the fragmentation mode region (Figure 3-125c) and bulk fly ash region (Figure 3-125d). Selenium correlates very closely to both calcium and iron in the fragmentation region. In the bulk fly ash region, the correlation of selenium with iron appears to be better than the correlation with calcium.

The correlation of selenium to calcium and iron using both evaluation methods for both submicron and supermicron fly ash sampled at Port 14 is shown in Table 3-82 for all six study coals.

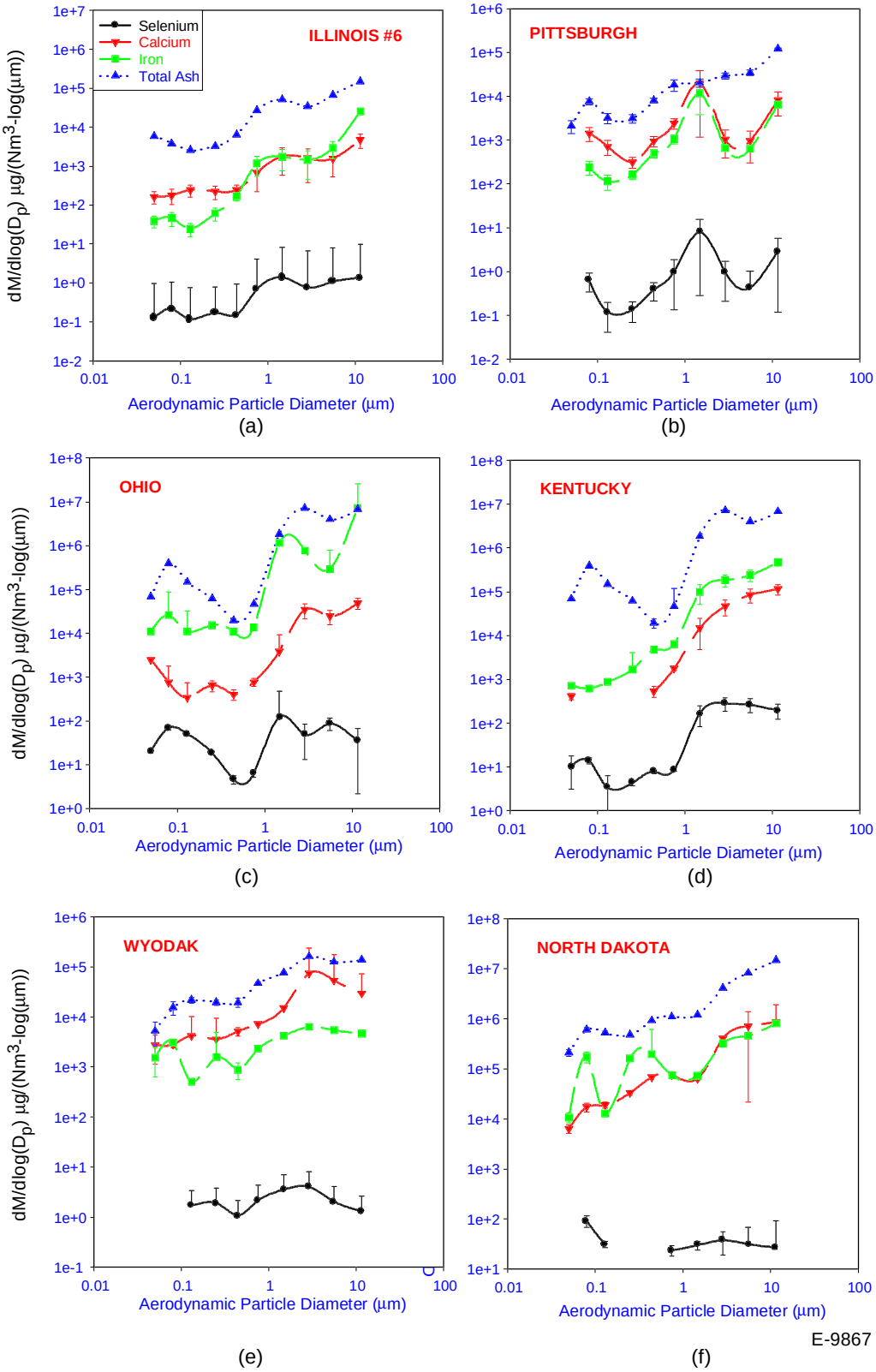

Figure 3-123. Differential mass distributions of selenium, calcium, iron, and total ash for the six study coals sampled at Port 14.

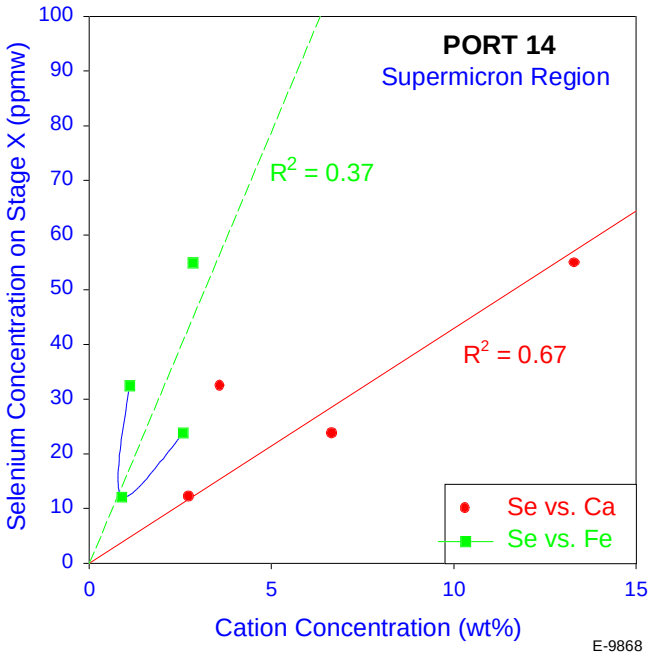

Figure 3-124. Cross correlation of Pittsburgh selenium to calcium and iron at baseline screening experimental conditions sampled at Port 14 for the supermicron region.

For the Illinois #6 coal, selenium appears to correlate with calcium in all three fly ash particle regimes. An apparent correlation with iron in the bulk fly ash particles was also calculated. Selenium in the Pittsburgh coal shows apparent correlations with both iron and calcium. This is due to the similarities in the iron and calcium distributions. Thus, it isn't possible to discern whether selenium is reacting with one cation or with both cations. For the Ohio coal, selenium does not show strong correlations with calcium or in any particle regime. Selenium in the Wyodak fly ash shows apparent correlations with calcium in the submicron and bulk fly ash regions but correlates better with iron the fragmentation region. Finally, the North Dakota selenium distribution appears to correlate with both calcium and iron in the fragmentation region but not in the bulk fly ash region[4].

This assessment of the distribution curves shown in Figure 3-123 suggests that the mechanisms controlling selenium partitioning:

1. Are different depending on the fly ash particle region
2. Are surface reaction controlled when there is sufficient calcium/iron compared to sulfur
3. When surface reaction controlled, the reaction is with iron and/or calcium active surface sites.

[4] Selenium data for the North Dakota submicron region was below the detection limit; no assessment can be made.

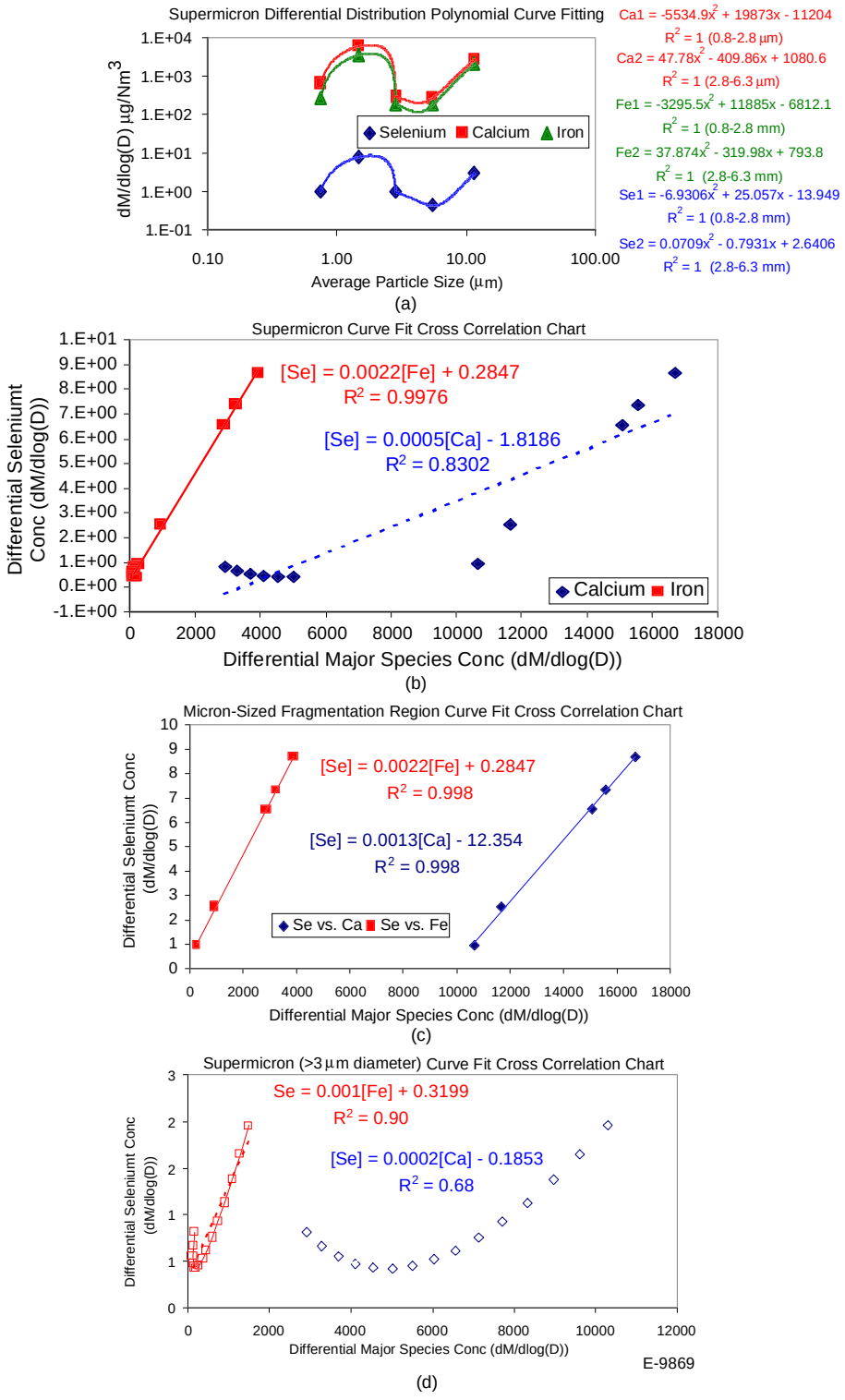

Figure 3-125. Cross correlation of Pittsburgh selenium to calcium and iron differential distribution curves at baseline screening experimental conditions sampled at Port 14 for the supermicron region; (a) best curve fit through the distribution data, (b) complete supermicron region cross correlation of data derived from the curves shown in (a), (c) cross correlation of data from 0.75 to 3.0 µm particle diameter (fragmentation region) derived from the curves shown in (a), (d) cross correlation of data from 3.0 to 10 µm particle diameter derived from the curves shown in (a).

Table 3-82. Correlation Coefficients for Selenium vs. Calcium and Iron in Fly Ash Particles from the Six Study Coals Sampled at Port 14

	Submicron Correlations			Supermicron Correlations		
Coal	**Absolute Concentrations**	**Differential Distributions**	**Overall Absolute Concentrations**	**Overall Differential Distributions**	**Fragmentation Region Differential Distributions**	**Bulk Fly Ash Region Differential Distributions**
Illinois: Se vs. Ca	0.82	~0	0.35	~0	0.73	0.80
Se vs. Fe	~0	~0	~0	~0	~0	0.71
Pittsburgh: Se vs. Ca	~0	0.99	0.67	0.83	1.0	0.68
Se vs. Fe	~0	0.99	0.37	1.0	1.0	1.0
Ohio: Se vs. Ca	~0	~0	0.48	~0	0.21	0.17
Se vs. Fe	~0	~0	~0	~0	~0	~0
Kentucky: Se vs. Ca	na*	na	~0	0.56	0.89	~0
Se vs. Fe	~0	1.0	0.13	0.86	1.0	~0
Wyodak: Se vs. Ca	~0	1.0	~0	0.15	0.58	0.94
Se vs. Fe	~0	~0	0.48	~0	0.94	0.54
N. Dakota: Se vs. Ca	na	na	~0	0.18	0.66	~0
Se vs. Fe	na	na	0.06	0.24	0.70	~0

*na = not available, analyses are below detection limit

The Illinois and Pittsburgh coals have moderate calcium contents and relatively high sulfur contents. The Ohio coal (where no size dependence was observed) has a low calcium content and high sulfur content. The Kentucky coal has a low calcium content and low sulfur content. The Wyodak and North Dakota coals have high calcium content, low sulfur content, and a lower maximum combustion temperature (than the four bituminous coals). Thus, the three parameters that appear to be important in determining the nature of selenium-cation surface reactions are: selenium-to-calcium ratio, coal sulfur content, and combustion temperature.

From these results, a set of hypotheses related to selenium partitioning was developed. To test these hypotheses, a set of special experiments was developed. Table 3-83 summarizes the hypotheses and special test matrix developed for validation.

One of the primary hypotheses proposed states that “selenium vapor-to-solid phase partitioning will be controlled by surface reaction if there are sufficient active cation surface sites to accommodate the selenium present in the flue gas”. To test this hypothesis, selenium was dissolved in dilute acid and then doped into the furnace at the burner outlet to increase the Se-to-Ca ratio in the combustion environment during Wyodak coal combustion to match the Ohio coal Se-to-Ca ratio. This was done at both the Wyodak maximum combustion temperature and an increased combustion temperature.

Table 3-83. Selenium Partitioning Mechanism Hypotheses and Validation Test Matrix

Hypothesis	Baseline Test and Fly Ash Region Where Observed	Test Number	Test Description
Vapor-to-solid phase selenium partitioning is controlled by surface reaction when sufficient surface sites are available for reaction	Ohio baseline coal versus other 5 coals; Ohio does not follow a dependence	99W-9, 00W-5	Selenium doped into Wyodak coal combustion until Se-to-Ca ratio matched Ohio ratio
		00O-1, 00O-2	Calcium blended into Ohio coal for combustion until Se-to-Ca ratio matched Wyodak ratio. Temperature decreased to match Wyodak combustion temperature
Selenium reacts with active calcium surface sites	Illinois submicron; Illinois fragmentation; Wyodak submicron; Wyodak bulk fly ash	99W-9, OOW-5	Selenium doped into Wyodak coal combustion until Se-to-Ca ratio matched Ohio ratio
Selenium reacts with active iron surface sites when sulfur is not available to consume all of the iron surface sites	Kentucky submicron; Kentucky fragmentation	00K-1	Sulfur was doped into the Kentucky coal combustion until the sulfur content matched the Ohio sulfur content
Selenium reacts with iron and/or calcium active surface sites	Illinois bulk fly ash; Pittsburgh submicron; Pittsburgh fragmentation; Pittsburgh bulk fly ash; Kentucky fragmentation; Wyodak fragmentation; North Dakota fragmentation	00P8-1, 00P8-2	Calcium was doped into Pittsburgh coal to assess recovery of selenium; then Iron was doped into Pittsburgh coal to assess recovery of selenium
Selenium partitioning is not controlled by reaction with iron or calcium when sufficient surface sites are not available for reaction	Ohio submicron; Ohio fragmentation; Ohio bulk fly ash	00K-1, 00O-1	Sulfur was doped into the Kentucky coal combustion until the sulfur content matched the Ohio sulfur content; Calcium blended into Ohio coal for combustion until Se-to-Ca ratio matched Wyodak ratio.
Increasing the maximum combustion temperature will increase the availability of active calcium and iron surface sites for reaction		00W-3, 00O-2	Oxygen blended into Wyodak combustion air; CO2 blended into Ohio combustion air.
Selenium is more reactive with iron than with calcium		00P8-1, 00P8-2	Calcium was doped into Pittsburgh coal to assess recovery of selenium; then Iron was doped into Pittsburgh coal to assess recovery of selenium

Figure 3-126 shows a comparison of the differential selenium distribution at the Wyodak baseline combustion conditions with Se-doped Wyodak coal and undoped Ohio coal (with CO_2 addition to the main combustion air to decrease the maximum combustion temperature) at the same combustion temperature. The Se-doped Wyodak distribution is more similar to the Ohio Se distribution than to the Wyodak baseline Se distribution. The cross correlation from differential distribution curves are R^2=0.89 for the Se-doped Wyodak versus the Ohio Se distribution and R^2=0.08 for the Se-doped Wyodak vs. the Wyodak Se distribution. This suggests that selenium partitioning for the doped case is controlled by the same mechanism as during Ohio combustion rather than the Wyodak selenium partitioning mechanism.

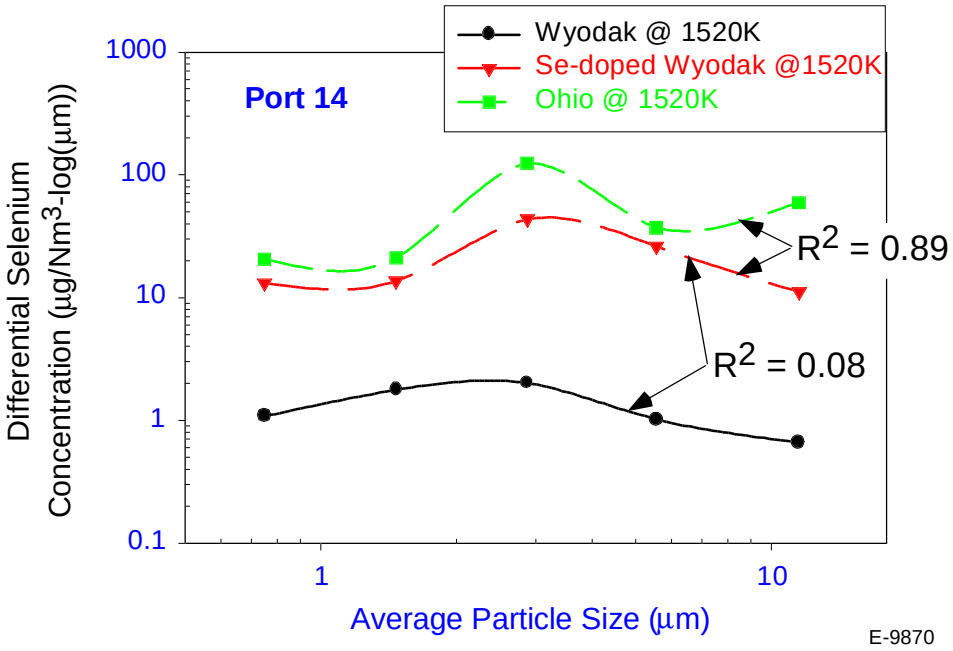

Figure 3-126. Comparison of selenium differential distributions when adjusting the selenium-to-calcium ratio at constant maximum combustion temperature in the Wyodak coal.

A similar comparison is shown in Figure 3-127. This figure shows a comparison of the differential selenium distribution at the Ohio baseline combustion conditions with Se-doped Wyodak coal at an elevated combustion temperature approaching the Ohio temperature and with an undoped Wyodak coal at the same elevated temperature.

Visually, it is difficult to discern whether the Se-doped Wyodak distribution is more similar to the Ohio Se distribution than to the Wyodak undoped distribution (due to the directional differences in the central data point). The correlation statistics are also unclear. Correlation coefficients from the cross correlation between the absolute concentration values on each relevant impactor stage are R^2=0.56 for the Se-doped Wyodak Se distribution versus the Ohio Se distribution and R^2=0.82 for the Se-doped Wyodak Se distribution versus the undoped Wyodak Se distribution. Most likely, the increased combustion temperature is increasing the availability of active iron surface sites (see Figure 3-120). Unlike the Ohio coal, the Wyodak

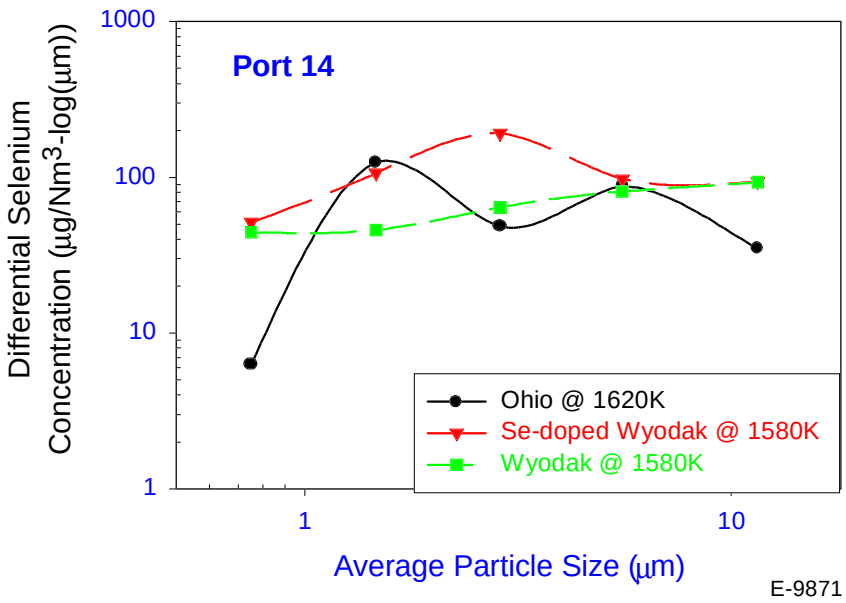

Figure 3-127. Comparison of selenium differential distributions when adjusting the selenium-to-calcium ratio of the Wyodak coal with combustion near the Ohio maximum combustion temperature.

coal has a low sulfur content. As will be shown below, it is postulated that the sulfur content affects the availability of iron cation surface sites for reaction with trace elements. The reaction of selenium with Fe will change the shape of both the undoped and doped Wyodak selenium distribution curves at the elevated combustion temperature conditions.

In another set of experiments, pulverized lime was blended into the Ohio coal in the entrance to the burner. The amount of lime added decreased the Se-to-Ca ratio to match the Se-to-Ca ratio of the Wyodak coal. Samples were collected at the Ohio maximum combustion temperature and at a depressed temperature similar to the Wyodak maximum combustion temperature (by adding CO_2 to the inlet air).

Figure 3-128 shows a comparison of the differential selenium distribution at the Ohio baseline combustion conditions with Ca-doped Ohio coal at the Ohio combustion temperature and with an undoped Wyodak coal at a similar elevated temperature. The Ca-doped Ohio coal selenium distribution has about the same degree of similarity to either the Wyodak distribution (elevated by O_2 enrichment of the combustion air) or the undoped Ohio distribution. The cross correlation between the absolute concentration values on each relevant impactor stage are R^2=0.46 for the Ca-doped Ohio Se distribution versus the Wyodak Se distribution and R^2=0.60 for the Ca-doped Ohio Se distribution versus the undoped Ohio Se distribution.

The uncertainty in the results of Figures 3-127 and 3-128 are similar. In both cases the doped distributions have similar Se-to-Ca ratios and combustion temperatures but with different coals as the feedstock. The addition of calcium at the higher temperature may be causing a sufficient excess of active cation sites to change the distribution curve. Analyzing the

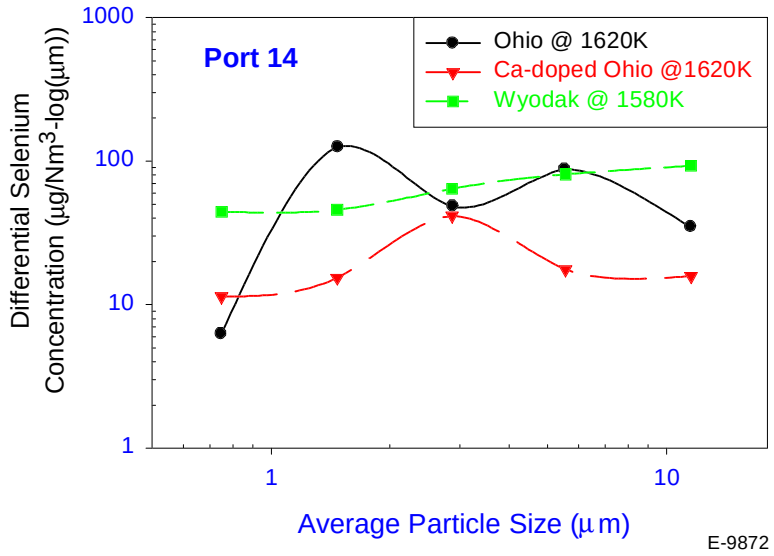

Figure 3-128. Comparison of selenium differential distributions when adjusting the selenium-to-calcium ratio of the Ohio with combustion at the Ohio maximum combustion temperature.

results for experiments in which Ohio coal is doped with calcium and the combustion temperature is depressed by CO_2 addition can test this hypothesis.

Figure 3-129 shows a comparison of the differential selenium distribution at the Ohio baseline combustion conditions with Ca-doped Ohio coal at the Wyodak combustion temperature and with an undoped Wyodak coal at its natural combustion temperature. The Ca-doped Ohio coal selenium distribution appears visually to be more similar to the Wyodak distribution than to the undoped Ohio distribution (temperature depressed by CO_2 addition to the combustion air). Correlation coefficients from the cross correlation between the absolute concentration values on each relevant impactor stage are R^2=0.90 for the Ca-doped Ohio Se distribution versus the Wyodak Se distribution and R^2=0.54 for the Ca-doped Ohio Se distribution versus the undoped Ohio Se distribution.

To summarize the results of this set of experiments, by manipulating the Se-to-Ca ratio and the maximum combustion temperature, the partitioning behavior of selenium can be manipulated in directionally predictable ways. Namely, the partitioning behavior of selenium during Wyodak combustion, which appears to be controlled by reaction with active calcium surface sites was changed to match the partitioning behavior of selenium during Ohio combustion (where partitioning does not appear to be controlled by reaction due to a lack of available cation surface sites) by adding selenium to the combustion environment so that the Se-to-Ca ratio matched the Ohio Se-to-Ca ratio. Then the partitioning behavior of selenium during Ohio combustion was changed to match the partitioning behavior of selenium during Wyodak combustion by adding calcium to the Ohio combustion environment and by reducing the combustion temperature through CO_2 addition.

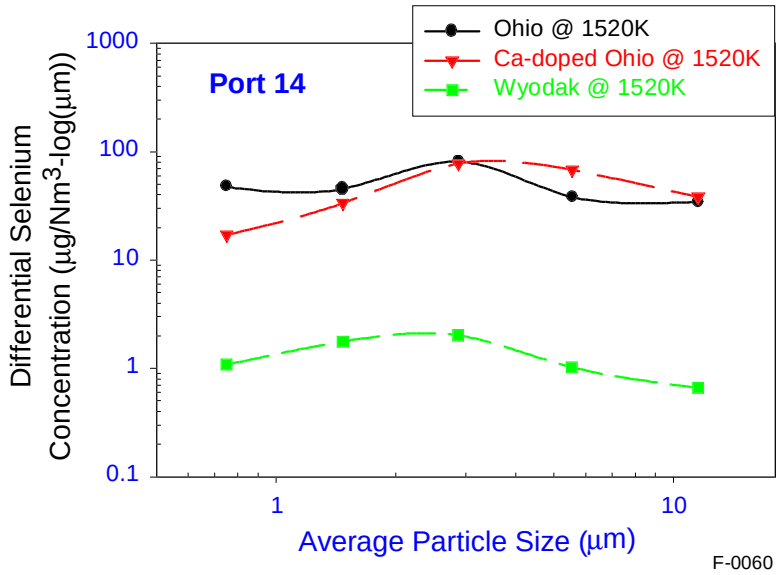

Figure 3-129. Comparison of selenium differential distributions when adjusting the selenium-to-calcium ratio of the Ohio with combustion at the Wyodak maximum combustion temperature.

In the Port 14 Kentucky baseline screening experimental results, the Se distribution most closely follows the iron distribution compared to the total ash or calcium distributions (see Figure 3-123). These results were initially surprising. Both the Ohio and Kentucky coals have similar calcium contents with similar forms of occurrence in the feedstock. Additionally, the Se-to-Ca ratios are similar. Yet in the Ohio coal experiments, selenium does not correlate with any cations while in the Kentucky coal experiments selenium appears to correlate with iron.

The one main difference between the Kentucky and Ohio coals is the sulfur content. Could sulfur be preferentially competing for available active cation sites in the Ohio experiments yet be insufficient to exhaust these sites in the Kentucky experiments? To examine the effect of sulfation on selenium partitioning, the main combustion air was doped with SO_2 during the combustion of the Kentucky coal. The amount of SO_2 added increased the sulfur content in the combustion environment to match the sulfur content of the Ohio coal. Table 3-84 shows a comparison of the Se supermicron size mass concentration distribution for the SO_2-doped Kentucky experiment versus the baseline Kentucky experiment. The Se concentration recovered is significantly lower for the SO_2-doped experiment indicating that less selenium is partitioning to supermicron fly ash particles when additional SO_2 is present.

Due to the similarity of selenium chemistry to that of sulfur, it was postulated that selenium is more reactive with iron surface sites than with calcium surface sites. Two sets of experiments were performed with the Pittsburgh seam coal to investigate whether selenium partitioning has a preference for reaction with calcium or with iron. The differential distributions of calcium and iron in Figure 3-123 are too similar to determine whether selenium is preferentially reacting with one or the other of these cations. In the first set of experiments the calcium content of the feedstock was increased by 50 mol% by pulverized lime addition. In the

Table 3-84. Comparison of Selenium Mass Concentration Values from Kentucky Coal SO_2 Doping Experiments

Particle Diameter (µm)	Baseline Experiment Selenium (µg/Nm^3)	SO_2-Doped Experiment Selenium (µg/Nm^3)
0.973	51	12
1.96	80	17
3.77	77	25
7.33	65	25

second set of experiments the iron content of the feedstock was increased by the same molar amount as in the calcium tests (this is a much small % increase since there is more iron in the Pittsburgh coal than calcium). The results are summarized in Table 3-85. There is a significant increase in the selenium concentration for the iron doping experiments whereas the calcium doping experiments yield Port 14 selenium concentrations similar to the base case. From this result we conclude that selenium is more reactive with active iron surface sites compared to calcium.

Table 3-85. A Comparison of Absolute Selenium Concentration Values from Pittsburgh Seam Coal Cation Doping Experiments

	Port 4		Se (ppmw)	Port 14		Se (ppmw)
Size	Baseline	Ca Doped	Fe Doped	Baseline	Ca Doped	Fe Doped
0.535	43	157	1483	55	75	909
0.973	36	260	331	381	33	377
1.96	32	132	69	33	20	178
3.77	19	53	35	12	9	30
7.33	7	15	8	24	6	18

The results from an interesting study by Niss et al. [151] can be more fully interpreted based on the current study results presented above. In the Niss study, three fly ash samples were subjected to an ion chromatography method to separate selenites from selenates. One fly ash sample was from an unidentified, pulverized coal process, a second from a source utilizing a calcium-based sorbent for SO_2 removal, and the third from a source where Na_2CO_3 was used for SO_2 removal. The results show that selenites were the dominant selenium form in the first two fly ash samples while selenates were the dominant form for the third fly ash sample. The first two results are consistent with selenium partitioning dominated by reaction with calcium surface sites to form calcium selenite complexes – the result predicted by the current study (unless the coal feedstock had a very high Se/Ca ratio and very low sulfur content; unfortunately this information is not included in the reference paper). The third result is consistent with selenium partitioning dominated by reaction with iron surface sites to form iron selenate complexes – the result we would predict since the volatilized sulfur is being scavenged by Na_2CO_3; leaving a greater percentage of the active iron cationic sites available for reaction with oxy-anions such as selenium.

Environmental Impact of Selenium from Fly Ash Surfaces

Based on the current study results, calcium selenite compounds are likely to make up the majority of selenium compounds (not calcium selenate – see Ghosh-Dastidar et al. [150]; Merrill et al. [152]; Niss et al. [151]; Wadge and Hutton [153]) that form due to selenium partitioning in coals with low Se/Ca ratios and high sulfur contents. Iron selenate compounds are likely to make up the majority of selenium compounds for coals with high Se/Ca ratios and low sulfur contents. For coals with high Se/Ca ratios and high sulfur contents, only a small portion of the Se will complex with surface cation sites while the majority of the Se will leave as vapor or condense onto the surface of the particle as SeO_2.

Metal selenite compounds have very low solubilities over a wide pH range [154]. For example, calcium selenite is only slightly soluble in neutral aqueous solutions [155]. By contrast, metal selenate compounds, such as iron selenate, are very soluble [154]. SeO_2 is partially soluble in water (38% is reported in Dean [156] and Weast [83]) and SeO_3 is very soluble in water [83]. These differences in solubility can be used to gain further insight into the nature of the Se present on fly ash particle surfaces.

In the current study, selected impactor stages were subjected to a sequential leaching protocol adapted from EPA method 1310 (TCLP) for five of the study coals. Selenium leaching results for the supermicron region post-combustion zone samples are summarized in Table 3-86. For the majority of the leachate obtained during this work, the selenium concentration was below the detection limit of the in-house GFAA utilized. A cold N_2 evaporation technique was employed to concentrate selected samples (one of the three impactor stages from each sampling location/particle regime/coal combination) by a factor of three. As a result, many of the results shown in Table 3-86 are from testing of a single impactor stage rather than testing of three impactor stages per particle regime (submicron or supermicron).

The Pittsburgh supermicron, Wyodak submicron, and North Dakota submicron and supermicron results are consistent with the solubility of selenites such as calcium- selenium complexes. The Pittsburgh submicron and Kentucky submicron and supermicron results are consistent with the solubility of selenates such as iron-selenium complexes. The Ohio submicron and supermicron results are most consistent with the solubility of selenides (such as SeO_2). These results support the conclusions derived from the distribution information and special experimental data described above.

There are distinct differences between some of the selenium solubility results for submicron particles compared to supermicron particles. For example, the Pittsburgh submicron solubility results are most consistent with iron-selenium complexes whereas the supermicron solubility results are more consistent with calcium-selenium complexes. This suggests that the partitioning mechanism may be different for the submicron and supermicron regimes due to differences in the availability of Ca versus Fe active surface sites.

Table 3-86. Summary of Selenium Solubility in Fly Ash from Baseline Screening Experiments

Coal/Sample Location	Submicron Size % Soluble at pH 4.9	Submicron Size % Soluble at pH 2.9	Supermicron Size % Soluble at pH 4.9	Supermicron Size % Soluble at pH 2.9
Pittsburgh Port 4	42%	67%	29%	51%
Pittsburgh Port 14	50%	65%	0%	0%
Ohio Port 4	14%	32%	0%	0%
Ohio Port 14	0%	32%	0%	11%
Kentucky Port 4	13%	69%	0%	43%
Kentucky Port 14	0%	58%	0%	55%
Wyodak Port 4	0%	32%	0%	26%
Wyodak Port 14	0%	0%	n/d	n/d
North Dakota Port 4	0%	0%	0%	0%
North Dakota Port 14	0%	0%	0%	0%

Note: n/d = not detectable in any of the samples.

The pH 4.9 leachability data helps assess the potential for selenium contained in submicron and supermicron particles to migrate into the water supply after ground deposition downwind of the combustor. The solubility of selenium from submicron particles is of particular concern because 1) the particles are enriched with selenium and 2) the collection efficiency of these particles in ESPs and baghouse filters is lower than for supermicron particles [10, 31, 32]. Calcium selenite complexes are not very soluble and are not expected to leach into groundwater. Selenate complexes are fairly soluble and are likely to contribute selenium to groundwater due to leaching. SeO_2 is partially soluble and is likely to contribute selenium to groundwater due to leaching. The potential environmental impact for selenium for fly ash for each of the five coals utilized in the solubility study is summarized in Table 3-87.

The pH 2.8 leachability data helps assess how selenium might leach from an ash disposal pile/landfill. As water migrates through the ash pile it can become much more acidic than the original water source. Calcium selenite complexes are not very soluble and are not expected to leach out of the fly ash. Iron selenate complexes and SeO_2 are fairly soluble and are likely to leach from the fly ash. The potential environmental impact for selenium from fly ash for each of the five coals utilized in the solubility study is included in Table 3-87.

Table 3-87. Environmental Impact of Selenium in Fly Ash Particles

Coal	Vapor-Phase Emission	Leachable from Ground Deposition[1]	Leachable from Disposal Pile[2]
Pittsburgh	Minor[3]	Submicron Major[4] Supermicron Negligible[5]	Submicron Major Supermicron Negligible
Ohio	Significant[6]	Submicron Minor Supermicron Negligible	Submicron Significant Supermicron Negligible
Kentucky	Minor	Negligible	Major
Wyodak	Minor	Negligible	Negligible
North Dakota	Significant	Negligible	Negligible

1. Based on pH 4.9 Solubility data
2. Based on pH 2.9 Solubility data
3. Minor < 20%
4. Major >50%
5. Negligible < 1%
6. Significant >20%

Temporal Resolution of Selenium Partitioning Processes

The analysis above has shown that selenium partitioning to fly ash surfaces may be dominated by surface reaction with calcium and/or iron active cation sites. Further insight can be gained into selenium partitioning mechanisms by examining size-segregated samples from Port 4 and comparing these results to those obtained from Port 14.

Insight into the timing of selenium volatilization can be gained by comparing the mass fraction of selenium still in the vapor phase at the combustion zone sampling location (Port 4) for the baseline screening experiments to the mass fraction of selenium still in the vapor phase at the post-combustion zone sampling location (Port 14). The mass fraction of selenium still in the vapor phase at both sampling locations for the six study coals is summarized in Table 3-80. The mass fraction of vapor-phase selenium is lower in the combustion zone sample for all of the study coals except the Kentucky coal. This indicates that significant selenium volatilization appears to continue after Port 4 for five of the study coals.

The timing of partitioning from the vapor phase back to particle surfaces can be evaluated by comparing the enrichment factors[5] of the submicron particles. Calculating a differential enrichment factor by subtracting the combustion zone enrichment factor from the post-combustion zone enrichment factor provides insight into when partitioning is occurring. Selenium enrichment factors at Ports 4 and 14 along with differential enrichment factors are shown in Table 3-81 for all six study coals.

A positive selenium differential enrichment factor is found for Illinois, Ohio, Wyodak and North Dakota submicron particles. This suggests that volatilized selenium continue to partition to submicron particle surfaces after Port 4. Care must be taken in using the Ohio,

[5] See Eq. (3-14) for the definition of the enrichment factors employed in this work.

Wyodak, and North Dakota data because the very low selenium concentrations present can exaggerate the enrichment factor calculation. By contrast the negative differential enrichment factors shown for the Pittsburgh and Kentucky submicron particles suggest that the majority of the selenium associated with submicron particle for these coals is present prior to Port 4.

Further insight into the timing of vapor-to-solid phase partitioning can be obtained using particle size dependence models based on transport theory. The particle size dependence of selenium associated with supermicron fly ash particles for the six study coals at the Port 4 sampling location is shown in Figure 3-130.

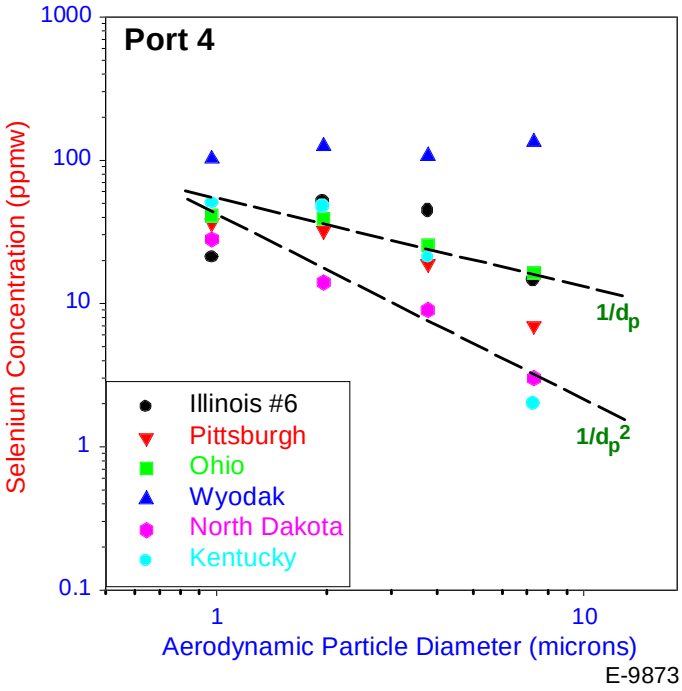

Figure 3-130. Particle size dependence of selenium in supermicron fly ash particles for all six study coals sampled at Port 4.

The results show that the Pittsburgh, Illinois and Ohio selenium distributions follow a near $1/D_p$ dependence. This indicates that the rate of partitioning of volatile selenium to supermicron particles is dominated by exterior surface reaction and that a significant portion of this process occurs prior to Port 4 for these coals. The Kentucky and North Dakota selenium distributions follow a near $1/D_p^2$ dependence that indicates that the reactivity of selenium with fly ash surface species is sufficiently rapid that the partitioning is limited by gas film transfer prior to Port 4. The Wyodak selenium distribution does not follow any dependence implying that partitioning may be occurring later for this coal (since at Port 14 a $1/D_p$ dependence is observed).

Note that the Pittsburgh and Ohio selenium distributions follow a $1/D_p$ dependence at Port 4 but not at Port 14. The results imply that active cation sites are available during or immediately after combustion but that additional sites are no longer available as the particles and

flue gas travel through the combustor. This hypothesis is supported by the special doping results for the Pittsburgh coal in which substantially higher concentrations of selenium were obtained when iron was doped into the combustion environment.

The size-segregated concentration of selenium in submicron particles is shown in Figure 3-131 for the six study coals at the Port 4 sampling location. There appears to be a decrease in concentration with particle size for the four bituminous coals. These results imply that the rate of partitioning of selenium to the particle surface is controlled by surface reaction and that this occurs early – prior to 0.5 residence seconds from the burner. No particle size dependence is apparent for the lower rank coals.

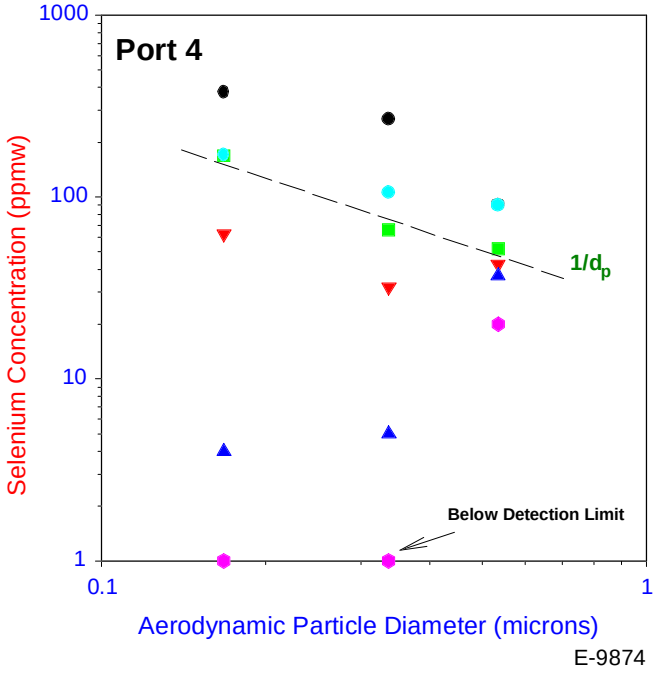

Figure 3-131. Particle size dependence of selenium in submicron fly ash particles for all six study coals sampled at Port 4.

Timing issues and any differences in Se-Fe or Se-Ca reactions as a dominant partitioning mechanism between Ports 4 and 14 can be evaluated by comparing the total ash size distribution and the size distributions of iron, calcium, and selenium. The differential mass concentration distributions of selenium, calcium, iron, and the total ash from full impactor sets for all six coals under baseline combustion conditions at the Port 4 sampling location are shown in Figure 3-132. The corresponding correlations of selenium to calcium and iron using both evaluation methods for both submicron and supermicron fly ash sampled at Port 4 is shown in Table 3-88 for all six study coals.

The distribution curves in Figure 3-132 and the cross correlations listed in Table 3-88 from the Port 4 samples can be compared to the selenium distributions and correlations at Port 14 (Figure 3-123, Table 3-82). The correlation of selenium in the Illinois fly ash distributions in both submicron and supermicron regions are different at Ports 4.

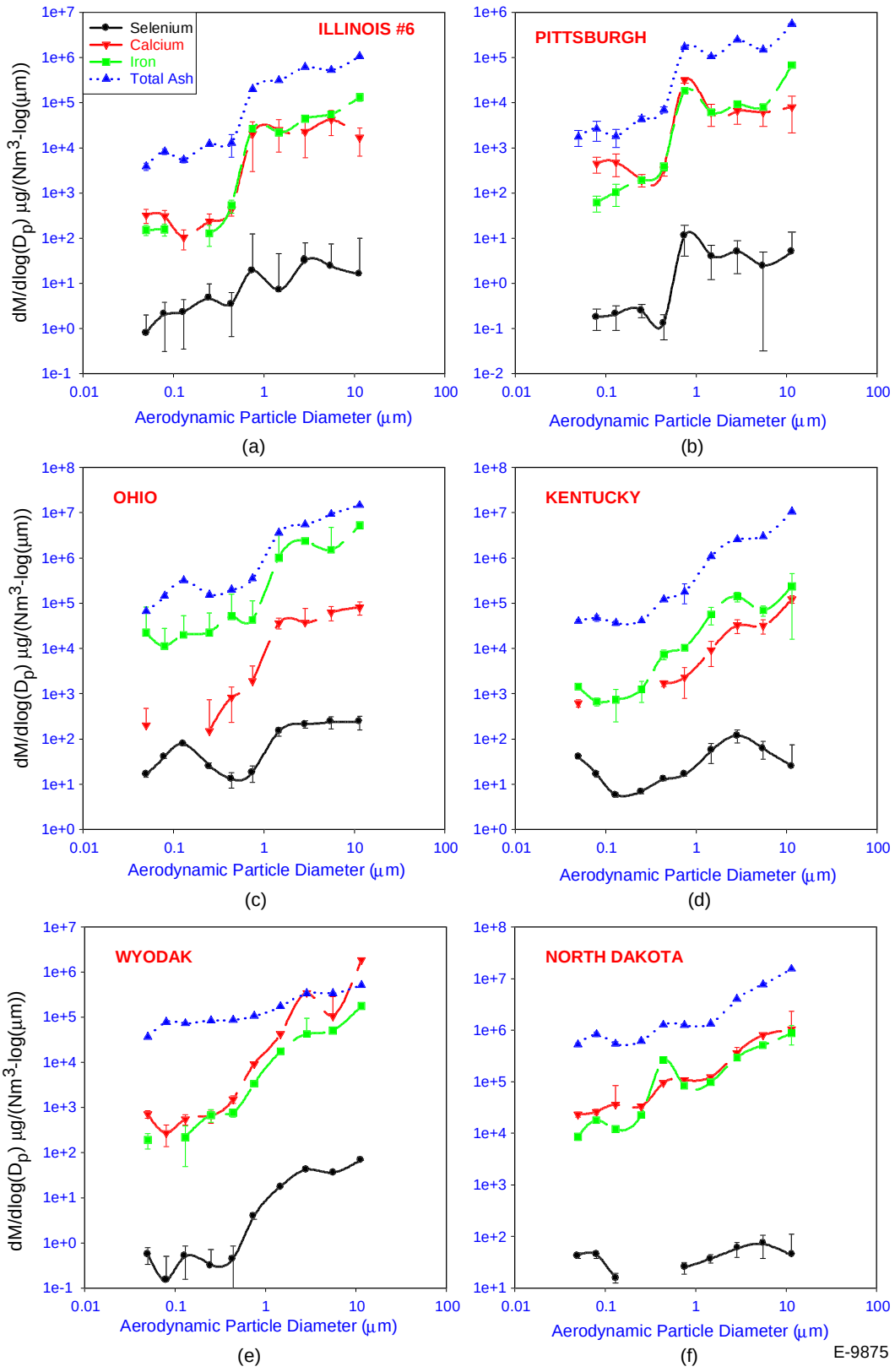

Figure 3-132 Differential mass distributions of selenium, calcium, iron, and total ash for the six study coals sampled at Port 4.

Table 3-88. Correlation Coefficients for Selenium Versus Calcium and Iron in Fly Ash Particles from the Six Study Coals Sampled at Port 4

Coal		Submicron Correlations			Supermicron Correlations		
		Absolute Concentrations	**Differential Distributions**	**Overall Absolute Concentrations**	**Overall Differential Distributions**	**Fragmentation Region Differential Distributions**	**Bulk Fly Ash Region Differential Distributions**
Illinois:	Se vs. Ca	<0	<0	0.35	0.16	~0	~0
	Se vs. Fe	<0	<0	0.14	0.66	0.80	~0
Pittsburgh:	Se vs. Ca	0.95	<0	0.49	0.91	0.99	~0
	Se vs. Fe	0.49	<0	0.90	0.89	0.95	~0
Ohio:	Se vs. Ca	<0	0.97	<0	0.86	0.94	0.96
	Se vs. Fe	<0	0.94	<0	0.94	0.93	0.46
Kentucky:	Se vs. Ca	na[1]	na	0.05	0.53	0.97	~0
	Se vs. Fe	<0	1.0	0.67	0.99	1.0	~0
Wyodak:	Se vs. Ca	<0	0.98	0.49	0.89	0.89	1.0
	Se vs. Fe	<0	<0	1.0	0.88	1.0	0.99
N. Dakota:	Se vs. Ca	na	na	0.14	0.87	0.85	~0
	Se vs. Fe	na	na	0.22	0.92	0.84	~0

1. na = not available, analyses are below detection limit

and 14. The submicron distributions may both follow calcium, but the iron and calcium submicron distributions at Port 4 are too similar to separate. The fragmentation region supermicron selenium distribution at Port 4 appears to follow the Fe distribution while at Port 14 it appears to correlate with calcium.

For the Pittsburgh selenium submicron and supermicron distributions, the dominant reactant cannot be discerned from Figure 3-132 and Table 3-88. Insight can be gained from the solubility data in Table 3-86. Submicron selenium solubility results are consistent with iron selenate at both sampling locations. For the supermicron fly ash, the Port 4 solubility results are consistent with iron selenate and the Port 14 solubility results are consistent with calcium selenite. Similar to the Wyodak submicron results, it appears that selenium is being displaced from iron by more reactive species after Port 4 and that selenium partitioning is then dominated by reaction with calcium.

The Ohio selenium distributions appear to correlate with calcium and/or iron at Port 4 in all three particle regions. By contrast, the Port 14 selenium distributions do not appear to correlate with either cation distribution. This suggests that selenium may initially be reacting with available active surface sites immediately after combustion and then is displaced by more thermodynamically favorable anions (most probably sulfur).

Summary of Selenium Partitioning

A comprehensive study has been performed to investigate the partitioning of selenium during pulverized coal combustion. The primary partitioning mechanisms for selenium during the combustion of the six coals investigated as predicted by this study are summarized in Figure 3-133 and Table 3-89.

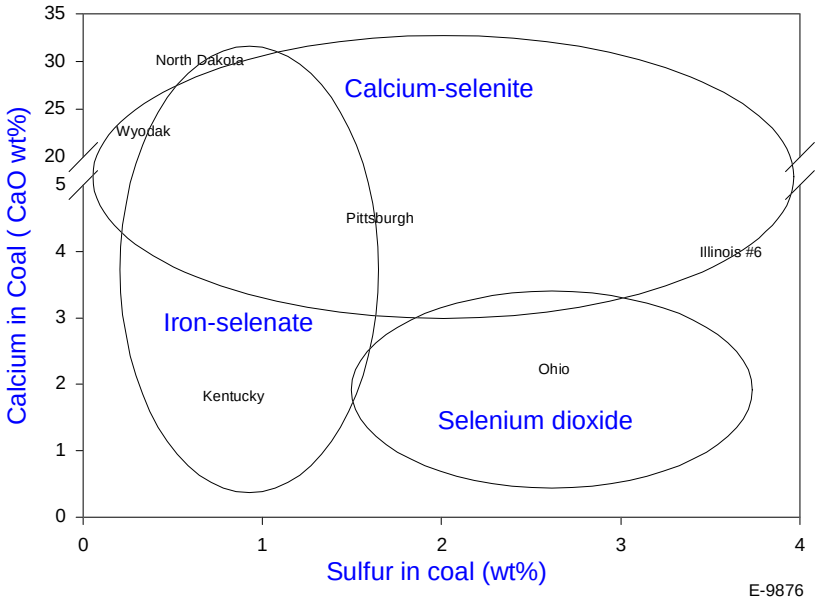

Figure 3-133. Summary of selenium partitioning mechanisms.

Table 3-89. Primary Partitioning Mechanisms for Selenium during the Combustion of the Six Study Coals

Coal	Submicron Region	Supermicron Region
Pittsburgh	Partitioning occurs and is essentially completed in the combustion zone (<2.2) residence seconds from the burner). Reaction with active calcium surface sites to form calcium selenite-type compounds. Sulfur partially inhibits reaction of selenium with active iron surface sites.	Partitioning to fly ash surfaces occurs in the combustion zone. Reaction with active calcium and iron surface sites form calcium-selenite and iron selenate-type compounds. Sulfur may partially inhibit reaction with active iron surface sites.
Illinois	Partitioning begins in the combustion zone and continues in the post-combustion zone (>2.2 res. sec.). Reaction with active calcium surface sites form calcium selenite-type compounds.	Partitioning to fly ash surfaces begins in the combustion zone. Initial reaction with active iron surface sites. In the post-combustion zone, sulfur displaces selenium from iron surface sites and the selenium reacts with active calcium surface sites form calcium selenite-type compounds.
Ohio	Partitioning begins in the combustion zone and continues in the post-combustion zone (>3.2 res. sec.). High sulfur/low calcium content results in a lack of available active surface cation sites, SeO_2 partitions to particle surfaces.	Partitioning begins in the combustion zone. High sulfur/low calcium content leads to a lack of available active surface cation sites, SeO_2 partitions to particle surfaces.
Kentucky	Partitioning occurs and is essentially completed in the combustion zone (<2.9 res. sec.). Active iron surface sites are available due to the low sulfur content of the coal. Reaction with active iron surface sites forms iron selenate-type compounds.	Partitioning to fly ash surfaces occurs in the combustion zone. Active iron surface sites are available due to the low sulfur content of the coal. Reaction primarily with active iron surface sites form iron selenate-type compounds and to a lessor extent with active calcium surface sites form calcium selenite-type compounds.
Wyodak	Partitioning begins in the combustion zone and continues in the post-combustion zone (>6.6 res. sec.). Active iron and calcium surface sites are available due to the low sulfur/high calcium content of the coal. Reaction with active calcium sites form calcium-selenite type compounds and to a lessor extent with iron sites form iron selenate-type compounds.	Partitioning to fly ash surfaces begins in the combustion zone. Active iron and calcium surface sites are available due to the low sulfur/high calcium content of the coal. Reaction with active calcium sites form calcium-selenite type compounds and to a lessor extent with iron sites form iron selenate-type compounds.
North Dakota	Partitioning begins in the combustion zone and continues in the post-combustion zone (>9.3 res. sec.). Active iron and calcium surface sites are available due to the low sulfur/high calcium content of the coal. Reaction with active calcium sites form calcium-selenite type compounds and to a lessor extent with iron sites form iron selenate-type compounds.	Partitioning begins in the combustion zone. Active iron and calcium surface sites are available due to the low sulfur/high calcium content of the coal. Reaction with active calcium sites form calcium-selenite type compounds and to a lessor extent with iron sites form iron selenate-type compounds.

The partitioning of selenium is governed primarily by the extent of selenium volatilization during combustion. For most coals selenium is bound in organic matter similar to sulfur or is substituted for sulfur in sulfides. Selenium in these forms is expected to volatilize during combustion. Volatilized selenium will heterogeneously transform to both submicron and supermicron particles primarily by reaction with active cation sites; although a significant minority (greater than 0.5 wt% of the total selenium) will remain in the vapor phase and exit the boiler due to selenium's relatively high vapor pressure.

The partitioning of selenium to fly ash surfaces is dependent on the availability of active cation sites. For coals with relatively low Se/Ca ratios, selenium is expected to react with calcium surface sites to form calcium selenite complexes. These selenite complexes are not very soluble and are not expected to leach into groundwater. If the Se/Ca ratio is relatively high and the sulfur content is low, selenium will most likely react with iron surface sites to form iron selenates. Selenate complexes are fairly soluble and are likely to contribute selenium to groundwater due to leaching. If the Se/Ca ratio is relatively high and the sulfur content is moderate to high, cationic surface sites will not be available for selenium partitioning. In these cases, most of the selenium is expected to exit the furnace in the vapor phase or as fly ash surface-based SeO_2 (e.g., the Ohio study coal). SeO_2 is partially soluble and is likely to contribute selenium to groundwater due to leaching.

Active cationic surface sites are primarily due to major elements (i.e., calcium and iron) volatilizing in the vicinity of the carbon oxidizing in the coal particles and then homogeneously and heterogeneously condensing. Increasing the combustion temperature can increase cationic surface site availability and subsequently reduce the emission of vapor phase or physically condensed SeO_2 from the furnace.

Arsenic

Arsenic Volatility

Finkleman and coworkers [7, 141, 142] determined the forms of occurrence of arsenic for the six coals utilized in this study. The results are summarized in Table 3-90. The majority of the arsenic for all six coals is attributed to pyrite/sulfide or mono-sulfide fractions although four of the coals have silicate fractions of 5 to 15%. Organically-associated arsenic was only detected in the Wyodak coal. Consistent with Bool and Helble [29], the large fraction of arsenic not contained in silicates is expected to volatilize during combustion.

Results from thermodynamic equilibrium simulations predict that AsO is the favorable form of occurrence at the combustion temperatures of all six coals studied in this research. Arsenic is predicted to remain as AsO throughout the post-combustion zone. If AsO is not an allowable formation product, the simulations predict As, As_2, and $AsCl_3$ as the most favorable forms of occurrence. In this case, arsenic is predicted to transform into oxy-anions (e.g., $Ca_3(AsO_4)_2$, As_2O_3, As_2O_5).

Table 3-90. Forms of Occurrence of Arsenic in the Six Study Coals[1]

Coal	Ammonium Acetate Leachable (organic)	HCl Leachable (mono-sulfide)	HF Leachable (silicate)	HNO3 Leachable (pyrite/sulfide)
Pittsburgh	0%	10%	0%	80%
Illinois	0%	20%	0%	60%
Kentucky	0%	30%	5%	35%
Ohio	0%	30%	5%	35%
Wyodak	5%	25%	15%	25%
North Dakota	0%	60%	10%	15%

1. From Ref. 7; Section 3.1.3.

Vapor-to-Particle Surface Arsenic Transport Mechanisms

Due to its low volatility, only a very small portion of the volatilized arsenic will exit the combustor in the vapor phase. In this study the average mass fraction of arsenic still in the vapor phase at the post-combustion zone sampling location (Port 14) for the baseline screening experiments was 4.5 wt% (compared to 13% for selenium). However, there was significant variation between coal types (see Table 3-91). For all of the study coals, most of the arsenic partitions back to the solid phase prior to exiting the combustor. For four of the coals – Pittsburgh, Illinois #6, Ohio, and Kentucky – very little (<3wt%) of the arsenic is still in the vapor phase at Port 14.

The average mass fraction of arsenic still in the vapor phase at the baghouse inlet sampling port for the baseline screening experiments was 14 wt% (compared to 20% for selenium). It should be noted that a portion of the bulk fly ash particles has been removed from the flue gas prior to this sample.

Due to the low concentration of arsenic compared to the major species in the coal, there is a very high probability that a volatilized arsenic molecule will contact submicron or supermicron particles prior to reaching the supersaturated conditions necessary for nucleation. Therefore, a majority of the volatilized arsenic is expected to heterogeneously partition onto the surfaces of both submicron and supermicron particles [30].

The heterogeneous vapor-to-solid phase partitioning theory described above for selenium is also proposed for arsenic. If this theory is valid, there will be an enrichment of arsenic onto submicron particles. Arsenic enrichment factors[6] for fly ash particles from the baseline screening experiments sampled at the Port 14 (post-combustion zone) sampling location are given in Table 3-92. All of the submicron fly ash samples taken at the post-combustion zone sampling location (Port 14) show enrichment of arsenic (values greater than 1.0). These results are consistent with observations by previous researchers [4, 6, 8-16, 24, 25, 32, 34, 35, 37, 71, 78, 81, 92, 93, 157].

[6] See Eq. (3-14) for the definition of the enrichment factors employed in this work.

Table 3-91. Mass Fraction of Arsenic in Vapor, Submicron, And Supermicron Regimes at Three Combustor Sample Locations

Coal/Location	Average Sampling Temperature (K)	Vapor Regime (Wt%)	Submicron Regime (Wt%)	Supermicron Regime (Wt%)
Pittsburgh				
Port 4	1440	0.4	57	43
Port 14	1140	1.3	15	84
Baghouse Inlet	470	9.7	16	74
Illinois				
Port 4	1410	3.3	19	78
Port 14	1130	0.6	20	79
Baghouse Inlet	220	11	11	78
Ohio				
Port 4	1330	8.2	5.1	87
Port 14	1040	2.8	1.2	96
Baghouse Inlet	610	36	19	46
Kentucky				
Port 4	1490	9.3	5.3	85
Port 14	1150	1.0	2.3	97
Baghouse Inlet	490	20	16	64
Wyodak				
Port 4	1080	0.7	1.8	98
Port 14	760	14	21	65
Baghouse Inlet	210	5.7	9.3	85
North Dakota				
Port 4	1250	16	11	72
Port 14	870	7.5	13	79
Baghouse Inlet	400	4.2	9.3	87
Average All Coals				
Port 4		6.4	17	77
Port 14		4.5	12	83
Baghouse Inlet		14	13	72

To be consistent with the heterogeneous vapor-to-solid phase partitioning theory, supermicron particles should contain a higher absolute mass fraction of arsenic than the submicron particles. In the current work, the average arsenic mass fraction in the supermicron particles was 83 wt% (see Table 3-91 for individual values). Vapor phase arsenic is believed to form an oxy-anion of the form As_2O_3 [11, 60] although many thermodynamic studies, including the work presented in Section 3.3.1, predict AsO as the primary form at coal

Table 3-92. Arsenic Enrichment Factors[1] for Submicron-Sized Fly Ash Samples

Coal/Location		Aerodynamic Particle Diameter (μm)			
		0.17	**0.34**	**0.54**	**Average**
Pittsburgh	Port 14	1.7	4.6	2.0	2.8
	Port 4	3.3	5.7	3.6	4.2
	Differential	-1.7	-1.1	-1.5	-1.4
Illinois	Port 14	3.0	2.6	4.4	3.3
	Port 4	2.2	1.7	0.6	1.5
	Differential	0.9	0.9	3.8	1.9
Kentucky	Port 14	4.6	4.8	3.2	4.2
	Port 4	6.4	3.8	3.1	4.4
	Differential	-1.8	1.0	0.2	-0.2
Ohio	Port 14	2.3	5.0	2.0	3.1
	Port 4	4.9	5.8	1.5	4.1
	Differential	-2.6	-0.8	0.5	-0.9
Wyodak	Port 14	2.0	1.9	1.9	1.9
	Port 4	0.0	0.1	0.3	0.1
	Differential	2.0	1.9	1.6	1.8
North Dakota	Port 14	1.9	3.3	1.8	2.3
	Port 4	1.4	1.6	1.7	1.6
	Differential	0.5	1.7	0.1	0.8

1. See Chapter 5.1.1.2 for the definition of the enrichment factors employed in this work

combustion conditions. However, when formation of AsO is constrained, oxy-anions (including As_2O_3) are the predicted forms of occurrence (see Section 3.3.1; Ref. [29]). The probability of As_2O_3 adherence to a particle's surface is primarily due to the number of active cation sites on the particle surface. As_2O_3 will become incorporated into the particle if subsequent reaction between the anion and cation (chemical bonding). The probability that chemical reaction will occur depends upon the rate at which the anion can migrate across the particle surface to the cation site and the kinetic reaction rate between the anion and cation.

Because of the low volatility of arsenic, gas-phase concentrations of As_2O_3 are insufficient in most combustion systems to initiate physical condensation prior to the stack. Therefore, As_2O_3 presence on/within fly ash particle surfaces is not expected to occur by this mechanism.

The particle size dependence of arsenic associated with supermicron fly ash particles for the six study coals at the Port 14 sampling location is shown in Figure 3-134. Only the Ohio arsenic distribution does not follow a near $1/D_p$ dependence[7]. This indicates that volatile arsenic partitioning to supermicron particles in the post-combustion zone is controlled by exterior surface reaction for Illinois, Pittsburgh, Kentucky, Wyodak, and North Dakota. For Ohio, the results indicate that this mechanism is not important after the combustion zone, most likely due to saturation of active cation sites by more abundant anions (the low arsenic-to-calcium ratio of

[7] Excluding the 1μm data point

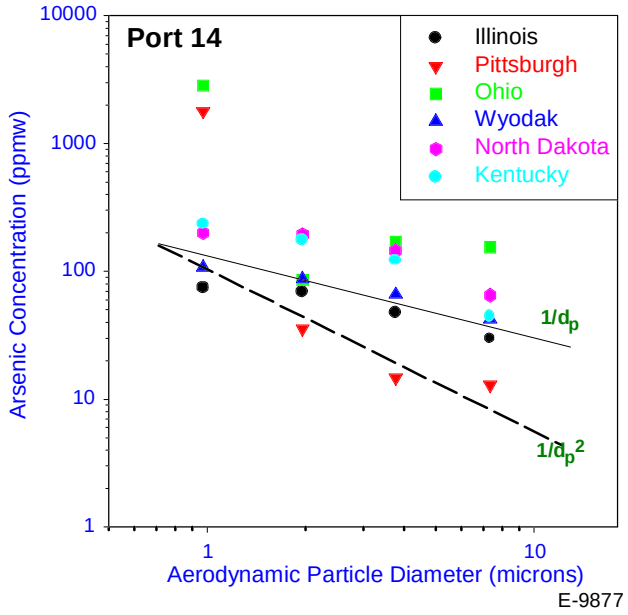

Figure 3-134. Particle size dependence of arsenic in supermicron fly ash particles for all six study coals sampled at Port 14.

this coal implies that less active cation sites are generated during combustion). These results are consistent with those reported by others [11, 12, 24, 29, 71] who report a $1/D_p$ arsenic concentration dependence for supermicron fly ash particles sampled at the end of the post-combustion zone.

The size-segregated concentration of arsenic in submicron particles from the current study is shown in Figure 3-135 for the six study coals at the Port 14 sampling location. No particle size dependence is apparent for any of the coals studied. In the study by Smith et al. [9] the arsenic concentration was also found to be independent of particle size in the submicron region.

Fly Ash Surface Arsenic Reaction Mechanisms

Many researchers have proposed a reaction of As_2O_3 with calcium cations as the most likely partitioning mechanism. If AsO is constrained as a reaction product, calcium arsenate is a favored form of occurrence (as predicted by thermodynamic simulation) for five of the six coals studied (except for Kentucky, see Section 3.3.1) in the post-combustion zone. In Irgolic et al. [158] examination of 11,000 fly ash particles they found arsenic only in the arsenate form and most likely in the form of calcium arsenate. Bool and Helble [29] performed equilibrium calculations that predicted the formation of calcium arsenate during the combustion of a Black Thunder coal. Gullett and Ragnunathan [149] demonstrated that Ca-based sorbents can increase solid-phase arsenic recoveries by >160% whereas kaolinite (Al-Si cation sites) and bauxite (Al cation sites) have only a small effect on arsenic recoveries. Mahuli et al. [123] also report

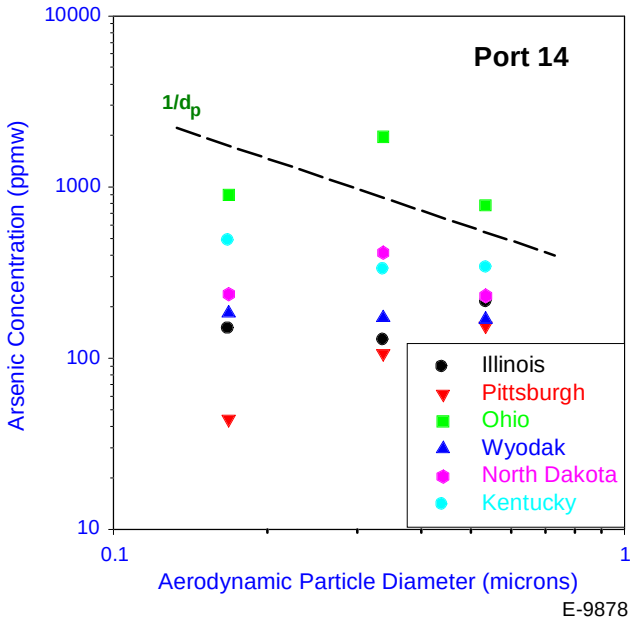

Figure 3-135. Particle size dependence of arsenic in submicron fly ash particles for all six study coals sampled at Port 14.

substantially higher solid-phase arsenic recoveries from Ca-based sorbents compared to kaolinite-, alumina-, or silica-based sorbents.

Due to the similarities in the oxy-anions of arsenic and selenium, it is postulated that arsenic may also react with active iron surface sites. Previous research pointing to the formation of As-Fe surface complexes has not been identified.

The potential for As-Fe or As-Ca reactions as a dominant partitioning mechanism can be evaluated by comparing the total ash size distribution and the size distributions of iron, calcium, and arsenic. The differential mass concentration distributions of arsenic, calcium, iron, and the total ash from full impactor sets for all six coals under baseline combustion conditions at the Port 14 sampling location are shown in Figure 3-136.

To examine the results more carefully, the distributions were decomposed into their submicron and supermicron components and cross correlation coefficients were calculated. The correlation of arsenic to calcium and iron using both evaluation methods for both submicron and supermicron fly ash sampled at Port 14 is shown in Table 3-93 for all six study coals.

Calcium in the Illinois #6 fly ash appears to correlate with both calcium and iron in the submicron and bulk fly ash regions. No correlation is discerned in the fragmentation region. By contrast, selenium showed correlation with calcium in all three particle regions. Like selenium, arsenic appears to correlate with both calcium and iron in all three particle regions for the Pittsburgh coal. This is due to the similarity between the iron and calcium distributions. It cannot be determined from this data whether arsenic correlates with one cation or with both.

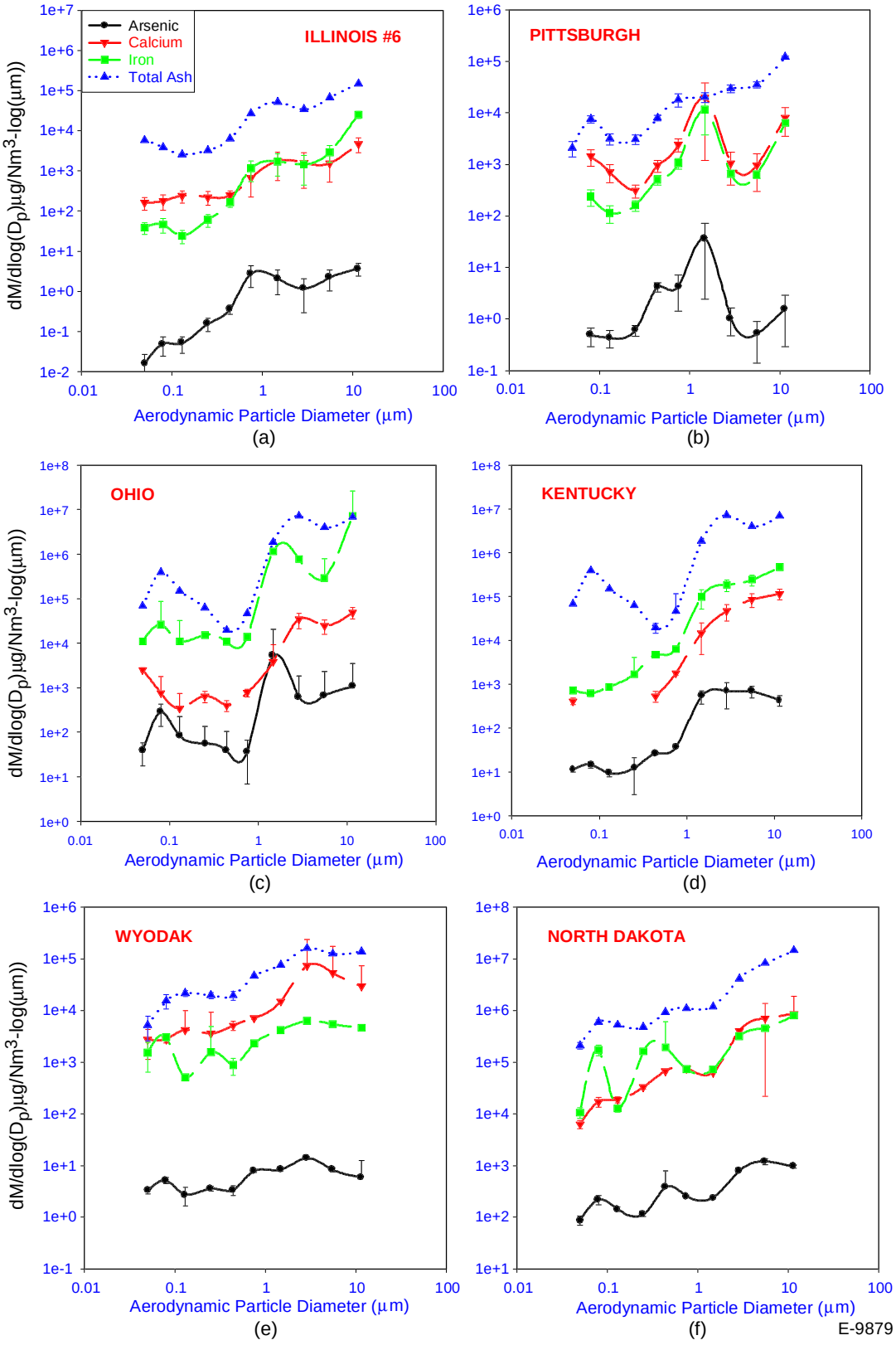

Figure 3-136. Differential mass distributions of arsenic, calcium, iron, and total ash for the six study coals sampled at Port 14.

Table 3-93. Correlation Coefficients for Arsenic vs. Calcium and Iron in Fly Ash Particles from the Six Study Coals Sampled at Port 14

Coal		Submicron Correlations			Supermicron Correlations		
		Absolute Concentrations	Differential Distributions	Overall Absolute Concentrations	Overall Differential Distributions	Fragmentation Region Differential Distributions	Bulk Fly Ash Region Differential Distributions
Illinois:	As vs. Ca	~0	0.92	0.31	~0	~0	0.80
	As vs. Fe	0.97	0.99	~0	~0	~0	0.87
Pittsburgh:	As vs. Ca	~0	0.99	1.0	0.84	1.0	~0
	As vs. Fe	0.51	0.99	0.99	1.0	1.0	0.16
Ohio:	As vs. Ca	0.92	~0	~0	~0	0.10	0.87
	As vs. Fe	0.89	~0	~0	~0	~0	1.0
Kentucky:	As vs. Ca	na	na	~0	0.45	0.76	~0
	As vs. Fe	~0	1.0	0.24	0.77	0.94	~0
Wyodak:	As vs. Ca	~0	~0	~0	0.50	1.0	0.98
	As vs. Fe	~0	~0	0.65	0.53	0.75	0.99
N. Dakota:	As vs. Ca	~0	0.82	~0	1.0	1.0	0.83
	As vs. Fe	~0	~0	0.34	1.0	1.0	0.53

The Ohio arsenic distribution does not correlate with calcium or iron in the submicron or fragmentation regions but shows an apparent correlation with both calcium and iron in the bulk fly ash region. For the Kentucky coal, arsenic correlates with iron in the submicron and fragmentation regions but shows no apparent correlation in the bulk fly ash region. Arsenic in the Wyodak coal correlates with calcium and iron in both supermicron region but shows no apparent correlation in the submicron region. For the North Dakota fly ash, arsenic correlates with calcium in all three particle regions but only strongly correlates with iron in the fragmentation region. This assessment of the distribution curves in Figure 3-136 and the cross correlations listed in Table 3-93 suggests that the mechanisms controlling arsenic partitioning:

1. Are different depending on the fly ash particle region,
2. Are often surface reaction controlled,
3. When surface reaction controlled, the reaction is with calcium and/or iron active surface sites.

The Illinois and Pittsburgh coals have moderate calcium contents and relatively high sulfur contents. The Ohio coal (where no size dependence is observed) has a low calcium content and high sulfur content. The Kentucky coal has a low calcium content and low sulfur content. The Wyodak and North Dakota coals have high calcium content, low sulfur content, and a lower maximum combustion temperature (than the four bituminous coals). Thus, the three parameters that appear to be important in determining the nature of arsenic-cation surface reactions are: arsenic-to-calcium ratio, coal sulfur content, and combustion temperature.

From these results a set of hypotheses related to arsenic partitioning were developed. To test these hypotheses, a set of special experiments was developed. Table 3-94 summarizes the hypotheses and the special test matrix developed for validation.

The control of arsenic vapor-to-solid phase partitioning by surface reaction is proposed when sufficient active cation sites are available to accommodate the arsenic present in the flue gas. To test this hypothesis, a set of special experiments was developed to explore these parameters in more detail. In one set of experiments using the Wyodak coal, arsenic was dissolved in dilute acid and then doped into the furnace at the burner outlet to increase the As-to-Ca ratio in the combustion environment to match the Ohio coal As-to-Ca ratio. This was done at both the Wyodak maximum combustion temperature and an increased combustion temperature.

Figure 3-137 shows a comparison of the differential arsenic distribution at the Wyodak baseline combustion conditions with As-doped Wyodak coal and undoped Ohio coal at the same combustion temperature. The As-doped Wyodak distribution is somewhat more similar to the Ohio As distribution (CO_2 addition to decrease maximum combustion temperature) than to the Wyodak baseline As distribution (except for the 11.5 μm data point). Correlation coefficients from the cross correlation between the absolute concentration values on each relevant impactor stage are R^2=0.94 for the As-doped Wyodak As distribution versus the Ohio As distribution and R^2=0.82 for the As-doped Wyodak As distribution versus the undoped Wyodak As distribution. The cross correlation from differential distribution curves are R^2=0.72 for the As-doped Wyodak versus the Ohio As distribution and R^2=0.64 for the As-doped Wyodak versus the Wyodak As distribution. This suggests that arsenic partitioning for the doped case is controlled by the same mechanism as during Ohio combustion rather than the Wyodak arsenic partitioning mechanism.

Table 3-94. Arsenic Partitioning Mechanism Hypotheses and Validation Test Matrix

Hypothesis	Baseline Test and Fly Ash Region Where Observed	Test Number	Test Description
Vapor-to-solid phase arsenic partitioning is controlled by surface reaction when sufficient surface sites are available for reaction	Ohio baseline coal vs. other five coals; Ohio does not follow a dependence	99W-8, 00W-4	Arsenic doped into Wyodak coal combustion until As-to-Ca ratio matched Ohio ratio
		00O-1, 00O-2	Calcium blended into Ohio coal for combustion until As-to-Ca ratio matched Wyodak ratio. Temperature decreased to match Wyodak combustion temperature
Arsenic reacts with active calcium surface sites	Wyodak fragmentation and bulk fly ash; North Dakota sub-micron and bulk fly ash	99W-8, OOW-4	Arsenic doped into Wyodak coal combustion until As-to-Ca ratio matched Ohio ratio
Arsenic reacts with active iron surface sites when sulfur is not available to consume all of the iron surface sites	Kentucky submicron and fragmentation;	00K-1	Sulfur was doped into the Kentucky coal combustion until the sulfur content matched the Ohio sulfur content
Arsenic reacts with iron and/or calcium active surface sites	Illinois submicron and bulk fly ash; Pittsburgh submicron and fragmentation; North Dakota fragmentation	00P8-1, 00P8-2	Calcium was doped into Pittsburgh coal to assess recovery of arsenic; then Iron was doped into Pittsburgh coal to assess recovery of arsenic
Arsenic partitioning is not controlled by reaction with iron or calcium when sufficient surface sites are not available for reaction	Ohio submicron; Ohio fragmentation; Ohio bulk fly ash	00K-1, 00O-1	Sulfur was doped into the Kentucky coal combustion until the sulfur content matched the Ohio sulfur content; Calcium blended into Ohio coal for combustion until As-to-Ca ratio matched Wyodak ratio.
Increasing the maximum combustion temperature will increase the availability of active calcium and iron surface sites for reaction		00W-3, 00O-2	Oxygen blended into Wyodak combustion air; CO2 blended into Ohio combustion air.
Arsenic has similar reactivity with iron as with calcium		00P8-1, 00P8-2	Calcium was doped into Pittsburgh coal to assess recovery of arsenic; then Iron was doped into Pittsburgh coal to assess recovery of arsenic

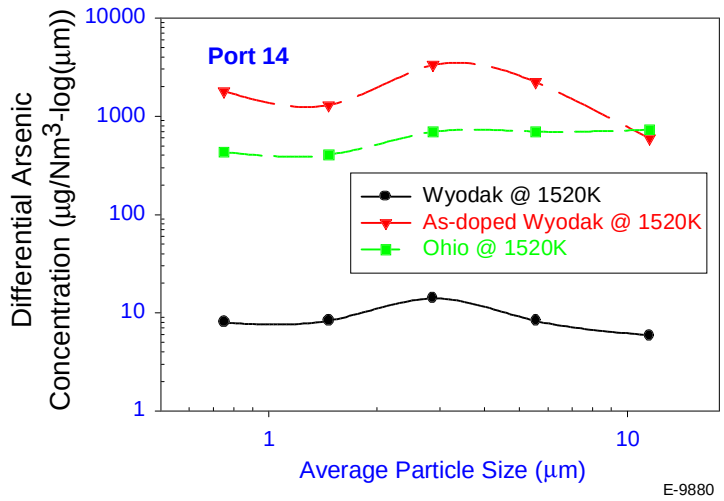

Figure 3-137. Comparison of arsenic differential distributions when adjusting the arsenic-to-calcium ratio at constant maximum combustion temperature in the Wyodak coal.

A similar comparison is shown in Figure 3-138. This figure shows a comparison of the differential arsenic distribution at the Ohio baseline combustion conditions with As-doped Wyodak coal at an elevated combustion temperature approaching the Ohio temperature and with an undoped Wyodak coal at the same elevated temperature. The As-doped Wyodak distribution does not resemble either of the other two distributions. Most likely, the increased combustion temperature is increasing the availability of active iron surface sites (see Figure 3-120).

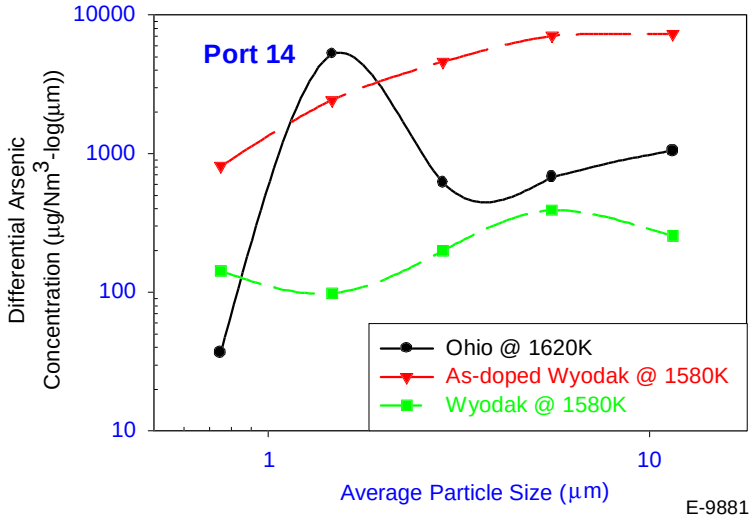

Figure 3-138. Comparison of arsenic differential distributions when adjusting the arsenic - to-calcium ratio of the Wyodak coal with combustion near the Ohio maximum combustion temperature.

Unlike the Ohio coal, the Wyodak coal has a low sulfur content. As will be postulated below, the sulfur content affects the availability of iron cation surface sites for reaction with trace elements. The reaction of arsenic with Fe will change the shape of both the undoped and doped Wyodak arsenic distribution curves at the elevated combustion temperature conditions. To gain some perspective on this hypothesis, Figure 3-139 shows the same information as Figure 3-138 but with the addition of the Kentucky baseline arsenic differential distribution curve. Even though the As-to-Ca ratio of the doped Wyodak coal exceeds the Kentucky As-to-Ca ratio, the doped Wyodak distribution has a shape that is more like the Kentucky coal than the other coals.

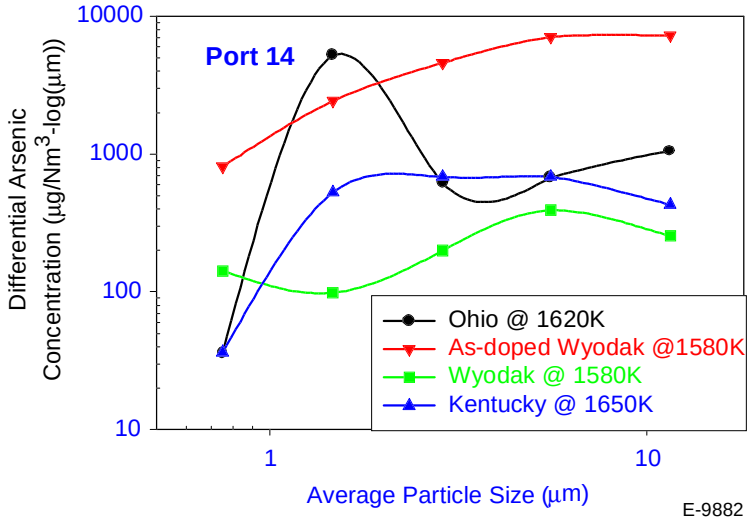

Figure 3-139. Comparison of arsenic differential distributions when adjusting the arsenic - to-calcium ratio of the Wyodak coal to the Ohio and Kentucky distributions with combustion near the Ohio maximum combustion temperature.

In another set of experiments, pulverized lime was blended into the Ohio coal in the entrance to the burner. The amount of lime added decreased the As-to-Ca ratio to match the As-to-Ca ratio of the Wyodak coal. Samples were collected at the Ohio maximum combustion temperature and at a depressed temperature similar to the Wyodak maximum combustion temperature (by adding CO_2 to the inlet air).

Figure 3-140 shows a comparison of the differential arsenic distribution at the Ohio baseline combustion conditions with Ca-doped Ohio coal at the Ohio combustion temperature and with an undoped Wyodak coal at a similar elevated temperature. The Ca-doped Ohio coal arsenic distribution is more similar to the Wyodak distribution (elevated by O_2 enrichment of the combustion air) compared to the undoped Ohio distribution. The cross correlation between the absolute concentration values on each relevant impactor stage are R^2=0.24 for the Ca-doped Ohio As distribution versus the Wyodak As distribution and R^2<0 for the Ca-doped Ohio As distribution versus the undoped Ohio As distribution. The cross correlation between the differential distributions are R^2=0.84 for the Ca-doped Ohio As distribution versus the Wyodak As distribution and R^2<0 for the Ca-doped Ohio As distribution versus the undoped Ohio As

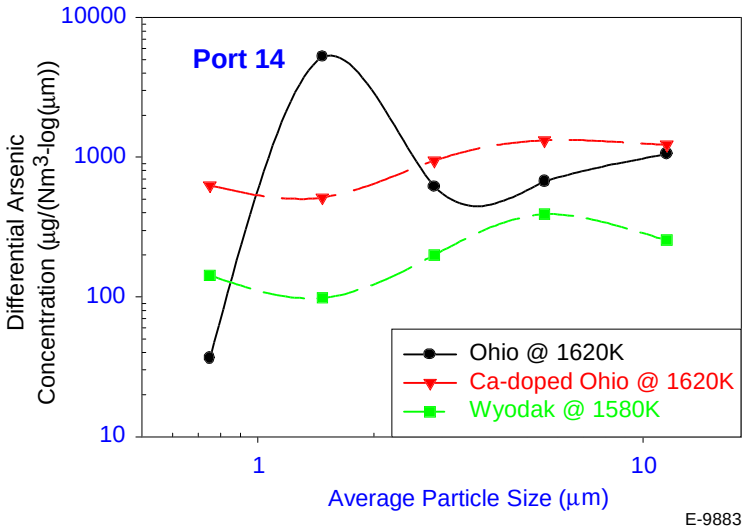

Figure 3-140. Comparison of arsenic differential distributions when adjusting the arsenic-to-calcium ratio of the Ohio with combustion at the Ohio maximum combustion temperature.

distribution. Figure 3-141 shows a comparison of the differential arsenic distribution at the Ohio baseline combustion conditions with Ca-doped Ohio coal at the Wyodak combustion temperature and with an undoped Wyodak coal at its natural combustion temperature. All three distribution curves are similar in shape so no useful information is gained. Useful information can be obtained by comparing the arsenic supermicron mass concentrations in the doped and undoped Ohio fly ash samples. This information is shown in Table 3-95 at two maximum combustion temperatures (with and without CO_2 doping of the combustion air). At both temperatures, there is an increase in arsenic recovery in the supermicron particles (where 83+ wt% of the arsenic

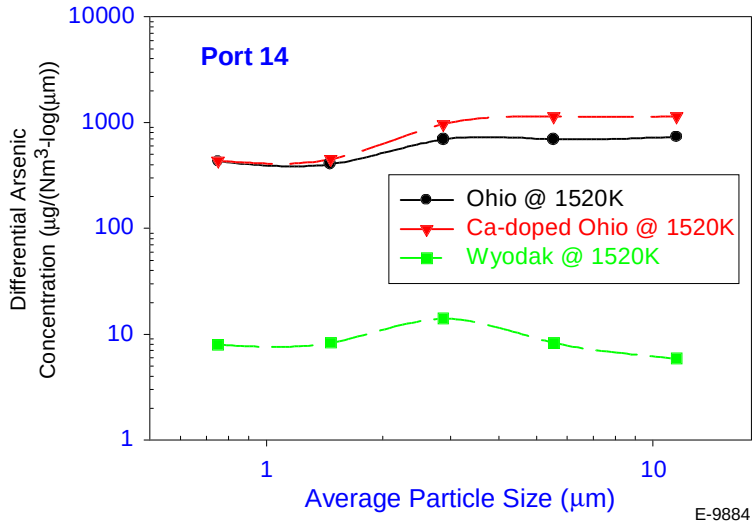

Figure 3-141. Comparison of arsenic differential distributions when adjusting the arsenic-to-calcium ratio of the Ohio with combustion at the Wyodak maximum combustion temperature.

Table 3-95. Comparison of Arsenic Mass Concentration Values from Ohio Coal Calcium Doping Experiments

Particle Diameter (µm)	Undoped Ohio Arsenic at 1620K (µg/Nm^3)	Calcium-Doped Ohio Arsenic at 1620K (µg/Nm^3)	Undoped Ohio Arsenic at 1520K (µg/Nm^3)	Calcium-Doped Ohio Arsenic at 1520K (µg/Nm^3)
1.96	176	269	197	275
3.77	194	381	201	329
7.33	348	405	241	377
Sum	718	1055	639	981

collected resides). Table 3-95 also provides information on the impact of combustion temperature upon arsenic recovery. The arsenic recovery is greater at the higher combustion temperature at the same As-to-Ca ratio. This result supports the hypothesis that the net impact of combustion temperature is the affect on the volatility of the cations (e.g., calcium and iron) not on the volatility of the trace element.

To summarize the results of this set of experiments, by manipulating the As-to-Ca ratio and the maximum combustion temperature, the partitioning behavior of arsenic can be manipulated in directionally predictable ways. Namely, the partitioning behavior of arsenic during Wyodak combustion, which appears to be controlled by reaction with active calcium surface sites was changed to match the partitioning behavior of arsenic during Ohio combustion (where partitioning does not appear to be controlled by reaction due to a lack of available cation surface sites) by adding arsenic to the combustion environment so that the As-to-Ca ratio matched the Ohio As-to-Ca ratio. Then the partitioning behavior of arsenic during Ohio combustion was changed to match the partitioning behavior of arsenic during Wyodak combustion by adding calcium to the Ohio combustion environment and reducing the combustion temperature through CO_2 addition. Further, the partitioning behavior of arsenic during Wyodak combustion was changed to match the partitioning behavior of arsenic during Kentucky combustion (where partitioning appears to be controlled by reaction with both iron and calcium surface sites) by making the As-to-Ca ratio similar to the Kentucky As-to-Ca ratio (which is similar to the Ohio As-to-Ca ratio) and making the maximum combustion temperature similar to the Kentucky combustion temperature through O_2 addition.

In the Port 14 Kentucky baseline screening experimental results, the As distribution appears to follow the iron distribution more closely than the calcium distribution (see Figure 3-126) but not as definitively as the selenium distributions reviewed above. The one main difference between the Kentucky and Ohio coals is the sulfur content. Could sulfur be preferentially competing for available active cation sites in the Ohio experiments yet be insufficient to exhaust these sites in the Kentucky experiments? To examine the effect of sulfation on arsenic partitioning, the main combustion air was doped with SO_2 during the combustion of the Kentucky coal so that the sulfur in the combustion environment matched the sulfur content of the Ohio coal. Table 3-96 shows a comparison of the As supermicron size mass concentration distribution for the SO_2-doped Kentucky experiment versus the baseline Kentucky experiment. The As concentration recovered is significantly lower for the SO_2-doped experiment indicating that less arsenic is partitioning to supermicron fly ash particles when additional SO_2 is present.

Table 3-96. Comparison of Arsenic Mass Concentration Values from Kentucky Coal SO_2 Doping Experiments

Particle Diameter (µm)	Baseline Experiment Arsenic (µg/Nm^3)	SO_2-Doped Experiment Arsenic (µg/Nm^3)
0.973	161	74
1.96	194	90
3.77	198	81
7.33	142	78

It was postulated that arsenic reactivity with calcium and iron were of similar magnitude. Two sets of experiments were performed with the Pittsburgh seam coal to investigate whether arsenic partitioning has a preference for reaction with calcium or with iron. The differential distributions of calcium and iron in Figure 3-126 are too similar to determine whether arsenic is preferentially reacting with one or the other of these cations. In the first set of experiments the calcium content of the feedstock was increased by 50 mol% by pulverized lime addition. In the second set of experiments the iron content of the feedstock was increased by the same molar amount as in the calcium tests (this is a much small % increase since there is more iron in the Pittsburgh coal than calcium). The results are summarized in Table 3-97. Doping with either calcium or iron increased the arsenic recovery in the supermicron fly ash particles. There is no definitive difference between the arsenic recoveries for the two dopants. This is in sharp contrast to the selenium results shown in Table 3-85, where the iron dopant showed a significant increase in selenium recovery compared to the calcium dopant. From these results we conclude that arsenic has similar reactivity with active iron surface sites compared to active calcium surface sites.

Table 3-97. A Comparison of Absolute Arsenic Concentration Values from Pittsburgh Seam Coal Cation Doping Experiments

Size	Port 4 Baseline	Ca Doped	As (ppmw) Fe Doped	Port 14 Baseline	Ca Doped	As (ppmw) Fe Doped
0.535	304	1144	935	233	795	1138
0.973	113	478	350	1787*	306	794
1.96	103	231	199	36	233	273
3.77	96	192	119	15	185	127
7.33	16	61	47	13	46	91

* This data point is considered to be an outlier.

Environmental Impact of Arsenic from Fly Ash Surfaces

Based on the current study results, calcium arsenate compounds are likely to make up the majority of arsenic compounds that form due to arsenic partitioning in coals with low As/Ca ratios and high sulfur contents. Both calcium and iron arsenate compounds are likely to make up the majority of arsenic compounds for coals with high As/Ca ratios and low sulfur contents. For

coals with high As/Ca ratios and high sulfur contents, only a small portion of the As will complex with surface cation sites while the majority of the As will be present on/within the particle in other forms.

In the current study, selected impactor plates were subjected to a sequential leaching protocol adapted from EPA method 1310 (TCLP) for five of the study coals. Arsenic leaching results for the supermicron region post-combustion zone samples are summarized in Table 3-98. Calcium arsenate is slightly soluble in neutral aqueous solutions and is soluble in acidic solutions [69, 83]. Iron arsenate has similar solubility characteristics to calcium arsenate – slightly soluble in neutral aqueous solutions and greater solubility in acidic solutions [156]. To further complicate the situation, arsenic trioxide (AsO_3) also has a low solubility in neutral aqueous solutions and is soluble in acidic solutions [83]. Of the species that are postulated as possibly present, only arsenic pentoxide (AsO_5) has different solubility characteristics. AsO_5 is very soluble in neutral aqueous solutions [69, 83].

Table 3-98. Summary of Arsenic Solubility in Fly Ash from Baseline Screening Experiments

Coal/Sample Location	Submicron Size % Soluble at pH 4.9	Submicron Size % Soluble at pH 2.9	Supermicron Size % Soluble at pH 4.9	Supermicron Size % Soluble at pH 2.9
Pittsburgh Port 4	45%	66%	42%	67%
Pittsburgh Port 14	20%	41%	28%	37%
Ohio Port 4	52%	92%	21%	52%
Ohio Port 14	39%	64%	49%	84%
Kentucky Port 4	16%	57%	18%	60%
Kentucky Port 14	38%	63%	17%	41%
Wyodak Port 4	30%	59%	13%	51%
Wyodak Port 14	33%	49%	18%	42%
North Dakota Port 4	31%	49%	17%	59%
North Dakota Port 14	47%	71%	10%	61%

For all of the coals except Ohio, the results are consistent with the solubility of calcium arsenate, iron arsenate, or As_2O_3. Arsenic in the Ohio supermicron fly ash is more soluble than arsenic in the fly ash from the other coals. This is most likely due to the oxidation of some of the As_2O_3 predicted to be present on Ohio fly ash surfaces to As_2O_5. There are no appreciable differences between the arsenic solubility results for submicron particles compared to supermicron particles. This is not surprising since all of the arsenic forms of occurrence expected to be present have similar solubility characteristics.

The pH 4.9 leachability data helps assess the potential for arsenic contained in submicron and supermicron particles to migrate into the water supply after ground deposition downwind of the combustor. In every case examined, arsenic is partially soluble and some arsenic is expected to leach out of ash particles exposed to aqueous environments (e.g., rainfall). If the dominant arsenic partitioning mechanism is physical absorption of As_2O_3 (e.g., Ohio coal), oxidation of As_2O_3 to As_2O_5 may result in increased arsenic leachability.

The pH 2.8 leachability data helps assess how arsenic might leach from an ash disposal pile/landfill. As water migrates through the ash pile it can become much more acidic than the original water source. All of the arsenic forms of occurrence are partially soluble and are likely to leach from the fly ash. If the dominant arsenic partitioning mechanism is physical absorption of As_2O_3 (e.g., Ohio coal), oxidation of As_2O_3 to As_2O_5 may result in increased arsenic leachability.

Querol et al. [41] reported arsenic leachability results for four subbituminous coals and associated fly ash from the Teruel mining district. They found arsenic in both the original coal and combusted fly ash to be only slightly leachable in water, a pH7 fluid, and a pH5 fluid but highly soluble in a concentrated nitric acid solution. They interpreted these results as implying that the arsenic was present as sulfide-bound material in both the coal and the fly ash since this explanation was consistent with previously reported forms of occurrence of arsenic in coal [60, 68, 69]. However, no attempts were made to ascertain the exact chemical composition of the leached arsenic material. The interpretation by Querol et al. [41] of their leaching results for the fly ash samples may need to be reexamined in light of the current understanding of arsenic partitioning onto fly ash surfaces. Their leaching results are consistent with a calcium and/or iron arsenate-controlled partitioning theory as well as with an As_2O_3 condensation-controlled partitioning theory.

Silberman and Harris [39] used a pH 5 citric acid solution. They selected this leaching acid because citric acid has been shown to dissolve large amount of iron and aluminum compounds from fly ash surfaces. Using this method, they report that most surface deposited arsenic on fly ash surfaces is in the As(+V) form rather than the As(+III) form. This result is consistent with the findings of Sato [154], Warren and Dudas [154], and Wadge and Hutton [153] but contradictory to leaching studies performed by others [159, 160] which conclude that the majority of arsenic present on fly ash surfaces may be in the As(+III) form and is inconsistent with the partitioning theory presented above. Jones [154] suggests that oxidation of As(+III) to As(+V) during the leaching test itself may be responsible for the inconsistency in results. This suggestion is supported by batch extraction experiments performed by Turner [159].

Temporal Resolution of Arsenic Partitioning Processes

The analysis above has shown that arsenic partitioning to fly ash surfaces may be dominated by surface reaction with calcium and/or iron active cation sites. Further insight can be gained into arsenic partitioning mechanisms by examining size-segregated samples from Port 4 and comparing these results to those obtained from Port 14.

Insight into the timing of arsenic volatilization can be gained by comparing the mass fraction of arsenic still in the vapor phase at the combustion zone sampling location (Port 4) for the baseline screening experiments to the mass fraction of arsenic still in the vapor phase at the post-combustion zone sampling location (Port 14). The mass fraction of arsenic still in the vapor phase at both sampling locations for the six study coals is summarized in Table 3-91. The mass fraction of vapor-phase arsenic is higher in the combustion zone sample for all of the study coals except the Wyodak and Pittsburgh coals (although the Pittsburgh values are similar at each location). This indicates that most arsenic volatilization occurs prior to Port 4 for four of the study coals. Only the Wyodak coal appears to have significant post-combustion zone volatilization. This is most likely due to continued carbon burnout after Port 4. As the carbon oxidizes, arsenic is subjected to the high temperatures required for volatilization.

The timing of partitioning from the vapor phase back to particle surfaces can be evaluated by comparing the enrichment factors[8] of the submicron particles. Calculating a differential enrichment factor by subtracting the combustion zone enrichment factor from the post-combustion zone enrichment factor provides insight into when partitioning is occurring. Arsenic enrichment factors at Ports 4 and 14 along with differential enrichment factors are shown in Table 3-92 for all six study coals.

A positive arsenic differential enrichment factor is found for Illinois, Wyodak, and North Dakota submicron particles. This suggests that volatilized arsenic continue to partition to submicron particle surfaces after Port 4. By contrast the negative differential enrichment factors shown for the Pittsburgh, Ohio, and Kentucky submicron particles suggest that the majority of the arsenic associated with submicron particle for these coals is present prior to Port 4.

Further insight into the timing of vapor-to-solid phase partitioning can be obtained using particle size dependence models based on transport theory (see above). The particle size dependence of arsenic associated with supermicron fly ash particles for the six study coals at the Port 4 sampling location is shown in Figure 3-142. The results show that the Pittsburgh, Ohio, and North Dakota arsenic distributions follow a near $1/D_p$ dependence. This indicates that the rate of partitioning of volatile arsenic to supermicron particles is dominated by exterior surface reaction and that a significant portion of this process occurs prior to Port 4 for these coals. The Kentucky arsenic distributions follow a near $1/D_p^2$ dependence that indicates that the reactivity of arsenic with fly ash surface species is sufficiently rapid that the partitioning is limited by gas film transfer prior to Port 4. The Illinois and Wyodak arsenic distributions do not follow any dependence implying that partitioning may be occurring later for these coals (since at Port 14 a $1/D_p$ dependence is observed for both coals).

[8] See Eq. (3-14) for the definition of the enrichment factors employed in this work.

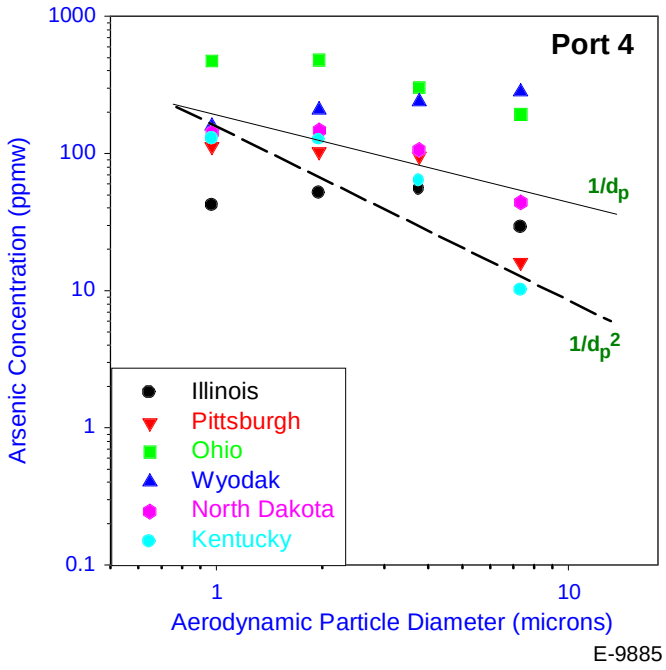

Figure 3-142. Particle size dependence of arsenic in supermicron fly ash particles for all six study coals sampled at Port 4.

Note that the Ohio arsenic distribution follows a $1/D_p$ dependence at Port 4 but not at Port 14. The results imply that active cation sites are available during or immediately after combustion but that additional sites are no longer available as the particles and flue gas travel through the combustor. This same scenario was observed for the Ohio selenium distribution.

The size-segregated concentration of arsenic in submicron particles is shown in Figure 3-143 for the six study coals at the Port 4 sampling location. There appears to be a decrease in concentration with particle size for the Illinois and Kentucky coals. These results imply that the rate of partitioning of arsenic to the particle surface is controlled by a transport process for the Illinois and Kentucky coals. No particle size dependence is apparent for the Pittsburgh, Ohio, Wyodak, or North Dakota coals.

Timing issues and any differences in As-Fe or As-Ca reactions as a dominant partitioning mechanism between Ports 4 and 14 can be evaluated by comparing the total ash size distribution and the size distributions of iron, calcium, and arsenic. The differential mass concentration distributions of arsenic, calcium, iron, and the total ash from full impactor sets for all six coals under baseline combustion conditions at the Port 4 sampling location are shown in Figure 3-144. The corresponding correlations of arsenic to calcium and iron using both evaluation methods for both submicron and supermicron fly ash sampled at Port 4 is shown in Table 3-99 for all six study coals.

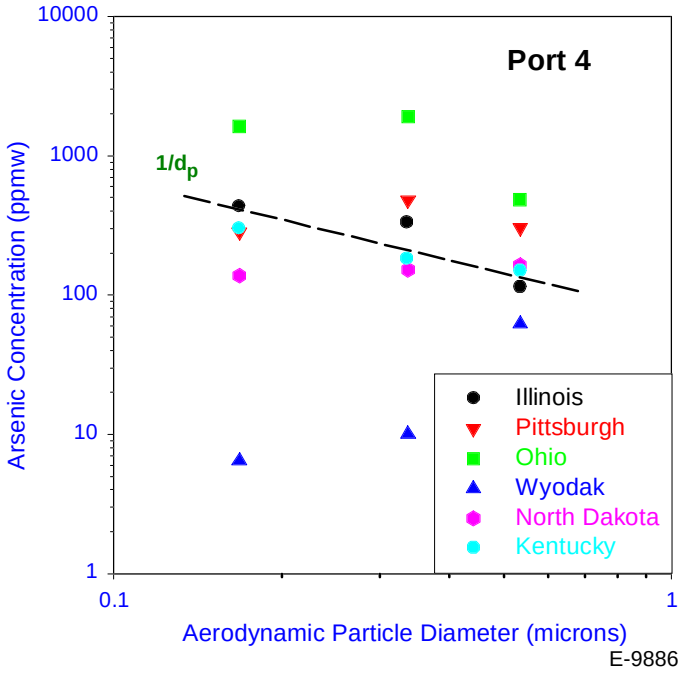

Figure 3-143. Particle size dependence of arsenic in submicron fly ash particles for all six study coals sampled at Port 4.

The differential distribution curves in Figure 3-144 and the cross correlations listed in Table 3-99 can be compared to the arsenic distributions and correlations at Port 14 (Figure 3-136, Table 3-93). The correlation of arsenic in the Illinois fly ash distributions in both submicron and supermicron regions are different at Ports 4 and 14. The submicron As distribution at Port 4 does not appear to follow either Ca or Fe while at Port 14, the As distribution follows the iron and calcium submicron distributions (which are too similar to separate). The fragmentation region supermicron arsenic distribution at Port 14 appears to follow the Fe distribution while at Port 4 no correlation is apparent. These results imply that active cation surface sites appear to develop after Port 4 and that arsenic then partitions to these sites in the post-combustion zone.

Similar to selenium, the Ohio arsenic distribution appears to correlate with calcium and/or iron at Port 4 in all three particle regions. By contrast, the Port 14 arsenic distributions do not appear to correlate with either cation distribution (except possibly in the bulk fly ash). This suggests that arsenic may initially be reacting with available active surface sites immediately after combustion and then is displaced by more thermodynamically favorable anions (most probably sulfur).

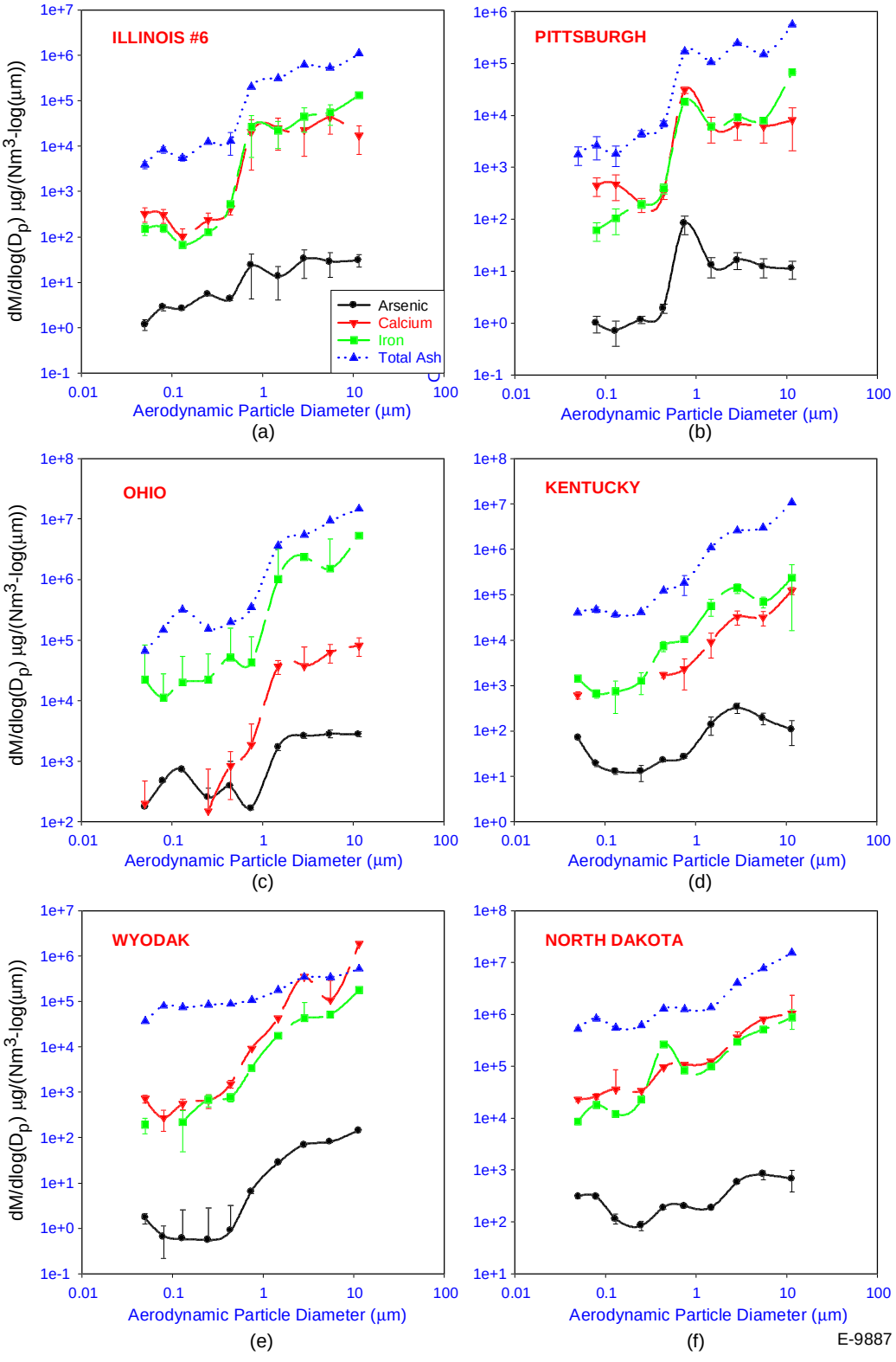

Figure 3-144. Differential mass distributions of arsenic, calcium, iron, and total ash for the six study coals sampled at Port 4.

Table 3-99. Correlation Coefficients for Arsenic Versus Calcium and Iron in Fly Ash Particles from the Six Study Coals Sampled at Port 4

Coal		Submicron Correlations			Supermicron Correlations		
		Absolute Concentrations	**Differential Distributions**	**Overall Absolute Concentrations**	**Overall Differential Distributions**	**Fragmentation Region Differential Distributions**	**Bulk Fly Ash Region Differential Distributions**
Illinois:	As vs. Ca	~0	~0	0.45	0.28	~0	~0
	As vs. Fe	~0	~0	0.21	0.78	0.76	~0
Pittsburgh:	As vs. Ca	0.28	0.88	1.0	0.93	1.0	0.57
	As vs. Fe	0.89	1.0	0.99	0.84	0.99	0.93
Ohio:	As vs. Ca	~0	0.99	~0	0.85	0.93	0.94
	As vs. Fe	~0	0.97	~0	0.96	0.94	0.40
Kentucky:	As vs. Ca	na	na	~0	0.67	0.96	~0
	As vs. Fe	~0	1.0	0.24	0.98	1.0	~0
Wyodak:	As vs. Ca	~0	1.0	0.97	0.96	0.96	1.0
	As vs. Fe	~0	~0	0.99	0.98	0.98	1.0
N. Dakota:	As vs. Ca	~0	1.0	0.36	0.95	0.99	0.84
	As vs. Fe	~0	0.99	0.30	0.98	0.98	0.98

Summary of Arsenic Partitioning

A comprehensive study has been performed to investigate the partitioning of arsenic during pulverized coal combustion. The primary partitioning mechanisms for arsenic during the combustion of the six coals investigated as predicted by this study are summarized in Figure 3-145 and Table 3-100.

The partitioning of arsenic is governed primarily by the extent of arsenic volatilization during combustion. The majority of the arsenic for all six coals is attributed to pyrite/sulfide or mono-sulfide fractions although four of the coals have silicate fractions of 5 to 15%. Organically-associated arsenic was only detected in the Wyodak coal. The large fraction of arsenic not contained in silicates is expected to volatilize during combustion. Volatilized arsenic will heterogeneously transform to both submicron and supermicron particles primarily by reaction with active cation sites. Only a small fraction (less than 5 wt% of the total arsenic at Port 14) will remain in the vapor phase and exit the boiler.

The partitioning of arsenic to fly ash surfaces is dependent on the availability of active cation sites. For coals with relatively low As/Ca ratios, arsenic is expected to react with calcium surface sites to form calcium arsenate complexes. These arsenate complexes are partially soluble and some of the arsenic in this form is expected to leach into groundwater. If the As/Ca ratio is relatively high and the sulfur content is low, arsenic will most likely react with both calcium and iron surface sites to form iron arsenates and calcium arsenates. These complexes are partially soluble and are likely to contribute arsenic to groundwater due to leaching. If the As/Ca ratio is relatively high and the sulfur content is moderate to high, cationic surface sites will not be

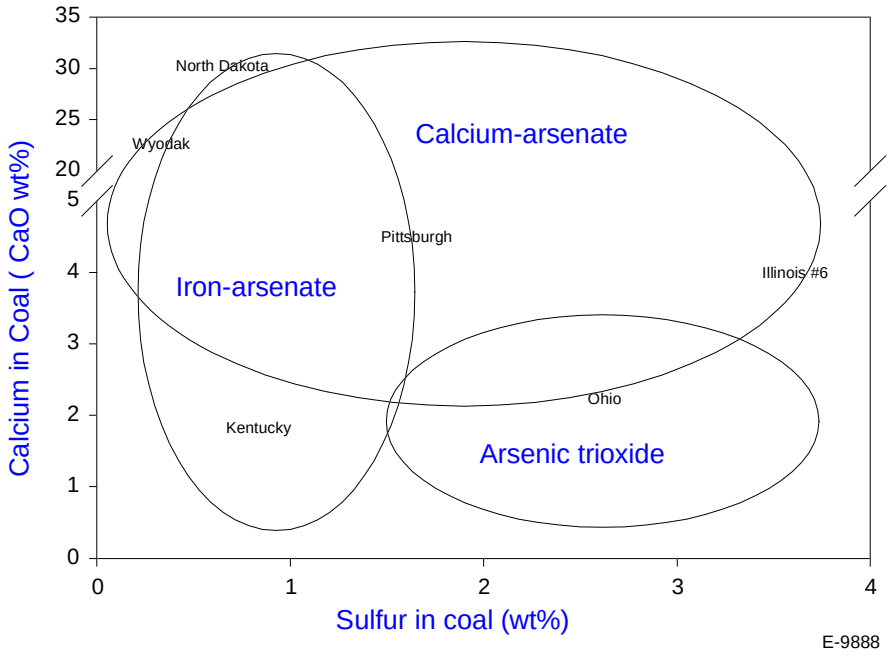

Figure 3-145. Summary of arsenic partitioning mechanisms.

Table 3-100. Primary Partitioning Mechanisms for Arsenic during the Combustion of the Six Study Coals

Coal	Submicron Region	Supermicron Region
Pittsburgh	Partitioning occurs and is essentially completed in the combustion zone (<2.2 residence seconds from the burner). Reaction with active calcium surface sites form calcium arsenate-type compounds. Sulfur partially inhibits reaction of arsenic with active iron surface sites.	Partitioning to fly ash surfaces occurs in the combustion zone. Reaction with active calcium surface sites form calcium arsenate-type compounds. Sulfur partially inhibits reaction of arsenic with active iron surface sites.
Illinois	Partitioning begins in the combustion zone and continues in the post-combustion zone (>2.2 res. sec.). Reaction with active calcium surface sites form calcium arsenate-type compounds.	Partitioning to fly ash surfaces begins in the combustion zone. Initial reaction with active iron surface sites. In the post-combustion zone, sulfur displaces arsenic from iron surface sites and the arsenic reacts with active calcium surface sites form calcium arsenate-type compounds.
Ohio	Partitioning occurs and is essentially completed in in the combustion zone (<3.2 res. sec.). High sulfur/low calcium content results in a lack of available active surface cation sites, As_2O_3 partitions to particle surfaces.	Partitioning begins in the combustion zone. High sulfur/low calcium content results in a lack of available active surface cation sites, As_2O_3 partitions to particle surfaces.
Kentucky	Partitioning occurs and is essentially completed in the combustion zone (<2.9 res. sec.). Active iron surface sites are available due to the low sulfur content of the coal. Reaction with active iron and calcium surface sites forms iron and calcium arsenate-type compounds.	Partitioning to fly ash surfaces occurs in the combustion zone. Active iron surface sites are available due to the low sulfur content of the coal. Reaction with active iron and calcium surface sites iron and calcium arsenate-type compounds.
Wyodak	Partitioning begins in the combustion zone and continues in the post-combustion zone (>6.6 res. sec.). Active iron and calcium surface sites are available due to the low sulfur/high calcium content of the coal. Reaction with active iron and calcium surface sites forms iron and calcium arsenate-type compounds	Partitioning to fly ash surfaces begins in the combustion zone. Active iron and calcium surface sites are available due to the low sulfur/high calcium content of the coal. Reaction with active iron and calcium surface sites forms iron and calcium arsenate-type compounds
North Dakota	Partitioning begins in the combustion zone and continues in the post-combustion zone (>9.3 res. sec.). Active iron and calcium surface sites are available due to the low sulfur/high calcium content of the coal. Reaction with active iron and calcium surface sites forms iron and calcium arsenate-type compounds	Partitioning begins in the combustion zone. Active iron and calcium surface sites are available due to the low sulfur/high calcium content of the coal. Reaction with active iron and calcium surface sites forms iron and calcium arsenate-type compounds.

available for arsenic partitioning. In these cases, most of the arsenic is expected to exit the furnace in the vapor phase or as fly ash surface-based As_2O_3 (e.g., the Ohio study coal). As_2O_3 is partially soluble and is likely to contribute arsenic to groundwater due to leaching. Further, a portion of the As_2O_3 may oxidize to As_2O_5. As_2O_5 is very soluble and any arsenic in this form will most likely leach out of fly ash particles when contacted by water.

Active cationic surface sites are primarily due to major elements (i.e., calcium and iron) volatilizing in the vicinity of the carbon oxidizing in the coal particles and then homogeneously and heterogeneously condensing. Increasing the combustion temperature can increase cationic surface site availability and subsequently reduce the emission of vapor phase or physically condensed As_2O_3 from the furnace.

Antimony

Antimony Volatility

Finkleman and coworkers [7, 141, 142] determined the forms of occurrence of antimony for the six coals utilized in this study. The results are summarized in Table 3-101. The most common form of occurrence of antimony for all six coals is attributed to organically associated antimony. Significant pyrite/sulfide and mono-sulfide fractions are also present in all coals. All of the coals have higher silicate-associated fractions than arsenic or selenium. Consistent with Bool and Helble [29], the large fraction of antimony not contained in silicates is expected to volatilize during combustion.

Table 3-101. Forms of Occurrence of Antimony in the Six Study Coals[1]

Coal	Ammonium Acetate Leachable or Unleachable (organic)	HCl Leachable (mono-sulfide)	HF Leachable (silicate)	HNO_3 Leachable (pyrite/ sulfide)
Pittsburgh	55%	10%	15%	20%
Illinois	50%	5%	20%	25%
Kentucky	70%	5%	20%	5%
Ohio	50%	10%	25%	15%
Wyodak	45%	5%	35%	15%
North Dakota	40%	5%	45%	10%

1. From Senior, et. al., 1997; Volker, 2000; Palmer, et. al., 1998

Results from thermodynamic equilibrium simulations predict that SbO is the favorable form of occurrence at the combustion temperatures of all six coals studied in this research. Antimony is predicted to remain either remain as SbO or condense to form AlSb(l) and AlSb(s) in the post-combustion zone. If SbO is not an allowable formation product, the simulations predict SbS, AlSb(l), and AlSb(s) as the most favorable forms of occurrence except for the North Dakota lignite. In this case, antimony is predicted to form SbS, AlSb(l), Sb_2O_4, $SbCl_3$, and $SbCl_5$. It should be noted that at the Port 14 and baghouse inlet sampling temperatures, North Dakota antimony is predicted to be in the chloride form.

Vapor-to-Particle Surface Antimony Transport Mechanisms

Due to its low volatility in the oxy-anion form, only a very small portion of the volatilized antimony is expected to exit the combustor in the vapor phase. If present in the chloride form substantially higher vapor-phase emissions could occur. In this study the average mass fraction of antimony still in the vapor phase at the post-combustion zone sampling location (Port 14) for the baseline screening experiments was 31 wt% (compared to 4.5% for arsenic and 13 wt% for selenium). However there was significant variation between coal types (see Table 3-102); more variation than arsenic or selenium. For the Illinois and Kentucky coals antimony in the vapor phase accounts for less than 1.5 wt% of the total antimony collected at Port 14 – a lower vapor phase mass fraction than arsenic or selenium. The Pittsburgh and Wyodak coals vapor phase antimony mass fractions are comparable to the arsenic mass fractions.

Table 3-102. Mass Fraction of Antimony in Vapor, Submicron, and Supermicron Regimes at Three Combustor Sample Locations

Coal/Location	Average Sampling Temperature (K)	Vapor Regime (Wt%)	Submicron Regime (Wt%)	Supermicron Regime (Wt%)
Pittsburgh				
Port 4	1440	1.6	61	37
Port 14	1140	4.2	14	82
Baghouse Inlet	470	42	19	38
Illinois				
Port 4	1410	3.7	21	75
Port 14	1130	1.3	15	83
Baghouse Inlet	220	11	12	77
Ohio				
Port 4	1330	22	2.9	76
Port 14	1040	81	7.1	11
Baghouse Inlet	610	20	22	58
Kentucky				
Port 4	1490	3.1	2.4	2.6
Port 14	1150	nd	2.5	98
Baghouse Inlet	490	nd	15	85
Wyodak				
Port 4	1080	0.7	25	75
Port 14	760	6.7	12	81
Baghouse Inlet	210	10	37	52
North Dakota				
Port 4	1250	59	40	0.6
Port 14	870	95	2.4	2.6
Baghouse Inlet	400	59	40	0.6
Average All Coals				
Port 4		15	26	59
Port 14		31	9.0	60
Baghouse Inlet		30	18	52

The Ohio and North Dakota coals have substantially higher vapor phase antimony mass fractions – 81 and 95 wt% at Port 14, respectively. The North Dakota results are particularly surprising since 45% of the antimony in the coal feed is associated with silicates and thus was not expected to volatilize in the furnace. These results imply that virtually all of the antimony in the North Dakota and Ohio coals volatilizes regardless of the form of occurrence in the feed coal. Furthermore, there is almost no partitioning to solid phase surfaces which is also surprising considering the behavior of arsenic and selenium. Even if surface reaction of antimony is not the controlling vapor-to-solid phase transport mechanism, a lower vapor phase mass fraction is expected due to the high probability of contact and partitioning of Sb_2O_3 to fly ash surfaces. These results suggest that antimony in the North Dakota flue gas is present as $SbCl_3$ and/or $SbCl_5$ as predicted by the thermodynamic equilibrium results shown in Section 3.3.1.

The thermodynamic equilibrium results shown in Section 3.3.1 do not predict antimony in the Ohio flue gas present as $SbCl_3$ and/or $SbCl_5$. Even though thermodynamic simulations do not predict antimony chloride formation, this may be the reason for the high vapor-phase emissions. However, higher vapor phase emissions of arsenic and selenium were also found in the Ohio coal compared to the other coals (although not nearly as high as antimony). This higher emission rate was attributed to the fact that oxy-anion partitioning for the Ohio coal is not controlled by surface reaction with iron and calcium cations. Thus, an alternate explanation for the higher Ohio emission could be that the ability of antimony trioxide to partition from the vapor phase to particle surfaces by a non-transport-controlled process is substantially less efficient than selenium dioxide or arsenic trioxide.

The average mass fraction of antimony still in the vapor phase at the baghouse inlet sampling port for the baseline screening experiments was 30 wt% (compared to 14% for arsenic and 20% for selenium). It should be noted that a portion of the bulk fly ash particles has been removed from the flue gas prior to this sample.

Due to the low concentration of antimony compared to the major species in the coal, there is a very high probability that a volatilized antimony molecule will contact submicron or supermicron particles prior to reaching the supersaturated conditions necessary for nucleation. Therefore for most coals, a majority of the volatilized antimony is expected to heterogeneously partition onto the surfaces of both submicron and supermicron particles [32].

The heterogeneous vapor-to-solid phase partitioning theory described above for selenium is also proposed for antimony partitioning for the Pittsburgh, Illinois, Kentucky, and Wyodak coals. If this theory is valid, there will be an enrichment of antimony onto submicron particles. Antimony enrichment factors[9] for fly ash particles from the baseline screening experiments sampled at the Port 14 (post-combustion zone) sampling location are given in Table 3-103. The Illinois, Kentucky, and Ohio coals show enrichment (values greater than 1.0) of antimony on all submicron stages for the Port 14 sampling location. The Port 14 Pittsburgh samples are inconclusive (two stages show depletion – $E_f < 1$ – and 1 stage shows enrichment). For the Wyodak and North Dakota coals, there is a depletion of antimony in the Port 14 fly ash samples.

[9] See Eq. (3-14) for the definition of the enrichment factors employed in this work.

Table 3-103. Antimony Enrichment Factors[1] for Submicron-Sized Fly Ash Samples

Coal/Location		Aerodynamic Particle Diameter (μm)			
		0.17	**0.34**	**0.54**	**Average**
Pittsburgh	Port 14	0.8	1.8	0.8	1.1
	Port 4	2.5	2.9	2.1	2.5
	Differential	-1.7	-1.1	-1.3	-1.4
Illinois	Port 14	2.7	1.3	2.9	2.3
	Port 4	2.2	1.4	0.6	1.4
	Differential	0.6	-0.1	2.3	0.9
Kentucky	Port 14	nd	5.0	5.2	3.4
	Port 4	14	nd	0.8	5.1
	Differential	-14	5.0	4.4	-1.7
Ohio	Port 14	11	21	19	17
	Port 4	1.5	4.6	0.9	2.4
	Differential	9.2	16	18	14
Wyodak	Port 14	0.3	0.6	0.7	0.5
	Port 4	0.1	0.1	4.9	1.7
	Differential	0.2	0.4	-4.3	-1.2
North Dakota	Port 14	0.7	1.0	0.4	0.7
	Port 4	19	5.2	0.7	8.2
	Differential	-18	-4.2	-0.3	-7.5

1. See Eq. (3-14) for the definition of the enrichment factors employed in this work

These results (both the vapor phase analysis and the submicron enrichment analysis) are in apparent contrast to the vast majority of previous studies. Enrichment of antimony in submicron particles is reported in many studies [4, 8, 11, 14, 17, 18, 30, 32, 34, 35, 65, 71, 72, 78-81, 92, 93, 144, 161, 162] while depletion of antimony in submicron particles was found reported in only one study [29]. However, most of these previous studies calculate enrichment by comparing the concentration in bulk samples collected at different locations in the combustion train (e.g., prior to the ESP versus after the ESP). For an equivalent comparison the average concentration in the submicron particles is referenced to the average concentration in the supermicron particles. Using this formula, a positive enrichment factor will be calculated for all six study coals and thus the current results are found to be consistent with previous work.

To be consistent with the heterogeneous vapor-to-solid phase partitioning theory, supermicron particles should contain a higher absolute mass fraction of antimony than the submicron particles. In the current work, the average antimony mass fraction in the supermicron particles for the four coals expected to follow this mechanism was 86 wt% (see Table 3-102 for individual values).

Deviation from this theory is expected for the Ohio and North Dakota coals. For these coals, vapor-to-solid phase partitioning may be controlled by the other means related to the volatility of Sb_2O_3, SbO, $SbCl_3$ and/or $SbCl_5$. Unfortunately, it was beyond the scope of this study to identify the exact forms of occurrence of vapor-phase antimony exiting the furnace.

Due to the similarity in chemistry with arsenic, vapor phase antimony is expected to form an oxy-anion of the form Sb_2O_3 during coal combustion although thermodynamic studies predict SbO as a major specie. The probability of Sb_2O_3 adherence to a particle's surface is primarily due to the number of active cation sites on the particle surface. Sb_2O_3 will become incorporated into the particle if subsequent reaction between the anion and cation (chemical bonding) occurs. The probability that chemical reaction will occur depends upon the rate at which the anion can migrate across the particle surface to the cation site and the kinetic reaction rate between the anion and cation.

Because of the very low concentrations of antimony in the feed coals, gas-phase concentrations of Sb_2O_3 are insufficient in most combustion systems to initiate physical condensation prior to the stack. Therefore, Sb_2O_3 presence on fly ash particle surfaces is not expected to occur by this mechanism.

The particle size dependence of antimony associated with supermicron fly ash particles for the six study coals at the Port 14 sampling location is shown in Figure 3-146. The following antimony distributions show a near $1/D_p$ dependence: Illinois, Pittsburgh[10], and Kentucky. This indicates that partitioning of vapor-phase antimony to supermicron particles in the post-combustion zone is controlled by exterior surface reaction. For the Wyodak coal, a $1/D_p^2$ dependence is shown when the 1 μm data point is excluded indicating gas film transfer-limited transport. There is no dependence for the Ohio and North Dakota antimony profiles indicating that this mechanism is not important after the combustion zone.

The size-segregated concentration of antimony in submicron particles from the current study is shown in Figure 3-147 for the six study coals at the Port 14 sampling location. No particle size dependence is apparent for any of the coals studied.

Fly Ash Surface Antimony Reaction Mechanisms

Due to the similarity of antimony to arsenic, a reaction of Sb_2O_3 with calcium and/or iron cations is a likely partitioning mechanism for the Illinois, Pittsburgh, Wyodak, and Kentucky coals. Gullett and Ragnunathan [149] demonstrated that Ca-based sorbents can increase solid-phase antimony recoveries by >135% whereas kaolinite (Al-Si cation sites) and bauxite (Al cation sites) had no measurable effect on antimony recoveries. For the Ohio and North Dakota coals, partitioning of SbO, Sb_2O_3, $SbCl_3$ and/or $SbCl_5$ by a non-transport-controlled is proposed. In the one previous study where submicron antimony depletion was observed [29], it was suggested that a Sb-Si interaction was involved. However oxy-anion forms of vapor-phase antimony are not expected to be as reactive with active Si cation surface sites as with Ca or Fe. But if antimony is present in a cationic form, such as SbO, it may be reacting with active oxy-aluminum anion surface sites in the Al-Si fly ash surface matrix. AlSb is also predicted by thermodynamic equilibrium simulations as a favorable form of occurrence at the Port 14 and baghouse inlet sampling temperatures.

[10] Excluding the 1 μm data point

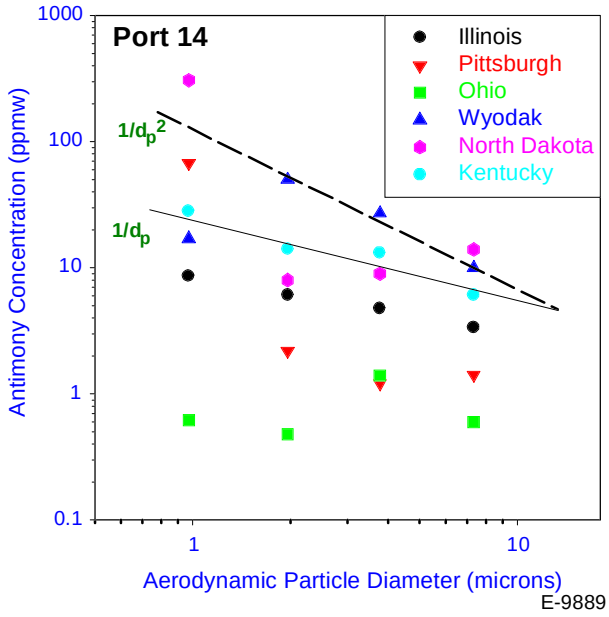

Figure 3-146. Particle size dependence of antimony in supermicron fly ash particles for all six study coals sampled at Port 14.

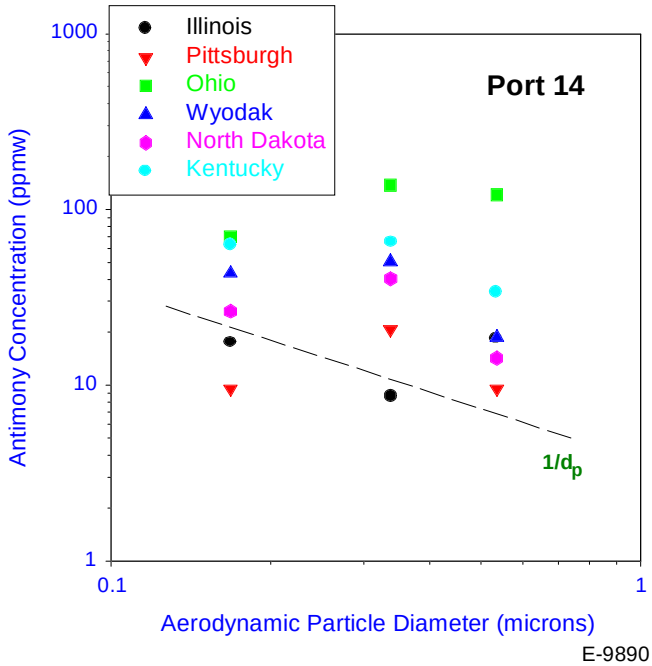

Figure3-147. Particle size dependence of antimony in submicron fly ash particles for all six study coals sampled at Port 14.

The potential for Sb-Fe, Sb-Ca, or Sb-Al reactions as a dominant partitioning mechanism can be evaluated by comparing the total ash size distribution and the size distributions of iron, calcium, aluminum, and antimony. The differential mass concentration distributions of the total ash, iron, calcium, aluminum, and antimony from full impactor sets for all six coals under baseline combustion conditions at the Port 14 sampling location are shown in Figure 3-148.

To examine the results more carefully, the distributions were decomposed into their submicron and supermicron components and cross correlation coefficients were calculated. The correlation of antimony to calcium, iron, and aluminum using both evaluation methods for both submicron and supermicron fly ash sampled at Port 14 is shown in Table 3-104 for all six study coals.

Antimony in the Illinois fly ash correlates with calcium and iron in all three particle regions. For Pittsburgh, correlation of antimony with calcium and iron is suggested for the fragmentation region and possibly the submicron region. No strong correlation was found for Ohio antimony with calcium, iron, or aluminum. Antimony correlation results for the Kentucky coal are unclear. Possible correlation with calcium, iron, and aluminum is suggested for both supermicron regions but not for the submicron region. Wyodak antimony appears to correlate with iron in the submicron region, with calcium in the fragmentation region, and with calcium, iron, and aluminum in the bulk fly ash region. For North Dakota, antimony does not appear to correlate with any major species in any particle region.

This assessment of the distribution curves in Figure 3-148 and the cross correlations listed in Table 3-104 suggests that the mechanisms controlling antimony partitioning:

1. Are different depending on the fly ash particle region,

2. May be surface reaction controlled if $SbCl_3$ and/or $SbCl_5$ are not formed,

3. When surface reaction controlled, the reaction is most likely with calcium and/or iron active surface sites; although it is not possible to rule out reaction with aluminum active surface sites (as predicted by thermodynamic equilibrium simulations for some coals).

The Illinois and Pittsburgh coals have moderate calcium contents and relatively high sulfur contents. The Ohio coal (where no size dependence is observed) has a low calcium content and high sulfur content. The Kentucky coal has a low calcium content and low sulfur content. The Wyodak and North Dakota coals have high calcium content, low sulfur content, and a lower maximum combustion temperature (than the four bituminous coals). The North Dakota coal also has a low chlorine content (0.0036 wt% compared to 0.17 wt% for the Kentucky coal). Thus, chlorine content is not the key parameter to account for the formation of antimony chloride during North Dakota lignite combustion.

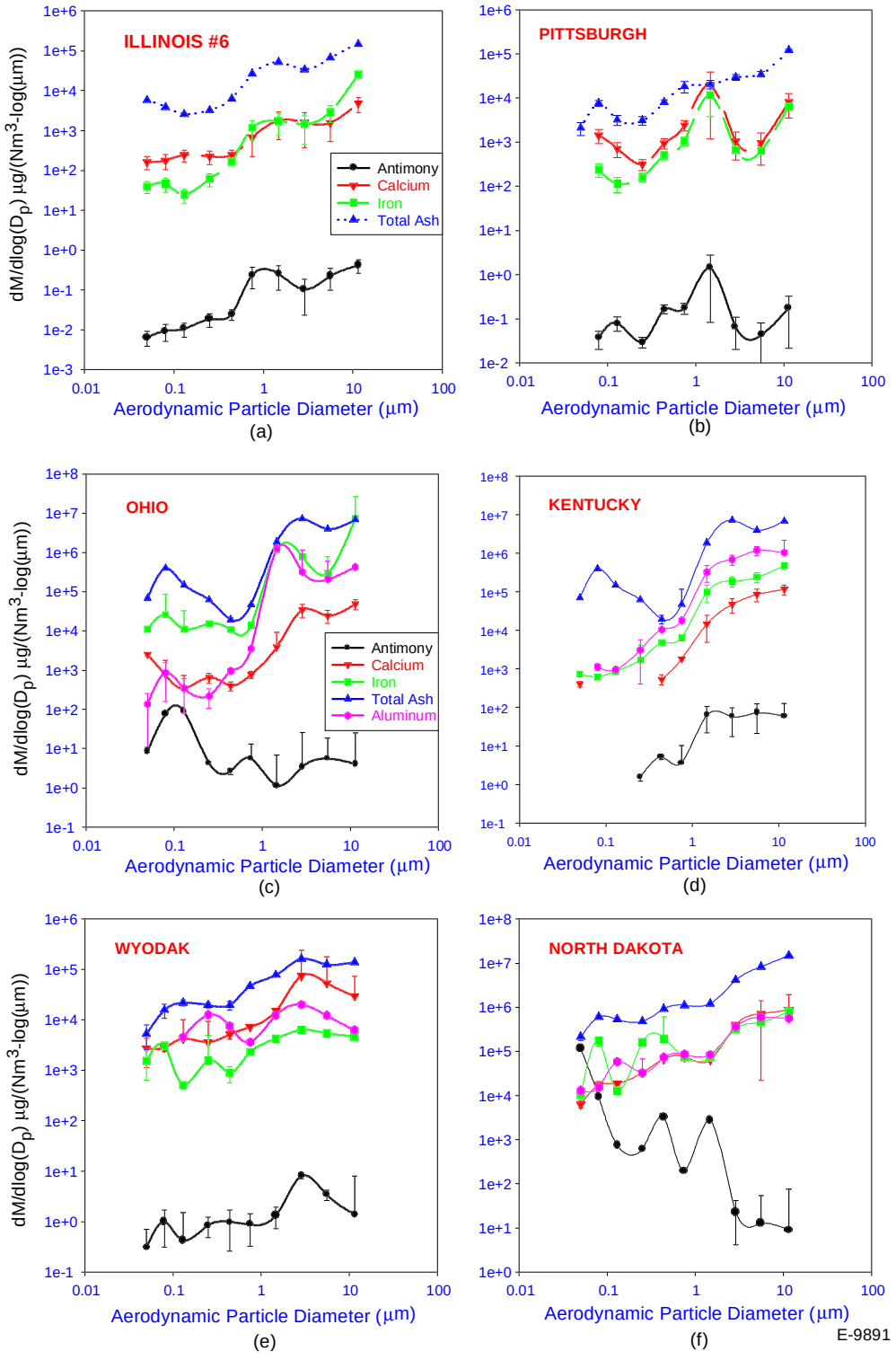

Figure 3-148. Differential mass distributions of antimony, calcium, iron, aluminum*, and total ash for the six study coals sampled at Port 14.

*Aluminum distribution data is not available for the two Phase I coals – Illinois #6 and Pittsburgh.

Table 3-104. Correlation Coefficients for Antimony versus Calcium, Iron, and Aluminum in Fly Ash Particles from the Six Study Coals Sampled at Port 14

Coal		Submicron Correlations			Supermicron Correlations		
		Absolute Concentrations	**Differential Distributions**	**Overall Absolute Concentrations**	**Overall Differential Distributions**	**Fragmentation Region Differential Distributions**	**Bulk Fly Ash Region Differential Distributions**
Illinois:	Sb vs. Ca	0.57	0.58	~0	0.12	1.0	1.0
	Sb vs. Fe	0.29	0.77	~0	~0	0.93	0.89
	Sb vs. Al	na[1]	na	na	na	na	na
Pittsburgh:	Sb vs. Ca	0.60	0.54	1.0	1.0	1.0	~0
	Sb vs. Fe	~0	0.40	0.99	0.82	1.0	~0
	Sb vs. Al	na	na	na	na	na	na
Ohio:	Sb vs. Ca	~0	~0	~0	0.10	~0	~0
	Sb vs. Fe	~0	~0	~0	0.26	0.51	0.32
	Sb vs. Al	~0	0.93	~0	~0	~0	~0
Kentucky:	Sb vs. Ca	nd[2]	nd	~0	0.34	0.54	0.68
	Sb vs. Fe	0.41	0.08	0.20	0.63	0.79	0.36
	Sb vs. Al	0.80	~0	~0	0.45	0.73	0.93
Wyodak:	Sb vs. Ca	0.24	~0	~0	0.87	1.0	0.98
	Sb vs. Fe	~0	0.83	~0	0.75	0.75	0.99
	Sb vs. Al	0.17	0.32	0.08	0.70	0.69	0.99
N. Dakota:	Sb vs. Ca	~0	0.98	~0	~0	~0	~0
	Sb vs. Fe	~0	~0	~0	~0	~0	~0
	Sb vs. Al	~0	0.99	~0	~0	~0	~0

1. Aluminum analyses not available for Illinois and Pittsburgh fly ash
2. Antimony concentrations below detection limit

The factors affecting antimony partitioning appear to be more complex than those for arsenic and selenium. The three parameters identified as important for As and Se partitioning (i.e., antimony-to-calcium ratio, coal sulfur content, and combustion temperature) also appear to be important in determining the nature of antimony surface reaction-controlled partitioning. Factors affecting the generation of antimony oxide (which would be expected to react with aluminum surface sites), antimony trioxide (which would be expected to react with calcium and/or iron surface sites), or antimony chloride (which is not expected to be reactive) may also be important. These factors have not been identified.

From these results a set of hypotheses related to antimony partitioning were developed. To test these hypotheses, a set of special experiments was developed. Table 3-105 summarizes the hypotheses and the special test matrix developed for validation.

The control of antimony vapor-to-solid phase partitioning by surface reaction is proposed for most coals when sufficient active cation sites are available to accommodate the antimony present in the flue gas. To test this hypothesis, a special set of doping experiments was also performed with antimony. In one set of experiments using the Wyodak coal, antimony was dissolved in dilute acid and then doped into the furnace at the burner outlet to increase the Sb-to-Ca ratio in the combustion environment to match the Ohio coal Sb-to-Ca ratio. This was done at both the Wyodak maximum combustion temperature and an increased combustion temperature.

Figure 3-149 shows a comparison of the differential antimony distribution at the Wyodak baseline combustion conditions with Sb-doped Wyodak coal and undoped Ohio coal at the same combustion temperature. The Sb-doped Wyodak distribution is much more similar to the Ohio antimony distribution than the Wyodak antimony distribution. The cross correlation between the absolute concentration values on each relevant impactor stage are R^2=0.9 for the Sb-doped Wyodak distribution versus the Ohio Sb distribution and R^2<0 for the Sb-doped Wyodak distribution versus the undoped Wyodak Sb distribution. The cross correlation between the differential distributions are R^2=1.0 for the Sb-doped Wyodak distribution versus the Ohio Sb distribution and R^2<0 for the Sb-doped Wyodak distribution versus the undoped Wyodak Sb distribution.

A similar comparison is shown in Figure 3-150. This figure shows a comparison of the differential antimony distribution at the Ohio baseline combustion conditions with Sb-doped Wyodak coal at an elevated combustion temperature approaching the Ohio temperature and with an undoped Wyodak coal at the same elevated temperature. Similar to the arsenic and selenium results, the Sb-doped distribution does not resemble either of the other two antimony distributions.

In another set of experiments, pulverized lime was blended into the Ohio coal in the entrance to the burner. The amount of lime added decreased the Sb-to-Ca ratio. Samples were collected at the Ohio maximum combustion temperature and at a depressed temperature similar to the Wyodak maximum combustion temperature (by adding CO_2 to the inlet air).

Table 3-105. Antimony Partitioning Mechanism Hypotheses and Validation Test Matrix

Hypothesis	Baseline Test and Fly Ash Region Where Observed	Test Number	Test Description
Vapor-to-solid phase antimony partitioning is controlled by surface reaction when sufficient surface sites are available for reaction	Ohio baseline coal versus other five coals; Ohio does not follow a dependence	99W-10, 00W-6	Antimony doped into Wyodak coal combustion until Sb-to-Ca ratio matched Ohio ratio
		00O-1, 00O-2	Calcium blended into Ohio coal for combustion until Sb-to-Ca ratio approached (+/- 25%) Wyodak ratio. Temperature decreased to match Wyodak combustion temperature
Antimony reacts with active calcium surface sites	Wyodak fragmentation and bulk fly ash; North Dakota submicron and bulk fly ash	99W-10, OOW-6	Antimony doped into Wyodak coal combustion until Sb-to-Ca ratio matched Ohio ratio
Antimony reacts with active iron surface sites when sulfur is not available to consume all of the iron surface sites	Kentucky submicron and fragmentation;	00K-1	Sulfur was doped into the Kentucky coal combustion until the sulfur content matched the Ohio sulfur content
Antimony reacts with iron and/or calcium active surface sites	Illinois submicron and bulk fly ash; Pittsburgh submicron and fragmentation; North Dakota fragmentation	00P8-1, 00P8-2	Calcium was doped into Pittsburgh coal to assess recovery of antimony; then Iron was doped into Pittsburgh coal to assess recovery of antimony
Antimony partitioning is not controlled by reaction with iron or calcium when sufficient surface sites are not available for reaction	Ohio submicron; Ohio fragmentation; Ohio bulk fly ash	00K-1, 00O-1	Sulfur was doped into the Kentucky coal combustion until the sulfur content matched the Ohio sulfur content; Calcium blended into Ohio coal for combustion until Sb-to-Ca ratio approached (+/- 25%) Wyodak ratio.
Increasing the maximum combustion temperature will increase the availability of active calcium and iron surface sites for reaction		00W-3, 00O-2	Oxygen blended into Wyodak combustion air; CO2 blended into Ohio combustion air.
Antimony has similar reactivity with iron as with calcium		00P8-1, 00P8-2	Calcium was doped into Pittsburgh coal to assess recovery of antimony; then Iron was doped into Pittsburgh coal to assess recovery of antimony

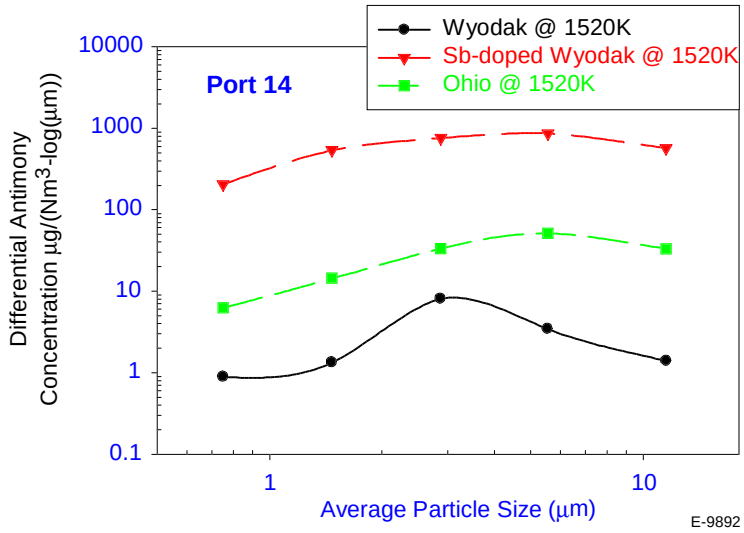

Figure 3-149. Comparison of antimony differential distributions when adjusting the antimony-to-calcium ratio at constant maximum combustion temperature in the Wyodak coal.

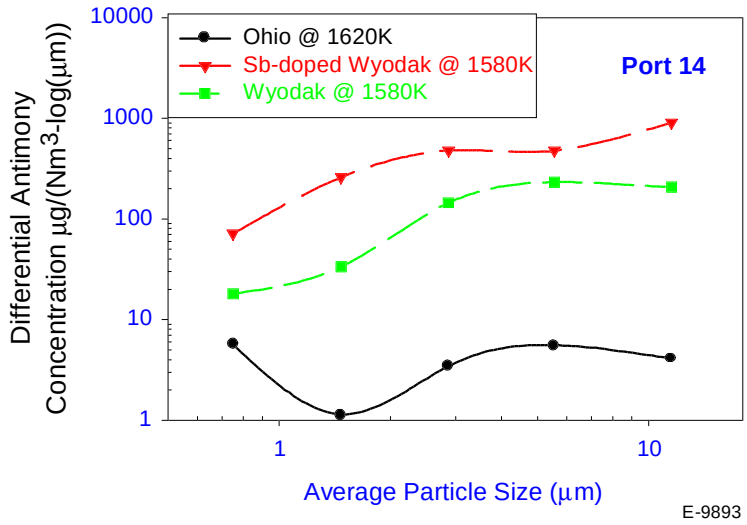

Figure 3-150. Comparison of antimony differential distributions when adjusting the antimony-to-calcium ratio of the Wyodak coal with combustion near the Ohio maximum combustion temperature.

Figure 3-151 shows a comparison of the differential antimony distribution at the Ohio baseline combustion conditions with Ca-doped Ohio coal at the Ohio combustion temperature and with an undoped Wyodak coal at a similar elevated temperature. The Ca-doped Ohio coal antimony distribution is less similar to the Wyodak distribution (elevated by O_2 enrichment of the combustion air) compared to the undoped Ohio distribution. In fact, the addition of calcium to the Ohio coal does not appear to have had any appreciable effect on the antimony profile for

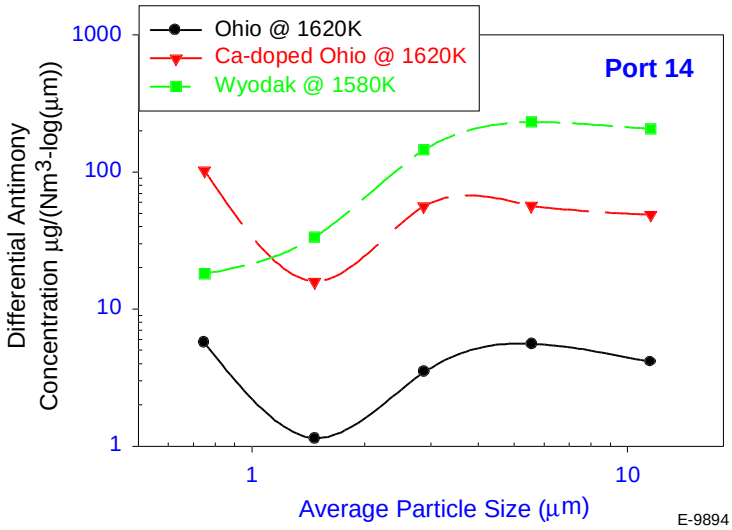

Figure 3-151. Comparison of antimony differential distributions when adjusting the antimony-to-calcium ratio of the Ohio with combustion at the Ohio maximum combustion temperature.

the Ohio coal. Recall from earlier analysis that over 80 wt% of the antimony recovered in the Ohio baseline fly ash Port 14 samples is in the vapor phase (see Table 3-102). The data shown in Figure 3-151 reinforces the hypothesis that the partitioning of antimony during Ohio coal combustion may be different than antimony partitioning for the other bituminous coals and also different from the partitioning of arsenic during Ohio coal combustion.

The results from two different experiments can be used to explore if the partitioning mechanism for the Ohio coal is related to combustion temperature. Figure 3-152 shows the differential antimony distribution of the Ohio coal at the baseline combustion temperature and at a depressed (by CO_2 addition to the main combustion air) combustion temperature. The profiles are very similar for data above 2 µm diameter although different below this point. By itself, this figure is not definitive. A second comparison is shown in Figure 3-153. In this figure, the differential antimony distribution at the Ohio baseline combustion conditions is compared to Ca-doped Ohio coal at the Wyodak combustion temperature and to an undoped Wyodak coal at its natural combustion temperature. Similar to Figure 3-151, the Ca-doped antimony distribution is more similar to the undoped Ohio distribution than the Wyodak distribution. However, there is an increase in the overall antimony recovery with the Ca-doped distribution. This does not imply that antimony is reacting with calcium, it may simply be an increase in physical absorption due to the increase in the number of particles present in the flue gas when the coal is doped with lime particles.

To summarize the results of this set of experiments, manipulating the Wyodak Sb-to-Ca ratio and/or combustion temperature results in changes in the antimony partitioning profile and these changes occur in a predictable manner similar to arsenic. However, manipulating the Ohio Sb-to-Ca ratio and/or combustion temperature has little effect on the antimony partitioning profile. This is consistent with previous analyses that indicate that Ohio antimony partitioning is

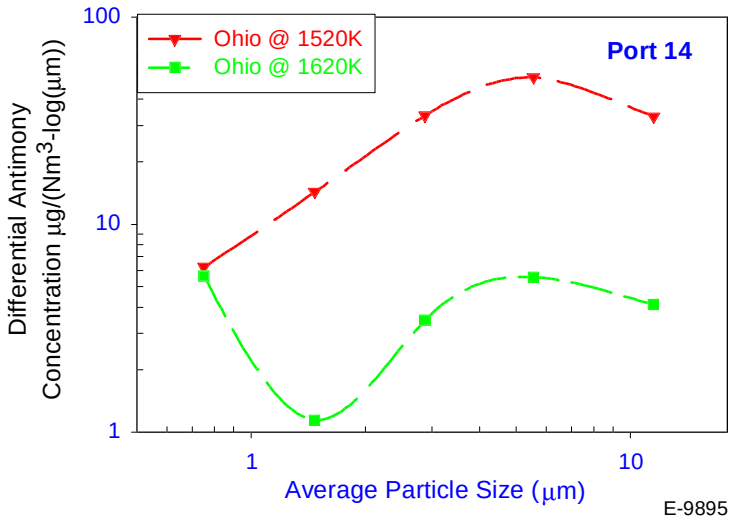

Figure 3-152. Comparison of antimony differential distributions of the Ohio coal at two different combustion temperatures.

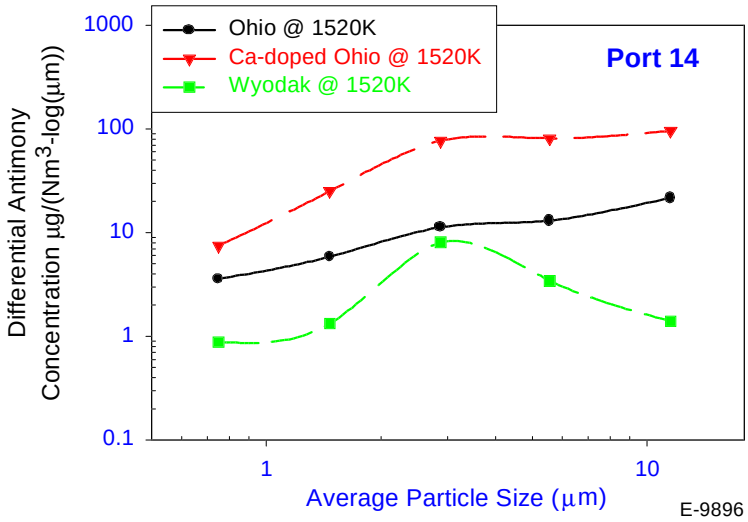

Figure 3-153. Comparison of antimony differential distributions when adjusting the antimony-to-calcium ratio of the Ohio coal with combustion at the Wyodak maximum combustion temperature.

not controlled by surface reaction mechanisms. The analysis has also shown that combustion temperature is not a critical parameter related to antimony partitioning during the Ohio coal combustion.

It was unclear from the Port 14 Kentucky baseline screening experimental results whether the antimony distribution follows the iron distribution more closely than the calcium distribution (see Figure 3-148). It is clear that the controlling antimony partitioning mechanism for the Kentucky coal is different than for the Ohio coal. Further, the particle size dependence analysis indicates that Kentucky antimony partitioning is controlled by a surface reaction mechanism similar to arsenic.

The one main difference between the Kentucky and Ohio coals is the sulfur content. Could sulfur be preferentially competing for available active cation sites in the Ohio experiments yet be insufficient to exhaust these sites in the Kentucky experiments? To examine the effect of sulfation on antimony partitioning, the main combustion air was doped with SO_2 during the combustion of the Kentucky coal. Table 3-106 shows a comparison of the Sb supermicron size mass concentration distribution for the SO_2-doped Kentucky experiment vs. the baseline Kentucky experiment. Contrary to the results for arsenic and selenium, the antimony concentration is essentially the same with the addition of SO_2 in the combustion air compared to the undoped antimony concentration. This result implies that 1) antimony partitioning is not controlled by reaction with iron surface sites, or 2) sulfur does not displace antimony that has reacted with iron surface sites.

Table 3-106. Comparison of Antimony Mass Concentration Values from Kentucky Coal SO_2 Doping Experiments

Particle Diameter (µm)	**Baseline Experiment Antimony (µg/Nm^3)**	**SO_2-Doped Experiment Antimony (µg/Nm^3)**
0.973	19	3
1.96	16	6
3.77	21	13
7.33	20	6

To explore this further, two sets of experiments were performed with the Pittsburgh seam coal to investigate whether antimony partitioning has a preference for reaction with calcium or with iron. The differential distributions of calcium and iron in Figure 3-148 are too similar to determine whether antimony is preferentially reacting with one or the other of these cations. In the first set of experiments the calcium content of the feedstock was increased by 50 mol% by pulverized lime addition. In the second set of experiments the iron content of the feedstock was increased by the same molar amount as in the calcium tests (this is a much small % increase since there is more iron in the Pittsburgh coal than calcium). The results are summarized in Table 3-107. Doping with either calcium or iron increased the antimony recovery in the supermicron fly ash particles. There is no definitive difference between the antimony recoveries for the two dopants. From these results we conclude that antimony has similar reactivity with active iron surface sites compared to active calcium surface sites.

The combined results from both the Kentucky SO_2 doping experiments and the Pittsburgh Ca/Fe doping experiments suggests that antimony is reactive with either calcium or iron surface sites and that sulfur does not displace antimony that has reacted with iron surface sites (in contrast to selenium and arsenic). This is a significant difference in the behavior of antimony

Table 3-107. Comparison of Absolute Antimony Concentration Values from Pittsburgh Seam Coal Cation Doping Experiments

Size	Port 4 Baseline	Ca Doped	Sb (ppmw) Fe Doped	Port 14 Baseline	Ca Doped	Sb (ppmw) Fe Doped
0.973	4	57	59	68	80	14
1.96	4	22	15	2	17	34
3.77	5	20	16	1	17	10
7.33	1	9	12	1	7	7

compared to arsenic and selenium and may account for the apparent correlation of antimony with iron under conditions where arsenic and selenium correlation with iron does not occur.

Environmental Impact of Antimony from Fly Ash Surfaces

In the current study, selected impactor stages were subjected to a sequential leaching protocol adapted from EPA method 1310 (TCLP) for five of the study coals. Antimony leaching results are summarized in Table 3-108. For all of the coals studied, antimony is soluble at pH 4.9 and very soluble at pH 2.9. This result is consistent with the following compounds: Sb, Sb_2O_4, and Sb_2O_5 [70, 155, 156] but is inconsistent with Sb_2O_3.

Table 3-108. Summary Of Antimony Solubility in Program Fly Ash from Baseline Screening Experiments

Coal/Sample Location	Submicron Size % Soluble at pH 4.9	Submicron Size % Soluble at pH 2.9	Supermicron Size % Soluble at pH 4.9	Supermicron Size % Soluble at pH 2.9
Pittsburgh Port 4	16%	85%	52%	80%
Pittsburgh Port 14	12%	87%	9%	86%
Ohio Port 4	36%	74%	49%	61%
Ohio Port 14	21%	63%	25%	50%
Kentucky Port 4	3%	56%	47%	86%
Kentucky Port 14	66%	94%	51%	84%
Wyodak Port 4	2%	15%	29%	91%
Wyodak Port 14	50%	100%	91%	100%
North Dakota Port 4	68%	72%	8%	59%
North Dakota Port 14	48%	100%	28%	50%

Unfortunately, solubility information on Ca-Sb and Fe-Sb complexes is not readily available. Therefore, it is not possible to correlate these results to those coals where surface reaction is the controlling vapor-to-particle surface antimony partitioning mechanism.

Earlier results were presented implying that non-reactive partitioning of vapor-phase antimony onto particle surfaces controlled the partitioning of antimony during the combustion of Ohio coal combustion. The Ohio fly ash solubility results imply that if this vapor-phase oxy-anion is Sb_2O_3 as postulated, Sb_2O_3 is not the ultimate form of occurrence on fly ash surfaces for these coals. If Sb_2O_3 is the dominant vapor-phase oxy-anion, these results, coupled with the substantial fraction of antimony still in the vapor-phase at Port 14 suggest that only Sb_2O_3 that transforms to another form (most likely oxidized to Sb_2O_5) will remain on the particle surface. Sb_2O_3 not transforming to another form on the particle surface will exit in the vapor phase.

The pH 4.9 leachability data helps assess the potential for antimony contained in submicron and supermicron particles to migrate into the water supply after ground deposition downwind of the combustor. In every case examined, antimony is soluble and antimony present on fly ash surfaces is expected to leach out of ash particles exposed to aqueous environments (e.g., rainfall).

The pH 2.8 leachability data helps assess how antimony might leach from an ash disposal pile/landfill. As water migrates through the ash pile it can become much more acidic than the original water source. For all of the coals studied, antimony was very soluble and is likely to leach from the fly ash.

Temporal Resolution of Antimony Partitioning Processes

The analysis above has shown that antimony partitioning to fly ash surfaces may be dominated by surface reaction with calcium, iron, and/or aluminum active sites. Further insight can be gained into antimony partitioning mechanisms by examining size-segregated samples from Port 4 and comparing these results to those obtained from Port 14.

Insight into the timing of antimony volatilization can be gained by comparing the mass fraction of antimony still in the vapor phase at the combustion zone sampling location (Port 4) for the baseline screening experiments to the mass fraction of antimony still in the vapor phase at the post-combustion zone sampling location (Port 14). The mass fraction of antimony still in the vapor phase at both sampling locations for the six study coals is summarized in Table 3-102. The mass fraction of vapor-phase antimony is lower in the combustion zone sample for all of the study coals except the Illinois and Kentucky coals. This indicates that significant antimony volatilization appears to continue after Port 4 for four of the study coals.

The timing of partitioning from the vapor phase back to particle surfaces can be evaluated by comparing the enrichment factors of the submicron particles. Calculating a differential enrichment factor by subtracting the combustion zone enrichment factor from the post-combustion zone enrichment factor provides insight into when partitioning is occurring. Antimony enrichment factors at Ports 4 and 14 along with differential enrichment factors are shown in Table 3-103 for all six study coals.

A positive antimony differential enrichment factor is found for Illinois and Ohio submicron particles. This suggests that volatilized antimony continue to partition to submicron particle surfaces after Port 4. By contrast the negative differential enrichment factors shown for the Pittsburgh, Kentucky, Wyodak, and North Dakota submicron particles suggest that the majority of the antimony associated with submicron particles for these coals is present prior to Port 4.

Further insight into the timing of vapor-to-solid phase partitioning can be obtained using particle size dependence models based on transport theory. The particle size dependence of antimony associated with supermicron fly ash particles for the six study coals at the Port 4 sampling location is shown in Figure 3-146. The results show that only the Illinois antimony distribution follows a near $1/D_p$ dependence. This indicates that for the Illinois coal, the rate of partitioning of volatile antimony to supermicron particles is dominated by exterior surface reaction and that a significant portion of this process occurs prior to Port 4 for this coal. The other antimony distributions do not follow any dependence implying that partitioning may be occurring later for the Pittsburgh, Wyodak, and Kentucky coals since particle size dependence is observed at Port 14 for these coals. The results also suggest that the partitioning of antimony for the Ohio and North Dakota coals is not a transport-controlled since no $1/D_p$ dependence is observed at either Port 4 or Port 14 for these coals.

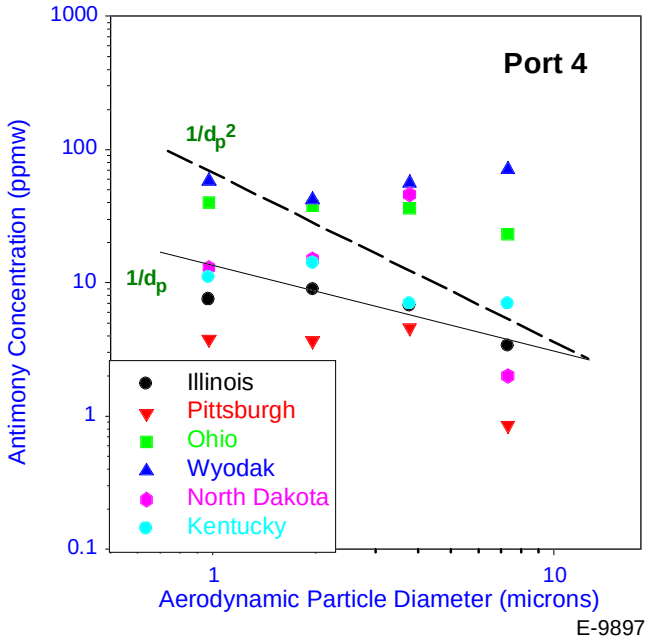

Figure 3-154. Particle size dependence of antimony in supermicron fly ash particles for all six study coals sampled at Port 4.

The size-segregated concentration of antimony in submicron particles is shown in Figure 3-155 for the six study coals at the Port 4 sampling location. There appears to be a $1/D_p$ dependence for the Illinois and Kentucky coals. These results imply that the rate of partitioning of antimony to the particle is transport process-controlled for the Illinois and Kentucky coals. No particle size dependence is apparent for the Pittsburgh, Ohio, or Wyodak coals. For North Dakota, a steep ($>1/D_p$) particle size dependence is shown. It is unclear if this apparent particle size dependence has any significance.

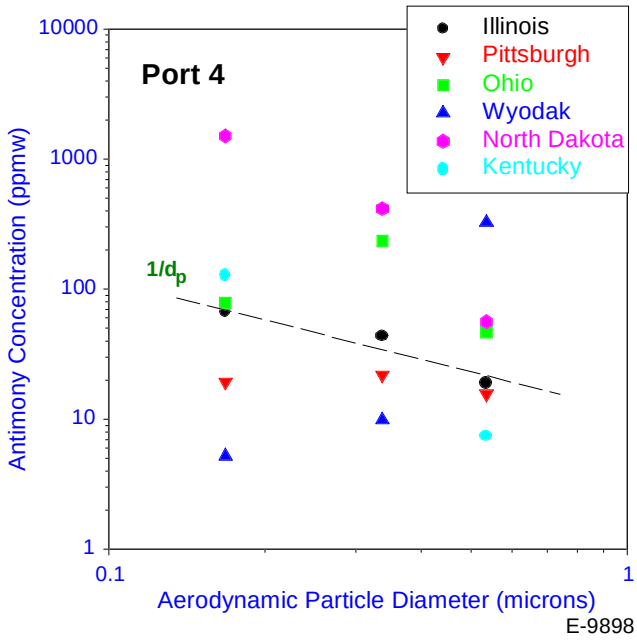

Figure 3-155. Particle size dependence of antimony in submicron fly ash particles for all six study coals sampled at Port 4.

Timing issues and any differences in Sb-Fe, Sb-Ca, or Sb-Al reactions as a dominant partitioning mechanism between Ports 4 and 14 can be evaluated by comparing the total ash size distribution and the size distributions of iron, calcium, aluminum, and antimony. The differential mass concentration distributions of antimony, calcium, iron, and the total ash from full impactor sets for all six coals under baseline combustion conditions at the Port 4 sampling location are shown in Figure 3-156. The corresponding correlations of antimony to calcium, iron, and aluminum using both evaluation methods for both submicron and supermicron fly ash sampled at Port 4 is shown in Table 3-109 for all six study coals.

Antimony in the Illinois fly ash appears to correlate only with iron in all three particle regions at Port 4 while at Port 14 it correlates with both calcium and iron. It is not clear why this situation exists. The most plausible explanations (calcium volatilization after Port 4, antimony reactivity greater with iron than calcium) are contradicted by other experimental results. The Pittsburgh, Kentucky, and North Dakota correlation results are similar at both sampling locations, suggesting that a similar partitioning mechanism is controlling at both locations.

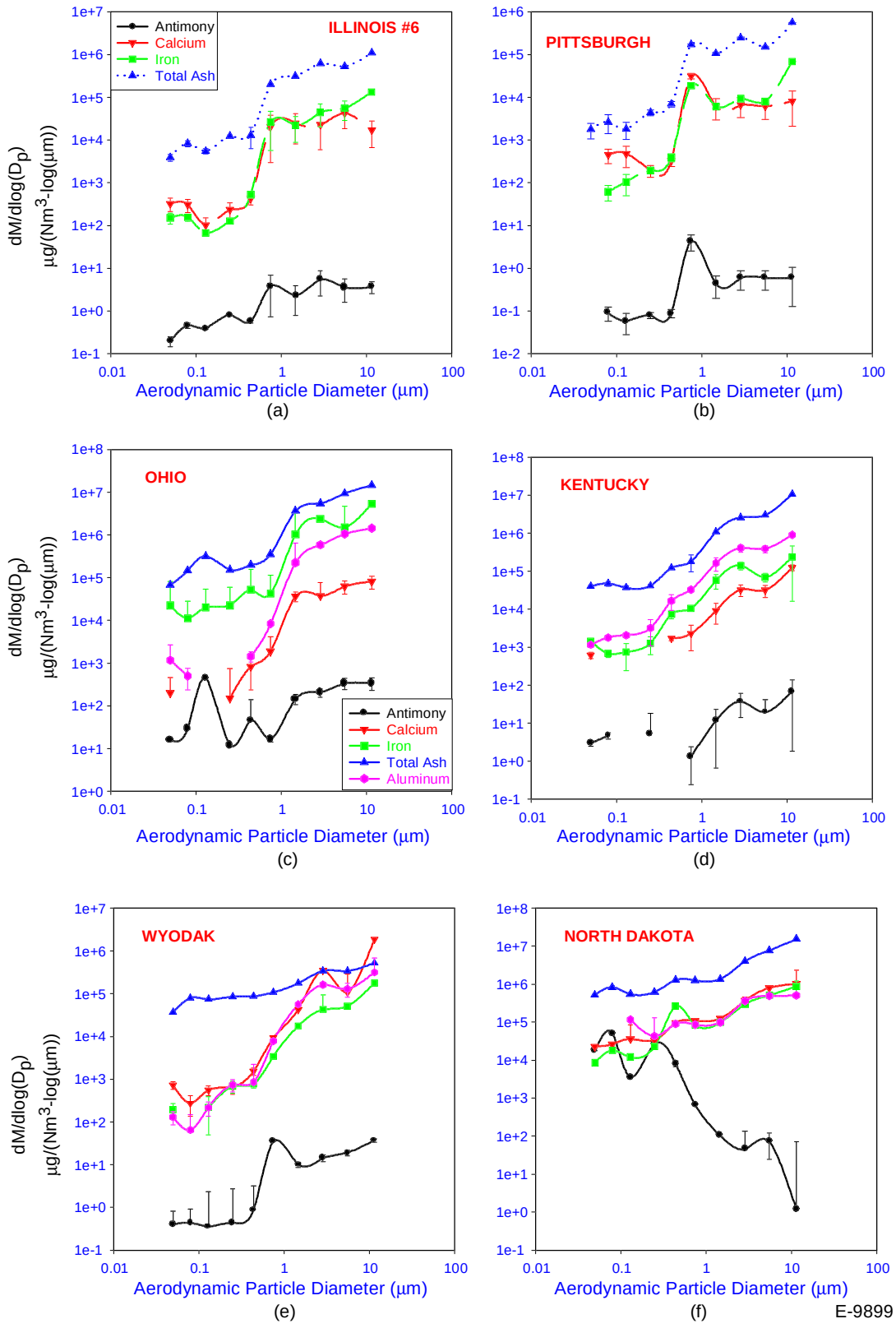

Figure 3-156. Differential mass distributions of antimony, calcium, iron, aluminum, and total ash for the six study coals sampled at Port 4.

Table 3-109. Correlation Coefficients for Antimony vs. Calcium, Iron, and Aluminum in Fly Ash Particles from the Six Study Coals Sampled at Port 4

Coal		Submicron Correlations			Supermicron Correlations		
		Absolute Concentrations	Differential Distributions	Overall Absolute Concentrations	Overall Differential Distributions	Fragmentation Region Differential Distributions	Bulk Fly Ash Region Differential Distributions
Illinois:	Sb vs. Ca	~0	~0	0.47	~0	~0	~0
	Sb vs. Fe	~0	~0	0.09	0.34	0.82	~0
	Sb vs. Al	na[1]	na	na	na	na	na
Pittsburgh:	Sb vs. Ca	0.84	~0	0.89	1.0	1.0	~0
	Sb vs. Fe	0.67	~0	~0	0.94	0.97	~0
	Sb vs. Al	na	na	na	na	na	na
Ohio:	Sb vs. Ca	~0	0.98	~0	0.95	0.95	0.96
	Sb vs. Fe	~0	0.95	~0	0.92	0.92	0.45
	Sb vs. Al	nd[2]	nd	~0	0.95	0.90	0.95
Kentucky:	Sb vs. Ca	nd	nd	~0	0.69	0.99	0.51
	Sb vs. Fe	nd	nd	0.20	0.97	0.99	0.96
	Sb vs. Al	nd	nd	0.08	0.75	0.99	0.54
Wyodak:	Sb vs. Ca	0.95	1.0	~0	~0	~0	1.0
	Sb vs. Fe	0.25	~0	~0	~0	~0	0.97
	Sb vs. Al	0.23	~0	~0	~0	~0	0.69
N. Dakota:	Sb vs. Ca	~0	~0	0.16	~0	~0	~0
	Sb vs. Fe	~0	~0	~0	~0	~0	~0
	Sb vs. Al	~0	~0	~0	~0	~0	~0

1. Aluminum analyses not available for Illinois and Pittsburgh fly ash
2. Antimony concentrations below detection limit

Similar to arsenic and selenium, antimony in the Ohio coal appears to correlate with calcium and iron at Port 4 but not at Port 14. Antimony in the Wyodak fragmentation region does not appear to correlate with any of the major species at Port 4 but does at Port 14. This is similar to arsenic and selenium. Fragmentation of Wyodak fly ash appears to occur after the Port 4 sampling location.

Summary of Antimony Partitioning

A comprehensive study has been performed to investigate the partitioning of antimony during pulverized coal combustion. Figure 3-157 and Table 3-110 summarize the primary partitioning mechanisms for antimony during the combustion of the six coals investigated as predicted by this study.

The partitioning of antimony is influenced by the extent of antimony volatilization during combustion. The most common form of occurrence of antimony for all six coals is attributed to organically associated antimony. Significant pyrite/sulfide and mono-sulfide fractions are also present in all coals. All of the coals have higher silicate-associated fractions than arsenic or selenium. The form of occurrence does not appear to affect the degree of volatilization. In order to achieve the antimony mass fractions collected for the Ohio and North Dakota coals in vapor phase impactor stages (at Port 14), antimony from silicate fractions must be vaporized.

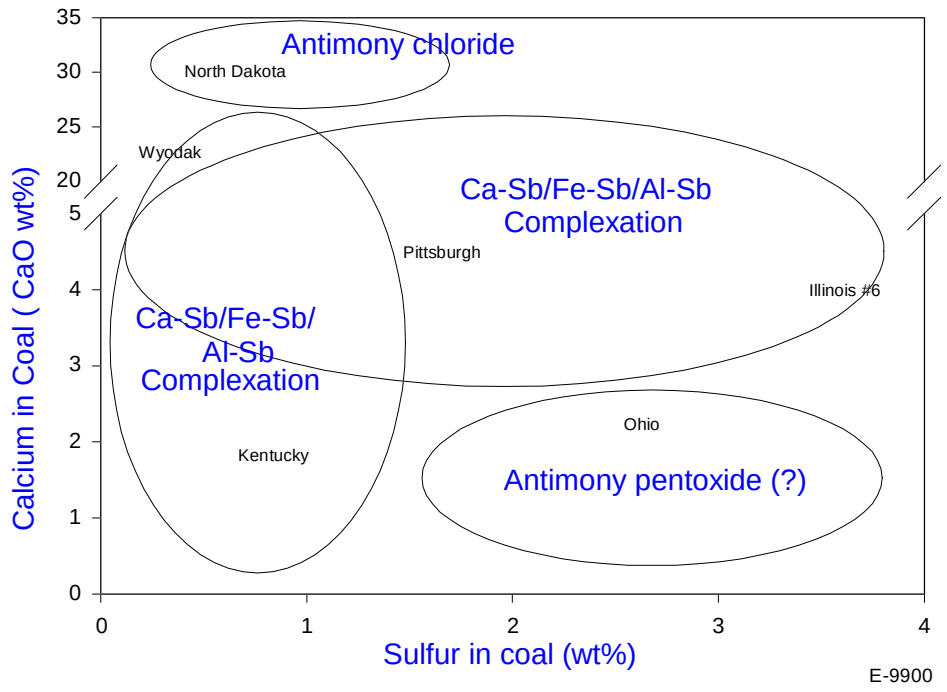

Figure 3-157. Summary of antimony partitioning mechanisms.

Table 3-110. Primary Partitioning Mechanisms for Antimony during the Combustion of the Six Study Coals

Coal	Submicron Region	Supermicron Region
Pittsburgh	Partitioning occurs and is essentially completed in the combustion zone (<2.2 residence seconds from the burner). Reaction with active calcium surface sites forms Ca-Sb compounds. Sulfur does not appear to inhibit reaction of antimony with active iron surface sites so Fe-Sb compounds are also formed	Partitioning to fly ash surfaces occurs in the combustion zone. Reaction with active calcium surface sites forms Ca-Sb compounds. Sulfur does not appear to inhibit reaction of antimony with active iron surface sites so Fe-Sb compounds are also formed
Illinois	Partitioning begins in the combustion zone and continues in the post-combustion zone (>2.2 res. sec.). Reaction with active calcium surface sites forms Ca-Sb compounds. Sulfur does not appear to inhibit reaction of antimony with active iron surface sites so Fe-Sb compounds are also formed	Partitioning to fly ash surfaces begins in the combustion zone. Reaction with active calcium surface sites form Ca-Sb compounds. Reaction with active calcium surface sites forms Ca-Sb compounds. Sulfur does not appear to inhibit reaction of antimony with active iron surface sites so Fe-Sb compounds are also formed
Ohio	Partitioning begins in the combustion zone and continues in the post-combustion zone (>3.2 res. sec.). High sulfur/low calcium content results in a lack of available active surface sites, antimony partitions to particle surfaces by means unrelated to surface reaction.	Partitioning begins in the combustion zone. High sulfur/low calcium content results in a lack of available active surface sites. Some antimony partitions to particle surfaces by means unrelated to surface reaction but most antimony leaves in the vapor phase.
Kentucky	Partitioning occurs and is essentially completed in the combustion zone (<2.9 res. sec.). Reaction with active iron and calcium surface sites forms Fe-Sb and Ca-Sb compounds.	Partitioning to fly ash surfaces occurs in the combustion zone. Reaction with active iron and calcium surface sites Fe-Sb and Ca-Sb compounds.
Wyodak	Partitioning occurs and is essentially completed in the combustion zone (<6.6 res. sec.). Reaction with active iron and calcium surface sites forms Fe-Sb and Ca-Sb compounds	Partitioning to fly ash surfaces occurs in the combustion zone. Reaction with active iron and calcium surface sites forms Fe-Sb and Ca-Sb compounds
North Dakota	Partitioning occurs in the combustion zone (<9.3 res. sec.). Some antimony partitions onto particle surfaces but most antimony leaves in the vapor phase as antimony chloride.	Partitioning begins in the combustion zone. Some antimony partitions onto particle surfaces but most antimony leaves in the vapor phase as antimony chloride.

Volatilized antimony will heterogeneously transform to both submicron and supermicron particles primarily by reaction if present as an oxide or oxy-anion. Reaction as an oxide will be with aluminum surface sites while reaction as an oxy-anion will be with calcium and/or iron if these sites are available. When these sites are not available very little antimony will partition to fly ash surfaces and most of the antimony will leave in the vapor phase. If volatilized antimony is in a chloride form very little antimony will partition to fly ash surfaces and most of the antimony will leave in the vapor phase.

The partitioning of antimony to fly ash surfaces is dependent on the availability of active cation sites. Since sulfur does not appear to inhibit the reactivity of antimony with iron surface sites, antimony is expected to react with both iron and calcium surface sites under all conditions where sufficient sites are available (in this study, all coals except the Ohio coal). These complexes are fairly soluble at moderate pH and antimony in these forms is expected to leach into groundwater. If the Sb/Ca ratio is relatively high and the sulfur content is moderate to high, cationic surface sites will not be available for antimony partitioning. In these cases, most of the antimony is expected to exit the furnace in the vapor phase.

Cobalt

Cobalt Volatility

The volatility of cobalt can be indirectly evaluated by calculating the enrichment of cobalt onto submicron particles. If a significant portion of the cobalt present in the feed coal is volatilized during combustion, there will be an enrichment of cobalt onto submicron particles due to homogeneous nucleation or heterogeneous transformation of vapor-phase cobalt.

Cobalt enrichment factors for fly ash particles from the baseline screening experiments sampled at the Port 14 (post-combustion zone) sampling location are given in Table 3-111. The Pittsburgh, Illinois, and Ohio coals show enrichment (values greater than 1.0) of cobalt on all submicron stages for the Port 14 sampling location. The Port 14 Kentucky, Wyodak, and North Dakota samples are less conclusive since at least one enrichment value is less than 1.0. These results imply that significant volatilization of cobalt occurs during combustion of all six study coals.

The enrichment of cobalt in submicron particles is reported in some previous studies [8, 17, 34, 65, 71, 95, 144, 161] but not in others [72, 78, 79, 92, 93, 163].

Vapor-to-Particle Surface Cobalt Transport Mechanisms

Due to its low volatility, only a small fraction of the volatilized cobalt will exit the combustor in the vapor phase. In this study the average mass fraction of cobalt still in the vapor phase at the post-combustion zone sampling location (Port 14) for the baseline screening experiments was 2.1 wt% with values ranging from 0.7 wt% to 6.4 wt% (see Table 3-111). The average mass fraction of cobalt still in the vapor phase at the baghouse inlet sampling port for the baseline screening experiments was 3.6 wt%. It should be noted that a portion of the bulk fly ash particles has been removed from the flue gas prior to this sample.

Table 3-111. Cobalt Enrichment Factors for Submicron-Sized Fly Ash Samples

Coal/Location		Aerodynamic Particle Diameter (μm)			
		0.17	**0.34**	**0.54**	**Average**
Pittsburgh	Port 14	1.9	2.6	1.6	2.0
	Port 4	1.7	4.2	2.0	2.6
	Differential	0.2	-1.7	-0.4	-0.6
Illinois	Port 14	1.9	2.2	1.1	1.7
	Port 4	0.003	0.009	0.04	0.02
	Differential	1.9	2.2	1.1	1.7
Kentucky	Port 14	0.2	3.7	1.1	1.7
	Port 4	5.2	3.6	1.8	3.5
	Differential	-5.0	0.2	-0.7	-1.8
Ohio	Port 14	1.1	2.8	2.1	2.0
	Port 4	2.1	3.0	3.5	2.9
	Differential	-1.0	-0.2	-1.4	-0.9
Wyodak	Port 14	2.5	1.3	0.9	1.6
	Port 4	0.02	0.04	0.2	0.07
	Differential	2.5	1.3	0.8	1.5
North Dakota	Port 14	0.81	2.9	1.15	1.6
	Port 4	0.63	0.95	1.18	0.9
	Differential	0.18	1.9	-0.02	0.7

Due to its low volatility, a volatilized cobalt molecule may reach nucleation conditions as it migrates away from burning carbon molecules into the bulk combustion gas. However since the concentration of cobalt is low compared to the major species in the coal, there is also a high probability that a volatilized cobalt molecule will contact submicron or supermicron particles prior to reaching the supersaturated conditions necessary for nucleation. Thus depending on the combustion conditions, volatilized cobalt may homogeneously nucleate into submicron particles or heterogeneously partition onto the surfaces of both submicron and supermicron particles [30].

If homogeneous nucleation is a significant partitioning mechanism for cobalt, there should be a substantial mass fraction of cobalt in the submicron particles at the Port 4 sampling location and then a decrease in value at Port 14 (due to agglomeration/coagulation of small particles). A substantial submicron mass fraction were found for the Pittsburgh coal at Port 4 (31 wt%) with a decrease to 13 wt% at Port 14. By contrast, the Wyodak coal has 16 wt% submicron cobalt at Port 14 but only 1.0 wt% at Port 4. Thus, homogeneous nucleation appears to be an important vapor-to-solid phase partitioning mechanism for cobalt in the Pittsburgh coal but not for cobalt in the Wyodak coal. The submicron mass fractions observed for the Pittsburgh and Wyodak coals are consistent with values reported by Quann [65] for combustion of a Montana lignite in a laboratory combustor system (17 wt%).

If heterogeneous vapor-to-solid phase partitioning is the dominant vapor to solid phase partitioning mechanism, supermicron particles should contain a much higher absolute mass fraction of cobalt than the submicron particles. In the current work, the average cobalt mass fraction in the supermicron particles for the six study coals was 90 wt% (see Table 3-112 for individual values).

Table 3-112. Mass Fraction of Cobalt in Vapor, Submicron, and Supermicron Regimes at Three Combustor Sample Locations

Coal/Location	Average Sampling Temperature (K)	Vapor Regime (Wt%)	Submicron Regime (Wt%)	Supermicron Regime (Wt%)
Pittsburgh				
Port 4	1440	0.6	31	68
Port 14	1140	2.8	13	84
Baghouse Inlet	470	3.8	9.3	87
Illinois				
Port 4	1410	nd[1]	0.1	99.9
Port 14	1130	2.4	5.8	92
Baghouse Inlet	220	7.5	9.6	83
Ohio				
Port 4	1330	0.6	4.7	95
Port 14	1040	0.3	0.5	99
Baghouse Inlet	610	8.8	29	62
Kentucky				
Port 4	1490	1.2	4.4	94
Port 14	1150	0.2	1.4	98
Baghouse Inlet	490	nd	13	87
Wyodak				
Port 4	1080	0.1	1.0	99
Port 14	760	6.4	16	78
Baghouse Inlet	210	0.6	3.4	96
North Dakota				
Port 4	1250	3.0	7.0	90
Port 14	870	0.7	9.4	90
Baghouse Inlet	400	0.8	4.4	95
Average All Coals				
Port 4		0.9	8.1	91
Port 14		2.1	7.6	90
Baghouse Inlet		3.6	11	85

1. nd = concentration on all vapor-phase impactor stages is below the analytical detection limit

Unlike the three previous trace elements studied, cobalt is not expected to form oxy-anions in the combustion flue gas (see Section 3.3.1). Therefore, cobalt is expected to form simple vapor-phase oxides during the combustion process. Cobalt in these forms will most readily act as a cation in reactions with active surface sites.

The controlling transport mechanisms for the partitioning of vapor-phase cobalt to the surfaces of fly ash particles can be investigated using a particle size dependence analysis. The particle size dependence of cobalt associated with supermicron fly ash particles for the six study coals at the Port 14 sampling location is shown in Figure 3-158. The Pittsburgh[11], Wyodak, and Kentucky distributions resemble a $1/D_p$ dependence indicating that volatile cobalt partitioning to supermicron particles in the post-combustion zone is controlled by exterior surface reaction. No particle size dependence is apparent for the Illinois, Ohio, and North Dakota distributions. Thus partitioning of cobalt for these coals does not appear to be controlled by a transport mechanism.

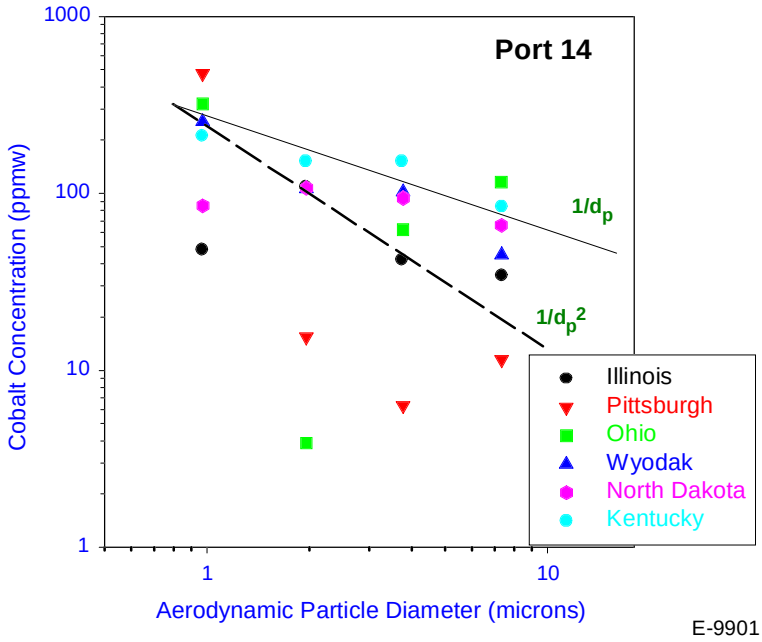

Figure 3-158. Particle size dependence of cobalt in supermicron fly ash particles for all six study coals sampled at Port 14.

The size-segregated concentration of cobalt in submicron particles from the current study is shown in Figure 3-159 for the six study coals at the Port 14 sampling location. A particle size dependence is indicated for the Kentucky and Wyodak coals. Surface reaction or gas film transfer most likely controls cobalt partitioning for these coals. No particle size dependence is apparent for the other coals studied.

[11] Excluding the 1 μm data point

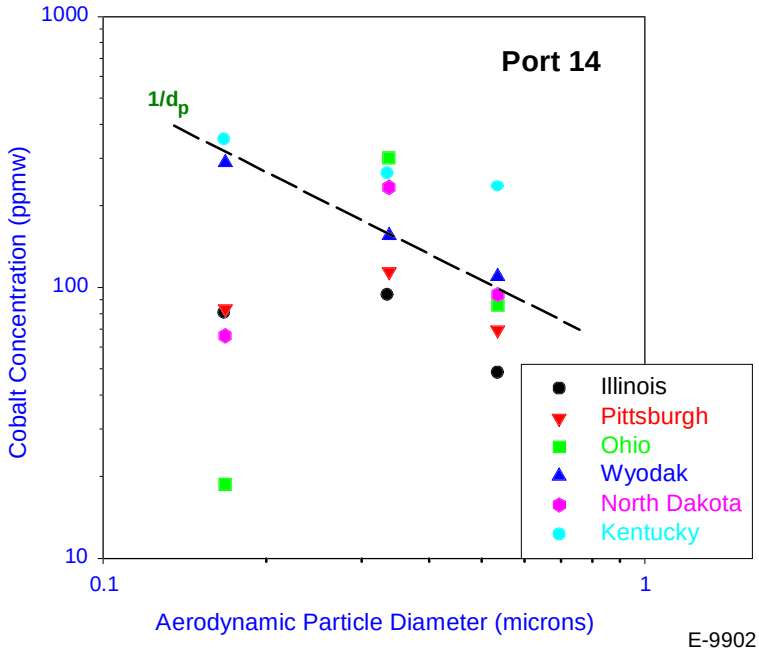

Figure 3-159. Particle size dependence of cobalt in submicron fly ash particles for all six study coals sampled at Port 14.

Fly Ash Surface Cobalt Reaction Mechanisms

The particle size dependence analysis indicates that cobalt partitioning for the Pittsburgh[12], Wyodak, and Kentucky coals is controlled by surface reaction. Cobalt is expected to be present in a cationic form, such as CoO. The most prevalent oxy-anion surface sites in the Al-Si fly ash surface matrix will be aluminum-based. To evaluate if cobalt is reactive with anionic surface sites (e.g., Al-oxyanions) as opposed to cationic surface sites (e.g., Ca, Fe), the total ash size distribution and the size distributions of iron, calcium, aluminum, and cobalt can be compared. The differential mass concentration distributions of these species from full impactor sets for the Pittsburgh, Kentucky, and Wyodak coals (the only three coals where surface reaction is expected) under baseline combustion conditions at the Port 14 sampling location are shown in Figure 3-160. Cross-correlation coefficients are shown in Table 3-113.

Cobalt in Pittsburgh fly ash appears to correlate with calcium and iron in the fragmentation region but not the bulk fly ash region (submicron cobalt is expected to be controlled by homogeneous nucleation). The Pittsburgh calcium and iron distributions are too similar to discern if cobalt reacts with one or both of these cations. It should be noted that aluminum concentration data are not available from the Pittsburgh baseline experiments performed during the Phase I testing period.

[12] Supermicron only; submicron partitioning is controlled by homogeneous nucleation.

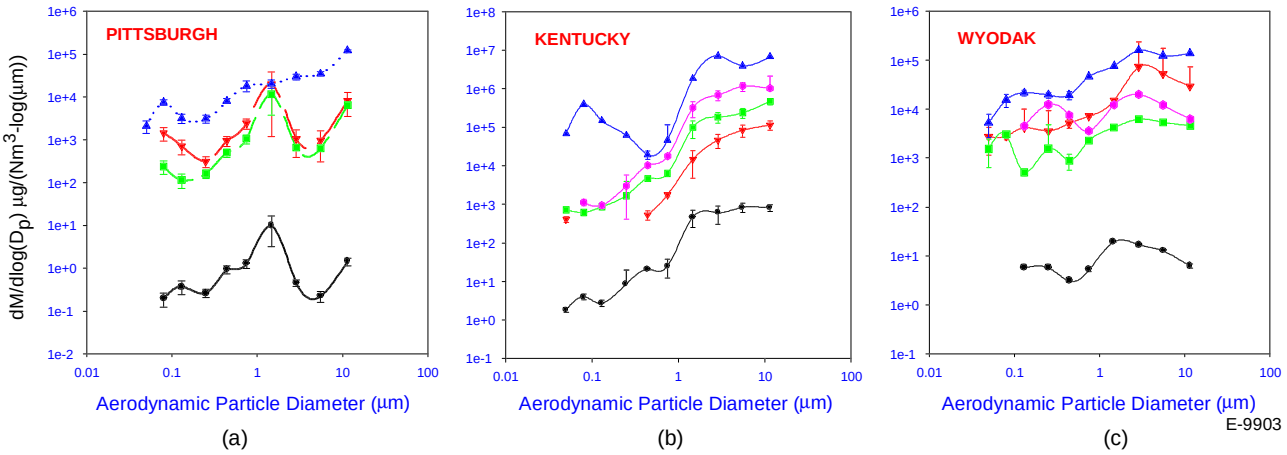

Figure 3-160. Differential mass distributions of cobalt, calcium, iron, aluminum,* and total ash for the Pittsburgh, Kentucky, and Wyodak coals sampled at Port 14

*Aluminum distribution data is not available for the Pittsburgh coal.

The Kentucky fly ash cobalt correlates with calcium, iron, and aluminum in both supermicron particle regions. Submicron Kentucky cobalt correlates with iron and less strongly with aluminum. It is not possible to discern which major specie cobalt is reactive with from these data.

The Wyodak cobalt correlates with calcium in the submicron and bulk fly ash regions but only weakly in the fragmentation region. Cobalt correlates more strongly with iron and aluminum in the fragmentation region than with calcium. The bulk fly ash cobalt appears to correlate strongly with all three major species.

From these results it appears that vapor-phase cobalt does partition to fly ash surfaces by surface reaction for these three coals. However, the results do not provide sufficient information to distinguish the actual controlling surface reactions.

In Phase IIb, three sets of experiments were performed with the Pittsburgh seam coal that can be used to gain insight into cobalt partitioning during coal combustion. First, an additional sample was collected at Port 14 under baseline combustion conditions to provide comparable cobalt, aluminum, calcium, and iron distributions. In the second set of experiments the calcium content of the feedstock was increased by 50 mol% by pulverized lime addition. In the third set of experiments the iron content of the feedstock was increased by the same molar amount as in the calcium tests (this is a much smaller % increase since there is more iron in the Pittsburgh coal than calcium). The results are summarized in Figure 3-161.

Table 3-113. Correlation Coefficients for Cobalt Versus Calcium, Iron, and Aluminum in Fly Ash Particles from the Pittsburgh, Kentucky, and Wyodak Study Coals Sampled at Port 14

Coal		Submicron Correlations			Supermicron Correlations		
		Absolute Concentrations	**Differential Distributions**	**Overall Absolute Concentrations**	**Overall Differential Distributions**	**Fragmentation Region Differential Distributions**	**Bulk Fly Ash Region Differential Distributions**
Pittsburgh:	Co vs. Ca	~0	0.99	1.0	0.81	1.0	~0
	Co vs. Fe	~0	0.98	1.0	1.0	1.0	~0
	Co vs. Al	na[1]	na	na	na	na	na
Kentucky:	Co vs. Ca	nd[2]	nd	~0	0.78	0.75	0.94
	Co vs. Fe	0.75	0.93	0.20	0.96	0.94	0.71
	Co vs. Al	0.74	0.50	0.03	0.87	0.90	1.0
Wyodak:	Co vs. Ca	~0	0.99	~0	~0	0.28	1.0
	Co vs. Fe	~0	~0	0.58	0.29	0.72	0.99
	Co vs. Al	~0	~0	0.91	0.58	0.77	0.98

1. Aluminum concentrations not available for Pittsburgh fly ash samples
2. Calcium concentrations below detection limit

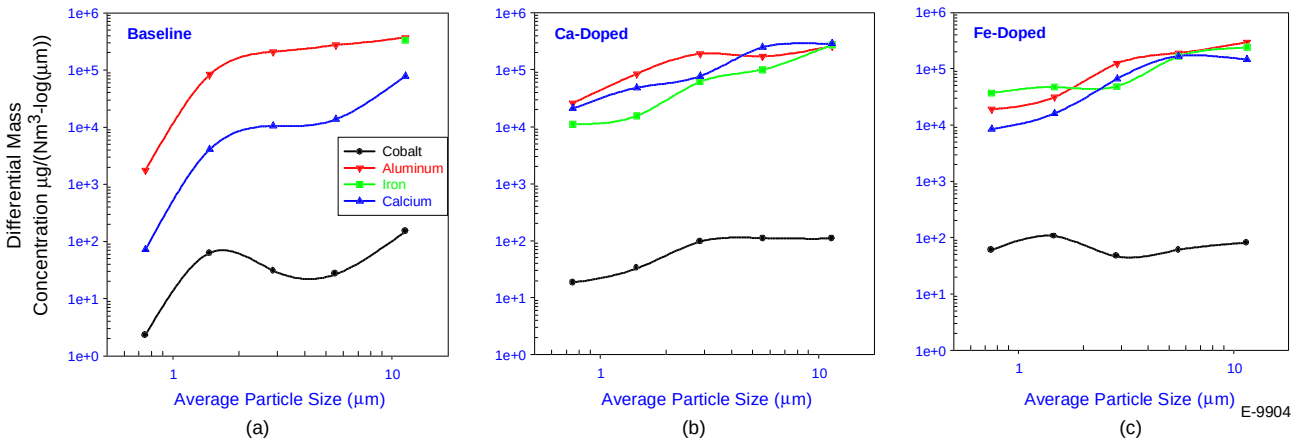

Figure 3-161. Differential mass distributions of cobalt, aluminum, iron, and calcium for the Pittsburgh baseline, Ca-doped, and Fe-doped experiments supermicron region sampled at Port 14.

In all three cases, the cobalt distribution most closely follows the iron distribution (in the baseline case the calcium and iron distributions have the same shape – see Figure 3-160a). In addition, there was no significant increase in cobalt recovery in any of the three cases. These results suggest that vapor-phase cobalt reacts with active iron surface sites in preference to aluminum sites in the combustion of the Pittsburgh coal. It also suggests that sufficient iron is present in the native coal to generate all of the active cation surface sites necessary to accommodate all of the cobalt that will partition by this mechanism (i.e., the addition of iron or calcium did not improve cobalt recovery in fly ash particles).

In the analysis of As, Se, and Sb partitioning, it was shown that sulfur can be a key parameter affecting partitioning. Could the present of increased sulfur in the combustion environment inhibit the reaction of cobalt with surface-active aluminum, iron, and calcium sites? To examine the effect of sulfation on cobalt partitioning, the main combustion air was doped with SO_2 during the combustion of the Kentucky coal. A comparison of the differential distributions at baseline and SO_2-doped conditions is shown in Figure 3-162. The addition of SO_2 decreases the overall recovery of cobalt. Furthermore the cobalt differential distribution curve from the SO_2-doped experiment most closely resembles the aluminum distribution curve compared to the iron or calcium curves. These results suggest that:

1) Sulfur species reduce the availability of active anion surface sites,

2) A significant portion of the vapor-to-solid phase cobalt partitioning is controlled by reaction with aluminum, and

3) Cobalt partitioning associated with aluminum surface sites is not affected by the sulfur content of the combustion environment.

The conclusion that cobalt partitioning to fly ash surfaces is not affected by sulfur content is reinforced by the Wyodak baseline experimental partitioning results shown in Figure 3-160.

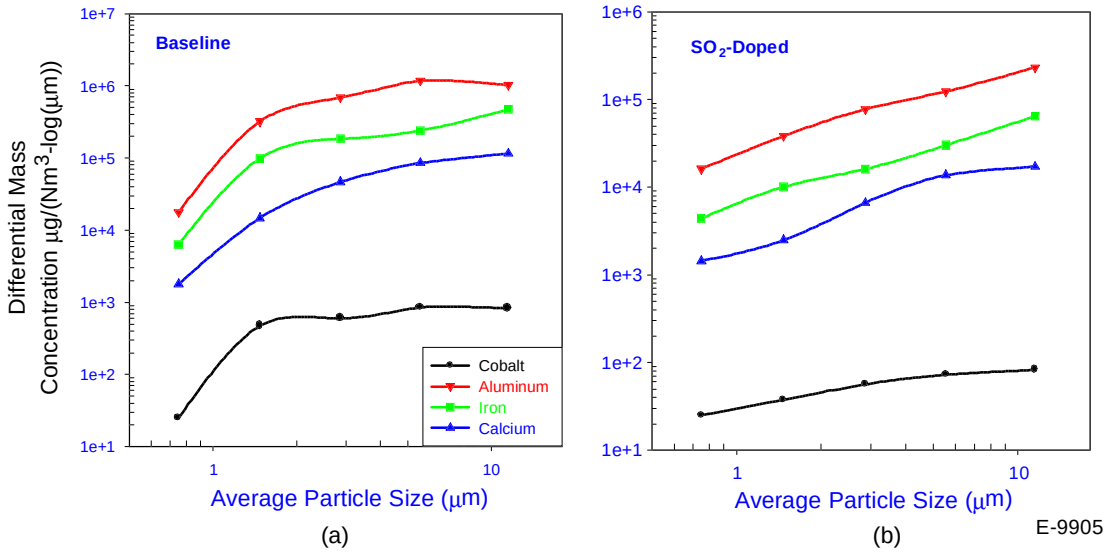

Figure 3-162. Differential mass distributions of cobalt, aluminum, iron, and calcium for the Kentucky baseline and SO_2-doped experiments supermicron region sampled at Port 14.

The Wyodak cobalt fragmentation distribution follows the iron and aluminum distributions more closely than the calcium or total ash distributions, but are too similar to distinguish between them. However, the mass fraction of cobalt in the submicron region is similar at 16 wt% to the Pittsburgh distribution (13 wt% Co in the submicron region) rather than to the Kentucky distribution (1.4 wt% Co in the submicron region). The Wyodak coal has a low sulfur content similar to the Kentucky coal. If increased sulfur affected which partitioning mechanism controls vapor-phase cobalt transformation to fly ash surfaces, the Wyodak distribution would be expected to more closely resemble the Kentucky distribution, not the Pittsburgh distribution.

Further insight into the partitioning mechanism for the Wyodak coal can be obtained by examining the results from the oxygen enrichment tests. If cobalt-iron complexation is the dominant reaction mechanism, there should be an increase in cobalt recovery at higher combustion temperatures due to the increase in active iron sites formed at the higher combustion temperatures (see Figure 3-120). This increase will be most notable in the submicron fly ash samples. By contrast, aluminum surface sites are not increased at higher combustion temperatures (Figure 3-120). Therefore if cobalt-aluminum complexation is the dominant reaction mechanism, there should be little increase in cobalt recovery at higher combustion temperatures.

To determine the impact of combustion temperature on the partitioning mechanisms for cobalt recovery, the differential mass fraction distributions of cobalt during Wyodak combustion at 1520 and 1580 K are compared in Figure 3-163. The results show an increase in the mass fraction of cobalt in the submicron region at the higher combustion temperature. This result is consistent with the Co-Fe complexation mechanism for the Wyodak and Pittsburgh coals proposed above.

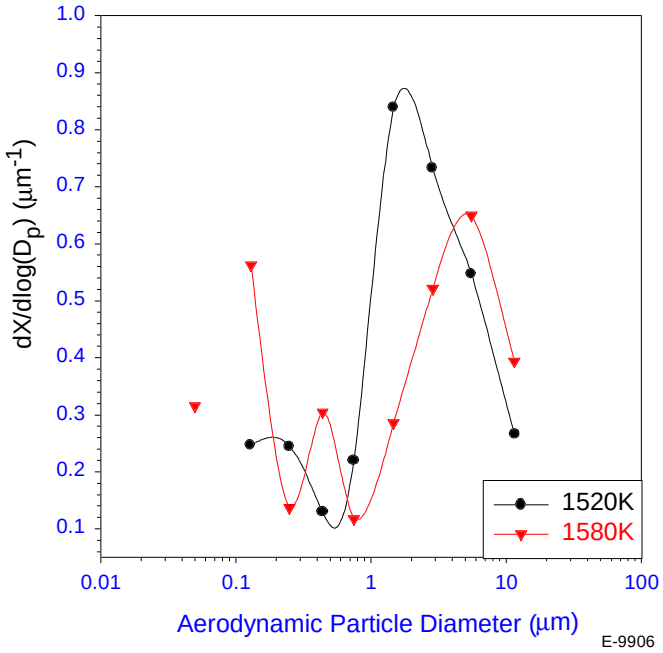

Figure 3-163. Differential mass fraction distributions of cobalt for the Wyodak coal at two combustion temperatures sampled at Port 14.

Environmental Impact of Cobalt from Fly Ash Surfaces

The solubility of cobalt in the TCLP 1310 fluids is shown in Table 3-114. For the Pittsburgh submicron, Ohio supermicron, Wyodak submicron and supermicron, Kentucky submicron, and North Dakota submicron and supermicron samples, cobalt is partially soluble at pH 4.9. For the Pittsburgh supermicron, Ohio submicron, and Kentucky supermicron samples, cobalt has very limited solubility at pH 4.9. At pH 2.9, cobalt is very soluble from the Ohio submicron and supermicron, Kentucky submicron, Wyodak submicron and supermicron, and North Dakota submicron and supermicron samples. For the Pittsburgh submicron and supermicron, and Kentucky supermicron samples, cobalt is partially soluble at pH 2.9. Information on the solubility Al-Co, Ca-Co, and Fe-Co complexes is not readily available.

The solubility results shown in Table 3-114 do not perfectly correlate to the partitioning information provided above. The lower solubility of the Kentucky samples is probably due to a lower solubility of Co-Al complexes. However the Pittsburgh and Wyodak solubility results are not consistent even though the previous analysis suggests that cobalt partitioning in these coals is controlled by similar Co-Fe complexation.

The Ohio and North Dakota results suggest that fly ash surface-based cobalt is fairly soluble in both leaching fluids.

The pH 4.9 leachability data helps assess the potential for cobalt contained in submicron and supermicron particles to migrate into the water supply after ground deposition downwind of the combustor. Unreacted fly ash surface-based cobalt is partially soluble and cobalt present in

Table 3-114. Summary of Cobalt Solubility in Fly Ash from Baseline Screening Experiments

Coal/Sample Location	Submicron Size % Soluble at pH 4.9	Submicron Size % Soluble at pH 2.9	Supermicron Size % Soluble at pH 4.9	Supermicron Size % Soluble at pH 2.9
Pittsburgh Port 4	52%	80%	19%	53%
Pittsburgh Port 14	25%	45%	9%	24%
Ohio Port 4	95%	100%	0%	69%
Ohio Port 14	0%	100%	37%	62%
Kentucky Port 4	20%	57%	3%	30%
Kentucky Port 14	43%	81%	5%	29%
Wyodak Port 4	0%	0%	16%	63%
Wyodak Port 14	45%	65%	60%	76%
North Dakota Port 4	44%	83%	35%	56%
North Dakota Port 14	33%	62%	42%	76%

this form on fly ash surfaces is expected to leach out of ash particles exposed to aqueous environments (e.g., rainfall). Cobalt present in Co-Al complexes and possibly in Co-Fe complexes is less soluble and less cobalt is expected to leach out of ash particles from this form.

The pH 2.8 leachability data helps assess how cobalt might leach from an ash disposal pile/landfill. As water migrates through the ash pile it can become much more acidic than the original water source. Unreacted fly ash surface-based cobalt is very soluble and should migrate out of the fly ash. Cobalt in Co-Al and possibly Co-Fe complexes is partially soluble and is expected to have an environmental impact.

Temporal Resolution of Cobalt Partitioning Processes

The analysis above has shown that cobalt partitioning to fly ash surfaces may be dominated by surface reaction with aluminum or iron active surface sites. Further insight can be gained into cobalt partitioning mechanisms by examining size-segregated samples from Port 4 and comparing these results to those obtained from Port 14.

Insight into the timing of cobalt volatilization can be gained by comparing the mass fraction of cobalt still in the vapor phase at the combustion zone sampling location (Port 4) for the baseline screening experiments to the mass fraction of cobalt still in the vapor phase at the post-combustion zone sampling location (Port 14). The mass fraction of cobalt in the vapor phase at both sampling locations for the six study coals is summarized in Table 3-112. The mass fraction of vapor-phase cobalt is lower in the combustion zone sample for the Pittsburgh, Illinois,

Wyodak, and North Dakota coals but not for the Ohio or Kentucky coals. This indicates that cobalt volatilization appears to continue after Port 4 for four of the study coals.

The timing of partitioning from the vapor phase back to particle surfaces can be evaluated by comparing the enrichment factors of the submicron particles. Calculating a differential enrichment factor by subtracting the combustion zone enrichment factor from the post-combustion zone enrichment factor provides insight into when partitioning is occurring. Cobalt enrichment factors at Ports 4 and 14 along with differential enrichment factors are shown in Table 3-111 for all six study coals.

A positive cobalt differential enrichment factor is found for Illinois, Wyodak, and North Dakota submicron particles. This suggests that volatilized cobalt continue to partition to submicron particle surfaces after Port 4. By contrast the negative differential enrichment factors shown for the Pittsburgh, Kentucky, and Ohio submicron particles suggest that the majority of the cobalt associated with submicron particles for these coals is present prior to Port 4.

Further insight into the timing of vapor-to-solid phase partitioning can be obtained using particle size dependence models based on transport theory. The particle size dependence of cobalt associated with supermicron fly ash particles for the six study coals at the Port 4 sampling location is shown in Figure 3-164. The results show that only the Kentucky and Pittsburgh cobalt distributions follow a near $1/D_p$ dependence. This indicates that for these coals, the rate of partitioning of volatile cobalt to supermicron particles is dominated by exterior surface reaction and that a significant portion of this process occurs prior to Port 4 for this coal. The other cobalt distributions do not follow any dependence. For the Wyodak coal, this suggests that partitioning may be occurring later for the Wyodak coal since particle size dependence is observed at Port 14 for this coal (Figure 3-158). This observation is consistent for all four trace elements examined.

The size-segregated concentration of cobalt in submicron particles is shown in Figure 3-165 for the six study coals at the Port 4 sampling location. There appears to be a decrease in concentration with particle size only for the Ohio coal. This is consistent with the results for arsenic and selenium, where particle size dependence is observed at Port 4 but no longer is apparent at Port 14. No particle size dependence is observed for the other coal submicron particles. These results suggest that the partitioning of vapor-phase cobalt to submicron particle surfaces for the Kentucky and Wyodak coal primarily occurs after Port 4 since particle size dependence is observed at Port 14 for these coals (Figure 3-159).

Timing issues and any differences in Co-Al or Co-Fe reactions as a dominant partitioning mechanism between Ports 4 and 14 can be evaluated by comparing the total ash size distribution and the size distributions of aluminum, iron, and cobalt. The differential mass concentration distributions of antimony, aluminum, and iron from full impactor sets for the Pittsburgh, Kentucky, and Wyodak coals under baseline combustion conditions at the Port 4 sampling location are shown in Figure 3-166. The corresponding correlations of antimony to iron and aluminum using both evaluation methods for both submicron and supermicron fly ash sampled at Port 4 is shown in Table 3-115 for the Pittsburgh, Kentucky and Wyodak coals. The results are consistent with the correlation results at Port 14.

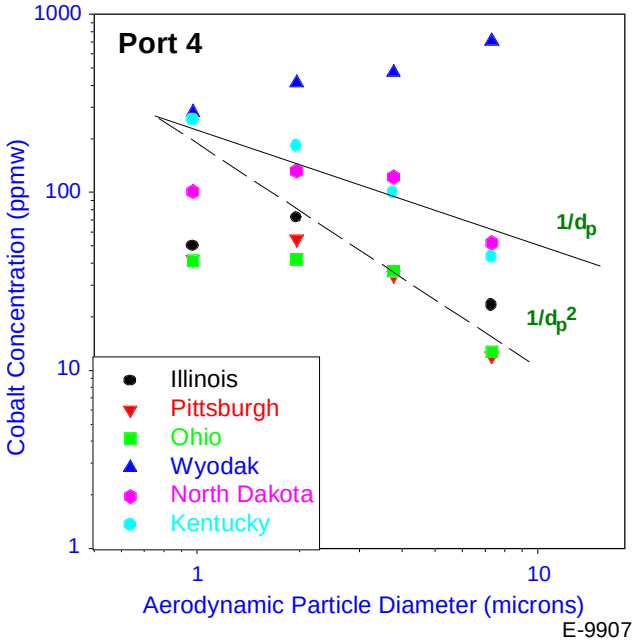

Figure 3-164. Particle size dependence of cobalt in supermicron fly ash particles for all six study coals sampled at Port 4.

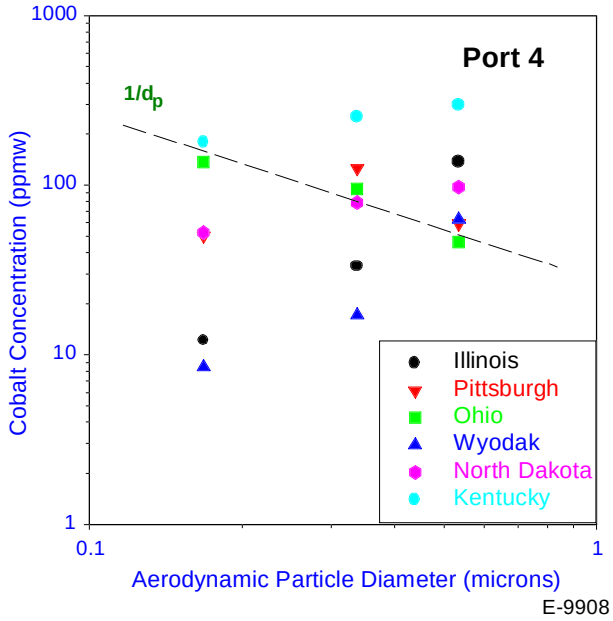

Figure 3-165. Particle size dependence of cobalt in submicron fly ash particles for all six study coals sampled at Port 4.

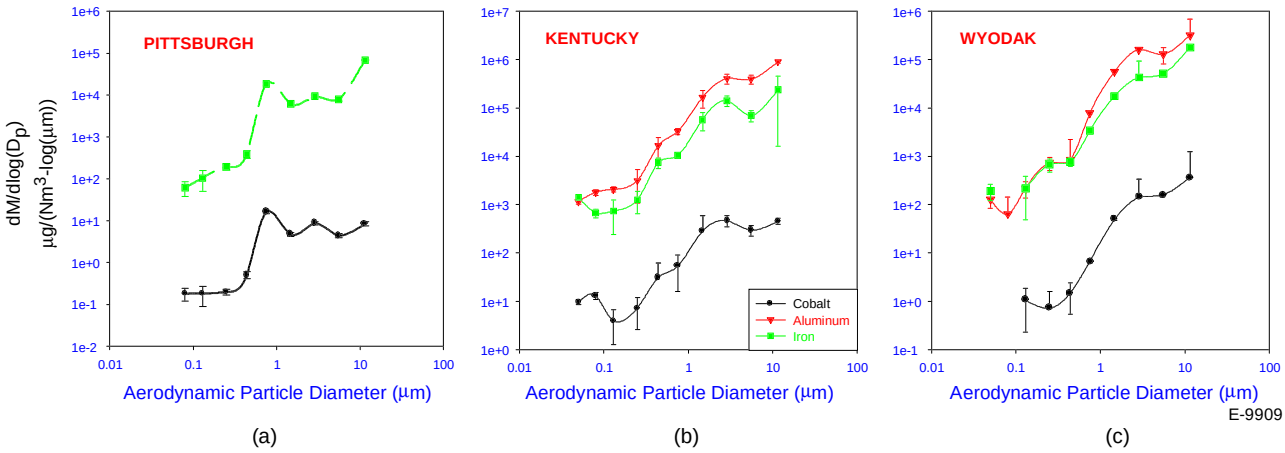

Figure 3-166. Differential mass distributions of cobalt, iron, and aluminum, for the Pittsburgh, Kentucky, and Wyodak coals sampled at Port 4.

Summary of Cobalt Partitioning

A comprehensive study has been performed to investigate the partitioning of cobalt during pulverized coal combustion. Table 3-116 summarizes the primary partitioning mechanisms for cobalt during the combustion of the six coals investigated as predicted by this study.

The partitioning of cobalt is influenced by the extent of cobalt volatilization during combustion. Enrichment of cobalt for half of the study coals suggests that significant cobalt volatilization may occur depending on the combustion conditions. Heterogeneous transformation of vapor phase cobalt to fly ash surfaces appears to be more important than homogeneous nucleation except for the Pittsburgh coal.

The partitioning for volatilized cobalt for many coals including the Illinois, Ohio, and North Dakota coals included in this study are not controlled by gas film transfer or surface reaction. Reaction with active aluminum fly ash surface sites can occur if sufficient sites are available. Reaction with active iron fly ash surface sites was also identified for two coals. This suggests that transition metals like cobalt can behave either as a cation or an oxy-anion depending on the combustion environment. Future work will be required to define a reaction pathway to explain these results.

Sulfur was shown to inhibit cobalt-iron complexation but does not appear to affect cobalt-aluminum complexation. However, this inhibition is less than for the reaction of arsenic or selenium with active iron fly ash surface sites during Kentucky coal combustion.

Table 3-115. Correlation Coefficients for Cobalt Versus Calcium, Iron, and Aluminum in Fly Ash Particles from the Pittsburgh, Kentucky, and Wyodak Study Coals Sampled at Port 4

Coal		Submicron Correlations			Supermicron Correlations		
		Absolute Concentrations	Differential Distributions	Overall Absolute Concentrations	Overall Differential Distributions	Fragmentation Region Differential Distributions	Bulk Fly Ash Region Differential Distributions
Pittsburgh:	Co vs. Ca	0.44	0.93	0.21	0.83	0.91	0.12
	Co vs. Fe	0.90	1.0	~0	0.15	~0	~0
	Co vs. Al	na[1]	na	na	na	na	na
Kentucky:	Co vs. Ca	nd[2]	nd	~0	0.51	0.86	~0
	Co vs. Fe	0.78	1.0	0.80	0.95	0.95	0.39
	Co vs. Al	0.91	1.0	0.61	0.62	0.95	~0
Wyodak:	Co vs. Ca	~0	0.99	~0	0.95	0.95	1.0
	Co vs. Fe	~0	~0	0.58	0.98	0.98	1.0
	Co vs. Al	~0	~0	0.91	0.89	1.0	0.82

1. Aluminum concentrations not available for Pittsburgh fly ash samples
2. Calcium concentrations below detection limit

Table 3-116. Primary Partitioning Mechanisms for Cobalt During the Combustion of the Six Study Coals

Coal	Submicron Region	Supermicron Region
Pittsburgh	Partitioning occurs and is essentially completed in the combustion zone (<2.2 residence seconds from the burner). Homogeneous nucleation accounts for most submicron Co. Additional submicron cobalt results from reaction of vapor-phase Co with active iron surface sites forms Fe-Co compounds.	Partitioning to fly ash surfaces occurs in the combustion zone. Reaction with active iron surface sites form Fe-Co compounds.
Illinois	Partitioning begins in the combustion zone and continues in the post-combustion zone (>2.2 res. sec.). Co partitioning onto particle surfaces is not transport controlled.	Partitioning to fly ash surfaces begins in the combustion zone. Co partitioning onto particle surfaces is not transport controlled.
Ohio	Partitioning occurs and is essentially completed in the combustion zone (<3.2 res. sec.). Co partitioning onto particle surfaces is not transport controlled.	Partitioning occurs in the combustion zone. Co partitioning onto particle surfaces is not transport controlled.
Kentucky	Partitioning occurs and is essentially completed in the combustion zone (<2.9 res. sec.). Reaction with active aluminum surface sites form Al-Co compounds and reaction with active iron surface sites form Fe-C0 compounds.	Partitioning to fly ash surfaces occurs in the combustion zone. Reaction with active aluminum surface sites form Al-Co compounds and reaction with active iron surface sites form Fe-C0 compounds.
Wyodak	Partitioning begins in the combustion zone and continues in the post-combustion zone (>6.6 res. sec.). Reaction with active iron surface sites form Fe-Co compounds.	Partitioning to fly ash surfaces begins in the combustion zone. Reaction with active iron surface sites form Fe-Co compounds.
North Dakota	Partitioning begins in the combustion zone and continues in the post-combustion zone (>9.3 res. sec.). Co partitioning onto particle surfaces is not transport controlled.	Partitioning begins in the combustion zone. Co partitioning onto particle surfaces is not transport controlled.

Radionuclides

Radionuclide Volatility

The volatility of cesium, thorium, and cerium can be indirectly evaluated by calculating the enrichment of these elements onto submicron particles. If significant portions of the radionuclides present in the feed coal are volatilized during combustion, there will be enrichment onto submicron particles due to homogeneous nucleation or heterogeneous transformation of vapor-phase material.

Cesium, thorium, and cerium enrichment factors for fly ash particles from the baseline screening experiments sampled at the Port 14 (post-combustion zone) sampling location are given in Table 3-117. The Pittsburgh, Illinois, and North Dakota coals show enrichment

Table 3-117. Cesium, Thorium, and Cerium Enrichment Factors for Submicron-Sized Fly Ash Samples

a) Cesium Enrichment Factors

Coal/Location		Aerodynamic Particle Diameter (µm)			
		0.17	**0.34**	**0.54**	**Average**
Pittsburgh	Port 14	1.2	1.1	1.8	1.4
	Port 4	0.2	0.4	0.3	0.3
	Differential	1.0	0.7	1.5	1.1
Illinois	Port 14	3.1	1.5	0.4	1.7
	Port 4	2.0	1.3	1.0	1.4
	Differential	1.1	0.2	-0.6	0.3
Ohio	Port 14	0.2	0.19	na[1]	0.22
	Port 4	0.3	0.17	na	0.25
	Differential	-0.1	-0.02		-0.03
Wyodak	Port 14	na	0.94	0.3	0.6
	Port 4	na	0.86	1.2	1.0
	Differential	--	0.08	-0.9	-0.4
North Dakota	Port 14	na	3.1	6.3	4.7
	Port 4	na	1.0	1.3	1.2
	Differential	--	2.1	5.0	3.5

na = data not available

b) Thorium Enrichment Factors

Coal/Location		Aerodynamic Particle Diameter (µm)			
		0.17	**0.34**	**0.54**	**Average**
Pittsburgh	Port 14	0.6	1.4	0.5	0.9
	Port 4	0.4	2.5	2.0	1.6
	Differential	0.2	-1.1	-1.5	-0.7
Illinois	Port 14	1.3	1.5	1.4	1.4
	Port 4	0.1	1.3	2.5	1.3
	Differential	1.2	0.2	-1.1	0.1
Ohio	Port 14	0.2	0.11	na[1]	0.2
	Port 4	0.4	0.16	na	0.3
	Differential	-0.2	-0.05	--	-0.1
Wyodak	Port 14	na	0.03	0.11	0.07
	Port 4	na	0.13	0.29	0.21
	Differential	--	-0.1	-0.18	-0.14
North Dakota	Port 14	na	4.0	3.06	3.5
	Port 4	na	0.3	na	0.3
	Differential	--	3.7	--	3.2

1. na = data not available

Table 3-117. (Continued) Cesium, Thorium, and Cerium Enrichment Factors for Submicron-Sized Fly Ash Samples

c) Cerium Enrichment Factors

	Aerodynamic Particle Diameter (μm)			
Coal/Location	**0.17**	**0.34**	**0.54**	**Average**
Pittsburgh Port 14	0.6	1.5	1.0	1.0
Port 4	0.9	3.1	2.8	2.3
Differential	-0.3	-1.6	-1.8	-1.3
Illinois Port 14	0.8	1.3	2.2	1.4
Port 4	0.6	2.0	3.6	2.1
Differential	0.2	-0.7	-1.4	-0.7
Ohio Port 14	0.2	0.1	na[1]	0.2
Port 4	0.5	0.3	0.46	0.4
Differential	-0.3	-0.2	--	-0.2
Wyodak Port 14	na	0.10	0.10	0.1
Port 4	na	0.24	0.43	0.3
Differential	--	-0.14	-0.33	-0.2
North Port 14	na	3.7	3.0	3.3
Dakota Port 4	na	0.1	9.7	4.9
Differential	--	3.6	-6.7	-1.6

1 data not available

(values greater than 1.0) of cesium for the Port 14 sampling location. The Port 14 Ohio and Wyodak samples predict depletion. These results imply that significant volatilization of cesium occurs for some coals during combustion but not for all coals.

Enrichment is shown for Thorium for the Illinois and North Dakota coals but depletion is indicated for the Pittsburgh, Ohio, and Wyodak coals at the Port 14 sampling location. These results imply that significant volatilization of thorium occurs for some coals during combustion but not for all coals.

For cerium, enrichment is shown for the Illinois and North Dakota coals. The Pittsburgh coal results are inconclusive. Depletion values are given for the Ohio and Wyodak coals. These results imply that significant volatilization of cerium occurs for some coals during combustion but not for all coals.

Dominant Vapor-to-Particle Surface Transport Mechanism

Due to low volatility, only a small fraction of volatilized cesium, thorium, and cerium molecules will exit the combustor in the vapor phase. In this study the average mass fraction of cesium still in the vapor phase at the post-combustion zone sampling location (Port 14) for the baseline screening experiments for the Pittsburgh, Illinois, and Ohio coals was 3 wt% with values ranging from 0.07 wt% to 7.7 wt% (see Table 3-118a). The average mass fraction of thorium still in the vapor phase at the post-combustion zone sampling location (Port 14) was 1.4 wt% with values ranging from 0.46 wt% to 2.2 wt% (Table 3-118b). For cerium, the average vapor phase mass fraction at Port 14 was 1.1 wt% with values ranging from 0.23 wt% to 2.0 wt% (Table 3-118c).

Vapor-phase cesium, thorium, and cerium molecules may reach the supersaturated conditions necessary for nucleation as they migrate away from burning carbon molecules into the bulk combustion gas. However since the concentration of these radionuclides is low compared to the major species in the coal, there is also a high probability that volatilized molecules will contact submicron or supermicron particles prior to reaching the supersaturated conditions necessary for nucleation. Thus depending on the combustion conditions, volatilized cesium, thorium, and cerium may homogeneously nucleate into submicron particles or heterogeneously partition onto the surfaces of both submicron and supermicron particles [30].

If homogeneous nucleation is a significant partitioning mechanism for these radionuclides, there should be a substantial mass fraction in the submicron particles and the mass fraction should be greater at Port 4 than at Port 14[13]. A significant submicron mass fraction is shown for all three radionuclides at Port 4 for the Pittsburgh fly ash which then decreases at Port 14. The Illinois and Ohio coals do not show this same behavior. These data imply that homogeneous nucleation is important for the partitioning of radionuclides during Pittsburgh coal combustion but less important during Illinois and Ohio coal combustion.

If heterogeneous vapor-to-solid phase partitioning is the dominant vapor-to-solid phase partitioning mechanism, supermicron particles should contain a much higher absolute mass fraction of cesium, thorium, and cerium than the submicron particles. In the current work, the average cesium mass fraction in the supermicron particles at Port 14 for the three study coals having available radionuclide data was 87 wt% (see Table 3-118 for individual values). The average thorium mass fraction in the supermicron particles at Port 14 for the three study coals having available radionuclide data was 86 wt% while the average cerium mass fraction in the supermicron particles at Port 14 for the three study coals having available radionuclide data was 89 wt%.

The controlling transport mechanisms for the partitioning of vapor-phase cesium, thorium, and cerium to the surfaces of fly ash particles can be investigated using a particle size dependence analysis. The particle size dependence of cesium associated with supermicron fly ash particles for five coals at the Port 14 sampling location is shown in Figure 3-167. The Illinois, Wyodak, and North Dakota distributions resemble a $1/D_p$ dependence indicating that partitioning of vapor-phase cesium to supermicron particles in the post-combustion zone is

[13] The submicron fraction will decrease due to agglomeration/coagulation.

Table 3-118. Mass Fraction of Cesium, Thorium, and Cerium in Vapor, Submicron, and Supermicron Regimes at Two Combustor Sample Locations

a) Cesium Partitioning

Coal/Location	Vapor Regime (Wt%)	Submicron Regime (Wt%)	Supermicron Regime (Wt%)
Pittsburgh			
Port 4	1.1	39	60
Port 14	0.07	19	81
Illinois			
Port 4	0.78	10	89
Port 14	1.3	3.1	96
Ohio			
Port 4	6.6	5.6	88
Port 14	7.7	9.8	83
Average			
Port 4	2.8	18	79
Port 14	3.0	10	87

b) Thorium Partitioning

Coal/Location	Vapor Regime (Wt%)	Submicron Regime (Wt%)	Supermicron Regime (Wt%)
Pittsburgh			
Port 4	0.78	25	74
Port 14	1.5	9.0	90
Illinois			
Port 4	0.35	11	89
Port 14	0.46	11	89
Ohio			
Port 4	0.82	3.2	96
Port 14	2.2	17	81
Average			
Port 4	0.65	13	86
Port 14	1.4	12	86

Table 3-118. (Continued) Mass Fraction of Cesium, Thorium, and Cerium in Vapor, Submicron, and Supermicron Regimes at Two Combustor Sample Locations

c) Cerium Partitioning

Coal/Location	Vapor Regime (Wt%)	Submicron Regime (Wt%)	Supermicron Regime (Wt%)
Pittsburgh			
Port 4	0.47	26	73
Port 14	0.96	4.7	94
Illinois			
Port 4	0.02	15	85
Port 14	0.23	13	87
Ohio			
Port 4	0.65	0.86	98
Port 14	2.0	13	85
Average			
Port 4	0.38	14	86
Port 14	1.1	10	89

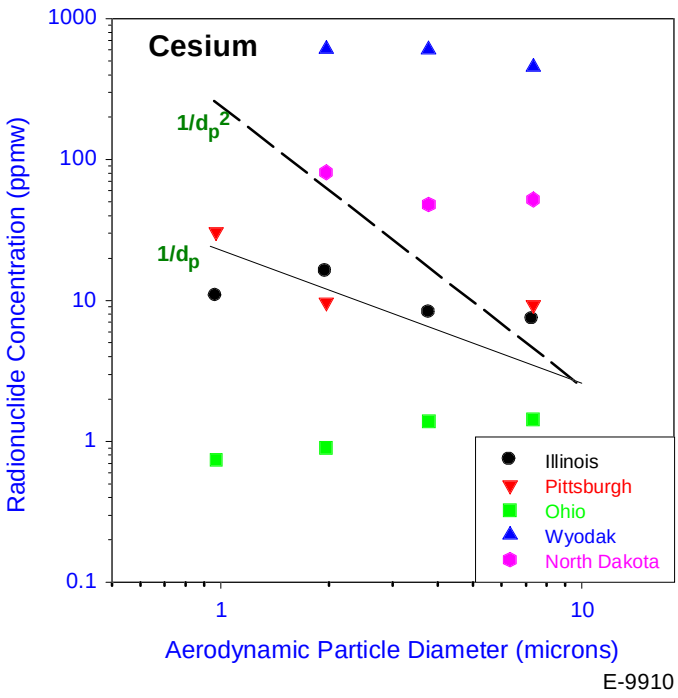

Figure 3-167. Particle size dependence of cesium in supermicron fly ash particles for five coals sampled at Port 14.

controlled by exterior surface reaction. No particle size dependence is apparent for the Pittsburgh and Ohio distributions. Thus, a transport process does not control vapor-phase cesium partitioning to supermicron particles in the post-combustion zone for these coals.

The particle size dependence of thorium associated with supermicron fly ash particles for five coals at the Port 14 sampling location is shown in Figure 3-168. No particle size dependence is apparent for any of the coals.

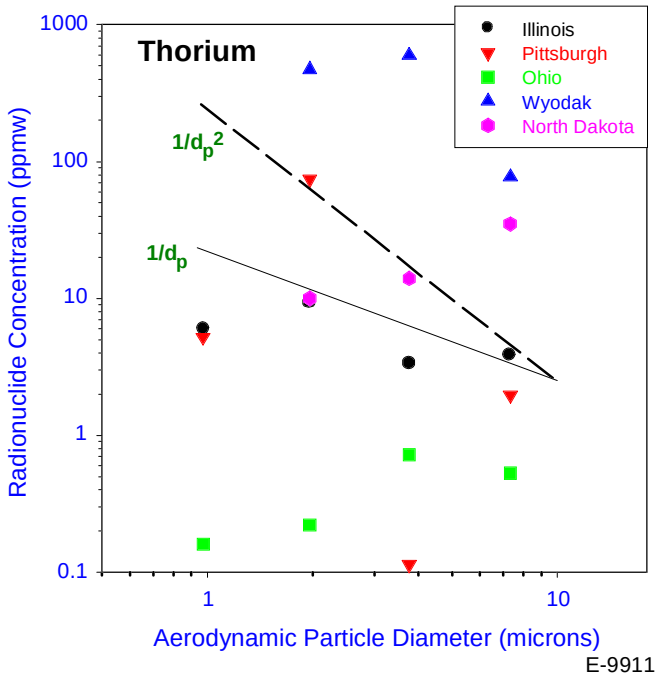

Figure 3-168. Particle size dependence of thorium in supermicron fly ash particles for five coals sampled at Port 14.

The particle size dependence of cerium associated with supermicron fly ash particles for five coals at the Port 14 sampling location is shown in Figure 3-169. No particle size dependence is apparent for any of the coals.

The size-segregated concentrations of cesium, thorium, and cerium in submicron particles for five coals at the Port 14 sampling location are shown in Figures 3-170, 3-171, and 3-172, respectively. No radionuclide particle size dependence is apparent for any of the coals evaluated.

Possible Fly Ash Surface Reaction Mechanisms

The particle size dependence analysis indicates that cesium partitioning for the Illinois, Wyodak, and North Dakota coals are controlled by surface reaction. Based on cesium sorbent study work by Amos [164] and an extensive study of sodium partitioning during coal combustion by Gallagher [165], cesium is expected to be present in a cationic form, such as Cs_2O. The most prevalent oxy-anion surface sites in the Al-Si fly ash surface matrix will be aluminum-based.

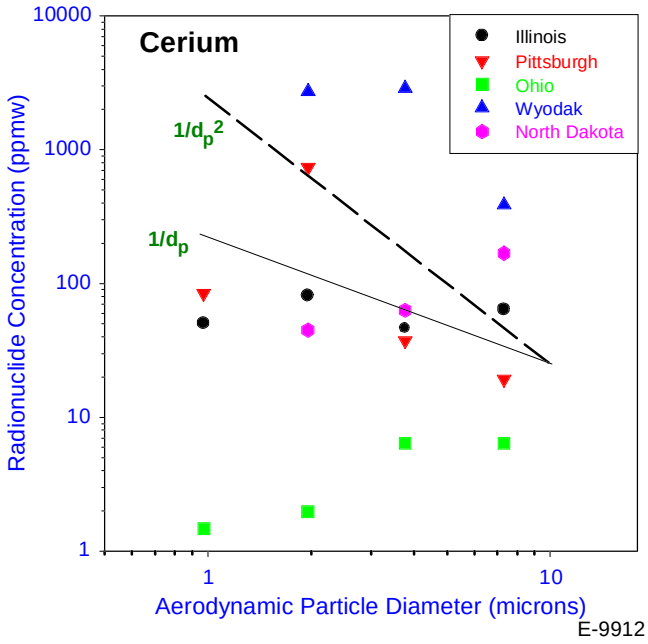

Figure 3-169. Particle size dependence of cerium in supermicron fly ash particles for five coals sampled at Port 14.

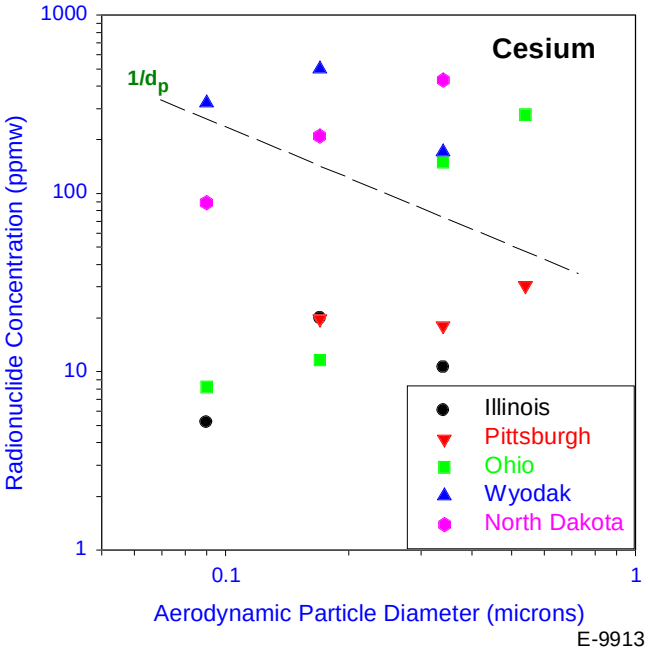

Figure 3-170. Particle size dependence of cesium in submicron fly ash particles for five coals sampled at Port 14.

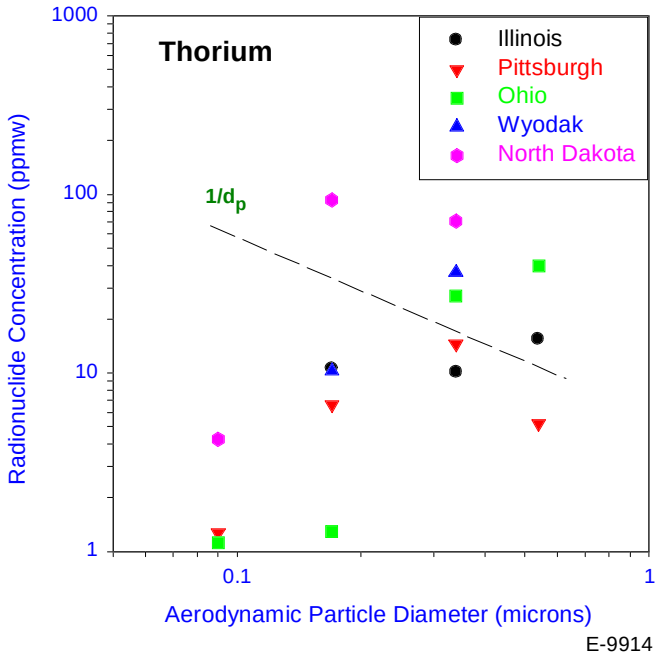

Figure 3-171. Particle size dependence of thorium in submicron fly ash particles for five coals sampled at Port 14.

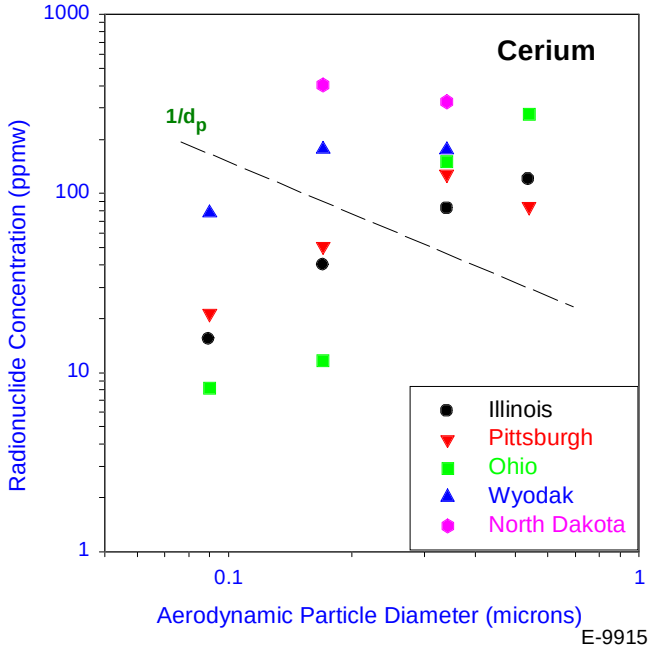

Figure 3-172. Particle size dependence of cerium in submicron fly ash particles for five coals sampled at Port 14.

To evaluate if cesium is reactive with anionic surface sites (e.g., Al-oxyanions) as opposed to cationic surface sites (e.g., Ca, Fe), a cross correlation analysis was performed. Figure 3-173 shows the absolute concentration of cesium on a supermicron impactor stage (stages 7-10) plotted versus the corresponding Al, Ca, and Fe concentration for the same impactor stage from Wyodak and North Dakota fly ash sampled at Port 14 (aluminum data is not available for the Illinois coal). Correlation coefficients were calculated for each relationship. The results suggest that cesium is more reactive with iron during Wyodak coal combustion and with calcium during North Dakota coal combustion. A Cs-Fe complexation mechanism for the Wyodak coal is consistent with the results for cobalt. Vapor-phase cobalt is also expected to be in a cationic form (e.g., CoO) yet analysis of results suggest Co-Fe complexation as the controlling vapor-to-solid phase partitioning mechanism.

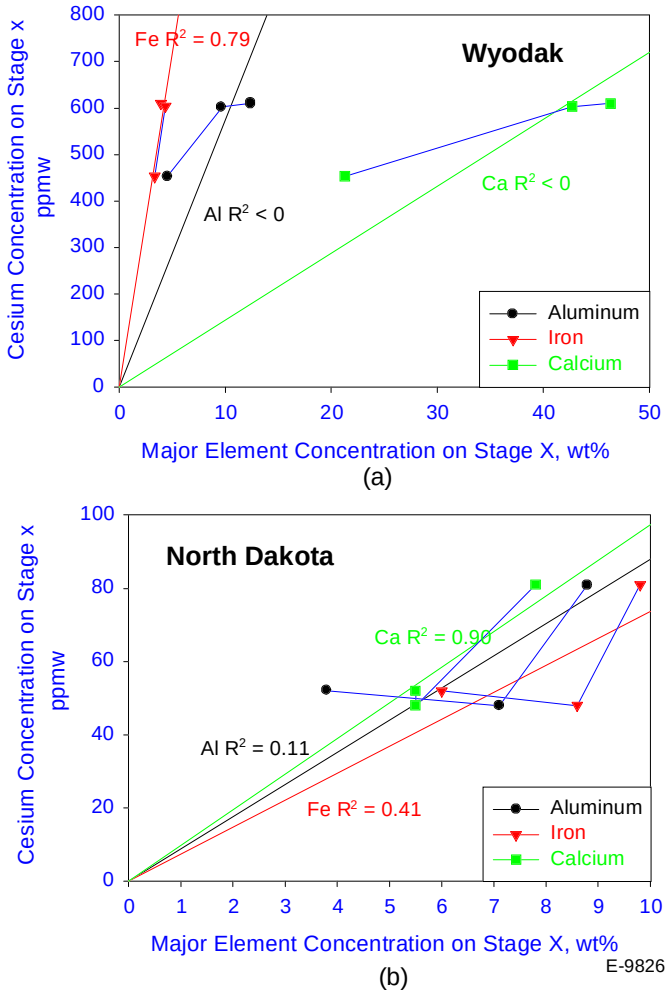

Figure 3-173. Cross correlation of cesium to aluminum, iron, and calcium in supermicron-sized impactor stages for (a) Wyodak and (b) North Dakota fly ash sampled at Port 14.

No previous published results documenting an apparent correlation of cesium with active cation surface sites (i.e., calcium and iron) rather than active anion surface sites (i.e., aluminum) have been found. In the sorbent study work by Amos [164], cesium doped into a natural gas flame was captured more efficiently by kaolinite (aluminum active anion sites) than by lime (calcium active cation sites).

These results should not be taken to imply that Cs-Al complexation is not a valid partitioning mechanism for some coals. The cobalt results suggest Co-Al complexation for the Kentucky coal (cesium data are not available for this coal) while Co-Fe complexation was predicted for the Wyodak and Pittsburgh coals.

The Timing of Partitioning Processes

The analysis above has shown that cesium partitioning to fly ash surfaces may be dominated by homogeneous nucleation, surface reaction with iron, calcium, and possibly aluminum active surface sites. Thorium and cerium partitioning to fly ash surfaces appears to be dominated by homogeneous nucleation or nontransport-controlled processes. Further insight can be gained into radionuclide partitioning mechanisms by examining size-segregated samples from Port 4 and comparing these results to those obtained from Port 14.

Insight into the timing of cesium, thorium, and cerium volatilization can be gained by comparing the mass fraction still in the vapor phase at the combustion zone sampling location (Port 4) for the baseline screening experiments to the mass fraction still in the vapor phase at the post-combustion zone sampling location (Port 14). These results are summarized in Table 3-118. The mass fraction of vapor-phase cesium is lower in the combustion zone sample for the Illinois and Ohio coals but not for the Pittsburgh coal. This indicates that cesium volatilization appears to continue after Port 4 for two of the three coals evaluated. For both thorium and cerium, the mass fraction in the vapor-phase is lower at Port 4 for all three coals indicating the thorium and cerium volatilization continues after Port 4.

The timing of partitioning from the vapor phase back to particle surfaces can be evaluated by comparing the enrichment factors of the submicron particles. Calculating a differential enrichment factor by subtracting the combustion zone enrichment factor from the post-combustion zone enrichment factor provides insight into when partitioning is occurring. Cesium, thorium, and cerium enrichment factors at Ports 4 and 14 along with differential enrichment factors are shown in Table 3-117 for five coals.

A positive cesium differential enrichment factor is found for Pittsburgh, Illinois, and North Dakota submicron particles. This suggests that volatilized cesium continues to partition to submicron particle surfaces after Port 4 for these coals. By contrast the negative differential enrichment factors shown for the Wyodak submicron particles suggests that the majority of the cesium associated with submicron particles for this coal is present prior to Port 4.

For thorium, a positive differential enrichment factor is only found for the Illinois submicron particles. Volatilized thorium may continue to partition to submicron particle surfaces after Port 4 only for this coal. Negative differential enrichment factors were calculated for cerium partitioning to submicron particles for all five coals.

Summary of Radionuclide Partitioning

A limited study has been performed to investigate the partitioning of cesium, thorium, and cerium during pulverized coal combustion. Table 3-119 summarizes the primary partitioning mechanisms during the combustion of five coals as predicted by this study.

Table 3-119. Primary Partitioning Mechanisms for Cesium, Thorium, and Cerium During the Combustion of Five Coals

Coal	Submicron Region	Supermicron Region
Pittsburgh	Cs partitioning occurs in the combustion zone (>2.2 residence seconds from the burner). Th and Ce partitioning begins in the combustion zone and continues in the post-combustion zone. Homogeneous nucleation accounts for most submicron Cs, Th, and Ce.	Partitioning to fly ash surfaces begins in the combustion zone. Cs, Th, and Ce are physically absorbed onto particle surfaces.
Illinois	Partitioning begins in the combustion zone and continues in the post-combustion zone (>2.2 res. sec.). Cs, Th, and Ce are physically absorbed onto particle surfaces. Cs may also transform by reaction with active surface sites.	Partitioning to fly ash surfaces begins in the combustion zone. Cs partitioning is controlled by reaction with active surface sites. Th and Ce are physically absorbed onto particle surfaces.
Ohio	Partitioning begins in the combustion zone and continues in the post-combustion zone in the combustion zone (>3.2 res. sec.). Cs, Th, and Ce are physically absorbed onto particle surfaces.	Partitioning begins in the combustion zone. Cs, Th, and Ce are physically absorbed onto particle surfaces.
Wyodak	Cs, Th, and Ce are physically absorbed onto particle surfaces. Cs may react with active iron surface sites to form Fe-Cs compounds.	Cs partitioning is controlled by reaction with active iron surface sites form Fe-Cs compounds. Th and Ce are physically absorbed onto particle surfaces.
North Dakota	Cs, Th, and Ce are physically absorbed onto particle surfaces. Cs may react with active calcium surface sites to form Ca-Cs compounds.	Cs partitioning is controlled by reaction with active calcium surface sites form Ca-Cs compounds. Th and Ce are physically absorbed onto particle surfaces.

The partitioning of these radionuclides is influenced by the extent of volatilization during combustion. Enrichment in submicron particle samples for some of the study coals suggests that significant volatilization may occur depending on the combustion conditions. Homogeneous nucleation was found to be a significant vapor-to-solid phase partitioning mechanism for one of the three coals evaluated. Heterogeneous transformation was found to be a more important partitioning mechanism to submicron particles for two other coals.

Heterogeneous transformation of vapor-phase thorium and cerium to fly ash surfaces is not transport controlled. For cesium, heterogeneous transformation from the vapor-phase to fly ash surfaces was found to be controlled by surface reaction for three coals and but not for two coals. For the Wyodak coal, Cs-Fe complexation is predicted (consistent with cobalt) while cesium partitioning for the North Dakota coal appears to be controlled by Cs-Ca complexation.

3.3.4 Summary and Recommendations

A comprehensive study has been conducted to investigate the post-combustion partitioning of trace elements during large-scale combustion of pulverized coal combustion. Trying to discern mechanistic information about trace elements from coal combustion experiments is extremely difficult

For many coals, there are three distinct particle regions developed by three separate mechanisms: 1) a submicron fume, 2) a micron-sized fragmentation region, and 3) a bulk (>3 μm) fly ash region. The controlling partitioning mechanisms for trace elements may be different in each of the three particle regions. A substantial majority of semi-volatile trace elements (e.g., As, Se, Sb, Cd, Zn, Pb) will volatilize during combustion. The most common partitioning mechanism for semi-volatile elements is reaction with active fly ash surface sites. Only the least volatile of these elements (e.g., cobalt) are expected to undergo significant vapor-to-solid phase partitioning by homogeneous nucleation. The presence of this mechanism is coal specific.

The submicron and fragmentation particle regions typically contain more active fly ash surface sites than the bulk fly ash region. The maximum combustion temperature affects the availability of active calcium and iron surface sites on submicron particles. Therefore, for most coals/combustion conditions, increasing the combustion temperature will decrease the vapor-phase emission of those trace elements that form oxy-anions during volatilization. The maximum combustion temperature does not affect the availability of active aluminum surface sites on submicron particles. Therefore, the recovery of volatilized trace elements that partition by reaction with active anion surface sites may be unaffected by combustion temperature.

Although not predicted by thermodynamic simulation, many volatilized trace elements appear to form oxy-anions during combustion. Volatilized transition metals (e.g., cobalt) may form simple oxides, oxy-anions, or a combination of both during combustion.

Sulfur will inhibit the reaction of most volatilized trace element oxy-anions with iron surface sites. The affect of sulfur on calcium reactivity appears to be less than the affect on iron reactivity. Sulfur content does not appear to affect the reactivity of aluminum surface sites. Therefore, coal sulfur content is an important parameter affecting the partitioning of many trace elements (e.g., selenium, arsenic) but not others (e.g., antimony, cesium). For coals with moderate (> 1 wt% as SO_2) to high sulfur contents (e.g., Pittsburgh, Illinois), volatilized trace elements that form oxy-anions will partition by reaction with active calcium surface sites if sufficient sites are available. For coals with low (<1 wt% as SO_2) sulfur contents (e.g., Kentucky, Wyodak, and North Dakota), volatilized trace elements that form oxy-anions will partition by reaction with active iron and/or calcium surface sites (depending on the reactivity of the individual trace element with iron versus calcium and the ratio of available iron to calcium surface sites). Volatilized trace elements that form oxy-anions will not partition by reaction for coals having a moderate to high sulfur content and low calcium content (e.g., Ohio) because there are insufficient active cation surface sites available for reaction.

Unreacted trace elements present on fly ash surfaces are usually very soluble in slightly acidic and acidic aqueous environments. The solubility of reacted trace elements present on fly ash surfaces is reaction product-dependent. Differences in partitioning mechanisms has a greater effect on trace element solubility from fly ash than which particle region the trace element resides in. Useful information can be obtained from leaching size-segregated fly ash samples collected on greased impactor membranes.

The following, element-specific conclusions can be derived from this work:

1. The volatilized form of antimony can have a substantial impact on the vapor phase emission. Almost all antimony present as antimony chloride is expected to leave in the flue gas and the remainder will partition as unreacted antimony to fly ash surfaces.

2. Volatilized selenium is more reactive with iron surface sites than with calcium surface sites. Therefore, coal sulfur content has a substantial impact on selenium partitioning.

3. Volatilized selenium is more reactive with both iron and calcium surface sites than arsenic or antimony.

4. Volatilized arsenic and antimony have similar reactivities with iron or calcium surface sites.

5. Volatilized selenium, arsenic, and antimony appear to form oxy-anions. These oxy-anions will react with active surface sites if available. Contrary to thermodynamic simulation predictions, formation of Al-As, Al-Se, or Al-Sb complexes were not observed under any of the conditions studied.

6. The forms of occurrence of selenium on fly ash surfaces can be distinguished by the solubility properties of the most likely forms of occurrence in slightly acidic and acidic aqueous leachates.

7. The forms of occurrence of arsenic on fly ash surfaces cannot be distinguished by the solubility properties of the most likely forms of occurrence in slightly acidic and acidic aqueous leachates.

8. All of the dominant forms of occurrence of antimony and cobalt on fly ash surfaces evaluated during this study were very soluble in slightly acidic and acidic aqueous leachates.

Areas for Future Work

Based on the work conducted in this research program, the following have been identified as areas where useful information can be developed in the future:

1. Methods need to be developed to identify the mechanisms controlling the partitioning of volatilized trace elements to fly ash surfaces when transport-controlled processes are not dominant such as for the Ohio coal in this study.

2. A leaching protocol needs to be developed to distinguish the forms of occurrence of arsenic on fly ash particle surfaces.

3. Solubility information needs to be developed for the most common forms of occurrence of antimony and cobalt on fly ash particle surfaces.

4. Further investigation is warranted into the mechanisms responsible for the fly ash fragmentation particle region. Also, what mechanism is responsible for the active cation and anion surface sites on these particles?

5. Determination of why North Dakota lignite antimony forms a volatilized antimony chloride would be useful.

6. Improved modeling tools for trace element partitioning need to be developed. Due to the rapid reactivity of most of the trace elements studied in this program in the very high temperature combustion environment, thermodynamic equilibrium does not seem to be an unreasonable assumption.

   However, thermodynamic simulations from this program and in virtually all published studies fail to accurately predict the most probable forms of occurrence of trace elements in the combustion and post-combustion environments for pulverized coal. This may be due to the use of bulk flue gas conditions in the simulations rather than point-source conditions.

7. Thermodynamic and transport data (e.g., heat capacities, thermal conductivity, etc.) for many postulated trace element reactants are not available. Development of these data may improve model prediction.

8. It would be useful to determine the mechanisms responsible for the formation of volatilized transition metal oxy-anions versus simple oxides.

9. Research is required to define the conditions required for volatilized Group 1 trace elements to partition by homogenous nucleation versus heterogeneous partitioning to the solid phase.

3.4 Post-Combustion Transformations of Mercury (EERC, UK, UC)

3.4.1. Background and Motivation

3.4.1.1 Mercury from Combustion Sources

Combustion processes remain the major source of mercury emissions to the atmosphere. The USEPA Mercury Study, submitted to Congress in February 1998, identifies emissions from combustion as the largest domestic source of mercury in the United States (Table 3-120). Electric utility boilers are the largest emitting single source category in this inventory, accounting for one-third of the anthropogenic emissions to the air in the U.S. Nearly all of the utility emissions result from coal combustion, as a result of mercury in coal concentrations typically between 0.08 ppmw and 0.22 ppmw for U.S. coals [166]. Municipal waste combustion and sewage sludge incineration are the second largest source of anthropogenic mercury emissions in the United States. Although there are regional differences - a similar inventory done for the northeastern U.S. identified municipal waste combustors as being responsible for 48% of mercury air emissions [167] - the study makes it clear that coal combustion remains an important source of mercury air emissions in the U.S.

Table 3-120. Mercury Emission Inventory for U.S. Sources, kg/yr
(Rounded to nearest 500) (U.S. EPA [168])

Source Type	Total Mercury
Medical Waste Incineration	12,000 (8%)
Municipal Waste Combustion and Sewage Sludge Incineration	32,500 (22%)
Electric Utility Boilers	45,500 (31%)
Non-Utility Fossil Fuel Boilers	25,500 (17%)
Non-Ferrous Metal Smelting	8,500 (6%)
Chlor-Alkali Sources	6,000 (4%)
Other Point Sources	12,000 (8%)
Area Sources	6,000 (4%)
Total	148,000

Anthropogenic mercury emissions from human activity take three forms: gaseous elemental mercury, gaseous divalent mercury, and particulate mercury. Table 3-121 presents speciated mercury emissions for domestic sources. Mercury circulates in the environment in different chemical forms and different physical states. Inorganic forms exist in three oxidation states: elemental, monovalent, or divalent. In organic form, mercury can exist as methyl mercury [167]. Other forms are also possible.

Mercury in the atmosphere can return to the surface of the earth by either dry or wet deposition. In the case of gaseous divalent mercury, it can be subject to rapid wet or dry deposition. Divalent mercury is soluble in water and it can also adhere to particles in the air. It has a residence time of just 5 to 14 days in the atmosphere [167]. Mercury in its elemental state can be expected to disperse on a regional and global scale. Bergan et al. [169] suggest an oxidation rate of Hg^0 to Hg^{+2} of 1.0 yr^{-1}, indicative of long atmospheric residence times. Elemental mercury is eventually removed from the atmosphere by dry deposition onto surfaces and by wet deposition after oxidation to water-soluble, divalent mercury [170, 171].

Table 3-121. Speciated Mercury Emission Inventory for U.S. Sources, kg/yr (U.S. EPA [168])

Source Type	Hg (0)	Hg(II)	Hg(P)
Medical Waste Incineration	2,410	7,230	2,410
Municipal Waste Combustion and Sewage Sludge Incineration	6,510	19,500	6,510
Electric Utility Boilers	22,700	13,600	9,080
Non-Utility Fossil Fuel Boilers	12,700	7,640	5,090
Non-Ferrous Metal Smelting	7,370	870	430
Chlor-Alkali Sources	4,270	1,830	0
Other Point Sources	9,600	1,200	1,200
Area Sources	5,950	0	0
Total	**71,510 (48%)**	**51,900 (35%)**	**24,720 (17%)**

Bergan et al. [169] have noted that global man-made emissions are at least 30% as large as natural emissions, implying the global average deposition rate, which is the rate at which mercury deposits on land or water bodies, has increased by at least 50% since pre-industrial times. In the most industrial regions (Europe, North America, Southeastern China), the deposition rate has increased by a factor of 2-10 during the past 200 years [169]. According to a study of mercury deposition in mid-continental North America, the rate of deposition of mercury to the earth surface has increased from 3.7 $\mu g/m^2$ in 1850 to approximately 12.5 $\mu g/m^2$ today [172].

3.4.1.2 Mercury Transformations at Post-Coal Combustion Conditions

During combustion, mercury escapes from the burning fuel as an elemental vapor, which may persist in elemental form or may be oxidized to the +2 (mercuric) state. The three most likely gas phase mercury compounds in combustion systems - Hg, HgO, and $HgCl_2$ - are all volatile at stack and air pollution control device temperatures. Table 3-122 presents physical property data for these three mercury compounds, and Figure 3-174 presents vapor pressure data for Hg and $HgCl_2$ taken from several investigators. The relatively high vapor pressure at stack temperatures for these mercury compounds (those most likely to appear in combustion stack gases) clearly indicates that removal of mercury from stack gases will be a challenging problem. Note that mercury also forms stable (+1) compounds, but these have not been observed in combustion systems.

The form of mercury emitted from point sources is a critical variable in modeling the patterns and amount of mercury deposited from the atmosphere [168]. In the combustion zone of a coal-fired power plant, all the mercury in coal is vaporized as elemental mercury, yielding vapor concentrations of mercury in the range of 10 to 20 $\mu g/Nm^3$ (1 to 2 ppbv). At furnace exit temperatures (1700 K), all of the mercury is expected to remain as the thermodynamically favored elemental form in the gas. As the gas cools after combustion, oxidation reactions can occur, significantly reducing the concentration of elemental mercury by the time the

Table 3-122. Physical/Chemical Properties of Mercury and Some of Its Compounds (Schroeder et al. [173] and references cited therein)

Property	Hg^0	$HgCl_2$	HgO
Melting Point (^oC)	-39	277	Decomposition @ +500 ^oC
Boiling Point (^oC)	357 at 1 atm	303 at 1atm	—
Vapor Pressure (Pa)	0.180 at 20°C	8.99×10^{-3} at 20°C	9.20×10^{-12} at 25°C
Water Solubility (g/l)	49.4×10^{-6} at 20°C	66 at 20°C	5.3×10^{-2} at 25°C
Henry's Law Coefficient [Pa m^3mol^{-1}]	729[a] at 20°C 0.32 at 25°C 0.18 at 5°C	3.69×10^{-5} at 20°C	$3.76x10^{-11}$ at 25°C
Octanol-Water Partition Coefficient	4.2[a]	0.5[a]	—

[a]Dimensionless

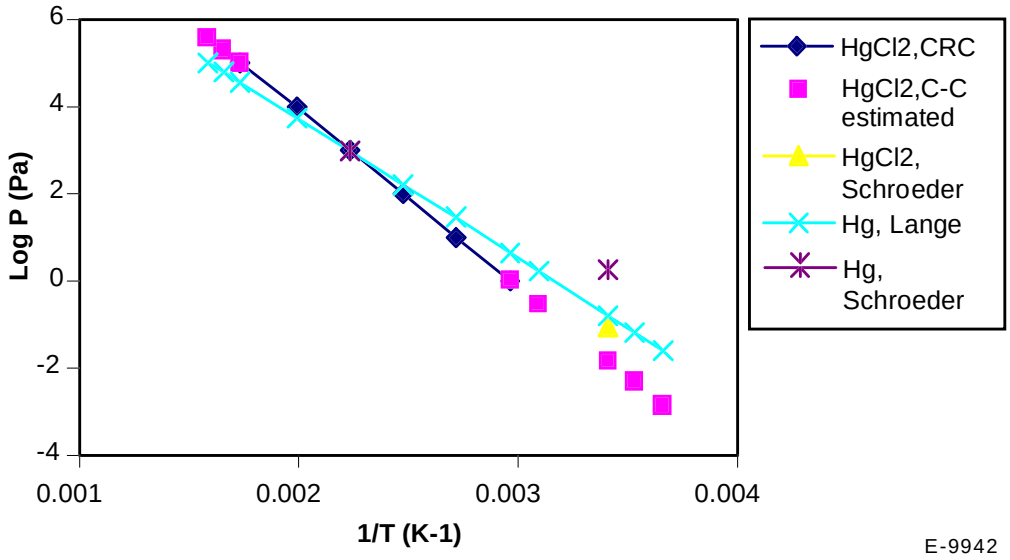

Figure 3-174. Vapor pressure - temperature data for Hg and $HgCl_2$. Source: Schroeder et al. [173], CRC, and Lange.

post-combustion gases reach the stack. Measurements of the concentration of mercury species taken in the stacks of pilot and full-scale coal combustion systems show more than half of the vapor phase mercury as the oxidized form which is likely to be $HgCl_2$ [174]. The range of observed values is broad: one study consisting of mercury speciation measurements from 14 different coal combustion systems reported anywhere from 30% Hg^{+2} to 95% Hg^{+2} upstream of the air pollution control device (APCD) [175]. In general, emissions of mercury from coal combustion sources are approximately 20-50% (Hg^0) elemental mercury and 50-80% divalent mercury (Hg^{+2}), which may be predominantly $HgCl_2$.

Equilibrium predicts complete oxidation of elemental mercury to $HgCl_2$ in coal-fired combustion flue gas at temperatures below about 725 K. The chlorine content of the coal determines the temperature below which $HgCl_2$ is thermodynamically stable. Measurements in full-scale combustion systems (circa 400 K) do not show complete oxidation of elemental mercury as predicted by equilibrium. The assumption of equilibrium for mercury species in coal combustion flue gas is then not valid. Consideration of a limited set of mercury speciation measurements indicates that mercury equilibrium in the flue gas is frozen at approximately 800 K. Kinetic limitations therefore need to be accounted for [174].

Recognition of the importance of kinetic limitations in mercury oxidation has led to several investigations of mercury reaction kinetics over the past decade. These are discussed below.

3.4.1.3 Previous Experimental Studies of Mercury Oxidation

A literature review encompassing previous experimental work regarding mercury (Hg) reactions under post-coal combustion conditions is presented. The objective was to gain a basic

understanding of previous mercury oxidation studies and the experimental conditions in which they were performed. Physical conditions and concentrations of the reactants vary from one system to another; however, important information about the nature of mercury transformations can be obtained. Their findings provide a framework for comparing our experimental system and expected results.

Hall et al. (1990)

Hall et al. [176] studied mercury chemistry in simulated flue gases related to waste incineration conditions. They built a system consisting of a propane-fueled furnace and a 12 m long temperature-controlled steel duct with a fabric filter. The gas flow was maintained by an induced draft ejector. Particles and trace gases were introduced either through or after the flame. Flue gas sampling was done at different ports through the steel duct. Flue gas was sampled at a constant flow of 1 standard liter per minute (slpm). A simple computer-controlled data acquisition system collected and stored temperature and combustion parameter data during the experiments. Elemental and total amounts of mercury were collected at different ports. Elemental mercury (Hg^0) was analyzed by cold vapor atomic absorption (CVAA) directly. For the total amount of mercury, the sampled flue gas passed through a Sn(II) solution to reduce most of the oxidized species prior to passing the CVAA analyzer. The difference between total and elemental amounts of mercury accounted for the amount of oxidized mercury.

The concentrations of mercury and HCl used by Hall et al. [176] and different studies are listed in Tables 3-123 and 3-124, as well as other parameters of their experimental runs. The existence of a temperature gradient should be emphasized. In the presence of 8% excess O_2, and at mercury concentration of 150 $\mu g/m^3$, 20 to 30% of the mercury was oxidized after 0.8 s residence time (T>500°C). The reaction product is assumed to be HgO, which has lower vapor pressure and tends to deposit in the walls of furnace ducts. In the presence of HCl (220 ppmv) in the gas, around 70% of the elemental mercury was oxidized after 0.8 s.

At lower temperatures in the flue gas, around 150 to 220°C, a reduction of oxidized mercury (to elemental mercury) occurs in many of the experiments. Hall et al. [176] assume that steel corrosion induced by HCl at these temperatures may give rise to an activated iron surface on which Hg(II) compounds may be reduced via

$$Fe + Hg(II) \Rightarrow Hg^0_{(g)} + Fe(II) \; . \qquad (3\text{-}15)$$

Hall et al. [176] also studied the effect of activated carbon (0.5-1.0 g/m^3, at NTP, specific surface 792 m^2/g (BET)). They found that the carbon that was collected contained 40-60 ppm mercury ($\mu g/g$ of carbon), which is equivalent to 14 to 20% of the mercury added. They affirm that activated carbon acts as a catalyst for the formation of mercuric oxide.

Table 3-123. Characteristics of Experiments Conducted Under Isothermal Conditions

Characteristics	Sliger et al. [177]	Ghorishi et al. [178]	Gaspar et al. [179]	Hall et al. [180]
Flue Gas Components	CO_2, H_2O, Air (O_2 and N_2), HCl	CO_2, H_2O, O_2, SO_2, HCl, N_2	CO, H_2O, O_2, HCl, N_2	N_2, HCl, Cl_2, O_2, NH_3,N_2O, SO_2,H_2S
Total Flow	N/A	300 cm^3/min	N/A	1 slpm
Hg Concentrations	53μg/m^3 or 137μg/m^3 (860°C)	400 μg/m^3	3000 μg/m^3	100 μg/m^3
[Cl species], ppm	HCl, 56-638	HCl 50, 100, 200 Cl_2, 50	HCl, 300, 3000	HCl, 100-300 Cl_2, 2-10
Test Temperatures	922, 860, 1071°C	150-754°C	423-876°C	20-900°C
Residence Time	1.4 s	2 s (at 850 °C)	0.7 s	0.7 s (900°C) 2.8 s (20°C)
Presence of Particles	No	Simulated Fly Ash	No	No
Sampling Method	EPA Method 29 (modified)	UV Analyzer	EPA Method 29 (not chilled)	Cold Vapor Atomic Absorption
Level of Mercury Oxidation	0-75%	27%(for high HCl and T>700°C) 100% (for Cl_2)	40-98% (HCl, 3000 ppm) 20-80% (HCl, at 300 ppm)	30-95% (20-900°C; HCl, 100-300 ppm); 50-95% (Cl_2)
Gas Environment	Natural Gas Furnace	Simulated	Simulated	Simulated
Oxygen Environment	No Information Available	O_2 Excess	Fuel Lean	10% O_2 excess for HCl runs

Table 3-124. Characteristics of Experiments Conducted with a Temperature Gradient

Characteristics	Galbreath et al. [181]	Hall et al. [180]	Hall et al. [176]
Flue Gas Components	CO_2, CO, O_2 and SO_2, NO_x, HCl	CO_2, CO, H_2O, O_2, HCl, Cl_2, NO_x, N_2	CO_2, CO, H_2O, O_2, HCl, NO_x, N_2
Total Flow Rate	N/A	700 slpm	N/A
Hg Concentrations	10 $\mu g/m^3$	140 $\mu g/m^3$	150 $\mu g/m^3$
[Cl species], ppm	HCl, 10-100	HCl,, 11,150 Cl_2, 11-150	HCl, 250
Test Temperature	200°C	500°C	>500°C
Tprofile	420 K/s	200-333 K/s	200-333 K/s
Res Time	2.5 s	1.5 s	0.8 s
Particles	In. heterogen. runs	No	Yes, activated carbon
Sampling Method	EPA Method 29 (modified)	Cold Vapor Atomic Absorption	Cold Vapor Atomic Absorption
Level of Mercury Oxidation	0-50%	62% for HCl 70% for Cl_2	70% for HCl 20-30% for O_2 only
Gas Environment	42 MJ/hr coal combustion (Absaloka subbit. coal)	Propane Furnace	Propane Furnace
Oxygen Environment	8.5 mol% O_2 excess	10%O_2 excess for HCl runs	8% O_2 excess

Hall et al. (1991)

Hall et al. [180] expanded their experimental studies regarding Hg reactions in the gas phase by studying reactions of mercury under more representative conditions (17 kW propane fired flue gas generator) and also through a continuous flow reactor. The 17 kW propane generator has the same characteristics as the one used in their previous work. Reactants were admitted near the burner providing a total gas flux of 750 slpm. In order to analyze elemental Hg present in the flue gas, 1 slpm of flue gas was withdrawn through a gas/liquid separator. Hg vapor was analyzed by cold-vapor atomic absorption (CVAA). To measure the total amount of Hg, another sampling port was used. The detection limit is claimed to be 3 $\mu g/m^3$ [180]. The continuous flow reactor system contained a pre-warming section, and a 45-cm long quartz reactor placed in two furnaces. Temperature was controlled by two microprocessors keeping the temperature within 0.5°C of a preset value. Reactant gases were premixed in two separate lines using N_2 as a matrix gas, with a total flow rate of 1 slpm.

Mercury was introduced in the system through a thermostated coil containing several droplets of Hg. The factors determining the final Hg concentration were therefore Hg vapor

pressure, N_2 flow rate, and dilution rate. The experimental conditions and extent of reaction of both systems are summarized in Tables 3-123 and 3-124. Based on their experiments, they concluded that mercury reacts with Cl_2, HCl, NO_2, and O_2. Mercury was not found to react with NH_3, N_2O, SO_2, or H_2S. The authors predicted that in waste incineration facilities, with high concentrations of HCl and Cl_2, most of the mercury will be oxidized. In coal combustion facilities, with lower HCl and Cl_2 concentrations, a slight oxidation would occur with NO_2. If soot and particles with a large surface area were present, they concluded that O_2 would cause considerable oxidation at 200°C.

Mercury was found to be oxidized up to 70% with Cl_2 concentrations ranging from 11 to 150 ppmv in the presence of a temperature gradient (17-kW propane burner). The peak temperature of the combustion chamber was between 800°C and 1000°C in these experiments, with a cooling rate between 200 to 333 K/s. The sampling was done at 500°C. Reaction time at this point is about 1.5 s. In the continuous flow reactor, up to 95% oxidation was achieved at constant temperatures ranging from 20 to 700°C, and with increasing Cl_2 concentrations from 1.7 to 10 ppmv.

The reaction time ranges from 2.8 s at 20 °C to 0.8 s at 700°C. Note that the Cl_2 concentrations in the continuous flow reactor were much lower than in the 17-kW propane burner.

Hall et al. [180] concluded from this data that the most probable products of the reaction with Cl_2 are Hg (I) and Hg (II) chlorides, and felt that heterogeneous reactions were important at low temperatures.

In the presence of a temperature gradient (17 kW propane generator), and with HCl concentrations up to 150 ppmv and a presence of 10% of O_2, mercury was oxidized up to a maximum of 74%, at a sampling temperature of 500°C, and with a residence time of 1.5 s. Note that these results differed from those obtained in the continuous flow reactor.

Hall et al. [180] found that the reaction rate increases with increasing constant temperatures, and at 900°C, more than 90% of mercury is oxidized. The reaction time is 0.7 s. at 900°C, and 2.8 s. at 20°C. The variation of HCl concentration, from 100 to 300 ppmv does not seem to cause further oxidation.

Sliger et al. (1998, 2000)

Sliger et al. [177] focused on homogeneous gas phase oxidation at high temperatures (between 860 and 1071°C), specifically with HCl. They compared their work to the low-temperature Cl_2-driven mechanism mentioned by Hall et al. and discussed in the preceding sections.

In the Sliger et al. [177] study, a natural gas furnace was used to model coal combustion. The natural gas furnace stands 2.4 m (7.9 ft) tall, with the main burner sitting on top. The furnace has a maximum power rating of 16.1 kW (54900 BTU/hr). It has a multiple layer refractory design. There are sampling ports along the center of the reactor. The maximum flame

temperature achieved is 1600°C (2900°F). Isothermal conditions are preferable but not met in the system. Four back-fired burners, forming two pairs of heating channels, are used to minimize the temperature drop along the test section. Mercury is introduced into the system through the vaporization of a mercury acetate solution which is atomized into the primary flame. Measurements without HCl showed the entire recovery of Hg as elemental. HCl is introduced through a dilution air inlet downstream of the burner. The residence time is approximately 1.4 s.

Flue gas was sampled with a variation of EPA Emissions Test Method 29 (the filter was omitted since there were no particles present). Nitric acid/ hydrogen peroxide impingers were used to capture oxidized forms of mercury and acidic $KMnO_4$ solution filled impingers are used to capture elemental mercury. Mercury was analyzed using CVAA.

Sliger et al [177] did not reproduce the Hall et al experimental results under similar HCl and Hg concentrations. They needed higher temperatures (922°C) and higher concentrations (HCl, 282 ppmv) to obtain 41% oxidation. At a temperature of 1071°C, and HCl concentration of 638 ppmv, the oxidation reached 71%. There is a trend of higher temperatures resulting in higher oxidation. Specific characteristics of the experimental runs can be seen in Table 3-123.

Sliger et al. [177] attribute the differences between their results and those of Hall et al. [180] to the lack of formation of large quantities of Cl atoms in the Sliger study. Hall et al. [180] pre-heated the gases before they entered reaction chamber, whereas in the Sliger et al. [177] system, HCl was introduced cold. Sliger et al. [177] hypothesize that this did not provide sufficient time for the buildup of Cl atom concentrations.

This interpretation is supported by kinetic modeling. Sliger et al. [177] developed a kinetic model to predict the behavior of reactions of mercury with chlorine species. A plug flow reactor model was utilized. The reaction mechanisms used in the model involved elementary reactions for the H_2-CO-O_2 system, without carbon-based reactions except those involving CO and CO_2. Reactions involving chlorine species were taken from a mechanism used to study chlorine inhibition of CO flames. For the interactions of Hg and chlorine, kinetic data for two reactions were considered. From Horne et al. [182]:

$$Hg + Cl + M \Rightarrow HgCl + M \quad (3\text{-}16)$$

This reaction is the initial step in the formation of $HgCl_2$. $HgCl_2$ was assumed to be formed by:

$$HgCl + HCl \Rightarrow HgCl_2 + H \quad (3\text{-}17)$$

The Cl_2 reaction from Hall et al. [180] was also included as a parallel oxidation path:

$$Hg + Cl_2 + M \Rightarrow HgCl_2 + M \quad (3\text{-}18)$$

Using this model, agreement with experimental results was found at low and moderate up HCl concentrations, up to the point at which the experimental results did not show further oxidation as the HCl concentration was increased. The model did not predict this plateau.

More recent modeling work by Sliger et al. [183, 184] presented a four step mechanisms for mercury oxidation:

$$Hg + Cl_2 \Rightarrow \text{oxidized products} \quad (3\text{-}19)$$

$$Hg + Cl \Rightarrow HgCl \quad (3\text{-}20)$$

$$HgCl + HCl \Rightarrow HgCl_2 + H \quad (3\text{-}21)$$

$$HgCl + Cl \Rightarrow HgCl_2 \quad (3\text{-}22)$$

The authors also considered possible competing high temperature pathways such as the abstraction reaction $HgCl + Cl \Rightarrow Hg + Cl_2$ at high temperatures, but deemed them unimportant relative to the proposed four step mechanism. Rate constants were obtained from the literature or from calculation. For the first reaction, the 1991 rate constant of Hall et al. [180] was used. The second reaction rate constant was based on the data of Horne et al. [182]. The third reaction rate constant was determined from transition state theory calculations, and the fourth reaction was assumed to proceed at the collision limit.

Using this newer kinetic model, the authors determined that nearly all of the oxidation observed in their experiments occurred during the quench phase at temperatures between 400 C and 700°C. They concluded that super-equilibrium Cl atom concentrations existing during quench were the major oxidant, and that high concentrations of vapor phase water significantly inhibited mercury oxidation.

Widmer et al. (2000)

Widmer et al. [185] have also studied the oxidation of mercury under high HCl concentrations relevant to waste combustion. Experiments indicated significant oxidation at temperatures of 700 to 800 K and in the presence of 300 to 3000 ppm HCl. Of more interest to our study of coal combustion is the 8-step model the authors construct to interpret their data. Combining their 8-step model

$$Hg + Cl + M \Rightarrow HgCl + M \quad (3\text{-}23)$$

$$Hg + Cl_2 \Rightarrow HgCl + Cl \quad (3\text{-}24)$$

$$Hg + HOCl \Rightarrow HgCl + OH \quad (3\text{-}25)$$

$$Hg + HCl \Rightarrow HgCl + H \quad (3\text{-}26)$$

$$HgCl + Cl_2 \Rightarrow HgCl_2 + Cl \quad (3\text{-}27)$$

$$HgCl + HCl \Rightarrow HgCl_2 + H \quad (3\text{-}28)$$

$$HgCl + Cl + M \Rightarrow HgCl_2 + M \quad (3\text{-}29)$$

$$HgCl + HOCl \Rightarrow HgCl_2 + OH \quad (3\text{-}30)$$

with the use the methane combustion model of Glarborg et al. [186] and the chlorine chemistry of Senkin at UCLA, the authors are able to model their mercury oxidation experimental data. They note, however, that their mechanism predicts little mercury oxidation at 10 to 50 ppm chlorine concentrations associated with coal fired combustors [185]. Nevertheless, this represents the most detailed characterization of homogeneous mercury chemistry to date.

Gaspar et al. (1997)

Gaspar et al. [179] used a simulated flue gas in a heated quartz reactor tube to study reactions of mercury with HCl, O_2, CO_2, and N_2. Water was introduced as moisture in N_2. All these gases were premixed. Hg was supplied to the system through a permeation device submerged in a tube with a constant temperature oil bath. The Hg line was heated before is mixed with flue gases. For sampling, flue gas went through three ambient temperature impingers to get oxidized mercury. Next, three chilled impingers were used to capture elemental mercury. The first three impingers were filled with a 5% HNO_3/ 10% H_2O_2 solution. The second set of impingers were filled with a 10% H_2SO_4 / 4% $KMnO_4$ solution. A constant temperature was maintained through the quartz tube reactor. The conditions at which the experiments were conducted are shown in Table 3-123 above. Two different concentrations of HCl, 300 ppm and 3000 ppm, were considered at different temperatures and using a fixed mercury concentration.

Gaspar et al. [179] report that 40 to 98% oxidation of mercury was achieved with high HCl concentrations (3000 ppmv) and a higher degree of oxidation was observed as the temperature increased. For low HCl concentrations (300 ppmv) 20 to 80% mercury oxidation was reported, with a higher degree of oxidation as the temperature increased. Note that one problem encountered by the investigators was the lowering of the permeation rate over many runs from 24.2 μg/min to 6.1 μg/min in the last run. Gaspar et al. [179] considered that this variation was within a reasonable level of the target of 1000 $\mu g/Nm^3$ of mercury.

For low HCl concentration tests, $HgCl_2$ formation approached equilibrium at high temperatures but the formation was significantly lower than what was achieved during high HCl concentrations. At 760°C, $Hg/HgCl_2$ equilibrium was achieved in 1 second. Kinetic limitations became evident at temperatures less than 760°C, when mercury chloride fell below equilibrium predictions. Adequate conversion of Hg to $HgCl_2$ was unlikely to occur in a system that rapidly quenched the gases. This is because Hg speciation reached equilibrium in 1 s.

Gaspar et al. [179] also concluded that in full-scale incinerator systems, poor bulk gas mixing, high waste composition variability, and stratified gas flow may further limit mercury chloride formation and the removal of mercury species.

Ghorishi et al. (1998)

Ghorishi et al. [178] conducted homogeneous and heterogeneous oxidation experiments in a quartz reactor surrounded by a temperature-controlled furnace. Mercury was provided through a permeation device using nitrogen as the carrier gas. Mixtures including N_2/H_2O, Air/CO_2, SO_2, and HCl were considered in the oxidation experiments. A bypass before the oxidation reactor was used to sample and measure total mercury by an on-line ultraviolet (UV) Hg^0 analyzer. The UV analyzer did not respond to oxidized forms of mercury. Before entering the Hg^0 analyzer, water vapor (which interfered with the readings) was removed from the flue gas through a NAFION gas sample dryer.

Ghorishi et al. [178] reported that at 40°C, 100% mercury oxidation occurred with chlorine as the oxidant (Cl_2= 50 ppmv, Hg=40 ppbv). The authors also concluded that homogeneous gas-phase oxidation of Hg^0 in the presence of HCl was very slow and proceeded at significant rates only at high temperatures (>700°C) and high HCl concentration (>200 ppmv). The effects of water vapor and SO_2 were also studied, and were found to have a significant inhibition effect ($H_2O_{(g)}$=1.7% mole, SO_2=500 ppmv)m consistent with the effects of water reported by Sliger et al. [177].

For the heterogeneous tests, the authors measured a high oxidative conversion of mercury (95%) in the presence of 14% Fe_2O_3 or 1% CaO, at temperatures between 150 and 200°C. These experiments were performed by passing simulated flue gas through a catalytic bed.

Galbreath et al. (1998)

Galbreath et al. [181] conducted mercury oxidation experiments in a 42 MJ/Hr down-fired furnace equipped with a baghouse for particulate control. Their primary goal was to determine whether chlorination is a dominant Hg transformation mechanism in real coal flue gases. A permeation device was used as a source of additional mercury as in other studies described previously in this section. HCl was introduced in the system as a mixture with N_2. Molecular Cl_2 was not introduced in the system but it was assumed to be a product of HCl reaction with oxygen (Deacon process). An on-line analyzer (Semtech Hg 2000) was used to verify the Hg^0 spike concentration. O_2, CO_2, CO, SO_2 and NO_x concentrations were measured in the CEPS using on-line analyzers (Beckman Instruments, Inc.). A modified EPA Method 29 sample train was used for determining Hg emissions and speciation. A tris(hydroxymethyl) aminomethane buffer solution was substituted for the HNO_3-H_2O_2 solutions in the first set of impingers of EPA method 29. Temperature changed from 1250°C to 200°C in about 2.5 seconds. This represented a cooling rate of 420 K/s. Hg and Cl speciation analyses of the resulting flue gases were performed at 200°C or 250°C.

Three different experimental runs were done. The first one was only in the presence of excess O_2 and N_2. The second incorporated 100 ppmv of HCl, and the third set involved the Absakola coal fly ash without mercury spikes. Refer to Table 3-124 for a list of experimental conditions.

In the presence of excess O_2, 85% of the mercury spike was recovered, with an oxidation of 50%. The product was assumed to be HgO. In the presence of 100 ppm HCl, an average of only 35% of initial mercury was recovered. From this recovered mercury, 72 to 83% was found to be oxidized mercury. Low recoveries of Hg^0 suggested that $HgCl_2$ was formed and deposited within the combustor. In the presence of Absakola coal, on average 41%, 19%, and 40% of the total Hg (~5.5 $\mu g/m^3$) were present as $Hg_{(p)}$ (particulate mercury), $Hg^{2+}X_{(g)}$ (oxidized), and $Hg^0_{(g)}$(elemental).

Niksa et al. (2001)

Niksa et al. [187] have proposed a modified version of the 8-step mechanism developed by Widmer et al. [185]. The framework of the Widmer et al. [185] mechanism is used, but based in part on work from this project, rate constants from Widmer et al. [185], Sliger et al. [184], and from kinetic theory are proposed. The suggested reactions and corresponding rate constants are presented in Table 3-125.

Table 3-125. Niksa et al. [187] Rate Constants for Hg Oxidation.
Rate Constants Are of the Form $k = AT^n \exp(-E/RT)$

	A	n	E (kcal mol^{-1})	Units	Source
$Hg+Cl+M \leftrightarrow HgCl+M$	9.00×10^{15}	0.5	0	$cm^6\ mol^{-2}\ s^{-1}$	Fit
$Hg+Cl_2 \leftrightarrow HgCl+M$	1.39×10^{14}	0	34.0	$cm^3\ mol^{-1}\ s^{-1}$	Widmer et al. [185]
$Hg+HCl \leftrightarrow HgCl+H$	4.94×10^{14}	0	79.3	$cm^3\ mol^{-1}\ s^{-1}$	Widmer et al. [185]
$Hg+HOCl \leftrightarrow HgCl+OH$	4.27×10^{13}	0	19.0	$cm^3\ mol^{-1}\ s^{-1}$	Widmer et al. [185]
$HgCl+Cl_2 \leftrightarrow HgCl_2+Cl$	1.39×10^{14}	0	1.0	$cm^3\ mol^{-1}\ s^{-1}$	Widmer et al. [185]
$HgCl+Cl+M \leftrightarrow HgCl_2+M$	1.16×10^{15}	0.5	0	$cm^6\ mol^{-2}\ s^{-1}$	Collision limt
$HgCl+HCl \leftrightarrow HgCl_2+H$	4.64×10^{3}	2.5	19.1	$cm^3\ mol^{-1}\ s^{-1}$	Sliger et al. [184]
$HgCl+HOCl \leftrightarrow HgCl_2+OH$	4.27×10^{13}	0	1.0	$cm^3\ mol^{-1}\ s^{-1}$	Widmer et al. [185]

The work of Niksa et al. [187] has suggested that the presence of NO can significantly affect the homogeneous oxidation kinetics of elemental mercury under some conditions. At low NO concentrations (< 20 ppm), trace amounts of NO are found to increase the extent of mercury oxidation. At higher concentrations, NO can inhibit Hg oxidation in systems, likely through NO + OH + M, but the extent of inhibition (or augmentation) was found to be highly dependent upon quench rate. These recent results suggest that future studies of homogeneous mercury oxidation should incorporate NO chemistry into the simulation. The work of Niksa et al. [187] also speculates that heterogeneous processes may be important in initiating the Hg oxidation sequence; experimental verification is needed.

3.4.2 Kinetic Modeling of Gaseous Mercury Oxidation

At the start of the Phase II effort and prior to initiating experiments, kinetic modeling of mercury reactions under post combustion conditions was done to provide a general understanding of the expected degree of reactivity of mercury in the flue gas under different conditions. In the kinetic modeling of mercury reactions, we studied the main factors affecting the degree of mercury oxidation. Based on previous studies, we concluded chlorine species concentrations, cooling rates, and temperature of the flue gas have all a strong effect on the amount of oxidized mercury in homogenous reactions. Chlorine species present in the Cl_2, HCl, and Cl forms were considered as potential oxidants.

3.4.2.1 Mercury and Chlorine Species at Specific Cooling Rates

Kinetics of Mercury Oxidation

To investigate the importance of reaction kinetics in determining the extent of mercury oxidation, kinetic calculations of mercury oxidation were conducted for conditions relevant to pulverized coal combustion. Two different kinetic models were considered. Global kinetics derived from studies of Hall et al. [180] and Gaspar et al. [179] were used to examine overall mercury oxidation under a range of conditions. To assess the importance of atomic chlorine, further kinetic calculations were conducted using elementary reactions derived from the early work of Sliger et al. [177].

As discussed in the previous section, Hall et al. [180] report data for total mercury and elemental mercury concentrations obtained in a flow reactor at a temperature of 500°C corresponding to a residence time of 1.5 seconds. Modeling the reactor as an isothermal plug flow device, a rate constant of $k= 1.07x10^{-15}$ $cm^3molecule^{-1}s^{-1}$ at 500 °C for the global oxidation of Hg by molecular chlorine is obtained. This rate constant represents a maximum possible value because of the uncertainties in gas thermal history and the likelihood that reaction occurred at temperatures greater than 500°C. It is of comparable magnitude to the value reported by Schroeder et al. [173], as $4x10^{-16}$ $cm^3molecule^{-1}s^{-1}$ for the same reaction under ambient conditions. Using these two values of the reaction rate constant and assuming an Arrhenius-type temperature dependence, the activation energy for this reaction is estimated to be 3.7 $kJmol^{-1}$.

For the global reaction with HCl to produce unspecified oxidized products, Gaspar et al. [179] report a rate constant of $k=2.20x10^{7}exp(-3460/T)$ $liters.mol^{-1}s^{-1}$ over the temperature range 400 to 900°C. This latter rate constant was derived from experiments conducted at HCl concentrations of 300 and 3000 ppmv, mercury concentrations of 0.37 ppmv, and approximate residence times of 1 second.

In considering the global reactions of Hg with Cl_2 and HCl, we evaluated oxidation considering both “reactions” simultaneously. The reason for doing this was that the rates were derived from studies in which only Cl_2 or HCl was injected, and thus represent reactions derived from those species alone. Since we believe Cl atom is responsible at the elementary level, this choice ignores interplay between Cl derived from Cl_2 and HCl, and could thus be considered a maximum rate of conversion.

Studies of the mechanism of mercury oxidation at temperatures of 600 °C and above by Kramlich et al. [188] suggest that the key oxidizing species is atomic Cl. We began by proposing a homogeneous pathway, governed by the principal steps,

$$Hg + Cl + M \Rightarrow HgCl + M \quad (3\text{-}31)$$

$$HgCl + Cl \Rightarrow HgCl_2 \quad (3\text{-}32)$$

$$HgCl + HCl \Rightarrow HgCl_2 \quad (3\text{-}33)$$

Kramlich et al. [188] note that super-equilibrium concentrations of Cl are required to account for observed $HgCl_2$ concentrations.

The consumption of elementary mercury in the mechanism proposed by Kramlich et al. [188] proceeds by the first reaction in the sequence. An average rate constant for this reaction, $1.5x10^{13}cm^3mol^{-1}s^{-1}$, is derived from the data of Horne et al. [182] and is equal to the value recommended by Kramlich et al. [188]. This value is approximately one order of magnitude less than the value derived from collision theory, $1.8x10^{14}cm^3mol^{-1}s^{-1}$. The rate constant for reaction two as a function of temperature was estimated from collision theory [189]:

$$k=\pi(\delta_{AB})^2(8k_bT/\pi m_r)^{0.5}p \quad (3\text{-}34)$$

where

p = 1 (steric factor, typical)
k_b = Boltzman constant
m_r = reduced mass
δ_{AB} = average diameter of hard spheres.

The information for the radius of each species was estimated from the National Institute of Standards and Technology (NIST) thermochemical webbook. Figure 3-175 gives the rate constant of the second reaction as a function of temperature from 273 to 973 K.

The rate constant for the third reaction in the sequence was estimated at a reference temperature (2000 K) from collision theory. Laidler [190] provides empirical methods to estimate activation energies based on enthalpies of reaction. In order to obtain a temperature dependency, an activation energy was estimated using the form:

$$k = k_{REF}\exp(-E/RT) \quad (3\text{-}35)$$

where k_{REF} in this case is estimated from collision theory at 2000 K. Using the Polanyi-Semenov equation, for exothermic reactions:

$$E = 48\ kJ/mol - 0.25\ Q \quad (3\text{-}36)$$

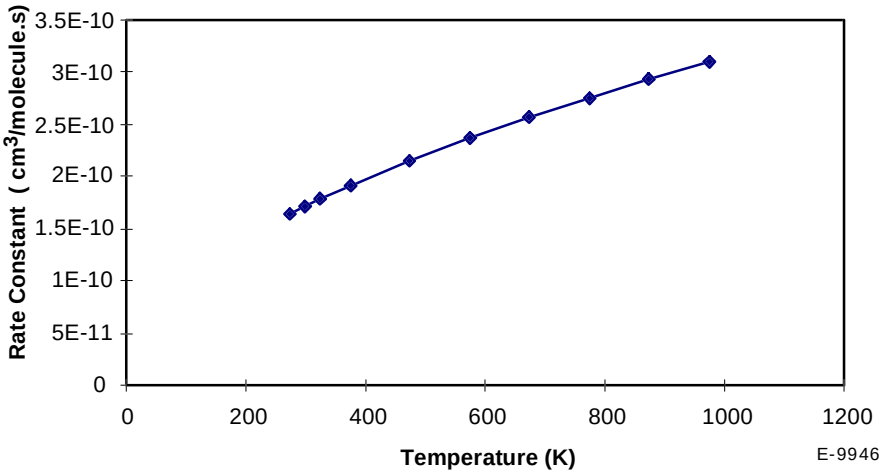

Figure 3-175. Rate constant of HgCl + Cl reaction as a function of temperature from 273 to 973 K.

where Q is the enthalpy of reaction. For the HgCl + HCl reaction the enthalpy of reaction is estimated to be 132 kJ/mol, base on NIST data. Thus the activation energy, E, is calculated to be 15 kJ/mol. The rate constant is therefore

$$k = 2.6 \times 10^{14} \exp(-15000/RT) cm^3/mol. \quad (3\text{-}37)$$

Results of Mercury Kinetic Calculations

Mercury consumption rates were derived from kinetic calculations conducted using both the global reaction sequence and the two primary steps of the mechanistic pathway. Mercury concentrations of 0.15 ppmw in the coal, corresponding to 0.01 ppmv (82 $\mu g/Nm^3$) in the flue gas, were used. Concentrations of the oxidants HCl, Cl_2, and Cl were taken from kinetic calculations of the combustion of CH_3Cl [174]. Reactions were examined at the isothermal conditions of 773 and 973 K as well as under cooling rates of 200 K/s and 500 K/s, in each case starting from a peak temperature of approximately 973 K.

In Figures 3-176 and 3-177, mercury conversion under isothermal conditions is presented as a function of HCl concentration at temperatures of 773 and 973 K, respectively. A residence time of 2 seconds was used in these calculations. Baseline Cl_2 and HCl concentrations were those obtained from the major constituent gas phase kinetic simulation at each temperature. Using the 773 K baseline concentrations of 0.013 ppm Cl_2 and 32 ppm HCl, mercury conversions of approximately 25% at 773 K and 45% at 973 K are obtained. In Figures 3-178 and 3-179 mercury conversion is presented as a function of Cl_2 concentration for the global kinetic sequence.

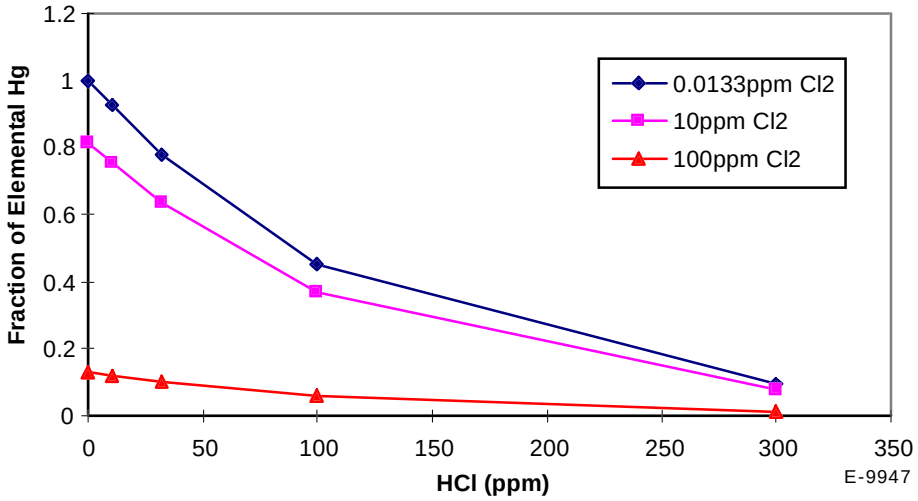

Figure 3-176. Hg conversion as a function of HCl concentration at 773 K using global kinetics.

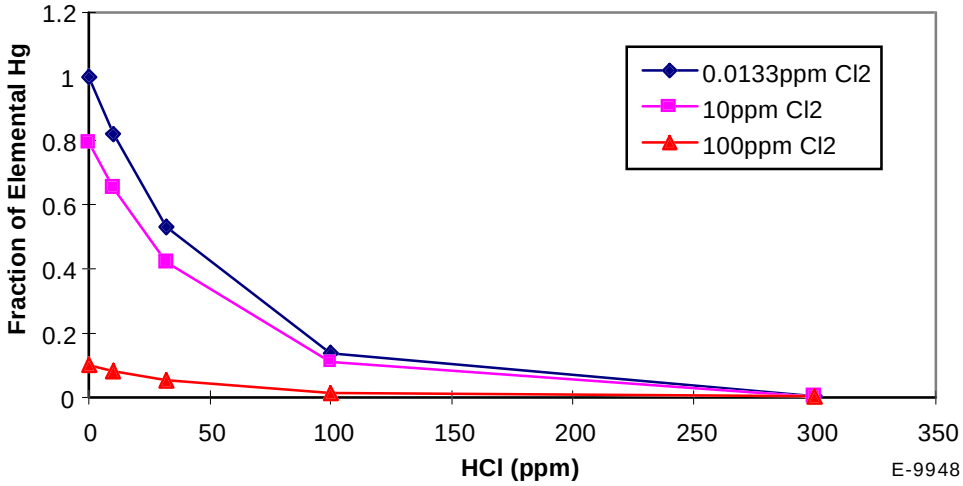

Figure 3-177. Hg conversion as a function of HCl concentration at 973 K using global kinetics.

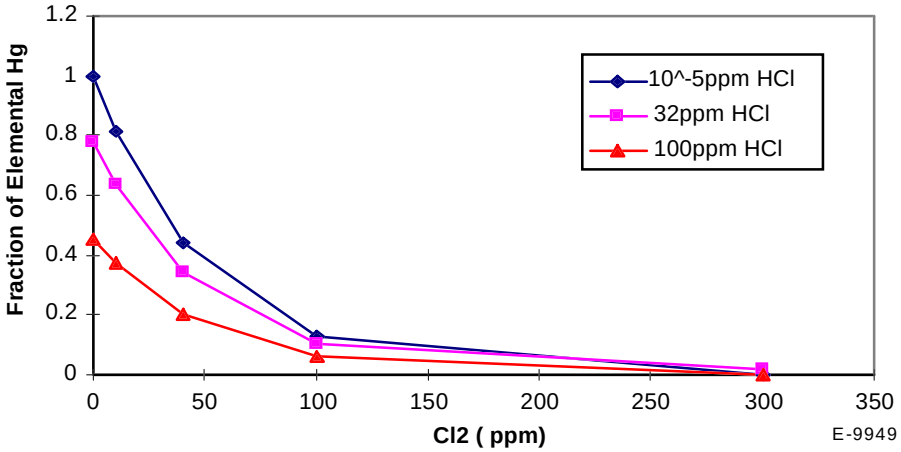

Figure 3-178. Hg conversion as a function of Cl_2 concentration at 773 K using global kinetics.

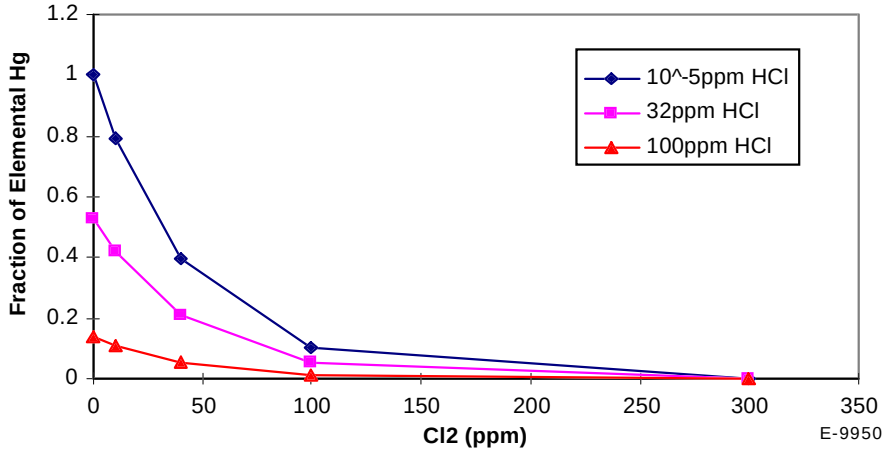

Figure 3-179. Hg conversion as function of Cl_2 concentration at 973 K using global kinetics.

To investigate mercury oxidation under thermal profiles associated with coal combustion, calculations using the combined global reactions were conducted at cooling rates of 200 and 500 K/s. Initial conditions for these calculations are presented in Table 3-126. As shown in Figure 3-180, mercury conversion is higher at the slower cooling rate, a result of increased residence time at higher temperatures. For the cooling rate of 200 K/s, an overall conversion of 24% is achieved in 2 seconds. At the higher cooling rate, an asymptotic value of 11% conversion is reached in 1 second.

Table 3-126. Initial Conditions for Global and Elementary Kinetics

-dT/dt	[Hg] (ppmv)	$[Cl_2]_0$ (ppmv)	$[HCl]_0$ (ppmv)	T range (K)
200 K/s	0.01	0.0046	32	962.6-300
500 K/s	0.01	0.0048	31.9	971.4-300

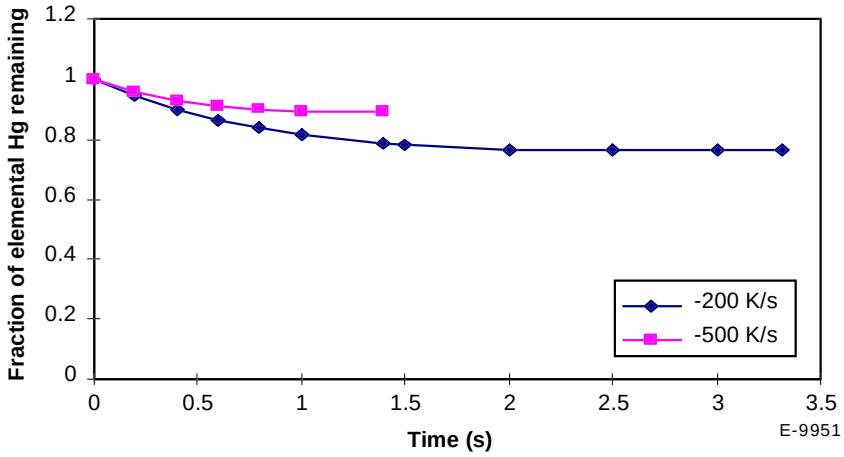

Figure 3-180. Hg conversion for two different cooling rates using global kinetics.

Mercury concentration profiles derived from the elementary reaction sequence at two different cooling rates are presented in Figure 3-181. Use of this reaction set is seen to result in complete conversion of elemental mercury within 200 ms. Order of magnitude reductions in the atomic Cl concentration were required to significantly reduce the conversion. Mercury conversions of comparable magnitude to the field data were obtained at atomic Cl concentrations of 0.00173 ppmv (Figure 3-182), one hundred-fold less than those suggested by the major constituent gas phase reaction chemistry. This suggests that accurate prediction of mercury speciation in coal combustion systems using a mechanistic model will require detailed knowledge of the super-equilibrium chlorine atom concentrations.

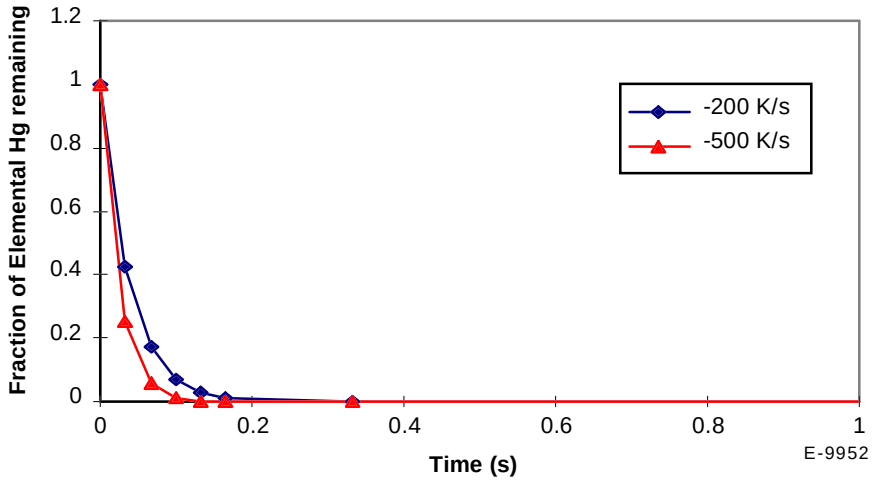

Figure 3-181. Fraction of elemental mercury converted for two different cooling rates using elementary reaction mechanism.

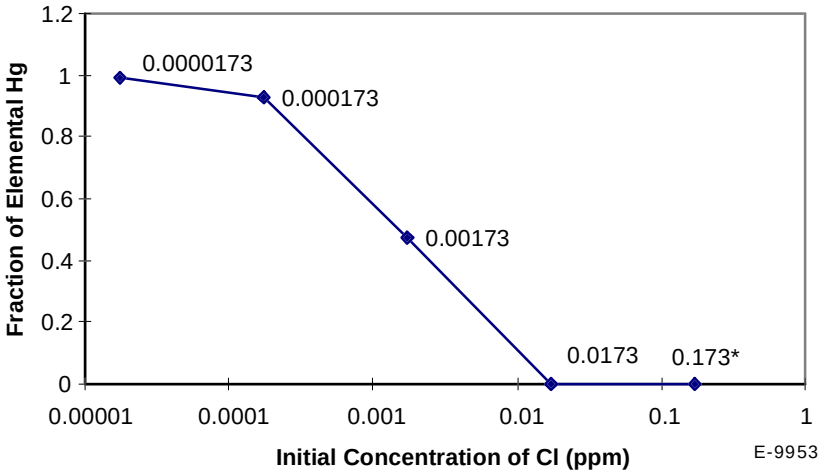

Figure 3-182. Hg conversion as a function of Cl atom concentration at 773 K and 1 second residence time using elementary reaction mechanism.

In summary, at air pollution control device (APCD) inlet temperatures, equilibrium predicts as much as half of the chlorine to be in the form of Cl_2, but kinetic calculations show that less than 1% of the chlorine is converted to Cl_2. Kinetic calculations of the homogeneous oxidation of elemental mercury by chlorine-containing species carried out using global reactions from the literature show that the levels of mercury oxidation, while of comparable magnitude to field observations, are still below the 40 to 80 % oxidation typically observed in field measurements. It is thus conceivable that heterogeneous reactions are also contributing to mercury oxidation in coal combustion systems. It must be stressed, however, that with the observed sensitivity of mercury conversion to Cl_2 concentrations, and the high level of uncertainty associated with field measurements of oxidized mercury at the low concentrations of stack gases, homogenous pathways alone may be important.

3.4.2.2 Mercury and Chlorine Species High Temperature Calculations

To extend Hg reaction calculations to higher initial temperatures, calculations using the global kinetic rates were also conducted using higher initial starting temperatures (Table 3-127). Calculations were conducted at initial temperatures of 1500 and 1200 K at a cooling rate of 200 K/s, and at initial temperatures of 1520 and 1220 K at a cooling rate of 500 K/s. The slight difference in initial temperatures was due to a desire to match the output of the chlorine calculations at the starting point.

Table 3- 127. Initial Conditions and Temperatures for Mercury Kinetic Calculations

Mechanism	**[Hg], ppm**	**[Cl2]o, ppm**	**[HCl]o, ppm**	**-dT/dt**	**T range, K**
Global kinetics	0.01	0.0001	31.4	200 K/s	1504-300
Global kinetics	0.01	0.0009	31.9	200 K/s	1204-300
Global kinetics	0.01	0.0001	31.3	500 K/s	1525-300
Global kinetics	0.01	0.001	31.8	500 K/s	1223-300

Results of these calculations are shown in Figures 3-183 and 3-184. In Figure 3-183, conversions of 50 to 80% were achieved after 2 seconds, corresponding to a cooling rate of 200 K/s and initial temperatures of 1500 and 1200 K, respectively. In Figure 3-184, conversions of 30 and 50% can be seen after 1 second, with initial temperatures of 1520 and 1220 K and a cooling rate of 500 K/s respectively. The final temperature is 300 K in all cases.

Comparing these results with those obtained at lower starting temperatures, conversions are in general much higher, not surprising given the higher initial starting temperature. Conversions to oxidized mercury are also observed to be within the range observed in field measurements (40 to 80% oxidation) when these higher starting temperatures are considered. Although global kinetic expressions were used to derive these results, it is instructive to note that chlorine atom concentrations are four times higher at 1520 K than at 970 K. The mechanistic assessment of the importance of chlorine atom in the oxidation of mercury is thus consistent with this finding, but it must be emphasized that it remains to be determined whether super-equilibrium concentrations of mercuric chloride can form at temperatures above approximately 1000 K, where equilibrium indicates that mercury should be present entirely as Hg(0) vapor.

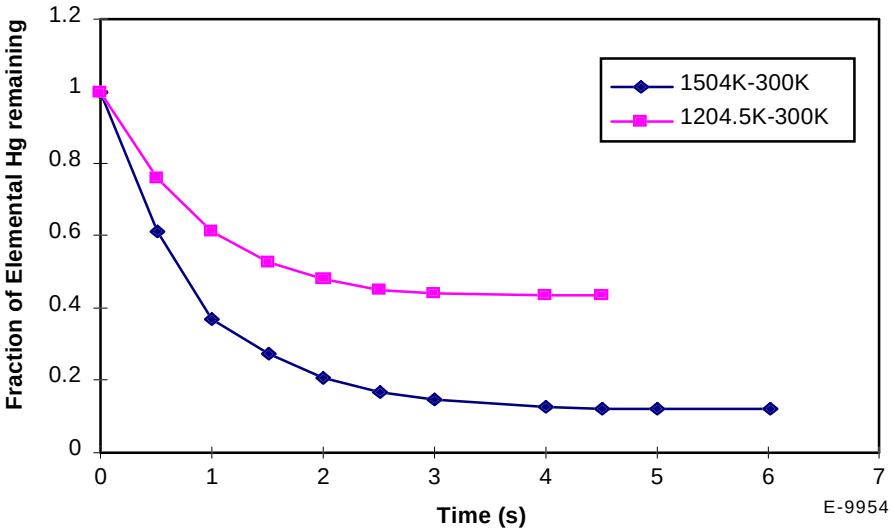

Figure 3-183. High temperature mercury oxidation at 200 K/s.

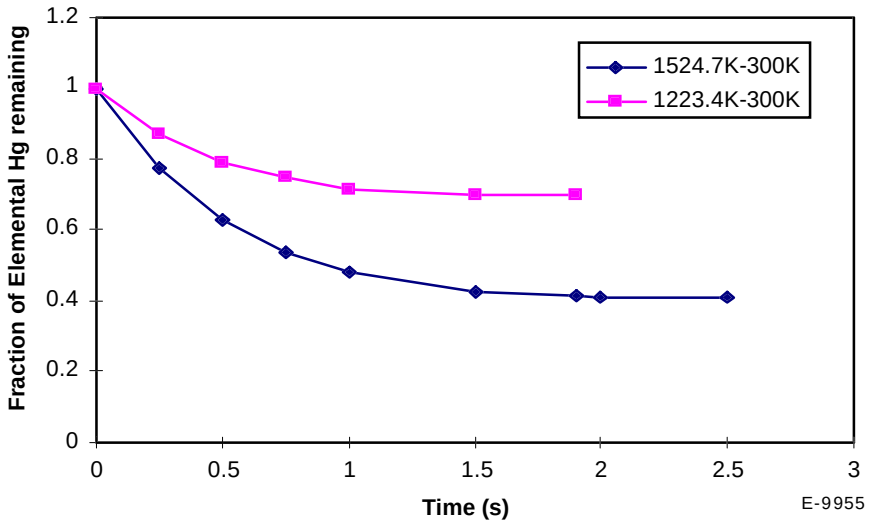

Figure 3-184. High temperature mercury oxidation at 500 K/s.

3.4.2.3 Mercury Reactions at Boiler Conditions

Additional calculations were conducted using a cooling rate calculated from the specifications for a small industrial boiler. The specifications and cooling rates derived from this calculation are provided in Table 3-128. Although the temperatures will be lower and the residence times in most sections shorter than those obtained in a large utility boiler, the shape of the temperature profile is representative of that encountered in a coal-fired utility boiler and thus can provide insight into the role of boiler temperature profile in mercury oxidation.

Table 3-128. Time-Temperature History of Effluent Gas

Location	**Tin, K**	**Tout, K**	**T-avg**	**Res. Time, s**	**Cooling rate, K/s**
Screen tubes	1368	1322	1345	0.025	1836
Superheater	1322	1147	1231	0.151	1163
Boiler bank	1147	711	903	1.162	1669
Rear cavity	711	708	709	1.162	3
Economizer	708	602	653	0.060	1766
Air heater	602	390	485	0.252 1.910328	842

Global kinetics and elementary kinetics were both used to determine mercury conversions attained at the end of the boiler using the temperature profile reported in Figure 3-185. The corresponding cooling rates are shown in Figure 3-186. Total Hg conversions are achieved within 0.2 seconds or less. The results are very similar to the ones observed at lower temperatures. Figures 3-187 and 3-188 show conversions similar to the Hg global reaction modeling done starting at 960 and 970 K reported previously. The conversions achieved were 23% for an initial temperature of 1370 K, and 13% for an initial temperature of 970 K. The sequences were run for 1.66 and 1.38 seconds, respectively. Note that the final observed conversions are below the 40 to 80% conversion reported in field measurements.

In summary, kinetic calculations were done under three different conditions: initial temperature of 973 K with –200 K/s and –500 k/s cooling rates, initial high temperatures of 1200 or 1500, with –200 K/s and –500 K/s cooling rates, and at boiler conditions with varying cooling rates. The results using the first and third conditions resulted in limited conversion of mercury, much below than the typical 40 to 80% field measurement Hg conversions. The results of the second condition are very similar to 40 to 80% Hg conversions. The total chlorine species concentration was kept at 32 ppmv, with variation in the distribution of Cl, HCl, and Cl_2, being HCl the most abundant, and Cl present in higher concentrations at high temperatures. These results imply that the temperature profile and cooling rates are important factors in the chemistry of chlorine and mercury species. We do not know how transcendent temperature profile is, therefore mercury transformation studies at specific temperatures profiles are important to provide trends of how cooling rates affect Hg conversion. The results of kinetic calculations show us that chlorine species concentrations are very important in the final conversion of mercury and that there seems to be a direct relation between initial chlorine concentration and final Hg conversion. The effect of changing Cl_2 and HCl concentrations on Hg conversion will

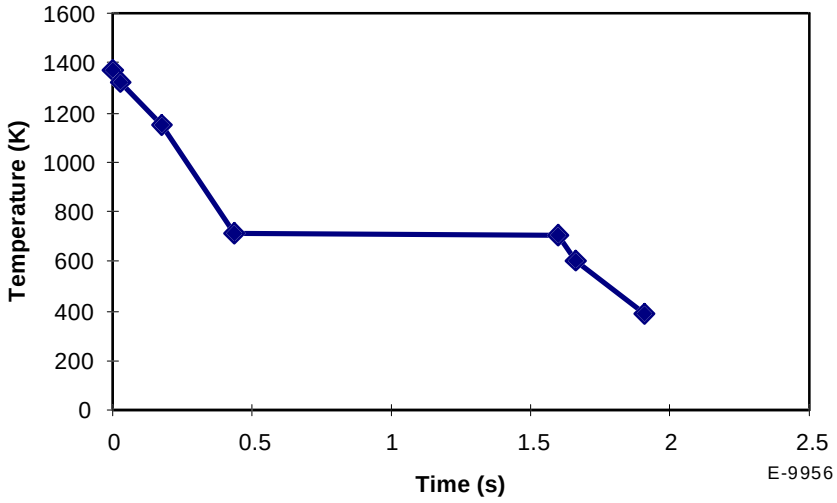

Figure 3-185. Calculated boiler temperature profile used in kinetic calculations.

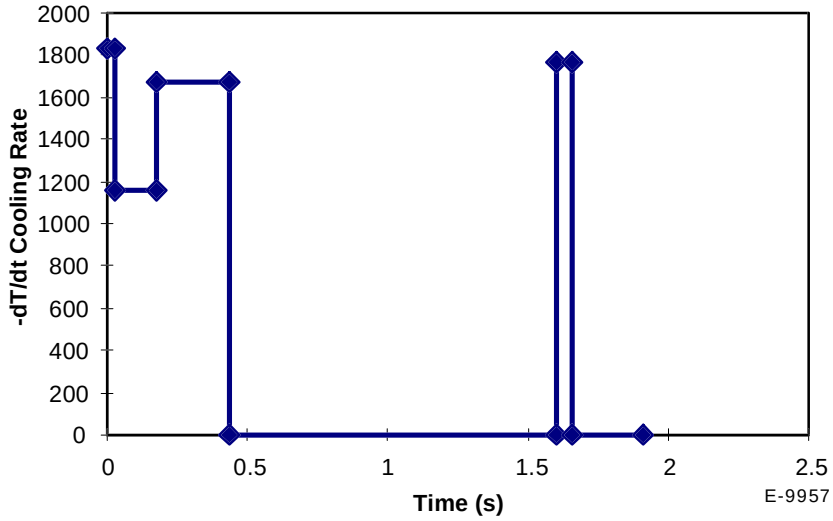

Figure 3-186. Calculated cooling rates for boiler temperature profile.

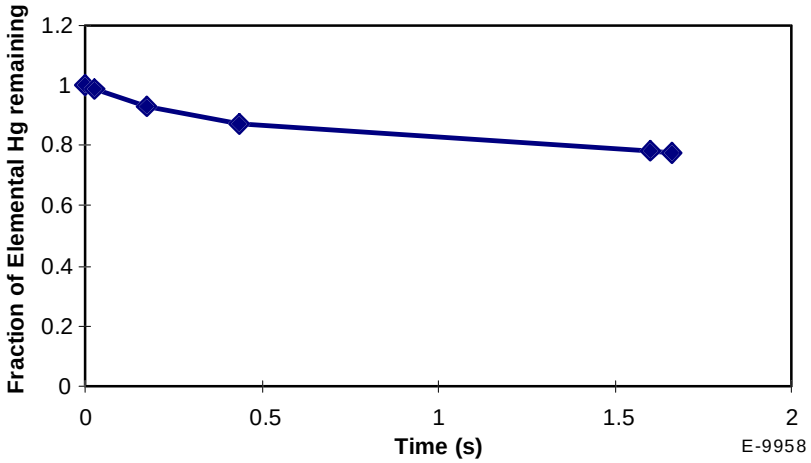

Figure 3-187. Conversion of Hg to $HgCl_2$ using boiler temperature profiles for calculations begun at 1370 K.

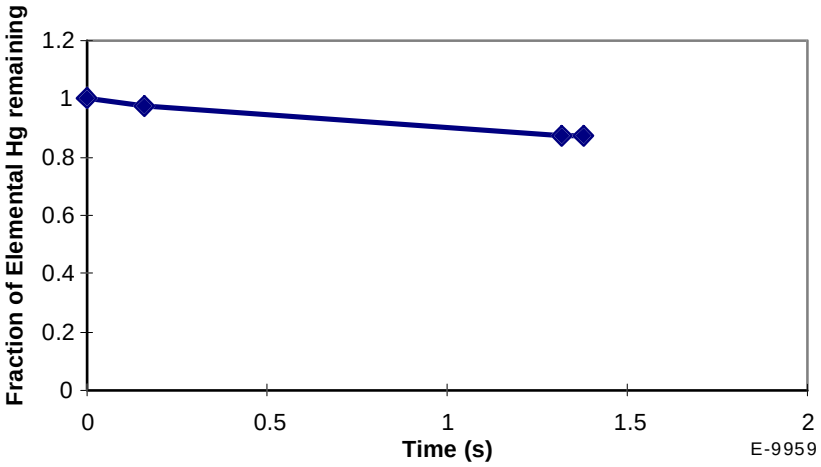

Figure 3-188. Conversion of Hg to $HgCl_2$ using boiler temperature profiles for calculations begun at 970 K.

be studied in experiments. Typical cooling rates will be used. We hope to get values from the kinetic rate constant in order to compare to the global kinetic model predictions. We expect they will agree to a good extent.

3.4.3 Bench-Scale of Investigation of Gaseous Mercury Oxidation

3.4.3.1 Introduction

The studies presented in the preceding section suggested that the presence of chlorine species (HCl and Cl_2), and temperature cooling rates were the most important factors affecting mercury oxidation. Molecular chlorine readily reacted with mercury. In the presence of a cooling rate (i.e., non-isothermal conditions), kinetic limitations were evident, according to several of the studies.

Most studies considered oxidation in the presence of HCl instead of Cl_2. The studies of Hall et al. [176], Hall et al. [180] and Galbreath et al. [181] showed that an excess of O_2 increased the degree of mercury oxidation by HCl. Ghorishi et al. [178] and Sliger et al. [177] concluded that the presence of water vapor has an inhibitory effect in the oxidation of mercury by HCl, meaning that higher concentrations of Cl atoms will be necessary to obtain previous oxidation results without the presence of water.

Past studies therefore demonstrated that HCl reacts with mercury at high concentrations and at high temperatures, and that molecular chlorine seems to be a more reactive oxidizing agent. Further, surface reactions may contribute, although high conversion by homogeneous pathways is reported under certain conditions. What remains unclear, however, is the influence of cooling rates in reactions of mercury with chlorine species. Experiments conducted under this program therefore focused on measuring mercury oxidation under cooling rates representative of the convective section of a coal-fired boiler to determine the extent of homogeneous mercury oxidation under these conditions.

3.4.3.2 Experimental System Design

A bench scale combustion system was constructed for the study of mercury transformations under a controlled gas environment. We wanted to study mercury reactions with chlorine species under typical cooling rates found at post-coal combustion conditions. The schematic diagram of this bench-scale facility is illustrated in Figure 3-189. It consists of a gas control panel, mercury generation unit, flat flame burner, mixing chamber, quartz tube reactor, probe, and an Ontario-Hydro analytical train. There are in total six feed lines of gases supplying both the flat flame burner and the mixing chamber. The quartz tube reactor was constructed with four sampling ports to permit flue gas sampling as a function of axial position (residence time). The tube itself was tilted five degrees from the horizontal to provide an outlet for condensed water on the inside walls as the flue gas cools down. The quartz reactor is not isothermal because we wanted to study the effect of cooling rates on Hg reactions. For this purpose, a flat flame burner is used to generate the desired high temperature flow which cools down as it travels the length of the quartz tube reactor. Details are provided in the following section.

Mercury Generation Unit

A mercury generation unit was assembled in order to provide the desired concentrations of mercury in the flue gas. It consists of a permeation device, a U-shape tube holder and a constant temperature heating bath. Figure 3-190 presents the configuration of the mercury generation unit and Figure 3-191 shows the relation of mercury permeation rate and bath temperature.

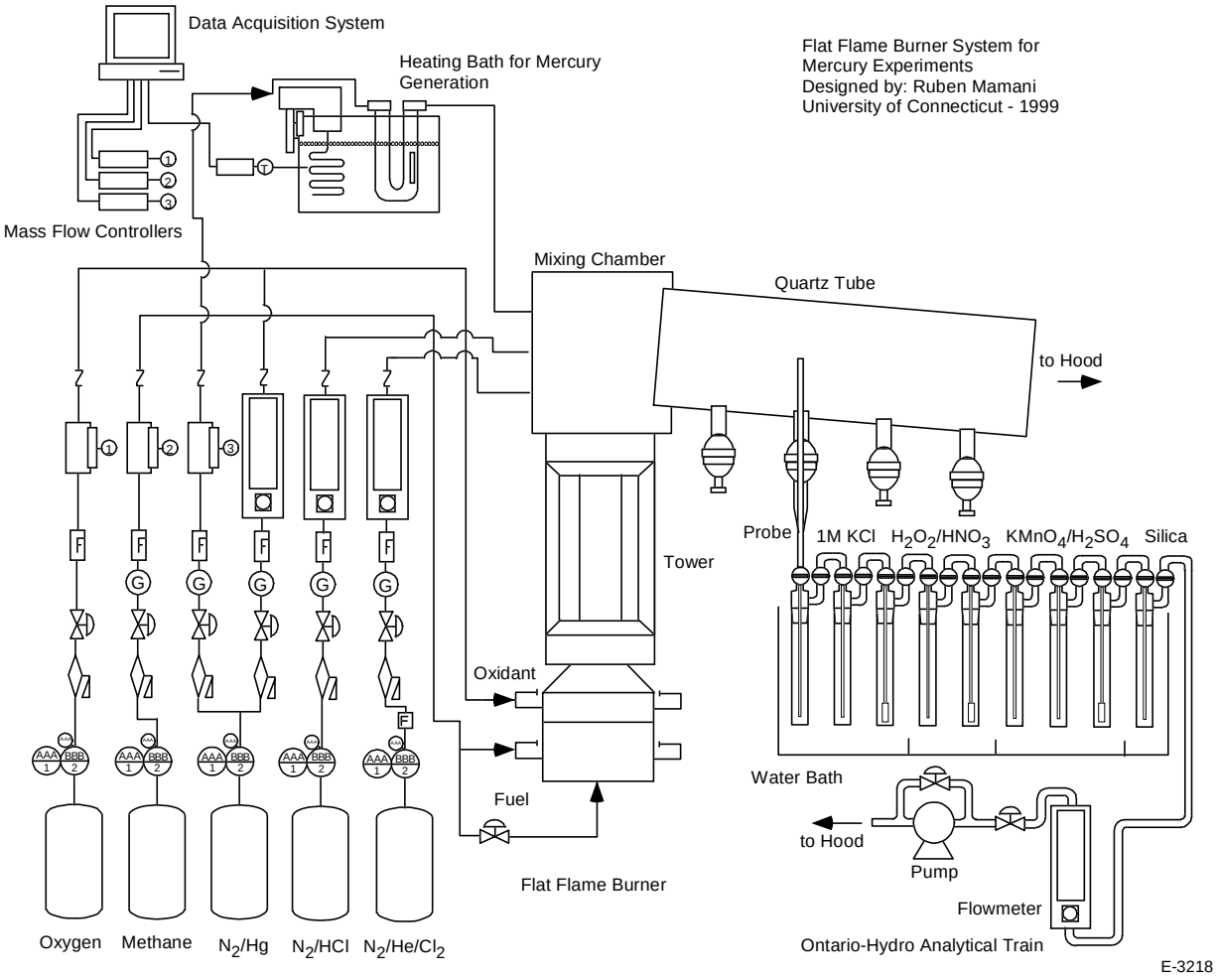

Figure 3-189. Experimental system for mercury oxidation experiments.

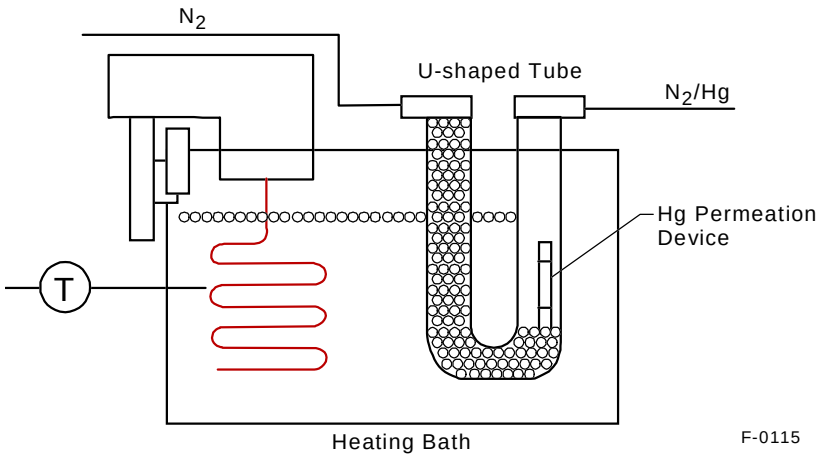

Figure 3-190. Mercury generation system

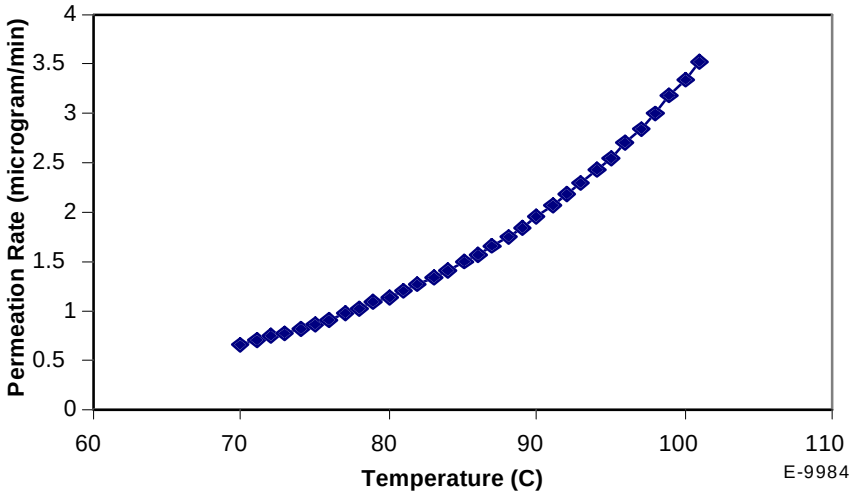

Figure 3-191. Permeation rate as a function of bath temperature (°C).

Permeation Device

A mercury permeation device from VICI Metronics is used to provide a steady feed of Hg to the reactor. The permeation rate (ng/min) as a function of the temperature was shown in Figure 3-191. The manufacturer (VICI Metronics) provided the following relation:

$$\text{Log(PR)} = \text{Log(3347)}+0.0234(\text{T-100}) \qquad (3\text{-}38)$$

to calculate the permeation rate (ng/min) of the permeation device at different temperatures. At 70°C the permeation rate corresponds to 665 ng/min, while at 100°C, it reaches 3347 ng/min.

U-shaped Tube Holder and Constant Temperature Heating Bath

The VICI mercury permeation device was placed on the right arm of the U-shaped tube holder. The tube holder is immersed in a constant temperature bath which is heated by a Fisher Scientific heater. Nitrogen (N_2) is used as the solvent gas for mercury and a specific volumetric rate is delivered to the mercury generation unit. N_2 enters the U-shaped tube holder from the left arm which contains glass beads (see Figure 3-190) to facilitate thermal exchange between the solvent gas and the heating medium. Next, N_2 carries the mercury generated from the permeation device and it exits through the right arm towards the mixing chamber.

The temperature of the heating bath is measured with an Omega thermistor which is connected to an Instrunet data acquisition system to provide a constant monitoring of temperature change. The liquid used in the heating bath is a mixture of standard automotive anti-freeze and water (1/3 parts of anti-antifreeze per 2/3 parts of water) in order to avoid rapid evaporation at working temperatures (70 to 100°C). In addition, Nalgene polypropylene plastic spheres (1/2 in. in diameter) were placed on top of the heating medium to minimize heat loss through evaporation and at the same time provide insulation. The heating solution required about 5 hours to reach steady state temperature.

The total volumetric flow of the flue gas determined ultimately the working temperature of the heating bath. The desired mercury concentration in the flue gas was approximately 50 $\mu g/m^3$. The total flow of the flue gas was determined to be 31 slpm. With the total volumetric flow, the time of operation of our experiments, and the desired mercury concentration, the temperature of operation was determined to be 85°C (See Table 3-129).

Table 3-129. Mercury Concentrations for Different Constant Heating Bath Temperatures

Temperature (°C)	**Hg Permeation Rate (μg/min)**	**At 30 slpm [Hg] ($\mu g/m^3$)**	**At 31 slpm [Hg] ($\mu g/m^3$)**	**At 32 slpm [Hg] ($\mu g/m^3$)**
70	0.665	22	21	21
75	0.870	29	28	27
85	1.492	51	50	48
95	2.557	85	82	80
100	3.347	112	108	105

Burner System, Mixing Chamber and Quartz Reactor

Flat Flame Burner and Viewing Tower

The central part of this system is a multi-element flat flame diffusion burner with central feed tube, manufactured by Research Technologies Inc. of Pleasanton, California. According to the manufacturer, the burner operates at optimum conditions between 25 and 40 standard liters per minute (slpm). The burner will operate under slightly fuel-lean conditions in all experiments.

Mixing Chamber

A stainless steel mixing chamber was placed directly on top of the burner as shown in Figure 3-189. The chamber itself has three incoming lines (N_2/Cl_2, N_2/HCl, and N_2/Hg) and a wide (13.5 cm) outlet to support the quartz reaction tube. The mixing chamber receives the gases resulting from the oxidation of methane (CO_2 and H_2O) and nitrogen. Mercury, HCl and chlorine are fed into the system through this unit, using nitrogen as carrier gas. Table 3-130 presents the temperatures obtained at the center of the outlet of the mixing chamber with different gas flow conditions (radiation error corrected).

Table 3-130. Radiation Corrected Temperatures at Outlet of Mixing Chamber

Run	1	2	3	4
Equiv. ratio	0.4	1	1	1
CH_4 slpm	2	3	4	4
O_2 slpm	10	6	8	8
N_2 slpm	14	17	14	17
Temperature center (°C)	532	775	804	858

It should be noted that these temperatures do not reflect the temperature inside the mixing chamber, which is much higher and which is reported in the following sections. Based on these results, gas flow conditions of Run 4 (Table 3-130) were selected for use in actual Hg oxidation experiments. The highest temperature (858°C) is reached under these flow conditions.

Quartz Tube Reactor

The outlet of the mixing chamber is connected to an 80-cm quartz tube which is inclined about 5 deg from horizontal in order to provide an outlet for water condensed on the inside walls. There are four side connectors along the quartz tube. The flue gas passes through the quartz tube and it is cooled as it exits to the hood. Four side connectors are used to insert the quartz probe which will sample flue gas at different distances along the length of the quartz tube. The quartz probe samples flue gas from the middle of the reaction tube. A thermocouple wire is attached to the quartz probe through a thin capillary tube inserted at the same time as the probe to monitor temperature at the sampling point.

Flame Temperature Profiles

In order to understand the temperature profile of the quartz tube reactor under the selected gas flows (N_2=17 slpm, O_2= 8 slpm, and CH_4= 2 slpm), the temperatures inside the tube were measured at different heights and distances away from the mixing chamber. Figure 3-192 displays the temperatures measured at 0, 3.75, 6.5, 9.75, and 13 cm from the bottom of the tube and along the centerline from the bottom of the tube upwards. These temperatures distributions were measured at the four inlets of the quartz tube reactor, located at 10, 30, 50 and 70 cm from the beginning of the tube. By looking at Figure 3-192 we can determine that the temperature in the flue gas is not evenly distributed, with the warmest region being at the top and center of the tube. The lowest temperatures are observed near the bottom of the quartz tube. Because the temperatures achieved in the center of the quartz tube are slightly lower than desired, heating tapes were wrapped around the quartz tube just after the mixing chamber. Figure 3-193 shows

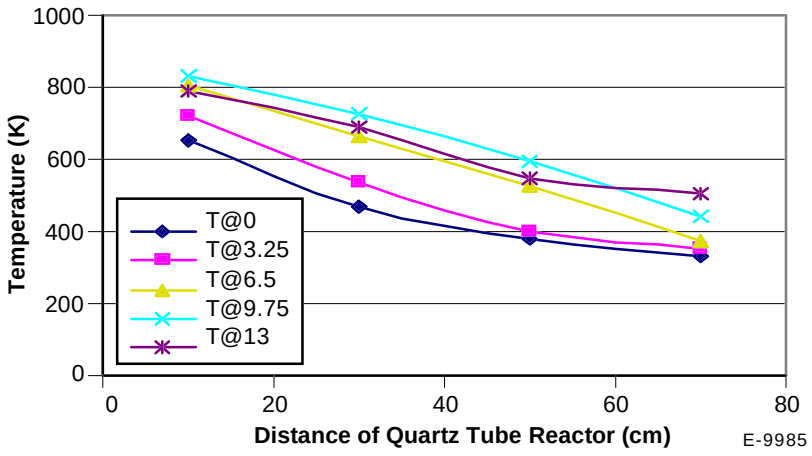

Figure 3-192. Temperature profile in quartz tube reactor.

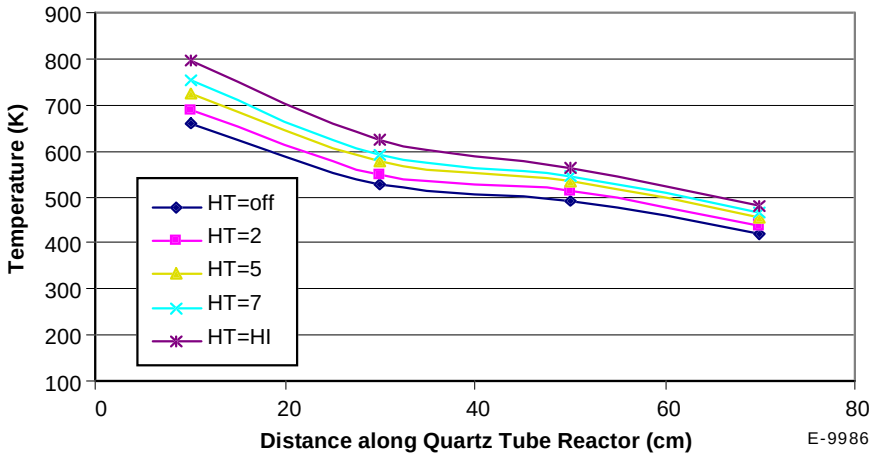

Figure 3-193. Temperature profile with varying heating tape settings

the effect of different heating tape settings on the temperature of the center of the tube, at different distances along the reactor. The highest settings (HI) were selected for all subsequent mercury oxidation experiments in order to approach temperatures close to coal post-combustion conditions.

Residence Time in Reactor

The residence time of the flue gas in the quartz tube reactor was used to estimate cooling rates at different sampling points (See Figure 3-194). Figure 3-195 shows the change in temperature as a function of distance from the center of the mixing chamber (approximately 15 cm above the flame surface) to the end of the quartz tube. Based on the total volumetric flow rate of 31 slpm, the ideal gas law was used to calculate flow at different temperatures. These volumetric flow values were then used to estimate the average velocity of the gas, v, at different points of the quartz tube reactor by using the cross-sectional area (Figure 3-196). Table 3-131 presents this information. With this information, residence times at the different sampling ports were obtained and are listed in Table 3-132. With the information of temperature and time at the different sampling ports, the cooling rates at such points were calculated and are also shown in Table 3-132. The cooling rates fall into the expected range, being 398 K/s at the first port and lower at the other three ports.

Flue Gas Sampling

The quartz probe conducts the flue gas into the Ontario-Hydro analytical train through quartz connectors build specially for the system. The Ontario-Hydro analytical train consists of nine impingers containing three kinds of solutions to capture oxidized and elemental mercury. A vacuum pump is used to generate a pressure difference in order to sample flue gas. The flow rate is measured by a rotameter before the gas exits to the fume hood.

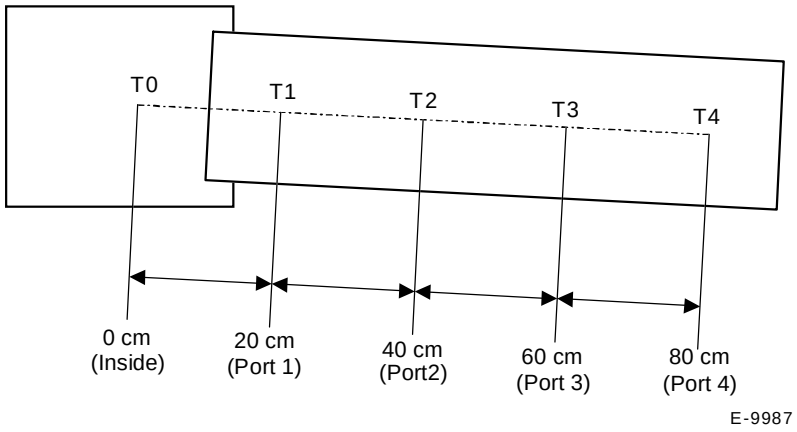

Figure 3-194. Temperature sampling points through quartz tube reactor.

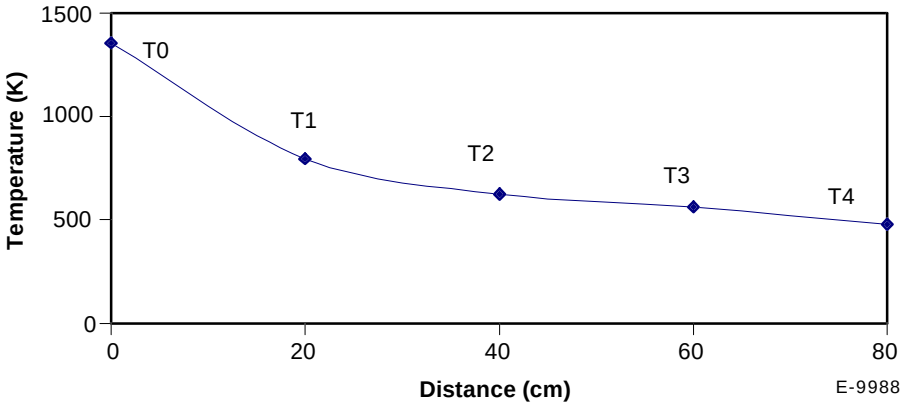

Figure 3-195. Temperature as a function of distance.

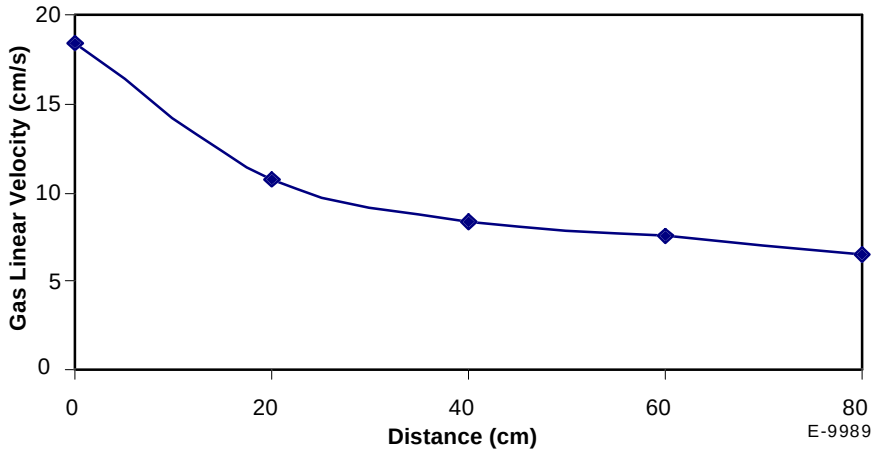

Figure 3-196. Gas velocity as a function of distance.

Table 3-131. Volumetric Flow Rates and Velocities at Different Distances from the Center of the Mixing Chamber (31slpm)

Sampling Point	Temperature, °K	Volumetric Flow l/min	Velocity of gas cm/s	Distance cm
T0	1373	138	18.5	0
Port 1, T1	795	80	10.7	20
Port 2, T2	624	63	8.4	40
Port 3, T3	561	56	7.6	60
Port 4, T4	479	48	6.4	80

Table 3-132. Residence Times and Cooling Rates at Different Sampling Points

Sampling Points	Temperature °K	Residence Times	Distance cm	Cooling Rate °K/s
T0	1353	0	0	N/A
Port 1, T1	795	1.4	20	398
Port 2, T2	624	3.6	40	78
Port 3, T3	561	6.2	60	25
Port 4, T4	479	9.0	80	29

Mercury Speciation Methods

Table 3-133 presents different advantages and disadvantages of mercury speciation sampling methods. The Ontario-Hydro method was selected since there is not a presence of SO_2 in our system. The Ontario-Hydro method is also a standard method for the determination of oxidized, elemental and particular mercury adopted by the Environmental Protection Agency. The Ontario-Hydro method is a derivative of EPA Method 29 developed specifically to capture gas phase mercury compounds. The main difference with EPA method 29 is that the first two acidified peroxide solutions are replaced by three impingers containing a solution of 1N potassium chloride dissolved in deionized water, the reason being that the acidic peroxide impingers were also capturing elemental mercury according to different studies [191].

Table 3-133. Trace Mercury Speciation Measurement Methods

Method	Advantages	Disadvantages
1. EPA Method 29	- Well known - Simple collection system	- Not specific for Hg. - Overestimation of Hg.
2. Ontario-Hydro	- Small variation of EPA method 29	- Loss of Hg if SO_2 is present.
3. Tris Method	- Removes Hg^{+2} without removing HgO	- Flue gas volume needs to be controlled carefully. - Possible loss of Hg.
4. Carbon Adsorption	- High specific area for adsorption. - Removal of Hg at low concentrations	- Compounds in sorbents oxidize Hg or vice versa. - Adsorption mechanisms not purely physical.
5. MESA	- High Specific area for adsorption. - Removal of Hg at low concentrations	- Presence of SO_2 and NO_x causes disturbance in measurements.

Ontario-Hydro Method (EPA Standard)

The Ontario-Hydro Method has become the U.S. Environmental Protection Agency standard test method for elemental, oxidized, particle-bound, and total mercury in flue gas generated from coal-fired stationary sources. The set up for the Ontario-Hydro sampling train is presented in Figure 3-197.

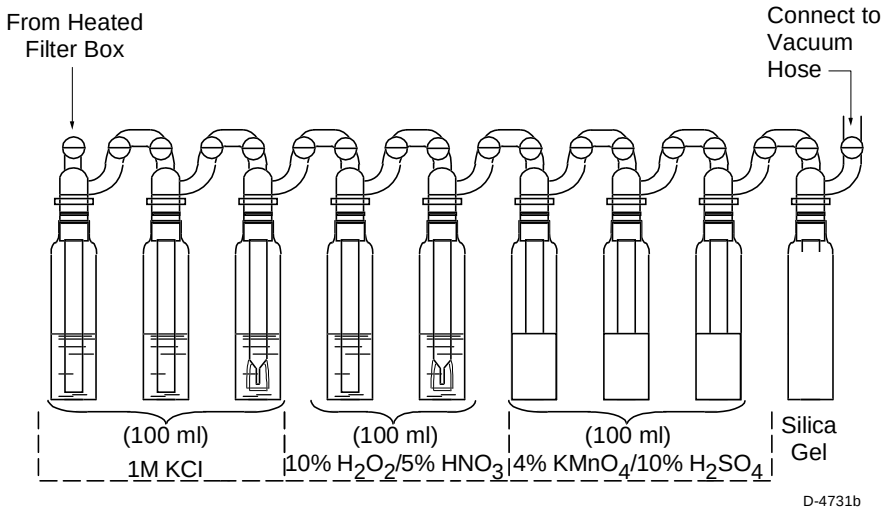

Figure 3-197. Ontario Hydro sampling train.

This method is applicable to total mercury concentrations ranging from approximately 0.5 to 100 μg/m^3 in the flue gas. This method can be used for sampling elemental, oxidized, and particle-bound mercury at the inlet and outlet of emission control devices and for calculating control device mercury collection efficiency. The volumetric flow of flue gas sampled should be between 1 dry cubic meters corrected to standards conditions (dcsm) and 2.5 dscm.

Total sampling for the method is between 2 and 3 hours. The use of this method is limited to flue gas stream temperatures kept within the thermal stability range of the sampling probe and filter components. A sample needs to be withdrawn from the flue gas stream isokinetically through a probe/filter system, maintained at 393 K (120°C) or the flue gas temperature, whichever is greater, followed by a series of impingers in an ice bath. Particle-bound mercury can be collected in the front half of the sampling train through a glass filter. Oxidized mercury is collected in impingers containing a chilled aqueous potassium chloride solution (1N KCl). Elemental mercury is collected in subsequent impingers. One impinger containing a chilled aqueous acidic solution of hydrogen peroxide (5% HNO_3, 10% H_2O_2) and three impingers containing chilled aqueous acidic solutions of potassium permanganate (4% $KMnO_4$/10% H_2SO_4). Figure 3-197 presents the volumes of the solutions present (100 ml) and the configuration of the train. Samples are recovered, digested, and then analyzed for mercury using cold-vapor atomic absorption (CVAA) or fluorescence spectroscopy (CVAFS). CVAA detection limit is approximately 0.2 ng/ml. (EPA Method 29 Guidelines). The analytical chemistry lab at the University of Connecticut Environmental Research Institute (ERI) has CVAA instrument with a detection limit is 0.08 μg/l and was therefore used in this study.

The prescribed sampling train was modified in our system by not including a filter for the capture of ash particles. Since we are burning methane, no fly ash is generated. Another modification was the addition of a second impinger to the 5% HNO_3,10% H_2O_2 solution because more than 20% of the flue gas will be present as water. Method guidelines recommend adding one more impinger under these conditions.

Since the total flue gas in our system was about 31 slpm, 15 slpm were sampled for about 1 hour, giving a high enough amount of mercury sampled. The expected recovery is in the order of 45 μg for total mercury sampled.

3.4.3.3 Experimental Procedures

Preliminary Procedures

A specific protocol was developed and then implemented prior to each experiment. First the heating bath of the mercury generation was set to the desired temperature and turned on about four hours before running experiments. The temperature in the bath was monitored continuously through a thermistor connected to the data acquisition system. Most of the Ontario-Hydro solutions were prepared the previous day, with the exception of the 4% w/v $KMnO_4$, 10% v/v H_2SO_4 solution. Three hundred fifty ml of this solution were prepared daily according to Ontario Hydro E.P.A. guidelines. In preparing all solutions, all glassware was first rinsed three times with deionized water.

The Ontario-Hydro train impingers (Ace Glass Inc.) were then each filled with 100 ml of their respective solutions. Each impinger has a 500 ml capacity. The first three impingers contained 1 M KCl, the next two impingers 10% v/v H_2O_2 / 5% v/v HNO_3, and the following three impingers, the freshly prepared acidic permanganate solution. The last impinger contained approximately 300 g of dried silica gel. The impingers were then weighed, and the impinger train then assembled inside a rectangular container located just below the quartz tube reactor. U-glass adapters were used to join one impinger to another, and the last impinger (silica gel) was connected to the vacuum pump and rotameter. The rectangular container was then filled with ice and water. The train was checked for leaks by starting the vacuum pump and closing the inlet of the Ontario Hydro impinger train.

Mass flow controllers are then adjusted to the desired setting, and the mercury permeation device placed in the U-shaped tube (VICI Metronics) once a temperature of 85°C was reached in the heating bath.

Combustion Procedure

To ignite the flame in the flat flame burner, the quartz tube reactor and mixing chamber were first disassembled. The burner was ignited as a true diffusion flame with no supplied oxidizer, using a low flow of methane (around 2 slpm) and a small spark igniter. Oxygen and nitrogen were then added to the burner with flows regulated by the mass flow controller and rotameter, respectively. Flow was adjusted slowly to 4 slpm for O_2, and 10 slpm for N_2. With

this low volumetric flow (16 slpm) the quartz tube reactor was then connected to the mixing chamber. The quartz tube connector was set in place by two chain clamps attached to a metal frame. It has upwards mobility by loosening the clamps slightly. In order to seal the mixing chamber and quartz tube reactor, furnace cement was mixed and used to fill gaps.

Once the quartz tube reactor was in place, a quartz probe carrying a type K thermocouple was connected to one of the four sampling ports. This quartz probe was then connected to the Ontario Hydro impinger train through quartz/glass adapters discussed above. The other ports were kept closed or another quartz probe with a thermocouple was inserted for additional temperature measurement.

High temperature heating tapes placed around the quartz tube reactor at the end closest to the mixing chamber and extending along the length of the tube were then adjusted to their desired setting. Regular heating tapes were also placed around the glass adapters leading to the Ontario-Hydro impinger train. Temperatures were kept above 200°C or above according to Ontario-Hydro guidelines. The inlet stainless steel line that feeds mercury doped N_2 into the mixing chamber was also surrounded by heating tapes set to the highest settings. The heating tapes were turned on as soon as the mixing chamber and tube quartz reactor were connected.

During an experiment, methane, oxygen flow rates and pure nitrogen were set to 4 slpm, 8 slpm and 17 slpm, respectively. Nitrogen for chlorine, hydrochloric acid and mercury flows were then initiated. The flow rate of these streams was typically 1 slpm, but varied according to the requirements of each experiment. Flue gas sampling was then started by turning the pump on at the outlet of the impinger train. Each experimental run lasted 1 hour.

An alternative flue gas sampling technique was also used for the determination of total mercury in selected experiments. It involved the use of coconut derived, steam-activated charcoal bead cartridges (12x30 mesh, 200 mg) doped with 5% potassium triiodide provided by M.I.T. as part of this project. A quartz probe was inserted to one of the quartz tube reactor outlets. This probe was connected through adapters to the charcoal cartridge. The charcoal cartridge was kept at 105°C through the use of heating tapes and thermocouples attached to a Love Control device. The gas was maintained at 1slpm for one hour, and controlled through a pump and rotameter. A drierite cartridge was installed after the charcoal cartridge to capture moisture and prevent clogging of the rotameter. This system was both set up at the same time as the Ontario-Hydro method and as an alternative for different runs.

Sampling Preparation Procedures

Once the flue gas sampling was finished, the system was left to cool for a few minutes. The mercury permeation device was taken out of the U tube with the aid of ventilation and under the hood and saved under refrigerated conditions for future experiments.

KCl Impingers

The impinger train was disassembled and the first three impingers (1 M KCl) weighed and recorded. A small volume of acidic permanganate solution was added to each for stabilization of mercury compounds. The impingers were shaken up and down for a few minutes and their volumes measured. All of the contents were then poured in a labeled 500 ml dark sampling bottle. Each impinger was rinsed with about 25 ml of 0.1 N HNO_3 solution, and the rinse poured in the sampling bottle. The first two U-glass adapters were also rinsed with about 20 ml of 0.1 HNO_3 and poured into the sampling bottle.

HNO_3/H_2O_2 Impingers

The third and fourth impingers were weighed and their weight recorded. Their volume was measured before pouring the contents into a clear 500 ml sampling bottle. Each impinger was then rinsed with 25 ml of 0.1 N HNO_3 solution. The volumes were then record ed before pouring the contents in the sampling bottle. The next two U-glass adapters were also rinsed with 25 ml of 0.1 N HNO_3 solution and poured into the 500 ml glass sampling bottle.

$KMnO_4/H_2SO_4$ Impingers

The fifth through seventh impingers were also weighed and shaken vigorously. Their weight and volume were measured and their contents poured into a 500 ml brown sampling bottle. Each of the impingers was then rinsed with 25 ml of 0.1 N HNO_3 solution and their volumes poured into the sampling bottle. Each of the impingers was also rinsed vigorously with 25 ml of 8 N HCl solution and their contents poured into the sampling bottle. A final rinse of 25 ml of 0.1 N HNO_3 solution was done for each impinger. The objective of the rinsing was to dissolve dark residues on the sides of the impingers. These procedures were done under the hood since vapors were evolved after mixing. The level of the liquid in the bottle was marked and a cap is placed loosely on the bottle.

The three sampling bottles were closed with their respective caps and they were then refrigerated and saved for later digestion. The weight of the silica gel impinger is also recorded.

Cleaning Procedure

After all the solvents are taken out, 10% v/v Citranox cleaning solution and water were used to brush and clean impingers and glass adapters. Next, all the glassware was placed under a 10% v/v HNO_3 solution for 4 hours. At the end of this time, the pieces were taken out and rinsed with deionized water three times and left to dry for the next series of experiments.

Analytical Procedures

Cold Vapor Atomic Absorption

Each Ontario-Hydro experiment resulted in three solution samples containing mercury. These samples were refrigerated and stored as described above. After many runs, the samples were taken to the Analytical Laboratory at the Environmental Research Institute (ERI), University of Connecticut, and analyzed using CVAA. The detection limit for CVAA is about 0.2 ng/ml, and the precision is 11% for mercury concentrations greater than 3μg/Nm^3 (Ontario-Hydro E.P.A. guidelines). According to ERI, the detection limit for their measurements is 0.08 μg/l of analyzed solution. The precision of the reported concentration is 10%.

Neutron Activation Analysis

The total amount of gas phase mercury present in a sample was captured by adsorption in the charcoal cartridges. The samples were then sent to Dr. Michael R. Ames, at the Environmental Research and Radiochemistry Center at M.I.T. For analysis the samples were neutron -irradiated in a nuclear reactor and the resulting mercury gamma ray emission measured to give a concentration of mercury in the charcoal. The detection limit is 5 ng of mercury per 200 mg of charcoal.

3.4.3.4 Experimental Data and Analyses

Results and Discussion

To assess the homogeneous speciation of mercury in the presence of selected oxidizing species, approximately 30 experiments were done under a range of oxidant concentrations. Three kinds of solutions were obtained in most experiments. The first container (KCl solution impingers, F1) contained oxidized mercury, while elemental mercury was present in the second (peroxide solution impingers, F2) and third (acidic permanganate solutions, F3) containers.

Summaries of the results of all the experiments conducted using the Ontario-Hydro impinger-based speciation method are shown in Appendix L, Tables L-1 through L-5. The first column of these tables presents the sample identification numbers for sets of three solutions corresponding to a single Ontario Hydro experimental run. An exception is found in experimental runs 20, 21, 22, 25, 26, and 27, where only KCl solution is reported. The second column indicates the sampling port and the flue gas sampling method (Ontario Hydro = OH, carbon adsorption = CHR). The third column shows the reactants involved and their concentrations in the flue gas in parts-per-million by volume (ppm). The fourth column reports the concentration of mercury in μg/liter of the Ontario Hydro impinger solutions measured by CVAA.

The fifth column in each table indicates the sample volume for each solution and the sixth column presents the amount of mercury captured in units of μg. The seventh column represents the expected total mercury recovery. The eighth column shows the percent of oxidized mercury in each experimental run. Results of selected experiments conducted using a combination of

Ontario Hydro impingers and charcoal cartridges, or conducted with cartridges alone, are also shown in this column.

Blank and Spiked Sample Testing

With the objective of testing the reproducibility of the CVAA analytical method used to determine mercury concentrations, blank experimental runs were performed and mercury spiked sample solutions were prepared. Experiments 1 and 10 (Table L-1) were blank experimental runs conducted without mercury but in presence of a flame. Experiments 2, 3, 8 and 9 (Table L-1) consisted of standard mercury test solutions prepared using Ontario Hydro USEPA draft guidelines, with no gas sampling involved.

Blank experimental runs were performed with the burner flame operating at a total gas flow rate of 30 slpm and an equivalence ratio of 1. The temperature profile for these two runs included an average mixing chamber temperature of 1080 °C. Flue gas sampling was done through the Ontario Hydro impinger train at a sampling temperature of 520°C (Port 1). The reaction time at this point is approximately 1.4 s. The flue gas was sampled continuously for 60 min, at a constant gas sampling rate of 15 slpm.

From the Ontario Hydro impinger train, three solutions were prepared according to the Ontario Hydro Method guidelines. KCl solution (F1) was used for oxidized mercury capture. Solutions of acidified peroxide (F2) and potassium permanganate (F3) were used for elemental mercury capture. The results of CVAA analysis are presented in Table L-1. In both experiments (EXP1 and EXP10), the KCl and peroxide solutions were reported as having no mercury present. The permanganate solution results showed a mass of 2 μg mercury. The results of KCl and H_2O_2 solutions reflected accurate measurements while the permanganate solution reflected an overestimation of 2 μg of mercury.

Mercury standard solution (VWR Inc., with a mercury concentration of 0.1+-0.001mg per 1 ml of solution) was used to prepare diluted mercury solutions of 10 μg/ml, 1 μg/ml, 0.1 μg/ml, and 0.01 μg/ml. These diluted solutions were used in the preparation of the "spiked" mercury solutions submitted for CVAA analysis. The "spiked" mercury solutions correspond to the three sampling solutions used in the Ontario Hydro sampling train: KCl solution for oxidized mercury capture, and peroxide and permanganate solutions for elemental mercury capture.

Experiments 2 and 3 were "spiked" solutions prepared with both low and high mercury concentrations. High concentration samples (Experiment 2, Table L-1) were prepared with calculated mercury concentrations of 200 μg/liter for the KCl container, and 130 μg/liter for the acidified peroxide and permanganate solutions, respectively. For the KCl container, the measured Hg was 11 μg less than the expected Hg mass. For the peroxide container a difference of 8 μg between measured (CVAA) and expected Hg mass was reported with the measured mass again being lower. For the permanganate container a difference of 5 μg between measured (CVAA) and expected Hg mass was observed, again, the measured mass was the lower value. The total measured mass of Hg was 175 μg, about 23 μg less than the expected 198 μg. At these

high concentrations, the accuracy was rated good since all of the obtained values were within 24% of the expected values. We attributed most of the errors to analytical methods since error values due to preparation of solutions are not high.

Low concentration samples (Experiment 3, Table L-1) were prepared with calculated mercury concentrations of 0.4 μg/liter for the KCl container, 0.2 μg/liter for the acidic peroxide container, and 0.4 μg/liter for the permanganate container. For the KCl solution no difference between measured (CVAA) and expected Hg mass was observed. For the peroxide container a difference of 0.3 μg between measured (CVAA) and expected Hg mass was observed. For the permanganate container a difference of 0.1 μg between measured (CVAA and expected Hg mass was observed. The total measured mass of Hg was 1 μg, about 0.5 μg greater than the expected 0.5 μg. There is some variability in the results but we concluded that mass balances in the system are reported to a reasonable degree.

The calculated relative standard deviation (rsd) for the high concentration spiking solutions in our system (EXP2) was 12.3% for the KCl impinger solutions, 32% for the peroxide solutions, 8.3% for the permanganate solutions, and 13% for total mercury mass. For the low concentration spiking solutions (EXP3) the rsd was 0% for the KCl impinger solutions, 75% for the peroxide solutions, 33% for the permanganate solutions, and 50% for total mercury mass.

We compared our results with the work reported by Brown et al. [192]. In a critical review of mercury measurement and its control, Brown et al. [192] listed statistical results for 20 individual Ontario Hydro Method sampling efforts. With analyte spiking, a relative standard deviation of 8.83% for the KCl impinger solutions was reported, and a relative standard deviation of 21.81% for the peroxide and permanganate impinger solutions was obtained. For total Hg, a relative standard deviation of 1.49% was calculated.

Except for the 75% error for the low mercury concentration in the peroxide solutions, most of the error values are of comparable magnitude to the relative standard deviation values reported by Brown et al. [192]. We concluded that the sample preparations and the CVAA ERI results are in good agreement and we could use the Ontario Hydro sampling method for future experiments.

Experiments 8 and 9 were also mercury spiked solutions. They were also prepared with known quantities of mercury standard solution. Only one solution of each (KCl, peroxide and permanganate) was prepared. The KCl solution had a mercury concentration of 25 μg/l, the peroxide and permanganate solutions had a mercury concentration of 20 μg/l each. These solutions were later split into two sample solutions for analysis and comparison of results. ERI CVAA results reported the expected consistency for both experiments. Only 1 μg difference was observed between peroxide solutions in Experiment 8 and Experiment 9 (EXP8 F2 and EXP9 F2 in Table L-1). The difference between measured and expected mercury was similar for both experiments. The measured (CVAA) mercury mass for the KCl solution was 7 μg, the expected mercury mass was 5 μg. There is an overestimation of 2 μg for both, Experiment 8 and Experiment 9. The measured mercury mass for the peroxide solution differs from Experiment 8 and Experiment 9. For Experiment 8, it is reported as 3 μg, while for Experiment 9, the mercury

mass is 4 μg. The expected mercury mass was 5 μg. There is an overestimation of 1-2 μg in the mass of mercury. The permanganate solution results show a measured mercury mass of 7 μg for Experiment 8 and 9. The expected mercury mass was 10 μg in each sample.

Initial Mass Balance Testing

With the objective of testing material balances in the burner system, experimental runs with only mercury (i.e., no chlorine species present) present in the flue gas were performed. Experiments 4, 5, 6, and 7 (Table L-2) were experimental runs conducted with mercury in presence of a flame.

Mass balance experimental runs were performed with the burner flame operating at a total gas flow rate of 31 slpm, a mercury concentration of 50 $\mu g/Nm^3$ and no chlorine species present. The composition of the flue gas on a volume percent basis was approximately 26% water, 13% CO_2 and 63% N_2, corresponding to a flue gas equivalence ratio close to 1. The flue gas did not contain O_2 in significant quantities. Flue gas sampling was done through the Ontario Hydro impinger train at temperatures of 520°C (Port 1), 350°C (Port 2), 290°C (Port 3), and 210°C (Port 4). The reaction times at these points are 1.4 s, 3.6 s, 6.2 s, and 9 s, respectively. The flue gas was sampled for 60 min in each case, at a gas sampling rate of 15 slpm.

For these conditions of a total gas flow rate of 31 slpm, a mercury concentration of 50 $\mu g/Nm^3$, 60 min sampling time, and 15 slpm flue gas sampling, a total of 45 μg Hg was expected to be recovered in the Ontario Hydro impinger solutions. For the first three ports (closest to the mixing chamber), good mass balance closure was obtained through CVAA analysis. In the Port 1 sample (EXP4), 46 μg of mercury were obtained. In the Port 2 sample (EXP5), 49 μg of mercury were captured, and the Port 3 sample (EXP6), 42 μg of mercury were collected. The result from the fourth sampling (EXP7) port, however, was 25 μg, which is almost half of the expected 45 μg. Because of the absence of chlorine species we expected most of the mercury to be in the elemental state. This was indeed observed in all of the experimental runs most of the mercury was reported in its elemental state. Very little oxidized mercury was observed in the Port 1 sample, with only 5 % present as oxidized mercury. Samples collected from the remaining ports contained no more than 3% mercury. Our results give a reasonable view of the degree of oxidation and indicate that in the absence of known oxidants (Cl_2, HCl or significant excess O_2), good mass balance closure is attained.

The results of the Port 4 samples further suggest that ambient air was being drawn in and collected with the Port 4 sample, resulting in the low value for reported total mercury mass. Port 4 is located very close to the open exit end of the quartz tube (see Figure 3-189). We therefore concluded that this port was not adequate for flue gas sampling in future experiments.

Reactions with HCl

With the objective of studying mercury reactions with typical concentrations of HCl present in a flue gas environment, experimental runs with mercury and HCl were performed.

Experiments 11, 12, and 13 (Table L-3) were such experiments conducted in the presence of a flame.

Experimental runs were performed with the burner flame operating at a total gas flow rate of 31 slpm, a mercury concentration of 50 μg/Nm^3 (6 ppb) and HCl concentration of 100 ppm. We selected such HCl concentrations because they fall between typical coal combustion and waste incinerator flue gas of concentrations 1-100 ppm and 400-1000 ppm, respectively [180]. Our mercury concentration also falls between the figures used by Galbreath et al. [181] of 10 μg/Nm^3, and Hall et al. [180], 140 μg/Nm^3. Concentrations of flue gas components were approximately, 26%v/v for water, 13% v/v for CO_2 and 63% v/v for N_2, resulting from combustion of methane in our burner at an equivalence ratio close to 1. The temperature profile corresponding to these three runs was shown in Section 3.4.3.1. Flue gas sampling was done through the Ontario Hydro impinger train at temperatures of 520°C (Port 1), 350°C (Port 2), and 290°C (Port 3). As noted previously, the calculated mercury residence times corresponding to these three sampling ports are 1.4 s, 3.6 s, and 6.2 s, respectively. As discussed in the previous section we used only the first three gas sampling ports since the fourth was sampling ambient air along with the flue gas.

The flue gas was sampled for 60 min, at a gas sampling rate of 15 slpm. At a total gas flow rate of 31 slpm, a mercury concentration of 50 μg/Nm^3, 60 min sampling time, and 15 slpm flue gas sampling, a total of 45 μg Hg was expected to be recovered in the Ontario Hydro impinger solutions.

The reported total mercury masses (CVAA) were 45 μg for the Port 1 sample (EXP11), 44 μg for the Port 3 sample (EXP12), and 65 μg for the Port 2 sample (EXP13). Most of the mass balances were met except for the last experimental run (EXP13) where the measured mass of mercury exceeded the expected amount by nearly 50%. Despite this variation in mass balance closure among these experiments, the percentage of oxidized mercury did not exceed 2% in any of the experimental runs. In addition, the speciation results showed no apparent dependence on flue gas sampling port position, and thus no dependence on residence time (or reaction time at these temperatures).

Our results did not agree with some of the previous studies done with mercury and HCl in a flue gas environment. Galbreath et al. [181] reported up to 50% oxidation of mercury at 100 ppmv of HCl, 10 μg/Nm^3 of mercury, 8.5% excess of O_2, and a sampling temperature of 200°C. Their reaction time was 2.5 s, with a calculated cooling rate of 420 K/s, with a peak temperature of 1250°C. Hall et al. [180] also reported 62% oxidation of mercury with 150 ppmv of HCl, 140 μg/Nm^3 of mercury, 10% excess O_2, and a sampling temperature of 500°C. The reaction time was 1.5 s, with a calculated cooling rate between 200 and 333 K/s.

Our system had a cooling rate of 400 K/s to the first sampling port (Port 1) which is of similar magnitude to the cooling rate of 420 K/s reported by Galbreath et al. [181], and higher than 200-333 K/s reported by Hall et al. [180]. Our sampling temperature was significantly higher than Galbreath et al. [181] and of similar magnitude to that of Hall et al. [180].

Our results do not show any significant mercury oxidation under similar HCl and Hg concentrations. The difference between our results and previous studies may be the presence of a 10% excess of O_2 in the published work, which may be causing further mercury oxidation, especially at lower temperatures, which is the case of Galbreath et al. [181]. Hall et al. [180] reported 20 to 30% mercury oxidation in a propane flue gas with an excess O_2 up to 8%. This happened after 0.8 s residence time in the furnace and the duct (T>500°C). We can speculate that the presence of excess O_2 caused further mercury oxidation by HCl, and that our system may not have had sufficiently high oxygen concentrations for oxidation to proceed.

Note, however, that other reports in the literature are consistent with our observation of little HCl-driver oxidation under these conditions. These other studies indicate very little mercury oxidation by HCl in systems without a significant cooling rate but at temperatures of comparable magnitude to our conditions. Sliger et al. [177] report very little mercury oxidation by HCl at temperatures closer to our sampling Port 1 (500 °C). At constant temperatures, about 860°C, and in the presence of 131 ppmv of HCl, Sliger et al. [177] reported only 11% mercury oxidation. Higher oxidation values were obtained at higher temperatures (922°C, 1071°C), high HCl concentrations (172 to 639 ppmv), and a residence time of 1.4 s. Ghorishi et al. [178] also reported that the oxidation of elemental mercury in the presence of HCl is very slow and proceeds at measurable rates only at high temperatures (>700°C) and high HCl concentrations (>200ppmv). Ghorishi et al. [178] reported only 9% mercury oxidation at 100 ppmv of HCl, and at a constant temperature of 515°C for a reaction time of 3 seconds. Gaspar et al. [179] also reported 20% mercury oxidation at HCl concentrations of 300 ppmv and at temperatures of 500 and 700°C. Reactions times of 0.70 to 1.15 seconds correspond to 430 and 870°C respectively. A comparison of our findings with these literature reports is presented in Figure 3-198.

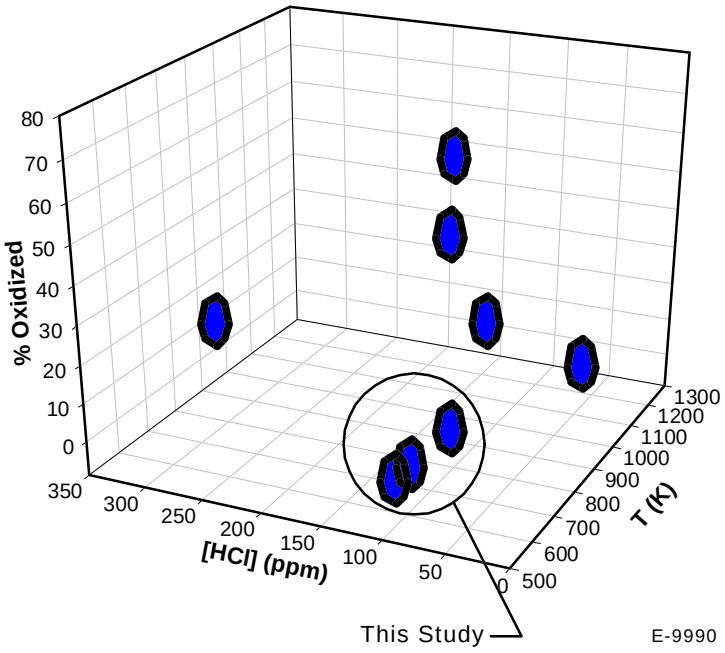

Figure 3-198. Comparison of HCl oxidation results with literature reported data.

The high amount of water present in the flue gas may also have had an effect on our results. Ghorishi et al [178] observed that the presence of water (1.7%) and SO_2 (500 ppmv) inhibited the reaction of HCl with mercury. They affirmed that the mechanism of this inhibition is unknown. They speculate that the observed inhibition effects may be caused by the scavenging of Cl atoms by compounds associated with SO_2 and H_2O.

Experimental runs at excess O_2, higher HCl concentrations, and less amount of moisture, are therefore needed to assess the importance of these two factors in mercury oxidation.

Reactions with Cl_2

Previous studies of mercury oxidation by Cl_2 in a simulated flue gas showed oxidation up to 70% at a temperature of 500°C, presence of a 200-333 K/s cooling rate, residence time of 1.5 s, and Cl_2 concentrations ranging from 50 to 150 ppmv [180]. At room temperatures (20°C) and without the presence of a cooling rate, Hg was oxidized by Cl_2 up to 95% at a residence time of 2.8 s [180]. With our objective of studying the effect of higher cooling rates typical of a flue gas environment, different experimental runs with mercury and Cl_2 were performed here. Experiments 14, 15, 16, 17, 18, 19, 23, 30, 31, 32, and 33 in Table L-4 were experimental runs with mercury using different chlorine concentrations and sampled at different ports along the reactor.

Experimental runs were performed with the burner flame operating at a total gas flow rate of 31 slpm, a mercury concentration of 50 $\mu g/Nm^3$ and Cl_2 concentrations of 50 ppmv, 100 ppmv, 300 ppmv, and 500 ppmv. Even though Cl_2 concentrations in coal flue gas are in the order of 0.004 ppmv (Table 3-129, Pittsburgh coal), we considered the importance of Cl_2 as a chlorine-atom producing compound at high temperatures. As discussed previously our mercury concentration falls between the figures used by Galbreath et al. [181], 10 $\mu g/Nm^3$, and Hall et al. [180], 140 $\mu g/Nm^3$, and is 50 $\mu g/Nm^3$. Which is twice the value of mercury in coal combustion flue gases. Mercury concentrations in coal flue gas range from 1 to 20 $\mu g/Nm^3$ (1 to 2 ppbv). Concentrations of flue gas components were approximately, 26%v/v for water, 13% v/v for CO_2 and 63% v/v for N_2, resulting from operation of the methane flame in an 26%O_2 /61%N_2 mixture and at an equivalence ratio close to 1. The flue gas did not have O_2 in significant quantities. The temperature profile of these three runs was shown in Figure 3-195. Again, flue gas sampling was done through the Ontario Hydro impinger train at temperatures of 520°C (Port 1), 350°C (Port 2), and 290°C (Port 3), with corresponding reaction times of 1.4 s, 3.6 s, and 6.2 s, respectively. At these operating conditions, and with a total gas flow rate of 31 slpm, a mercury concentration of 50 $\mu g/Nm^3$, 60 min sampling time, and 15 slpm flue gas sampling, a total of 45 μg Hg was expected to be recovered.

The reported total mercury masses (CVAA) varied considerable in these experiments. Experiments 14, 15, 16, 17, 18, 19, 23, and 33, resulted in higher than expected mercury capture. The average mass of mercury captured in these three experiments was 64 with a standard deviation of +/- 4 μg. The largest amount captured of total mercury collected was obtained in experiment 14, with 73 μg. Experiments 30, 31, and 32 had an underestimation of total mercury, being the lowest experiment 32, with 31 μg. Possible causes include (1) release of mercury that

may have deposited on the walls previously, (2) analytical error, which was evident in the blank runs discussed previously, and (3) varying permeation rate of mercury. The temperature of the bath was not identical on all of the experiments, having a variation between 83 and 85°C, even though nitrogen flow was kept constant through the use of a mass flow controller.

In the first series of experiments (Experiments 14 to 16), the concentration of chlorine was 50 ppmv. Flue gas was sampled at three different ports. With a chlorine concentration of 50 ppmv and a mixing chamber temperature of 1080 °C, the highest degree of oxidation was found at the first sampling port with 10% of Hg oxidized. Samples extracted from Ports 3 and 2 have 7% and 8% oxidized mercury, respectively. According to the experiments of Hall et al. [180] 67% of the mercury should be oxidized at Cl_2 concentrations of 50 ppmv, and 78% of mercury is oxidized at Cl_2 concentrations of 150 ppmv with 500°C sampling temperature in both cases. Cooling rates in our system are somewhat higher, however, being 400 K/s from the chamber to the first port. Hall et al. [180] cooling rate was calculated to be between 200 and 333 K/s. Hall et al. [180] mentioned that Cl_2 reaction with mercury also occurs at room temperature (25°C). If this statement is true we would expect to see more conversion as mercury moves through the system.

Studies at higher chlorine concentrations were also conducted. We used 500 ppmv chlorine concentrations for the following experiments: 17, 18, and 19. We need to note that the higher nitrogen gas flow rates required to increase the Cl_2 concentration to 500 ppmv caused the temperature in the mixing chamber to decrease by approximately 200 °C. The temperatures at sampling ports 1, 2 and 3 under this condition were 500°C, 300°C and 270°C, respectively. Despite the lower temperatures, the percent of mercury oxidized was found to be 93% in all samples. We observed that high Hg conversion can be obtained at these temperature, consistent with Hall et al. [180], but note that higher Cl_2 concentrations were required to achieve this value in our experiments.

Before conducting experiments at intermediate chlorine concentrations, an additional experiment was conducted using 50 ppmv Cl_2 to verify initial results. As shown in Table L-4 (Experiment 23), the measured percentage of mercury oxidized was 12%, nearly identical to the result obtained previously at the same conditions (Experiment 14, Table L-4).

In an attempt to obtain intermediate values of mercury conversion, experiments were then conducted at chlorine concentrations of 300 ppmv, with gas sampling at Ports 1 and 3. The percent mercury oxidation obtained was 69% for sampling Port 3 (Experiment 30, Table L-4) and 66% for sampling Port 1 (Sample 32, Table L-3). Again, no appreciable difference was observed in mercury oxidation with port location.

Experiments 33 and 31 were performed at chlorine concentrations of 100 ppmv, with samples extracted from Ports 1 and 3 respectively. The percent of oxidation obtained was 36% for sample taken from Port 3 and 45% for sample taken from Port 1. No appreciable difference was observed in the selection of sampling ports.

Figure 3-199 shows our experimental results indicating that as the concentration of chlorine increases, the amount of mercury oxidized is higher. The same pattern is seen in the results of Hall et al. [180] except at lower chlorine concentrations. The cause for this discrepancy can be explained by the higher cooling rates (and thus shorter reaction times at elevated temperature) achieved in our system, the presence of excess oxygen in Hall et al. [180] system, and the high moisture content in the flue gas environment.

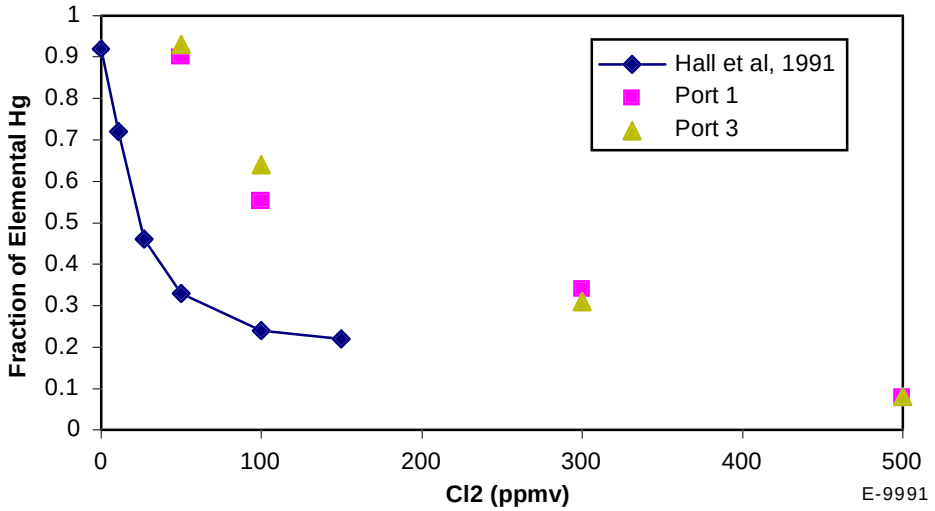

Figure 3-199. Fraction of elemental mercury as a function of initial chlorine concentration.

Ghorishi et al. [178] reported that at a constant temperature of 40°C and in the presence of 50 ppm Cl_2, 100% of Hg is oxidized. Similar results are obtained by Hall et al. [180] at Cl_2 concentrations of 10 ppmv, using Hg concentrations of 40 ppbv (330 μg/m^3), and at constant temperatures ranging from 20°C to 700 °C. In experiments with the presence of a cooling rate, however, the highest oxidation attained is no longer 100% but 78% [180].

The high amount of water present in our flue gas may also have had an effect on Hg oxidation in our system. Ghorishi et al. [178] observed that the presence of water (1.7%) and SO_2 (500 ppmv) inhibited the reaction of HCl with mercury was inhibited. They affirmed that the mechanism of this inhibition is unknown. HCl and Cl_2 can be considered as generators of Cl atoms at higher temperatures. Ghorishi et al. [178] speculated that the observed inhibition effects may be caused by the scavenging of Cl atoms by compounds associated with SO_2 and H_2O. Thus it is conceivable that in the high H_2O environment of our experiments, radical scavenging reduced the pool of Cl atoms and thus reduced reaction rates.

Reactions Involving HCl/Cl_2

Experiment 24 was performed with both HCl and Cl_2 simultaneously in order to study mercury interactions with a specific ratio of HCl/Cl_2 under flue gas conditions. This experimental run was done with the burner flame operating at a total gas flow rate of 31 slpm, a mercury concentration of 50 μg/Nm^3, a Cl_2 concentration of 50 ppmv, and an HCl concentration

of 100 ppmv. Concentrations of flue gas components were approximately, 26%v/v for water, 13% v/v for CO_2 and 63% v/v for N_2, resulting from the operation of the methane flame at an equivalence ratio close to 1. The temperature profile of this run was shown in Figure 3-195. Flue gas sampling was done through the Ontario Hydro impinger train at a temperature of 520°C (Port 1), with corresponding residence time of 1.4 s. The flue gas was sampled for 60 min, at a gas sampling rate of approximately 15 slpm. At a total gas flow rate of 31 slpm, a mercury concentration of 50 $\mu g/Nm^3$, 60 min sampling time, and 15 slpm, a total of 45 μg Hg was expected to be recovered in the Ontario Hydro impinger solutions. The result of this experimental run indicated that only 10% of the mercury is oxidized (Table L-3). We attributed this oxidation to the presence of Cl_2. No previous studies were reported with a mixture of specific ratios of Cl_2 and HCl.

Carbon Adsorption Experiments

To examine an alternative flue gas sampling method for total mercury recovery, experimental runs with a carbon adsorption flue gas sampling system were performed. The reason for this examination was to provide shorter experimental times, including sample preparation, in order to have more than one experimental run per day. This system was sometimes used in conjunction with the Ontario Hydro experimental runs or in separate runs. The key component of the carbon adsorption system consisted of a 200 mg of steam-activated coconut charcoal cartridge (12x30 mesh), doped with 5% potassium triiodide. It acted as an adsorption bed for the capture of gaseous mercury.

Tables 3-134 and 3-135 present information regarding the different flue gas sampling experiments conducted with the carbon adsorption system. The first column indicates previously reported Ontario Hydro experimental run (EXP) which was conducted at conditions equivalent to a carbon adsorption experimental run (CHR). The second column is the actual carbon adsorption experimental run number. The third column has information regarding the type of reactants, sampling port, and the concentrations of reactants in ppmv. The fourth column is the expected amount of mercury mass captured per 200 mg of coconut charcoal. At a total flue gas flow rate of 31 slpm, a mercury concentration of 50 $\mu g/Nm^3$, 60 min sampling time, and 1 slpm flue gas sampling, a total of 3 μg was expected to be recovered. The fifth column presents the measured amount of mercury in the carbon cartridges reported by the Environmental Research and Radiochemistry Center at MIT. The sixth column shows the standard deviation of the value shown in the previous column. The experimental sampling time is recorded in the seventh column.

Carbon adsorption Experiments 1 to 3 (CHR1 to CHR3) were done at sampling Port 4, but were disregarded based on the Ontario Hydro results discussed previously, which reported atmospheric air sampling along with the flue gas. Lower than expected masses of captured Hg were seen with the cartridges as well, as shown in the second and third rows of Table 3-134.

Table 3-134. Carbon Adsorption Experimental Results

Sample ID	Sorbant #	Type/ Port/ ppmv	Sampling Time (min)	Expected Hg (μg)	Measured Hg (μg)	Standard Deviation +/-(μg)
EXP 10	CHR1	Blank 4	62	0	0.41	0.020
EXP 11	CHR2	HCl 4 100	60	3.00	0.06	0.003
	CHR3	Hg 4	60	3.00	1.40	0.070
	CHR4	Hg 1	61	3.05	3.57	0.180
EXP 12	CHR5	HCl 1 100	65	3.25	1.87	0.100
	CHR6	Hg 3	60	3.00	2.36	0.120
EXP 13	CHR7	HCl 3 100	65	3.25	3.56	0.180
EXP 14	CHR8	Cl2 2 50	68	3.40	5.32	0.270
EXP15	CHR9	Cl_2 1 50	65	3.25	0.630	0.040
EXP16	CHR10	Cl_2 1 50	60	3.00	1.320	0.080
EXP17	CHR11	Cl_2 1 500	60	3.00	0.500	0.030
EXP18	CHR12	Cl_2 1 500	60	3.00	0.610	0.040
EXP19	CHR13	Cl_2 3 500	60	3.00	0.550	0.040
EXP23	CHR17	Cl_2 3 50	60	3.00	1.620	0.090
EXP24	CHR18	Cl_2,HCl 3 50,100	60	3.00	2.570	0.150

Table 3-135. Combined Carbon Adsorption-Ontario Hydro Experimental Runs

Sample ID	Sorbant #	Type/ Port/ (ppm)	Sampling Time (min)	Expected Hg (μg)	Measured Hg (μg)	Standard Deviation +/- (μg)
EXP20	CHR14	Blank 1	60	0	0.110	0.030
EXP21	CHR15	Hg 1	62	3	1.240	0.070
EXP22	CHR16	Cl2 1 50	60	3	0.860	0.060
EXP25	CHR19	Blank 1	60	0	0.036	0.003
EXP26	CHR20	Hg 1	61	3	1.910	0.110
EXP27	CHR21	Cl2 1 50	60	3	1.330	0.070

To test material balance closure, experiments in which mercury is added to the post-combustion flue gas in the absence of HCl or Cl_2 were conducted. Experiments 4 and 6 measured total mercury values of 3.57 μg and 2.36 μg. Comparing to the expected value of 3 μg, a variation of approximately ± 20% was observed, slightly larger than the ± 10% mass balance closure observed in comparable experiments using the complete Ontario-Hydro impinger train. Experiments in the presence of HCl at Ports 1 and 3 were also performed (CHR5 and CHR7). Based on the results discussed previously, we expected most of the mercury to be in the elemental state, therefore mercury captured by the adsorption system should be in similar quantities as mercury without any reactant. The results were different. At the first port (CHR5) the measured value of mercury mass was about 40% less than the expected value. At the third port (CHR7) and under the same conditions (HCl concentration), the measured value of mercury was about 10% higher than the expected value, yielding a considerable variability in the analytical results. In a similar experimental run, this time with Cl_2 concentration of 50 ppmv (CHR), no significant oxidation was also expected based on the results discussed previously. The measured mercury concentration was about 60% higher than the expected value. Again, a high variability was observed.

The charcoal cartridges were used in experimental runs in the presence of the oxidizing species HCl or Cl_2 to test if total mercury present in the flue gas agreed with Ontario-Hydro results under these conditions. Experiments CHR 9 through CHR 13, and CHR 17 and CHR 18 were done in this manner. The results are shown in Table 3-135 and underreport expected mercury levels by up to 85%. In experiments CHR9, CHR11, CHR12, and CHR13, a constant measured value of around 0.57 μg is reported, which means that the concentrations of mercury are not accurate (not close to 3 μg) but were repetitive and may need to be subject to calibration.

A combination of the first three impingers of the Ontario Hydro sampling train (KCl solutions), and the carbon adsorption system was then assembled for the study of mercury speciation in the flue gas. Six experiments were performed with the flame operating at a total gas flow rate of 31 slpm. The temperature profile corresponding to these runs was shown in Figure 3-195. Flue gas sampling was done through the first three Ontario Hydro impingers train at a temperature of 520°C (Port 1). The residence time at this point is 1.4 s. As in other experiments, the flue gas was sampled for 60 min, at a gas sampling rate of approximately 15 slpm. The sampling through carbon adsorption system was done through a T connection following the first three impingers of the Ontario Hydro. The gas sampling rate was approximately 1 slpm through the carbon adsorption system.

CHR14 and CHR 19 were blank experimental runs (Table 3-135). The results for the adsorption system part showed 0.11 and 0.036 μg of mercury per 200 mg of coconut charcoal, where values of 0 μg were expected. The results from the KCl solutions corresponding to experiments 20 and 25 (EXP20 and EXP25) measured no presence of mercury. Both systems therefore demonstrated reasonable in the absence of mercury.

In order to study the material balance of the combined system, adsorption experiments CHR15 (or EXP21) and CHR 20 (or EXP26) were conducted under flue gas conditions mentioned earlier with a mercury concentration of 50 $\mu g/Nm^3$ and sampling time of 60 min. The results of both adsorption charcoal cartridges showed values of 1.24 and 1.91 μg for CHR14 and CHR20, respectively. Both numbers are well below the expected 3 μg but both results show the same trend. The results of the Ontario Hydro KCl impingers showed concentrations of 1 μg of mercury for both experimental runs (EXP21 and EXP26). Based on our previous experiments using the Ontario Hydro train, all of the Hg was expected to be elemental, so no capture in the KCl impinger solutions was expected.

Two experiments were also performed in the presence of 50 ppmv of Cl_2. The flue gas flow rate and temperature profile conditions were the same as mentioned earlier, with a mercury concentration of 50 $\mu g/Nm^3$. Based on the Ontario Hydro results from experiments 14, 15, 16, and 23 in Table L-4, no oxidized mercury was expected to be captured by the KCl impinger solutions. We would therefore expect Hg loading in the carbon cartridges similar to these from experiments without any Cl_2, such as adsorption experiments CHR15 and CHR 20. For the charcoal cartridges, the results showed the following mercury amounts: 0.86 μg (CHR16) and 1.33 μg (CHR21). There was no expected similarity between both results. They also are much lower than the expected 4 μg mercury. The KCl solutions showed much higher concentration of mercury, being 4 μg (EXP27) and 5 μg (EXP22). They are much higher than the expected 1 μg of mercury obtained in previous experiments. We can conclude that a slight mercury oxidation may be occurring with Cl_2 concentration 50 ppmv. We cannot, however quantify the degree of oxidation since the results of the adsorption system did not meet material balance requirements.

The results from these experiments can not be considered reliable since previous experiments involving total mercury present in flue gas do not match or come close to a similar Ontario-Hydro value. It is possible that mercury mass balance closure could have been improved had the system been completely disassembled, rinsed, and all rinses analyzed for mercury (to

assess deposition within lines and the sample holder). We chose, however, to continue employing the Ontario-Hydro impinger train for future experiments since it had shown more consistency in their results.

Examination of Potential Ontario Hydro Artifacts in Cl_2 Experiments

Our oxidation experiments using molecular chlorine as an oxidant demonstrated a trend of increasing oxidation with increasing chlorine concentration. In comparing these results with the only comparable study in the literature, that of Hall et al. [180], we find level of mercury conversion that is 20 to 25% less as shown in Figure 3-200. While there is some concern that surface reactions may have affected the oxidative conversion in the Hall et al. [180] data, the relatively low surface to volume ratio in our system suggests that the conversions observed herein are the result of homogeneous gas phase reactions.

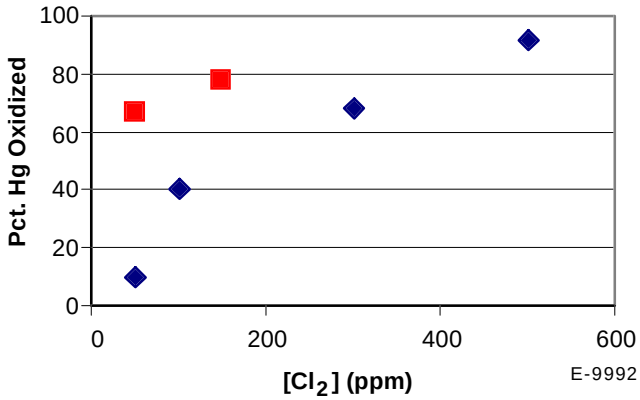

Figure 3-200. Results of oxidation experiments in the presence of Cl_2. Red squares represent Hall et al. [180] data; blue diamonds are from this project.

One important concern, however, is whether the Ontario Hydro sampling train reports "false positives" for mercury oxidation when molecular Cl_2 is used as the oxidizing agent. Linak et al. [193] suggest that the impinger solutions achieve saturation at low concentrations of Cl_2. This means that as the Cl_2 concentration increases there is no major increase in the oxidation of mercury. Specifically, Linak et al. [193] conducted experiments using one impinger filled with the solution of the first impinger of the Ontario-Hydro impinger train. They then bubbled carrier gas containing Cl_2 at concentrations of from 1, 10 and a 100 ppm through this solution. After 1 hour, they terminated the flow of the chlorine containing mixture and then bubbled mercury containing gas through the solution. Total duration of the experiment was 2 hours, with 1 hour for each gas mixture. From analysis of the oxidized fraction of mercury, Linak et al. [193] concluded that a positive bias of between 10 to 20% was possible. The authors suggested adding $Na_2S_2O_3$ to the solutions in order to avoid reaction with OCl^- which they claim is the active oxidizing species and hence the cause of the mercury bias.

A similar experiment was conducted in our laboratory as part of this study. In our experiment, first three impingers of the Ontario Hydro train were used, with each filled with the standard Ontario Hydro KCl solution. Carrier gas containing Cl_2 at a concentration of 100 ppm

was then bubbled through the impinger. Analysis of the solution indicated between 5 to 10% oxidation was occurring.

From these experiments and the analysis of the Linak et al. [193] data, we conclude that there is at most a 10% bias in our reported extents of mercury conversion in the presence of molecular chlorine. Although we did not examine concentrations higher than 100 ppm Cl_2, the lack of a consistent trend with Cl_2 concentration in the Linak et al. [193] study (at 10 ppm Cl_2 there was no significant mercury oxidation) and the observation that the 100 ppm Cl2 experiments did not differ from the 1 ppm Cl_2 experiments in terms of extent of Hg oxidation in solution suggest that bias is minimal.

Check of Permeation Rate

With the objective of testing the permeation rate of mercury from the mercury permeation device, experimental runs with direct flue gas sampling were performed. Experiments 28 and 29 (Table L-5) were conducted in the absence of a flame, using only a background flow of N_2. The dilution N_2 containing mercury was connected to the background flow of N_2 through a Swagelock T fitting. The burner system was modified by by-passing the mixing chamber using a stainless steel line which was followed by the Ontario Hydro sampling train. In Experiment 28, all the gas was sampled through the Ontario Hydro sampling train at 15 slpm. In Experiment 29, the gas flow rate was increased to 18 slpm, and part of it was sampled at 15 slpm with the use of the Ontario Hydro sampling train. In both experiments the stainless steel duct was kept at a temperature of 170°C with the use of heating tapes. In both experimental runs, the heating bath was kept at 85°C, which is the same temperature used in all of the experimental runs. The mercury permeation rate was constant at approximately 1.5 μg/min (see Eq. (3-38)), giving a concentration of 50 $\mu g/m^3$ at total gas flow rate of 31 slpm (most of our experiments). In Experiments 28 and 29, the permeation rate was constant but the total gas flow rate changed, being 15 slpm and 18 slpm respectively.

Experiment 28 was conducted at a total gas flow rate of 15 slpm, a mercury concentration of 100 $\mu g/Nm^3$, 60 min sampling time, and 15 slpm flue gas sampling. A total of 90 μg Hg was expected to be recovered in the Ontario Hydro impinger solutions. Only 57 μg of mercury were recovered in Experiment 28, which implied about 37% of initial mercury loss through the system.

Experiment 29 was run at a total gas flow rate of 18 slpm, a mercury concentration of 80 $\mu g/Nm^3$, 60 min sampling time, and 15 slpm gas sampling through the Ontario Hydro impinger train. A total of 70 μg Hg was expected to be recovered in the Ontario Hydro impinger solutions. Only 47 μg of mercury were recovered, which implied 33% mercury loss in the system. In both cases our results gave an underestimation of mercury present in flue gas. Possible causes for this discrepancy are the possibility of mercury being adsorbed on surfaces since most of the flue gas line was stainless steel tubing. In experiments with the presence of the mixing chamber and the quartz tube reactor, less stainless steel area of contact is available and the impact of adsorption may not be significant.

Kinetic Information from Chlorine Reactions

For chlorine reactions, the results show a clear correlation between initial chlorine concentrations and mercury conversion. The results are similar to the trends reported by Hall et al. [128]. The main difference is the required Cl_2 concentrations to achieve total Hg oxidation are much higher in our experiments.

Figure 3-199 shows the fraction of elemental mercury remaining as a function of initial Cl_2 concentrations at sampling Ports 1 and 3. Recall that sampling Port 1 is the one closest to the mixing chamber, and sampling Port 3 is the third one from the mixing chamber.

The temperatures at each sampling port were approximately 520°C (793 K) and 300°C (573 K), respectively (See Table 3-136). Figure 3-199 shows that at initial chlorine concentrations of 500 ppmv, 92% of the elemental mercury was consumed. At chlorine concentrations of 50 ppmv, only 10% of the elemental mercury reacted. The results for both sampling ports are very similar. The factor that changed between the two sampling ports is the cooling rate. From the mixing chamber to sampling port 1 a cooling rate of 400 K/s is calculated from measured temperatures and estimated cooling rates.

Table 3-136. Physical Conditions at Different Quartz Tube Reactor Sampling Ports

Port	Distance (m)	Temperature (K)	Residence Time (s)	Cooling Rate dT/dt (K/s)
1	0.2	795	1.4	400
2	0.4	624	3.6	80
3	0.6	561	6.2	20
4	0.8	479	9.0	30

From sampling Port 1 to sampling Port 3, a cooling rate of 40 K/s is obtained. We assume that mercury reaction with chlorine depends mainly on the time and temperature of the reactor. From the values of conversion of mercury and initial chlorine concentration reported in Figure 3-199 the kinetic rate constant values were determined for the global reaction:

$$Hg + Cl_2 \Rightarrow HgCl_2 \qquad (3\text{-}39)$$

These values were obtained by modeling a plug flow reactor with non-isothermal conditions. Temperature varied along the length of the quartz tube. The average value of the reaction rate constant for the global reaction was $k_1 = 3.6\text{x}10^3$ +/-$1.3\text{x}10^3$ m^3/mol.s ($5.97\text{x}10^{-15}$ cm^3/ molecule.s), for the experiments at the first sampling port. For the third sampling port, an average reaction rate constant of $k_3 = 1.8\text{x}10^3$ +/-$0.7\text{x}10^3$ m^3/mol.s ($2.99\text{x}10^3$ cm^3/molecule.s) was calculated. The reaction rate constant obtained from Hall et al. [180] data was $1.07\text{x}10^{-5}$ cm^3/ molecule.s. The obtained reaction rate constants values are six times and three times the magnitude of Hall et al. [180] reaction rate constant value.

Kinetic calculations in Section 3.4.2 predicted 11% of oxidized mercury at a cooling rate of 500 K/s, a mercury concentration of 0.01 ppmv (82 $\mu g/m^3$), a Cl_2 concentration of 0.0048, an HCl concentration of 31.9 ppmv and 1 second residence time. In addition, 24% of oxidized mercury was predicted at a cooling rate of 200 K/s, a mercury concentration of 0.01 ppmv, a Cl_2 concentration of 0.0046 ppmv, an HCl concentration of 32 ppmv, and 2 seconds residence time. Even though chlorine species concentrations are smaller in the kinetic runs than actual chlorine concentrations used in our experiments, they predicted an important trend regarding the degree of mercury oxidation and cooling rates of the system. At very high cooling rates, very little mercury oxidation is predicted. This was also shown in Figure 3-188, in which boiler conditions were simulated with cooling rates in the order of 1000 K/s, and with only 20% of mercury oxidation. If we compare cooling rate data (200 to 333 K/s) from Hall et al. [180] and our system (400 K/s), we should expect less mercury oxidation, which is our case.

In respect to chlorine concentrations, kinetic calculations were made to test the degree of mercury oxidation under constant temperatures (773 and 973 K). About 40 to 45% of mercury oxidation is expected with Cl_2 concentration of 50 ppmv. Our experimental results tell us that much higher chlorine concentrations are needed for such mercury oxidation value.

Heterogeneous Mercury Oxidation Experiments

Although it was not the focus of this task, limited experimentation was also conducted to determine whether the presence of ash-like particulate affected mercury oxidation. Commercial alumina (Figure 3-201) of nominal size < 10 microns (Figure 3-202) was therefore injected into the mixing chamber in the presence of either 100 ppm HCl, or 100 or 300 ppm Cl_2. Powder injection rates were such that an alumina concentration of 5000 mg Nm^{-3} was maintained to provide concentrations within the range of typical fly ash particle loadings in flue gas.

As the results in Figure 3-203 demonstrate, mercury oxidation by HCl increased in the presence of the alumina particles for the stoichiometric combustion conditions employed throughout this study. In the presence of the particles, conversion levels of 7% were obtained. Experiments in the presence of Cl_2 demonstrated a significant decrease in the fraction of oxidized gas phase mercury collected. Powder samples were collected and analyzed for chlorine, but no chlorinated species were detected. This indicates that the solid did not absorb or react with chlorine to reduce conversion. Other possible explanations will be investigated in future experiments.

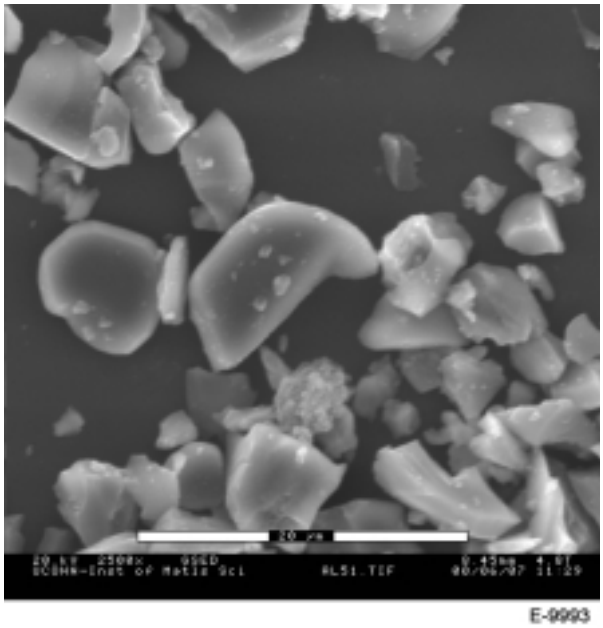

Figure 3-201. SEM micrograph of alumina powder used as fly ash surrogate.

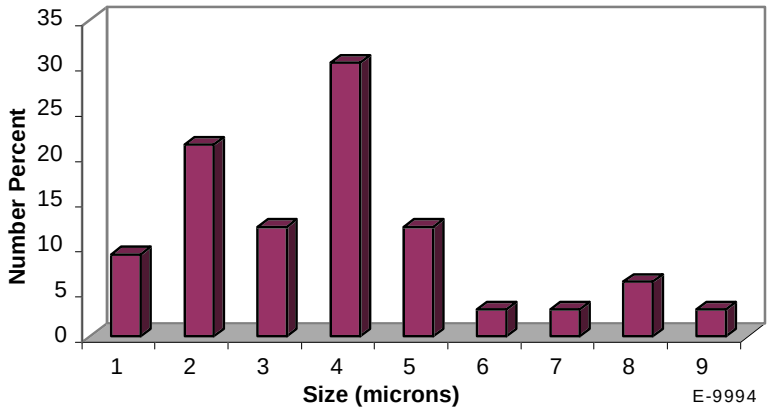

Figure 3-202. Number size distribution of alumina particles taken from SEM micrographs.

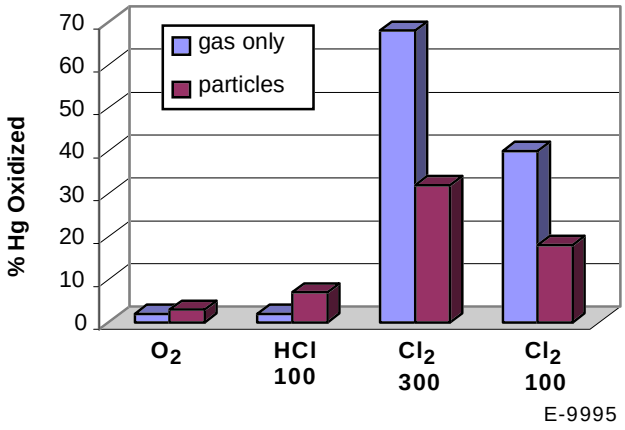

Figure 3-203. Mercury conversion in the absence and presence of alumina particles.

Sources of Error

Major sources of error can be identified as experimental errors, and chemical analysis errors. The main uncertainty while running experiments was the actual permeation rate of mercury from the mercury generation unit. Calculations were made to estimate the amount of total mercury expected after 1 hour of flue gas sampling. The calculated value was 45 μg of total mercury at a flue gas sampling rate of 15 slpm. The results from CVAA ranged from 25 μg to 73 μg. The main factors in this variation of total mercury are: the time of sampling, the actual gas sampling rate, temperature of heating bath, and possible accumulation of mercury inside the system.

The time of sampling was a constant during most of the sampling, varying within ±10 min. The actual gas sampling rate was not 15 slpm but about 14 slpm. This was factored in the calculations of amount of Hg expected by extending the sampling time for about 5 min. The temperature of the bath was kept at about +/-2°C of 85°C in all of the runs. The possible accumulation of mercury inside the system can explain the higher mercury concentrations found in EXP12 in relation to EXP13 (Table L-3). The mercury permeation device was left overnight inside the U tube for that particular experiment. The impact of this error was estimated not significant since the conversion of mercury was measured for each experiment and the concentrations of chlorine species were very high in comparison to mercury concentrations.

Other errors affect our system to a lesser degree. Specifically, instrumentation errors like the Omega mass flow controllers with ± 3% error of the smallest flow used. These instruments were used for methane, oxygen, and the nitrogen for the mercury generation unit. Large rotameters introduced an error of 5% of the smallest flow used. About thermocouple errors, the errors were minimal. The instrumentation error for a K-type thermocouple was between ±2.2°C or ±0.75%(whichever is greater) for a range of temperatures between 0°C to 1250°C. The error of the thermistor probe was ±0.1°C.

3.4.3.5 Summary

Kinetic modeling of reactions of mercury with chlorine species under different cooling rate conditions established the importance of cooling rates as one of the main factors determining the degree of mercury oxidation in post-coal combustion. Kinetic calculations showed that the chemistry involving Cl atom reactions with mercury is fast. Therefore the presence of high concentrations of Cl atoms causes rapid mercury oxidation to occur, and the degree to which Cl_2 and HCl generate Cl atoms is important.

The results of mercury oxidation experiments under different chlorine concentrations showed that, relative to what has been reported in the literature, much higher chlorine concentrations are needed to obtain higher mercury oxidation. We demonstrated that total mercury oxidation can be achieved at cooling rates of 400 K/s by increasing the amount of chlorine up to 500 ppmv. Similar trends as Hall et al. [180] results were obtained but higher chlorine concentrations were needed.

At typical HCl concentrations (100 ppmv) no reaction is observed with mercury. Results can be compared to the ones obtained by Kramlich et al. [188] in which at low concentrations (100 ppm HCl) little or no reaction with mercury is observed. Kramlich et al. [188] reported that HCl concentrations in the order of 282 ppm were required to produce 41% mercury oxidation at 922 °C. Ghorishi et al. [178] also reported that oxidation of elemental Hg in the presence of HCl is very slow and only measurable at high temperatures (>700 °C). Gaspar et al. [179] obtained significant mercury oxidation at temperatures above 760°C, but with HCl concentrations of 300 ppmv and 3000 ppmv. These studies along our results suggest that the Hall et al. [180] data may not be valid, and were perhaps influence by heterogeneous reactions on surfaces within their reactor system.

The consistent observation that no change in mercury conversion was observed between Port 1 and Port 3 samples suggests that no further mercury oxidation occurs as the temperature decreases. Data from Hall et al. [180] suggesting complete mercury oxidation at room temperature do not agree with our findings. Again, surface catalytic effects may have contributed to their findings.

Experiments with SiO_2 particles need to be performed to assess the effects of surfaces in mercury oxidation. This is particularly important given concerns about Hall et al. [180] room temperature data. In this case the Ontario-Hydro method specifies a glass filter for the collection of particles. Introduction of NO should also be considered to provide experimental assessment of the role of NO that has been proposed recently by Niksa et al. [187].

3.4.4 Mercury-Ash Interactions in Fixed Bed Tests

3.4.4.1 Introduction

On December 14, 2000, the U.S. Environmental Protection Agency (EPA) announced that it would regulate mercury emissions from coal-fired utility boilers, with regulations being proposed in 2003 and implementation expected by 2007. Before electric utilities can implement emissions minimization strategies for mercury, they must have an accurate means of predicting emissions in all effluent streams for the range of fuels and operating conditions commonly utilized. Results from the information collection request (ICR) sampling indicate a wide range of mercury concentrations and splits between elemental, oxidized, and particulate-bound mercury. Some pilot-scale testing has shown that ash can play a significant role in determining the amount of oxidized mercury in the flue gas. As a result, it becomes very important to understand the interactions between fly ash, mercury, and other flue gas constituents. The overall goal of this project is to develop a "Toxics Partitioning Engineering Model." The specific goal of this task is to perform bench-scale tests to evaluate the interactions of mercury with ash and ash components at temperatures characteristic of cold-side particulate collection devices.

3.4.4.2 Experimental

A bench-scale system has been developed at the Energy & Environmental Research Center (EERC) for evaluating mercury sorbents and fly ashes in a fixed-bed configuration. Figure 3-204 is a schematic of the bench-scale system. The system is composed of three subsystems: the mercury/gas delivery system, the fixed bed, and the mercury measurement system. Mass flow controllers are used to maintain constant gas flow for most of the flue gas constituents, and flowmeters are used for flow verification. The mercury and mercuric chloride permeation tubes are maintained at a constant temperature and continuously purged with nitrogen to ensure constant outlet mercury concentrations. The output from each of the permeation tubes is periodically verified by taking EPA Method 101A samples at the inlet of the fixed-bed system.

A simulated flue gas was used for all tests, and the mixtures used for some of the ashes were based on the proximate/ultimate analysis data for the parent coal. The flue gas blends are presented in Table 3-137. The flue gas mixture used for the other ash samples is the baseline mix used for evaluating sorbents for mercury control and is also presented in Table 3-137.

The fixed-bed is a Teflon-coated 2.5-in.-diameter EPA Method 5 dust loading filter holder. A quartz filter loaded with fly ash makes up the actual fixed bed. The filters are uniformly coated with the ash by pulling a vacuum on the outlet side of the filter holder and feeding the ash at the inlet side. It has been demonstrated with carbon sorbents that the process is very repeatable for mass loadings down to 10 mg. The fixed-bed assembly is maintained at the desired temperature inside an oven which can be controlled to ±1°F. A slipstream of the flue gas can be taken at the inlet of the filter holder or after it passes through the fixed bed and is sent to the mercury CEMs (continuous emission monitors). The remainder of the flue gas is vented.

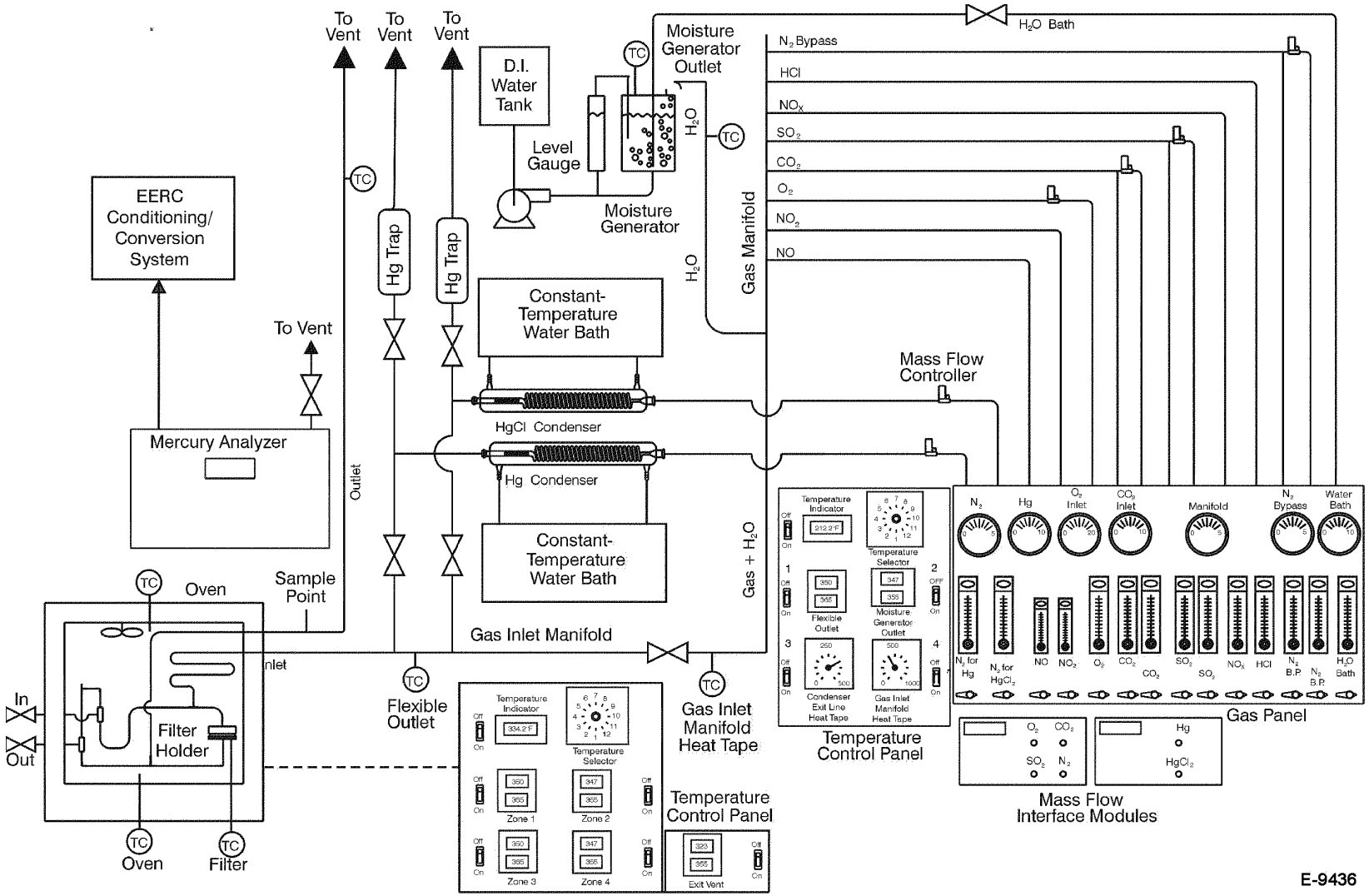

Figure 3-204. Schematic of the EERC bench-scale system.

Table 3-137. Flue Gas Mixture for Bench-Scale Tests

Flue Gas Component	Ohio Blend	ND Lignite	Wyodak	Blacksville, AA, DA, DMA, GA, MA	Valmy, Comanche, Dale, Valmont, Black Thunder, Cordero Rojo, Absaloka
O_2, %	3.3	3.0	3	4	6
CO_2, %	14	14	14	14	12
H_2O, %	8	14.7	12	6	8
SO_2, ppm	1900	840	300	1700	1600
NO, ppm	300	300	300	550	300
NO_2, ppm	15	15	15	27	20
HCl, ppm	60	5	5	50	50

The mercury measurement system consists of a conditioning/conversion system and several mercury CEMs. The conditioning/conversion system conditions the sample gas by removing moisture and acid gases before sending it to the mercury CEMs. In order to speciate between elemental and oxidized forms of mercury, the conditioning/conversion system either reduces all forms of mercury to elemental mercury for a measurement of total mercury concentration, or removes the oxidized forms of mercury from the flue gas stream for a measurement of elemental mercury concentration. The oxidized forms are reduced by passing the flue gas through a $SnCl_2$ solution. The difference between the total mercury and Hg^0 is assumed to be some form of Hg^{2+}. Three different CEMs have been used to measure outlet mercury concentrations from the bench-scale system: a Semtech 2000, a PS Analytical Sir Galahad, and a Tekran Model Tekran 2537A. The Semtech 2000 mercury analyzer continuously measures the elemental mercury concentration and utilizes a Zeeman shift in the light source to eliminate interferences from SO_2, water vapor, and particulate. Both the PSA and Tekran instruments are based on atomic fluorescence sampling and provide a reading every 2.5 min. Figure 3-205 is a plot of the outlet mercury concentration as a function of time from one run where all three instruments were being used to measure the mercury concentration. The agreement between the instruments is very good. For most of the tests, the results will be presented as mercury concentration (normalized to a percentage of the inlet mercury concentration) as a function of time. Normalizing the data to the inlet concentration removed any variations in mercury concentration due to temperature swings or mass flow controller calibration drift. In addition to having good agreement between instruments, the results from the system have been shown to be very repeatable. Figure 3-206 is a plot of the outlet mercury concentration from three repeat runs of the same test conditions where an iodine-impregnated activated carbon was evaluated for mercury capture.

The fixed-bed tests are not intended to simulate the conditions where an ash is injected continuously upstream of a particulate control device, but they give a good indication of mercury ash interactions, provided the exposure conditions are similar among comparative tests. For all tests, the total flow of gases across the fixed bed was held constant at 29.9 scfh, and the mass loading of ash was nominally 1.5 g. The exposed ash for some of the tests was analyzed to verify the amount of mercury captured by the ash and to calculate mass balances.

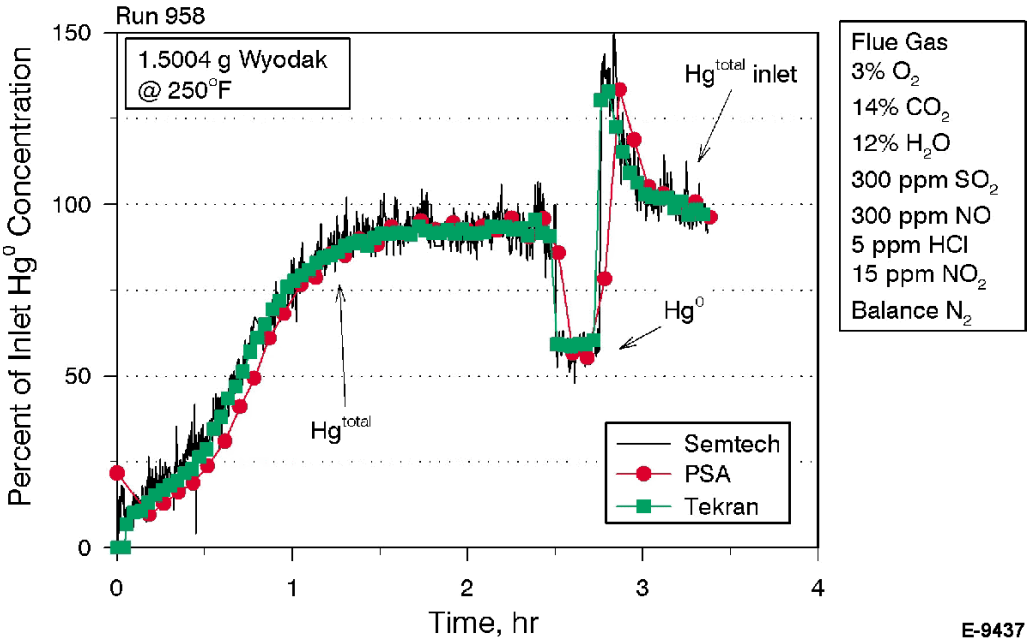

Figure 3-205. Plot of outlet mercury concentration as a function of time, from one run with three different mercury CEMs.

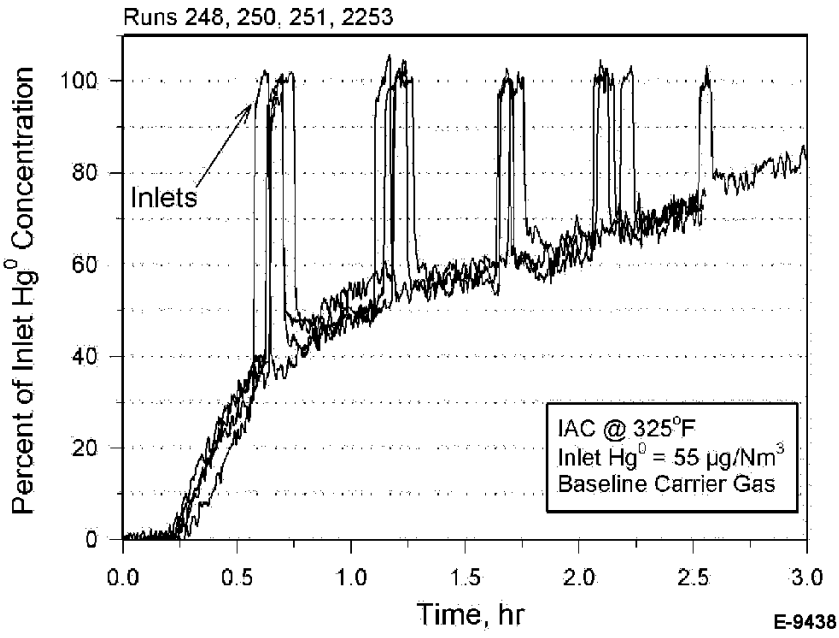

Figure 3-206. Outlet mercury concentration from three repeat runs of the same test conditions.

3.4.4.3 Objectives

In the original scope of work, there were five different test series planned to evaluate the effects of temperature, mercury concentration, mercury species, stoichiometric ratio of combustion air, and ash source. The plan was to first identify a temperature or temperature range for optimum interactions between elemental mercury and the fly ash. A second series was set up to identify the optimum temperature for interactions with $HgCl_2$. Using the optimum temperature, a series of to be conducted to find the optimum mercury concentration to observe interactions. The fourth series was designed to evaluate the effects of mercury species and operating temperature on the interactions between mercury and the fly ash samples as well as the effects of stoichiometric ratio. The fifth series was designed to compare results from lab-prepared ash samples with ash samples obtained from utility boilers. Tests were conducted at two different temperatures for both mercury species, and the baseline mercury concentrations were found to be sufficient. The focus of the remaining tests was to identify ashes that were reactive with mercury or $HgCl_2$ in a simulated flue gas.

3.4.4.4 Ash Characterization

Under this program, 17 different ash samples were evaluated in the bench-scale unit. Some of the characteristics of the ashes are presented in Table 3-138. A brief discussion of the origin of each ash follows.

Table 3-138. Results of Ash Analysis

Fly Ash	LOI, % (dry)	Moisture, %	Surface Area, m^2/g	Mercury, µg of Hg/g of Ash
Ohio Blend	6.79	0.64	1.40	0.276
ND Lignite	2.86	0.38	0.68	0.536
Wyodak	4.45	0.73	9.33	1.29
Comanche	0.90	0.62	1.35	1.05
Valmy	4.50	0.68	5.98	0.557
Blacksville	4.3	0.25	1.95	0.140
Coal Creek	0.01	0.07	ND	0.0067
Valmont	0.88	0.09	1.49	ND
Black Thunder	1.38	ND	3.0	2.13
AA	37.12	ND	4.36	0.282
MA	44.4	ND	3.92	0.060
DA	6.22	ND	6.17	0.114
GA	0.67	ND	0.17	0.002
DMA	1.5	ND	0.96	0.051
Absaloka	1.34	ND	3.04	0.223
Cordero Rojo	0.21	ND	0.74	0.183
Dale Station	54.94	ND	156.96	0.001

Ohio Blend, Wyodak, and North Dakota Lignite Ashes. The Ohio blend, Wyodak, and North Dakota lignite samples were generated in a combustor with 20% excess air at UA. Each ash sample consisted of two separate fractions collected at different locations in the UA combustion system. The first fraction was collected in a postcombustion zone knockout chamber. The second fraction was collected from the baghouse hopper. Because of the apparent high carbon content, it was decided that the fraction collected in the knockout chamber was not representative and would not be used during these tests. The LOI (loss on ignition) values for these samples were considered on the high end, but it was decided to use the ash samples.

Coal Creek Ash. An ash sample obtained from the ESP hopper at Coal Creek Station located in North Dakota was also evaluated. This is the same parent coal as the North Dakota lignite sample received from UA. The Coal Creek Station has two tangentially pc-fired boilers with an electrostatic precipitator (ESP) followed by a wet scrubber. The ash samples were collected by the EERC as part of a mercury-sampling activity at the plant.

Valmy Station Ash. The Valmy Station in Nevada burns a western bituminous coal in two units with low-NO_x burners. Unit 1 is equipped with a reverse-gas baghouse; Unit 2 has a spray dryer followed by a reverse-gas baghouse. The ash evaluated was from Unit 2. Sampling at the station indicated nearly all of the mercury in the flue gas was captured by the fly ash.

Comanche Station Ash. A sample of ash from the Comanche Station (Public Service of Colorado) was sent by PSI to be evaluated in the bench-scale simulator. The sample was collected by ADA Technologies on 1/23/98 when the plant was burning a PRB (Powder River Basin) coal from the Belle Ayr Mine. The station has two combustion units. Unit 1 is a dry-bottom, tangential-fired boiler with no NOx controls. Unit 2 is a dry-bottom wall-fired boiler using overfire air for NOx control. Both units are equipped with a fabric filter dust collector. It was not specified from which unit the sample was collected. According to information from Tom Brown's Critical Review on Mercury, the mercury removal across the reverse-gas baghouse was 34 to 78% at 280°F and <30% at 330 to 350°F. The concentration of mercury on the fly ash indicates a significant amount of mercury capture by the fly ash during combustion. This is consistent with the reported data which show less than 2 $\mu g/m^3$ vapor-phase mercury in the flue gas. The mercury concentration in the coal indicates roughly a total 5.4 $\mu g/m^3$ mercury in the flue gas.

Valmont Station Ash. A western bituminous coal is burned at Valmont station in a dry-bottom, tangential-fired boiler equipped with low-NO_x burners. Particulate control is achieved with a fabric filter baghouse. Ash samples were collected from this plant as part of ICR sampling activity. There was very little mercury present in the flue gas.

Blacksville Ash. During Run PTC-BV-457, the Blacksville bituminous coal was burned in the EERC particulate test combustor (PTC) which is a pilot-scale combustion system burning roughly 60 lb/hr of coal. The ash was collected at 345°F in a fabric filter pulse-jet baghouse equipped with Ryton bags. Sampling with EPA Method 29 was conducted during this test. The total mercury concentration at the inlet of the baghouse was 6.9 $\mu g/m^3$ with 0.7 $\mu g/m^3$ equivalent mercury on the fly ash. Based on the Method 29 results (this method has since been shown to overestimate the fraction of oxidized mercury), 85% of the mercury in the flue gas was oxidized.

Absaloka and Cordero Rojo Ashes. The Absaloka and Cordero Rojo subbituminous coals were also burned in the PTC, but the ash was collected in the advanced hybrid particulate collector (AHPC) which is a combined ESP–baghouse also equipped with W.L. Gore all-PTFE (polytetrafluoroethylene) bags. No mercury sampling was associated with these samples.

Black Thunder Ash. The Black Thunder subbituminous coal was burned in the Big Stone plant in Milbank, South Dakota. The unit is a cyclone-fired boiler with overfire air for NO_x control. The ash was collected in a demonstration AHPC. No mercury sampling was associated with this sample.

Dale Station Ash. The William C. Dale Station ash was evaluated as a possible mercury sorbent under another program. No other information is available.

AA, MA, DMA, GA, DA Ashes. These five ash samples were taken from the ESP hoppers of full-scale power plants burning eastern bituminous coals and were supplied by PSI. Additional information on these ashes is provided in Table 3-139.

Table 3-139. Characteristics of Eastern Bituminous Coal Ash Samples

Parameter	GA Ash	DMA Ash	DA Ash	AA Ash	MA Ash
Hg in coal, ppm	0.18	0.09	0.12	0.09	0.09
Cl in coal, ppm	1300	1600	1100	1100	2300
Coal ash content, %	13.6	10.9	13.9	18.5	10.1
LOI (ESP ash), %	0.1	1	4	35	42
ESP in: $\%Hg_p + Hg^{2+}$	73	81	80	89	76
Hg removal by ash, %	6.8	7.8	24.0	10.1	42.4
Boiler type	pc	pc	pc	Cyclone	Stoker

In addition to analysis performed at the EERC, samples of the three baseline ashes (Ohio, Wyodak, ND lignite) were characterized by UU, and the results were presented in Quarterly Report 15. Results showed the Wyodak sample had larger surface area per mass when compared to the other two samples. The investigation of particle morphology was carried out with a scanning electron microscope, and the Ohio and North Dakota samples were found to contain large irregular-shaped particles and no ultrafine aggregates, whereas the Wyodak sample was found to contain ultrafine aggregates. With the background information and the SEM pictures, the conclusion was made that the Wyodak sample contained some soot and the other two samples did not.

Characterization of Ash Samples for Bench-Scale Mercury Studies

Morphology of Selected Ash Samples

The samples from the UA combustor which were tested at bench scale at EERC (Subsection 3.4.2) were also examined at the UU be scanning electron microscopy. The carbon content of these samples was high, particularly that of the two low rank coals. In addition, the surface area of the Wyodak ash was abnormally high, and suggested that perhaps this ash sample contained soot. Therefore, a small study was undertaken of the morphology of these ash samples. The LOI and surface area data, of each sample are listed in Table 3-140.

Table 3-140. Surface Area and LOI of Ash Samples for Morphological Analysis

Sample No.	Identity Number	Type	LOI in %	Surface Area m^2/g
1	INO24-1	Ohio	6.79	1.52
2	INO24-2	N.Dakota	2.86	0.55
3	INO24-3	Wyodak	4.45	13.42

Method

The samples were prepared for electron microscopy by suspending the materials in ethyl alcohol using an ultrasonic agitator. The ultrasonic agitator was run for 2 min to ensure a thorough suspension. The suspension was subsequently diluted to one-tenth and one-hundredth of the original strength. The material was then deposited on a 0.4 µm pore size polycarbonate membrane filter by vacuum filtration, dried in room temperature overnight and then mounted, for investigation with SEM (Cambridge S 240, tungsten filament, kavex energy dispersive X-ray, Dapple energy dispersive X-ray analyzer). Each microscopy sample had a strip of filter for both the strengths (1/10 & 1/100).

The imaging was done with the scanning electron microscope in the Material Sciences department, University of Utah, Salt Lake City.

To identify the carbon, the samples were examined for the presence of large irregular shaped particles or aggregates of ultrafine particles. The hypothesis of this investigation is that the large chunks of irregular shaped particles are unburnt coal and that the fine aggregates are soot. This hypothesis is based on previous investigations of carbon in coal combustion products [194, 195]. The EDS study on the samples was not conducted for problems mentioned in the discussion.

Observations with Electron Microscopy

Sample 1: (Ohio). Large irregular shaped particles, suggesting char, were found in the sample along with large spherical particles that looked like mineral ash due to their glassy or crystalline appearance. At higher magnification, the pores of the polycarbonate membrane filter were clearly seen. No aggregates of ultrafine particles were seen.

The four pictures (Figures 3-207 through 3-210), though not a zoom-sequence, are representative of the sample. The first picture, Figure 3-207, shows the general collection of particles of different sizes and shapes. The most common particles are the spherically shaped ones. From this picture it can be safely stated that they are 2 to 10 µm in size. At higher magnification, it was found that they had a glassy or crystalline surface suggesting the presence of mineral ash particles [196-198]. A large number of irregularly shaped particles can also be seen in this picture, suggesting unburnt char [194]. Figures 3-208 and 3-209 show such particles. Figure 3-210 shows that at higher magnification, no aggregates or ultrafine particles are seen.

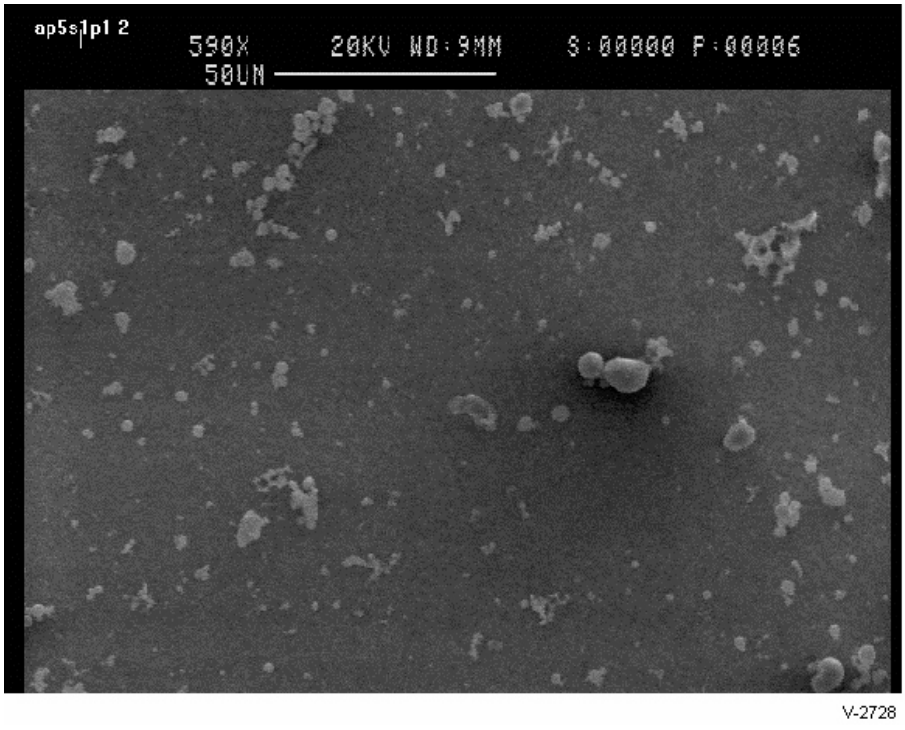

Figure 3-207. SEM photograph of Ohio ash sample (590 times magnification).

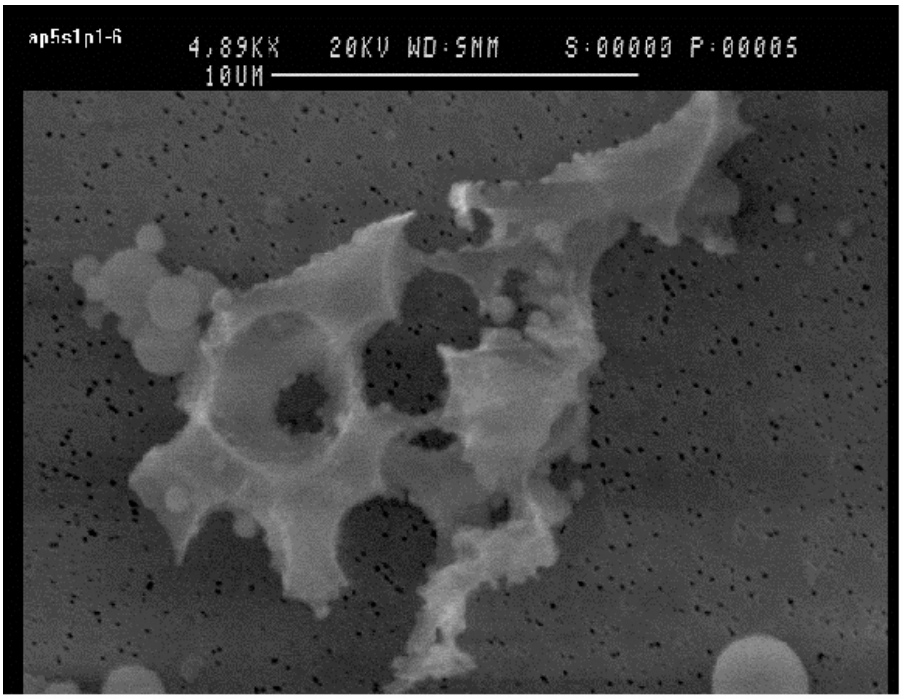

Figure 3-208. SEM photograph of Ohio ash sample (4,890 times magnification).

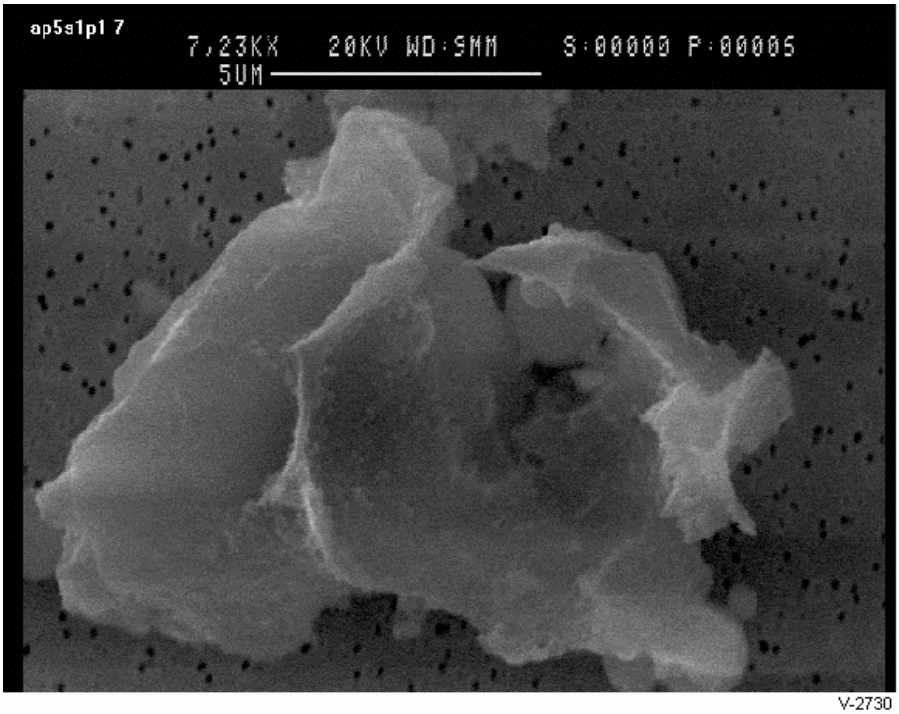

Figure 3-209. SEM photograph of Ohio ash sample (7,230 times magnification).

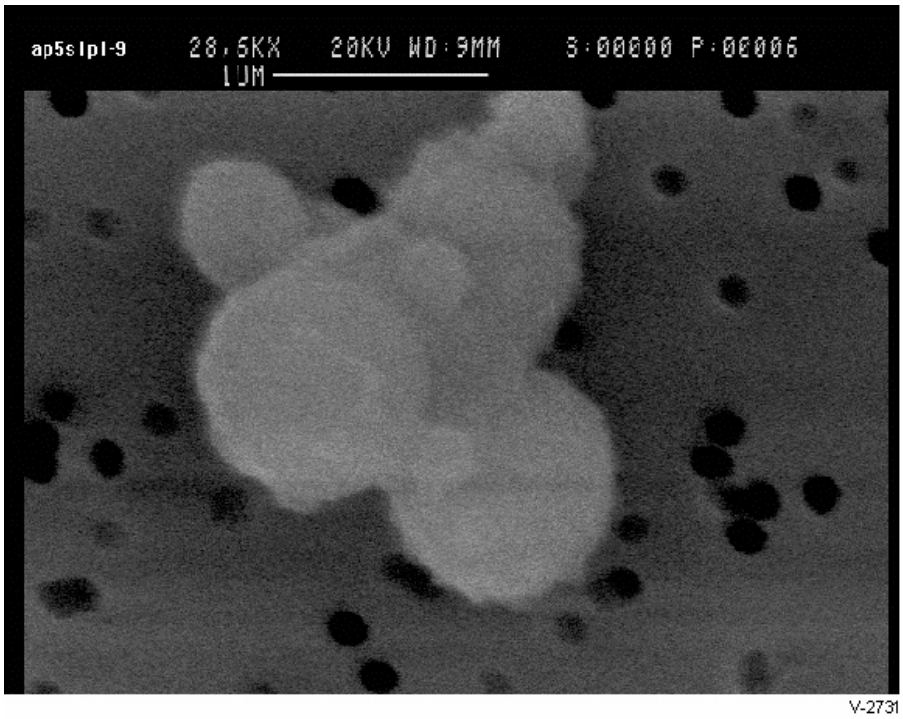

Figure 3-210. SEM photograph of Ohio ash sample (28,600 times magnification).

Sample 2: (North Dakota). Sample 2 has a large number of spherical particles that are glassy or crystalline suggesting mineral ash particles formed by coalescing of minerals during combustion [196-198]. The zoom-sequence of Figures 3-211 through 3-214 shows the mineral ash particles.

After a thorough study of the sample it was found that it contained a lot of irregularly shaped particles. No aggregates of ultrafine particles were found in the sample. The following pictures (Figures 3-215 and 3-216) show the spherically shaped particles and the irregularly shaped particles in the sample.

The first four pictures show a zoom in sequence of a particular area in the North Dakota sample filter strip. Lots of spherical shaped particles are seen in these pictures suggesting mineral ash content. Figure 3-214 shows a particle covered with micro-crystals that look similar to crystals of calcium sulfate as reported in earlier works [137]. The remaining pictures show some irregularly shaped particles that could possibly be unburnt char as suggested by the hypothesis framed. The aggregates of ultrafines discussed earlier were not found in this sample also. This leads to the conclusion that the carbon in the North Dakota sample is found in the large irregular shaped particles and not the ultrafine aggregates. This was surprising since previous samples of fly ash from North Dakota lignite have contained clusters of ultrafine particles [199].

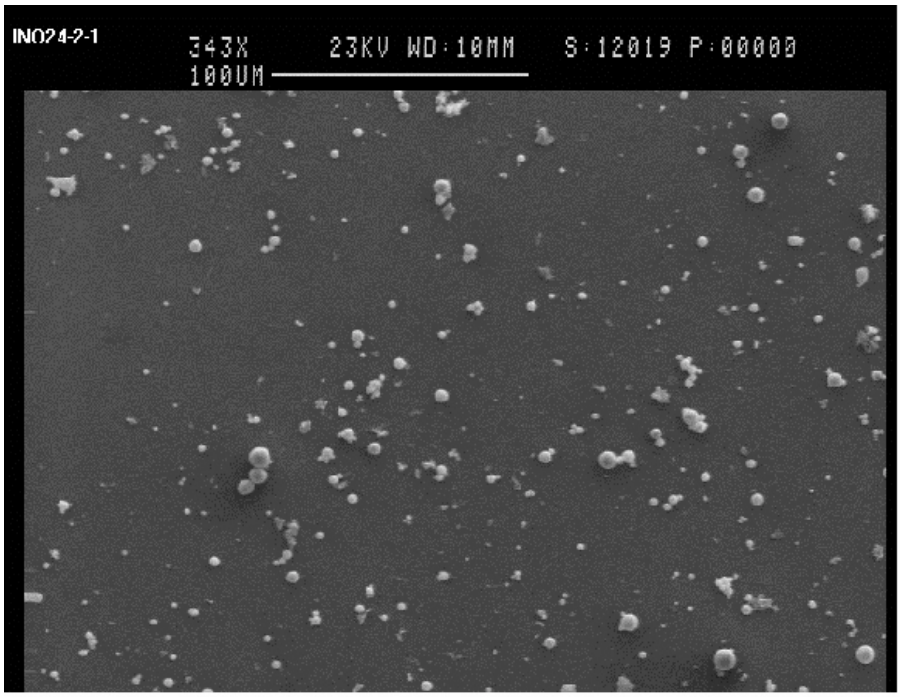

Figure 3-211. SEM photograph of North Dakota lignite ash sample (343 times magnification).

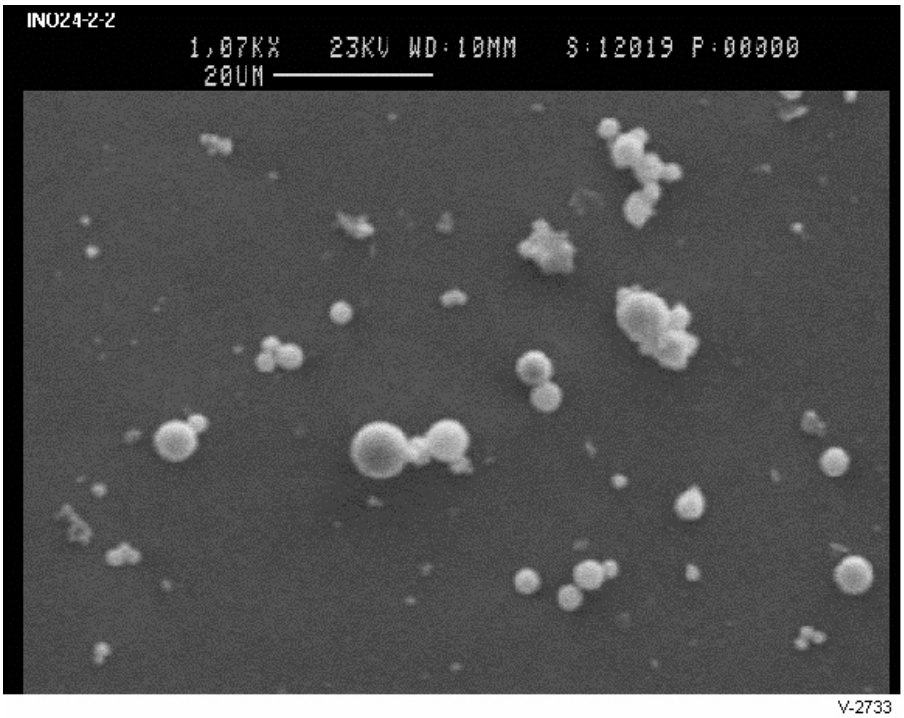

Figure 3-212. SEM photograph of North Dakota lignite ash sample (1,070 times magnification).

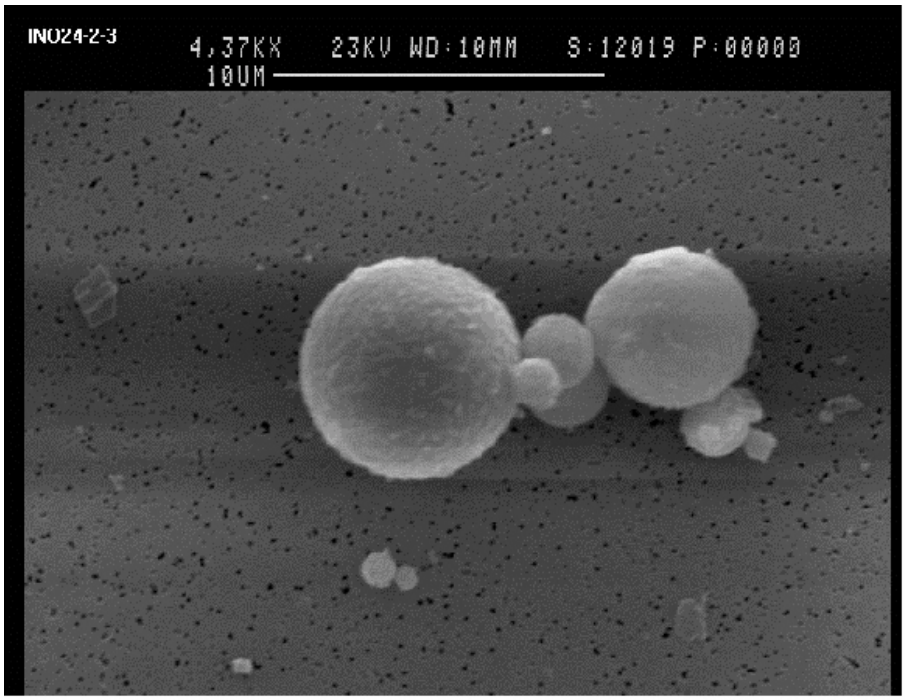

Figure 3-213. SEM photograph of North Dakota lignite ash sample (4,370 times magnification).

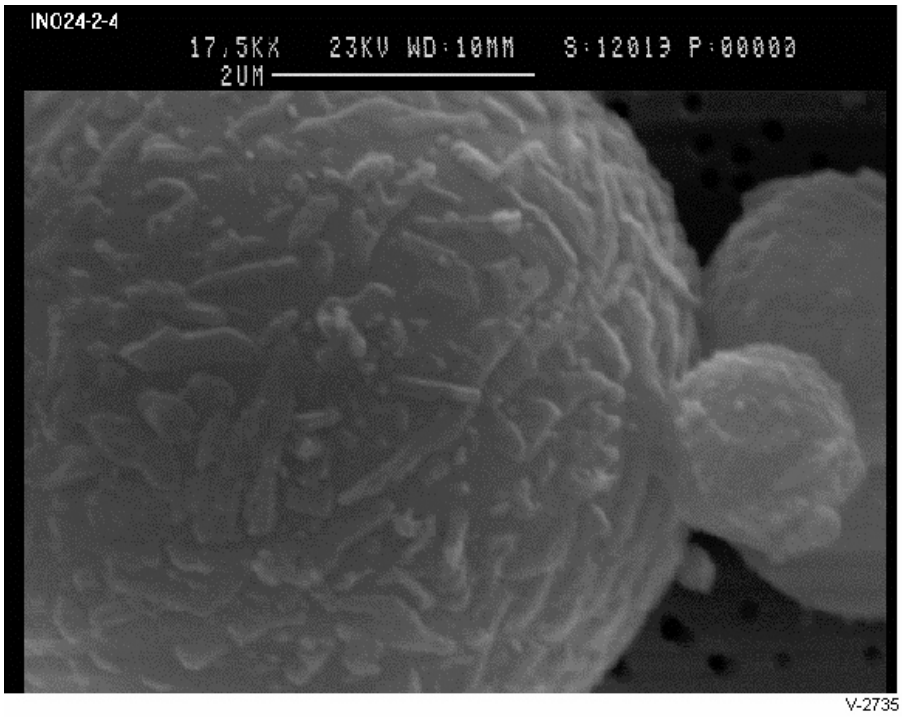

Figure 3-214. SEM photograph of North Dakota lignite ash sample (17,500 times magnification).

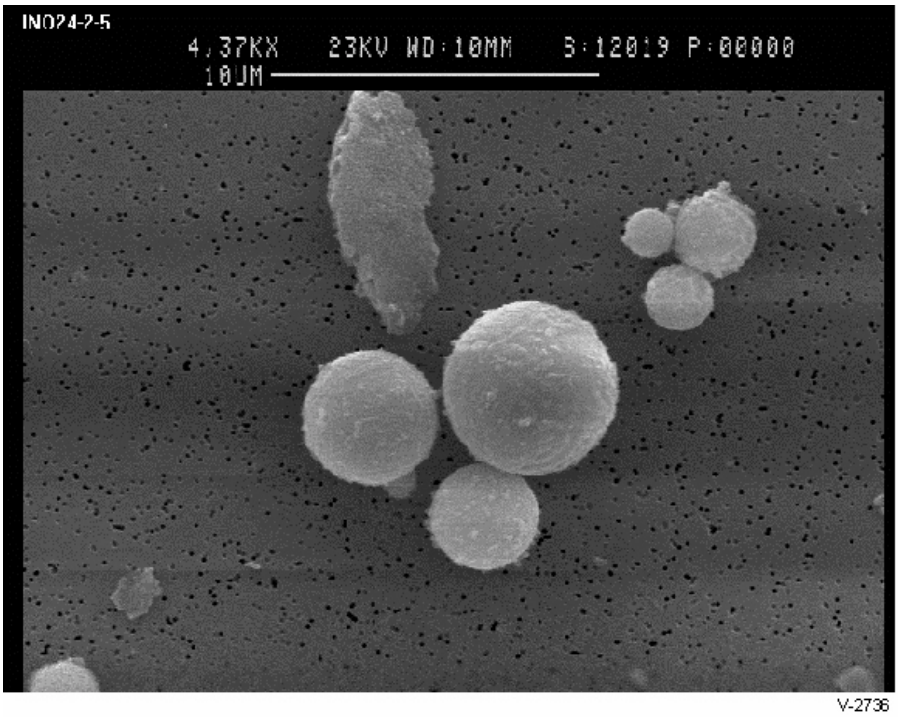

Figure 3-215. SEM photograph of North Dakota lignite ash sample (4,370 times magnification).

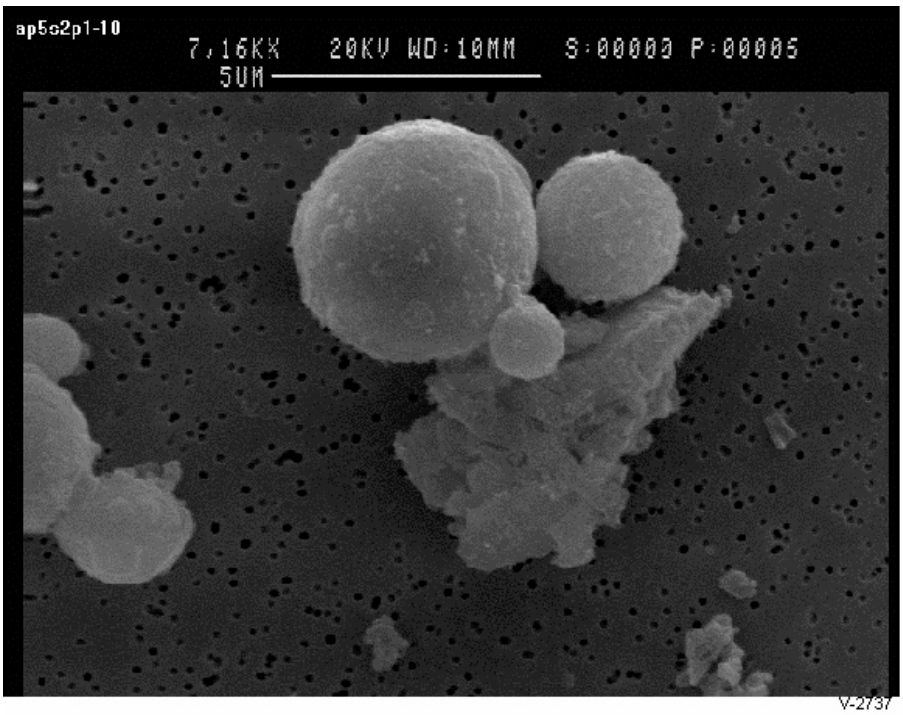

Figure 3-216. SEM photograph of North Dakota lignite ash sample (7,160 times magnification).

Sample 3: (Wyodak). The third sample showed a large number of spherical particles along with some ultrafine aggregates. The irregular shaped particles mentioned earlier were not found in this sample.

The first three pictures, Figures 3-217 through 3-219, in the third sample are a zoom-sequence showing the general types of particles present in the sample. The third picture in the sequence shows some aggregates present in it. This is the general trend, as observed in from the investigation. The number of irregulars is very small in comparison with the other two samples.

The next sequence (Figures 3-220 through 3-223) is also from the third sample (Wyodak) and shows large (2 to 5 µm) irregular particles which might be char and ultrafine aggregates 200 to 500 nm in size with primary particles on the order of tens of nanometers.

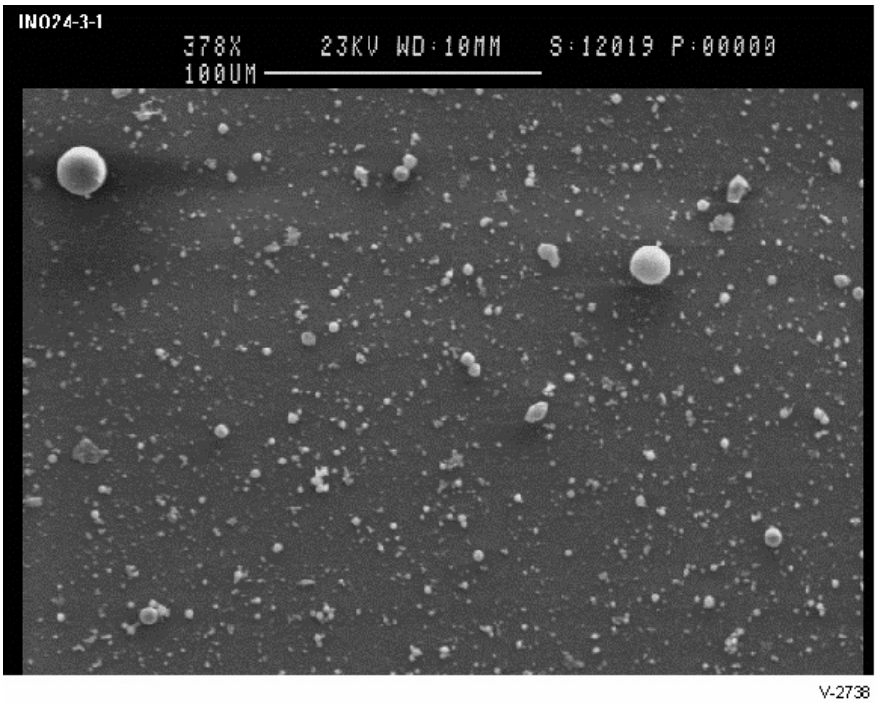

Figure 3-217. SEM photograph of Wyodak ash sample (378 times magnification).

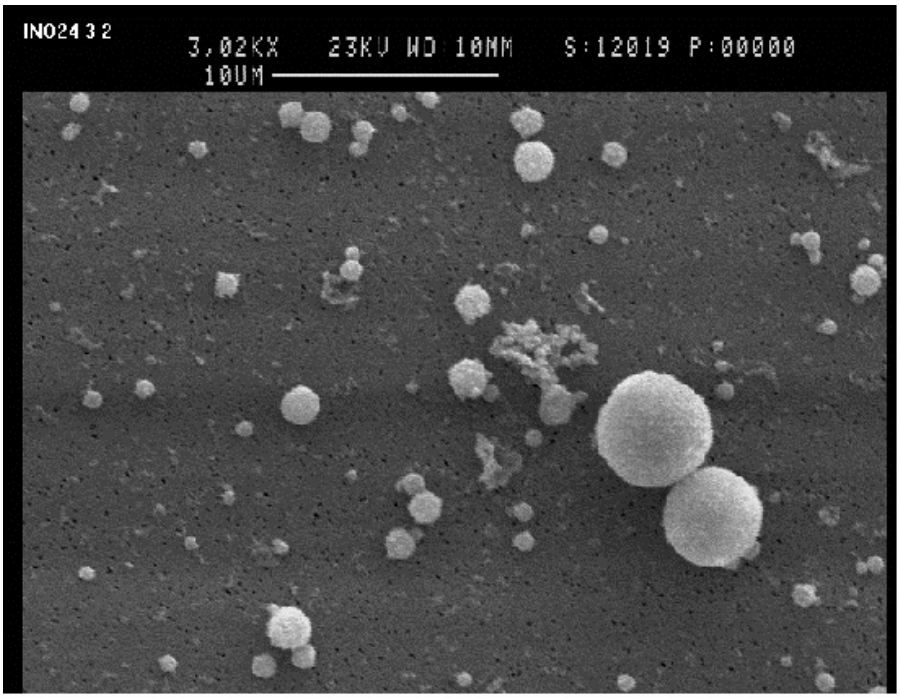

Figure 3-218. SEM photograph of Wyodak ash sample (3,020 times magnification).

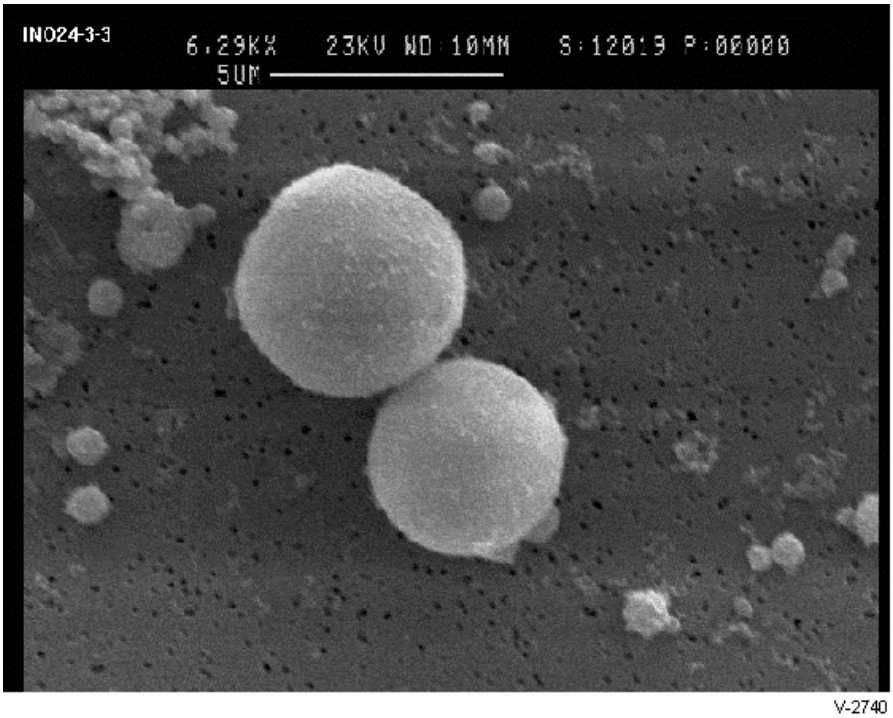

Figure 3-219. SEM photograph of Wyodak ash sample (6,290 times magnification).

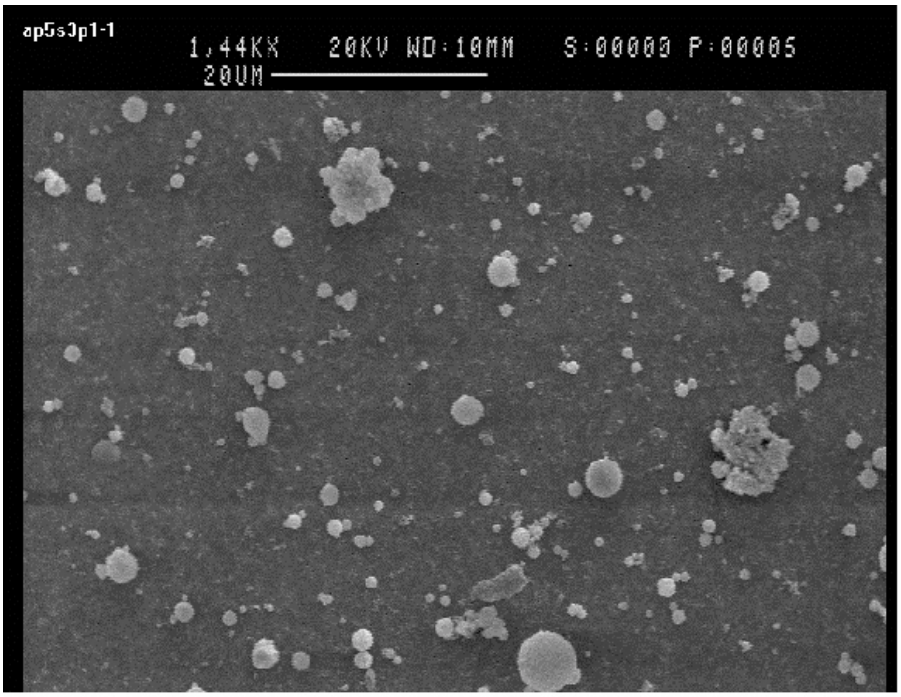

Figure 3-220. SEM photograph of Wyodak ash sample (1,440 times magnification).

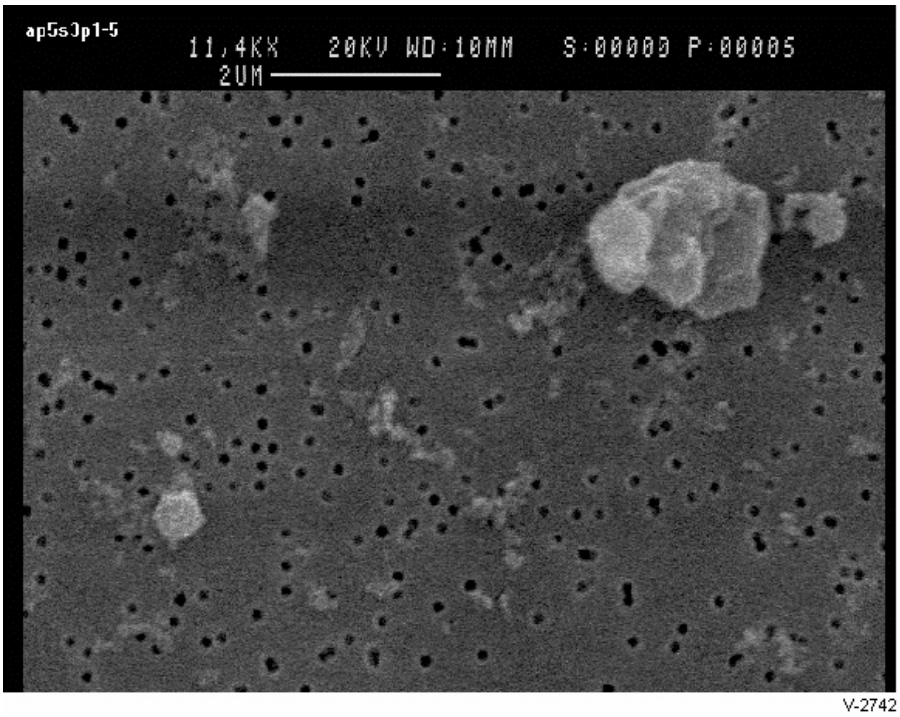

Figure 3-221. SEM photograph of Wyodak ash sample (11,400 times magnification).

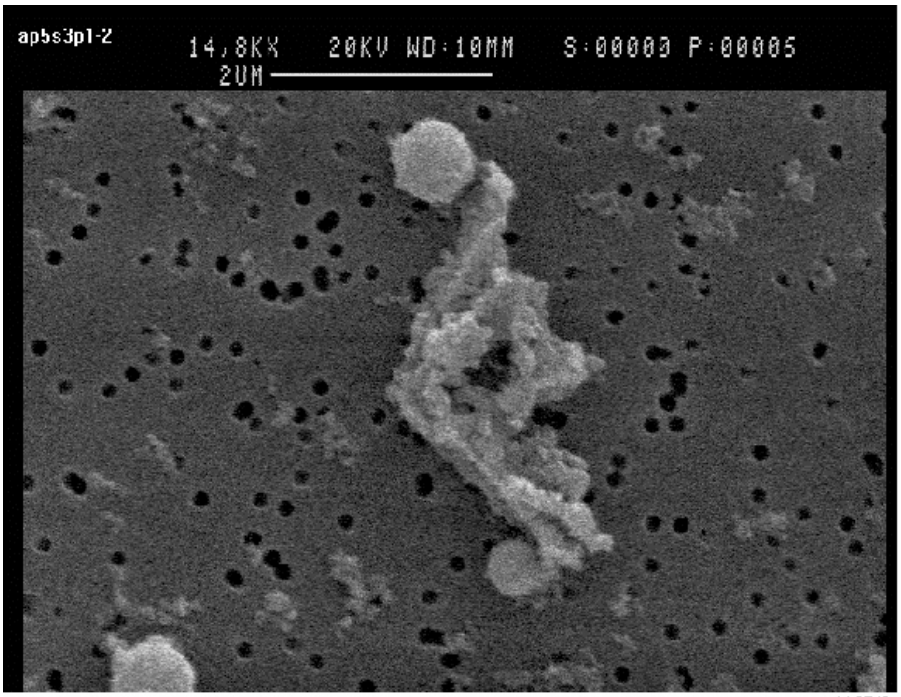

Figure 3-222. SEM photograph of Wyodak ash sample (14,800 times magnification).

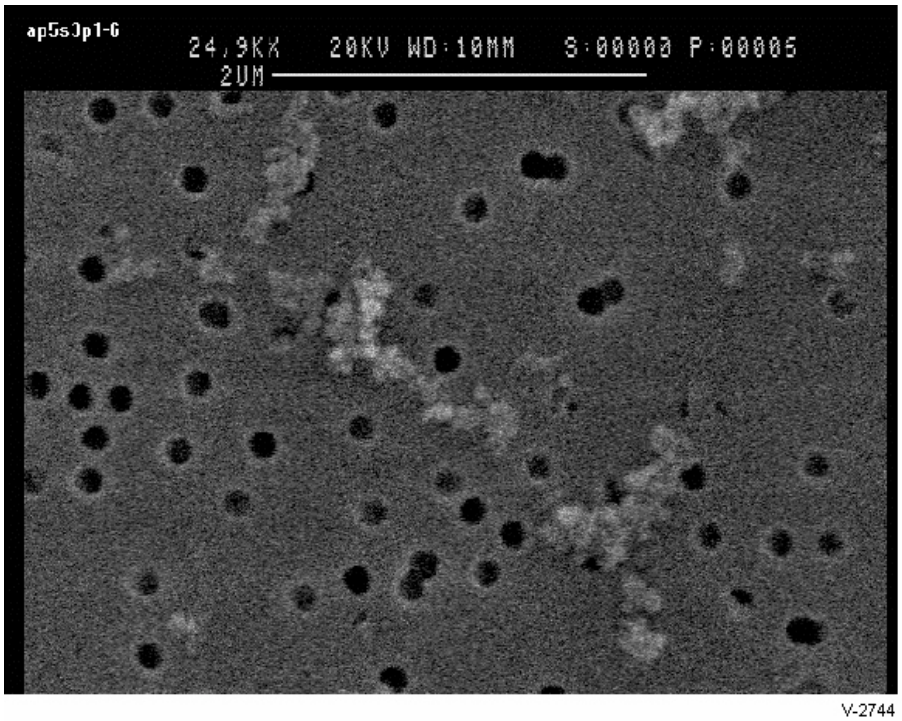

Figure 3-223. SEM photograph of Wyodak ash sample (24,900 times magnification).

Discussion

From the literature, it can said that the spherical particles found in the samples are mineral ash particles formed by the coalescence of minerals during combustion. The large irregularly shaped particles could be unburnt char and the small aggregates, found in abundance only in the Wyodak sample, could possibly be soot. However, these ultrafine particles could also be mineral ash formed by vaporization and condensation. The inference that the Wyodak sample contained soot was made by the fact that a large amount ultrafine aggregates was found by microscopy (that also explains that large surface area of the sample). The sample did not contain the large irregularly shaped particles, suggestive of char, that were found in the other two samples, even though the LOI measurement showed that unburnt carbon was present. Hence the carbon in the sample could be in the form of soot.

The EDS or a qualitative analysis is very useful in determining whether the ultrafine particles are carbon or metal oxides. EDS analysis was not performed on these particles due to limitations of the instrument in the Material Sciences department. The instrument tended to lose focus, when the working distance was changed for the purpose the EDS analyses. Direct viewing at large working distances was also not possible due to limitations of the instrument. The instrument will soon be replaced. Further studies in-depth are hence possible. From the origin of particles (based on the surface area data and what is known about the formation of particle during coal combustion) and the images that were taken, the conclusion made was that the North Dakota and the Ohio samples contained char and the aggregates suggesting soot was not seen. Hence all the carbon in these samples is in the form of char. The Wyodak sample hardly had any char in it. The aggregates suggesting soot were present. Hence the carbon in the sample is in the form of soot also.

XAFS and Mössbauer Characterization

Two suites of fly-ash samples are being characterized and tested at EERC for their propensity for mercury sorption in order to ascertain what parameters might be of most significance for mercury capture from combustion gases at low temperatures. As part of this investigation, ^{57}Fe Mössbauer and sulfur XAFS experiments were conducted at U. Kentucky to complement the testing and characterization being done at EERC. Chlorine XAFS spectroscopy was also attempted on the same samples, but the experiments were not very successful as the chlorine contents were at or below the detection limit of the chlorine XAFS experiment at beam-line X-19A at NSLS.

The first suite of samples examined consisted of a suite of eight ash samples, some of which were fly-ash samples as collected from commercial coal-burning plants and some that had been prepared by thermal treatment either at 400 or 750^{o}C. As indicated in Table 3-141, the Mössbauer data show that iron in all samples is present as Fe^{3+} either in glass or in oxide phases. Two different sub-suites of samples can be identified in these materials depending on whether the Ca ferrite phases are significant or not. The Ca ferrite phases are principally distinguished from Fe^{3+} in glass by their lower isomer shift values, consistent with values reported in the literature [42]. Representative spectra are shown in Figure 3-224.

Table 3-141. Mossbauer Data for First Set of EERC Fly-Ash Samples

Sample ID	IS	QS	Ho	%Fe	Phase
UNDEERC Comanche Ash	0.27	0.88		36	Ca ferrite
	0.24	1.59		57	Ca ferrite
	0.31	-0.19	496	7	Ca ferrite (magnetic)
Valmont Ash Hopper #9	0.31	1.12		47	Fe3+ glass
	1.03	2.08		19	Fe2+ glass
	0.37	-0.03	501	5	Hematite
	0.33	0	480	17	Magnetite A
	0.51	0	444	11	Magnetite B
Valmy Fly-Ash	0.28	1.11		41	Ca ferrite
	0.96	1.86		13	Fe2+ glass
	0.3	-0.1	486	22	Ca ferrite
	0.29	0.08	416	10	Ca ferrite
Blacksville Hopper Ash #1	0.32	0.97		20	Fe3+ glass
	0.37	-0.08	514	10	Hematite
	0.32	0	488.5	34	Magnetite A
	0.52	0	453	22	Magnetite B
	0.52	0	398	13	Magnetite B
Wyodak ashed at 400C	0.28	0.85		42	Ca ferrite
	0.26	1.56		41	Ca ferrite
	0.36	-0.09	512	17	Hematite
Ohio ashed at 750C	0.32	0.61		9	Fe3+ glass
	0.29	1.03		17	Fe3+ glass
	0.35	5.85		3.5	spm Fe3+ oxide
	0.37	-0.1	510	46.5	Hematite
	0.28	0	480	15	Magnetite A
	0.33	0	389	9	spm Fe3+ oxide
Ohio ashed at 400C	0.32	1.11		24	Fe3+ glass
	0.36	-0.09	514.5	37	Hematite
	0.3	0	492	13	Magnetite A
	0.58	0	461	10	Magnetite B
	0.5	0	422.5	15	Magnetite B
Wyodak ashed at 750C	0.3	0.73		32	Ca ferrite
	0.3	1.36		34	Ca ferrite
	0.37	-0.11	513	13	Hematite
	0.25	0.01	433	20	Ca ferrite (magnetic)

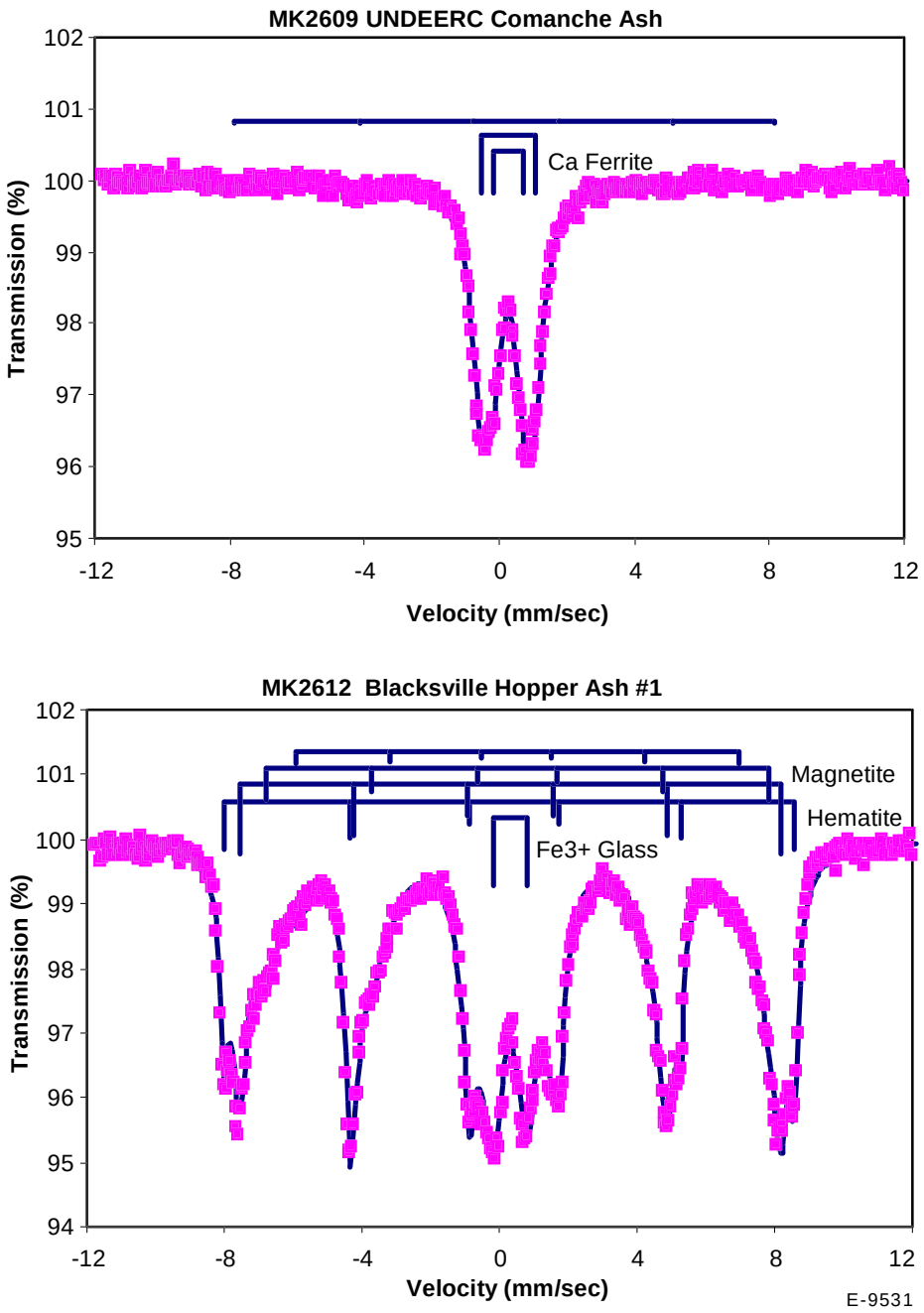

Figure 3-224. Mössbauer spectra of Comanche fly-ash and Blacksville Hopper ash.

The Mössbauer spectra of the eight samples show significant variation. The spectra can be subdivided into two groups: a group of four samples (Ohio 400°C, Ohio 750°C, Valmont, and Blacksville) that exhibited a significant fraction (33-80% of the total iron) of magnetic iron oxides, both hematite and magnetite, and a group (Valmy, Wyodak 400°C, Wyodak 750°C, Comanche) that was dominated by one or both of the calcium ferri-aluminate phases ($Ca(Al,Fe)_2O_4$, or $Ca_2(Al,Fe)_2O_5$). The Wyodak ashes were somewhat transitional since they did exhibit a minor fraction of hematite, but no magnetite. As will be seen below, the four samples

in the calcium ferri-aluminate group also exhibited the four most intense sulfur XANES spectra and this is clearly a further manifestation of the well-known relationship between the sulfur content and calcium content of fly-ashes.

In the sulfur XANES spectra of the same eight ash samples (Figure 3-225), there was observed to be a 100-fold difference in the sulfur K-edge step-height among the different samples and this was reflected mostly in the quality of the spectral data obtained, rather than in differences in the sulfur forms. Sulfate forms dominated (>95% of the sulfur) seven of the eight spectra. Two samples (Valmont and Blacksville) exhibited the presence of reduced sulfur forms (organic sulfur forms, probably thiophenic), but the amounts were very minor (<5% of the total sulfur). Only one sample demonstrated a significantly different spectrum and this was the Valmy ash, with the highest sulfur content. The spectrum of this sample clearly showed evidence for a significant sulfite (SO_3^{2-}) species, in addition to sulfate. Except for the Valmont, Valmy, and Blacksville fly-ash samples, the major species present in these fly-ash samples could be identified as calcium sulfate, ($CaSO_4$), from the sulfur XANES spectra. Attempts to measure the chlorine XAFS spectra of some of these same coal fly-ash samples indicate that the chlorine contents are at or below the detection limit of the method. No useful information was obtained.

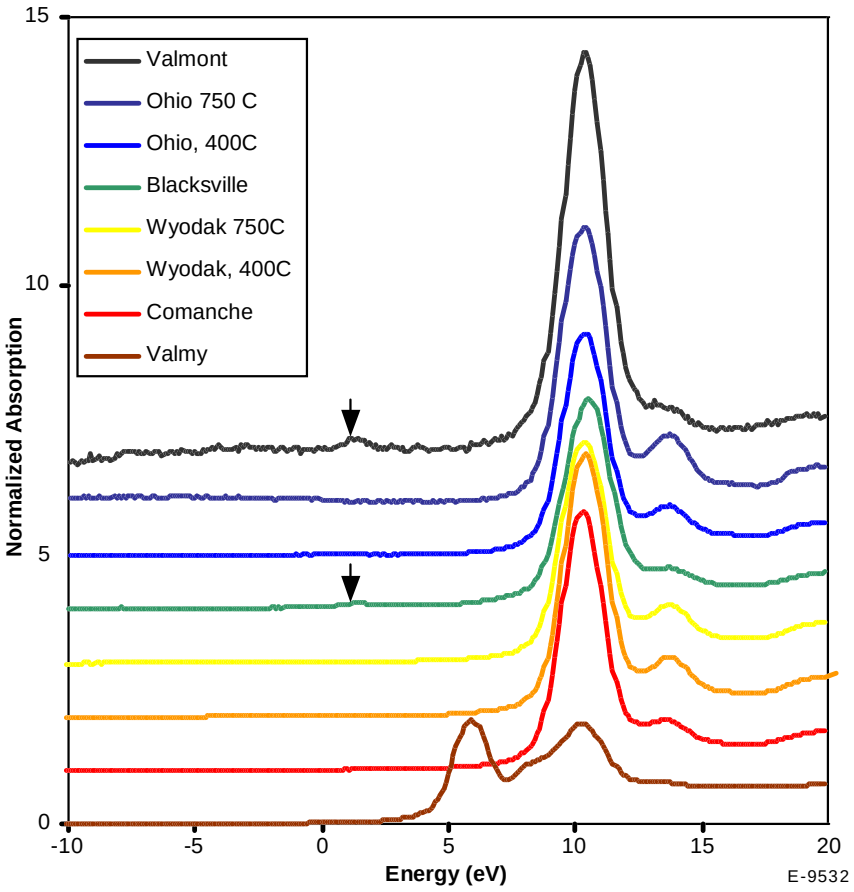

Figure 3-225. Sulfur XANES of first set of samples from EERC.

Similar Mössbauer and sulfur XAFS data were obtained for the second set of samples received from EERC. Results of the analyses are summarized in Figure 3-226 and Table 3-142. In the sulfur XANES spectra (Figure 3-226), there is observed to be a wider range in sulfur forms among the different samples than in the first set of eight samples reported above. Three of the five spectra exhibit minor sulfide forms; in two cases (samples "AA" and "MA"), the amounts of sulfide sulfur are quite significant (>30% of the S). Only one sample ("GA") contained all of its sulfur as sulfate.

The least-squares fitting of the sulfur XAFS data for both sets of samples are summarized in Table 3-143 and examples of the least-squares fitting are given in Figure 3-227. The wide range in step-height should be noted; for one series of ash samples, the step-height, which is a very approximate measure of the sulfur concentration, varies by a factor of 250, while for the other series the factor is about 10. It is likely that the calcium content of the ash is important in controlling the sulfur retention by these ashes.

Attempts to measure the chlorine XAFS spectra of some of these same coal fly-ash samples indicate that the chlorine contents are at or below the detection limit of the method for four of the five samples. Only sample "DMA" contained detectable chlorine, but no useful information could be obtained.

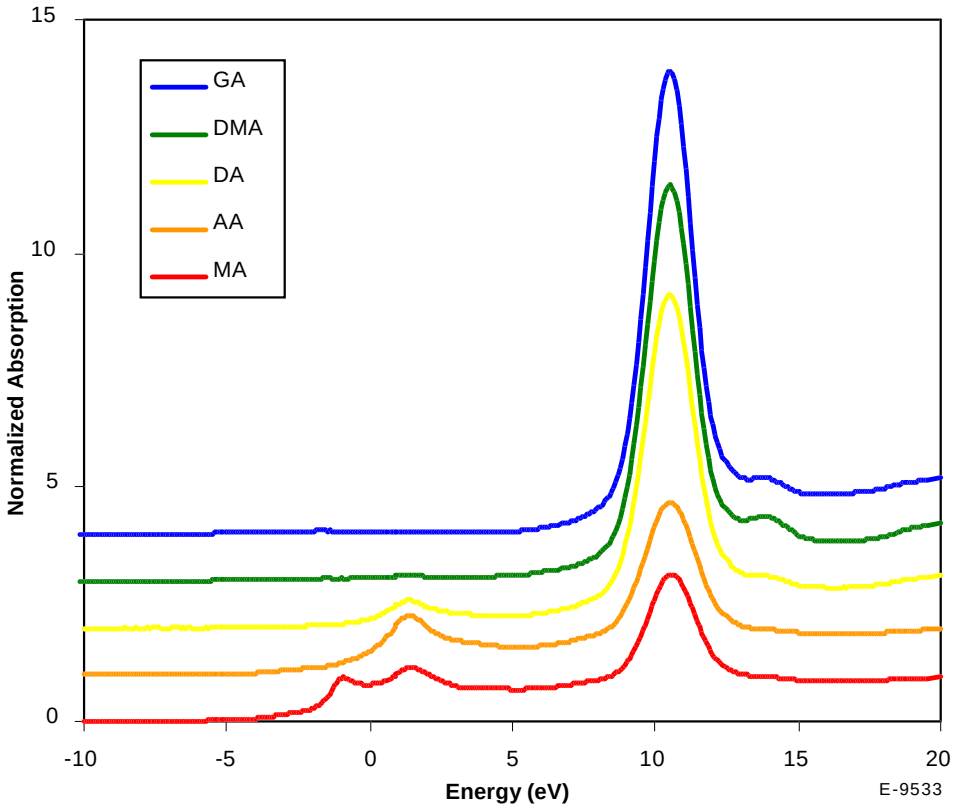

Figure 3-226. Sulfer XANES of second set of samples from EERC.

Table 3-142. Mossbauer Data for the Second Set of Samples from EERC

Sample ID	IS	QS	Ho	%Fe	Phase
AA Ash UNDEERC	0.43	0.67		9	Fe3+ glass
	0.92	2.01		26.5	Fe2+ glass
	0.37	-0.09	515	8	Hematite
	0.29	0	488	21.5	Magnetite A
	0.66	0	454	35	Magnetite B
DA Ash UNDEERC	0.31	1.07		18	Fe3+ glass
	1.02	2.01		11	Fe2+ glass
	0.36	-0.09	514	10.5	Hematite
	0.3	0	490	29.5	Magnetite A
	0.64	0	457	18	agnetite B1
	0.61	0	419	13	agnetite B2
DMA Ash UNDEERC	0.27	0.98		39	Fe3+ glass
	0.93	1.13		18	Fe2+ glass
	0.95	1.95		18	Fe2+ glass
	0.27	0	475	5	Magnetite A
	0.63	0	442	20	Magnetite B
GA Ash UNDEERC	0.32	1.04		25.5	Fe3+ glass
	0.95	2.04		10	Fe2+ glass
	0.37	-0.09	513	15.5	Hematite
	0.31	0	489	21	Magnetite A
	0.61	0	452	27.5	Magnetite B
MA Ash UNDEERC	0.34	0.95		30	Fe3+ glass
	0.99	1.97		19.5	Fe2+ glass
	0.37	-0.09	513	7	Hematite
	0.31	0	488	16	Magnetite A
	0.57	0	448	16	Magnetite B

Table 3-143. Results of Least-Squares Fitting S XANES Spectra – EERC Ash Samples

Ash	Relative Step-Height	%S in				
		Pyrrhotite	Pyrite	Thiophene	Sulfite	Sulfate
Set 1						
Valmont ash	1			3		97
Ohio 750°C	3					100
Ohio 400°C	18					100
Blacksville hopper	25			4		96
Wyodak 750°C	42					100
Wyodak 400°C	50					100
Comanche	53					100
Valmy ash	250			0	47	53
Set 2						
Sample “AA”	8.9	10	23	27		41
Sample "DA"	2.5					
Sample "DMA"	1.6			3		97
Sample "GA"	1					100
Sample "MA"	6.5	9	56	17		18

The Mössbauer spectra of this group of five samples also showed significant variation and the results are summarized in Table 3-143. However, compared to the data for the earlier series (Table 3-142), there is no evidence for Ca ferrite phases in these samples, with the possible exception of sample “DMA” so that all samples are more like one of the sub-groups in the earlier series of samples. Four of the five samples exhibited both magnetic oxides, hematite and magnetite, as well as ferric and ferrous glass absorption features, in their Mössbauer spectra. The fifth sample, “DMA” contained no detectable hematite, but possibly some calcium ferrite phases instead, as the magnetite parameters are a little unusual. Sample “GA”, which exhibited the highest fraction of sulfur as sulfate, also had the highest fraction of iron as ferric, indicating both elements are fully oxidized.

3.4.4.5 Bench-Scale Test Results

Table 3-144 lists the runs completed with elemental mercury injection and includes the concentration of mercury on the spent ash (if it was submitted for analysis), the amount of mercury generated during the test, the mass balance based on data from each of the mercury CEMs used during the test, and the mercury collection efficiency of the ash at 100% breakthrough. The mass balance is the ratio of the mercury measured (on the ash and in the flue gas) to the mercury generated (based on the average mercury permeation rate determined with wet-chemistry measurements). The collection efficiency at 100% breakthrough is based on the mercury on the spent ash, or the integrated area under the curve if ash analysis is not available, and the amount of mercury generated (permeation rate) in the time it took to reach 100% breakthrough. It appears the collection efficiencies based on the integrated breakthrough curve

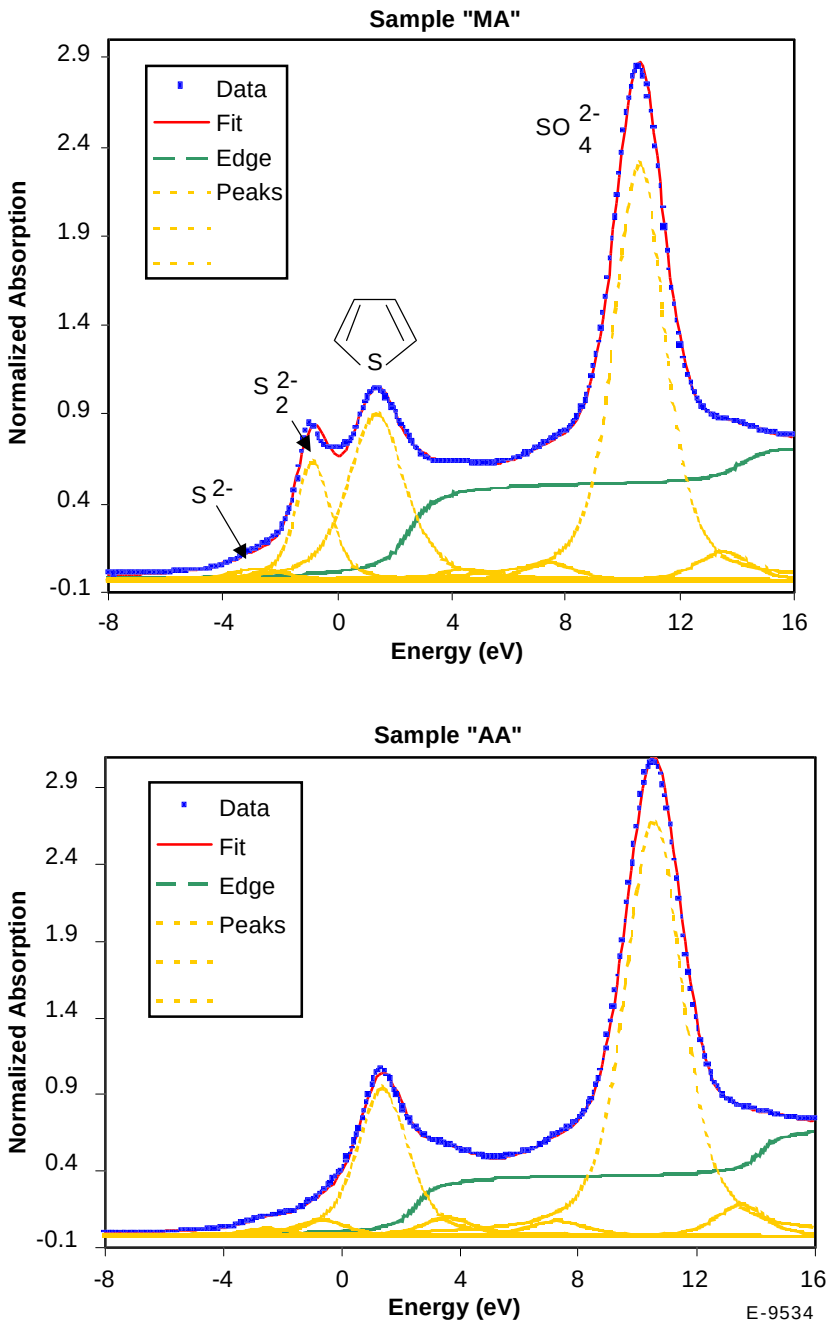

Figure 3-227. Examples of LSQ fitted sulfur XANES spectra for EERC ash samples. Peaks are due to pyrrhotite (S^{2-}), pyrite (S_2^{2-}), thiophenic sulfur and sulfate (SO_4^{2-}), respectively, with increasing energy.

Table 3-144. Results from Tests with Hg^0 Injection

Run No.	Fly Ash	Temp., °F	Hg^0 on Ash, µg/g	Hg^0 on Spent Ash, µg/g	Hg^0 Gen., µg	Semtech Mass Balance, %	PSA Mass Balance, %	Tekran Mass Balance, %	Collection Efficiency @ 100% Breakthrough
957	Ohio	250	0.276	ND[a]	ND	ND	ND	ND	ND
960	Ohio	350	0.276	ND	ND	ND	ND	ND	ND
988	Ohio ashed @ 400°C	300	ND	ND	ND	ND	ND	ND	ND
989	Ohio ashed @ 750°C	300	ND	ND	ND	ND	ND	ND	ND
958	Wyodak	250	1.29	2.51	43.8	98	101	98	10[b]
962	Wyodak	350	1.29	ND	ND	ND	ND	ND	42[c]
990	Wyodak ashed @ 400°C	350	ND	ND	ND	ND	ND	ND	ND
991	Wyodak ashed @ 750°C	350	ND	ND	ND	ND	ND	ND	ND
959	ND lignite	250	0.536	ND	ND	ND	ND	ND	ND
961	ND lignite	350	0.536	ND	ND	ND	ND	ND	ND
963	Coal Creek	350	0.0067	ND	ND	ND	ND	ND	ND
1149	Blacksville	250	0.140	1.21	30.6	80	108	86	13[b]
964	Blacksville	350	0.140	ND	ND	ND	ND	ND	ND
974	Valmy	250	0.557	ND	ND	ND	ND	ND	ND
1104	Valmy	250	0.557	1.40	28.8	75	85	76	ND
1127	Valmy	250	0.557	1.67	24.1	106	121	104	43[b]
1153	Valmy	350	0.557	ND	ND	ND	ND	ND	ND
1155	Valmont	250	ND	ND	ND	ND	ND	ND	ND
1111	Valmont	350	ND	0.09	24.3	95	123	95	3[b]
975	Comanche	250	1.05	ND	ND	ND	ND	ND	ND
1112	Comanche	350	1.05	0.40	18.2	113	127	115	0[b]
1150	Comanche	350	1.05	ND	ND	ND	ND	ND	ND
1103	AA	250	0.282	0.93	26.2	71	78	70	12[b]
1126	AA	250	0.282	1.28	33.7	103	117	102	17[b]
1154	AA	350	0.282	ND	ND	ND	ND	ND	ND
1048	DA	250	0.114	ND	ND	ND	ND	ND	64[c]
1049	DMA	250	0.051	ND	ND	ND	ND	ND	ND
1044	GA	250	0.002	ND	ND	ND	ND	ND	ND
1109	MA	250	0.060	0.87	21.5	106	111	115	31[b]
1113	MA	350	0.060	0.20	22.9	95	113	104	14[b]

Table 3-144. (Continued) Results from Tests with Hg^0 Injection

Run No.	Fly Ash	Temp., °F	Hg^0 on Ash, µg/g	Hg^0 on Spent Ash, µg/g	Hg^0 Gen., µg	Semtech Mass Balance, %	PSA Mass Balance, %	Tekran Mass Balance, %	Collection Efficiency @ 100% Breakthrough
1114	MA	250	0.060	0.74	23.3	102	114	107	13[b]
1105	Dale	250	0.0010	10.27	40.2	72	83	80	48[b]
1108	Dale	250	0.0010	30.0	71.4	119	134	128	ND
1110	Dale	250	0.0010	12.0	21.9	180	191	179	309[b]
1138	Black Thunder	250	2.13	ND	ND	ND	ND	ND	ND
1141	Black Thunder	350	2.13	ND	ND	ND	ND	ND	ND
1139	Cordero Rojo	250	0.183	ND	ND	ND	ND	ND	ND
1142	Cordero Rojo	350	0.183	ND	ND	ND	ND	ND	ND
1140	Absaloka	250	0.223	2.33	27.3	93	93	89	26[b]
1143	Absaloka	350	0.223	0.51	16.9	96	100	89	5[b]

[a] Not determined.
[b] Mercury captured based on mercury on spent ash.
[c] Mercury captured based on integration of breakthrough curve.

are higher than those based on ash analysis. The difference may be caused by offgassing of collected mercury during the remainder of the test, then the ash analysis would give artificially low collection efficiencies or if there is a lag time in the mercury (particularly $HgCl_2$) passing through the system. The difference may be caused by one or both of these, but it does give a basis for comparison of ashes and their ability to capture mercury. For many samples, the collection efficiency is zero, and the ash showed no ability to capture mercury.

Test Results

To help with the interpretation of the results, the test protocol for each run is essentially the same. At the start of each test, the concentration of total mercury at the outlet of the fixed bed is measured until 100% breakthrough is reached (outlet mercury concentration equals the inlet mercury concentration). At this point, the conditioning/conversion system is switched to measure the elemental mercury concentration at the outlet of the fixed bed (noted on the plots as Hg^0). If no oxidation is taking place, the concentration will remain at 100% of the inlet elemental mercury concentration. However, if any of the elemental mercury is being oxidized across the filter, it will show as a drop in the outlet concentration of elemental mercury. After the outlet elemental mercury concentration is measured, the system is switched to measure the total inlet mercury concentration. When the elemental mercury concentration is measured at the outlet of the fixed-bed when $HgCl_2$ is injected, the expected concentration is zero. If it is higher than zero, this indicates some of the $HgCl_2$ has been reduced to elemental mercury.

The intention was to run the first four series of tests with the ash samples generated at UA. The first series of tests was to determine an optimum operating temperature for observing interactions between the fly ash samples and mercury in a simulated flue gas. Figures 3-228 through 3-230 plot the results from the tests with the Ohio blend, Wyodak, and North Dakota lignite samples at both 250 and 350°F. Figure 3-230 also plots the results from a test with an ash sample from the Coal Creek Station, which burns the North Dakota lignite. The results from these tests showed the Ohio blend and North Dakota lignite ash samples had no capacity for mercury capture and the Ohio blend showed the ability to oxidize elemental mercury at the higher temperature. The Wyodak ash showed some capacity for mercury capture at both temperatures, with the capacity decreasing with increasing temperature. In an effort to look at the capture efficiencies of the ashes on an equal basis, the capture efficiency at 100% breakthrough was calculated for those samples that showed some capture, and the results are presented in Table 3-144. For those ashes that showed no capture of mercury (ND), the efficiency can be assumed to be zero. The capture efficiency was calculated as:

$$\frac{\text{mercury captured}}{\text{mercury generated at 100\% breakthrough}} * 100\% .$$

For those samples that were not analyzed for mercury concentration, the amount of mercury captured was determined by integrating the breakthrough curve. There are potential problems with both methods. The efficiency based on the measured mercury on the spent sorbent may be low because it does not take into account any mercury that offgases from the surface after 100%

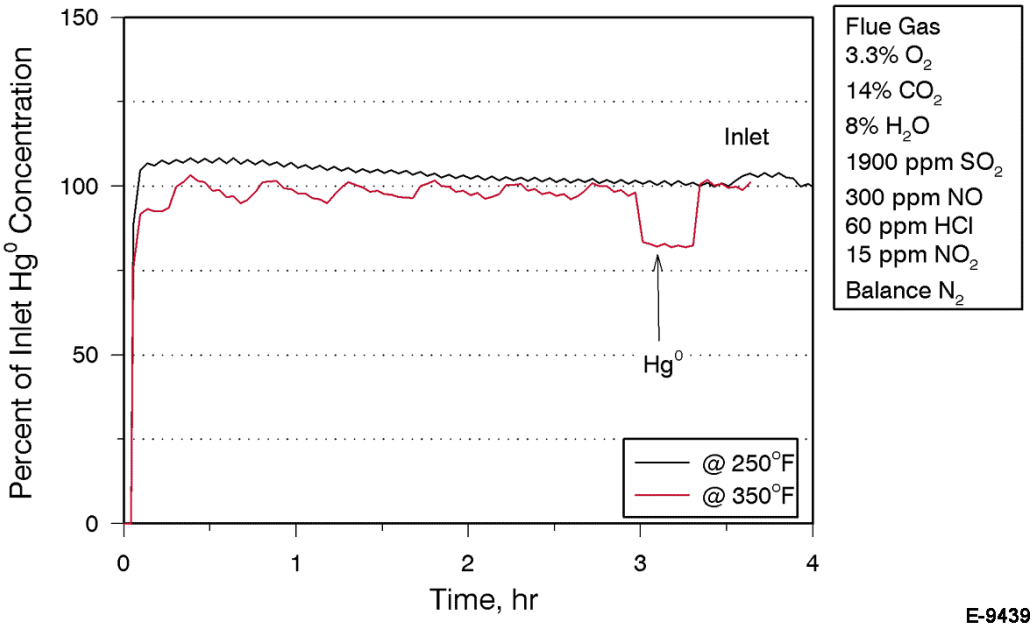

Figure 3-228. Outlet mercury concentration as a function of time for Ohio blend ash at 250 and 350°F.

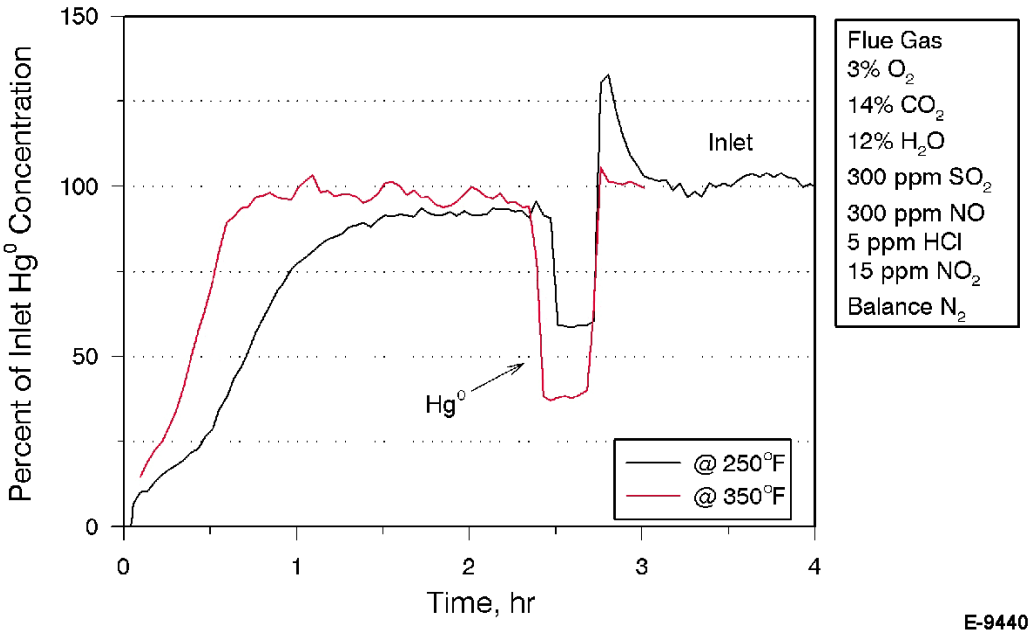

Figure 3-229. Outlet mercury concentration as a function of time for Wyodak ash at 250 and 350° F.

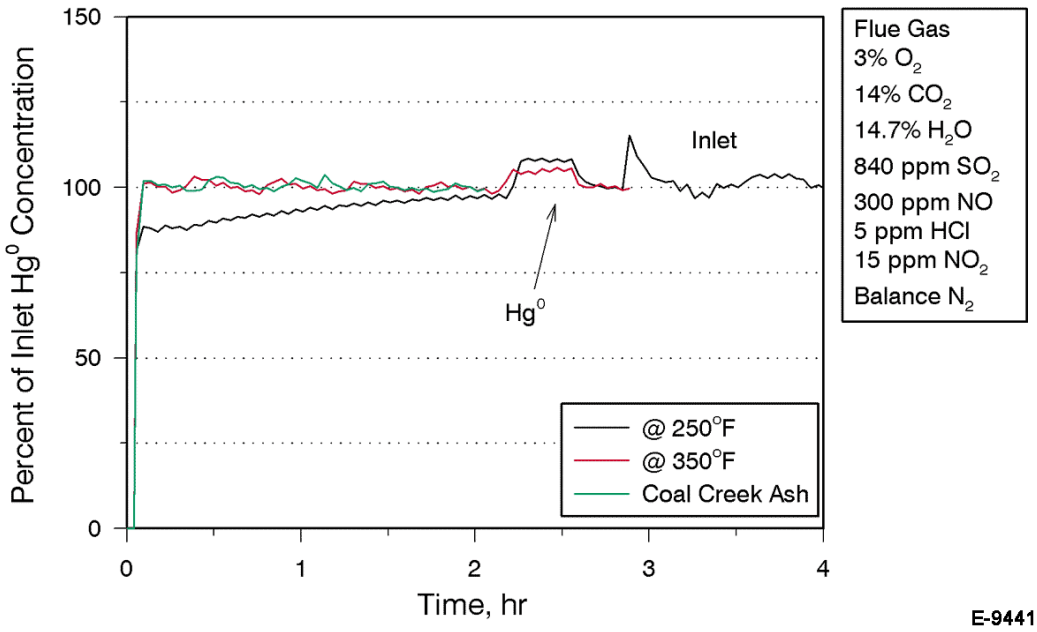

Figure 3-230. Outlet mercury concentration as a function of time for the North Dakota lignite ash at 250 and 350° F and the Coal Creek ash at 350°F.

breakthrough is reached. On the other hand, the efficiency based on the integration of the breakthrough curve may be high because of a lag in the breakthrough. Mercury capture efficiency for the Wyodak ash at 250°F is based on the amount of mercury measured on the spent sorbent, while the efficiency at 350°F is based on the integration of the breakthrough curve. The mass balance for the test at 250°F indicates there was no offgassing of mercury from the sorbent once 100% breakthrough was reached. This indicates the efficiency at 350°F is most likely high. The Wyodak ash also showed a temperature effect on oxidation of elemental mercury. Roughly 40% of the elemental mercury was oxidized at 250°F and 60% at 350°F.

Because two of the baseline ashes were essentially nonreactive, no conclusions could be made about the optimum temperature to observe interactions between the fly ash samples and mercury in the simulated flue gas. As a result, there were deviations from the original test plan. Additional tests were conducted to identify other reactive ash samples. Based on the UU results which showed the Wyodak ash contained soot, a new series of tests was conducted to evaluate the role of the carbon in the ash. Several ash samples were ashed to remove the unburned carbon, and these ashed samples were evaluated in the bench-scale unit to determine carbon's role in the capture of mercury.

Since it is not clear if the carbon in the ash was responsible for the high capture, samples of the Wyodak ash and Ohio blend ash were subjected to a high- (750°C) and low- (400°C) temperature ashing process to remove the unburned carbon. These samples were then evaluated in the bench-scale system. Samples of the Blacksville and Valmy ash were also ashed, but were only evaluated with $HgCl_2$ injection. The LOI and mercury concentration of the ashed samples were measured and found to be zero. The samples ashed at 400°C showed a slight color change from the baseline ash which was consistent with the removal of the unburned carbon (i.e.,

changing from a grey to a light tan color). However, the ashing process significantly changed the color of the samples ashed at 750°C, indicating there may have been a change to the mineralogy of the samples. Therefore, samples of each ashed sample were sent to PSI for additional surface area determination and Mössbauer analysis, which are presented in Table 3-145.

Table 3-145. Mössbauer Data

Ash Sample	Hematite, %	Magnetite, %	Fe3+ Oxide, %	Fe3+ Glass, %	Fe2+ Glass, %	Ca Ferrite, %	Mg, Ca Ferrite, %
Ohio ashed @ 400°C	37	38		24			
Ohio ashed @ 700°C	46.5	15	12.5	26			
Wyodak ashed @ 400°C	17					83	
Wyodak ashed @ 700°C	13					66	20
Blacksville	10	69		20			
Comanche						93	7
Station A	5	28		47	19		
Station B					13	87	
GA ash	15.5	48.5		25.5	10		
AA ash	8	56.5		9	26.5		
DMA ash		25		39	36		
DA ash	10.5	60.5		18	11		
MA ash	7	43		30	19.5		

Figure 3-231 is a plot of the outlet total mercury concentration as a function of time for the Ohio blend fly ash, ashed at 400 and 750°C and evaluated at 300°F, and the results from the baseline tests at 250 and 350°F. The results from these tests are similar to those for the base ash evaluated at 350°F. Initial breakthrough is immediate, and the outlet concentration quickly reaches 100% of the inlet concentration. After 1 hour, the 400°C ashed sample oxidized roughly 30% of the elemental mercury, and the 750°C ashed sample oxidized only 10% of the elemental mercury. The color of the sample ashed at 400°C was a light tan, which would be expected when the carbon was removed from the parent ash. However, as mentioned, there was a drastic change in the color of the ash from the sample ashed at 400°C to the sample ashed at 750°C which was a reddish-orange color. The color change indicates a transformation of the base ash material when subjected to the ashing process.

Figure 3-232 plots the outlet mercury concentration as a function of time for the Wyodak samples ashed at 400 and 750°C and evaluated at 350°F and the results from the baseline tests at 250 and 350°F. The ashed samples of Wyodak ash showed no reactivity during these test. Again, there was a color change in the ash from the sample ashed at 400°C and the sample ashed at 750°C. The baseline Wyodak ash was very reactive to elemental mercury at both 250 and 350°F; both capture and oxidation of the elemental mercury were observed. It is unknown if the change in reactivity was a result of removing the carbon from the ash or if there was a mineralogical change in the baseline ash.

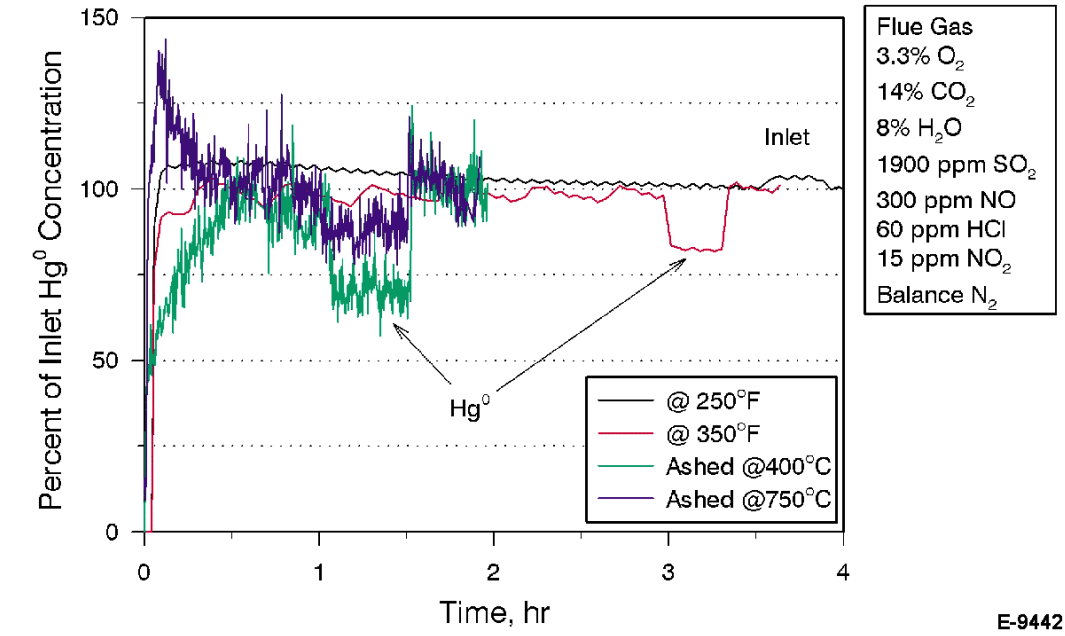

Figure 3-231. Outlet mercury concentration as a function of time for the Ohio blend fly ash, ashed at 400 and 750°C and evaluated at 300°F, and the results from the baseline tests at 250 and 350°F.

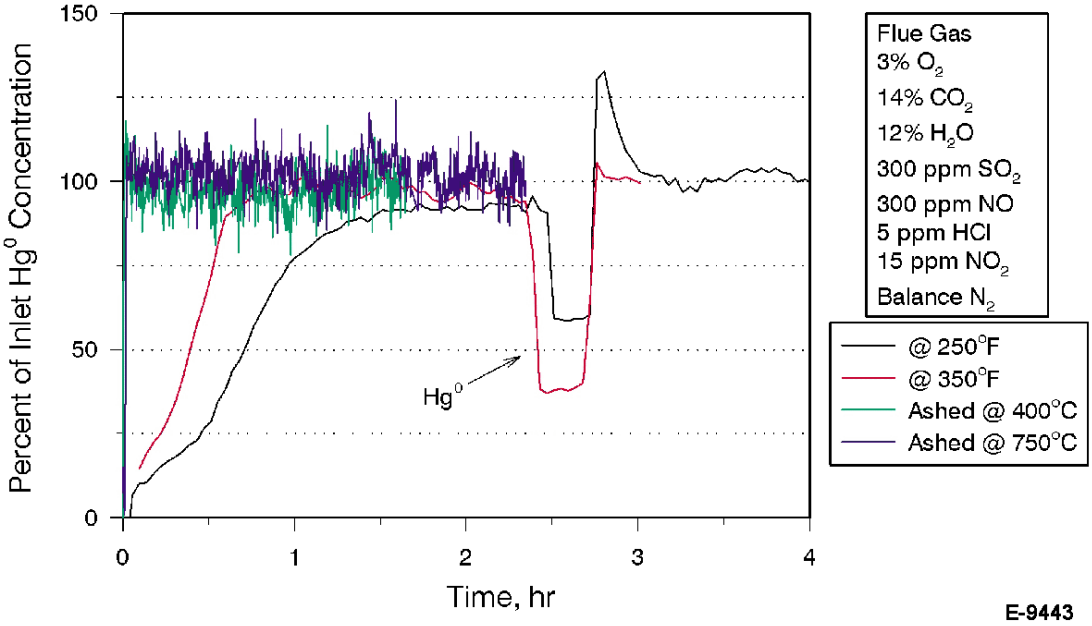

Figure 3-232. Outlet mercury concentration as a function of time for the Wyodak samples ashed at 400 and 750°C and evaluated at 350°F, and the results from the baseline tests at 250 and 350°F.

Based on the results with the initial ash samples, it did not appear there was an optimum temperature for observing capture and oxidation effects with elemental mercury injection, and as mentioned, two of the three ashes were unreactive. Therefore, a number of different ashes were evaluated to find ash samples that were reactive with elemental mercury. These ash samples were also characterized in terms of LOI and surface area in order to develop correlations between the LOI, surface area, mercury capture, and oxidation of elemental mercury.

Figure 3-233 plots the results from the tests with the Blacksville ash at 250 and 350°F. Others have reported that the Blacksville ash is very reactive, but they used a flue gas that did not have all of the reactive gases present [200]. The results at 250 and 350°F are very similar and show the ash has almost no capacity for mercury capture but oxidized between 25% and 45% of the elemental mercury, with the higher oxidation taking place at the lower temperature.

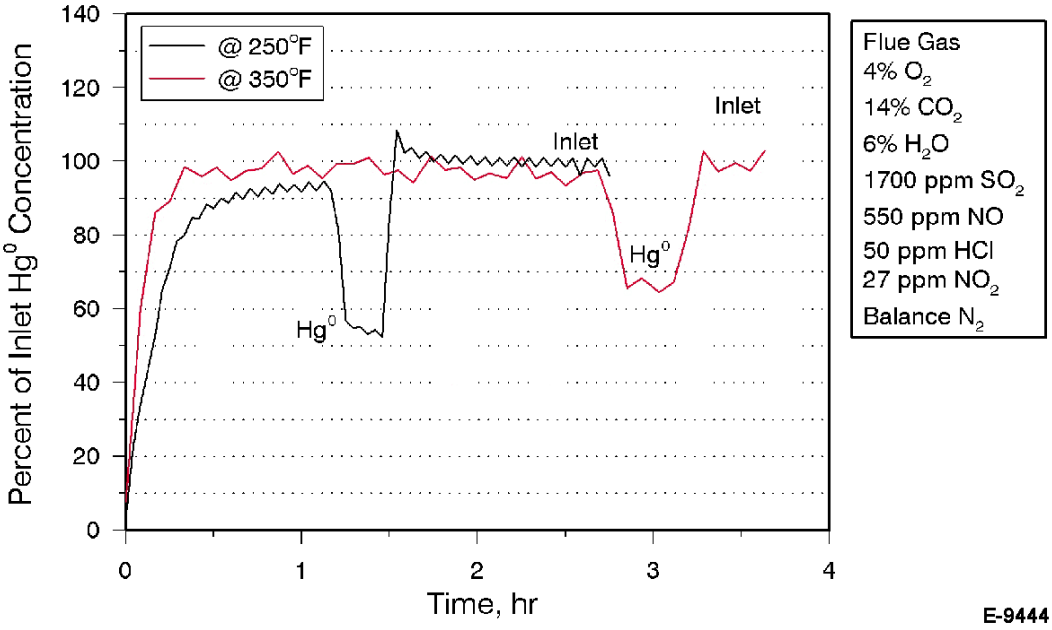

Figure 3-233. Outlet mercury concentration as a function of time for the Blacksville ash at 250 and 350°F.

There were problems with the first two runs with the Valmy ash at 250°F, and the results are not plotted here. Figure 3-234 plots the results from the tests with the Valmy ash at 250°F (Run 1127) and 350°F with elemental mercury injection. The baseline flue gas mixture was used during this test. The ash showed some capacity for mercury capture, with 43% capture at 100% breakthrough for the test at 250°F. The ash also oxidized roughly 50% of the elemental mercury at 250°F and 40% at 350°F.

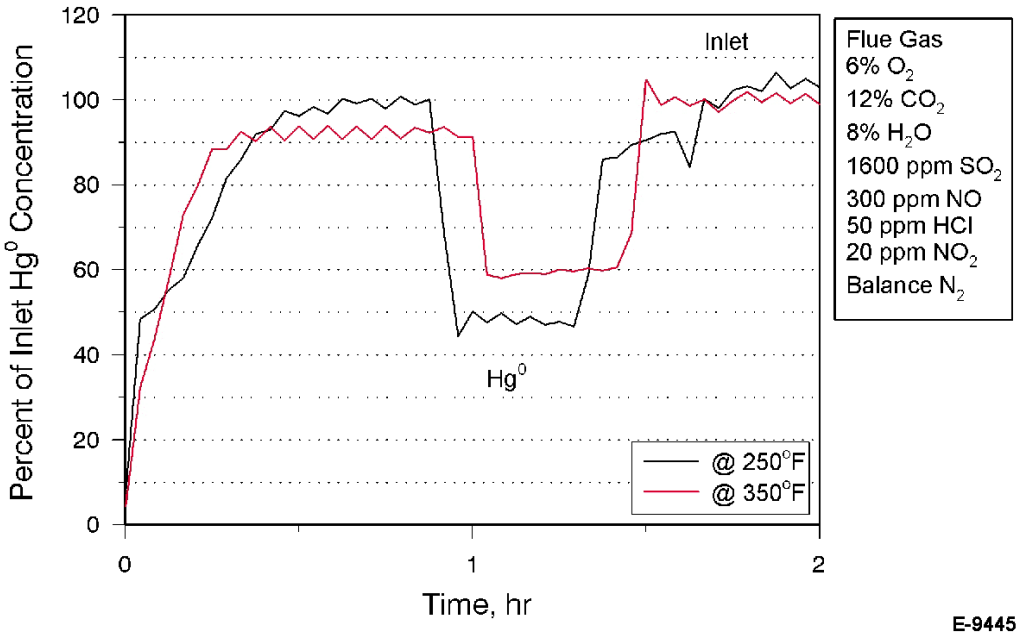

Figure 3-234. Outlet mercury concentration as a function of time for the Valmy ash at 250 and 350°C.

A second western bituminous ash, from the Valmont Station, was evaluated, and the results are plotted in Figure 3-235. This ash showed almost no capacity for elemental mercury capture, but did show a significant temperature effect on the oxidation of elemental mercury. At 250°F, roughly 70% of the elemental mercury was oxidized while only 30% was oxidized at 350°F.

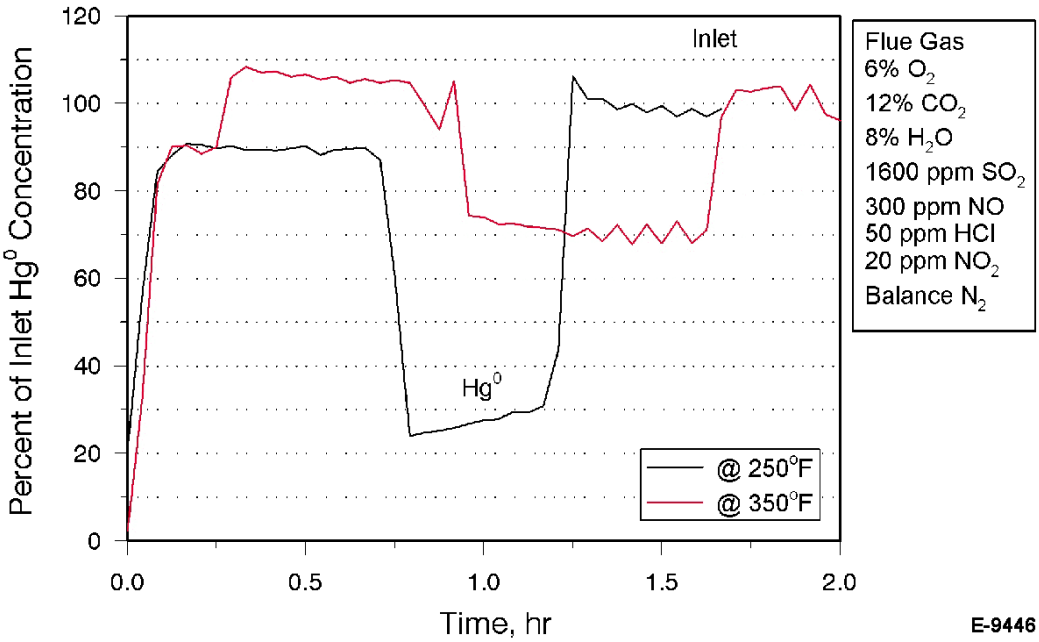

Figure 3-235. Outlet mercury concentration as a function of time for the Valmont ash at 250 and 350°F.

Six ash samples sent by PSI were also evaluated in the bench-scale unit. These samples included ash from the Comanche Station and the five eastern bituminous ash samples. Figure 3-236 plots the results from the tests with the Comanche ash at 250° and 350°F. The baseline flue gas was used with these tests. The ash captured some mercury at 250°F but nothing at 350°F. Less than 20% of the elemental mercury was oxidized at 350°F and roughly 25% at 250°F.

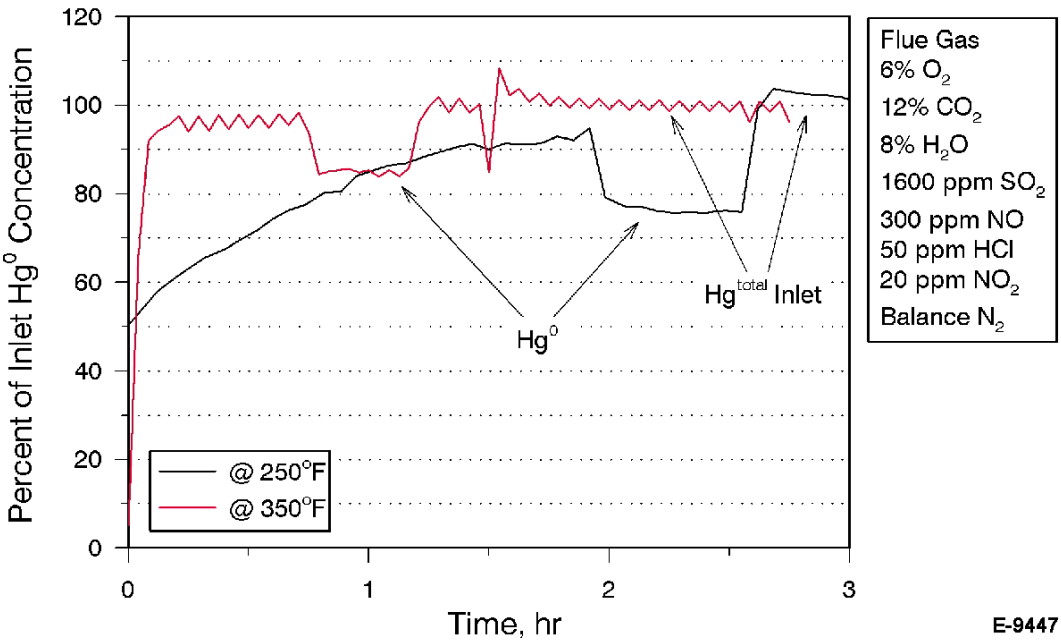

Figure 3-236. Outlet mercury concentration as a function of time for the Comanche ash at 250 and 350°F.

The results from an initial test (Run 1103) with the AA ash were questionable because of low inlet mercury concentrations. The information from this run was presented in Table 3-144, but the results are not plotted here. Figure 3-237 plots the results for the repeat test at 250°F and the test at 350°F with elemental mercury injection. The five samples of ash from eastern bituminous coals (AA, DA, DMA, GA, MA) were all evaluated with the Blacksville flue gas mixture, with the exception of the MA which had an increased HCl concentration of 75 ppm. This ash showed some capacity for capture. At 250°F, the capture efficiency at 100% breakthrough was 17%. This ash also showed a significant amount of oxidation of the elemental mercury with increased oxidation at the lower temperature.

Figure 3-238 plots the results from the test with the DA ash at 250°F with elemental mercury. Based on the integrated breakthrough curve, the collection efficiency at 100% breakthrough was 64%, but it appears there was offgassing of captured mercury after breakthrough. While this ash did show some capacity for capture and significant oxidation, it was not evaluated further with elemental mercury.

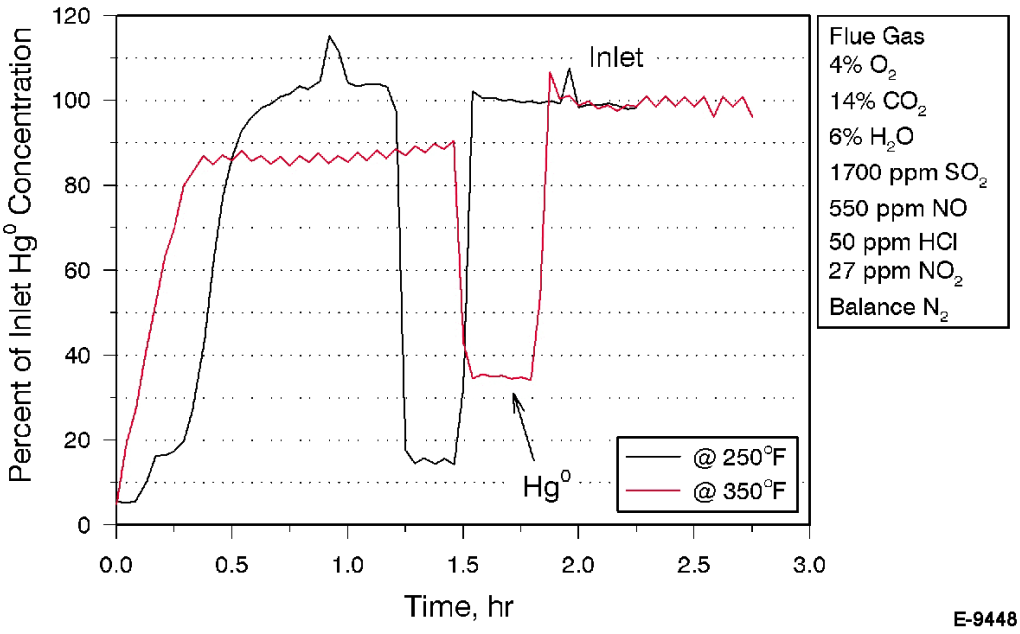

Figure 3-237. Outlet mercury concentration as a function of time for the AA ash at 250 and 350°F.

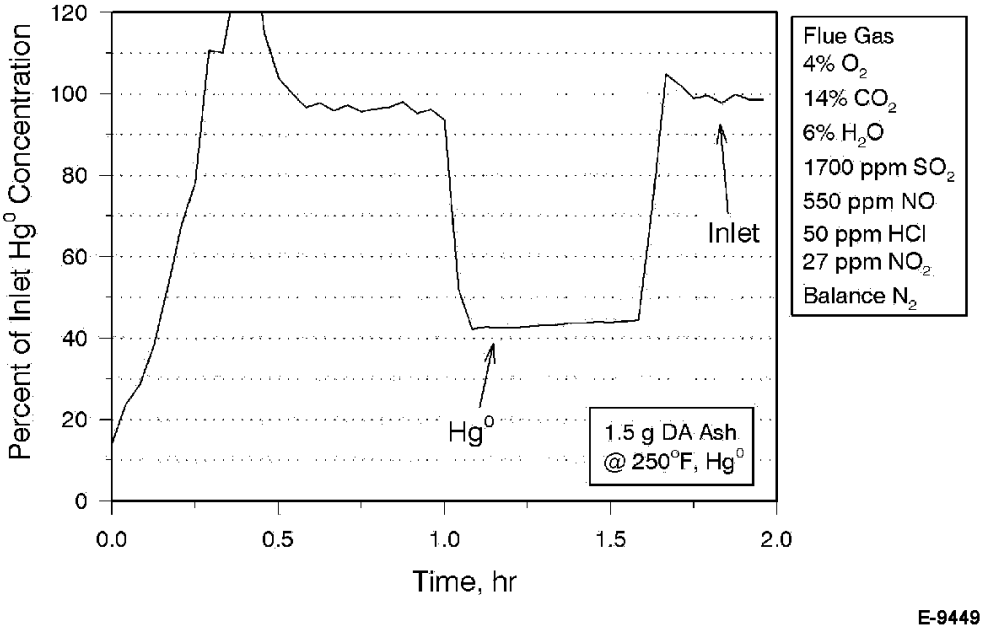

Figure 3-238. Outlet mercury concentration as a function of time for the DA ash at 250 and 350°F.

Results from the GA and DMA ash samples at 250°F are plotted in Figure 3-239. Results from these tests indicated the ash samples were relatively unreactive with elemental mercury and were not tested further with elemental mercury.

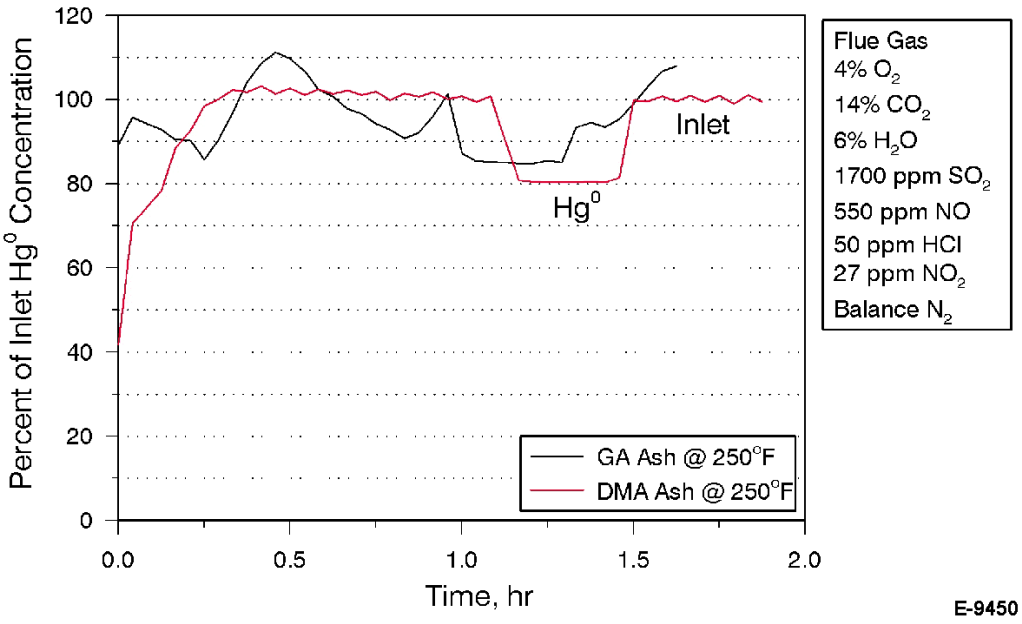

Figure 3-239. Outlet mercury concentration as a function of time for the GA and DMA ashes at 250°F.

The MA ash was evaluated at 250 and 350°F, and the results are plotted in Figure 3-240 along with the results from a test with only 50 ppm HCl at 250°F. Results from the tests with elemental mercury injection show a temperature effect. At the lower temperature, the ash captured slightly more mercury and oxidizes less than at the higher temperature. There may also be an HCl concentration effect. It appears there is more oxidation at 250°F with less HCl present in the flue gas.

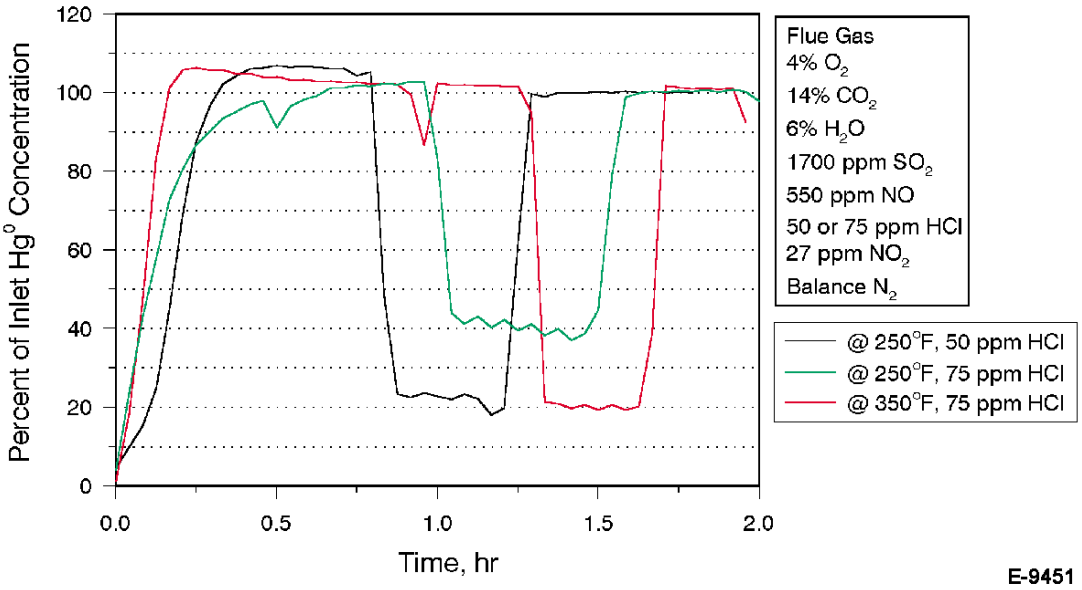

Figure 3-240. Outlet mercury concentration as a function of time for the MA ash at 250 and 350°F with 75 ppm HCl and with 50 ppm HCl at 250°F.

Three tests were completed with an ash sample from the Dale Station with the baseline simulated flue gas. This ash had 70% LOI and was initially evaluated under a different program as a mercury sorbent. The results from the previous tests indicated the ash did not work well as a sorbent, but for an ash did capture and oxidize a significant portion of the elemental mercury. Under the previous test program, samples of the baseline Dale Station ash were also treated with sulfur to enhance mercury capture. Results from tests with these treated ash samples indicated the more sulfur on the ash, the lower the percentage of the inlet elemental mercury that was oxidized.

Based on these results, it was decided this would be an ash suitable for further testing. The results from the first test were questionable because of the low inlet concentration (8 µg/m^3). The ash was reevaluated at 250°F, and the results are plotted in Figure 3-241. The results from the repeat test and the mass balance data indicated the Dale Station ash collected 30 µg Hg/g carbon. It was at this point it was discovered that the Dale Station ash had been activated by the original customer. The surface area was measured at 157 m^2/g, which is two orders of magnitude greater than the ash samples, but still lower than the 500–1000 m^2/g typical of activated carbons. The results from this run, however, did not look like those for other activated carbons. There was immediate mercury breakthrough but to only 50%; the ash then captured roughly 50% of the elemental mercury for the next 6 hours. A typical activated carbon captures roughly 100% of the elemental mercury for the first hour to hour and a half followed by rapid breakthrough to 100% of the inlet concentration. The Dale Station ash did behave the same as activated carbon in terms of oxidizing the elemental mercury in the flue gas stream. Since the difference may have been caused by the increased mass loading (1.5 g as an ash as opposed to 150 mg for an activated carbon), it was decided to evaluate this ash at the lower mass loading to

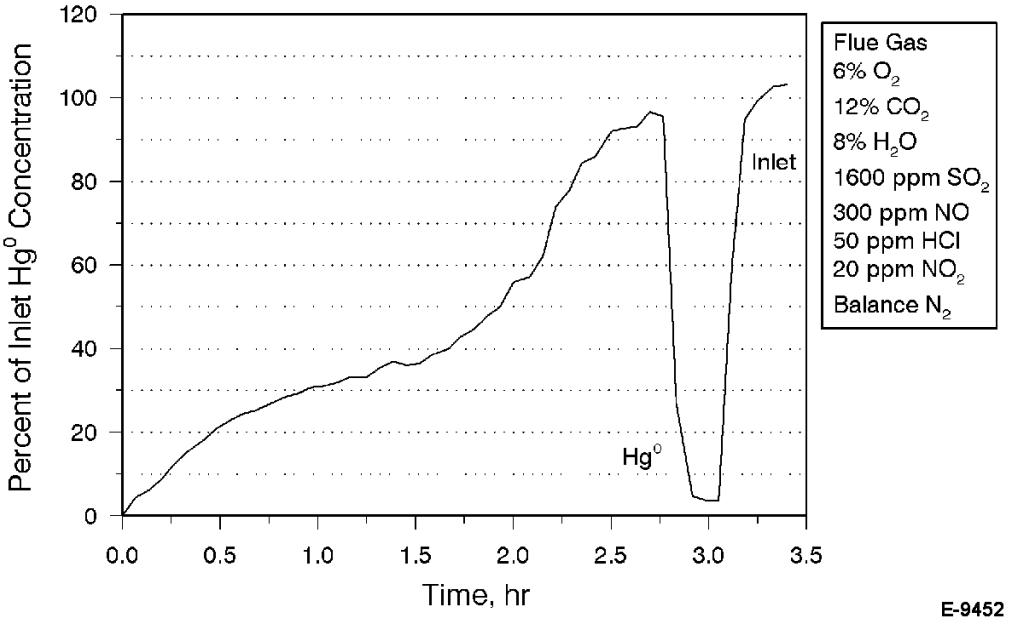

Figure 3-241. Outlet mercury concentration as a function of time for the Dale Station ash at 250°F.

see how it compared to an activated carbon. The third test was completed with the Dale Station ash at 250°F with only 150 mg of the ash in the fixed bed. Results from this test are plotted in Figure 3-242. The results from this test are similar to those for activated carbons with the same mass loading, with the exception that breakthrough occurred much earlier in the test. Even at the lower mass loading, the ash oxidized nearly 100% of the elemental mercury. Analysis of the spent ash indicated there was more mercury on the ash than was generated during the test. This may have been caused by a sample of ash with a higher than normal amount of mercury on it. Since the Dale Station ash had undergone an activation process, it was decided not to test it further.

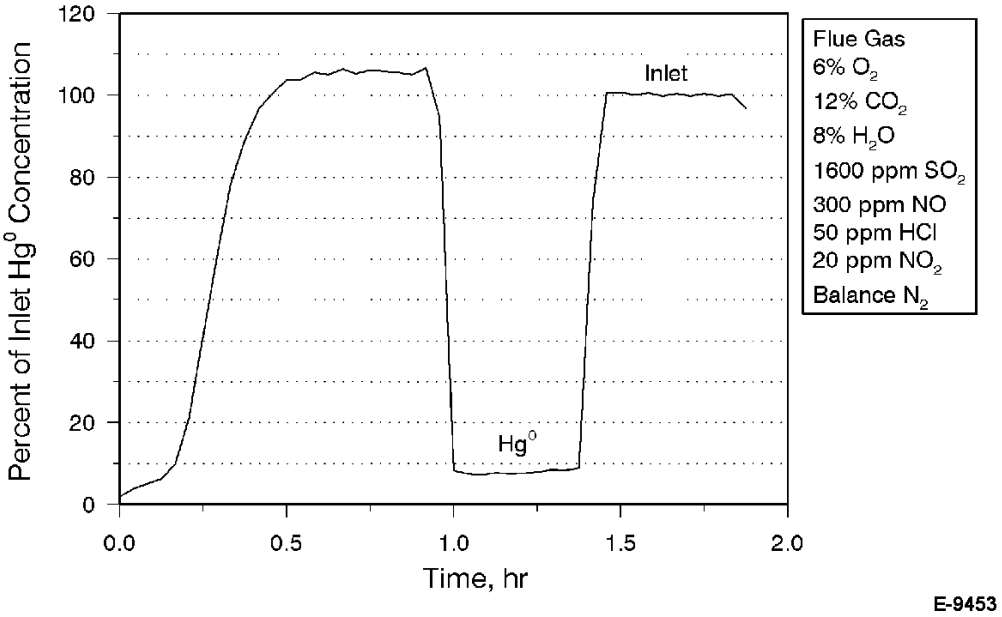

Figure 3-242. Outlet mercury concentration as a function of time for the Dale Station ash at 250°F with 150 mg ash.

Since the western bituminous ashes showed higher capacity for elemental mercury capture and oxidation, it was decided to evaluate samples of ash from different parent western subbituminous coals. Figure 3-243 plots the results from two tests with the Black Thunder ash at 250 and 350°F. The baseline flue gas mixture was used for these tests. This ash showed no capacity for mercury capture and only oxidized 30 to 40% of the elemental mercury.

Figure 3-244 plots the results from two tests with the Cordero Rojo ash at 250 and 350°F. The baseline flue gas mixture was used for these tests. This ash also showed no capacity for mercury capture and oxidized roughly 20% of the elemental mercury at both temperatures.

Figure 3-245 plots the results from two tests with the Absaloka ash at 250 and 350°F. The baseline flue gas mixture was used for these tests. This ash showed significant capacity for capture at 250°F (26% at 100% breakthrough) and oxidized roughly 70% of the elemental mercury at both temperatures. There is also a temperature effect with this ash on the capacity, with increasing temperature decreasing the capacity.

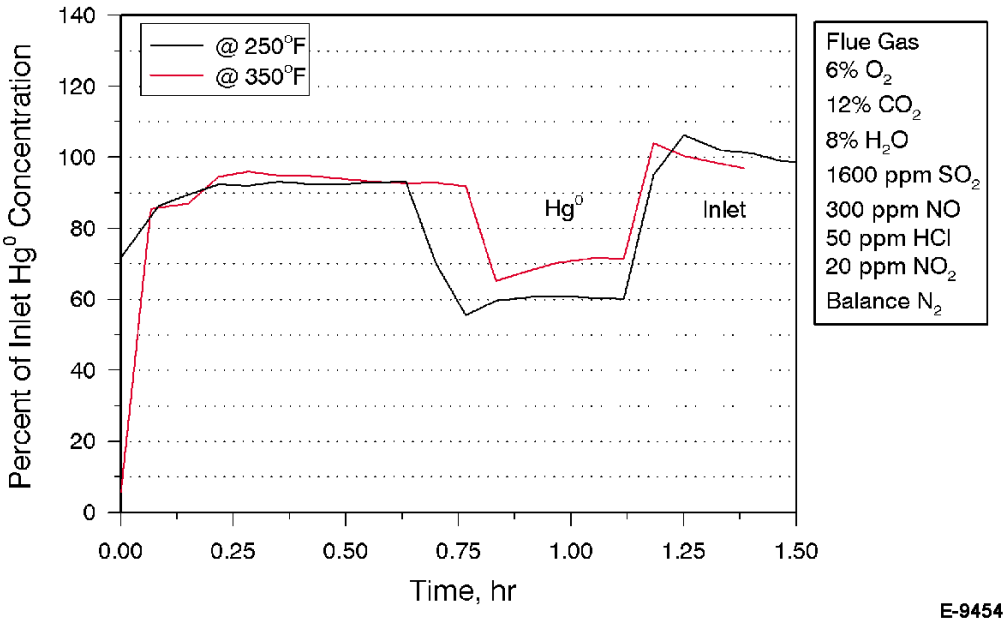

Figure 3-243. Outlet mercury concentration as a function of time for the Black Thunder ash at 250 and 350°F.

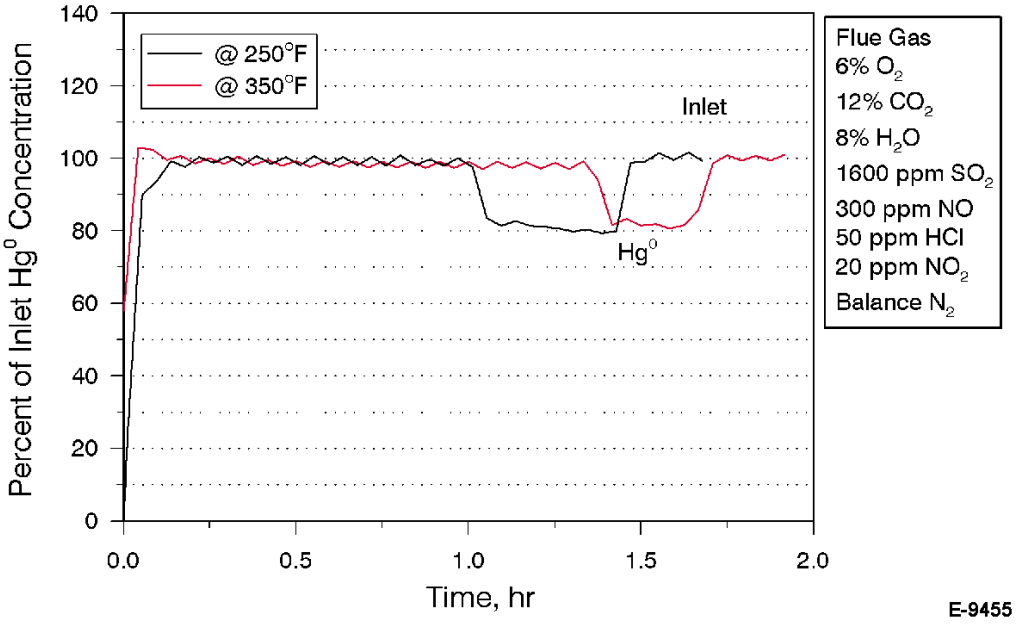

Figure 3-244. Outlet mercury concentration as a function of time for the Cordero Rojo ash at 250 and 350°F.

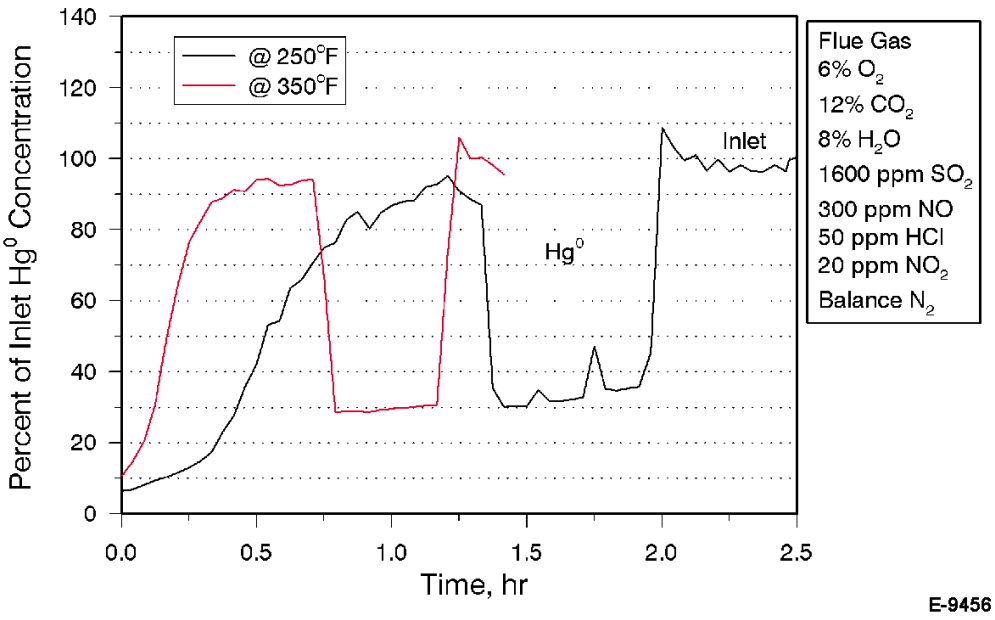

Figure 3-245. Outlet mercury concentration as a function of time for the Absaloka ash at 250 and 350°F.

Figure 3-246 plots the percent oxidation as a function of LOI, temperature, and coal type for the tests with elemental mercury in the flue gas. When plotted on a log scale, there is a trend of increasing oxidation with increasing LOI, particularly with the bituminous and subbituminous coals. Of the 11 ash samples evaluated at two temperatures, two showed increasing oxidation with increasing temperature (one bituminous and one subbituminous), six showed increasing oxidation with decreasing temperature, and three showed no temperature effect (two subbituminous and one bituminous). Figure 3-247 plots the percent of oxidation as a function of ash surface area, temperature, and ash type. Again, there is no strong correlation, but a general trend of increasing oxidation with increasing surface area. Since there is no strong correlation between LOI or surface area and the amount of oxidation, the type of surface area may be more important than the amount. The process the ash goes through in terms of time–temperature profile between the boiler outlet and the inlet to the particulate collection device may be important in determining the type of carbon surfaces available. From the plots, there are a number of low LOI and low surface area ashes that oxidized significant amounts of the elemental mercury, indicating also it is the type of surface and not the amount that is important.

Figure 3-248 plots the mercury capture efficiency of the ash samples at 100% break-through as a function of LOI, temperature, and ash type. Figure 3-249 plots the efficiency as a function of ash surface area. From these two plots, it is evident there is no correlation because most of the samples did not capture any mercury. It is clear that most of the mercury capture took place at the lower temperature, indicating a physical sorption mechanism.

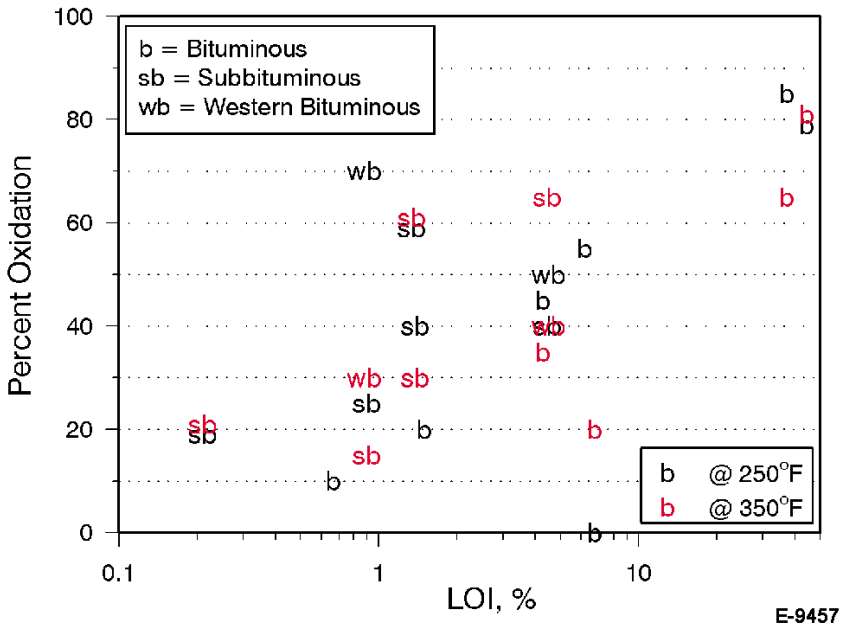

Figure 3-246. Percent oxidation of elemental mercury as a function of ash LOI.

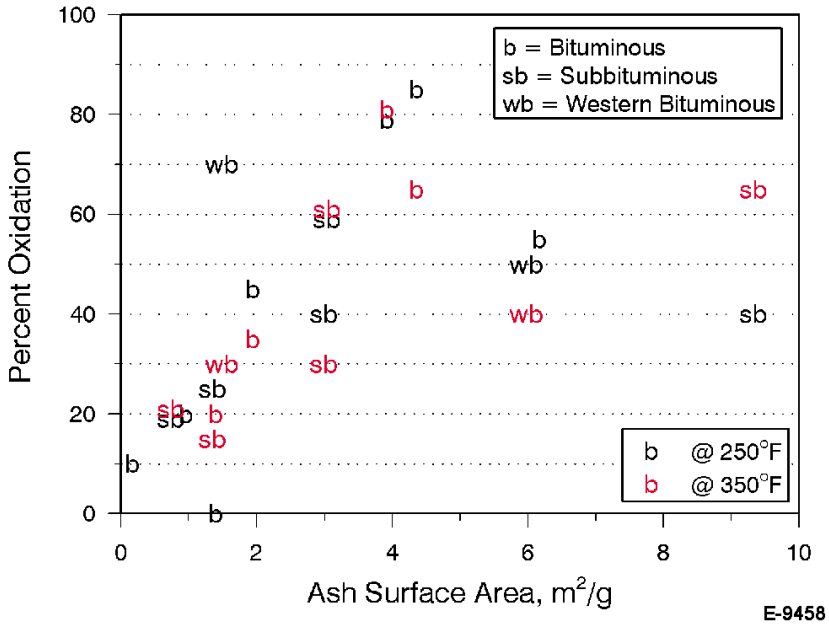

Figure 3-247. Percent oxidation of elemental mercury as a function of ash surface area.

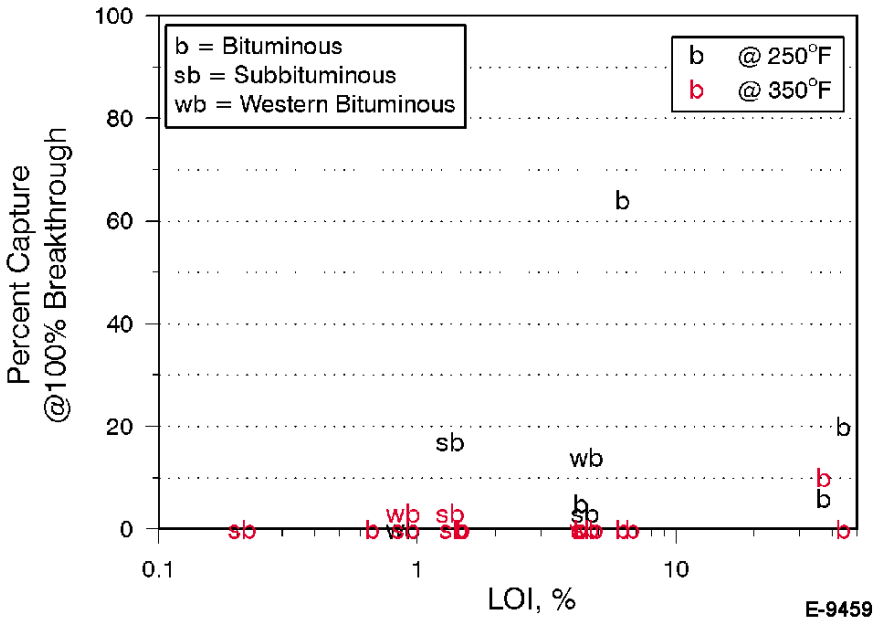

Figure 3-248. Percentage of elemental mercury capture at 100% breakthrough as a function of ash LOI.

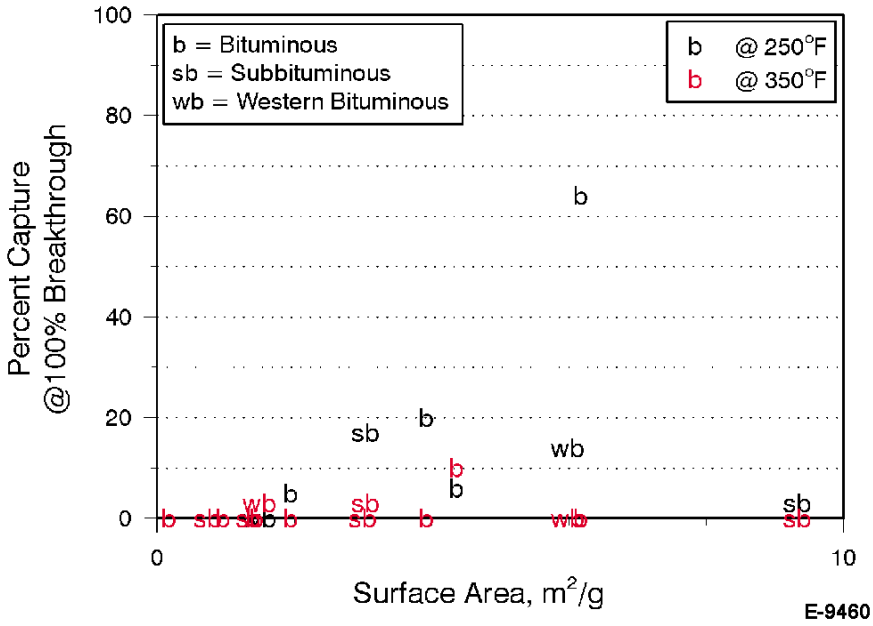

Figure 3-249. Percentage of elemental mercury capture at 100% breakthrough as a function of ash surface area.

The objective of the second test series was to determine the optimum temperature to observe interactions between the fly ash samples and Hg^{++}. Table 3-146 lists the runs completed with $HgCl_2$ injection and includes the concentration of mercury on the spent ash (if it was submitted for analysis), the amount of mercury generated during the test, the mass balance based on data from each of the mercury CEMs used during the test, and the mercury collection efficiency of the ash at 100% breakthrough. Because the North Dakota lignite showed no reactivity with the elemental mercury and there is no oxidized mercury in the Coal Creek flue gas stream, it was decided not to evaluate that ash with $HgCl_2$ injection.

Figure 3-250 plots the results from the tests with the Ohio blend ash at 250 and 350°F and the ashed samples of the Ohio blend ash at 350°F, all with $HgCl_2$ in the simulated flue gas. The results are clear that this ash was unreactive with $HgCl_2$ with the possible exception of the base ash at 350°F which may have reduced some of the $HgCl_2$ to elemental mercury. However, only one mercury CEM was used during this test, and it was showing some noise. It is very possible there was no reduction of $HgCl_2$ across the ash bed during this test. The mass balances for these tests are all low, indicating not all of the mercury generated is accounted for. Similar tests with a blank filter in place also show a slight lag in mercury breakthrough. From this, it appears some of the $HgCl_2$ is trapped in the bench-scale system and would explain the low mass balances for the $HgCl_2$ tests. The analysis of the spent base samples indicates there was some capture of $HgCl_2$. At 100% breakthrough, the capture efficiency was 6% at 250°F and 7% at 350°F.

Figure 3-251 plots the results from tests with the baseline Wyodak ash at 250 and 350°F and the two ashed Wyodak samples at 350°F, all with $HgCl_2$ in the simulated flue gas. During these tests, there was some noise experienced with the mercury CEMs, as is evident in the plots. It appears there was capture with the baseline ash, and the capture efficiency at 100% breakthrough was 7% at 250°F and 10% at 350°F. At the elevated temperature, it appears there is some reduction of the $HgCl_2$ across the ash.

Figure 3-252 plots the results from tests with the baseline Blacksville ash at 250 and 350°F and the two ashed Blacksville samples at 350°F, all with $HgCl_2$ in the simulated Blacksville flue gas. The results indicate there was no capture of $HgCl_2$ or reduction to elemental mercury for any of the samples. The large dip in the curve for the sample ashed at 750°C occurred because the heaters for the conditioning/conversion system tripped out. The system returned to normal when the heaters were turned on again.

Figure 3-253 plots the results from tests with the baseline Valmy ash at 250 and 350°F and the two ashed Valmy samples at 350°F, all with $HgCl_2$ in the baseline simulated flue gas. The results indicate there was only capture of $HgCl_2$ at 250°F with the baseline ash sample. Based on the mercury measured on the fly ash, the collection efficiency at 100% breakthrough was 30%.

Table 3-146. Results from Tests with $HgCl_2$ Injection

Run No.	Fly Ash	Temp., °F	Hg on Ash, µg/g	Hg on Spent Ash, µg/g	$HgCl_2$ Generated, µg	Semtech Mass Balance, %	PSA Mass Balance, %	Tekran Mass Balance, %	Efficiency @ 100% Break-through
1122	Ohio	250	0.276	0.50	24.2	67	86	68	9[a]
1000	Ohio	350	0.276	0.88	42	ND	ND[b]	88	11[a]
1037	Ohio ashed @ 400°C	350	ND	0.04	33	74	ND	71	ND
1029	Ohio ashed @ 750°C	350	ND	0.08	23	79	ND	77	ND
1120	Wyodak	250	1.29	2.90	23.5	70	84	76	14[a]
999	Wyodak	350	1.29	2.12	45	ND	ND	81	10[a]
1005	Wyodak ashed @ 400°C	350	ND	0.13	61	ND	ND	64	ND
1003	Wyodak ashed @ 750°C	350	ND	0.03	46	ND	ND	68	ND
1124	Blacksville	250	0.14	0.63	20.1	72	87	77	10a
1023	Blacksville	350	0.140	0.26	27	69	ND	66	ND
1033	Blacksville ashed @ 400°C	350	ND	0.08	25	83	ND	74	ND
1034	Blacksville ashed @ 750°C	350	ND	0.66	37	72	ND	74	ND
1121	Valmy	250	0.557	2.52	22.4	82	93	83	46[a]
1022	Valmy	350	0.557	0.60	24	78	ND	72	3[a]
1026	Valmy ashed @ 400°C	350	ND	0.16	20	89	ND	97	ND
1027	Valmy ashed @750°C	350	ND	0.38	20	87	ND	97	ND
1035	AA	350	0.282	ND	31	ND	ND	ND	43[c]
1030	DA	350	0.114	ND	32	ND	ND	ND	ND
1123	DMA	250	0.051	0.38	26.7	81	91	79	12[a]
1032	DMA	350	0.051	ND	24	ND	ND	ND	ND
1028	GA	350	0.002	ND	21	ND	ND	ND	ND
1125	MA	250	0.060	0.57	28.7	76	91	77	17[a]
1038	MA	350	0.060	ND	ND	ND	ND	ND	44[c]
1144	Black Thunder	350	2.13	ND	ND	ND	ND	ND	ND
1145	Cordero Rojo	350	0.183	ND	ND	ND	ND	ND	ND
1147	Absaloka	250	0.223	0.93	16.5	86	94	80	29[a]
1146	Absaloka	350	0.223	0.37	14.4	71	90	72	8[a]

a Mercury captured based on mercury on spent ash.
b Not determined.
c Mercury captured based on integration of breakthrough curve.

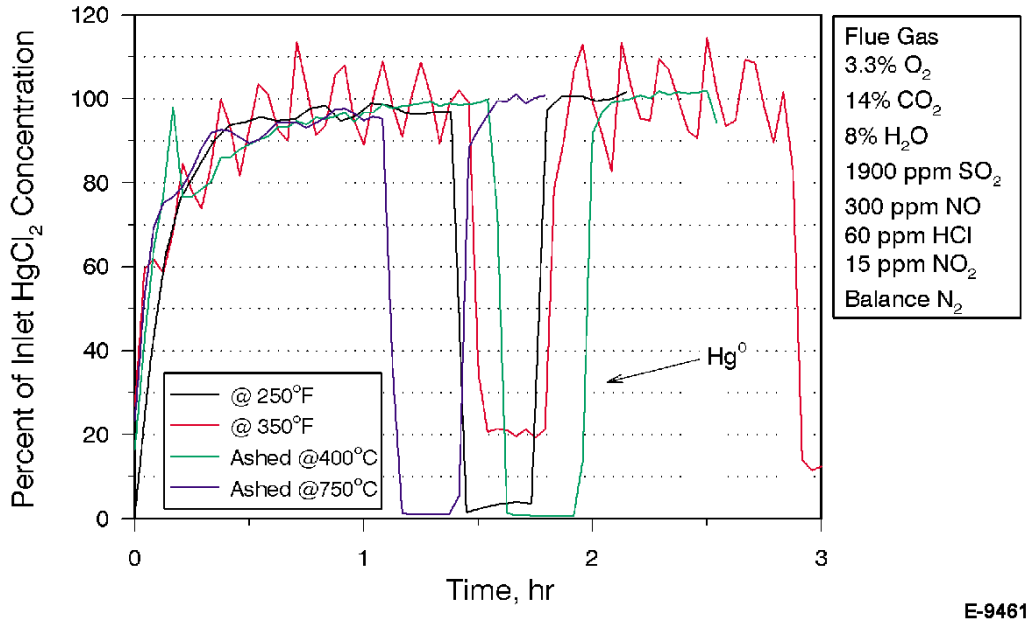

Figure 3-250. Outlet mercury concentration as a function of time for the Ohio blend fly ash, ashed at 400 and 750°C and evaluated at 300°F, and the results from the baseline tests at 250 and 350°F with $HgCl_2$ injection.

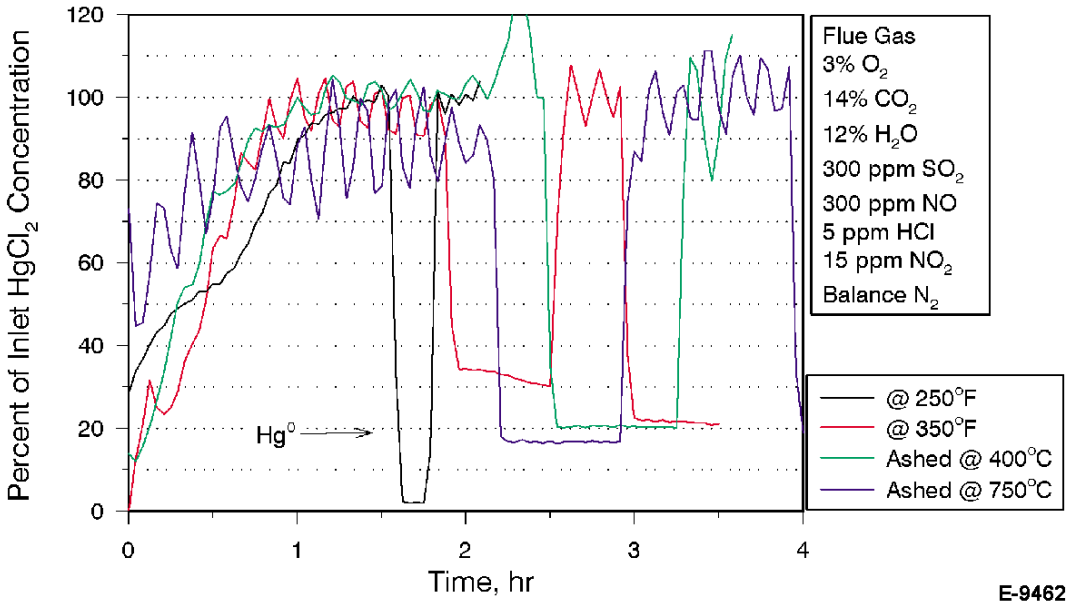

Figure 3-251. Outlet mercury concentration as a function of time for the Wyodak fly ash, ashed at 400 and 750°C and evaluated at 300°F, and the results from the baseline tests at 250 and 350°F with $HgCl_2$ injection.

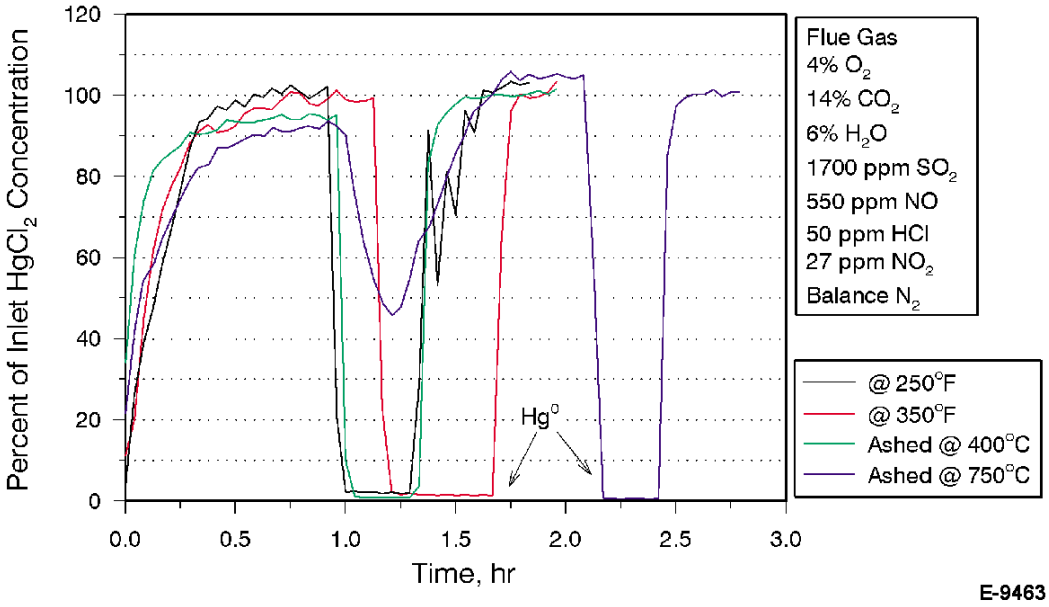

Figure 3-252. Outlet mercury concentration as a function of time for the Blacksville fly ash, ashed at 400 and 750°C and evaluated at 300°F, and the results from the baseline tests at 250 and 350°F with $HgCl_2$ injection.

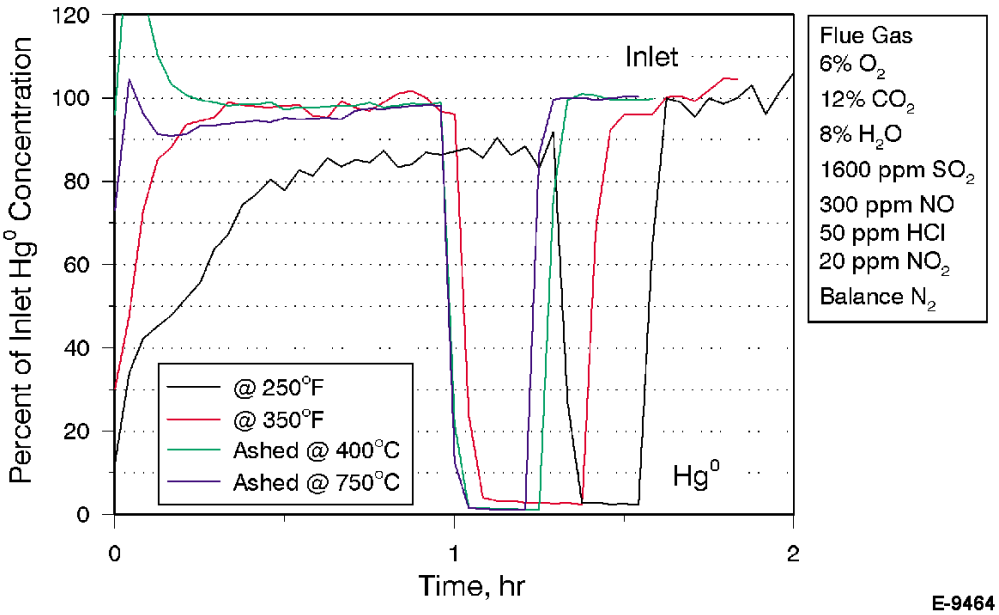

Figure 3-253. Outlet mercury concentration as a function of time for the Valmy fly ash, ashed at 400 and 750°C and evaluated at 300°F, and the results from the baseline tests at 250 and 350°F with $HgCl_2$ injection.

Figure 3-254 plots the results from tests with the AA, DA, and GA ash samples at 350°F, all with $HgCl_2$ in the Blacksville simulated flue gas. The results indicate there was some capture of $HgCl_2$ by the AA and DA ashes, but there appears to be an offgassing of mercury from the system at the beginning of the test with the GA ash. The AA ash captured roughly 43% of the mercury generated at 100% breakthrough, based on the integrated breakthrough curve. These ashes showed no ability to reduce $HgCl_2$ to elemental mercury.

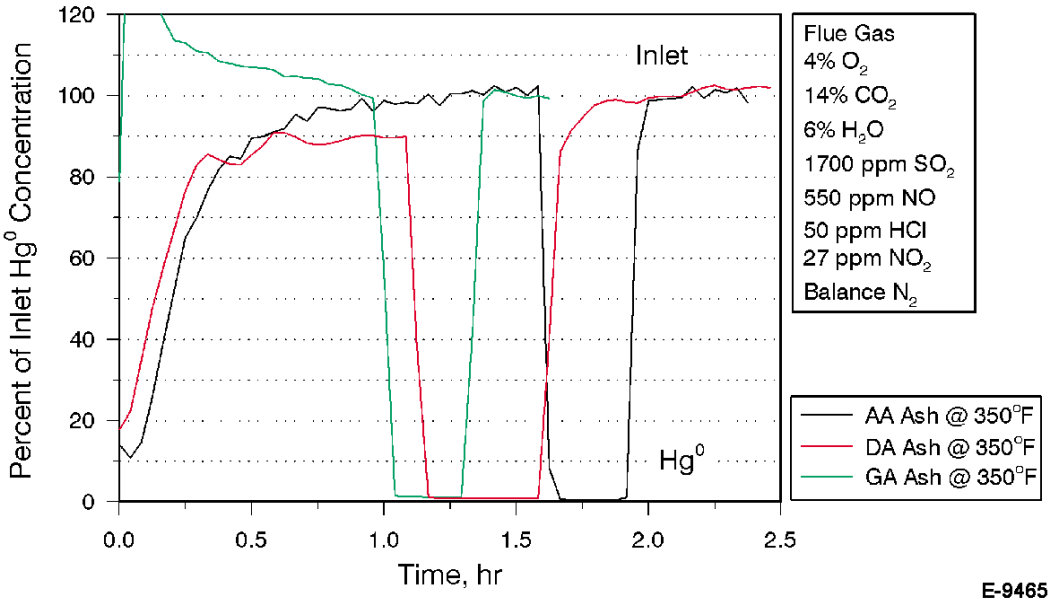

Figure 3-254. Outlet mercury concentration as a function of time for the AA, DA, and GA fly ashes at 350°F with $HgCl_2$ injection.

Figure 3-255 plots the results from tests with the DMA ash at 250 and 350°F with $HgCl_2$ in the Blacksville simulated flue gas. The results indicate there was very little capture of $HgCl_2$ and no reduction of $HgCl_2$ to elemental mercury. The capture efficiency at 100% breakthrough for the test at 250°F was 8%.

Figure 3-256 plots the results from tests with the MA ash at 250 and 350°F with $HgCl_2$ in the Blacksville simulated flue gas with 75 instead of 50 ppm HCl. The results indicate there was some capture of $HgCl_2$, roughly 17% at 100% breakthrough at 250°F and 44% at 350°F. The efficiency at 350°F was based on the integrated breakthrough curve. This ash showed no ability to reduce $HgCl_2$ to elemental mercury.

Figure 3-257 plots the results from tests with the Black Thunder and Cordero Rojo ash samples at 350°F. Neither of these ash samples showed capacity for capture or reduction of $HgCl_2$.

Figure 3-258 plots the results from the tests with the Absaloka ash at 250° and 350°F with $HgCl_2$ injection in the baseline simulated flue gas. The breakthrough curves appear similar, but the ash captured more $HgCl_2$ at 250° than at 350°F, based on the analysis of the spent ash samples. The capture at 100% breakthrough for the test at 250°F was significant at 29%.

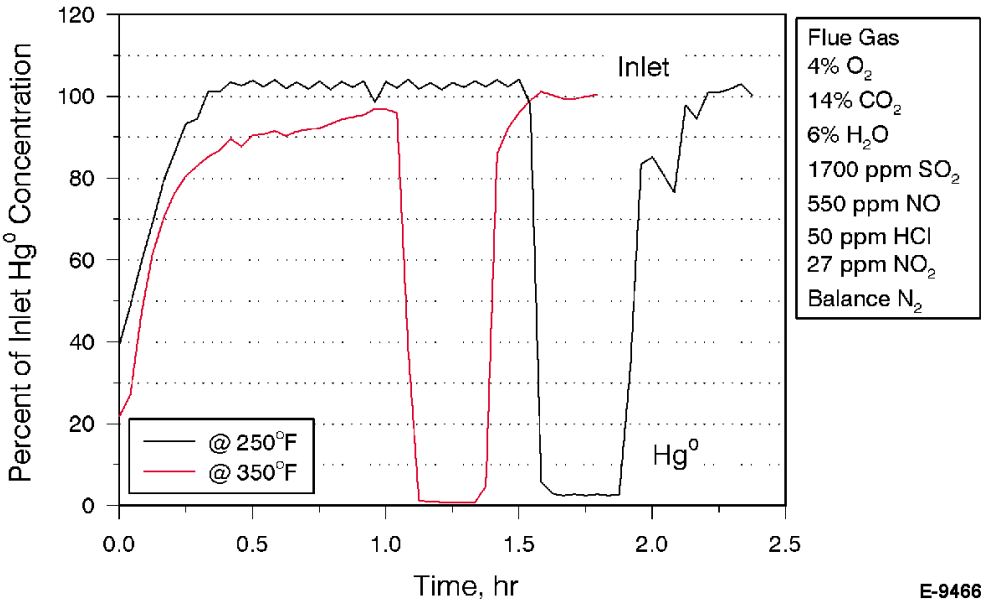

Figure 3-255. Outlet mercury concentration as a function of time for the DMA fly ash at 250 and 350°F with $HgCl_2$ injection.

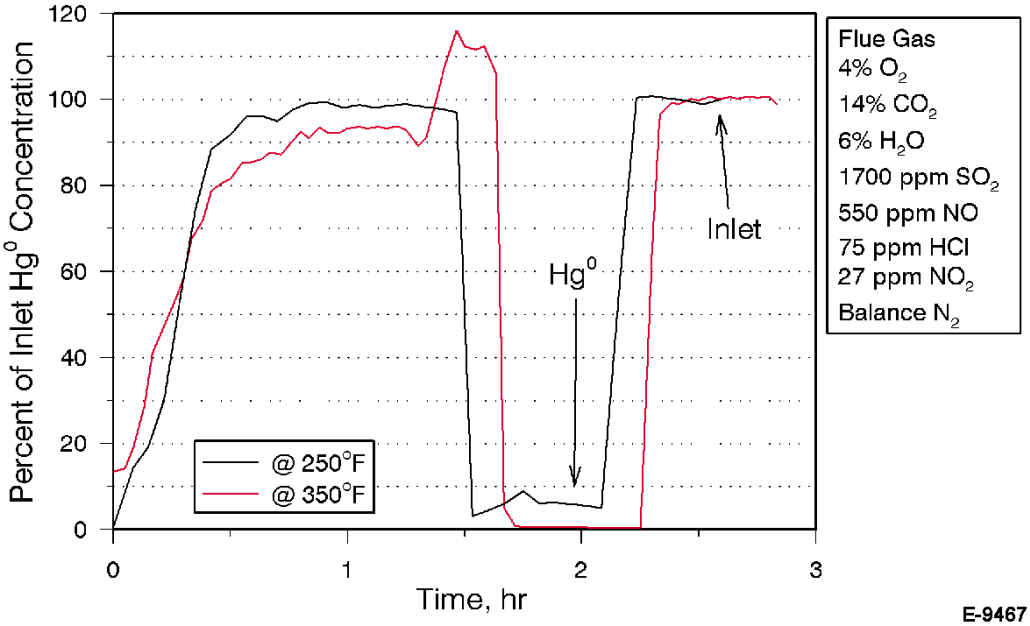

Figure 3-256. Outlet mercury concentration as a function of time for the MA fly ash at 250 and 350°F with $HgCl_2$ injection.

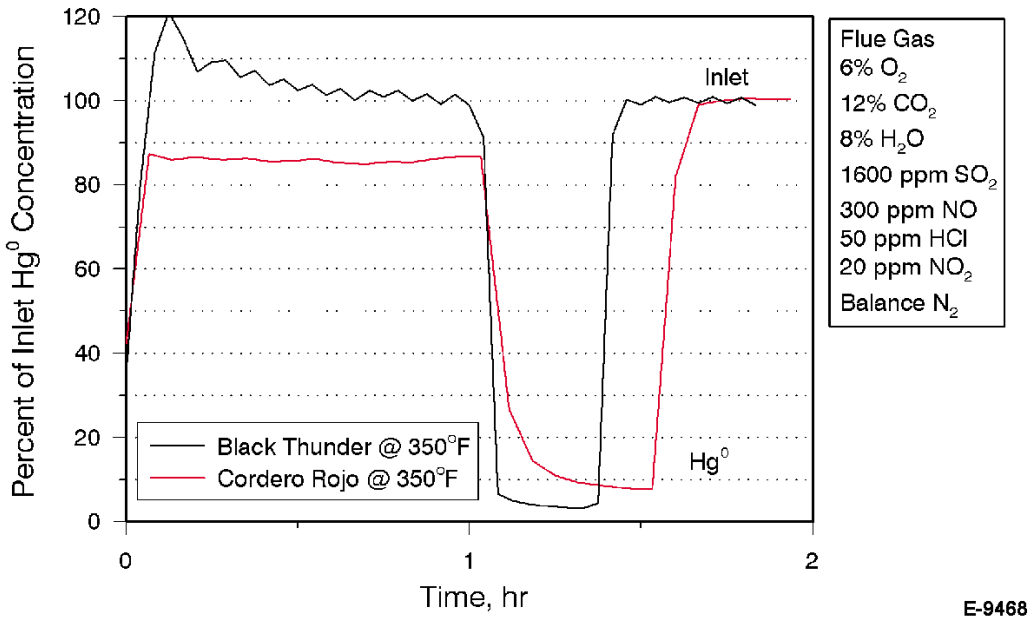

Figure 3-257. Outlet mercury concentration as a function of time for the Black Thunder and Cordero Rojo ashes at 350°F with $HgCl_2$ injection.

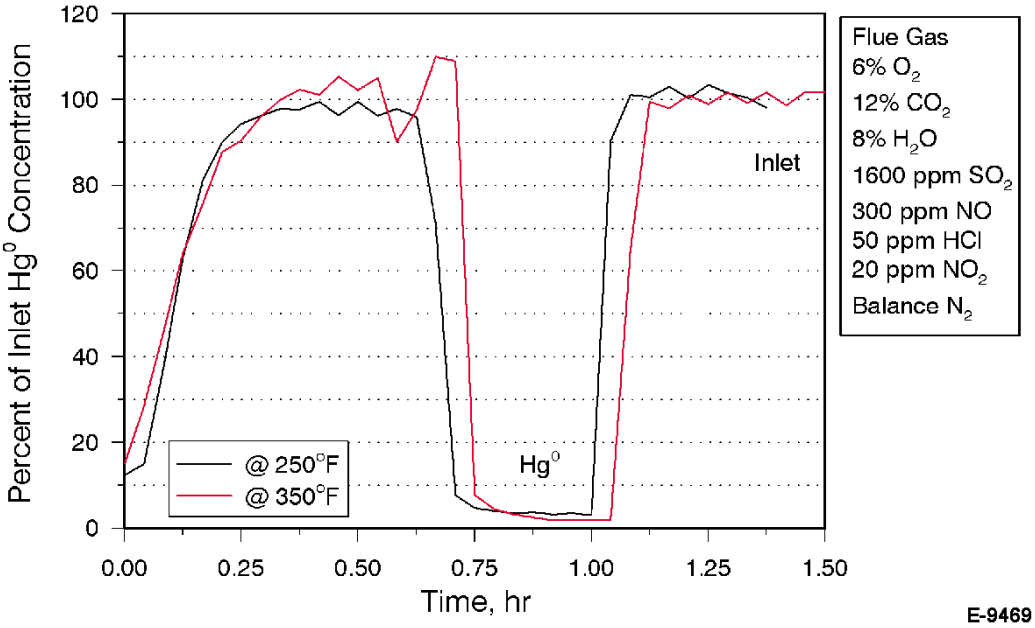

Figure 3-258. Outlet mercury concentration as a function of time for theAbsaloka fly ash at 250 and 350°F with $HgCl_2$ injection.

Figure 3-259 plots the capture efficiency of the ash samples at 100% breakthrough as a function of LOI, temperature, and ash type. The only trend there appears to be is increased capture with decreasing temperature. This would be expected with physisorption of the $HgCl_2$

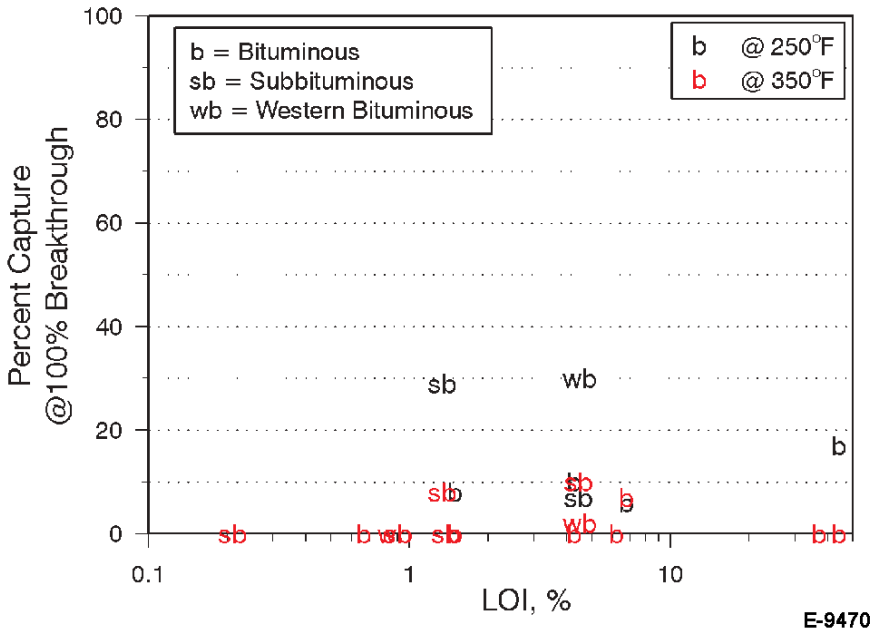

Figure 3-259. Percentage of $HgCl_2$ capture at 100% breakthrough as a function of ash LOI.

on the surface of the ash. Figure 3-260 plots the capture efficiency of the ash samples at 100% breakthrough as a function of ash surface area, temperature, and ash type. There appears to be a slight trend of increasing capture with increasing surface area. Again, the temperature effect is apparent.

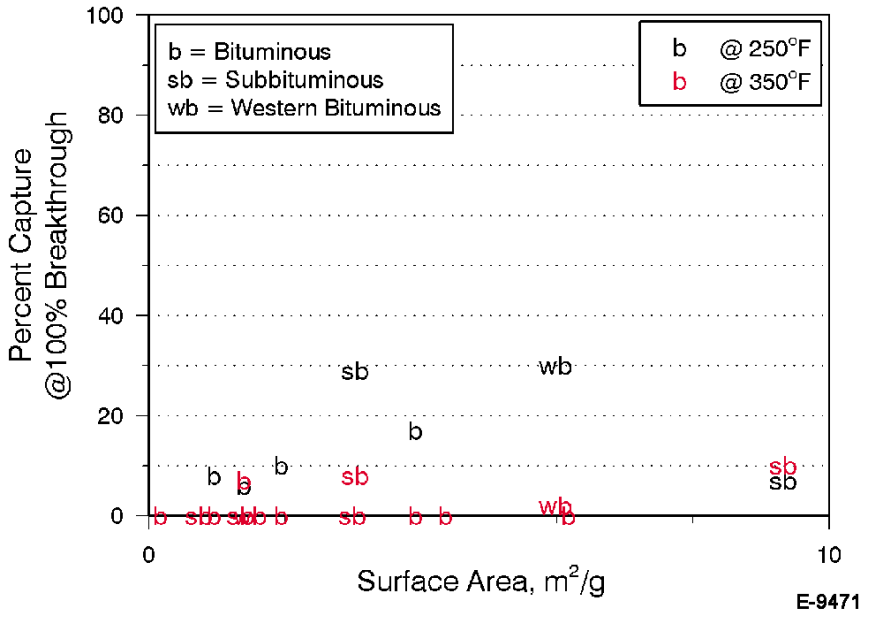

Figure 3-260. Percentage of $HgCl_2$ capture at 100% breakthrough as a function of ash surface area.

3.4.5 Trace Metal Speciation on Solid Samples

3.4.5.1 Arsenic XANES Spectra of Calcium Compounds Reacted with As Vapor

Arsenic XAFS spectra were obtained for various samples submitted by Prof. J.J. Helble (UC). These were samples of inorganic arsenic compounds produced in pulverized coal combustion in a bench-scale study conducted under fuel-lean combustion conditions [201]. Such experiments were conducted in the presence or absence of various calcium compounds (Ca_2SiO_4 pure, Ca_2SiO_4 - II, and Ca acetate) using cacodylic acid, $(CH_3)_2AsOOH$, as the source of arsenic in the vapor phase. In the absence of calcium compounds, the dominant arsenic phase observed by XAFS spectroscopy and chromatography was As_2O_3; however, after reaction, in the presence of calcium compounds, all samples exhibited virtually identical As XANES and RSFs (Figure 3-261). All (>95%) of the arsenic was present as As(V), in a form similar to that found in arsenates, and it would appear that the same calcium arsenate form is present in all three materials. The arsenic XANES spectra of the SiO_2 and the cacodylic acid samples indicate that the dominant oxidation state of arsenic is trivalent in these materials. The RSFs are also

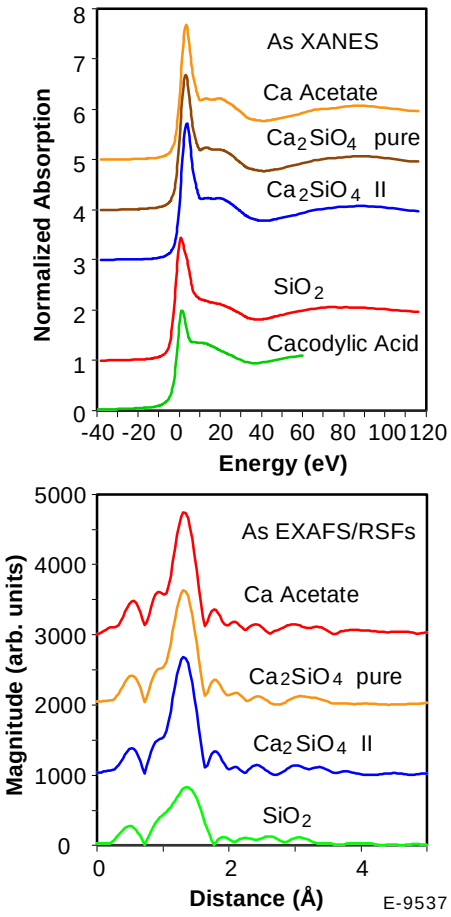

Figure 3-261. XANES and EXAFS/RSFs of arsenic compounds produced in bench-scale study designed to determine arsenic speciation during pulverized coal combustion [201].

consistent with these observations, as the RSFs for the Ca-based materials are closely similar with the main peak occurring at 1.31 ± 0.02 Å, whereas the RSF for the SiO_2 material is rather different and the main peak occurs at 1.37 ± 0.02 Å. Further details of this work are published elsewhere [201].

3.4.5.2 University of Arizona Ash Filter Characterization

Some XAFS measurements were made directly on a filter from UA combustion unit that was used to collect fly-ash particulate matter in order to establish whether or not it was feasible to perform XAFS measurements of trace elements on thin filter materials without removal of the material. Both the As and Cr absorption edges were examined at SSRL and the quality of the XAFS data obtained from such a sample is indicated in Figure 3-262. Although noisy, it is clear that the oxidation states of chromium and arsenic are predominantly, if not entirely, Cr^{3+} and As^{5+}, respectively. However, direct measurements of trace element occurrences do appear feasible from filter samples from combustion systems and we have now begun to examine filter samples of combustion-derived particulate matter collected on filters, including ambient air-particulate ($PM_{2.5}$) samples [202, 203].

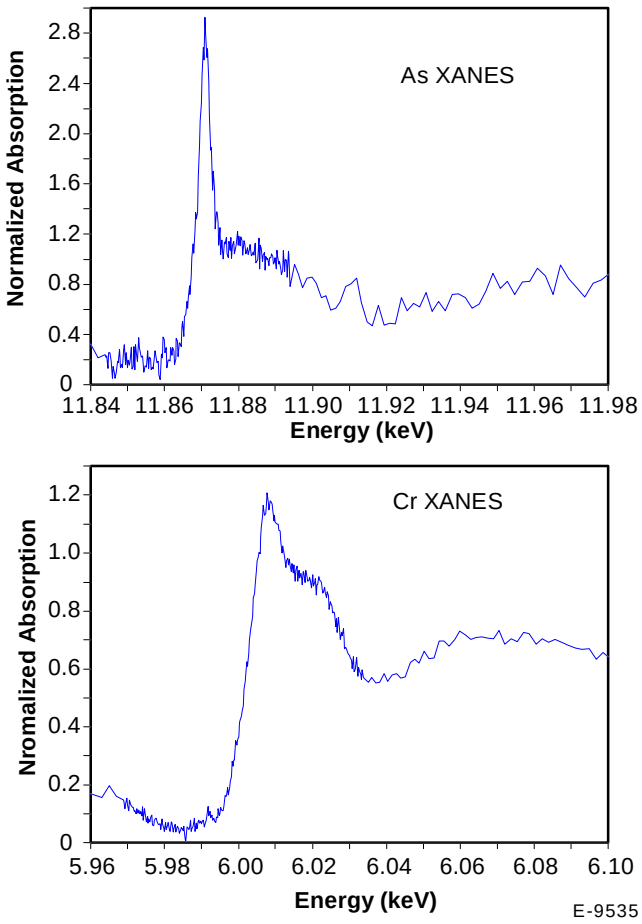

Figure 3-262. XANES of arsenic and chromium on a filter used to collect fly-ash and particulate matter from the UA combustion unit.

3.4.5.3 Chromium Speciation in Fly-Ash

In previous work, it was noted [204] that, although the chromium in most fly-ash samples from coal combustion is predominantly (>95%) trivalent (Cr^{3+}), there are many exceptions in which the much more toxic and carcinogenic hexavalent (Cr^{6+}) chromium oxidation state is found in amounts up to 20% of the total chromium, and exceptionally even up to 50% of the chromium. Our work on the mode of occurrence of chromium in coal [57-59] has established that it is found in coal in exclusively trivalent forms. Hence, the occurrence of the Cr(VI) oxidation state in fly-ash is not a reflection of the chromium speciation in the coal. Further, it is unlikely that such variation is due to the combustion conditions, because conditions among different pulverized combustion units do not vary greatly. More likely, the occurrence of Cr(VI) in combustion ash is a reflection of the chemical composition of the ash. For example, we have already presented data (Subsection 3.4.5.1 and Ref. [201]) that indicate that the higher oxidation state of arsenic, As(V), is stabilized by the presence of calcium.

We have started to address this problem of why certain coal ashes contain significant Cr(VI) by examining how chromium occurs in the well-characterized ash samples that we received from Grant Dunham, EERC. Shown in Figure 3-263 are chromium XANES spectra of three ash samples; all three samples exhibit a fairly prominent pre-edge peak that reflects the presence of Cr(VI) as chromate (CrO_4^{2-}) in them. The Cr(VI) contents were determined following the procedure described elsewhere [204]. Results of the fitting are shown in Table 3-147. Other samples examined showed no evidence for the presence of any Cr(VI). Moreover, as the intensity of the pre-edge peak increases, the remainder of the spectrum becomes flatter as one would predict [204] for a mixture of Cr(III) and Cr(VI) species. Further, we note

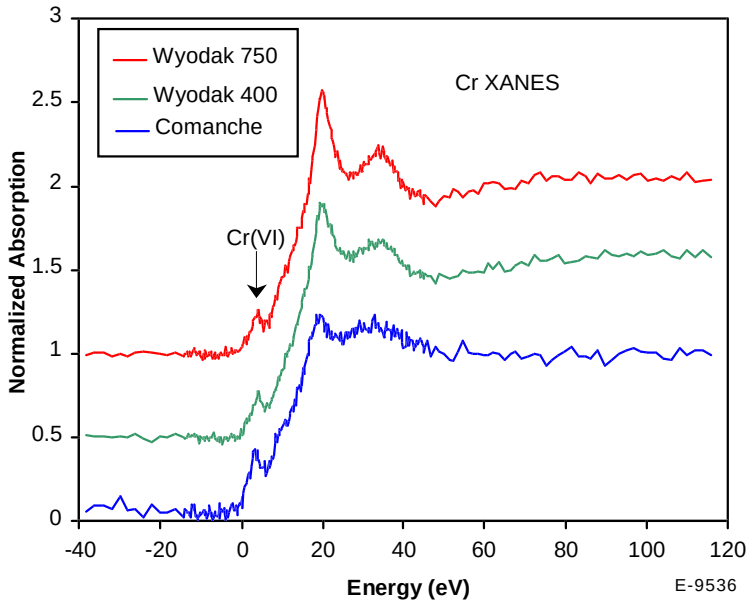

Figure 3-263. XANES spectra of chromium in three fly-ash samples from EERC.

Table 3-147. Estimates of Cr(VI) Contents of EERC Ash Samples

Sample	Cr(VI) as % of total Cr
Wyodak 750°C	19
Wyodak 400°C	20
Comanche	24
Valmont	<5

that these three samples all belong to the subset of samples that exhibit Ca ferrites in their Mössbauer spectra (Figure 3-224) and the likely presence of calcium sulfate in their sulfur XANES spectra (Figure 3-225). This would appear to indicate, if only circumstantially, that calcium might be responsible for the stabilization of the Cr(VI) oxidation state, possibly in much the same way that calcium stabilizes the As(V) oxidation state in particulate matter [201].

3.4.5.4 Mercury Sorbent Characterization

Introduction

A major research effort in Phase II, building on some preliminary work started in Phase I [205-207], was the XAFS spectroscopic characterization of mercury adsorbed on various carbon-based and other sorbent materials. In a number of cases, ancillary XAFS data on sulfur and chlorine were also obtained. Such sorbents came from a number of sources including:

- Coal chars from UA combustion unit (actually started in Phase I)
- Activated carbon and zeolite-based sorbents from Physical Sciences Inc. (C. Senior, P.I.)
- Lignite-activated chars from UNDEERC (S. Miller and G. Dunham, P.I.s)
- Fly-ash carbon from Cherokee Station, CO (ADA Technologies, Inc.)
- Various carbon-based and inorganic sorbents from Ghorishi and Gullett (US EPA)
- Carbon felts from Gullett (US EPA)

In addition, it was necessary to carry out significant background work in order to develop spectral data analysis procedures for extracting the necessary information from the mercury XAFS spectrum. As we shall see, one of the major achievements was the development of the inflection point difference (IPD) parameter for interpreting the mercury XAFS spectrum. The background development work will be described first and then the results obtained for the various sorbent materials will be presented.

Mercury XAFS Developmental Work

Mercury XAFS Spectroscopy

Mercury XAFS spectroscopy was conducted principally at beam-line IV-3 at the Stanford Synchrotron Radiation Laboratory (SSRL), Palo Alto, CA. Additional experiments were also carried out at beam-line X-18B at the National Synchrotron Light Source (NSLS), Brookhaven National Laboratory, NY. Virtually identical experimental practice was carried out at both synchrotrons. The mercury L_{III} edge at 12,284 eV was used for the absorption experiments and all measurements on mercury sorbents were carried out in fluorescence geometry. The mercury contents of the sorbents varied from as much as 8.5 wt% to as little as 8 parts per million (ppm) and a Lytle-type detector was used for the more concentrated samples, whereas a 13-element germanium detector was used to record the spectra from less concentrated samples. A 6 μ gallium filter and Soller slits [208] were used to enhance the signal/noise ratio with both types of detector. For the most dilute samples (< 300 ppm Hg), multiple scanning was also used to improve the signal/noise ratio. Additionally, the spectra of a number of mercury compounds were recorded. These spectra were measured in absorption geometry using pressed pellets of the compound in a plastic medium or thin smear mounts on tape. A droplet of elemental mercury pressed and sealed between two thin plastic sheets served as the calibration standard. The single inflection point in the XAFS spectrum of elemental mercury was taken to be the zero-point of energy for calibrating the XAFS spectra obtained in this investigation. Where possible, this spectrum was measured simultaneously in an absorption experiment after the main experiment, so that each XAFS spectrum would be individually calibrated.

Analysis of the calibrated spectral data consisted of dividing the XAFS spectrum into separate X-ray absorption near-edge structure (XANES) and extended X-ray absorption fine structure (EXAFS) regions. Analysis of the XANES region consisted of smoothing and differentiating the spectrum to obtain (Figure 3-264) the $d^2Abs/(dE)^2$ spectrum, from which the inflection point difference (IPD) could be most precisely determined. The isolated EXAFS region was analyzed in the usual manner [209, 210] by fitting a five-region cubic spline to the data to obtain the chi spectrum and then converting from real space to reciprocal (k) space. A Fourier transform was then applied to the k^3-weighted chi vs. wavevector spectrum to obtain the radial structure function (RSF). The RSF is a one-dimensional representation of the local structure around the absorbing mercury atom.

Mercury Compound XAFS Systematics

During the course of this project, we have accumulated much XAFS data on mercury in various sorbents and on a wide range of Hg compounds. Almost without exception, the first features that occur on the mercury absorption edge are two inflection points, which appear as distinct peaks in the first derivative spectrum (Figure 3-264), whose positions and intensities appear to be related to chemical bonding differences. In particular, the separation of these inflection points, the inflection point difference (IPD), appears to correlate with differences in the ionicity of the Hg-NN bond. The more ionic compounds of mercury, such as HgO, mercury sulfate, etc., in which the Hg ion is surrounded by relatively small, ionic oxygen anions, have large values for the separation of the inflection points, whereas the least ionic and largest anionic species, such as Se^{2-} and I^- in Hg selenide, and Hg iodides give rise to small separations. Two parameters can be readily defined from the first derivative spectrum. These are the inflection point difference (IPD), defined as:

$$IPD = P_1 - P_2 \tag{3-40}$$

and the peak height ratio (H_R) defined as:

$$H_R = H_1 / H_2 \tag{3-41}$$

where P_1, H_1 and P_2, H_2 are the positions and heights of the low-energy and high energy peaks in the first-derivative spectrum, respectively (Figure 3-264). Data for these parameters are presented in the Table 3-148 for 16 mercury compounds. Interestingly, it seems to make little difference whether the mercury is Hg(I) or Hg(II) as the pair of mercuric and mercurous sulfates and the corresponding pair of chlorides have essentially the same IPD values. Compounds with large effective height ratios (H_R >4) have high symmetry crystal structures or are liquid. Also listed in Table 3-148 are values determined for the position of the first major peak (phase-shift uncorrected) in the mercury EXAFS/RSF spectrum, which corresponds to the bond distance between the mercury atom and its nearest neighbor ligand atoms.

It is well known that features in the XANES region can reflect bond lengths and other structural details, and, as can be readily seen in Table 3-148, there appears to be an inverse correlation between the separation (IPD parameter) of the mercury L_{III} edge inflection points and the phase-shift uncorrected RSF peak position, as might be expected based on previous investigations of systematics in XANES spectra [211, 212]. Similar trends can be seen in other compilations of mercury compound data [213].

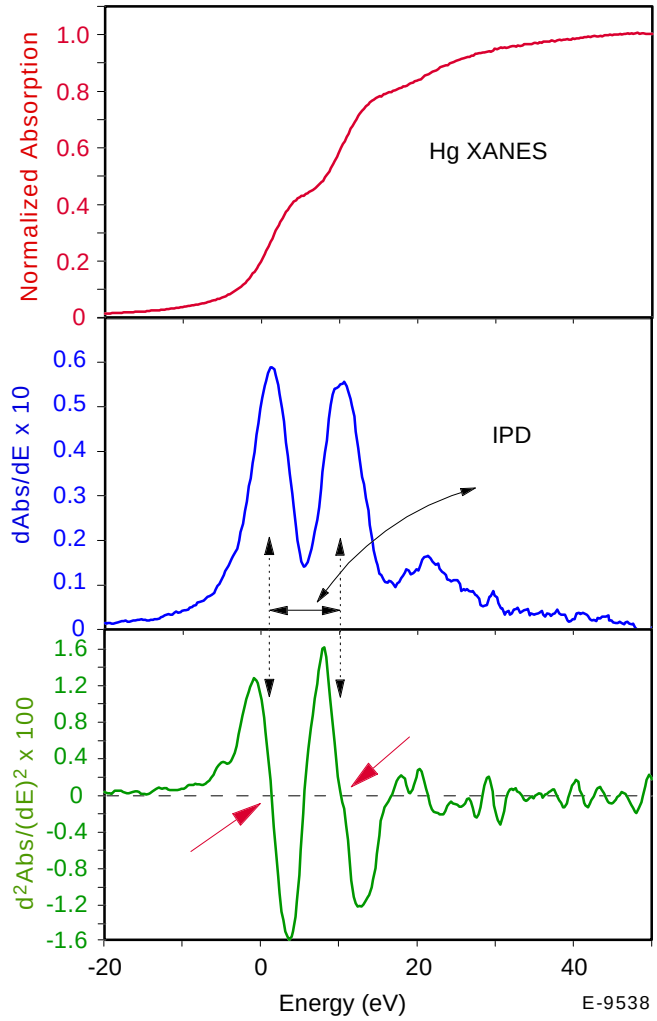

Figure 3-264. Definition of the IPD parameter from Hg XANES spectrum of a carbon-based sorbent. Red arrows show measurement positions. Zero-point of energy corresponds to 12,284 eV.

However, regardless of whether the IPD parameter reflects bond distance or bond ionicity or both, the important point for this work is that, as shown in Figure 3-265, the IPD parameter can be used as an effective indicator of the local structure and chemistry of Hg-sorbent complexes, and hence also the probable Hg sorption mechanism. It should be emphasized that the value of the IPD parameter measured from an Hg XANES spectrum is a single, average value that reflects the amount and nature of different possible bonding sites for mercury sorption in the sorbent material. As a result, it may not be too useful for complex real-world samples, where sorption might take place at a number of different sites.

Table 3-148. Hg XAFS Systematics for Mercury Compounds

Hg Compound	IPD, eV	H_R	RSF, Å
HgO (yellow)	13.3	1.95	
HgO (red)	12.8	1.75	1.68
$HgNO_3$	11.3	1.05	
Hg acetate	10.6	1.55	1.72
Hg_2SO_4	9.6	1.10	
$HgSO_4$	9.5	1.35	
Hg_2Cl_2	8.4	1.00	
$HgCl_2$	8.4	1.00	2.02
HgS (metacinnabar)	7.7	>4	2.12
HgS (cinnabar)	7.5	1.40	2.05
$HgCH_3I$	6.9	1.40	2.49
Hg diphenyl	6.8	3.60	
HgI_2	6.5	0.90	
HgSe	6.4	>4	
K_2HgI_4	4.6	1.00	2.52
Hg (liquid)	0.0	∞	

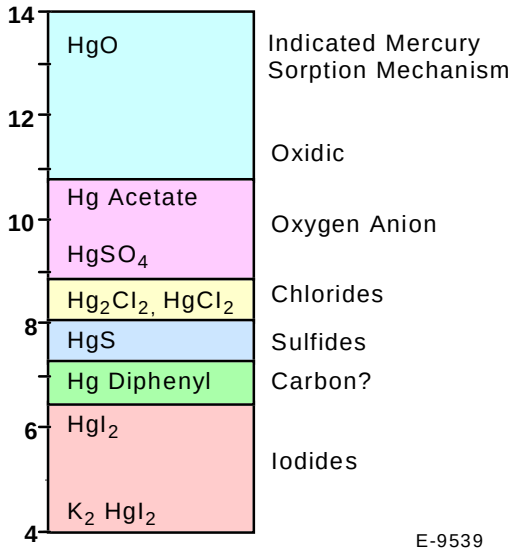

Figure 3-265. Diagram showing the relationship of the IPD parameter to different possible mercury sorption species represented by different ligand types.

Physisorption Versus Chemisorption

Another aspect of these investigations was to see if we could identify whether or not XAFS spectroscopy could be used to distinguish between chemisorption and physisorption process on carbonaceous sorbents. The former process involves the formation of chemical bonds between the mercury and the ligand species on the sorbent materials, for which the mercury would have to be oxidized, whereas the latter could involve the sorption of elemental mercury (Hg^0), since the adsorption would not involve chemical bonding *per se*, but weaker van der Waals type attraction only. Hence, the sorption of mercuric species would represent chemi-sorption and the adsorption of elemental mercury would represent physisorption, especially from atmospheres in which the mercury is present in elemental form.

It is quite easy to distinguish between elemental and oxidized mercury from the XAFS spectrum because elemental mercury gives rise to a single peak only in the first-derivative of the mercury XANES spectrum, whereas mercuric compounds give rise to a two-peak spectrum. Furthermore, the single peak due to elemental mercury overlaps significantly with the lower energy peak of mercuric species. Hence, in the case of a mixture of elemental mercury and mercuric species, we would also expect to see a two-peak spectrum, albeit weakened or more asymmetric due to the presence of the elemental mercury. Consequently, the height ratio, H_R, of the two peaks might be useful as a parameter that reflects the fraction of elemental mercury involved in the adsorption.

To explore the usefulness of this parameter, we performed two types of simulation and from the calculated spectra obtained H_R as a function of the IPD parameter. The first simulation consisted of adding the XANES spectrum of elemental mercury to that of mercuric sulfide or mercuric chloride in various proportions and determining the two parameters from the first and second derivatives of the simulated spectra. Such simulated spectra for the series Hg^0-$HgCl_2$ are shown in Figure 3-266. The derived data on the IPD and H_R parameters are plotted as the "experimental" trends from HgS and $HgCl_2$ towards elemental mercury in Figure 3-267. The "theoretical" trends for the same mixtures, the solid lines in Figure 3-267, were calculated by simulating the shape of the derivative spectra for elemental mercury and the mercuric compounds as single and double lorentzian-shaped peaks, respectively. The peak positions and height ratio were then determined mathematically by differentiation of the mathematical equation representing specific mixtures of elemental mercury and the mercuric compound. By minor adjustment of the initial parameters, reasonably good agreement was obtained between the two simulations, as shown in Figure 3-267.

Also shown in Figure 3-266 are data points for experimental determinations of the two parameters made from the XANES spectra of mercury species adsorbed on various sorbent materials. These data will be discussed in more detail below; however, it can be seen from the plot that these experimental data for actual sorbents trend, for the most part, between HgS and $HgCl_2$ or away from $HgCl_2$ to more ionic values. None of these experimental data has a value for H_R that in any way might be interpreted as resulting from significant elemental mercury in them.

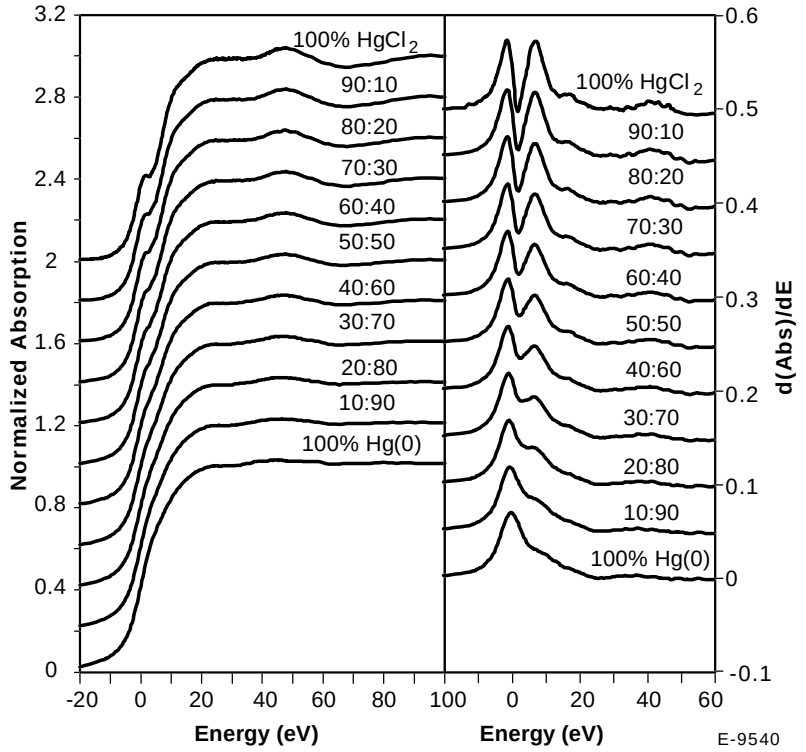

Figure 3-266. Simulated mercury XANES spectra for mixtures of elemental mercury and mercuric chloride based on weighted additions of the experimental spectra for the two end-members.

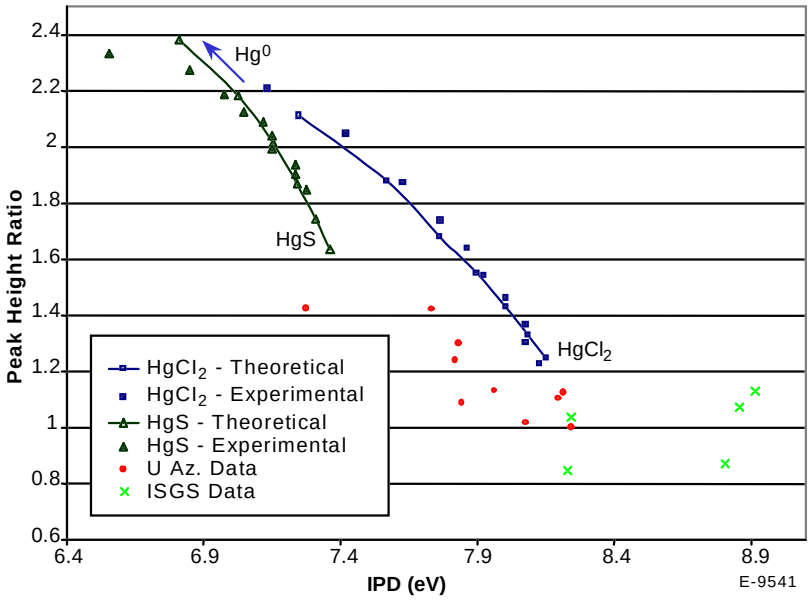

Figure 3-267. Comparison of the relationship between the HR and IPD XANES parameters calculated for simulated spectra of mixtures of elemental mercury and mercuric sulfide or mercuric chloride and experimental determinations for mercury in various sorbent materials.

All other experimental XANES data obtained for sorbent materials, but not shown in Figure 3-267, are also consistent with the fact that there is little or no elemental mercury present in the sorbent materials. From this result, we can infer that chemisorption is the dominant process involved in adsorption of mercury under the low-temperature conditions that these sorption experiments have taken place.

Hg XANES Data For Mercury Sorption on Various Sorbent Materials

Data are now presented for the various suites of samples that have been examined using mercury L_{III} XAFS spectroscopy. Most of these samples have been subjected to a mercury-laden (either as Hg^0 or as $HgCl_2$) atmosphere that simulates a typical coal combustion flue gas. As discussed elsewhere [205], the presence or absence of specific acidic species in the simulated flue-gas atmosphere has a major effect on the extent of the mercury adsorbed by the sorbent and quite possibly the mercury speciation as well.

University of Arizona Sorbent Samples

Some 10 samples from UA combustion unit were run at the mercury L_{III} edge at 12,284 eV. The samples investigated were coal-derived chars and, after exposure to the Hg-laden simulated flue gas atmosphere, the mercury contents varied from 8.5 wt.% to 160 ppm. The Hg XAFS spectra were all obtained in fluorescence geometry using a Lytle detector for the more concentrated samples and a 13-element germanium detector for less concentrated samples. In both cases, Soller slits and gallium filters were used to enhance the signal/noise ratio. Counting times varied from a single scan taking about 45 min to multiple scans lasting as much as 8 hours. Experimental and data analysis procedures were the same as described in the Final Report for Phase I of the project [7].

The mercury XANES data for UA samples are shown in Figures 3-268 and 3-269 and the IPD values are tabulated in Table 3-149. The spectra all look quite similar; however, as discussed further below, there are some quite subtle differences among the different samples that appear to correlate with differences in the samples preparation, chemistry, or conditions of sorption. In addition, the EXAFS data for UA chars was sufficiently strong to provide good radial structure functions (RSFs). These are shown in Figures 3-270 and 3-271. Again, they are very similar and indicate a Hg-nearest neighbor (NN) phase-shift uncorrected distance of about 2.0 Å ± 0.1.

Sorbent Samples from Physical Sciences Inc. (C. Senior, P.I.)

Five sorbents exposed to a simulated Hg-laden flue gas were provided for XAFS analysis by C. Senior of PSI. The samples consisted of two zeolite sorbents, two activated carbon samples, and one sulfur-activated carbons. The Hg XAFS data were collected at the same session as UA samples described above. The XANES data for the five samples are shown in Figure 3-272 and the data are tabulated in Table 3-150. However, due to their low mercury contents, these sorbent samples did not provide sufficient EXAFS signal for a useful RSF. Note the IPD value for the two zeolite sorbents compared to those for the carbon-based sorbents.

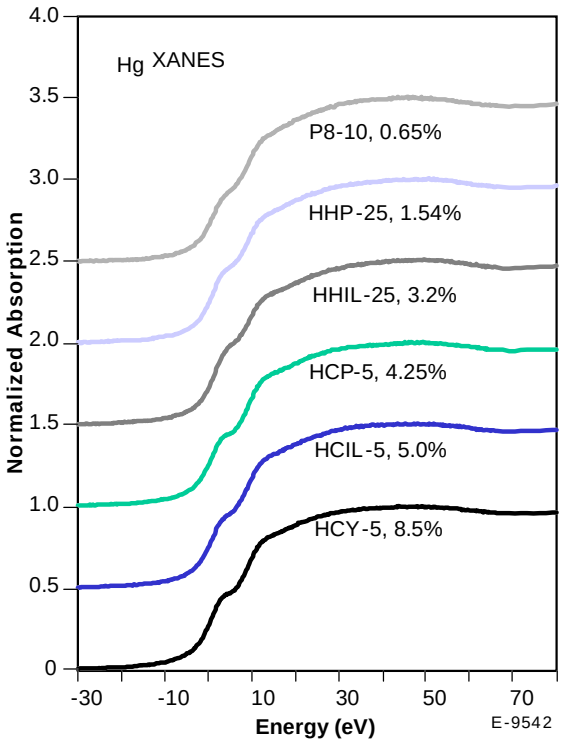

Figure 3-268. Hg XANES spectra of high mercury sorbent samples prepared at UA.

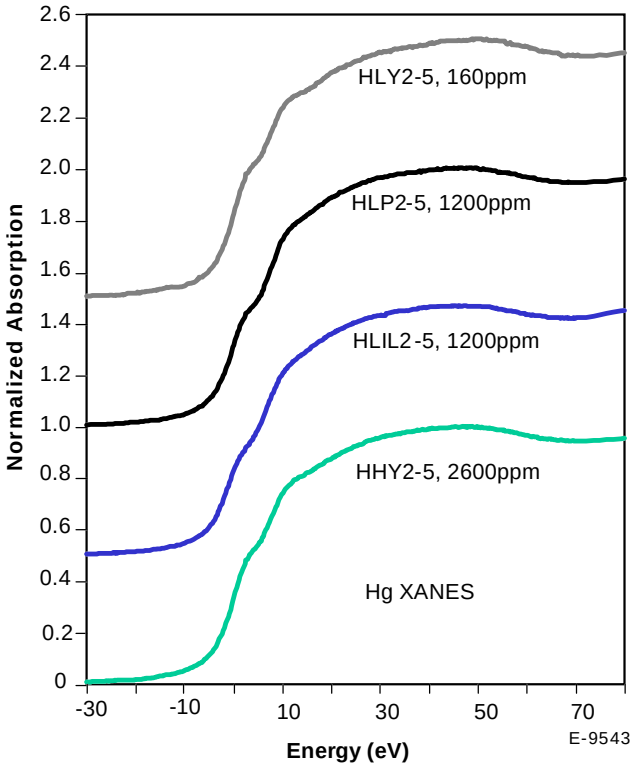

Figure 3-269. Hg XANES spectra of low mercury sorbent samples prepared at UA.

Table 3-149. Experimental Results for Coal-Based Chars After Exposure to Hg-Laden Flue Gas in UA Combustion Unit

UA Sorbent	Hg Content, wt%	Coal	Hg/Vapor Species	IPD, eV
HCP-5	4.25	Pitt	$HgCl_2$	8.4
HCY-5	8.5	Wy	$HgCl_2$	8.3
CIL-5	5.0	IL	$HgCl_2$	8.1
P8-10	0.65	Pitt	Hg	8.0
HLIL-25	0.12	IL	Hg	8.0
HLP-25	0.12	Pitt	Hg	8.0
HHIL-25	3.2	IL	Hg	7.9
HHP-25	1.54	Pitt	Hg	7.8
HHY-25	0.26	Wy	Hg	7.7
HLY-25	0.016	Wy	Hg	7.3

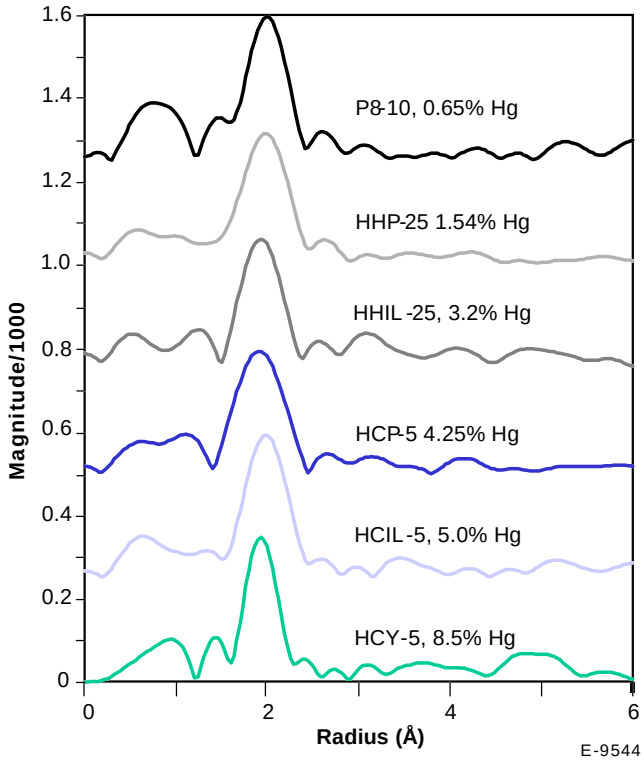

Figure 3-270. Hg EXAFS/RSFs for high mercury sorbents prepared at UA.

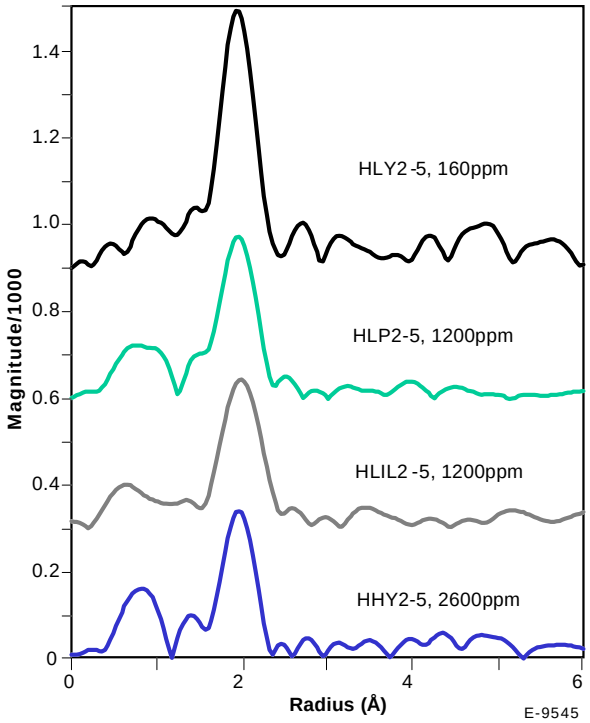

Figure 3-271. Hg RSFs for low mercury sorbents prepared at UA.

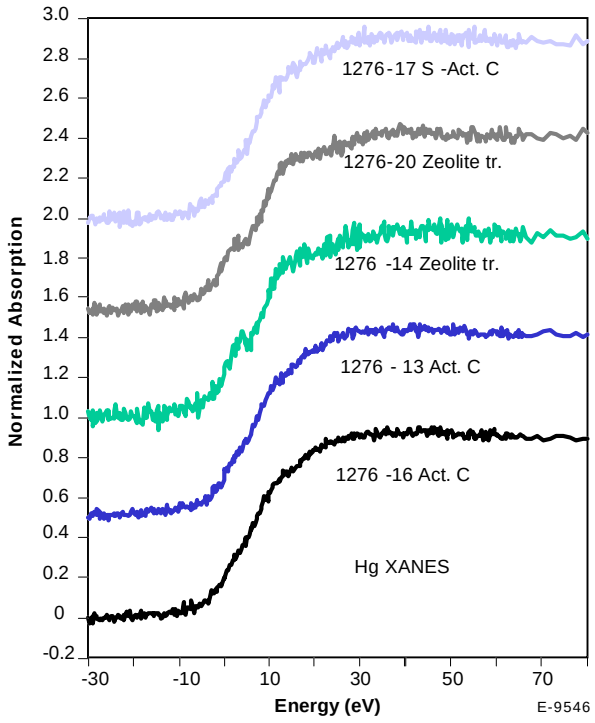

Figure 3-272. Hg XANES spectra of very low mercury sorbent samples prepared at PSI.

Table 3-150. Experimental Results for Zeolite and Activated Carbon Sorbents After Exposure to a Simulated Hg-Laden Flue Gas at Physical Sciences Inc.

Sorbent	Coal/Hg Vapor Species	IPD, eV
PSI-20	Zeolite, treat	10.0
PSI-14	Zeolite, treat	9.0
PSI-13	Act. C, treat	6.9
PSI-17	S-AC, treat	6.9
PSI-16	Act. C	6.1

Lignite-Activated Chars from UNDEERC (S. Miller and G. Dunham, P.I.s)

In XAFS sessions in early 1999, Hg XAFS experiments were conducted at SSRL for mercury and at NSLS for sulfur and chlorine in three lignite activated carbon (LAC) sorbents used for Hg capture from different formulations of the synthetic flue gas (SFG) in the experimental rig at the Energy and Environmental Research Center (EERC) at the University of North Dakota (prepared by Grant Dunham and Stan Miller, EERC). As shown in Figure 3-273, there are some significant differences in the appearance of the Hg L_{III} absorption edge that must relate to differences in how the mercury is bound to the different sorbent matrices. The parameters derived from the XANES spectra are shown in Table 3-151 for each sorbent.

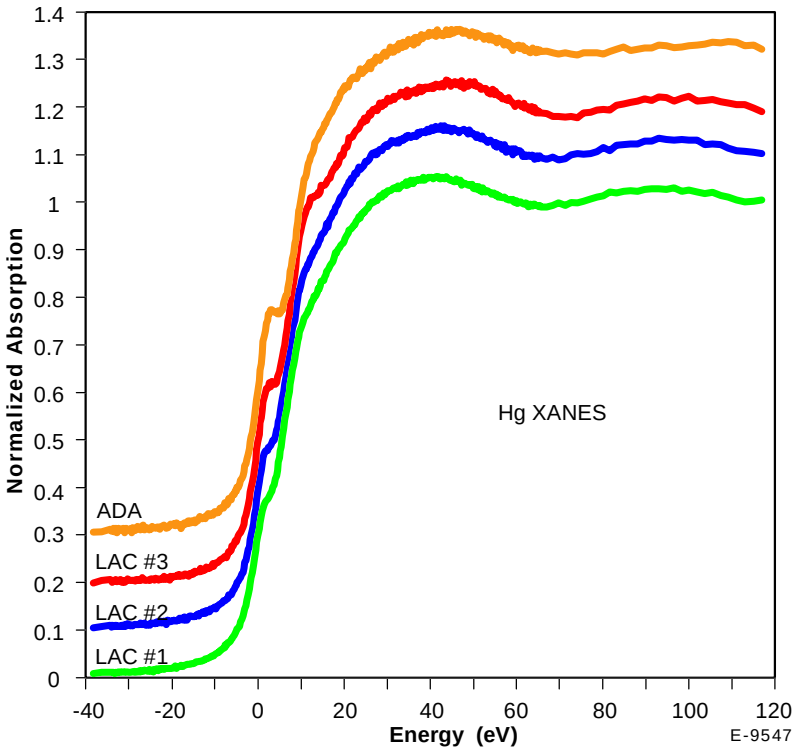

Figure 3-273. Hg XANES spectra of three lignite-activated carbons (LAC) from UNDEERC and the Cherokee fly-ash sample from ADA Technologies.

Table 3-151. Mercury XAFS Systematics for EERC LAC Sorbent Samples

Sample	IPD, eV	Mean Position, eV	RSF Peak, A	Peak Height Ratio
LAC #1	6.8	2.8	1.98	0.95
LAC #2	7.0	3.2	1.95	1.00
LAC #3	7.9	3.8	1.91	1.05

Table 3-152 summarizes data on the mercury, sulfur and chlorine step-heights for the LAC sorbent exposed to different flue-gas formulations. The step-height is an approximate measure of the elemental concentration. The data are normalized relative to those for LAC #2.

Table 3-152. Hg, S and Cl Step-Height Data for EERC LAC Sorbent Samples

Sample	Relative Step-Height Mercury	Relative Step-Height Sulfur	Relative Step-Height Chlorine
LAC #1	1.2	0.5	12
LAC #2	1.0	1	1
LAC #3	0.9	3.5	0.2

The step-height data given in Table 3-152 indicate that there are significant differences in the sulfur and chlorine contents of the lignite activated carbon (LAC) samples after exposure to the different formulations of the simulated flue gas. Sample LAC #1 has clearly adsorbed significant chlorine and furthermore the chlorine XANES spectra show (Figure 3-274) that the form of chlorine adsorbed is in the form of HCl, whereas the Cl XANES spectra of samples LAC #2 and LAC #3 clearly show the presence of organochlorine species. There are also significant differences among the three samples in sulfur contents, but the spectral differences are less marked. All three samples contained predominantly sulfate sulfur with small fractions (<10%) of the sulfur as elemental sulfur (Figure 3-275). The fraction of sulfur in elemental form decreased as the step-height increased, indicating that sulfur was being adsorbed in a sulfate form.

Fly-Ash Carbon from Cherokee Station, CO (ADA Technologies, Inc.)

Also received for XAFS examination were a number of fly-ash samples from ADA Technologies, Inc. (courtesy of Jason Albiston and Sheila Haythornthwaite). These particular fly-ash samples had been shown to have a great propensity for mercury adsorption. Included among the samples was a baghouse-hopper ash sample from the Cherokee Power station, CO, that had been impregnated with Hg in flue-gas experiments at ADA Technologies. The Hg XANES spectrum is included in Figure 3-273 for comparison with the LAC samples.

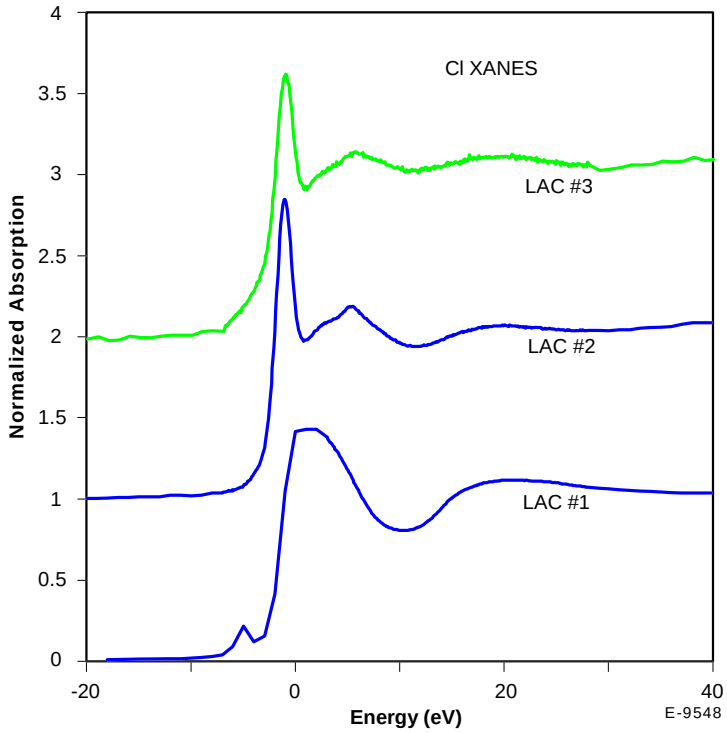

Figure 3-274. Chlorine XANES spectra of three lignite-activated carbons (LAC) from UNDEERC. Note the difference in appearance of the spectrum of sample LAC #1.

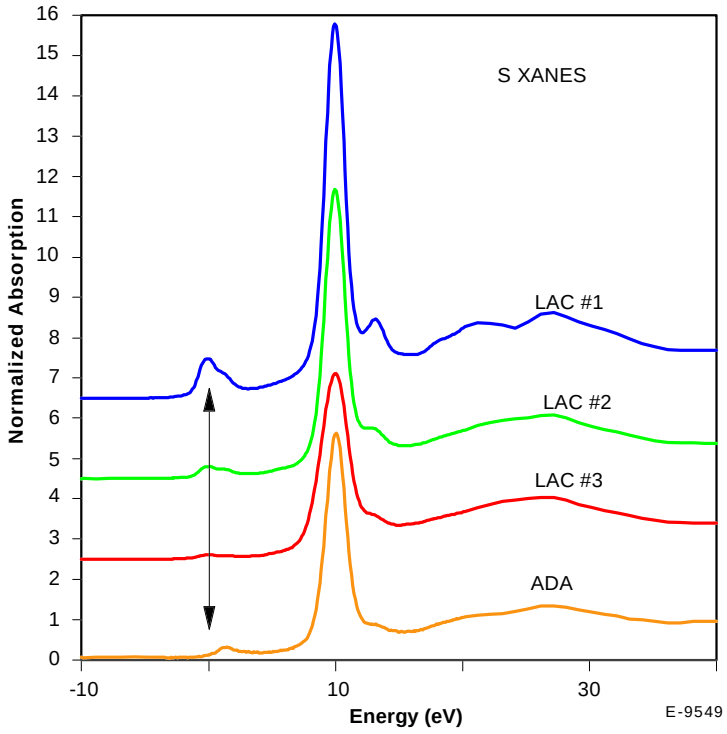

Figure 3-275. Sulfur XANES spectra of three lignite-activated carbons (LAC) from UNDEERC and the Cherokee fly-ash from ADA Technologies.

Unfortunately, the other samples were not enriched, or at least not sufficiently so, and some only contained the mercury that they had adsorbed during their residence in the power plant. These samples proved to be too low in mercury for successful Hg XAFS experiments.

As listed in Table 3-153, the mercury XAFS parameters indicate that the IPD for the Hg-enriched fly-ash sample is equivalent to or slightly greater than that for $HgCl_2$. However, the ash contains virtually no chlorine (below the XAFS detection limit, <100 ppm); hence, the IPD value may represent an average value for different Hg components in the ash. The ADA Cherokee ash also contained significant sulfate sulfur (Figure 3-275), but with a very minor fraction of organic (thiophene) sulfur present, rather than elemental sulfur, when compared to the LAC samples.

Table 3-153. Mercury XAFS Parametric Data for the Hg-Enriched ADA Cherokee Ash and Fractions Prepared by Triboelectrostatic Separation

Sample	Step-Height	RSF distance, Å	RSF Height	Peak Height Ratio, H_R	IPD, eV
Bulk	*	1.86	245	1.3	8.4
Negative TES fraction	0.58	1.88	250	1.3	8.5
Center TES fraction	0.60	1.86	225	1.4	8.3
Positive TES fraction	0.37	1.83	230	1.4	7.9

* not measured at the same time, so a comparison of the step-height is not valid.

Data were also obtained on the Cherokee fly-ash sample subjected to triboelectrostatic separation (TES) [214] and the analytical data shown in Table 3-154 were obtained for the three fractions generated by this separation technology, as well as for the original material. The mercury contents were determined by CVAAS and the carbon contents by LOI. These measurements were conducted at the University of Kentucky Center for Applied Energy Research. The results seem to imply that there is a carbonaceous fraction that is enriched in mercury because of the positive correlation of mercury content and carbon content (Figure 3-276). However, the fact that the correlation is by no means linear (Figures 3-276a, 3-276b) indicates that the system

Table 3-154. Data for Triboelectrostatic separation on ADA Cherokee Fly-Ash Sample

Sample (fraction)	Wt%	Carbon Content (wt %)	Mercury Content (ppm)
Bulk Sample	100	8.2	158
Positive Fraction	49.9	3.6	81
Middle Fraction	38.9	6.4	87
Negative Fraction	11.3	13.8	745

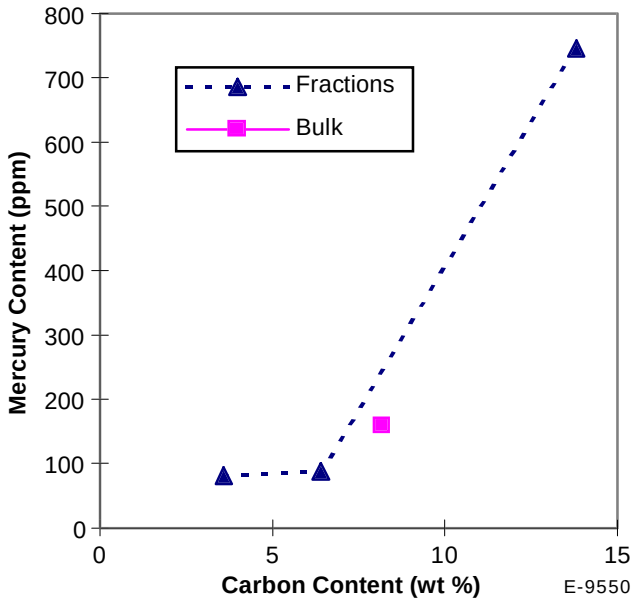

(a)

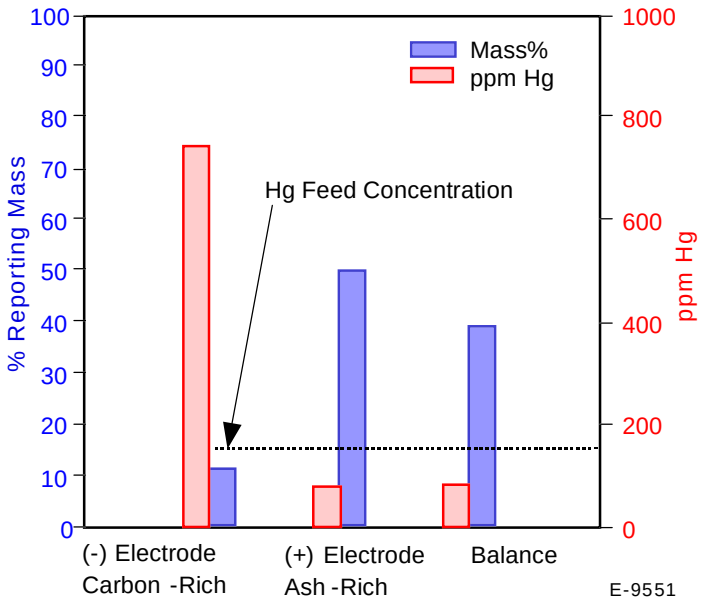

(b)

Figure 3-276. (a) Correlation between carbon content and mercury content for fractions of ADA baghouse-hopper fly-ash separated by triboelectrostatic separation. (b) Partitioning of mercury among different fractions separated from the Cherokee fly-ash by a laboratory-scale triboelectrostatic method.

is not a simple two-component system with respect to mercury; that is, it is not simply a mixture of a carbon component with an uniformly high mercury content and a non-carbonaceous component (aluminosilicate glass?) with an uniformly low or zero mercury content. Rather, one must speculate that the mercury content of the carbon is variable and that there are more than one carbonaceous component. Also, as noted by James Neathery, who did the separation, the middle fraction, which is not deflected towards either electrode, typically contains much coarse carbon particulate matter. Hence, the finest carbonaceous particulate matter, which concentrates towards the negative electrode, has the highest mercury concentration. This observation would be consistent with a mechanism of surface capture of mercury because the smallest particles have the highest surface area and therefore would have the highest mercury concentrations.

Figure 3-277 shows the mercury XANES spectra and first-derivative XANES spectra obtained from different fractions of the Cherokee fly-ash after TES separation. The spectra show relatively little variation from each other or from the spectrum of the bulk fly-ash sample. However, there is some subtle variation in the spectra that the first-derivative spectra accentuate. Results of the mercury XAFS data analysis are summarized in Table 3-153.

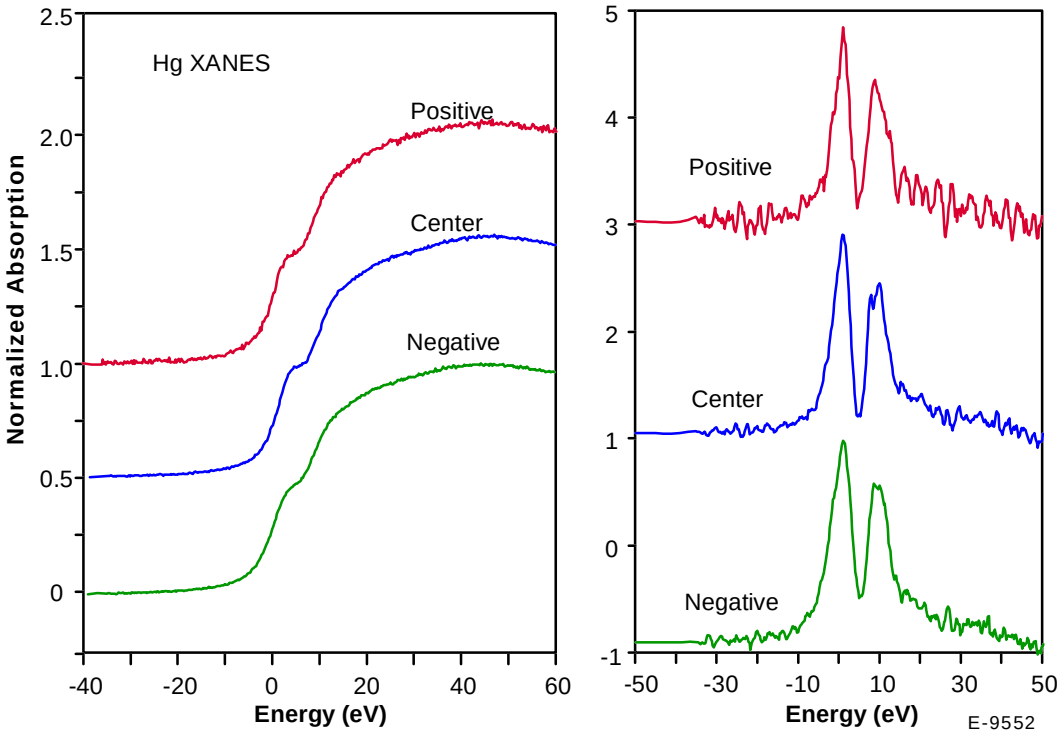

Figure 3-277. Mercury XANES spectra (left) and first-derivative spectra (right) of fractions of Cherokee fly-ash separated in a laboratory-scale triboelectrostatic separation technique. Zero-point of energy corresponds to 12,284 eV.

Given the uncertainties due to the signal/noise of the data and errors associated with the data analysis, the differences between the derived XAFS parametric data for the bulk Cherokee fly-ash sample and those for the TES fractions are relatively small. The IPD values determined for the fly-ash sample and fractions appear close to that observed for mercuric chloride (q.v. Table 3-153) and are similar to values obtained previously for carbonaceous sorbents, particularly those exposed to gaseous HCl or $HgCl_2$ [206, 207]. However, the values for H_R, the peak-height ratio, and for the RSF distance data for the fly-ash, are significantly different from those observed for mercuric chloride (H_R = 1.0-1.1, RSF distance = 2.05 Å) and other carbonaceous sorbents [205-207]. Furthermore, the chlorine XAFS data discussed above indicate that the chlorine content of the fly-ash is extremely low (<100 ppm). Hence, although it is likely that Hg-Cl bonding does contribute to the Hg XAFS spectrum (since only about 56 ppm of chlorine would be needed to bond with 158 ppm of Hg as $HgCl_2$), it is probable that the Hg XAFS spectrum of the Cherokee fly-ash reflects other mercury species as well. Such species would have to have values for H_R that are greater than that observed for mercuric chloride. One possibility would be a relatively small elemental mercury component. Another would be an Hg-O species as recent studies to be discussed below and elsewhere [215] have indicated that such species are formed on lime-based sorbents and exhibit highly asymmetric first-derivative XANES spectra and smaller RSF distances. Further discrimination of the mercury species on the basis of the XAFS data alone may yet be possible based on RSF data. More detailed discussion of these relationships are presented elsewhere [216].

Various Carbon-Based and Inorganic Sorbents (Ghorishi and Gullett, US EPA)

Two series of sorbents were received from Drs. Ghorishi and Gullett (US EPA, RTP, NC) for Hg XAFS analysis. These series consisted respectively of six carbonaceous sorbents and five inorganic sorbents that had been exposed to a Hg-enriched simulated flue gas atmosphere. XAFS data were collected for these samples at SSRL in July 1999. The normalized XANES and first derivative spectra are shown in Figure 3-278 and the various parametric data derived from the spectra are summarized in Table 3-155.

There is a clear distinction in the Hg XAFS spectra and data between the carbonaceous sorbents and the two $Ca(OH)_2$-based sorbents, which were the only ones to give rise to acceptable XAFS data. For these latter two samples, it is clear that the sorption of $HgCl_2$ involves the formation of a Hg-O bond as the IPD value for both samples is in excess of 10 eV. In addition, the RSF distance is significantly shorter and the RSF peak-heights for both lime-based samples are significantly less than those observed for the carbonaceous sorbents. Both the shortened RSF distance and the smaller RSF height are compatible with Hg-O bonding, in contrast to the Hg-S or Hg-Cl bonding that is indicated for the carbonaceous samples. The following sorption reaction is suggested for the lime-based sorbents:

$$Ca(OH)_2 + HgCl_2 \rightarrow CaCl_2 + Hg(OH)_2 \qquad (3\text{-}42)$$

This reaction indicates that mercuric chloride will undergo chemisorption when the conditions are right.

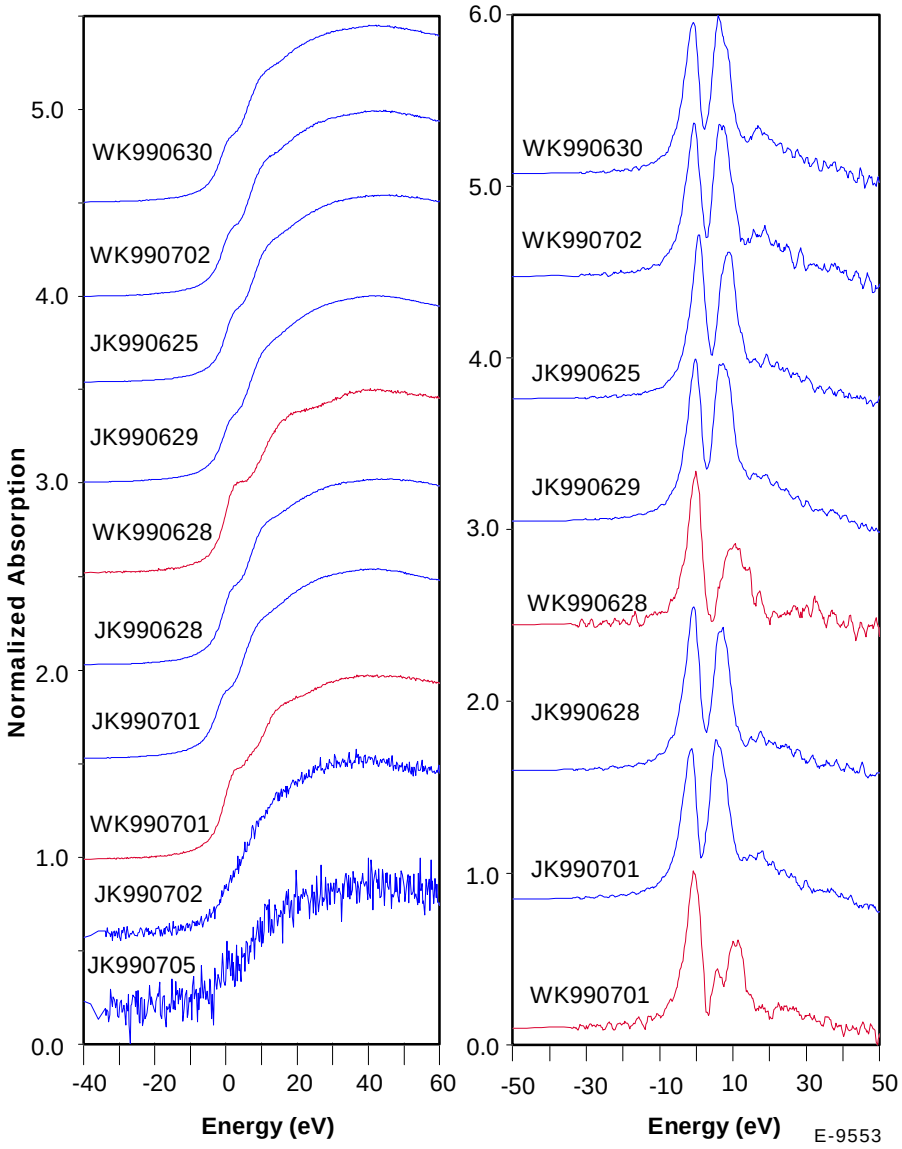

Figure 3-278. Hg XANES and first derivative spectra for sorbent samples from Drs. Ghorishi and Gullett (US EPA). Lime-based sorbents highlighted in red. Note that there are no derivative spectra presented for the bottom two XANES spectra because of their poor signal/noise ratios.

The bottom-most derivative spectrum from a lime-based sorbent (WK990701) suggests the possibility of a mixture of sorbent reactions as the dual-peaked nature of the peak at high energy might arise from a combination of minor Hg-S and major Hg-O bonding. This sample was exposed to SO_2 in the vapor phase whereas the other lime-based sorbent (WK990628) was not and shows no development of an interior peak. Finally it should be noted that the six carbonaceous sorbents were prepared from two different treated carbon materials (FGD-C and PC-100 type carbons) and subjected to the same three sorption experiments. As summarized in

Table 3-155. Hg XAFS Systematics of Various Sorbents from Ghorishi and Gullett (EPA)

Sample	Conditions Sorbent/Gas species/T°C	Step-Height	RSF, distance	RSF, height	Peak Height Ratio	IPD, eV
WK990630	FGD-C/$HgCl_2$/140	0.72	1.93	347	0.9	8.0
WK990702	PC-100/$HgCl_2$/140	0.71	1.94	360	1.0	7.5
JK990625	FGD-C/Hg,HCl/60	0.68	1.90	290	1.2	8.2
JK990629	PC-100/Hg,HCl/60	0.68	1.94	356	1.0	7.2
WK990628	$Ca(OH)_2$/$HgCl_2$/60	0.53	1.70	199	2.0	10.7
JK990628	FGD-C/Hg,HCl+SO_2/60	0.71	1.93	317	1.2	7.5
JK990701	PC-100/Hg,HCl+SO_2/60	0.72	1.93	394	0.9	7.2
WK990701	$Ca(OH)_2$/$HgCl_2$, SO_2/60	0.60	1.93	210	4.0 2.0	6.3 11.5
JK990702	Gypsum/Hg, HCl/60	0.22	--	--	--	--
JK990703	Gypsum/Hg, HCl+SO_2/60	n.d.			--	
JK990705	Fe_2O_3-Al_2O_3-SiO_2/Hg, O_2+CO_2+NO_2/100	0.05	--	--	--	--

Table 3-155 and also in Figure 3-279, the FGD-C derived sorbents always gave a higher IPD value than the PC-100 derived sorbents. The significance of this observation is not clear at this time, but may imply that the Cl/S ratio on the carbon surface is systematically different for the two types of carbon during the sorption experiments.

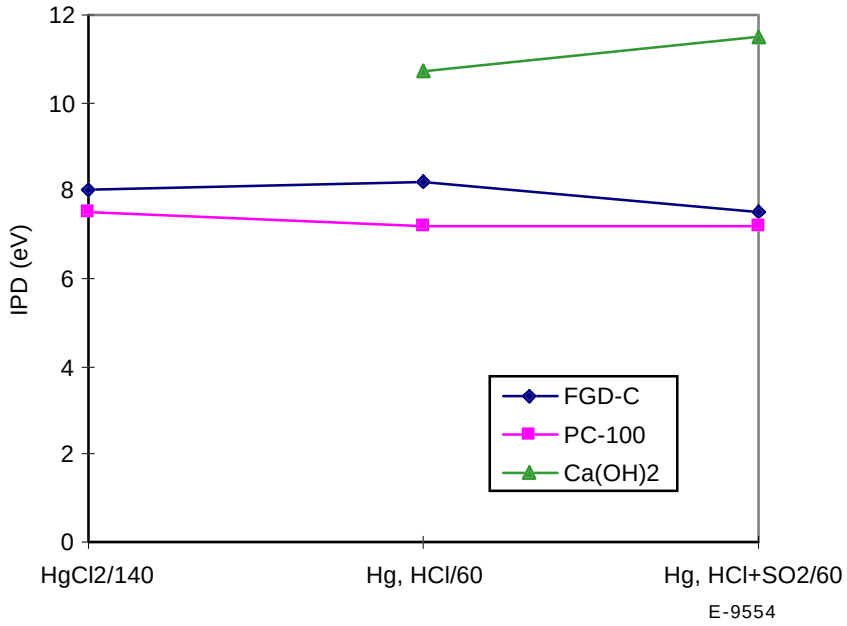

Figure 3-279. Plot of IPD values for different carbon-based sorbents and two lime-based sorbents for comparable experiments.

Carbon Felts (Gullett, et al., US EPA)

New Hg XAFS investigations were carried out during December 1999 at SSRL on beam-line IV-3 using a 6 μ Ga filter and the 13-element Ge detector. A total of 13 sorbent samples were supplied to us that had been exposed to Hg in a simulated flue-gas atmosphere. Six of the sorbents consisted of activated carbon felts, the remainder were activated carbons. Even though the mass of the activated carbon felts was small, only 20 to 30 mg, they covered a large area and the spectra obtained were reasonably satisfactory. Figure 3-280 shows the Hg XANES spectra of five of the activated carbon felt samples; the sixth gave a too weak spectrum. Hg XAFS systematics for these samples are summarized in Table 3-156. Of the other seven samples, only the two BPL activated carbons gave a reasonably strong spectra for analysis. As shown in Table 3-156, estimates of the inflection point difference (IPD) for the activated carbon felts vary between 8.4 and 9.8 eV and indicate a transitional bonding environment between Hg-Cl and Hg-O for the mercury. The one activated carbon sample that gave a strong signal exhibited a highly asymmetric first derivative spectrum and an IPD value of 9.2 eV.

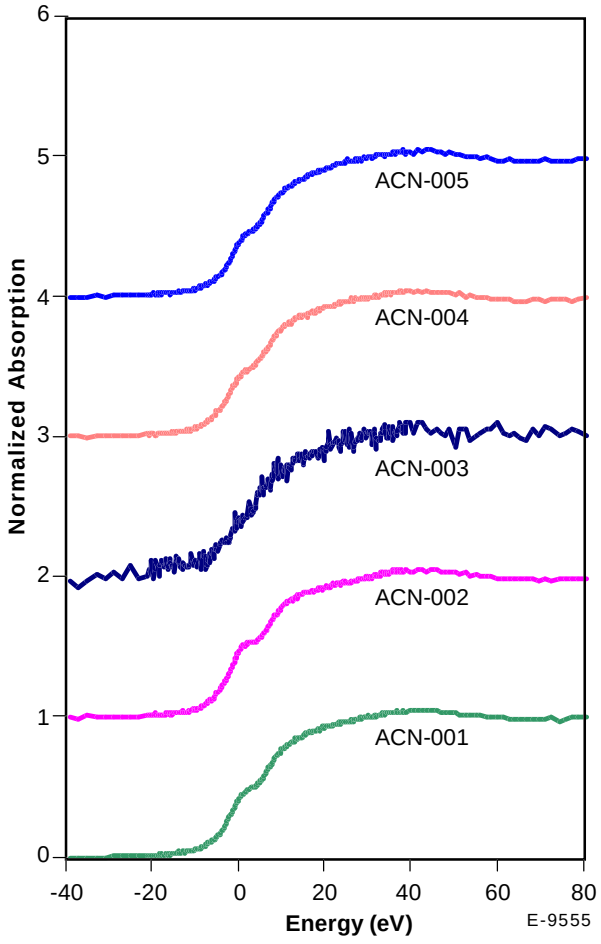

Figure 3-280. Hg XANES spectra of activated carbon felt samples obtained from Dr. Brian Gullett, US EPA and co-workers.

Table 3-156. Hg XAFS Systematics of Carbon "Felt" Sorbents from Gullett (EPA)

Sample	IPD, eV	Peak Height Ratio	Step Height	RSF, distance	RSF, height
ACN-1	9.0	1.2	1.82	1.85	148
ACN-2	9.1	1.4	1.56	--	--
ACN-3	--	--	0.17	--	--
ACN-4	9.3	1.1	1.95	1.91	263
ACN-5	8.4	1.2	1.05	1.94	276
ACN-6	--	--	--	--	--
BPL-1	9.2	1.5	0.60	1.79	155
BPL-2	9.2	1.3	0.21	--	--
ACN-c	9.8	1.2	14.00	--	--
BPL-c	10.3	1.2	17.00	--	--

Two additional series of carbon felts received from Brian Gullett and co-workers at EPA have been examined by mercury, sulfur and chlorine XAFS spectroscopy. Each series consisted of (a) the as-received material, (b) the material after a chemical pre-treatment, and (c) the material after exposure to a mercury-laden flue gas. As anticipated, only the materials exposed to mercury exhibited a significant mercury XANES spectrum and the spectra were of excellent quality. From the values obtained from the separation of the two peaks in the derivative of the mercury XANES spectra (Figure 3-281, Table 3-156), it is clear that the mercury bonding in

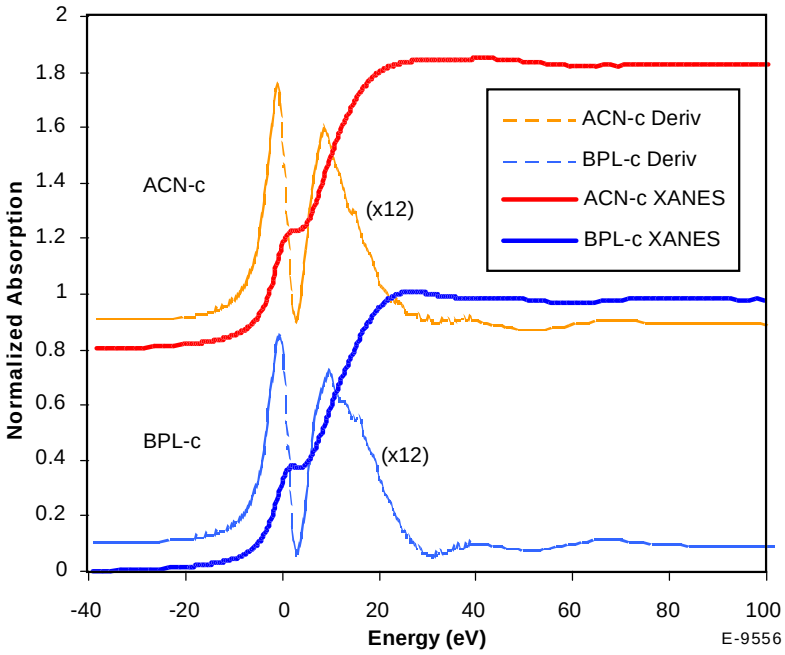

Figure 3-281. Mercury XANES and first derivative spectra of pre-treated carbon felts exposed to a mercury-laden flue gas. Zero-point of energy corresponds to 12,284 eV.

these materials involves oxygen anions. Values of 9.8 and 10.3 eV were obtained for the ACN-c and BPL-c carbon felts, respectively, which are well into the range anticipated for Hg bound to oxygen anions.

Sulfur XANES spectra were also recorded for the two carbon-based materials, both the as-received samples and the chemically pre-treated samples (Figure 3-282). Quite different sulfur XANES spectra were recorded for the two as-received materials; whereas the spectrum of sample ACN-a was dominated by sulfate, the spectrum of the BPL-a material was dominated by an organic sulfide (thiophene?) form of sulfur. The chemical pre-treatment had some effect on the sulfur forms in these two samples. In the case of the ACN carbon felt, the dominant sulfate peak was altered to a bisulfate (HSO_4^-) form in sample ACN-b, whereas the organic sulfide peak in the spectrum of sample BPL-b shifted by about 0.25 eV to higher energy. Only a very weak chlorine edge (ACN-b) or none at all (BPL-b) was detected.

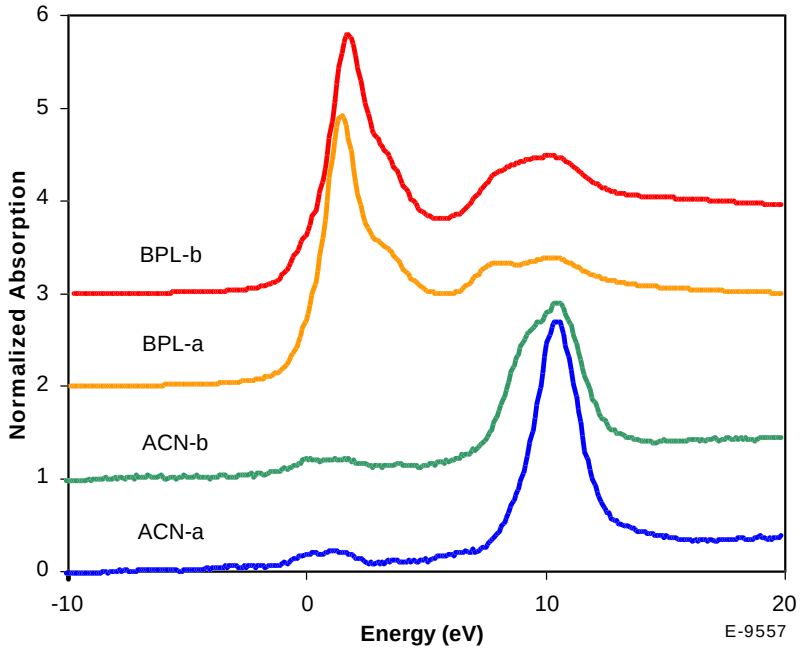

Figure 3-282. Sulfur XANES spectra of ACN and BPL carbon felt materials: a. as received; b. after chemical pre-treatment. Zero point of energy corresponds to 2,472 eV.

Discussion of Hg XAFS Systematics

During the course of this investigation, we have obtained Hg XAFS data for mercury adsorbed on a number of different sorbents, varying from carbonaceous materials, such as element-activated carbons and carbon felts, to various inorganic-based materials, such as lime-derived sorbents and zeolites. As a result, we have seen significant variation in the mercury XAFS spectra of these materials, particularly in the variation of the IPD parameter, which we have developed as an indicator of the local bonding around Hg in these sorbent materials. Also,

the asymmetry of the inflection point, as indicated by the peak-height ratio, H_R, has been used in conjunction with the IPD parameter to model anticipated trends for mixtures of chemisorption and physisorption of oxidized and elemental mercury, respectively. In the data we have obtained, there is little or no evidence for physisorption of elemental mercury on any of the sorbent materials. Our results would therefore appear to indicate that almost all mercury sorption occurs by chemisorption. All materials we have examined exhibit the characteristic inflection point indicative of the formation of Hg-anion bonds. It would appear that the anion could be virtually any available electronegative species, as we have seen evidence for the formation of Hg-I, Hg-Cl, Hg-S, and Hg-O in this work and related studies [205]. However, we have not been able to prove whether or not Hg-C bonding exists as a viable chemisorption mechanism. Our data suggest that it is unlikely, however

As discussed in more detail elsewhere [207], IPD values tend to cluster between about 7.0 and 9.0 eV, with a few values outside this range. A histogram of the different IPD values for the sorbent samples in Tables 3-149 and 3-150 and from Rostam-Abadi et al. [214] at Illinois Sate Geological Survey (ISGS) is shown in Figure 3-283. This figure clearly indicates separate regimes for the different suites of samples, although there is some degree of overlap. When the IPD values for the sorbents are compared with those for standards, we find that most of the UA samples have values comparable to chlorides and sulfides. The IPD values for the ISGS samples are somewhat higher and may reflect bonding of mercury to chloride and/or oxygen-containing species such as sulfate or nitrate. However, the IPD values for the PSI activated-carbon samples

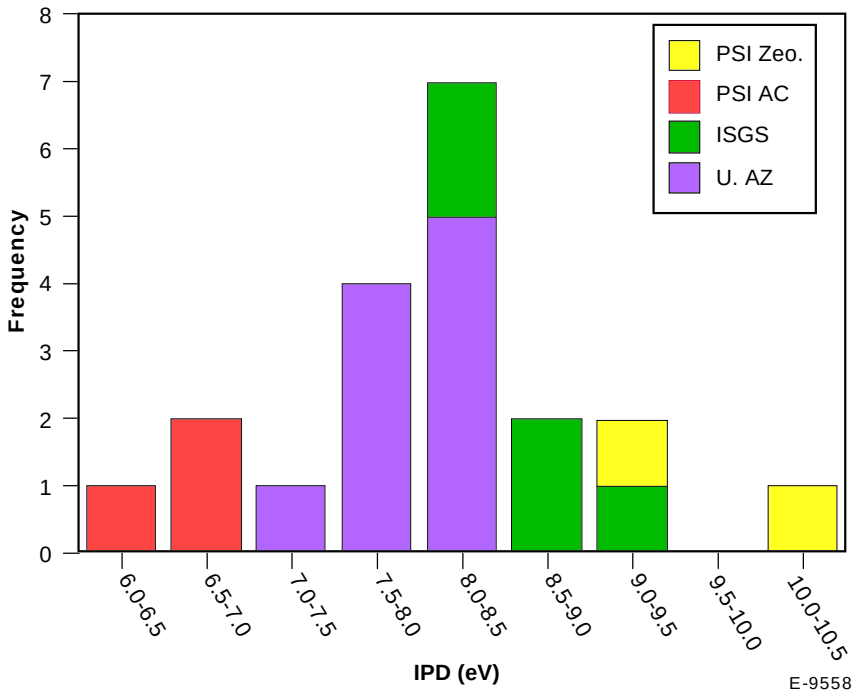

Figure 3-283. Histogram of IPD values for mercury sorption experiments on various sorbent materials in four investigations conducted at UA, at PSI and at Illinois State Geological Survey and Radian (ISGS).

are significantly lower, whereas the values for the PSI zeolite samples are significantly higher than those for the other samples. In experiments carried out with mercuric chloride ($HgCl_2$) in the SFG, the IPD values are higher than those obtained in experiments with Hg^0 vapor. Finally, within the sets of UA samples (q.v. Table 3-149 and References [7, 207]), there is clearly a trend towards lower IPD values for the experiments carried out with the Wyodak coal than with the Illinois #6 and Pittsburgh coals. Such differences most likely reflect the different chlorine contents of the coals. The Wyodak coal is known to have a much lower content of chlorine than the other two coals.

The data shown in Figure 3-283 make a further interesting point in that they appear *not* to show a bimodal distribution around the values for HgS and $HgCl_2$. Consequently, we speculate that the IPD value may reflect the S/Cl ratio at the sorption sites; *i.e.*, the formation of an "average" or mixed $HgS_xCl_{2(1-x)}$ species rather than a specific sulfide or chloride species. For the PSI sorbents, the values are not compatible with either chloride or sulfide formation. The two zeolite samples have high values for IPD that are more compatible with mercury bonded to oxygen anions, as would be anticipated for zeolites and their aluminosilicate framework structure. The IPD values for the PSI activated carbon samples may indicate that the principal bonding is between Hg and C, as they are lower than those for mercury sulfides and closer to that for diphenyl mercury. However, we note with interest that often a peak for selenium was seen in the Hg XAFS spectra for some of these samples.

Finally, in experiments in which NO_x was added to the flue gas formulation, we have seen evidence for Hg-O bonding [207, 217] in carbonaceous sorbents, as well as in inorganic sorbents such as zeolites (Table 3-150) and lime-based sorbents (Table 3-155). Further, such bonding appears to be present in the carbon "felt" sorbents, as the IPD values are significantly larger than would be expected for S- or Cl-based Hg capture.

With the exception of the iodine-activated carbons discussed elsewhere [205], the EXAFS/RSF spectra of virtually all such sorbents consist of a single peak, uncorrected for phase shift, at a position within ±0.05 Å of 1.95 Å. The range exhibited in this peak position by these samples is not much greater than the error of the determination. Consequently, as shown in Figure 3-284, there appears to be little or no correlation between this peak position and the IPD value, unlike that suggested by the data shown in Table 3-148 for the mercury standards. However, the height parameter of the RSF may yet be useful as indicating light or heavy anions surrounding the Hg, as the height of the EXAFS/RSF peak is a function of the number and mass of the anions that coordinate the mercury cation [209, 210]. The values shown in Table 3-155 for the RSF peak height are significantly lower, by a factor of 2, for the lime-based sorbents compared to those for the carbonaceous sorbents. This is consistent with oxygen anions as the ligands around Hg for the lime-based sorbents and Cl and/or S as the ligands around Hg for the carbonaceous sorbents. The utility of this particular parameter needs to be explored further.

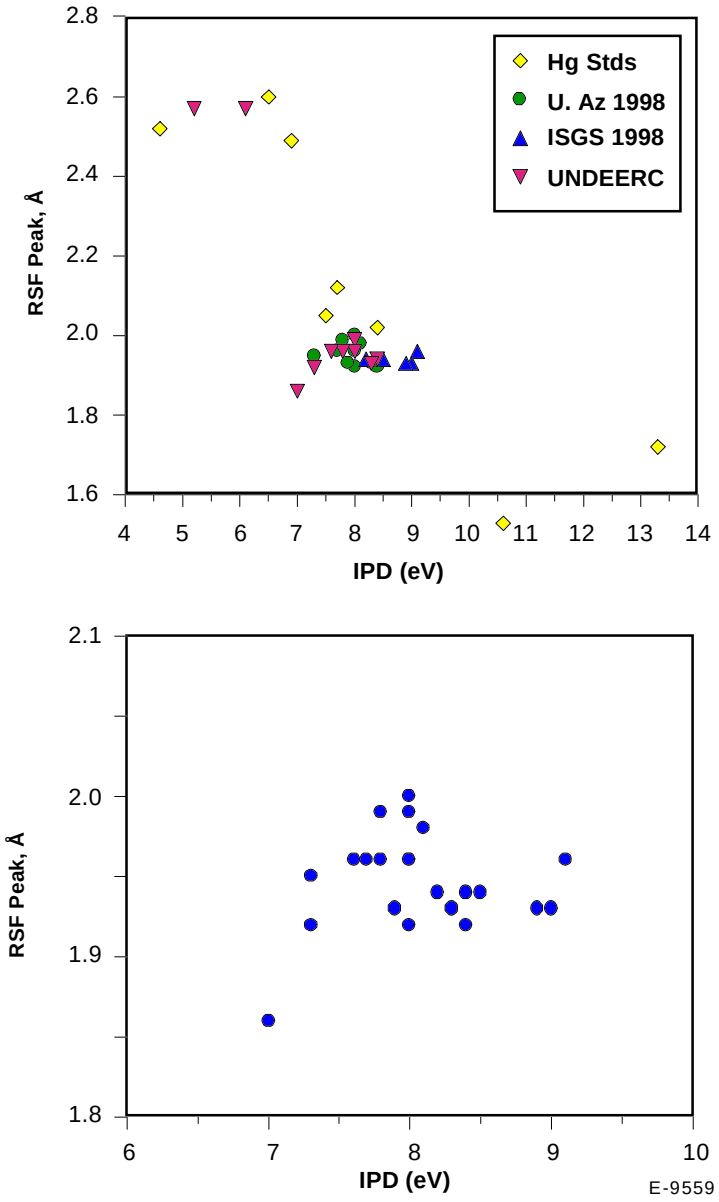

Figure 3-284. (Top) Plot of RSF peak positions against IPD values for mercury compounds and for various sorbents. Note the approximate inverse relationship for the Hg compounds. (Bottom) Detail for sorbents only.

Conclusions

In this work we have used XAFS and Mössbauer spectroscopies to characterize elements in combustion ash materials and in mercury sorbents. For ash, these techniques were used to characterize ash samples with respect to the occurrence of hazardous elements in them and with respect to their use as sorbent materials. For mercury sorption studies, Hg XAFS spectroscopy, complemented by similar investigations of S and Cl, was used to characterize the occurrence of mercury in sorbents that had been exposed to synthetic flue gas of various formulations. Key findings include:

Ash

- Recognition of calcium aluminoferrites as major iron-bearing components in high calcium ash samples.
- Direct observation of sulfite as a major sulfur form in one ash sample.
- XAFS spectroscopy contributed to the realization of the importance of calcium in controlling the oxidation state of arsenic and possibly other elements as well (e.g., chromium).
- Successfully demonstrated the feasibility of performing speciation studies by XAFS spectroscopy directly on filters.

Sorbents

- Demonstrated the usefulness of XAFS spectroscopy for the speciation of mercury captured on low-temperature sorbents from combustion flue gases. Developed XAFS parameters for such analyses.
- Demonstrated that all mercury sorption processes appeared to involve chemisorption rather than physisorption.
- Chloride, sulfide, iodide and oxygen anions were all shown to be effective for capturing mercury.
- Mechanism of capture reflects the gas-phase composition in terms of the speciation of mercury and of acid-gas components.

Acknowledgements

The authors wish to acknowledge the assistance of Nora Yap, an undergraduate student who contributed significantly to this body of work. In particular, Nora did much of the XAFS work on mercury associated with this project. We also wish to acknowledge various persons who contributed samples for our investigations, including H. Belkin (USGS), B. Ghorishi and B. Gullett, (US EPA), S. Haythornthwaite and J. Albiston (ADA Technologies), M. Rostam-Abadi (ISGS), C. Richardson (Radian), as well as our co-investigators on the project. We also wish to thank Drs. B. K. Parekh and J. K. Neathery (UK CAER) for carrying out various important separations and chemical analyses associated with the project.

The authors also acknowledge the U.S. Department of Energy for its support of the synchrotron facilities at SSRL and NSLS, where the XAFS experimentation was carried out.

3.4.6 Summary and Recommendations

Combustion processes remain the major source of mercury emissions to the atmosphere. Electric utility boilers are the largest emitting single source category in this inventory, accounting for one-third of the anthropogenic emissions to the air in the U.S. Anthropogenic mercury emissions from human activity take three forms: gaseous elemental mercury, gaseous divalent mercury, and particulate mercury. Mercury circulates in the environment in different chemical forms and different physical states. Inorganic forms exist in three oxidation states: elemental, monovalent, or divalent. Mercury in the atmosphere can return to the surface of the earth by either dry or wet deposition. In the case of gaseous divalent mercury, it can be subject to rapid wet or dry deposition. Divalent mercury is soluble in water and it can also adhere to particles in the air. It has a residence time of several days to a week. Mercury in its elemental state can be expected to disperse on a regional and global scale. The oxidation rate of Hg^0 to Hg^{+2} is on the order of a year, indicative of long atmospheric residence times.

The form of mercury emitted from point sources is a critical variable in modeling the patterns and amount of mercury deposited from the atmosphere. During combustion, mercury escapes from the burning fuel as an elemental vapor, which may persist in elemental form or may be oxidized to the +2 (mercuric) state. The three most likely gas phase mercury compounds in combustion systems - Hg, HgO, and $HgCl_2$ - are all volatile at stack and air pollution control device temperatures. At furnace exit temperatures, all of the mercury is expected to remain as the thermodynamically favored elemental form in the gas. As the gas cools after combustion, oxidation reactions can occur, significantly reducing the concentration of elemental mercury by the time the post-combustion gases reach the stack. Measurements of the concentration of mercury species taken in the stacks of pilot and full scale coal combustion systems show more than half of the vapor phase mercury as the oxidized form that is likely to be $HgCl_2$. The range of observed values is broad.

Many laboratory studies in the literature have suggested that the presence of chlorine species (HCl and Cl_2), and temperature cooling rates were the most important factors affecting mercury oxidation. Molecular chlorine readily reacted with mercury. In the presence of a cooling rate (i.e., non-isothermal conditions), kinetic limitations were evident, according to several of the studies. Further, surface reactions may contribute, although high conversion by homogeneous pathways is reported under certain conditions.

Experiments conducted under this program at UC therefore focused on measuring mercury oxidation under cooling rates representative of the convective section of a coal-fired boiler to determine the extent of homogeneous mercury oxidation under these conditions.

Although the oxidation of elemental mercury in the convective pass is assumed to proceed primarily via gas-phase reaction, experimental evidence suggests that some fly ash can catalyze oxidation of elemental mercury. Iron oxide has been shown to promote this oxidation. Other constituents in the fly ash (carbon, calcium compounds) may also contribute. The presence of acid gases (HCl, SO_2, NO, NO_2) in the flue gas has also been shown to cause oxidation in the presence of fly ash. Thus, the coal composition (in terms of chlorine content and ash composition), the operation of the combustion system (in terms of unburned carbon in the

ash), and temperature and residence time in the particulate control device will all affect mercury speciation in the gas and the amount of mercury adsorbed on the particulate matter.

Experiments conducted at the Energy & Environmental Research Center (EERC) at the University of North Dakota measured oxidation of elemental mercury and adsorption of elemental and mercuric chloride on ash samples. The ash samples were in a heated fixed bed reactor.

3.4.6.1 Gaseous Mercury Oxidation

Kinetic modeling of reactions of mercury with chlorine species under different cooling rate conditions established the importance of cooling rates as one of the main factors determining the degree of mercury oxidation in post-coal combustion. Kinetic calculations showed that the chemistry involving Cl atom reactions with mercury is fast. Therefore the presence of high concentrations of Cl atoms causes rapid mercury oxidation to occur, and the degree to which Cl_2 and HCl generate Cl atoms is important.

The results of mercury oxidation experiments under different chlorine concentrations showed that, relative to what has been reported in the literature, much higher chlorine concentrations are needed to obtain higher mercury oxidation. At typical HCl concentrations (100 ppmv) no reaction is observed with mercury. We demonstrated that total mercury oxidation can be achieved at cooling rates of 400 K/s by increasing the amount of chlorine up to 500 ppmv.

Experiments with SiO_2 particles need to be performed to assess the effects of surfaces in mercury oxidation. This is particularly important given concerns about Hall et al. [180] room temperature data. In this case the Ontario-Hydro method specifies a glass filter for the collection of particles. Introduction of NO should also be considered to provide experimental assessment of the role of NO that has been proposed recently.

3.4.6.2 Mercury-Ash Interactions

In the original scope of work, five different test series were planned to evaluate the effects of temperature, mercury concentration, mercury species, stoichiometric ratio of combustion air, and ash source. Tests were run at temperatures of 250 and 350°F. With the tests with elemental mercury injection, there was no clear temperature effect. Oxidation of the elemental mercury either increased or decreased or was not affected by increasing temperature. With elemental mercury capture, there appeared to be a slight effect, but this can be attributed to physisorption of the elemental mercury on the ash samples. With the $HgCl_2$ injection tests, capture efficiency increased with decreasing temperature. Again, this can be attributed to physisorption on the ash surface. The objective was to identify a temperature to optimize interactions between the mercury in the simulated flue gas and the ash samples. Based on the results, there was no need to find an “optimum” temperature for either the elemental or $HgCl_2$ tests. The temperatures used were adequate for observation of effects. Tests were planned to find optimum mercury concentrations, but again the baseline concentrations were adequate. No ashes were generated with different stoichiometric combustion ratios at UA, so none was tested. The main body of the testing performed was to identify reactive ash samples and determine the

effects of ash properties on capture, oxidation of elemental mercury, and reduction of oxidized mercury. As a result, 17 different ash samples were evaluated with elemental mercury or $HgCl_2$ injection. The results from these tests and analysis of the ash samples indicate there is a slight correlation between LOI and oxidation of elemental mercury across the fixed bed of ash. This effect was more evident with the bituminous and subbituminous ashes. There was also a general trend of increasing oxidation with increasing surface area. These trends most likely represent increasing active sites on the carbon that is in the ash. There was no correlation between temperature and the amount of oxidation of elemental mercury. There was also no correlation between LOI, surface area, and capture of elemental mercury. Also, no conclusions could be made about the effect of ash type on oxidation or capture of elemental mercury. Results from tests where ash samples were ashed at 400 and 750°C to remove carbon and evaluated in the fixed bed showed this process rendered active ashes inert. The baseline Wyodak ash which showed capacity for capture and oxidation of elemental mercury showed no reactivity even after the low-temperature ashing at 400°C. This was observed with all the ash samples that were ashed. The loss of active sights when the carbon was ashed is most likely responsible for the change in reactivity and not a change in the inorganic matter in the ash.

Results from the tests with $HgCl_2$ in the simulated flue gas indicate there is increased capture of $HgCl_2$ at lower temperatures. However, this is most likely due to physisorption and not an ash surface effect. As expected, the ash samples did not reduce $HgCl_2$ across the fixed bed. No conclusions could be made about the effects of LOI, surface area, or ash type on the capture of $HgCl_2$ in the fixed-bed system.

Extensive work was carried out at UK during this program to develop new methods for identification of mercury species in fly ash and sorbents. We demonstrated the usefulness of XAFS spectroscopy for the speciation of mercury captured on low-temperature sorbents from combustion flue gases and developed XAFS parameters for such analyses. We demonstrated that all mercury sorption processes appeared to involve chemisorption rather than physisorption. Chloride, sulfide, iodide and oxygen anions were all shown to be effective for capturing mercury. The mechanism of capture reflects the gas-phase composition in terms of the speciation of mercury and of acid-gas components.

3.5 Field Data (PSI, UC)

3.5.1 Semi-Volatile Trace Metals

3.5.1.1 Background

Pulverized coal combustion remains an important anthropogenic source of trace metallic element emissions. Because the concentration of trace metals in coal is typically in the parts per million range [3, 218], emissions from individual utility sources should remain well below the annual 10 ton per element major source threshold identified in the 1990 U.S. Clean Air Act Amendments [219]. Nevertheless, the large quantities of coal consumed worldwide ensure that in aggregate, coal combustion contributes significantly to the total air burden of trace metals. Using 1983 emissions data from Western Europe, the United States, Canada, and the former Soviet Union, Nriagu and Pacyna [220] estimated worldwide trace metals emissions from a variety of sources. They concluded that electric utility coal combustion contributed 2 to 6% of the anthropogenic atmospheric arsenic emissions, 2 to 3% of the cadmium emissions, 14 to 17% of chromium emissions, 9 to 17% of the mercury emissions, 10 to 14% of the antimony emissions, and 6 to 13% of the selenium emissions. For each of these elements, anthropogenic sources constituted 40 to 85% of the total annual atmospheric emissions [221].

Trace elements are emitted from coal-fired utility sources as a consequence of vaporization during combustion. Volatile trace metals such as selenium and mercury are completely vaporized at combustion temperatures, and are sufficiently volatile to remain partly in the vapor phase as temperatures decrease through air pollution control devices and the stack. Other trace elements such as arsenic, antimony, and lead will partially vaporize at flame temperatures and subsequently condense on the surfaces of fly ash particles generated during combustion. For many trace elements, condensation leads to concentration enrichment in the submicron fly ash particle size range because of the high underlying surface area of this particulate. Studies of trace element partitioning conducted over the past 25 years have been consistent in reporting enrichment of selected elements in the submicron fly ash particulate. In Table 3-157, the findings of these studies are reported, grouped by coal type and the size of the facility in which measurements were made. Although most of these studies considered partitioning for a broad range of elements, results presented in Table 3-157 are restricted to the subset of elements listed in Title III of the Clean Air Act Amendments that are emitted primarily in the particulate matter. Antimony, arsenic, beryllium, cadmium, chromium, cobalt, lean, manganese, nickel, and selenium are therefore included in Table 3-157, whereas mercury is specifically excluded because of its emission primarily in the vapor phase. The results in Table 3-157 demonstrate that arsenic, antimony, lead, cadmium, cobalt, and selenium are nearly always enriched in the finest particulate, independent of the type of coal burned or the size of the combustion facility. In contrast, chromium and nickel show behavior that is dependent upon the rank of the parent coal. Whereas enrichment has been reported for sub-bituminous coals, it is infrequently reported for bituminous and lignitic coals. In many of the early field studies, possible contamination of particulate samples by stainless steel probes and impaction substrates has obscured interpretation of results for these elements [18, 222]. More recent bench scale studies have suggested that rank-specific differences may, however, arise as a result of differences in the form-of-occurrence of chromium and nickel within specific coals [79]. Both elements may be present in organic and mineral forms, and the limited available data suggest the existence of large coal to coal variations [7, 69].

Table 3-157. Trace Metal Enrichment in Submicron Fly Ash Particulate
(elements identified in Title III of 1990 Clean Air Act Amendments, excluding Hg)

Coal Type/Source	Boiler Size	enriched	no trend or depleted	method	reference (citation)
Field Studies					
B Ill./Ky.	290 MWe cyclone	Sb, As, Cd, Cr, Pb, Ni, Se	Co, Mn	[c] FA BA	Klein et al. [92]
B U	350 MWe	Sb, As, Pb, Hg, Se		[c] f(dp), ESP-O	Gladney et al. [93]
B Poland	17.2 kg/s	As	Mn, Ni	[c] FA BA	Kauppinen and Pakkan. [36]
B Colombia	350 MWe	As, Cd, Pb, Se	Cr, Ni	[c] FA BA	Sander [223]
B Russia/Can	250 MWe	As, Cd, Pb, Se	Cr, Ni	[c] FA BA	Sander [223]
B US	295 MWe	As, Cd, Pb, Se	Cr, Ni	[c] FA BA	Sander [223]
B US, Austral.	115-645 MWe	Sb, As, Se		RE FA BA	Meij [17]
B UK	2000 MWe station	As, Pb	Cr, Mn, Ni	[c] FA BA	Martinez-Tarazona,Spears [157]
B Illinois	U	As, Sb, Se	Cr, Ni, Mn	RE FA BA	Demir et al. [224]
B Poland	160, 113 MWe	As, Cd, Co, Pb, Se	Be, Cr, Mn, Ni	RE FA BA	Aunela-Tapola et al. [225]
S US	750 MWe	Sb, As, Se		[c] f(dp), APCD-O	Ondov et al. [157]
S US	160, 203, 654 kg/s	Sb, As, Se		[c] f(dp), APCD-O	Ondov et al. [157]
S US	520 MWe	Sb, As, Cd, Cr, Ni, Se	Mn	[c] f(dp), ESP-I	Markowski et al. [226]
S Wyoming	37.5 MWe	Sb, As, Hg, Ni, Se		[c] f(dp), FF-I	Shendrikar et al. [32]
S US	113 MWe	Sb, As, Se	Mn	[c] f(dp), APCD-I	Markowski and Filby [81]
S Spain	1050MWe station	As, Se, Cd	Be, Cr, Mn, Ni	[c] f(dp), ESP-I	Querol et al. [41]
S Spain	1050MWe station	Sb, As, Co, Pb, Ni, Cr		[c] f(dp), ESP ash	Querol et al. [41]
L Texas	U	As, Sb, Se	Mn	[c] FA BA	James and Acevedo [227]
Br, L Bulgaria	U	As	Cr, Pb, Ni	[c] FA BA	Vassilev [228]
L Greece	U	As		[c] f(dp), ESP ash	Bogdanovic et al. [229]
U	U	Sb, As, Cd, Cr, Pb, Ni, Se	Mn	[c] f(dp), FA	Davison et al. [35]
U	180 MWe	Sb, As, Pb, Se		[c] FA BA	Kaakinen et al. [4]
U	U	Sb, As, Cd, Pb, Se,	Mn	[c] f(dp) ESP-O	Coles et al. [34]
U	500 – 700 MWe	As, Pb (Sb, Cr, Ni, Se also but data not shown)		[c] f(dp), ESP ash	Smith et al. [9]
U	U	As, Cr, Pb, Se	Mn	[c] f(dp), ESP ash	Smith et al. [230]
U	430, 750, 180 MWe	As, Se		[c] f(dp) ESP-O	Bierman and Ondov [231]
U	25 MWe	As, Ni	Se	RE f(dp) ESP-I	McElroy et al. [73]

Table 3-157. (Continued) Trace Metal Enrichment in Submicron Fly Ash Particulate
(elements identified in Title III of 1990 Clean Air Act Amendments, excluding Hg)

Coal Type/Source	Boiler Size	enriched	no trend or depleted	method	reference(citation)
Laboratory and Pilot Scale Studies					
B Pittsburgh	Pilot 1. 5 MM Btu h^{-1}	Sb, As,Cd, Pb	Se	c f(dp), ESP-I	Tumati and Devito [232]
L No. Dakota	Lab 17 kW	As, Pb	Mn	RE f(dp)	Linak and Peterson [233]
Bench Scale (Drop Tube) Studies					
B, S, L US	20% O_2	Sb, As, Co, Cr, Mn		RE f(dp)	Quann et al. [234]
B Illinois (b)	10.5% O_2	As Sb	Cr, Co	[c] f(dp)	Helble [79]
B, S Pitt., Wyo.	SR 1.2	Sb, As, Cr, Se		[c] f(dp)	Bool and Helble [29]
S Wyoming	30% O_2	Mn, Cr		[c] f(dp)	Helble [79]
L Montana	20% O_2	Sb, As		[c] f(dp)	Neville and Sarofim [235]
L Montana	20% O_2	Sb, As, Cr, Co		[c] f(dp)	Quann et al. [66]
L Montana	20% O_2	Sb, As, Mn, Hg		[c] f(dp)	Haynes et al. [11]
L Montana	20% O_2	Sb, As, Cr		[c] f(dp)	Neville et al. [71]

Key: Coal: B bituminous S subbituminous L lignite Br brown coal
U unspecified
ESP electrostatic precipitator
FF fabric filter (baghouse)
APCD air pollution control device (various)
RE relative enrichment factor as defined by Meij (1994) in Ref. [17]. RE = {(TE conc. in ash)(% ash in coal)}/(TE conc. in coal)
RE > 3 considered enriched, a more restrictive definition than that adopted by Meij.
TE trace element
BA bottom ash
FA fly ash, either extractively sampled at the inlet to an air pollution control device, or removed from ESP hoppers
[c] f(dp) concentration measured as function of particle size, I at ESP or APCD inlet, O at ESP or APCD outlet
(b) beneficiated coal
SR stoichiometric ratio

Coal source information listed as nation, state (US), or region of origin as specified in cited reference.
Elements not listed were either not measured, or presented RE: 1.5 < RE < 3.
Table represents expansion and reclassification of studies summarized by Linak and Wendt [125].

The enrichment of trace metals in submicron fly ash is potentially problematic because air pollution control equipment is generally less efficient in collecting particles less than 1 μm in size. Electrostatic precipitators (ESPs), used on 91% of the coal-fired power plants in the U.S. (corresponding to 91% of the coal-fired megawattage, [236]), have a collection efficiency minimum in the 0.1 to 1 μm size range. Trace elements enriched in this size range will be captured with reduced collection efficiencies relative to the total particulate mass. Particulate emissions will therefore be enriched in some of these trace metallic species. This is seen in Table 3-158 for coal-fired power plants recently studied as part of Electric Power Research Institute (EPRI) and Department of Energy-sponsored programs in the United States. Only facilities utilizing an ESP for particulate control are represented. For elements such as arsenic and selenium, the metal capture efficiency is lower than the particulate capture efficiency. For others such as beryllium and manganese, metal capture efficiency is comparable to particulate capture efficiency.

Table 3-158. Trace Element Capture Efficiencies: Field Data Facilities Utilizing ESP Alone for Particulate Control

Element	Average Particulate Capture Efficiency	Average Element Capture Efficiency	Ratio	Number of Data Points (Sites)
Hg	99.1	28.9	0.291	17
Se	99.0	49.1	0.496	16
As	99.2	96.1	0.969	19
Cd	99.1	96.1	0.970	8
Pb	99.2	96.8	0.976	18
Ni	99.1	97.6	0.985	16
Cr	99.2	98.0	0.989	19
Co	98.9	98.2	0.992	11
Be	99.0	98.3	0.993	11
Mn	99.2	98.5	0.993	21
Sb	98.9	98.5	0.996	6

Because the concentration of individual trace elements varies from coal to coal, and because the capture efficiency of trace elements differs from that of the particulate, predictive models to assess the level of trace element emissions from a given coal-fired facility are required. Such estimates are an important component of risk assessment studies that consider individual exposure to potentially hazardous air pollutants [236, 237]. The simplest models are based on 'emissions factors' in which field data are collected and combined to yield an average emissions level for a particular fuel or unit type. Emission factors are generally reported on a mass per unit fuel consumption basis, and therefore do not account for the concentration of a trace element in a particular coal. Brooks [238] derived emissions factors from published field test data, but observed that the range of trace metal emissions was extremely broad. Brooks' findings are reported in Table 3-159 for selected elements. Emissions data span nearly four orders of magnitude for some elements. This is contrasted with the narrower range reported by Chow et al. [222] for facilities measured as part of the EPRI-sponsored Power Plant Integrated Systems: Chemical Emissions Studies (PISCES) test program in the United States [222]. Data from the Brooks report shown in Table 3-159 were obtained by combining data from bituminous, sub-bituminous, and lignitic coals for both wet and dry bottomed pulverized coal fired utility

Table 3-159. Emissions Factors for Selected Trace Metals Emitted by Utility Pulverized Coal Combustion (lb/10^{12} Btu) Median (Range)

	Brooks (1989)[a]	**Chow et al. (1994)[b]**
As	42 (0.17 - 242)	32 (6-120)
Cd	3.8 (0.22 - 52.8)	2 (0.06 - 8)
Cr	2300 (1.6 - 7970)	22 (9 - 45)
Mn	440 (1 - 9240)	---
Pb	44 (1.1 - 184)	12 (4 - 40)
Ni	2100 (70 - 5760)	15 (5 - 30)

[a] From Ref. 238. Average of all coal types for utility boilers firing pulverized coal and utilizing electrostatic precipitators. Both wet and dry bottom units included in average. Individual boilers treated as single data points in deriving Table 3-159.
[b] From Ref. 222. ESPs and fabric filters combined.

plants equipped with electrostatic precipitators. Data in the Chow et al. study include facilities equipped with fabric filters as well as those equipped with electrostatic precipitators. Chow et al. attributed the large differences in emission factors for chromium and nickel to the use of stainless steel sampling lines in many of the studies comprising the Brooks report.

A related method for predicting trace metal emissions incorporates capture efficiencies that are trace element specific, thus allowing coal-dependent variations in trace element concentrations to be examined. Capture efficiencies reported by Brooks [238] and Szpunar [239] are summarized in Table 3-160. The capture efficiencies reported by Szpunar are estimates for a new 500 MWe power plant with 99.8% particulate capture assumed. The values reported by Szpunar are closer to those obtained in the field testing programs of the early 1990s (Table 3-158), and thus are likely to represent reasonable estimates for a well-maintained power plant operating with high efficiency particulate control equipment.

Table 3-160. Average Capture Efficiency for Selected Trace Metals

	Brooks ESPs (1989)[a]	**Szupnar (1993)[b]**
As	87.5	97.2
Cd	74.6	97.3
Cr	71.5	99.0
Mn	78.1	98.0
Pb	---	98.2
Ni	79.1	99.6

[a] data from Ref. 238
[b] data from Ref. 239

The data reported by Szpunar incorporate trace element enrichment as a function of particle size by categorizing elements according to relative volatility [218, 239]. While an improvement over the emission factors summarized in Table 3-159, the use of capture efficiencies neglects element-specific variations in volatility, and is restricted to providing estimates for facilities with comparable particulate control efficiencies. Rubin and co-workers [240] have incorporated the variability in field data by utilizing the distributions of measured trace element

concentrations and capture efficiencies in the PISCES study to develop a probability-based emissions factor model. Results are reported as probabilistic outputs by specifying the percentage of facilities with a given set of input variables that would have emissions within a given range. Using a subset of approximately 12 data points to define the expected emissions range, the authors used the probabilistic model to predict emissions at one specific plant. Predicted means for chromium and selenium showed good agreement with measured emissions, whereas arsenic showed poor agreement.

While these models represent increasing levels of complexity, none incorporate the element specific vaporization occurring within the flame, nor do they address element-specific partitioning to different size classes of fly ash occurring downstream. Recognizing this, Meserole and Chow [241] improved upon the emission factor methodology by calculating hypothetical emissions for a trace metal compound based upon air pollution control device capture efficiency and trace element enrichment in the submicron fly ash (as a function of the fraction vaporized for a generic trace element). Rizeq et al. [242] later expanded this approach by adapting a model originally developed for waste incineration. In the Rizeq et al. model, trace element vaporization and condensation during coal combustion were explicitly treated by using equilibrium vapor pressures to determine the extent of vaporization of each element, and homogeneous and heterogeneous condensation to distribute the trace elements in the particulate phase. While this methodology represents a more fundamental and thus more general approach, there are limitations associated with the prediction of trace element vaporization using equilibrium thermochemistry. Previous studies have shown that mass transport and kinetic considerations affect vaporization rates and extents [7, 66, 243], thus establishing the thermodynamic values as upper limits. Creation of submicron ash particulate through the decomposition of pyrite minerals has also been suggested [244]; this may also contribute to submicron enrichment of trace elements such as arsenic that are contained in pyrite [69]. In addition, aluminosilicate mineral phases are typically neglected in calculating vaporization because of the scarcity of thermodynamic data for these compounds. Aluminosilicates are, however, important mineral phases in coal [7] and may contain substantial quantities of certain trace elements [69]. The limiting effects are best seen in equilibrium predictions that all of the lead, arsenic, antimony, and cadmium present in all coals will vaporize during combustion regardless of temperature or reaction stoichiometry [242]. In addition, chromium is predicted to vaporize completely under oxidizing conditions, but shows lower vaporization under locally reducing conditions. Bench experiments conducted under variable temperatures would therefore be expected to show either no change or a decrease in the amount of trace element associated with the submicron particulate phase. For arsenic and chromium, two elements for which recent bench data are available, the amount of each element present in the submicron fly ash (and taken to be indicative of the amount vaporized) is found to increase with increasing particle temperature [7].

A general model for trace element emissions must therefore be based upon fundamental partitioning behavior within the combustion environment. It must address coal-specific trace element concentrations, element specific volatility, element specific partitioning among the different size classes of ash particles, and element and particle size-specific penetration through air pollution control devices such as the electrostatic precipitator. In this paper, a model that incorporates the framework of these fundamentally-based efforts while utilizing experimental

data to define elemental partitioning is described. The model further considers element-specific partitioning by utilizing models for heterogeneous condensation, surface reaction, or retention within the mineral phase that are element-specific and derived from fundamental combustion studies of trace element partitioning.

3.5.1.2 Model Development

Extensive field data on trace element emissions recently obtained in DOE and EPRI-sponsored projects provides a large database which can be used to assess model predictions of trace element emissions. This database provides information on coal rank, ash content, sulfur content, trace element concentrations, coal higher heating value, trace element emissions rate, and particulate matter emissions rate for the ten trace elements listed in Table 3-157 at over 40 U.S. sites. From this tabulated data, the capture efficiency of air pollution control devices for total particulate matter as well as individual trace metals can be derived. Comparison of these efficiencies provides a means for determining whether selected trace elements are preferentially emitted from coal-fired utility power plants, and whether there is any rank, control device, or facility-type dependence in such emissions.

The particulate collection efficiency of an air pollution control device is defined as

$$\eta = 1 - PM_{out}/PM_{in} \quad (3\text{-}43)$$

where PM_{out} is the particulate matter concentration (mass per unit heat input, e.g., lb per million Btu) at the outlet of the air pollution control device, and PM_{in} is the corresponding value at the inlet of the air pollution control device. PM_{out} can be expressed in terms of coal parameters as

$$PM_{out} = PM_{in} (1-\eta) = f_a (1-\eta) / H \quad (3\text{-}44)$$

where f_a is the mass fraction of ash in coal on an as-received basis, and H is the higher heating value of the coal on an energy content per unit mass basis. For any trace element *i* present in the coal, the emissions E_i on a mass per fuel energy content basis (e.g., lb trace element *i* per 10^{12} Btu) can be determined by analogy to Eq. (3-44),

$$E_i = A_{i,in} (1-\eta_i) = C_i (1-\eta_i) / H \quad (3\text{-}45)$$

where $A_{i,in}$ is the concentration of trace element *i* at the inlet to the air pollution control device (mass per unit fuel energy content), C_i is the concentration (mass fraction) of trace element *i* in the coal on an as received basis, and η_i is the capture efficiency of trace element *i* in the air pollution control device, defined as in Eq. (3-43). Combination of Eqs. (3-44) and (3-45) yields an expression for trace element emissions as a function of measurable parameters:

$$E_i = \frac{C_i \ PM_{out} (1 - \eta_i)}{f_a (1 - \eta)} \tag{3-46}$$

Thus, if trace element capture efficiency were correlated with particulate capture efficiency, a linear plot of E_i as a function of (C_i PM_{out} / f_a) would pass through the origin with slope equal to (1-η_i)/ (1-η). Typically, however, a broad range is observed in emissions measurements made at different facilities. Modification of Eq. (3-46) to the empirical

$$E_i = a_i \left[\frac{(C_i \ PM_{out})^{bi}}{f_a} \right] \tag{3-47}$$

can also be considered, and is the form recommended by EPRI for interpretation of the DOE and PISCES data [245]. Although the large size of the underlying database makes it probable that the development of Eq. (3-47) for each trace metal will be more accurate than emissions factors proposed elsewhere (c.f. Tables 3-159 and 3-160), this approach remains a correlational one that does not account for the enrichment of many trace metals in the smallest particle sizes.

A more accurate model useful for predicting the emissions of trace metals from pulverized coal combustion sources equipped with electrostatic precipitators can be derived if trace element concentrations are predicted as a function of ash particle size, and if size-dependent particulate capture efficiencies are considered. Previous efforts have addressed these issues, but have used thermodynamic models for trace element vaporization [242] and have restricted consideration to homogeneous and heterogeneous condensation [241, 242]. Fundamental bench scale studies have demonstrated, however, that minerals and trace elements transform through condensation as well as by surface reaction of vapor phase species with ash particles and by coalescence of ash particles within the burning coal char [11, 79, 125, 126, 242]. Trace element concentrations can therefore exhibit size dependence expressed as

$$CE_{i,j\ ash} = k_{i,j} \ dp_j^{\ n} \tag{3-48}$$

where $CE_{i,j\ ash}$ represents the concentration of trace element *i* in ash particles of size dp_j, $k_{i,j}$ is a proportionality constant, and n is the exponent representing the size dependence of concentration. The exponent n will equal –1 for heterogeneous condensation in the free molecular regime, -2 for heterogeneous condensation in the continuum regime, -1 for heterogeneous surface reaction control, and 0 for complete mass apportionment resulting from mineral coalescence (size independence) [11, 125, 246]. Recall that in a previous model, Rizeq et al. treated only condensation, but allowed for size-regime dependent condensation flux [242, 247]. Messerole and Chow incorporated a 1/dp dependence in trace element concentration, which, although labeled as condensation, represents assumptions of condensation on the smallest submicrometer-scale ash particles (free molecular regime) and external surface reaction control on the larger fly ash particles (continuum regime) [241]. In the work described herein, the size dependence was selected from mechanistic assessments derived from bench-scale experimental studies and is element-specific.

In order to predict trace element emissions, ash particle size distributions at the inlet to the electrostatic precipitator are needed. Models that predict the size distribution of fly ash particles formed during pulverized coal combustion are available, but require coal mineralogical data as input [248]. Because such data were not provided as part of any published field studies, site-specific calculation of fly ash particle size and composition distributions, a long-term goal of trace element emissions models [7], is not presently possible. Fly ash particle size distributions were therefore derived from field measurements of ash particle size distributions conducted at the inlet to a power station cold-side electrostatic precipitator. Measurements were conducted on two separate occasions, permitting sampling of ash during combustion of two bituminous coals [249]. Data (Figure 3-285) were obtained by extractive sampling and subsequent size segregation using cyclones and a low pressure impactor (BLPI). An average particle size distribution at the ESP inlet was then obtained by averaging the two distributions and renormalizing. In the 4 to 8 μm region where data collected by the cyclone and impactor overlapped, particle concentrations were considered additive. The fraction of ash in the submicron particle size range calculated from these combined data was 1.9%, comparable to the 0.5 to 2% observed in prior field studies [73, 250, 251]. Fly ash particle size distributions were subsequently calculated for individual facilities by adjusting the mass in each size bin by the relative ash content of the fuel. The normalized fly ash particle size distribution (i.e., percentage of total fly ash mass within a given size range) remained fixed at the value derived from Figure 3-285.

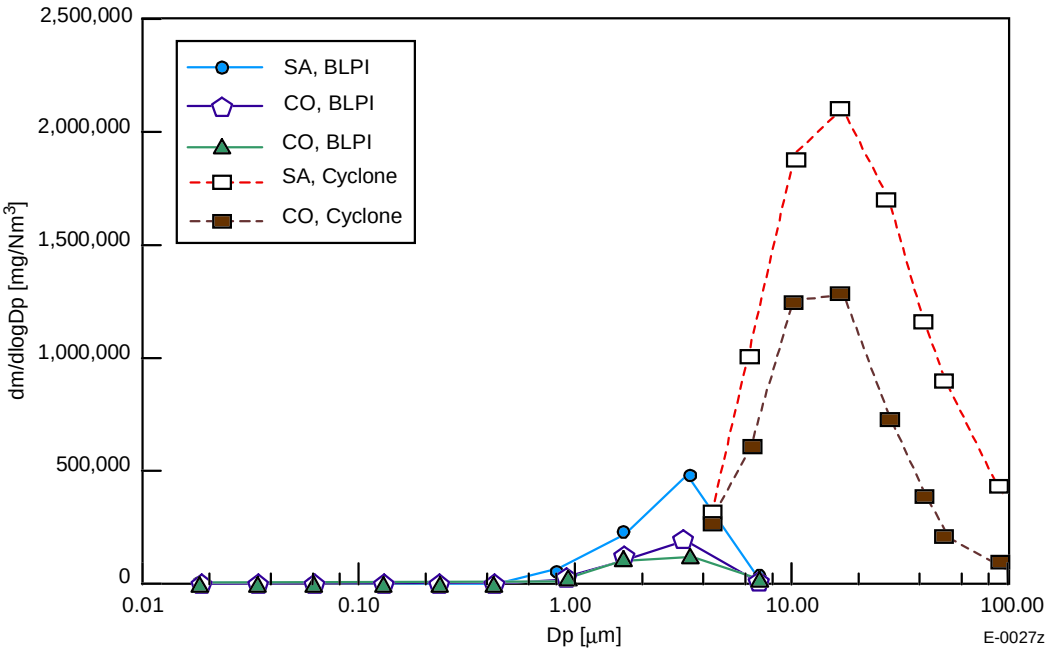

Figure 3-285. Fly ash particle size distributions obtained from field measurements (Lind [249]) and used to assign baseline size distribution at ESP inlet. CO represents Colombian coal, SA South African.

Particulate penetration through the electrostatic precipitator was determined through additional low pressure impactor and cyclone measurements at the electrostatic precipitator outlet at the same facility represented by the data in Figure 3-285. Aluminum penetration data [249] were used rather than total mass penetration data to avoid complications introduced by condensation and particle formation within cold-side ESPs [252]. The penetration curve derived from these measurements is presented in Figure 3-286 along with other ESP penetration measurements from the published literature. Data reported by McElroy et al. [73] demonstrate higher penetration, whereas 1998 data reported by Ylatalo and Hautanen [253] for combustion of a Polish coal are similar to the aluminum penetration data of Lind [249]. Mohr et al. [252] data are overall mass penetration data in the submicron regime for the two coals used to derive the aluminum data of Lind [249]. Although these data demonstrate higher penetration in the 0.1 to 0.6 μm range for the same two coals, evidence of particulate formation within the precipitator was observed. The aluminum data of Lind were therefore taken as being representative of particulate penetration through a well-operated current-generation ESP neglecting particle formation within the precipitator.

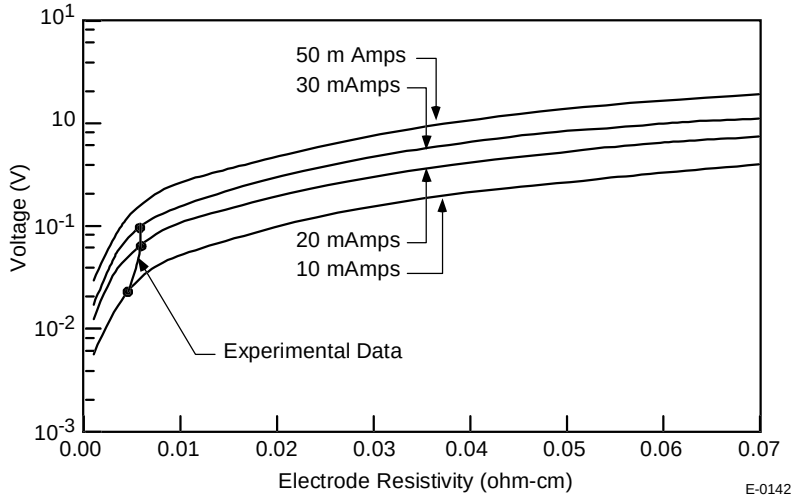

Figure 3-286. Particle penetration through cold-side electrostatic precipitators as a function of particle size. Lind [249] data used in the model are reported for aluminum, all others are for total mass. Ylatalo and Hautanen [253] data are for the 234 MWe baseline case with all fields operative. Ensor et al. [254] data for hot-side ESP. Penetration peak at particle sizes less than 0.1 μm reported by Mohr et al. [252] excluded from figure.

With the establishment of a fly ash particle size distribution at the electrostatic precipitator inlet, the distribution of trace elements as a function of ash particle size can be established. This was accomplished by defining the fraction of a trace element associated with the submicron fly ash, and then distributing it among all fly ash particles as a function of particle size. Selenium, arsenic, and chromium were selected for detailed modeling because of differences in partitioning behavior observed at the bench scale. Selenium is a volatile element that may remain partially in the vapor phase at stack conditions. Arsenic is representative of a second type of volatile element that will vaporize significantly during combustion, but will condense completely before exiting the power plant. Based upon the field and bench studies

summarized in Table 3-157, antimony, cadmium, cobalt, and lead are expected to follow similar partitioning patterns. Chromium is representative of elements that are only partially volatile, with enrichment sensitive to coal type or combustion conditions. Nickel has demonstrated behavior similar to that of chromium in field and laboratory studies (Table 3-157). Based upon these observations and data from bench scale studies, the trace elements were distributed as indicated in Table 3-161. Particle size-dependent electrostatic precipitator penetration efficiencies were then used to determine the fraction of particulate and thus the fraction of trace element emitted.

Table 3-161. Partitioning Functions used in Development of Emissions Model

	Submicron	**Supermicron**
chromium	heterogeneous condensation	coalescence (mass apportionment)
arsenic	surface reaction	surface reaction
selenium	vapor + surface reaction	surface reaction

Using these partition functions, trace element emissions from a given facility can be expressed as

$$E_{ijk} = Pt_j \, [Pt_k/Pt_{baseline}] \, CE_{ijk} \qquad (3\text{-}49)$$

where *i* represents a specific trace element, *j* represents a specific size (bin) of fly ash, *k* represents a specific utility boiler or site, E represents trace element emissions (mass per unit heat input of the fuel), Pt represents overall particulate mass penetration through the electrostatic precipitator, $Pt_{baseline}$ represents the overall particulate mass penetration through the baseline electrostatic precipitator (Figure 3-286), and CE represents the concentration of the trace element in a specific size class of fly ash particles at the inlet to the electrostatic precipitator. Overall emissions of trace element *i* from site *k* can then be determined from the mass weighted sum over all size bins,

$$E_{ik} = \sum_j m_{jk} E_{ijk} \qquad (3\text{-}50)$$

where m_{jk} represents the mass of fly ash in size bin *j* at site *k*. CE is a discontinuous function of particle size,

$$CE = k_{1ik} \, dp^n \, f_{v,i} \qquad dp < 1 \, \mu m \qquad (3\text{-}51a)$$

$$CE = k_{2ik} \, dp^n \, (1\text{-}f_{v,i}) \qquad dp > 1 \, \mu m \qquad (3\text{-}51b)$$

where k1 and k2 are normalization constants and fv represents the fraction of trace element *i* associated with the submicron fly ash. Although size dependencies reported for heterogeneous condensation are strictly valid only for particle sizes much greater than or less than the mean free path of the gas (approximately 0.1 μm at typical cold side ESP inlet temperatures of 140°C, and 0.4 μm at 1500°C), they are taken as being valid throughout the transition regime, with sharp transitions in mechanism occurring at a particle size of 1 μm. A cutoff size of 1 μm is

convenient because experimental studies have assigned trace element volatility from the fraction of an element appearing in the submicron size range [234].

3.5.1.3 Results and Discussion

An initial characterization of trace metal emissions can be obtained by applying Eqs. (3-43) through (3-47) to field data generated in the EPRI PISCES and DOE sampling programs. Taking arsenic as a typical element, a plot of the data shows a lack of correlation between stack emissions E and the parameter C PM/fa specified by Eq. (3-46) (Figure 3-287). The linear least squares correlation coefficient R^2 was determined to be 0.20 for 36 sites [7], with emissions ranging from less than one pound arsenic per 10^{12} Btu up to several hundred pounds per 10^{12} Btu. Using the empirical approach described by Eq. (3-47), an improved fit is obtained (Figure 3-288, $R^2 = 0.72$), a trend that holds true for all ten of the trace elements considered [7]. Further improvement in agreement between predicted and measured arsenic emissions was observed when the subset of facilities using fabric filtration for particulate control was considered ($R^2 = 0.92$), suggesting that much of the variability observed in Figure 3-287 stems from the emission of small particulate enriched in arsenic.

The dependence of arsenic emissions on air pollution control device type further suggests that the approach outlined by Eqs. (3-48) through (3-51) should be useful in improving emissions estimates for arsenic and other compounds with comparable combustion partitioning behavior. It is not clear, however, whether improved prediction would be obtained for less volatile elements such as chromium. The partitioning / penetration emissions model outlined by Eqs. (3-48) through (3-51) was thus applied to chromium by generating emissions estimates and comparing them to data measured in the DOE and EPRI PISCES studies. The amount of chromium present in the submicron ash particle size range was used as an adjustable parameter to obtain the best fit to measured data. Goodness of fit was determined by minimizing the sum of squared residuals R, defined as

$$R_i = \sum_k (E_{ik,predicted} - E_{ik,measured})^2 \qquad (3\text{-}52)$$

A comparison of the model-predicted values of chromium emissions with those derived from Eq. (3-47), using an a_i value of 6.10 and b_i of 0.284 (both derived from EPRI PISCES data for coal-fired facilities utilizing ESPs, with or without flue gas desulfurization) is shown in Figure 3-289. The partitioning / penetration model demonstrates no difference when compared to the empirical approach. This is attributed to the relatively low volatility of chromium and the small percentage of sub-bituminous coal-fired boilers in the dataset. In the discussion of Table 3-157 it was noted that chromium enrichment was only observed at field sites burning subbituminous coal. Analysis of the EPRI/DOE database suggests similar results for facilities burning sub-bituminous coal (Figure 3-290), but given the dominance of bituminous coal-fired systems in the database, the influence of selective partitioning in sub-bituminous systems on the overall correlation is minimal. Bench scale experiments in which the amount of chromium in the submicron ash particulate correlated with the fraction of silicon in the submicron particulate, rather than the amount of chromium in the coal, provide further evidence in support of coal-specific chromium volatility [234].

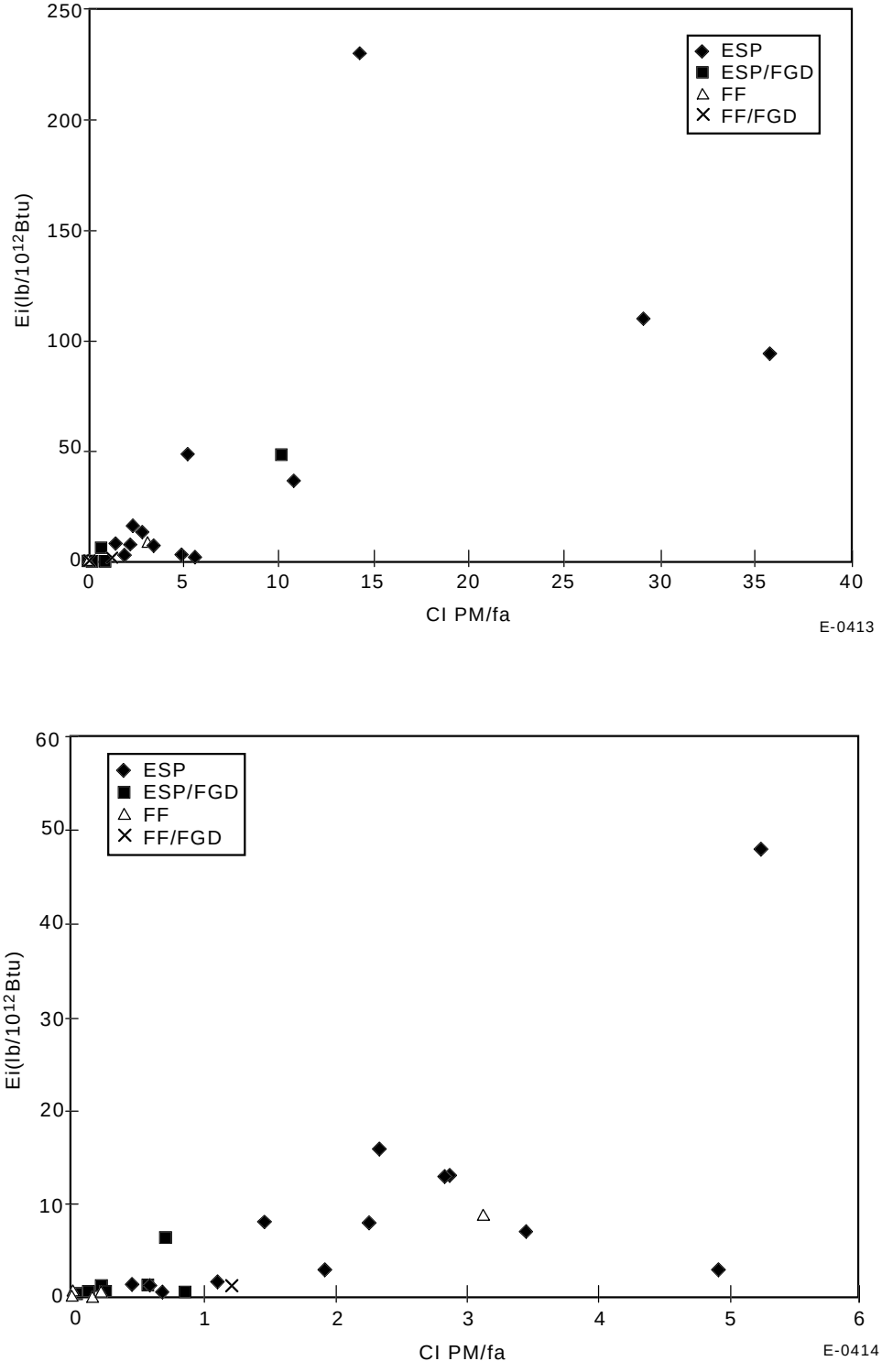

Figure 3-287. Arsenic emissions data obtained from field measurements as a function of C*PM /fa as per Eq. (3-46). Different symbols represent different types of particulate control device. $R^2 = 0.20$ for these data. (a) entire dataset, (b) CI PM/fa < 5 only.

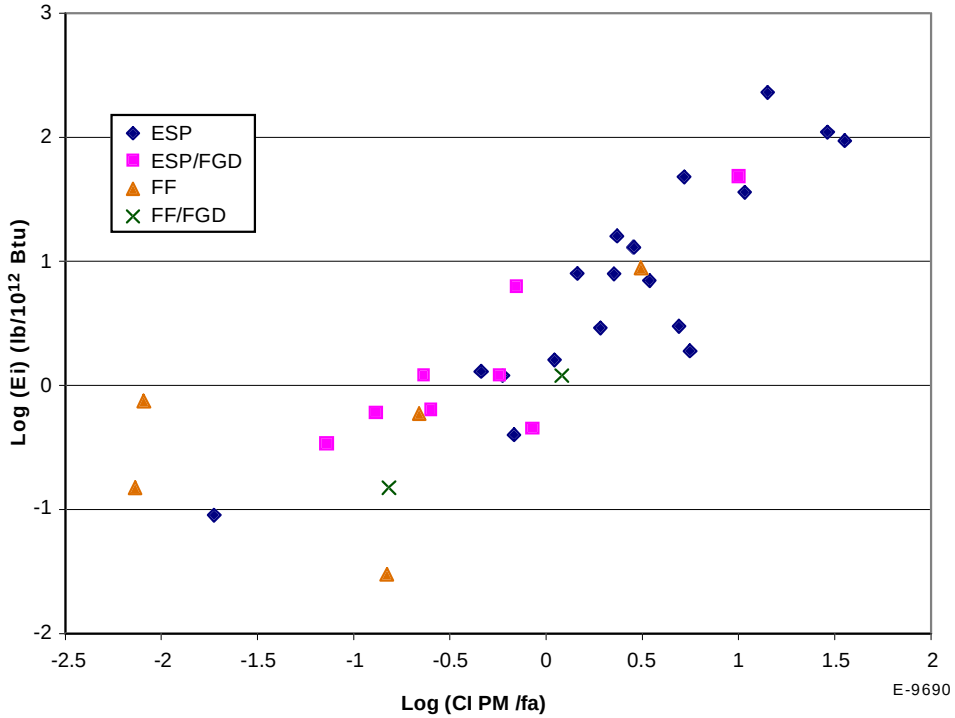

Figure 3-288. Arsenic emissions data obtained from field measurements as a function of C*PM/fa, plotted according to Eq. (3-47). Different symbols represent different types of particulate control device. $R^2 = 0.72$ for these data.

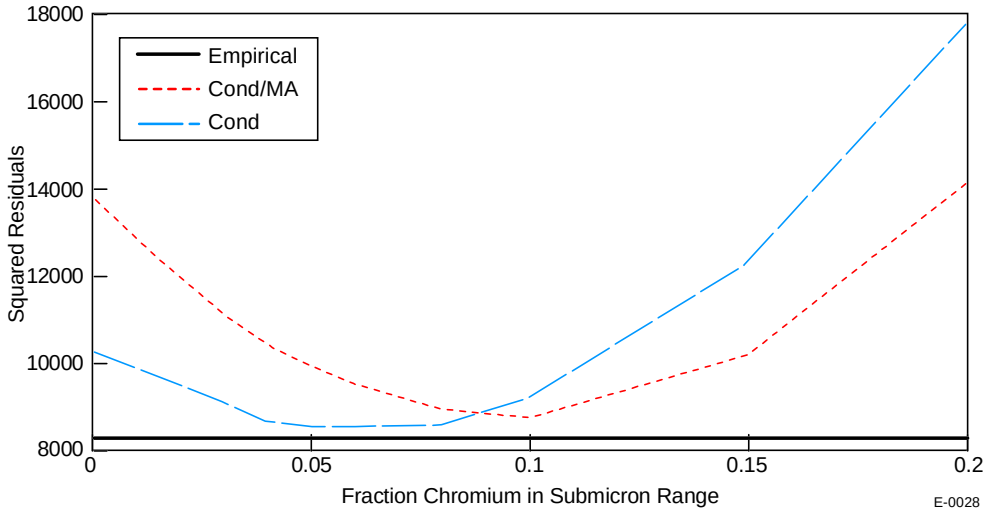

Figure 3-289. Comparison of field measurements of chromium emissions with empirical model derived from database fit and partitioning / penetration model described by Eqs. (3-48) through (3-51). COND represents condensation, MA mass apportionment.

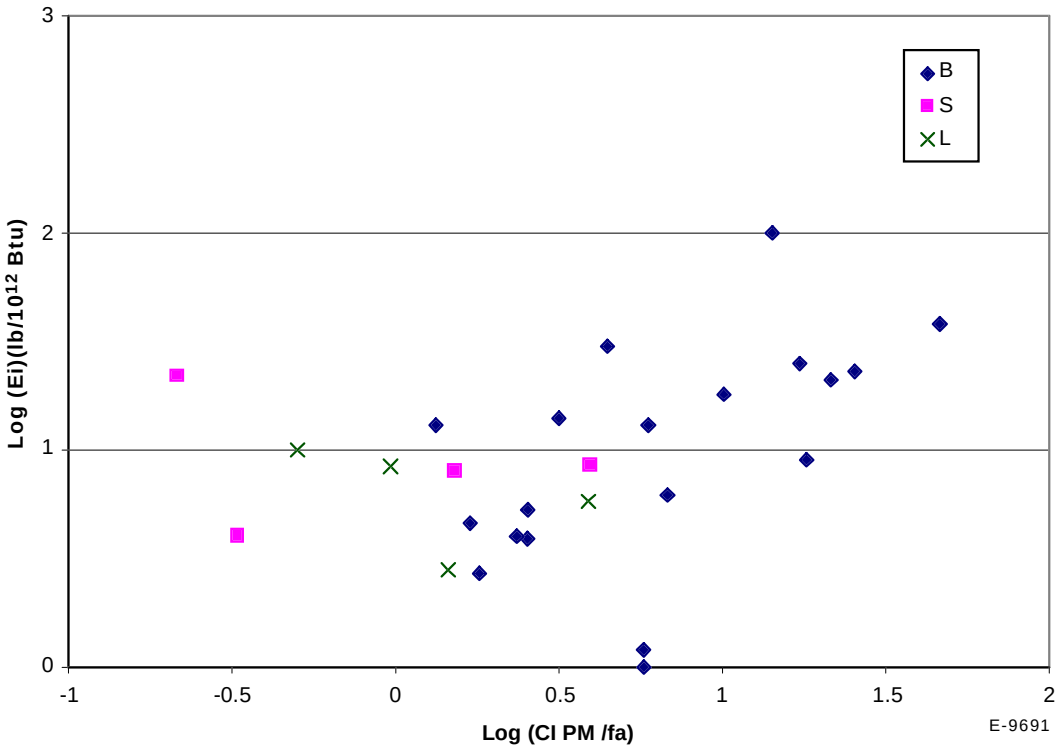

Figure 3-290. Chromium emissions data obtained from field measurements as a function of C*PM /fa as per Eq. (3-46). Different symbols represent different coal rank as indicated. Data shown for facilities using ESP or ESP in conjunction with flue gas desulfurization only. $R^2 = 0.57$ for these data ($R^2 = 0.26$ using Eq. (3-46)).

Application of the model described in Eqs. (3-48) through (3-51) to arsenic yields different results. Comparison of model-predicted arsenic emissions with those derived from Eq. (3-47), using an a_i value of 3.14 and b_i of 0.887 is shown in Figure 3-291. Using the fraction of arsenic in the submicron ash as an adjustable parameter, improved agreement with measured field emissions data is found for fractions of arsenic in the submicron ash between 0.01 and 0.28. When the fractional partitioning of arsenic is set equal to 0.14, the minimum in the curve shown in Figure 3-291, agreement with measurements is greater than 20% improved over that derived from empirical correlation of the field data. Predicted emissions based on particulate capture alone are also shown in Figure 3-291; greater than 50% improvement in agreement with the data is observed for the partitioning model.

The arsenic fractional partitioning of 0.14 found by minimizing the difference between predicted and measured emissions in the available field data is consistent with reported experimental values. In Table 3-162, experimental partitioning data are provided for several trace elements. For arsenic, most data cluster between fractions of 0.10 and 0.42 in the submicron ash. Values determined in field measurements were generally lower than those observed in the laboratory, with an average value of 0.15 obtained from the four field measurements. Although the single bituminous coal field measurement yielded a value greater than

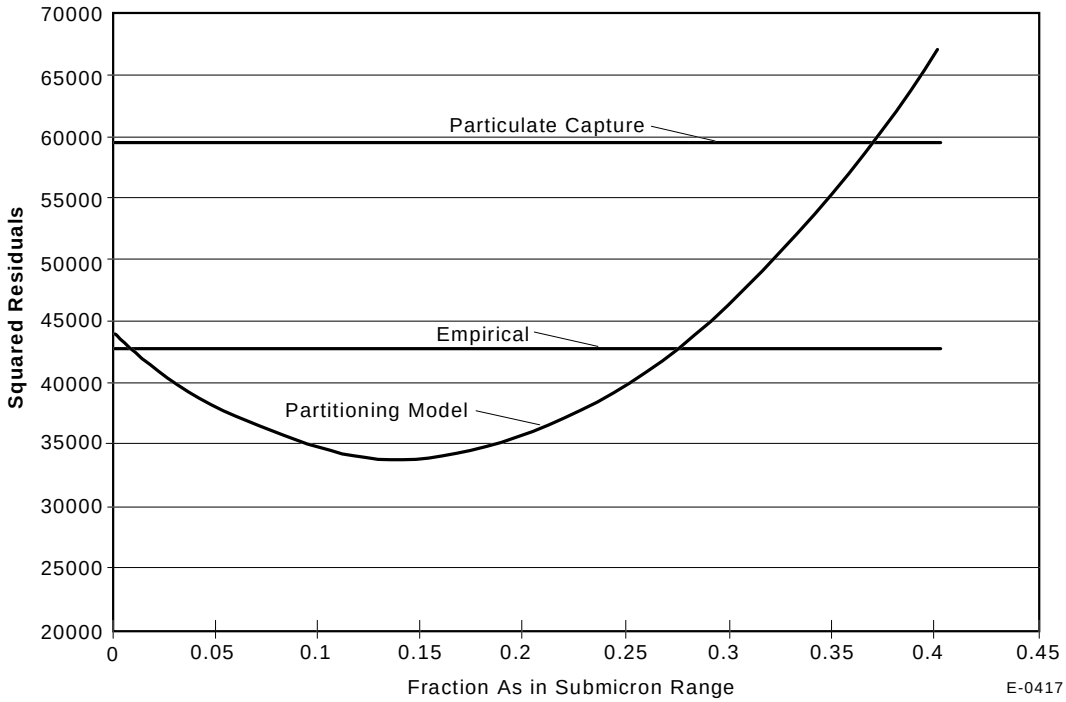

Figure 3-291. Comparison of field measurements of arsenic emissions with (a) empirical model derived from database fit and (b) partitioning / penetration model described by Eqs. (3-48) through (3-51).

those derived from the sub-bituminous coals, the extensive laboratory dataset reported by Quann et al. [234] did not identify any rank-specific differences for arsenic. The model fit value of 0.14 is thus within the range of reported partitioning values for arsenic, and is in good agreement with the small amount of data available from field measurements.

Using the penetration / partitioning model, arsenic emissions were predicted for three Canadian power plants comprising 12 boilers in total and representing units not contained within the PISCES field testing database [255]. Emissions predictions were also made using the PISCES database-derived empirical parameters and by assuming that arsenic emissions were proportional to total particulate emissions. As shown in Figure 3-292, the partitioning model provided the best agreement with measured emissions, with the sum of the residuals being at least 80% less than that derived from the other two models. A partitioning value of 0.14 derived from the study of the PISCES database was used in this calculation. The partitioning value of 0.14 does not represent the minimum in the residuals curve for this dataset (the minimum occurred at 0.20); nevertheless, a significant improvement over other approaches was identified.

Similar calculations were performed to assess selenium emissions for the facilities contained within the PISCES database. Meij [17], in a study of trace element emissions from a power station in the Netherlands burning a coal from the eastern U.S., reported that 25% of the selenium remained in the vapor phase at stack conditions. The partitioning model for selenium was thus modified to incorporate the fraction of vapor phase selenium as an adjustable

Table 3-162. Fraction of Trace Element Associated with Submicron Ash

Scale	Coal Type	As	Sb	Cr	Mn	Cd	Se	Reference (citation no.)	Comment
Bench	B	33	36				67	Bool and Helble [29]	1 coal, all size fractions < 0.97 μm included
Bench	B	42*		2-24				Quann et al. [234]	4 coals, size segregated
Bench	B	20	23				16	Senior et al. [7]	3 coals
Bench	B+L	42*		12				Zeng [243]	size segregated coals
Lab	B (I6)	10-12						Wendt et al. [256]	Illinois 6; all size fractions LE 0.535 μm
Lab	B (P8)	70						Wendt et al. [256]	Pittsburgh 8; all size fractions LE 0.535 μm
Pilot	B	20	32	1	12	61	42	Tumati and Devito [232]	fraction present 'fine' mode d_{mean} = 0.7 μm
Field	B	10		6	3			Martinez-T. and Spears [157]	total < 2.5 μm
Bench	S	18	22				19	Senior et al. [7]	1 coal
Bench	S	8	11				35	Bool and Helble [29]	1 coal, all size fractions < 0.97 μm included
Bench	S	42*		13-20				Quann et al. [234]	2 coals, size segregated
Bench	S	42*		35				Zeng [243]	3 coals, size segregated
Field	S	22	19	21	13			Shendrikar et al. [32]	derived from dm/dlog(dp) data at FF inlet
Field	S	15	10	21	10			Ensor et al. [254]	derived from dm/dlop(dp) at ESP inlet
Field	S	14	24		1		9	Markoswki and Filby [81]	tabulated data
Bench	L	42*		7-15				Quann et al. [234]	3 coals, size segregated.

* Value derived from entire combined Quann et al. [234] and Zeng [243] database and therefore taken to be independent of coal type.

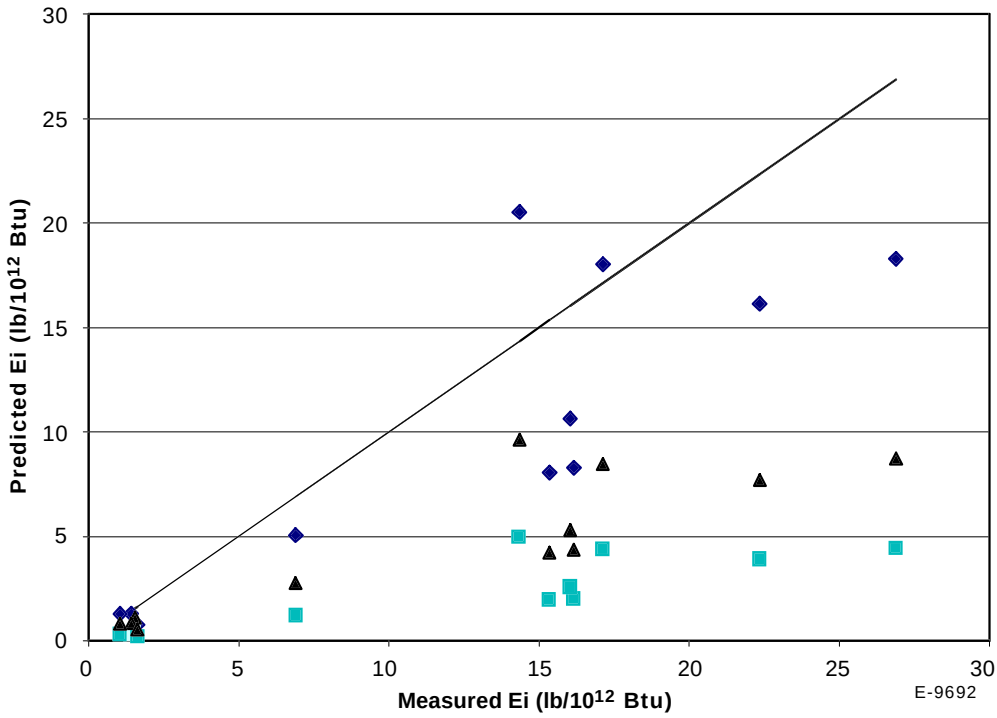

Figure 3-292. Comparison of field measurements of arsenic emissions from 12 Canadian boilers with (a) empirical model derived from database fit, using U.S. database, and (b) partitioning / penetration model described by Eqs. (3-48) through (3-51).

parameter. Four values of the fraction of selenium in the vapor phase were considered: 0, 0.05, 0.10, and 0.20. As shown in Figure 3-293, best agreement with experimental measurements was obtained for vapor fractions of 0.05 to 0.10, with 80% of the remaining selenium associated with the submicron ash particulate. At these optimum conditions, a 50% improvement in agreement (versus the empirical database-derived model) was obtained. Using a value of 20% vapor and 30% of the remainder in the submicron size range, consistent with the limited selenium partitioning data reported in Table 3-162, provided 40% improvement over the database-derived model. In either case, calculations indicate that improved emissions estimates could be obtained by considering size-dependent partitioning for this element.

3.5.1.4 Summary and Conclusions

A model for the emission of trace elements from electric utility coal-fired power plants has been developed. The model partitions trace elements among fly ash particles as a function of ash particle size, and incorporates size-dependent particulate penetration through electrostatic precipitators to obtain emissions estimates. Comparison with recent field measurements and a database-derived model demonstrated that improved agreement could be obtained for relatively volatile elements such as arsenic and selenium. In contrast, agreement for chromium was comparable to that obtained with the database-derived model, and was attributed to the relatively low volatility of this element. A review of the literature in this area suggests that this conclusion

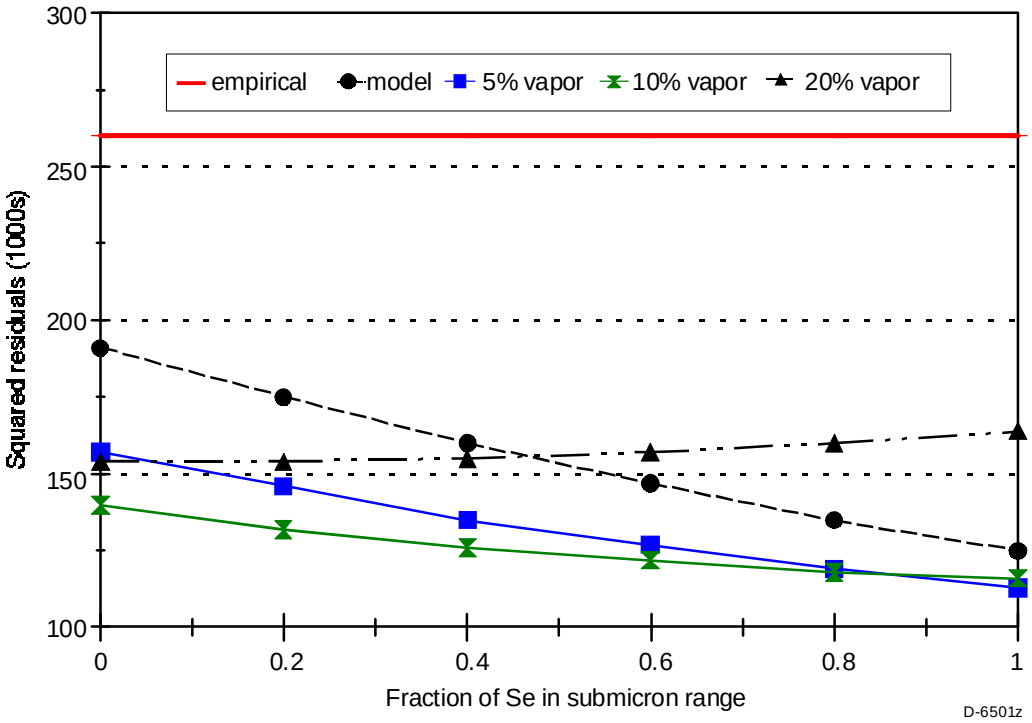

Figure 3-293. Comparison of field measurements of selenium emissions with empirical model derived from database fit (solid line) and partitioning / penetration model described by Eqs. (3-48) through (3-51), with ● 0% selenium vapor, ■ 5% vapor, ♦ 10% vapor, ▲ 20% vapor.

may be restricted to facilities combusting bituminous coals, as facilities firing sub-bituminous coals generally produced greater fractions of chromium in the submicron ash particulate. The partitioning model might thus be a more appropriate mechanism for predicting chromium emissions for such facilities.

Although the fraction of an element in the submicron size range was treated as an adjustable parameter in this study, the values obtained for each of these elements were consistent with partitioning data reported in both field and laboratory studies. It is therefore concluded that for volatile elements such as arsenic and selenium, a model based upon partitioning and overall ESP capture efficiency offers the most accurate predictions of trace element emissions, even for facilities contained within the PISCES database. Recommended values for arsenic are 14% in the submicron range, and for selenium, 20% vapor and 30% in the submicron fly ash size range. Further improvement in emissions prediction could be achieved by measuring the size-dependent particulate penetration though an ESP at an individual facility, but given the general absence of such data, the results presented herein suggest that an average value coupled to an overall particulate collection efficiency can provide improved predictions of trace element emissions. It is anticipated that first principles prediction of elemental partitioning, when coupled to the model presented herein, will provide the most accurate model of trace element emissions for all coals over a broad range of combustion conditions.

3.5.2 Mercury Field Data

3.5.2.1 Introduction

The United Stated Environmental Protection Agency (EPA) has estimated that during the period 1994-1995 annual emissions of mercury from human activities in the United States were 159 tons [168]. Approximately 87% of these emissions were from combustion sources. Coal-fired utilities in the U.S. were estimated to emit 51 tons of mercury per year into the air during this period.

The form of mercury emitted from point sources is a critical variable in modeling the patterns and amount of mercury deposition from the atmosphere [168,257]. Both elemental and oxidized mercury are emitted to the air from combustion point sources. Elemental mercury has a lifetime in the atmosphere of up to a year, while oxidized forms of mercury have lifetimes of a few days or less [168] as a result of the higher solubility of Hg^{+2} in atmospheric moisture. Elemental mercury can thus be transported over long distances, whereas oxidized and particulate mercury deposit near the point of emission. Once mercury has deposited on land or water, it can transform into methylmercury, an organic form, and thereby enter the food chain. Humans are most likely to be exposed to methylmercury through consumption of fish.

In December of 2000, the US EPA made a decision to regulate the emission of mercury from coal-fired power plants. A proposed regulation will be due no later than December 2003 and promulgated no later than December 2004. Utility industry compliance would have to be in place by December 2007. Compliance with the proposed regulation may in some cases necessitate additional controls for mercury. Since some mercury is removed by existing air pollution control devices (APCDs), it is vital to understand the behavior in existing equipment in order to cost-effectively control emissions. The speciation of mercury in the flue gas of a coal-fired power plant affects the amount of mercury retained in the air pollution control devices (and not emitted out the stack) because the chemistry of elemental mercury in flue gas is different from that of oxidized mercury.

In order to understand the technical and economic feasibility of mercury controls on coal-fired power plants, it is therefore necessary to understand the chemistry of mercury in flue gas and the potential physical and chemical interactions at various points in the system. A predictive model for both mercury emissions and speciation has been developed [258]. In this paper, data from full scale power power plants are used to develop the model further and to test it.

3.5.2.2 Behavior of Mercury in Combustion Systems

Theoretical Considerations

Mercury is present in coal in low concentrations, on the order of 0.1 ppmw. In the combustion zone of a coal-fired power plant, all the mercury in coal is vaporized as elemental mercury, yielding vapor concentrations of mercury in the range of 1 to 20 mg/m^3 (1 to 20 ppbw). At furnace exit temperatures (1700 K), all of the mercury is expected to remain as the thermodynamically favored elemental form in the gas. As the gas cools after combustion, oxidation reactions can occur, significantly reducing the concentration of elemental mercury by the time the post-combustion gases reach the stack. Equilibrium thermochemical calculations predict that $HgCl_2$ will be formed at low temperatures in coal combustion flue

gas [174]. However, the complete oxidation of elemental mercury that is predicted from equilibrium is rarely observed in practice (as discussed below). This has led to the conclusion that there are kinetic limitations to the oxidation of mercury in flue gas from coal-fired power plants.

The major kinetic pathway to formation of $HgCl_2$ in flue gas is believed to be through the reaction of atomic chlorine Cl with elemental mercury [174,184,185,259]. Although the oxidation of elemental mercury in the convective pass is assumed to proceed primarily via gas-phase reaction, experimental evidence suggests that some fly ash can catalyze oxidation of elemental mercury. Iron oxide has been shown to promote this oxidation [260]. Other constituents in the fly ash (carbon, calcium compounds) may also contribute. The presence of acid gases (HCl, SO_2, NO, NO_2) in the flue gas has also been shown to cause oxidation in the presence of fly ash [261,262]. Furthermore, selective catalytic reduction (SCR) technology for NO_x control has been observed to oxidize a portion of elemental mercury [263].

Thus, the coal composition (in terms of chlorine content and ash composition), the operation of the combustion system (in terms of unburned carbon in the ash), and temperature and residence time in the particulate control device will all affect mercury speciation in the gas and the amount of mercury adsorbed on the particulate matter. Other components of the air pollution control system such as FGD and selective catalytic reduction (SCR) systems have also been shown to affect both the speciation of mercury in the stack and the amount of mercury removed in the air pollution control equipment as a whole.

Behavior in Practical Combustion Systems

The Information Collection Request (ICR) initiated by the United States EPA in 1999 was designed to provide more information which could be useful for making a regulatory determination about mercury emissions from coal-fired power plants. Part 3 of the ICR is comprised of measurements of mercury speciation from coal-fired power plants. Data from 83 boilers selected for testing are now available on the web (http://utility.rti.org). Plants were selected based on the configurations of air pollution control equipment and fuel type. For each plant, the input value of mercury in the coal was measured (along with other coal composition data). Mercury measurements were made at the stack and at the inlet to the last air pollution control device (APCD) using the Ontario Hydro method that gives elemental, oxidized, and particulate-bound mercury. Table 3-163 summarizes the configurations for the ICR data sets, comparing the distribution of units tested with the distribution of the boiler population in the United States.

Coal-fired power plants already have air pollution control devices (APCDs) such as fabric filters and electrostatic precipitators (ESPs) for particulate control, scrubbers for SO_2 control and low-NO_x burners (LNBs), selective catalytic reduction (SCR) or selective non-catalytic reduction (SNCR) for NO_x control. Most of these have some impact on mercury speciation and emissions [264].

Table 3-164 summarizes the average inlet speciation and decrease in elemental and oxidized mercury across various air pollution control devices. In some cases, an increase in one of the mercury species was observed, which is indicated by a negative value. Changes in mercury are reported across wet scrubbers (FGDs) only, although the upstream particulate removal device is indicated in parentheses. For dry scrubbers (SDAs), the change in mercury is computed across both the SDA and particulate removal device (either ESP or FF).

Table 3-163. Summary of APCD and Coal Type Information for ICR Data Sets

APCD Equipment	Coal Type	% of Units Tested	% of Existing Units
Cold-side ESP	Bituminous	7.2	48.3
Cold-side ESP	Low Rank	7.1	11.7
Hot-side ESP	Bituminous	7.2	6.6
Hot-side ESP	Low Rank	3.6	2.4
Cold-side ESP + FGD	Bituminous	6	8.8
Cold-side ESP + FGD	Low Rank	9.2	2.5
Hot-side ESP + FGD	Bituminous	4.8	0.7
Hot-side ESP + FGD	Low Rank	3.6	1
FF	Bituminous	3.6	2.9
FF	Low Rank	7.2	2.7
FF + Wet FGD	Bituminous	7.2	1.6
FF + Wet FGD	Low Rank	3.6	1.6
SDA + FF	Bituminous	3.6	2.9
SDA + FF	Low Rank	7.2	1.3
SDA + ESP	Bituminous	2.4	0.2
SDA + ESP	Low Rank	3.6	0.3
FF + FBC	Bituminous	3.6	2.9
Other	Other	9.3	1.6

ESP: Electrostatic Precipitator
FF: Fabric Filter
FGD: Flue Gas Desulfurization
SDA: Spray Dryer Absorber
FBC: Fluidized Bed Combustor

The average change in *gaseous* mercury (the sum of elemental and oxidized) across the device is also reported in Table 3-164. The changes in elemental and oxidized mercury by themselves reflect both gas-phase oxidation of elemental mercury and removal of gaseous mercury (by adsorption on particles or absorption into scrubber solution). However, changes in total gaseous mercury indicate only removal by adsorption/absorption.

The computed averages in Table 3-164 suggest that species of mercury can sometimes increase across air pollution control devices. However, sometimes the negative average decrease is due to one very large negative number overly influencing the average. It is important, therefore, to look at the general trends for changes in mercury species across the device and not follow averages strictly.

Removal of mercury in the APCD depends on chlorine content, temperature and type of particulate control device. For particulate control devices, the mercury removal increases with coal chlorine content. At hot-side temperatures of 250 to 400 C (475 to 750 F), very little mercury was found in the particulate phase; this manifests itself in the low removal of mercury by HESPs. For cold-side devices – ESPs and FFs operating in the range of 130 to 170 C (270 to 350 F) – most of the mercury at the inlet to the PCD was elemental for coals with low chlorine contents (less than about 150 ppm on a dry basis). For coals with chlorine greater than about 200 ppm, most of the mercury was found in the particulate phase at the PCD inlet with the amount of oxidized gaseous mercury varying from 0 to 50%.

Table 3-164. Average Values of Inlet Mercury Speciation and Removal Of Gaseous Mercury Species for Combinations of Coal and APCD

APCD	Coal	Inlet Hg_p	Inlet Hg^0	Avg Hg^{+2} Decrease	Avg Hg^0 Decrease	Avg Gaseous Decrease
ESP	Bitum.	48.4%	19.2%	17.5%	-28.3%	8.5%
HESP	Bitum	9.1%	48.7%	-33.1%	21.9%	11.5%
FF	Bitum	51.1%	29.2%	9.5%	39.6%	21.8%
FGD-ESP	Bitum			87.2%	-11.4%	49.3%
FGD-HESP	Bitum			138.4%	-174.5%	8.4%
FGD-FF	Bitum			86.8%	-1.1%	74.0%
FGD-WS	Bitum			78.2%	-336.2%	9.4%
FGD-All	Bitum			91.0%	-53.8%	46.5%
SDA-FF	Bitum	69.1%	19.2%	52.1%	8.1%	51.7%
ESP	Low Rank	11.1%	73.9%	-83.4%	-19.1%	-14.0%
HESP	Low Rank	6.5%	76.3%	14.3%	-14.9%	-8.3%
FF	Low Rank	27.7%	45.7%	-61.6%	59.1%	14.7%
WS	Low Rank	3.4%	67.9%	91.2%	-12.1%	24.4%
FGD-ESP	Low Rank			127.5%	-16.2%	33.9%
FGD-HESP	Low Rank			66.5%	4.4%	27.0%
FGD-WS	Low Rank			81.7%	-246.3%	-47.9%
FGD-All	Low Rank			99.0%	-72.0%	10.3%
SDA-ESP	Low Rank	14.9%	61.0%	88.7%	-8.2%	26.6%
SDA-FF	Low Rank	13.1%	73.9%	47.7%	-76.3%	2.2%
FF	Other	99.2%	0.5%	71.6%	57.9%	72.5%

If there is mercury in the particulate phase at the inlet to an ESP or fabric filter, these devices will remove it efficiently. Unburned carbon has been suspected of adsorbing mercury for both eastern and western bituminous and sub-bituminous coals. Often a consequence of low-NO_x burners or a low-NO_x combustion systems, pulverized coal boilers can produce high levels of unburned carbon when burning bituminous coals [265], or less commonly, sub-bituminous coal [266]. Mercury has been found to concentrate in the carbon-rich fraction of fly ash [216,267]. However, it is not possible to generalize and conclude that high carbon in ash will always give high levels of particulate-bound mercury. Unfortunately, data collected as part of the ICR do not include any information on the carbon content of the ash. As discussed below, this will limit the utility of the ICR data for use in developing prediction methods for speciation and emissions.

Sorption of mercury by fly ash has been observed to be dependent on temperature for both eastern bituminous coals and western sub-bituminous coals [266,268]. Some fly ash has been observed to oxidize elemental mercury in both laboratory scale apparatus [200,269] and pilot scale baghouses [268]. Laboratory experiments using well-controlled gas compositions indicate that the composition of the gas, particularly the amounts of HCl, NO_x, and SO_2, influences mercury oxidation. The composition of the ash is also important. Experiments with model fly ash compounds [260] exposed to mercury in a laboratory fixed bed reaction have shown that iron oxide is particularly effective at oxidizing elemental mercury in simulated flue gas. Many eastern bituminous coals and lignites contain substantial amounts of iron oxide in the ash.

From Table 3-164, there is little decrease in total gaseous mercury across particulate control devices on average; FFs have the largest apparent decrease in gaseous mercury (15 to 22%). Venturi scrubbers show the highest degree of removal, although there are very few data points in that category. In general, therefore, the mercury removed across particulate control devices comes primarily from the particulate-bound mercury. Although not obvious from Table 3-164, fabric filters often remove about half of the gaseous mercury for bituminous coals. A few large negative values of gaseous removal skew the average value.

Fabric filters produce decreases in elemental mercury, which can be attributed to oxidation for the most part. Thus, we conclude that fabric filters oxidize 40 to 60% of the elemental mercury and, particularly for bituminous coals, gaseous mercury is sometimes adsorbed across fabric filters.

FGDs remove oxidized mercury with an efficiency of approximately 90%. Elemental mercury is not removed to any degree across FGDs (although the average decreases in Table 3-164 are influenced by a few very large negative values). Bituminous coals produce flue gas with predominantly oxidized gaseous mercury. Consistent with this observation, FGDs on boilers burning bituminous coals remove about half the gaseous mercury. In boilers burning low rank coals, the mercury is predominantly elemental and little gaseous mercury is removed in the FGD.

In some cases, elemental mercury is observed to increase across FGDs. In the ICR data, this is observed for systems containing hot-side ESP followed by FGD and venturi scrubber followed by FGD. The reason for this is not known at this time.

Based on a detailed study of the behavior of mercury in a pilot scale wet scrubber [268], the adsorption of oxidized mercury appears to be strongly correlated with the mass transfer in the scrubber, usually expressed as liquid-to-gas (L/G) ratio and weakly dependent on pH of the scrubber solution [268]. The type of FGD system (forced versus natural oxidation, for example, or limestone versus magnesium-lime) also affects the amount of oxidized mercury removed in the scrubber [185].

Under some conditions, limestone scrubbers have been observed to reduce adsorbed mercury back to Hg^0 giving rise to higher concentrations of elemental mercury at the outlet than at the inlet [268]. Assuming that no Hg^0 is adsorbed by the scrubber, the amount of adsorbed Hg^{+2} that is reduced can be calculated from the ratio of the increase in elemental mercury to the decrease in Hg^{+2} across the scrubber. Based on very limited data, this also appears to be related to the L/G ratio in the scrubber. The ICR data, however, do not have complete information on scrubber operation (SO_2 removal and L/G) for every boiler and this type of detailed correlation cannot be made, limiting the accuracy of the predictions.

SDAs remove similar amounts of gaseous oxidized mercury as compared to FGDs, but often remove a significant amount of gaseous elemental mercury as well, particularly those on boilers burning bituminous coal that are coupled with a fabric filter.

The stack speciation of mercury appears to depend on the chlorine content of the coal because conversion of elemental mercury to an oxidized form is probably most strongly influenced by chlorine chemistry, either heterogeneously or homogeneously. Data from EPA's Information Collection Request (Figure 3-294) show anywhere from almost no Hg^0 to

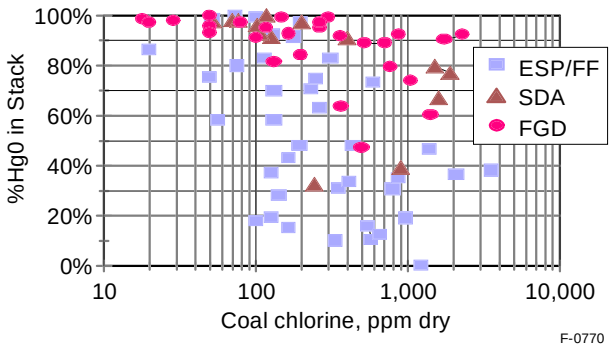

Figure 3-294. Observed speciation of mercury in the stacks of coal-fired power plants (as percent elemental mercury) as a function of coal chlorine content.

95% Hg^0 emitted from coal-fired power plants. Units with scrubbers emit very little oxidized mercury, as would be expected. Units with only particulate control devices have a much broader range of mercury speciation in the stack.

3.5.2.3 Modeling Mercury Emissions

A simple predictive model for mercury speciation and emissions has been developed [258], but tested on only a small number of data sets to date. The previous work focused on mercury removal across wet scrubbers, but neglected removal and/or oxidation across particulate control devices because there were not sufficient field data available. In this task, the ICR data will be used to create and test some simple models of mercury removal across particulate control devices.

Although the model has been described elsewhere in more detail [258], a brief explanation will be given here. A simple mass balance model for emissions of mercury from coal-fired power plants was in which the post-combustion region of the boiler was divided into three parts: 1) convective section to air heater (AH); 2) particulate control device (PCD); and 3) flue gas desulfurization unit (FGD). Concentrations of mercury species (gaseous and condensed) in each section were either calculated from equilibrium or plant parameters, or assigned based upon limited available from field data as explained below. All of the mercury was assumed to start as gaseous elemental mercury (Hg^0). In the AH section, elemental mercury can oxidize to Hg^{+2}, nominally the sum of HgO and $HgCl_2$. In addition, Hg^{+2} can be adsorbed on particulate matter in the AH section, converting it to Hg_p. In the scrubber section (which may be a wet or dry scrubber), both Hg^0 and Hg^{+2} can be absorbed into the scrubber solution. The model therefore predicts the speciation and emissions of mercury from the boiler based upon coal mercury content, equilibrium at elevated temperatures, assumed mercury partitioning coefficients in the various sections of the boiler, and scrubber operation.

Previous work has shown that the oxidation of mercury in post-combustion flue gas is kinetically limited [174]. Efforts are underway to determine the appropriate kinetic rate constants for mercury oxidation [184,185,259]. In this work, a simple empirical equilibrium approach has been taken, although more sophisticated kinetics may be used in the future. In this approach, mercury oxidation has been assumed to proceed according to equilibrium until a specific temperature is reached, at which point chemical reactions cease (or are frozen). The degree of conversion of mercury at the inlet to the particulate control device is

determined by the chlorine content of the coal for cold-side devices (Figure 3-295) and by the device temperature for hot-side devices (Figure 3-296).

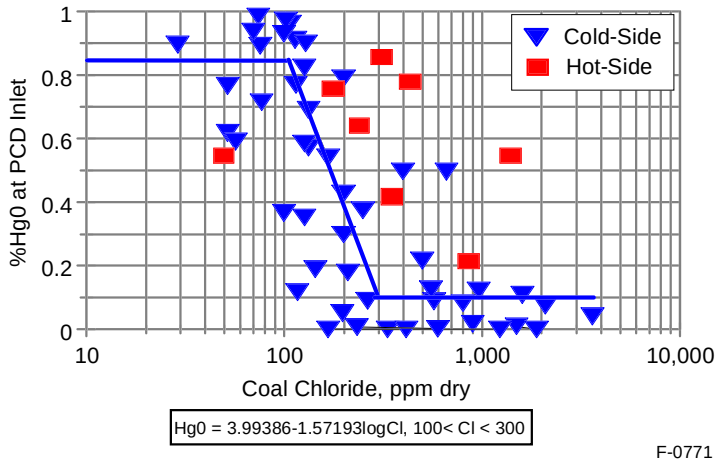

Figure 3-295. Speciation of mercury (in terms of gaseous elemental) at the inlet to air pollution control devices as a function of coal chlorine content. Solid line indicates empirical correlation for cold-side devices.

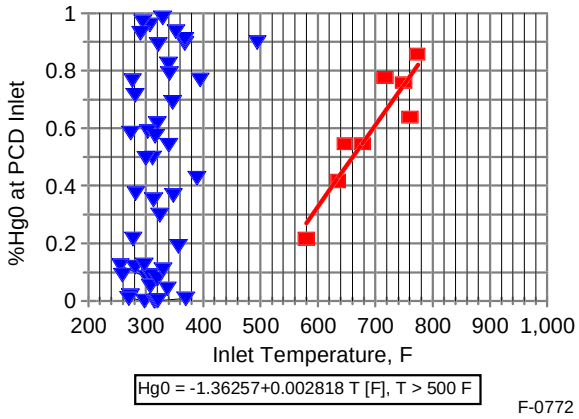

Figure 3-296. Speciation of mercury (in terms of gaseous elemental) at the inlet to air pollution control devices as a function of device temperature. Solid line indicates empirical correlation for hot-side devices.

Note that there is considerable scatter in the ICR data with respect to chlorine content (although not with respect to temperature). There is considerable uncertainty in the measurement of chlorine in coal, particularly for reported values less than 1000 ppm [270].

Once the degree of oxidation of mercury at the inlet to the particulate control device is determined, the partitioning between gaseous and particulate must be determined. In a previous work [258] this split was computed from the carbon content of the fly ash for bituminous coals. However, those data are not available in the ICR set. The lack of carbon-in-ash data reduces the accuracy of predictions based on ICR data. Therefore, the amount of particulate mercury was correlated with the coal chlorine content, as shown in Figure 3-297. The solid line indicates the calculated amount of particulate mercury.

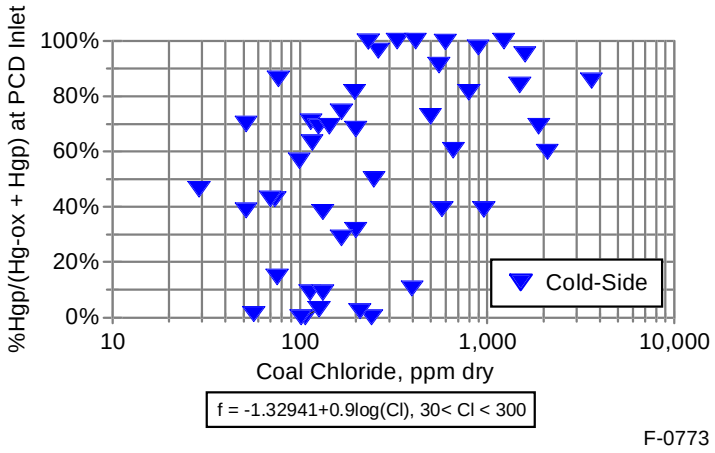

Figure 3-297. Particulate mercury (as fraction of particulate and oxidized mercury) at the inlet to the particulate control device for cold-side devices.

In this work, the approach taken was to look at average values of the change in gaseous elemental and oxidized mercury across individual air pollution control devices as a function of coal chlorine for the most part because chlorine has been shown to be the single most important factor for mercury oxidation in flue gas.

These values are shown in Table 3-165. Where values differ from those in Table 3-164, some effort has been directed to remove from consideration measurements that are obviously in error before computing average percent change across the device and improve the correlation between calculated values and observed values (derived from ICR data).

Examination of the trends in Table 3-165 provides some insight into behavior of mercury in various air pollution control devices. Particulate control devices appear to affect gaseous mercury. Fabric filters have the largest effect, causing on average a 40 to 85% decrease in elemental mercury and a 25% decrease in oxidized mercury for bituminous coals, while low rank coals have an increase in oxidized mercury in the model. The large decrease in elemental mercury suggests that some of the elemental mercury is being oxidized across the fabric filter. SDAs produce decreases in oxidized mercury (50 to 90%).

ESPs and HESPs have a smaller effect on gaseous mercury. ESPs (cold and hot) have a smaller effect on gaseous mercury; ICR data do indicate a number of cases in which gaseous mercury (elemental or oxidized) increases across the precipitator. This may be a measurement artifact related to oxidation of elemental mercury in the Ontario Hydro measurement train.

The correlations in Table 3-165 were used to calculate mercury speciation at the inlet and outlet of the individual air pollution control devices based on the coal mercury content. The speciation of mercury at the inlet to APCDs was calculated as shown in Figures 3-295 through 3-297. For the case of wet scrubbers (FGDs), the appropriate particulate control device correlations were applied to calculate the mercury concentrations at the inlet to the FGD. In all cases, the only pieces of information used were the coal mercury content, the

Table 3-165. Correlations Between Mercury Removal and Chlorine Content: Fractional Removal ($f = A \log_{10}Cl + B$) and Coefficient of Regressions (RSQ)

Variables:	A logCl [ppm dry]	B Constant	RSQ
ESPs:			
Hg^{+2}	0.6609	-1.9173	0.11
Hg^{0}	-0.6176	1.2279	0.18
Total Hg	0.3803	-0.6083	0.48
FFs:			
Hg^{+2}	-0.0579	0.0390	0.00
Hg^{0}	0.0482	0.3938	0.00
Total Hg	0.5387	-0.6832	0.27
HESPs:			
Hg^{+2}	0.0464	-0.2086	0.00
Hg^{0}	0.4232	-1.0149	0.29
Total Hg	0.2814	-0.6006	0.57
SDA/ESP:			
Hg^{+2}	-0.1610	1.2198	0.93
Hg^{0}	-0.6805	1.7446	0.78
Total Hg			
SDA/FF:			
Hg^{+2}	0.2634	-0.1599	0.09
Hg^{0}	0.5117	-1.6187	0.05
Total Hg	0.7060	-1.2878	0.88
FGD-ESP:			
Hg^{+2}	0.9000		
Hg^{0}	0.0000		
Total Hg	0.1167	0.2334	0.10
FGD-HESP:			
Hg^{+2}	0.9000		
Hg^{0}	0.0000		
Total Hg	1.5164	-3.1080	0.61
FGD-WS:			
Hg^{+2}	0.9000		
Hg^{0}	0.0000		
Total Hg	-0.0933	0.3163	0.03

coal chlorine content and the temperature of the particulate control device. Although the correlation coefficients in Table 3-165 are not always high, particularly for mercury species, this method allows the calculation of speciation within the particulate control devices, which is necessary for application of this model to problems such as design of mercury control systems.

The total mercury removal (coal to stack) and the fraction of elemental mercury in the stack were computed. The standard error or regression between the calculated values and the ICR values was computed as a quantitative measure of the agreement between the model and the ICR values. In Table 3-166, the standard errors were also computed based on correlations between total Hg removal or stack speciation with coal chlorine. The end result of the calculation is displayed in a series of figures (Appendix M).

Table 3-166. Average Error of Prediction for ICR Values Versus Calculated Values, Where Calculated Values Were Derived From (a) Correlations From Species-Based Model and (b) Correlations Based on Total Removal or Stack Speciation with Chlorine Content

Variables:	Hg removal, by species (a)	Hg removal, total (b)	Hg^0 (stack) (a)	Hg^0, total (b)
ESPs:	0.18	0.16	0.19	0.18
FFs:	0.22	**0.27**	**0.29**	0.21
HESPs:	0.09	0.09	0.12	**0.16**
SDA/ESP:	**0.42**	0.12	0.01	0.01
SDA/FF:	**0.28**	0.12	0.08	0.08
FGD-ESP:	**0.31**	0.18	0.08	0.06
FGD-HESP:	**0.24**	0.19	0.07	0.07
FGD-WS:	0.18	0.15	0.06	0.05

Chu [270] has computed total removal and speciation based on coal chlorine as in Table 3-166. The approach taken for this model, the use of correlations of Hg species, yields standard error values that are similar in most cases. The species-based approach has the advantage of providing more information about the process.

3.5.2.4 Summary

Data from the Information Collection Request (ICR) may be used to increase our knowledge of the effect of coal type, combustion system, and air pollution control devices on mercury speciation and emissions. These data must be evaluated carefully, however, if they are to be useful. In many cases, critical information may be missing or measurements in error. Several sources of inaccuracy in the predictions were identified, specifically,

- Lack of ash composition data which could be used to improve the prediction of the adsorption of mercury on fly ash the oxidation of mercury in particulate control devices;
- Uncertainty in the measurement of coal chlorine, a key parameter for mercury oxidation in flue gas;
- Over-reporting of oxidized mercury by the Ontario Hydro method when applied to flue gas containing high ash loadings.

APCD systems have not previously been tuned to maximize mercury capture; such a strategy may be considered in the future, if mercury regulations are imposed. Most APCDs have been associated with reductions in mercury emissions, although the speciation of mercury is very important in determining the magnitude of reduction. However, a considerable increase in our understanding of the behavior of mercury in APCDs will be required even to get consistent mercury reductions without having an impact on removal efficiency of particulate, SO_2 or NO_x. With these caveats in mind, wet FGD's, dry scrubbers, and fabric filters can all remove a significant amount (circa 50%) of the gaseous mercury in the flue gas under certain conditions. Fabric filters showed an average of 40 to 85% decrease in elemental mercury. The large decrease in elemental mercury suggests that some of the elemental mercury is being oxidized across the bag filter. SDAs produce decreases in oxidized mercury (50 to 60%) but not generally for elemental mercury. ESPs and HESPs have a smaller effect on gaseous mercury. ICR data do indicate a number of cases in which gaseous mercury (elemental or oxidized) increases across the precipitator, particularly for low rank coals.

3.6 Model Development (PSI, UU, UC)

3.6.1 Overview

The objective of the modeling task is to develop a fundamentally-based predictive model to allow utility operators to predict trace element emissions from their plants. The ToPEM will be applicable to *all* combustion conditions including new fuels and coal blends, low-NO_x combustion systems, and new power generation plants. Development of ToPEM will be based on PSI's existing EMAF.

The existing program (EMAF) consists of the following blocks, see also Figure 3-298

(1) Data reading

(2) A - Generation of coal particles at various sizes with a particle size distribution similar to the input
B - Generation of mineral particles and formation of included and excluded

(3) A - Distribution of mineral particles to coal particles
B - Combustion of coal particles
C - Formation of ash particles assuming a certain degree of coalescence.

As a first step in developing the ToPEM, we developed a sub-model that calculates the evaporation of major elements (Na, K, Fe, Si, Al, Ca and Mg) from both inherent and extraneous minerals of coal. Subsequently, this sub-model was included into EMAF, which formed the ToPEM. Experimental data were used to test and modify the sub-model and the ToPEM.

3.6.2 Coal Mineralogy

3.6.2.1 Measurement of Coal Mineralogy

Inorganic compounds get into coal in a number of ways as discussed in Section 2. Inorganic elements are sometimes found in the organic matrix, primarily by ion-exchange, and are always found in discrete particles of minerals. When coal is pulverized for use in utility boilers, the mineral particles can either be embedded in the coal (included minerals) or liberated during the grinding process (excluded minerals).

There are only a small number of minerals that predominate in US coals and these are summarized in Table 3-167. Quartz and kaolinite are often the major mineral types. Other clays (montmorillonite or illite) are sometimes also important. In general, pyrite is a significant mineral in bituminous coals. Pyrite can comprise as much as 25% of the minerals in the case of high sulfur coals. Calcium in bituminous coals, although not in high concentrations, is frequently found in calcite. In low rank coals, calcium is more likely to be organically-bound.

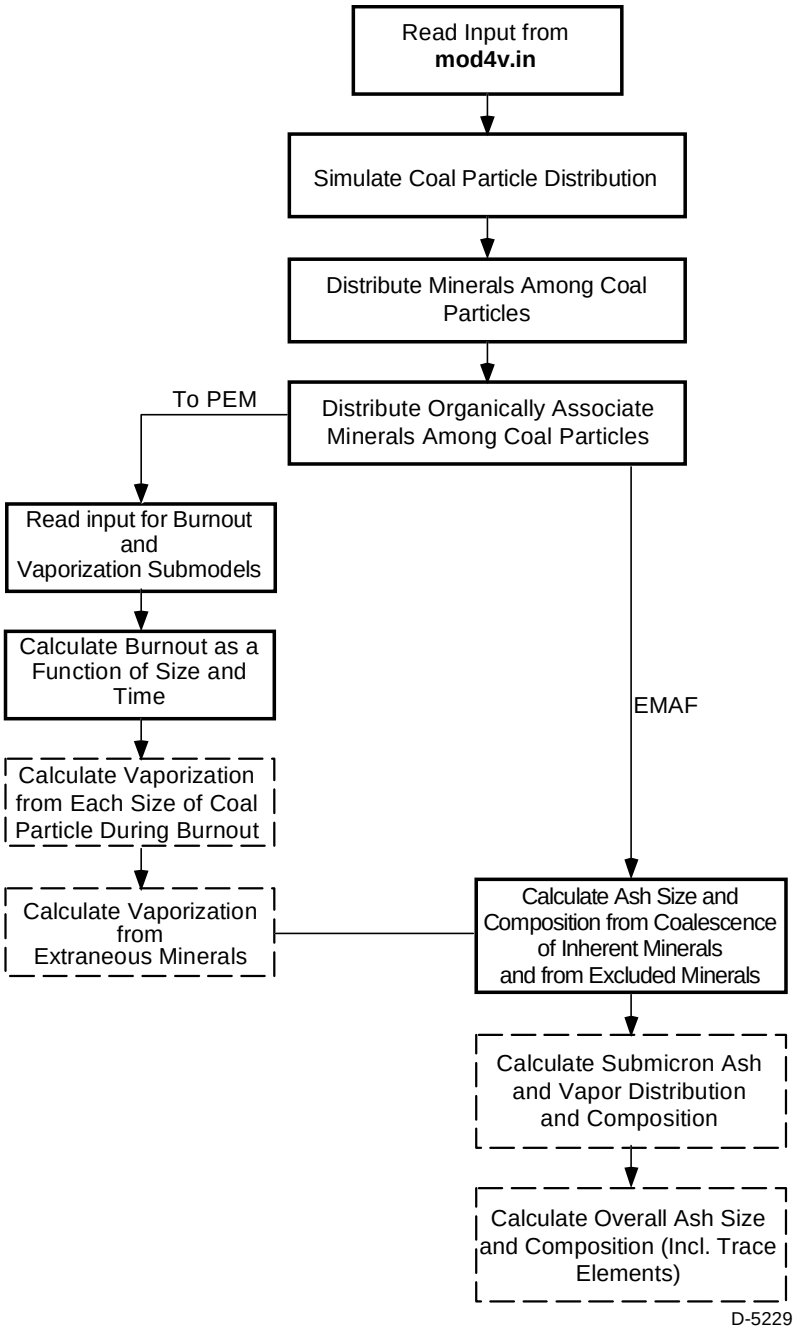

Figure 3-298. Flow chart for engineering model for ash formation.

Table 3-167. Common Minerals Occurring in US Coals

Quartz

Shale group
Species: illite, montmorillonite, muscovite, bravaisite
General formula: $(K, Na, H_3O, Ca)_2\ (Al, Mg, Fe, Ti)_4\ (AlSiO_8O_{20}(OH,F)_4)$

Kaolin group
Species: kaolinite, livesite, metahalloysite
Formula: $Al_2(Si_2O_5)(OH)_4$

Sulfide group
Species: pyrites, marcasite
Formula: FeS_2

Carbonate group
Species: calcite, dolomite, ankerite
Formula: $(Ca,Mg,Fe,Mn)\ CO_3$

Chloride Group
Species: sylvite, hallite
Formula: KCl, NaCl

Early methods for characterizing inorganic elements in coal were indirect, for example, ash content or fusibility of the ash. It was acknowledged early on that the composition of coal ash strongly influenced the tendency to form deposits in the combustion system. Beginning in the 1930's, the contribution of specific minerals to slagging and fouling problems was recognized using methods of density separation to isolate mineral-rich fractions of coal. With the advent of cyclone boilers for pulverized coal, viscosity measurements were made on coal ash.

Mineralogical characterization of coal continued, resulting in a fairly comprehensive understanding of the occurrence and formation of the major minerals in coal by techniques such as physical separation, selective leaching, and x-ray diffraction analysis.

Since the 1960's, low rank coals have become more widely used for steam generation because of their low ash and sulfur contents. Low rank fuels have a major proportion of inorganic elements organically bound to the coal matrix instead of in discrete minerals. Selective leaching (or chemical fractionation) methods have been used to identify and characterize the organically bound elements, primarily Ca, Na, and Mg in subbituminous and lignite coals [48]. As described elsewhere in this report, selective leaching and advanced analytical methods such as X-Ray absorption fine structure spectroscopy have been applied to the problem of determining the forms of occurrence of major and trace elements in coal.

Computer Controlled Scanning Electron Microscopy or CCSEM analysis is a method for analyzing the minerals in coal. How is CCSEM different from ASTM ash analysis? ASTM ash analysis gives <u>one composition</u>, the bulk ash composition, which is equivalent to mixing all the

minerals together. CCSEM analysis gives the size and composition of individual mineral particles in the coal sample. CCSEM provides much more information on the minerals in coal, information that is used by advanced models such as EMAF to predict the size and composition of ash particles.

CCSEM analysis begins with 1 to 2 grams of coal which is mixed with a binder, usually an epoxy resin, and formed into a pellet. A cut is made through the pellet to expose a cross-section. First a beam of electrons is systematically swept over the entire specimen. The SEM has electron detectors that measure the back-scattered electron (BSE) signal which depends on the atomic number of the element under the electron beam. The BSE signal from areas containing minerals is much brighter than that from the surrounding organic material. This creates a map of the mineral particles, as the figure shows, giving the size and location of each mineral particle.

Several thousand mineral particles are catalogued for each analysis. The diameter and cross-sectional area of each mineral particle are recorded. Mineral particles as small as 1 micron can be seen.

In the second step, a special energy detector called for energy dispersive x-rays (EDX) is used to measure the composition of each mineral particle. Most EDX detectors cannot see oxygen or carbon, so the amounts of heavier atoms (Al, Si, etc.) are reported and the amount of oxygen and carbon is inferred from the mineral type. The analysis procedure associates the composition with a particular mineral type (pyrite, kaolinite, etc.).

CCSEM analysis cannot locate organically-bound elements. For example, in Powder River Basin coals calcium, magnesium, and sodium are not always located in mineral particles, but are found in the organic matrix as individual atoms. A comparison of the ASTM ash analysis and the CCSEM analysis tells how much of each element in organically-bound. Chemical fractionation can be used to quantify organically-bound elements.

The detailed information provided by CCSEM analysis, when combined with more standard coal analyses, are used to predict the size and composition of the bulk ash particles by models such as EMAF and ToPEM. However, CCSEM analysis is not routinely performed on coals. In order to lower barriers to the use of ToPEM by the utility industry, a procedure has been developed to estimate the mineralogy (CCSEM analysis) of US coals.

In this task, the objective was to develop a calculational procedure for estimating the mineralogy (the size and composition of the minerals) of pulverized coals. A database of CCSEM analyses of US coals was assembled. Correlations were developed based on the coal rank and origin and on the bulk ash composition.

3.6.2.2 Coal Database

The database consists of 31 US coals (Table 3-168) from the major coal-producing regions. The data needed to make an estimate of the mineralogy are as follows:

- Coal rank
- Coal origin
- Sulfur content, dry basis
- Ash content, dry basis
- Ash composition, wt% as oxides.

In Table 3-168, the coals are sorted by rank, origin, and sulfur content as follows:

- Lignite
- Western Sub-bituminous
- Illinois Basin, Low Sulfur (< 1 wt% dry)
- Illinois Basin, High Sulfur (> 1 wt% dry)
- Appalachian Basin, Low Sulfur (< 1 wt% dry)
- Appalachian Basin, High Sulfur (>1 wt% dry)

3.6.2.3 Procedure for Calculation

Correlations were developed between the standard coal ash properties and the minerals as measured by CCSEM for all the coals in the database. The correlations were incorporated into a calculational procedure as described in this section.

The first step in the procedure is to convert the ash composition to a sulfur-free basis. Then the ash composition is converted from an oxide basis (in weight percent) to an elemental basis (in atom percent). Because this composition is based on the measured bulk composition, it includes both organically-bound and mineral-bound inorganic elements. Low rank coals contain a significant amount of organically-bound inorganic elements, while bituminous coals do not. Therefore, low rank coals must be corrected for organically-bound elements before the mineralogy can be estimated. For bituminous coals, no correction is made for organically associated elements; all major elements are assumed to be associated with discrete minerals.

For low rank coals (lignites and sub-bituminous coals) the amounts of selected elements (Ca, Mg, Na, K) that are organically-bound are subtracted from the composition. For Ca and Mg, relationships between the fraction of the element associated with the minerals and the amount of that element present in the ash (on a wt% oxide basis) were derived from the database. Figures 3-299 and 3-300 show the correlation between fraction of a given element in the minerals and the concentration of the oxide in the ash.

Table 3-168. Properties of Coals in Mineralogy Database

Coal	Rank	State	County	Basin	Seam	HHV	Moisture	Ash	Sulfur
L-1	Lignite	TX	Panola	Gulf Coast Lignite	Wilcox	8,015	24.27%	13.18%	1.86%
L-2	Lignite	TX	Atacosa	Gulf Coast Lignite	Jackson	4,100	20.40%	40.40%	1.40%
PRB-1	Sub-bituminous	WY	Campbell	PRB	Wyodak	8,578	29.30%	4.36%	0.28%
PRB-2	Sub-bituminous	WY	Campbell	PRB	Wyodak	8,686	29.00%	4.13%	0.14%
PRB-3	Sub-bituminous	WY	Campbell	PRB	Wyodak-Anderson	8,897	28.01%	4.90%	0.34%
PRB-4	Sub-bituminous	WY	Campbell	PRB	Smith	8,176	29.00%	5.20%	0.37%
PRB-5	Sub-bituminous	WY	Campbell	PRB	Wyodak-Anderson	8,432	29.36%	5.49%	0.36%
PRB-6	Sub-bituminous	WY	Campbell	PRB	Wyodak	8,381	29.00%	6.43%	0.35%
PRB-7	Sub-bituminous	WY	Campbell	PRB		8,411	29.00%	5.63%	0.41%
PRB-8	Sub-bituminous	WY	Campbell	PRB	Roland/Smith	8,519	29.00%	4.59%	0.25%
PRB-9	Sub-bituminous	WY	Campbell	PRB	Wyodak	8,618	29.00%	4.81%	0.31%
PRB-10	Sub-bituminous	WY	Campbell	PRB	Wyodak	8,346	29.18%	5.23%	0.46%
PRB-11	Sub-bituminous	WY	Campbell	PRB	Wyodak-Anderson	8,758	26.24%	5.12%	0.29%
PRB-12	Sub-bituminous	WY	Campbell	PRB	Wyodak-Anderson	8,595	29.00%	4.37%	0.27%
APH-1	High-volatile Bituminous	KY	Pike	Appalachian	Elswick	13,968	1.54%	6.41%	2.89%
APH-2	High-volatile Bituminous	PA	Indiana	Appalachian	Upper Freeport	14,346	0.00%	6.01%	1.90%
APH-3	High-volatile Bituminous	PA	Belmont	Appalachian	Pittsburgh	12,115	5.30%	11.20%	4.30%
APH-4	High-volatile Bituminous	PA	Monongahela?	Appalachian	Pittsburgh	14,391	0.00%	4.86%	1.69%
APH-5	High-volatile Bituminous	PA	Greene?	Appalachian	Pittsburgh	13,725	1.10%	7.04%	1.72%
APL-1	Medium-volatile Bituminous	VA	Buchanan	Appalachian	Pocahontas #3	14,079	6.13%	4.83%	0.74%
APL-2	Medium-volatile Bituminous	WV	Mingo	Appalachian	Alma/Cedar Grove	12,696	8.40%	7.74%	0.83%
ILH-1	High-volatile Bituminous	IL		Illinois	Illinois 5	13,818	0.00%	4.56%	1.50%
ILH-2	High-volatile Bituminous	IL	Gallatin	Illinois	Illinois 5	13,264	2.02%	9.20%	3.03%
ILH-3	Medium-volatile Bituminous	IL	Perry	Illinois	Illinois 6	12,675	0.00%	9.00%	3.00%
ILL-1	Medium-volatile Bituminous	IN	Knox	Illinois	Carbondale	11,106	18.40%	6.20%	0.48%
ILL-2	Medium-volatile Bituminous	IN	Pike?	Illinois	Carbondale	10,964	19.60%	6.75%	0.58%
ILH-4	High-volatile Bituminous	KY		Illinois	W.Ky #9	13,222	2.36%	9.04%	5.11%
ILH-5	High-volatile Bituminous	KY	Union	Illinois	W.Ky #11	12,334	7.12%	6.90%	3.05%
ILH-6	High-volatile Bituminous	KY		Illinois	W.Ky #6	12,566	4.47%	8.65%	2.90%
ILH-7	High-volatile Bituminous	IL	Gallatin	Illinois	Illinois 5	12,725	6.60%	7.90%	2.70%
ILH-8	High-volatile Bituminous	KY	Union	Illinois	W.Ky #11	11,719	12.09%	5.92%	2.50%

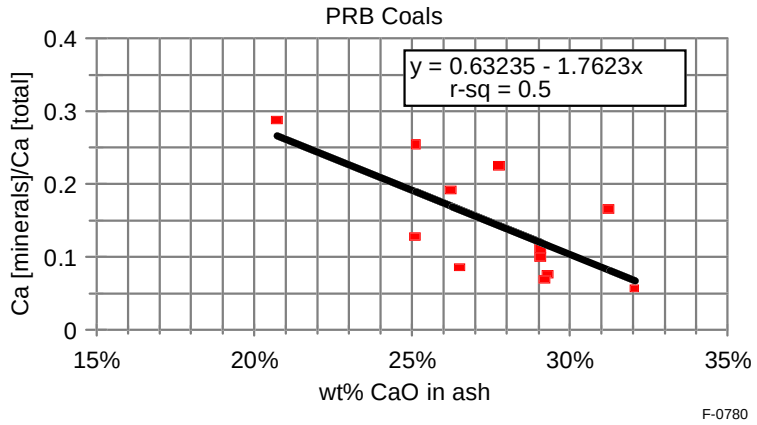

Figure 3-299. Fraction of calcium in the minerals as a function of CaO content of ash for Powder River Sub-bituminous coals.

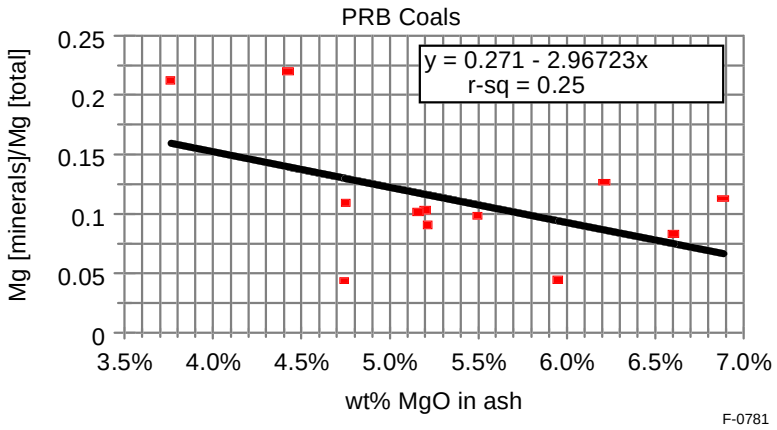

Figure 3-300. Fraction of magnesium in the minerals as a function of MgO content of ash for Powder River Sub-bituminous coals.

The correlations between the fraction of the element in minerals and the amount of the element in the ash were not good enough for Na and K. This may be because these elements are often present in lower amounts and the accuracy of their measurement is lower. For these elements, it was assumed that 63% of the K and 5% of the Na resided in the minerals. These values were based on a previous comparison between selective leaching and CCSEM for a Powder River Basin coal. Since the concentrations of these elements in the ash are typically only about 1-2 wt% (as oxides), average values will probably adequate.

The major mineral categories used are as follows:

- Quartz
- Kaolinite
- Other clays (illite, montmorillonite)
- Miscellaneous silicates
- Pyrite (includes pyrrhotite and jarosite)
- Calcite (includes dolomite)
- Other minerals.

For each coal in the database, there are data on the composition and size distribution of each mineral category. Average compositions of each mineral category were computed from the database, allowing the atoms in the mineral phase to be distributed among the major minerals. Figure 3-301 shows an example of the distribution of Si in one coal type (sub-bituminous). For each coal type, average distributions were computed for each element. An example of the average distribution for all coal types for Si is given in graphical form in Figure 3-302. Appendix N gives the average values for all elements and coal types. The distribution matrices in the appendix were used for the calculational procedure.

For certain minerals, ratios of key elements were adjusted to reflect the average ratios observed in the CCSEM measurements. Table 3-169 gives the average ratios of S/Fe in pyrite and Al/Si in clays. Once the pyrite and clays have been adjusted, the mineral composition is complete.

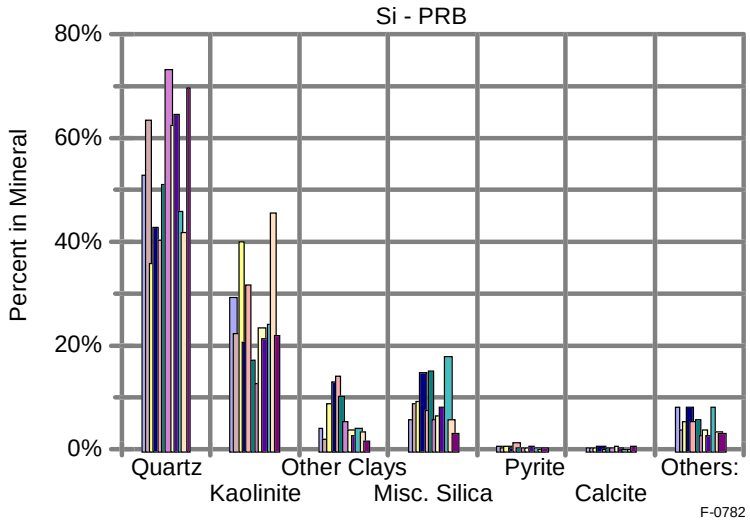

Figure 3-301. Distribution of silicon among the mineral categories for sub-bituminous coals.

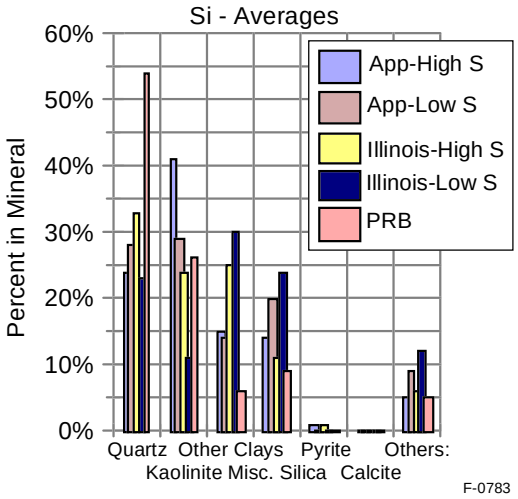

Figure 3-302. Distribution of silicon among the mineral categories for different coal types, based on average values in a given coal type.

Table 3-169. Average Atomic Ratios in Selected Minerals from CCSEM Analysis

Coal	Pyrite, S/Fe	Kaolinite, Al/Si	Other Clay, Al/Si
PRB subbituminous	1.9	1.1	0.7
Low sulfur Appalachian bituminous	2.6	0.9	0.6
High sulfur Appalachian bituminous	2.8	0.9	0.7
Low sulfur Illinois bituminous	2.1	0.8	0.5
High sulfur Illinois bituminous	2.7	1.0	0.6

The size distribution of the minerals is assigned by using average distributions of individual minerals. Figure 3-303 gives an example of the size distributions of kaolinite in Appalachian and subbituminous coals. Appendix O gives the average mineral distributions.

3.6.2.4 Summary

A calculational procedure was developed for estimating both the size and composition of coal minerals in common US coals. The procedure was based on correlations derived from a database of CCSEM measurements of 31 US coals. This will allow the estimation of coal mineralogy from more standard coal analyses. The coal mineralogy can be used as input to ToPEM (and other advanced models for ash behavior).

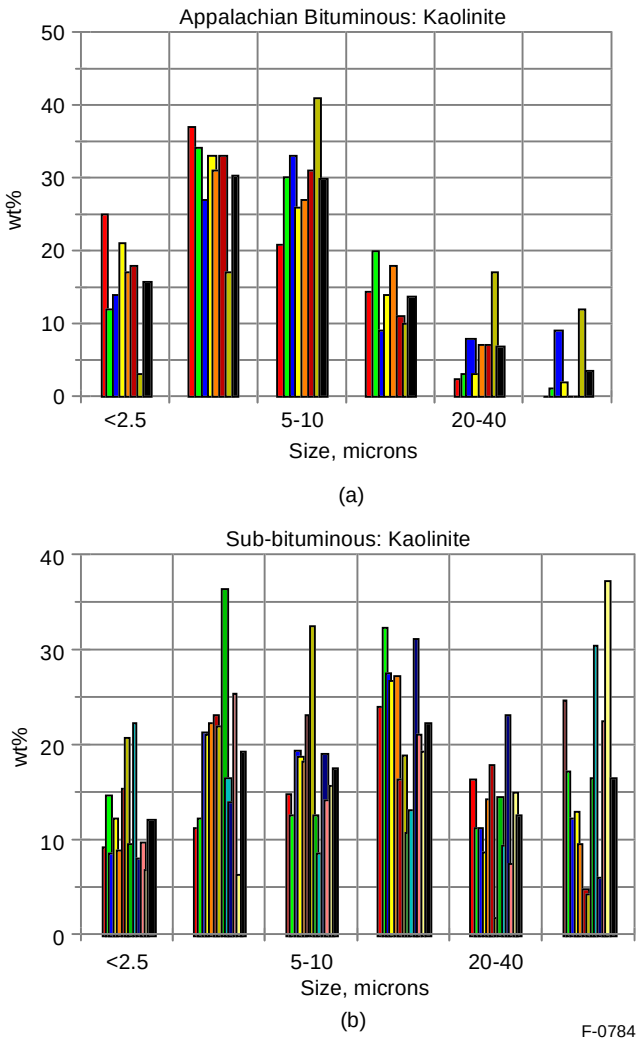

Figure 3-303. Distribution of kaolinite minerals by diameter of mineral grains for (a) Appalachian bituminous coals and (b) subbituminous coals.

3.6.3 Modeling Vaporization from Single Particles

ToPEM was used to model the combustion and ash vaporization of coals used in Phase I. These coals were three bituminous coals, Elkhorn-Hazard, Illinois 6 and Pittsburgh, and one low rank coal, Wyodak. In this section, we present results of the modeling effort and the steps taken to improve the accuracy of the model.

Initially we will present the mineral distribution for the various coals particle sizes, predicted by ToPEM and its implications to the submicron ash composition. Then we will present the ash vaporization model starting from the older versions to newer versions with improved accuracy. Finally, we will describe ash vaporization results from ToPEM, compare these results to experimental data and recommend ways to improve the model.

Mineral Composition of Coal Particles

The ToPEM model creates a sample of coal particles of various sizes based on actual coal particle size distribution data. Subsequently, it creates a sample of mineral particles based on CCSEM and ASTM ash analysis data. The minerals are then distributed in the coal particles using statistical methods. To check the validity of the statistical representation of the coal particles after the mineral distribution, the overall mineral composition of the coal sample is calculated and compared to that from the CCSEM data.

Mineral particles that are too big to fit in coal particles become excluded minerals. ToPEM assumes that organically bound metals such as Na, Ca and Mg in low rank coals exist in very small particles with a diameter of 0.1 μm. Table 3-170 shows the percent of ash and excluded minerals calculated by ToPEM for each of Elkhorn-Hazard, Illinois 6, Pittsburgh and Wyodak coals. There is a good agreement between the calculated and the actual amount of ash.

Figures 3-304 through 3-307 show the composition of minerals as a function of coal particle size for the four coals. The total composition does not add up to 100%, because only selected elements are presented. While in Elkhorn-Hazard the mineral composition is fairly independent of coal particle size, this is not true with the three other coals. Excluded minerals in Illinois 6 are characterized by large amounts of sodium and aluminum. This is a result of large silicate particles present in the coal which end up as excluded particles. Similarly in Pittsburgh,

Table 3-170. Amount of Excluded Mineral Particles as Calculated by ToPEM

Coal	% Ash Calculated (Measured)	% Excluded Minerals Calculated
Elk.-Haz.	7.29 (7.59)	21.81
Illinois 6	10.04 (10.61)	12.62
Pittsburgh	5.61 (7.11)	19.04
Wyodak	7.03 (8.47)	20.04

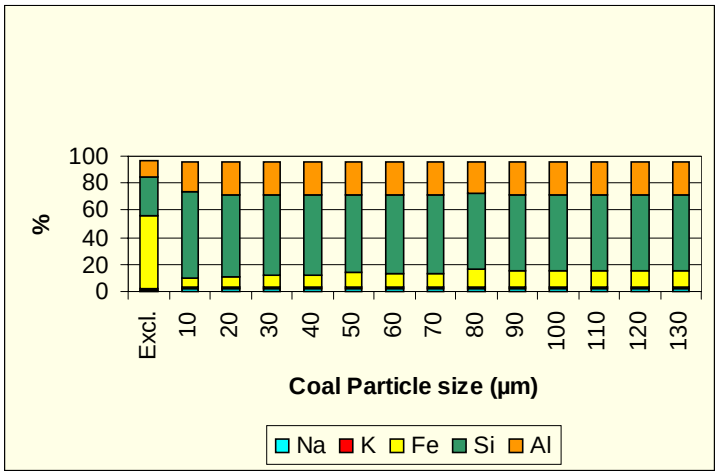

Figure 3-304. Elkhorn-Hazard: Mineral composition as a function of coal particle size, predicted by ToPEM.

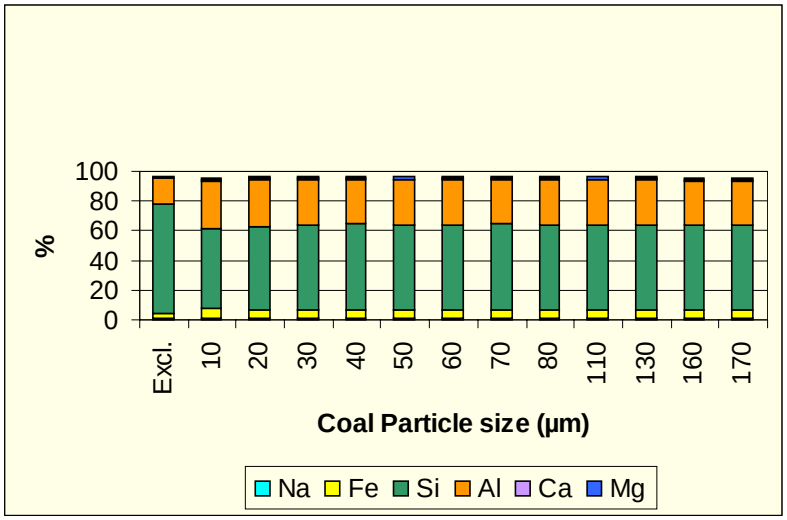

Figure 3-305. Illinois 6: Mineral composition as a function of coal particle size, predicted by ToPEM.

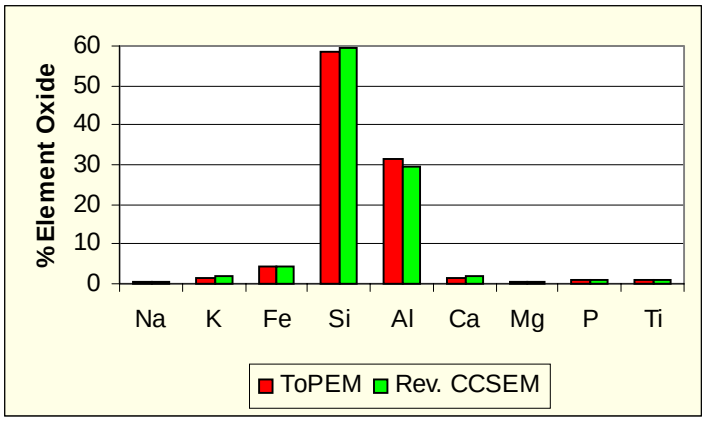

Figure 3-306. Pittsburgh: Mineral composition as a function of coal particle size, predicted by ToPEM

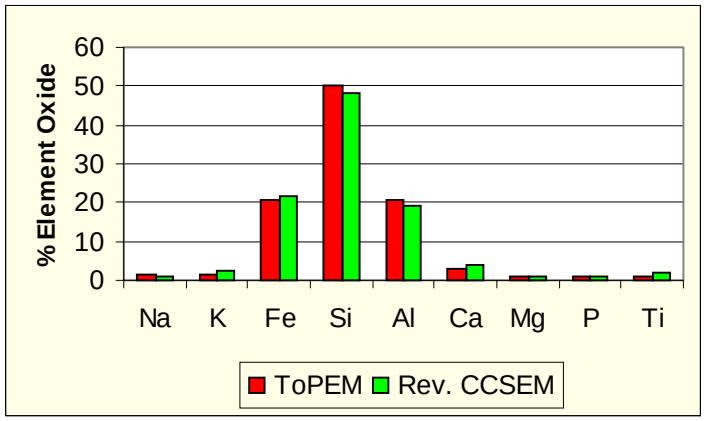

Figure 3-307. Wyodak: Mineral composition as a function of coal particle size, predicted by ToPEM.

a substantial amount of pyrite ends up as excluded minerals, which explains the high iron content of excluded particles. Finally in Wyodak, excluded particles are characterized by high silica content and 10 μm coal particles are characterized by high Ca and Mg content.

Figures 3-308 through 3-311 show the bulk ash composition of the four coals estimated from ToPEM. Also plotted are the actual bulk ash compositions derived directly from CCSEM data. In all coals there is a very good agreement between the two estimates, an indication that the coal sample generated by ToPEM represents accurately the actual coal.

Figure 3-312 shows the cumulative mass distribution of coal particles as a function of particle size for the four coals, based on measurements. In all coals 25 to 40% of the total mass of the coal resides in 10 μm particles and 70 to 90% of the coal mass, in coal particles 60 μm and smaller. Figure 3-313 shows the mineral content predicted by ToPEM for each coal particle size. It can be seen that the mineral content of the smallest particle size, 10 μm, is very low, 7 to 10 times lower than that of larger coal particles.

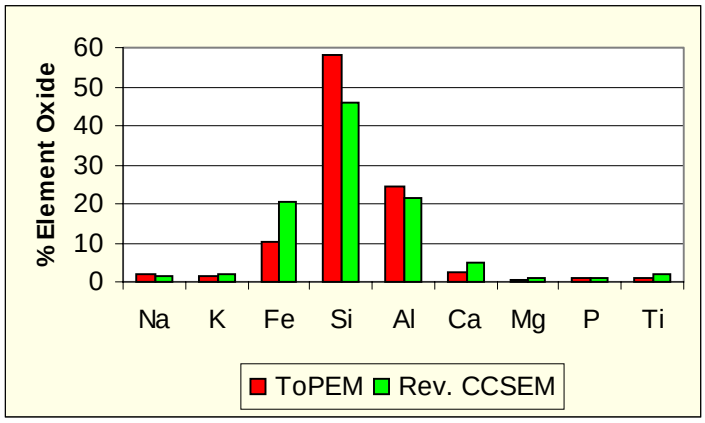

Figure 3-308. Elkhorn-Hazard: Bulk ash composition (a) predicted by ToPEM and (b) estimated from CCSEM data.

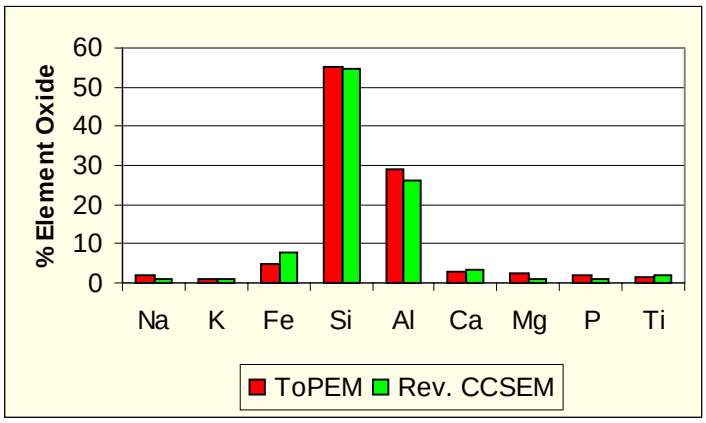

Figure 3-309. Illinois 6: Bulk ash composition (a) predicted by ToPEM and (b) estimated from CCSEM data.

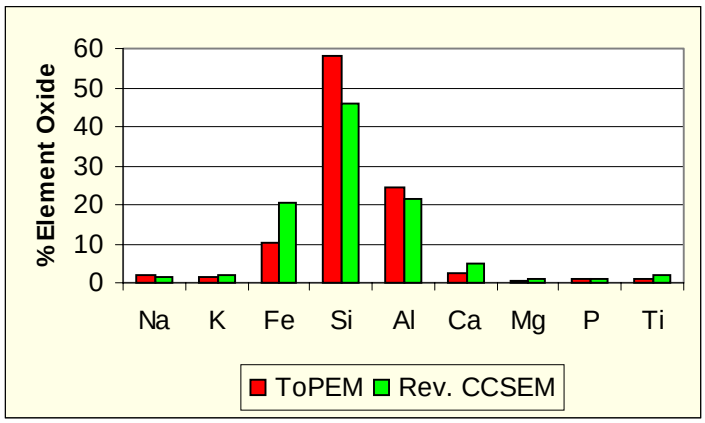

Figure 3-310. Pittsburgh: Bulk ash composition (a) predicted by ToPEM and (b) estimated from CCSEM data.

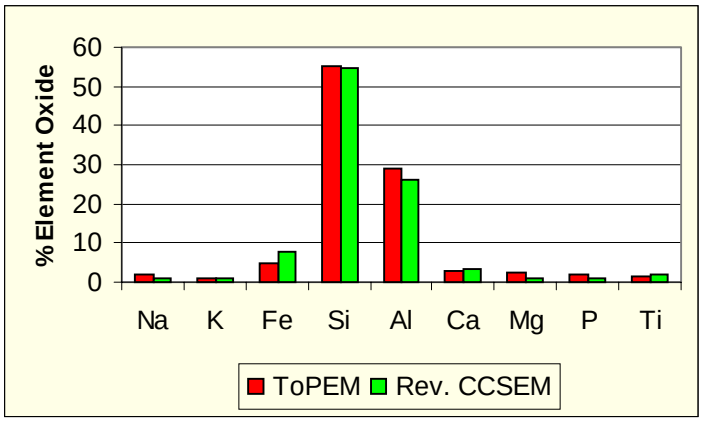

Figure 3-311. Wyodak: Bulk ash composition (a) predicted by ToPEM and (b) estimated from CCSEM data.

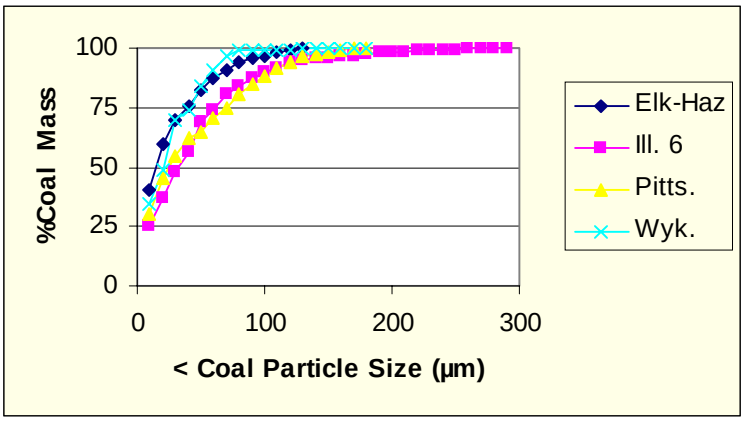

Figure 3-312. Cumulative mass distribution of coal particles as a function of coal particle size. This plot is based on measured particle size distributions.

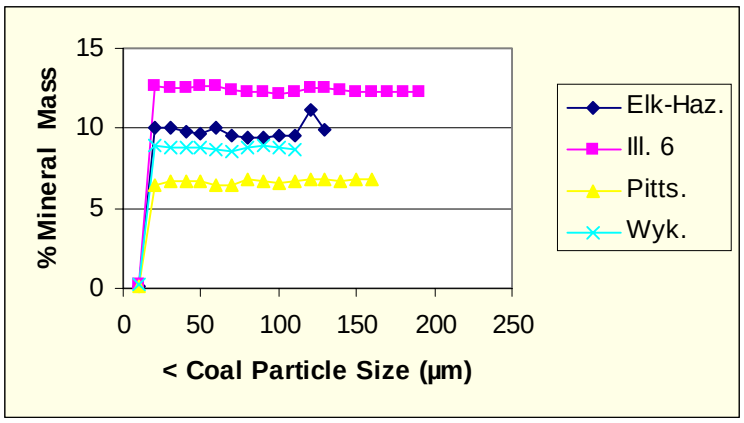

Figure 3-313. Mineral content that corresponds to various sizes of coal particles, as predicted by ToPEM for the four coals.

Figure 3-314 shows the fraction of the total ash in the coal in each size of coal particles. It can be seen that only 50 to 75% of the total amount of ash is contained in coal particles less than 60 μm, while 70 to 90% of the total mass of coal is contained in this size range. Therefore, we expect that larger coal sizes contribute more to the submicron ash than smaller sizes.

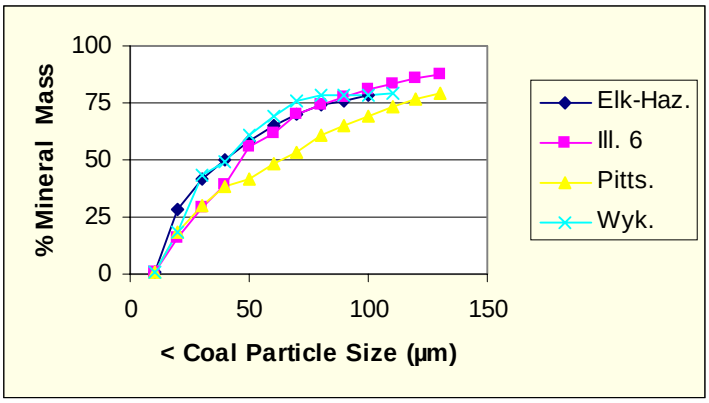

Figure 3-314. Cumulative distribution of mineral mass in the various sizes of coal particles.

Major Metal Vaporization Model

Vaporization Model

Previous work on vaporization of inorganic elements during *single particle* combustion in a Drop Tube Furnace was done by Quann [65], Quann and Sarofim [62], and Mims [271]. This work was both experimental and theoretical. The effects of coal rank, particle size, particle temperature and oxygen concentration were examined experimentally. Also, a theoretical analysis on vaporization from included, excluded and atomically dispersed minerals was accomplished. This theoretical analysis indicates that the element vaporization depends on one or more of the following parameters: coal rank, coal type, bulk O_2 and CO_2 concentration, particle size and composition of inherent ash. Results of this effort for Si, Ca and Mg were in very good agreement with the experiments.

For the case where we have vaporization from both internal inclusions and exposed inclusions on the char surface, Mims gives for the fractional vaporization rate of a metal:

$$\frac{f_v}{t_b} = \frac{9\theta c}{r_i^2 C_o \rho_p}\left[\frac{r_i D_e x_i^e}{2r_o(3\theta)^{1/2}} + \frac{D_m x_i^{es}}{5}\right] \qquad (3\text{-}53)$$

where,

f_v = fraction of metal that vaporizes
t_b = burnout time
C_o = metal concentration in coal
θ = volume ratio of inclusions in coal

r_i = inclusion radius
r_0 = char radius
D_e = effective diffusivity
D_m = metal diffusivity
x_i^e = equilibrium mole fraction metal at internal inclusion surface
x_i^{es} = equilibrium mole fraction metal at surface of exposed inclusion
ρ_p = density of the char particle
c = molar concentration coefficient.

In the limiting case of vaporization from the external or excluded particles, $D_e << D_m$. Therefore Eq. (3-53) becomes:

$$\frac{f_v}{t_b} = \frac{9\pi\theta c}{r_i^2 C_o \rho_p}\left[\frac{D_m x_i^{es}}{5}\right] \tag{3-54}$$

In the limiting case of vaporization from discrete inclusions, $D_e >> D_m$. Therefore Eq. (3-53) becomes:

$$\frac{f_v}{t_b} = \frac{9\pi\theta c}{r_i\, C_o \rho_p}\left[\frac{D_e x_i^e}{2r_o(3\theta)^{1/2}}\right] \tag{3-55}$$

For vaporization from organically associated minerals, which are in the form of fine inclusions, we assume $r_i << r_o$ then:

$$\frac{f_v}{t_b} = \frac{4cD_m x_i^e}{r_o^2 C_o} \tag{3-56}$$

Instead of calculating the fractional vaporization rate directly from Eqs. (3-53) through (3-56), we utilize as reference two sets of past experimental data for fractional vaporization rate. One set of these data was obtained for a bituminous coal and the other set for a low rank coal. Both were obtained at reference combustion conditions, which were 20% oxygen and gas temperature of 1750 K. These data correspond *single particle* combustion experiments conducted by Quann and Sarofim [62, 65]. To calculate metal vaporization of a different coal, we adjust the reference vaporization data for the combustion conditions and the properties of the coal in question.

Experimental results show that vaporization of most metals depends on the metal concentration in coals [62, 65]. Exceptions are Mg and Fe, the vaporization of which was found to be independent of concentration. Dependence of metal vaporization on concentration is also predicted from the theoretically analysis presented in References 62, 65, 271 and expressed with Eq. (3-53).

To account for this effect, another set of equations was derived, Eqs. (3-57) through (3-59), assuming different concentrations of a specific metal in the reference coal and the coal in question. These equations were derived from Eqs. (3-54) through (3-56).

The following formula was derived for discrete mineral particles:

$$\frac{f_v}{t_b} = \left(\frac{f_v}{t_b}\right)_r \left(\frac{x_i^e}{x_{ir}^e}\right)\left(\frac{r_{or}}{r_o}\right)\left(\frac{C_{or}}{C_o}\right) \tag{3-57}$$

The following formula was derived for organically bound elements:

$$\frac{f_v}{t_b} = \left(\frac{f_v}{t_b}\right)_r \left(\frac{x_i^{es}}{x_{ir}^{es}}\right)\left(\frac{r_o}{r_{or}}\right)^2\left(\frac{C_{or}}{C_o}\right) \tag{3-58}$$

The following formula was derived for excluded minerals:

$$\frac{f_v}{t} = \left(\frac{f_v}{t_b}\right)_r \left(\frac{r_o}{r_{or}}\right)^2\left(\frac{C_{or}}{C_o}\right) \tag{3-59}$$

Variable t in Eq. (3-59) is the residence time of the excluded particles in the boiler. This is different than the burnout time of coal particles and usually at least twice as long.

In diffusion-controlled combustion, which is usually the case for coal particle combustion in boilers, there is a simple relationship between the burnout time, t_b, the initial coal particle radius, r_o, and the oxygen volume fraction, x_{O_2}. This relationship has the following form:

$$t_b \propto \left(\frac{r_o^{\,2}}{\ln(1+x_{O_2})}\right) \tag{3-60}$$

If we substitute Eq. (3-60) into Eqs. (3-57) through (3-59), we get an expression for the *fraction* of the metal that vaporizes for discrete, organically bound and excluded minerals. For discrete mineral particles:

$$f_v = \left(\frac{f_v}{t_b}\right)_r \left(\frac{x_i^e}{x_{ir}^e}\right)\left(\frac{\ln(1+x_{O_2 r})}{\ln(1+x_{O_2})}\right)\left(\frac{r_o}{r_{or}}\right)\left(\frac{C_{or}}{C_o}\right) t_{b,r} \tag{3-61}$$

For organically bound elements:

$$f_v = \left(\frac{f_v}{t_b}\right)_r \left(\frac{x_i^{es}}{x_{ir}^{es}}\right)\left(\frac{\ln(1+x_{O_2 r})}{\ln(1+x_{O_2})}\right)\left(\frac{C_{or}}{C_o}\right) t_{b,r} \tag{3-62}$$

The following formula was derived for excluded minerals:

$$f_v = \left(\frac{f_v}{t_b}\right)_r \left(\frac{r_o}{r_{or}}\right)^2 \left(\frac{C_{or}}{C_o}\right) t \qquad (3\text{-}63)$$

A series of calculations were performed, in which the concentration term for a specific metal in Eqs. (3-61) through (3-63) was either considered or omitted. Generally better results were obtained when the concentration of Mg and Fe was not considered, which is consistent with Quann's experimental results. However it appears that the vaporization of a particular metal is not a unique function of the concentration of this metal in the coal, but depends on the type and rank of the coal.

Effect of Bulk CO_2 Concentration on Vaporization of Major Metals

In this section we will investigate the effect of bulk CO_2 on vaporization of major metals. Quann has shown experimentally that the presence of CO_2 in the exhaust gases depresses vaporization, as long as oxygen concentration is held constant. By performing his experiments at constant oxygen concentration environment, Quann was able to isolate the effect of burnout times and char temperatures, which remained constant, from the effect of CO_2 concentration in the combustion gases. Results of these experiments revealed that CO_2 decreases vaporization of all metals, but the effect is more pronounced in two atomically dispersed metals, Ca and Mg.

The above experimental results are consistent with the proposed mechanism for metal vaporization. The vaporization mechanism involves reduction of solid metal oxides with CO and production of metal vapors in reduced form along with CO_2. This mechanism predicts, indeed, that presence of CO_2 decreases metal vaporization, as long as O_2 concentration stays constant.

However, in real life combustors, O_2 concentration decreases as CO_2 forms, which results in increase of combustion times and decreases in char temperatures. Since both combustion times and char temperatures affect metal vaporization, the net result of bulk CO_2 should be the combined effect of longer combustion times, lower combustion temperatures and change in the molar fraction of metal vapors due to presence of CO_2.

Initially we will describe our past approach, which assumes that there is no bulk CO_2. This is a reasonable assumption for single particle combustion, but it may not be so for interactive combustion of coal particles, which is the case in industrial combustors. Subsequently we will present another approach, which more correctly assumes that there is bulk CO_2 due to combustion of other coal particles.

Past Approach – No Bulk CO_2. We assume that there is equilibrium between the metal oxide in the char, a reduced form of the metal oxide, CO and CO_2. For example, for SiO_2 we have:

$$SiO_{2(s)} + CO \rightarrow SiO_{(g)} + CO_2 \qquad (3\text{-}64)$$

The equilibrium constant can be expressed in terms of partial pressures of gaseous species in the following way:

$$K_{eq} = \frac{p_{SiO} \cdot p_{CO_2}}{\alpha_{SiO_2} \cdot p_{CO}} \tag{3-65}$$

where α_{SiO2} is the activity coefficient and p are the partial pressures of the various species on the surface of the mineral particle. For simplicity we assume that the partial pressures of the gaseous species are equal to those at the char surface.

The equilibrium constant, K_{eq}, for the above chemical equation is a function of temperature and is given by the following:

$$K_{eq} = \exp(A - \frac{B \cdot 10^4}{T_p}) \tag{3-66}$$

where T_p is the temperature of the burning char.

We assume that combustion is controlled by gas phase diffusion, which is true for most industrial combustors. Oxygen reacts with the coal particle and forms CO at the surface of the particle. There is no CO_2 at the surface of the char as a result of combustion. The partial pressure of CO on the char surface is a function of the oxygen bulk concentration, $p_{o_{2b}}$, and is given by the equation:

$$p_{CO} = \frac{2 \cdot p_{O_{2b}}}{1 + p_{O_{2b}}} \tag{3-67}$$

For single particle combustion, the char temperature is a function of bulk oxygen concentration and gas temperature, and is given by the equation:

$$T_p = T_g + 2000 \cdot p_{O_{2b}} \tag{3-68}$$

If we assume that there is no bulk CO_2, Eq. (3-64) indicates that the partial pressure of CO_2 on the surface, $p_{CO2,}$ is equal to the partial pressure of vaporized oxide, p_{SiO}. Under this assumption, the partial pressure of the vaporized oxide is given by the equation:

$$P_{SiO} = (K_{eq} \cdot \alpha_{SiO_2} \frac{2 \cdot p_{O_{2b}}}{1 + p_{O_{2b}}})^{1/2} \tag{3-69}$$

Equation (3-69) can be used to calculate the ratio of the molar fractions of vaporized metals, which correspond to the coal in question and the reference coal, as following:

$$\frac{P_{SiO}}{(P_{SiO})_r} = \frac{x_i^{es}}{x_{ir}^{es}} = \frac{\left(K_{eq} \frac{2 \cdot p_{O_{2b}}}{1 + p_{O_{2b}}} \right)^{1/2}}{\left(K_{eq} \frac{2 \cdot p_{O_{2b}}}{1 + p_{O_{2b}}} \right)_r^{1/2}} \tag{3-70}$$

The fractional vaporization rates were calculated using Eqs. (3-65) through (3-70) in conjunction with Eqs. (3-61) and (3-63). Results were presented in past quarterly reports.

New Approach –CO_2 Present in Bulk Gas. At any instant of time in a boiler environment, coal particles are at different stages of combustion and burn interactively with other particles close by. In this case, there is CO_2 in the bulk gas, resulting from the volatile and char combustion of particles. Equation (3-65) indicates that the presence of CO_2 in the bulk gas affects the partial pressure of the vaporized oxide and therefore influences the vaporization rate.

In the case that bulk CO_2 is present, Eqs. (3-64) through (3-68) still hold. The concentration of the vaporized oxide is not equal to CO_2 and O_2 concentration, as was the case without bulk CO_2 present. In this case we have:

$$P_{SiO} = \frac{K_{eq}}{p_{CO_2}} \cdot \alpha_{SiO_2} \cdot \frac{2 \cdot p_{O_{2b}}}{1 + p_{O_{2b}}} \tag{3-71}$$

If we neglect the effect of the activity coefficient, the ratio of the vapor pressures of the coal in question and the reference coal is:

$$\frac{P_{SiO}}{(P_{SiO})_r} = \frac{x_i^{es}}{x_{ir}^{es}} = \frac{\left(K_{eq} \frac{2 \cdot p_{O_{2b}}}{p_{CO_{2b}} \left(1 + p_{O_{2b}}\right)} \right)}{\left(K_{eq} \frac{2\, p_{O_{2b}}}{p_{CO_{2b}} \left(1 + p_{O_{2b}}\right)} \right)_r} \tag{3-72}$$

To account for this effect, we will first estimate the bulk composition of the gaseous phase both after the complete combustion of volatiles and after the overall combustion. These calculations will provide us with a range of CO_2 concentrations in the bulk gas that we can use for vaporization calculations.

The following is the overall combustion equation for a stoichiometric ratio ϕ:

$$C_a\ H_b N_c O_d S_e Cl_f + \frac{1}{2}\varphi\left(2a + \frac{b-f}{2} + 2e - d\right)(O_2 + 3.78N_2) \rightarrow aCO_2 + \frac{b-f}{2} H_2O + eSO_2 +$$

$$fHCl + \frac{1-\varphi}{2}\left(2a + \frac{b-f}{2} + 2e - d + \frac{c}{2}\right)O_2 + \left[\frac{\varphi}{2} 3.78\left(2a + \frac{b-f}{2} + 2e - d\right) + \frac{c}{2}\right]N_2 \tag{3-73}$$

The following is the combustion equation that describes the complete combustion of the volatiles:

$$C_x H_y N_z O_w + \frac{1}{2}\left(2x + \frac{y}{2} - w\right)(O_2 + 3.78N_2) \rightarrow xCO_2 + \frac{y}{2} H_2O + \frac{1}{2}\left[z + 3.78\left(2x + \frac{y}{2} - w\right)\right]N_2 \tag{3-74}$$

The chemical formulas of the coal and the volatiles can be calculated from the ultimate and proximate analyses of coal. By subtracting this last equation from the overall combustion equation and assuming that the chlorine content in the coal is negligible, the combustion of char can be obtained from the following equation:

$$C_{X'}S_{Y'} + \frac{1}{2}\frac{X' + 2Y'}{X'}(A\,O_2 + B\,N_2 + C\,H_2O + D\,CO_2) \rightarrow X'\,CO + Y'SO_2 + \frac{1}{2}\frac{X' + 2Y'}{X'}(B\,N_2 + C\,H_2O + D\,CO_2) \quad (3\text{-}75)$$

The coefficients X', Y', A, B, C and D are calculated from Eqs. (3-73) and (3-74). The composition of the gases after the volatile combustion for the coals burned in Phase I at a stoichiometric ratio of 1.2 is shown in Table 3-171. For the same coals and stoichiometric ratio, the composition of the gases after complete combustion is shown in Table 3-172.

Table 3-171. Bulk Composition of Gas Phase after Volatile Combustion

Species		Elk.-Haz.	Illinois 6	Pittsburgh	Wyodak
CO_2	%	3.8	4.1	2.2	6.6
H_2O	%	5.6	6.2	5.3	9.2
O_2	%	13.2	12.7	14.8	9.1
N_2	%	77.2	76.9	77.1	75.1

Table 3-172. Bulk Composition of Gas Phase after Overall Combustion

Species		Elk.-Haz.	Illinois 6	Pittsburgh	Wyodak
CO_2	%	14.2	13.7	14.3	13.1
H_2O	%	5.2	6.1	5.5	8.9
O_2	%	3.3	3.2	3.3	2.9
N_2	%	77.1	76.6	77.2	75.1
SO_2	%	0.06	0.27	0.11	0.02

The above results indicate that CO_2 bulk concentrations in a boiler may be very different than those in single particle combustion. It is possible that presence of bulk CO_2 affects the vaporization rate of metals, as can be inferred from the equations above. However, it is important that we make a distinction between the bulk CO_2 and the CO_2 at the surface of inclusions.

Before combustion starts there is no CO_2 inside the pores of a coal particle. During diffusion controlled combustion, CO_2 forms far away from the surface of the particle, which contributes to the bulk CO_2. Eventually CO_2 may diffuse though the pores of the coal particle. It is possible, however, that the time scales of combustion and CO_2 diffusion are equivalent, since gas diffusion controls both processes. If this is the case, bulk CO_2 may not influence much metal

vaporization from inclusions, although it may still influence vaporization of atomically dispersed metals and vaporization of excluded minerals.

Choice of Equilibrium Equations. Another variable which affects the vaporization calculations is the choice of equilibrium equations that take place during the vaporization process. Three sets of equations were evaluated as listed in Table 3-173. The first set of equations (Eqs. (1) through (7) as defined in Table 3-173) involves the reduction of metal oxides with CO. In the second set (Eqs. (1) through (4) and (6) through (8) as defined in Table 3-173), the initial aluminum equilibrium equation is replaced with another, which is favored more thermodynamically. Finally, in the third set of equations (Eqs. (1), (2), (4) and (6) through (9) as defined in Table 3-173), the vaporization of iron is considered to result from the combustion of pyrite, which is the form of occurrence of iron in many high rank coals.

Table 3-173. Equilibrium Equations and Constants for Vaporization of Metals

Equation #	***ln(K) = a + 10^4b/T***	***a***	***b***
1	$Na_2O_{(l)}$ + CO <=> 2Na + CO_2	17.8966	-2.8487
2	$K_2O_{(l)}$ + CO <=> 2K + CO_2	17.9507	-2.0891
3	$FeO_{(l)}$ + CO <=> Fe + CO_2	11.4942	-4.2064
4	$SiO_{2(l)}$ + CO <=> SiO + CO_2	18.8256	-5.9700
5	$Al_2O_{3(l)}$ + CO <=> 2AlO + CO_2	42.7695	-17.8851
6	CaO(l) + CO <=> Ca + CO_2	13.2182	-6.1507
7	MgO(l) + CO <=> Mg + CO_2	14.4976	-5.4094
8	$Al_2O_{3(l)}$ + 2CO <=> Al_2O + $2CO_2$	19.3480	-10.1851
9	$FeS_{(l)}$ + CO <=> Fe + CO S	10.9323	-5.1305

Effect of Mineral Distribution in Various Coal Particles Sizes on Ash Vaporization. As mentioned earlier, the way the minerals are distributed within the various sizes of coal particles is likely to affect ash vaporization. Ash vaporization from a certain coal size depends on the burnout time and the ash composition of that particular coal size. Smaller coal particles have shorter burnout times and therefore ash vaporization is lower than that of larger coal particles. Eqs. (3-61) and (3-62) indicate that metal vaporization decreases as the metal concentration in the coal increases.

Therefore, high concentration of a metal in one size of coal particles decreases the vaporization of the metal. Furthermore, excluded particles experience only the gas temperatures, which are substantially lower than the temperatures of burning particles. Under these conditions, low volatility elements such as Na and K vaporize more extensively than other more refractory metals such as Si and Fe.

To examine the effect of mineral distribution on ash vaporization, we examined two cases. In the first case we calculated vaporization directly from the bulk ash composition and we call it "bulk ash model." The implication here is that the minerals are uniformly distributed in all coal particles, independently of their size. It was assumed that all minerals were included. In the second case we used ToPEM to generate coal particles, distribute the minerals and form excluded mineral particles; vaporization was calculated from an ensemble of coal particles.

Results from Vaporization Modeling

Effect of bulk CO_2. To assess the effect of CO_2 on ash vaporization, we calculated the amount of ash that vaporizes during combustion at three different bulk CO_2 concentrations. Subsequently we compared the calculated values with experimental data for each of the four coals of Phase I. For the calculations we used the "Bulk Ash Model" which implies that the minerals are distributed uniformly within the various coal sizes. The following is a more detailed description of the three sets of calculations.

In Case 1, combustion of char and volatiles is assumed to take place with 20% oxygen at 1750 K gas temperature. No CO_2 is present in the combustion gases. The underlying assumption to this approach is that the coal particles are far from each other and burn individually as single particles. In Case 2, combustion is assumed to occur in two discrete stages: (a) combustion of volatiles without metal vaporization and (b) char combustion where metal vaporization takes place. The oxygen content during char combustion is the initial oxygen flow rate minus the oxygen consumption during volatile combustion. In Case 3, combustion is assumed to occur in two discrete phases as described in Case 2. This time, the oxygen content during char combustion is the initial oxygen flow rate minus the oxygen consumption during the overall combustion (volatiles plus char). This case applies to poorly mixed pockets in the boiler with high particle concentration.

In each of these cases, the char temperature was calculated from Eq. (3-68), assuming 20% O_2 for the first case, and, depending on the coal, 9 to 14% O_2, for the second case and 2 to 4% O_2 for the third. The equilibrium reactions that were considered were Eqs. (1) through (4), (6) through (8) as defined in Table 3-173. Note that Case 1 is not affected by the equilibrium reactions because combustion is assumed to take place at reference conditions, 20% O_2 and at 1750 K.

Table 3-174 shows the partial pressure of vaporized metals calculated for 0 to 14% bulk CO_2 at 1750 K gas temperature. These results are plotted in Figure 3-315. The partial pressure of Na and K from these calculations results in values greater than 1. This was observed earlier and was decided that in such cases we assume that partial pressure is 1. Generally the partial pressures calculated by Case 1 are higher that those calculated by the other cases. This is to be expected since Case 1 corresponds to the highest char temperature. Also the bulk CO_2 concentration is assumed to be zero in this case.

Figures 3-316 through 3-322 show the ash vaporization calculations for three different oxygen concentrations (and therefore bulk CO_2 concentrations) described earlier. For the three bituminous coals the presence of CO_2 affects the amount of ash that vaporizes and especially the

Table 3-174. Calculated Partial Pressure of Metals under Various Assumptions

Reduced Oxide	20% O_2 (0% CO_2)	14% O_2 (4% CO_2)	4% O_2 (14% CO_2)
SiO	6.36E-03	1.14E-04	3.28E-07
AlO	1.50E-06	5.57E-10	1.57E-12
Fe	4.86E-03	2.88E-05	7.07E-07
Ca	5.30E-04	9.98E-07	4.33E-09
Mg	5.03E-03	1.09E-04	6.65E-07
Na	4.03E+00	1.56E+01	1.96E+00
K	1.73E+01	1.54E+02	2.30E+01

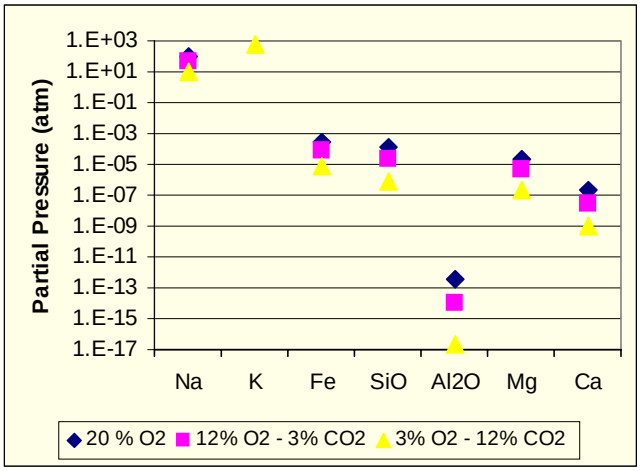

Figure 3-315. Partial pressure of vaporized metals calculated for 20-3% O_2 (0-14% bulk CO_2) at 1750 K gas temperature.

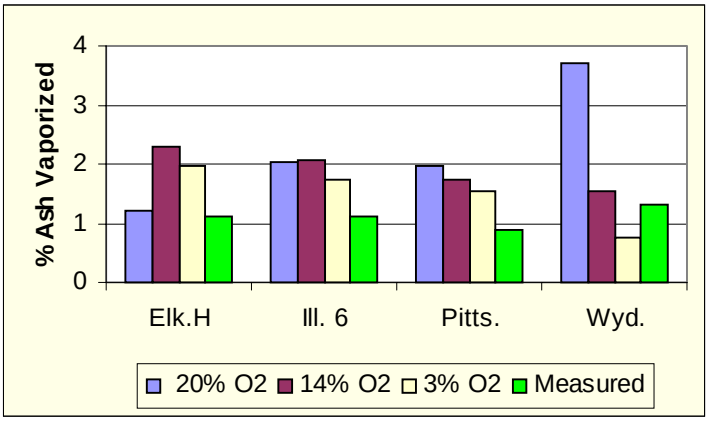

Figure 3-316. Ash vaporization for 20%, 14% and 3% bulk O_2 (0%, 3% and 14% CO_2).

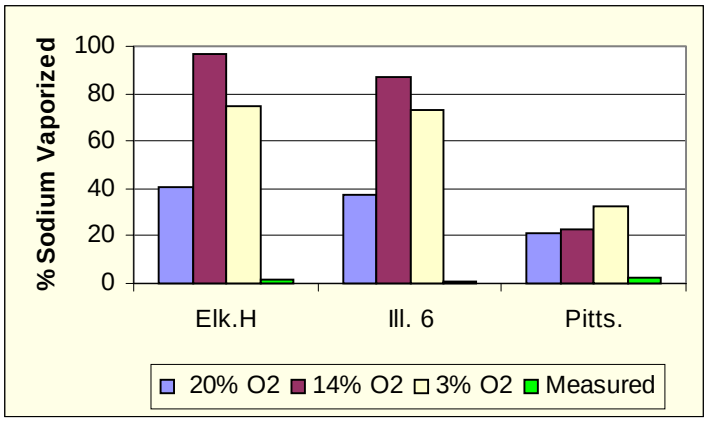

Figure 3-317. Sodium vaporization for 20%, 14% and 3% bulk O_2 (0%, 3% and 14% CO_2).

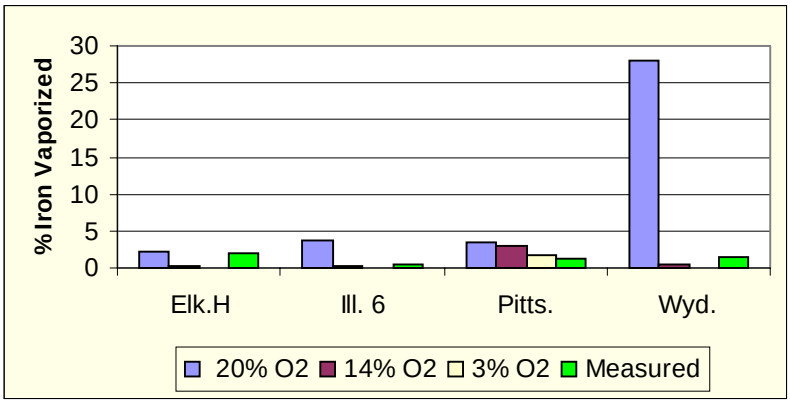

Figure 3-318. Iron vaporization for 20%, 14% and 3% bulk O_2 (0%, 3% and 14% CO_2).

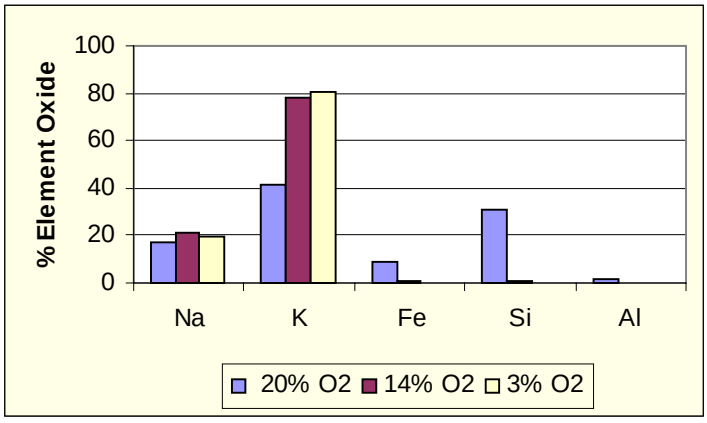

Figure 3-319. Elkhorn-Hazard: Submicron ash composition predicted from bulk ash for 20%, 14% and 3% bulk O_2 (0%, 3% and 14% CO_2).

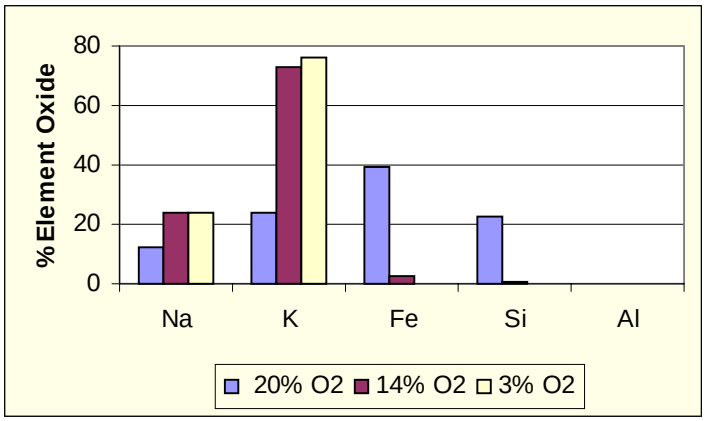

Figure 3-320. Illinois 6: Submicron ash composition predicted from bulk ash for 20%, 14% and 3% bulk O_2 (0%, 3% and 14% CO_2).

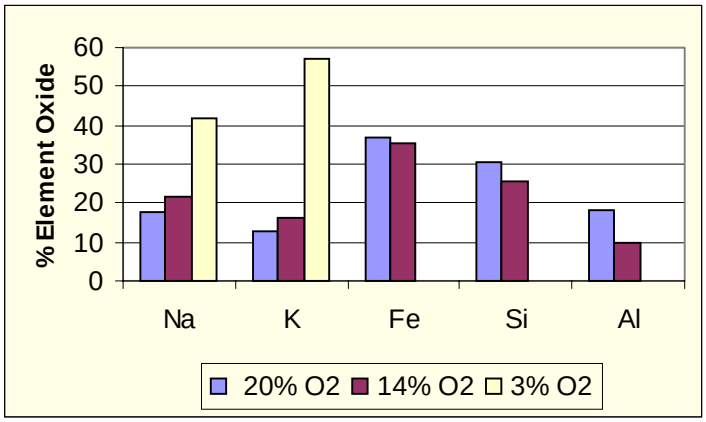

Figure 3-321. Pittsburgh: Submicron ash composition predicted from bulk ash for 20%, 14% and 3% bulk O_2 (0%, 3% and 14% CO_2).

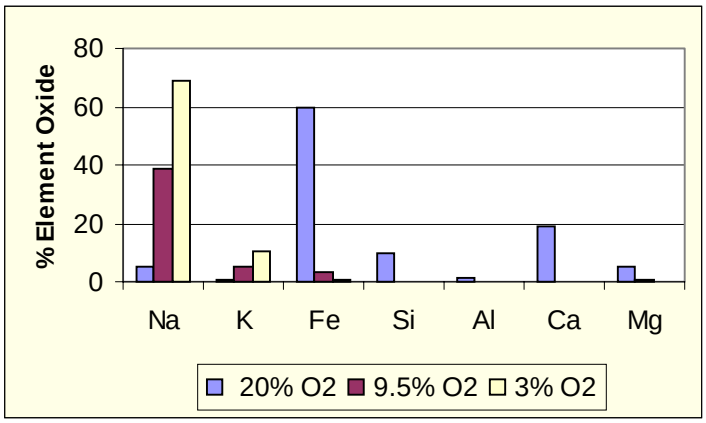

Figure 3-322. Wyodak: Submicron ash composition predicted from bulk ash for 20%, 9.5% and 3% bulk O_2 (0%, 3% and 14% CO_2).

ash composition. In most cases the amount of submicron ash is predicted within 40%. The amount of sodium is overpredicted by at least ten times in every case. The amount of iron that vaporizes is predicted better when we assume that CO is present.

Figures 3-319 through 3-322 show the predicted composition of the submicron ash for all coals under different bulk O_2/CO_2 concentrations. The two cases where 14% CO_2 is present and 3% O_2, predict higher K concentrations and lower concentrations of Si and Fe than the experimentally observed. Predictions from the 20% O_2 case are closer to experimental data.

Effect of Equilibrium Equations. Equation (5) of Table 3-173 was used in the past to calculate aluminum vaporization at conditions other than the reference. Presently, Eq. (8) of Table 3-173 is used since it is more thermodynamically favored. Figure 3-323 shows the fraction of Al that vaporizes at 14% O_2, using the two different equations. Equation (9) of Table 3-173 describes the iron vaporization through pyrite oxidation. Figure 3-324 compares the iron vaporization calculated by the two methods.

Effect of Mineral Distribution in Coal Particles. Figures 3-325 through 3-328 show submicron ash composition as calculated by ToPEM for the different sizes of coal particles. Combustion conditions were assumed to be 20% O_2 and 1750 K gas temperature.

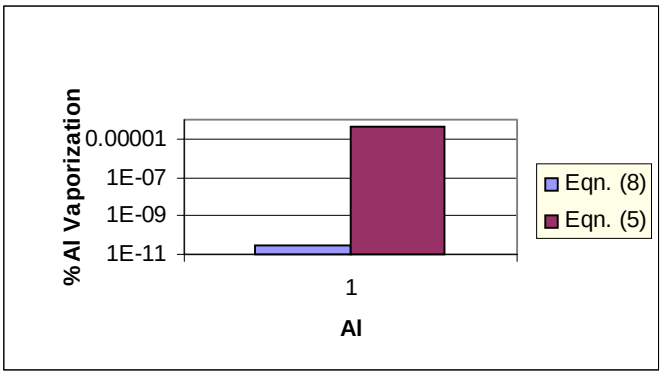

Figure 3-323. Fraction of Al that vaporizes at 14% O_2 (a) using equilibrium Eq. (8) and (b) using equilibrium Eq. (5). (See Table 3-173.)

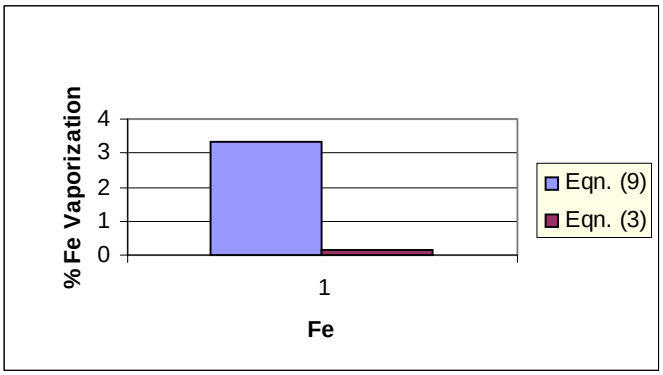

Figure 3-324. Fraction of Fe that vaporizes at 14% O_2 (a) using equilibrium Eq. (9) and (b) using equilibrium Eq. (3). (See Table 3-173.)

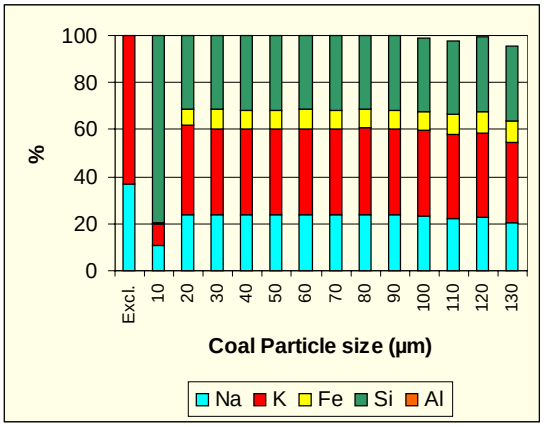

Figure 3-325. Elkhorn-Hazard: Submicron ash composition predicted for 20% O_2 predicted by ToPEM for different sizes of coal particles.

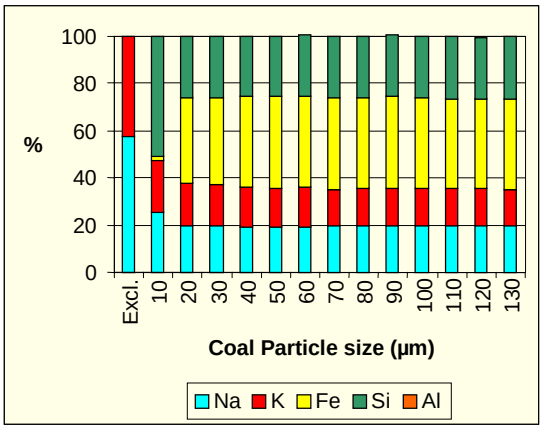

Figure 3-326. Illinois 6: Submicron ash composition predicted for 20% O_2 predicted by ToPEM for different sizes of coal particles.

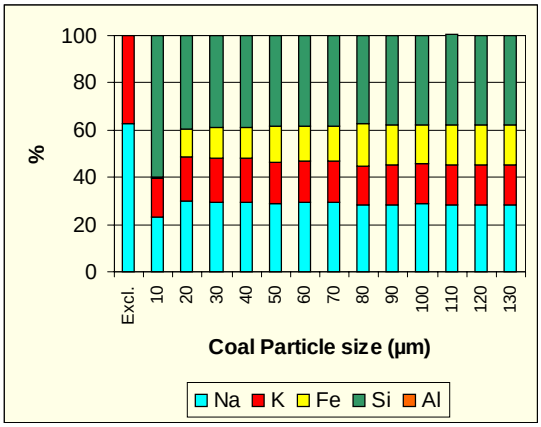

Figure 3-327. Pittsburgh: Submicron ash composition predicted for 20% O_2 predicted by ToPEM for different sizes of coal particles.

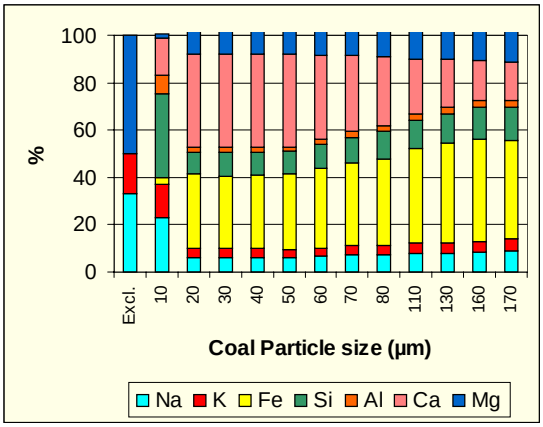

Figure 3-328. Wyodak: Submicron ash composition predicted for 20% O_2 predicted by ToPEM for different sizes of coal particles.

In all bituminous coals submicron ash from excluded particles consisted of Na and K, as expected, due to the relatively low temperature experienced by excluded particles in the boiler. In the same coals, submicron ash from 10 µm coal particles was enriched in Si and contained only minimal amounts of iron. The submicron ash composition from the other sizes of coal particles was similar and close to that of the bulk composition of the submicron ash.

Figures 3-329 through 3-331 show the amounts of ash, Na and Fe that vaporize, as calculated from the bulk ash model and from ToPEM. The differences between the two methods are small and can be attributed to non-uniform mineral distribution predicted by the ToPEM.

Effect of Temperature. The equilibrium equations suggest that char temperature greatly affects the vaporization of metals. Eq. (3-68) used to calculate char temperatures is valid for single particles and in cases were the furnace temperature is uniform throughout. This is not the case in most industrial boilers, since there is usually a temperature profile along the boiler. Furthermore experimental studies found that char temperature of single particles is different than char temperature of particles burning in groups due to competition for oxygen [272, 273].

Therefore some of the discrepancies between the observed and calculated figures may stem from the fact that the char temperature is overestimated. Furthermore, the assumption that bulk CO_2 affects the vaporization equilibrium may not be entirely correct, either. At the beginning of combustion the pores of the coal particles are filled with air. As CO_2 forms it diffuses inside the pores, but in diffusion controlled combustion the two diffusion times may be similar. If this is true, then the vaporization of minerals may not be affected as much by the presence of CO_2.

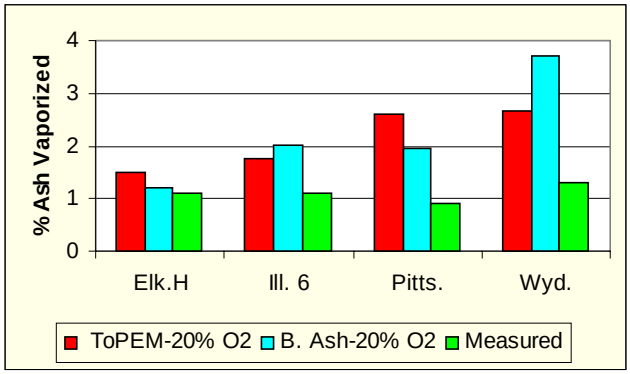

Figure 3-329. Ash vaporization for 20% bulk O_2 (a) from ToPEM and (b) from the bulk ash model.

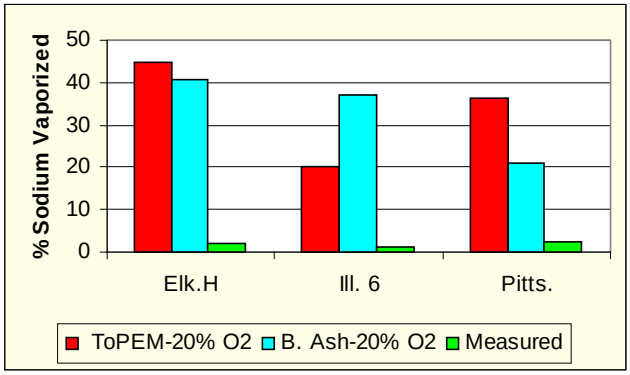

Figure 3-330. Sodium vaporization for 20% bulk O_2 (a) from ToPEM and (b) from the bulk ash model.

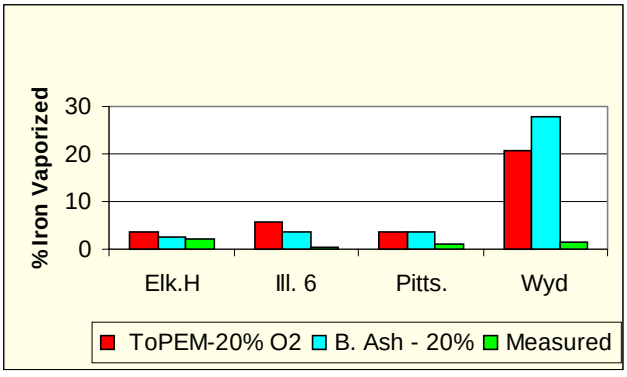

Figure 3-331. Iron vaporization for 20% bulk O_2 (a) from ToPEM and (b) from the bulk ash model.

SECTION 4

SUMMARY

4. SUMMARY

4.1 Coal Properties

The coals in Phase II were chosen in an attempt to (1) represent a broad range of elemental forms of occurrence and (2) represent the major coal ranks and commercial coal seams used for pulverized coal power generation in the U.S. A bituminous coal from Ohio coal was selected for study. The particular coal sample was a blend of three seams: Ohio 5, Ohio 6, and Ohio 7. The second coal in Phase II was a lignite from North Dakota (Hagel Bed). This coal is burned at a mine-mouth utility power plant in North Dakota. While lignites are not major steam producing coals throughout the United States, they are important regionally. The mineralogy of lignites from this seam is different from other coals. This coal is also burned at a full scale power plant which will be sampled for trace element emissions in another DOE-sponsored program. The third coal was from the Wyodak seam. This is a sub-bituminous coal from the Powder River Basin and is an important steam coal.

In this work UK has used XAFS and Mössbauer spectroscopies to characterize elements in project coals. For coals, the principal use was to supply direct information about certain hazardous and other key elements (iron) to complement the more complete indirect investigation of elemental modes of occurrence being carried out by colleagues at USGS.

- For comparing speciation information, XAFS experiments should be conducted directly on the residues from the leaching experiments. Using the identical fractions enables the assumptions in the leaching protocol to be tested and provides cleaner fractions for the XAFS investigation.

- Arsenic principally exists in association with pyrite in U.S. bituminous coals and as As^{3+}-O species in lower rank coals. Both forms are easily oxidized to arsenate forms.

- Chromium was found largely in organic association in both bituminous and lower-rank coals. Cr associated with clays (illite) was relatively minor in all three coals.

- Iron was found to be present predominantly as pyrite in all three coals; minor Fe^{2+}/clay and/or siderite were also present, more so in the lower-iron, lower-rank coals. Jarosite was a common oxidation product of pyrite.

- Zinc was not present as zinc sulfide (sphalerite), except possibly in minor amount in the bituminous coal. The major zinc forms in all three coals remain to be identified.

- Selenium is largely associated with pyrite in the bituminous coal; its contents in the lower rank coals were too low to obtain useful information.

Iterative selective leaching using ammonium acetate, HCl, HF, and HNO_3, used in conjunction with mineral identification/quantification, and microanalysis of individual mineral grains, has allowed USGS to delineate modes of occurrence for 44 elements in the Ohio 5/6/7, Wyodak, and North Dakota Program coals. These results provide basic information on the

distribution of elements in these coals, information needed for characterization and combustion model development.

The Phase II coals show rank-dependent systematic differences in trace-element modes of occurrence. For example, the Ohio 5/6/7 sample shows a greater proportion of chalcophile elements residing in pyrite, compared to the two lower rank coals. These associations are quantified by selective leaching results for each element, and supporting data where obtainable. Microanalysis shows that each of the Phase II coals have pyrite containing isolated domains enriched in one or more potentially harmful elements. Pyrite in the Ohio 5/6/7 coal has the most arsenic-rich micro-domains (approaching 2.0 wt. %), but these show no appreciable enrichment in associated chalcophile elements. Grain-scale concentrations of other chalcophile elements (e.g., Cd, Se) may be higher in pyrite in the two lower rank coals, but pyrite is less abundant in these coals than the Ohio 5/6/7 sample. The association of mercury and pyrite was confirmed using laser ablation ICP-MS, for the Ohio 5/6/7 sample, and for the Illinois #6 and Pittsburgh coals studied in Phase I. Chromium and other transition metals in illite/smectite were determined using the SHRIMP-RG ion microprobe, providing concentrations of silicate-hosted metals, at levels below those that can be quantified with the electron microprobe.

4.2 Combustion Zone Behavior

The work at UU focused on the behavior of trace metals in the combustion zone by studying vaporization from single coal particles. The coals were burned at 1700 K under a series of fuel-rich and oxygen-rich conditions. The combustion atmosphere varied from 0 to 100% oxygen with the balance being either nitrogen or carbon dioxide. The nitrogen provided an inert environment for the reaction. Carbon dioxide was used to investigate the governing reaction for metal reduction. Carbon dioxide was expected to keep the metals in their less volatile oxidized state, and also to affect the particle temperature. The impact of the carbon dioxide is particularly important since early interpretations of the vaporization data did not properly account for the gas composition in the pores.

After combustion, the particles were rapidly cooled to between 120 and 140°C by addition of 21 liters per minute of nitrogen gas through a water-cooled probe. An Andersen Mark II cascade impactor, located directly below the furnace collected and sized the particles. A side stream of the final exhaust was pulled through a small activated carbon plug to absorb any gas phase mercury and complete the mass balance. After collection, selected impactor stages, representing the residual and submicron ash, and the carbon plug were analyzed using instrumental neutron activated analysis (INAA).

During pyrolysis, the volatile organics are removed, and the remaining char is often assumed to include all of the mineral components of coal. Surprisingly, a number of elements showed enrichment in the submicron ash under pyrolyzing conditions. It appears likely that, with the exception of mercury, these elements were associated with volatile compounds. Mercury is not associated with organics, but is more likely enriched because of the ability of carbon to absorb mercury.

As the oxygen concentration was increased, there was an enrichment of several elements in the submicron ash. Several significant minor elements were also reduced in the submicron ash by using a carbon dioxide rich atmosphere. These data support the hypothesis that the carbon dioxide controls vaporization rates for metal species according to the governing reaction. The carbon lowers the reaction constant, however the affect cannot simply be explained with empirical models because of the intricacies of the carbon dioxide reactions.

The data collected in this study will be applied to a model that accounts for the full equilibrium between carbon monoxide and carbon dioxide. The model also considers many other reactions taking place in the combustion zone, and involves the diffusion of gases into the particle and combustion products away from the particle.

UU also investigated chlorine speciation in the flue gas because one possible means of reducing emissions of mercury is to reduce elemental mercury by reacting it with a radical chloride ion. It has been suggested that sulfur dioxide would interfere with the speciation, so this was first tested that theory with a synthetic flue gas.

4.3 Post-Combustion Behavior of Semi-Volatile Metals

A comprehensive study has been conducted at UA to investigate the post-combustion partitioning of trace elements during large-scale combustion of pulverized coal combustion. For many coals, there are three distinct particle regions developed by three separate mechanisms: 1) a submicron fume, 2) a micron-sized fragmentation region, and 3) a bulk (>3 μm) fly ash region. The controlling partitioning mechanisms for trace elements may be different in each of the three particle regions. A substantial majority of semi-volatile trace elements (e.g., As, Se, Sb, Cd, Zn, Pb) will volatilize during combustion. The most common partitioning mechanism for semi-volatile elements is reaction with active fly ash surface sites. Only the least volatile of these elements (e.g., cobalt) are expected to undergo significant vapor-to-solid phase partitioning by homogeneous nucleation. The presence of this mechanism is coal-specific.

The submicron and fragmentation particle regions typically contain more active fly ash surface sites than the bulk fly ash region. The maximum combustion temperature affects the availability of active calcium and iron surface sites on submicron particles. Therefore, for most coals/combustion conditions, increasing the combustion temperature will decrease the vapor-phase emission of those trace elements that form oxy-anions during volatilization. The maximum combustion temperature does not affect the availability of active aluminum surface sites on submicron particles. Therefore, the recovery of volatilized trace elements that partition by reaction with active anion surface sites may be unaffected by combustion temperature.

Although not predicted by thermodynamic simulation, many volatilized trace elements appear to form oxy-anions during combustion. Volatilized transition metals (e.g., cobalt) may form simple oxides, oxy-anions, or a combination of both during combustion.

Sulfur will inhibit the reaction of most volatilized trace element oxy-anions with iron surface sites. The effect of sulfur on calcium reactivity appears to be less than the effect on iron reactivity. Sulfur content does not appear to affect the reactivity of aluminum surface sites.

Therefore, coal sulfur content is an important parameter affecting the partitioning of many trace elements (e.g., selenium, arsenic) but not others (e.g., antimony, cesium). For coals with moderate (> 1 wt% as SO_2) to high sulfur contents (e.g., Pittsburgh, Illinois), volatilized trace elements that form oxy-anions will partition by reaction with active calcium surface sites if sufficient sites are available. For coals with low (<1 wt% as SO_2) sulfur contents (e.g., Kentucky, Wyodak, and North Dakota), volatilized trace elements that form oxy-anions will partition by reaction with active iron and/or calcium surface sites (depending on the reactivity of the individual trace element with iron versus calcium and the ratio of available iron to calcium surface sites). Volatilized trace elements that form oxy-anions will not partition by reaction for coals having a moderate to high sulfur content and low calcium content (e.g., Ohio) because there are insufficient active cation surface sites available for reaction.

Unreacted trace elements present on fly ash surfaces are usually very soluble in slightly acidic and acidic aqueous environments. The solubility of reacted trace elements present on fly ash surfaces is reaction product-dependent. Differences in partitioning mechanisms has a greater effect on trace element solubility from fly ash than which particle region the trace element resides in. Useful information can be obtained from leaching size-segregated fly ash samples collected on greased impactor membranes.

The following, element-specific conclusions can be derived from this work:

1. The volatilized form of antimony can have a substantial impact on the vapor phase emission. Almost all antimony present as antimony chloride is expected to leave in the flue gas and the remainder will partition as unreacted antimony to fly ash surfaces.

2. Volatilized selenium is more reactive with iron surface sites than with calcium surface sites. Therefore, coal sulfur content has a substantial impact on selenium partitioning.

3. Volatilized selenium is more reactive with both iron and calcium surface sites than arsenic or antimony.

4. Volatilized arsenic and antimony have similar reactivities with iron or calcium surface sites.

5. Volatilized selenium, arsenic, and antimony appear to form oxy-anions. These oxy-anions will react with active surface sites if available. Contrary to thermodynamic simulation predictions, formation of Al-As, Al-Se, or Al-Sb complexes were not observed under any of the conditions studied.

6. The forms of occurrence of selenium on fly ash surfaces can be distinguished by the solubility properties of the most likely forms of occurrence in slightly acidic and acidic aqueous leachates.

7. The forms of occurrence of arsenic on fly ash surfaces cannot be distinguished by the solubility properties of the most likely forms of occurrence in slightly acidic and acidic aqueous leachates.

8. All of the dominant forms of occurrence of antimony and cobalt on fly ash surfaces evaluated during this study were very soluble in slightly acidic and acidic aqueous leachates.

4.4 Post-Combustion Behavior of Mercury

Combustion processes remain the major source of mercury emissions to the atmosphere. Electric utility boilers are the largest emitting single source category in this inventory, accounting for one-third of the anthropogenic emissions to the air in the U.S. Anthropogenic mercury emissions from human activity take three forms: gaseous elemental mercury, gaseous divalent mercury, and particulate mercury. Mercury circulates in the environment in different chemical forms and different physical states. Inorganic forms exist in three oxidation states: elemental, monovalent, or divalent. Mercury in the atmosphere can return to the surface of the earth by either dry or wet deposition. In the case of gaseous divalent mercury, it can be subject to rapid wet or dry deposition. Divalent mercury is soluble in water and it can also adhere to particles in the air. It has a residence time of several days to a week. Mercury in its elemental state can be expected to disperse on a regional and global scale. The oxidation rate of Hg^0 to Hg^{+2} is on the order of a year, indicative of long atmospheric residence times.

The form of mercury emitted from point sources is a critical variable in modeling the patterns and amount of mercury deposited from the atmosphere. During combustion, mercury escapes from the burning fuel as an elemental vapor, which may persist in elemental form or may be oxidized to the +2 (mercuric) state. The three most likely gas phase mercury compounds in combustion systems - Hg, HgO, and $HgCl_2$ - are all volatile at stack and air pollution control device temperatures. At furnace exit temperatures, all of the mercury is expected to remain as the thermodynamically favored elemental form in the gas. As the gas cools after combustion, oxidation reactions can occur, significantly reducing the concentration of elemental mercury by the time the post-combustion gases reach the stack. Measurements of the concentration of mercury species taken in the stacks of pilot and full scale coal combustion systems show more than half of the vapor phase mercury as the oxidized form that is likely to be $HgCl_2$. The range of observed values is broad.

Many laboratory studies in the literature have suggested that the presence of chlorine species (HCl and Cl_2), temperature, and cooling rates were the most important factors affecting mercury oxidation. Molecular chlorine readily reacted with mercury. In the presence of a cooling rate (i.e., non-isothermal conditions), kinetic limitations were evident, according to several of the studies. Further, surface reactions may contribute, although high conversion by homogeneous pathways is reported under certain conditions.

Experiments conducted under this program at UC therefore focused on measuring mercury oxidation under cooling rates representative of the convective section of a coal-fired boiler to determine the extent of homogeneous mercury oxidation under these conditions.

Although the oxidation of elemental mercury in the convective pass is assumed to proceed primarily via gas-phase reaction, experimental evidence suggests that some fly ash can catalyze oxidation of elemental mercury. Iron oxide has been shown to promote this oxidation. Other constituents in the fly ash (carbon, calcium compounds) may also contribute. The presence of acid gases (HCl, SO_2, NO, NO_2) in the flue gas has also been shown to cause oxidation in the presence of fly ash. Thus, the coal composition (in terms of chlorine content and ash composition), the operation of the combustion system (in terms of unburned carbon in the ash), and temperature and residence time in the particulate control device will all affect mercury speciation in the gas and the amount of mercury adsorbed on the particulate matter.

Experiments conducted at the Energy & Environmental Research Center (EERC) at the University of North Dakota measured oxidation of elemental mercury and adsorption of elemental and mercuric chloride on ash samples. The ash samples were in a heated fixed bed reactor.

Gaseous Mercury Oxidation

Kinetic modeling of reactions of mercury with chlorine species under different cooling rate conditions established the importance of cooling rates as one of the main factors determining the degree of mercury oxidation in post-coal combustion. Kinetic calculations showed that the chemistry involving Cl atom reactions with mercury is fast. Therefore the presence of high concentrations of Cl atoms causes rapid mercury oxidation to occur, and the degree to which Cl_2 and HCl generate Cl atoms is important.

The results of mercury oxidation experiments under different chlorine concentrations showed that, relative to what has been reported in the literature, much higher chlorine concentrations are needed to obtain higher mercury oxidation. At typical HCl concentrations (100 ppmv) no reaction is observed with mercury. We demonstrated that total mercury oxidation can be achieved at cooling rates of 400 K/s by increasing the amount of chlorine up to 500 ppmv.

Mercury-Ash Interactions

In the original scope of work, five different test series were planned to evaluate the effects of temperature, mercury concentration, mercury species, stoichiometric ratio of combustion air, and ash source. Tests were run at temperatures of 250 and 350°F. With the tests with elemental mercury injection, there was no clear temperature effect. Oxidation of the elemental mercury either increased or decreased or was not affected by increasing temperature. With elemental mercury capture, there appeared to be a slight effect, but this can be attributed to physisorption of the elemental mercury on the ash samples. With the $HgCl_2$ injection tests, capture efficiency increased with decreasing temperature. Again, this can be attributed to physisorption on the ash surface. The objective was to identify a temperature to optimize interactions between the mercury in the simulated flue gas and the ash samples. Based on the results, there was no need to find an “optimum” temperature for either the elemental or $HgCl_2$ tests. The temperatures used were adequate for observation of effects. Tests were planned to find optimum mercury concentrations, but again the baseline concentrations were adequate. The main body of the testing performed was to identify reactive ash samples and determine the

effects of ash properties on capture, oxidation of elemental mercury, and reduction of oxidized mercury. As a result, 17 different ash samples were evaluated with elemental mercury or $HgCl_2$ injection. The results from these tests and analysis of the ash samples indicate there is a slight correlation between LOI and oxidation of elemental mercury across the fixed bed of ash. This effect was more evident with the bituminous and subbituminous ashes. There was also a general trend of increasing oxidation with increasing surface area. These trends most likely represent increasing active sites on the carbon that is in the ash. There was no correlation between temperature and the amount of oxidation of elemental mercury. There was also no correlation between LOI, surface area, and capture of elemental mercury. Also, no conclusions could be made about the effect of ash type on oxidation or capture of elemental mercury. Results from tests where ash samples were ashed at 400 and 750°C to remove carbon and evaluated in the fixed bed showed this process rendered active ashes inert. The baseline Wyodak ash which showed capacity for capture and oxidation of elemental mercury showed no reactivity even after the low-temperature ashing at 400°C. This was observed with all the ash samples that were ashed. The loss of active sights when the carbon was ashed is most likely responsible for the change in reactivity and not a change in the inorganic matter in the ash.

Results from the tests with $HgCl_2$ in the simulated flue gas indicate there is increased capture of $HgCl_2$ at lower temperatures. However, this is most likely due to physisorption and not an ash surface effect. As expected, the ash samples did not reduce $HgCl_2$ across the fixed bed.

Extensive work was carried out at UK during this program to develop new methods for identification of mercury species in fly ash and sorbents. We demonstrated the usefulness of XAFS spectroscopy for the speciation of mercury captured on low-temperature sorbents from combustion flue gases and developed XAFS parameters for such analyses. We demonstrated that all mercury sorption processes appeared to involve chemisorption rather than physisorption. Chloride, sulfide, iodide and oxygen anions were all shown to be effective for capturing mercury. The mechanism of capture reflects the gas-phase composition in terms of the speciation of mercury and of acid-gas components.

4.5 Field Data Evaluation

Semi-Volatile Trace Metals

Based on a review of field data, a model for the emission of trace elements from electric utility coal-fired power plants has been developed. The model partitions trace elements among fly ash particles as a function of ash particle size, and incorporates size-dependent particulate penetration through electrostatic precipitators to obtain emissions estimates. Comparison with recent field measurements and a database-derived model demonstrated that improved agreement could be obtained for relatively volatile elements such as arsenic and selenium. In contrast, agreement for chromium was comparable to that obtained with the database-derived model, and was attributed to the relatively low volatility of this element. A review of the literature in this area suggests that this conclusion may be restricted to facilities combusting bituminous coals, as facilities firing sub-bituminous coals generally produced greater fractions of chromium in the

submicron ash particulate. The partitioning model might thus be a more appropriate mechanism for predicting chromium emissions for such facilities.

Although the fraction of an element in the submicron size range was treated as an adjustable parameter in this study, the values obtained for each of these elements were consistent with partitioning data reported in both field and laboratory studies. It is therefore concluded that for volatile elements such as arsenic and selenium, a model based upon partitioning and overall ESP capture efficiency offers the most accurate predictions of trace element emissions, even for facilities contained within the PISCES database. Recommended values for arsenic are 14% in the submicron range, and for selenium, 20% vapor and 30% in the submicron fly ash size range. Further improvement in emissions prediction could be achieved by measuring the size-dependent particulate penetration though an ESP at an individual facility, but given the general absence of such data, the results presented herein suggest that an average value coupled to an overall particulate collection efficiency can provide improved predictions of trace element emissions. It is anticipated that first principles prediction of elemental partitioning, when coupled to the model presented herein, will provide the most accurate model of trace element emissions for all coals over a broad range of combustion conditions.

Mercury

Data from the EPA Information Collection Request (ICR) may be used to increase our knowledge of the effect of coal type, combustion system, and air pollution control devices on mercury speciation and emissions. These data must be evaluated carefully, however, if they are to be useful. In many cases, critical information may be missing or measurements in error. Several sources of inaccuracy in the predictions were identified, specifically,

- Lack of ash composition data which could be used to improve the prediction of the adsorption of mercury on fly ash the oxidation of mercury in particulate control devices;

- Uncertainty in the measurement of coal chlorine, a key parameter for mercury oxidation in flue gas;

- Over-reporting of oxidized mercury by the Ontario Hydro method when applied to flue gas containing high ash loadings;

- Poor mercury mass balance closure.

Air Pollution Control Devices (APCDs) have not previously been tuned to maximize mercury capture; such a strategy may be considered in the future, if mercury regulations are imposed. Most APCDs have been associated with reductions in mercury emissions, although the speciation of mercury is very important in determining the magnitude of reduction. However, a considerable increase in our understanding of the behavior of mercury in APCDs will be required even to get consistent mercury reductions without having an impact on removal efficiency of particulate, SO_2 or NO_x. With these caveats in mind, wet FGD's, dry scrubbers, and fabric filters can all remove a significant amount (circa 50%) of the gaseous mercury in the flue gas under

certain conditions. Fabric filters showed an average of 40 to 85% decrease in elemental mercury and a 25% decrease in oxidized mercury. The large decrease in elemental mercury suggests that some of the elemental mercury is being oxidized across the bag filter. SDAs produce decreases in oxidized mercury (50 to 60%) and elemental mercury (20 to 30%). ESPs and HESPs have a smaller effect on gaseous mercury. For bituminous coals, ESPs and HESPs appear to decrease elemental mercury (perhaps via oxidation). For low rank coals, precipitators have a smaller effect on gaseous mercury; ICR data do indicate a number of cases in which gaseous mercury (elemental or oxidized) increases across the precipitator, particularly for low rank coals.

4.6 Model Development

This work aimed to develop a model that predicts the vaporization of metals during coal combustion and to incorporate this model into the existing Engineering Model for Ash Formation (EMAF). The model is based on theoretical analysis for metal vaporization, experimental data and data correlations. The existing program, EMAF, was substantially modified to accommodate the vaporization sub-model.

The new Toxics Partitioning Engineering Model (ToPEM) was used to model the combustion and ash vaporization of coals used in Phase I. In certain coals, vaporization from excluded minerals and the smallest coal particles has a significant impact on the composition of the vaporized material. The vaporization equations were revised, so the effect of metal concentration in the coal is accounted for more accurately. The effects of the bulk CO_2 and char temperature were examined in detail. The calculated values for metal vaporization were compared with measured values from four different coals obtained in Phase I. The best agreement between the amount of vaporization and the composition of the submicron ash was obtained by assuming that the coal particles burn in 20% oxygen.

SECTION 5

REFERENCES

5. REFERENCES

1. Raask, E. (1985), "The modes of occurrence and concentration of trace elements in coal", Progress in Energy Combustion Science, **11**:97-118.

2. Gluskoter, H.J., Ruch, R.R., Miller, W.G., Cahill, R.A., Dreher, G.B., and Kuhn, J.K. (1977), "Trace elements in coal: occurrence and distribution", Illinois State Geological Survey Circular No. 499.

3. Devito, M.S., Rosendale, L.W. and Conrad, V.B. (1994), Comparison of trace element contents of raw and clean commercial coals, Fuel Proc Tech, **39**:87-106.

4. Kaakinen, J.W., Jorden, R.M., Lawasani, M.H., and R.E. West(1975), "Trace Element Behavior in Coal-Fired Power Plant", Environmental Science and Technology, **9:**862-869.

5. Raask, E., (1985), Mineral Impurities in Coal Combustion, Hemisphere Publishing Corp., Washington.

6. Linak, W.P. and Wendt, J.O.L. (1994), "Trace Metal Transformation Mechanisms During Coal Combustion", Fuel Processing Technology, **39**:173-198.

7. L. E. Bool, III, C. L. Senior, F. Huggins, G. P. Huffman, N. Shah, J. O. L. Wendt, F. Shadman, T. Peterson, W. Seames, A. F. Sarofim, I. Olmez, T. Zeng, S. Crowley, R. Finkelman, J. J. Helble, and M. J. Wornat, *Toxic Substances from Coal Combustion – A Comprehensive Assessment.* **Final Report, DOE Contract No. DE-AC22-95PC95101**, U.S. Department of Energy, July 1997.

8. Campbell, J.A., Laul, J.C., Nielson, K.K., and Smith, R.D. (1978), "Separation and Chemical Characterization of Finely-Sized Fly-Ash Particles", Analy Chem, **50**:163-173

9. Smith, R.D., Campbell, J.A., and Nielson, K K. (1979), "Characterization and formation of submicron particles in coal-fired plants", Atmos Environ, **13**:607-617.

10. Clarke, L.B. (1993), "The Fate of Trace Elements During Coal Combustion and Gasification: An Overview", Fuel, **72**:731-736.

11. Haynes, B.S., Neville, M., Quann, R.J., and Sarofim, A.F. (1982), "Factors Governing the Surface Enrichment of Fly Ash in Volatile Trace Species", J. Colloid & Interface Sci, **87**:266-279

12. Smith, R.D., Campbell, J.A., and Nielson, K K. (1979), "Concentration Dependence upon Particle Size of Volatilized elements in Fly Ash", Env Sci Tech, **13**:553-558.

13. Biermann, A.H. and Ondov, J.M. (1980), "Selenium in Coal-fired steam plant emissions", Atmos Environ, **14**:289-295.

14. Damle, A.S., Ensor, D.S., and Ranade, M.B. (1982), “Coal combustion aerosol formation mechanisms: a review”, Aeros Sci Tech, **1**:119-133.

15. Senior, C.L. and Flagan, R.C. (1982), “Ash vaporization and condensation during combustion of a suspended coal particle”, Aeros Sci Tech, **1**:371-383.

16. Flagan, R.C. and Friedlander, K. (1976), “Particle Formation in Pulverized Coal Combustion - A Review”, in Recent Developments in Aerosol Science (ed: D.T. Shaw) Chpt. 2, Wiley-Interscience, pp. 25-59.

17. Meij, R. (1994), “Trace element behavior in coal-fired power plants,” *Fuel Processing Technology* 39: 199-217.

18. Raask, E. and L. Goetz (1981), “Characteristics of captured ash, chimney solids, and trace elements”, J. of the Institute of Energy, September, **54:**163-173.

19. Lauf, R.J., Harris, L. A., and S.S. Rawiston (1982), “Pyrite Framboids as the source of magnetite spheres in fly ash”, Env. Sci. Tech, **16**:218-220.

20. Linak, W.P. and T. W. Peterson (1984), “Effect of Coal Type and Residence Time on the Submicron Aerosol Distribution from Pulverized Coal Combustion”, Aerosol Science and Technology, **3**:77-96.

21. McNallan, M.J., Yurek, G.J., and J.F. Elliott (1981), “The formation of inorganic particulates by homogeneous nucleation in gases produced by the combustion of coal”, Combustion and Flame, **42**:45-60.

22. Mulholland, J.A. and Sarofim, A.F. (1990), “Mechanisms of Inorganic particle formation during suspension heating of simulated aqueous wastes”, Environ Sci & Tech, **25**:268-274.

23. Sarofim, A.F., Howard, J.B., and Padia, A.S. (1977), “The physical transformation of mineral matter in pulverized coal under simulated combustion conditions”, Combustion Science and Technology, **16**:187-204.

24. Natusch, D.F.S., Wallace, J.F., and Evans, C.A.(1974), “Toxic trace elements: preferential conc. in respirable particles”, Science, **183:**202-204.

25. Taylor, D.D. and Flagan, R.C. (1983), “The influence of combustor operation on fine particles from coal combustion’, Aeros Sci Tech, **1**:103-117.

26. Helble, J.J. and Sarofim, A.F. (1989), “Influence of char fragmentation on ash particle size distributions”, Combustion and Flame, **76**:183-196.

27. Wall, T.F., Lowe, A., Wibberley, L.J., and Stewart, I.M. (1979), “Mineral Matter in Coal and the Thermal Performance of Large Boilers”, Prog Energy Combust Sci, **5**:1-29.

28. Smith, R.D. (1980), "The trace element chemistry of coal during combustion and the emissions from coal-fired plants", Prog. Energy and Combust. Sci., **6**:53-119.

29. Bool, L.E. and Helble, J.L. (1995), "A Laboratory Study of the Partitioning of Trace Elements during Pulverized Coal Combustion", Energy & Fuels, **9**:880-887.

30. Ratafia-Brown, J.A. (1994), "Overview of trace element partitioning in flames and furnaces of utility coal-fired boilers", Fuel Proc Tech, **39**:139-157.

31. Germani, M.S. and Zoller, W.H. (1988), "Vapor-Phase Concentrations of As, Se, Br, I, and Hg in the Stack of a Coal-fired Power Plant", Env Sci Tech, **22**:1079-1085.

32. Shendrikar, A.D., Ensor, D.S., Cowen, S.J., and Woffinden, G.J. (1983), "Size-dependent penetration of trace elements through a utility baghouse", Atmos Environ, **17**:1411-1421.

33. Esmen, N.A. and Corn, M. (1971), "Residence Time of Particles in Urban Air", Atmospheric Environment, **5:** 571-578.

34. Coles, D.G., Ragaini R.C., and Ondov, J.M. (1978), "Behavior of Natural Radionuclides in Western Coal-fired Power Plants," Environ. Science and Technology, **12:**442-466.

35. Davison, R.L., Natusch, D.F.S., Wallace, J.R., and Evans, C.A. (1974), "Trace elements in fly ash dependence of concentration on particle size", Env Sci Tech, **8**:1107-1113.

36. Kauppinen, E.I, and Pakkanen, T.A. (1990), "Coal Combustion Aerosols: A field study", Environmental Science & Technology, **24**/12: 1811-1818.

37. Swaine, D.J. (1994), "Trace elements in coal and their dispersal during combustion", Fuel Proc Tech, **39**:121-137.

38. Linton, R.W., Williams, P., Evans, C.A., and Natusch, D.F.S. (1977), "Determination of the Surface Predominance of Toxic elements in Airborne Particles by Ion Microprobe Mass Spectrometry and Auger Electron Spectrometry", Analyt Chem, **49**:1514-1521.

39. Silberman, D. and Harris, W.R. (1984), "Determination of arsenic (III) and arsenic (V) in coal and oil fly ashes", Intern J Environ Anal Chem, **17**:73-83.

40. Meserole, F.B., Schwitzgebel, K., Magee, R.A., and Mann, R.M. (1979), "Trace element emissions from coal-fired power plants", Trans. ASME, **101**:620-624.

41. Querol, X., Juan, R., Lopez-Soler, A., Fernandez-Turiel, J., and Ruiz, C. (1996), "Mobility of trace elements from coal and combustion wastes", Fuel, **75**:821-838.

42. G. P. Huffman, and F. E. Huggins, "Mössbauer studies of coal and coke: quantitative phase identification and direct determination of pyritic and iron-sulfide sulfur content," Fuel, **57**, 592-604 (1978).

43. F. E. Huggins, and G. P. Huffman, *Mössbauer analysis of the iron-bearing phases in coal, coke, and ash.* **Analytical Methods for Coal and Coal Products**, Vol. III, (ed. C. Karr, Jr.), Chapter 50, 371-423, Academic Press, New York, NY, (1979).

44. N. N. Greenwood and T. C. Gibb, **Mössbauer Spectroscopy**, Chapman and Hall, London, 1971.

45. Hosterman, J. W., and Dulong, F. T., 1985, A computer program for semi-quantitative mineral analysis by X-ray diffraction: in Pevear, D. R., and Mumpton, F. A., eds., Qualitative mineral analysis of clays: CMS Workshop, Lectures, v. 1, The Clay Minerals Society, Evergreen, CO, p. 38-50.

46. Palmer, C.A. (ed.), 1997, The chemical analysis of the Argonne Premium Coal Samples: U. S. Geological Survey Bulletin 2144, 106 p.

47. Palmer, C. A., Krasnow, M.R., Finkelman, R. B., and D'Angelo, W.M., 1993, An evaluation of leaching to determine modes of ocurrence of selected toxic elements in coal: Journal of Coal Quality, v. 12, no. 4, p. 135-141.

48. Finkelman, R. B., Palmer, C. A., Krasnow, M.R., Aruscavage, P. J., Sellars, G. A., and Dulong, F. T., 1990, Combustion and leaching behavior of elements in the Argonne Premium Coal Samples: Energy and Fuels, v. 4, no. 5, p. 755-766.

49. ASTM (American Society for Testing and Materials), 1998a, D2492-90 Standard test method for forms of sulfur in coal: in Annual book of ASTM standards, v. 5.05, Gaseous fuels, coal and coke, ASTM, Philadelphia, PA, p. 262-267.

50. ASTM (American Society for Testing and Materials), 1998b, D2797-95 Standard practice for preparing coal samples for microscopical analysis by reflected light: in Annual book of ASTM standards, v. 5.05, Gaseous fuels, coal and coke, ASTM, Philadelphia, PA, p. 282-285.

51. Pontolillo, J., and Stanton, R. W., 1994, Coal petrographic laboratory procedures and safety manual II: U.S. Geological Survey, Open-File Report 94-631, 69 p.

52. A. Kolker, S. Crowley, C. A. Palmer, R. B. Finkelman, F. E. Huggins, N. Shah, and G. P. Huffman, "Mode of occurrence of arsenic in four U.S. coals," Fuel Proc. Technol. (Air Toxics special issue), **63**, 167-178, (2000).

53. Wilson, Robert G, Stevie, Fred A., and Magee, Charles W., 1989, Secondary ion mass spectrometry, a practical handbook for depth profiling and bulk impurity analysis: Wiley, New York.

54. F. E. Huggins, S. Srikantapura, B. K. Parekh, L. Blanchard, and J. D. Robertson, "XANES spectroscopic characterization of selected elements in deep-cleaned fractions of Kentucky #9 coal," Energy & Fuels, **11**, 691-701, (1997).

55. F. E. Huggins, J. Zhao, N. Shah, F. Lu, G. P. Huffman, L. E. Bool, III, and C. L. Senior, *Investigation of the oxidation of arsenical pyrite in coal and its effect on the behavior of arsenic during combustion*, **Proceedings, ICCS '97, 9th International Conference on Coal Science, (Essen, Germany),** (eds. A. Ziegler, K. H. van Heek, J. Klein, and W. Wanzl), 1, 381-384, P & W Druck und Verlag GMBH, Essen (1997).

56. F. E. Huggins, F. Goodarzi, and C. J. Lafferty, "Mode of occurrence of arsenic in subbituminous coals," Energy & Fuels, **10**, 1001-1004, (1996).

57. F. E. Huggins, G. P. Huffman, A. Kolker, S. Mroczkowski, C. A. Palmer, and R. B. Finkelman, "Direct comparison of XAFS spectroscopy and sequential extraction for arsenic speciation in coal," Preprints, ACS Div. Fuel Chem., **45**(3), 547-551, (2000).

58. F. E. Huggins, and G. P. Huffman," Modes of occurrence of trace elements in coal from XAFS spectroscopy," Int. J. Coal Geol., **32**, 31-53, (1996).

59. F. E. Huggins, N. Shah, G. P. Huffman, A. Kolker, S. Crowley, C. A. Palmer, and R. B. Finkelman, "Mode of occurrence of chromium in four U.S. coals," Fuel Proc. Technol. (Air Toxics special issue), **63**, 79-92, (2000).

60. F. E. Huggins, N. Shah, J. Zhao, F. Lu, and G. P. Huffman, "Nondestructive determination of trace element speciation in coal and ash by XAFS spectroscopy," Energy & Fuels**, 7**, 482-489, (1993).

61. Lee, C.M. Modeling of the Vaporization and Subsequent Reactions of Selected Minerals During Pulverized Coal Combustion. University of Utah, MS thesis. 2000.

62. Quann, R.J. and Sarofim, A.F. "Vaporization of Refractory Oxides During Pulverized Coal Combustion," Nineteenth Symposium (International) on Combustion, (The Combustion Institute, Pittsburgh, PA) pp. 1429-1440, 1982.

63. Haynes, B.S., personal communication, 2001.

64. Baxter, L.L., Mitchell, R.E., and Fletch, T.H., "Release of Inorganic Material During Coal Devolatilization." Combustion and Flame, **108**, 494-502 (1997).

65. Quann, R.J. Ash Vaporization Under Simulated Pulverized Coal Combustion Conditions, Massachusetts Institute of Technology, ScD Thesis, 1982.

66. Quann, R., Neville, M., Janghorbani, M, Mims, C.A. and A.F. Sarofim (1982), "Mineral Matter and Trace-Element Vaporization in a Laboratory-Pulverized Coal Combustion System", Environmental Science and Technology, **16:**778-781.

67. Procaccini, C., et al. "Presence of Chlorine Radicals and Formation of Molecular Chlorine in the Post-Flame Region of Chlorocarbon Combustion." Environmental Science and Technology, **34**:21, pp 4565-4570. 2001.

68. Finkelman, R.B., Stanton, R.W., Cecil, C.B., and Minkin, J.B. (1979), "Modes of Occurrence of Selected trace elements in several appalachian coals", J. Am. Chem. Soc., Prepr Fuel Chem Div, **39:**236-241

69. Finkelman, R.B. (1994), "Modes of occurrence of potentially hazardous elements in coal: levels of confidence", Fuel Processing Technology, **39:**21-34.

70. Norman, N.C. (1998), Chemistry of Arsenic, Antimony, and Bismuth, Blackie Academic & Professional, New York.

71. Neville, M., McCarthy, J.F., and Sarofim, A.F. (1983), "Size fractionation of submicrometer coal combustion aerosol for chemical analysis", Atmos Environ, **17**:2599-2604.

72. Kaleta, P. and U. Tomza (1988), "Trace Elements in size-fractionated coal ash from two polish power plants", J Radioanal Nucl Chem, **121**:237-244.

73. McElroy, M.W., Carr, R.C., Ensor, D.S., and G.R. Markowski (1982), "Size distribution of fine particles from coal combustion", Science, **215**:13-19.

74. Zingaro, R.A. and W.C. Cooper (1974), Selenium, Van Nostrand Reinhold Co., New York.

75. Eary, L.E., Rai, D., Mattigod, S.V., and C.C. Ainsworth(1990), "Geochemical factors controlling the mobilization of inorganic constituents from fossil fuel combustion residues: II. Review of the Minor Elements", J. Environ. Qual., **19**:203-214.

76. Pupp, C., Lao, R.C., Murray, J.J., and R.F. Pottie (1974), "Equilibrium vapor concentrations of some polycyclic aromatic hydrocarbons, As4O6 and SeO2", Atmospheric Environment, **8**:915-925.

77. Andren, A.W., Klein, D.H., and Y. Talmi (1975), "Selenium in Coal-fired steam plant emissions", Env. Sci. Tech., **9**:856-858.

78. Block, C. and Dams, R. (1976), "Study of Fly Ash Emission During Combustion of Coal", Env Sci Tech, **10**:1011-1017.

79. Helble, J.J., (1994), "Trace element behavior during coal combustion: results of a laboratory study", Fuel Processing Technology, **39**:159-172.

80. Lee, R.E., Crist, H.L., Riley, A.E., and K. E. MacLeod (1975), "Concentration and size of trace metal emissions from a power plant, a steel plant, and a cotton gin", Env. Sci. Technol., **9**:643-647.

81. Markowski, G.R. and R. Filby (1985), "Trace Element Concentration as a function of particle size in fly ash from a pulverized coal utility boiler", Environ Sci & Tech, **19**:796-804.

82. Pyatnitskii, I.V., Analytical Chemistry of Cobalt, translated from the original Russian by N. Kaner, Israel Program for Scientific Translations, Jerusalem, 1966.

83. Weast, R.C., Handbook of Chemistry and Physics (68th ed.), CRC Press, Cleveland, (1987).

84. Beck, H.L., Gogolak, C.V., Miller, K.M,. and Lowder, W.M., 1980, "Perturbations on the natural radiation environment due to the utilization of coal as an energy source"; in The Natural Radiation Environment III (T.F. Gesell and W.M. Lowder, eds), U.S. Department of Energy, Washington, D.C., CONF-89-42, Vol 2.; pp. 1521-1558.

85. Eisenbud M. and Gesell, T. (1997), Environmental Radioactivity from natural, industrial and military sources, 4th Ed., Academic Press, San Diego, Ca., pp. 175-180.

86. Wilkerson, D.F., Arya, S., and Wilson, B.L. (1993) , "Investigations of Radionuclides in Aqueous Sediment Env. Surrounding A Coal Burning Power Plant", J. of Env. Sci and Health: Part A, **28A**:1005-1016.

87. Corbett, J.O. (1985), "The radiation dose from coal burning: a review of pathways and data", Radiation Protection Dosim., **4**:5-19.

88. Nakaoka, A., Takagi, S.l Fukushimia, M., and Ichikawa, Y. (1985), "Evaluation of radiation dose from a coal-fired power plant", Health Phys., **48**:215-220.

89. Alvarez, M.C., and Garzon, L., "Assessment of Radiological Emissions from Spanish Coal Power Plants: Radioactive Releases and Associated Risks", Health Phys., **57**:765-769.

90. Nowina-Konopka, M. (1993), "Radiological hazard from coal-fired power plants in Poland", Radiation Protection Dosim., **46**:171-180.

91. International Atomic Energy Agency (1963), "A Basic Toxicity Classification of Radionuclides", Report of Joint Study of a Group of Consultants to the International Atomic Energy Agency, Technical Report Series No. 15, Vienna.

92. Klein, D.H., Andren, A.W., Carter, J.A., Emery, J.F., Feldman, C., Fulkerson, W., Lyon, W.S., Ogle, J.C., Talmi, Y., Van Hook, R.I., and Bolton, N. (1975), "Pathways of 37 Trace Elements Through Coal-Fired Power Plant", Env. Sci. & Tech., **9**:973-979.

93. Gladney. E.S., Small, J.A., Gordon, G.E., and W.H. Zoller (1976), "Composition and size distribution of in-stack particulate material at a coal-fired power plant", Atmos. Environ., **10**:1071-1077.

94. Gordon, S. and B.J. McBride (1994), "Computer Program for Calculation of Complex Chemical Equilibrium Compositions and Applications", NASA Reference Publication 1311.

95. Dugwell, D. (2000), "Trace element emissions from combustion and gasification processes", Intl. Conf. on Ind. Furnaces and Boilers, Portugal, April 2000.

96. Owens, T.M., Chang-Yu, W., and P. Biswas (1995), "An equilibrium analysis for reaction of metal compounds with sorbents in high temperature systems", Chem. Eng. Comm., **133**:31-52.

97. Yan, R., Gauthier, D., Flamant, G., and J. M. Badie (1999), "Thermodynamic study of the behaviour of minor coal elements and their affinities to sulphur during coal combustion, Fuel Proc Tech, **78**:1817-1829.

98. Barin, I. (1995), Thermochemical Data of Pure Substances, Weinheim, FRG, VCH.

99. Knacke O., Kubaschewski O., and Hesselman K.(1991), Thermochemical properties of inorganic substances, 2nd ed., Springer-Verlag, Berlin, pp.1-1113.

100. Glusko V. P., et al. (1965), Termiceskie konstanty vescestv, Nauka, Moskova.

101. Glusko V. P., et al. (1968), Termiceskie konstanty vescestv, Nauka, Moskova.

102. Glusko V. P., et al. (1970), Termiceskie konstanty vescestv, Nauka, Moskova.

103. Glusko V. P., et al. (1971), Termiceskie konstanty vescestv, Nauka, Moskova.

104. Glusko V. P., et al. (1972), Termiceskie konstanty vescestv, Nauka, Moskova.

105. Pankratz L. B.(1984a), "Thermodynamic data for mineral technology", U.S. Dept. of the Interior, Bureau of Mines, Bulletin **677**:355.

106. Pankratz L.B.(1984b), "Thermodynamic Properties of Halides", U.S. Dept. of the Interior, Bureau of Mines, Bulletin **674.**

107. Pankratz L.B.(1995), "Thermodynamic Properties of Carbides, Nitrides, and other Selected Substances", U.S. Dept. of the Interior, Washington, DC, pp. 957.

108. Pankratz L. B. and King E. G. (1982), "Thermodynamic properties of elements and oxides", U.S. Dept. of the Interior, Bureau of Mines, Bulletin **672**:509.

109. Pankratz L.B., Mah A. D., and Watson S. W. (1987), "Thermodynamic Properties of Sulfides", U.S. Dept. of the Interior, Bureau of Mines, Bulletin **689:**427.

110. Ruzinov L. P. and Guljanickij B. S. (1975), “Ravnovesnye prevrasoenija metallugiceskin reaktseij”, Moskva, 416.

111. Karapet’yants M. Kh. (1978), Chemical thermodynamics, MIR Publishers, Moscow, 690.

112. Karapet'yants M. Kh. and Karapet'yans M. L. (1970), Thermodynamic constants of inorganic and organic compounds, Ann Arbor- Humprey Science Publishers, London, 461.

113. Karapet'yants, M. Kh., Maier, A.I., and Soldatova, T.A. (1970), “Enthalpies of Formation of Certain Praseodymium Selenites”, Inorganic Materials, Vol. 6, No. 6, pp. 976-979.

114. Karapet'yants, M. Kh., Maier, A.I., and Bas'kova, N.A. (1977), “Enthalpies of Formation of Rare Earth and Yttrium Carbonates”, Inorganic Materials, Vol. 13, No. 7, pp. 1032-1034.

115. Philips, S. L., Hale, F. V., Siegel, M. D. and L. F. Silvester (1988), “Thermodynamic Tables for Nuclear Waste Isolation”, Lawrence Berkeley Laboratory and Sandia National Laboratories, 182.

116. Mills K. C. (1974), Thermodynamic Data for Inorganic Sulfides, Selenides and Tellurides, Butterworths, London.

117. Kubaschewski O., Evans E. LL (1951), Metallurgical thermochemistry, Butterworth-Springer ltd, London.

118. Kubaschewski O. and Catterall J.A. (1956), Thermodynamical data of alloys, Pergamon press, Bath.

119. Kubaschewski, O., Kubaschewski-von Goldbeck, O., Rogl, P., and Franzen, H.F. (1983), “Titanium, Physico-Chemical Properties of its Compounds and Alloys”, Atomic Energy Review, Special Issue No. **9**, pp. 1-460.

120. Kubaschewski O., Alcock C. and Spencer P.J. (1993), Materials Thermochemistry, 6th Ed., Pergamon Press, U.K.

121. Fabricius G., Liukkonen S., and Sundholm G. (1994), Fysikaalisen kemian taulukoita. Otatieto, Espoo.

122. Wouterlood,H.J., Bowling, K.M., Removal and Recovery of Arsenious Oxide from Flue Gases, Environ. Sci Technol., **13**, 93-97 (1979).

123. Mahuli,S., Agnihtori, R., Chauk, S. Ghost-Dastidar, A., and Fan, L., Mechanism of arsenic sorption by hydrated lime, Environ. Sci Technol. **31**, 3226-3231 (1997).

124. Jadhav, R.A., Fan, L., Capture of Gas Phase Arsenic Oxide by Lime: Kinetic and Mechanism, Environ. Sci Technol., **35**, 794-799. (2001).

125. Linak, W.P., and Wendt, J.O.L, Toxic Metal Emissions from incineration: mechanism and control, Progr. Energy Combust.Sci. **19**, 145-185 (1993).

126. Neville, M and Sarofim, A.F., The fate of sodium during pulverized coal combustion, Fuel **64**, 384-390 (1985).

127. Johnson, W.L. (1995), A Laboratory Combustion System for Emission Studies, Masters Thesis, University of Arizona.

128. Bool, L.E. (1993), The Partitioning of Iron During the Combustion of Pulverized Coal, Doctoral Dissertation, University of Arizona.

129. Davis, S.B. (1999), Interactions Between Semi-Volatile Toxic Metals and Sorbents in Combustions, Doctoral Dissertation, University of Arizona.

130. Hillamo, R.E. and Kauppinen, E.I. (1991), "On the Performance of the Berner Low Pressure Impactor", Aeros Sci Tech, **14**:33-47.

131. Markowski, G.R. and Ensor, D.S. (1977), "A Procedure for Computing Particle size Dependent Efficiency for control devices from cascade impactor data", Proceeding of 70th Annual Meeting of the Air Pollution Control Association, Toronto.

132. Davis, S.B., Gale, T.K., Wendt, J.O.L., and W. P. Linak (1998), "Multi-component Coagulation and Condensation of Toxic Metals in Combustors", Proc. Combust. Inst., **27:**1785-1791.

133. Seames, W.S. "The Partitioning of Trace Elements During Pulverized Coal Combustion," Ph.D. Thesis, University of Arizona, August 2000.

134. Mamane, Y., Miller, J.L., and T.G. Dzubay (1986), "Characterization of Individual fly ash particles emitted from coal and oil fired power plants", Atmospheric Environment, **20**: 2125-2135.

135. Helble, J.J., Neville, M., and Sarofim, A.F. (1986), "Aggregate formation from vaporized ash during pulverized coal combustion", Proc. Combust. Inst., **21:**411-417.

136. Schure, M.R., Soltys, P.A., Natusch, D.F.S., and T. Mauney (1985), "Surface Area and Porosity of Coal Fly Ash", Environ Sci & Tech, **19**:82-86.

137. Fisher, G.L., Change, D.P. Y., and M. Brummer (1976), "Fly Ash Collected from Electrostatic Precipitators: Microcrystalline Structures and the Mystery of the Spheres", Science, **192**:553-555.

138. Desrosiers, R.C., Riehl, J.W., Ulrich, G.D., and A.S. Chiu (1979), "Submicron Fly Ash Formation in Coal-Fired Boilers", Proc. Combust. Inst., **17**: 1395-1403.

139. Hazrati, A. and Schrodt, J.T. (1988), "Microcharacterization of micron/submicron fly ash from a pulberized-dry-coal-burning power plant", Surface and Interface Analysis, **13**:142-148.

140. Kang, S., Helble, J.J., Sarofim, A.F., and J. Beer (1988), "Time-resolved evolution of fly ash during pulverized coal combustion", Proc. Combust. Inst., **22**:231-238.

141. Finkelman, R.B. (1999), Unpublished Correspondence.

142. Kolker, A. (2000), Unpublished Correspondence.

143. Conzemius, R.J., Welcomer, T.D., and H.J. Svec (1984), "Elemental Partitioning in Ash Depositories and Material Balances for a Coal Burning Facility by Spark Source Mass Spectrometry", Env. Sc. Tech., **18:**12-18.

144. Ragaini, R.C. and J. M. Ondov (1976), "Trace-element emissions from western US coal-fired power plants", Proc. Int. Conf. On Modern Trends in Activation Analysis, Munich, Germany, 654-663.

145. Agnihotri, R., Chauk, S., Mahuli, S., and Fan, L.S. (1998), "Selenium Removal Using Ca-Based Sorbents: Reaction Kinetics", Env. Sci. & Tech., **32**:1841-1846.

146. Dismukes, E.B. (1994), "Trace Element Control in Electrostatic Precipitators and Fabric Filters", Fuel Processing Technology, **39**:403-416.

147. Oehm, G.L., Crisp, P.T., and J.Ellis (1991), "The Recovery of Selenious Acid Aerosols on Glass Fiber Filters", J. Air Waste Management Assoc., **41**:190-195.

148. Hidy, G.M. and Brock, J.R. (1970), The Dynamics of Aerocolloidal Systems, Pergamon Press, New York.

149. Gullett, B.K. and Ragnunathan, K. (1994), "Reduction of Coal-Based Metal Emissions by Furnace Sorbent Injection", Energy & Fuels, **8**:1068-1076.

150. Ghosh-Dastidar, A., Mahuli, S., Agnihotri, R., and L.S. Fan (1996), "Selenium capture using sorbent powders: mechanism of sorption by hydrated lime", Env. Sci. Tech., **30**:447-452.

151. Niss, N.D., Schabron, J.F., and T.H. Brown (1993), "Determination of selenium species in coal fly ash extracts", Env. Sci. Tech., **27**:827-829.

152. Merrill, D.T., Manzione, M.A., Parker, D.S., Petersen, J.J., Chow, W., and A.O. Hobbs (1987), "Field Evaluation of Arsenic and Selenium Removal by Iron Coprecipitation", Env. Progress, **6**:82-89.

153. Wadge, A. and M. Hutton (1987), "The leachability and chemical speciation of selected trace elements in fly ash from coal combustion and refuse incineration", Environ. Pollut., **48**:85-99.

154. Jones, D.R. in Swaine, D.J. and Goodarzi, F. (1995), Environmental Aspects of Trace Elements in Coal, Kluwer Academic, Boston, Chapter 12.

155. Coney, A.M. and Hahn, D.A., A Dictionary of Chemical Solubilities, MacMillan (1921).

156. Dean, J.A. (1992), Langes Handbook of Chemistry, 14th Edition, McGraw-Hill.

157. Martinez-Tarazona, M., and Spears, D.A. (1996), "The fate of trace elements and bulk minerals in pulverized coal combustion in a power station", Fuel Proc Tech, **47**:79-92.

158. Irgolic, K.J., Hass, G., and Goesseler, W. (1997), "Arsenic Compounds in Fly Ash from Coal-Fired Power Plants", Managing Hazardous Air Pollutants, 4th Intl. Conf.; Washington, D.C., Nov. 12-14.

159. Turner, J.R. (1981), "Oxidation State of Arsenic in Coal Ash Leachate", Env. Sci. & Tech., **15**:1062-1066.

160. Hansen, L.D., Silberman, D., Fisher, G.L., and D.J. Eatough (1984), "Chemical Speciation of Elements in stack-collected, respirable-size coal fly ash", Env. Sci. & Tech., **18**:181-186.

161. Nodelman, I.G., Pisupati, S.V., Miller, S.F., and A.W. Scaroni (2000), "Partitioning behavior of trace elements during pilot-scale combustion of pulverized coal and coal-water slurry fuel", J. Haz. Matls., **74**:47-59.

162. Ondov, J.M., Ragaini, R.C., and Biermann, A.H. (1978), "Elemental particle size emissions from coal-fired power plants: use of an inertial cascade impactor," Atmospheric Environment **12**: 1175-1185.

163. Hansen, L.D. and G.L. Fisher (1980), "Elemental Distribution in Coal Fly Ash Particles", Env. Sci. & Tech., **14:**1111-1117.

164. Amos, J.M. (1999), High Temperature Reactive Capture of Cesium and Strontium by Sorbents, Masters Thesis, University of Arizona.

165. Gallagher, N.E. (1992), Alkali Metal Partitioning in a Pulverized Coal Combustion Environment, Doctoral Dissertation, University of Arizona.

166. Toole-O'Neil, B., Tewalt, S.J., Finkelman, R.B., and Akers, D.J., "Mercury concentration in coal - unraveling the puzzle," Fuel **78**, 47-54 (1999).

167. Tatsutani, M., Round, M., Brown, D., Groves, T., D'Urso, J., Marin. A., Alter, L., Goldberg, T., and Pilgrim, W., Northeast States and Eastern Canadian Provinces Mercury Study, NESCAUM, NEWMOA, NEIWPCC and EMAN, February 1998.

168. Keating, M.H., Mahaffey, K.R., Schoeny, R., Rice, G.E., Bullock, O.R., Ambrose, R.B., Swartout, J., and Nichols, J.W., *Mercury Study Report to Congress, Volume I: Executive Summary*, EPA-452/R-97-003, December 1997.

169. Bergan, T., Gallardo, L., and Rodhe, H. "Mercury in the Global Trophosphere: a Three-dimensional Model Study," Atmospheric Environment **33**(1999) 1575-1585.

170. Carpi, Anthony, "Mercury from Combustion Sources: A Review of the Chemical Species Emitted and their Transport in the Atmosphere," Water, Air, and Soil Pollution, **98**: 241-254, 1997.

171. Xu, X., Yang, X., Miller, D.R., Helble, J.J., and Carley, R.J., "A regional scale modeling study of atmospheric transport and transformation of mercury. I. Model development and evaluation," Atmospheric Environment **34**, 4933-4944 (2000).

172. Swain, E. B., Swain, D., Engstrom, R., Brigham, M.E., Henning, T.A., and Brezonik, P.L., "Increasing Rates of Atmospheric Mercury Deposition in Midcontinental North America," Science **257**, 784-788 (1992).

173. Schroeder, W.H., and Munthe, J. "Atmospheric Mercury – An Overview," Atmospheric Environment, **32**(5) pp. 809-822, 1998.

174. Senior, C.L., Sarofim, A.F., Zeng, T., Helble, J.J., and Mamani-Paco, R., "Gas-Phase Transformations of Mercury in Coal-Fired Power Plants," Fuel. Proc. Technol., 2000, **63**(2-3), 197-214.

175. Prestbo, E. M., and Bloom, N.S. "Mercury Speciation Adsorption (MESA) Method for Combustion Flue Gas: Methodology, Artifacts, Intercomparison, and Atmospheric Implications," Water, Air, Soil Poll. **80**, 145-158 (1995).

176. Hall, B., Lindqvist, O., and Ljungstrom, E., "Mercury Chemistry in Simulated Flue Gases Related to Waste Incineration Conditions," Environ. Sci. Technol., **24**(1) pp 108-111, 1990.

177. Sliger N. R., Going J. D., and Kramlich, J. C., "Kinetic Investigation of the High-Temperature Oxidation of Mercury by Chlorine Species," Western State Section/The Combustion Institute, Fall 1998 Meeting, Seattle, Washington.

178. Ghorishi, S.G., Lee, C.W., and Kilgroe, J.D., "Mercury Control Research: Effects of Fly Ash and Flue Gas Parameters on Mercury Speciation" 6th Annual Waste-to-Energy Conference, Proceedings, May 11-13, 1998, Miami Beach, Florida.

179. Gaspar, J.A., Widmer, N.C., Cole, J.A., and Seeker, W.R. "Study of Mercury Speciation in a Simulated Municipal Waste Incinerator Flue Gas" International Conference on Incineration and Thermal Treatment Technologies Proceedings, May 12-16, 1997, Oakland, California.

180. Hall, B., Schager, P., and Lindqvist, O., "Chemical Reactions of Mercury in Combustion Flue Gases," Water, Air, and Soil Pollution **56**: 3-14, 1991.

181. Galbreath, K.C., Zygarlicke, C.Z., and Toman, D. L. "Mercury-Chlorine-Fly Ash Interactions in a Coal Combustion Flue Gas" Air & Waste Management Association's 91st Annual Meeting & Exhibition, June 14-18, 1998, San Diego, California.

182. Horne, D.G., Gosavi, R., and Strausz, O.P., "Reactions of Metal Atoms I. The Combination of Mercury and Chlorine Atoms and the Dimerization of HgCl," J. Chem. Phys. 1968 **48**(10), 4758-4764.

183. Sliger, R.N., Kramlich, J.C., and Marinov, N.M. (2000a), "Towards the development of a chemical kinetic model for the homogeneous oxidation of mercury by chlorine species," *Fuel Processing Technology* (in press).

184. Sliger, R.N., Kramlich, J.C., and Marinov, N.M. (2000b), "Development of an Elementary Homogeneous Mercury Oxidation Mechanism," *Proc. A&WMA Annual Conference*, Salt Lake City, June.

185. Widmer, N.C., West, J., and Cole, J.A. (2000), "1Thermochemical Study of Mercury Oxidation in Utility Boiler Flue Gases," *Proc. A&WMA Annual Conference*, Salt Lake City, June.

186. Glarborg, P., Miller, J.A., and Kee, R.J., Combustion and Flame **65**(2), 177-202 (1986).

187. Niksa, S., Helble, J.J., and Fujiwara, N., Kinetic modeling of homogeneous mercury oxidation: the importance of NO and H_2O in predicting oxidation in coal-derived systems, Environmental Science & Technolgy (submitted) (2001).

188. Kramlich, J.C., Sliger, R.N., and Going, D.J., "Reduction of Inherent Mercury Emissions in Pulverized Coal Combustion," DOE Grant DE-FG22-95PC95216, presentation at DOE University Coal Research Contractor's Meeting, Pittsburgh, June, 1997.

189. Benson, S.W., The Foundations of Chemical Kinetics, McGraw-Hill: New York, NY (1960).

190. Laidler, K.J., Theories of Chemical Reaction Rates, McGraw-Hill: New York, NY, 1968, 38, 39.

191. Laudal, D.L., Heidt, M.K., and Galbreath, K.C. "State of the Art: Mercury Speciation Measurement in Coal Combustion" Air & Waste Management Association's 90th Annual Meeting & Exhibition, June 8-13, 1997, Toronto, Ontario, Canada.

192. Brown, T. D., Smith, D.N., Hargis, R.A. Jr., and O'Dowd, W.J. "Mercury Measurement and Its Control: What We Know, Have Learned, and Need to Further Investigate," J. Air & Waste Manage. Assoc., pp. 1-97, June 1999.

193. Linak, W.P., Ryan, J.V., Ghorishi, B.S., and Wendt, J.O.L., Issues related to solution chemistry in mercury sampling impingers," J. Air and Waste Management Association 2001, 51:688-698.

194. John M. Veranth, Thomas H. Fletcher, David Pershing , Adel Sarofim, Measurement of soot and char in pulverised coal fly ash, Fuel.

195. John M. Veranth, David W. Pershing, Adel F. Sarofim and Jefferey E. Shield, "Sources of unburned carbon in the fly ash produced from low NO_x pulverised coal combustion," 27th Symposium (International) on Combustion (The Combustion Institute, Pittsburgh, PA), pp 1737-1744, 1998.

196. Tiiu Alliksaar, Jan Mati Punning, Water, Air & Soil Pollution, v **106** 219-239, 1998 Kluwer Academic Publishers.

197. Tiiu Alliksaar, Per Horstedt, Ingenar Renberg, Water, Air & Soil Pollution, v **104**, 149-160 1998, Kluwer Academic Publishers.

198. J. Watt, Water, Air & Soil Pollution, v **106** n 3-4 Sept. 1998 Kluwer Academic Publishers p 309-327 0049-6979.

199. Personal communication with John M. Veranth, Research Assistant Professor, Chemical and Fuels Engineering Department, University of Utah, Salt Lake City, Utah.

200. Ghorishi, S.B., Lee, C.W, and Kilgroe, J.D., "Speciation of Mercury in the Presence of Coal and Waste Combustion Fly Ashes," paper presented at the Air & Waste Management Association 93rd Annual Conference and Exhibition, Salt Lake City, UT, June 19-22, 2000.

201. M. E. Hirsch, R. O. Stirling, F. E. Huggins, and J. J. Helble, "Speciation of combustion-derived particulate phase arsenic," Environ. Engineering Science, **17,** 315-327, (2000).

202. F. E. Huggins, N. Shah, G. P. Huffman, and J. D. Robertson, "XAFS spectroscopic characterization of elements in combustion ash and fine particulate matter," Fuel Proc. Technol. (Proceedings, Conf. Air Quality, McLean, VA), **65-66**, 203-218, (2000).

203. G. P. Huffman, F. E. Huggins, N. Shah, S. Pattanaik, H. L. C. Meuzelaar, S. J. Jeon, D. Smith, B. Harris, M. S. Seehra, and A. Manivannan, Structure of primary $PM_{2.5}$ derived from diesel truck exhaust**,** Preprints, ACS Div. Fuel Chem., **45**(3), 441-445, (2000).

204. F.E. Huggins, M. Najih, and G. P. Huffman, Direct speciation of chromium in coal combustion by-products by X-ray absorption fine structure spectroscopy. Fuel (Special Issue, 1997 International Ash Utilization Symposium), **78**, 233-242, (1999).

205. F. E. Huggins, G. P. Huffman, G. E. Dunham, and C. L. Senior, XAFS examination of mercury sorption on three activated carbons. Energy & Fuels, **13**, 114-121, (1999).

206. F. E. Huggins, N. Yap, and G. P. Huffman, XAFS Investigation of mercury sorption on carbon-based and other sorbent materials. Jpn. J. Appl. Phys. (Proc. Internat. Conf. SRMS-2, Kobe, Japan) **38** (Suppl. 38-1), 588-591, (1999).

207. F. E. Huggins, N. Yap, G. P. Huffman, and C. L. Senior, *Identification of mercury species in unburned carbon from pulverized coal combustion.* **Proceedings, Air & Waste Management Association 92nd. Annual Meeting** (St. Louis, MO), Paper 99-A72 on CD-ROM, (1999).

208. E. A. Stern and S. M. Heald, Rev. Sci. Instrum**. 50**, 1579-1582, (1979).

209. Eisenberger, P. and B. M. Kincaid, Science, **200** 1441-1447, (1978).

210. P. A. Lee, P. H. Citrin, P. A. Eisenberger and B. M. Kincaid, Rev. Mod. Phys., **53**, 769-808, (1981).

211. A. Bianconi, E. Fritsch, G. Calas and J. Petiau**,** Phys. Rev. B, **32**, 4292-4295, (1985).

212. F. W. Lytle, R. B. Greegor and A. Panson, Phys. Rev. B, **37**, 1550-1562, (1988).

213. R. Åkesson, I. Persson, M. Sandström and U. Wahlgren, Inorg. Chem., **33**, 3715-3723, (1994).

214. H. Ban, J. L Schaefer, and J.M. Stencel, Fuel, **76**, 801-805, (1996).

215. B. K. Gullett, B. Ghorishi, R. Keeney, and F. E. Huggins, Mercuric chloride capture by alkaline sorbents, **Proceedings, Air & Waste Management Association 93rd. Annual Meeting (Salt Lake City, UT),** Paper 259, CD-ROM, (2000).

216. F. E. Huggins, Nora Yap, G. P. Huffman, and J. K. Neathery, *Investigation of mercury adsorption on Cherokee fly-ash using XAFS spectroscopy*, **Proceedings, Air & Waste Management Association 93rd. Annual Meeting (Salt Lake City, UT),** Paper 528, CD-ROM, (2000).

217. F. E. Huggins, informal report to Dr. Rostam-Abadi, ISGS, on S and Hg XANES analysis of various sorbents, August, 1998.

218. Clarke, L.B., and Sloss, L.L. (1992), Trace Elements, Report No. IEACR/49, IEA Coal Research, London.

219. United States Public Law 101-549, Amendments to the Clean Air Act (1990), 101st Congress, 104 Statutes Part 4, 2399-2712.

220. Nraigu, J.O., and Pacyna, J.M. (1988), "Quantitative assessment of worldwide contamination of air, water, and soils by trace metals," Nature **333**, 134-139.

221. Nriagu, J.O. (1989), "A global assessment of natural sources of atmospheric trace metals," Nature **338**, 47-49.

222. Chow, W., Miller, M.J., and Torrens, I.M. (1994), "Pathways of trace elements in power plants: interim research results and implications," Fuel Process. Technol. **39**: 5-20.

223. Sander, B. (1993), "Measurements of trace element mass balances in coal-fired power plants equipped with different types of FGD systems," *Proceedings of the 2nd EPRI International Conference on Managing Hazardous Air Pollutants*, Washington DC, July.

224. Demir, I., Hughes, R.E., Lytle, J.M., and Ho, K.K (1997), "Atmospheric emissions of trace elements at three types of coal-fired power plants," American Chemical Society Division of Fuel Chemistry Preprints, **42**(1), 1101-1106.

225. Aunela-Tapola, A., Hatanpaa, E., Hoffren, H., Laitinen, T., Larjava, K., Rasila, P., and Tolvanen, M. (1998), "A study of trace element behaviour in two modern coal-fired power plants II: trace element balances in two plants equipped with semi-dry flue gas desulphurization facilities," Fuel Process. Tech. **55**: 13-34.

226. Markowski, G.R., Ensor, D.S., Hooper, R.C., and Carr, R.C. (1980), "A submicron aerosol mode in flue gas from a pulverized coal utility boiler," Environ. Sci. Tech. **14**(11), 1400-1402.

227. James, W.D., and Acevedo, L.E. (1993), "Trace element partitioning in Texas lignite combustion," J. Radioanalytical and Nuc. Chem. **171**(2): 287-302.

228. Vassilev, S.V. (1994), "Trace elements in solid waste products from coal burning at some Bulgarian thermoelectric power stations," Fuel **73**(3): 367-374.

229. Bogdanovic, I., Fazinic, S., Itskos, S., Jaksic, M., Karydas, E., Katselis, V., Paradellis, T., Tadic, T., Valkovic, O., and Valkovic, V. (1995), "Trace element characterization of coal fly ash particles," Nuc. Instrum. and Methods in Phys. Res. B **99**: 402-405.

230. Smith, R.D., Campbell, J.A., and Nielson, K.K. (1980), "Volatility of fly ash and coal," Fuel **59**: 661-665.

231. Biermann, A.H., and Ondov, J.M. (1980), "Application of surface deposition models to size-fractionated fly ash," Atmospheric Environment **14**: 289-295.

232. Tumati, P.S., and Devito, M.S. (1991), "Retention of condensed/solid phase trace elements in an electrostatic precipitator," *Proceedings of the 1st EPRI International Conference on Managing Hazardous Air Pollutants: State of the Art*, Washington DC, November.

233. Linak, W.P., and Peterson, T.W. (1986), "Mechanisms governing the composition and size distribution of ash aerosol in a laboratory pulverized coal combustor," *Proc. of the 21st Symposium (Int'l) on Combustion*, The Combustion Institute, Pittsburgh, pp. 399-410.

234. Quann, R.J., Neville, M., and Sarofim, A.F. (1990), "A laboratory study of the effect of coal selection on the amount and composition of combustion generated submicron particles," Combust. Sci. Tech. **74**: 245-265.

235. Neville, M., and Sarofim, A.F. (1982), "The stratified composition of inorganic submicron particles produced during coal combustion," *Proc. of the 19th Symposium (Int'l) on Combustion*, The Combustion Institute, Pittsburgh, pp. 1441-1449.

236. U.S. Environmental Protection Agency (1996), Study of Hazardous Air Pollutant Emissions from Electric Utility Steam Generating Units: Interim Final Report, Volume 1, EPA Report Number EPA-453/R-96-013a.

237. U.S. Environmental Protection Agency (1998), Study of Hazardous Air Pollutant Emissions from Electric Utility Steam Generating Units: Final Report, Executive Summary, Report to Congress, February.

238. Brooks, G. (1989), "Estimating air toxic emissions from coal and oil combustion sources," Radian Corporation Report to the U.S. Environmental Protection Agency, EPA Report No. EPA-450/2-89-001.

239. Szpunar, C.B. (1993), "Projections of air toxic emissions from coal-fired utility combustion: input for hazardous air pollutant regulators," *Proceedings of the 2nd EPRI International Conference on Managing Hazardous Air Pollutants*, Washington DC, July.

240. Rubin, E.S., Berkenpass, M.B., Frey, H.C., and Toole-O'Neill, B. (1993), "Modeling the uncertainty in hazardous air pollutant emissions," *Proceedings of the 2nd EPRI International Conference on Managing Hazardous Air Pollutants*, Washington DC, July.

241. Meserole, F.B., and Chow, W. (1991), "Controlling trace species in the utility industry," *Proceedings of the 1st EPRI International Conference on Managing Hazardous Air Pollutants: State of the Art*, Washington DC, November.

242. Rizeq, R.G., Hansell, D.W., and Seeker, W.R. (1994), "Predictions of metals emissions and partitioning in coal-fired combustion systems," Fuel Processing Tech. **39**: 219-236.

243. Zeng, T. (1998), "Transformation of iron and trace elements during coal combustion," Sc.D. Thesis, Department of Mechanical Engineering, Massachusetts Institute of Technology, Cambridge MA, March.

244. Baxter, L.L., and Mitchell, R.E. (1992), "The release of iron during the combustion of Illinois No. 6 coal," Combust. Flame **88**, 1-14.

245. Electric Power Research Institute (1994), Electric Utility Trace Substances Synthesis Report, Report No. EPRI TR-104614, Project 3081.

246. Helble, J.J., Srinivasachar, S., and Boni, A.A. (1990), "Factors influencing the transformation of minerals during pulverized coal combustion," Progr. in Energy and Combust. Sci. **16**:4, 267-280 (1990).

247. Barton, R.G., Clark, W.D., and Seeker, W.R. (1990), "Fate of metals in waste combustion systems," Combust. Sci. Technol. **74**(6), 327-342.

248. Wilemski, G., and Srinivasachar, S. (1994), "Prediction of ash formation in pulverized coal combustion with mineral distribution and char fragmentation models," in The Impacty of Ash Deposition on Coal Fired Plants, J. Williamson and F. Wigley, eds., Taylor and Francis Publishers, London, pp. 151-164.

249. Lind, T. (1996). Ash particle size distributions and electrostatic precipitator penetration data obtained in field measurements were generously provided by Ms. Terttaliisa Lind of the Aerosol Technology Group, VTT, Espoo Finland. Samples were obtained during 1994 measurements at the facility described by Mohr et al., (1996).

250. Schulz, E.J., Engdahl, R.B., and Frankenberg, T.T. (1975), "Submicron particles from a pulverized coal fired boiler," Atmospheric Environment **9**: 111-119.

251. Schmidt, E.W., Gieseke, J.A., and Allen, J.M. (1976), "Size distribution of fine particulate emissions from a coal-fired power plant," Atmospheric Environment **10**: 1065-1069.

252. Mohr, M., Ylatalo, S., Klippel, N., Kauppinen, E.I., Riccius, O., and Burtscher, H. (1996), "Submicron fly ash penetration through electrostatic precipitators at two coal power plants," Aerosol Sci. Tech. **24**: 191-204.

253. Ylatalo, S.I., and Hautanen, J. (1998), "Electrostatic precipitator penetration function for pulverized coal combustion," Aerosol Sci. Tech. **29** 17-30.

254. Ensor, D.S., Markowski, G., Woffinden, G., Legg, R., Cowen, S., Murphy, M., Shendrikar, A.D., Pearson, R., and Scheck, R. (1983), "Evaluation of electrostatic precipitator performance at San Juan Unit number 1," Final Report submitted to the Electric Power Research Institute, report number EPRI CS-3252, Project 780-1.

255. Orr, D (1996), Radian Corporation compiled database. Original data taken from Evans, J.C., Abel, K.H., Olsen, K.B., Lepel, E.A., Sanders, R.W., Wilkerson, C.L., and Hayes, D.J. (1985), "Characterization of trace constituents at Canadian coal-fired plants. Phase I – Final Report, Appendices H to K (data)," Battelle Pacific Northwest Laboratories report to the Canadian Electrical Association.

256. Wendt, J.O.L., Davis, S.D., Gale, T.K., and Seames, W.S. (1998), "Formation and control of semi-volatile toxic metals in combustion processes," Proc. 12th Members Conference, International Flame Research Foundation, Noordwijkerhout, The Netherlands, May.

257. Pai, P., Karamchandani, P., and Seigneur, C. "Uncertainties in Modeling Long-Range Transport and Fate of Mercury Emissions in North America," presented at EPRI Managing Hazardous Air Pollutants, Fourth International Conference, Washington, DC, November 12-14, 1997.

258. Sarofim, A.F., Senior, C.L., and Helble, J.J., "Emissions of Mercury, Trace Elements, and Fine Particles from Stationary Combustion Sources," Fuel. Proc. Technol., 2000, **65-66**, 263-288.

259. Helble, J.J. and Mamani-Paco, R.S., "Bench Scale Examination of Mercury Oxidation Under Non-isothermal, Post-combustion Conditions," presented at the Air and Waste Management Association Annual Meeting, Salt Lake City, Utah, June 18-22, 2000.

260. Ghorishi, S.B., "Fundamentals of Mercury Speciation and Control in Coal-Fired Boilers," EPA-600/R-98-014, February 1998.

261. Carey, T.R., Hargrove, O.W., Richardson, C.F., Chang, R., and Meserole, F.B., "Factors Affecting Mercury Control in Utility Flue Gas Using Activated Carbon," J. Air & Waste Manage. Assoc., 1998, **48,** 1166-1164.

262. Miller, E.S., Dunham, S.J., Olson, and Brown, T.D., "Mercury Sorbent Development for Coal-Fired Boilers," paper presented at the Conference on Air Quality, McLean, VA, December 1-4, 1998.

263. Fahlke, J. And Bursik, A. "Impact of the State-of-the-Art Flue Gas Cleaning on Mercury Species Emissions from Coal-Fired Steam Generators," Water, Air, Soil Poll. 1995, **80**, 209-215.

264. Senior, C.L., "Predicting the Speciation of Mercury Emissions from Coal-Fired Power Plants," presented at the Conference on Air Quality II, McLean, Virginia, September 19-21, 2000.

265. DeVito, M.S and Rosenhoover, W.A., "Flue Gas Mercury and Speciation Studies at Coal-Fired Utilities Equipped with Wet Scrubbers," presented at 15th International Pittsburgh Coal Conference, Pittsburgh, PA, September 15-17, 1998.

266. Butz, J., Smith, J., Grover, C., Haythornthwaite, S., Fox, M., Hunt, T., Chang, R., and Brown, T.D., "Coal Fly Ash as a Sorbent for Mercury," Proceedings of the Mercury in the Environment Specialty Conference, Air & Waste Management Association, Minneapolis, MN, September 15-17, 1999.

267. Li, Z. and Hwang, J.-Y., "Mercury Distribution in Fly Ash Components," Paper WP72B.05 presented at the Air &Waste Management Association 90th Annual Meeting, Toronto, Ontario, Canada, June 8-13, 1997.

268. Amrhein, G.T., Holmes, M.J., Bailey, R.T., Kudlac, G.A., Downs, W., and Madden, D.A., *Advanced Emissions Control Development Program*, Phase III-Approved Final Report, DOE Contract DE-FC22-94PC94251, July 1999.

269. Norton, G.A., Yang, H., Brown, R.C., Laudal, D.L., Dunham, G.E., and Okoh, J.M., "Effects of Fly Ash on Mercury Oxidation in Simulated Flue Gas Environments," paper presented at the Air & Waste Management Association 93rd Annual Conference and Exhibition, Salt Lake City, UT, June 19-22, 2000.

270. Chu, P., "Total and Speciated Mercury Emissions from U.S. Coal-Fired Power Plants," presented at the Conference on Air Quality II, McLean, Virginia, September 19-21, 2000.

271. Mims, C.A., Neville, M., Quann, R.J. and Sarofim, A.F. "Laboratory Studies of Trace Element Transformations During Coal Combustion," Presented at 87th AIChE Meeting, Boston, MA 1979.

272. Panagiotou, T. and Levendis, Y. " Observations on the Combustion of Polymers (Plastics): from Single Particles to Groups of Particles". Combust. Sci. and Tech., **137**:121-147, 1998.

273. Levendis, Y., Atal, A., Courtemance, B. and Carlson, J.B." Burning Characteristics and Gaseous/Solid Emissions of Blends of Pulverized Coal with Waste Tire-Derived Fuel". Combust. Sci. and Tech., **131**:147-185, 1998.

274. Lawless, P. A. and C.E. Rodes (1999), "Maximizing Data Quality in the Gravimetric Analysis of Personal Exposure Sample Filters", J. of the Air & Waste Management Assoc., **49**:1039-1049.

275. Laul, J.C. (1979), "Neutron Activation analysis of geological materials", Atomic Energy Rev., **17**:603-695.

APPENDIX A

Phase II Coal Results

Table A-1. Coal Analysis Report - Ohio

Analyzed on: 06/17/98
Air Dry Loss……..0.00 %
Residual Moisture……..2.33 %

	As Received	Dry	Dry Ash-Free
PROXIMATE ANALYSIS D3172			
Moisture	2.33		
Ash	9.70	9.93	
Volatile Matter	39.19	40.12	44.55
Fixed Carbon	48.78	49.95	55.45
	100.00	100.00	100.00
ULTIMATE ANALYSIS D3176			
Hydrogen	5.07	4.92	5.47
Carbon	71.07	72.77	80.79
Nitrogen	1.37	1.40	1.56
Sulfur	2.62	2.68	2.98
Oxygen	10.17	8.30	9.20
Ash	9.70	9.93	
	100.00	100.00	100.00
Heating Value (btu/Lb) D1989	12865	13172	14624
FORMS OF SULFUR D2492			
Sulfate Sulfur	0.02	0.02	0.02
Pyritic Sulfur	1.39	1.42	1.58
Organic Sulfur	1.21	1.24	1.38
Free Swelling Index D720	4.0		

Ash Fusion (Reducing Atmosphere)

	Initial D.	Softening T.	Hemi T.	Fluid T.
Temp F	2130	2240	2390	2490

Table A-2. Coal Analysis Report - North Dakota

Analyzed on: 06/17/98
Air Dry Loss……..25.22 %
Residual Moisture……..14.25 %

	As Received	Dry	Dry Ash-Free
PROXIMATE ANALYSIS D3172			
Moisture	35.88		
Ash	9.38	14.64	
Volatile Matter	28.15	43.90	51.42
Fixed Carbon	26.59	41.46	48.58
	100.00	100.00	100.00
ULTIMATE ANALYSIS D3176			
Hydrogen	6.59	4.02	4.71
Carbon	38.57	60.15	70.46
Nitrogen	0.42	0.65	0.77
Sulfur	0.63	0.98	1.15
Oxygen	44.41	19.56	22.91
Ash	9.38	14.64	
	100.00	100.00	100.00
Heating Value (btu/Lb) D1989	6392	9969	11678
FORMS OF SULFUR D2492			
Sulfate Sulfur	0.09	0.14	0.16
Pyritic Sulfur	0.18	0.28	0.33
Organic Sulfur	0.36	0.56	0.66
Free Swelling Index D720	0.0		

Ash Fusion (Reducing Atmosphere)

	Initial D.	Softening T.	Hemi T.	Fluid T.
Temp F	2050	2070	2090	2110

Table A-3. Coal Analysis Report - Wyodak

Analyzed on: 10/06/98

	As Received	Dry	Dry Ash-Free	
PROXIMATE ANALYSIS D3172				
Moisture	25.81			
Ash	6.03	8.13		
Volatile Matter	34.85	46.97	51.13	
Fixed Carbon	33.31	44.90	48.87	
	100.00	100.00	100.00	
ULTIMATE ANALYSIS D3176				
Hydrogen	6.51	4.88	5.31	
Carbon	51.19	69.00		80.10
Nitrogen	0.72	0.97	1.06	
Sulfur	0.32	0.43	0.47	
Oxygen	35.23	16.59	18.06	
Ash	6.03	8.13		
	100.00	100.00	100.00	
Heating Value (btu/Lb) D1989	8869	11955	13013	
FORMS OF SULFUR D2492				
Sulfate Sulfur	0.01	0.01	0.01	
Pyritic Sulfur	0.04	0.05	0.06	
Organic Sulfur	0.27	1.37	0.40	
Free Swelling Index D720	0.0			

Ash Fusion (Reducing Atmosphere)

	Initial D.	Softening T.	Hemi T.	Fluid T.
Temp F	2100	2120	2140	2230

APPENDIX B

Composition and Analyses of Phase I Coals

Table B-1. Coal Properties Phase I Program Coals

	Elkhorn/Hazard		Pittsburgh		Illinois No. 6		Wyodak	
	Dry Basis	**As Received**	**Dry Basis**	**As Received**	**Dry Basis**	**As Received**	**Dry Basis**	**As Received**
Proximate (wt %):								
Fixed Carbon	57.80	56.46	62.23	61.99	54.98	53.16	49.62	43.14
Volatile Matter	34.61	33.80	30.66	30.22	34.41	33.27	41.91	36.44
Moisture	0.00	2.33	0.00	1.44	0.00	3.31	0.00	13.06
Ash	7.59	7.41	7.11	7.01	10.61	10.26	8.47	7.36
Ultimate (wt %):								
Carbon	76.66	74.87	77.74	76.62	70.02	67.70	61.19	53.20
Hydrogen	4.70	4.59	4.87	4.80	4.89	4.73	5.28	4.59
Nitrogen	1.46	1.43	1.50	1.48	1.22	1.18	0.95	0.83
Sulfur	0.84	0.82	1.66	1.64	3.72	3.60	0.25	0.22
Oxygen	8.58	8.38	7.01	6.91	9.50	9.20	23.86	20.74
Chlorine	0.17	0.17	0.099	0.098	0.035	0.034	**	**
Moisture	0.00	2.33	0.00	1.44	0.00	3.31	0.00	13.06
Ash	7.59	7.41	7.11	7.01	10.61	10.26	8.47	7.36
Ash Composition (wt%):								
SiO_2	55.83		42.92		44.38		31.76	
Al_2O_3	34.27		22.87		17.35		18.04	
Fe_2O_3	5.18		19.18		19.80		5.81	
TiO_2	1.71		1.08		0.91		1.80	
CaO	1.84		4.51		4.00		24.35	
MgO	0.60		0.97		0.85		2.61	
Na_2O	0.32		1.28		0.63		0.90	
K_2O	1.53		1.21		1.80		0.70	
SO_3	1.45		5.40		4.62		12.93	
P_2O_5	0.23		0.57		0.12		1.10	

Table B-2. Forms of Sulfur in Phase I Program Coals

	Elkhorn/Hazard		**Pittsburgh**		**Illinois No. 6**		**Wyodak**	
Sulfur (wt%, dry basis)	0.87		2.12		3.82		0.46	
Forms of sulfur:	Wt % in Coal (Dry Basis)	Percent of Total Sulfur	Wt % in Coal (Dry Basis)	Percent of Total Sulfur	Wt % in Coal (Dry Basis)	Percent of Total Sulfur	Wt % in Coal (Dry Basis)	Percent of Total Sulfur
Sulfate	0.03	3.4	0.01	0.5	0.04	1.0	0.02	4.3
Pyritic	0.12	13.8	0.91	42.9	1.57	41.1	0.03	6.5
Organic	0.72	82.8	1.2	56.6	2.21	57.9	0.41	89.1

Table B-3. Chemical Analyses of Phase I Coals by NAA

Element	Pittsburgh Concentration (ppm)	Elkhorn/Hazard Concentration (ppm)	Illinois No. 6 Concentration (ppm)	Wyodak Concentration (ppm)
Na	600	340	400	710
Sc	1.8	3.9	2.2	1.8
Cr	13	20	14	7
Fe	8220	2970	13700	2700
Co	2.5	6.2	.6	1.7
Zn	17	18	70	33
As	4.1	4	2.7	1.3
Se	0.62	3.1	2.2	1.6
Br	17	25	3.7	2.4
Rb	8	5.1	13	3.6
Sr	160	120	ND	ND
Mo	0.85	4	4.9	1.7
Cd	0.06	0.31	0.15	0.30
Sb	0.26	1	0.38	0.23
Cs	0.55	0.45	0.99	0.26
Ba	110	130	52	370
La	4.5	14	4.7	4.9
Ce	8.8	27	9.3	8.7
Sm	0.78	2.5	0.9	0.71
Eu	0.2	0.37	0.19	0.18
Yb	0.38	1.4	0.032	0.35
Lu	0.063	0.24	0.0054	0.057
Hf	0.44	1.1	0.056	ND
Au (in ppb)	0.95	0.98	0.51	1.1
Hg	0.11	0.13	0.22	0.19
Th	1.2	4.3	0.095	1.7
U	0.31	1.9	ND	ND

APPENDIX C

Comparison of Whole Coal Elemental Compositions for Original and Blind Replicate Analyses

Table C-1. Comparison of Whole Coal Elemental Results for Original and Blind Replicate Analyses (Only Analyses Done by the Same Method Are Compared)

	Replicate	Original	Replicate	Original	Replicate	Original
Element	**OHIO**	**OHIO**	**WYODAK**	**WYODAK**	**ND**	**ND**
Li	11	9.5	3.7	3.2	5.1	4.6
Be	2.6	2.6	0.3	0.3	0.8	0.8
B	86	100	42	56	130	160
Na	280	270	860	910	3800	3900
Mg	340	360	1900	2000	4000	4500
Al	9100	10000	7400	6500	9000	8900
Si	19000	19000	13000	8200	25000	21000
P	270	290	570	570	170	160
Ca	1100	1000	11000	10000	15000	16000
Ti	580	600	670	530	410	400
V	25	24	18	18	15	16
Mn	20	20	8.2	8.5	59	62
Ni	18	21	4.8	5.8	4.3	5.5
Cu	9.6	7.4	14	13	5.5	4.0
Zn	21	22	8.2	7.9	12	12
Ga	6.0	5.5	2.5	2.1	2.3	2.5
Ge	9.8	10	0.37	0.34	1.3	1.6
Sr	100	97	260	280	420	430
Y	9.7	9.7	3.5	3.5	4.8	4.9
Zr	14	19	18	15	26	28
Nb	3.0	3.4	2.8	2.9	3.1	2.7
Mo	4.9	3.2	1.1	0.65	2.3	1.4
Ag	<0.2	0.1	<0.2	<0.1	<0.3	-0.2
Cd	0.1	0.078	0.1	0.084	<0.1	0.072
Sn	1.0	1.4	<0.9	0.35	<1.5	0.78
Te	<0.2	0.045	<0.2	0.13	<0.3	0.10
Ba	66	71	450	430	590	560
Au	<1.0	<1.0	<0.9	<1.0	<1.5	-2.0
Hg	0.18	0.15	0.13	0.09	0.08	0.09
Tl	1.3	1.2	<0.2	0.1	<0.3	0.11
Pb	9.1	8.1	1.9	1.5	1.5	1.6
Bi	<0.2	0.1	<0.2	0.074	<0.3	0.087

APPENDIX D

CCSEM Mineral Compositions of Phase II Coals

Table D-1. Coal Minerals in Wyodak Coal

#	Mineral Species	Na	Mg	Al	Si	P	S	Cl	K	Ca	Ti	Fe	Wt %
453	Quartz	0	0	0	99	0	0	0	0	0	0	0	37.9
227	Kaolinite	0	0	49	50	0	0	0	0	1	0	0	20.1
15	Illite	0	0	33	58	0	0	0	7	1	0	1	1.2
1	K-Feldspar	0	0	19	54	0	0	0	27	0	0	0	0
9	Montmorillonite	0	0	23	66	0	2	0	0	7	2	0	0.6
215	Misc. Silicates	0	0	32	60	0	1	0	1	3	1	0	15.1
18	Pyrite	0	0	0	0	0	65	0	0	0	0	34	2.4
2	Ferrous Sulfate	0	0	0	0	0	46	0	0	0	0	54	0.2
2	Gypsum	0	0	0	0	0	47	0	0	53	0	0	0.3
3	Chalcopyrite	0	0	0	1	0	48	0	0	2	0	32	0.6
27	Misc. sulf.	0	0	2	1	0	52	0	1	11	11	16	1.9
80	Misc. Phosphate	0	0	39	1	28	1	0	0	29	1	0	8.6
11	Fe-rich	0	1	0	1	0	0	0	0	2	0	96	1.8
8	Mixed Carbonate	0	1	4	6	5	2	0	0	38	0	44	0.4
12	Ti-rich	0	0	2	5	0	2	0	0	7	73	0	1.3
1	Quartz-Sulfate	8	0	0	37	0	37	0	0	0	18	0	0
1	Alumina-rich	0	0	100	0	0	0	0	0	0	0	0	0.2
97	Misc. Mixed	0	0	32	23	12	5	0	0	24	2	1	7.4
1182	Grand Totals	0	0	21	60	3	4	0	0	6	2	3	100

Table D-2. Coal Minerals in North Dakota Lignite

#	Mineral Species	Na	Mg	Al	Si	P	S	Cl	K	Ca	Ti	Fe	Wt %
305	Quartz	0	0	1	99	0	0	0	0	0	0	0	24.4
33	Kaolinite	0	0	47	50	0	1	0	0	1	0	0	1.7
138	Illite	0	1	30	56	0	0	0	10	1	0	2	12.6
11	K-Feldspar	0	0	18	60	0	1	0	20	1	0	0	0.7
72	Montmorillonite	4	0	23	65	0	1	0	0	5	0	1	5.8
284	Misc. Silicates	0	2	21	65	0	1	0	3	3	0	6	21.9
1	Elem. Sulfur	0	0	0	0	3	97	0	0	0	0	0	0
45	Pyrite	0	0	0	0	0	66	0	0	0	0	33	9.6
3	Ferrous Sulfate	0	0	1	3	0	50	0	0	1	0	45	0.2
2	Jarosite	2	0	0	0	0	41	0	13	0	0	44	0.1
58	Gypsum	0	0	0	1	0	50	0	0	49	0	0	5.1
60	Misc. Sulf.	1	0	1	3	0	48	0	0	15	17	12	5.9
2	Misc. Phosphate	4	1	0	31	38	3	3	6	9	0	1	0.2
10	Fe-Rich	0	0	1	1	0	1	0	0	1	0	96	0.7
5	Calcite	0	0	0	0	0	0	0	0	100	0	0	0.7
24	Mixed Carbonate	0	3	2	3	0	8	1	0	32	0	48	2.2
2	Ti-Rich	0	1	0	12	0	0	0	0	5	76	0	0.1
2	Quartz-Sulfate	0	0	5	50	0	25	1	0	15	1	2	0.1
2	Sil-Sulf	0	0	18	40	0	23	0	0	14	3	2	0.1
1	Silicate-Pyrite	0	0	11	29	0	26	0	2	0	0	32	0
1	Alumina-Rich	0	0	95	0	0	5	0	0	0	0	0	0
139	Misc. Mixed	1	2	19	35	0	11	0	1	23	1	6	7.9
1200	Grand Totals	1	1	12	54	0	13	0	2	8	1	8	100

Table D-3. Coal Minerals in Ohio Coal

#	Mineral Species	Na	Mg	Al	Si	P	S	Cl	K	Ca	Ti	Fe	Wt %
157	Quartz	0	0	0	99	0	0	0	0	0	0	0	10.4
152	Kaolinite	0	0	47	50	0	1	0	1	0	0	0	8.4
210	Illite	0	0	37	52	0	1	0	9	0	0	1	16
2	K-Feldspar	0	0	20	59	0	0	0	20	0	0	0	0.3
1	Chlorite	0	0	28	29	0	0	2	0	0	0	42	0
1	Montmorillonite	4	0	14	72	0	9	0	0	0	0	0	0
257	Misc. Silicates	0	0	35	59	0	2	0	2	0	0	1	16.5
296	Pyrite	0	0	0	0	0	67	0	0	0	0	33	39.3
5	Ferrous Sulfate	0	0	0	0	0	52	0	0	0	0	47	0.2
1	Jarosite	6	0	5	2	0	36	3	0	0	0	47	0
4	Gypsum	0	0	0	0	0	49	0	0	50	0	1	0.1
32	Misc. Sulf.	0	0	1	1	0	65	0	0	0	0	32	1.8
8	Apatite	0	0	1	1	33	0	0	0	65	0	0	0.5
9	Misc. Phosphate	0	0	12	7	32	2	0	0	45	0	1	0.4
10	Fe-Rich	0	0	0	0	0	1	1	0	0	0	97	2.2
2	Calcite	0	0	0	0	0	0	0	0	100	0	0	0.3
1	Dolomite	0	34	0	0	0	0	0	0	66	0	0	0.1
11	Mixed Carbonate	0	0	2	2	0	10	0	0	46	0	39	0.5
3	Ti-Rich	0	0	2	2	0	1	0	0	0	82	0	0.2
1	Trace-Rich	0	0	0	0	0	0	0	0	3	0	0	0
1	Quartz-Sulfate	0	0	7	60	0	27	0	2	0	0	4	0
4	Quartz-Pyrite	0	0	4	43	0	33	0	0	0	0	20	1
4	Sil-Sulf	0	1	33	32	0	26	0	0	3	0	4	0.1
3	Silicate-Pyrite	0	0	21	26	0	35	0	0	0	0	18	0.1
25	Misc. Mixed	1	1	20	30	3	15	2	4	11	0	12	1.3
1200	Grand Totals	0	0	16	34	0	29	0	2	1	0	17	100

APPENDIX E

Trace Metal Content of Mineral Grains by Electron Microprobe Analysis

Table E-1. Electron Microprobe Results for Pyrite in Ohio 5/6/7 Coal

No.	Pb	Se	Cu	Cd	As	Ni	Zn	Co*	Fe	S	Total	Comment	Size/Form
10	0.02	0.01	0.00	0.02	0.00	0.00	0.00	0.05	47.34	53.04	100.48	OhioB1.1	30
11	0.00	0.00	0.00	0.01	0.00	0.00	0.00	0.05	42.22	52.38	94.65	OhioB1.2	subhedral
13	0.00	0.00	0.05	0.03	0.07	0.13	0.00	0.06	44.40	50.13	94.86	OhioB3.1	10x25
14	0.06	0.01	0.03	0.01	0.16	0.24	0.00	0.06	44.05	50.01	94.63	OhioB3.2	subhedral
15	0.00	0.02	0.00	0.00	0.00	0.01	0.00	0.05	46.99	52.94	100.01	OhioB41	80x80
16	0.00	0.00	0.00	0.00	0.07	0.02	0.00	0.06	47.08	51.81	99.04	OhioB4.2	subhedral
18	0.00	0.00	0.00	0.01	0.11	0.01	0.00	0.05	47.19	51.83	99.19	OhioB4.4	
19	0.00	0.00	0.00	0.01	0.04	0.01	0.00	0.06	47.35	51.88	99.35	OhioB4.5	
20	0.01	0.01	0.00	0.03	0.00	0.00	0.00	0.05	46.81	52.75	99.66	OhioB5.1	90x90
21	0.00	0.01	0.00	0.02	0.00	0.00	0.01	0.04	46.67	53.32	100.07	OhioB5.2	round
22	0.02	0.02	0.02	0.02	0.00	0.00	0.00	0.07	46.08	53.06	99.29	OhioB5.3	
23	0.10	0.02	0.02	0.04	0.00	0.00	0.00	0.04	45.82	51.73	97.76	OhioB5.4	
24	0.03	0.01	0.00	0.01	0.01	0.00	0.00	0.05	46.51	51.18	97.80	OhioB6.1	35x120
25	0.00	0.02	0.00	0.04	0.01	0.00	0.00	0.05	46.75	51.17	98.03	OhioB6.2	subhedral
26	0.00	0.01	0.01	0.01	0.02	0.01	0.00	0.05	46.49	52.00	98.60	OhioB6.3	
27	0.04	0.00	0.03	0.04	0.35	0.03	0.00	0.05	45.54	50.62	96.70	OhioB7.1	60x60
28	0.04	0.00	0.01	0.04	0.01	0.03	0.01	0.04	46.22	50.24	96.65	OhioB7.2	round
29	0.03	0.00	0.01	0.01	0.30	0.05	0.00	0.06	45.82	49.33	95.60	OhioB7.3	
30	0.02	0.00	0.01	0.00	0.04	0.05	0.00	0.06	46.30	50.30	96.78	OhioB7.4	
39	0.00	0.00	0.01	0.00	0.02	0.00	0.00	0.05	47.54	51.80	99.43	OhioB10.1	120x170
40	0.00	0.01	0.04	0.01	0.04	0.06	0.00	0.06	47.07	51.90	99.17	OhioB10.2	subhedral
41	0.00	0.00	0.04	0.03	0.02	0.04	0.00	0.05	47.37	51.59	99.13	OhioB10.3	
42	0.03	0.00	0.00	0.00	0.01	0.00	0.00	0.06	47.39	51.41	98.90	OhioB10.4	
43	0.01	0.00	0.03	0.03	0.04	0.03	0.01	0.05	46.78	51.55	98.52	OhioB10.5	
44	0.00	0.01	0.03	0.01	0.04	0.01	0.00	0.05	45.44	49.55	95.14	OhioB11.1	70x190
45	0.00	0.02	0.03	0.03	0.03	0.00	0.00	0.05	45.22	50.02	95.39	OhioB11.2	oval
46	0.01	0.00	0.04	0.00	0.03	0.01	0.01	0.06	45.20	49.26	94.63	OhioB11.3	
47	0.00	0.02	0.03	0.03	0.04	0.00	0.00	0.05	46.13	50.41	96.70	OhioB11.4	
48	0.01	0.02	0.00	0.03	0.03	0.01	0.00	0.05	46.82	51.76	98.73	OhioB11.5	
No.	**Pb**	**Se**	**Cu**	**Cd**	**As**	**Ni**	**Zn**	**Co***	**Fe**	**S**	**Total**	**Comment**	**Size/Form**
49	0.00	0.00	0.00	0.01	0.01	0.00	0.00	0.06	46.89	51.24	98.22	OhioB12.1	70x120
50	0.00	0.00	0.00	0.03	0.02	0.00	0.00	0.05	46.79	51.02	97.90	OhioB12.2	subhedral
51	0.00	0.00	0.00	0.02	0.01	0.00	0.00	0.06	46.72	50.85	97.67	OhioB12.3	
52	0.00	0.00	0.00	0.02	0.07	0.06	0.00	0.06	46.46	50.93	97.60	OhioB12.4	
53	0.01	0.00	0.00	0.00	0.00	0.00	0.00	0.04	46.15	51.12	97.32	OhioB12.5	

No.	Pb	Se	Cu	Cd	As	Ni	Zn	Co*	Fe	S	Total	Comment	Size/Form
54	0.04	0.00	0.01	0.01	0.11	0.01	0.00	0.03	45.97	50.39	96.58	OhioB13.1	50x60
55	0.03	0.01	0.00	0.02	0.17	0.01	0.00	0.06	45.43	50.63	96.35	OhioB13.2	irregular
10	0.02	0.00	0.00	0.01	0.02	0.00	0.00	0.04	46.75	55.25	102.09	OhioA1.1	35x80
11	0.02	0.01	0.00	0.01	0.02	0.00	0.01	0.06	46.45	55.64	102.21	OhioA1.2	subhedral
12	0.01	0.01	0.00	0.02	1.79	0.00	0.00	0.06	47.20	53.43	102.51	OhioA1.3	
13	0.00	0.00	0.01	0.01	1.54	0.00	0.00	0.06	46.81	54.69	103.13	OhioA1.4	
14	0.01	0.00	0.00	0.01	1.74	0.02	0.00	0.08	46.92	53.16	101.93	OhioA1.5	
15	0.02	0.01	0.00	0.01	0.00	0.00	0.02	0.06	47.50	55.85	103.46	OhioA2.1	35x60
16	0.00	0.00	0.00	0.02	0.00	0.00	0.01	0.05	47.82	54.72	102.62	OhioA2.2	composite
17	0.01	0.00	0.02	0.00	0.00	0.00	0.00	0.05	46.86	54.59	101.53	OhioA2.3	subhedral
18	0.00	0.00	0.00	0.02	0.00	0.00	0.00	0.04	47.49	55.32	102.86	OhioA2.4	
19	0.02	0.02	0.01	0.01	0.00	0.00	0.00	0.05	46.70	54.52	101.32	OhioA2.5	
20	0.01	0.00	0.01	0.00	0.05	0.03	0.00	0.05	45.75	52.53	98.42	OhioA3.1	50x100
21	0.01	0.00	0.00	0.01	0.04	0.02	0.00	0.06	44.79	50.96	95.88	OhioA3.2	composite
22	0.02	0.00	0.00	0.00	0.04	0.05	0.01	0.06	45.40	52.64	98.24	OhioA3.3	zoned
23	0.02	0.01	0.00	0.02	0.01	0.00	0.01	0.05	43.82	50.81	94.74	OhioA3.4	subhedral
24	0.02	0.00	0.00	0.00	0.03	0.00	0.00	0.05	44.43	51.33	95.86	OhioA3.5	
25	0.04	0.01	0.00	0.01	0.00	0.01	0.00	0.06	46.87	55.71	102.71	OhioA3.6	
26	0.03	0.00	0.01	0.01	0.00	0.00	0.00	0.04	46.79	53.26	100.13	OhioA4.1	45
27	0.00	0.00	0.01	0.00	0.00	0.01	0.01	0.06	47.92	54.57	102.56	OhioA4.2	framboid?
28	0.01	0.02	0.01	0.00	0.00	0.01	0.00	0.05	46.39	53.47	99.95	OhioA4.3	
29	0.00	0.00	0.01	0.02	0.05	0.00	0.00	0.05	46.71	54.11	100.95	OhioA5.1	45x60
30	0.00	0.00	0.01	0.00	0.04	0.01	0.00	0.05	46.38	54.83	101.32	OhioA5.2	zoned
31	0.00	0.03	0.00	0.01	0.04	0.01	0.00	0.05	46.85	54.66	101.64	OhioA5.3	subhedral
32	0.01	0.00	0.00	0.01	0.23	0.01	0.00	0.04	46.72	54.56	101.58	OhioA5.4	
33	0.00	0.00	0.02	0.02	0.00	0.01	0.00	0.05	46.72	53.89	100.71	OhioA5.5	
No.	**Pb**	**Se**	**Cu**	**Cd**	**As**	**Ni**	**Zn**	**Co***	**Fe**	**S**	**Total**	**Comment**	**Size/Form**
34	0.00	0.00	0.00	0.01	0.01	0.07	0.01	0.06	46.02	53.67	99.83	OhioA6.1	100x110
35	0.00	0.01	0.00	0.00	0.02	0.01	0.00	0.04	45.60	54.05	99.72	OhioA6.2	subhedral
36	0.00	0.01	0.00	0.01	0.05	0.01	0.02	0.04	46.67	54.50	101.32	OhioA6.3	
37	0.00	0.00	0.00	0.00	0.00	0.02	0.01	0.06	46.30	53.92	100.30	OhioA6.4	
38	0.00	0.00	0.01	0.01	0.01	0.00	0.01	0.05	46.94	54.35	101.37	OhioA6.5	
39	0.01	0.00	0.01	0.01	0.02	0.06	0.00	0.05	46.34	54.58	101.07	OhioA6.6	
40	0.00	0.03	0.19	0.01	0.00	0.03	0.02	0.04	45.47	55.97	101.76	OhioA7.1	25x50
41	0.01	0.01	0.16	0.03	0.00	0.01	0.02	0.05	46.38	56.14	102.80	OhioA7.2	double
42	0.01	0.02	0.20	0.02	0.00	0.04	0.03	0.05	45.64	54.81	100.81	OhioA7.3	framboid?
43	0.00	0.02	0.00	0.02	0.00	0.01	0.00	0.04	46.62	54.19	100.91	OhioA8.1	50x60
44	0.02	0.01	0.00	0.02	0.00	0.00	0.01	0.05	46.66	54.72	101.48	OhioA8.2	subhedral

No.	Pb	Se	Cu	Cd	As	Ni	Zn	Co*	Fe	S	Total	Comment	Size/Form
45	0.08	0.00	0.00	0.02	0.16	0.07	0.02	0.07	44.89	52.16	97.47	OhioA8.3	
46	0.00	0.00	0.02	0.01	0.11	0.06	0.00	0.05	46.46	53.19	99.90	OhioA8.4	
47	0.01	0.00	0.01	0.01	0.02	0.01	0.01	0.03	44.94	52.86	97.89	OhioA9.1	60x180
48	0.00	0.00	0.00	0.01	0.01	0.07	0.00	0.06	45.10	53.06	98.30	OhioA9.2	subhedral
49	0.00	0.01	0.00	0.01	0.00	0.03	0.02	0.04	46.08	52.99	99.18	OhioA9.3	
50	0.01	0.00	0.01	0.02	0.00	0.00	0.00	0.05	46.86	54.11	101.04	OhioA9.4	
51	0.00	0.00	0.01	0.03	0.00	0.01	0.00	0.05	46.87	53.56	100.53	OhioA9.5	
52	0.00	0.00	0.00	0.00	0.00	0.00	0.01	0.05	48.22	55.11	103.39	OhA10.1	80x90
53	0.00	0.01	0.01	0.00	0.00	0.05	0.00	0.05	47.68	55.48	103.28	OhA10.2	subhedral
54	0.00	0.00	0.00	0.01	0.00	0.00	0.01	0.05	46.83	54.79	101.70	OhA10.3	
55	0.01	0.01	0.00	0.01	0.06	0.03	0.00	0.05	44.64	51.77	96.57	OhA10.4	
56	0.00	0.00	0.02	0.00	0.00	0.01	0.00	0.04	47.04	53.32	100.44	OhA10.5	
57	0.00	0.00	0.00	0.01	0.10	0.00	0.00	0.05	46.74	56.08	102.99	OhA11.1	120x130
58	0.00	0.01	0.00	0.00	0.02	0.00	0.02	0.04	47.42	55.01	102.52	OhA11.2	subhedral
59	0.00	0.00	0.00	0.01	0.01	0.00	0.01	0.05	47.06	54.99	102.13	OhA11.3	
60	0.02	0.01	0.00	0.01	0.00	0.00	0.01	0.04	47.04	54.95	102.08	OhA11.4	
61	0.02	0.00	0.00	0.02	0.06	0.00	0.00	0.05	47.05	56.20	103.40	OhA11.5	
62	0.00	0.01	0.00	0.00	0.10	0.00	0.00	0.05	46.59	54.27	101.01	OhA11.6	
63	0.01	0.00	0.15	0.01	0.08	0.20	0.01	0.05	45.67	53.64	99.81	OhA12.1	120x120
64	0.01	0.00	0.14	0.01	0.10	0.20	0.00	0.05	45.99	53.32	99.81	OhA12.2	subhedral
65	0.03	0.00	0.11	0.02	0.11	0.21	0.00	0.03	45.96	53.16	99.63	OhA12.3	
66	0.00	0.00	0.15	0.02	0.11	0.29	0.00	0.06	45.61	53.04	99.28	OhA12.4	
No.	**Pb**	**Se**	**Cu**	**Cd**	**As**	**Ni**	**Zn**	**Co***	**Fe**	**S**	**Total**	**Comment**	**Size/Form**
67	0.00	0.00	0.04	0.02	0.00	0.02	0.00	0.05	45.86	55.17	101.15	OhA13.1	175x150
68	0.00	0.00	0.06	0.01	0.00	0.01	0.00	0.05	47.10	56.27	103.49	OhA13.2	composite
69	0.00	0.01	0.01	0.01	0.00	0.02	0.00	0.04	46.60	55.41	102.10	OhA13.3	subhedral
70	0.01	0.01	0.01	0.00	0.00	0.02	0.00	0.05	47.24	55.35	102.69	OhA13.4	
71	0.01	0.00	0.01	0.01	0.00	0.09	0.00	0.05	46.77	55.74	102.67	OhA13.5	
72	0.01	0.01	0.03	0.01	0.00	0.02	0.00	0.05	46.76	54.47	101.36	OhA13.6	
54	0.00	0.00	0.06	0.00	0.00	0.00	0.00	0.04	46.69	52.59	99.38	OH-1 1.1	190x150
55	0.00	0.01	0.04	0.00	0.03	0.00	0.01	0.06	46.47	52.06	98.68	OH-1 1.2	composite
56	0.00	0.00	0.05	0.00	0.04	0.00	0.01	0.04	45.89	51.99	98.02	OH-1 1.3	subhedral
57	0.00	0.00	0.05	0.00	0.00	0.00	0.00	0.04	45.68	51.80	97.57	OH-1 1.4	
58	0.00	0.03	0.04	0.00	0.01	0.00	0.01	0.05	42.77	52.11	95.02	OH-1 1.5	
60	0.00	0.01	0.02	0.00	0.00	0.00	0.00	0.05	47.10	52.60	99.77	OH-1 2.1	90x50
61	0.00	0.00	0.01	0.00	0.00	0.00	0.00	0.06	46.59	53.24	99.91	OH-1 2.2	subhedral
62	0.00	0.00	0.03	0.00	0.00	0.00	0.01	0.04	46.53	52.49	99.10	OH-1 2.3	
66	0.00	0.00	0.01	0.00	0.00	0.00	0.00	0.05	47.28	52.54	99.88	OH-1 4.1	140x40

No.	Pb	Se	Cu	Cd	As	Ni	Zn	Co*	Fe	S	Total	Comment	Size/Form
67	0.00	0.00	0.04	0.00	0.00	0.07	0.01	0.04	46.64	50.71	97.51	OH-1 4.2	framboid
68	0.00	0.01	0.01	0.00	0.00	0.00	0.00	0.05	47.23	52.55	99.84	OH-1 4.3	cluster
70	0.00	0.01	0.03	0.00	0.00	0.01	0.00	0.05	45.23	52.66	97.99	OH-1 4.5	
71	0.00	0.00	0.06	0.00	0.00	0.01	0.00	0.05	46.40	52.23	98.74	OH-1 4.6	
72	0.00	0.00	0.03	0.00	0.00	0.00	0.00	0.05	46.57	51.65	98.29	OH-2 1.1	170x150
73	0.00	0.00	0.02	0.00	0.00	0.00	0.00	0.04	46.06	51.99	98.12	OH-2 1.2	composite
74	0.00	0.02	0.04	0.00	0.00	0.01	0.00	0.05	46.61	51.49	98.21	OH-2 1.3	subhedral
75	0.00	0.00	0.01	0.00	0.00	0.00	0.00	0.06	43.10	52.10	95.26	OH-2 1.4	
76	0.00	0.01	0.00	0.00	0.00	0.01	0.00	0.06	47.14	51.83	99.04	OH-2 1.5	
77	0.00	0.00	0.02	0.00	0.00	0.00	0.00	0.05	47.36	52.33	99.75	OH-2 1.6	
78	0.00	0.00	0.01	0.00	0.00	0.00	0.02	0.05	45.09	51.03	96.20	OH-2 1.7	
80	0.00	0.01	0.01	0.00	0.00	0.00	0.01	0.05	45.76	52.10	97.93	OH-2 2.2	75x60
81	0.00	0.00	0.00	0.00	0.00	0.00	0.01	0.04	47.81	52.72	100.58	OH-2 2.3	subhedral
82	0.00	0.00	0.00	0.00	0.00	0.00	0.00	0.06	47.32	52.53	99.91	OH-2 2.4	
83	0.00	0.02	0.01	0.00	0.04	0.01	0.00	0.04	43.63	51.72	95.47	OH-2 5.1	150x90
84	0.00	0.02	0.01	0.00	0.00	0.00	0.00	0.05	46.49	51.34	97.90	OH-2 5.2	framboid
85	0.00	0.05	0.03	0.00	0.07	0.01	0.00	0.05	45.90	51.81	97.91	OH-2 5.3	cluster
86	0.00	0.03	0.03	0.00	0.09	0.01	0.00	0.04	45.84	51.95	97.99	OH-2 5.4	
87	0.00	0.03	0.04	0.00	0.04	0.00	0.00	0.05	44.77	51.56	96.48	OH-2 5.5	
88	0.00	0.01	0.02	0.00	0.00	0.00	0.00	0.05	46.01	50.66	96.75	OH-2 5.6	
89	0.00	0.00	0.00	0.00	0.00	0.00	0.01	0.05	47.29	50.94	98.29	OH-2 5.7	
90	0.00	0.01	0.00	0.00	0.00	0.00	0.00	0.06	46.98	52.35	99.40	OH-2 6.1	140x120
91	0.00	0.00	0.01	0.00	0.00	0.00	0.00	0.05	45.42	52.50	97.98	OH-2 6.2	composite
92	0.00	0.00	0.00	0.00	0.00	0.00	0.00	0.05	47.60	52.52	100.18	OH-2 6.3	subhedral
93	0.00	0.00	0.00	0.00	0.00	0.00	0.00	0.05	46.94	52.24	99.23	OH-2 6.4	
94	0.00	0.00	0.01	0.00	0.00	0.00	0.00	0.04	43.78	52.54	96.37	OH-2 6.5	
95	0.00	0.00	0.01	0.00	0.03	0.00	0.00	0.05	47.74	52.79	100.61	OH-2 6.6	

* Cobalt data reflect a constant background of 0.05 $\pm$ 0.02 wt.%, due to an interference with iron. Results for Co are not background-subtracted.

Detection limit for other elements is 0.01 wt. %. Grain sizes are in micrometers. Different runs are indicated by normal, italicized, and underlined analysis numbers, respectively.

Table E-2. Electron Microprobe Results for Pyrite in North Dakota Coal

No.	Pb	Se	Cu	Cd	As	Ni	Zn	Co*	Fe	S	Total	Comment	Size/Form
57	0.00	0.01	0.02	0.01	0.08	0.00	0.00	0.04	46.63	52.26	99.06	NDakA2.1	35x35
59	0.03	0.01	0.00	0.02	0.05	0.00	0.00	0.05	46.90	50.69	97.74	NDakA2.3	irregular
60	0.00	0.00	0.00	0.02	0.00	0.00	0.00	0.05	44.56	49.41	94.03	NDakA3.1	10x25
													subhedral
62	0.00	0.00	0.02	0.02	0.00	0.15	0.00	0.06	46.61	48.75	95.60	NDakA4.1	20x25
63	0.02	0.00	0.00	0.01	0.00	0.08	0.00	0.06	46.58	52.17	98.92	NDakA4.2	subhedral
64	0.00	0.00	0.00	0.00	0.01	0.01	0.03	0.05	45.42	48.47	93.98	NDakA5.1	20x20
													irregular
66	0.00	0.01	0.00	0.01	0.10	0.05	0.00	0.07	46.23	52.79	99.25	NDakA6.1	15x25
67	0.01	0.00	0.00	0.02	0.06	0.07	0.00	0.06	46.00	51.49	97.70	NDakA6.2	subhedral
68	0.05	0.00	0.00	0.02	0.00	0.00	0.00	0.05	46.29	50.50	96.92	NDakA7.1	15x20
													subhedral
70	0.00	0.01	0.00	0.04	0.07	0.00	0.00	0.05	46.91	52.08	99.15	NDakA8.1	30x50
71	0.00	0.00	0.00	0.02	0.13	0.00	0.00	0.07	46.86	50.37	97.45	NDakA8.2	irregular
72	0.00	0.01	0.01	0.03	0.14	0.00	0.00	0.05	46.41	51.59	98.25	NDakA8.3	
73	0.00	0.00	0.00	0.00	0.24	0.00	0.00	0.06	46.04	52.33	98.67	NDakA9.1	30x35
74	0.01	0.00	0.01	0.02	0.24	0.01	0.01	0.06	46.57	51.63	98.56	NDakA9.2	subhedral
75	0.00	0.00	0.00	0.02	0.24	0.00	0.00	0.05	46.34	51.82	98.47	NDakA9.3	
81	0.00	0.00	0.00	0.05	0.00	0.09	0.00	0.06	46.29	50.37	96.86	NDak11.1	60x70
83	0.00	0.01	0.00	0.01	0.00	0.11	0.00	0.06	45.64	51.06	96.89	NDak11.3	irregular
84	0.01	0.01	0.01	0.02	0.14	0.00	0.00	0.06	46.28	49.01	95.53	NDak12.1	15
													framboid
86	0.01	0.00	0.00	0.01	0.03	0.00	0.00	0.05	45.81	52.16	98.08	NDak13.2	35x40
87	0.04	0.01	0.02	0.02	0.00	0.00	0.00	0.06	46.15	50.17	96.45	NDak13.3	irregular
75	0.00	0.00	0.01	0.02	0.07	0.00	0.00	0.05	47.73	48.89	96.77	NDakB2.1	40x50
76	0.00	0.00	0.01	0.01	0.01	0.03	0.00	0.07	47.56	53.29	100.97	NDakB2.2	multiple
77	0.00	0.02	0.00	0.01	0.03	0.00	0.00	0.06	48.02	48.59	96.72	NDakB2.3	framboid
78	0.01	0.01	0.01	0.01	0.00	0.01	0.01	0.06	47.06	55.41	102.58	NDakB3.1	15x15
79	0.00	0.00	0.00	0.00	0.01	0.00	0.01	0.06	47.00	56.73	103.80	NDakB3.2	subhedral
No.	**Pb**	**Se**	**Cu**	**Cd**	**As**	**Ni**	**Zn**	**Co***	**Fe**	**S**	**Total**	**Comment**	**Size/Form**
80	0.00	0.01	0.00	0.00	0.03	0.00	0.00	0.06	44.69	52.03	96.81	NDakB4.1	40x40
81	0.00	0.03	0.02	0.00	0.03	0.01	0.01	0.04	44.75	53.36	98.25	NDakB4.2	irregular
82	0.00	0.00	0.01	0.00	0.00	0.02	0.00	0.04	46.04	54.48	100.58	NDakB4.3	
89	0.00	0.00	0.00	0.02	0.00	0.00	0.00	0.06	48.74	54.84	103.67	NDakB7.1	15x15

No.	Pb	Se	Cu	Cd	As	Ni	Zn	Co*	Fe	S	Total	Comment	Size/Form
90	0.00	0.01	0.00	0.01	0.00	0.00	0.00	0.05	47.78	56.46	104.31	NDakB7.2	subhedral
91	0.00	0.00	0.00	0.02	0.03	0.00	0.00	0.05	47.06	55.89	103.05	NDakB8.1	30x35
92	0.01	0.00	0.00	0.01	0.00	0.00	0.01	0.06	45.99	54.24	100.32	NDakB8.2	subhedral
93	0.00	0.00	0.00	0.01	0.03	0.00	0.00	0.05	46.52	54.35	100.96	NDakB8.3	
94	0.00	0.00	0.01	0.00	0.00	0.00	0.00	0.04	46.97	56.23	103.25	NDakB9.1	17x35
95	0.00	0.00	0.00	0.01	0.00	0.01	0.00	0.06	46.37	55.51	101.95	NDakB9.2	cleat?
99	0.01	0.00	0.01	0.01	0.00	0.01	0.00	0.04	47.89	47.19	95.15	NDkB10.3	35
													euhedral
100	0.02	0.00	0.02	0.01	0.01	0.01	0.00	0.05	45.86	53.62	99.59	NDkB11.1	30x60
101	0.00	0.00	0.00	0.02	0.00	0.02	0.00	0.05	47.66	54.78	102.54	NDkB11.2	irregular
104	0.01	0.00	0.00	0.03	0.00	0.01	0.00	0.05	47.66	55.81	103.57	NDkB12.1	40x40
													irregular
107	0.01	0.00	0.00	0.02	0.02	0.00	0.00	0.04	47.67	51.82	99.57	NDkB13.1	35x35
													subhedral
42	0.00	0.03	0.03	0.00	0.78	0.12	0.00	0.05	45.56	51.95	98.53	ND-2 3.1	
43	0.00	0.04	0.02	0.00	0.80	0.12	0.00	0.05	45.72	52.01	98.76	ND-2 3.2	65x40
44	0.00	0.05	0.03	0.00	0.83	0.10	0.00	0.06	46.08	51.94	99.09	ND-2 3.3	subhedral
45	0.00	0.07	0.03	0.00	0.78	0.09	0.01	0.04	45.14	51.85	98.01	ND-2 3.4	
46	0.00	0.05	0.02	0.00	0.78	0.12	0.00	0.05	45.60	52.23	98.85	ND-2 3.5	
47	0.00	0.05	0.01	0.00	0.77	0.11	0.02	0.06	45.72	52.03	98.78	ND-2 3.6	
48	0.00	0.05	0.02	0.00	0.71	0.11	0.02	0.06	45.88	52.10	98.95	ND-2 3.7	
49	0.00	0.04	0.02	0.00	0.32	0.03	0.02	0.05	46.28	52.47	99.23	ND-2 3.8	
50	0.00	0.02	0.03	0.00	0.18	0.00	0.00	0.05	46.72	52.44	99.44	ND-2 3.9	
51	0.00	0.01	0.03	0.00	0.02	0.00	0.02	0.06	47.41	52.75	100.28	ND-2 4.1	70x30
52	0.00	0.01	0.01	0.00	0.00	0.00	0.01	0.06	47.73	52.76	100.59	ND-2 4.2	subhedral
53	0.00	0.02	0.01	0.00	0.00	0.00	0.00	0.06	46.56	52.39	99.04	ND-2 4.3	

* Cobalt data reflect a constant background of 0.05 ± 0.02 wt.%, due to an interference with iron. Results for Co are not background-subtracted.

Detection limit for other elements is 0.01 wt. %. Grain sizes are in micrometers. Different runs are indicated by normal, italicized, and underlined analysis numbers, respectively.

Table E-3. Electron Microprobe Results for Pyrite in Wyodak Coal

No.	Pb	Se	Cu	Cd	As	Ni	Zn	Co	Fe	S	Total	Comment	Size/Form
88	0.06	0.04	0.17	0.04	0.15	0.07	0.01	0.06	45.26	50.21	96.06	WdakB1.1	30x40
89	0.07	0.02	0.14	0.03	0.21	0.09	0.00	0.07	44.61	49.93	95.17	WdakB1.2	framboid
90	0.07	0.06	0.17	0.02	0.18	0.09	0.00	0.07	44.17	50.70	95.52	WdakB1.3	cluster
92	0.00	0.01	0.00	0.01	0.00	0.00	0.00	0.07	47.68	52.88	100.65	Wdak2.1	30x30
94	0.00	0.00	0.01	0.02	0.01	0.00	0.01	0.07	48.04	52.63	100.78	Wdak2.3	subhedral
95	0.01	0.00	0.00	0.04	0.01	0.00	0.00	0.06	47.41	52.87	100.39	Wdak3.1	15x25
96	0.03	0.00	0.00	0.03	0.01	0.00	0.00	0.06	48.10	52.58	100.81	Wdak3.2	subhedral
97	0.04	0.00	0.00	0.03	0.00	0.00	0.00	0.06	46.32	51.71	98.15	Wdak4.1	60x80
98	0.00	0.01	0.01	0.02	0.00	0.00	0.00	0.05	46.36	51.28	97.73	Wdak4.2	subhedral
99	0.02	0.00	0.00	0.03	0.00	0.00	0.00	0.05	46.42	51.20	97.72	Wdak4.3	
100	0.00	0.01	0.00	0.03	0.00	0.00	0.00	0.05	46.30	51.45	97.84	Wdak4.4	
101	0.00	0.02	0.00	0.02	0.00	0.00	0.00	0.07	45.50	51.99	97.60	Wdak4.5	
102	0.02	0.00	0.01	0.02	0.00	0.00	0.00	0.06	45.21	51.16	96.46	Wdak4.6	
104	0.00	0.00	0.00	0.03	0.00	0.00	0.00	0.07	45.91	51.43	97.43	Wdak5.2	40x50
													irregular
106	0.00	0.06	0.03	0.04	0.15	0.09	0.00	0.06	44.32	49.15	93.89	Wdak6.1	20x25
													subhedral
108	0.01	0.03	0.00	0.01	0.00	0.00	0.00	0.04	47.01	53.85	100.95	Wdak7.1	15x25
109	0.00	0.00	0.01	0.04	0.00	0.00	0.00	0.06	45.95	53.65	99.70	Wdak7.2	subhedral
111	0.00	0.00	0.00	0.00	0.00	0.01	0.00	0.05	46.44	54.87	101.37	WydkA2.1	15x30
112	0.00	0.00	0.01	0.01	0.00	0.00	0.00	0.04	46.09	55.12	101.26	WydkA2.2	subhedral
114	0.29	0.04	0.45	0.01	0.11	0.16	0.00	0.10	46.27	53.71	101.15	WydkA3.2	10
													framboid
115	0.00	0.01	0.01	0.01	0.00	0.00	0.00	0.07	47.15	55.39	102.64	WydkA4.1	10
													framboid
119	0.40	0.15	0.12	0.02	0.47	0.47	0.00	0.10	45.18	56.50	103.40	WydkA6.1	35x50
120	0.27	0.11	0.09	0.03	0.34	0.32	0.00	0.10	45.65	55.93	102.83	WydkA6.2	cleat?
121	0.30	0.10	0.11	0.02	0.39	0.39	0.00	0.09	45.79	55.71	102.88	WydkA6.3	
122	0.17	0.08	0.01	0.01	0.27	0.49	0.01	0.16	44.59	54.20	100.00	WydkA6.4	
No.	**Pb**	**Se**	**Cu**	**Cd**	**As**	**Ni**	**Zn**	**Co***	**Fe**	**S**	**Total**	**Comment**	**Size/Form**
124	0.08	0.01	0.00	0.01	0.00	0.00	0.00	0.05	43.68	55.23	99.06	WydkA7.2	20x30
													subhedral
127	0.00	0.00	0.01	0.00	0.00	0.00	0.00	0.04	45.77	56.95	102.76	WydkA8.2	10x15
													irregular
128	0.00	0.13	0.01	0.00	0.20	0.17	0.02	0.08	46.72	47.77	95.09	WydkA9.1	20x25
													subhedral
131	0.00	0.02	0.02	0.01	0.00	0.02	0.00	0.06	47.05	56.41	103.59	WydkA10.2	20

No.	Pb	Se	Cu	Cd	As	Ni	Zn	Co	Fe	S	Total	Comment	Size/Form
													framboid
133	0.04	0.00	0.04	0.01	0.00	0.05	0.00	0.07	46.21	55.91	102.33	WydkA11.1	20
134	0.03	0.01	0.04	0.02	0.01	0.05	0.00	0.07	46.56	56.17	102.96	WydkA11.2	framboid
30	0.00	0.00	0.02	0.00	0.03	0.01	0.00	0.05	46.30	52.36	98.77	WY-1 1.1	120x50
31	0.00	0.01	0.01	0.00	0.02	0.01	0.00	0.06	44.96	52.07	97.13	WY-1 1.2	irregular
32	0.00	0.00	0.02	0.00	0.04	0.00	0.00	0.06	47.05	51.96	99.13	WY-1 1.3	
33	0.00	0.00	0.04	0.00	0.02	0.00	0.00	0.05	47.46	52.04	99.62	WY-1 1.4	
34	0.00	0.00	0.01	0.00	0.03	0.01	0.00	0.05	44.60	51.99	96.69	WY-1 1.5	
35	0.00	0.00	0.03	0.00	0.01	0.00	0.00	0.06	44.35	52.00	96.44	WY-1 1.6	
36	0.00	0.00	0.04	0.00	0.00	0.00	0.00	0.05	46.82	51.67	98.57	WY-1 2.1	120x45
37	0.00	0.00	0.01	0.00	0.00	0.00	0.00	0.03	46.86	51.84	98.75	WY-1 2.2	irregular
38	0.00	0.00	0.01	0.00	0.00	0.00	0.00	0.06	46.25	51.82	98.14	WY-1 2.3	
39	0.00	0.00	0.01	0.00	0.00	0.00	0.00	0.05	44.78	51.37	96.21	WY-1 2.4	
41	0.00	0.00	0.02	0.00	0.00	0.00	0.00	0.04	44.54	52.52	97.12	WY-1 2.6	

* Cobalt data reflect a constant background of 0.05 ± 0.02 wt.%, due to an interference with iron. Results for Co are not background-subtracted.

Detection limit for other elements is 0.01 wt. %. Grain sizes are in micrometers. Different runs are indicated by normal, italicized, and underlined analysis numbers, respectively.

Table E-4. Electron Microprobe Data for Illite/Smectite and Kaolinite (K)

No.	Na_2O	K_2O	CaO	MgO	FeO	MnO	TiO_2	Cr_2O_3	Al_2O_3	SiO_2	Total*	Comment
						Ohio 5/6/7						
14	0.22	3.13	0.03	0.27	0.42	0.00	0.17	0.01	34.93	42.68	81.87	Map2Ohio2.1
15	0.11	8.20	0.02	2.60	4.67	0.01	0.35	0.03	29.69	49.15	94.82	Map2Ohio2.2
16	0.18	5.09	0.06	0.84	1.38	0.00	0.85	0.00	27.46	45.85	81.72	Map2Ohio2,3
182	0.16	4.83	0.24	1.15	1.66	0.01	0.98	0.01	27.62	44.54	81.20	Ohio(a) gr1 1.2
186	0.18	4.89	0.23	1.14	1.63	0.00	0.84	0.02	27.64	45.55	82.11	Ohio(a)gr1 1.6
191	0.47	8.01	0.00	1.38	2.20	0.01	0.16	0.02	33.29	48.81	94.35	Ohio(a)gr3 3.1
192	0.17	4.75	0.12	1.29	1.71	0.00	0.24	0.01	34.38	50.19	92.85	Ohio(a)gr3 3.2
193	0.01	0.02	0.02	0.04	0.10	0.02	0.03	0.01	39.69	47.94	87.87	Ohio(a)gr4 4.1
195	0.10	1.19	0.10	0.26	0.62	0.00	0.00	0.00	27.13	52.11	81.51	Ohio(a) 6.1
196	0.81	8.15	0.04	0.37	1.67	0.01	0.13	0.01	33.16	43.13	87.49	Ohio(a) 7.1
197	0.03	0.05	0.06	0.11	0.40	0.00	0.03	0.00	39.77	47.63	88.08	Ohio(a) 8.1
198	0.03	0.04	0.04	0.07	0.26	0.00	0.00	0.00	39.35	47.89	87.68	Ohio(a) 8.2
199	0.16	5.96	0.13	2.30	1.94	0.03	0.29	0.04	28.58	47.29	86.72	Ohio(a) 9.1
200	0.31	3.98	0.01	0.36	0.73	0.01	0.30	0.01	33.84	49.96	89.50	Ohio(a) 9.2
51	0.32	8.54	0.02	0.30	0.90	0.00	0.17	0.01	39.09	47.12	96.48	Map12Ohio12.1
58	0.17	4.29	0.20	0.87	0.85	0.00	0.09	0.00	31.51	49.42	87.40	Map13Ohio13.3
59	0.06	2.07	0.03	0.63	0.50	0.00	0.04	0.01	37.87	48.44	89.63	Map13Ohio13.4
60	0.11	0.74	0.11	0.20	0.19	0.00	0.02	0.00	36.49	47.23	85.09	Map13Ohio13.5
61	0.03	0.41	0.01	0.07	0.13	0.00	0.00	0.00	39.82	48.00	88.48	Map13Ohio13.6
62	0.12	2.64	0.00	0.19	0.30	0.02	0.03	0.00	39.44	48.08	90.81	Map13Ohio13.7
63	0.04	0.52	0.13	0.12	0.14	0.00	0.02	0.00	37.70	46.54	85.21	Map13Ohio13.8
83K	0.00	0.05	0.06	0.08	0.16	0.01	0.00	0.00	41.20	49.74	91.31	Ohio(b)gr1 1.1
84K	0.00	0.02	0.01	0.01	0.16	0.00	0.01	0.00	40.91	48.97	90.09	Ohio(b)gr1 1.2
85K	0.00	0.11	0.05	0.09	0.15	0.01	0.01	0.00	40.77	48.97	90.15	Ohio(b)gr1 1.3
89K	0.00	0.00	0.02	0.02	0.13	0.00	0.00	0.00	41.67	49.61	91.46	Ohio(b)gr1 1.7
96	0.92	5.26	0.04	0.77	1.30	0.00	1.56	0.02	33.35	49.49	92.72	Ohio(b)gr3 3.1
97	0.58	4.58	0.17	0.99	1.35	0.00	0.69	0.00	31.49	44.04	83.89	Ohio(b)gr3 3.2
100	0.40	4.51	0.05	0.89	1.53	0.01	0.21	0.03	30.30	43.00	80.93	Ohio(b)gr3 3.5
107	0.03	0.20	0.02	0.14	0.31	0.00	0.02	0.00	40.34	49.47	90.54	Ohio(b)gr5 5.1
108	0.02	0.26	0.02	0.18	0.45	0.00	0.05	0.01	40.39	49.89	91.27	Ohio(b)gr5 5.2

No.	Na_2O	K_2O	CaO	MgO	FeO	MnO	TiO_2	Cr_2O_3	Al_2O_3	SiO_2	Total*	Comment
117	0.08	1.73	0.07	1.38	2.32	0.01	0.04	0.01	31.83	50.44	87.91	Ohio(b)gr6 6.5
						North Dakota						
39	0.18	5.60	0.22	3.85	10.56	0.05	0.06	0.02	16.91	46.80	84.25	Map8ND8.1
40	0.15	6.76	0.18	1.96	1.88	0.00	0.00	0.01	32.19	51.85	94.97	Map8ND8.2
41	0.14	6.53	0.13	2.13	2.85	0.00	0.02	0.01	31.62	49.42	92.85	Map8ND8.3
42	0.16	4.19	0.15	3.78	6.97	0.06	0.00	0.01	32.30	48.55	96.16	Map8ND8.4
126	0.37	3.13	0.42	2.91	3.97	0.01	0.13	0.03	18.89	53.39	83.27	ND(b) gr1 1.1
128	0.14	2.83	0.49	2.02	2.85	0.04	0.02	0.00	18.09	59.35	85.83	ND(b) gr1 1.3
129	0.11	2.01	0.44	2.53	3.56	0.00	0.35	0.01	19.49	50.72	79.22	ND(b) gr1 1.4
130	0.11	2.43	0.55	1.95	4.51	0.04	0.26	0.02	15.29	58.28	83.42	ND(b) gr1 1.5
131	0.13	1.93	0.57	1.20	2.62	0.01	0.22	0.01	14.09	61.89	82.67	ND(b) gr2 2.1
132	0.12	3.20	0.41	1.49	2.45	0.01	0.19	0.01	16.96	61.80	86.64	ND(b) gr2 2.2
133	0.16	2.74	0.54	1.31	2.42	0.02	0.40	0.02	16.24	56.42	80.27	ND(b) gr2 2.3
135	0.14	1.67	0.34	1.05	3.01	0.02	0.15	0.02	25.16	54.39	85.95	ND(b) gr3 3.1
136	0.13	2.53	0.54	2.46	6.38	0.00	0.44	0.01	18.07	48.50	79.05	ND(b) gr3 3.2
138	0.10	4.96	0.32	1.74	4.26	0.01	0.24	0.02	29.67	51.89	93.20	ND(b) gr3 3.4
139	0.29	1.88	0.84	1.63	4.05	0.01	2.80	0.03	16.78	52.73	81.01	ND(b) gr4 4.1
141	0.13	4.60	0.16	1.05	1.33	0.03	0.35	0.01	26.86	57.87	92.39	ND(b) gr4 4.3
142	0.34	5.94	0.56	1.13	3.05	0.02	0.13	0.01	18.16	58.60	87.95	ND(b) gr4 4.4
145	0.63	2.96	0.51	2.51	5.23	0.04	0.13	0.01	19.53	55.74	87.28	ND(b) gr5 5.2
147	0.10	2.73	0.49	2.27	3.65	0.02	0.96	0.02	16.12	55.53	81.88	ND(b) gr5 5.4
152	0.12	3.48	0.21	0.97	1.78	0.00	0.15	0.01	20.00	60.13	86.85	ND(b) gr6 6.4
154	0.11	8.08	0.06	2.38	5.36	0.01	0.43	0.02	26.49	47.33	90.27	ND(b) gr7 7.1
155	0.15	1.49	0.70	1.58	4.58	0.00	0.15	0.01	17.40	55.55	81.60	ND(b) gr7 7.2
158	0.10	6.30	0.08	2.30	4.57	0.01	0.70	0.01	29.69	50.30	94.06	ND(b) gr7 7.5
159	0.13	2.31	0.58	1.16	1.59	0.00	0.15	0.01	17.10	57.54	80.56	ND(b) gr8 8.1
207	0.09	6.78	0.15	2.62	2.91	0.00	0.10	0.01	28.20	49.74	90.58	NDak(a) 4.1
						Wyodak						
165	0.12	1.44	0.71	0.95	2.69	0.00	0.68	0.00	24.70	50.98	82.26	Wdk(b) gr1 1.4
168	0.03	0.27	0.27	0.20	0.34	0.00	0.16	0.00	37.21	45.87	84.34	Wdk(b) gr2 2.3
169	0.07	0.50	0.44	0.38	0.43	0.01	0.21	0.00	37.06	47.16	86.26	Wdk(b) gr2 2.4
178	0.09	1.50	0.64	0.78	1.00	0.02	1.27	0.02	28.79	47.42	81.52	Wdk(b) gr4 4.2

No.	Na_2O	K_2O	CaO	MgO	FeO	MnO	TiO_2	Cr_2O_3	Al_2O_3	SiO_2	Total*	Comment
21	0.06	3.75	0.08	0.87	2.20	0.00	0.09	0.00	36.45	48.20	91.69	Map4Wyodak4.1
22	0.04	1.80	0.22	0.43	0.89	0.01	0.13	0.00	39.18	47.02	89.73	Map4Wyodak4.2
26	0.01	0.01	0.17	0.02	0.30	0.01	0.06	0.00	39.53	46.35	86.45	Map5Wyodak5.1
27	0.04	0.04	0.16	0.05	0.35	0.00	0.00	0.00	38.71	42.00	81.35	Map5Wyodak5.2
210	0.00	0.00	0.03	0.02	0.03	0.00	0.00	0.00	39.12	47.23	86.44	Wyodak(a) 1.1
211	0.00	0.01	0.02	0.01	0.02	0.00	0.03	0.00	39.51	46.70	86.31	Wyodak(a) 1.2
214	0.89	7.45	0.11	0.40	0.72	0.03	0.44	0.00	35.13	46.99	92.17	Wyodak(a) 4.1
215	0.67	6.15	0.18	0.29	0.56	0.00	0.25	0.01	33.93	45.63	87.69	Wyodak(a) 4.2
216	0.00	0.05	0.59	0.05	0.06	0.01	0.00	0.00	37.56	42.53	80.85	Wyodak(a) 5.1

*Desired totals 85-95% due to presence of structural water and/or hydroxyl not determined.

Table E-5. Electron Microprobe Analyses of Calcite in Ohio 5/6/7

No.	MnO	MgO	PbO	CaO	FeO	SrO	BaO	ZnO	Total*	Comment
39	0.39	0.38	0.03	55.71	0.37	0.20	0.06	n.d.	57.14	OhioB clc1.1
40	0.47	0.47	0.00	55.53	0.49	0.30	0.00	n.d.	57.26	OhioB clc1.2
41	0.81	0.21	0.00	57.66	1.53	0.02	0.04	n.d.	60.27	OhioB clc2.1
42	0.67	0.22	0.03	58.02	1.67	0.07	0.00	n.d.	60.67	OhioB clc2.2
43	0.80	0.19	0.01	57.01	1.37	0.02	0.00	n.d.	59.40	OhioB clc2.3
141	0.50	0.23	0.01	54.35	0.86	0.08	0.04	0.01	56.08	OhioB clc2.4
142	0.54	0.20	0.01	51.13	0.89	0.05	0.00	0.00	52.81	OhioB clc2.5
44	0.00	0.39	0.01	59.16	2.05	0.06	0.00	n.d.	61.66	OhioB clc4.1
45	0.03	0.63	0.03	56.74	1.89	0.06	0.00	n.d.	59.37	OhioB clc4.2
46	0.32	0.41	0.00	56.88	1.04	0.17	0.00	n.d.	58.82	OhioB clc5.1
47	0.32	0.43	0.00	56.32	1.25	0.20	0.00	n.d.	58.52	OhioB clc5.2
48	0.29	0.43	0.02	56.76	1.30	0.22	0.00	n.d.	59.01	OhioB clc5.3
49	0.22	0.49	0.00	55.86	1.23	0.19	0.05	n.d.	58.03	OhioB clc5.4
143	0.26	0.40	0.00	54.67	0.75	0.28	0.00	0.00	56.35	OhioBclc5.5
144	0.32	0.35	0.03	54.64	0.85	0.20	0.00	0.00	56.38	OhioBclc5.6

*Desired total for pure $CaCO_3$ is 56.0 wt. % CaO.

APPENDIX F

USGS Leaching Results

Table F-1. Complete USGS Leaching Results

USGS Leaching Results for OHIO 5/6/7

Element	NH4Ac	HCl	HF	HNO3	Total	Element	NH4Ac	HCl	HF	HNO3	Total
Li	0%	0%	65%	0%	65%	**Sn**	0%	5%	35%	0%	40%
Be	0%	5%	50%	0%	55%	**Sb**	0%	5%	20%	15%	40%
Na	25%	10%	40%	10%	85%	**Cs**	5%	5%	75%	5%	90%
Mg	10%	5%	70%	0%	85%	**Ba**	5%	0%	90%	5%	100%
Al	0%	0%	100%	0%	100%	**La**	0%	5%	5%	55%	65%
P	0%	50%	50%	0%	100%	**Ce**	0%	5%	5%	60%	70%
K	0%	5%	90%	0%	95%	**Sm**	0%	25%	5%	35%	65%
Ca	30%	30%	5%	5%	70%	**Eu**	5%	25%	5%	30%	65%
Sc	0%	5%	40%	0%	45%	**Tb**	5%	20%	5%	25%	55%
Ti	0%	0%	65%	0%	65%	**Yb**	0%	5%	10%	25%	40%
V	0%	0%	35%	0%	35%	**Lu**	0%	5%	10%	30%	45%
Cr	0%	0%	30%	0%	30%	**Hf**	0%	0%	50%	0%	50%
Mn	15%	30%	20%	30%	95%	**Ta**	0%	0%	35%	5%	40%
Fe	0%	10%	10%	80%	100%	**W**	5%	10%	25%	0%	40%
Co	15%	30%	10%	20%	75%	**Tl**	10%	15%	15%	50%	90%
Ni	5%	15%	10%	25%	55%	**Pb**	0%	35%	10%	40%	85%
Cu	0%	10%	5%	65%	80%	**Th**	0%	10%	10%	35%	55%
Zn	5%	30%	10%	30%	75%	**U**	0%	5%	20%	5%	30%
As	0%	25%	5%	60%	90%	**Hg**	15%	15%	15%	50%	95%
Se	0%	0%	0%	50%	50%						
Rb	0%	5%	70%	10%	85%						
Sr	5%	5%	60%	5%	75%						
Y	0%	20%	10%	25%	55%						
Zr	0%	5%	70%	25%	100%						
Mo	5%	10%	20%	25%	60%						
Cd	5%	20%	5%	35%	65%						

Table F-1 (Continued). Complete USGS Leaching Results

USGS Leaching Results for North Dakota

Element	NH4Ac	HCl	HF	HNO3	Total	Element	NH4Ac	HCl	HF	HNO3	Total
Li	10%	0%	35%	0%	45%	**Ce**	0%	60%	10%	20%	90%
Be	0%	70%	20%	0%	90%	**Sm**	5%	70%	10%	15%	100%
Na	85%	5%	5%	0%	95%	**Eu**	0%	60%	15%	10%	85%
Mg	50%	35%	10%	0%	95%	**Tb**	0%	60%	15%	10%	85%
Al	0%	25%	65%	0%	90%	**Yb**	0%	60%	20%	10%	90%
P	0%	85%	10%	0%	95%	**Lu**	0%	60%	15%	0%	75%
K	10%	5%	80%	0%	95%	**Hf**	0%	0%	60%	5%	65%
Ca	40%	60%	0%	0%	100%	**Ta**	5%	0%	45%	0%	50%
Sc	0%	15%	80%	5%	100%	**W**	10%	10%	50%	5%	75%
Ti	0%	20%	60%	0%	80%	**Tl**	ND	ND	ND	ND	ND
V	0%	35%	45%	0%	80%	**Pb**	0%	85%	10%	5%	100%
Cr	0%	10%	35%	5%	50%	**Th**	0%	20%	45%	15%	80%
Mn	15%	75%	10%	0%	100%	**U**	0%	45%	45%	5%	95%
Fe	0%	65%	15%	10%	90%	**Hg**	0%*	5%	5%	90%	100%
Co	0%	55%	40%	0%	95%						
Ni	0%	45%	25%	15%	85%						
Cu	0%	30%	10%	20%	60%						
Zn	0%	65%	10%	5%	80%						
As	0%	50%	15%	15%	80%						
Se	10%	5%	0%	25%	40%						
Rb	0%	5%	70%	0%	75%						
Sr	40%	60%	0%	0%	100%						
Y	0%	80%	10%	5%	95%						
Zr	0%	5%	65%	0%	70%						
Mo	0%	0%	60%	0%	60%						
Cd	ND	ND	ND	ND	ND						
Sn	ND	ND	ND	ND	ND						
Sb	0%	0%	40%	10%	50%						
Cs	0%	5%	75%	5%	85%						
Ba	0%	80%	15%	5%	100%						
La	0%	55%	10%	20%	85%						

* DMA Hg value of ammonium acetate leached fraction was used as whole coal value.

Table F-1 (Continued). Complete USGS Leaching Results

USGS Leaching Results for WYODAK

Element	NH4Ac	HCl	HF	HNO3	Total	Element	NH4Ac	HCl	HF	HNO3	Total
Li	0%	0%	35%	0%	35%	**Ba**	5%	80%	5%	0%	90%
Be	0%	55%	35%	0%	90%	**La**	0%	60%	5%	15%	80%
Na	90%	5%	0%	0%	95%	**Ce**	0%	65%	5%	15%	85%
Mg	55%	30%	0%	0%	85%	**Sm**	0%	70%	5%	10%	85%
Al	0%	25%	55%	0%	80%	**Eu**	0%	60%	10%	10%	80%
P	0%	80%	10%	0%	90%	**Tb**	0%	70%	5%	10%	85%
K	30%	5%	50%	0%	85%	**Yb**	5%	40%	15%	15%	75%
Ca	45%	55%	0%	0%	100%	**Lu**	5%	45%	15%	10%	75%
Sc	0%	60%	35%	0%	95%	**Hf**	0%	0%	45%	5%	50%
Ti	0%	20%	60%	0%	80%	**Ta**	0%	0%	40%	5%	45%
V	0%	65%	25%	0%	90%	**W**	10%	5%	45%	5%	65%
Cr	0%	10%	45%	0%	55%	**Tl**	ND	ND	ND	ND	ND
Mn	5%	80%	5%	5%	95%	**Pb**	0%	70%	20%	10%	100%
Fe	0%	75%	10%	10%	95%	**Th**	0%	30%	25%	15%	70%
Co	0%	30%	60%	5%	95%	**U**	10%	50%	30%	5%	95%
Ni	0%	25%	15%	20%	60%	**Hg**	20%	0%	0%	50%	70%
Cu	0%	20%	5%	20%	45%						
Zn	0%	50%	10%	25%	85%						
As	0%	40%	15%	15%	70%						
Se	5%	5%	0%	20%	30%						
Rb	10%	0%	65%	0%	75%						
Sr	30%	65%	5%	0%	100%						
Y	0%	65%	10%	10%	85%						
Zr	0%	5%	60%	0%	65%						
Mo	0%	0%	45%	0%	45%						
Cd	0%	70%	5%	10%	85%						
Sn	ND	ND	ND	ND	ND						
Sb	0%	5%	35%	15%	55%						
Cs	5%	5%	60%	5%	75%						

Table F-2. Interpreted Leaching Results

Element	OHIO	WYODAK	NORTH DAKOTA
Li	65% Silicates 35% Organic	35% Silicates 65% Organic	35% Silicates 65% Organic (15%)[1]
Be	50% Silicates 5% Gibbsite (?) 45% Organic	35% Silicates 55% Gibbsite (?) 10 % Organic	20% Silicates 70% Gibbsite 10 % Organic
Na	25% Exchangable 10% HCl Soluble 40% Silicates 10% HNO_3 Soluble	90 % Exchangable 5% HCl Soluble	85% Exchangable 5% HCl Soluble 5% Silicates
Mg	70% Silicates 25% Organic (10%)[1] 5% Carbonates	70% Organic (55%)[1] 30 % Carbonates	10% Silicates 55% Organic (50%)[1] 35% Carbonates
Al	100% Silicates	55% Silicates 25% Gibbsite (?) 20% Organic	65% Silicates 25% Gibbsite (?) 10% Organic
P	50% Phosphates 50% Silicates	80% Phosphates 10% Silicates 10% Organic	85% Phosphates 10% Silicates 5% Organic
K	90% Silicates	50% Silicates 45% Organic (30%)[1]	80% Silicates 15% Organic (10%)[1]
Ca	60% Carbonates 5% Silicates 30% Organic	100% Carbonates	100% Carbonates
Sc	40% Silicates 5% Fe-Oxides 55% Insolubles[2]	35% Silicates 60% Fe-Oxides 5% Insolubles[2]	80% Silicates 15% Fe-Oxides
Ti	65% Silicates 35% Insoluble (TiO_2)	60% Silicates 20% Insoluble (TiO_2) 20% Fe-Oxides	60% Silicates 20% Insoluble (TiO_2) 20% Fe-Oxides
V	35% Silicates 65% Organic	25% Silicates 10% Organic 65% Fe-Oxides	45% Silicates 20% Organic 35% Fe-Oxides

Table F-2 (Continued). Interpreted Leaching Results

Element	OHIO	WYODAK	NORTH DAKOTA
Cr	30% Silicates	45% Silicates	35% Silicates
	70% Insolubles[2]	45% Insolubles[2]	50% Insolubles[2]
		10% Fe-Oxides	10% Fe-Oxides
Mn	45% Carbonates[3]	85% Carbonates[3]	90% Carbonates[3]
	20% Silicates	5% Silicates	10% Silicates
	30% Pyrite	5% Pyrite	
Fe	80% Pyrite	10% Pyrite	10% Pyrite
	10% Fe-Oxides[4]	75% Fe-Oxides[4]	65% Fe-Oxides[4]
	10% Silicates	10% Silicates	15% Silicates
Co	10% Silicates	60% Silicates	40% Silicates
	30% HCl Soluble[5]	30% HCl Soluble[5]	55% HCl Soluble[5]
	40% Organic (15%)	5% Organic	5% Organic
	20% Pyrite	5% Pyrite	
Ni	25% Pyrite	20 Pyrite	15% Pyrite
	10% Silicates	15% Silicates	25% Silicates
	15% HCl Soluble[5]	25% HCl Soluble[5]	45% HCl Soluble[5]
	50% Organic (5%)	40% Organic	15% Organic
Cu	65% Pyrite[6]	20% Pyrite[6]	20% Pyrite[6]
	5% Silicates	5% Silicates	10% Silicates
	10% HCl Soluble[5]	20% HCl Soluble[5]	30% HCl Soluble[5]
	20% Organic	55% Organic	40% Organic
Zn	30% Sphalerite	50% Sphalerite	65% Sphalerite
	30% Pyrite	25% Pyrite	5% Pyrite
	10% Silicates	10% Silicates	10% Silicates
	30% Organic (5%)[1]	15% Organic	20% Organic
As	60% Pyrite	15% Pyrite	15% Pyrite
	25% Arsenate	40% Arsenate	50% Arsenate
	5% Silicates	15% Silicates	15% Silicates
	10% Organic	30% Organic	20% Organic
Se	50% Pyrite	20% Pyrite	25% Pyrite
	50% Organic	75% Organic (5%)[1]	70% Organic (10%)[1]
Rb	70% Silicates	65% Silicates	70% Silicates
	15% Organic	35% Organic (10%)	25% Organic
Sr	10% Carbonates	95% Carbonates	100% Carbonates
	60% Silicates	5% Silicates	

Table F-2 (Continued). Interpreted Leaching Results

Element	OHIO	WYODAK	NORTH DAKOTA
Y	45% Phosphates	75% Phosphates	85% Phosphates
	10% Silicates	10% Silicates	10% Silicates
	45% Organic	15% Organic	5% Organic
Zr	70% Silicates (Zircon)	60% Silicates (Zircon)	65% Silicates (Zircon)
	5% HCl Soluble[7]	5% HCl Soluble[7]	5% HCl Soluble[7]
	25% HNO_3 Soluble[7]	35% Insoluble (Zircon)	30% Insoluble (Zircon)
Mo	20 % Silicate	45% Silicates	60% Silicates
	45% Organic (5%)[1]	55% Organic	40% Organic
	25% Pyrite		
Cd	20% Sphalerite	70% Sphalerite	ND
	35% Pyrite	10% Pyrite	ND
	40% Organic (5%)[1]	15% Organic	ND
Sn	35% Silicates	ND	ND
	60% Organic	ND	ND
Sb	20% Silicates	35% Silicates	40% Silicates
	60% Organic	45% Organic	50% Organic
	15% Pyrite	15% Pyrite	10% Pyrite
Cs	75% Silicates	60% Silicates	75% Silicates
	10% Insolubles[8]	25% Insolubles[8]	15% Insoluble[8]
	5% HCl Soluble	5% HCl Soluble	5% HCl Soluble
Ba	5% Barite	80% Barite	85% Barite
	90% Silicates	5% Silicates	15% Silicates
	5% Organic (5%)[1]	15% Organic (5%)[1]	
La	55% HNO_3 Soluble[9]	15% HNO_3 Soluble[9]	20% HNO_3 Soluble[9]
	5% HCl Soluble[9]	60% HCl Soluble[9]	55% HCl Soluble[9]
	5% Silicates	5% Silicates	10% Silicates
	35% Organic	20% Organic	15% Organic
Ce	60% HNO_3 Soluble[9]	15% HNO_3 Soluble[9]	20% HNO_3 Soluble[9]
	5% HCl Soluble[9]	65% HCl Soluble[9]	60% HCl Soluble[9]
	5% Silicates	5% Silicates	10% Silicates
	30% Organic	15% Organic	10% Organic
Sm	35% HNO_3 Soluble[9]	10% HNO_3 Soluble[9]	15% HNO_3 Soluble[9]
	25% HCl Soluble[9]	70% HCl Soluble[9]	70% HCl Soluble[9]
	5% Silicates	5% Silicates	10% Silicates
	35% Organic	15% Organic	

Table F-2 (Continued). Interpreted Leaching Results

Element	OHIO	WYODAK	NORTH DAKOTA
Eu	30% HNO_3 Soluble[9] 25% HCl Soluble[9] 5% Silicates 40% Organic (5%)	10% HNO_3 Soluble[9] 60% HCl Soluble[9] 10% Silicates 20% Organic	10% HNO_3 Soluble[9] 60% HCl Soluble[9] 15% Silicates 15% Organic
Tb	25% HNO_3 Soluble[9] 20% HCl Soluble[9] 5% Silicates 40% Organic (5%)	10% HNO_3 Soluble[9] 70% HCl Soluble[9] 5% Silicates 15% Organic	10% HNO_3 Soluble[9] 60% HCl Soluble[9] 15% Silicates 15% Organic
Yb	25% HNO_3 Soluble[9] 5% HCl Soluble[9] 10% Silicates 60% Organic	15% HNO_3 Soluble[9] 40% HCl Soluble[9] 15% Silicates 30% Organic (5%)	10% HNO_3 Soluble[9] 60% HCl Soluble[9] 20% Silicates 10% Organic
Lu	30% HNO_3 Soluble[9] 5% HCl Soluble[9] 10% Silicates 55% Organic	10% HNO_3 Soluble[9] 45% HCl Soluble[9] 15% Silicates 30% Organic (5%)	 60% HCl Soluble[9] 15% Silicates 25% Organic
Hf	50% Silicates 50% Organic	45% Silicates 50% Organic	60% Silicates 35% Organic
Ta	35% Silicates 60% Organic	40% Silicates 55% Organic	45% Silicates 55% Organic (5%)[1]
W	25% Silicates 10% HCl Soluble 65% Organic (5%)[1]	45% Silicates 5% HCl Soluble 45% Organic (10%)[1]	50% Silicates 10% HCl Soluble 35% Organic (10%)[1]
Tl	50% Pyrite 15% Silicates 15% Monosulfides 10% Organic	ND ND ND ND	ND ND ND ND
Pb	35% Galena 40% Pyrite 10% Silicates 15% Organic	70 Galena 10% Pyrite 20% Silicates	85% Galena 5% Pyrite 10% Silicates
Th	45% Phosphates 10% Silicates 45% Organic	45% Phosphates 25% Silicates 30% Organic	35% Phosphates 45% Silicates 20% Organic

Table F-2 (Continued). Interpreted Leaching Results

Element	OHIO	WYODAK	NORTH DAKOTA
U	20% Silicates 5% HCl Soluble[10] 70% Organic[11]	30% Silicates 50% HCl Soluble[10] 15% Organic (10%)[1,11]	45% Silicates 45% HCl Soluble[10] 15% Organic[11]

NOTES:

[1] Number in parentheses after Organic % indicates percent in exchangeable sites.
[2] Organic association or insoluble species such as chromite.
[3] May also include Fe oxides, oxidized pyrite, and mono-sulfides.
[4] May also include oxidized pyrite, carbonates and mono-sulfides.
[5] No evidence for any particular species. This element may be associated with carbonates, sulfates, oxides, or mono-sulfides.
[6] Includes pyrite and most chalcopyrite.
[7] Zircon may be partially soluble in HCl and HNO_3.
[8] Species unknown—may be organically associated.
[9] Likely associated with phosphates, especially rare earth bearing phosphates. There is conflicting evidence as to whether HCl-soluble and HNO_3 -soluble rare earth elements are associated with different species.
[10] Species unknown, may be associated with organic chelates, small amounts may be associated with zircon.
[11] Small amounts may be associated with zircon.

APPENDIX G

Trace Metal Content of Mineral Grains by SHRIMP-RG Analysis

Table G-1. SHRIMP-RG data reduction showing raw counts for a representative Ohio illite/smectite, counts per ppm or weight percent (Al_2O_3, CaO, SiO_2) for standards (SRM 610, GSE, and BHVO), and comparison of results for this illite obtained by each standard. From electron microprobe analysis, the SiO_2 and Al_2O_3 contents of illite/smectite are known to be about 50 and 30 weight percent, respectively. SHRIMP-RG results for these elements are given in weight percent to facilitate comparison to the microprobe data.

Aug 25 '99		**Counts/ppm or wt. % (Al_2O_3,CaO, SiO_2)**			**Illite Concentration by Standard**		
Ohio gr1-2L	**Raw Counts**	**SRM 610**	**GSE**	**BHVO**	**Conc. 610**	**Conc. GSE**	**Conc. BHVO**
Mg	21391	9.44	13.00	13.06	2266	1645	1637
Al_2O_3	325487	10252	16810	11708	31.75	19.36	27.80
CaO	5442	90615	111287	104267	0.06	0.05	0.05
SiO_2	1059325	18292	27723	19627	57.91	38.21	53.97
Sc	4163	362.6	240.5	349.6	11.48	17.31	11.91
Ti	29024	18.13	20.55	17.24	1601	1413	1683
V	13766	175.0	190.0	129.8	78.68	72.47	106.04
^{52}Cr	14022	180.2	215.9	163.0	77.82	64.95	86.01
^{53}Cr	1587	20.25	24.53	18.53	78.37	64.72	85.65
Mn	7009	200.6	303.2	253.2	34.94	23.12	27.69
Co	173	108.3	186.0	165.0	1.60	0.93	1.05
Ni	687	21.94	43.81	34.70	31.30	15.67	19.79
Rb	68370	617.4	718.8	584.2	110.74	95.12	117.02
Sr	11821	239.3	280.4	233.1	49.40	42.15	50.70

Table G-2. SHRIMP-RG Results Showing Reproducibility of GSE Standard (in Counts per ppm or Weight Percent) During Runs on Feb 2 and Feb. 3, 2000 (Results for GSE_L1 were excluded from the calibration)

GSE Std	**Counts per ppm or weight percent (Al_2O_3, SiO_2, CaO)**				
	2 Feb 00	**2 Feb 00**	**3 Feb 00**	**3 Feb 00**	**3 Feb 00**
	GSE_L1	**GSE_L2**	**GSE_L1**	**GSE_L2**	**GSE_L3**
^{26}Mg	236.5	227.5	241.7	230.0	222.7
^{43}AlO	48462	46832	47833	50470	47871
^{44}Ca	320743	307322	310075	333787	315280
^{44}SiO	81609	79356	81572	85734	81213
^{45}Sc	762.3	738.3	700.7	798.6	728.8
^{47}Ti	63.08	60.09	59.64	66.63	61.58
^{51}V	608.0	572.0	552.0	644.1	585.8
^{52}Cr	650.5	611.0	588.9	668.6	618.6
^{53}Cr	72.98	68.83	64.97	75.45	69.67
^{55}Mn	864.3	844.1	723.5	897.6	827.7
^{55}KO	7.17	6.97	6.22	7.20	6.71
^{59}Co	475.9	474.3	370.9	493.0	446.3
^{60}Ni	103.8	104.1	77.93	107.07	96.12
^{63}Cu	165.3	166.7	118.0	170.9	151.2
^{64}Zn	84.54	87.33	57.32	85.92	76.38
^{72}FeO	15.82	15.67	10.46	16.33	14.67
^{85}Rb	1673.3	1673.4	741.2	1926.4	1523.8
^{88}Sr	736.0	723.9	405.7	866.0	710.6

APPENDIX H

Trace Metal Content of Mineral Grains by Laser Ablation Mass Spectrometry

Table H-1. Laser Ablation ICP-MS Data for Pyrite in Ohio 5/6/7 (in ppm)
Data are Corrected for In-Run Drift. Fe Content is Fixed and Assumed to be Stoichimetric

	ohio1 py1.1	**ohio1 py1.2**	**ohio1 py4.1**	**ohio2 py6.1**	**ohio2 py6.1a**	**ohio2 py6.2**	**ohio2 py1.1**	**ohio2 py5.1**	**ohio2 py5.2**
Cr	4.1	8.4	25	720	1.2	9.2	0.77	1.2	0.37
Mn	304	523	501	833	141	473	92	336	368
Fe	465500	465500	465500	465500	465500	465500	465500	465500	465500
Co	135	255	12	57	9.1	7.6	1.7	12	16
Ni	889	974	941	420	15	13	22	75	95
Cu	314	339	298	361	63	52	88	27	8.4
Zn	16	26	14	42	2.8	4.3	5.3	14	17
As	735	835	47	471	171	166	44	176	247
Se	720	898	86	596	12	31	67	133	161
Mo	7.1	12	6.9	46	5.3	10	0.24	41	45
Cd	1.8	1.6	0.30	0.45	0.30	0.52	0.29	0.68	0.92
Sb	23	94	12	55	0.94	3.3	0.53	1.9	2.3
Hg	24	23	1.7	9.0	0.59	0.97	0.98	14.6	18
Hg	29	27	2.1	12	0.65	0.98	1.1	16.3	20
Tl	183	140	8.3	4.1	23	19	0.54	24	29
Pb	547	1268	273	518	70	91	27	3.6	4.8

APPENDIX I

Procedures for Large Scale Combustion Experiments

I.1 Combustion Experimental Procedures

I.1.1 Pre-Experimental Preparatory Activities

A number of activities were performed prior to the start of each experimental run to insure that the experimental objectives were achieved. These are described below.

BLPI Media Preparation

Sample collection media for the BLPI were prepared by cutting the polycarbonate membranes (Phase IIb utilized precut membranes) plus membrane backing paper and/or aluminum foil (these last two types are denoted herein as "blanks") to the proper size and shape and then spraying them with a high purity grease (Apezion L) dissolved in toluene or hexane. These were allowed to dry under a fume hood for at least 48 hours or were dried in a vacuum dessicator for a minimum of 24 hours. Dried media were stored in disposable plastic Petri dishes.

One and a half milliliter PVC sample vials (Fisher microcentrifuge tubes with snap caps) were used to contain the particulate-laden membranes. The empty vials were preweighed on a microbalance and stored in zip-loc sealed polyethylene "snack" (0.165 x 0.0825 m) bags. Once the vials were weighed, they were only handled using tweezers and surgical gloves to minimize vial mass deviations during handling. Typically, vials were preweighed less than one month prior to use. See Appendix J, Quality Control, for an analysis of the error introduced by preweighing the sample vials.

The dried sample media were weighed on the microbalance (Ohaus Analytical Plus) just prior to loading into the BLPI. Usually, membranes were weighed in the morning and then used in the afternoon of the same day. Once the membranes and foil were cut, they were handled using only tweezers and surgical gloves.

All microbalance weights were repeated. Two readings with a deviation of less than 0.00005 g in Phase I, 0.00003 g in Phase IIa, and 0.00002 g in Phase IIb were required before the weight data were accepted as accurate. A discussion of error associated with the gravimetric measurements in included in Appendix J, Quality Control.

For samples requiring the use of the preseparator cyclone on the BLPI, the bottom of a Petrie disk together with a ChemWipe was also preweighed and placed in a sealed zip-loc sealed "sandwich" (0.165 x 0.165 m) bag. Once the dish and wipe were weighed, they were handled using only tweezers and surgical gloves.

Air Supply Measurement Device Description and Calibration

The manometers used to meter the various air systems were calibrated once prior to the start of the test period. Calibration equations for these systems are given below. This section describes the compressed air supply system (see Section 3.3.3) associated with the combustion facility utilized in the experimental work associated with this research and the calibrations performed.

During Phases I and IIa, this air was provided by a 25 HP (18.7 kW), 9 scfm (standard cubic feet per minute) [0.00425 Nm^3/s, normal cubic meters per second] reciprocating air compressor. A 30.5 ft^3 (0.86m^3) vertical detached volume tank is included to smooth out the air supply pressure and flow. A second air compressor system was used during Phase IIb. This compressor is a Speedaire cast-iron series air compressor vertically mounted on a volumetric tank. Interconnections were installed to allow either compressor to be used with any of the combustors located within the facility (there are currently three). Air supply headers were used to transport the 150 psig (1136kPa) air from the compressors to the combustion systems. These headers were supplied with knockout traps for collection of aqueous and hydrocarbon liquids entrained in the air supply [127]. A pressure regulator was used to reduce the combustion air to 60 psig (515kPa).

A portion of this air was routed to the UV detector purge system which utilized a Matheson Gas Products model FM-1050 rotameter for manual flow control. An UV detector is mounted in a special port 2 ¾ in. (0.0699 m) below the top of the furnace. The detector senses the presence of OH^- radicals generated during combustion. Johnson [127] gives a detailed explanation of the emergency shutdown system operating off of the UV detector signal. Purge air is required to prevent the UV detector from overheating and from being coated with soot/fly ash particulate.

Calibration of the UV purge air rotameter yields the following least squares fit linear regression:

$$\text{Flow (acfm)} = 0.0023\ (\text{rotameter reading}) + 0.001 \qquad \text{(I-1)}$$

Another portion of this air was used for coal feeder transport air (see Section 3.3.3 for a description of the coal feeder system). During Phase I and a portion of Phase IIa (the Ohio and Wyodak baseline screening experiments), an inclined manometer (Meriam Instrument Model 40HE35WM) was used to manually control pressure and flow rate of this transport air [127].

Calibration of the upper inclined manometer used for coal feeder transport air at 4 psig (129kPa) feed pressure yields the following least squares linear regression equation:

$$\text{Flow (acfm)} = 2.5375(\text{reading}) - 0.2429 \quad R^2=0.9975 \qquad \text{(I-2)}$$

The transport air control system was redesigned and modified to allow the use of either air or nitrogen for transport. A Matheson Model FM-1050 rotameter was utilized for manual flow control in this revised system. Calibration with nitrogen for the rotameter yields the following least squares fit linear regression:

$$\text{Flow (acfm)} = 0.0136(\text{reading}) - 0.1961 \qquad R^2=0.9958 \qquad \text{(I-3)}$$

This second transport system was used during the Phase IIa North Dakota and Kentucky baseline screening experiments and the Phase IIb Wyodak doping experiments.

An additional transport air system was commissioned in 1999 for use with a new coal feeder. This new transport air system used a McMillan Model CE mass flow controller to automatically control transport air. The calibration curve for this mass flow controller is:

$$\text{Flow (acfm)} = 2.254(\text{meter voltage}) - 0.8106 \qquad \text{(I-4)}$$

This system was used during the Phase IIb Ohio, Kentucky, and Pittsburgh doping experiments.

The main combustion air was controlled using an inclined manometer (Meriam Instrument Model 40HE35WM). The calibration curve for this manometer, generated using air at 20 psig (239kPa), is:

$$\text{Flow (acfm)} = 7.2197(\text{reading}) + 0.3289 \qquad R^2=0.9997 \qquad \text{(I-5)}$$

During Phase I and the Ohio experiments in Phase II, this air was routed directly to the coal burner located at the top of the furnace (see Section 3.3.3 for a description of the burner).

As part of the major rebuild in 1997, an electric air preheater was added to the main combustion air supply system. The inconel-sheaved heating elements (six) from an inoperable Chromalox heater were refurbished and utilized in the new heater. The shell was constructed of 3 in. (0.076 m) diameter schedule 40 304 stainless steel pipe with a 150# endcap and 150# mating flange. A new heater power supply, control system, and safety system were provided. A Watlow model 935 PID controller operating off of an Omega K-type thermocouple signal mounted in the discharge elbow of the heater provided control. A three-phase power relay, (Watlow Din-a-mite solid state power controller protected by a square-D 40 amp 3-phase fuse block) was used to energize the heating elements. Over-temperature protection was provided by two Watlow model 947 latching relays. Each relay is designed to open the power circuit at temperatures of 1100 ^{o}F (866 K) from separate sensing thermocouples. One relay operates off of an Omega K-type thermocouple signal mounted in the discharge elbow of the heater. The other relay operates off the signal of an Omega K-type thermocouple flush mounted to the outside shell of the preheater located approximately 0.25M below the outlet of the heater. If either relay trips, there is a required manual reset from a common reset button located on the control panel.

The preheater was mounted at the side of the furnace adjacent to ports 0-6 in order to reduce heat loss between the preheater and the burner. Six inches of Knauff fiberglass pipe insulation, rated to 1000^{o}F (811 K) was used on the outside of the preheater and the air discharge lines. The outlet piping of the preheater was configured to allow supply from the preheater to either of the large furnaces in the combustion laboratory. Two ½ in. (0.0127 m) stainless steel gate valves rated to 1100^{o}F (866 K) were utilized as isolation valves.

The preheater was utilized for the Wyodak, North Dakota, and Kentucky experiments conducted in Phase IIa and for all Phase IIb tests. The air exiting the preheater was maintained at 588 K; a typical air preheat temperature utilized in commercial combustors.

An air supply header consisting of four Speed-Aire regulators and portable supply hoses was used to provide air services for all other systems.

Liquid Dopant Calibration

The liquid rate for water or the liquid dopant (arsenic, selenium, or antimony dissolved in dilute acid or iron nitrate dissolved in water) was controlled by adjusting the stroke rate on the metering supply pump. To calibrate, liquid was collected from the supply tube (at the point where it connected to the atomizer nozzle) in a graduated cylinder. A stop watch was used to determine the flow rate.

Lime Feeder Calibration

For the low flow rate case (adding calcium to the Pittsburgh coal in Phase IIb), the lime feeder supply tube (the line that connected the feeder discharge nozzle to the burner inlet nozzle) was connected to a bucket. This bucket had a cloth filter-covered outlet line to allow air to escape while trapping the lime particles. The amount of lime collected at a given screw turning rate and constant transport air rate per unit time was measured gravimetrically. The calibration curve developed by this procedure is shown in Figure I-1.

For the high flow rate case (adding calcium to the Ohio coal in Phase IIb), the feed rate exceeded the capacity of the bucket collection system. For this case, the transport air was shutoff and the coal was collected as it fell off of the screw tip. The amount of lime collected at a given screw turning rate was measured gravimetrically. The calibration curve developed by this procedure is shown in Figure I-2.

I.1.2 Experimental Activities

Preheat on Gas

For a cold furnace, the first step was to preheat the upper refractory using a propane torch located in the pilot port at the top of the furnace. The outlet vacuum blower was operated at a low flow rate to slowly draw the hot combustion gases down the furnace. A typical pilot preheat time was one hour. In Phase II, the baghouse heaters were also commissioned to preheat the baghouse to 105^{o}C (378 K). Some time during this step, water flow to the coal burner radiant shield was initiated.

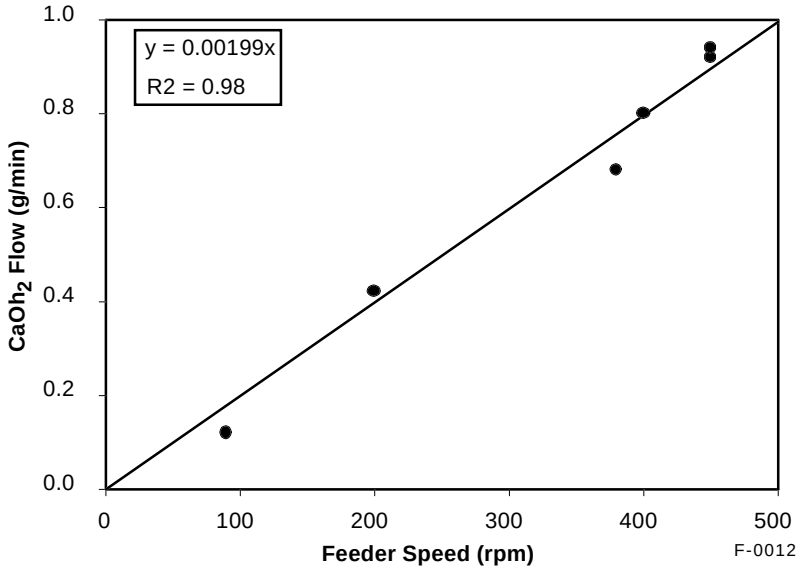

Figure I-1. Lime feeder calibration curve for Phase IIb Pittsburgh calcium doping experiments.

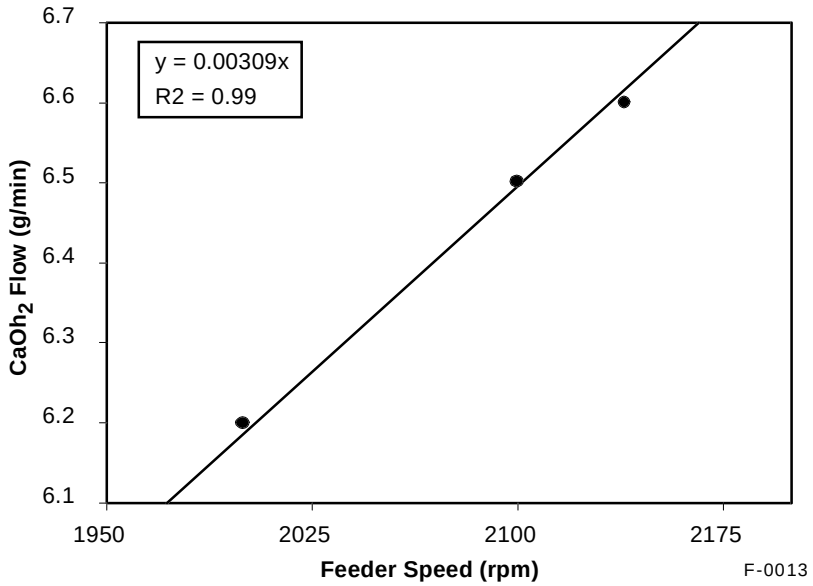

Figure I-2. Lime feeder calibration curve for Phase IIb Ohio calcium doping experiments.

Next, the outlet vacuum blower speed was increased to insure negative pressure in the furnace. Then, combustion air and natural gas were introduced into the furnace (with the propane pilot lit and in place) at the lowest stable operating level. After 5 min, the propane pilot was removed from the furnace. Cooling water flow to the baghouse outlet condenser was then initiated.

Over the course of 12 to 48 hours, the heating load in the furnace was slowly increased until the desired gas combustion conditions were reached. The maximum sustainable gas feed rate was used in this preheat for the bituminous coals. A typical methane feed rate for bituminous coal preheat was 305 slpm (0.0051 Nm^3/s). For the lower rank coals, the gas rate was set so that the steady-state gas temperature would be close to the steady-state coal combustion temperature.

Furnace flue gas generated during the preheat step was routed through a bypass line instead of through the particulate removal baghouse during the Phase I tests (1995 baghouse – see Section 3.3.3 for a description of the baghouse) to avoid condensation in the baghouse. In Phase II, a bypass was not required since heaters were used to preheat the new baghouse to 105°C (378 K).

For Phase I, the baghouse was commissioned and allowed to warm-up until the gas temperature in the baghouse was approximately 100°C (373 K) after the gas preheat step was completed. This warm-up was normally accomplished in 15 min or less. This step was not required in Phase II.

If the air preheater was being used (Phase IIa North Dakota, Wyodak, and Kentucky baseline screening experiments, and all Phase IIb experiments), it was energized and the controller setpoint was adjusted to the desired conditions. It typically takes around 90 min for the air to reach 315°C (588 K).

Switchover and Preheat With Coal

Switchover from natural gas firing to coal combustion was accomplished by the following procedure:

1. Increase the vacuum blower speed to insure negative pressure in the furnace during coal combustion (coal combustion generates a high combustion product gas flow rate compared to gas combustion at comparable heat duties).

2. Start the coal feeder transport air/nitrogen at the desired rate.

3. Energize the pneumatic vibrators on the coal feeder supply bin with compressed air.

4. Reduce the natural gas flow rate to around 30 slpm (0.0005 Nm^3/s).

5. Adjust the main combustion air rate to around 20% above the final desired rate.

6. Start the coal screwfeeder and quickly increase the screw turning rate to the approximate final desired rate.

7. Observe the flame visually to insure proper combustion characteristics.

8. After 10 min, the natural gas can be shut off and the air rate reduced to the approximate final desired rate.

9. Insert the gas sampling probe in Port 4 (Port 4b in Phase I) and measure the oxygen content in the flue gas. Adjust the coal feed rate so that the O_2 concentration in the flue gas at Port 4 (Port 4b in Phase I) is at the desired level.

The time required for furnace warm-up on coal varied depending on how hot the furnace was at the time of switchover from gas to coal and the heating value of the coal. A typical warm-up time for bituminous coals was 1.5 to 3 hours. Lower rank coals could reach steady-state in around 1 hour. A typical mid-point temperature warmup curve for the two Phase I coals are shown in Figure I-3.

Determining the optimum time at which to begin the first set of samples requires a balance of factors. First, the rate of change of the temperature in the furnace with time is considered. The furnace is considered to be operating at steady state when the rate of change in the temperature profile (arbitrarily defined as +/- 5K) is slower than the time required obtaining an impactor sample. As seen from Figure I-3, a relatively flat profile was obtained in less than 180 min.

In Phase I, the time required to achieve steady-state had to be balanced against slag buildup in the furnace. As slag forms along the walls, the gas and the pressure profile in the furnace change. If a shelf of slag builds up too far, it will begin to affect the streamlines in the furnace. When these laminar streamlines are affected, it affects the ability to extract a representative sample from the centerline of the furnace. Therefore in Phase I, sampling was initiated before the furnace was completely at steady state. Instead, we tried to start sampling when we had reached the flat profile region of the unsteady-state temperature curve; typically after around 130 min.

After the furnace rebuild, slag buildup was not a problem. Therefore in Phase II, the furnace was allowed to operate longer prior to sampling so that steady-state conditions were achieved.

Gas-Phase Analyzer Calibration Procedures

During the gas or coal feed warm-up periods the gas sampling and analysis system was commissioned. Each of the analyzers was zeroed using nitrogen and calibrated to span with a certified span gas prior to gas data collection. Details of the calibration procedures for the oxygen and NO_x analyzers used in both phases plus the CO and CO_2 analyzers used in Phase I can be found in Johnson [127].

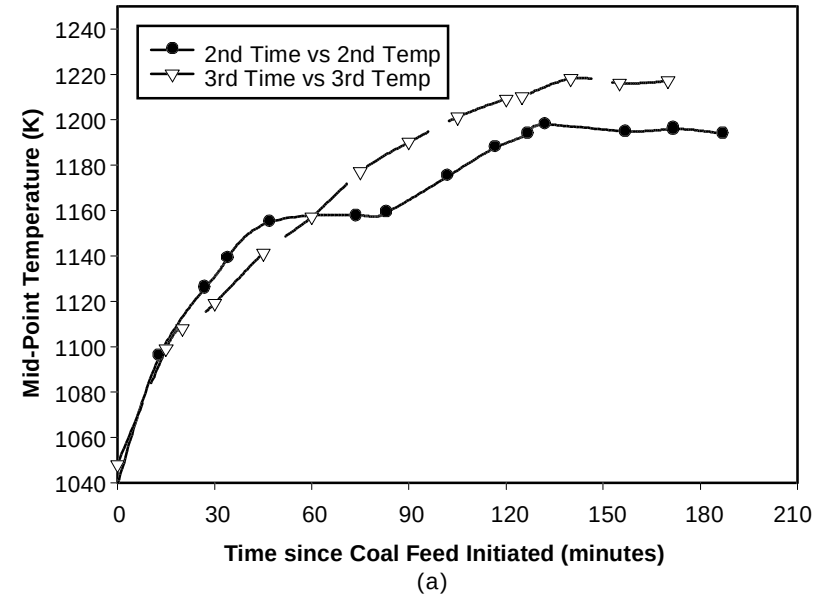

(a)

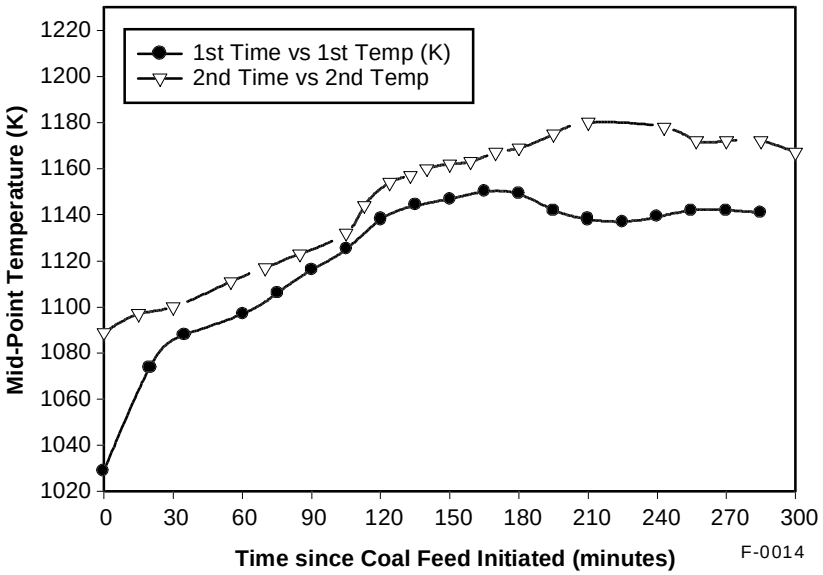

(b)

Figure I-3. Typical furnace warmup measured at the mid-point for combustion of (a) Pittsburgh seam coal and (b) Illinois #6 coal.

For the California Analytics dual component CO/CO_2 analyzer used in Phase II, the following procedure was followed:

1. Introduce nitrogen into the analyzer at the normal gas sampling rate (as controlled by a rotameter) and purge any residual gases out of the analyzer.

2. When the analyzer is only full of nitrogen, as indicated by a stable reading, zero both CO and CO_2 signals. First depress the "zero" button on the faceplate of the analyzer. The

signals should flash. Then, depress the "enter" key. The displays should both be reset to 0.00.

3. Introduce one of the two span calibration gases (either CO or CO_2) into the analyzer at the normal gas sampling rate. Flush the nitrogen completely out of the analyzer as indicated by a stable reading.

4. The span of the relevant component detector is now reset. First, depress the "span" button on the faceplate of the analyzer. If the incorrect display is flashing (e.g., CO_2 is flashing when you entered the CO calibration gas) depress the "func" key. Verify that the correct display is now flashing. Then, depress the "enter" key. The correct display should be reset to the preset calibration value (see the analyzer manual for information on how to modify the preset span gas calibration values).

5. Close the first span calibration gas and open the second span calibration gas so that this gas is introduced to the analyzer. Flush the first span gas completely out of the analyzer as indicated by a stable reading.

6. Repeat step 4 for the second detector.

7. Close the second span calibration gas and open the nitrogen feed valve so that nitrogen is reintroduced into the analyzer. Flush the second span gas completely out of the analyzer as indicated by a stable reading.

8. Repeat steps 1 through 7 until the readings during zero and span read correctly within the accuracy of the analyzer without manual reset.

Gas and Temperature Profile Determination

For most experiments, there was insufficient time in a single run day to obtain complete gas and temperature profiles from the furnace as well as perform particle sampling. Therefore, gas and temperature profiles were obtained separately and only selected temperature/gas readings were obtained during particle sampling.

To generate the furnace profile, readings were obtained using the portable "R-type" thermocouple probe (see Section 3.3.3) from the centerline of the furnace through the following sample ports:

Phase I: 1, 2, 3, 4a, 4b, 4c, 5, 7, 9, 11, 14
Phase IIa: 0, 1, 2, 3, 4, 5, 6, 8, 10, 12, 14, 16, Baghouse inlet

Impactor Calibration

The bottom stage of the BLPI serves as a sonic orifice that controls the total flow rate through the particulate sampling system. The exact flow rate must be known in order to

correctly set the sampling rate. The BLPI was loaded with the first set of preweighed membranes or with blanks and then connected to the particulate sampling system.

Thirty slpm (standard liters per minute; 0.0005 Nm^3/s) of nitrogen was fed to the sampling probe. Next, the sample vacuum pump was turned on and nitrogen was drawn through the impactor and through a wet test meter. Since the BLPI flow rate was typically 22 to 24 slpm (0.00037 to 0.0004 Nm^3/s), excess nitrogen continued to leave the sampling probe; preventing contamination of the membranes in the impactor. The time required for 1 acfm (actual cubic foot per minute; 0.00047 am^3/s – actual cubic meters per second) of nitrogen to flow through the wet test meter was measured using a stopwatch. Two successive readings within 0.05 seconds were required before the readings were accepted. Corrections from actual to standard/normal conditions and vice-versa were calculated using the actual laboratory temperature and barometric pressure measured at the time of the calibration test.

The calibrated flow rate determined by this procedure was not affected by whether the preseparator cyclone was attached to the inlet of the BLPI unless there was a leak in the cyclone. If a leak was detected, the cyclone was disassembled and vacuum grease was added to seal the top to the cyclone body.

Particle Sampling Rate Determination

In order to maximize the accuracy of the analytical results from these experiments, it was desirable to optimize the particle loading on the impactor stages [130]. The optimum is achieved by maximizing the particle loading on the smallest stages of interest without overloading the larger size stages. Overloaded stages result in bounce off and carryover to adjacent stages which skews the particle size distribution (PSD). In addition, an overloaded impactor plate typically has particle residue on the surfaces of the plate retention collars that cannot be effectively collected, further skewing the PSD.

The optimum sampling time was determined for each coal/sample location combination prior to collection of the first set of samples obtained for that coal/sample location combination. This procedure was often performed the day prior to the first day of particle testing in conjunction with the gas and temperature profile determination.

Sample time determination was accomplished via the following procedure:

1. Load blanks into the BLPI.

2. Follow the sampling procedure described in the *Particle Sampling Procedure* section, below; however, cease sampling well short of the expected sampling time.

3. Visually inspect the impactor stages to determine if overloading has occurred on any of the stages.

4. If no overloading is observed, repeat step two for another increment of time.

5. Repeat steps 2 through 4 until overloading occurs.

6. The optimum sampling time is the cumulative time up to the second to last sampling period (that is, ignore the sampling period that added enough material to overload the impactor).

For the bituminous coal total impactor experiments (performed in Phase I and Phase IIa), this procedure was performed both with and without the preseparator cyclone attached to the impactor inlet.

Particle Sampling Procedure

The following procedure was performed for collection of size-segregated particles using the BLPI:

1. Obtain the furnace gas temperature at the port where sampling will be performed.

2. Insert the gas sampling probe in Port 4 (Port 4b in Phase I) and adjust the main combustion air rate to insure that the proper excess oxygen content was present (typically to match 20% excess air conditions).

3. The theoretical combustion product flue gas flow rate and composition are calculated using these conditions. These results are then used to calculate the theoretical isokinetic sampling rate (assumed to be 90% of the maximum velocity in a laminar flow profile).

4. Insert the gas sampling probe in the port where sampling will be performed. Use the oxygen concentration value to determine dilution of the flue gas flow rate in the furnace due to leakage. These results are used to adjust the theoretical isokinetic sampling rate calculated in step 3. From this calculation the nitrogen flow rate is calculated as the difference between the total impactor flow rate (determined per step *Impactor Calibration* section, above) and the isokinetic sampling rate.

5. The isokinetic NO_x concentration in the diluted particle sampling gas stream is also calculated.

6. Connect the outlet line from the vacuum sampling pump to the gas analyzer system inlet sampling conditioning system.

7. For the baseline screening tests of bituminous coals in Phase I and Phase IIa, the first particulate sample was collected using the preseparator cyclone on the BLPI. For the lower rank coals in Phase IIa and for all of the Phase IIb experiments, the preseparator cyclone was not required.

8. Adjust the nitrogen flow controller setpoint to match the nitrogen flow rate calculated in step 4, above.

9. Begin nitrogen flow to the particle sampling probe.

10. Insert the particle sampling probe into the desired sample port in the furnace (typically ports 4b and 12 in Phase I and ports 4, 14, and the baghouse inlet port in Phase II).

11. Start the vacuum pump while simultaneously starting a stopwatch to measure the sampling time. The vacuum pump draws the nitrogen and sample through the BLPI.

12. For samples of longer than 10 min in duration, the NO_x concentration in the sample gas is monitored. The nitrogen flow rate to the sample probe is adjusted as required until the NO_x concentration matches the isokinetic NO_x concentration calculated in step 5, above.

    If the sample time is shorter than 10 min, an impactor sample must be collected using blanks in the BLPI (with the preseparator cyclone attached to the BLPI inlet) prior to taking the actual sample so that the nitrogen rate can be adjusted to match isokinetic sampling conditions.

13. When the desired sampling time is reached, turn off the vacuum pump. This halts the influx of furnace material into the particle sampling probe.

14. For Phase IIa tests involving the North Dakota and Kentucky baseline screening tests and for all Phase IIb tests, two impactors were available for particle sampling. In these experiments, the particle sampling probe was not immediately removed from the furnace. Instead, the first impactor was replaced in the particle sampling system by the second impactor and steps 11 through 13 were repeated.

    For the Kentucky experiments, the preseparator cyclone was attached to the first impactor to obtain samples from the submicron stages (1-6) while the second impactor was configured without the cyclone in order to obtain samples from the supermicron impactor stages (6-11). The nitrogen flow rate during second impactor sampling was maintained at the same rate as the isokinetic rate determined during first impactor sampling.

    For the North Dakota and Phase IIb experiments, neither impactor was configured with the preseparator cyclone. The nitrogen flow rate was maintained at the same rate for both impactor sampling periods.

15. Remove the particle sampling probe from the furnace.

16. Shutoff the nitrogen flow controller to halt nitrogen flow to the particle sampling probe.

17. Reconnect the gas sampling probe outlet line to the gas analyzer sample conditioning system inlet.

18. Obtain O_2, CO_2, CO, and NO_x readings from the sampling port and from Port 4 (Port 4b in Phase I) to verify the combustion conditions of the furnace.

19. Obtain temperature readings at the sampling port to verify the sampling temperature.

20. Unload the impactor and preseparator cyclone (if utilized). For impactor stages containing membranes, carefully fold the membrane to avoid loss of particulate matter and place in the correct preweighed microcentrifuge vial (see the *BLPI Media Preparation* section, above). For the baseline screening tests of bituminous coals in Phase I and Phase IIa, blanks were used in stages 7-11 when using the cyclone and in stages 1-5 when the cyclone was not being used.

    For impactor sets collected without the cyclone, discard the blanks in stages 1-5 (unweighed). For impactor sets collected with the cyclone, store the blanks in stages 7-11 in Petrie dishes until they are weighed on the microbalance.

    If the cyclone was used, disassemble and empty into the preweighed petrie dish. Remove residual material from the cyclone inlet fitting, outlet fitting, and internal walls using the preweighed wipe. Place the contaminated wipe in the Petrie dish with the loose material collected from the cyclone.

When additional samples were to be obtained, the impactor was reassembled and loaded with the appropriate membranes/blanks for the next sample. For the baseline screening tests of bituminous coals in Phase I, the second particulate sample was collected at the same sampling location using the BLPI without the preseparator cyclone attached. For these samples, the nitrogen flow rate for the second sample was maintained at the same value as was used for the first impactor sample.

Switchover to Gas

After all experimental activities were completed on a given experimental day, the combustion fuel was switched from coal to gas. This was accomplished by the following procedure:

1. Increase the main combustion air flow rate to 120% of the desired final flow rate for gas combustion (this rate was always higher than the experimental air flow rate during coal combustion).

2. Start gas flow at around 30 slpm (0.0005 Nm^3/s).

3. Reduce coal feed rate by 50%.

4. Increase gas flow to the final desired flow rate.

5. Stop coal feeder screw revolutions.

6. Reduce the vacuum blower speed to maintain a slightly negative pressure in the furnace. This speed was typically slightly higher than the speed used during warmup because ash

and slag residue deposited on the walls of the furnace during coal combustion increased the pressure drop in the furnace slightly.

7. After approximately 2 min, stop air flow to the coal feeder pneumatic vibrators.

8. After an additional 2 min, stop air or nitrogen transport gas feed to the coal feeder.

9. Reduce main combustion air flow rate to the final desired flow rate.

When additional experiments were to be performed on subsequent days, the furnace was left in this gas combustion state overnight. For additional safety, the coal feeder tube was usually disengaged from the coal burner inlet fitting (which was capped) to avoid any possibility of coal entering the burner while unattended.

When furnace shutdown was planned, the furnace was operated with gas combustion for a minimum of 15 min prior to shutdown to insure that all coal in the burner and furnace had oxidized.

Shutdown Procedure

The procedure outlined in the *Switchover to Gas* section above was always performed prior to furnace shutdown to insure that all coal in the furnace was completely oxidized prior to shutdown.

For shutdown, the following procedure was followed after the procedure outlined in the *Switchover to Gas* section above:

1. Stop natural gas flow to the burner.

2. Reduce the main combustion air flow rate to around 10% of the original flow.

3. Let the furnace purge with air for at least 10 min then shutoff the main combustion air flow. The UV air flow rate can also be eliminated.

4. Reduce the vacuum blower speed to approximately 7 Hz to draw a vacuum on the furnace. Leave for around 10 min.

5. Shutoff the vacuum blower. Stop the flow of cooling water to the baghouse outlet condenser.

6. After at least 12 hours of cooling, stop the flow of water to the burner radiant shield. Turn off the baghouse heating strips. Open all traps and drains on the furnace outlet system.

I.1.3 Post-Experimental Activities

Particle Sample Gravimetric Determination

Blanks and Cyclone Catch

Contaminated impactor blanks removed from BLPI stages 7-11 collected using the preseparator cyclone were weighed on the microbalance (Ohaus Analytical Plus) on the same day as they were collected. All microbalance weights were repeated. Two readings with a deviation of less than 0.00005 g in Phase I and 0.00003 g in Phase IIa were required before the weight data were accepted as accurate.

Similarly, the petrie dish containing the material removed from the cyclone and the contaminated wipe was also weighed on the same day as collected. Typically, the weight was allowed to stabilize on the balance for at least 30 min. If two weights within 0.00005 g could not be obtained (around 70% of the time), the average of five separate weighings was used to represent the weight.

Membrane Gravimetric Determination

The ash-laden membranes collected during particle sampling were stored in capped microcentrifuge tubes enclosed in sealed polyethylene snack bags. The combined membrane+ash+vial weight was typically not determined on the day of the experiment. Instead, the weights were typically determined after all experiments in the set were completed (usually within four weeks of the day of the experiment). All microbalance weights were repeated. Two readings with a deviation of less than 0.00005 g in Phase I, 0.00003 g in Phase IIa, and 0.00002 g in Phase IIb were required before the weight data were accepted as accurate.

Slag and Particulate Removal

The burner assembly and ash trap were removed to allow the interior of the furnace to be inspected. Slag tends to build up on the interior walls in the upper portion of the furnace. This slag was physically removed in Phase I by abrasion with a sharp steel spear. In Phase II, a chimney sweep brush was used. In order to get the chimney sweep brush into and out of the furnace, a portion of the 2 in. inlet quarl was removed. After the furnace was cleaned, moldable fibrous alumina (Zircar AX moldable) was used to rebuild the quarl prior to the next set of experiments in the furnace.

Slag and other particulate matter in sampling ports was also removed by physical impaction and compressed air.

Slag and ash was removed from the ash trap and particle trap. Any unburned coal buildup in the burner assembly was also removed.

Air and Cooling Water Systems

All rotating equipment, filters, and lines were inspected, serviced, and cleaned to remove contaminants. Air compressor oil was replaced every 500 operating hours.

The air blower was also disassembled and residual particulate was removed from the cover and blower vanes.

Sampling Probes

The gas and particulate sampling probes were cleaned with isopropyl alcohol and flushed with water to remove any residual contaminants. The gas sample lines were water flushed daily. The particulate sample line was renewed from new tygon tubing periodically. This sampling line was reserved and used only in particle sampling service.

I.2 Sample Preparation for In-House Analyses

Particle sample sets that most closely represented the average or typical particle size distribution for a particular experiment were selected for elemental analysis. Some of these sample sets were sent to MIT for analysis by INAA. Since this method is a dry analytical method, no sample preparation was required.

Other sample sets were identified for analysis at UA by atomic absorption spectroscopic methods (i.e., AAS, AES, and GFAA). These methods are wet methods and the inorganic elements in the fly ash had to be dissolved into a liquid media prior to analysis.

Prior to this research, analysis of trace elements in milligram level ash samples obtained from impactors had not been accomplished at UA. However, analysis of major inorganic elements from ash samples at the 0.1-g level obtained from impactors was routinely performed.

The main challenge in developing a sample preparation protocol for inorganic elemental analysis by AES/AAS/GFAA was to balance four conflicting factors:

1. Provide sufficient oxidation by acids to dissolve all inorganic material from the ash mounted on the greased membranes.

2. Minimize the acid strength in order to maximize the life of the graphite tubes, graphite contact cylinders, and Teflon autosampler pipette tips in the GFAA. This was a major concern because of the high cost of these consumables.

3. Minimize the quantity of liquid utilized in dissolution in order to maximize the detection range for trace elements (primarily selenium, antimony, and cobalt).

4. Maximize the quantity of liquid available after dissolution in order to analyze all of the major and minor elements desired from a single sample set.

Obviously, a protocol had to be developed that resulted in an acceptable compromise of these four factors.

The protocol developed was based on a modification of the existing in-house sample preparation protocols [165]. One of the keys was utilizing the correct vessel for digestion. Sample digestion was performed in 10 ml-capacity capped, graduated, polypropylene transport tubes (Perfector Scientific Transport Tube, Cat #2010).

I.2.1 In-House Digestion Protocol

The digestion protocol for inorganic elements in fly ash samples mounted on greased inertial impactor membranes is as follows:

1. Remove the membrane from the microcentrifuge vial with tweezers and place in a marked transport tube (Perfector Scientific Transport Tube, Cat #2010 or equivalent). Loosen the folds of the membrane somewhat to insure that all surfaces will be in contact with the dissolving acid.

2. Rinse out the microcentrifuge vial with one (1) ml of dissolving acid (see *Dissolving Acid* section below for composition of this acid) into the same transport tube containing the membrane.

   Note: accuracy in measurement of the digestion fluids is critical for accurate analytical results. See Appendix J, Quality Control for a discussion of this source of error.

3. Add another 3 ml of dissolving acid to the vial containing the membrane.

4. Sonicate the vial (unheated) for 12 min.

5. Allow samples to rest for 24 hours.

6. Sonicate the samples a second time for 12 min.

7. Add 4 ml of boric acid solution (see *Boric Acid* section below) to the vial containing the membrane.

8. Sonicate the samples for 5 mins.

I.2.2 Digestion Fluids

All dissolving fluids should be made using purified water. Typical laboratory grade ion-exchange quality water is acceptable for many of the trace elements of interest including arsenic, selenium, antimony, cobalt, cadmium, chromium, and cesium. However for analysis of sodium, lead, iron, calcium, magnesium and other similar elements by GFAA (not by AAS/AES), an ultrapure grade water is required.

Dissolving Acid

500 ml water
300 ml HF(49%)
100 ml HCl(37%)
100 ml HNO_3(70%)

Boric Acid

56.6 g Boric acid crystals dissolved to 1000 ml in water

I.2.3 Validation

The method was validated by two separate methods. First, a typical set of fly ash impactor samples (a total of 12) was subjected to the protocol. The membrane was removed from the digestion fluid and placed in a new transport tube. Then it was subjected to the protocol again. Both the original and secondary fluids were analyzed for arsenic, selenium, antimony, cadmium, and cobalt to determine the degree of digestion into the original fluid. For all elements, the concentration in the secondary fluid was below the detection limit of the GFAA.

To further validate the method, a sample of NIST standard reference material 1633b, Constituent elements in Coal Fly Ash was obtained. Three separate samples of the NIST fly ash were dissolved using the in-house digestion protocol. Analyses were completed for Si, Ca, Fe, Mg, and Al by AAS, for Na by AES, and for As, Se, Sb, and Co by GFAA.

In addition to these validation methods, the results obtained using the in-house digestion and analytical procedures was compared to results obtained by INAA at MIT. It was found that the variability between samples analyzed in-house was comparable to the variability between samples analyzed at both locations.

I.3 Size-Segregated Fly Ash Solubility Study

A leachability protocol was developed to investigate the solubility of the inorganic constituents of size-segregated fly ash particles collected on greased membranes in impactors (such as the BLPI used in this program work). The objectives of this program of study were:

1. Develop and demonstrate a technique applicable for examining the leachability of inorganic constituents on submicron-sized fly ash particles contained on greased impactor membranes.

2. Gain insight into the environmental impact of submicron particle deposition in a) soil downwind of coal-fired combustors and b) fly ash disposal sites and to compare this impact to that of supermicron particles.

3. Gain insight into how As, Se, and Sb partition to both submicron and supermicron particle surfaces by determining the degree of solubility of fly ash particle compounds containing these trace elements.

It was not the intent of this work to utilize the extensive leaching protocols typically used to investigate the forms of occurrence of trace elements in coal and fly ash.

I.3.1 Summary of Leaching Experiments

Selected size-segregated particle sample sets from baseline screening experiments were subjected to the protocol described in Section I.3.2, below to assess the solubility of arsenic-, selenium-, antimony-, and cobalt-containing species from submicron and supermicron fly ash. Table I-1 summarizes the sample sets and impactor stages utilized in this study.

Table I-1. Summary of Baseline Screening Sampling Sets
Utilized in the Sequential Solubility Study

Sample ID:stages	Coal	Particle Regime	Sample Location
PL1:1-2	Pittsburgh	Vapor	Port 14
PL1:3-5	Pittsburgh	Submicron	Port 14
PL1:6-10	Pittsburgh	Supermicron	Port 14
PL2:1-2	Pittsburgh	Vapor	Port 14
PL2:3-5	Pittsburgh	Submicron	Port 14
PL2:6-10	Pittsburgh	Supermicron	Port 14
PL3:3-5	Pittsburgh	Submicron	Port 4
PL3:8-10	Pittsburgh	Supermicron	Port 4
O8:3-5	Ohio	Submicron	Port 4
O8:8-10	Ohio	Supermicron	Port 4
O5:3-5	Ohio	Submicron	Port 14
O5:8-10	Ohio	Supermicron	Port 14
K5:3-5	Kentucky	Submicron	Port 4
K5:8-10	Kentucky	Supermicron	Port 4
K7:3-5	Kentucky	Submicron	Port 14
K7:8-10	Kentucky	Supermicron	Port 14
W3:3-5	Wyodak	Submicron	Port 4
W3:8-10	Wyodak	Supermicron	Port 4
W2:3-5	Wyodak	Submicron	Port 14
W2:8-10	Wyodak	Supermicron	Port 14
N1:3-5	North Dakota	Submicron	Port 4
N1:8-10	North Dakota	Supermicron	Port 4

I.3.2 Leaching Experiment Procedures

The procedure developed for this study is a modification of the standard EPA toxicity characterization leaching protocol method 1310 (TCLP 1310). The principal modifications are:

1. Sequential leaching is performed using both TCLP 1310 fluids. In method 1310, a sample of ash is tested to determine which fluid will be used.

2. The fly ash can be fixed on greased impactor membranes or free. In method 1310, the ash sample is a free sample.

3. Variable quantities of ash can be used and the quantities can be as small as in the 0.01 mg range. In method 1310, a fixed amount of ash in the 100 g range is required.

4. It is important that a very accurate net weight of ash be determined.

5. A fixed quantity of leachate will be generated regardless of the sample weight.

The modified method was developed to achieve the limited objectives listed above. A more rigorous leaching protocol is beyond the scope of work of the present program.

Procedure

This procedure allows an assessment of the solubility of inorganic constituents from size segregated fly-ash samples analogous to EPA's method TCLP 1310. The method is designed for use with fly ash samples collected using an impactor onto greased polycarbonate membrane substrates. The distribution of ash mass on these membranes is typically 0.1 mg to 100 mg. The method can also be used for loose solids samples by the addition of filtration or drying steps during fluid transfer.

1. PART 1: 1st Solubility Fluid (pH 4.93 step)

1.1 Determine net weight of fly ash on substrate.

1.2 Place substrate in a sealable test tube/vial (we used Perfector Scientific 10 ml Transport Tube, Cat #2010)

1.3 Add 5ml of the first solubility fluid (pH 4.93).

1.4 After the designated amount of fluid 1 is added, shake the solution by hand for a few seconds and check the pH.

1.4.1 If the solution has strayed from the initial pH of 4.99, then add the correct buffer solution dropwise while monitoring the pH. (See Item 4.3-below for buffer solutions).

1.5 Place the samples in an auto-shaking apparatus, for 18 +/- 2 hrs. After a period of 20 min, recheck the pH to insure that it has not changed from the expected pH.

1.5.1 The pH should be checked every hour until two consecutive pH readings are essentially the same.

1.6 After 18 hours, remove the samples from the auto-shaker and allow them to rest for approximately 1 hour. Recheck the pH and adjust if necessary.

1.7 Once the contents in the vial has settled, decant the solution into another resealable test tube/vial. This vial now contains fluid 1 leachate.

1.8 Remove trace amount of liquid from the samples.

1.8.1 Place the membrane in a syringe (no tip) and gently squeeze the remaining moisture out of the membrane.

1.8.2 Place the membrane back in a resealable test tube/vial.

2. PART 2: 2^{nd} Solubility Fluid (pH 2.88 step)

2.1 Add 5ml of the second solubility fluid 2 (pH 2.88).

2.2 Shake the solution by hand for a few seconds and check the pH.

2.2.1 If the solution has strayed from the pH of 2.88, add the correct buffer solution dropwise while the pH is read.

2.3 Place the samples in an auto-shaking apparatus, for 18 +/- 2 hrs. After a period of 20 min, recheck the pH to insure that it has not changed from the expected pH.

2.3.1 The pH should be checked every hour until two consecutive pH readings are essentially the same.

2.4 After 18 hours, remove the samples from the auto-shaker and allow them to rest for approximately 1 hour. Recheck the pH and adjust if necessary.

2.5 Once the contents in the vial has settled, decant the solution in another resealable test tube/vial. This vial now contains fluid two leachate.

2.6 Remove trace amount of liquid from the samples.

2.6.1 Place the membrane in a syringe (no tip) and gently squeeze the remaining moisture out of the membrane.

2.6.2 Place the membrane back in a resealable test tube/vial.

3. PART 3: Total inorganic dissolution step

3.1 Add 4ml of dissolving acid solution #1 to the vial containing the membrane.

3.2 Sonicate the vial (unheated) for 12 min.

3.3 Allow samples to rest for 24 hours

3.4 Sonicate the samples for an additional 12 min.

3.5 Add 4ml of dissolving acid solution #2 to the vial containing the membrane.

3.6 Sonicate the samples for 5 min.

4. PART 4: Fluids and solutions (purified water should be used)

4.1 Solubility Fluid #1 – (pH ~ 4.93 +/- 0.05)
Acetic acid - 5.7 ml
Water - 500 ml
Sodium OH (1N)= 1M NaOH - 64.3 ml

4.2 Solubility Fluid #2 – (pH ~ 2.88 +/- 0.05)
Acetic acid - 5.7 ml
Water - 94.3 ml

4.3 Buffer solutions

4.3.1 pH~1
HCl (1N) – 20 ml of HCl
Water - 480 ml

4.3.2 pH ~14
NaOH (1N) – 40g NaOH pellets
Water - up to 500 ml

4.4 GFAA solutions

4.4.1 Dissolving acid #1
500 ml water
300 ml HF(49%)
100 ml HCl(37%)
100 ml HNO_3(70%)

4.4.2 Dissolving acid #2
56.6 g boric acid crystals
up to 1000 ml water

Method Validation

Special sample sets were collected at Port 14 during the combustion of Pittsburgh seam coal under baseline screening combustion conditions to validate the method. In these sample sets, the membranes were cut in half and each half was defined gravimetrically. The "A" set of membranes were subjected to the modified TCLP 1310 protocol described above. The "B" set was digested directly per section 3 of the modified TCLP1310 protocol.

By adding up the mass of arsenic collected for each fluid and for each impactor stage, the mass balance closure of the modified protocol was determined. We also determined the mass of

fly ash collected on the "A" and "B" membranes which provides an indication of the error in the gravimetric measurements. The results of both calculations are summarized in Table I-2.

Table I-2. Leaching Protocol Validation: Arsenic Closure

Impactor Stage	As Recovery in all three fluids (ppmw)	As Recovery in Control Sample (ppmw)	Relative Difference (%)	Ash Mass Leached Membranes (g)	Ash Mass Control Membranes (g)	Relative Difference (%)
1c*	327	263	20	0.000465	0.000495	6
2c	507	371	27	0.000415	0.000575	39
3c	538	549	2	0.000275	0.00027	2
4c	754	940	25	0.00019	0.000185	3
5	648	419	35	0.000165	0.00026	58
6c	489	327	33	0.00039	0.000615	58
6	778	308	60	0.000155	0.00029	87
7	535	494	8	0.0003	0.00031	3
8	339	203	40	0.00043	0.00055	28
9	213	169	21	0.00073	0.000625	14
10	102	95	7	0.00116	0.00117	1
11	141	146	3	0.0008	0.000675	16

* indicates sample collected with inlet preseparator cyclone attached to impactor

In Figure I-4 the error in the arsenic mass balance for each impactor membrane is plotted versus the difference in the fly ash mass measured on the "A" and "B" membranes. The results in Figure I-4 along with the cross correlation coefficient calculated indicate that error in the arsenic mass balance closure correlates with the differences in the fly ash mass determination (within the accuracy of this experimental program) and therefore that errors in the mass balance are primarily due to gravimetric measurement uncertainty rather than due to errors from the leaching protocol or analytical procedures.

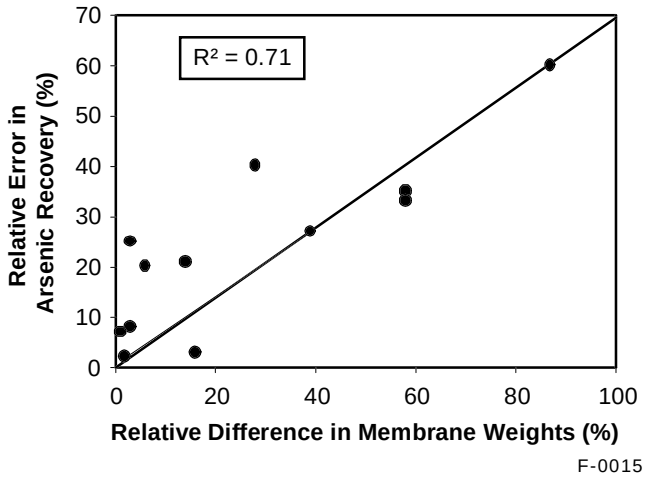

Figure I-4. Cross correlation of arsenic closure error to membrane gravimetric variability.

APPENDIX J

Quality Assurance and Control for Large Scale Combustion Studies

This section provides a qualitative and, when possible, a quantitative assessment of the error associated with this experimental program. It also describes the quality assurance program implemented to maximize the probability that the results and analyses derived from these experiments are accurate.

J.1 Quality of the Combustion Experiments

It is not possible, due to the size and complexity of combusting coal in UA's downflow combustor, to be assured of accurate and reliable results during every experiment. Therefore multiple experiments were run for all baseline screening tests. Reliability improved over the course of the program due to improvements in the functionality, operability, and reliability of the experimental equipment (see Section 3.3.3, Equipment for more details) and due to increased experience in running coal combustion experiments with this equipment.

In Phase I, experiments were run until duplicate sample sets from both ports 4b and 12 that were obtained that were judged to be truly representative of typical combustion conditions. In Phase IIa, a minimum of four good experimental sampling days and at least one good experimental day for gas and temperature profiles was considered the minimum acceptable experimental scope to insure quality results. As an additional requirement, there had to be at least three sample sets that could be used to characterize the typical combustion condition.

In Phase IIb the objectives were more limited and confidence in operating the equipment was at a maximum. Furthermore, many different experimental conditions were investigated. Therefore, using the stringent quality guidelines from Phase IIa was not feasible. In this phase only one good experimental day with duplicate sample sets was required at each combustion condition/sampling location combination.

Some of the main sources of error associated with the actually operation of the combustion system were:

1. The inability to accurately define the coal feed rate.
    - It was not possible to calibrate the coal feeder to match actual combustion conditions. The vacuum induced on the coal transport line by the burner could not be simulated accurately and this difference in feed resistance had a substantial effect on the coal feed rate.
    - Leakage through cracks in furnace walls and sample ports made it difficult to accurately back calculate the actual coal feed rate from the oxygen consumption or CO_2/CO generation in the furnace.
    - The accuracy of the coal proximate analysis and theoretical combustion calculations limited the ability to infer coal feed rate from excess oxygen or CO_2/CO generation in the furnace.

2. The lack of consistency of coal feed rate over time.
   - The feed rate changed with changes in the coal profile in the feed hopper. The gas composition had to be constantly monitored so that the coal feeder screw speed could be adjusted to accommodate these changes.
   - Bridging and "rat-hole" formation (these coals have over 25 wt% water contents) in the coal feed hopper for lower rank coals sometimes significantly affected the feed rate. Sometimes this problem required shutting down the coal feed and redistributing or replacing the coal in the hopper. This made assessment of steady-state conditions more difficult. For the North Dakota lignite, it was necessary to pulse the hopper with compressed argon every 12 minutes to avoid bridging.
   - The feed rate changes with changing pressure profile in the furnace. The gas composition had to be constantly monitored so that the coal feeder screw speed could be adjusted to accommodate these changes.

3. The variations in the coal composition.
   - This problem was greater for lower rank coals which have a greater variation in composition. The gas composition had to be constantly monitored so that the coal feeder screw speed could be adjusted to accommodate these changes.

4. The difficulty in maintaining steady-state conditions during particle sampling.
   - This problem was greatest for the lower rank coals due to the variations in coal composition and the variations in feed rate for a given screwfeeder speed.

No attempt was made to quantify any of these sources of error. Instead, replication of the total ash particle size distribution was used as the primary quality measure for whether the experiments were valid. On-site evaluation of furnace operation also played a part in determining when experiments were considered to generate reliable results.

J.2 Error Associated With Particulate Sampling

Particle sampling was carried out using a portable, water-cooled, stainless steel, aspirated isokinetic sampling probe. Samples extracted by the probe from the centerline of the furnace were routed through a Berner Low Pressure Impactor (BLPI) [130] using a dilution nitrogen gas stream and a vacuum pump. The bottom stage of the BLPI acts as a sonic orifice to control the total flow rate from the sampling probe. During these experiments the total gas flow rate was maintained at a constant value by this sonic orifice. Isokinetic sampling was accomplished by adjusting the dilution nitrogen flow rate.

The major sources of error during particle sampling were:

1. The loss of particles to the interior walls of the probe and tubing prior to the BLPI.
   - Losses are not expected to be evenly distributed (large particles are expected to be lost at a higher fraction than smaller particles).

2. The difference between the actual total flow rate and the calibrated total flow rate through the impactor.
   - The impactor total flow rate was determined prior to sampling. Changes in laboratory temperature/atmospheric pressure or resistance in the sampling system could result in differences between the actual total flow rate and the calibrated total flow rate.

3. The introduction of inaccuracies in determining the isokinetic sampling rate.
   - The theoretical isokinetic sampling rate calculation was determined to be within +/- 20% of the actual isokinetic sampling rate based on NOx measurements. All of the Phase I and most of the Phase IIa experiments were based on a theoretical isokinetic sampling rate calculation.
   - Even when actual NOx measurements were used to determine the isokinetic sampling rate, most of the sample collection times were too short to make this determination during sampling. In these cases, the isokinetic sampling rate was determined prior to sampling using blanks in the impactor. Changes in the operating conditions of the furnace between rate determination and sampling could result in over- or under-sampling.

4. The inability to be sure that all material was obtained from the preseparator cyclone and included in the cyclone catch weight.
   - It was difficult to remove all of the particles collected in the preseparator cyclone for the Phase I and Phase IIa bituminous coal experiments.
   - The use of a preweighed tissue improved this in Phase IIa compared to Phase I but did not completely eliminate this problem.

5. The evaporation of grease off of membranes during sampling.
   - All membranes were sprayed with grease dissolved in a hydrocarbon. During Phase I, membranes were dried for at least 24 hours prior to use. However negative weights were experienced on the lowest sampling stages due to evaporation of the residual hydrocarbon and possibly elements of the grease during sampling.
   - In Phase II, all membranes were vacuum desiccated for 24 hours prior to use. This reduced the number of negative weight readings recorded but did not completely eliminate them.
   - Loss of weight due to evaporation was likely present on all impactor stages during these experiments. The impact of this weight loss on the particle size distribution is probably fairly linear, although the more rapid loading of particles on the larger-size impactor stages may have inhibited evaporation somewhat.

6. Loss of particles to the exterior surface of the sampling probe in the furnace due to thermophoresis.
   - Losses to the water-cooled exterior surface of the particle sampling probe are not expected to be evenly distributed.

No attempt was made to quantify any of these sources of error. Instead, replication of the total ash particle size distribution was used as the primary quality measure for whether the experiments were valid.

In Phase IIa, procedures were followed to replace negative weights on selected impacted stages (usually stages 1 or 2) with predicted weights. For the Ohio, Wyodak, and Kentucky baseline screening experiments, the negative weight was replaced with a weight that allowed the weight fraction (grams of ash on stage x per grams of ash on all stages) to equal the average weight fraction from all other valid experimental sample sets collected under identical conditions. Whenever feasible, these sample sets were not selected for analysis.

For the North Dakota baseline screening experiments in Phase IIa and for all Phase IIb experiments, back-to-back sample sets were collected using two impactors. Therefore, the negative weight was replaced with a weight that allowed the weight fraction on that stage to equal the weight fraction from the twin sample set. Again whenever feasible, these sample sets were not selected for analysis.

J.3 Gravimetric Error

Accurate particle size distributions and size-segregated elemental concentrations in the BLPI sample sets requires accurate measurement of the weight of the ash collected on the membranes and, when applicable, in the preseparator cyclone. Lawless and Rodes [274] performed a detailed study of the sources of error when collecting impactor samples in systems similar to the one used in these experiments. They determined that gravimetric error was the primary source of error introduced into the results derived from a gravimetric-type impactor loaded with stabilized (e.g., vacuum desiccated for 24 hours) greased membranes.

This source of error was given considerable attention during this program. The causes of gravimetric error can be divided into those that result in random error and those that result in systematic error. Both of these categories are described below.

The error bars shown with the results (Section 3.3.3) from this program include a gravimetric uncertainty factor. The gravimetric uncertainty factor is the sum of the random gravimetric error factor plus the systematic error factor (To be rigorously accurate, the systematic error factor should only be applied to the positive uncertainty of the gravimetric weight. However it made the calculations much simpler to include this factor in both positive and negative uncertainty. Since this factor is relatively minor, the difference in the reported uncertainty will not affect any of the conclusions derived from these results). The source of these values is discussed below.

J.3.1 Random Error

All microbalance weights were repeated in an independent fashion. Where independent, means a vial, blank, or membrane was not weighed and then immediately reweighed again. Instead, a set of three to six items were weighed and then the entire set was reweighed. When a vial, blank, or membrane had to be reweighed immediately, the scale was allowed to come to

complete zero (retared to zero if necessary) prior to replacing the item on the balance. Two readings with a deviation of less than 0.00005 g in Phase I, 0.00003 g in Phase IIa, and 0.00002 g in Phase IIb were required before the weight data were accepted as accurate. Usually, the deviation was less than the accepted tolerance.

Using the gravimetric data from all of the sample sets collected in the course of this research program, the average standard deviation for measurements from each program phase and for each type of weight have been determined. The results are shown in Table J-1. The method chosen to convey this uncertainty is to define the random gravimetric uncertainty factor for a given sample as the sum of the single standard deviation values representing the uncertainty from each of the gravimetric measurements utilized in calculating the net ash mass on a membrane.

J.3.2 Systematic Error

Lawless and Rodes [274] concluded that the largest cause of gravimetric error was the buildup of static charge on the membranes. Static charge was also observed to be a problem with a significant minority of the membranes utilized in this work. This error will vary depending on the charge buildup on the membrane and other external factors including the amount of residual charge on the microbalance pan. No attempt was made to quantify this source of error during these experiments. Since this error is not quantified a systematic uncertainty correction term for this error is not included in this analysis. Some perspective on the degree of error that may be introduced by this decision can be inferred from the Lawless and Rodes (1999) study. In their study, they estimated the increase in apparent mass due to static charges to be 4-46 μg.

As stated in Appendix I, the empty sample vials were preweighed prior to executing a set of experiments. The vials were then stored in two layers of sealed polyethylene until used. On average, the vials were preweighed approximately one month before they were reweighed filled with an ash-laden membrane. This procedure may introduce a systematic error into the gravimetric measurements.

To test for this error, a series of sample vials were weighed in March 1999. Repeat weights were performed until two readings were observed to within a variance of 30 μg. The vials were then stored in two layers of resealable polyethylene bags (snack bags enclosed in a freezer-size bag). The vials were reweighed in December 1999 using the same microbalance and with the same tolerance criterion. Once the initial weight was taken, the vials were handled only with tweezers to avoid contamination from skin oils.

A comparison of the results is shown in Table J-2 and Figure J-1. The average absolute error of the nine vials included in this test was +40 μg with a range of –43 to +95 μg. Seven of the vials weighed higher at the 2nd reading and two of the vials weighed less at the 2nd reading. The average relative error was 0.0036%. The average error is twice the acceptable uncertainty of the readings and the maximum value is three times the acceptable uncertainty. It must be concluded that vial preweighing does add systematic error that should be included in the uncertainty of the measurement.

Table J-1. A Summary of the Gravimetric Error Associated with Particulate Sample Results

Tests	Avg. Empty Vial uncertainty	# of Empty Vial Measure-ments	Avg. Empty Cyclone Uncertainty	# of Empty Cyclone Measure-ments	Avg. blank membrane uncertainty	# of Blank Membrane Measure-ments	Avg. filled vial uncertainty	# of Filled Vial Measure-ments	Avg. filled cyclone uncertainty	# of Filled Cyclone Measure-ments
Ohio P4[1]	1.53E-05	185	6.27E-04	19	8.67E-05	270	1.27E-05	258	3.78E-04	12
Ohio P14	1.86E-05	133	3.60E-04	12	1.28E-05	222	2.46E-05	232	1.01E-03	17
Ohio BG[2]	1.02E-04	46	4.50E-04	5	5.00E-06	59	1.51E-05	62	1.00E-05	2
Wy[3] P4	1.62E-05	90			1.59E-05	89	1.55E-05	90		
Wy P14	1.46E-05	92			1.40E-05	101	1.22E-05	100		
Wy BG	1.18E-05	66			1.18E-05	67	1.64E-05	66		
ND P4	1.64E-05	110			8.12E-06	116	7.15E-06	114		
ND P14	1.04E-05	111			2.91E-06	110	5.15E-06	112		
ND BG	2.86E-05	111			2.42E-05	113	1.27E-06	110		
Ky P4	1.66E-05	114	3.13E-03	13	1.09E-05	171	1.19E-05	165	2.67E-05	6
Ky P14	1.42E-05	120	1.62E-02	13	7.41E-06	170	1.00E-05	170	6.53E-04	6
Ky BG	1.89E-05	111			9.50E-06	112	9.64E-06	110		
IL P4a	2.00E-05	72	2.23E-03	8	1.75E-05	132	1.40E-05	133	6.26E-04	9
IL P12	1.60E-05	84	3.10E-04	6	1.44E-05	154	2.06E-05	155	3.89E-03	10
IL BG	2.19E-05	56			1.05E-05	44	1.64E-05	44		
P8 P4a	1.07E-04	49	2.50E-05	6	2.73E-05	98	2.49E-05	93	1.40E-05	5
P8 P12	5.36E-05	51	1.40E-05	5	2.63E-05	93	2.20E-05	97	2.20E-05	5
P8 BG	1.50E-05	44			6.36E-06	44	7.73E-06	44		
WS -4	6.78E-06	367			7.92E-06	367	8.74E-06	367		
WS-14	6.57E-06	380			6.14E-06	379	9.54E-06	377		
OS-4	9.00E-06	60			4.67E-06	60	7.67E-06	60		
OS-14	7.33E-06	60			3.67E-06	60	1.03E-05	60		
PS-4	8.75E-06	48			7.50E-06	48	4.58E-06	48		
PS-14	9.17E-06	48			5.83E-06	48	4.58E-06	48		
KS-4	9.17E-06	24			4.17E-06	24	4.17E-06	24		
KS-14	1.00E-05	24			9.17E-06	24	9.17E-06	24		

[1] P4 = from Port 4 (Phase II furnace) sampling location sample sets, P14 = from Port 14 sampling location sample sets, BG = from Baghouse inlet sampling location sample sets, P4a = from Port 4a (Phase I furnace) sampling location sample sets, P12 = from Port 12 sampling location sample sets

[2] BG – from Baghouse Inlet sampling location sample sets

[3] Oh = Ohio Phase IIa, Wy = Wyodak Phase IIa, ND = North Dakota Phase IIa, Ky = Kentucky Phase IIa, IL = Illinois Phase I, P8 = Pittsburgh Phase I, WS = Wyodak Phase IIb, OS = Ohio Phase IIb, PS = Pittsburgh Phase IIb, KS = Kentucky Phase IIb

Table J-1. (Continued) A Summary of the Gravimetric Error Associated with Particulate Sample Results

Tests	Avg. Empty Vial uncertainty	# of Empty Vial Measure-ments	Avg. Empty Cyclone Uncertainty	# of Empty Cyclone Measure-ments	Avg. blank membrane uncertainty	# of Blank Membrane Measure-ments	Avg. filled vial uncertainty	# of Filled Vial Measure-ments	Avg. filled cyclone uncertainty	# of Filled Cyclone Measure-ments
Summary	**of Results**									
Phase I	2.10E-05	256	3.98E-04	25	1.01E-05	477	9.95E-06	478	7.70E-04	29
Phase IIa	9.82E-06	1389	2.17E-03	62	1.16E-05	1688	6.24E-06	1677	3.01E-04	43
Phase IIb	3.60E-06	1011			3.31E-06	1010	4.29E-06	1008		

Testing Phase	Type of Sample	Avg. Std. Dev. For Empty Vial	Avg. Std. Dev. For Blank Membrane	Avg. Std. Dev. For Filled Vial	1/5 Avg. Std. Dev. For Empty Cyclone	1/5 Avg. Std. Dev. For Filled Cyclone	Random Uncertainty Factor	Systematic Uncertainty Factor	Total Gravimetric Uncertainty Factor (g/sample)
I	Supermicron size stages sampled with cyclone	2.10E-05	1.01E-05	9.95E-06	7.96E-05	1.54E-04	2.75E-04	5.00E-06	**2.75E-04**
	Submicron size stages	2.10E-05	1.01E-05	9.95E-06			4.11E-05	5.00E-06	**4.11E-05**
	Supermicron size stages samples without cyclone	2.10E-05	1.01E-05	9.95E-06			4.11E-05	5.00E-06	**4.11E-05**
IIa	Supermicron size stages samples with cyclone	9.82E-06	1.16E-05	6.24E-06	4.35E-04	6.02E-05	5.22E-04	5.00E-06	**5.22E-04**
	Submicron size stages	9.82E-06	1.16E-05	6.24E-06			2.76E-05	5.00E-06	**2.76E-05**
	Supermicron size stages samples without cyclone	9.82E-06	1.16E-05	6.24E-06			2.76E-05	5.00E-06	**2.76E-05**
IIb	Submicron size stages	3.60E-06	3.31E-06	4.29E-06			1.12E-05	5.00E-06	**1.12E-05**
	Supermicron size stages samples without cyclone	3.60E-06	3.31E-06	4.29E-06			1.12E-05	5.00E-06	**1.12E-05**

Table J-2. A Comparison of Empty Vial Weights after Nine Months Storage

Vial #	March 99 Weight (g)	Dec. 99 Weight (g)	Absolute Error (g)	Relative Error (%)
11	0.99474	0.994745	0.000005	0.0005
10	0.989615	0.98967	0.000055	0.0056
8	0.96956	0.969635	0.000075	0.0077
7	0.963795	0.96389	0.000095	0.0099
6	0.918613	0.91857	-0.000043	-0.0047
4	0.98339	0.983455	0.000065	0.0066
3	0.993255	0.993215	-0.000040	-0.0040
2	0.99375	0.99382	0.000070	0.0070
1	0.965215	0.965255	0.000040	0.0041
		Average ➔	0.00004	0.0036

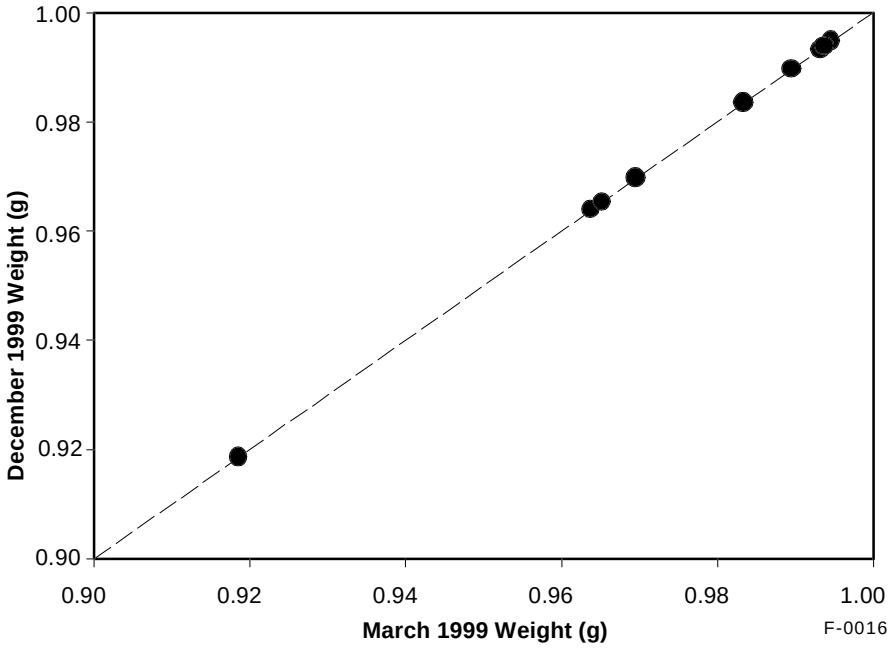

Figure J-1. Assessment of error due to preweighing empty sample vials for particle sampling.

Since the gap in time was 9 months compared to the 1 month typically experienced, the test results represent a conservative upper limit of the error that might be incurred due to preweighing of sample vials. Using this data, the additional deviation due to preweighing sample vials is estimated at +/- 5 μg (40/2-30/2). This additional deviation is used as the systematic gravimetric uncertainty factor (see Table J-1).

J.4 Analytical Error

The complexity of coal combustion fly ash makes analysis far more challenging than "clean" samples such as wastewater. There are three major sources of analytical error: 1) measurement inaccuracies during sample preparation, 2) elemental contamination in the membrane material and grease, and 3) errors in the actual analytical readings.

A number of quality assurance steps were implemented to maximize the accuracy and reliability of the results:

1. Sample sets were selected for analysis based on how closely these sets reflected the typical total ash particle size distribution.

2. Sample sets with zero or negative net weights were not selected for analysis unless no other sample sets were available.

3. For the Phase IIa baseline screening tests (except the Kentucky sample sets), sample sets were analyzed by two different laboratories utilizing different analytical methods for the Port 4 and Port 14 sampling location. One sample set at each location was analyzed by MIT using INAA and two sample sets at each location were analyzed at Arizona using AAS/AES/GFAA. In general, the differences between the analytical methods were within the variances between results generated at Arizona from multiple sample sets using the same analytical methods.

4. Three separate sample sets were analyzed at Arizona using AAS/AES/GFAA for Phase IIa Baghouse inlet port results and the Kentucky baseline screening results.

5. When possible, sample sets taken from the same experimental day were analyzed by the same method.

6. Unusual results based on comparison between sample sets were reverified by the original analytical method.

A description of the sources of error and quality control procedures for each analytical location is provided below. In addition, quantification of uncertainty is also presented.

J.4.1 Instrumental Neutron Activation Analytical Error

Samples sent to MIT for INAA analysis were not subject to sample preparation measurement errors since the INAA technique is a dry technique.

A thorough discussion of the INAA technique and the factors affecting the accuracy of INAA analyses can be found in Laul [275]. According to Laul, the basic criteria controlling sensitivity for determining multi-elements by sequential INAA are: 1) the neutron flux in the reactor, 2) the irradiation times, 3) the decay interval prior to counting, 4) the half-life and γ-ray energy of a radionuclide, and 5) the resolution and efficiency of the Ge(Li) detector. At MIT,

two irradiation periods were used to accommodate the substantial variations in irradiation times for the elements of interest.

Laul also lists the most common systematic errors as: 1) incorrect preparation of elemental standards, 2) different neutron fluxes for sample and standard, 3) thermal neutron self-shielding by large amounts of high cross-section elements such as boron and cadmium, 4) consistent unknown interference from another activation product, and 5) uncorrected deadtime losses caused by different activities of sample and standard. To mitigate most of these sources of error, a NIST certified fly ash was used as the quality control check during these analyses.

For INAA analyses the uncertainty in elemental mass per sample was reported by MIT as a measure of the analytical uncertainty. This value was converted into an uncertainty in element mass/ash mass (ppmw) and the average value for each element in each program phase was then computed. These analytical uncertainty factors are shown in Table J-3.

In addition, blank greased membranes were also analyzed by INAA in both Phase I and Phase IIa. These results are also shown in Table J-3. The typical background contamination values shown in Table J-3 were subtracted from the raw analytical data prior to applying any uncertainty factors. Phase I data was corrected with the Phase I background contamination values and Phase II data was corrected with the Phase II background contamination values. Corrected elemental data are given for all of the INAA results reported in Section 3.3.3.

J.4.2 Measurement Error during In-house Sample Preparation for Atomic Absorption/Atomic Emission/Graphite Furnace Spectroscopy

Measurement errors for in-house samples were incurred because of inaccuracies in metering the exact volume of liquid solution used in the dissolution procedure (see Appendix I). Liquid solutions were metered using Rainin Pipetman 1000 and 2000 µl micropipettors. These devices were routinely calibrated using fixed glass pipets. Due to the strong acids used in the digestion procedure, the micropipettors had to be cleaned and recalibrated fairly often (approximately every 3 weeks when in routine use). In addition, the transport tubes used to hold the sample solution were also graduated. These graduation markings were used to verify that the micropipettor had metered the correct volume of solution.

No attempt was made to exactly define the measurement error introduced during the sample preparation procedure. Based on the need to clean and recalibrate frequently, the micropipettor manufacturer's stated accuracy is believed to be too optimistic. Therefore, a conservative estimate of 0.05 ml per measurement was chosen based on the limit of a person's ability to discern the accuracy of micropipettor operation compared to the transport tube graduated markings (Perfector Scientific has not published the accuracy of the transport tube markings).

For example, to obtain the arsenic concentration for Ohio Run 11c, stage 3, the original sample was prepared by first adding 4 ml of dissolving acid to the membrane-containing transport tube. Then, 4 ml of boric acid were added. Finally, the sample was diluted by a factor

Table J-3. Summary of the Analytical Error
Associated with Elemental Results for Elements Analyzed by INAA

Element	Phase I Uncertainty (ppmw Element/ash)	Phase I Contamination Correction (ppmw)	Phase II Uncertainty (ppmw Element/ash)	Phase II Contamination Correction (ppmw)
Na			5.22E+02	1.95E+01
Mg			9.15E+02	6.99E+00
Al			2.53E+03	5.89E+01
Ca	7.65E+03	0[1]	3.85E+03	4.42E+01
Cl			4.18E+02	2.39E+01
K			4.47E+03	0[a]
Sc	5.00E-02	3.38E-03	2.52E+00	6.25E-03
Ti			6.34E+02	0
V			2.77E+02	3.02E-02
Cr			1.58E+02	2.87E+01
Mn			1.79E+02	9.20E-01
Fe	6.00E+02	2.36E+01	3.06E+03	5.89E+01
Co	1.20E+00	5.09E-02	1.03E+01	2.43E-01
Zn	9.00E+01	5.45E+00	3.05E+02	5.89E+00
Ga			1.33E+01	0
As	4.75E+00	3.64E-03	4.74E+01	3.68E-02
Se	1.21E+01	1.16E-02	3.37E+01	4.05E-01
Br			7.45E+01	1.58E+00
Rb	2.40E+01	3.31E-01	5.37E+00	0
Sr			1.09E+02	0
Mo	1.62E+01	3.13E-02	2.40E+01	0
Cd	3.50E+03	2.80E-02	5.66E+01	1.25E-01
In			3.59E-01	0
Sb	6.00E-01	2.15E-03	3.08E+00	1.91E-02
Cs	2.00E+00	5.82E-02	6.19E+00	0
Ba			3.78E+01	0
La	1.00E-01	4.73E-03	1.65E+00	1.07E-02
Ce	1.65E+00		9.23E+00	0
Nd			2.56E+01	5.89E-01
Sm	2.65E-02	8.36E-04	4.51E-01	1.73E-03
Eu	2.80E-01	2.25E-02	3.20E-01	0
Yb	8.00E-02	3.24E-03	1.23E+00	0
Lu	4.00E-02	1.05E-03	1.61E-01	0
Au	4.15E+00	5.09E-04	4.95E-02	1.66E-04
Hg	2.00E-01	3.05E-02	6.60E-01	3.38E-02
Th	7.00E-01	1.02E-02	2.19E+00	8.09E-02
U			7.25E-01	0

[a] 0 = contamination level below detection limit

of 9 (in a single dilution step) to the final concentration. There are three micropipettor measurements involved in this preparation, so the uncertainty is 3 x 0.05 ml or 0.15 ml/sample. Since this sample weighs 8.33E-06 g/ml, the measurement uncertainty factor is +/-1.3 ppmw (As/ash).

As with the INAA samples, blank greased membranes were dissolved and analyzed for all of the elements of interest. The average of four values was used and is reported in Table J-4. The typical background contamination values shown in Table J-4 were subtracted from the raw analytical data prior to applying any uncertainty factors. Corrected elemental data are given for all of the AAS/AES/GFAA results reported in Section 3.3.3.

Table J-4. Analytical Error Associated with Elemental Results for Elements Analyzed by AAS, AES, and GFAA from Fly Ash Samples (excluding leaching study analyses)

Element	Uncertainty (ppmw/ sample)	Contamination Correction (ppmw)
AAS/AES		
Si	3.86E+03	1.85E+02
Ca	1.45E+03	5.57E+01
Na	2.88E+02	1.91E+02
Mg	5.07E+01	1.81E+01
Fe	1.27E+03	2.92E+03
Al	9.62E+02	1.42E+02
GFAA		
As (high)[a]	3.90E+01	1.10E+00
As (low)[b]	5.29E+00	1.10E+00
Se	4.38E+00	2.32E-01
Co	3.75E+00	5.98E-01
Sb	5.88E+00	5.61E-01

[a] As(high) applies to samples from the Phase IIa Ohio baseline screening and the Phase IIb Wyodak Special Doping experiments

[b] As(low) applies to all samples not utilizing As (high

J.4.3 AAS and AES Analytical Error

Atomic absorption flame spectroscopy was used for all major inorganic species analyzed in-house except for sodium which was analyzed by atomic emission flame spectroscopy. The primary sources of error are: 1) background interference by other elemental emissions within the measured spectrum, 2) sensitivity limits of lamps and instrument, and 3) accuracy of the calibration curve generated.

All calibration standards were developed from certified standards (99.99+% accurate) using purified water. Serial dilutions of no more than 10:1 were used to minimize measurement errors. A new calibration curve was developed for each analyzer run. Blanks and quality control standards were also used. For most of the analyses, triplicate NIST-certified fly ash samples (from the same batch used at MIT for INAA) were used as an additional quality check. Samples

were diluted when required to insure that detection values were within the limits of the calibration curve.

Duplicate or triplicate measurements were obtained for each sample. If a sample result appeared questionable or the variance in the measurements was great, the sample was rerun to verify or correct the results. For each element, the average standard deviation in the sample measurements was calculated and is shown in Table J-4. The analytical uncertainty factor for these samples includes this single standard deviation of variation based on these average values.

An estimate of the uncertainty for samples from the leaching study was determined separately. Each fluid in the leaching protocol has a different acid composition and concentration which will affect the repeatability of the results. For each element/leaching fluid combination, the average standard deviation in the sample measurements was calculated and is shown in Table J-5. The analytical uncertainty factor for these samples includes this single standard deviation of variation based on these average values. The third leaching fluid uses the identical acid as the normal digestion utilized for total fly ash dissolution. So, the analytical uncertainty factors values in Table J-4 have used for these samples.

Table J-5. A Summary of the Analytical Error Associated with Elemental Results for Leaching Study Samples Analyzed by AAS, AES, and GFAA

Element	Fluid 1 Uncertainty (µg/l)	Fluid 2 Uncertainty (µg/l)
AAS		
Ca	9.36E+01	4.59E+01
Fe	0.00E+00	0.00E+00
Al	0.00E+00	0.00E+00
GFAA		
As	2.84E-01	2.87E-01
Se	1.28E-01	7.71E-02
Sb	0.00E+00	0.00E+00
Co	0.00E+00	0.00E+00

J.4.4 GFAA Analytical Error

Graphite furnace atomic absorption spectroscopy was used for all trace inorganic species analyzed in-house. The primary sources of error are: 1) background interference by other elemental emissions within the measured spectrum, 2) sensitivity limits of lamps and instrument, 3) trace contamination from the water or matrix modifier sources, 4) accuracy of the calibration curve generated, 5) integrity of the graphite tube and contact cylinders, and 6) integrity and accuracy of the automatic sampling system micropipettor.

All calibration standards were developed from certified standards (99.99+% accurate) using purified water. Serial dilutions of no more than 10:1 were used to minimize measurement errors. A new calibration curve was developed each time the graphite tube was replaced or more often if failure of quality checks (independent quality control standard check or spike/recovery test) occurred. A linear calibration curve, passing through zero was required to have a Pearson's correlation coefficient of 0.995 for all trace elements except cobalt which required a 0.985 coefficient (0.995 was not possible with this element due to high interference levels).

Blanks, spikes, and quality control standards were also used. Spikes were developed from the same original standard as was used to produce the calibration curve. The quality control standards were produced from a separate certified standard (Perkin-Elmer QC-21 multi-element standard). Spikes and control samples were run on average every ten samples. In addition, triplicate NIST-certified fly ash samples (from the same batch used at MIT for INAA) were used as an additional quality check. Samples were diluted when required to insure that detection values were within 110% of the limits of the calibration curve. The automatic sampling system was used for dilutions up to 10:1. For samples still beyond the calibration range, manual dilutions (performed serially at no more than 10:1) were used.

The manufacturer's recommended matrix modifier was used with all analyses to improve sensitivity and recovery during analysis. In addition, end-cap tubes were used to further improve sensitivity of the results. In these tubes, there is a reduction in the diameter of the optical opening at the ends of the graphite tubes to reduce losses of material during pyrolysis.

Triplicated analyses were performed for each sample. Values greater than one standard deviation from the mean were rejected. Additionally, if the mean sample result appeared questionable or the variance in all three measurements was great, the sample was rerun to verify or correct the results. For each element, the average standard deviation in the sample measurements was calculated and is shown in Table J-4. The analytical uncertainty factor for these samples includes this single standard deviation of variation based on these average values.

An estimate of the uncertainty for samples from the leaching study was determined separately. Each fluid in the leaching protocol has a different acid composition and concentration which will affect the repeatability of the results. For each element/leaching fluid combination, the average standard deviation in the sample measurements was calculated and is shown in Table J-5. The analytical uncertainty factor for these samples includes this single standard deviation of variation based on these average values. The third leaching fluid uses the identical acid as the normal digestion utilized for total fly ash dissolution. So, the analytical uncertainty factors values in Table J-4 have used for these samples.

J.5 Overall Assessment Of Error

J.5.1 Total Ash Distribution

A typical total ash particle size distribution (PSD) was developed for each coal/combustion condition/sampling location combination. These were developed by calculating the average distribution of all of the relevant sample sets that had accepted as valid experiments.

The gravimetric uncertainty factors shown in Table J-1 were applied to the typical total ash PSD's to generate the error bars and overall uncertainty values reported in Section 3.3.3.

J.5.2 Elemental Concentrations and Distributions

A typical elemental concentration and a typical elemental size distribution were developed for each coal/combustion condition/sampling location combination. These were developed by considering the data of all relevant sample sets that were selected for analysis. How these data was treated varied somewhat depending on 1) the number of sample sets available, 2) the variability of the data between sample sets, 3) the uncertainty of the data within a given sample set, and 4) the analytical method (s) used to generate the data.

Phase I Elemental Data

In Phase I, one set of samples for each coal/combustion condition/sampling location was selected for analysis by INAA. No data was analyzed in-house by AAS/AES/GFAA. Therefore, the results from these single sample selections are reported as the typical values shown in Section 3.3.3. The uncertainty reported in Section 3.3.3 was calculated by applying the gravimetric uncertainty factor from Table J-1 to the ash mass of the associated sample plus applying the appropriate elemental analytical uncertainty factor from Table J-3 to the concentration value.

Phase IIa Elemental Data for Ohio, Wyodak, and North Dakota Fly Ash at Ports 4 and 14

One set each of Port 4 and Port 14 sample sets from the Phase IIa baseline screening experiments for the Ohio (stages 1-11), Wyodak (stages 3-5, 8-10), and North Dakota lignite (stages 3-5, 8-10) coals were analyzed by INAA at MIT. Two sets each of Port 4 and Port 14 sample sets from the Phase IIa baseline screening experiments for the Ohio, Wyodak, and North Dakota lignite coals were analyzed in-house by AAS/AES/GFAA.

For elements only analyzed by INAA, the results from these single sample selections are reported as the typical values shown in Section 3.3.3. The uncertainty reported in Section 3.3.3 was calculated by applying the gravimetric uncertainty factor from Table J-1 to the ash mass of the associated sample plus applying the appropriate elemental analytical uncertainty factor from Table J-3 to the concentration value.

For elements only analyzed by AAS or GFAA, the uncertainty of both sets of results was calculated by applying the gravimetric uncertainty factor from Table J-1 to the ash mass of the associated sample, adding the appropriate measurement uncertainty factor (see Section J.4.2), and applying the appropriate elemental analytical uncertainty factor from Table J-5 to the concentration value.

The results from the two sets were usually averaged to produce the typical concentrations reported in Section 3.3.3. The uncertainty values were averaged likewise. Occasionally, a value was rejected as out-of-range where it was definitively wrong (e.g., the concentration of the individual element was much greater than 100 wt% of the total ash).

For elements analyzed by both AAS and INAA, AES and INAA, or GFAA and INAA, the uncertainty of each set of results was calculated using the appropriate method, described above. If all three concentration values were within the range of the uncertainty of the individual samples, an average of all three values and all three uncertainties is reported as the typical value and typical uncertainty in Section 3.3.3.

If one of the three concentration values was outside of the range of the uncertainty of the other two samples and the other two samples were within the range of each other, the outlier was discarded and the average of the other two values and the other two uncertainties is reported as the typical value and typical uncertainty in Section 3.3.3.

If no two concentration values lie within the uncertainty of each other, all average of all three values is reported as the typical value. The variability of the three values is then reported as the uncertainty (this being larger than the uncertainty of the individual samples).

Phase IIa Elemental Data for Kentucky Fly Ash at Ports 4 and 14 and all Baghouse Inlet Port Samples

Three sample sets were analyzed in-house by AAS/AES/GFAA for the Kentucky fly ash sampled at all three port locations, for the North Dakota fly ash sampled at the baghouse inlet, and for the Wyodak fly ash sampled at the baghouse inlet. A single sample set was analyzed in-house for the Ohio baghouse inlet sample location and two sample sets were analyzed in-house for the Pittsburgh and Illinois baghouse inlet sample location.

The uncertainty of each set of results was calculated by applying the gravimetric uncertainty factor from Table J-1 to the ash mass of the associated sample, adding the appropriate measurement uncertainty factor (see Section J.4.2), and applying the appropriate elemental analytical uncertainty factor from Table J-5 to the concentration value.

In the cases where three sample sets were analyzed, if all three concentration values were within the range of the uncertainty of the individual samples, an average of all three values and all three uncertainties is reported as the typical value and typical uncertainty in Section 3.3.3. If one of the three concentration values was outside of the range of the uncertainty of the other two samples and the other two samples were within the range of each other, the outlier was discarded and the average of the other two values and the other two uncertainties is reported as the typical

value and typical uncertainty in Section 3.3.3. If no two concentration values lie within the uncertainty of each other, all average of all three values is reported as the typical value. The variability of the three values is then reported as the uncertainty (this being larger than the uncertainty of the individual samples).

For the cases with two sample sets, the average of the two sample sets and their uncertainties are reported as typical values in Section 3.3.3. The only exception occurs when one of the sample results is below the detection limit, but the other is above. In this case, the value above the detection limit is reported as the typical value.

For the Ohio baghouse inlet sample, the results and uncertainty from the single sample set are reported as typical values in Section 3.3.3.

Phase IIb Elemental Data

For the special tests in Phase IIb, single sample sets were analyzed in-house by AAS/GFAA. The uncertainty of each set of results was calculated by applying the gravimetric uncertainty factor from Table J-1 to the ash mass of the associated sample, adding the appropriate measurement uncertainty factor (see Section J.4.2), and applying the appropriate elemental analytical uncertainty factor from Table J-5 to the concentration value. These elemental concentrations and uncertainties are reported as typical values in Section 3.3.3.

Leaching Study Results

Selected impactor stage membranes from single sample sets were subjected to the leaching protocol. Three concentration values are generated from each sample – fluid 1, fluid 2, and total dissolution.

The fluid 1 and fluid 2 elemental concentration uncertainty was calculated by applying the measurement uncertainty factor (see Section J.4.2) plus the relevant analytical uncertainty factor from Table J-5. The total dissolution uncertainty was calculated by applying the measurement uncertainty factor (see Section J.4.2) plus the relevant analytical uncertainty factor from Table J-4.

The fraction soluble at pH 4.9 was calculated by taking the ratio of the fluid 1 elemental concentration value over the total dissolution elemental concentration value. The uncertainty is calculated by adding the uncertainties from both numerator and denominator values.

The fraction soluble at pH 2.9 was calculated by summing the elemental concentration values at pH 4.9 and 2.9 then dividing this sum by the total dissolution elemental concentration value. The uncertainty is calculated by taking adding the average uncertainty of the two numerator values to the uncertainty of the denominator value.

APPENDIX K

Experimental and Sampling Conditions for Large Scale Combustion Studies

Table K-1. A Summary of the Pittsburgh Seam Coal Baseline Experiments

Test Run #	Date	Coal Feed Rate (kg/hr)	Sample Set #	Sampling Times	Sample Port Used
97P8-1	1/29/97	1.4	97P8-1c	60 min	12
			97P8-1	2 min	12
			97P8-2c	60 min	12
			97P8-2c	2 min	12
97P8-2	1/30/97	1.4	97P8-3c	60 min	4b
			97P8-3	2 min	4b
			97P8-4c	60 min	4b
			97P8-4	2 min	4b
97P8-3	2/4/97	1.4	97P8-5c	60 min	4b
			97P8-5	2 min	4b
			97P8-6c	60 min	4b
			97P8-6	2 min	4b
			97P8-7c	60 min	4b
			97P8-7	2 min	4b
97P8-4[1]	2/7/97	2.2	97P8-8c	120 min	4b
97P8-5	2/18/97	2.2	97P8-9c	120 min	4b
			97P8-9	6 min	4b
			97P8-10c	120 min	12
			97P8-10	6 min	12
97P8-6	2/20/97	2.2	97P8-11c	120 min	4b
			97P8-11	6 min	4b
			97P8-12c	120 min	12
			97P8-12	6 min	12
99P8-1	08/01/99	2.2	99P8-1[2]	20 min	BG[3]
			99P8-2	5 min 2 sec	BG
			99P8-3	5 min	BG

[1] The coal feeder screw broke in the middle of the first sample and the run was aborted
[2] This sample set rejected due to impactor overload
[3] BG – baghouse inlet sample port

Table K-2. Summary of Pittsburgh Seam Coal Baseline Screening Experimental Sampling Conditions

Sample Set # (Port Sampled)	Total Combustion Gas Rate (slpm)	Sampling Rate (slpm)	Sampling Temp. (^{O}K at port where sample was taken)	Port 4b O_2 Conc (%)	Port 4b Co_2 Conc (%)	Port 12 O_2 Conc (%)	Port 12 Co_2 Conc (%)
97P8-9/9c (4b)	535	1.72	1440	3.3	18.6	--	--
97P8-10/10c (12)	535	1.84	1139	3.5	18.2	5.1	17.1
97P8-11/11c (4b)	535	1.72	1432	3.2	17.7	--	--
97P8-12/12c (12)	535	1.72		3.0	17.3	3.0	16.2
99P8-1 (BG[1])	460	1.56	472	3.2[2]		5.1[3]	
99P8-2 (BG)	460	1.56	472	3.2		5.1	
99P8-3 (BG)	460	1.56	472	3.2		5.1	

[1] BG – baghouse inlet port
[2] Port 4 location after furnace rebuild
[3] Port 14 location after furnace rebuild

Table K-3. A Summary of the Illinois #6 Baseline Experiments

Test Run #	Date	Coal Feed Rate (kg/hr)	Sample Set #	Sampling Times	Sample Port Used
97IL-1	2/25/97	2.2	97IL-1c	120 min	4b
			97IL-1	6 min	4b
			97IL-2c	120 min	12
			97IL-2	6 min	12
97IL-2	2/27/97	2.2	97IL-3c	120 min	4b
			97IL-3	6 min	4b
			97IL-4c	120 min	12
97IL-3	3/3/97	2.2	97IL-5c	120 min	4b
			97IL-5	6 min	4b
97IL-4	3/5/97	2.2	97IL-6c	120 min	12
			97IL-6	6 min	12
			97IL-7	6 min	12
			97IL-4	6 min	12
99IL-1	03/14/99	2.2	99IL-1	10 min 41 sec	BG[1]
			99IL-2	15 min	BG

[1] BG – Baghouse inlet sample port

Table K-4. A Summary of Illinois #6 Baseline Screening Experimental Sampling Conditions

Sample Set # (Port Sampled)	Total Combustion Gas Rate (slpm)	Sampling Rate (slpm)	Sampling Temp. (^{O}K at port where sample was taken)	Port 4b O_2 Conc (%)	Port 4b Co_2 Conc (%)	Port 12 O_2 Conc (%)	Port 12 Co_2 Conc (%)	Port Bg* O_2 Conc (%)	Port Bg Co_2 Conc (%)
97IL-1/1c (4b)	527	1.70		3.7	15.0	--	--	--	--
97IL-2/2c (12)	527	1.70		3.6	15.0	3.8	15.0	--	--
97IL-3/3c (4b)	518	1.67	1443	3.4	15.2	--	--	--	--
97IL-4/4c (12)	518	1.83	1144	3.4	15.2	5.6	13.7	--	--
97IL-5/5c (4b)	547	1.70	1379	4.1	14.2	--	--	--	--
97IL-6/6c	540	2.1	1115	3.9	16.1	7.0	12.2	--	--
97IL-7	540	1.96	1115	3.6	15.6	6.8	11.9	--	--
99IL-1 (BG)	418*	1.22	217	3.7	16.0	5.4	14.4	8.1	11.8
99IL-2 (BG)	418	1.22	217	3.7	16.0	5.4	14.4	8.1	11.8

* Sampling rate for BG samples are 65% of isokinetic

Table K-5. A Summary of Ohio Screening Experiments

Test Run #	Date	Coal Feed Rate (kg/hr)	Sample Set #	Sampling Times	Sample Port Used
98O-1	11/19/98	2.8	none[1]		
98O-2	11/21/98	2.9	98O-1c[2]	120 min	4
			98O-1*	4 min	4
			98O-2c[2]	120 min	14
			98O-2[2]	4 min	14
98O-3	11/23/98	2.6	98O-3c[3]	120 min	4
			98O-3[3]	4 min	4
			98O-4c	30 min	4
			98O-4	1 min	4
			98O-5c	30 min	14
			98O-5	45 secs	14
98O-4	11/24/98	2.6	98O-6c	45 mins	4
			98O-6	15 secs.	4
			98O-7c	25 mins	14
			98O-7	10.2 secs	14
98O-5	11/28/98	2.6	98O-8c	22 mins	4
			98O-8	10.3 secs	4
			98O-9c	10 mins	4
			98O-9	10.2 secs	4
			98O-10c	22 mins	14
			98O-10	10.3 secs	14
98O-6	11/30/98	2.8	98O-11c	8 mins	4
			98O-11	40 secs	4
			98O-12c	60 min	14
			98O-12	45 secs	14
98O-7	12/3/98	2.5	none[1]		
98O-8	12/21/98	2.4	98O-13c[2]	10 mins	Baghouse
			98O-13[2]	1 min	Baghouse
			98O-14c[2]	20 mins	Baghouse
			98O-14[2]	6 mins	Baghouse
98O-9	12/22/98	2.5	98O-15c	25 mins	Baghouse
			98O-15	6 mins	Baghouse
			98O-16	30 mins	Baghouse

1 Complete temperature and gas profiles were obtained using this run
[2] Sampling system problems encountered; results not valid
[3] Overloaded impactor; results not valid

Table K-6. Summary of Ohio Baseline Screening Experimental Sampling Conditions

Sample Set # (port sampled)	Total Combustion Gas Rate (slpm)	Sampling Rate (slpm)	Sampling Temp. (^{O}K at port where sample was taken)	Port 4 O_2 Conc (%)	Port 4 Co_2 Conc (%)	Port 14 O_2 Conc (%)	Port 14 Co_2 Conc (%)	Port Bg[1] O_2 Conc (%)	Port Bg Co_2 Conc (%)
98O-6/6c (4)	425	1.62	1346	4.0	15.33				
98O-7/7c (14)	425	2.05	1060	3.9	15.4	6.3	13.7		
98O-9/9c (4b)	425	2.05	1308	4.3[2]	14.6[2]				
98O-10/10c (14)	425	2.15	1032	4.3[2]	14.6[2]	8.5	11.1		
98O-11/11C (4)	459	2.38	1331	3.5[2]	15.9[2]				
98O-12/12c (14)	459	2.55	1041	3.7[2]	15.6[2]	9.0	11.0		
98O-16 (BG[1])	401	1.20	612	4.3	15.2	6.4	13.5	8.7	11.1

[1] BG = baghouse inlet sampling port
[2] Gas Readings Measured at Port 3

Table K-7. A Summary of the Wyodak Baseline Experiments

Test Run #	Date	Coal Feed Rate (kg/hr)	Sample Set #	Sampling Times	Sample Port Used
99W-1	03/15/99	2.2	none[1]	none	
99W-2	03/19/99	2.2	99W-1c	20 min	4
			99W-1	1 min 20 sec	4
			99W-2c	38 min	14
			99W-2	2 min	14
99W-3	03/20/99	2.2	99W-3	40 min	4
			99W-4	40 min	14
			99W-5	60 min	BG[2]
99W-4	03/22/99	2.2	99W-6	40 min	4
			99W-7	40 min	14
			99W-8	60 min	BG
99W-5	03/26/99	2.2	99W-9	40 min	4
			99W-10	40 min	4
			99W-11	40 min	14
			99W-12	60 min	BG
99W-6	03/27/99	2.2	none[1]	none	

[1] Complete temperature and gas profiles were obtained using this run
[2] BG – Baghouse inlet sample port

Table K-8. A Summary of the Wyodak Baseline Screening Experimental Sampling Conditions

Sample Set # (port sampled)	Total Combustion Gas Rate (slpm)	Sampling Rate (slpm)	Sampling Temp. (^{O}K at port where sample was taken)	Port 4 O_2 Conc (%)	Port 4 Co_2 Conc (%)	Port 14 O_2 Conc (%)	Port 14 Co_2 Conc (%)	Port Bg* O_2 Conc (%)	Port Bg Co_2 Conc (%)
99W-3 (4)	222	0.73	1058	3.7	16.3				
99W-4 (14)	277	0.93	738	3.7	16.3	7.5	12.8		
99W-5 (BG)	277#	0.93+	202	3.7	16.3	7.5	12.8	9.7	10.5
99W-6 (4)	222	0.73	1083	4.0	16.4				
99W-7 (14)	273	0.89	779	4.0	16.4	6.7	13.6		
99W-8 (BG)	273	0.89	217	4.0	16.4	6.7	13.6	9.4	11.5
99W-9 (4)	224	0.72	1092	3.3	16.0				
99W-10 (4)	224	0.72	1092	3.3	16.0				
99W-11 (14)	274	0.88	756	3.3	16.0	6.9	13.4		
99W-12 (BG)	274	0.88	200	3.3	16.0	6.9	13.4	8.0	11.9

Combustion rate for BG samples are assumed to equal rate at Port 14
+ BG sampling rate is set equal to Port 14 rate; this is not an isokinetic sample

Table K-9. A Summary of the North Dakota Lignite Baseline Experiments

Test Run #	Date	Coal Feed Rate (kg/hr)	Sample Set #	Sampling Times	Sample Port Used
99ND-1	07/16/99	2.2	none[1]	none	
99ND-2	07/17/99	2.2	none	none	
99ND-3	07/24/99	2.2	99ND-1	4 min	4
			99ND-2	3 min	4
			99ND-3	4 min 30 sec	14
			99ND-4	3 min 30 sec	14
			99ND-5	5 min 30 sec	BG[2]
			99ND-6	4 min 30 sec	BG
99ND-4	7/25/99	2.2	99ND-7	3 min 30 sec	4
			99ND-8	3 min 30 sec	4
			99ND-9	4 min	14
			99ND-10	4 min	14
			99ND-11	6 min 21 sec	BG
			99ND-12	6 min	BG
99ND-5	7/26/99	2.2	none[3]	none	
99ND-6	7/31/99	2.2	99ND-13	3 min 30 sec	4
			99ND-14	4 min	14
			99ND-15	6 min	BG

[1] Complete temperature and gas profiles were obtained using this run
[2] BG – Baghouse inlet sample port
[3] Complete temperature and gas profiles obtained; blank sample running natural gas obtained

Table K-10. Summary of North Dakota Lignite Baseline Screening Experimental Sampling Conditions

Sample Set # (port sampled)	Total Combustion Gas Rate (slpm)	Sampling Rate (slpm)	Sampling Temp. (^{O}K at port where sample was taken)	Port 4 O_2 Conc (%)	Port 4 Co_2 Conc (%)	Port 14 O_2 Conc (%)	Port 14 Co_2 Conc (%)	Port Bg[*] O_2 Conc (%)	Port Bg Co_2 Conc (%)
99ND-1 (4)	174	0.59	1268	3.3	15.0				
99ND-2 (4)	174	0.59	1268	3.3	15.0				
99ND-3 (14)	202	0.69	916	3.3	15.0	5.7	13.7		
99ND-4(14)	202	0.69	916	3.3	15.0	5.7	13.7		
99ND-5 (BG)	202[#]	0.69[+]	405	3.3	15.0	5.7	13.7	10.8	8.7
99ND-6 (BG)	202	0.69	405	3.3	15.0	5.7	13.7	10.8	8.7
99ND-7 (4)	172	0.59	1274	3.2	15.4				
99ND-8 (4)	172	0.59	1274	3.2	15.4				
99ND-9 (14)	218	0.74	884	3.2	15.4	6.9	12.3		
99ND-10 (14)	218	0.74	884	3.2	15.4	6.9	12.3		
99ND-11 (BG)	218	0.74	398	3.2	15.4	6.9	12.3	12.5	6.1
99ND-12 (BG)	218	0.74	398	3.2	15.4	6.9	12.3	12.5	6.1
99ND-13 (4)	174	0.59	1146	3.4	--[1]				
99ND-14 (14)	220	0.75	735	3.4	--	7.0	--		
99ND-15 (BG)	220	0.75	409	3.4	--	7.0	--	11.0	--

[#] Combustion rate for BG samples are assumed to equal rate at Port 14
[+] BG sampling rate is set equal to Port 14 rate; this is not an isokinetic sample
[1] CO_2 analyzer out of service during these sample sets

Table K-11. A Summary of the Kentucky Elkhorn/Hazard Coal Baseline Experiments

Test Run #	Date	Coal Feed Rate (kg/hr)	Sample Set #	Sampling Times	Sample Port Used
99KY-1	08/11/99	2.2	none[1]	none	
99KY-2	08/12/99	2.2	99KY-1	2 min	4
			99KY-1c	12 min 9 sec	4
			99KY-2	2 min	14
			99KY-2c	15 min 2 sec	14
			99KY-3	20 min	BG[2]
			99KY-6	20 min 1 sec	BG
99KY-3	8/13/99	2.2	99KY-4	2 min 31 sec	4
			99KY-4c	16 min 1 sec	4
			99KY-5	2 min 39 sec	4
			99KY-5c	16 min	4
			99KY-7	2 min 31 sec	14
			99KY-7c	16 min	14
			99KY-8	3 min 30 sec	14
			99KY-8c	25 min	14
99KY-4	8/18/99	2.2	99KY-10	3 min 30 sec	4
			99KY-10c	25 min	4
			99KY-11	3 min 30 sec	4
			99KY-11c	25 min	4
			99KY-13	3 min 30 sec	14
			99KY-13c	25 min 1 sec	14
			99KY-14	3 min 32 sec	14
			99KY-14c	25 min 1 sec	14
99KY-5	8/19/99	2.2	99KY-9	25 min	BG
			99KY-12	16 min	BG
			99KY-15	16 min	BG

[1] Complete temperature and gas profiles were obtained using this run
[2] BG – Baghouse inlet sample port

Table K-12. A Summary of Kentucky Elkhorn/Hazard Coal Baseline Screening Experimental Sampling Conditions

Sample Set # (port sampled)	Total Combustion Gas Rate (slpm)	Sampling Rate (slpm)	Sampling Temp. (^{O}K at port where sample was taken)	Port 4 O_2 Conc (%)	Port 4 Co_2 Conc (%)	Port 14 O_2 Conc (%)	Port 14 Co_2 Conc (%)	Port Bg* O_2 Conc (%)	Port Bg Co_2 Conc (%)
99KY-1/1c (4)	401	1.36	1500	3.4	15.2				
99KY-2/2c (14)	410	1.39	1176	3.3	15.2	3.7	15.1		
99KY-3/6 (BG)	410#	1.39+	470	3.3	15.2	3.7	15.1	5.5	13.4
99KY-4/4c (4)	401	1.36	1530	3.4	15.6				
99KY-5/5c (4)	401	1.36	1522	3.2	15.6				
99KY-7/7c (14)	417	1.42	1182	3.3	15.6	4.1	15.0		
99KY-8/8c (14)	417	1.42	1189	3.3	15.6	4.0	15.1		
99KY-10/10c (4)	401	1.36	1458	3.4	15.4				
99KY-11/11c (4)	401	1.36	1444	3.4	15.4				
99KY-13/13c (14)	424	1.44	1102	3.4	15.4	4.3	14.5		
99KY-14/14c (14)	424	1.44	1102	3.4	15.4	4.3	14.5		
99KY-9/12/ 15 (BG)	424	1.44	495	3.4	15.4	4.4	14.4	5.3	13.7

Combustion rate for BG samples are assumed to equal rate at Port 14

+ BG sampling rate is set equal to Port 14 rate; this is not an isokinetic sample

Table K-13. Summary of Wyodak As/Se/Sb Doping Experiments

Test Run #	Date	Coal Feed Rate (kg/hr)	O2 Enrichment (%)	Dopant Used	Sample Set #	Sampling Times	Sample Port Used
99W-7	12/15/99	2.2	0	none	none[1]	none	
99W-8	12/19/99	2.2		As	WS-1	20 min	4
					WS-2	20 min	4
					WS-3	25 min	14
					WS-4	25 min	14
99W-9	12/20/99	2.2	0	Se	WS-5	21 min	4
					WS-6	20 min	4
					WS-7	25 min	14
					WS-8	25 min	14
99W-10	12/21/99	2.2	0	Sb	WS-9	20 min	4
					WS-10	20 min	4
					WS-11	25 min	14
					WS-12	25 min	14
00W-1	1/5/00	2.2	testing[2]	none	none		
00W-2	1/6/00	2.2	testing[3]	none	none[1]		
00W-3	1/7/00	2.2	22	none	WS-13	25 min	4
					WS-14	25 min	4
					WS-15	30 min	14
					WS-16	30 min	14
00W-4	1/8/00	2.2	22	As	WS-17	25 min	4
					WS-18	25 min	4
					WS-19	30 min	14
					WS-20	30 min	14
00W-5	1/10/00	2.2	22	Se	WS-21	25 min	4
					WS-22	25 min	4
					WS-23	30 min	14
					WS-24	30 min	14
00W-6	1/11/00	2.2	0	Sb	WS-25	20 min	4
			22	Sb	WS-26	25 min	4
			22	Sb	WS-27	25 min	4
			22	Sb	WS-28	30 min	14
			22	Sb	WS-29	30 min	14
			0	Sb	WS-30	25 min	14

[1] Complete temperature and gas profiles were obtained using this run
[2] Test aborted due to problems with temperature probe
[3] 22% enrichment determined to be optimum

Table K-14. Summary of Wyodak As/Se/Sb Doping Experimental Sampling Conditions

Sample Set # (port sampled)	Total Combustion Gas Rate (slpm)	Sampling Rate (slpm)	Sampling Temp. (^{O}K at port where sample was taken)	Port 4 O_2 Conc (%)	Port 4 Co_2 Conc (%)	Port 14 O_2 Conc (%)	Port 14 Co_2 Conc (%)	Dopant/ Concen-tration (g/liter)	Max Combustion Temp (K)
WS-1 (4)	210	2.09	1255	3.8	15.3			As/616	1480
WS-2 (4)	210	2.09	1255	3.8	15.3			As/616	1480
WS-3 (14)	210	2.11	983	3.8	15.3	5.4	14.0	As/616	1480
WS-4 (14)	210	2.11	983	3.8	15.3	5.4	14.0	As/616	1480
WS-5 (4)	210	1.90	1267	4.1	14.6			Se/42	1483
WS-6 (4)	210	1.90	1267	4.1	14.6			Se/42	1483
WS-7 (14)	210	1.90	983	4.1	14.6	5.3	14.0	Se/42	1483
WS-8 (14)	210	1.90	983	4.1	14.6	5.3	14.0	Se/42	1483
WS-9 (4)	210	1.60	1288	3.8	15.0			Sb/74	1525
WS-10 (4)	210	1.60	1288	3.8	15.0			Sb/74	1525
WS-11 (14)	210	1.60	969	3.8	15.0	6.4	12.7	Sb/74	1525
WS-12 (14)	210	1.60	969	3.8	15.0	6.4	12.7	Sb/74	1525
WS-13 (4)	145	0.85	1303	3.8	19.7			none	1582
WS-14 (4)	145	0.85	1303	3.8	19.7			none	1582
WS-15 (14)	145	0.85	923	3.8	19.7	5.8	17.7	none	1582
WS-16 (14)	145	0.85	923	3.8	19.7	5.8	17.7	none	1582
WS-17 (4)	145	0.70	1283	3.6	>20			As/616	1573
WS-18 (4)	145	0.70	1283	3.6	>20			As/616	1573
WS-19 (14)	145	0.70	932	3.6	>20	4.8	>20	As/616	1573
WS-20 (14)	145	0.70	932	3.6	>20	4.8	>20	As/616	1573
WS-21 (4)	145	0.64	1273	3.8	19.4			Se/42	1580
WS-22 (4)	145	0.64	1273	3.8	19.4			Se/42	1580
WS-23 (14)	145	0.64	891	3.8	19.4	5.6	18.0	Se/42	1580
WS-24 (14)	145	0.64	891	3.8	19.4	5.6	18.0	Se/42	1580
WS-25 (4)	210	1.55	1283	3.8	14.8			Sb/74	1478
WS-26 (4)	145	0.96	1251	3.6	>20			Sb/74	1553
WS-27 (4)	145	0.96	1251	3.6	>20			Sb/74	1553
WS-28 (14)	145	0.96	902	3.6	>20	5.8	18.3	Sb/74	1553
WS-29 (14)	145	0.96	902	3.6	>20	5.8	18.3	Sb/74	1553
WS-30 (14)	210	1.55	917	3.8	14.8	6.1	12.8	Sb/74	1510

Table K-15. Summary of Ohio Calcium Doping Experiments

Test Run #	Date	Coal Feed Rate (kg/hr)	CO_2 Added to Air?	Calcium Dopant Used?	Sample Set #	Sampling Times	Sample Port Used
00O-1	2/23/00	2.2	No	Yes	OS-1	2 min	4
					OS-2	2 min	4
					OS-3	2 min 10 sec	14
					OS-4	2 min 10 sec	14
00O-2	2/24/00	2.2	Yes	No	OS-5	2 min 15 sec	4
				Yes	OS-6	2 min	4
				Yes	OS-7	2 min	4
				No	OS-8	2 min	14
				Yes	OS-9	2 min	14
				Yes	OS-10	2 min	14

Table K-16. Summary of Ohio Ca Doping Experimental Sampling Conditions

Sample Set # (port sampled)	Total Combustion Gas Rate (slpm)	Sampling Rate (slpm)	Sampling Temp. (^{O}K at port where sample was taken)	Port 4 O_2 Conc (%)	Port 4 Co_2 Conc (%)	Port 14 O_2 Conc (%)	Port 14 Co_2 Conc (%)	Calcium Feed Rate (kg/hr)	Max Combustion Temp (K)
OS-1 (4)	356	1.86	1400	3.4	15.6			0.4	1636
OS-2 (4)	356	1.86	1400	3.4	15.6			0.4	1636
OS-3 (14)	356	1.86	1087	3.4	15.6	4.5	14.6	0.4	1636
OS-4 (14)	356	1.86	1087	3.4	15.6	4.5	14.6	0.4	1636
OS-5 (4)	548	2.82	1450	3.2	>20			0.0	1494
OS-6 (4)	548	2.82	1449	3.2	>20			0.4	1491
OS-7 (4)	548	2.82	1449	3.2	>20			0.4	1491
OS-8 (14)	548	2.82	1449	3.2	>20	2.8	>20	0.0	1491
OS-9 (14)	548	2.82	1449	3.2	>20	2.8	>20	0.4	1491
OS-10 (14)	548	2.82	1449	3.2	>20	2.8	>20	0.4	1491

Table K-17. Summary of Wyodak Iron Doping Experiments

Test Run #	Date	Coal Feed Rate (kg/hr)	O2 Enrichment (%)	Dopant Used	Sample Set #	Sampling Times	Sample Port Used
00W-7	2/27/00	2.2	0	Fe	WS-31	5 min	4
					WS-32	5 min	4
					WS-33	4 min 30 sec	14
					WS-34	4 min 30 sec	14
00W-8	2/28/00	2.2	22	Fe	WS-35	5 min	4
					WS-36	5 min	4
					WS-37	4 min 30 sec	14
					WS-38	4 min 30 sec	14

Table K-18. Summary of Wyodak Iron Doping Experimental Sampling Conditions

Sample Set # (port sampled)	Total Combustion Gas Rate (slpm)	Sampling Rate (slpm)	Sampling Temp. (^{O}K at port where sample was taken)	Port 4 O_2 Conc (%)	Port 4 Co_2 Conc (%)	Port 14 O_2 Conc (%)	Port 14 Co_2 Conc (%)	Dopant/ Concen-Tration (g/Liter)	Max Combustion Temp (K)
WS-31 (4)	273	2.75	1295	3.5	15.1			Fe/860	1478
WS-32 (4)	273	2.75	1295	3.5	15.1			Fe/860	1478
WS-33 (14)	273	2.75	983	3.5	15.1	4.7	14.1	Fe/860	1478
WS-34 (14)	273	2.75	983	3.5	15.1	4.7	14.1	Fe/860	1478
WS-35 (4)	273	2.75	1318	3.4	19.7			Fe/860	1537
WS-36 (4)	273	2.75	1318	3.4	19.7			Fe/860	1537
WS-37 (14)	273	2.75	974	3.4	19.7	4.6	20	Fe/860	1537
WS-38 (14)	273	2.75	974	3.4	19.7	4.6	20	Fe/860	1537

Table K-19. Summary of Kentucky SO_2 Doping Experiments

Test Run #	Date	Coal Feed Rate (kg/hr)	SO_2 Added to Air (Ncm^3/min)	Sample Set #	Sampling Times	Sample Port Used
00K-1	2/20/00	2.2	490	KS-1	1 min 30 sec	4
				KS-2	1 min 30 sec	4
				KS-3	1 min 35 sec	14
				KS-4	1 min 35 sec	14

Table K-20. Summary of Kentucky SO_2 Doping Experimental Sampling Conditions

Sample Set # (port sampled)	Total Combustion Gas Rate (slpm)	Sampling Rate (slpm)	Sampling Temp. (^OK at port where sample was taken)	Port 4 O_2 Conc (%)	Port 4 Co_2 Conc (%)	Port 14 O_2 Conc (%)	Port 14 Co_2 Conc (%)
KS-1 (4)	378	3.18	1469	3.4	15.9		
KS-2 (4)	378	3.18	1469	3.4	15.9		
KS-3 (14)	378	3.18	1103	3.4	15.9	4.3	15.0
KS-4 (14)	378	3.18	1103	3.4	15.9	4.3	15.0

Table K-21. Summary of Pittsburgh Ca/Fe Doping Experiments

Test Run #	Date	Coal Feed Rate (kg/hr)	Dopant Used	Sample Set #	Sampling Times	Sample Port Used
00P8-1	2/18/00	2.2	Ca	PS-1	2 mn	4
				PS-2	2 min	4
				PS-3	2 min 15 sec	14
				PS-4	2 min 15 sec	14
00P8-2	2/19/00	2.2	Fe	PS-5	2 min	14
				PS-6	2 min	14
				PS-7	1 min 45 sec	4
				PS-8	1 min 45 sec	4

Table K-22. Summary of Pittsburgh Ca/Fe Doping Experimental Sampling Conditions

Sample Set # (port sampled)	Total Combustion Gas Rate (slpm)	Sampling Rate (slpm)	Sampling Temp. (^{O}K at port where sample was taken)	Port 4 O_2 Conc (%)	Port 4 Co_2 Conc (%)	Port 14 O_2 Conc (%)	Port 14 Co_2 Conc (%)	Dopant/Feed Rate (G/Min)
PS-1 (4)	392	3.36	1472	3.3	16.0			Ca/0.87
PS-2 (4)	392	3.36	1472	3.3	16.0			Ca/0.87
PS-3 (14)	392	3.36	1087	3.3	16.0	4.3	15.0	Ca/0.87
PS-4 (14)	392	3.36	1087	3.3	16.0	4.3	15.0	Ca/0.87
PS-5 (14)	392	3.36	1098	3.3	15.6	3.4	15.6	$Fe(NO_3)_3$/3.6
PS-6 (14)	392	3.36	1098	3.3	15.6	3.4	15.6	$Fe(NO_3)_3$/3.6
PS-7 (4)	392	3.36	1453	3.3	15.6			$Fe(NO_3)_3$/3.6
PS-8 (4)	392	3.36	1453	3.3	15.6			$Fe(NO_3)_3$/3.6

APPENDIX L

Measurements of Gaseous Mercury Oxidation in Bench-Scale Reactor

Table L-1. Blank Experimental Runs and Mercury "Spiked" Solutions

Sample ID#	Port/ Sampling	Reactant ppmv	CVAA, Hg ERI (μg/liter)	Sample Volume (liters)	Hg Measured (μg)	Hg Expected (μg)	% Hg Oxidized
EXP1 F1	1rst/OH	Blank	0.4	0.587	0	0	
EXP1 F2	1rst/OH	Blank	1.6	0.289	0	0	
EXP1 F3	1rst/OH	Blank	2.6	0.596	2	0	N/A
				Total:	2	0	
EXP10 F1	1st/OH	Blank	ND	0.503	ND	0	
EXP10 F2	1st/OH	Blank	1.1	0.257	0	0	
EXP10 F3	1st/OH	Blank	3.1	0.502	2	0	N/A
				Total:	2	0	
EXP2 F1	None/OH	Spike	178.8	0.500	89	100+/-5*	
EXP2 F2	None/OH	Spike	99.4	0.250	25	33+/-2*	
EXP2 F3	None/OH	Spike	120.6	0.500	60	65+/-3*	N/A
				Total:	175	198+/-6*	
EXP3 F1	None/OH	Spike	0.3	0.500	0.2	0.2+/-0.02*	
EXP3 F2	None/OH	Spike	1.5	0.250	0.4	0.1+/-0.01*	
EXP3 F3	None/OH	Spike	0.6	0.500	0.3	0.2+/-0.02*	N/A
				Total:	1	0.5+/-0.03	
EXP8 F1	None/OH	Spike	14.5	0.500	7	5+/-0.5*	
EXP8 F2	None/OH	Spike	12.3	0.250	3	5+/-0.5*	
EXP8 F3	None/OH	Spike	13.6	0.500	7	10+/-1*	N/A
				Total:	17	20+/-1*	
EXP9 F1	None/OH	Spike	14.9	0.500	7	5+-0.5*	
EXP9 F2	None/OH	Spike	14.2	0.250	4	5+-0.5*	
EXP9 F3	None/OH	Spike	14.1	0.500	7	10+-1*	N/A
				Total:	18	20+/-1*	

*Based on propagation of measurement error only.

Table L-2. Material Balance Experimental Runs

Sample ID#	Port/ Sampling	Reactant ppmv	CVAA, Hg ERI (μg/liter)	Sample Volume (liters)	Hg Measured (μg)	Hg Expected (μg)	% Hg Oxidized
EXP4 F1	1st/OH	none/0	4.3	0.523	2		
EXP4 F2	1st/OH	none/0	12.3	0.281	3		
EXP4 F3	1st/OH	none/0	80.3	0.500	40		5
				Total:	46	45	
EXP5 F1	2nd/OH	none/0	1.7	0.555	1		
EXP5 F2	2nd/OH	none/0	10.5	0.287	3		
EXP5 F3	2nd/OH	none/0	86.4	0.523	45		2
				Total:	49	45	
EXP6 F1	3rd/OH	none/0	2.1	0.582	1		
EXP6 F2	3rd/OH	none/0	12.1	0.290	4		
EXP6 F3	3rd/OH	none/0	70.5	0.535	38		3
				Total:	42	45	
EXP7 F1	4th/OH	none/0	0.3	0.500	0		
EXP7 F2	4th/OH	none/0	3.1	0.256	1		
EXP7 F3	4th/OH	none/0	48.6	0.500	24		1
				Total:	25	45	

Table L-3. Hg and HCl (HCl/Cl_2) Experimental Runs

Sample ID#	Port/ Sampling	Reactant ppmv	CVAA, Hg ERI (μg/liter)	Sample Volume (liters)	Hg Measured (μg)	Hg Expected (μg)	% Hg Oxidized
EXP11 F1	1/OH	HCl, 100	1.0	0.510	1		
EXP11 F2	1/OH	HCl, 100	8.5	0.252	2		
EXP11 F3	1/OH	HCl, 100	84.2	0.504	42		1
				Total:	45	45	
EXP12 F1	3/OH	HCl,100	1.1	0.512	1		
EXP12 F2	3/OH	HCl,100	8.0	0.255	2		
EXP12 F3	3/OH	HCl,100	83.5	0.500	42		1
				Total:	44	45	
EXP13 F1	2/OH	HCl,100	2.3	0.535	1		
EXP13 F2	2/OH	HCl,100	14.6	0.259	4		
EXP13 F3	2/OH	HCl,100	115.4	0.522	60		2
				Total:	65	45	
EXP24 F1	1/OH	Cl2,HCl;50,100	8.7	0.588	5		
EXP24 F2	1/OH	Cl2,HCl;50,100	9.4	0.270	3		
EXP24 F3	1/OH	Cl2,HCl;50,100	81.0	0.553	45		10
				Total:	52	45	

Table L-4. Hg and Cl_2 Experimental Runs

Sample ID#	Port/ Sampling	Reactant ppmv	CVAA, Hg ERI (µg/liter)	Sample Volume (liters)	Hg Measured (µg)	Hg Expected (µg)	% Hg Oxidized
EXP14 F1	1/OH	Cl2,50	13.4	0.546	7		
EXP14 F2	1/OH	Cl2,50	14.6	0.262	4		
EXP14 F3	1/OH	Cl2,50	122.5	0.502	61		10
				Total:	**73**	**45**	
EXP15 F1	3/OH	Cl2,50	8.5	0.525	4		
EXP15 F2	3/OH	Cl2,50	10.3	0.253	3		
EXP15 F3	3/OH	Cl2,50	117.2	0.500	59		7
				Total:	**66**	**45**	
EXP16 F1	2/OH	Cl2,50	9.9	0.546	5		
EXP16 F2	2/OH	Cl2,50	10.4	0.256	3		8
EXP16 F3	2/OH	Cl2,50	106.8	0.526	56		
				Total:	**64**	**45**	
EXP17 F1	2/OH	Cl2,500	116.0	0.515	60		
EXP17 F2	2/OH	Cl2,500	13.0	0.254	3		
EXP17 F3	2/OH	Cl2,500	2.8	0.501	1		93
				Total:	**64**	**45**	
EXP18 F1	3/OH	Cl2,500	114.4	0.524	60		
EXP18 F2	3/OH	Cl2,500	12.5	0.270	3		
EXP18 F3	3/OH	Cl2,500	3.9	0.503	2		92
				Total:	**65**	**45**	
EXP19 F1	1/OH	Cl2,500	110.9	0.536	59		
EXP19 F2	1/OH	Cl2,500	17.4	0.262	5		
EXP19 F3	1/OH	Cl2,500	3.2	0.510	0		92
				Total:	**64**	**45**	
EXP23 F1	1/OH	Cl2/50	14.0	0.550	8		
EXP23 F2	1/OH	Cl2/50	7.7	0.249	2		
EXP23 F3	1/OH	Cl2/50	103.5	0.518	54		12
				Total:	**63**	**45**	
EXP30 F1	3/OH	Cl2, 300	42.28	0.582	25		
EXP30 F2	3/OH	Cl2, 300	20.5	0.266	5		
EXP30 F3	3/OH	Cl2, 300	10.18	0.526	5		69
				Total:	**35**	**45**	
EXP31 F1	3/OH	Cl2, 100	25.13	0.591	15		
EXP31 F2	3/OH	Cl2, 100	28.22	0.244	7		
EXP31 F3	3/OH	Cl2, 100	36.88	0.529	20		36
				Total:	**41**	**45**	
EXP32 F1	1/OH	Cl2, 300	43.37	0.472	20		
EXP32 F2	1/OH	Cl2, 300	24.79	0.269	7		
EXP32 F3	1/OH	Cl2, 300	7.04	0.522	4		66
				Total:	**31**	**45**	
EXP33 F1	1/OH	Cl2, 100	43.78	0.58	25		
EXP33 F2	1/OH	Cl2, 100	33.28	0.271	9		
EXP33 F3	1/OH	Cl2, 100	39.87	0.544	22		45
				Total:	**56**	**45**	

Table L-5. Direct Measurements and Combined Experimental Runs

Sample ID#	Port/ Sampling	Reactant ppmv	CVAA, Hg ERI (μg/liter)	Sample Volume (liters)	Hg Measured (μg)	Hg Expected (μg)	% Hg Oxidized
EXP20 F1	1/CHR	Blank	0.7	0.558	0		
EXP25 F1	1/CHR	Blank	0.1	0.573	0		
EXP21 F1	1/CHR	none/0	1.6	0.569	1		
EXP26 F1	1/CHR	none/0	1.1	0.553	1		
EXP22 F1	1/CHR	Cl2/50	7.9	0.575	5		
EXP27 F1	1/CHR	Cl2/50	6.7	0.549	4		
EXP28 F1	Direct/OH	none/0	0.25	0.4062	0		
EXP28 F2	Direct/OH	none/0	0.54	0.273	0		
EXP28 F3	Direct/OH	none/0	105.95	0.537	57		0
				Total:	**57**	**90**	
EXP29 F1	Direct/OH	none/0	0.55	0.3755	0		
EXP29 F2	Direct/OH	none/0	0.63	0.242	0		
EXP29 F3	Direct/OH	none/0	89.11	0.523	47		0
				Total:	**47**	**70**	

APPENDIX M

Correlations Between Calculated Mercury Removal and Speciation with ICR Data

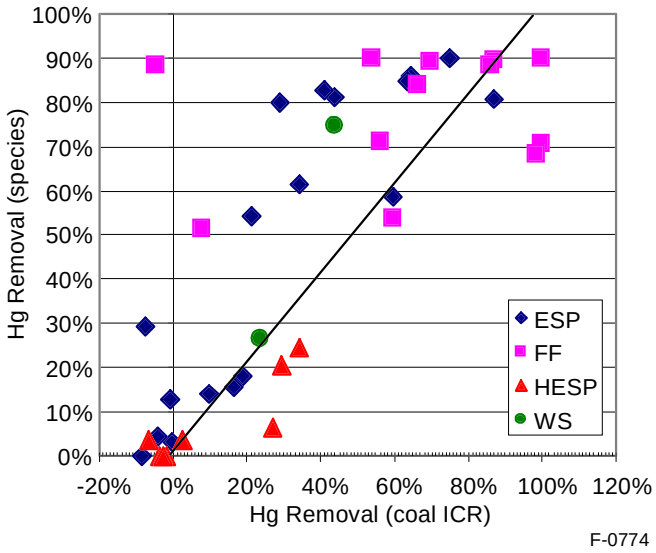

Figure M-1. Calculated total mercury removal for particulate control devices compared with ICR data.

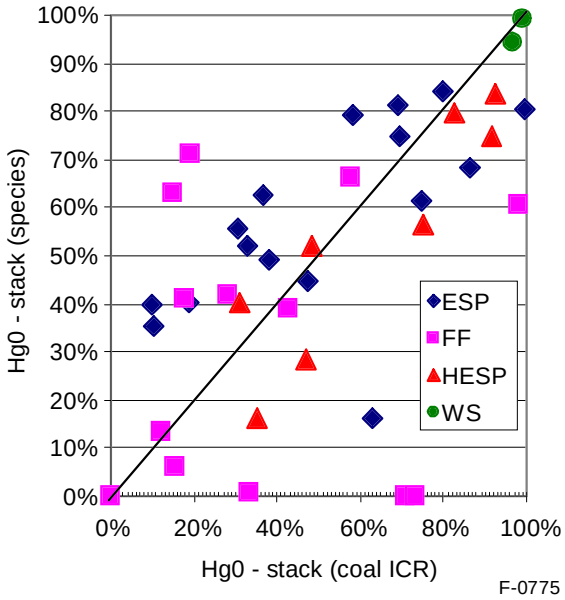

Figure M-2. Calculated mercury stack speciation for particulate control devices compared with ICR data.

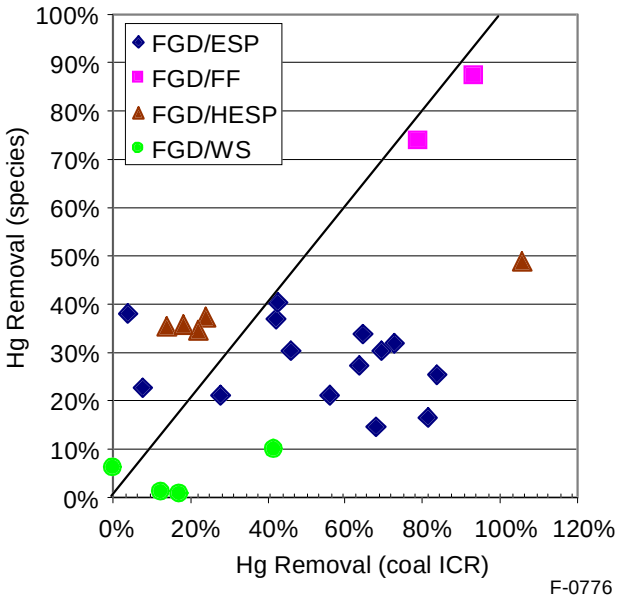

Figure M-3. Calculated total mercury removal for wet scrubbers compared with ICR data.

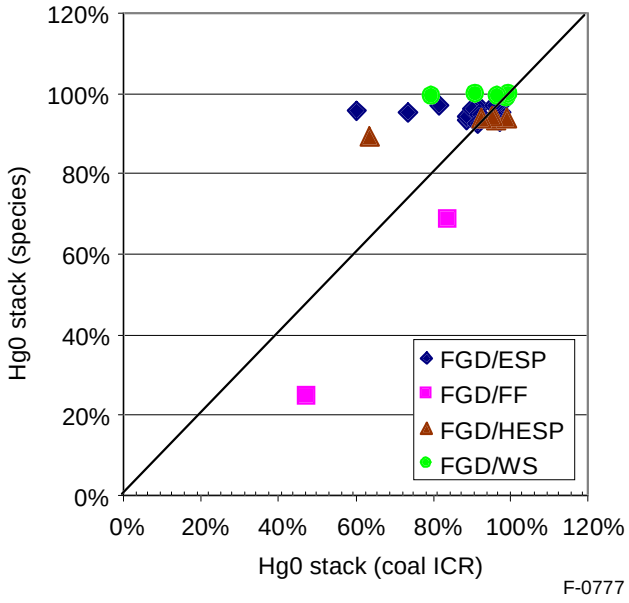

Figure M-4. Calculated mercury stack speciation for wet scrubbers compared with ICR data.

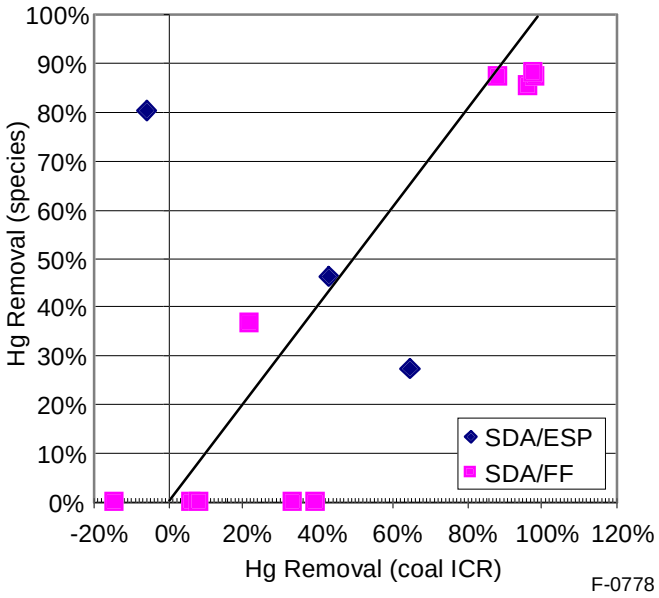

Figure M-5. Calculated total mercury removal for dry scrubbers compared to ICR data.

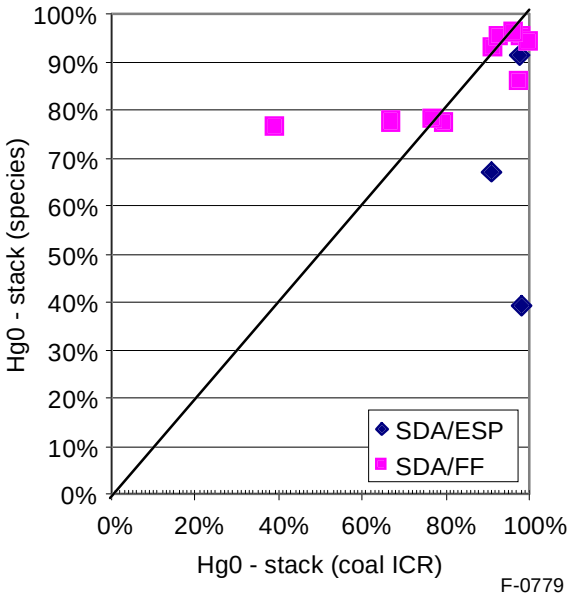

Figure M-6. Calculated mercury stack speciation for dry scrubbers compared with ICR data.

APPENDIX N

Distribution of Elements in Mineral Categories Bases for Major Coal Types

Table N-1. Elemental Distribution Matrix for Low Ranks Coals (Sub-bituminous and Lignite)

Na	Mg	Al	Si	P	S	Ca	Ti	Fe	Ba
7%	15%	2%	54%	20%	3%	0%	37%	4%	13%
20%	20%	60%	26%	9%	5%	1%	12%	7%	11%
4%	6%	10%	6%	2%	1%	4%	4%	3%	4%
8%	14%	11%	9%	5%	3%	7%	10%	5%	7%
2%	4%	0%	0%	1%	47%	0%	1%	65%	1%
3%	5%	0%	0%	1%	2%	51%	2%	0%	21%
56%	36%	17%	5%	62%	39%	37%	34%	16%	43%

Table N-2. Elemental Distribution Matrix for Low Sulfur Illinois Basin Coals

Na	Mg	Al	Si	P	S	Ca	Ti	Fe	Ba
6%	7%	1%	23%	5%	3%	3%	10%	3%	11%
7%	3%	25%	11%	7%	2%	2%	9%	3%	7%
18%	22%	43%	30%	24%	9%	7%	28%	13%	30%
20%	33%	23%	24%	25%	9%	16%	23%	19%	23%
1%	2%	0%	0%	1%	34%	1%	2%	28%	2%
2%	6%	0%	0%	4%	1%	41%	2%	1%	2%
46%	27%	8%	12%	34%	42%	30%	26%	33%	25%

Table N-3. Elemental Distribution Matrix for High Sulfur Illinois Basin Coals

Na	Mg	Al	Si	P	S	Ca	Ti	Fe	Ba
11%	7%	1%	33%	0%	0%	2%	12%	1%	8%
17%	7%	49%	24%	16%	1%	5%	15%	2%	18%
18%	23%	32%	25%	9%	2%	6%	20%	3%	27%
11%	14%	10%	11%	8%	3%	4%	9%	5%	11%
21%	25%	1%	1%	33%	79%	5%	17%	76%	14%
3%	4%	0%	0%	7%	5%	68%	5%	1%	6%
19%	20%	7%	6%	27%	10%	10%	22%	12%	16%

Table N-4. Elemental Distribution Matrix for Low Sulfur Appalachian Basin Coals

Na	Mg	Al	Si	P	S	Ca	Ti	Fe	Ba
1%	1%	0%	28%	2%	2%	0%	8%	3%	11%
15%	1%	51%	29%	7%	7%	1%	12%	4%	22%
1%	0%	20%	14%	1%	8%	4%	7%	6%	10%
16%	20%	18%	20%	8%	3%	7%	13%	18%	9%
4%	2%	1%	0%	4%	53%	0%	4%	29%	18%
5%	14%	0%	0%	10%	6%	51%	5%	2%	4%
58%	62%	10%	9%	68%	21%	37%	51%	38%	26%

Table N-5. Elemental Distribution Matrix for High Sulfur Appalachian Basin Coals

Na	Mg	Al	Si	P	S	Ca	Ti	Fe	Ba
5%	8%	0%	24%	0%	0%	1%	12%	1%	11%
26%	7%	65%	41%	11%	2%	8%	31%	4%	22%
9%	7%	18%	15%	5%	1%	4%	11%	2%	10%
19%	11%	12%	14%	8%	2%	11%	10%	3%	9%
22%	29%	1%	1%	26%	82%	7%	18%	81%	18%
3%	22%	0%	0%	5%	6%	61%	4%	0%	4%
16%	16%	4%	5%	45%	7%	8%	14%	9%	26%

APPENDIX O

Mineral Size Distributions for U.S. Coals Based on Rank

Table O-1. Average Lignite CCSEM Mineral Size Distribution

Diameter, microns	Quartz	Kaolinite	Other Clay	Misc. Silicate	Pyrite	Calcite	Other
<2.5	11.5	18	18.9	8.3	9	12.3	15.3
2.5-5	27.9	25.6	23.45	15.45	11.8	18.8	17.9
5-10	16.35	20.25	21.5	14.95	10	11.8	17.7
10-20	13.3	19.8	20.3	28.55	18.6	41.3	24.8
20-40	11.95	9.65	10.8	20.25	18.05	15.8	15.65
>40	19	6.2	4.5	11.95	32.6	0	8.65

Table O-2. Average Subbituminous CCSEM Mineral Size Distribution

Diameter, microns	Quartz	Kaolinite	Other Clay	Misc. Silicate	Pyrite	Calcite	Other
<2.5	14.0	12.1	14.9	23.1	12.2	47.5	28.9
2.5-5	22.2	19.3	27.3	30.7	12.1	31.5	42.6
5-10	18.9	17.4	18.9	13.4	13.5	5.4	13.6
10-20	19.9	22.3	17.4	13.0	21.8	4.1	6.3
20-40	15.4	12.5	11.3	12.6	19.0	8.8	4.8
>40	9.7	16.5	10.2	7.4	21.3	2.7	3.9

Table O-3. Average Appalachian CCSEM Mineral Size Distribution

Diameter, microns	Quartz	Kaolinite	Other Clays	Misc. Silicate	Pyrite	Calcite	Other
<2.5	16.0	15.7	22.2	23.3	10.1	5.7	31.9
2.5-5	30.8	30.3	35.7	37.7	13.5	14.7	33.0
5-10	27.2	29.8	24.3	25.0	27.4	22.6	18.0
10-20	15.3	13.8	9.7	9.0	21.4	22.0	7.5
20-40	7.7	6.8	5.8	4.6	19.7	23.6	5.3
>40	3.0	3.4	2.1	0.3	8.1	11.4	4.5

Table O-4. Average Illinois CCSEM Mineral Size Distribution

Diameter, microns	Quartz	Kaolinite	Other Clays	Misc. Silicate	Pyrite	Calcite	Other
<2.5	19.4	17.2	22.2	29.5	9.9	7.1	37.3
2.5-5	39.5	37.8	44.4	39.2	15.1	19.2	31.7
5-10	25.5	24.5	20.0	15.5	22.6	21.9	13.8
10-20	10.5	12.0	9.0	9.4	29.1	16.4	8.5
20-40	3.4	6.9	3.3	5.0	17.7	21.8	6.4
>40	1.4	1.6	1.0	0.9	5.4	13.5	2.1